Stacked Greenfield and Brownfield ROZ Fairways in the Illinois Basin Geo-Laboratory: Co-Optimization of EOR and Associated CO_2 Storage

Final Report

Federal Agency and Organization: DOE Office of Fossil Energy

Award Number: DE-FE0031700

Principal Investigator and Report Submitted by:
Nathan D. Webb, MS
Associate Research Scientist, Petroleum Geologist
ndwebb2@illinois.edu
217-244-2426

Date of Report Submission: 10/30/2023

Unique Entity Identifier (UEI) Number: Y8CWNJRCNN91

Recipient Name: University of Illinois at Urbana-Champaign

Recipient Address: 1901 South First Street, Suite A, Champaign, IL 61820

Project Period: 02/01/2019 to 07/31/2023

Reporting Period End Date: 07/31/2023

Report Frequency: Final

Signature of Submitting Official:



DISCLAIMER

This report was prepared as an account of work sponsored by an agency of the United States Government. Neither the United States Government nor any agency thereof, nor any of their employees, makes any warranty, express or implied, or assumes any legal liability or responsibility for the accuracy, completeness, or usefulness of any information, apparatus, product, or process disclosed, or represents that its use would not infringe privately owned rights. Reference herein to any specific commercial product, process, or service by trade name, trademark, manufacturer, or otherwise does not necessarily constitute or imply its endorsement, recommendation, or favoring by the United States Government or any agency thereof. The views and opinions of authors expressed herein do not necessarily state or reflect those of the United States Government or any agency thereof.

CONTRIBUTORS

The chapters of this final report generally follow the project Statement of Project Objectives (SOPO). Zohreh Askari was the leader for Task 2. Nathan Webb was the leader for Tasks 3 and 5. Nate Grigsby was the leader for Task 4. Fang Yang was the leader for Task 6. For each subsection within this report, an effort was made to credit authorship to the appropriate members of the project team.

Bi-Petro, Inc., provided access to and field support for the Huff and Puff test in the Holsapple 2B well at the Greenfield Laboratory Site. Specific thanks to Skip Homier, Collin Homier, and Brad Richards from Bi-Petro for their support and guidance throughout the project. Projeo Corporation (Nick Malkewicz) facilitated the well testing by rigging up equipment and sensors and coordinating the efforts of many oilfield vendors and service companies. MacCARB supplied the CO_2 for the well test and Robert McCarthy was incredibly helpful in coordinating the logistics of CO_2 deliveries and troubleshooting issues during CO_2 injection. Natural Gas Services (Kevin Lock) provided support and guidance on the production portion of the field testing.

Podolsky Oil Company provided field access and facilitated the drilling of the Carrie Winter 10 well at the Brownfield Laboratory Site. Specifically, Michael Podolsky and Stephanie Storckman were very supportive of the project and provided real-time input during the drilling and field data collection. Stephanie provided expert project management during the drilling of the well. Projeo Corporation (Nick Malkewicz) oversaw the open-hole geophysical logging of the well by Schlumberger Wireline Services.

Support from the following ISGS staff was indispensable for completing the project:

Dmytro Lukhtai provided critical field operation leadership and support during the Greenfield tests.

Damon Garner provided database support.

Steve Sargent developed a custom field instrumentation and datalogging system for the Greenfield tests.

Michelle Johnson provided project management support.

Jill Monroe provided editing and formatting of the final report.

Torie Strole provided financial management support.

EXECUTIVE SUMMARY 4

1. INTRODUCTION 7

1.1 OBJECTIVES 7
1.2 MOTIVATION 7

2. SCREENING AND SELECTION OF ILB ROZS FOR RESOURCE ASSESSMENT 12

2.1 SCREENING AND SELECTION OF ILLINOIS BASIN ROZS FOR RESOURCE ASSESSMENT 12
2.2 REVIEW OF ANALOGOUS BASINS 51

3. ILLINOIS BASIN ROZ CHARACTERIZATION 73

3.1 GEOLOGICAL CHARACTERIZATION OF ROZS AND SEALS 73
3.1.1 Tar Springs Sandstone 73
3.1.2 Cypress Sandstone 93
3.1.3 Carper Sandstone 107
3.1.4 Middle Devonian 154
3.2 MODEL OIL SOURCE AND MIGRATION INTO ROZ FAIRWAYS 167

4. GREENFIELD FIELD LABORATORY: STACKED ROZ STORAGE COMPLEX 173

4.1. HOLSAPPLE 2B HUFF AND PUFF TEST 173
4.1.1 Pre-Test Reservoir Characterization 174
4.1.2 Field Operations 193
4.1.3 Post-Test Interpretation 258
4.1.4 Post-Test Reservoir Simulations 271
4.2 STRATEGIES TO MAXIMIZE STORAGE, EOR, AND NET PRESENT VALUE 276

5. BROWNFIELD FIELD LABORATORY: STACKED ROZS AND CONVENTIONAL RESERVOIR STORAGE COMPLEX 282

5.1 GEOLOGY OF THE STACKED RESERVOIRS IN THE NOBLE OIL FIELD, RICHLAND COUNTY, IL 282
5.2 CARRIE WINTER 10 REPORT 338
5.3 DRILL STEM TEST ANALYSIS 372
5.4 STRATEGIES TO MAXIMIZE STORAGE, EOR, AND NET PRESENT VALUE 386

6. CO-OPTIMIZATION, LCA, AND CLASSIFICATION OF STACKED RESERVOIR EOR AND STORAGE RESOURCES 392

6.1 CO_2 SOURCES AND PIPELINES TO SUPPLY FIELD LAB SITES 392
6.2 CO-OPTIMIZED ECONOMIC CO_2-EOR AND STORAGE 406
6.2.1 Brownfield 406
6.2.2 Greenfield 436
6.2.3 Economic Analysis of Brownfield and Greenfield ROZ Development Strategies 474
6.3 LIFE CYCLE ANALYSIS OF BROWNFIELD AND GREENFIELD DEVELOPMENTS WITH POTENTIAL ILB CO_2 SOURCES 485
6.4 CO_2 STORAGE AND EOR RESOURCE ASSESSMENT OF SELECTED ILB ROZ FAIRWAYS 493

7. APPENDICES 526

7.1 GEOCHEMICAL CHARACTERIZATION OF ALTERATION OF HOLSAPPLE 2B OILS AND CORRELATION WITH HOLSAPPLE 2B GASES, CUMBERLAND CO., ILLINOIS 526
7.2 CARPER WATER-OIL-CO_2 RELATIVE PERMEABILITY 599

REFERENCES 600

EXECUTIVE SUMMARY

Residual oil zones (ROZs) have proven to be economically viable targets for carbon dioxide enhanced oil recovery (CO_2-EOR); the thick, carbonate ROZs in the San Andres Formation in the Wasson Field of the Permian Basin (Gupta et al., 2022) are an example. Incremental oil produced from CO_2-EOR can achieve a negative carbon balance through associated storage of injected CO_2 (i.e., CO_2 that ultimately becomes trapped in the formation and exceeds the carbon emissions created by the combustion of the produced oil; Núñez-López and Moskal, 2019). Given the regional extent of Permian Basin ROZ fairways and generally higher net utilization of CO_2 (compared to conventional CO_2-EOR), ROZs around the world provide the opportunity for significant carbon neutral to carbon negative oil production with associated CO_2 storage, and therefore should be a priority target for exploration. However, ROZs have not been widely recognized or identified due to poor or no conventional oil production. Hence, in places like the Illinois Basin (ILB), exploratory analyses are required to recognize the existence of an ROZ.

ROZs represent a bypassed resource and there is a need for characterization, simulation, and field laboratory studies of greenfield and brownfield ROZs and combinations of stacked ROZs with depleted and bypassed conventional oil reservoirs. Delineating the ROZ resource and providing guidelines for economic low-carbon oil production strategies could incentivize construction of CO_2 source and distribution infrastructure and help overcome the inexperience of local operators in dealing with CO_2-EOR to meet the challenge of commercial-scale implementation of associated storage projects in the ILB.

In support of these goals, this research project addressed two technical research needs:

1) ROZ formation, characterization, and associated storage in conjunction with EOR, and
2) Co-optimizing CO2-EOR with associated storage in storage complexes with stacked reservoirs

These needs were addressed by advancing methods to screen for and characterize siliciclastic ROZs to quantitatively assess the stacked ROZ resource in the ILB. The project leveraged field laboratory data to build reservoir models to identify scenarios in which CO_2-EOR and associated storage are systematically co-optimized in stacked reservoirs to economically produce low carbon oil. The defined scenarios were then assessed for real-world business case implementation by conducting techno-economic analyses, including lifecycle analysis, of the two field laboratory sites.

Findings of this study are supported by data from two field laboratory sites, one with stacked greenfield ROZs and the other with a stacked complex that includes a brownfield ROZ and depleted conventional reservoirs. The field laboratory sites were used to collect data and conduct tests to validate ROZ detection methodologies and identify economic field-deployable strategies to co-optimize CO_2-EOR and associated storage in stacked ROZs. Findings from these field sites were extrapolated to characterize the basin-wide stacked ROZ fairway resource.

To provide a framework for identification and characterization of ILB ROZs, a literature review of several basins with reservoirs analogous to those in the ILB is provided in **Chapter Two**. The ROZs within the Williston, Big Horn, Powder River, Wind River, and Green River Basins have much in common with those that are believed to occur within the ILB than those in the Permian Basin. They often occur within siliciclastic formations, and the oil-bearing intervals are on the order of 10s of feet thick (in contrast to the 100s of feet thick ROZs that have been economically produced in the Permian Basin carbonates). The availability of CO_2, coupled with existing oil production infrastructure and confirmed ROZs, makes more ROZ-focused studies likely, which could yield synergistic opportunities in the future.

Chapter Two also describes the screening of seven candidate ILB formations with ROZ potential. Three formations were selected for detailed regional characterization and analysis: Carper Sandstone (part of the Borden Siltstone), Tar Springs Sandstone, and Middle Devonian (Geneva Dolomite and associated Dutch Creek Sandstone). The Cypress Sandstone, which was subjected to rigorous regional geologic characterization and ROZ resource assessment as part of a previous project (Webb et al., 2019), was analyzed along with the selected formations, adding new data to strengthen and expand upon the findings that were already available. The four selected formations have a high degree of overlap, particularly in the northern half of the ILB near the field laboratory sites. **Chapter Three** describes the regional geological characterization of the formations of interest within the ILB stacked complex (including greenfield and brownfield ROZs and conventional oil reservoirs) to develop a regional geologic framework for the ROZs and their overlying seals.

Chapter Four focuses on the Greenfield Laboratory Site in which a well of opportunity was used to conduct a CO_2 Huff and Puff (HnP) test within a greenfield ROZ in the Carper Sandstone in Cumberland County, Illinois. Field activities commenced in February 2020, and concluded in September 2021. 1,010 tons of CO_2 were injected, and 349 tons were produced, along with 20,492 bbls of water and 63 bbls of oil. The field test had two objectives; to demonstrate the efficacy of CO2-EOR in a siliciclastic greenfield ROZ, and to characterize the rock and fluid properties of the ROZ. The HnP accomplished the first objective by producing oil and storing CO_2. The second objective was accomplished by analysis of the amount, properties, and composition of the produced fluids (oil, gas, brine). Fluid properties and results from core flood tests using proxies for the produced fluids were used to improve the characterization of the ROZ following the conclusion of field activities. The low oil recovery is attributed to the reservoir properties of the Carper Sandstone; natural fractures within a low permeability, very-fine grained sandstone to coarse siltstone that resulted in limited contact between CO_2 and matrix bound oil. Both EOR and CO_2 storage exceeded expectations defined by pre-test reservoir simulations.

Previous research postulated the existence of a brownfield ROZ underlying the MPZ in the top of the thick Cypress Sandstone at the Brownfield Laboratory Site in Noble oil field (Webb and Grigsby, 2020). **Chapter Five** details the drilling of a new research well, the Carrie Winter #10, to validate the existence and properties of the ROZ. Core was collected through the MPZ and ROZ of the Cypress Sandstone and confirmed the presence of oil saturation within the ROZ. The core also provided confirmation that the ROZ is bounded above and below by carbonate cemented intervals within the sandstone that log correlations have shown to be persistent (Webb and Grigsby, 2020; Grigsby and Webb, 2020). A drill stem test was completed within the ROZ and confirmed that the oil is immobile. An advanced geophysical log suite, including the Schlumberger Dielectric Scanner, was collected. Analysis of the advanced logs and traditional well log analysis techniques applied to the triple combo logs support the existence of an MPZ overlying an ROZ in the Cypress Sandstone. The combination of log analysis techniques calibrated to core validates the concept of identifying and characterizing siliciclastic ROZs using well logs.

Chapter Six addresses the co-optimization and life cycle analysis of CO_2-EOR and associated storage at the two field laboratory sites and presents a regional assessment of the EOR and associated storage resources of the stacked ROZs. The multi-reservoir model for the Greenfield (in which all targets were developed simultaneously via shared wells) showed that the contrast in reservoir properties between the relatively low permeability Carper Sandstone and the higher permeability Geneva Dolomite required each formation to be developed separately to optimize oil production and CO_2 storage. For the Brownfield, the development strategies are biased towards the two most prolific formations, the Cypress Sandstone and

Ste. Genevieve Limestone, which together account for approximately 90% of the oil that has been produced from the field. Because of significant differences in the two reservoirs (e.g., thickness, continuity, compartmentalization), different pattern sizes were required to maximize the performance of CO_2 injection in each reservoir individually, but shared wells can be leveraged to optimize the development of several units within the stacked complex simultaneously.

In analyzing the economic metrics of the two field laboratory sites several tradeoffs are presented as selection of a development strategy based on economic criteria will be specific to the business strategy of an individual company. The Brownfield site generally offers lower economic risk because existing infrastructure results in lower capital investment. However, the presence of numerous legacy wellbores presents a different kind of risk in that improperly plugged wells may present leakage pathways for CO_2. Many of the Brownfield cases also are shorter lived as CO_2 recycling costs increase over time while the revenue generated from bringing in new CO_2 declines. Conversely, the Greenfield site requires greater capital investment, but the lack of legacy well penetrations and all new wells may be more attractive for operators adverse to dealing with legacy wellbore issues.

When considering regional CO_2 sources, field development costs (CAPEX and OPEX) controlled the variability of the total unit costs for the two field laboratory sites. For the greenfield case using both CO_2 emitting sectors, carbon capture costs controlled the scenario variability. However, on a percentage basis, carbon capture costs at the CO_2 emitting facility were the largest proportion of the total project unit costs, ranging from 53-88% of the total project costs. Technology advancements that reduce the CO_2 capture costs could increase the economic viability of ROZ EOR projects such as the examples modeled here. The gate-to-gate emission factors were 9-14 $kgCO_2$ eq/stb for brownfield and 4-9 $kgCO_2$ eq/stb for greenfield. The two contributing factors were electricity and land use, and electricity is the dominating factor that generated 99% of the gate-to-gate emissions. However, the gate-to-gate emissions were found to be negligible compared to the cradle-to-gate emissions. These findings suggest that the choice of development strategies evaluated here had only a negligible impact on global warming potential relative to upstream operations.

Finally, the distribution of ROZs in the Illinois Basin was found to be controlled by the geological setting and oil migration history of the basin. ILB ROZ fairways that are stratigraphically proximal to the source rock are generally widespread whereas fairways developed in formations with a greater thickness of intervening strata are more discrete, an indication of influence from fault systems and fracturing associated with major structures. Within these fairways, over 40 ROZ prospects were defined across three formations (Tar Springs Sandstone, Cypress Sandstone, Carper Sandstone) containing an estimated 4.6 billion barrels of original oil in place (OOIP), which is 30 to 40% of the OOIP of the conventional reservoirs in the ILB. The CO_2-EOR resource of these ROZ prospects exceeds 466 million bbls of oil using CO_2 injection via pattern flooding. Associated CO_2 storage is estimated to be 394 million tonnes of CO_2.

Chapter Seven concludes with the unabridged reports and data provided by Stratum Reservoir detailing 1) laboratory analysis of Carper Sandstone oil and gas samples collected as part of the HnP testing, and 2) core flooding experiments to determine relative permeability of a CO_2-brine-oil system within the Carper Sandstone at the Greenfield site. These data were discussed in context of the greenfield laboratory work in Chapter Four.

1. INTRODUCTION

1.1 Objectives

The overall objective of the Stacked Greenfield and Brownfield ROZ Fairways in the Illinois Basin Geo-Laboratory project was to identify economic strategies to co-optimize carbon dioxide enhanced oil recovery (CO_2-EOR) and associated storage in stacked, primarily siliciclastic, reservoirs in the Illinois Basin (ILB). This entailed characterization, simulation, and field laboratory studies of greenfield and brownfield residual oil zones (ROZs) and combinations of stacked ROZs with depleted and bypassed conventional oil reservoirs.

Sub-objectives in support of the overall objective were to: 1) design field laboratory data collection and injection tests based on preliminary characterization and modeling of the ROZs and conventional oil reservoirs of two field laboratory sites; 2) implement and complete field laboratory data collection and injection tests to characterize the ROZs in multiple formations and demonstrate the efficacy of CO_2-EOR and associated storage in siliciclastic ROZs; 3) evaluate the performance of CO_2-EOR and associated storage in vertically stacked ROZs using reservoir simulations calibrated with the field laboratory data; 4) determine strategies to co-optimize CO_2-EOR and associated storage in vertically stacked ROZs based on techno-economic analyses and life-cycle analyses (LCA) for the two field laboratory sites; 5) develop a methodology that can be effectively used to identify geologic formations with ROZs and to quantify the ROZs' oil-in-place through the use of field laboratories; and 6) apply the findings from these sub-objectives to finalize an ILB ROZ resource assessment.

Economic strategies to co-optimize carbon dioxide enhanced oil recovery (CO_2-EOR) and associated storage in stacked, primarily siliciclastic, residual oil zones (ROZs) in the Illinois Basin (ILB) are needed. These ROZs represent a bypassed resource and there is a need for characterization, simulation, and field laboratory studies of greenfield and brownfield ROZs and combinations of stacked ROZs with depleted and bypassed conventional oil reservoirs. Delineating the ROZ resource and providing guidelines for economic low-carbon oil production strategies could incentivize construction of CO_2 source and distribution infrastructure and help overcome the inexperience of local operators in dealing with CO_2-EOR to meet the challenge of commercial-scale implementation of associated storage projects in the ILB.

1.2 Motivation

Operators in the Permian Basin have been using CO_2-EOR to produce oil economically from extensive carbonate ROZs for years, resulting in established methodologies to locate and delineate ROZs in carbonates (Trentham and Melzer, 2016). Though these methodologies have documented key ROZ screening criteria, there remain unique challenges to identifying and characterizing ROZs in siliciclastic formations. Recent Illinois State Geological Survey (ISGS) research has used well log analysis to delineate areas of the ILB where both brownfield ROZs (beneath a main pay zone) and greenfield ROZs (intervals of residual oil with no overlying main pay zone) are likely to occur in the Cypress Sandstone (Webb et al., 2019). Furthermore, recent exploratory work by ILB operators has yielded evidence of an extensive greenfield ROZ in the Carper Sandstone via oil shows with limited oil production at high water cuts. These findings are promising but require further field validation. A method that combines direct and indirect indicators to identify and characterize siliciclastic ROZs will address critical gaps in our understanding of CO_2-EOR of ILB ROZs and associated CO_2 storage opportunity. The method will need to be validated by

field data and iteratively improved to address the range of heterogeneities present across different siliciclastic depositional settings in the ILB.

Within siliciclastic ROZs, another challenge is determining the proper development strategies for producing the low oil saturation of an ROZ economically. Techniques used to produce oil from ROZs in the Permian Basin may not be applicable elsewhere, since they were developed in thick carbonate ROZs and are designed to maximize oil production. From a CO_2-EOR perspective, historically overlooked siliciclastic ROZ fairways may contain large volumes of oil that could be economically produced, especially when considered as part of a stacked reservoir complex in which depleted and bypassed conventional reservoirs also occur. From a storage perspective, stacked, widespread, porous and permeable ROZs separated by laterally extensive caprocks provide favorable capacity and containment for associated storage. However, due to the low oil saturations with very high water production, projects must be carefully designed to properly leverage the potential of ROZs for low carbon oil production.

Unlike natural sources of CO_2 that are commonly used in CO_2-EOR projects, anthropogenic CO_2 sources may fluctuate or even shut-down for emergency or routine maintenance. Moreover, sales of captured CO_2 will not provide the sole revenue for any emissions source; therefore, businesses expending capital for added-value projects will require assurance of the long-term availability of CO_2. The potential for a more versatile CO_2-EOR and associated storage resource is greatly expanded where ROZ fairways in different formations are stacked, especially in areas that also contain mature conventional oilfields. Stacked storage uses the three-dimensional properties of the geology to combine CO_2-EOR and saline-storage types where EOR provides an attractive market for CO_2 (Hovorka, 2013). By linking CO_2-EOR with vertically and horizontally adjacent saline storage volumes, the infrastructure, experience, and community acceptance developed for EOR can provide a substantive boost for using the entire subsurface for storage of very large volumes of CO_2 (Hovorka, 2013). However, there is currently a lack of understanding of how to deploy economic strategies to co-optimize CO_2-EOR and associated storage systematically in stacked storage complexes that include ROZs. A challenge of co-optimizing EOR and storage in a stacked reservoir complex is the chronology in which each reservoir is targeted. There will be differences in the pressure and volume of the produced CO_2 relative to the reservoir pressure and volume of CO_2 required. Such issues may be mitigated if reservoirs with different properties could be targeted individually or systematically, as needed.

b) Current State-of-the-Art Technologies: CO_2-EOR was developed as a tertiary recovery technique to produce residual oil from depleted main pay zones (MPZs) following waterflooding. In search of additional CO_2-EOR opportunities within existing CO2-EOR operations, in the Permian Basin, wells were deepened below the producing oil water contact to produce oil from what were believed to be long capillary transition zones (now recognized as brownfield ROZs). Recent projects in the Permian Basin have also been able to economically produce oil from greenfield ROZs far from conventional oil fields. However, because they occur away from existing oil fields, greenfield ROZs are difficult to identify and produce. Research on Permian Basin ROZs led to the development of a set of indirect indicators of ROZs (e.g. sulfur, biodegraded oil, fresh water, and tilted oil-water contacts) that have been used to identify and map the extent of greenfield fairways (Trentham and Melzer, 2016). Areas with suspected ROZs are subjected to more costly screening methods (e.g. drilling to collect core and run modern, open hole well logs) to find direct indicators of the ROZ before investing in CO_2-EOR projects. Lessons learned from these projects can be useful but are generally site specific and may not apply broadly to other basins, especially siliciclastics.

Further study is required to demonstrate that significant ROZs exist elsewhere and that they can be identified with a universal methodology and economically produced.

Conventional CO_2-EOR (targeting depleted MPZs) has established reliable projections of oil recovery and storage (i.e., net and gross CO_2 utilization) from field applications, laboratory tests, and modeling. CO_2-EOR of nonconventional ROZ reservoirs, which have a significantly higher storage potential, has received much less attention. Because conventional CO_2-EOR commonly follows waterflooding and is associated with water-alternating-gas injection schemes, the literature includes field and laboratory studies of CO_2-EOR in the presence of high water saturation (Stalkup, 1970; Tiffin and Yellig, 1983). CO_2 injection in high water saturation within ROZs will have similar effects of water blocking (restricting contact to oil) and loss of CO_2 via dissolution in brine, but an integrated reservoir study with this specific saturation and permeability distribution was not found in the literature.

In addition to estimating the CO_2-EOR resource that ROZs represent, an element of this study is maximizing CO_2 storage. Traditional CO_2-EOR design seeks the maximum oil recovery while injecting the minimum amount of CO_2, which is clearly contrary to CO_2 storage operations. Fortunately, several large-scale CO_2 injection projects, including the Illinois Basin-Decatur Project, have produced information about the fate and transport of CO_2 in siliciclastics that can be applied to the study of co-optimizing carbon storage and oil recovery. Kovscek and Cakici (2004) have defined an objective function for evaluating development strategies to serve the purpose of co-optimizing CO_2-EOR and storage. This objective function combines dimensionless oil recovery and reservoir utilization. Like all similar approaches that generalize CO_2-EOR performance, there is no rigor to the geologic description or unique geologic settings, and are applicable when technology is more mature like those used for MPZ CO_2-EOR performance (e.g. CO_2 Prophet).

Existing studies that have investigated the co-optimization of CO_2-EOR and associated storage in depleted MPZs evaluate reservoirs on an individual basis. A new generation of research is needed that involves the study of stacked reservoirs in a systematic manner, as a stacked storage complex. One solution is the use of saline reservoirs for stacked storage of CO_2. Saline reservoirs that occur within the storage complex above or below the ROZ or depleted reservoirs could be used to store CO_2 that could be produced during downtime of the facility providing the anthropogenic CO_2 or if the facility stops providing CO_2 sometime in the future. Studying the ability of a reservoir to produce previously stored CO_2 would improve understanding of the feasibility of this option for added-value stacked storage. The CO_2 would remain stored in the subsurface but would be transferred from formation to formation based on added value need for each reservoir.

c) Feasibility of the Proposed Concept: The proposed project takes an integrated approach (Figure 1-1) to addressing the first two technical research needs identified in the FOA (*ROZs-formation, characterization, -and associated storage in conjunction with EOR,* and *Co-optimizing CO_2-EOR with associated storage in storage complexes that have stacked reservoirs*) by advancing methods to screen for and characterize siliciclastic ROZs to quantitatively assess the stacked ROZ resource in the ILB. The approach will leverage field laboratory data to build reservoir models to identify scenarios in which CO_2-EOR and associated storage are systematically co-optimized in stacked reservoirs to economically produce low carbon oil. The defined scenarios will then be assessed for real-world business case implementation by conducting techno-economic analysis, including lifecycle analysis, of two field laboratory sites.

Findings of this study will be supported by data from two field laboratory sites, one with stacked greenfield ROZs and the other with a stacked complex that includes a brownfield ROZ and depleted conventional reservoirs. The field laboratory sites will be used to collect data and conduct tests to validate ROZ detection methodologies and identify economic field-deployable strategies to co-optimize CO_2-EOR and associated storage in stacked ROZs. Findings from these field sites will be extrapolated to characterize the basin-wide stacked ROZ fairway resource (Figure 1-1).

Relevant oilfield data (including well files [e.g., drilling, completion and perforations], well logs, core data [e.g., whole core, core descriptions, core analyses], production records, oil saturation data [e.g., oil shows, oil saturation from core analysis, and drill stem test data] and past reports and maps) will be compiled and analyzed to establish an understanding of the formations of interest at the field laboratory sites and regionally across the ILB. Data from the greenfield and brownfield laboratory tests will be collected and used for detailed geologic and petrophysical characterizations to ensure usable field test results.

At the regional scale, direct and indirect indicators of ROZs will be assessed through data mining of ISGS institutional datasets and by surveying operators who can provide additional observations of ROZ indicators for at least five siliciclastics and two carbonate formations that have historically exhibited ROZ characteristics (Figure 1-2). ROZ potential maps based on these indicators will be compared to maps developed by modeling oil source and migration pathways and a ROZ identification methodology based on well log analysis previously developed as part of a current ISGS ROZ study (Grigsby and Frailey, *in prep*). Results from these methods will then be compared to each other, and to direct measures of oil saturations from the field laboratory tests, to determine if they can be used to properly identify and characterize siliciclastic ROZs. The three most promising ROZs to come out of this screening process will undergo advanced, detailed studies based on the field sites.

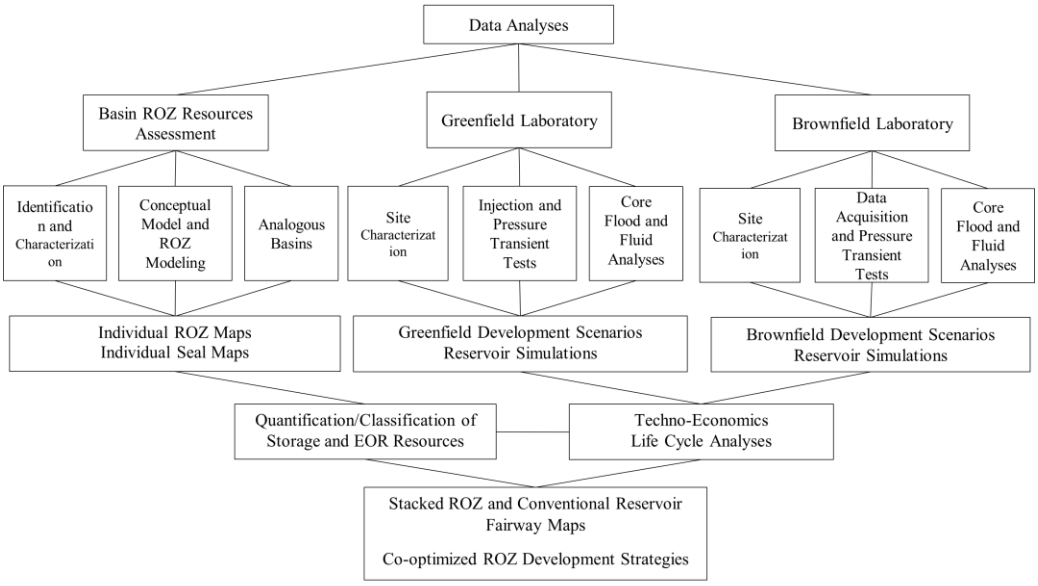


Figure 1-1. Workflow that shows the integration of the research that flows down from the initial data analysis to the work at regional and field laboratory site scales. The products of the research at both scales are fed into the resource classification and techno-economic and lifecycle analysis, ultimately resulting in fairway maps and co-optimized development strategies.

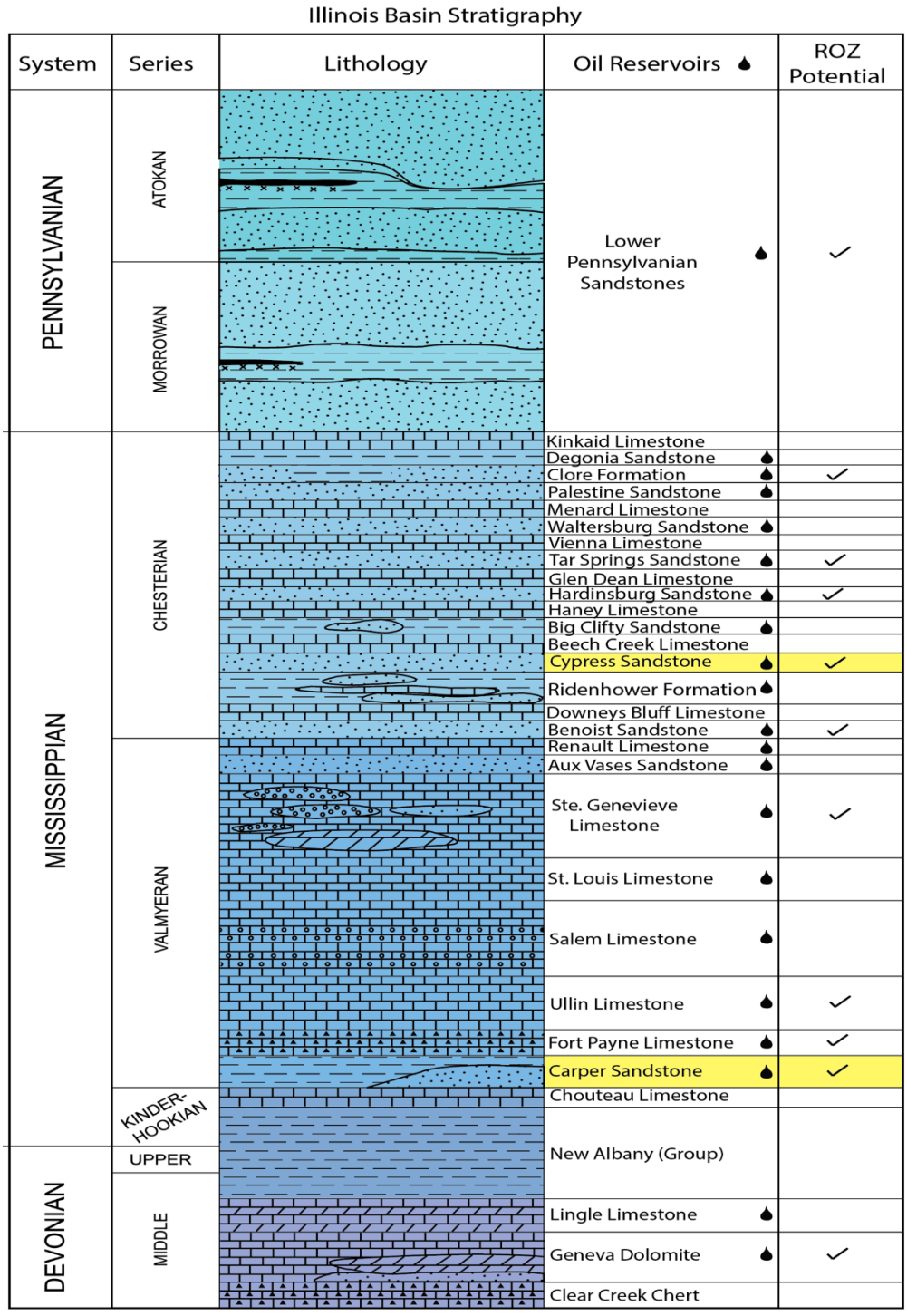


Figure 1-2. Upper Paleozoic stratigraphic column of the Illinois Basin showing known oil reservoirs as well as formations that have ROZ potential.

2. Screening and Selection of ILB ROZs for Resource Assessment

Direct and indirect indicators of ROZs will be assessed through data mining of Illinois State Geological Survey institutional datasets and surveying operators who can provide additional observations of ROZ indicators for at least five siliciclastics and two carbonates. This task ends with the selection of three ILB ROZs for detailed resource assessment through synthesis and analyses of existing data to establish an understanding of the formations of interests at the field laboratory sites and regionally across the ILB. Siliciclastic ROZ indicators identified and used in a current ISGS ROZ study will be tested for general applicability in other ILB ROZs.

2.1 Screening and Selection of Illinois Basin ROZs for Resource Assessment

Authors: Nathan Webb, Zohreh Askari, Nathan Grigsby, Damon Garner, Hannes Leetaru, Carl Carman
Published as Technical Report DOE-UIUC-31700-1, OSTI ID: 1846284, https://doi.org/10.2172/1846284

Residual oil zones (ROZs) are naturally occurring areas of immobile oil found below or outside of the primary oil-producing regions of an oil field. Brownfield ROZs, which are commonly associated with conventional oil reservoirs or main pay zones (MPZs), are found below the producing oil-water contact. Greenfield ROZs are believed to occur within formations that are laterally extensive and hydrodynamically connected that extend beyond the boundaries of conventional oil fields and have no overlying MPZ. These ROZs represent a potentially significant opportunity for carbon dioxide enhanced oil recovery (CO_2-EOR) and associated CO_2 storage.

The overall objective of this research is to identify economic strategies to co-optimize CO_2-EOR and associated storage in stacked, primarily siliciclastic reservoirs in the Illinois Basin (ILB). Stacked reservoirs occur in geologic settings in which several reservoirs are vertically stacked one above the other and separated by one or more seals. ROZs are believed to create an economic incentive for CO_2-EOR, but depleted reservoirs that lack ROZs also have associated storage potential.

It is the purview of this study to conduct regional geologic characterization on at least three formations that have the potential to contain ROZ fairways. Detailed geologic characterization will also take place at two field laboratory sites (Figure 2-1). The brownfield site is in Noble Field, Richland County, and contains several stacked MPZs and at least one identified ROZ within the Cypress Sandstone. The greenfield site is in south-central Cumberland County and contains at least one ROZ within the Carper Sandstone, with other ROZs indicated by log analysis within the Cypress Sandstone and a Pennsylvanian sandstone.

In order to select the formations potentially containing ROZ fairways for regional geologic characterization, a preliminary geologic assessment was conducted on seven candidate formations (five siliciclastic and two carbonate formations). The formations included in the screening are the Tar Springs Sandstone, Cypress Sandstone, Bethel/Yankeetown (Benoist) Sandstones, Spar Mountain Sandstone, Carper Sandstone, Salem/Ullin Limestones, and the Geneva Dolomite/Dutch Creek Sandstone (Figure 2-2). Well data, including drilling and completion reports, well logs, core data (i.e., core descriptions, core analyses), production records, oil saturation indicators (i.e., oil shows, oil saturation from core analysis, and drill stem test data), and previous reports and maps were compiled and analyzed to determine which formations exhibited the greatest potential for ROZs. This report summarizes the efforts to screen the seven candidate formations as well as the selection of three formations (Carper Sandstone [part of Borden Siltstone], Tar Springs Sandstone, and Geneva Dolomite/Dutch Creek Sandstone) for further characterization and detailed analysis.

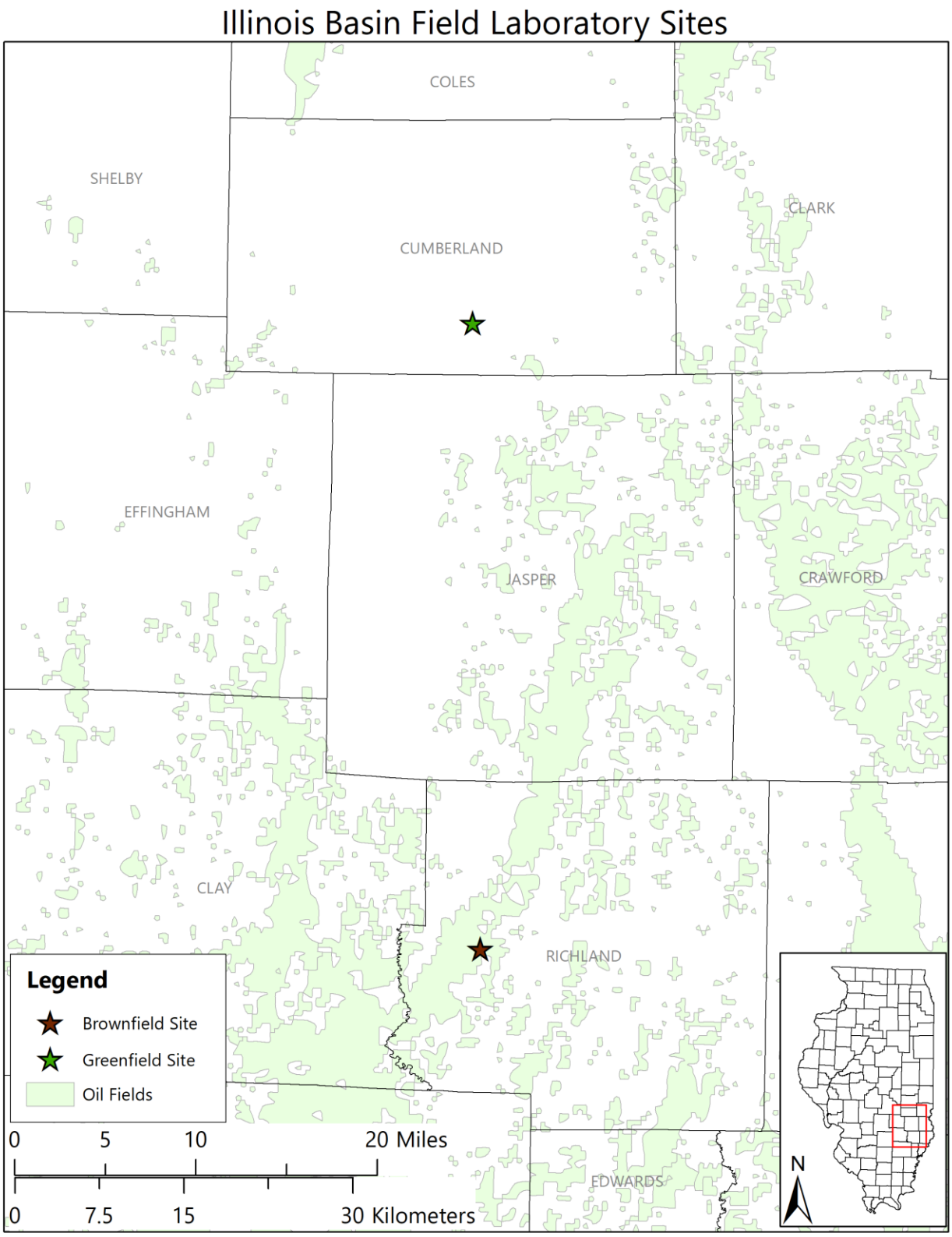


Figure 2-1. Map showing the location of brownfield and greenfield laboratory sites.

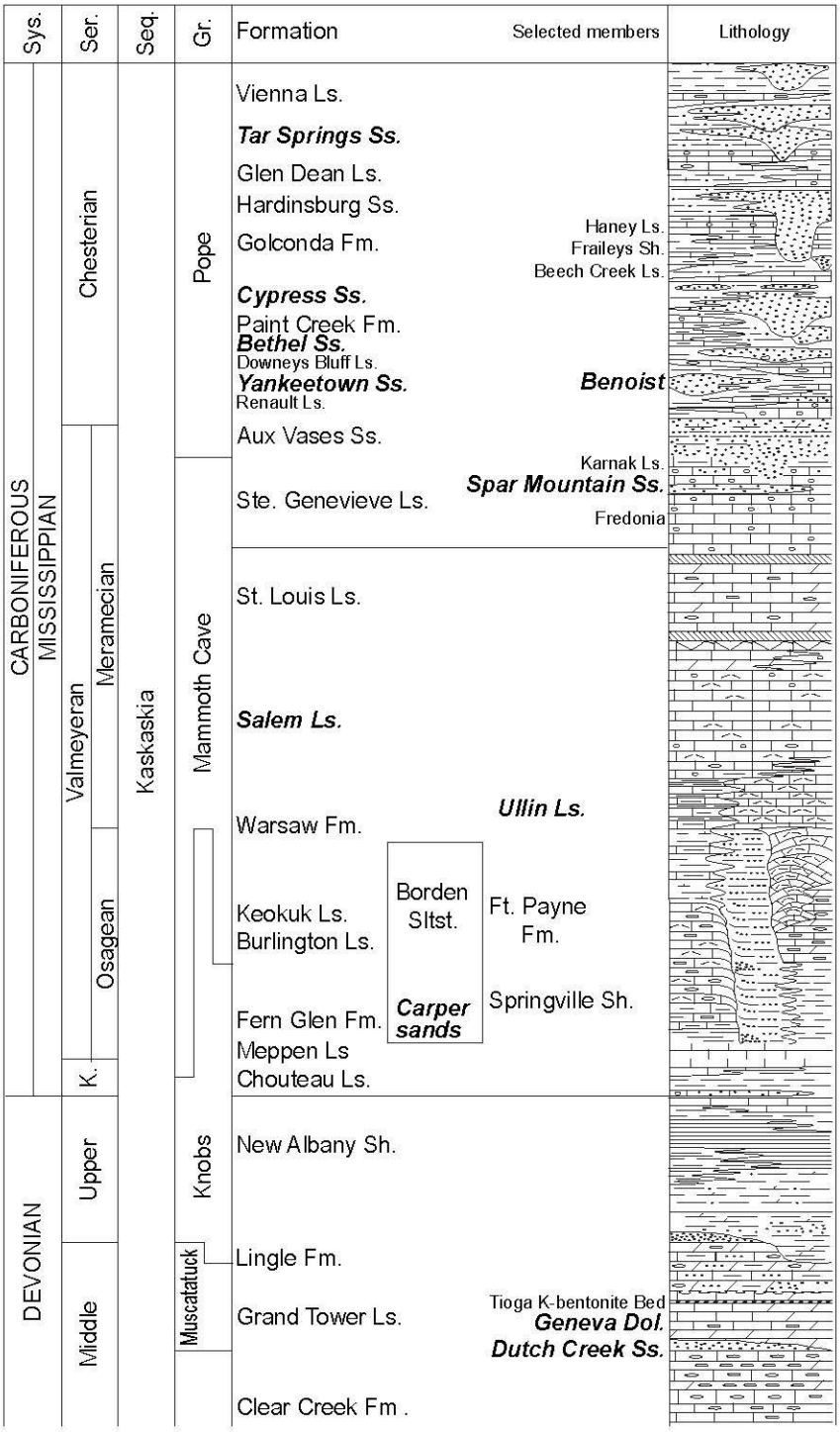


Figure 2-2. Generalized stratigraphic column of the ILB (in bold are units assessed for ROZ potential). Abbreviations: K., Kinderhookian; Dol., dolomite; Fm., formation; Ls., limestone. Modified from Kolata (2005).

Data Quality and Availability

Well Records

For over two decades, the Illinois State Geological Survey (ISGS) has been progressively transitioning from paper records to a database system to support the public's need to access information and the results of scientific studies. The Petroleum Geology section has paper records for roughly 200,000 wells, which provides a sense of the scale and time commitment being given to complete this transition. To meet the data objectives of this project (regional geologic characterization, ROZ screening), an assessment of needed data was performed. Comparing data needs against available digital data highlighted what digitization efforts needed to be prioritized to meet these objectives.

Well location and completion data are critical in determining the spatial distribution of oil produced from various formations across the ILB and assessing historical oil migration. Although well location data was reasonably accurate for the 85,000 wells that have produced oil, it was determined that the well completion data was incomplete, and more than 50% of the data may have been missing from the digital database. Completion data from two sources were compiled into an improved dataset. Even though recent scanning of well documents have made these data more accessible, identifying well completions is a slow process and will continue for the duration of this project. Data from several thousand core analysis reports are being added to the existing data from 7,296 wells currently in the database. Thousands of shows of oil are already present in the ISGS database, as are roughly 18,500 drill stem test records.

To identify potential greenfield and brownfield ROZs, the spatial distribution of oil saturation values from core analysis reports, oil shows from driller reports, data from drill stem tests, and geophysical logs are being analyzed. Together, these various data types are considered "oil indicators" for a given formation. Of these data types, successful production perforations and drill stem tests can be inferred to indicate mobile oil. The other data types do not distinguish between mobile and residual oil and are not considered to be quantitative measures of oil saturation, but instead are considered direct evidence of oil presence within the formation at that well location. The oil indicators were compiled and mapped to understand the distribution of oil encountered within each screened formation and were compared against well completion data to determine if the zones were produced.

Geophysical Logs

Basin-Wide

Geologic characterization, geocellular and reservoir models for simulations, and oil and water saturation calculations all rely on geophysical well logs. Most oil wells drilled since the 1930s in the ILB were logged. The availability and quality of well logs are dependent on when and where the wells were drilled; there is generally higher data distribution in oil fields and higher data quality in newer wells.

Logging technology has evolved over time, so the completion date of a given well can often be used to infer the type of available log suites. Old oil fields will have a disproportionate number of wells with old e-logs (SP and resistivity). Conversely, new completions are more likely to have more sophisticated log suites (modern resistivity and porosity logs). Modern well logs are necessary for reducing uncertainty in some calculations, but qualitative interpretations (such as picking the top and base of a formation or the volume of shale calculations) can often be accomplished with older logs (Table 2-1).

Raster logs can be used to pick formation tops, estimate extent and thickness, as well as for general, qualitative assessments, but they must be digitized to LAS format to quantify oil saturation and for

geocellular/reservoir modeling. The ISGS has raster logs for 112,368 wells and LAS logs for 7,368 wells. Because so few logs in the ILB are in the digital LAS format, raster logs are being, and will continue to be, evaluated and digitized in strategic locations (near the field laboratory sites and areas that have high ROZ potential). So far, more than 200 additional logs have been digitized to support this project.

Table 2-1. Estimated date intervals when log suites were in use.

		Start	Stop
SP		1930s	NA
Resistivity	Induction logs (SN, LN)	1950s	1960s
	Dual induction (LL8/SFL, ILM, ILD)	1960s	NA
	Array	1990s	NA
Gamma ray	Gamma ray neutron	1950s	1960s
	Gamma ray	1970s	NA
	Spectral	1980s	NA
Porosity	Sidewall neutron	1960s	1970s
	Compensated neutron	1970s	NA
	Compensated density	1970s	NA
	Neutron-density porosity	1980s	NA
	Sonic	1960s	NA
NMR		1990s	NA

Near-Field Sites

The brownfield laboratory site is Noble Field (part of Clay City Consolidated Field) and its immediate vicinity (Figure 2-1). There are approximately 540 wells in the study site, 400 of which have LAS files as a result of digitization for a previous project (DE-FE0024431). Most of the wells were drilled before widespread adoption of neutron-density porosity logs, resulting in a high proportion (approximately 75%) that only have old e-logs.

The Cypress Sandstone, Aux Vases Sandstone, Ste. Genevieve (McClosky) Limestone, St. Louis Limestone, and Salem Limestone (Figure 2-2) were the primary targets for oil production at Noble Field. As such, most of the wells fully penetrate and log the Tar Springs and at least the upper portion of the Cypress Sandstone; fewer capture the Yankeetown Sandstone, Spar Mountain Sandstone, Salem and Ullin Limestones, and the Dutch Creek Sandstone. The Geneva Dolomite and Carper Sandstone are not present in Noble Field.

The greenfield laboratory site is in Cumberland County, away from established oil fields (Figure 2-1). There are only approximately 40 wells in the vicinity of the study site (10 in LAS format). The Carper Sandstone

and Geneva Dolomite have oil shows in the area, so although there are few wells, those that do exist often penetrate most of the candidate formations.

Seismic Lines

The ISGS has access to a collection of proprietary 2D and 3D seismic reflection data that has been donated to the ISGS as well as publicly available seismic data acquired through DOE funded programs. The collection is composed of more than 5,633 km (3,500 mi) of seismic reflection data. Most of this data has never been interpreted but is being evaluated for its usefulness in determining the continuity of ROZ formations, especially in areas where well data is lacking.

A 2D seismic reflection profile across Noble Field in Richland County, Illinois (Figure 2-3) is being acquired as part of the DOE funded CarbonSAFE Illinois – East Sub-Basin project (DE-FE0029445). The goal of this data acquisition is to characterize thick sandstone packages outside of oil fields to evaluate their CO_2 storage potential and to better understand the lateral continuity of the formations in the brownfield study area that extend outside of the densely drilled area.

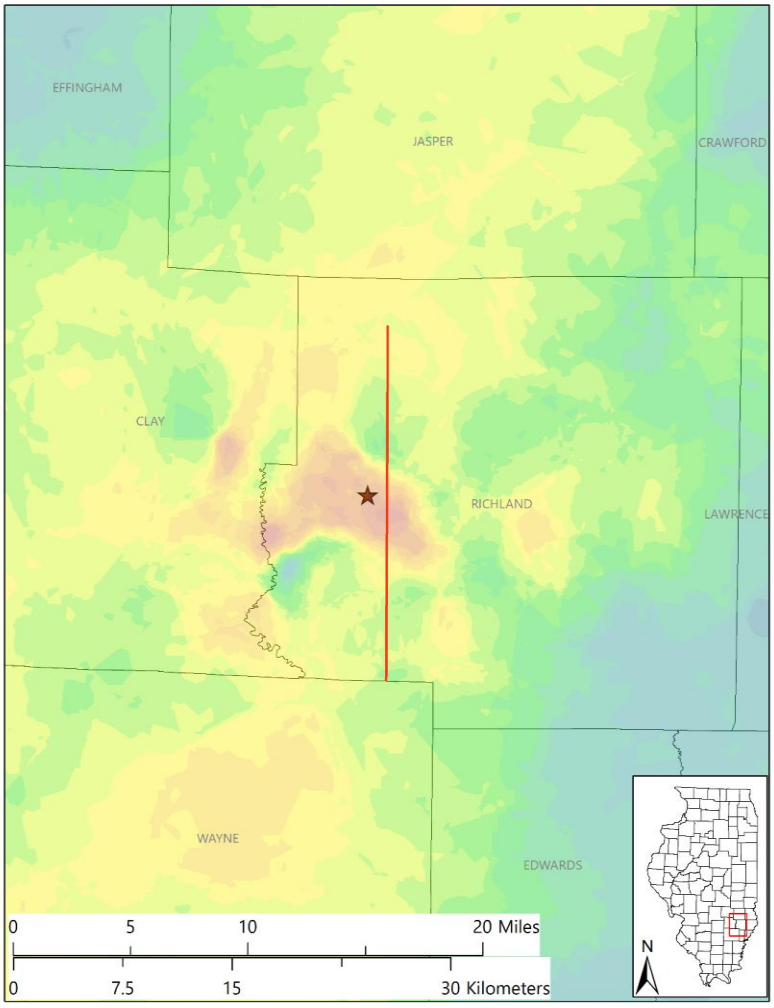


Figure 2-3. Map showing the location of the 2D seismic reflection profile (red line) acquired for CarbonSAFE Illinois – East Sub-Basin project in Richland County. Brownfield site within Noble Field where new stratigraphic test well will be drilled is indicated by the star. The base map shows the net thickness of the Cypress Sandstone; warmer colors are thicker.

Criteria for Selecting Formations for ROZ Resource Assessment

Each candidate formation was evaluated for ROZ potential by reviewing available literature and querying and mapping well data from the ISGS oil field database. Screening criteria for the candidate formations include: 1) geology, 2) ROZ indicators, and 3) data availability. Those candidate formations with the highest ROZ potential and data availability will be selected for more detailed ROZ resource assessment in the next phase of this project.

Geology

ROZs occur within widespread, hydraulically connected formations that have experienced an accumulation and sweep of paleo oil reserves over geologic time. A broad understanding of the geology of each candidate formation can be used to determine if its geology supports the existence of an ROZ fairway. Certain depositional environments (e.g., fluvial channels, turbidites) and diagenetic processes (e.g., dolomitization) are naturally conducive to the development of regionally extensive ROZ fairways.

ROZ Indicators

Indirect indicators of oil saturation have been used to identify areas that have the potential to contain ROZs in the Permian (West, 2014; Trentham and Melzer, 2016), Williston (Burton-Kelly et al., 2015; Yang and Qing, 2016), Bighorn (Yin et al., 2012), and Illinois Basins (Webb et al., 2019). These indicators can be interpreted from data commonly recorded when an oil well is drilled. Indirect indicators being evaluated to screen for ILB ROZs are:

- Oil shows
- Oil production
- Drill stem tests
- Core-derived oil saturation
- Sulfur water or odor
- Fresh water
- Tilted oil-water contacts
- Biodegraded oil
- Extensive dolomitization

Areas that have a high concentration of these indirect indicators are generally considered to have ROZ potential, but thoughtful evaluation of the indicators is vital. For example, indicators at the periphery of an oil field may indicate an associated brownfield ROZ, but may also reflect a depleted or a thin, non-commercial MPZ. Conversely, sparse or scattered indirect indicators may indicate a greenfield ROZ in data-poor regions. Areas with a disproportionate number of wells with oil shows to wells with oil production are likely to have ROZ potential.

Data Availability

In addition to the data used to evaluate ROZ potential described above, candidate formations should have adequate available data for detailed characterization that is necessary to 1) establish the existence of an ROZ and 2) evaluate the potential CO_2-EOR and the associated storage resource.

Detailed characterization uses interpretations and analyses of core, logs, cross sections, and seismic data to understand regional variations in geology (e.g., lithology, porosity, depositional or diagenetic trends). Adequate well log coverage is needed in areas with ROZ potential (e.g., at the periphery of brownfield ROZs or in areas with abundant indications of greenfield ROZs) to better estimate residual oil saturation

and constrain the thickness and spatial extent of the ROZ. Modern well logs are preferred, where available, to quantify residual oil saturation.

Formation Screening

Preliminary review of the more than 60 oil producing formations in the ILB resulted in the selection of two carbonate and five siliciclastic candidate formations with ROZ potential for screening. The candidate formations include the Geneva Dolomite/Dutch Creek Sandstone and Salem/Ullin Limestone (primarily carbonates), and the Tar Springs, Cypress, Bethel/Yankeetown, Spar Mountain, and Carper Sandstones (siliciclastics) (Figure 2-2). Based on the screening, three were subsequently selected for detailed characterization. The following is a summary of the geologic attributes, ROZ indicators, and data availability for each formation. For each formation, a map is presented showing the distribution of producing oil wells and oil indicators, as well as their relation to the two field laboratory sites. The boundaries of the porous and permeable rock within each formation is also shown. The mapped boundaries are generally based on regional isopach and/or isolith maps from previously published reports (citations given). As such, in some cases, mapped oil production or oil indicators may fall outside of the delineated boundary.

Carbonate Formations

Geneva Dolomite/Dutch Creek Sandstone

The Grand Tower Limestone (Middle Devonian) (Figure 2-4) is subdivided into three members, which include the Dutch Creek Sandstone, Geneva Dolomite, and Cooper Limestone from base to top (e.g., Meents and Swann, 1965; Willman et al., 1975). The Geneva Dolomite and Dutch Creek Sandstones are prolific oil reservoirs in the ILB. The Geneva Dolomite is the basal member of the Grand Tower across the northern part of the ILB (Figure 2-5). Toward the southeast, the Geneva overlies and/or grades into the Dutch Creek Sandstone (Meents and Swann, 1965). The Geneva Dolomite is present at the greenfield site, and the Dutch Creek Sandstone is present at the brownfield site.

The Geneva Dolomite consists of brown to dark brown, coarsely crystalline pure dolomite with vugular and intercrystalline porosities (Seyler et al., 2003). In some localities, floating grains of rounded, coarse to fine quartz sand occur in the Geneva, particularly in its lower part. The Dutch Creek Sandstone is composed of fine- to medium-grained, rounded, well-sorted, and fossiliferous sandstone with sandy limestone interbeds (Collinson and Atherton, 1975). The contact between the Geneva Dolomite and the underlying Dutch Creek Sandstone is conformable.

Geneva Dolomite thickness ranges from 0 to 15 m (0 to 50 ft) and, locally, up to 27 m (90 ft) thick. Oil is trapped within the Geneva on pronounced, closed structures. Many of these structures are related to tectonics, but, in many cases, the closure is also caused or enhanced by the draping of younger, Middle Devonian strata over Silurian reefs (Seyler et al., 2003).

The porous and permeable Geneva Dolomite and Dutch Creek Sandstone and their associated oil production is mainly distributed across the northern portion of the ILB. Over 150 wells have produced oil from the Geneva Dolomite, and 36 wells have produced from the Dutch Creek Sandstone (Figure 2-5). Devonian reservoirs have been cored in 628 wells. The Geneva Dolomite was cored in nine wells, with two wells in Cumberland County (API 120350010700 and 120352137100), and one well in Richland County (API 121590044700) near the greenfield and brownfield sites, respectively (Figure 2-6).

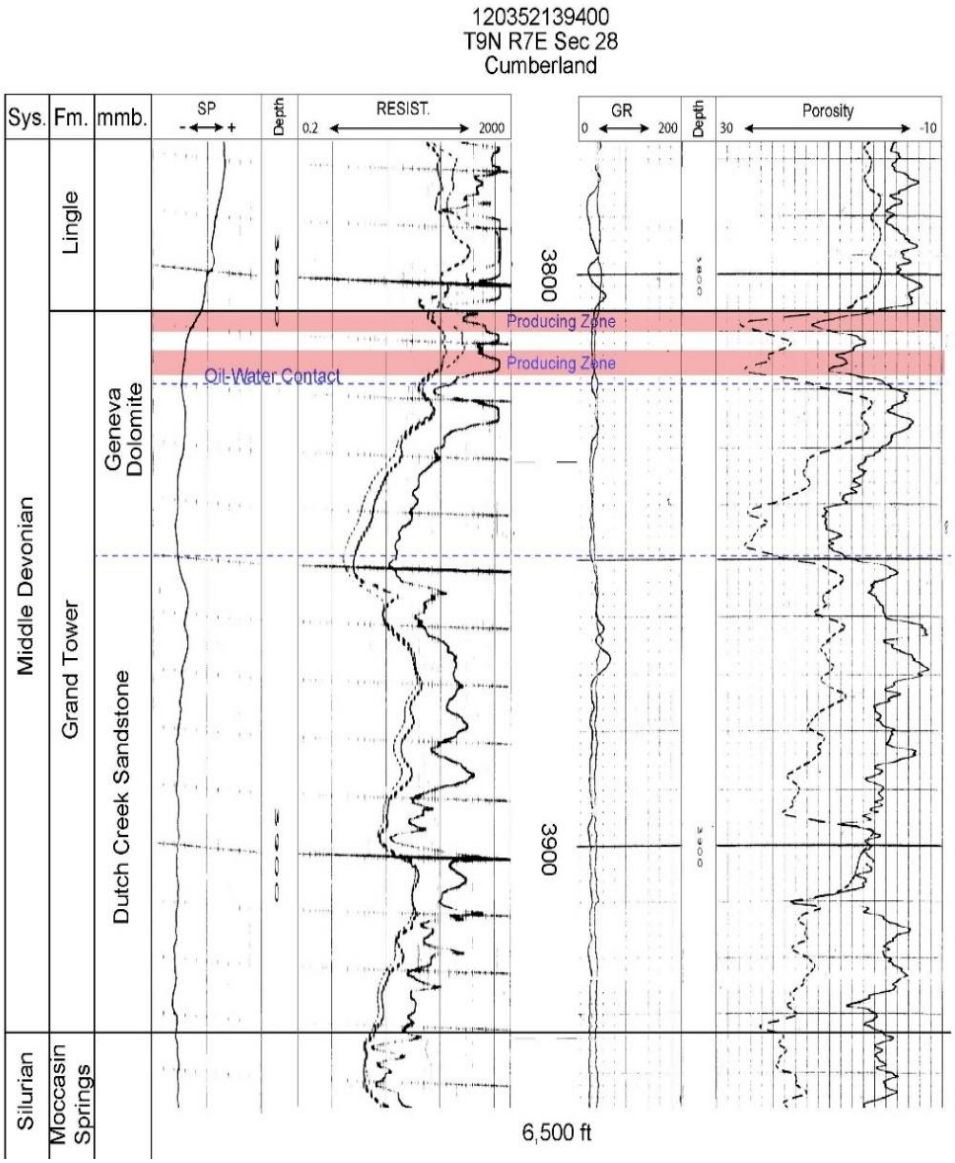


Figure 2-4. Geneva Dolomite type log in the Lillyville Field, Cumberland County.

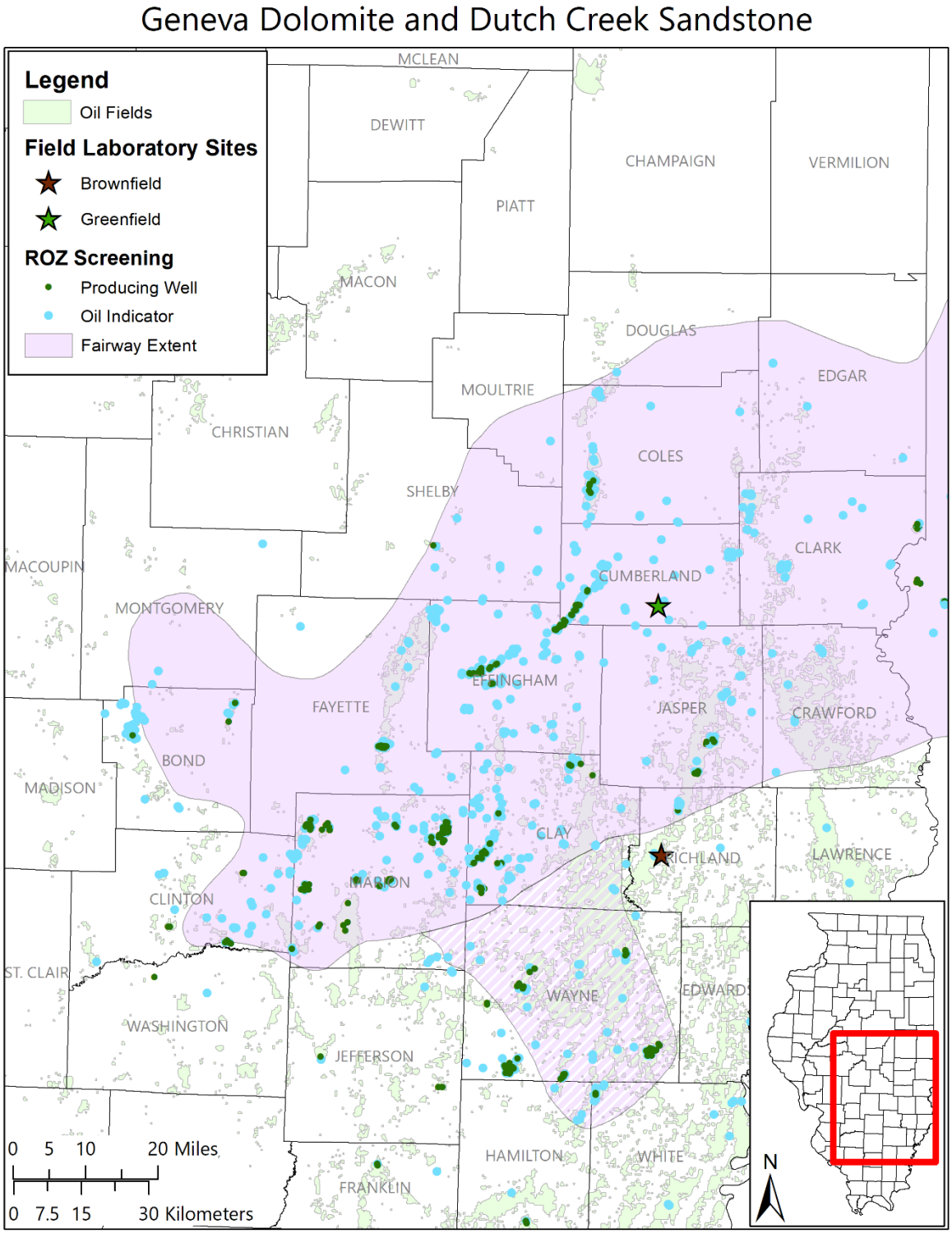


Figure 2-5. Map showing distribution of oil indicators in the Geneva Dolomite and Dutch Creek Sandstone overlaid with wells producing oil from both zones. The extent of porous and permeable rock for the Geneva is shaded in purple and the extent for the Dutch Creek Sandstone is striped (based on Meents and Swann, 1965; Seyler et al., 2003).

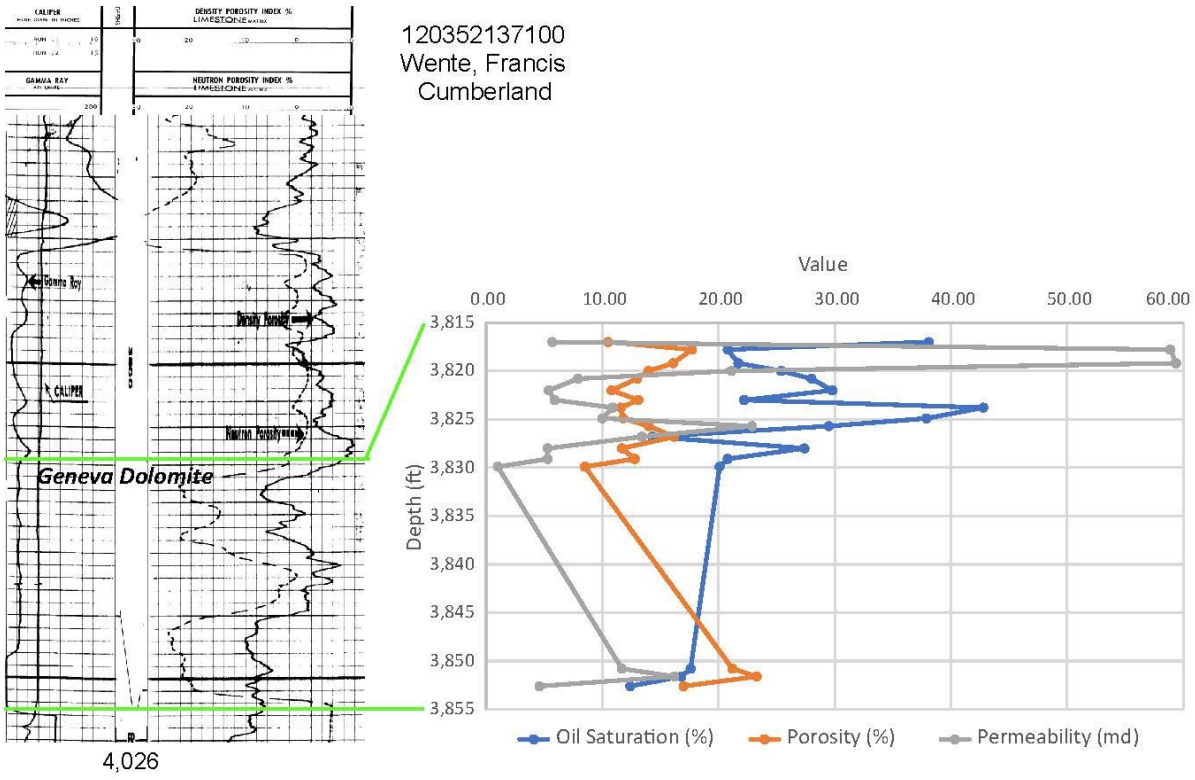


Figure 2-6. Example of Geneva Dolomite core analysis from Wente #1 well (API 120352137100), Cumberland County.

Ullin and Salem Limestone

The Ullin and Salem limestones (Middle Mississippian) consist of a pair of limestone units that reflect progressively shallowing carbonate deposition within the ILB. The lower part of the Ullin is up to 185 m (607 ft) thick, varies in thickness inversely with the underlying Fort Payne Formation, and is absent where the Fort Payne reaches its maximum thickness (Figure 2-8). The upper part of the Ullin Limestone is up to 60 m (197 ft) thick and is relatively uniform in thickness but thins somewhat toward the basin center. The upper Ullin occurs across the ILB, overlying the lower Ullin (where present) and the Fort Payne Formation. The Ullin Limestone is directly overlaid by the Salem Limestone.

Overall, the Ullin Limestone is composed of light to medium gray, fine-grained skeletal mudstone to wackestone, with beds of bryozoan and crinoid-rich grainstone and packstone (Lineback and Cluff, 1985). The Ullin Limestone contains 1) Waulsortian-type carbonate mound complexes, 2) transported mound-like to lenticular bryozoan-crinoid sand piles (packstones to grainstones), and 3) storm-generated sandwaves (Lasemi et al., 1994). Oil reservoirs typically develop in the bioclastic grainstone sandwave facies within the upper Ullin Limestone (Lasemi et al., 1998). Hydrocarbon traps occur in tectonic structures, but also occur in areas where bryozoan-crinoidal bioherms and, in some cases, carbonate mud mounds, develop positive structures over which porosity zones in the overlying units drape. The Salem Limestone (Figure 2-8) is a bioclastic, oolitic limestone consisting of several shallowing-upward sequences (Cluff and Lineback, 1981).

Oil production and oil indicators from both formations are well distributed across the south-central portion of the ILB. Over 250 wells have produced oil from Ullin, and 1,174 have produced oil from the Salem Limestone (Figure 2-7). Both units occur and are oil productive at the brownfield site. The Salem Limestone is present at the greenfield site.

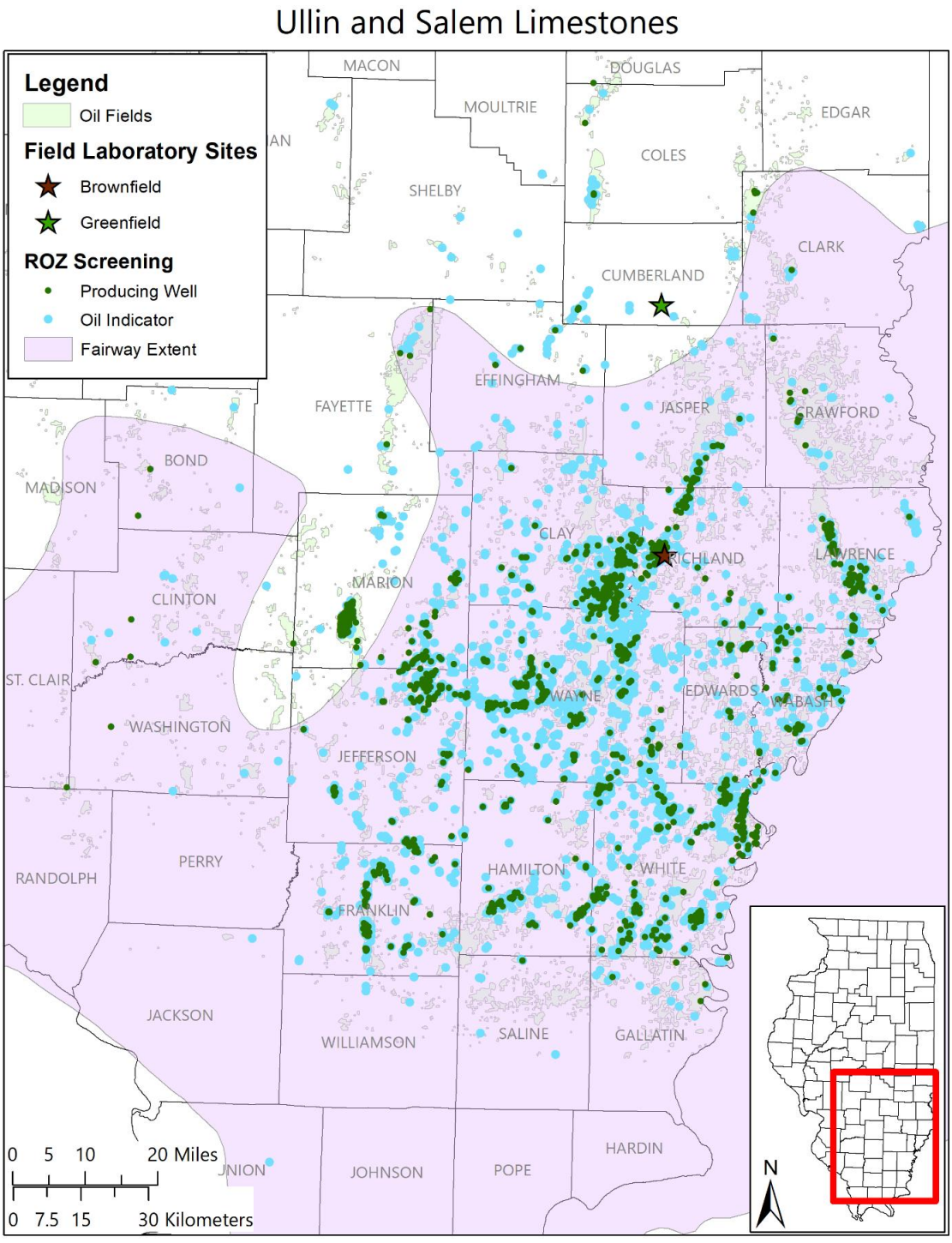


Figure 2-7. Map showing distribution of oil indicators in the Ullin and Salem Limestones overlaid with wells producing oil from the Ullin and Salem Limestones. The extent of the Ullin Limestone is shaded in purple (based on Lineback, 1966).

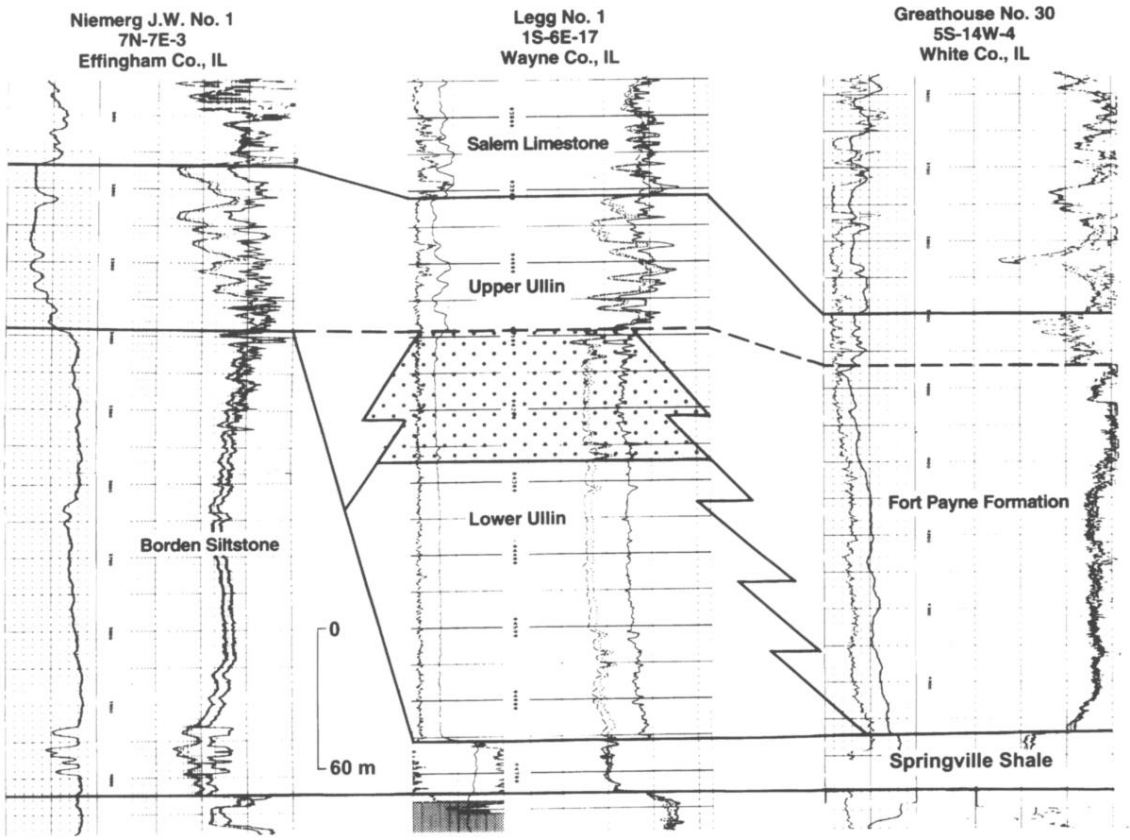


Figure 2-8. Three-well cross section showing the typical log signature and correlations of the upper Ullin into the Salem Limestone. Also shown is the complex stratigraphic relationship among the Borden Siltstone, lower Ullin Limestone, and Fort Payne Formation. The upper Ullin into the overlying Salem Limestone is the focus of the ROZ screening effort. From Lasemi et al. (1998).

Siliciclastic Formations

Tar Springs Sandstone

The Tar Springs Sandstone (Upper Mississippian) was deposited across Illinois, southwestern Indiana, and western Kentucky as a tidally influenced, river-dominated delta (Morse, 2001). The Tar Springs Sandstone, like the Cypress Sandstone, is thick and persistent across the ILB. It conformably overlies the Glen Dean Limestone and underlies the Vienna Limestone (Morse, 2001) (Figure 2-9). The Tar Springs Sandstone is 23 to 40 m (75 to 130 ft) thick for most of its extent across Illinois (Figure 2-10) and, locally, may reach a thickness exceeding 46 m (150 ft) (Willman et al., 1975). The formation is either almost entirely sandstone or almost entirely shale, with local, thin beds of coal. The sandstone is white to light gray, very fine- to fine-grained, locally medium-grained, angular, and friable to well-cemented. A conglomerate with coarse sand grains and limestone pebbles occurs at the base but is rare.

The Tar Springs Sandstone is produced from stacked, distributary channel sandstone reservoirs. Most Tar Springs oil production occurs in southeastern Illinois in oil fields along the Wabash River. Typical reservoir porosity ranges from 16% to 19%, and permeability ranges from 60 to 700 millidarcies (Morse, 2001). Out of more than 1,290 Tar Springs oil producing wells in Illinois, fewer than nine wells have been producing oil in Richland County. A cross section shows the typical log characteristics of the Tar Springs Sandstone and oil reservoirs near the brownfield lab site in Richland County (Figure 2-9). The Tar Springs is present at the greenfield site.

Spar Mountain Sandstone

The Spar Mountain Sandstone Member (also informally referred to as the Rosiclare sandstone) of the Ste. Genevieve Limestone (Middle Mississippian) is named after Spar Mountain, Hardin County, where the type section consists of 2.4 to 4.6 m (8 to 15 ft) of light gray to greenish gray, calcareous, glauconitic sandstone or siltstone grading to very sandy limestone (Atherton et al., 1975). The Spar Mountain underlies the Karnak Member of the Ste. Genevieve Limestone (Figure 2-11) and extends across much of the ILB. The thickest and most continuous deposits of the Spar Mountain Sandstone occur in the north-central portion of the ILB (Leetaru, 2000) (Figure 2-12).

Oil production from the Spar Mountain Sandstone is well distributed across the ILB (and generally is outside of the boundary of thick, continuous sandstone, where it occurs in more compartmentalized reservoirs). Out of more than 700 Spar Mountain oil producing wells in Illinois, about 65 wells have been producing oil in Cumberland and Richland Counties; most of these wells are in Richland County. The Spar Mountain isopach map shows a north-south trend through the central portion of Illinois (Leetaru, 2000) (Figure 2-12). There is significant thinning of the Spar Mountain Sandstone to the East and West. The map of the Spar Mountain Sandstone shows its distribution relative to the field laboratory sites (Figure 2-12).

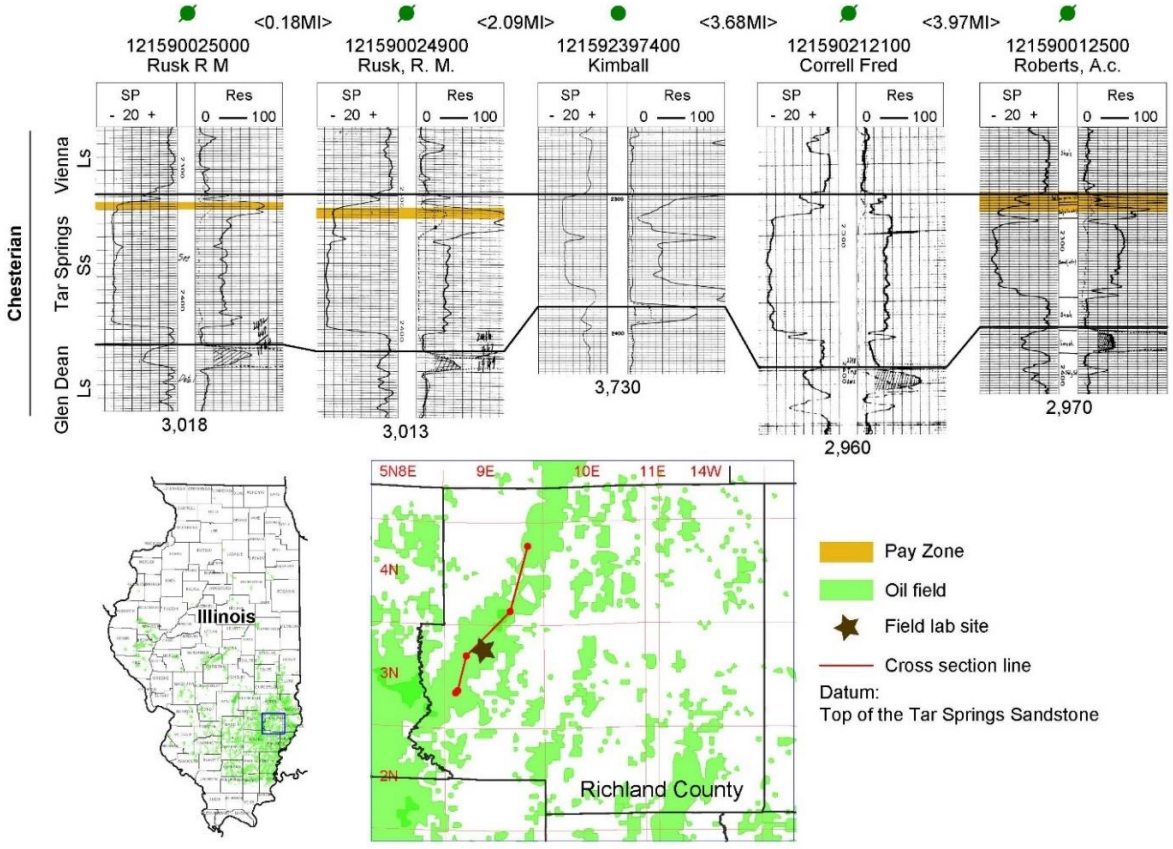


Figure 2-9. Stratigraphic cross section flattened on top of the Tar Springs Sandstone in the Clay City Consolidated oil field.

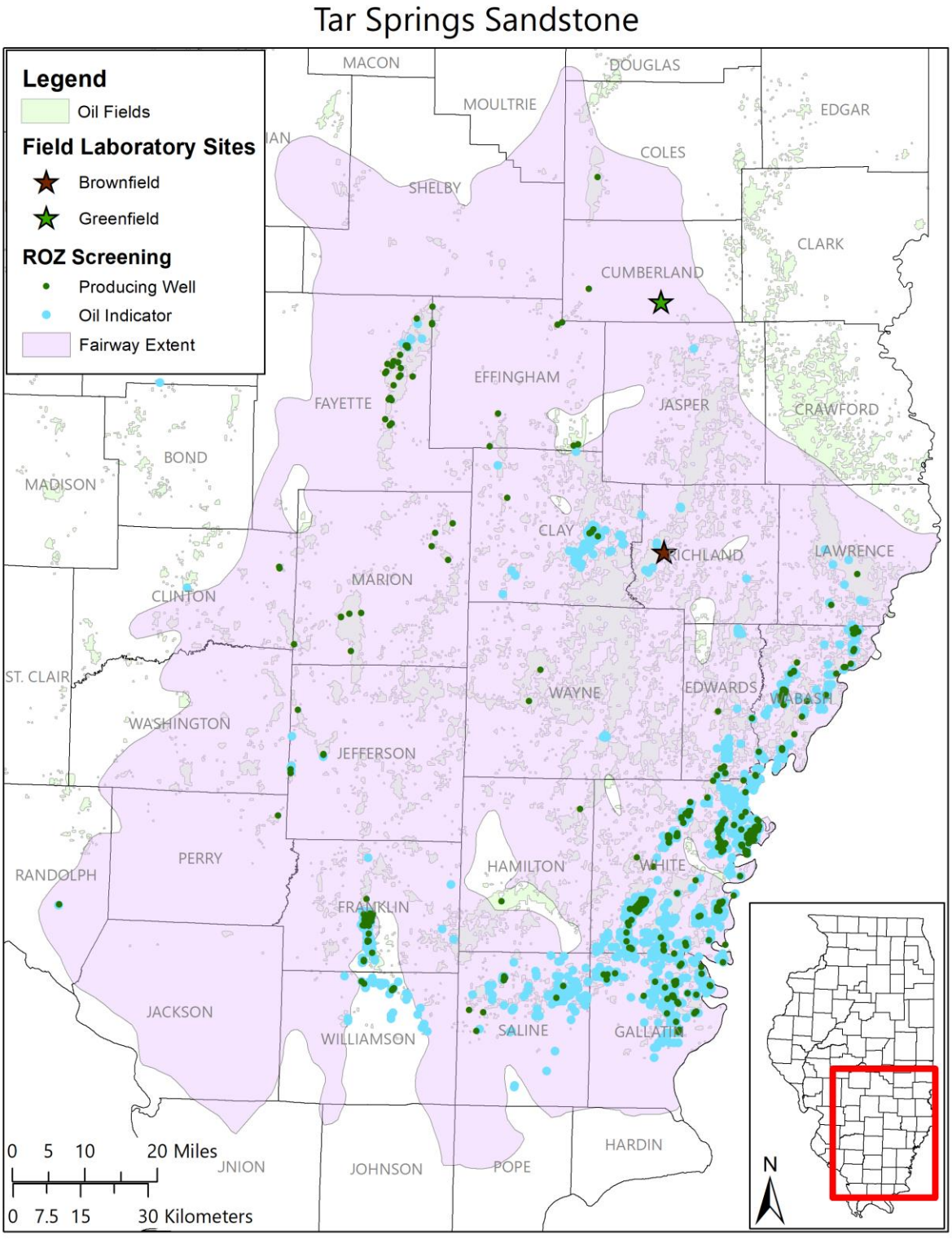


Figure 2-10. Map showing the distribution of oil indicators in the Tar Springs Sandstone overlaid with wells producing oil from the formation. The extent of the Tar Springs Sandstone is shaded in purple (based on Morse, 2001).

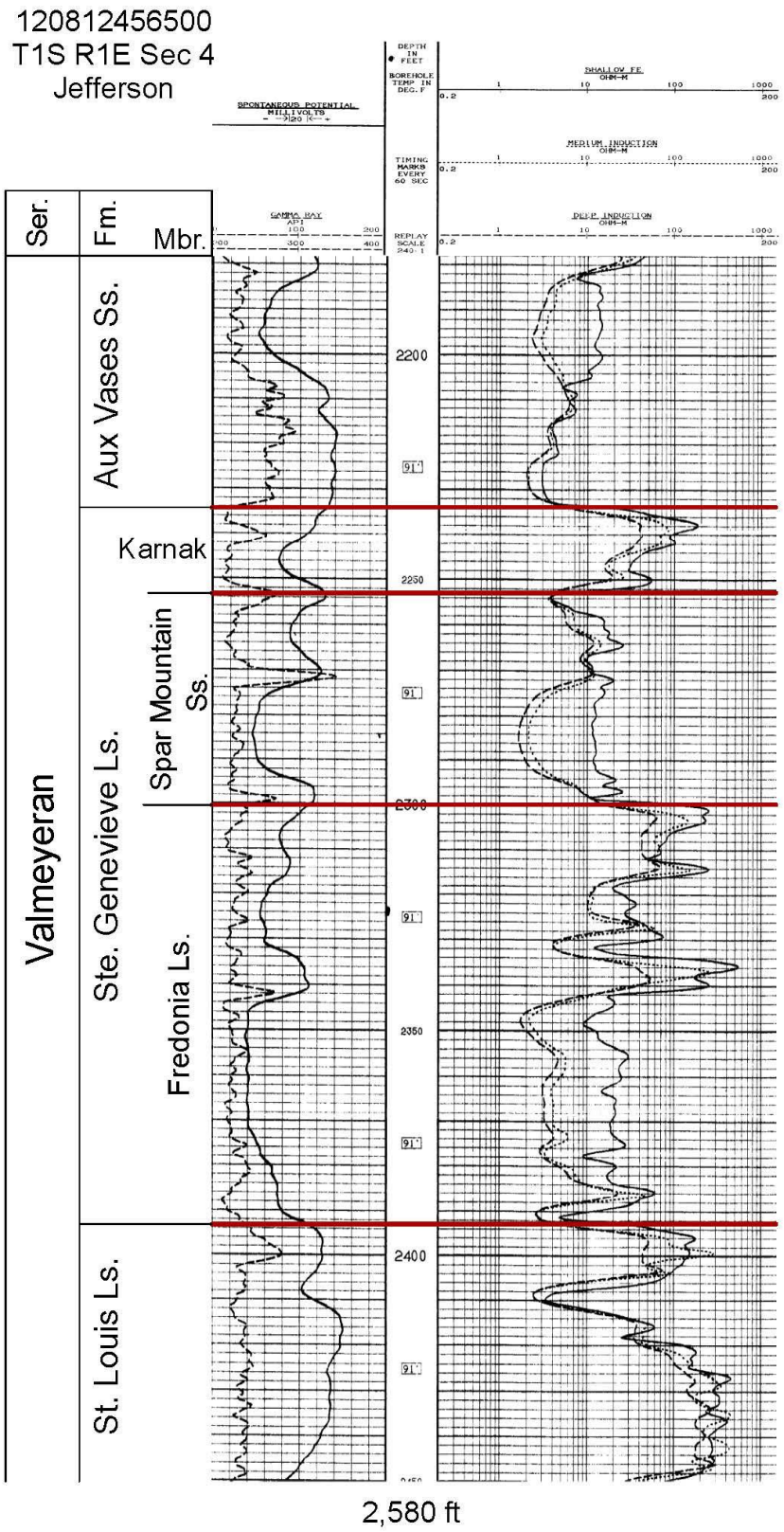


Figure 2-11. Log showing the typical presentation of the Spar Mountain Sandstone.

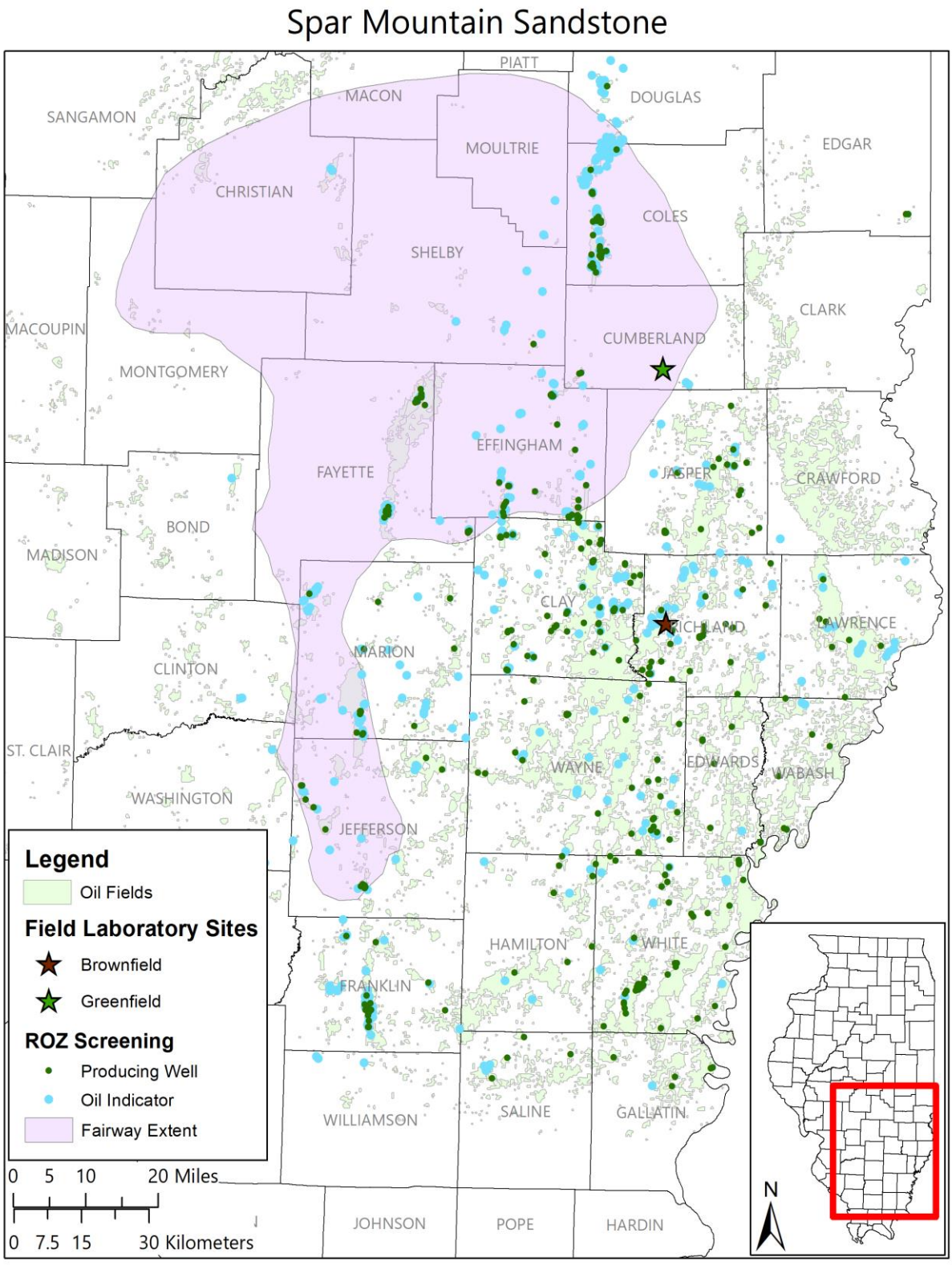


Figure 2-12. Map showing the distribution of oil indicators in the Spar Mountain Sandstone overlaid with wells producing oil from the formation. The extent of porous and permeable rock for the Spar Mountain is shaded in purple (based on Leetaru, 2000).

Cypress Sandstone

The Cypress Sandstone (Upper Mississippian) is a dominantly siliciclastic unit that contains the most prolific oil reservoirs in the ILB. Cypress Sandstone bodies (Figure 2-13) up to 60 m (200 ft) thick define a northeast-southwest trend that is approximately 230 km (140 mi) long and 100 km (60 mi) wide across the central portion of the ILB (Figure 2-14). These sandstones commonly contain relatively thin oil reservoirs and, as part of a comprehensive study of the nonconventional CO_2-EOR opportunities of the thick Cypress Sandstone, were found to have widespread associated ROZs (Webb et al., 2019).

The Cypress Sandstone is composed of thick sandstone in some areas and is shale-interbedded with numerous lenticular, well-cemented sandstone bodies in others. The Cypress Sandstone is predominantly sublitharenitic and subarkosic in composition (Pitman et al., 1998). Two mostly parallel, northeast-southwest trending clastic belts composed of generally thick sandstone bodies are found within the Cypress Sandstone and are thought to represent fluvial systems (Nelson et al., 2002).

The fluvial facies of the Cypress Sandstone are between 30 and 60 m (100 and 200 ft) thick (Figure 2-13) but thins and changes facies to the East and West (Willman et al., 1975). These sandstones are sometimes referred to as the “massive,” “main,” or “lower” Cypress Sandstone in literature and drilling records, and are commonly overlaid by thin, lenticular sandstone bodies encased in shale (Fituri, 1987).

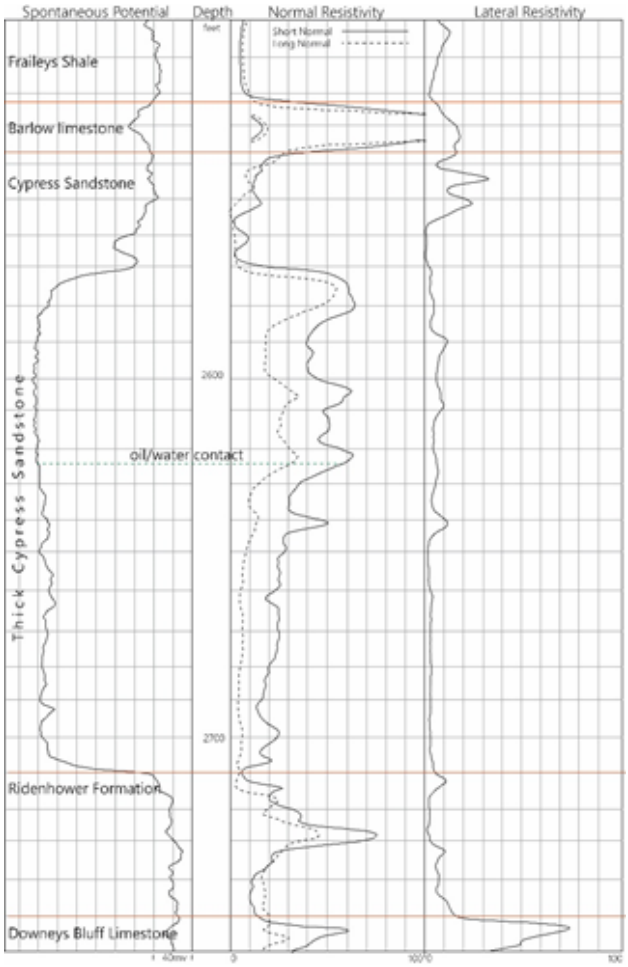


Figure 2-13. Example geophysical logs from Noble Field (left) showing the fluvial facies of the Cypress Sandstone as well as the presence of an oil zone developed in the top of the formation, as indicated by the higher resistivity values.

The fluvial Cypress Sandstone features generally fining-upward sequences, characteristic of their interpreted deposition as bar deposits in fine-grained channel belts. Permeability increases at channel bases as a function of coarsening grain size within typical reservoir units (Howell, 2017). In outcrops, this facies exhibits stacked, imbricate sand bars (Cole and Nelson, 1995). Coarse lag deposits of marine fossil hash in the bases of channels indicate a close proximity to marine/estuarine conditions (Seyler et al., 2000). Regional characterization has shown that the thick, multistory fluvial facies of the Cypress Sandstone exhibits porosity from 15% to 21%, and horizontal and vertical permeability up to approximately 0.98 μm^2 (1,000 mD).

Oil production from thick sandstones in the central part of the ILB is relatively sparse, as most production comes from the tidal bar facies along the eastern border of Illinois, outside of the thick, porous, and permeable sandstone trend. Within the thick sandstone trend, the majority of mapped oil production is derived from thin sandstone lenses that overlie the thick Cypress Sandstone, though thin oil zones are a common feature in the top of thick Cypress Sandstone deposits (Figure 2-13). The presence of a thick brine aquifer underlying the ROZ and high vertical permeability results in characteristically low primary oil recovery caused by excessive brine production from the aquifer. As the leading oil producing formation in the ILB, over 1,950 wells produce oil from the Cypress Sandstone. There are 110 wells with core available for study, and more than 1,500 wells with core analysis data from the Cypress Sandstone.

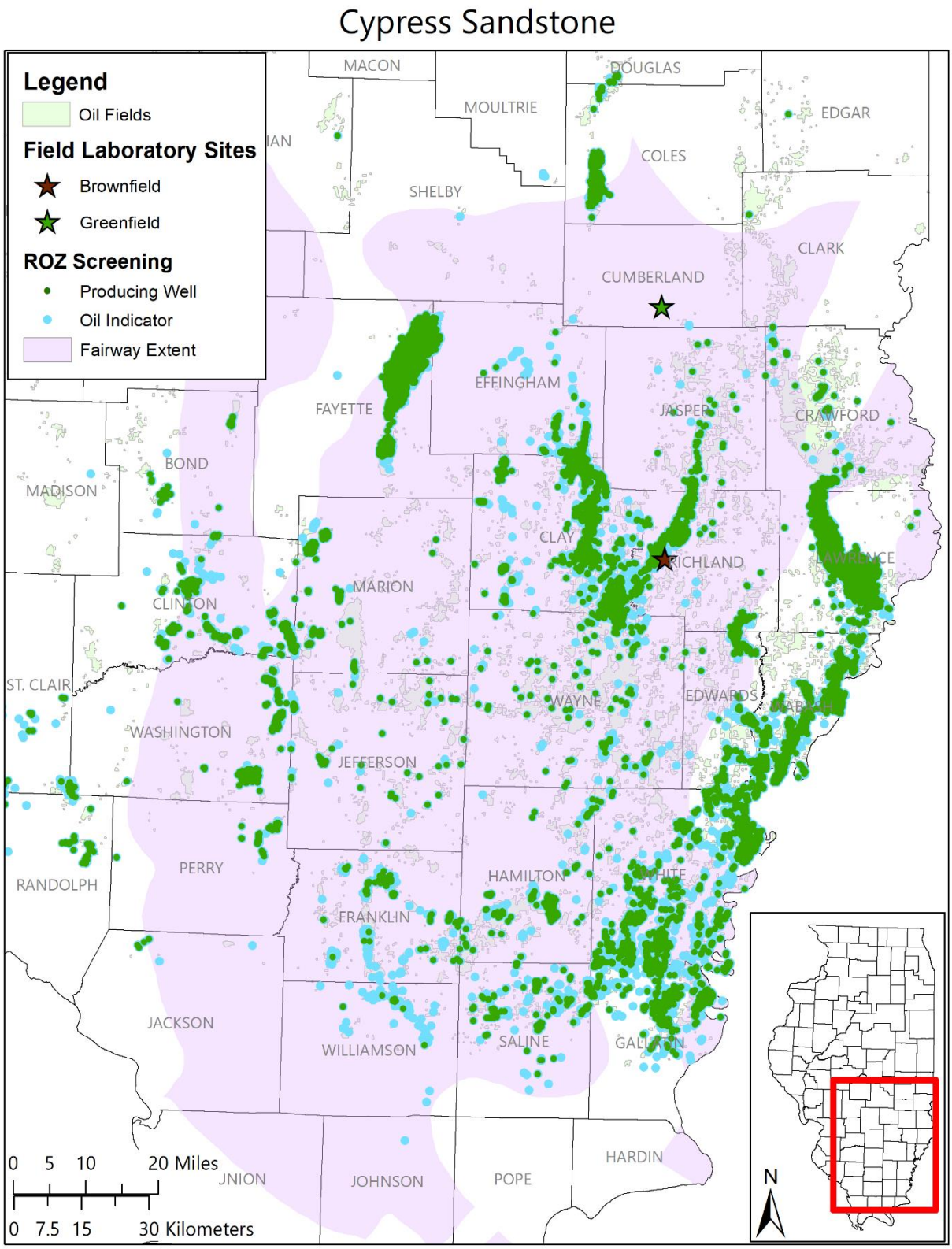


Figure 2-14. Map showing the distribution of oil indicators in the Cypress Sandstone overlaid with wells producing oil from the formation. The extent of the thick Cypress Sandstone is shaded in purple (based on Webb et al., 2019).

Carper Sandstone

The Carper Sandstone forms discrete sandstone lobes within the thick Borden Siltstone (Lower to Middle Mississippian) delta deposits in the northern part of the ILB. The Borden Siltstone forms a tongue-shaped body, extending in a southwest direction across central and southern Illinois, that is 120 to 210 m (400 to 700 ft) thick (Swann et al., 1965). The Carper Sandstone bodies within the Borden Siltstone have been interpreted as the deposits of turbidites. They are composed of very fine-grained quartz sandstone that is well sorted and exhibits graded bedding (Lineback, 1968).

Mapping of the Borden Siltstone interval between the underlying Kinderhookian (Lower Mississippian) Chouteau Limestone and the overlying Valmeyeran (Middle Mississippian) carbonates illustrates a large area of deeper water clastics deposition than is normally associated with the ILB (Figure 2-15). The Borden Siltstone contains large volumes of clay, particularly in the lowermost portions of the formation near the contact with the Chouteau Limestone.

The Carper Sandstone consists of bodies of very fine-grained sandstone to coarse silt that are up to approximately 30 m (100 ft) thick. The Carper Sandstone occurs in isolated lenses located near the base of the Borden Siltstone with 6 to 15 m (20 to 50 ft) of dark grey Springville Shale separating it from the underlying Chouteau Limestone. These stratigraphic relationships are shown in the cross section in Figure 2-15. The Chouteau Limestone directly overlies the Devonian New Albany Shale, a black, organic-rich shale that is likely the major source rock in the ILB (Barrows and Cluff, 1984).

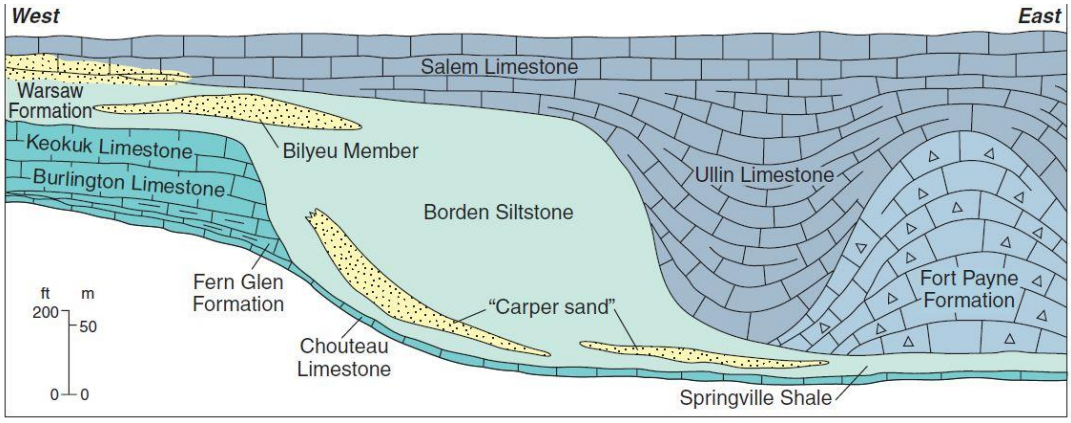


Figure 2-15. Regional cross section illustrating the stratigraphic and vertical relationship of Carper sandstone bodies within the Borden Siltstone (Devera et al., 2011).

The Borden Siltstone has been interpreted as a deltaic deposit, extending across east-central and southwestern Illinois with the source of sediments located far to the northeast (Figure 2-16). Previous research mapped the Borden Siltstone delta using electric log characteristics, where topset, foreset, and bottomset beds were identified within the delta (Lineback, 1968). A series of five separate sandstone accumulations comprise the Carper A, B, C, D, and E sandstones (Figure 2-16). These discontinuous sandstone bodies are composed of extremely fine-grained sandstone and are located near the base of the Borden Siltstone in some areas of central and east central Illinois and near the top in others (Figure 2-16; Lineback, 1968). Carper Sandstones are sandy facies located within finer-grained dark shales that make up the bottomset beds of the Borden delta. The sand accumulated on the foreset slope of the Borden Siltstone delta off the mouths of major distributaries (Lineback, 1968). According to the deltaic deposition model, sand and other clastics were moved downslope in turbidity currents that carried the sand across the prodelta plain and eventually deposited it as submarine fans.

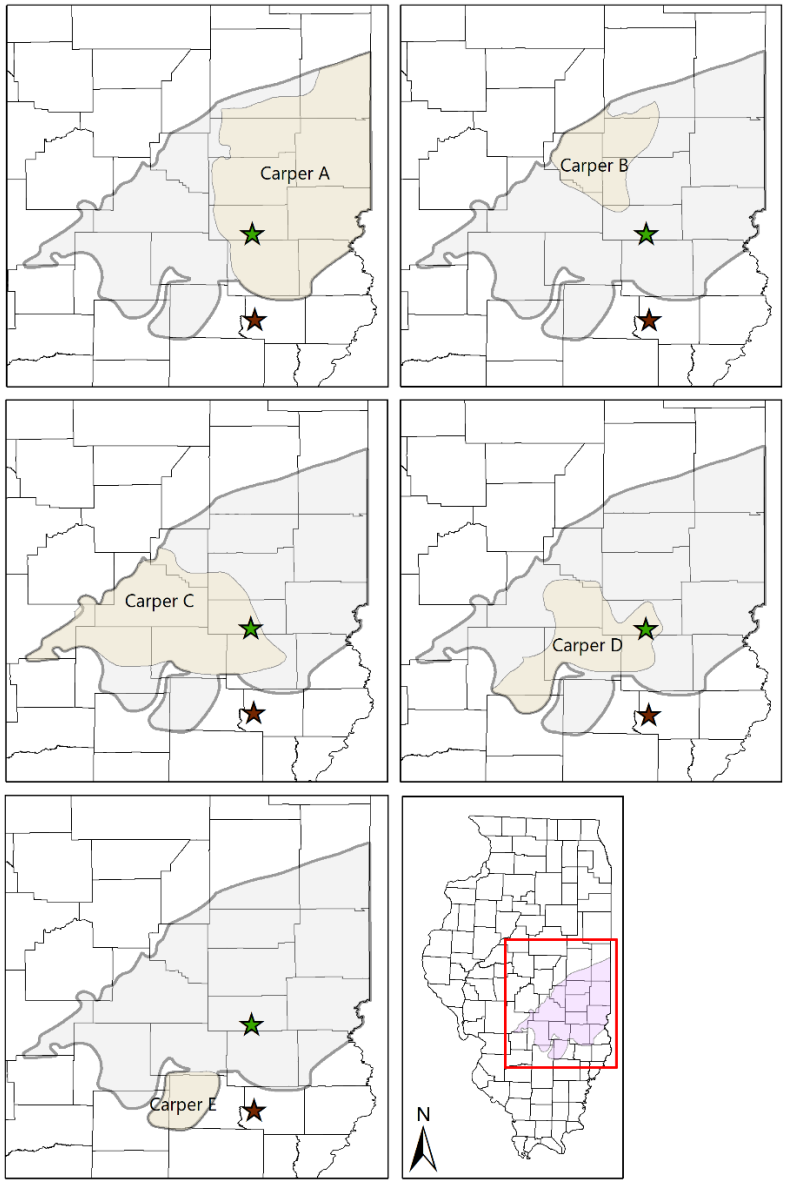


Figure 2-16. Series of maps showing the distribution of each lobe of the Carper Sandstone (A, B, C, D, and E) within the overall boundary of Carper deposition (modified from Lineback, 1968).

Carper Sandstone bodies located in the lower portion of the Borden Siltstone are localized and usually fan shaped (Figure 2-16). Carper Sandstone deposits are lenticular in transverse cross sections; however, in longitudinal cross sections, the bottom surface slopes upward with respect to the base of the Borden Siltstone in one direction and slopes downward, closer to the base, in the other. Downslope, the geometry of Carper Sandstone bodies thin and pinch out. Upslope, the sandstone body may thicken (Figure 2-15; Lineback, 1968). Several Carper Sandstone bodies were recognized and mapped in the Borden Siltstone. The interpretation of deposition by turbidity currents was based on the geometry of mapped Carper Sandstone bodies, their stratigraphic position, and the graded bedding of the lowermost bottomset sandstone bodies (Lineback, 1968). These maps illustrate several episodes of turbidite submarine fan deposition within the Borden Siltstone.

The Carper Sandstone's depositional trend arcs across the northern portion of the ILB, with a footprint similar to that of the Geneva Dolomite. Oil production occurs mainly in a handful of fields that are situated on anticlines, but oil indicators are common outside of established oilfields. At least 233 wells have produced oil from the Carper Sandstone. Core analysis data is available for 78 wells and 19 wells have core available for study.

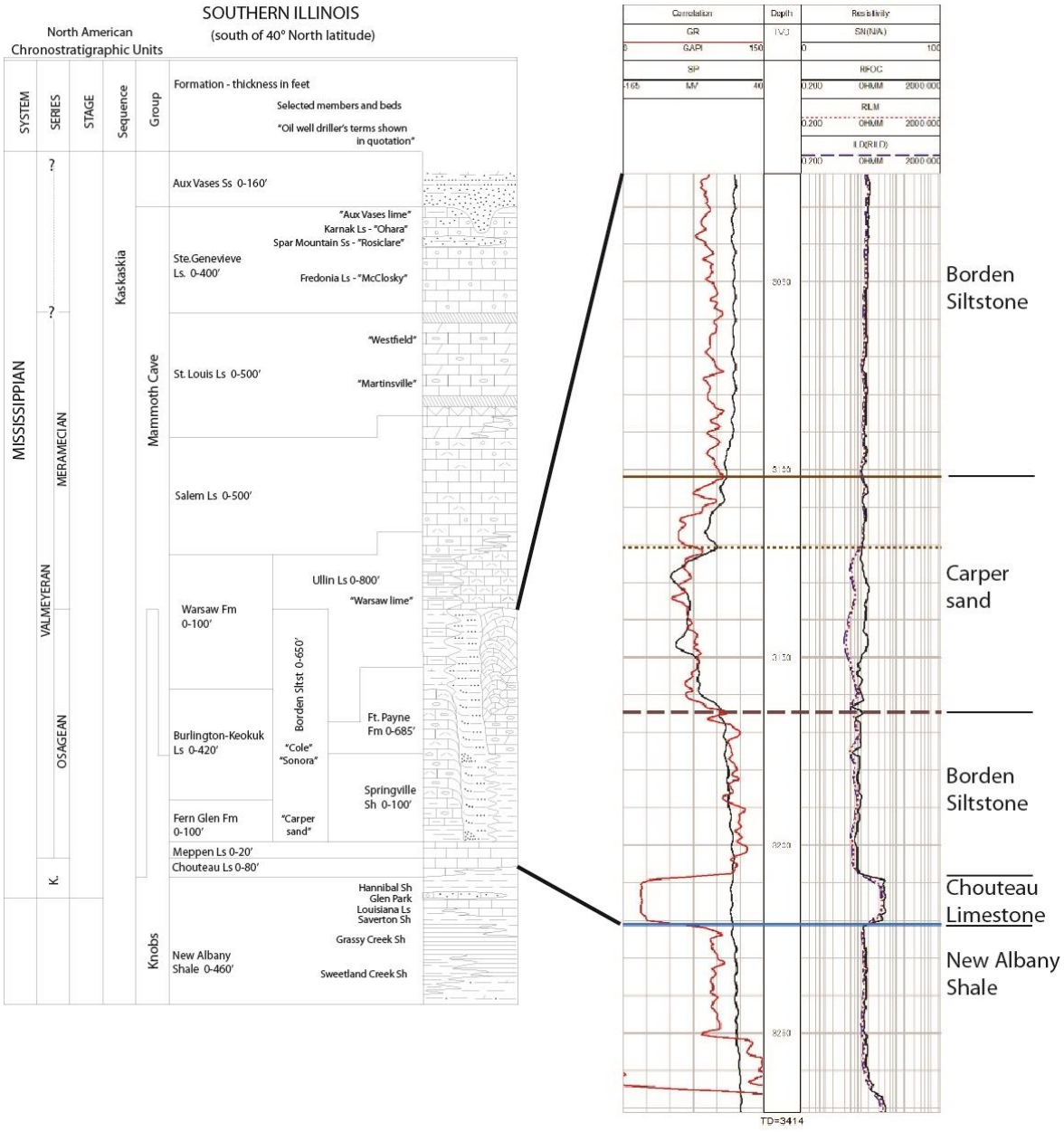


Figure 2-17. Left: Portion of the generalized stratigraphic column for Illinois. Rocks below the New Albany Shale and above the Aux Vases Sandstone are not shown. Formal formation names are listed, along with gross thicknesses of the formations. Oil industry terms are listed in quotes. Right: Type log of the Kistler Unit #19 Well (API 120512794100) showing the interval that was used to map the Carper Sandstone reservoir in St. James Field.

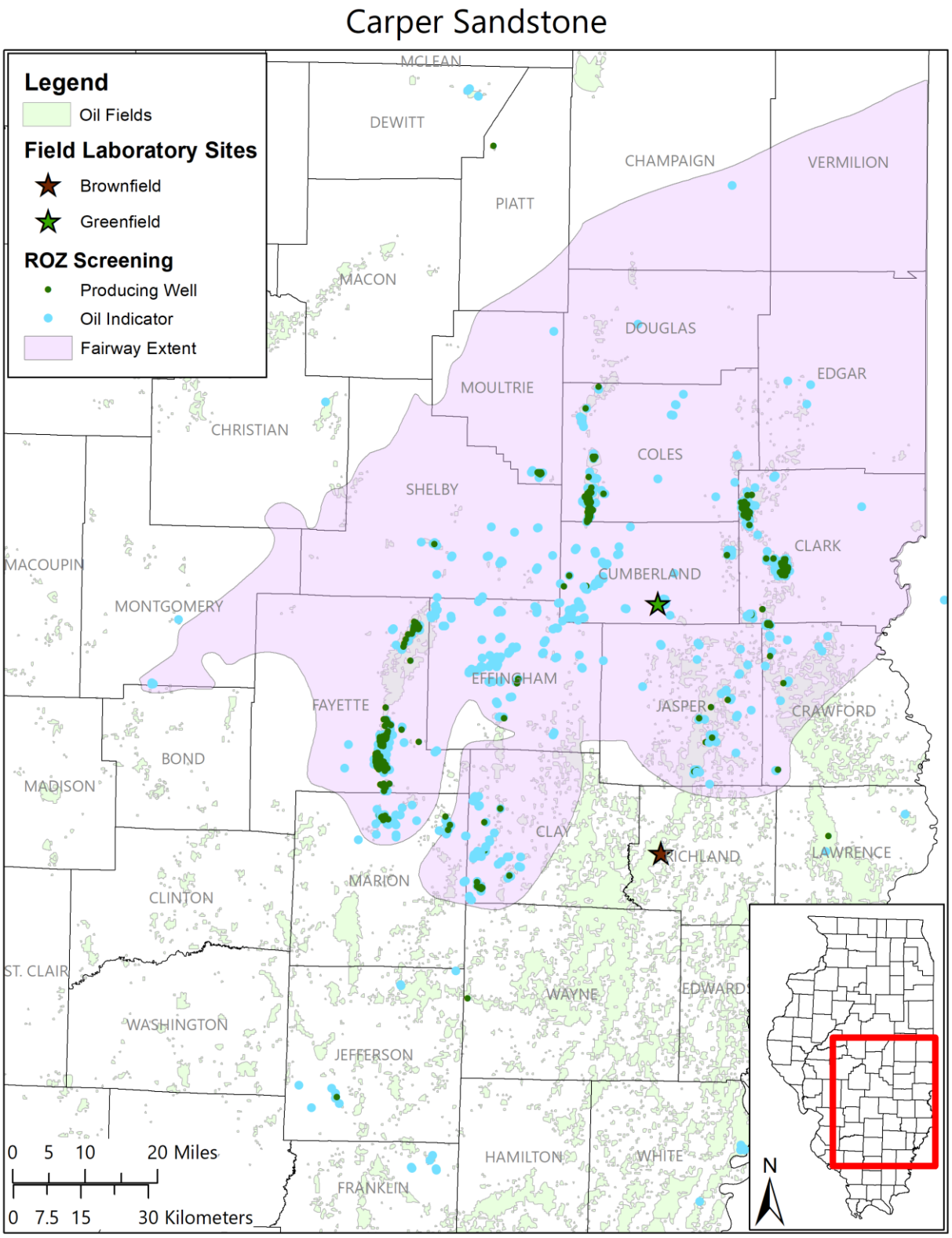


Figure 2-18. Map showing the distribution of oil indicators in the Carper Sandstone overlaid with wells producing oil from the formation. The extent of Carper Sandstone deposition is shaded in purple (based on Lineback, 1968).

Yankeetown and Bethel Sandstone

The Yankeetown (Benoist) Sandstone (Upper Mississippian) is an oil-producing horizon in south-central Illinois that has been used for natural gas storage (Figure 2-20). The Benoist Sandstone, Yankeetown Chert, and Bethel Sandstone were miscorrelated until the 1950s, when the stratigraphic equivalency of the Benoist and Yankeetown was established. The Bethel and Benoist have similar wireline signatures and lithologies, and were therefore frequently confused (Leetaru et al., 2005).

The Benoist Sandstone is a subarkosic sandstone, deposited in a fluvial-deltaic coastal plain environment. It is relatively continuous and roughly 12 to 18 m (40 to 60 ft) thick with stratified layers of high and low permeability. The Benoist consists of two primary facies: 1) a laminated sandstone with flaser-to-lenticular bedding, and 2) a shale layer roughly 1.5 m (5 ft) thick, which separates the upper and lower reservoir zones. Facies identified in the Benoist include:

- conglomerate
- bryozoan-rich mudstone
- fossiliferous red shale
- slickensided mudstone
- bioturbated sandstone
- parallel-laminated to rippled sandstone
- contorted sandstone
- structureless to cross-bedded sandstone
- fractured sandstone
- calcareous mudstone

The Benoist is primarily a moderately to well-sorted, fine- to medium-grained quartz arenite, containing up to 5% potassium feldspar and up to 2% polycrystalline lithic chert grains. The original quartz grains were subrounded to subangular but were subsequently altered by quartz overgrowth cementation. The observed porosity in the Benoist reservoir facies is both primary and secondary (via dissolution). Some pores have been partially or completely occluded by calcite cement. Scanning electron microscopy indicated that individual sand grains were coated with clay minerals such as ferrous chlorite and illite (Widmyer at al., 1988).

Leetaru et. al. (2005) studied the Benoist Sandstone in six oil fields in Illinois: Boyd, Dix South, Salem, Centralia, Fairman, and Kinmundy North. They concluded that the reservoirs in five of the six studied fields are laterally discontinuous, and that many wells are required to determine the local lateral continuity of these reservoirs.

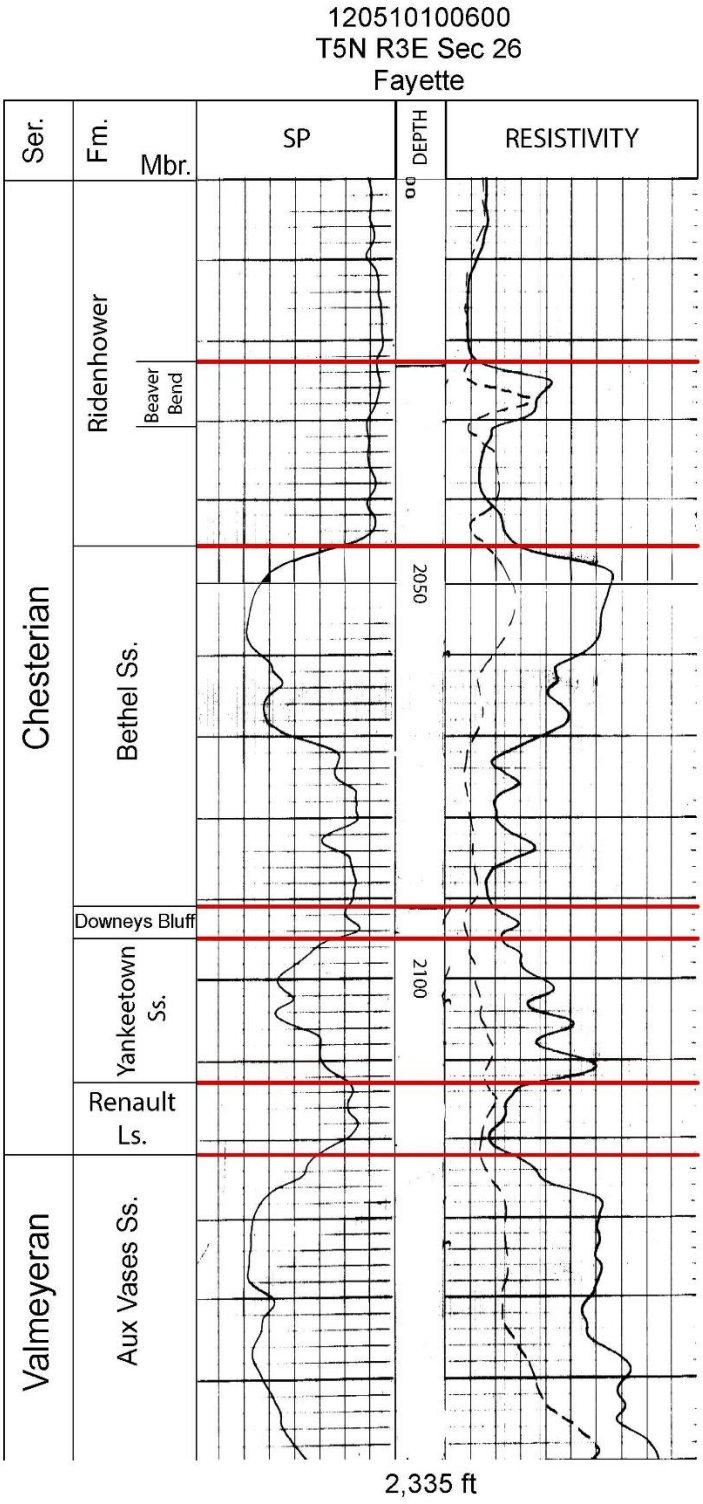


Figure 2-19. Type log showing an example well where both the Bethel and Yankeetown (Benoist) Sandstones are present.

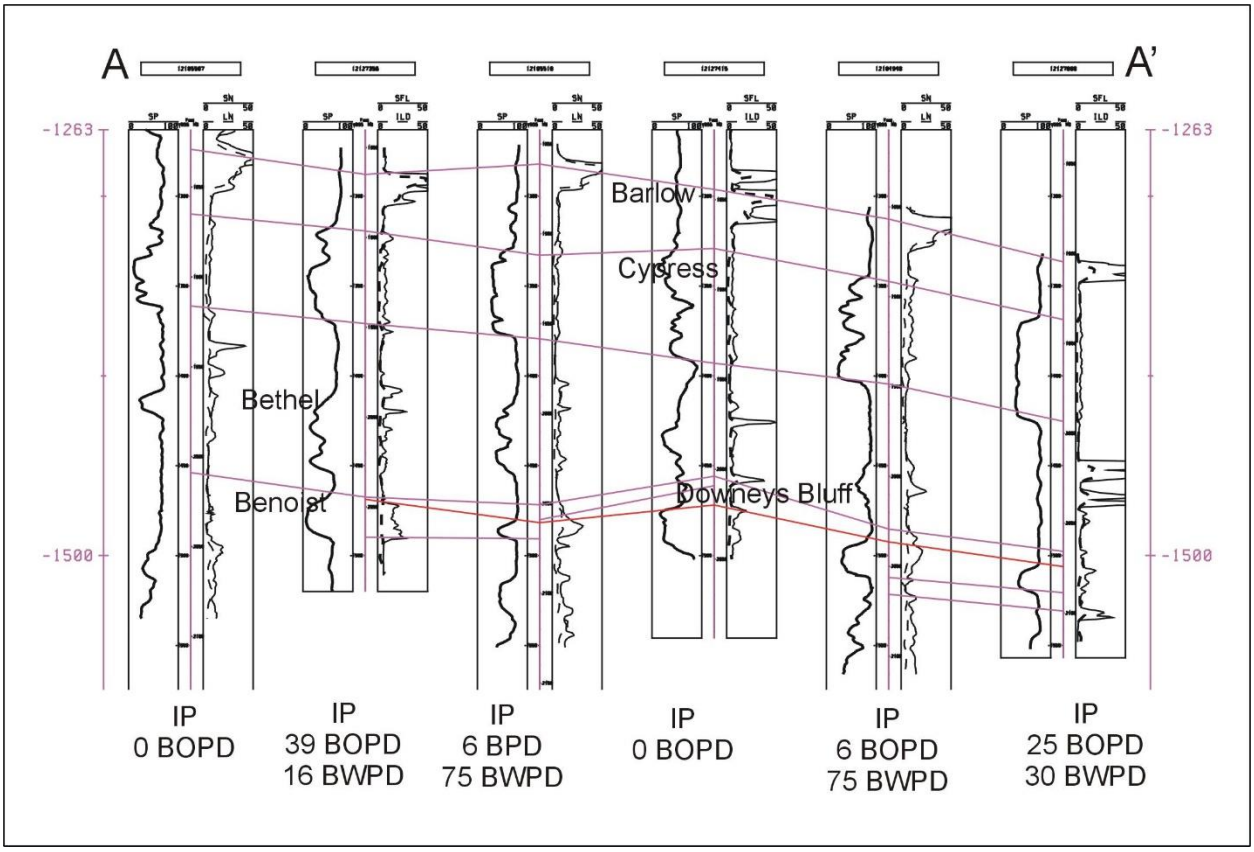


Figure 2-20. Example cross section from Kinmundy Field showing the relationship of the Bethel and Yankeetown (Benoist) Sandstones in an area where both are present.

The Bethel Sandstone is 6 to 12 m (20 to 40 ft) thick in the northwestern portion of its extent, but it is locally thinned by pre-Cypress erosion. It thickens to the southeast to just over 30 m (100 ft) in eastern Gallatin County (Figure 2-21).

The Bethel is primarily sandstone, but grades to shale in the west. It can locally contain small quartz pebbles and a basal conglomerate of limestone and shale pebbles. The sandstone is dominantly light gray to light greenish gray with a few lenses of green or medium gray. It commonly contains dark greenish to gray shale partings with occasional carbon and mica flakes. The presence of red and green shales increases as the Bethel grades westward to shale. These shale beds may range from a fraction of an inch to several feet thick. A persistently prominent bed of red clay about 15 ft thick is observed in southwestern Illinois.

The Bethel Sandstone is fine-grained and varies from white to brownish in color. Its grains are extremely well-sorted with high sphericity. The Bethel is generally poorly- to well-cemented with silica, with occasional calcareous lenses from the recrystallization of fossil remains; where well-cemented, the Bethel is lighter in color.

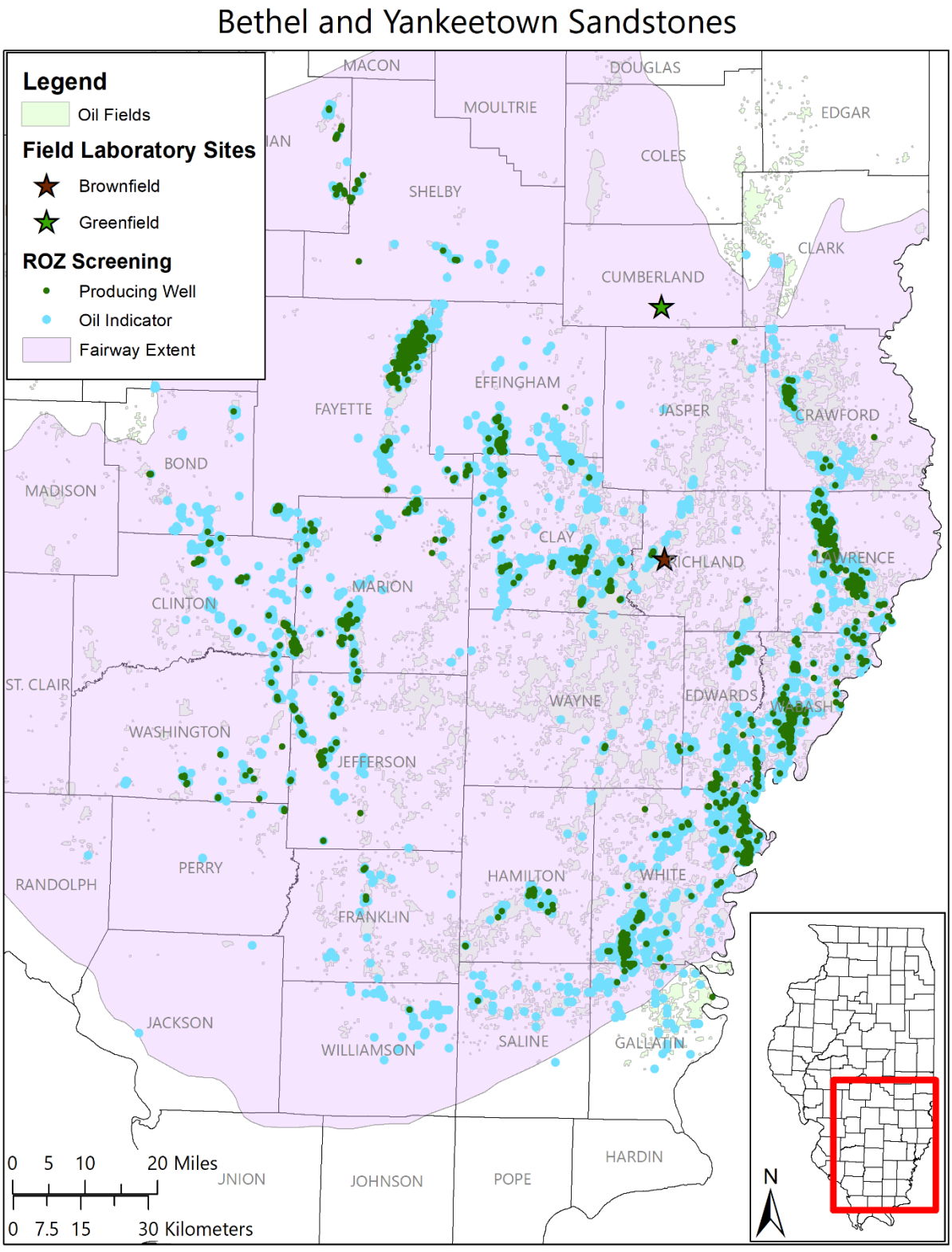


Figure 2-21. Map showing the distribution of oil indicators in the Bethel and Yankeetown Sandstones overlaid with wells producing oil from the formation. The extent of the Bethel and Yankeetown Sandstones is shaded in purple (based on Willman et al., 1975).

Selecting Formations for ROZ Resource Assessment

Screening multiple formations for their potential to contain ROZs highlights the utility of historical oil well records to understand the regional geology, ROZ indicators, and data availability. Although the ISGS digital oilfield database is incomplete, it is a useful tool for analyzing the extent of oil indicators across the ILB and allows for the identification of areas where oil is indicated but production is lacking. Digitizing additional well records and adding them to the database over time will ultimately decrease uncertainty in the existence of prospective ROZs.

All seven candidate formations have ROZ potential. Based on the analysis of available data, three formations have been selected for detailed regional characterization and analysis. The three formations are the Carper Sandstone (part of the Borden Siltstone), Tar Springs Sandstone, and Middle Devonian (Geneva Dolomite and associated Dutch Creek Sandstone) (Figure 2-22). A fourth formation, the Cypress Sandstone, was subjected to rigorous regional geologic characterization and ROZ resource assessment as part of a previous project (Webb et al., 2019). However, as the Cypress Sandstone is shallower than the Carper and Middle Devonian formations, and is stratigraphically near the Tar Springs Sandstone, there should be data pertaining to the Cypress in all wells that will be analyzed by this project. Thus, the Cypress Sandstone will be analyzed along with the selected formations, and any new data will serve to strengthen or expand upon the findings that are already available.

The Carper Sandstone is deeper than all the other candidate formations (save the Geneva/Dutch Creek). There are relatively few wells that reach the depth of the Carper, especially outside of oil fields, creating some uncertainty regarding the lateral continuity of Carper Sandstone bodies. This fact highlights the integral role that seismic reflection profiles will play during the regional characterization. However, well records document many oil shows in non-productive areas, especially in Cumberland, Effingham, and Shelby counties, where regionally extensive lobes of Carper Sandstone overlap (Figure 2-18). Also, as a low porosity/permeability, very fine-grained sandstone to coarse siltstone, the Carper provides a contrasting siliciclastic end member for the application of well log analyses compared to the previously studied Cypress, which is a clean sandstone and a nearly ideal Archie rock (i.e., petrophysically simple). Because the Carper is the subject of a CO_2 injection test at the greenfield field laboratory, it is obviously a high priority for regional characterization and resource assessment.

The Tar Springs Sandstone has ROZ potential in the southeastern ILB and, like the Cypress, is thick and widespread across much of the ILB. The occurrence of thin MPZs in the tops of the thick Tar Springs Sandstone (Figure 2-9) make the Tar Springs a direct analog for Cypress Sandstone reservoirs. Production difficulties from such reservoirs may mean that oil indicators are underreported in the central part of the ILB. The geologic similarities with the Cypress Sandstone make the Tar Springs Sandstone a natural choice for characterization and resource assessment.

The Geneva Dolomite/Dutch Creek Sandstone are widespread, porous, and permeable throughout the northern flank of the ILB (Figure 2-5). They are the deepest of the candidate formations, but wells that encounter them commonly have oil shows with no production. Many drill stem tests from the formations report sulfur water (including at Noble Field). The dolomite lithology makes the Geneva analogous to the San Andres Formation of the Permian Basin, where ROZs are prolific, as well as its association with the underlying Dutch Creek Sandstone make for an interesting mixed-lithology target for characterization and resource assessment.

In addition to exhibiting features–such as extensive, porous, and permeable rock–that are favorable for ROZ prospecting, the extent of each of the selected formations have a high degree of overlap, particularly in the northern flank of the ILB near the field laboratory sites (Figure 2-22). The overlap will allow for the direct investigation of the possibility of stacked ROZs, maximizing the utility of each well that will be analyzed. The Carper Sandstone and Geneva Dolomite/Dutch Creek Sandstones are stacked across much of the same area in the northern ILB (Figure 2-18, Figure 2-5). The Tar Springs Sandstone covers a much larger area of the ILB (Figure 2-10). Previous investigation of the Cypress Sandstone also identified several ROZ prospects concentrated in the north flank of the ILB (Webb et al., 2019). By focusing further geologic characterization on this specific area of the ILB, wells chosen to characterize the three selected formations will also contribute to better characterizing the Cypress Sandstone ROZ prospects that were previously defined.

Despite not being selected for regional characterization, the remaining candidate formations that were part of this screening were nevertheless found to have ROZ potential. The Ullin and Salem Limestones are also good ROZ prospects. The widespread Ullin/Salem Limestones exhibits extensive oil indicators. However, the proportion of oil shows to production is low (i.e., too many wells produced oil which indicates MPZ instead of ROZ presence). Similarly, the Yankeetown and Bethel Sandstones have widespread oil indicators and production, but the sandstone bodies themselves are thinner and less regionally continuous when compared to the Cypress or Tar Springs. The Spar Mountain Sandstone has indications of an ROZ in the northern ILB. Wells in Shelby, Effingham, and Coles counties that encounter the formation often have oil shows with no production. However, the distribution of porous and permeable sandstone is limited when compared against other formations. Although these formations were not selected for characterization as part of the regional resource assessment, they will be evaluated where they occur at the two field laboratory sites.

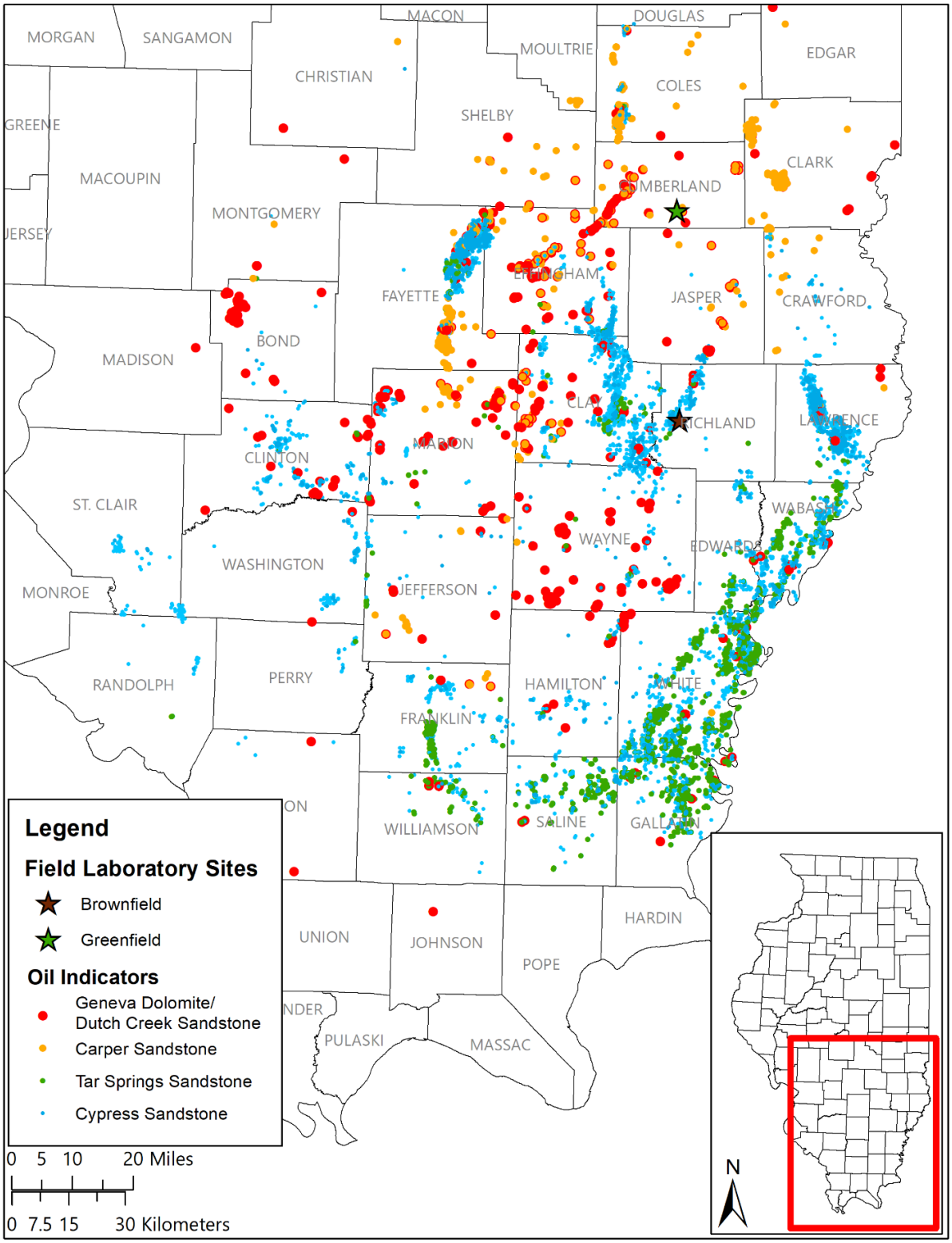


Figure 2-22. Map showing the distribution of wells with perforations or oil indicators from the three selected formations (and the Cypress Sandstone). Areas of significant overlap for all formations occur in the northern half of the mapped area. Overlap of the Cypress and Tar Springs sandstone occurs predominantly along the southeastern border of the state.

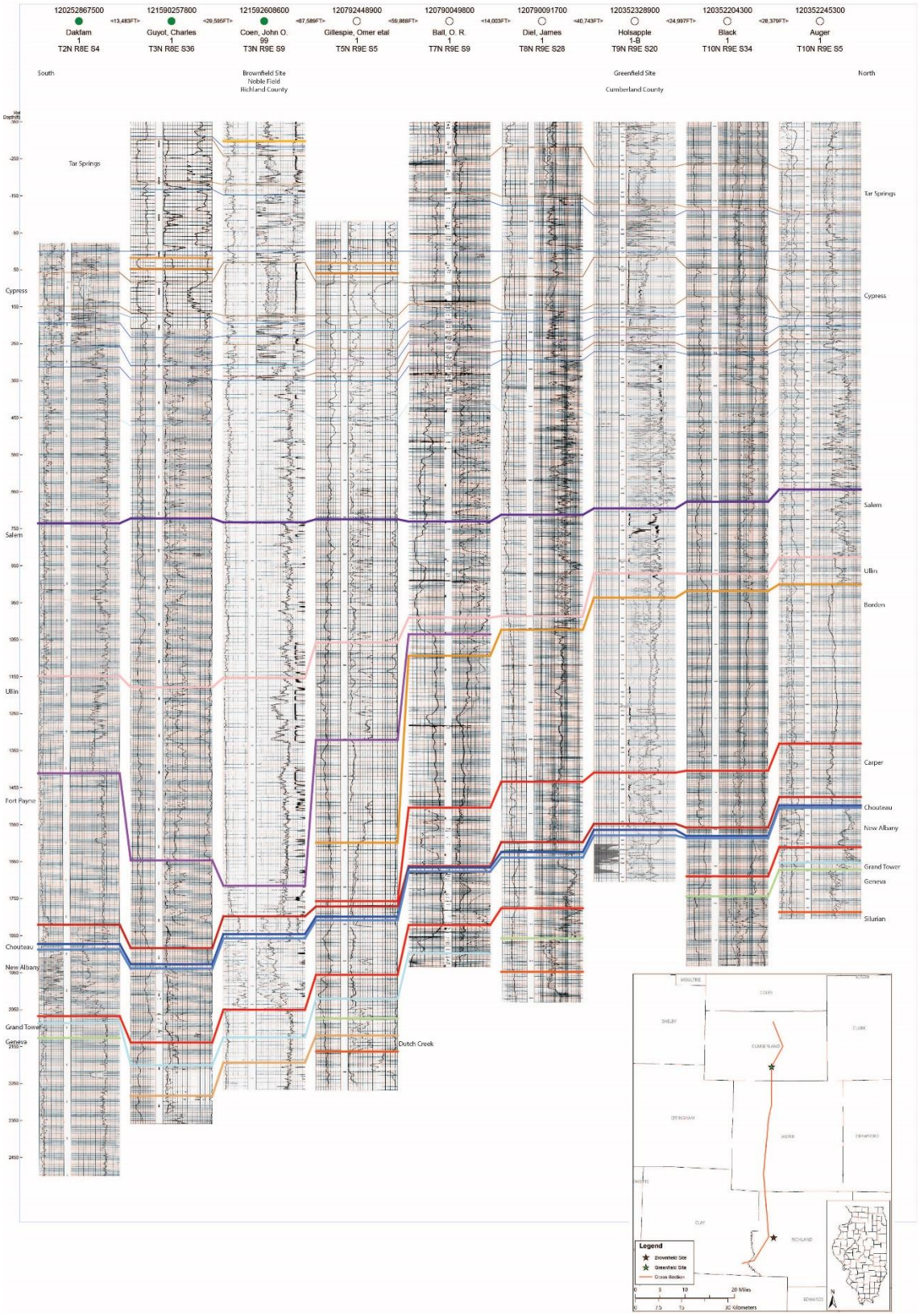


Figure 2-23. Cross-section showing the continuity of the candidate formations between the brownfield and greenfield sites.

Appendix 2-1 – Formation Data Availability Tables

Simple database queries were conducted to gain a basic understanding of the data availability and attributes of each of the candidate formations. As the database is incomplete and constantly evolving, the numbers provided in the tables below are considered provisional and were used only for comparison purposes.

Geneva Dolomite/Dutch Creek Sandstone

Formation aliases			Geneva Dolomite, Dutch Creek Sandstone		
Major producing fields			Salem, Centralia, Raccoon Lake, Sandoval, Patoka, Lillyville, Mattoon		
Dominant reservoir lithology			Dark brown, crystalline, porous, pure dolomite		
Number of wells that encounter formation			>9,800		
Number of wells with oil indicators			2,471 (Devonian)		
Number of wells with production			>152 (Geneva)/1,707 (Devonian)		
Number of wells with DSTs			107 (Geneva)/ 593 (Devonian)		
Number of wells with core			9 (Geneva)/109 (Devonian)		
	Minimum	Maximum	Mean	Median	Standard Deviation
Typical depth (ft)	420	5,018	1,897	1,973	1,018
Subsea elevation (ft)	282	-1,660	-1,299	-1,353	1,088
Thickness (ft)	0	60	23	16	17
Porosity (%)	4	30	17	18	6
Permeability (mD)	0	355	36	10	57

Ullin and Salem Limestone

Formation aliases	Ullin Limestone, Warsaw Lime, Salem Limestone
Major producing fields	Ullin – New Harmony, Enfield, Concord, Johnsonville, Bessie, Benton North Salem – Salem, Clay City, Divide, New Harmony, Phillipstown, Iuka, Benton
Dominant reservoir lithology	Ullin – bioclastic grainstone sandwave Salem – bioclastic oolitic limestone
Number of wells that encounter formation	>18,000
Number of wells with oil indicators	661 (Ullin), 1,774 (Salem)
Number of wells with production	>257 (Ullin), 1,174 (Salem)
Number of wells with DSTs	493 (Ullin), 1,039 (Salem)
Number of wells with core	11 (Ullin), 7 (Salem)

	Minimum	Maximum	Mean	Median	Standard Deviation
Typical depth (ft)	213	4396	3398	3716	860
Subsea elevation (ft)	-3977	488	-2932	-3256	897
Thickness (ft)	2	748	54	12	109
Porosity (%)	0.2	19.5	6.5	6.3	4.3
Permeability (mD)	0	486	17.3	0.2	52.2

Tar Springs Sandstone

Formation aliases	Tar Springs Sandstone
Major producing fields	Benton, New Harmony Consolidated, Phillipstown Consolidated, Loudon, Benton
Dominant reservoir lithology	White to light gray, very fine grained to fine grained sandstone
Number of wells that encounter formation	>19,500
Number of wells with oil indicators	2,263
Number of wells with production	>1,300
Number of wells with DSTs	367
Number of wells with core	44

	Minimum	Maximum	Mean	Median	Standard Deviation
Typical depth (ft)	60	3200	2117	2244	438
Subsea elevation (ft)	358	-2784	-1667	-1819	473
Thickness (ft)	50	150	85	84	22
Porosity (%)	0	30	15	16	5
Permeability (mD)	60	700			

Spar Mountain Sandstone

Formation aliases	Spar Mountain Sandstone / Rosiclare Sandstone
Major producing fields	Clay City Consolidated, Lawrence, Salem Consolidated, Phillipstown Consolidated
Dominant reservoir lithology	Light gray to greenish gray, calcareous, glauconitic sandstone
Number of wells that encounter formation	>17,000
Number of wells with oil indicators	3,700
Number of wells with production	744
Number of wells with DSTs	1211
Number of wells with core	202

	Minimum	Maximum	Mean	Median	Standard Deviation
Typical depth (ft)	650	3,350	2,576	2,826	656
Subsea elevation (ft)	-110	-2,950	-2,083	-2,359	714
Thickness (ft)	0	120	15	11	12
Porosity (%)	0	32	11	12	5
Permeability (mD)	0	1,180	64	3	197

Cypress Sandstone

Formation aliases		Cypress Sandstone, Kirkwood Sand, Weiler Sand			
Major producing fields		Lawrence, Loudon, Clay City, sailor Springs, Bible Grove, Dale			
Dominant reservoir lithology		Very-fine to fine-grained sandstone			
Number of wells that encounter formation		>52,000			
Number of wells with oil indicators		>17,600			
Number of wells with production		>11,600			
Number of wells with DSTs		1,641			
Number of wells with core		110			
	Minimum	Maximum	Mean	Median	Standard Deviation
Typical depth (ft)	0	3,994	2,290	2,542	611
Subsea elevation (ft)	-3,529	762	-1,814	-2,082	644
Thickness (ft)	0	250	52	38	44
Porosity (%)	4.6	26.7	17.9	18.4	3.7
Permeability (mD)	0	750	78.2	42.5	113

Carper Sandstone

Formation aliases	Carper Sandstone, Borden Siltstone, Sonora sand, Bilyeu sand
Major producing fields	Mattoon, Martinsville, Westfield, Loudon, St. James, Wilburton, Kinmundy
Dominant reservoir lithology	Very fine-grained sandstone to coarse siltstone
Number of wells that encounter formation	>570
Number of wells with oil indicators	>570
Number of wells with production	>260
Number of wells with DSTs	40
Number of wells with core	16 with core; 78 with core analyses

	Minimum	Maximum	Mean	Median	Standard Deviation
Typical depth (ft)	350	4240	1800	1380	1011
Subsea elevation (ft)	333	-3702	-1183	-793	1040
Thickness (ft)	20	50	30	30	7
Porosity (%)	1.6	28	15	15.3	3.6
Permeability (mD)	0.01	313	5.7	1.9	13.8

Yankeetown and Bethel Sandstone

Formation aliases	Yankeetown (Benoist) Sandstone; Bethel Sandstone
Major producing fields	Boyd, Salem, Centralia, Fairman, Kinmundy
Dominant reservoir lithology	Very-fine to medium-grained sandstone
Number of wells that encounter formation	>24,000
Number of wells with oil indicators	>3,000
Number of wells with production	>6,000
Number of wells with DSTs	788
Number of wells with core	47

	Minimum	Maximum	Mean	Median	Standard Deviation
Typical depth (ft)	40	3,707	2,322	2,566	651
Subsea elevation (ft)	536	-3,182	-1,835	-2,071	683
Thickness (ft)	0	175	27	24	18
Porosity (%)	6.5	21.9	16.5	16.6	2.8
Permeability (mD)	0	1,060	132.8	94.5	164.3

2.2 Review of Analogous Basins

Authors: Zohreh Askari, Nathan Grigsby, Yaghoob Lasemi, Nathan Webb, Charles Monson
Published as Technical Report DOE-UIUC-31700-2, OSTI ID: 1846288, https://doi.org/10.2172/1846288

Sedimentary basins comprise extensive porous sandstone and carbonate reservoirs capable of hosting economically significant greenfield and brownfield residual oil zones (ROZs). Several basins in the United States, including the intracratonic Illinois Basin (ILB), have stacked, predominantly siliciclastic ROZs that are potential targets for tertiary recovery of petroleum and for storing large volumes of anthropogenic carbon in the subsurface. The rocks in these basins share facies and depositional settings with many reservoirs that have already been major producers in primary production and, in some cases, as carbon dioxide enhanced oil recovery (CO_2-EOR) targets. The lessons learned from field data collection and testing of these intervals in a basin like the ILB have broad applications to analogous basins with potential ROZs.

The object of this research was to study analogous basins within the United States with reservoirs and ROZ potential analogous to the ILB formations. To provide a framework for identification and characterization of ROZs and apply development strategies, a literature review of sedimentary basins was conducted, and several basins with reservoirs analogous to the ILB were identified. The analogous basins include the Los Angeles Basin in southern California, Uinta Basin in eastern Utah, Piceance Basin in western Colorado, and Big Horn, Powder River, Wind River, Green River, and Williston basins in Wyoming, Montana, South Dakota, and North Dakota (Figure 2-24). These basins, which encompass reservoirs that are analogous to ILB reservoir targets, are described below:

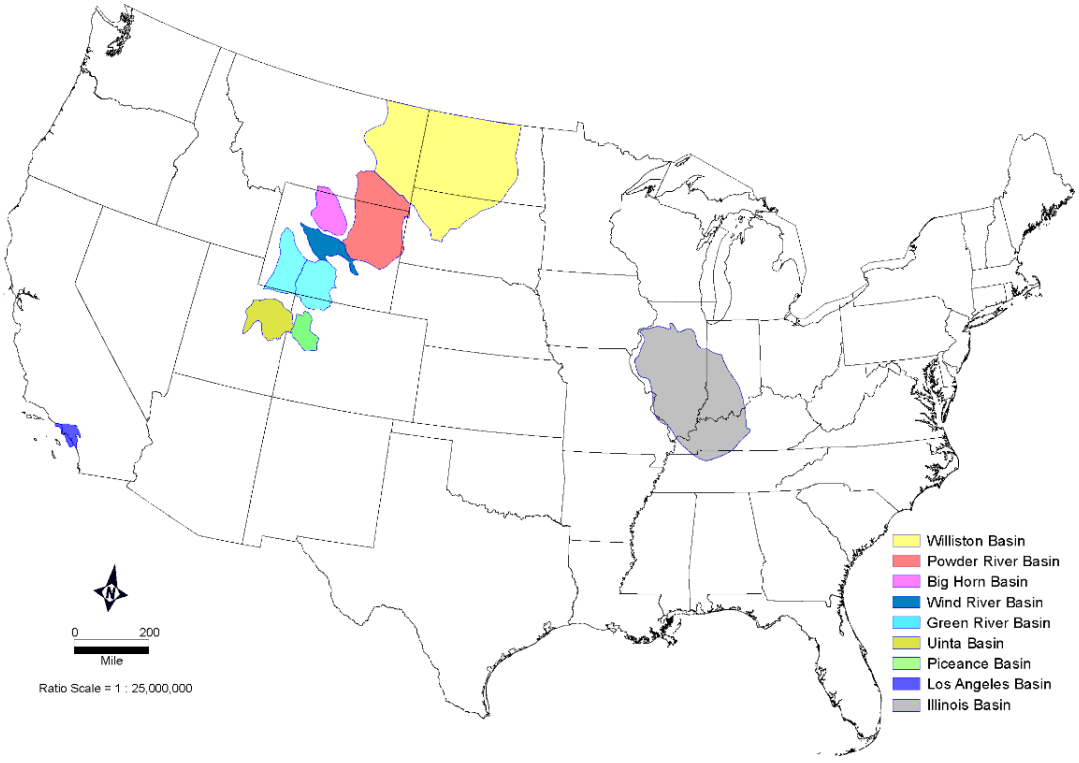


Figure 2-24. Location map of the basins mentioned in this report.

Basin Matrix

Extensive fairways of thick sandstone can be deposited in a range of geologic settings, including fluvial valleys, deltas, eolian dune fields, coastal strandplains, and turbidites, among other settings. Though all of these are lithologically classified as siliciclastics, their specific geological settings impact the properties (e.g., texture, mineralogy, internal heterogeneity, the presence of carbonate or clay mineral cements, etc.) that are important for ROZ development, ROZ detection through well log analysis, CO_2-EOR and associated storage.

Several basins in the US have extensive sandstone fairways capable of hosting economically significant ROZs (Table 2-2). The primary reservoir targets for this proposal share sedimentological characteristics and depositional settings with many other reservoirs nationwide that have already been major producers in primary production and, in some cases, as CO_2-EOR targets. The shelf clastic Cypress reservoir is comparable to the Domengine Formation of the Sacramento Valley Basin; the Upper Tuscaloosa Formation of the US Gulf Coast; the Kuparuk Formation of the North Alaska Basin; the Missourian sandstones of the Anadarko-South Oklahoma Basin; the Sussex and Shannon members of the Pierre Shale in the Denver Basin; and the Frontier Formation of the San Juan Basin. The Carper turbidites are like the Puente of the Los Angeles Basin; the Fleming Group in the Gulf of Mexico; the Frio Sandstone of the Louisiana Gulf Coast; the Torok and Channing Formations in the North Alaska Basin; and the Monterey turbidites in multiple California basins.

Table 2-2. Basin matrix listing general properties of basins that contain analogous formations to those being studied in the Illinois Basin.

Basin	Los Angeles Basin	Uinta/Piceance	Powder River Basin
Field	Wilmington	Rangely (Colorado)	Teapot Dome
Reservoir and lithology	Puente Fm (Miocene): Union Pacific, Ford, and Lower Ranger zones; Lower Pico Fm, Upper Ranger zone. Siliciclastic turbidites.	Weber Sandstone (Permian)	Tensleep Sandstone (Pennsylvanian-Permian). Dominantly sandstone, some carbonate.
Reservoir depth	Upper Ranger ~2,250 ft; Lower Ranger ~2,500 ft; Union Pacific ~4,100 ft; Ford ~4,900 ft (Otott and Clarke, 1996)	Average depth 6,400 ft (Wackowski, 2004)	5,525 ft (Jafri et al., 2016)
Reservoir porosity and permeability/injectivity ranges	Modeled mean porosity 31% for Pico and 24% for Puente. Kozeny-Carman permeability estimate 283 mD for Pico and 124 mD for Puente (Bruno et al., 2014)	Average effective porosity 12%; average effective permeability 8 md (Cooper, 2016)	Effective porosity 4-20%; permeability 0.001-234 mD (Jafrai et al, 2016).
Reservoir capacity estimates	185 million tonne CO_2 storage capacity estimate (including Pliocene Repetto Fm as well as Pico and Puente) (Bruno et al., 2014)	IEAGHG (2000) predicted 0.03 Gt of storage for a Chevron CO_2 flood project that was in progress at that time.	3597MM SCFD CO_2 storage (Garcia, 2005)
Caprock	Interbedded shales and siltstones within the Puente and Pico	State Bridge Formation (Permian-Triassic)	Opeche Shale (Goose Egg Fm)
Caprock thickness	Variable	650 ft (Hefner and Barrow, 1992)	300 ft (Raja et al., 2016)
Caprock an unconventional reservoir in the basin?	No	No	No
To what extent are reservoirs and caprocks naturally fractured?	Wilmington anticline is faulted (Colazas and Strehle, 1995)	Both local and extensive fractures (Bowker and Jackson, 1989)	Reservoir (Tensleep) is highly fractured (Chiaramonte et al., 2011). Opeche/Goose Egg caprock is intact (Friedmann and Stamp, 2006).
Field production history	Field discovered in 1936. Water injection began in 1961. CO_2 immiscible flooding of "tar zone" 1981-86; chemical EOR, caustic waterflood, and steam flood also attempted in 1960s-80s. Horizontal drilling commenced in 1993. Over 2.4 billion bbl produced to date. (Otott and Clarke, 1996)	Discovered 1933; waterflooding began 1958; CO_2 flooding began 1986; targeted infill drilling in 2000s. Cumulative production over 900 MMBbl as of December 2016 (Cooper, 2016)	First production 1908; became a Naval Petroleum Reserve in 1915; closed to development, 1920s; reopened 1976; became geological carbon storage test center 2003; sold to Stranded Oil Resources Corp. 2014
Is proposed reservoir an ROZ? Has it been previously exploited?	Unknown whether reservoir is ROZ. Various EOR techniques have been applied here (Otott, 1996).	Conventional reservoir; CO_2-EOR is ongoing at the field.	Tensleep is an ROZ in the Bighorn Basin (Yin et al., 2012). Teapot Dome has been investigated for possible CO_2-EOR activities.
Local state of stress	SH-max orientations in Wilmington Field ~N50E to S10E; substantial variability due to structural complexity of basin (Stock et al., 2016)	8,550 psi (horizontal at N70E) > 6,300 psi (vertical) > > 4,550 psi (horizontal at N20W) (Haimson, 1972)	Maximum compressive stress N80W (Schwartz, 2006)
Distance to basement from deepest reservoir	Onshore: ~1,500 ft from top of Ford to basement. Offshore: ~4,000 ft from top of Ford to basement	Approximately 2,500 ft (Raleigh et al., 1976)	Approximately 1,500 ft from granite basement to top of Tensleep (Black et al., 2010)
Potential CO_2 sources	Several industrial CO_2 sources exist in the Los Angeles Basin (Childers, 2012)	Exxon Shute Creek plant near LaBarge, WY, and natural CO_2 fields	Major sources of CO_2 in the Rocky Mountains are the Shute Creek and Lost Cabin plants in Wyoming
Other basins/formations where results gained from this project should be directly applicable?	Carper, Illinois Basin; Puente, Los Angeles Basin; Fleming Group, Gulf of Mexico; Frio Sandstone, Louisiana Gulf Coast; Torok and Channing Formations, North Alaska Basin; Monterey turbidites in California basins.	Cypress, Illinois Basin; Domengine, Sacramento Valley Basin; Upper Tuscaloosa, US Gulf Coast; Kuparuk Formation, North Alaska Basin; Missourian sandstones, Anadarko-South Oklahoma Basin; Sussex and Shannon members of Pierre Shale, Denver Basin; Frontier Formation, San Juan Basin.	Cypress, Illinois Basin; Domengine, Sacramento Valley Basin; Upper Tuscaloosa, US Gulf Coast; Kuparuk Formation, North Alaska Basin; Missourian sandstones, Anadarko-South Oklahoma Basin; Sussex and Shannon members of Pierre Shale, Denver Basin; Frontier Formation, San Juan Basin.

Los Angeles Basin - Southern California

Authors: Zohreh Askari and Yaghoob Lasemi

The Upper Miocene Puente Formation in the Los Angeles Basin consists of shale and stacked siliciclastic reservoirs whose facies and depositional setting are comparable to the Mississippian Borden Siltstone in the ILB. Both Illinois and Los Angeles Basins have a long history of oil exploration and production, but the two basins are quite different in areal extent, tectonic evolution, and subsidence history. The Los Angeles Basin was a rapidly subsiding, deep, active continental margin structural feature during Upper Miocene when the Puente Formation was being deposited (Yerkes et al., 1965; Wright, 1991). It is a basin with a young petroleum system in which petroleum was likely generated in the Pliocene after the Puente Formation was deposited. The ILB, however, was a slowly subsiding, relatively shallow intracratonic basin during the Cambrian through Permian time (Buschbach and Kolata, 1991; Kolata and Nelson, 1991). Compared to the ILB, the Los Angeles Basin is much smaller in areal extent, but massive source and reservoir rocks, and large anticlinal traps have resulted in the highest concentrations of crude oil in the world (Gautier et al., 2013). Here, we review the geology of the two basins and characterize their basin fill stratigraphic architecture to demonstrate that, with a few exceptions, the sandstone reservoirs in the Miocene Puente Formation in the Los Angeles Basin are comparable to the "Carper Sandstone" reservoir within the Mississippian Borden Siltstone in the ILB.

Geological Setting

The present-day Los Angeles Basin is a northwest-trending lowland plain about 50 miles (80.5 km) long and 20 miles (32.2 km) wide on the southern California coast, covered by alluvial deposits (Figure 2-25). It is bounded by mountains and hills that expose Pleistocene and Mesozoic or older basement rocks (Yerkes et al., 1965).

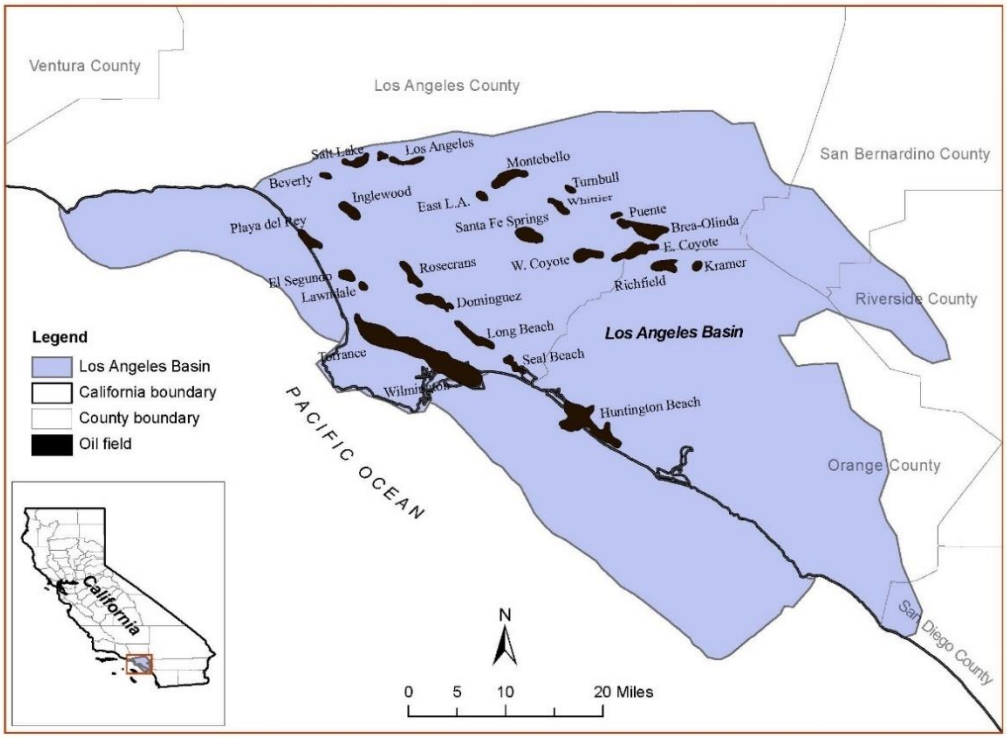


Figure 2-25. Map of southern California showing the location of the Los Angeles Basin (not all oil fields are shown).

The physiographic province is underlain by a structural depression comprised of four primary structural blocks (Figure 2-26) whose contacts are zones of faulting and flexure on which vertical and lateral movement occurred intermittently since Middle Miocene times (Yerkes et al., 1965). The Los Angeles Basin is a rapidly subsiding, deep structural feature that formed as strike-slip extensional basin in Late Miocene times, about 7 million years ago (Wright, 1991). It was formed by large-magnitude crustal extension beginning in latest Oligocene through earliest Miocene times (Crouch and Suppe, 1993), like those predicted for pull-apart basins (Biodlz, 1991).

The ILB, however, was a slowly subsiding intracratonic basin during the Cambrian through Permian times (e.g., Kolata and Nelson, 2010). It is bounded by arches and domes and covers the main part of Illinois, southeast Indiana, and western Kentucky (Kolata and Nelson, 2010).

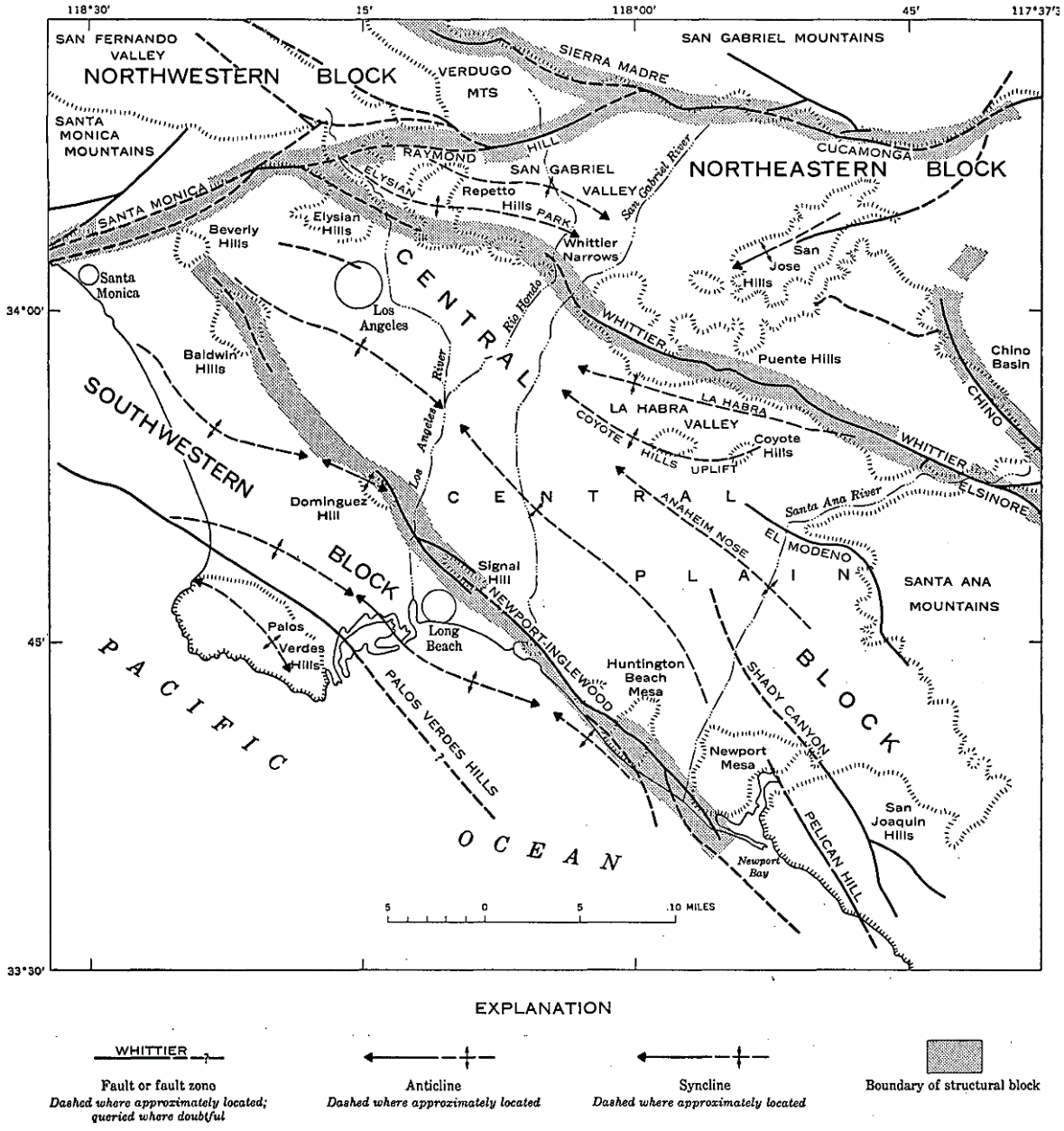


Figure 2-26. Major basement structural features of the Los Angeles Basin (Yerkes et al., 1965).

Production History and Future Potential

The Los Angeles Basin is the most prolific oil-producing district in California. The basin has a long history of oil exploration and production; oil was first discovered in 1880 (Barbat, 1958). The area contains several oil and gas fields, including the giant Wilmington-Belmont Field in Long Beach. The Wilmington-Belmont oil field produces more oil than any other field in the Los Angeles Basin and is the third largest oil field in the United States (Figure 2-27). At the end of 2014, the Wilmington oil field produced more than two billion barrels of oil (Bruno et al., 2014).

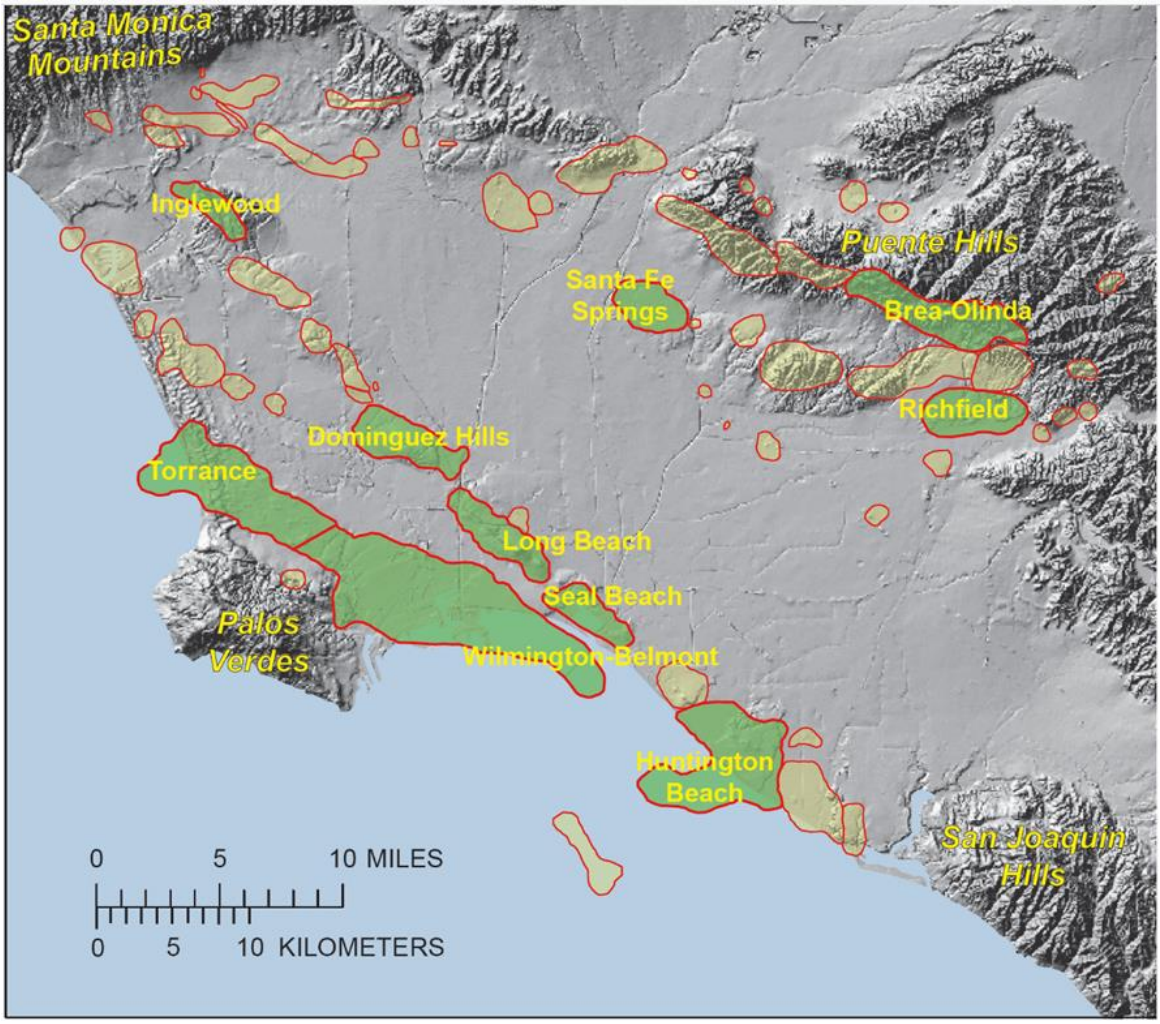


Figure 2-27. Map of the Los Angeles Basin, showing oil fields (outlined in red). Ten oil fields evaluated in the USGS assessment are shaded green (Gautier et al., 2013).

Oil is produced chiefly from Lower Pliocene and Upper Miocene strata. Several minor oil reservoirs have been discovered in Pleistocene sandstones, Upper Pliocene sandstones, and Middle Miocene sandstones. Sixty-eight oil fields have been found in an area of about 450 square miles, one of which, the Wilmington-Belmont, is the fourth largest oil field in the United States (Figure 2-27).

A large volume of original oil in place (OOIP) in the Los Angeles Basin is residual oil below pay zones and in depleted reservoirs and remains to be produced through CO_2-EOR projects. Based on the United States Geological Survey (USGS) assessment, in ten oil fields of the Los Angeles Basin, between 1.4 and 5.6 billion

barrels of additional oil could be recovered with extensive water, steam, and CO_2 floods, with additional recoverable oil remaining in the other existing oil fields, in yet-to-find conventional oil fields, and in unconventional resources (Gautier et al., 2013).

The Los Angeles Basin area is home to more than a dozen major power plants and oil refineries. In the central Wilmington Graben (offshore Los Angeles) alone, more than 100 million tons of storage capacity are available within the Pliocene and Miocene Formations (Bruno et al., 2014). The massive reservoir facies in the Puente Formation provide the opportunity for both CO_2-EOR and large-scale geologic storage of CO_2.

In the ILB, more than 4 billion barrels of oil have been produced mostly from Pennsylvanian and Mississippian siliciclastic and carbonate reservoirs. The main source rock in the ILB is the organic-rich New Albany Shale (Upper Devonian to lowermost Mississippian). A large volume of OOIP in the Illinois Basin is residual oil in depleted reservoirs. It is estimated that an additional 4 billion barrels of oil remain to be produced through water flooding and CO_2-EOR methods that would result in significant oil recovery and storage of carbon dioxide. The ILB area has several major CO_2 producing plants, including ADM ethanol producing facilities in Macon County and several power plants and oil refineries in Crawford County. Geologic investigations indicate that hundreds of million tons of storage capacity are available within the Paleozoic saline and petroleum reservoirs.

Stratigraphy

Puente Formation in the Los Angeles Basin

The stratigraphic succession of the Los Angeles Basin consists of several unconformity-bounded sequences comprising the Cretaceous, Tertiary, and Quaternary deposits (Figure 2-28). The Cretaceous succession overlies the basement rocks, which include metamorphic and igneous crystalline rocks of Precambrian to early Late Cretaceous age (Yerkes et al., 1965). The major basin-fill units include the Middle Miocene Topanga, Upper Miocene Puente, and the Paleocene Fernando Formations (Figure 2-28).

The Puente Formation (Upper Miocene) was named by Eldridge and Arnold (1907) for its outcrop exposures in the Puente Hills. It is locally referred to as the Modelo or Monterey Formation. The formation is overlain by the Pliocene Fernando Formation and underlain, with unconformable contact, by the Middle Miocene Topanga Group (Durham and Yerkes, 1964; Yerkes et al., 1965; Yerkes, 1972). The formation has a composite maximum thickness of about 3,900 m (12,800 ft) in the eastern Puente Hills. It is considerably thinner to the south in the Santa Ana Mountain and to the north in the San Jose Hills (Yerkes et al., 1965). The Puente Formation is coeval with the deep marine Monterey and Modelo Formations (e.g., Durham and Yerkes, 1964; Yerkes et al., 1965; Yerkes, 1972). It consists of conglomerate, arkosic sandstone, and mudrock characterized by a succession of alternating thin-bedded sandstone and shale that grade to thick-bedded sandstone and conglomerate in two upward-thickening and coarsening megacycles reflecting submarine-fan progradation (Salvatore et al., 1995). The formation is divided into four stratigraphic units (Figure 2-28), including (1) thin-bedded sandstone and shale (La Vida Member), grading to (2) thick-bedded sandstone and conglomerate (Soquel Member), (3) thin-bedded mudrock and sandstone (Yorba Member), grading to (4) thick to very thick-bedded sandstone and conglomerate (Sycamore Canyon Member).

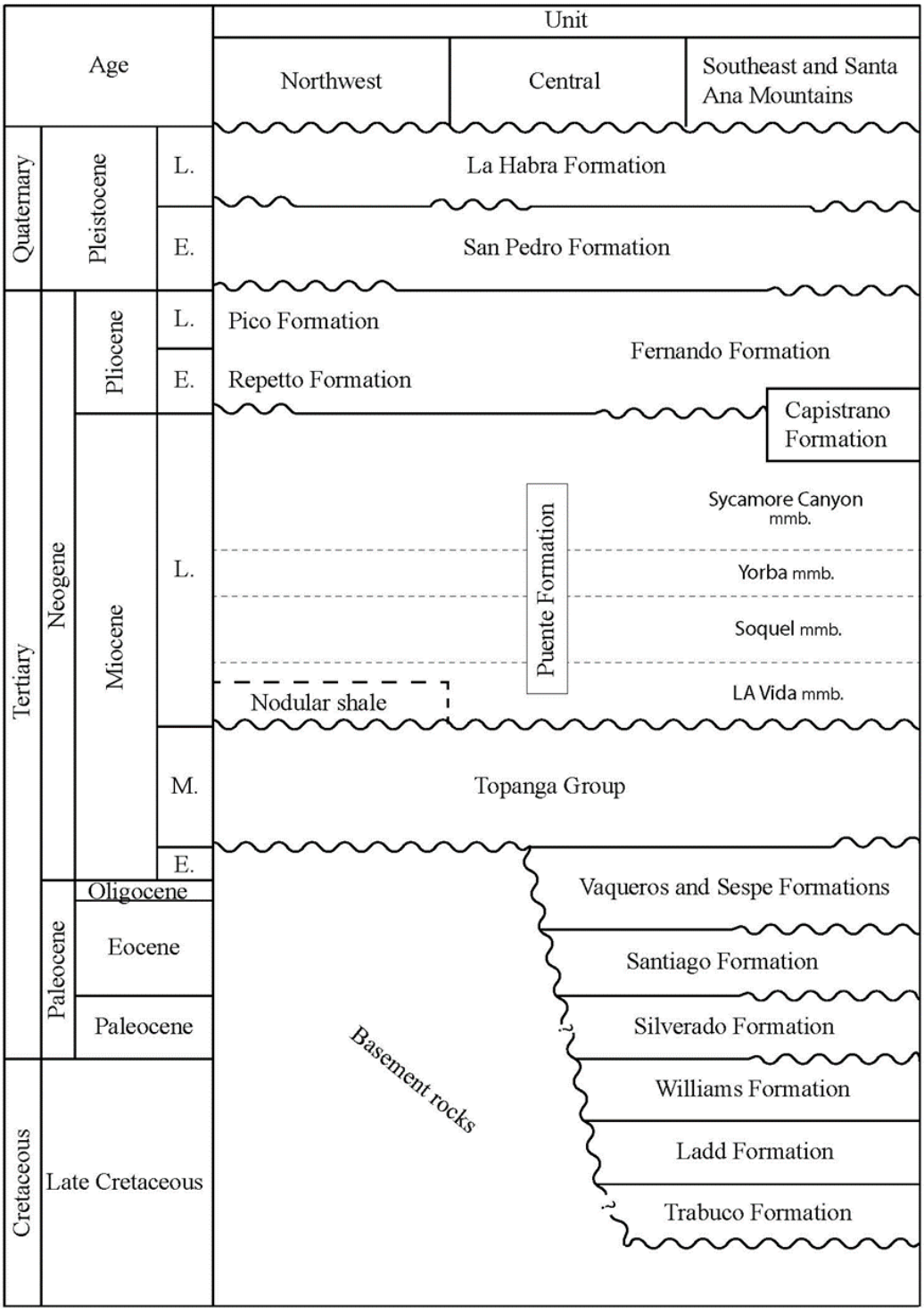


Figure 2-28. Stratigraphic column of Los Angeles Basin. From Beyer (1995).

Borden Siltstone in the Illinois Basin

The sedimentary succession of the Illinois Basin consists of alternating Cambrian through Permian, chiefly shallow marine siliciclastic and carbonate platform deposits, reflecting in a rather slowly subsiding interior cratonic basin, like the Michigan and Williston Basins. The Middle Mississippian Borden Siltstone (nearly

200 m thick) consists of mudrock and beds of fine sandstone to coarse siltstone. It overlies the Lower Mississippian Chouteau Limestone and underlies Ullin Limestone (Figure 2-29) (Lineback, 1968). The Borden Siltstone, Warsaw Shale, and Springville Shale are laterally equivalent and represent parts of a delta system that invaded and restricted the deep-water basin. In the lowermost part of the Borden Siltstone, thin, laterally discontinuous, graded sandstone beds occur that are informally named "Carper sandstone" (Lineback, 1968).

Reservoir Facies and Depositional Setting

In this section, reservoir characteristics of the Puente Formation and the Borden Siltstone ("Carper sandstone") are discussed. Geological characteristics of the Puente Formation in the Los Angeles Basin and the Borden Siltstone in the Illinois Basin are summarized in Table 2-3.

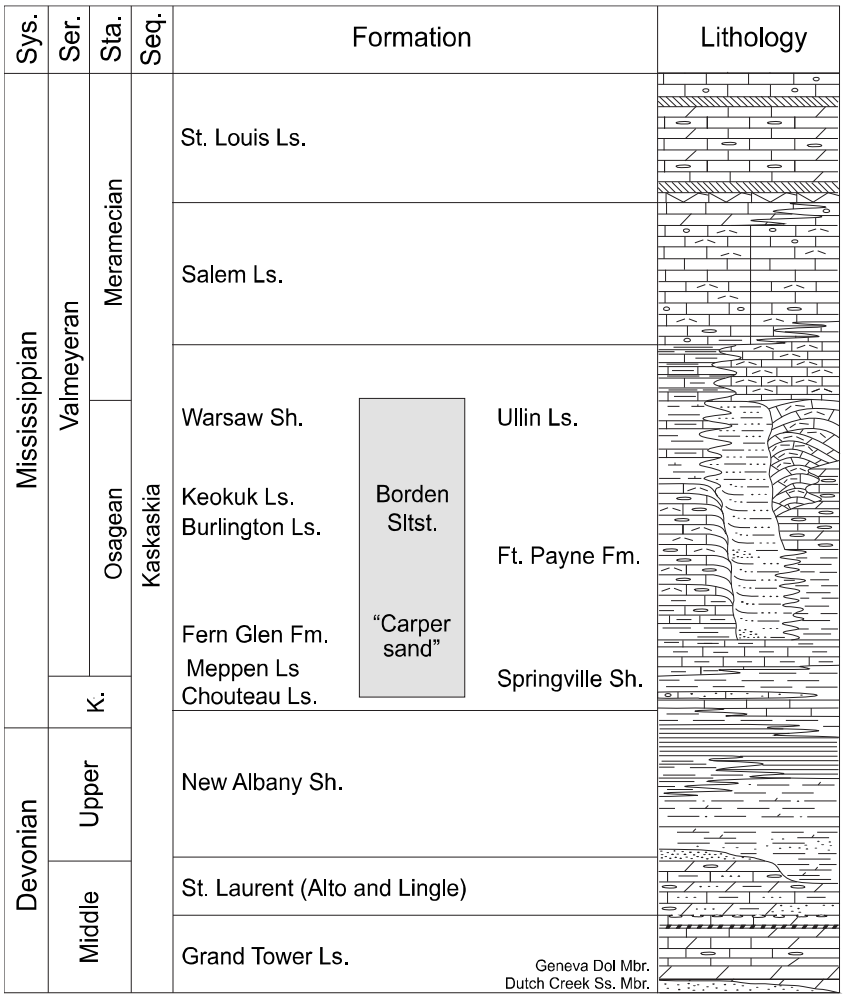


Figure 2-29. Stratigraphic column of the Middle Devonian through Middle Mississippian succession. Modified from Kolata (2005).

Puente Formation

In the Los Angeles Basin, the Upper Miocene Puente Formation is a major basin-fill unit of nearly 4,000 m (13,123 ft) thick, which was deposited in a rapidly subsiding deep basin (Yerkes et al., 1965; Wright, 1991). It is composed of massive organic rich mudrock and coarse siliciclastics (conglomerate and sandstone) that were deposited as debris flow and turbidite deposits associated with a submarine fan depositional

system at bathyal depths (e.g., Durham and Yerkes, 1964; Yerkes et al., 1965; Yerkes, 1972). The reservoir rocks are massive, prolific oil producers in the upper part of the formation. They are arkosic sandstone and conglomerate intervals with average porosity of 24% and permeability of 124 md (Bruno et al., 2014). They are capped by thick, organic-rich source rocks and petroleum traps that consist mostly of faulted anticlines and noses.

Borden Siltstone

In the ILB, the Middle Mississippian Borden Siltstone (nearly 200 m [656 ft] thick) consists of mudrock and beds of fine sandstone to coarse siltstone. In the lowermost part of the Borden Siltstone, thin, oil-bearing sandstone beds occur that were informally named "Carper sandstone" (Lineback, 1968). The Carper reservoirs are generally fan-shaped, lenticular sand bodies (Lineback, 1968; Seyler and Cluff, 1991). Their average porosity and permeability are 14% and 5 md, respectively. They are laterally discontinuous, encased in shale, and form small stratigraphic or stratigraphic-structural combination traps. The "Carper" was deposited as turbidites in the offshore setting (pro-delta) of a deltaic system. Graded bedding and geometry of the sand bodies indicate deposition by turbidity currents when sand carried by a river system moved down-slope across the gently sloping delta front in a pro-delta plain of the Borden Siltstone deltaic system (Lineback, 1968). A relatively small amount of oil has been produced from the "Carper sandstone". Intervals with immobile residual oil and ROZ in the depleted reservoir underlying the pay zone would result in commercial oil production and CO_2 storage through enhanced oil recovery methods.

Table 2-3. Comparison of the geological characteristics of the Puente Formation in the Los Angeles Basin and the Borden Siltstone in the Illinois Basin.

Stratigraphic units and basin	Puente Formation (Los Angeles Basin)	Borden Siltstone (Illinois Basin)
Age	Tertiary (Late Miocene)	Paleozoic (Middle Mississippian)
Formation thickness	3,900 m	200 m
Basin type	Active margin pull-apart basin	Interior cratonic basin
Lithology	Interbedded mudrock, sandstone, and conglomerate	Interbedded mudrock, sandstone, and siltstone
Reservoir facies	Massive sandstone and conglomerate in the upper part of the formation	Thin sandstone beds in the lower part of Borden informally named "Carper Sandstone"
Depositional setting	Deeper marine pro-delta plain of a deltaic system	Proximal to distal setting of a submarine fan system
Porosity and permeability	24 percent/ 124 millidarcy	14 percent/ 5 millidarcy
Caprock/seal	Pro-delta plain shale up to 6 m	Massive basin plain shale
ROZ potential	Thick ROZ in the depleted reservoirs; EOR techniques have locally been applied	ROZ is present but has not been evaluated
Potential CO_2 source	More than a dozen major power plants and oil refineries	ADM ethanol facilities power plants and refinery in the vicinity of oil fields
Reservoir capacity for CO_2 storage	In Wilmington Graben offshore Los Angeles alone, more than 100 million tons of storage capacity in Pliocene and Miocene rocks	Reservoir capacity has not been evaluated

Uinta and Piceance Basins - Utah and Colorado

Author: Nathan D. Webb

Geological Setting

The Uinta and Piceance Basins are (Tertiary) Laramide structures located in eastern Utah and Western Colorado, respectively, and are separated by the Douglas Creek arch (Figure 2-30). The basins lie within the Colorado Plateau and Basin and Range Petroleum Region (e.g., Dolton et al., 1981) in an area commonly referred to as the Uinta-Piceance Province (Figure 2-30). The Uinta Basin is east-west oriented and has >30,000 ft of Phanerozoic sediments where it is deepest on the north side; the Piceance Basin is deepest on the east side with >20,000 ft of Phanerozoic sediments (Spencer and Wilson, 1989; Figure 2-31).

General stratigraphy of the Uinta-Piceance Province includes Phanerozoic rocks from Cambrian to Tertiary in age (Figure 2-32). The following summary is based on Spencer and Wilson (1989). Most Ordovician to Middle Devonian rocks are absent due to erosion and/or nondeposition. Late Devonian to Mississippian marine strata were deposited on a shallow shelf east of the main depocenter in western Utah and eastern Nevada. Pennsylvanian rocks are mostly continental and marine siliciclastics with some marine carbonates. A relatively thin (<500 to 1,000 ft) succession of marine and continental strata of Permian age was deposited over much of the Uinta and Piceance province. Triassic and Jurassic continental siliciclastics were deposited over much of the area and are separated by a few tongues of marine shale and carbonate from the west. Lower Cretaceous sandstones, conglomerates, and shales are thin (generally <500 ft) and are overlain by a thick (6,000 to >8,000 ft) section of Upper Cretaceous marine shale and continental and marine sandstone, mudstone, shale, and siltstone with some coal.

The Uinta and Piceance Basins, as they are known today, began to form in the Paleocene and subsided rapidly through the Eocene (Johnson, 1985). Maximum subsidence occurred in the Uinta Basin where more than 15,000 ft of fluvial and lacustrine deposits accumulated. Tertiary sedimentation was dominated by the development of Lake Uinta, which covered large parts of both basins during Eocene times and resulted in the deposition of Green River Formation source rock (Figure 2-32).

Numerous oil and gas fields have been discovered in the Uinta and Piceance basins with exploitation beginning in 1890. More than 1.2 billion bbl of oil and 1.1 tcf of gas have been produced from thirty-four fields in the Uinta Mountains and northern Uinta-Piceance basins (Osmond, 1986). The Weber Sandstone is the most prolific hydrocarbon producer, being responsible for about two-thirds of the production from eight fields (Hefner and Barrow, 1992). The largest field in the province is the Rangely Field. The balance of oil production is derived from lacustrine sandstones of the Eocene Green River and Uinta Formations and fluvial sandstones of the Eocene Wasatch Formation (Figure 2-32) from fields including Red Wash and Bluebell-Altamont.

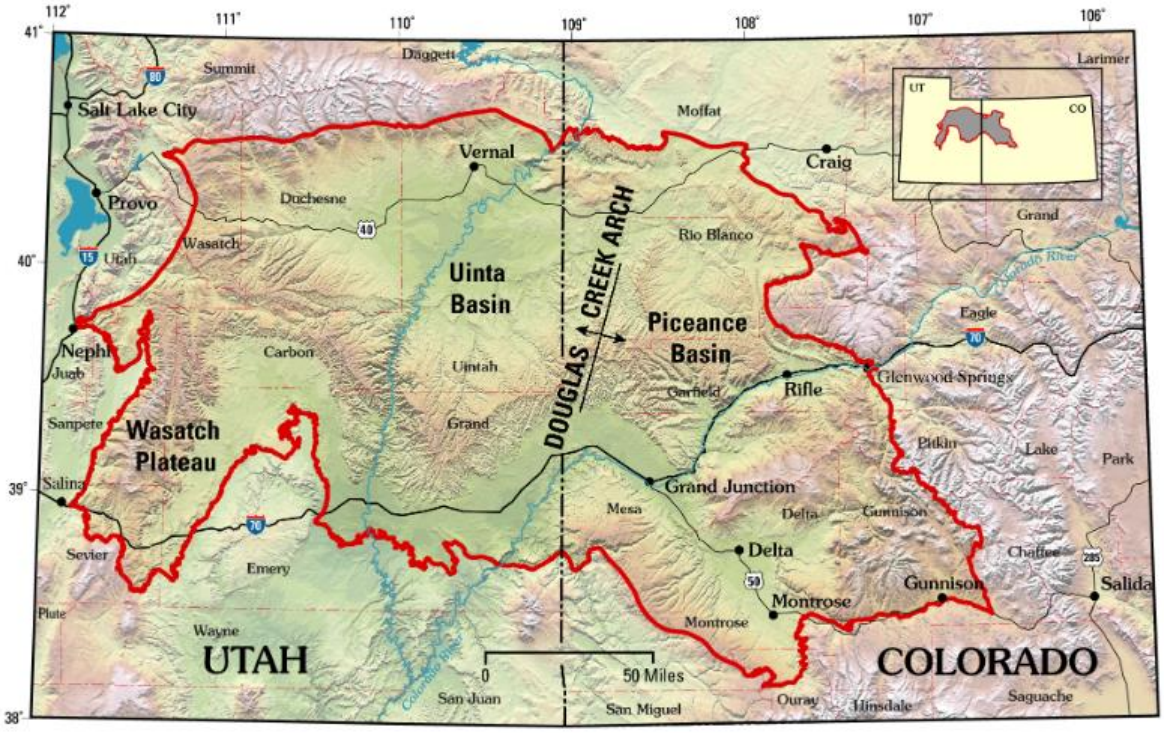


Figure 2-30. Location of the Uinta-Piceance Province (red outline) that contains the Uinta and Piceance Basins in eastern Utah and western Colorado.

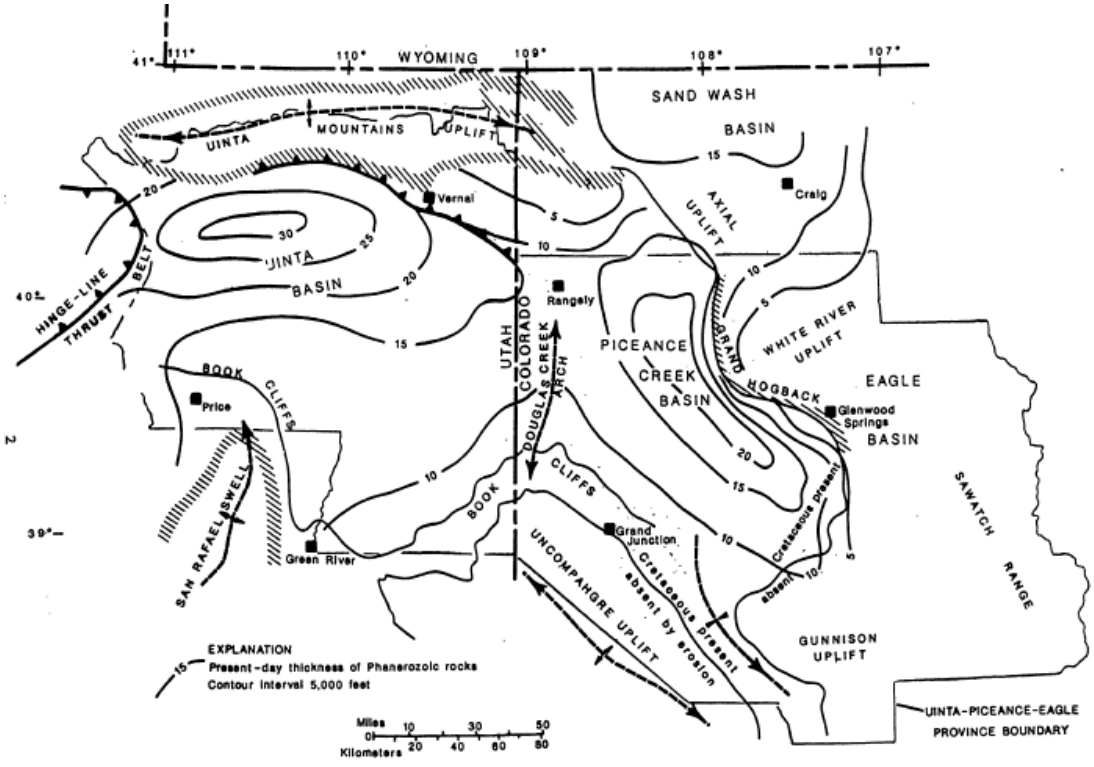


Figure 2-31. Map showing present thickness of Phanerozoic strata within the Uinta and Piceance Basins. From Spencer and Wilson (1988).

Petroleum Systems and Plays

There are five recognized total petroleum systems (e.g. source rock, reservoir rock, seal, and trap; Figure 2-33) in Pennsylvanian and younger rocks in the basins, including the Minturn, Phosphoria, Mancos, Mesaverde, and Green River systems (Lillis et al., 2003; Figure 2-32). A total petroleum system is a mappable entity encompassing genetically related petroleum that occurs in seeps, shows, and accumulations (discovered or undiscovered) that have been generated by a pod or by closely related pods of mature source rock (Figure 2-33). Spencer (1995) assessed the basins and identified six conventional and seven unconventional hydrocarbon plays (Table 2-4).

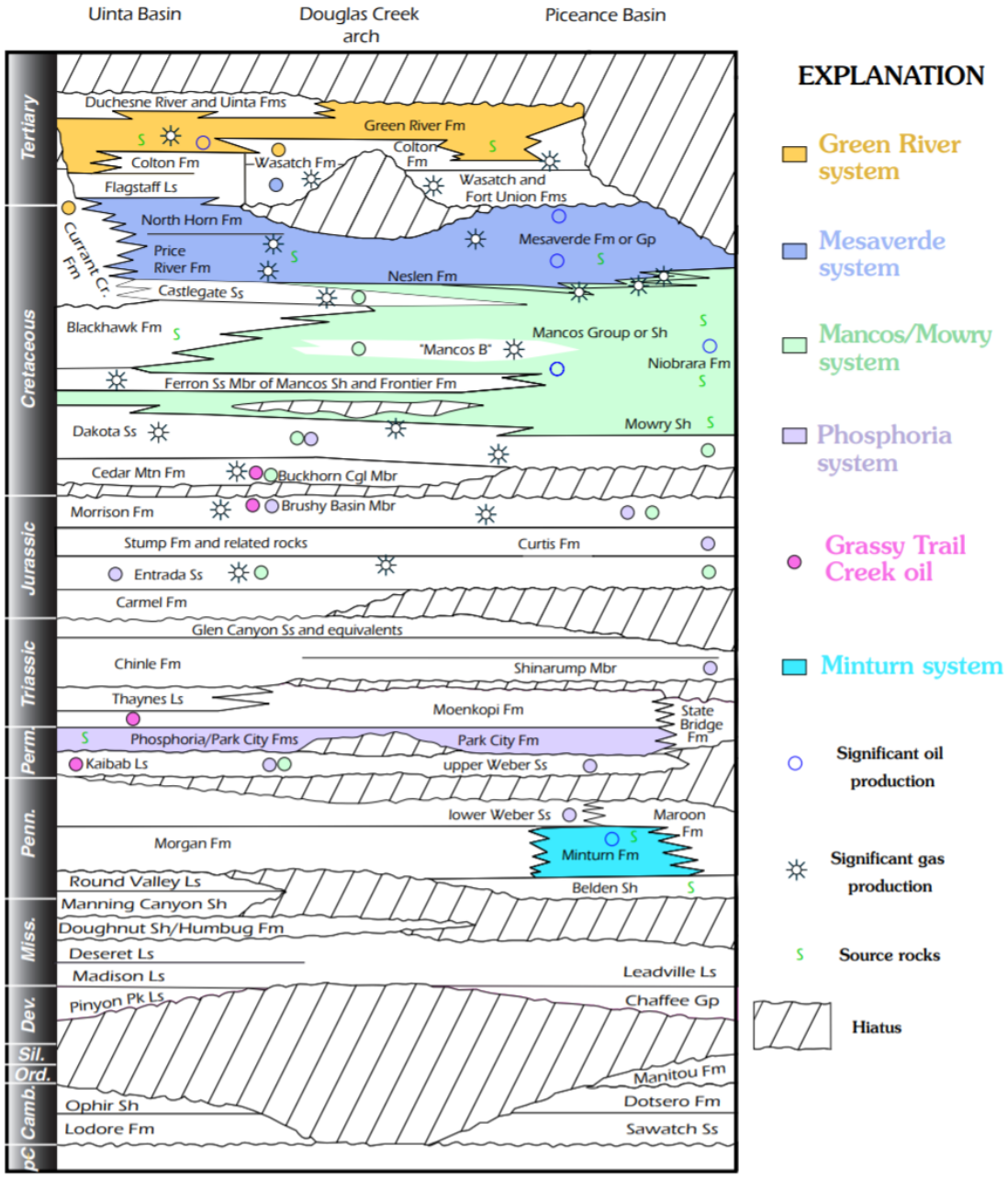


Figure 2-32. Generalized stratigraphic column of the Uinta-Piceance Province showing the distribution of petroleum system source rocks (shaded) and associated oil types (circles). From Lillis et al. (2003).

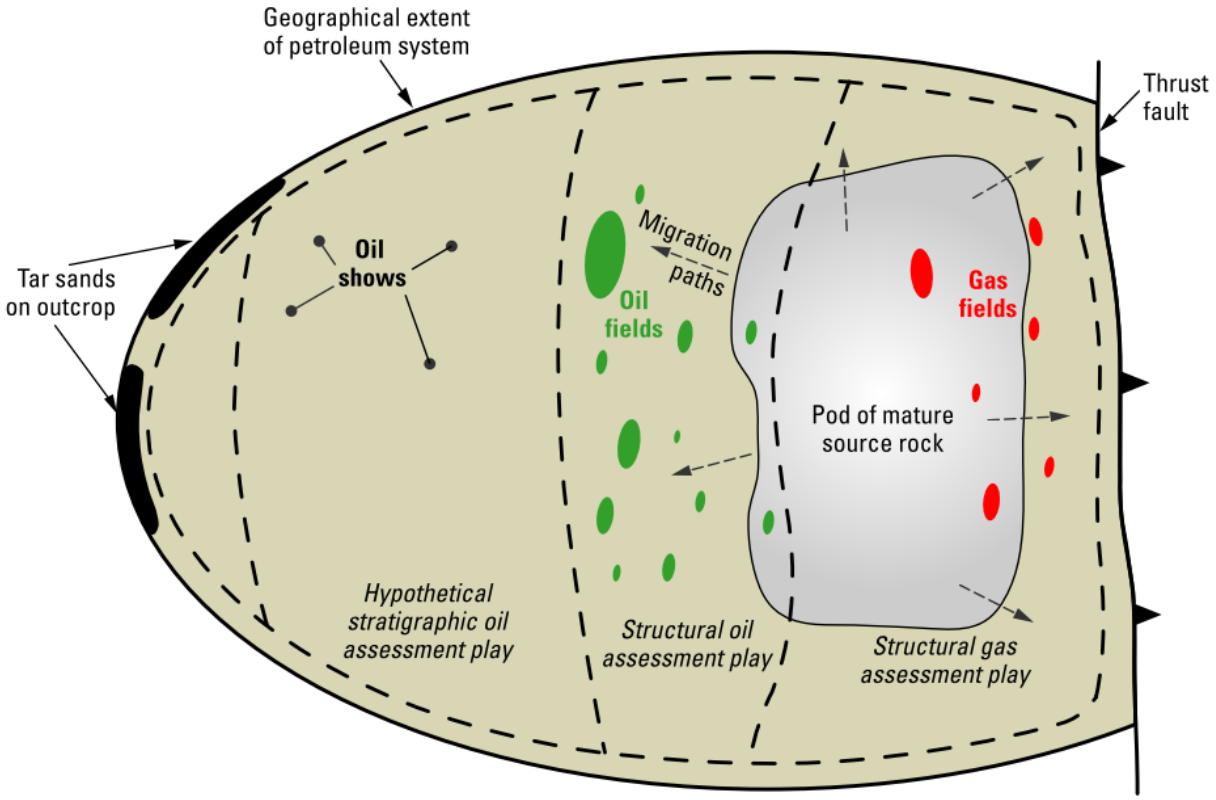


Figure 2-33. Schematic plan view of a total petroleum system, showing a pod of mature source rock, the distribution of known petroleum occurrences, and the boundaries of the assessment units. From Team (2003).

*Table 2-4. Summary of plays in the Uinta-Piceance Province as described by Spencer (1995). *Illinois Basin analog formations were assigned based on lithology and depositional environment are listed in the rightmost column.*

Play	Type	Source	Reservoirs	Lithology	Porosity (%)	Fields	ILB Analogue*
Piceance Tertiary	Conv	Mesaverde; Green River?	Tertiary Wasatch Fm and Douglas Creek Member of Green River Fm	Fluvial to marginal lacustrine litharenites to feldspathic litharenites	11 to 15+	Not listed	Chesterian fluvial sandstones
Uinta Tertiary	Conv	Mesaverde; Green River?	Wasatch and Green River Formations	Fluvial and lacustrine litharenites and feldspathic litharenites	10 to 15+	Altamont-Bluebell; Red Wash	Chesterian fluvial sandstones
Upper Cretaceous	Conv	Mesaverde	Mesaverde Group	Marginal-marine, fluvio-deltaic, and fluvial environments very fine-grained sandstone and siltstone			Chesterian sandstones
Cretaceous Dakota to Jurassic	Conv	Mowry and Mancos Shales	Dakota, Morrison, Entrada Fms.	Fluvial/Eolian sandstone	<11 to 25	Wilson Creek; Maudlin Gulch	
Permian-Pennsylvanian Sandstones and Carbonates	Conv	Phosphoria; local?	Weber Sandstone	sandstone and carbonate	11 to 14	Ashley Valley; Rangely	
Basin Margin Subthrusts (hypothetical)	Conv	Lower Tertiary, Upper Cretaceous, and Pennsylvanian Belden Shale	Paleozoic to Tertiary; especially Mississippian carbonates				
Cretaceous Self-Sourced Fractured Shales	Unconv	Mancos Shale - enclosing marine shale	Upper Cretaceous Mancos Shale - open fractures	brittle siltstones, carbonates, and calcareous shale and siliceous shale		Rangely	
Tight Gas Piceance Mesaverde Williams Fork	Unconv	Mesaverde Group	Williams Fork Member	medium- to fine-grained litharenites that were deposited in fluvial environments			
Tight Gas Piceance Mesaverde Iles	Unconv	Mesaverde Group; Mancos Shale	Iles Member	medium- to fine-grained litharenites			
Tight Gas Uinta Tertiary East and West	Unconv	Mesaverde Group	Uteland Butte, Chapita, and Buck Canyon zones of Wasatch Formation	medium- to fine-grained feldspathic litharenites, and litharenites mostly deposited in fluvial environments			
Basin Flank Uinta Mesaverde (hypothetical)	Unconv	Mesaverde Group	Mesaverde Group	fine- to medium-grained litharenites to feldspathic litharenites	<4 to 12		
Deep Synclinal Uinta Mesaverde (hypothetical)	Unconv	Mesaverde Group	Mesaverde Group	sandstone	3 to 8		

CO_2-EOR Projects

The Rangely Field is located on the Raven Park anticline in Rio Blanco County in NW Colorado (Hefner and Barrow, 1992; Figure 2-34). Oil production is derived primarily from the Pennsylvanian-Permian Weber Sandstone (Figure 2-32). The Rangely Field is the largest field in the Rocky Mountain Region in terms of daily and cumulative oil production (Hild and Wackowski, 1999).

The Weber Sandstone discovery occurred in 1933, and a few dozen successful wells were drilled in the subsequent two decades, with development coincidental with the onset of World War II (Hefner and Barrow, 1992). At the time Rangely Field was unitized for waterflooding and gas reinjection in October 1957, it was the second largest unit in the United States. In October 1986, tertiary CO_2 flooding of the field began.

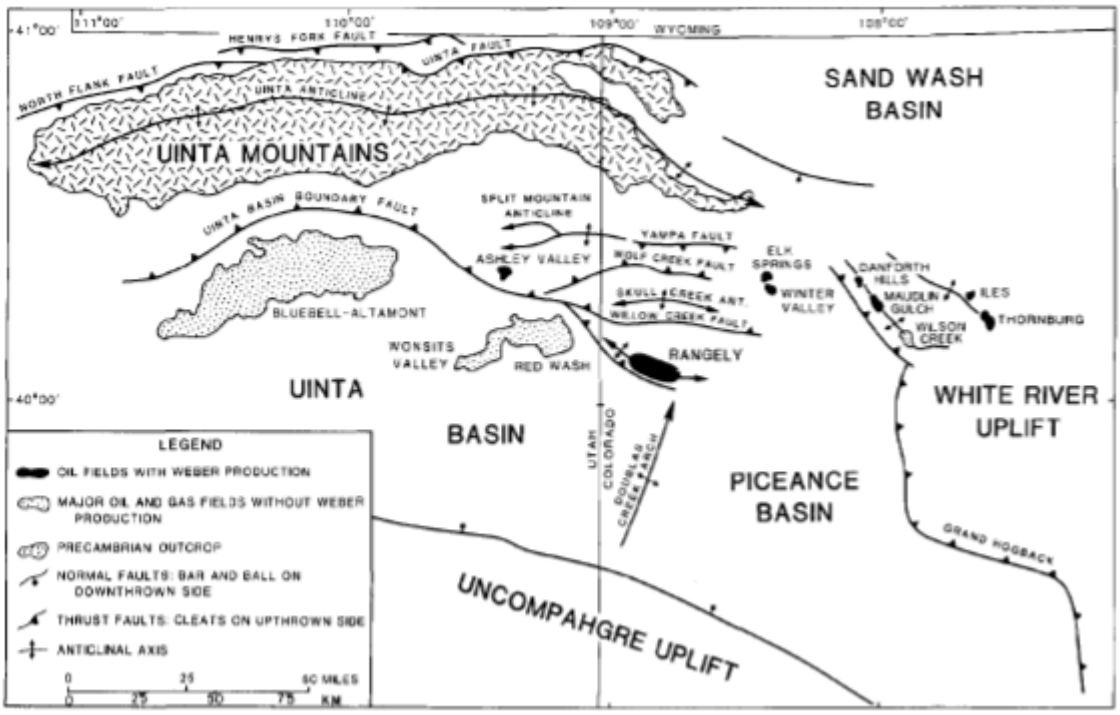


Figure 2-34. Location map showing Rangely Field in relation to structural features within the Uinta-Piceance Basin. From Hefner and Barrow (1992).

ROZ Potential

There have been no formally published studies of ROZ potential in the Uinta-Piceance Province. Despite this, the initial discovery of ROZs was in carbonate rocks of the Permian Basin, and much of the ROZ exploration outside of the Permian Basin has been in carbonate formations. However, some of the most prolific carbon storage reservoirs are within extensive siliciclastic formations. When extensive siliciclastic formations are hydrocarbon bearing, they are often associated with strong bottom water drive aquifers that dissuade operators from attempting production due to water issues. However, these reservoirs may be ideal for CO_2-EOR and associated storage because of their bypassed oil resources and significant storage potential.

Powder River, Bighorn, Wind River, and Williston Basins - Wyoming, Montana, and the Dakotas

Author: Nathan P. Grigsby

Wyoming, North Dakota, and Montana have five basins that are believed to contain ROZs: the Williston, Big Horn, Powder River, Wind River, and Green River Basins (Figure 2-35). Burton-Kelly et al., (2018) identified ROZs in The Mission Canyon and Red River Formations in the Williston Basin and conducted basin evolution modeling to investigate their CO_2-EOR and associated storage potential. Strong indications of ROZs have been documented in the Tensleep Sandstone in the Big Horn Basin (Koperna and Kuuskraa, 2006a; Yin et al., 2014; Jones, 2016). No large-scale ROZ exploration projects have been completed in the Powder River, Wind River, or Green River Basins, but there are indications that ROZs may exist. For example, Burton Kelley et al. (2018) identified five formations in the Powder River Basin that have ROZ potential, and oil has been identified in non-productive wells between Lost Soldier and Wertz Fields in the Green River Basin and outside Big Sand Draw Field in the Wind River Basin (Yin et al., 2012).

This region has a pipeline network that can distribute CO_2 from Shute Creek and Riley Ridge gas plants in western Wyoming to fields in the Wind River, Green River, Powder River, and Williston Basins (Figure 2-35). This has allowed for several large-scale CO_2-EOR projects to commercially produce oil from depleted siliciclastic reservoirs and encouraged characterization and assessment of other fields along the pipeline for tertiary recovery potential. The depleted reservoirs that these projects targeted are functionally like naturally occurring ROZs, so they may provide insight into CO_2 injection strategies and storage potential for ROZ-bearing siliciclastic reservoirs. The availability of CO_2 and successful CO_2-EOR projects have led to basin-scale economic studies of CO_2-EOR (Cook, 2012).

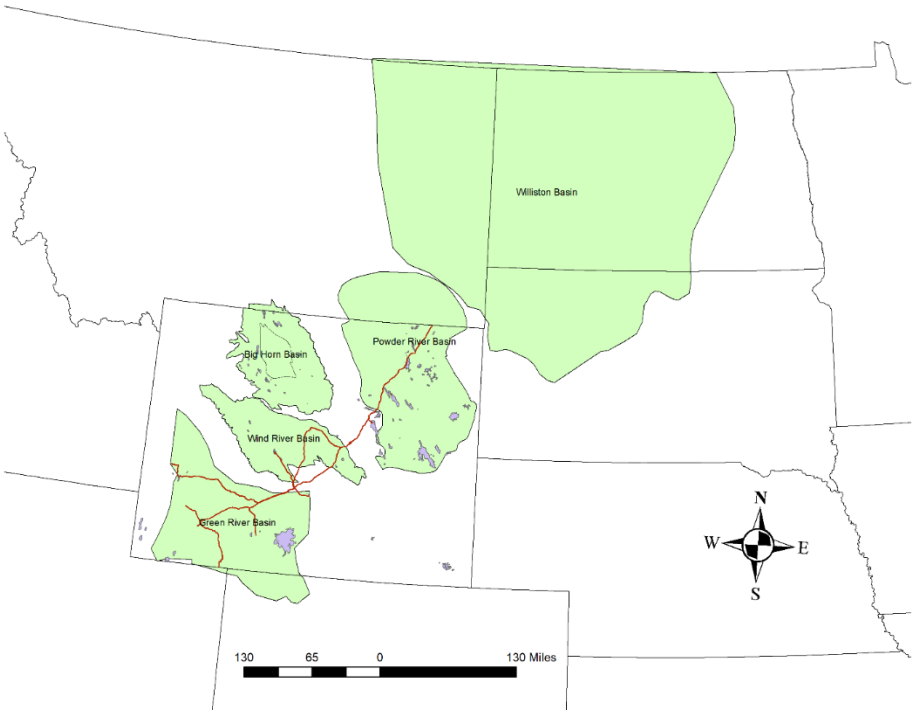


Figure 2-35. Map of basins in Wyoming, Montana, South Dakota, and North Dakota. Fields with CO_2-EOR projects or that have been characterized for CO_2-EOR injection in Wyoming are shaded purple. CO_2 pipeline shown with red line and provided by Wyoming Pipeline Authority.

Powder River Basin

The USGS conducted a large-scale resource assessment of the Powder River Basin (Anna, 2009). The study attempted to identify and quantify overlooked oil and gas accumulations by characterizing the source rock and migration pathways for five Total Petroleum Systems (TPSs) (Table 2-5). The oil migration pathways described in this report are believed to serve as conduits for ROZ creation, so the detailed geologic characterization conducted on each can be leveraged for basin-scale ROZ studies.

Table 2-5. Total Petroleum Systems and their reservoir units for the Powder River Basin. Modified from Anna (2009).

TPS	Conventional	Unconventional
Pennsylvanian-Permian Composite	Minnelusa Tensleep Sandstone Leo	
Mowry	Fall River Lakota Sandstone Muddy Sandstone	Mowry Shale
Niobrara	Frontier-Turner Sandstone Sussex-Shannon Sandstone Mesaverde-Lewis Sandstone	Niobrara
Paleozoic-Mesozoic Composite	Eastern Basin Margin Upper Fort Union Sandstone	
Cretaceous Biogenic Gas		Shallow Continuous Biogenetic Gas

Burton Kelly et al. (2018) focused on the Williston Basin but did identify four formations in the Powder River Basin that have ROZ potential based on formation geometry (thick, continuous, porous fairways necessary for ROZ formation), proximity to source rocks, and likely oil migration pathways: The Sussex, Shannon, Muddy, and Minnelusa. An ongoing research project funded by the DOE in 2019 entitled "Developing CO_2-EOR and associated storage within the residual oil zone fairways of the Powder River Basin, Wyoming" is likely to produce more information.

The four potential ROZ-bearing formations identified by Burton Kelly et al. (2018) are siliciclastic. The Sussex and Shannon Sandstones represent distal ends of a transgressive-regressive wedge of a deltaic system (Dolton and Fox, 1996; Anna, 2009; Craddock et al., 2012). The Muddy Sandstone has a complex depositional system, but primarily produces oil from valley fill fluvial and estuarine sandstones and transgressive nearshore marine sandstones. The Minnelusa is eolian (similar to Tensleep) and is a complex mixture of dunes and dolomite (Foster, 1958; Dolton and Fox, 1996; Anna, 2009; Craddock et al., 2012).

Table 2-6. Properties of the candidate formations in the Powder River Basin. Values derived from Dolton and Fox (1996) and Craddock et al. (2012).

Formation	Lithology	Depositional Environment	Typical Pay Thickness	Typical Porosity	Typical Permeability
Sussex-Shannon	Sandstone	Deltaic	5-32 ft	10-15%	1-3,000 mD
Muddy	Sandstone	Valley fill fluvial and estuarine	10-25 ft	9-22%	100 mD
Minnelusa	dolomite, evaporite, sandstone	Eolian	5-35 ft	14-20%	100 mD

CO_2-EOR Projects

Several CO_2-EOR projects have been completed in ROZ-bearing formations within the Powder River Basin. These studies have targeted depleted oil reservoirs but have produced findings that can be applied to (naturally occurring) ROZs. A water alternating gas (WAG) CO_2-EOR project in the Second Wall Creek (a fluvial/deltaic member of the Turner Sandstone) began at Salt Creek Field in 2004. This flood injected 181 billion cubic tonnes of CO_2 as of February 2010 (Hendricks, 2009; Roux and Andersen, 2010). The Teapot Dome Oil Field is immediately to the southeast of Salt Creek along the Salt Creek Anticline. The field is owned and operated by the federal government and therefore has a large amount of publicly available data. Both the Tensleep and Second Wall Creek Sandstones have been characterized at the Teapot Dome in preparation for CO_2 injection (Friedmann and Stamp, 2006; Jafri et al., 2016).

Bighorn Basin

The hydrodynamic regime of the Tensleep Sandstone across the Bighorn Basin has properties that are indicative of ROZs (i.e. tilted oil water contacts) (Hubbert, 1954; Bredehoeft et al., 1992). Koperna and Kuuskraa (2006) screened the basin and concluded that 13 oil fields have potential ROZs that contain an estimated 4.4 Bbbls of oil (~1.1 Bbbls of which is technically recoverable). Since then, the Enhanced Oil Recovery Institute has bolstered the case for a basin-scale ROZ fairway in the Tensleep by developing a more detailed understanding of the basin's oil migration pathways, identifying indirect indicators of ROZs, such as oil shows in non-productive wells, high water cuts, fresh water, and calcite, and gathering anecdotal evidence from local operators (Yin et al., 2012, 2014; Jones, 2016). Their studies have focused on data-rich oil fields and the immediate vicinity to identify brownfield ROZs connected by associated greenfield ROZs (Figure 2-36).

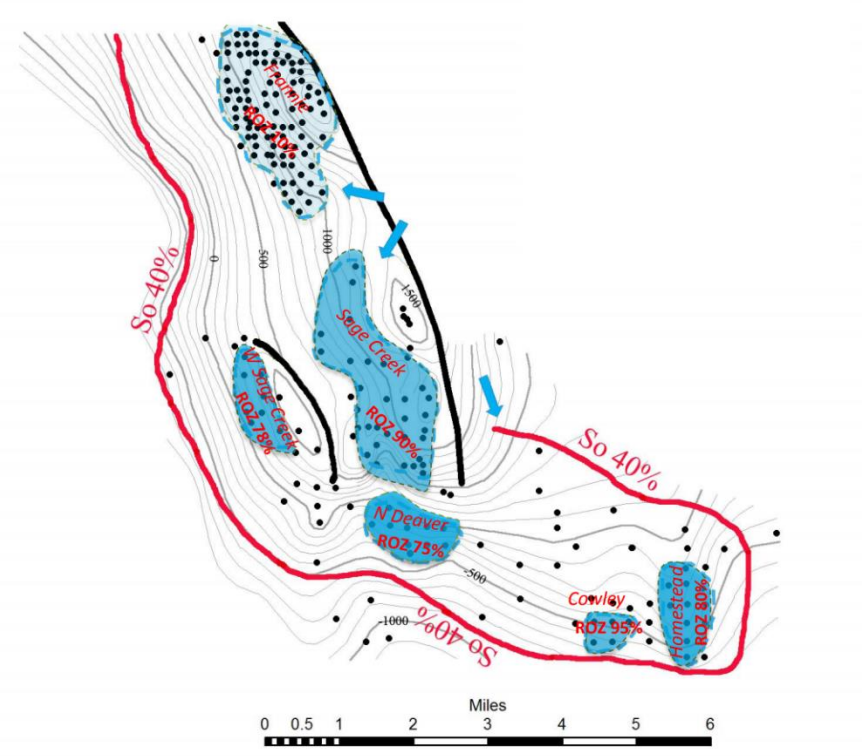


Figure 2-36. Frannie-Sage Creek-Homestead ROZ taken from Yin et al., 2014. Red line is 40% oil saturation contour. Evidence suggests that brownfield ROZs exist beneath oil fields (shaded blue) with a greenfield ROZ filling the space between them.

Tensleep Sandstone

The Tensleep is the most productive formation in Wyoming. It produces oil throughout the Bighorn Basin, on the western side of the Wind River Basin, and the northeastern edge of the Green River Basin. Several successful CO_2-EOR projects have targeted the Tensleep (Salt Creek/Teapot Dome, Big Sand Draw, Wertz/Lost Soldier) (Jafri et al., 2016; Kleinsteiber, 1990). The ROZ potential of the Tensleep has been well characterized in the Big Horn Basin, but there is evidence that it may have ROZs in other basins. Oil shows in non-productive wells have been identified between Wertz and Lost Soldier Fields and outside the Big Sand Draw Field in the Wind River Basin.

The Tensleep has been divided into an upper productive eolian cross-bedded sandstone and a lower dolomite member. Flow beds are often compartmentalized due to the highly variable nature of the depositional environment. Furthermore, natural fractures exert a strong influence on the hydrodynamic regime (Cooper and Lorenz, n.d.; Bredehoeft et al., 1992) and may be responsible for widespread Type 2 ROZs.

Table 2-7. Tensleep formation properties. Taken from Craddock et al. (2012).

Formation	Lithology	Depositional Environment	Typical Pay Thickness	Typical Porosity	Typical Permeability
Tensleep	Limestone, some sandstone	Eolian	75-150 ft	16%	100 mD

Wind River Basin

ROZs have not been studied in the Wind River Basin, but the basin does have two successful CO_2-EOR projects; Madison Formation in Beaver Creek Field and Tensleep in Big Sand Draw Field. Wells with high water cut and non-productive oil shows have been observed in the vicinity of Big Sand Draw Field, which may indicate an associated greenfield ROZ beyond the field's boundaries (Yin et al., 2012).

Green River Basin

Lost Soldier and Wertz Fields on the northeastern edge of Green River Basin have both had successful CO_2-EOR projects. Injection into the Tensleep at Wertz began in 1986 (Kleinstelber, 1990). A line drive WAG was started in 1989 in the Tensleep at Lost Soldier Field (Brokmeyer et al., 1996). The success of these projects led to additional studies to prolong or increase production (Eves and Nevarez, 2009; Aryana et al., 2014). Wells drilled between the fields have oil shows and low oil cut/high water cut production, which indicates that an associated ROZ may extend between them (Figure 2-37).

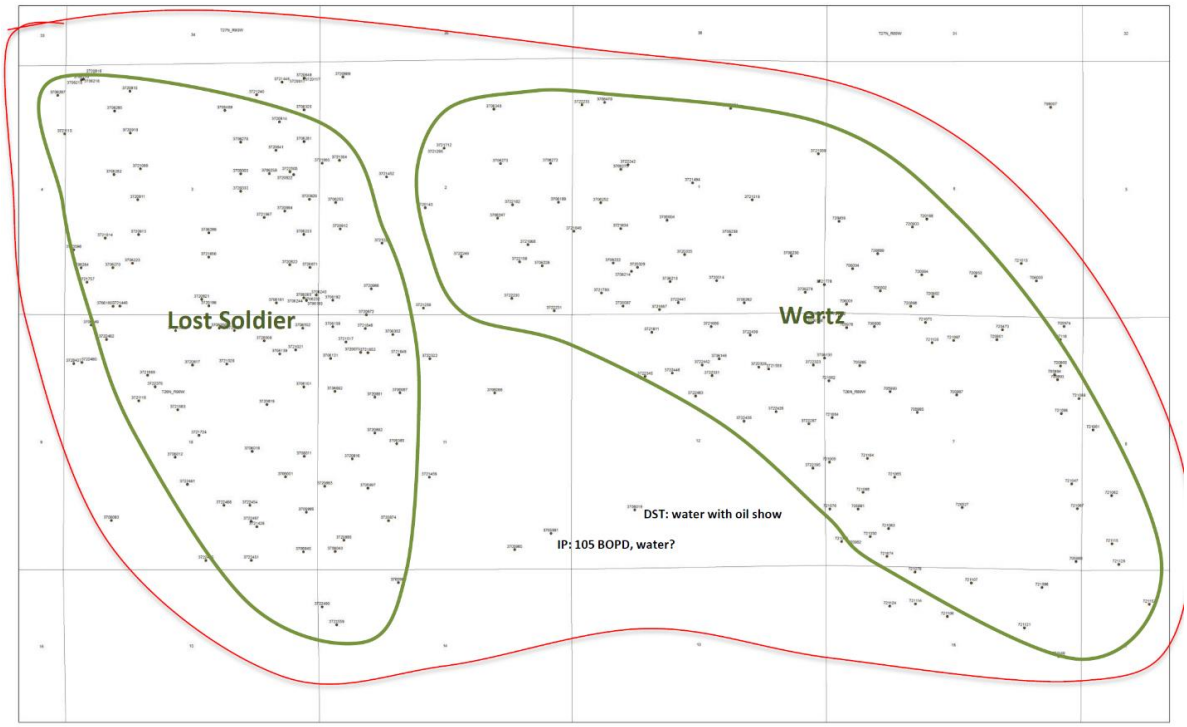


Figure 2-37. Map of Lost Soldier and Wertz fields showing indications of ROZ between fields. Taken from Yin (2012).

Williston Basin

Several studies have looked at the undiscovered oil resources (USGS, 2013) and ROZ potential (Koperna and Kuuskraa, 2006b; Burton-Kelly et al., 2018) of the Williston Basin. The USGS study identified ten TPSs with undiscovered oil resources (Table 2-8; Anna, 2011).

Table 2-8. Williston Basin Total Petroleum Systems. From Anna (2011).

TPS	Conventional	Unconventional
Bakken-Lodgepole		
Winnipeg-Deadwood	Winnipeg-Deadwood	Winnipeg-Icebox
Red River	Red River Fairway Red River East Margin Interlake-Stonewall-Stony Mountain	
Winnipegosis	Winnipegosis	
Duperow	Dawson Bay Souris River Duperow-Birdbear	
Cedar Creek-Paleozoic Composite	Cedar Creek Structural	
Madison	Mission Canyon -Charles	
Tyler	Tyler Sandstone	Tyler Shale
Shallow Biogenic Gas		
Coalbed Gas		

Burton Kelley et al. (2018) assessed the thickness, heterogeneity, oil production, and indirect indicators of ROZ of the major formations in the Williston Basin and concluded that the Mission Canyon and Red River Formations have the highest ROZ potential (Table 2-9). They then created basin evolution models for both formations, identified areas that had the potential to contain ROZs, and estimated the oil within ROZs in the Williston Basin.

The Mission Canyon is a primarily carbonate Mississippian Formation (Fischer et al., 2005). The formation is one of the most prolific oil producers in the basin, but reservoir characteristics are difficult to generalize because the petrophysical properties are controlled by seven spatially variable facies. The Red River is a primarily dolomitized limestone Ordovician and Silurian (Carroll, 1979; Fischer et al., 2008).

Table 2-9. Properties of candidate formations in the Williston Basin. Values taken from Fischer et al. (2005); Fischer et al., (2008).

Formation	Lithology	Depositional Environment	Typical Pay Thickness	Typical Porosity	Typical Permeability
Red River	Mostly dolomite	Marine to shallow marine to sabkha	10-20 ft	15-16% in unit B 8-25% in unit C	7 mD
Mission Canyon	Mostly dolomite	Marine	15 ft	8%	32 mD

Conclusion

The ROZs within the Williston, Big Horn, Powder River, Wind River, and Green River Basins have much in common with those that are believed to occur within the Illinois Basin. They often occur within siliciclastic formations, and the oil-bearing intervals are on the order of 10s of feet thick (in contrast to the 100s of feet thick ROZs that have been economically produced in the Permian Basin carbonates). The availability of CO_2, coupled with existing oil production infrastructure and confirmed ROZs, makes more ROZ-focused studies likely, which could yield synergistic opportunities soon.

3. Illinois Basin ROZ Characterization

Regional geologic characterization was conducted for the formations of interest within the ILB stacked complex (including greenfield and brownfield ROZs and conventional oil reservoirs) to develop a regional geologic framework for the ROZs and their overlying seals. ROZ fairway maps were also developed but will be discussed in detail in Chapter 6.

This chapter will cover each of the four formations identified as part of the screening process described in Chapter 2. The four formations include the Tar Springs Sandstone, Cypress Sandstone, Carper Sandstone, and Geneva Dolomite/Dutch Creek Sandstone.

3.1 Geological Characterization of ROZs and Seals

3.1.1 Tar Springs Sandstone

Authors: Zohreh Askari and Yaghoob Lasemi
Published as Technical Report DOE-UIUC-31700-4, OSTI ID: 1905583

The upper Mississippian (Chesterian) Tar Springs Sandstone (Figure 3-1) is a major oil producing unit in Illinois. It is one of several Mississippian sandstone units that together have contributed more than 60% of the cumulative oil production in the Illinois Basin (Howard, 1990). The Tar Springs is present in the southern part of the Illinois Basin; the basin covers southeastern Illinois, western Kentucky, and southwestern Indiana (Figure 3-2). Like other Mississippian sandstones, the Tar Springs consists of conventional reservoirs and produces from mature oil fields showing declining primary and secondary production trends. Substantial amounts of immobile oil are remaining in the depleted Tar Springs Sandstone reservoirs. Most of the remaining oil could be recovered by the implementation of enhanced oil recovery methods. The average recovery factor for mature reservoirs is estimated to be between 20% to 40% and application of tertiary recovery techniques is effective at mobilizing the remaining oil and increasing the recovery factors up to 50%–70% (Muggeridge et al., 2014).

Conventional oil reservoirs occur in association with residual oil zones (ROZs) that contain naturally occurring immobile oil (Melzer, 2006). The ROZs found below conventional oil reservoirs are named brownfield ROZs that can also extend beyond the boundaries of conventional oil fields (e.g., Sanguinito et al., 2020). ROZs are potential targets for carbon dioxide enhanced oil recovery (CO_2-EOR) and for storing large volumes of anthropogenic carbon in the subsurface (Melzer, 2006; Sanguinito et al., 2020).

The Tar Springs Sandstone consists of interbedded shale and sandstone reservoir intervals (Figure 3-3), which may be oil productive and/or have ROZ potential. It was one of the candidates selected for geologic characterization related to the brownfield lab site in Richland County, Illinois. Here we focus on regional and field scale geological characterization of the Tar Springs in Illinois. We have used well records, including drilling and completion reports, well logs, and core data (core descriptions/core analyses) to analyze and interpret geological variations. In addition, oil saturation indicators (oil shows, oil saturation from core analysis, and drill stem test data) were analyzed to determine the ROZ potential of the Tar Springs Sandstone.

Geological and Stratigraphic Settings

The Illinois Basin was formed in the Cambrian over the northeast extension of the Reelfoot Rift system (Kolata and Nelson 1990, 2010). The basin is bordered by a series of prominent structures and includes southern Illinois, western Kentucky, and southwestern Indiana (Kolata and Nelson, 1990). During the Chesterian (upper Mississippian), the rate of subsidence in the Illinois Basin increased due to

compressional stress related to the Ouachita and Alleghenian orogenies (Kolata and Nelson, 1990). As the result, the basin interior was rapidly subsiding and was open to the southwest at the edge of the Ouachita Trough (Nelson, 1995).

The Tar Springs Sandstone constitutes the upper part of the Chesterian Series that is comprised of cyclic alternation of (Figure 3-1) carbonate and siliciclastic unites (Swann, 1964; Nelson et al., 2002). It was deposited as the result of basinward advance of the Michigan River system (Swann, 1964). The Tar Springs is named for the Tar Springs in western Kentucky and consists of very fine- to fine-grained, friable to well-cemented sandstone (Atherton et al., 1975). It overlies the Glen Dean Limestone and underlies the Vienna Limestone (Figures 3-1 and 3-3). A widespread shale interval is present in the uppermost part of the Tar Springs. The upper part of this shale may be carbonaceous and could contain thin coal beds (Morse, 2001; Nelson et al., 2002). According to Atherton et al. (1975), the upper and lower contacts of the Tar Springs are conformable. However, Swann (1963) and Morse (2001) reported local erosion along the lower boundary and removal of up to 40 ft (12 m) of the upper part of the Glen Dean Limestone. Morse (2001) recognized channelized sandstone bodies directly above the Glen Dean Limestone and suggested a widespread minor disconformity at the base of the Tar Springs. The isopach contour map (Figure 3-4) shows the areal extent and lateral thickness variation of the Tar Springs sandstone in Illinois. The thickness of the Tar Springs ranges from zero to more than 140 ft (0 to 43 m).

Lithofacies and Depositional Setting

The Tar Springs Sandstone consists of massive and stacked lenticular sandstone bodies interbedded with shale/siltstone (Figures 3-5 and 3-6). The lower part of the Tar Springs commonly consists of massive fluvial channel sandstone bodies that overlie directly on the Glen Dean Limestone or on a shale/siltstone interval in the basal part of the Tar Springs (Figures 3-3, 3-5, and 3-6). The massive sandstone is generally widespread, but its thickness is very variable ranging from zero to over 100 feet. It may locally consist of stacked channel deposits separated by thin shale or shale partings. The upper part of the Tar Springs is comprised of shale and lenticular sandstone intervals; the lower massive sandstone interval may also change laterally to compartmentalized lenticular sand bodies with shale interbeds (Figures 3-3 and 3-6).

Geophysical log motifs, including gamma ray, spontaneous potential (SP), and resistivity log signatures of the Tar Springs sandstone bodies display barrel/blocky, bell (fining upward) or funnel (coarsening upward) log signatures with shale interbeds (Figures 3-3, 3-5, and 3-6). The log motifs of sand bodies and interbedding with shale are interpreted as fluvio-deltaic depositional system (e.g., Coleman and Prior 1982). The depocenters of the sandstone bodies as indicated by net sandstone isopach map (Figure 3-7), log motifs, and facies analysis (Wescott, 1982; Morse, 2001; Henderson et al., 2020) indicate a heterogeneous unit recording a general northeast-southwest transition and depositional change from mainly coastal fluvial systems to tidally influenced deltaic and shallow-marine environments.

The stacked lenticular sandstones showing coarsening upward and barrel shape log motifs (for examples see wells API# 121592628300 and 121592354600 in Figure 3-5 and well API# 121933213700 in Figure 3-6) represent deltaic distributary mouth bars and distributary channel facies, respectively. The shale intervals correspond to interdistributary bay and deeper marine prodelta settings. Massive sandstone showing barrel or fining upward log signatures (for examples see wells API#121592608400 and 121590025000 in Figure 3-5 and wells API#121933213100 and 121933217900 in Figure 3-6) that locally cut into the lower shale interval of the basal Tar Springs represent narrow southwest trending fluvial

channel belts. The fluvial channel deposits commonly constitute the lower part of the Tar Springs and change laterally and vertically to coastal and mainly delta front and delta plain facies.

Reservoir Facies and Trap Mechanism

The Tar Springs Sandstone consists of quartzose sandstone bodies with siltstone and gray shale interbeds. Morse (2001) and Henderson et al. (2020) described the Tar Springs reservoirs as well-sorted, fine- to medium-grained quartz arenites with less than 5% feldspar and chert containing abundant cross bedding, ripple cross-lamination and planar bedding. Digenetic quartz overgrowth and clay mineral cement (mainly kaolinite and chlorite) partially occlude pore throats impacting porosity and permeability (Morse, 2001; Henderson et al., 2020).

The impact of post-depositional diagenesis on reservoir porosity and permeability of the Tar Springs varies in various parts of the basin. In the Roland consolidated, Inman east consolidated, and Rock Hill oil fields (Figure 3-8) for example, measured porosity ranges from 14 to 23% and permeability varies in the range of zero to 740 millidarcies (md). In the Roland consolidated field, White County (see below) core analysis report of 15 wells indicated porosity ranges from 6% to 25% and permeability from zero to 740 md with average measured core porosity and permeability of 17% and 76 md, respectively. In the Inman east consolidated oil field, Gallatin County, Morse (2001) measured porosity and permeability values in cores of 31 wells and measured reservoir porosity that ranged from 16% to 19% and permeability from 60 to 700 md with average permeability of 107 md and average core porosity of 17%. In the Rock Hill field, southwest Indiana, Henderson et al. (2020) used core plugs from three wells and measured average porosity and permeability of 20.5% and 644.3 md, respectively.

The Tar Springs reservoirs in Illinois have been productive in several oil fields with more than 1,290 producing wells. Entrapment and accumulations of oil in the Tar Springs was controlled by structural, stratigraphic (sandstone body lateral pinch out), or structural-stratigraphic combination traps. Structural control is the main trap mechanism in most oil fields. Along the Clay City Anticline near the brownfield lab site in Richland County, Illinois, few wells produce from the Tar Springs Sandstone (Figure 3-5). Most of the Tar Springs oil production in southeastern Illinois is from oil fields along the Wabash River (Figure 3-9). Here, production is mainly from fault controlled anticlinal structures in Gallatin and White Counties.

Oil Field Characterization

The Roland Consolidated Field along the Albion-Ridgway Fault Zone (Figure 3-10) in southeastern Illinois was selected for field scale geological characterization and ROZ evaluation of the Tar Springs Sandstone. The rationale for this selection was that the field has produced from compartmentalized lenticular sandstones and the upper part of the massive sandstones both of which have Roz potential. The oil fields in southeast Illinois, including the Roland consolidated field were developed along the fault zones in the Wabash Valley fault system. The fault system consists of a series of high-angle normal faults (Nelson 1995).

Roland Consolidated Field

The Roland Field is developed along the Albion-Ridgway Fault Zone, a north-northeast trending high angle normal fault in southeastern Illinois (Figure 3-10). The producing wells and those with show of oil indicators in the Tar Springs occur mostly along the eastern margin of the field (Figure 3-10), where a dragged fold anticlinal structure (Figure 3-11) was developed in the upthrown side of the Albion-Ridgway Fault Zone. The field was discovered in 1940 and is primarily located in southwestern White

County, Illinois (Figures 3-8 and 3-10). More than 1,500 wells were drilled in the field and nearly 70 million barrels of oil have been produced from various Chesterian carbonate and siliciclastic units including the Tar Springs. A structural-stratigraphic combination trap mechanism was generally responsible for oil entrapment. The shale in the uppermost part of the Tar Springs Sandstone, the Vienna limestone, and the underlying shale of the sandstone of the Waltersburg Formation provide caprock/seal for the Tar Springs reservoirs (Figure 3-12).

In the Roland Field, like other areas of the basin, the Tar Springs consists of massive and stacked lenticular sandstone bodies the upper part of which may be oil saturated and productive of oil (Figure 3-6 and Figures 3-13 through 3-15). Blocky, bell, and funnel geophysical log motifs (Figures 3-6, 3-14, and 3-15) indicate a general northeast-southwest trend of the sand bodies suggesting fluvial and coastal deltaic and tidal flat depositional setting. Based on core analysis data of the upper and lower sandstone intervals from 15 wells in the Roland Field, reservoir porosity ranges from 6% to 25% and permeability from zero to 740 md with average measured core porosity and permeability of 17% and 76 md, respectively (Figure 3-16).

Production has been from the upper lenticular sandstone and the upper part of the massive sandstone. The wells with show of oil in the Tar Springs reservoirs could have in fact been oil productive because: (1) they are located near the crest of the fold (Figures 3-14 and 3-15), (2) geophysical log signatures show porous intervals with high true resistivity (Figures 3-13 through 3-15), (3) drill stem tests (for example, well API#121930682800 in Figure 3-14 and Wells API#121930192600 and 121930195500 in Figure 3-15) recorded several to hundreds of feet of oil, and (4) core analysis reports (for examples see Figure 3-13) indicate oil saturation. In the Roland Field, several formations are oil productive. The common practice is production from the deeper reservoirs followed by perforating the shallower reservoirs after depletion of the deeper pays. Operators generally do not report any future workover; thus, the database underrepresents the number of wells producing from the Tar Springs.

This study revealed that substantial amounts of immobile residual oil remain in the depleted Tar Springs Sandstone reservoirs and those that extend beyond the boundaries of conventional oil fields in which their ROZ potential has been established through the available subsurface records in the subsurface. Well completion reports, oil shows/oil saturation from core analysis and drill stem test data suggest that the Tar Springs Sandstone has an excellent potential for CO_2-EOR and storage of anthropogenic carbon dioxide. CO_2-EOR is effective at mobilizing the residual oil from the ROZs and would also store anthropogenic carbon in the subsurface (e.g., Sanguinito et al., 2020).

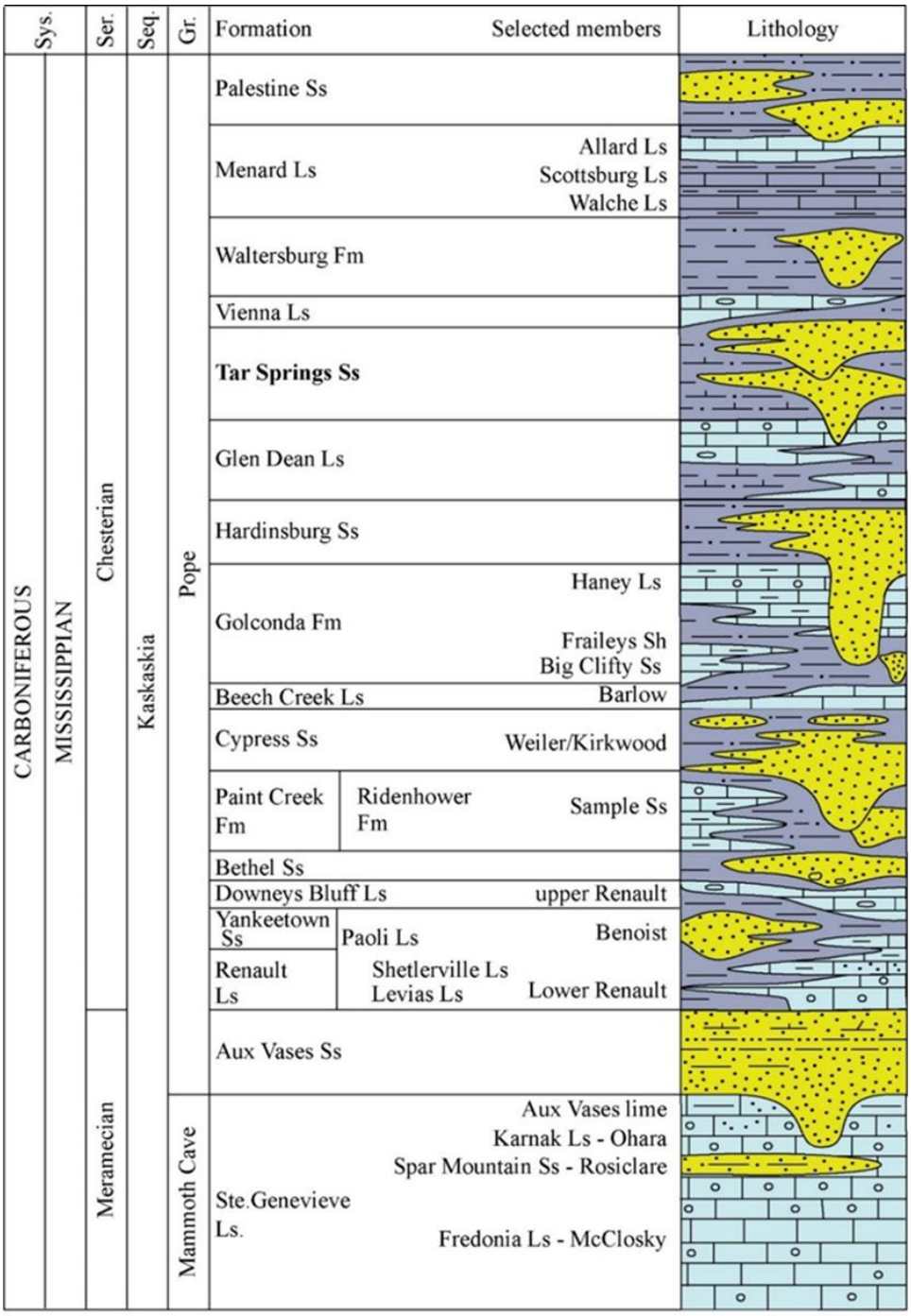


Figure 3-1. Upper Mississippian stratigraphic column in Illinois (modified from Kolata, 2005). Abbreviations: Dol., dolomite; Fm., formation; Ls., limestone

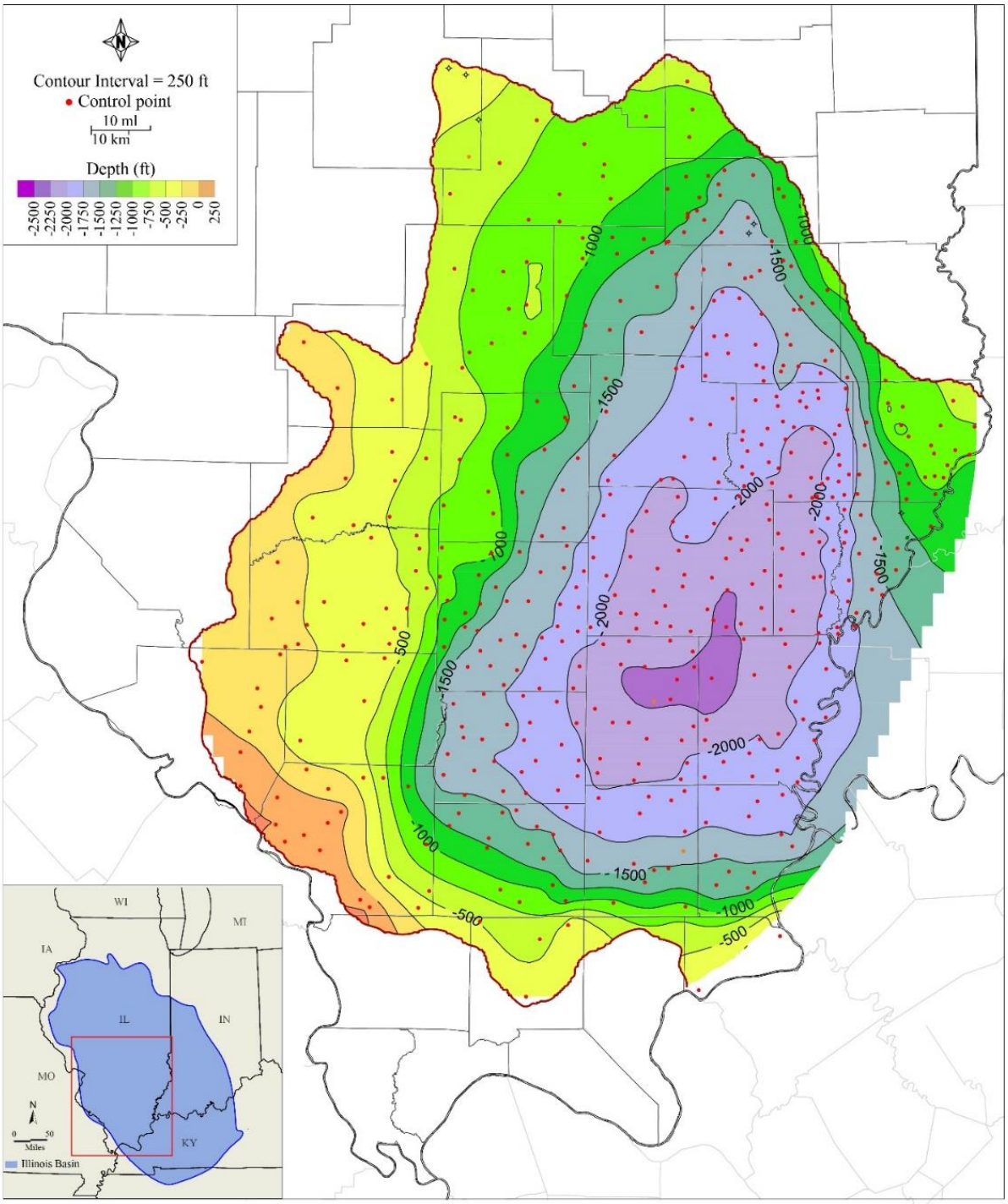


Figure 3-2. Structure contour map showing the extent of the Illinois Basin in Illinois during deposition of the Tar Springs Sandstone (datum is the base of the upper shale unit of the Tar Springs). The outline of the Illinois Basin (in blue) is shown in the index map.

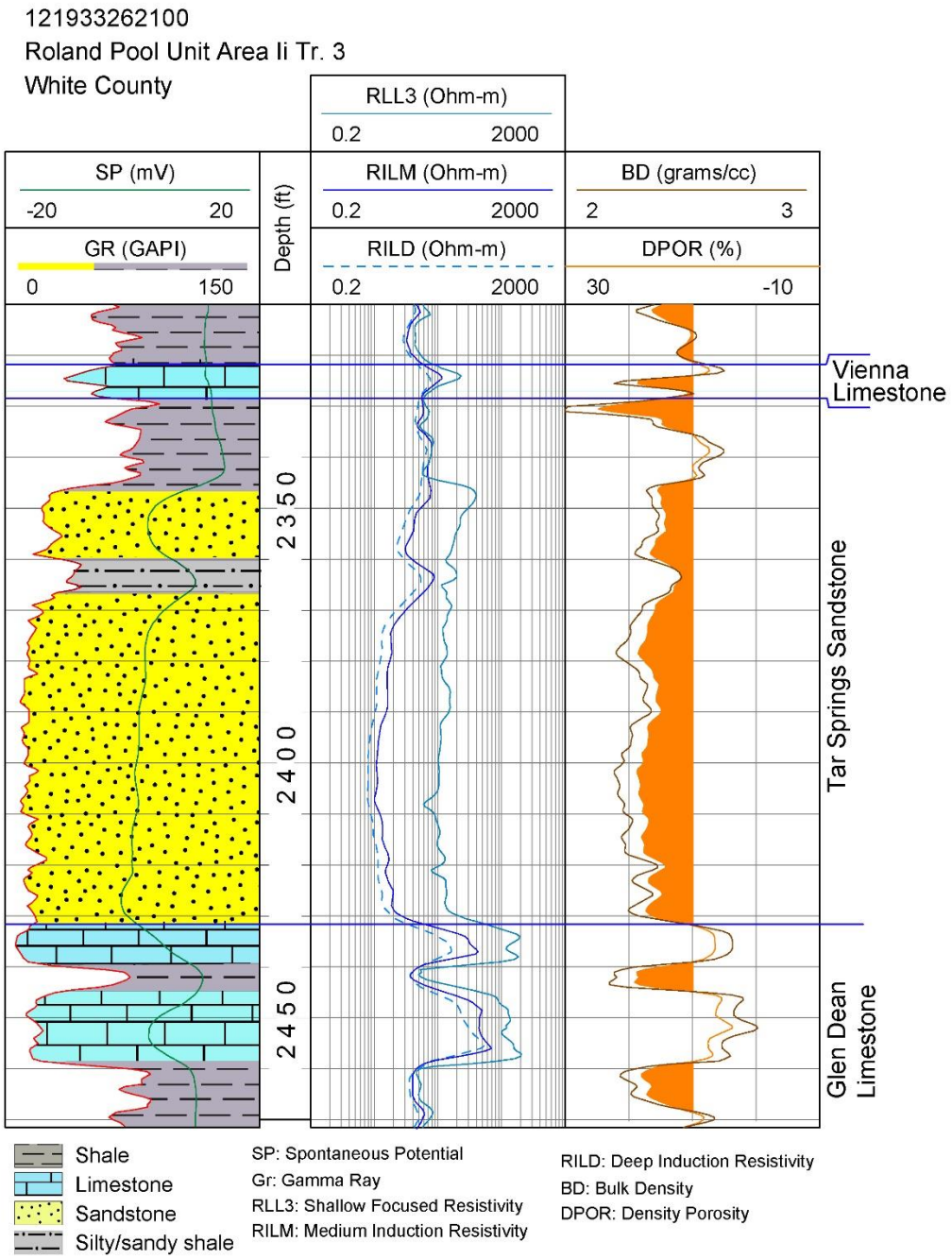


Figure 3-3. Type log and lithologic column in white County, Illinois (well API 121933262100) showing the stratigraphic relationship of the Tar Springs Sandstone with the underlying and overlying carbonate formations. Gamma ray log signature indicates blocky, coarsening, and finning upward motifs. massive sandstone and thin lenticular sandstone that occur in the lower and upper part of the Tar Springs, respectively.

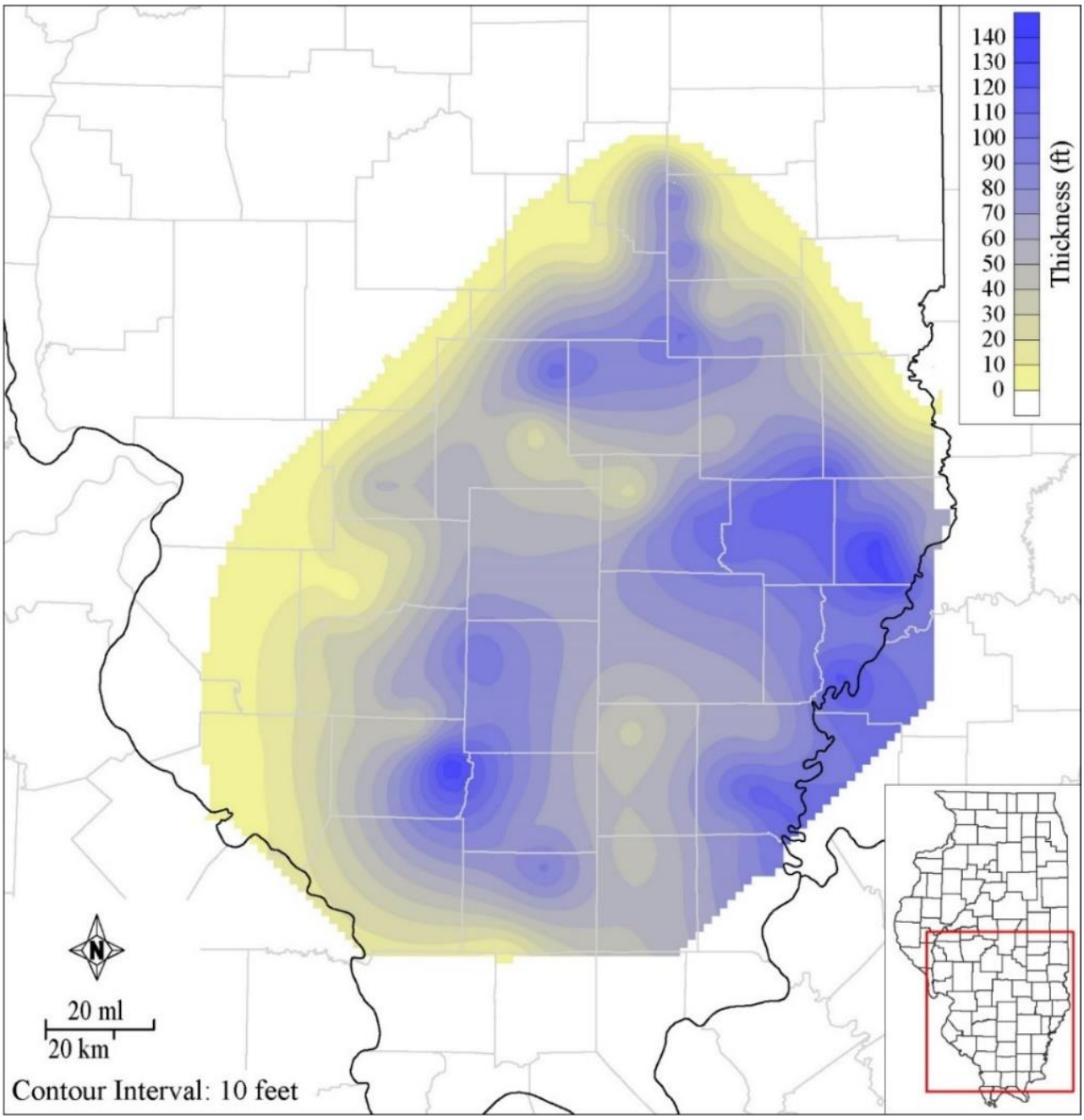


Figure 3-4. Isopach contour map showing the Tar Springs Sandstone thickness and its areal extent in Illinois. Note that the Tar Springs depocenters in Illinois display an overall north-south/northeast-southwest trend.

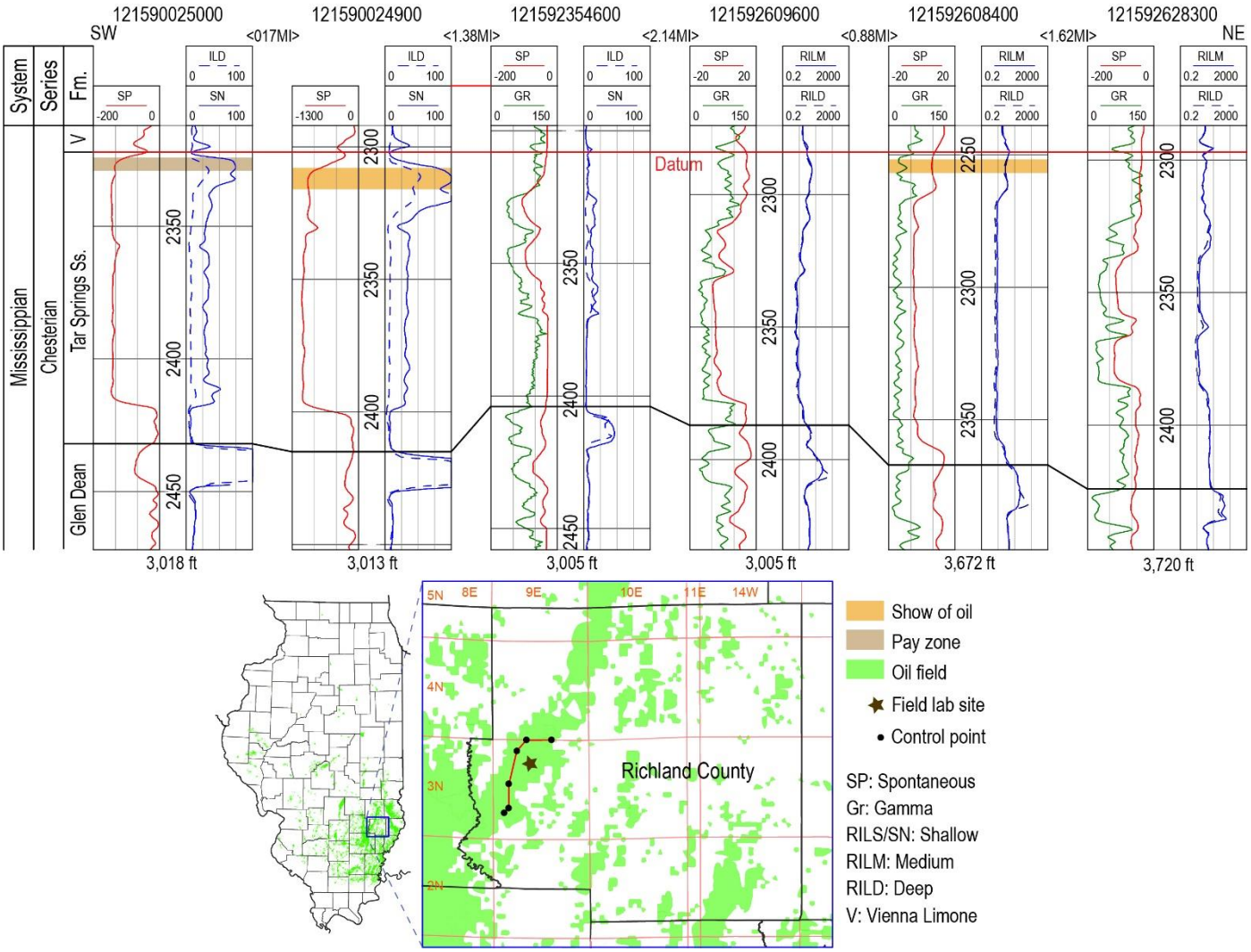


Figure 3-5. SW-NE stratigraphic cross section along the Clay City Consolidated oil field, Richland County showing lateral and vertical variations of the massive and lenticular sandstone intervals in the Tar Springs Sandstone. Note gamma ray log signatures showing blocky, coarsening, and finning upward profiles. Note also lateral change of massive sandstone to lenticular sandstone (datum base of the Vienna Limestone).

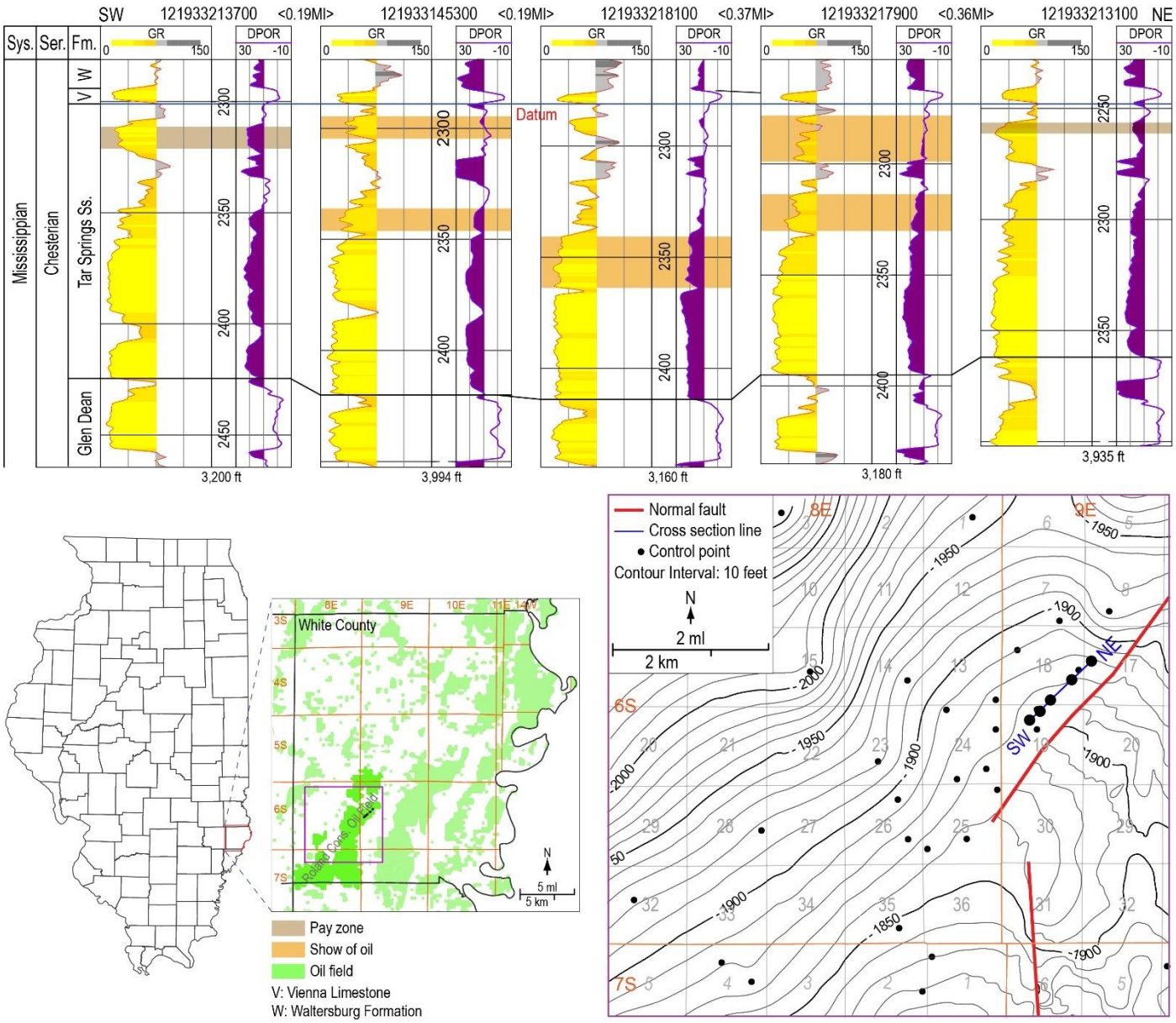


Figure 3-6. Stratigraphic geophysical log cross section showing lateral continuity and vertical lithologic variation of the massive and stacked lenticular sand bodies of the Tar Springs Sandstone in the northeast of the Roland Field, White County. Note the oil shows and oil productive intervals (Datum is the base of the Vienna Limestone). Note also that the wells with show of oil (database record) should be productive because the subsea elevation of these wells are nearly the same as in the productive wells (Datum is the base of the Vienna Limestone).

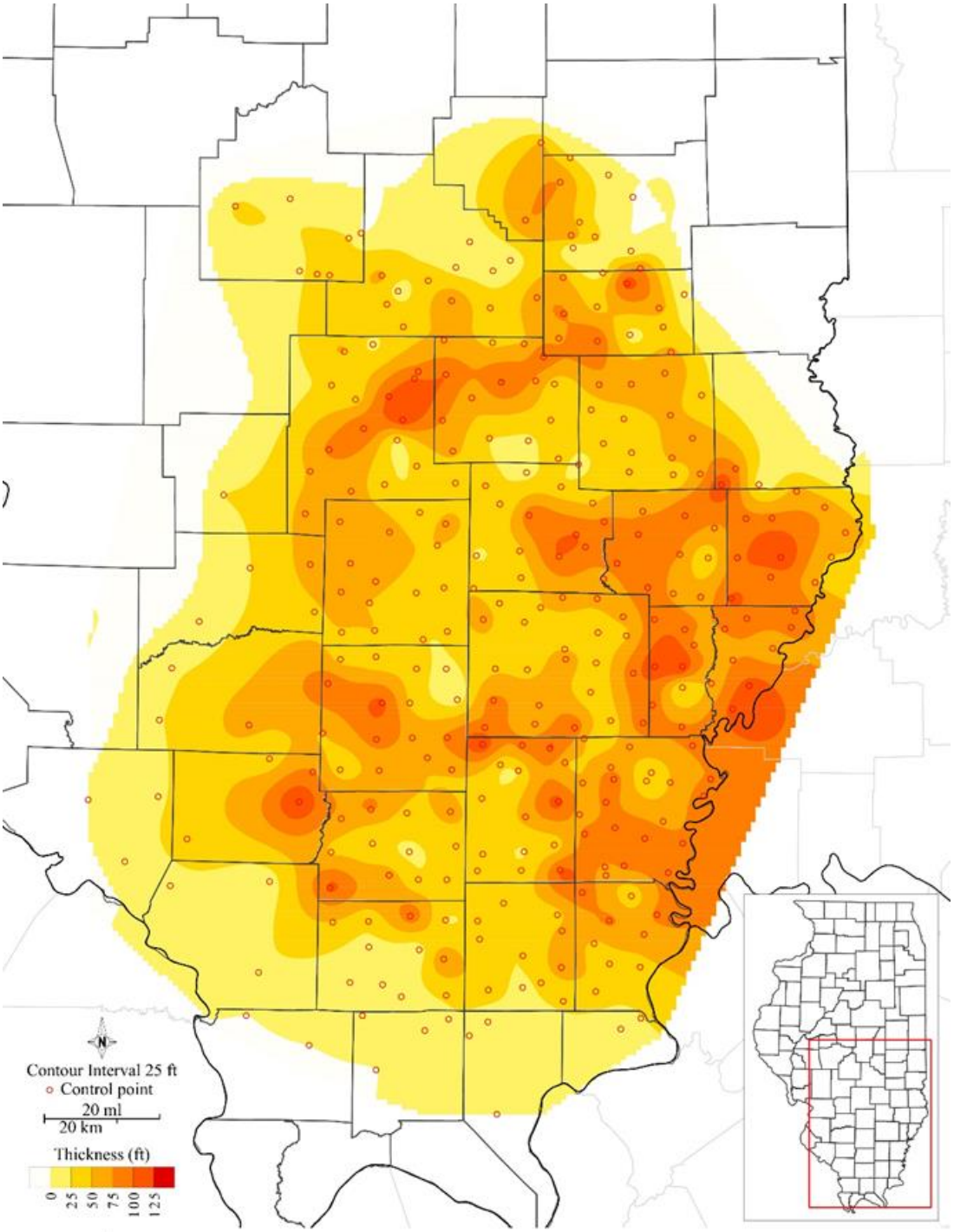


Figure 3-7. Net sand isopach map of the Tar Springs in Illinois showing. The overall paleo-shoreline perpendicular northeast-southwest/north-south trend.

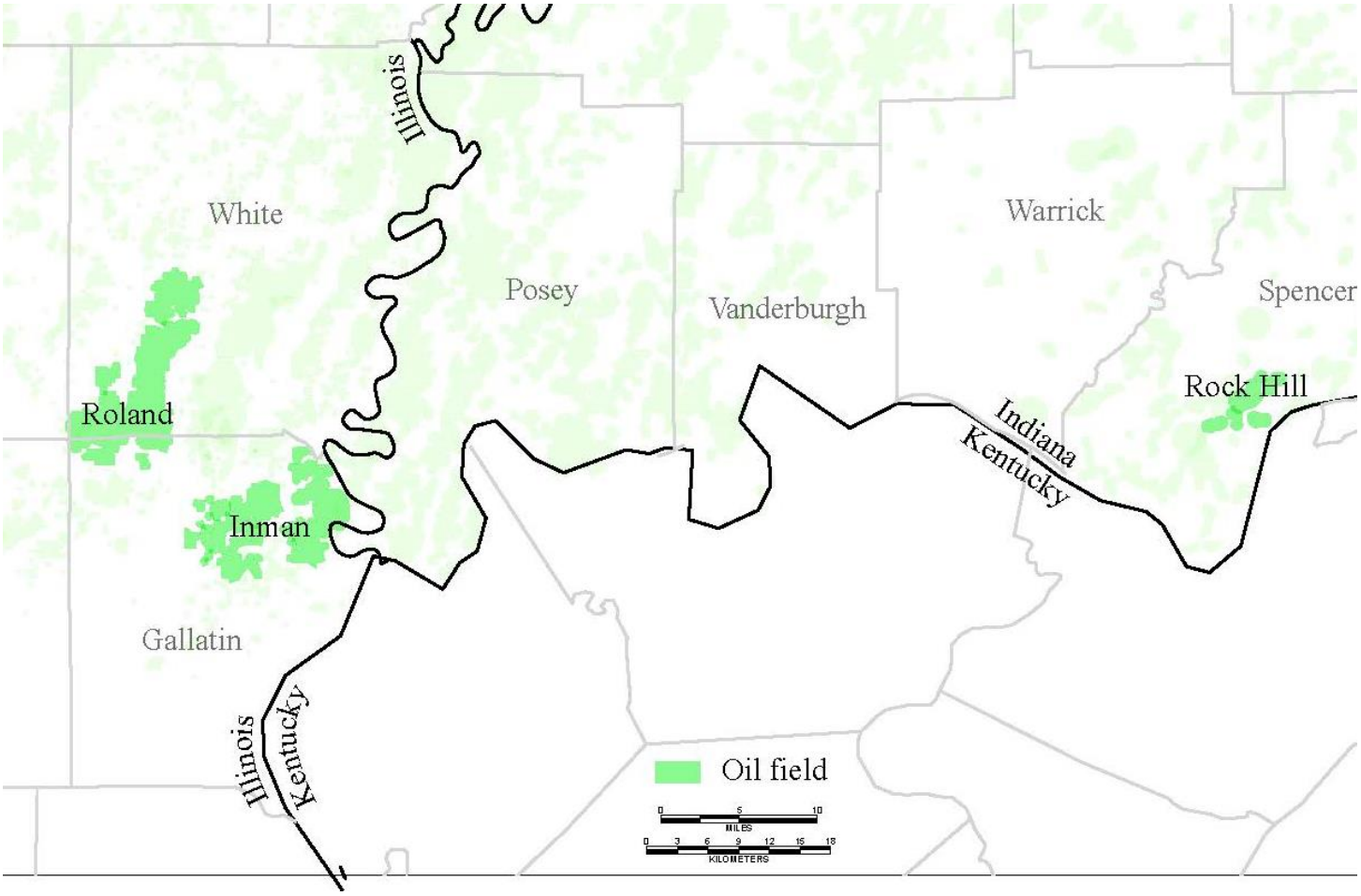


Figure 3-8. Index map showing Roland Consolidated, Inman East Consolidated, and Rock Hill fields in the southwestern part of the Illinois Basin.

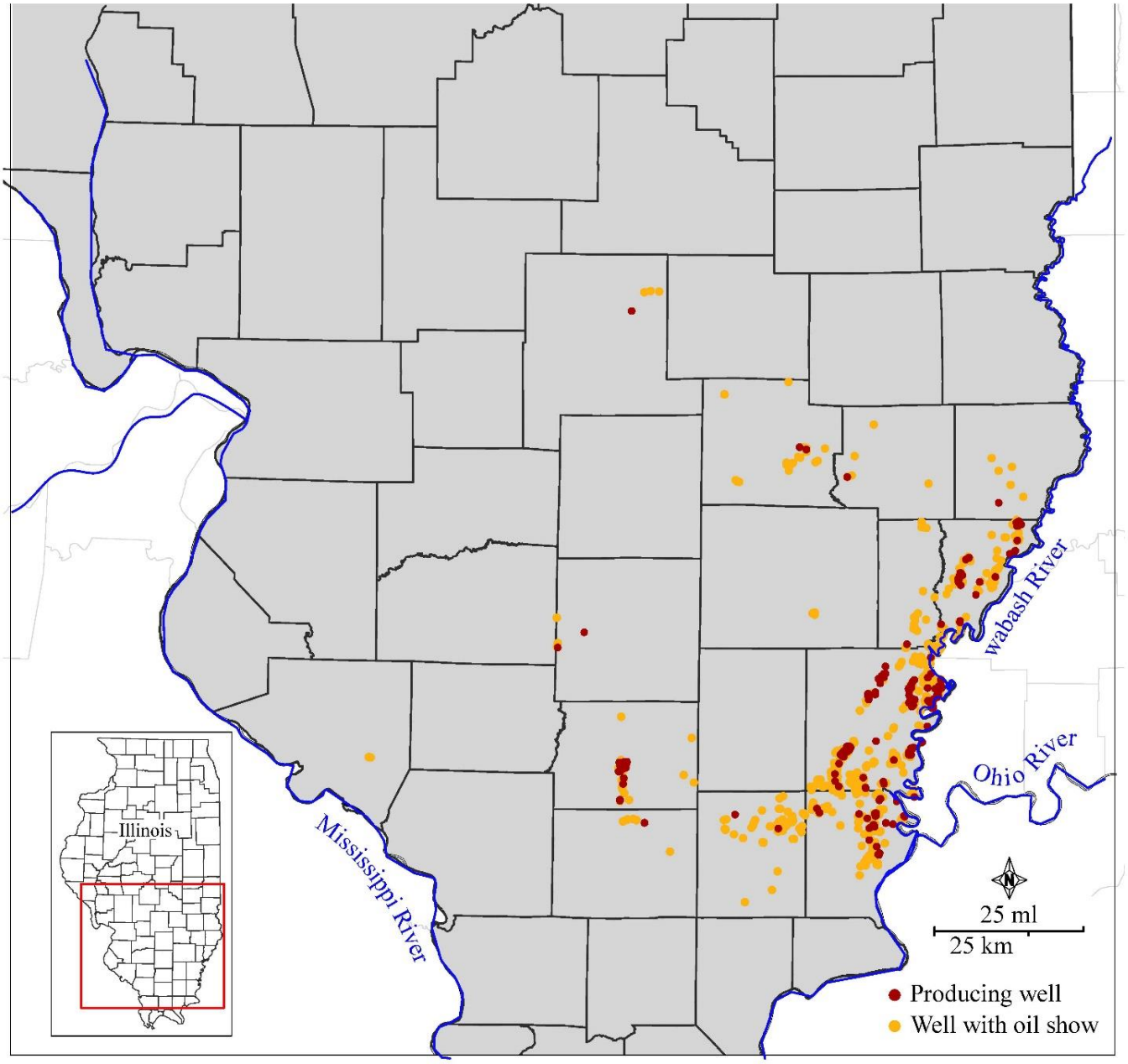


Figure 3-9. Distribution of wells (not all wells are shown) and oil indicators in the Tar Springs Sandstone. Note that some of the wells with oil show could have produced. Wells along the crest of the anticlines encounter more than one reservoir but the normal practice is production from the deeper reservoir during early life of a well. Operators do not report any future workover on producing wells.

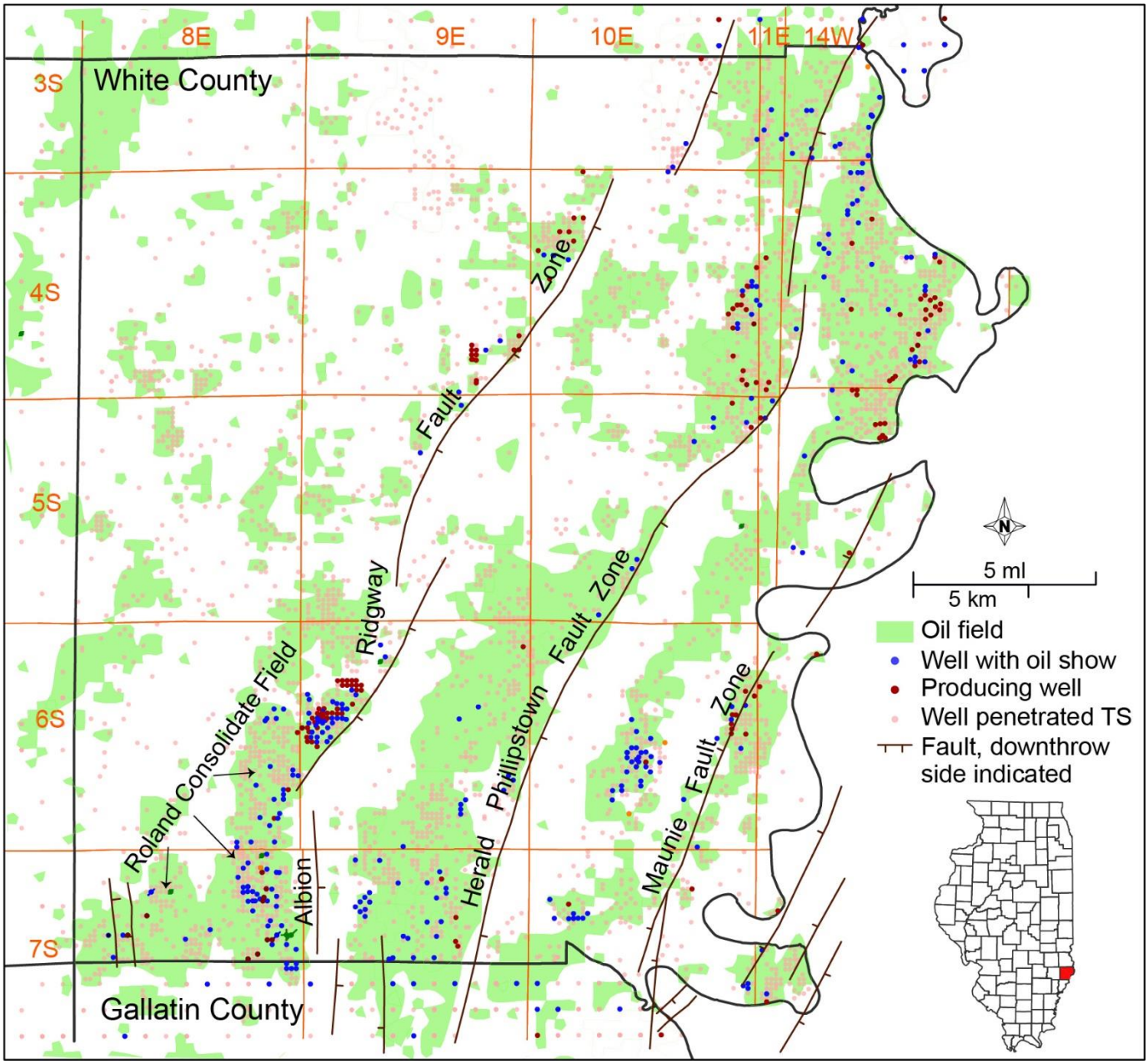


Figure 3-10. Map showing the fault zones along the Wabash Valley fault system in White County, Illinois (from Nelson, 1995). Note the wells that penetrated the Tar Springs Sandstone and the producing wells, and wells with show of oil in the Tar Springs.

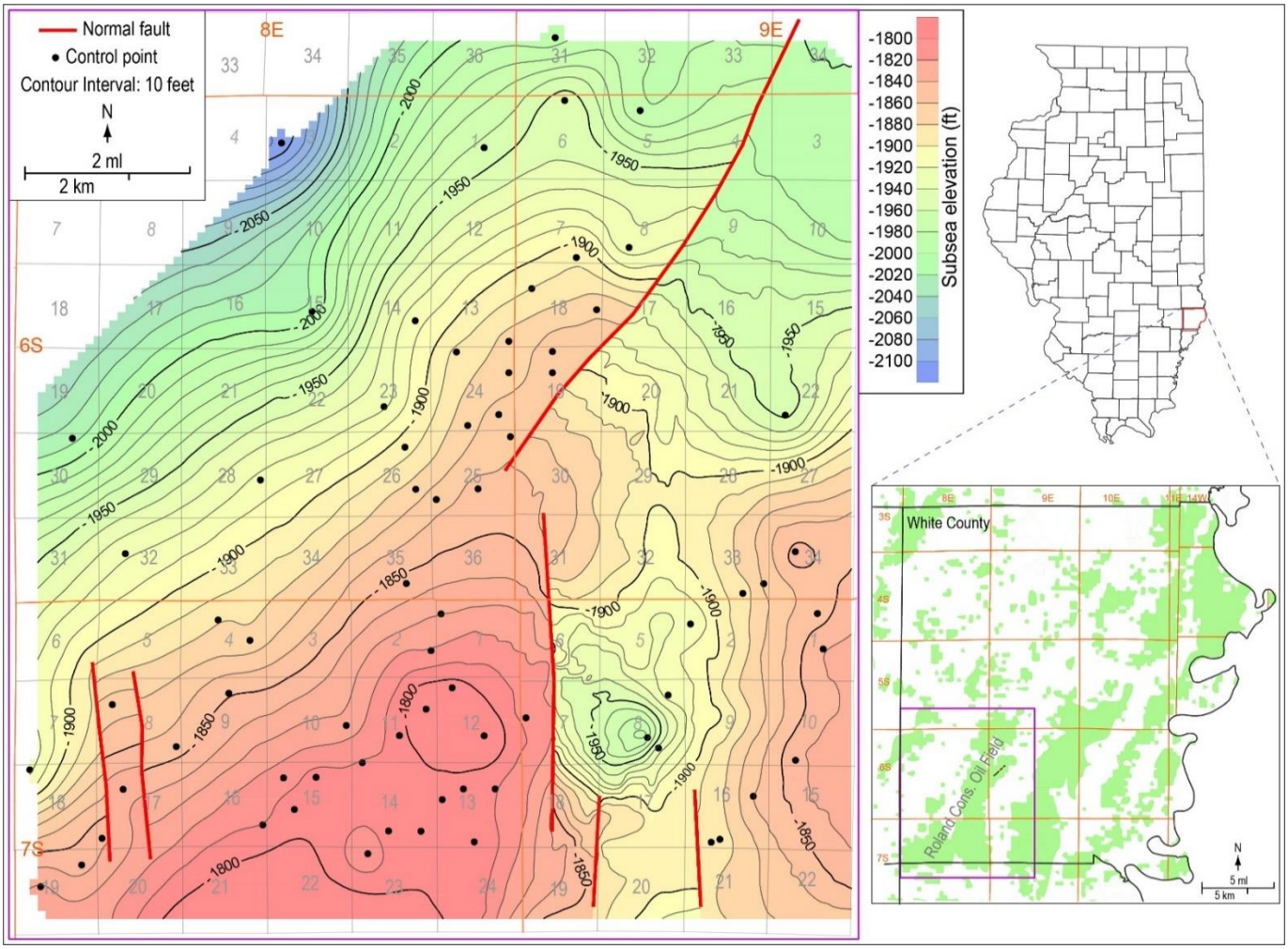


Figure. 3-11. Structural contour map of the Roland Consolidated Field area showing the dragged fold structures developed along the Wabash valley fault zones.

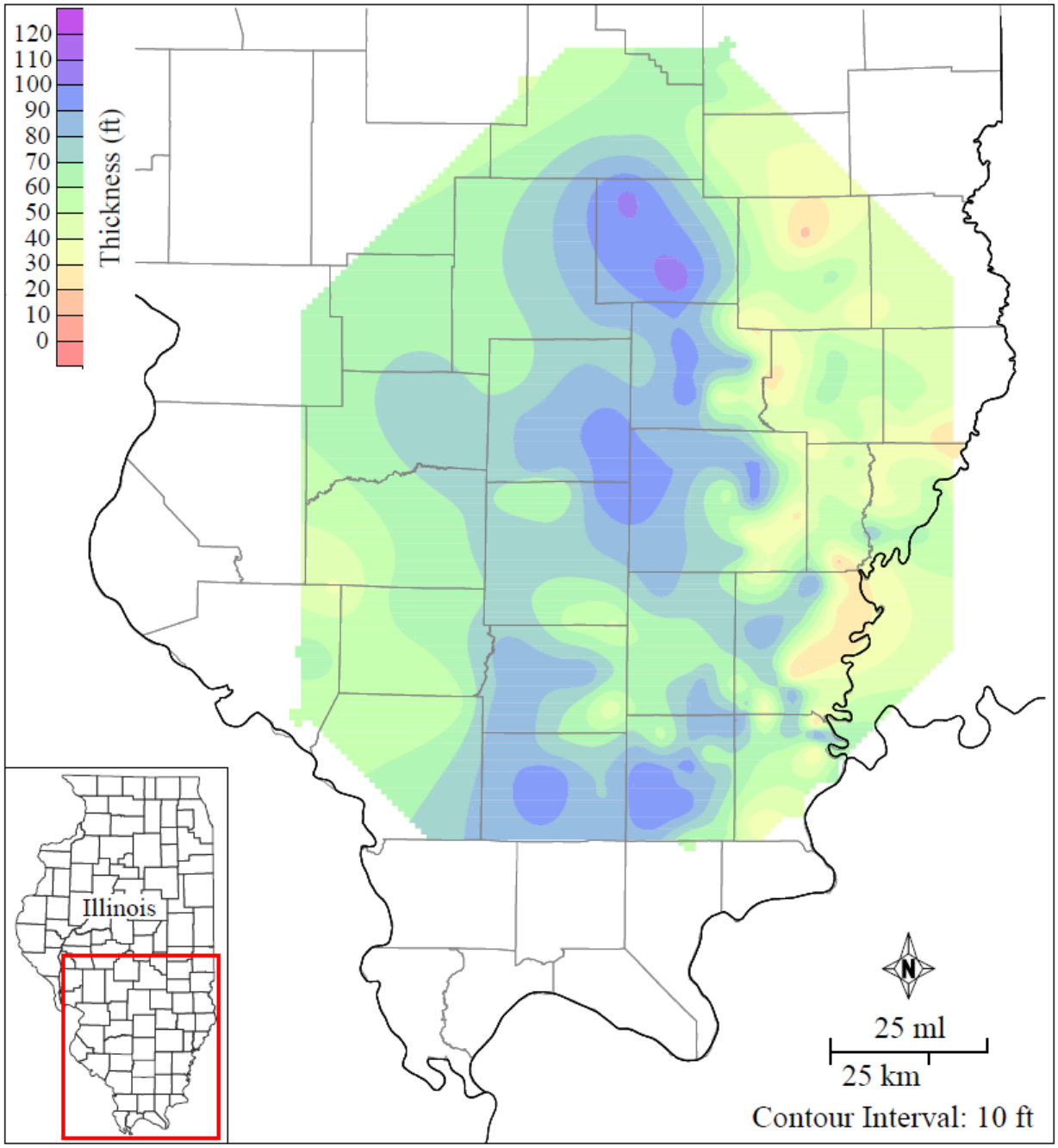


Figure 3-12. Isopach map of the seal for the Tar Springs sandstone reservoirs. The map is prepared using the combined thickness of the shale in the uppermost part of the Tar Springs Sandstone, the Vienna limestone, and the shale interval underlying the sandstone unit of the Waltersburg Formation.

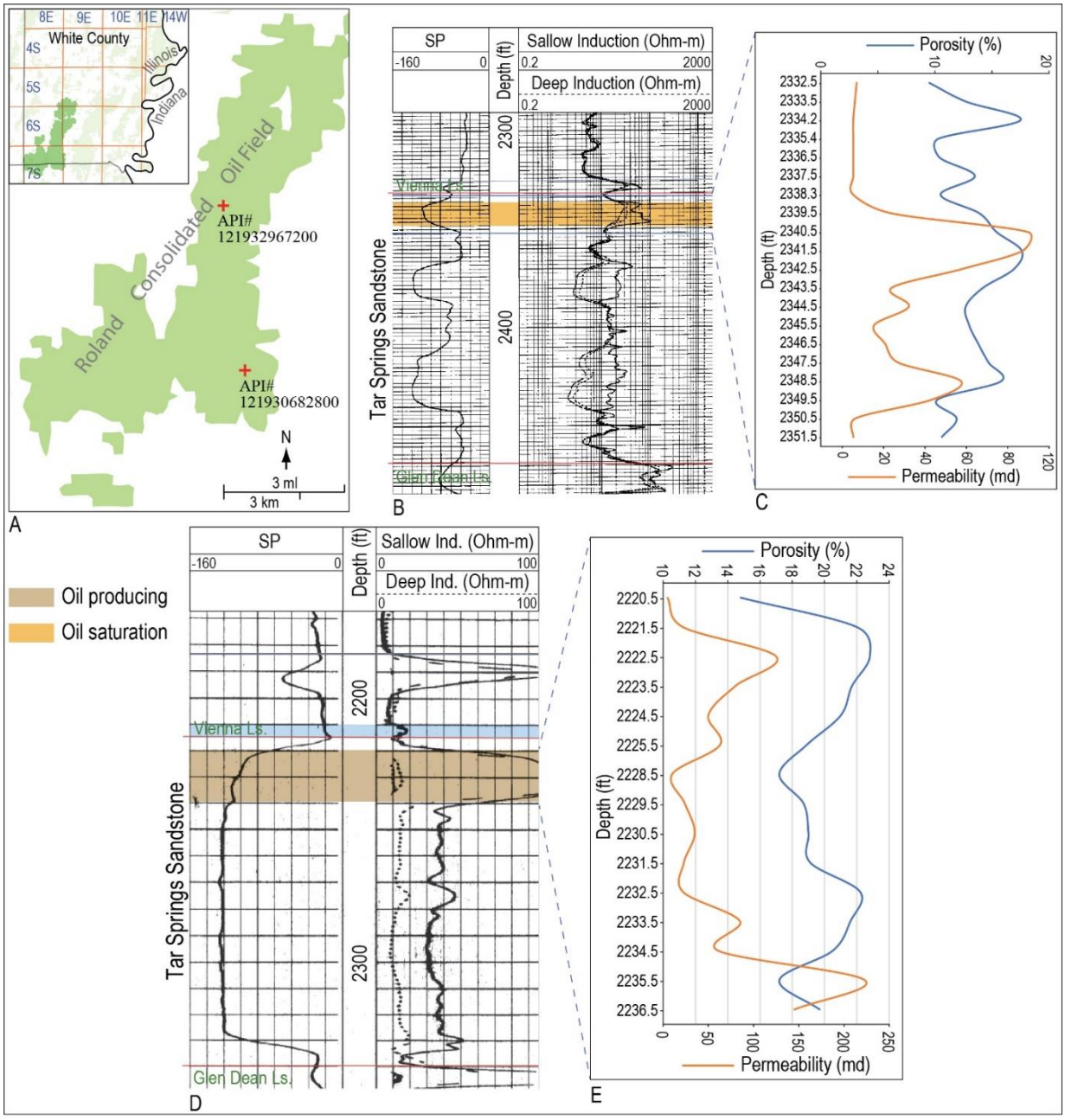


Figure. 3-13. Core analyses of two wells in the Roland Consolidated Field, White County, Illinois. (A) Location map. (B) Electric log of well API#121932967200. (C) Plot of porosity versus permeability from core analysis report of the upper Tar Springs oil saturated lenticular sandstone reservoir. (D) Electric log of well API#21930682800. (E) Plot of porosity versus permeability from core analysis report of the upper part of the massive Tar Springs sandstone reservoir.

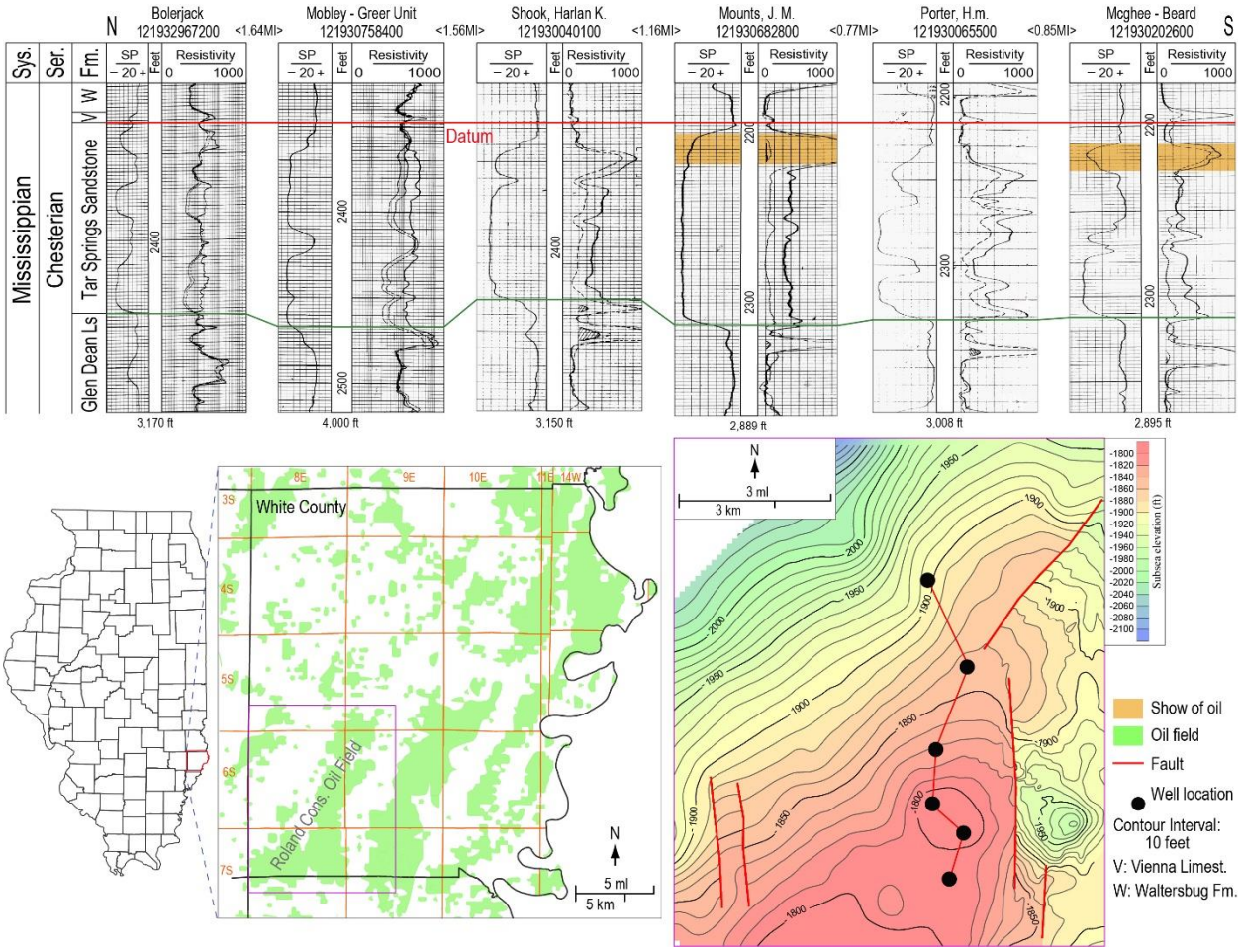


Figure 3-14. N-S stratigraphic electric log cross section in the Roland anticlinal structure, eastern margin of Roland Field. Note lateral and vertical variations of the Tar Springs Sandstone in which massive sandstone change laterally to lenticular non-massive reservoir bodies. Core analysis report and electrical resistivity of the sandstones indicate that all of the lenticular sandstones in the upper part of the Tar Spring are oil saturated (datum base of the Vienna Limestone).

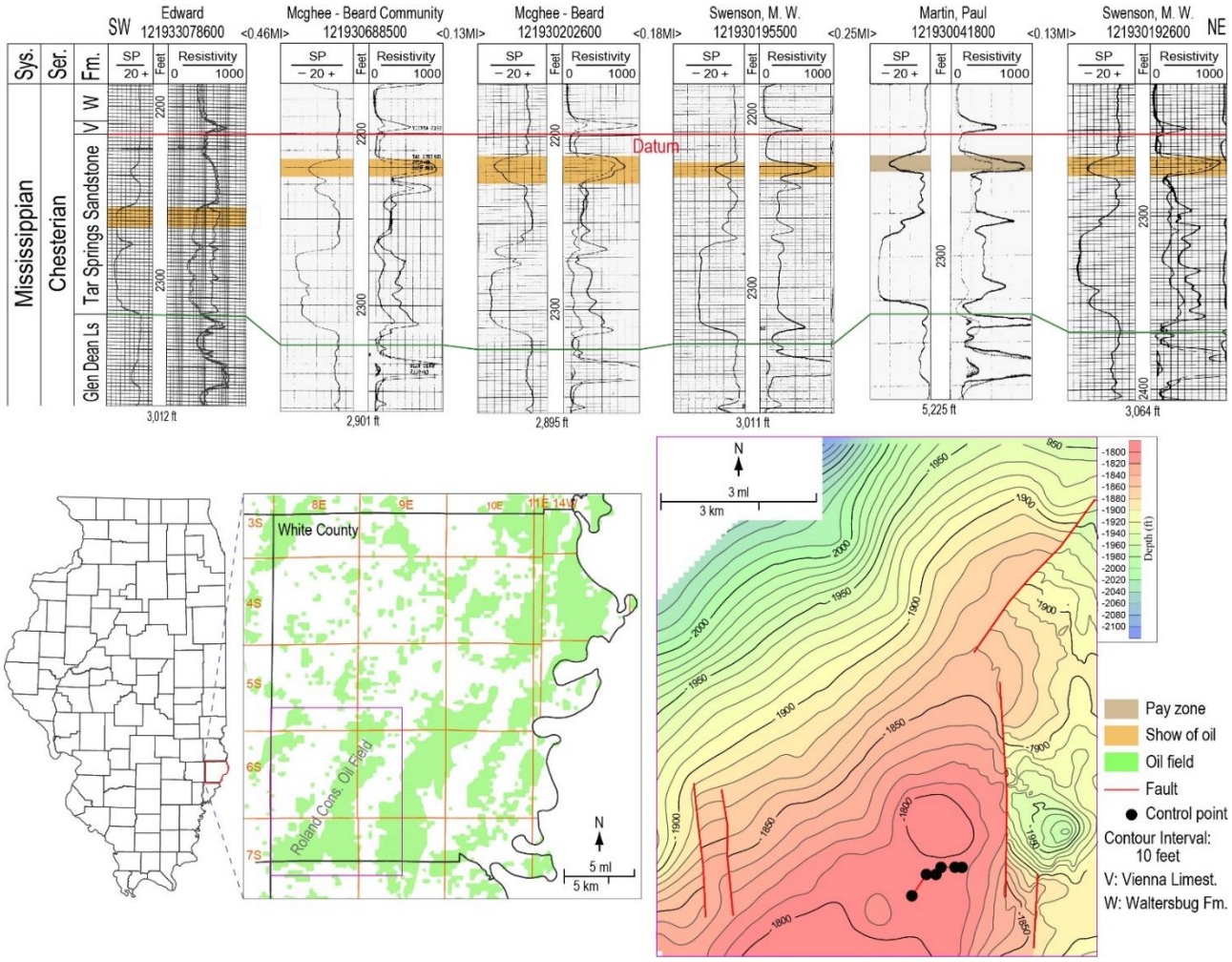


Figure 3-15. SW-NE stratigraphic electric log cross section in the Roland anticlinal structure, southeastern corner of Roland Field. Note lateral and vertical variations of the Tar Springs Sandstone in which massive sandstone in the lower part change to lenticular non-massive reservoir bodies (datum base of the Vienna Limestone).

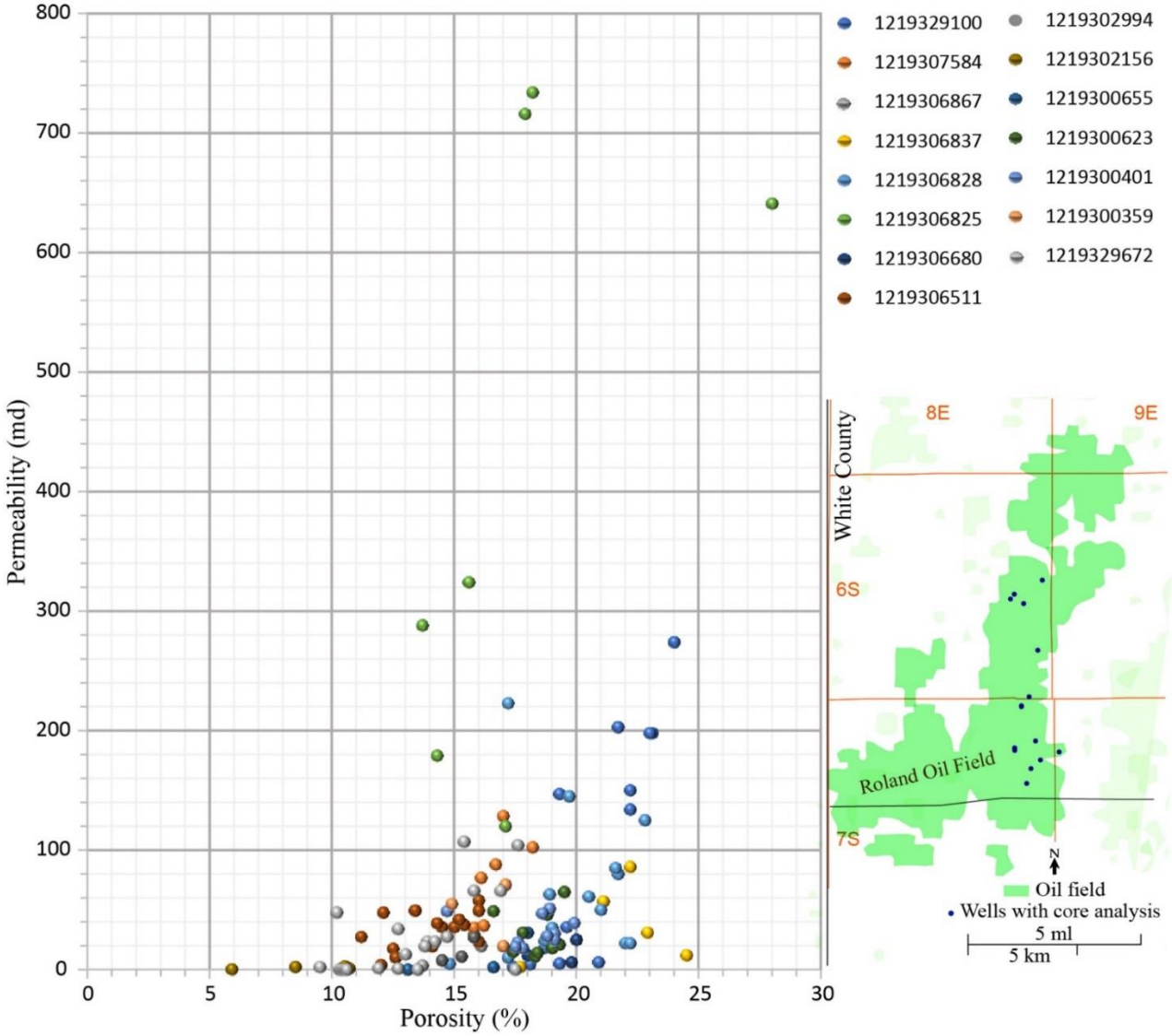


Figure 3-16. Permeability vs Porosity Xplot of 15 wells in the Roland Field based on core analysis report.

3.1.2 Cypress Sandstone

The Cypress Sandstone was previously characterized as part of DOE Project Number DE-FE0024431. The reader is referred to that final report (https://doi.org/10.2172/1545654) for a full treatment on the geology and reservoir characteristics of the Cypress Sandstone. The following summary is derived from that report.

Up to 60 m thick Cypress Sandstone bodies define a northeast-southwest fairway that is approximately 230 km long and 100 km wide across the central portion of the ILB. These sandstones commonly contain relatively thin oil reservoirs and were found to have associated underlying residual oil zones (ROZs). The presence of a thick brine aquifer underlying the ROZ and high vertical permeability results in characteristic low primary oil recovery caused by excessive brine production from the aquifer. Nonconventional CO_2-EOR in these oil reservoirs are expected to require more CO_2 to produce a unit of oil compared to conventional CO_2-EOR. Consequently, nonconventional CO_2-EOR will have a higher storage component and offer a unique storage opportunity.

An integrated approach of detailed site-specific geologic reservoir characterization, 3D geocellular modeling, and reservoir simulation of multiple development cases at Noble Field was employed to determine development strategies for CO_2-EOR and storage. The findings of Noble Field research were leveraged to assess the regional CO_2-EOR and associated storage resource within the nonconventional reservoirs of the thick Cypress Sandstone in the ILB.

Regional characterization shows that thick, multistory fluvial facies of the Cypress Sandstone exhibits porosity from 15% to 21% and horizontal and vertical permeability up to approximately 0.98 µm2 (1,000 mD). Oil saturation indicators screened from well records and well log analyses were used to map 27 brownfield and greenfield ROZ prospects with residual oil saturation (SOR) values ranging from 14 to 35%. ROZ thickness varies from 2.7 to 21.6 m (9 to 71 ft).

3.1.2.1 Cypress Seal System

Authors: Nathan Webb and Donna Willette
Published as Technical Report DOE-UIUC-31700-3, OSTI ID: 1905579, https://doi.org/10.2172/1905579

The Cypress Sandstone is the youngest and shallowest unit in the Illinois Basin that was featured in the United States Carbon Utilization and Storage Atlas IV as a target for saline carbon storage with an estimated 0.2 to 2.3 GT of storage potential (NETL, 2012). Additional research on a residual oil zone (ROZ) developed within the Cypress Sandstone has delineated 27 prospects with approximately 290.8 million m^3 (1.8 billion barrels) of oil in place (Webb et al., 2019). 21 to 31 million m^3 (144 to 196 million barrels) of oil is estimated to be recoverable using carbon dioxide enhanced oil recovery (CO_2-EOR). Storage of CO_2 associated with EOR in these ROZ prospects alone, not accounting for associated main pay zones (MPZs), underlying brine formation, or intervals adjacent to or between prospects, is estimated to be up to 10.4 billion tonnes.

The Cypress Sandstone is thus well understood to be a CO_2 injection target, both for EOR and associated storage. However, the seal system overlying the Cypress Sandstone is poorly understood. Unlike deeper formations such as the Mt. Simon Sandstone or the St. Peter Sandstone which are either in use as a CO_2 sink or being characterized for prospective storage, respectively, the Cypress is not overlain by hundreds of feet of impermeable shale. Rather, the Cypress is overlain by a lithologically variable interval that is composed generally of shales and limestones with some sandstone in the part of the Basin where the

Cypress is deep enough to facilitate CO_2 storage. Also, due to its status as one of the shallowest and most prolific oil reservoirs in the Basin, the seal system overlying the Cypress Sandstone has a relatively high number of legacy well penetrations.

The purpose of this report is to characterize the Cypress Sandstone seal system using well logs and available core. Gross thickness, lithology (facies), and mineralogy of seals is described and mapped across the Basin. The column height of CO_2 that can be held is calculated using capillary pressure data from a representative core.

Methods

Maps of the Cypress Sandstone seal system were developed using a combination of prior published maps as well as additional original data. Geophysical well logs were used to identify and correlate lithology and thickness of the seal system in the Basin interior. Outcrop mapping studies were reviewed to provide additional detail about lithologic and mineralogical heterogeneity of the formations in the seal system.

Modern well logs and a core were collected from the Carrie Winter #10 well at the Brownfield Laboratory site in Richland County, IL, through the lower portion of the seal system to provide details on the lithology and mineralogy of the units where they are rarely sampled in the Basin interior. The core provided an opportunity to describe the lithology and facies and collect samples for mineralogical and mercury injection capillary pressure (MICP) analyses.

Stratigraphy

The seal system overlying the Cypress Sandstone is composed of shales at the top of the Cypress Formation, limestones and shales of the Golconda Formation and Hardinsburg Formation, and the Glen Dean Limestone (Figure 3-17). The composite thickness of this section is generally from 30 to 61 m (100 to 200 ft) thick. Sandstone bodies that occur as both thin lenses and thick channel forms are present within both the Golconda and Hardinsburg Formations, but their distribution, in particular the thick channel sandstones are known and spatially restricted. These lithologically complex formations are described in detail by both Willman et al. (1975) and Nelson et al. (2002), but their general characteristics are summarized below.

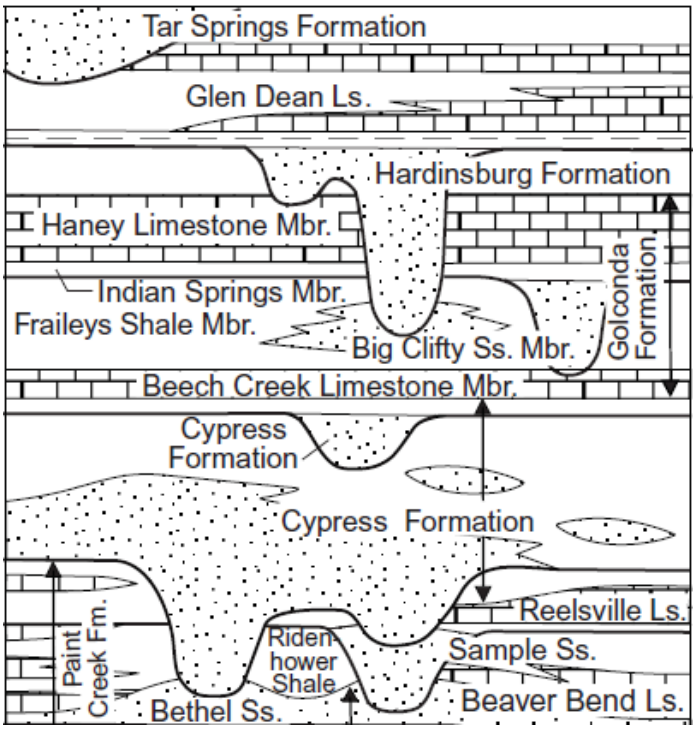


Figure 3-17. Stratigraphic column showing the lithologic variability of the seal interval overlying the Cypress Sandstone. Modified from Nelson et al. (2002).

A geophysical log through the seal interval is shown for the Carrie Winter 10 well and includes descriptions of samples and core (Figure 3-18). This well is a representative example of the seal interval in an area where the Fraileys Shale Member and Hardinsburg Formations are predominantly shaley. A 130 mi (210 km) long geophysical log cross section shows the stratigraphic and lithologic variability of the seal system overlying the Cypress Sandstone in the central part of the Illinois Basin (Figure 3-19). Nelson et al. (2002; see Figure 3-20) show another example cross section through this stratigraphic interval.

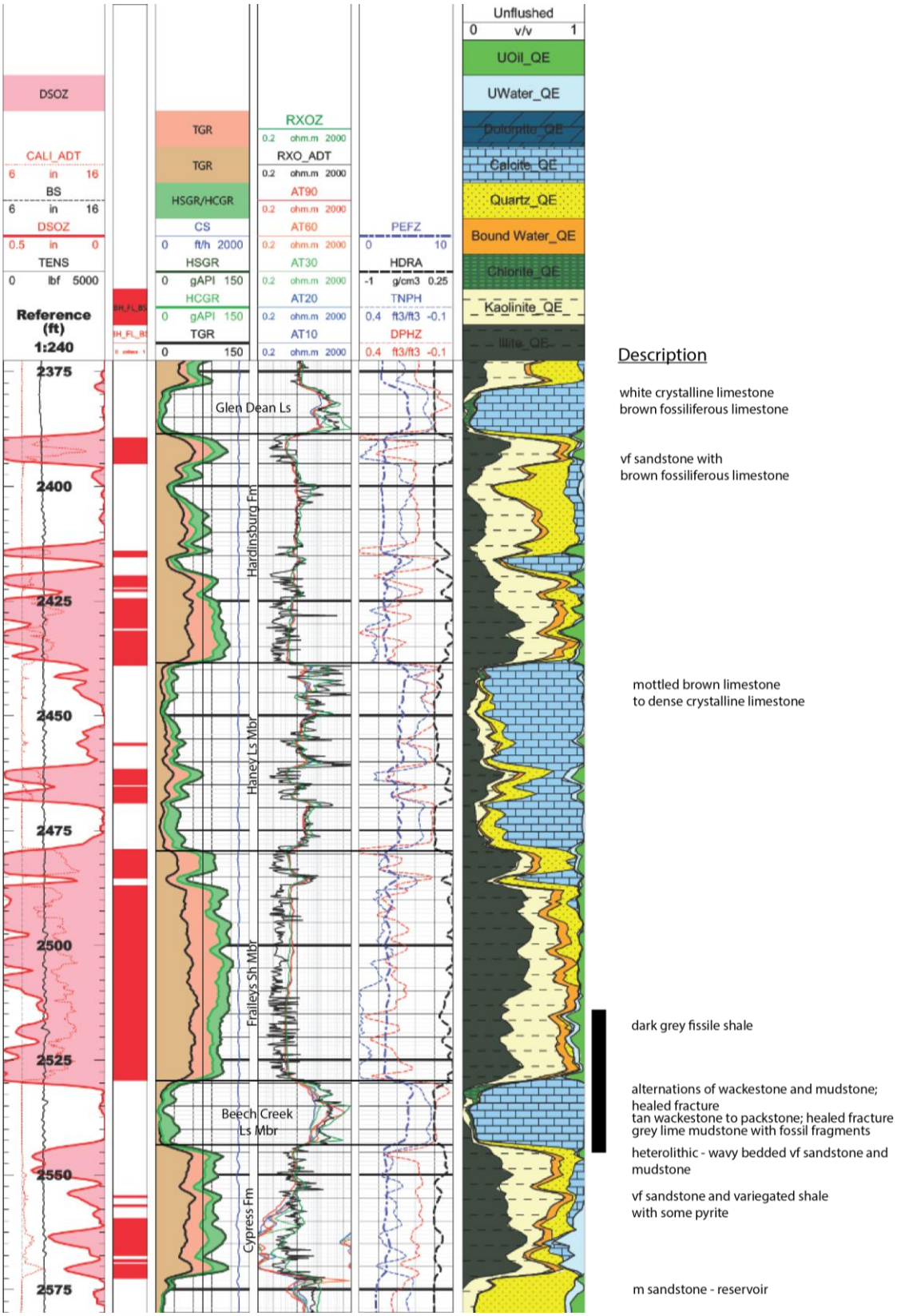


Figure 3-18. Geophysical log (including Gamma Ray, Resistivity, Porosity, and ELAN) from the Carrie Winter 10 well through the seal interval over the Cypress Sandstone. Descriptions are listed to the right. Cored interval indicated by black bar.

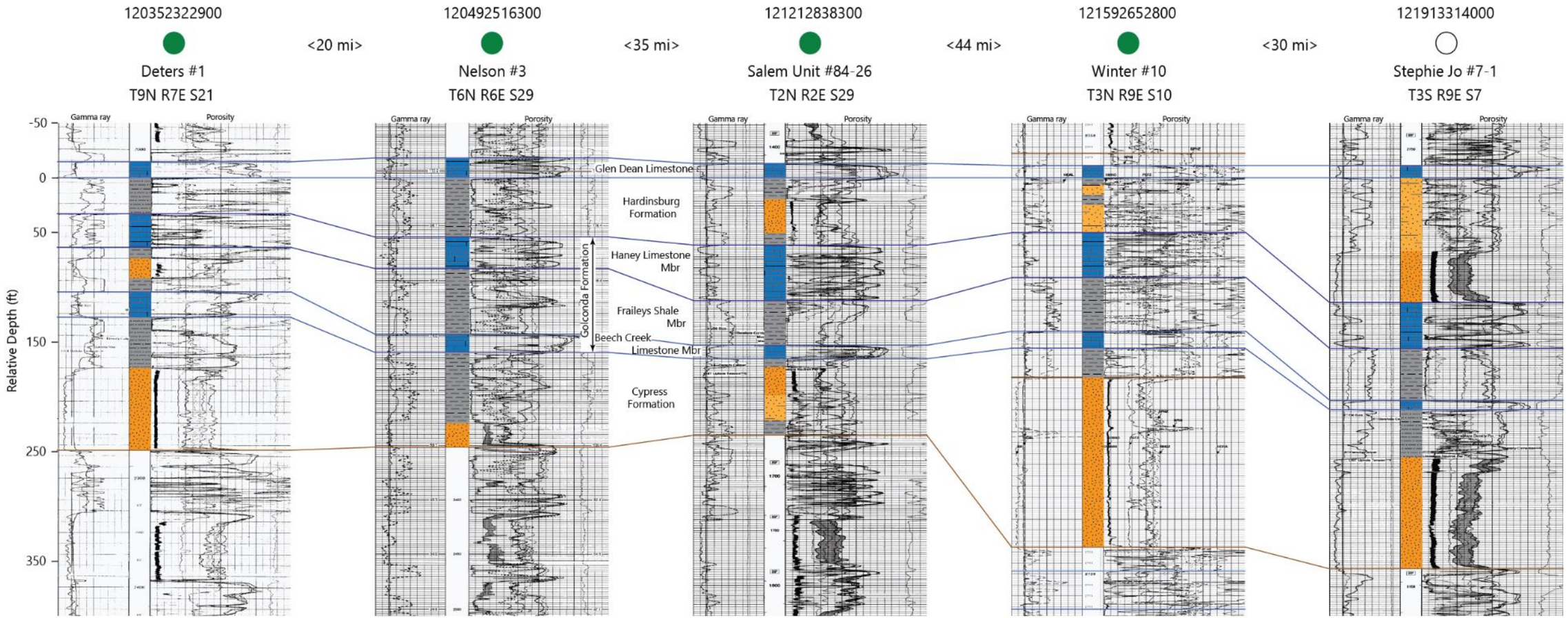


Figure 3-19. North-South cross section showing variation in lithology through the seal interval overlying the Cypress sandstone. Lithology is indicated by symbol and color for each log. Orange = sandstone, yellow = shaley sandstone, blue = limestone, grey = mudstone. Sandstones occur in the Fraileys Shale Member and the Hardinsburg Formation in some areas, but they are otherwise composed of shale.

Cypress Formation

The Cypress Formation is 30 to 61 m (100 to 200 ft) thick in the central part of the Illinois Basin and thins outward towards the Basin margins (Willman et al., 1975). Typically, the upper part of the formation contains 3 to 15 m (10 to 50 ft) of shale to sandy shale at the top (e.g. Figure 3-18, Figure 3-19).

Golconda Formation

The Golconda Formation consists generally of limestone and shale in the central part of the Illinois Basin with a sandstone member that occurs along the eastern shelf of the Basin (Willman et al., 1975). The formation consists of the Beech Creek Limestone Member, the Fraileys Shale/Big Clifty Sandstone Member, and the Haney Limestone Member.

Beech Creek Limestone Member

The Beech Creek Limestone Member is up to 11 to 12 m (35 to 40 ft) but more commonly 3 to 4.5 m (10 to 15 ft) thick. The base of the Beech Creek in southern Indiana has a lag deposit of sandy oolitic limestone and shale-pebble conglomerate (Harris, 1992). The lower part of the Beech Creek is argillaceous, dark brownish gray, skeletal and pelletal to lithographic limestone, usually with scattered, black, rounded grains and a few fossils (Willman et al., 1975; Nelson et al., 2002). The limestone coarsens upward into fine to coarse grained, fossiliferous grainstone that is light brownish gray (Willman et al., 1975; Nelson et al., 2002). The overall succession likely records a transition from deposition below wave base to later shoaling and higher wave and current energy (Harris, 1992).

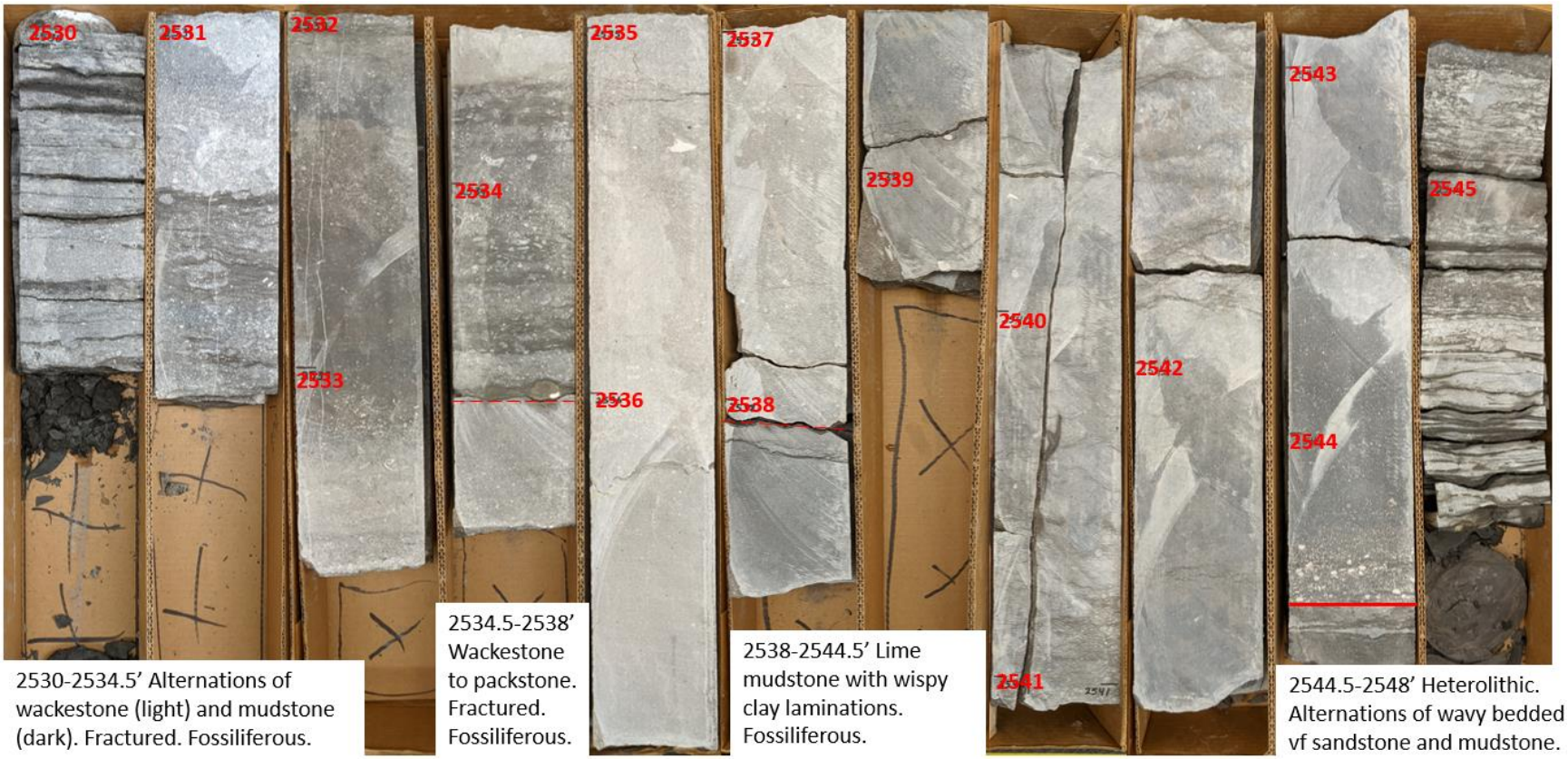


Figure 3-20. Photographs of core and brief description through the entire Beech Creek Limestone Member in the Carrie Winter #10 well. Core corresponds to the geophysical log in Figure 3-18. The red line marks the base of the limestone above which a lag can be seen (e.g. Harris, 1992).

Fraileys Shale and Big Clifty Sandstone Members

The Fraileys Shale and Big Clifty Sandstone Members are lateral facies of one another, with the former generally occurring throughout southern Illinois where the Cypress Sandstone contains ROZs and is deep enough to be a potential CO_2-EOR and storage target. Isolated lenses of Big Clifty Sandstone do occur in southern Illinois. The Big Clifty Sandstone is well developed as a thick and continuous sandstone body on much of the eastern flank of the Illinois Basin.

The lower part of the Fraileys Shale Member is typically dark gray to black, fissile clay-shale that contains siderite nodules. The shale grades upwards to greenish to olive-gray and is somewhat silty, calcareous, and fossiliferous. Limestone interbeds are common and become more so toward the north and west. Local "buildups" of coarse, highly fossiliferous limestone up to 10 m thick occur in the middle part of the Fraileys in southern Illinois, both in subsurface and on the outcrop. Their depositional setting is uncertain, but high-energy conditions are strongly implied. A thin but widely traceable bed of buff, micritic dolomite or dolomitic limestone occurs near the top of the Fraileys. Near the top of the Fraileys-Big Clifty is a nearly basinwide interval of red, green, and gray variegated shale and mudstone that has been interpreted as a paleosol.

Core was collected through the lower dark grey Fraileys Shale in the Carrie Winter 10 well. Three samples were collected from the core and analyzed for mineralogy using X-Ray diffraction. Results of the analysis show that the Fraileys Shale is dominantly composed of quartz with 16% clay (Figure 3-21). The clay fraction is nearly one half illite, one quarter illite-smectite, with the remainder being kaolinite and chlorite.

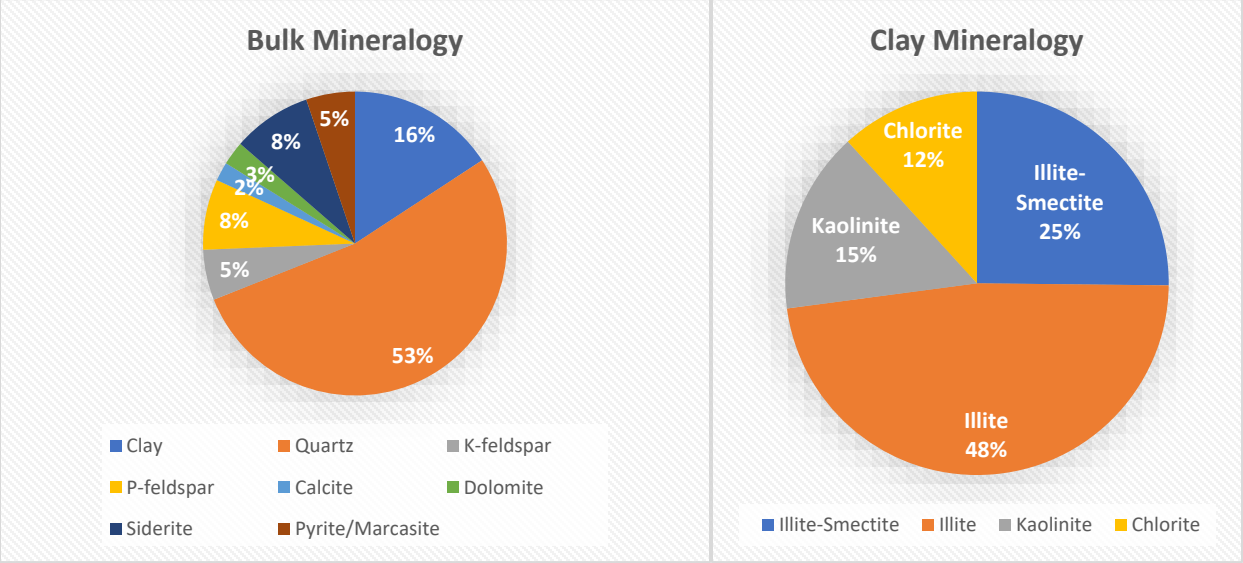


Figure 3-21. Charts showing the mineralogical composition of the Fraileys Shale in the Carrie Winter 10 well for the bulk rock (left) and clay (<16 µm) fraction (right).

Haney Limestone Member

The Haney Limestone Member is dominantly limestone, with some interbedded shale. In southern Illinois the Haney is up to 100 ft thick but thins northward and is approximately 15 ft thick near its northern erosional limit. The limestone of the Haney is typically light gray to brownish gray or dark gray, coarse grained, fossiliferous and largely oolitic. In many places the oolitic beds alternate with non-oolitic beds or with shale. A little chert is commonly present in the Haney, and much of the limestone is shaly. The shale is dark gray and generally calcareous and fossiliferous. The individual limestone beds generally are

markedly lenticular and are much less persistent laterally than are beds in the younger Chesterian limestones.

Hardinsburg Formation

The Hardinsburg Formation consists primarily of shale and sandstone and is commonly 50-100 feet thick and thins to the north and west. Subordinate siltstone and thin limestones and coals also occur within the Hardinsburg Formation. The sandstones within the Hardinsburg Formation are generally thin and tabular within the shale, except within a well-defined NE-SW trending paleovalley system where the sandstones become thick, channel-fill deposits.

Glen Dean Limestone

The Glen Dean limestone is generally 15 to 30 ft thick and is found across the Basin. The limestone consists of crinoid-bryozoan wackestone and packstone; oolitic grainstone is common (especially at the top), and beds of microgranular dolomite and lime mudstone occur (Nelson et al., 2002).

Regional Facies Distribution

The general distribution of facies within the Cypress seal interval has been previously mapped (see Willman et al., 1975; Nelson et al., 2002). Facies trends from those previous maps have been synthesized here to show the general distribution of facies above the Beech Creek Limestone and below the Glen Dean Limestone where porous sandstones tend to occur. The facies pattern shows a change from more shales, limestones, and isolated sandstone lenses on the west side of the Basin to more thick sandstones in the Big Clifty and Hardinsburg intervals on the east side of the Basin. In the central part of the Basin where the Cypress is deep enough to be a CO_2 injection target, the seal interval is largely composed of shales and limestones with isolated sandstone bodies as well as some narrow, discreet channel-form sandstones in the Hardinsburg Formation (Figure 3-19).

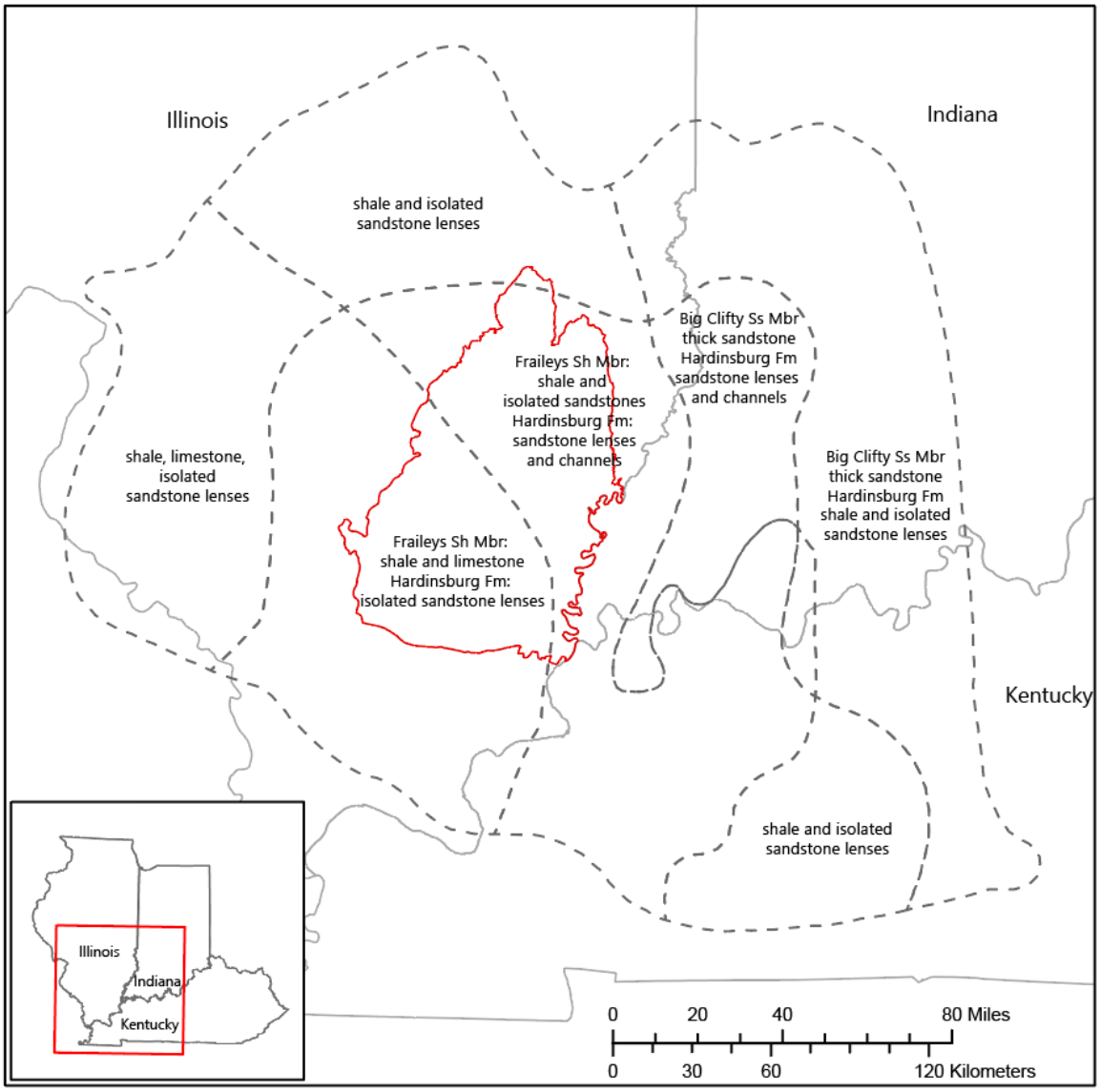


Figure 3-22. Map showing the distribution of facies in the Cypress seal interval above the Beech Creek Limestone and below the Glen dean Limestone. Facies boundaries are generalized based on maps in Nelson et al. (2002). The red line on the map is the 2,000 ft subsea elevation contour on the base of the Barlow Limestone and approximates the part of the Basin where the Cypress is at least 2,500 ft deep and amenable to miscible CO_2 injection (see Figure 3-20).

The overall seal interval has an average thickness of approximately 165 ft. At its thinnest, it is approximately 100 ft thick. If the clayey shale interval at the top of the Cypress Formation is included as part of the seal system, the average thickness increases to approximately 200 ft. Overall, the seal interval thickens southward (Figure 3-20). The Fraileys shale is the most consistent impermeable clay shale within the seal interval and its thickness ranges from approximately 22 to 88 ft, with an average thickness of approximately 55 ft.

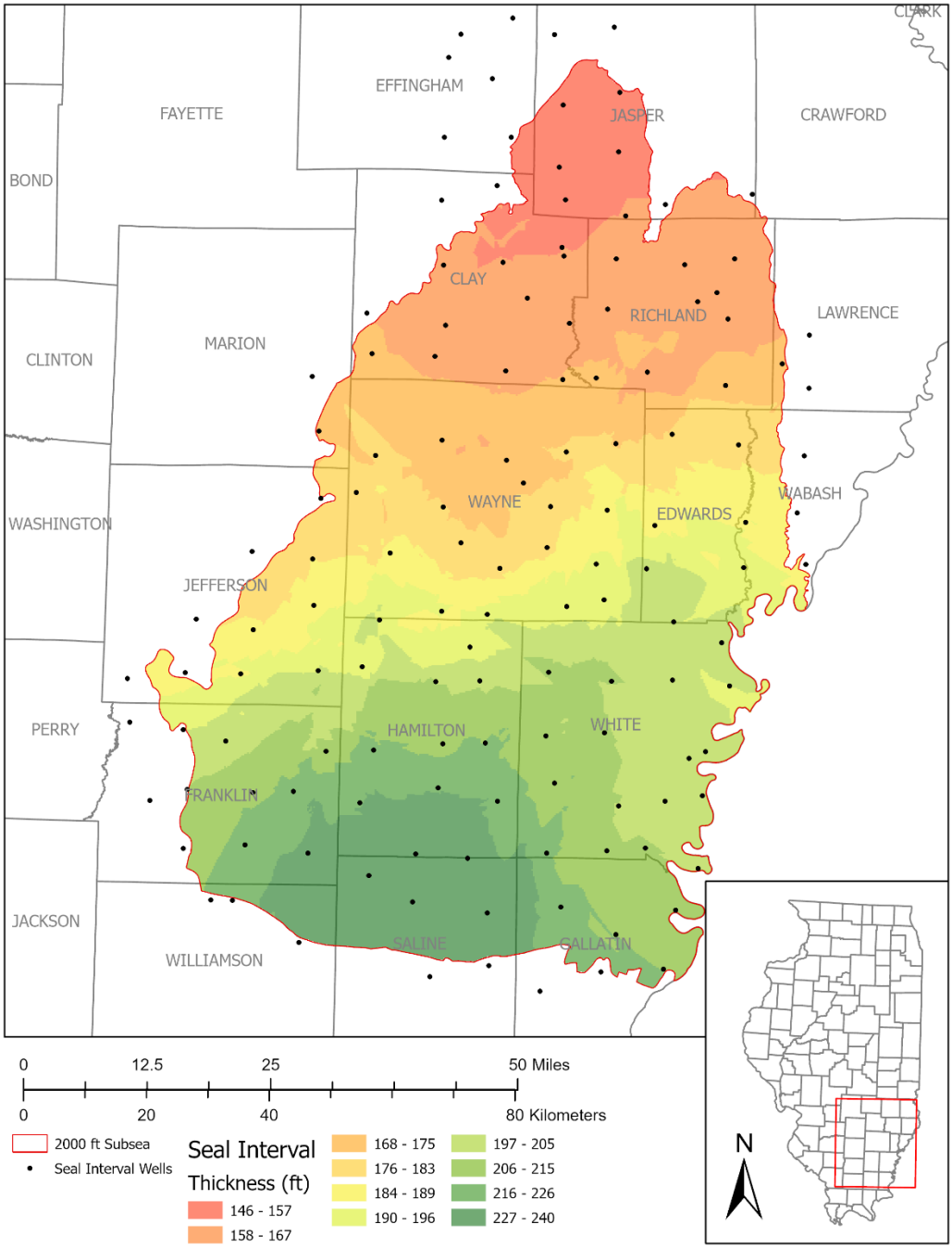


Figure 3-23. map showing the thickness of the Cypress seal interval from the base of the Beech Creek Limestone to the base of the Glen Dean Limestone.

Capillary Column Height

Two samples of the Fraileys Shale, which though relatively thin is the most laterally persistent shale in the seal interval, were collected from the Carrie Winter 10 well and were analyzed using mercury injection capillary pressure (MICP) analysis (Table 3-1). MICP entry pressures allow calculation of the column height of CO_2 that the caprocks can hold (Table 3-2). A rigorous evaluation of threshold pressures using detailed

MICP data created a range of minimum to maximum $scCO_2$ column heights based upon a range of CO_2 contact angles and Hg/air threshold pressures. This provides additional insight into seal capacity and leakage potential. Generally, prior to 2006, $scCO_2$/water/rock interfaces in the sub-surface, were assumed to have a contact angle (θ) of 0°, as water was thought to be the wetting phase (Daniel and Kaldi, 2008). More recent experimental studies using quartz, mica, and clay substrates and $scCO_2$ immersed in brine indicate that these substrates become less water-wet in the presence of $scCO_2$, i.e. contact angles varying from 0° to 40° (Sarmadivaleh, et al., 2015). An increase in contact angle becomes more pronounced at higher pressures up to 20mPa, ranging from 30° to 60°. For the purposes of this study, a range of column heights was calculated using a contact angle of 0°, 20°, 40°, 60° to bracket the wettability uncertainty.

In addition, based upon the sample MICP entry pressure (Hg/air), the threshold pressure of the CO_2/brine system was modified by 20% (either low or high) to capture some of the variability in pore volume and permeability of changing caprock composition and resultant diagenesis. This allowed a maximum/minimum comparison of column heights relative to the data derived from the sample.

Variability of capillary pressure using a range of contact angles follows the wettability transformation from an air/mercury system to brine equation (after Schowalter 1979):

$$(1)\quad P_{b/CO2} = P_{a/m} (\sigma_{b/CO2} \cos\theta_{b/CO2}) / (\sigma_{a/m} \cos\theta_{a/m})$$

Where $P_{b/CO2}$ is the capillary pressure in the brine/CO_2 system, $P_{a/m}$ is the capillary pressure in the air/mercury system, $\sigma_{b/CO2}$ and $\sigma_{a/m}$ are the interfacial tensions of the brine/CO_2 and the airmercury systems respectively, $\theta_{b/CO2}$ and $\theta_{a/m}$ are the contact angles of the brine/CO_2/substrate and air/mercury/substrate systems respectively.

Calculation of the column height uses the standard equation:

$$(2)\quad h_{scCO2}\ \text{max} = (Pth_s - Pth_r) / (\rho_f - \rho_{scCO2})*0.433$$

Where Pth_s is the entry pressure of the seal in the $scCO_2$/brine system, Pth_r is the entry pressure of the reservoir in the $scCO_2$/brine system, $\rho_f - \rho_{scCO2}$ is the density difference of the brine and $scCO_2$, and 0.433 the normal hydrostatic gradient of water in psi/ft, and h_{scCO2} max is the maximum column height or caprock capacity (Daniel and Kaldi, 2009). The interfacial tension (IFT) used in the Hg/air to brine/CO_2 conversion for each sample is based upon studies indicating that it typically ranges between 21 – 27 dynes/cm under $scCO_2$ conditions (Espinoza, et al., 2010). By using this methodology, MICP entry pressures allow a range column height estimates to bracket a realistic evaluation of seal capacity to Cypress reservoirs. (Table 3-2).

The contact angle (CA) ranges for CO_2 reported in Table 3-2 are between 0 and 60° based upon the assumed properties (clay lithology, high salinity, high pressure) of the caprock (e.g. Chiquet et al., 2005). Experimental work Daniel and Kaldi (2009) suggest that at higher pressures, 40 to 60° may be more accurate. A fully water-wet interface in the pores would have a CA between 0° to 25°.

Table 3-1. Seal samples collected from core and data used in the column height calculation for seal capacity.

Formation	Depth (ft)	Pressure (psia)	Temp (°F)	Salinity (ppm)	Brine density (g/cc)	Threshold entry pressure (psia)
Fraileys Shale	2523.5	1107.4	86.2	98,000	1.070	27.31
Fraileys Shale	2529.3	1109.9	86.3	98,000	1.070	28.3

Table 3-2. The four columns in the table represent column height calculations at contact angles (CA) of 0°, 20°, 40°, and 60°. For CO_2, CA is generally assumed to be between 20° and 40°. Column heights were calculated using the threshold pressure of the sample derived from mercury injection capillary pressure. Min and Max values derived by decreasing and increasing (respectively) the threshold pressure by 20%.

Formation	CO_2 Column Height ft. (m) @ CA 0°	CO_2 Column Height ft. (m) @ CA 20°	CO_2 Column Height ft. (m) @ CA 40°	CO_2 Column Height ft. (m) @ CA 60°
	min – sample - max	**min – sample - max**	**min – sample - max**	**min – sample - max**
Fraileys Shale	**87.3** (26.6) – **110.4**(33.6) –**136.5** (41.6)	**82.1** (25.0) – **103.7**(31.6) – **128.3** (39.1)	**66.9** (20.4) – **84.6**(25.8) – **104.6** (31.9)	**43.7** (13.3) – **55.2** (16.8) – **68.3** (20.8)

^ CO_2 will be in vapor phase at sample depths

When injecting CO_2 into depleted oil reservoirs or ROZs, injection at or below original reservoir pressure is often considered safe for maintaining seal integrity since the seal was effective in retaining the hydrocarbon reservoir. However, when the hydrocarbons are replaced by the injected CO_2, the lower interfacial tension (IFT) of the CO_2/brine system relative to that of the original hydrocarbon/brine system results in a reduced capillary sealing pressure of the caprock and hence, the sealing capacity is diminished (Li et al., 2006).

Well Penetrations

The Cypress Sandstone is one of the most prolific oil reservoirs in the Illinois Basin. It is also one of the shallowest oil reservoirs meaning most wells were drilled to the Cypress Sandstone or deeper formations. The result is the Cypress seal interval is penetrated by tens of thousands of legacy wellbores (Figure 3-24) which should be considered when the Cypress is being evaluated for CO_2 storage.

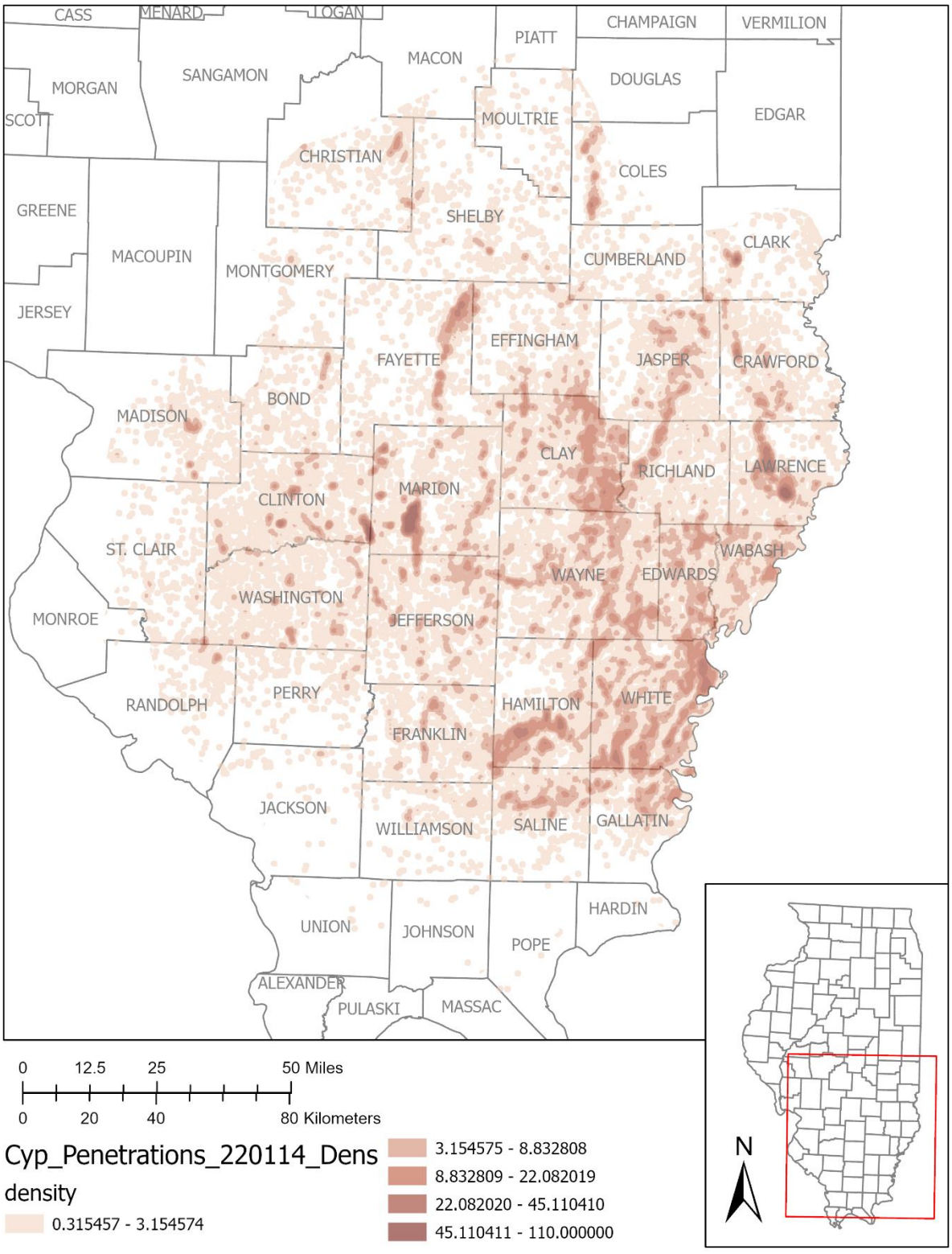


Figure 3-24. Heatmap showing density of legacy well penetrations through the Cypress seal interval.

Discussion

As has been shown, the sealing interval is pervasive and has a thickness of at least 46 m (150 ft) within the area where the Cypress would be targeted for miscible CO_2 injection. However, the lithology does vary, meaning a specific site assessment would be required. Here we use the Noble Field as an example for illustrative purposes to determine the seal capacity.

Kaldi (2011) developed a qualitative seal potential yardstick that can be applied to assess relative seal capacity graded on a 0 to 1 (0 – 100%) scale. The parameters of the assessment are as follows:

1. Capacity = Hmax/structure (in feet or meters).
   At Noble Field 30 m of Fraileys Shale /33.5 m of Structural closure. Thus, capacity is 0.9 since the seal thickness is slightly less than the thickness of structural closure.
2. There are two parts to qualitatively estimate the geometry portion of the seal evaluation:
   a. H (seal thickness in meters) / 15 m.
   b. Area of seal / area of closure.

   Because the Fraileys Shale is thicker than 15 m (a) and it is continuous over the area of the field and well beyond it (b), both would be 1.
3. Seal Quality or fracture potential estimated from 0 – 1, with 1 being unfractured and 0 being completely fractured.
   At Noble Field, we will assume 0.75 since the 19% carbonate content of the Frailey Shale (Figure 3-21) is adequate for some microfracturing to occur.
4. The final calculation is to multiply all the values together.
   For Noble Field the qualitative calculation for seal quality would be 0.9 x 1 x 1 x 0.75, giving a seal quality value of 0.68 or 68%.

Conclusions

Unlike the typical deep targets for carbon storage, the Mt. Simon and St. Peter Sandstones, which are overlain by the thick Eau Claire and Maquoketa Shales, the Cypress has a thinner seal system comprised of three lithologically varied formations. In general the thickness of the interval is adequate and the composition favorable to provide an impermeable seal, but localized areas exist where the Hardinsburg Formation contains channelized sandstone bodies that can diminish the thickness of the Fraileys Shale, which should be considered the primary confining unit. The qualitative evaluation of overall seal potential of 68% indicates the Fraileys Shale may be effective in some locations.

In general, the thickness of the sealing interval should provide a suitable seal for CO_2 in the part of the Basin where the Cypress is deep enough for miscible injection. However, Because of the variability in lithology, site specific evaluation of seal integrity and capacity is recommended before commencing with any CO_2 injection in the Cypress Sandstone in the Illinois Basin.

3.1.3 Carper Sandstone

Authors: Nathan Webb, Nathan Grigsby, Jack Brown, and Mingyue Yu
This manuscript is currently in review for publication as part of the ISGS Circular Series.

The Carper Sandstone Member consists of a series of extensive lobate sandstone deposits of variable thickness (0 to 200 ft [0 to 61 m]) that occur within the Borden Siltstone (early Middle Mississippian) that tongues into the northern portion of the Illinois Basin (Swann et al., 1965; Lineback, 1968). The Carper is unlike any other Mississippian sandstone in the Basin in that it is finer grained, naturally fractured, is well cemented by clay and carbonate minerals, and has lower porosity and permeability, all of which make it

more akin to a tight oil reservoir (e.g., Yang et al., 2016). Oil is produced conventionally from the Carper Sandstone in several fields on structures in the northern part of the Basin (Stevenson, 1964).

Given the broad lateral extent of its deposits (>16,800 km^2 in Illinois), its stratigraphic proximity above the New Albany Shale, the primary hydrocarbon source rock in the Illinois Basin (Barrows and Cluff, 1984), and the widespread distribution of oil indicators in untested areas indicating low in situ oil saturation, we propose that the Carper Sandstone is an atypical resource in Illinois that is likely underexploited. The widespread oil indicators likely reflect secondary migration through and along Carper Sandstone beds, which may have been an important carrier bed. The low in situ oil saturation may be an indication that the Carper is a siliciclastic residual oil zone (ROZ), a volume of rock into which oil accumulated and was later naturally displaced, leaving behind a low, largely immobile remaining oil saturation.

The objective of this report is to provide details about the reservoir (rock and fluid) properties of the Carper Sandstone that may prove useful for ongoing conventional development as well as future nonconventional development as a potential carbon dioxide enhanced oil recovery (CO_2-EOR) and associated carbon storage target, both within existing fields and in greenfield areas downdip and far removed from existing producing areas.

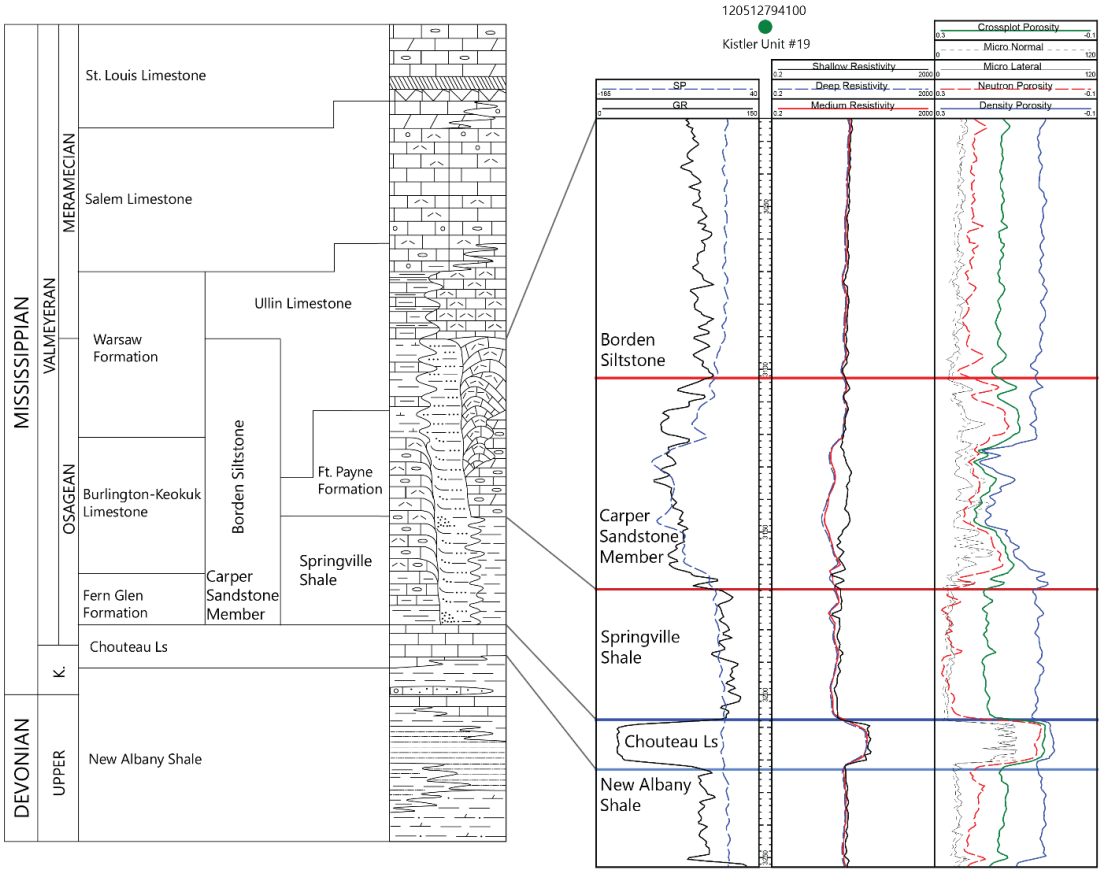


Figure 3-25. Left: Portion of the generalized stratigraphic column for Illinois (Modified from Kolata, 2005). Rocks below the New Albany Shale and above the St. Louis Limestone are not shown. Right: Type log of the Kistler Unit 19 well (API 120512794100) from St. James Field, Fayette County, IL, showing typical presentation of the Carper Sandstone.

GEOLOGIC SETTING

North America

The Acadian orogeny was a middle-Devonian to early Carboniferous Period mountain-building event that involved the collision of the exotic Avalonian terrane with the eastern margin of present-day North American (Laurentia; Figure 3-26). The Avalonian terrane was largely comprised of dense, Pre-Cambrian igneous rock (Greenhough et al., 1985; Murphy et al., 1990) that, when combined with the rate of convergence of the two plates, produced the uplift of the Acadian Mountains on the Laurentian continental margin, and subsidence of new and reactivated continental interior foreland and intracratonic basins.

Acadian uplift also created a significant sediment source, and sediment shed from the growing mountain belt was routed westward as part of a continental-scale siliciclastic depositional system known as the Borden-Price-Pocono-Grainger clastic sequence (Ettensohn et al., 2002; Figure 3-27). The Price-Pocono group, in the proximal Appalachian Basin of Pennsylvania, Maryland, and West Virginia, contains coarser, sandstone units deposited in fluvial to coastal environments (Pelletier, 1958). Distal, continental interior locations (e.g., the Illinois Basin) received finer, hemipelagic sediments, which compose the Borden Siltstone (Kepferle, 1977). Research on the Borden-Price-Pocono-Grainger clastic sequence emphasizes the generic ties between ancient tectonic processes during the Acadian orogeny with the resulting myriad of sediment processes, deposition, and dispersal (Kreisa and Bambach, 1973).

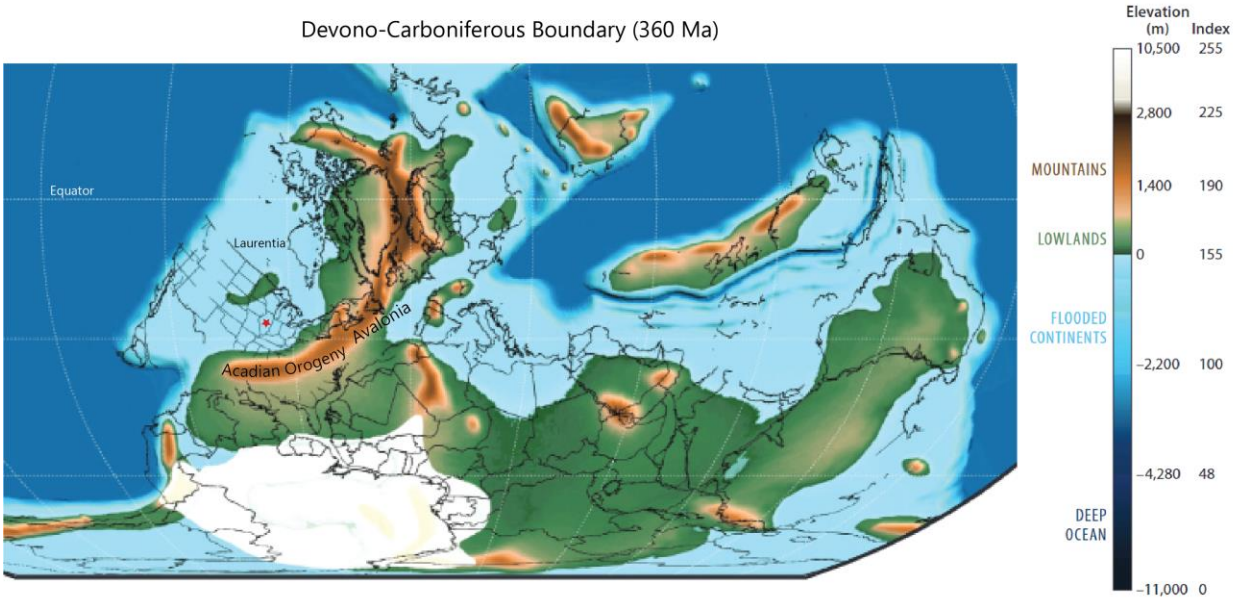


Figure 3-26. Palaeogeographical setting of the study area in the Illinois Basin during Mississippian shown with a red star. Modified from Scotese (2021).

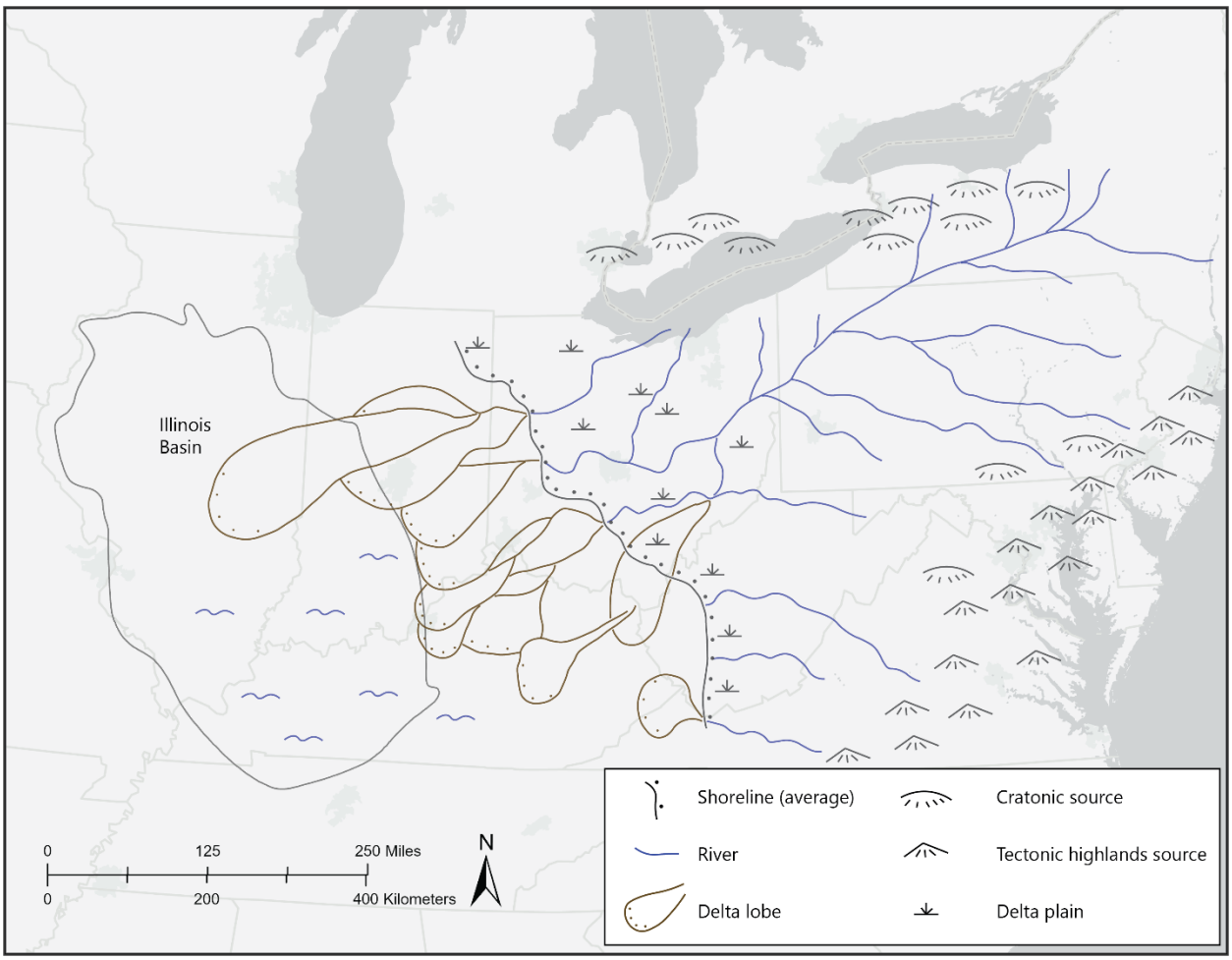


Figure 3-27. Map of the eastern United States depicting the hypothetical drainage pattern established following uplift associated with the Acadian Orogeny. The present-day outline of the Illinois Basin is shown for reference. Modified from Kepferle (1977).

Illinois Basin

The Illinois Basin, a spoon-shaped structural basin that covers 285,000 km^2 (110,000 mi^2), was reactivated because of stresses related to the Acadian Orogeny. Prior to reactivation, the Basin had low sedimentation rates paired with low subsidence rates resulting in deposition of fine-grained New Albany Shale group sediments (Borden, 1874; Collinson et al., 1967; Figure 3-25). New Albany Shale thickness and facies associations indicate a relatively deep-water, anoxic depositional environment (Kolata and Nelson, 1991). Northward migration of the continent concurrent with and following the deposition of the shale placed the Basin a position of about 5°S latitude (Craig et al., 1979; Scotese and McKerrow, 1990). The equatorial location played a role in promoting the deposition of the Chouteau Limestone, which overlays the New Albany Shale group (Treworgy and Devera, 1991; Figure 3-25). Around the time that there was a transition from carbonate to siliciclastic deposition, the Illinois Basin was located at the southern boundary of Euramerica (Figure 3-26). The Illinois Basin's subsidence rate abruptly exceeded the rate of sedimentation at the start of the Mississippian (Kolata and Nelson, 1991). A concomitant increase in sediment input to the Basin resulted in deposition of the Borden Siltstone (Cumings, 1922).

The Borden Siltstone in the Illinois Basin has been interpreted as a submarine, basin-fill, deltaic sequence (Swann et al., 1965). With deformation of the continent associated with the Acadian orogeny, a large river

system developed and followed the gradient to carry terrigenous sediment to the continental interior (Figure 3-27). Sediment size is correlated to transport distance, therefore the Illinois Basin received silt-sized sediments in its distant continental interior location. The fluvial system carrying silt to the Illinois Basin from the north-east would eventually begin to carve out channels as a medium to carry the sediment and water. These channels would begin to penetrate the Basin and establish a delta distributary network. Individual distributary channel mouths are presumed to be the source of sediment gravity flows.

Stratigraphy

The New Albany Shale and Chouteau Limestone are reliable marker beds throughout the study area that underlie the Springville Shale/Borden Siltstone succession (Figure 3-25). The Springville Shale overlies the Chouteau Limestone or, where the limestone is absent, the New Albany Shale. The Springville Shale has been interpreted to represent the deep-water bottomset beds of the Borden delta that extended into the basin beyond the delta front beds of the Borden Siltstone (Lineback, 1966). Based on this interpretation, the Springville Shale name was only applied beyond a vertical cutoff where the Borden Siltstone thinned to less than 30 m (100ft). This application of a vertical cutoff is a lithostratigraphic convenience and likely reflects a limitation of the subsurface data available at the time (generally old e-logs) in being able to clearly differentiate the Springville from the Borden where the latter thickens. However, given that foreset beds prograded over the bottomset beds through the temporal evolution of the Borden delta, it is reasonable that the Springville Shale can be differentiated from the Borden Siltstone wherever the latter occurs irrespective of thickness. Lithologically, the Springville Shale is more clayey than the Borden Siltstone (as the name suggests) and modern geophysical logs show a distinct difference between the two units, with the Springville Shale having higher Gamma Ray, higher Neutron Porosity, and lower Density Porosity than the Borden. For the purposes of this report, the Springville Shale name will be applied broadly to the higher Gamma Ray interval that underlies the Carper Sandstone or, where the sandstone is absent, the Borden Siltstone.

The Borden Siltstone, which includes the Carper Sandstone Member in its lower half, is up to 650 ft thick and preserves a subaqueous deltaic succession, including generally southward-dipping imbricate topset, foreset, and bottomset beds (Swann et al., 1965; Lineback, 1966). Foreset slopes dipped 5.7 to 17 m per km (30 to 90 ft per mile, 0.6 to 0.9°) and prograded south-westward in water 152.4 to 213.4 (500 to 700 ft) deep (Swann et al., 1965). The low-angle slope of the foresets left the submarine fan system susceptible to mass wasting events of fine-grained material.

Near the base of the Borden Siltstone, widespread bodies of very-fine grained sandstone are interbedded with the siltstone. These sandstones are referred to as the Carper Sandstone Member of the Borden Siltstone (e.g., Moulton, 1926) and have been interpreted as turbidite deposits (Lineback, 1968). The thickness of the Carper Sandstone ranges from 0 to 61 m (0 to 200 ft).

Five lobe-shaped bodies of Carper Sandstone were previously mapped in Illinois and assigned letters (from oldest to youngest) Carper A through E (Lineback, 1968; Figure 3-29). The depositional locus of each lobe varies spatially with a general anticlockwise trend around the deep part of the Basin and the outer portions of the lobes commonly overlap (Figure 3-29). Two additional lobes have been identified in subsequent subsurface mapping in Indiana (Al-Aswad, 1986). In general, 6.1 to 15 m (20 to 50 ft) of Springville Shale separates the sandstone from the underlying Choteau Limestone (Figure 3-28).

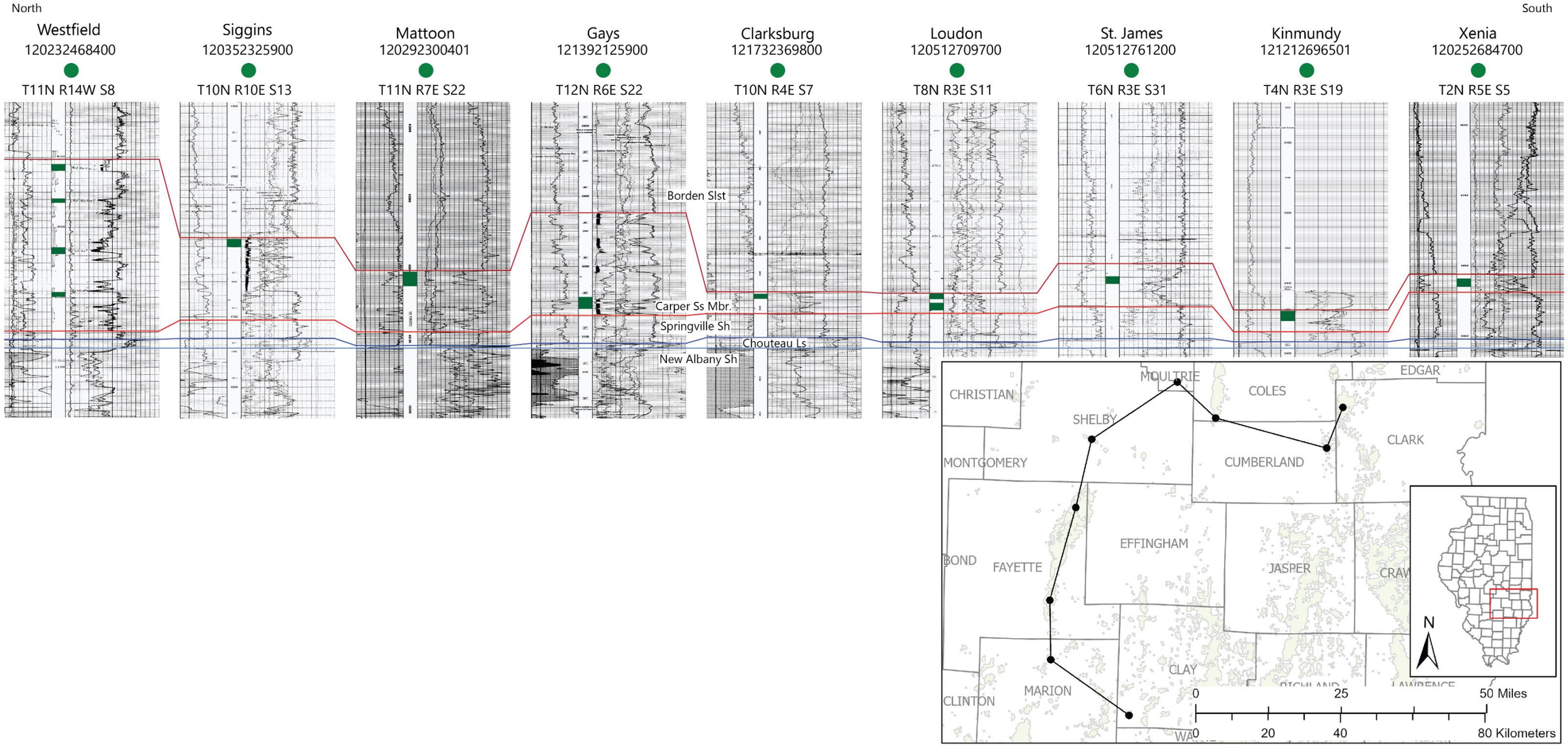


Figure 3-28. Cross-section from Westfield in the northeast to Xenia in the southwest arcing through several Carper producing areas. Datum is the base of the Chouteau Limestone. The red correlation line is the base of the Carper Sandstone. Green shading in the depth track indicates production perforations in the well. The cross section shows the varying thickness of the Springville Shale between the Chouteau Limestone and Carper sandstone. Also note the variability in the number of Carper Sandstone bodies and which ones are oil productive.

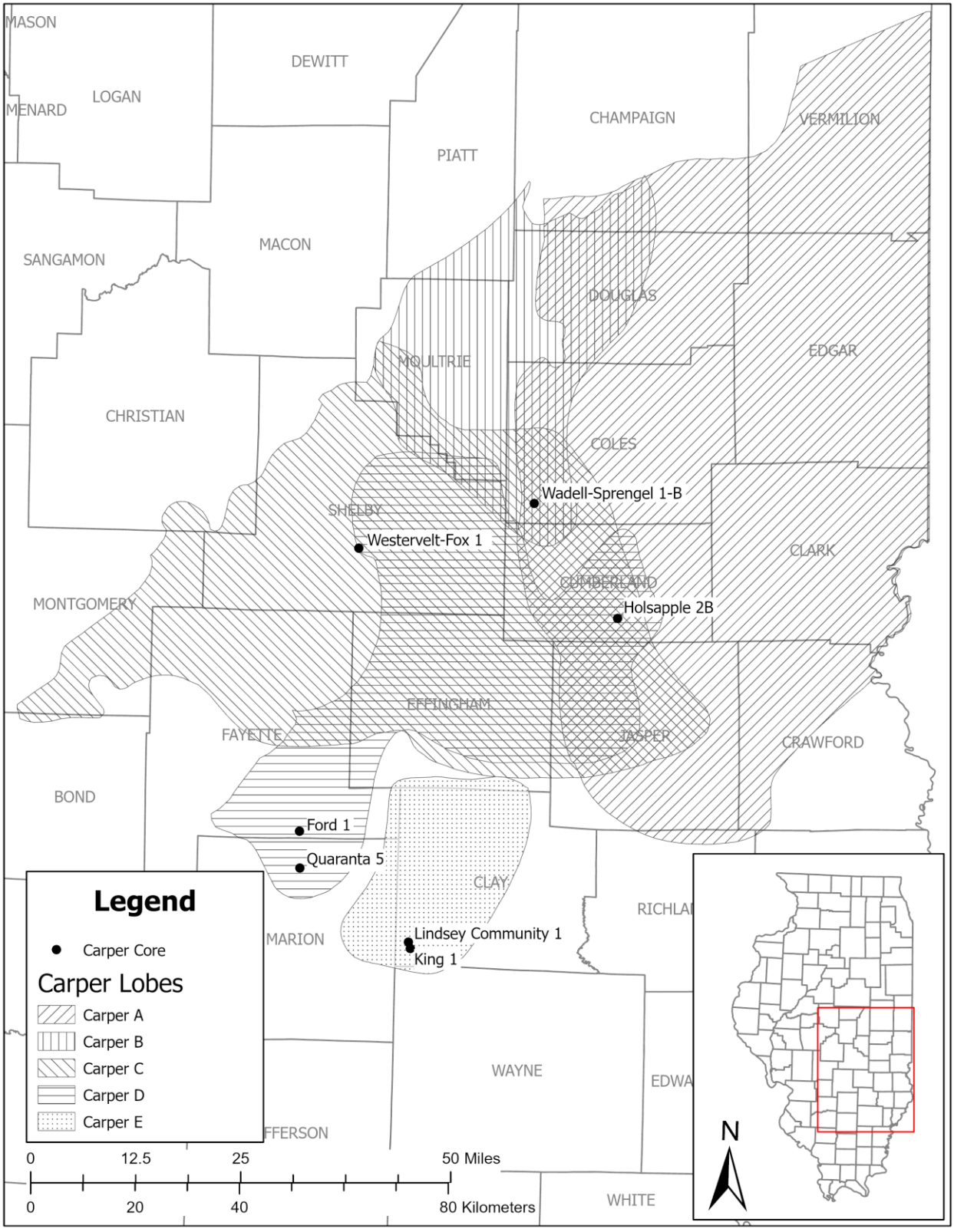


Figure 3-29. Map showing locations of depositional lobes for Carper A, B, C, D, and E sandstones (after Lineback, 1968). Black dots indicate wells with core and are labeled with the well name.

RESERVOIR CHARACTERIZATION

Sedimentary Facies Analysis

Data and Methods

A facies analysis was conducted to refine the subaqueous gravity flow environmental interpretation developed previously (e.g., Swann et al., 1965; Lineback, 1968; Al-Aswad, 1986) and better understand the impact on reservoir quality. The facies analysis was based on new descriptions of 72.5 m (237.75 ft) of Carper Sandstone cores from seven wells (Table 3-3). The wells are distributed such that the core represent four of the five previously mapped lobes (e.g., Figure 3-29). Five lithofacies were observed that represent the features and depositional history of each sequence. The lithofacies defined here include *massive-bedded sandstone* (Sm), *parallel-laminated sandstone* (Sp), *interlaminated sandstone and mudstone* (Sl), *sandy mudstone* (Ms), and *mudstone* (M) (Table 3-4). Also present in the cores were shale and limestone facies, belonging to the Springville Shale and the Chouteau Limestone, respectively, that underlie the Carper Sandstone (see Figure 3-17).

Table 3-3. Listing of core described for this study. Well locations are shown in Figure 3-29.

Well	API	Core Top m (ft)	Core Base m (ft)	Carper Lobes
Holsapple 2B	1203523296	1,120.8 (3,677)	1,154.6 (3,788)	A, C, D
King 1	1202528436	1,223.2 (4,013)	1,226.5 (4,024)	E
Lindsey Community 1	1202527421	1,300.0 (4,265)	1,315.2 (4,315)	E
Quaranta 5	1212126965	1,014.7 (3,329)	1,032.1 (3,386)	D
Westervelt-Fox 1	1217323476	875.1 (2,871)	877.8 (2,880)	C
Ford 1	1205101748	1,010.1 (3,314)	1,017.4 (3,338)	D
Wadell-Sprengel 1-B	1202923336	923.5 (3,030)	940.9 (3,087)	A

In addition to the facies analysis, 21 samples were collected from the Holsapple 2B and Quaranta 5 cores for petrographic thin section preparation and mineralogical analysis via X-Ray diffraction (Table 3-5 and 3-6). The samples were selected to represent the range of Carper Sandstone lithofacies as well as a few samples of the lithologies in adjacent formations including siltstone (Borden Siltstone), shale (Springville Shale), and limestone (Chouteau Limestone). Thirteen of these samples correspond to core plugs that were collected for routine core analysis. Twelve of the sandstone petrographic slides were point counted for textural and diagenetic analysis, including 400 compositional data points and 100 textural data points (Table 3-7).

Lithofacies

Lithofacies identified in this study are summarized in Table 3-4. Lithofacies belonging to formations outside the Borden Siltstone (Springville Shale and Chouteau Limestone) are not included.

Table 3-4. Characteristics of lithofacies defined in this report.

Code	Name	Description	Process	Environment
Sm	Massive-bedded Sandstone	Grayish tan, very-fine grained structureless sandstone. Dominantly quartz, with sparse mm-sized flat mudstone intraclasts throughout. Occasionally displays red-coloration due to oxidization processes. Beds range in thickness from 0.2m to 2.5 m, with a typical thickness of 1.5m.	High density turbidity current	Submarine Slope Deposit
Sp	Parallel laminated Sandstone	Gray, very-fine grained quartz sandstone. Planar, ripple and low-angle cross-lamination present. Isolated clay laminations can occur along bedding surfaces. Exhibits soft-sediment deformation structures including fluid escape pipes, flame structures, load casts and deformed bedding. Bioturbation was sparsely observed. Average bed thickness of 0.3 m.	Transitional currents	Submarine Slope Deposit
Sl	Interlaminated sandstone and mudstone	Dark gray, very-fine sandstone to siltstone and muddy sandstone and siltstone. Predominately characterized by horizontal, mm-scale mud and clay chips that are largely deformed by sand loading and shearing. Instances where mud clasts align horizontally near the facies' upper boundary surface.	Transitional cohesive debris flow, deformed under sand injection from beneath	Submarine Slope Deposit
Ms	Sandy Mudstone	Interlaminated planar beds of tan siltstone and gray claystones that fine upwards. Isolated examples of ripple laminations present. Soft-sediment deformation (e.g., flame structures) and bioturbation observed. Average bed thickness <0.3 m.	Depositional sorting and traction by dilute turbulent wake	Submarine Slope Deposit
M	Mudstone	Light to medium gray, fine clay mudstone with thin brown (sometimes black) slightly curved ichnofossils, syneresis cracks, isolated pyrite nodules, and some deformed clay laminations. Pyrite and siderite bands formed near several mudstone contacts. Coarser intervals contained faint planar lamination and flaser bedding. Variable thickness.	Low Energy background suspension settling	Submarine/Ocean floor

Lithofacies Sm - Massive-bedded Sandstone to Siltstone

Description

Lithofacies Sm comprises massive (structureless) grayish-tan very-fine grained sandstone to coarse siltstone organized in beds ranging in thickness from 0.2 to 2.5 m, with a typical thickness of 1.5 m (Figure 3-30). In the King 1 core (Carper lobe E), there are tool marks, including groove marks, found at the bottom of a massive sandstone unit (Figure 3-30). Generally flat, elongate mm-scale mudstone chips occur throughout. Both gradational and sharp contacts with associated lithofacies were observed. Gradational contacts are ubiquitous where the massive-bedded sandstone is in association with laminated sandstone (lithofacies Sp). Where Lithofacies Sm was observed in association with interlaminated sandstone and mudstone (lithofacies Sl), the contact was general sharp and planar. The contact was generally sharp and undulatory at the base and top of the facies where in association with sandy mudstone (lithofacies Ms) or hemipelagic mudstone (lithofacies M).

Interpretation

The lack of observed internal bedding in the sandstone suggests that it was deposited under turbulent, upper flow regime conditions in the submarine fan system. Outcrop-scale context is required to define a more precise location in the overall submarine fan system (Stow and Johansson, 2000).

Massive sandstone deposits represent the initial sandy flow that occurs in the base of sediment gravity flow deposits. Sandy subaqueous gravity flow deposits occur within a continuum of flow regime from turbid flow (resulting in turbidite deposits) to laminar flow (resulting in debrite deposits). The single observation of tool marks on the bottom of a sandstone supports a process interpretation of laminar flow as recent work has shown that groove marks require fixed and suspended clasts found in debrite deposits (Peakall et al., 2020).

The erosional contacts of the massive-bedded sandstones, when in association with mudstones, indicate that the sediment gravity flow scoured the underlying muds before deposition of the coarser sandstone. The process of a sandstone scouring a muddy substrate is a common result from turbidity current flow in both laboratory experiments (Cartigny et al., 2014) and numerical models (Fildani et al., 2006). The lack of observed conglomerates in the sandstone suggests that the incision of the underlying mudstone was not strong enough to produce floating clasts but was adequate to entrain small mudstone chips in the flow.

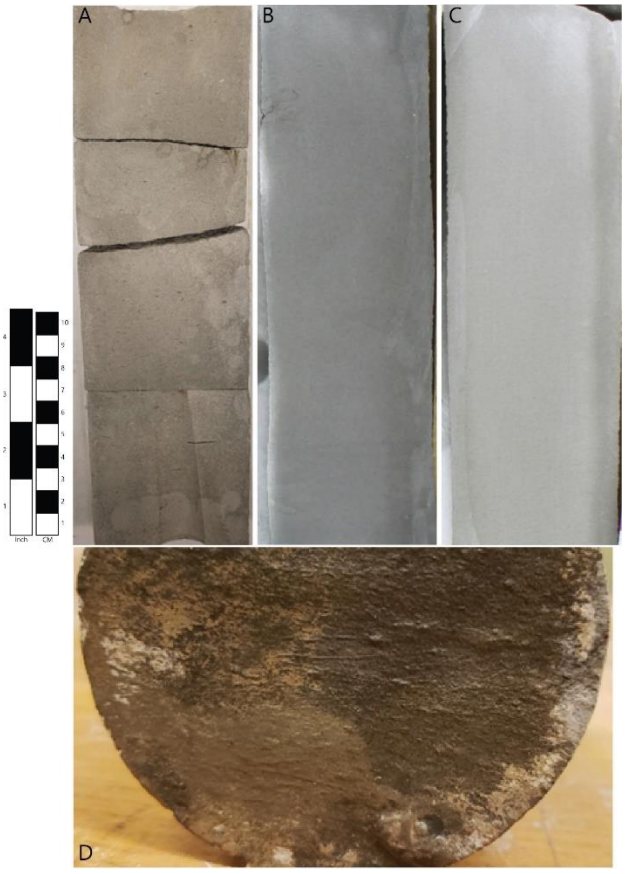


Figure 3-30. Examples of massive sandstone from A) Holsapple 2B, 1,126.5 m (3,696 ft). B) Ford 1, 1,011.6 m (3,319 ft). C) Lindsey Community 1 1,314.9 m (4,314 ft). D) Enlarged photo showing groove marks (generally oriented left-right) found at the bottom of a massive sandstone (King 1, 1,226.5 m [4,024 ft]). Core diameter = 8.9 cm (3.5 in).

Lithofacies Sp - Parallel-Laminated Sandstone to Siltstone

Description

Lithofacies Sp consists of a grayish-tan very-fine grained sandstone to coarse siltstone. The sandstone beds range in thickness from 0.076 m to 0.6 m and contain faint, parallel horizontal laminations, with few instances of low-angle laminae and cross-laminae (Figure 3-31). Much like Lithofacies Sm, the parallel-laminated sandstone contains isolated mudstone chips and can have a variety of contacts in association with other facies; although, lithofacies Sp was rarely found in association with lithofacies M. The laminated sandstone was generally found to alternate with the massive sandstone in sequence. The sandstone has localized examples of thin clay drapes that occur along bedding surfaces and in a few places contains thicker (up to approximately 2.5 cm) mudstone beds (Figure 3-31). Soft-sediment deformation is present, including instances of deformation of clay laminae, flame structures, load casts and fluid escape pipes (Figure 3-31).

Interpretation

Lithofacies Sp reflects turbulence suspension which permitted sufficient laminar flow behavior to allow for the deposition of discrete laminae. The transition from an initial turbulent state (reflected by lithofacies Sm) to a more laminar state is common to both turbidites (e.g., Bouma, 1962) and HEBs (e.g., Haughton, Davis, and Barker, 2009). The similarities of the facies compared with the massive sandstone facies suggest that they both represent the early stages of a sediment gravity flow. The sharp to gradational contacts that exist between lithofacies Sp and lithofacies Sm and Ms respectively, are expected in both traditional Bouma sequences (e.g., Bouma, 1962) and within the typical sequence of fine-grained turbidites (e.g., Stow and Shanmugam, 1980; Stow and Piper, 1984). The post-depositional deformation suggests loading of sand on mobile mud laminae in the lithofacies, most likely relate to subsequent submarine gravity flows.

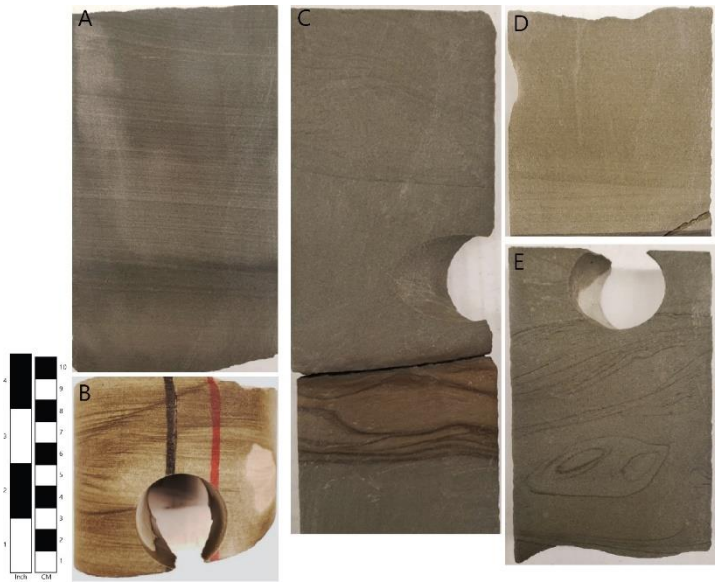


Figure 3-31. A) Low-angle parallel laminations of Facies Sp (Quaranta 5, 1,014.9 m [3,329.8 ft]). B) Rare occurrence of parallel laminations forming incipient climbing ripples (Holsapple 2B 1,125.9 m [3,694 ft]). C). Clay laminations and bedding deformed into unique geometry, present in parent sandstone (Holsapple 2B 1,131.9 m [3,713.7 ft]) D.) Faint laminations in clean, very fine-grained sandstone (Quaranta 5, 1,020.2 m (3,347 ft)). E) Soft-sediment deformation processes resulted in fluid escape pipes, load casts and flame structures (Holsapple 2B, 3,710.5 ft).

Lithofacies Sl - Interlaminated Sandstone and Mudstone

Description

Lithofacies Sl contains interlaminations of dark grey claystones and lighter gray siltstones (Figure 3-32). Bed thickness varies from laminations up to 0.30 m in thickness. Beds are generally planar with local instances of incipient ripple cross lamination (Figure 3-32). Facies Sl is not as abundant in the core, but when found, overlies a thicker sandstone (Sm or Sp) bed. The contacts with the other facies tend to be sharp, although there are several instances of undulating or erosive contacts. Soft-sediment deformation (including deformed, convolute bedding, and rarely, flame structures) and bioturbation are also found in this facies.

Interpretation

The rapid transitional nature of this facies combined with its isolated cases of ripple lamination suggest a drastic change in flow intensity from the previous facies. According to the bedform phase diagram (e.g., Southard, 1991), lithofacies Sl's fluctuating fine-grain size indicates that the unit transitioned from micro-ripple structures to upper stage plane beds. They are a product of a turbulent, but progressively more laminar unidirectional flow caused by turbulence dampening in the clay-rich flow (Baas and Best, 2002). Facies Sl represents depositional sorting and occurs in the upper part of both Bouma sequences and HEBs. Ripple structures are found in turbidites and HEBs alike and are present in many systems including the Belage formation (Kuswandaru et al., 2018), Ross formation (Pierce et al., 2018), and Karoo-basin (Jobe et al., 2012; Morris et al., 2014). Erosive and undulating contacts that occur at both the base and the cap of the facies are the product of bioturbation and deformation.

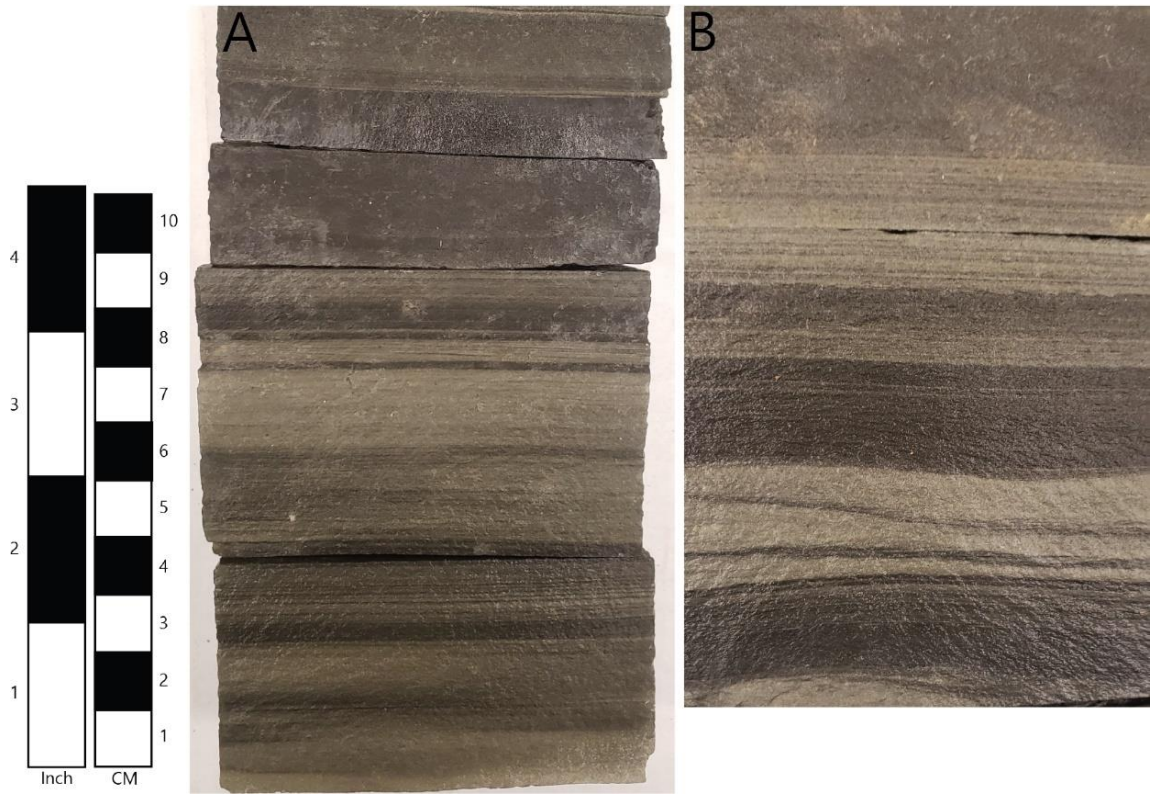


Figure 3-32. Example of lithofacies Sl Alternating succession of interlaminated silt and clay from the Holsapple 2B A) 1,125.8 m (3,693.5 ft), and B) 1,104.3 m (3,623 ft).

Lithofacies Ms - Sandy Mudstone

Description

Lithofacies Ms consists of a sandstone to siltstone unit that is darker grey with a higher proportion of admixed mud and common soft sediment deformation. Mud and clay clasts range from mudstone chips to pebble-sized. Sand loading is common, and sand pockets are present in variable shapes, sometimes preserving ptygmatic-folding geometry. The cap of the Su lithofacies sometimes contains systematic horizontal aligning of mudstone chips (Figure 3-33). The lithofacies often separates a sandy base (Sp and Sm) from an upper sequence containing sandstone laminations or hemipelagic deposition (Sl or M). The contact with the sandy base is either gradual or is deformed with ample sand loading. A scour surface often separates the Su lithofacies from a well-defined Sl or M lithofacies (Figure 3-33).

Interpretation

The Su lithofacies strongly resembles a less defined H3 division in the ideal HEB model (Figure 3-35). Haughton (2003) described an argillaceous sandstone unit with a transition from mudclasts surrounded by heterogenous matrix and patches of cleaner sand into a mudclast breccia with more uniform muddy matrices. The Su lithofacies in the Carper Sandstone is less distinct and often fails to show this upward trend. However, smaller clasts of carbonaceous material can be found more regularly near the top of the unit (Figure 3-33). Horizontal alignment of the clasts is present in select areas of the core (Figure 3-33). Variability of the clay and mud clast size shows a transition from turbulent driven flow that scours small shale clasts, to a dampened turbulent and highly cohesive debris flow depositing larger pebble-sized clasts. Sand patches and deformation suggest lithification within an unconsolidated mud matrix. In the idealized hybrid event bed sequence, the H3 division is followed by a coarser, laminated sandstone (P. Haughton et al., 2009), which reasonably describes the scour mark between the Su lithofacies and the laminations provided by the Sp and Ml lithofacies.

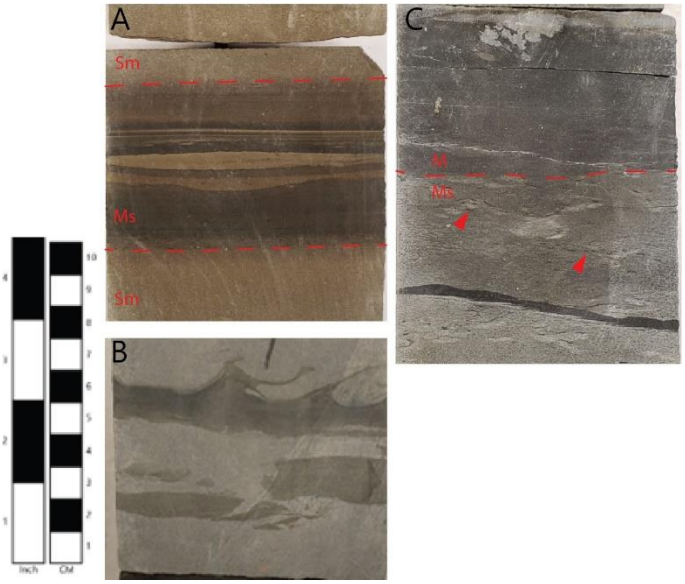


Figure 3-33. A) Thin bed of muddy sandstone meeting massive sandstone above and below along gradational contacts. Holsapple 2B, 1,138.1 m (3,734 ft) B) Soft-sediment deformation processes resulted in fluid escape pipes, load casts and flame structures (Holsapple 2B, 3,710.5 ft). C) Red arrows pointing at small Cosmoraphe ichnogenera, part of the Nereities ichnofacies. Holsapple 2B, 1,142.7 m (3,749 ft).

Lithofacies M - Mudstone

Description

Lithofacies Mf consists of structureless to faintly horizontally bedded, dark-gray mudstone. Although the facies occurs infrequently in the core, where it does occur, it forms the thickest beds ranging from 0.23 to 2.87 m thick. The mudstone exhibits both gradational and sharp contacts with associated facies. The mudstone contains blebs of pyrite and siderite concretions. Bioturbation is commonly present in the mudstone and previous workers identified trace fossils of the Nereities-Zoophycos ichnofacies (Ahmad, 2003). Subaqueous sedimentary cracks are common and are generally filled with coarse silt to very fine sandstone and are ptygmatically folded.

Interpretation

The mudstone represents hemipelagic background sedimentation of the Borden deltaic complex. Periods of quiescent marine conditions allowed for slow suspension fall-out sedimentation that allowed colonization of the seafloor. The siderite horizons are evidence for diagenetic alteration in times of very limited clastic deposition. The subaqueous sedimentary cracks contain a ptygmatically folded fill presumably because the crack-fill was more resistant to burial compaction than the matrix (McMahon et al., 2017).

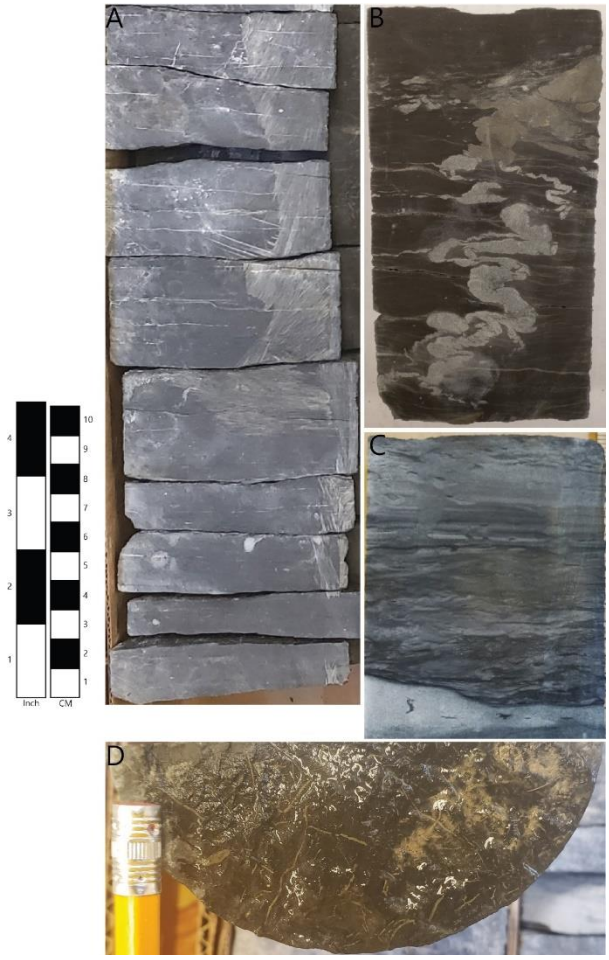


Figure 3-34. Examples of fossiliferous mudstone from A) Holsapple 2B, 1,126.5 m (3,764 ft). B) Holsapple 2B, 1,122.4 m (3,682.5ft), showing sandstone to siltstone filled subaqueous sedimentary crack with ptygmatic folding and some pyrite mineralization. C) Quaranta 5, 1,020.5 m (3,348 ft), showing bioturbation in mudstone and coarse siltstone. D) surface of mudstone bed showing subaqueous sedimentary cracks.

Facies Associations

The Carper Sandstone was previously interpreted as a series of turbidite deposits in a prograding submarine fan system (e.g., Lineback, 1968). The turbidite interpretation was based on repetitive graded sequences observed within Carper Sandstone cores (Stevenson, 1964). Only a few years prior to these interpretations, ideal turbidite architecture was outlined by Bouma (1962) in a facies model (Figure 3-35a). These graded beds, so-called Bouma sequences, include five-fold division that represent the laminar to turbulent change in flow regime that occur as part of turbidite deposition.

Research on submarine fan deposits has proliferated in the years since the Bouma sequence was proposed with new classification schemes being proposed that better account for the range of grain sizes and facies that can occur in deep-water systems. The classical five-fold Bouma sequence is now considered too limited to encompass deep-water sediment gravity flows of different grain size and transitional flow regime. In the 1980s, a novel paradigm for fine-grained turbidite systems was introduced (Stow and Shanmugam 1980; Stow and Piper 1984). Fine-grained turbidites are those in which over 50% of grains are silt sized (<63 μm). An idealized silt turbidite (>70% silt particles) facies model is shown in Figure 3-33b (Stow and Piper, 1984). Unique to this facies model is the inherently fine-grain sizes in all internal divisions, and the attenuation of explicit ripple to dune sedimentary structures that require coarser drains to develop. The very-fine grained nature of the Carper Sandstone makes it amenable to analysis within the context of siltstone turbidite sequences.

In addition to grain size, flow regime plays an equally important role in sequence patterns in deep-water systems. Sediment gravity flow sequences may include beds that do not conform to the typical upward grading pattern and sedimentary features that (Bouma, 1962) initially described. More distal reaches of deep-water systems show evidence of turbulence suspension and a transition from dilute turbulent flow (turbidite deposits) to cohesive, laminar flow (debris flow deposits) (Figure 3-36). Transitional flows are more complex than gradual turbulence-dampening flow and can have repeated interspersed clay suspension-driven plug flows (Baas et al., 2009). Non-typical beds, called Hybrid Event Beds (HEBs), are beds that capture depositional events of a single flow event that begins as a turbidite, then progresses through the transitional intervals and is capped by a laminar debrite. HEB sequences are organized into five internal divisions: H1, H2, H3, H4, and H5 (Figure 3-35c) (P. Haughton et al., 2009). HEBs typically range from 5 to 200 cm (2 to 78 in) thick. Much like the Bouma sequence, individual divisions may be absent, leading to an incomplete sequence that can give insight into the co-genetic turbulent and laminar flow regime, varying flow intervals, and location of the sequence within the basin (Talling, 2013). Recent work has demonstrated the application of HEB classification to outcrops that record distal marine successions (Fonnesu et al., 2018; Pierce et al., 2018).

The five lithofacies identified in the Carper Sandstone can be rationalized into two facies associations within the overall sediment gravity flow environment: Turbidite and Hybrid Event Bed (HEB) deposits (e.g., Figure 3-37), which are interpreted to represent single flow events. Criteria for identifying turbidite and HEB deposits include i.) clear internal divisions that reflect the ideal facies schemes in Figure 3-35 and, ii.) each deposit must contain two or more internal divisions. Upon meeting the above criteria, each turbidite or HEB deposit was characterized by its internal architecture, e.g., a H1-H3-H5 deposit is a single-flow event HEB that maintained its H1, H3, and H5 divisions in the core. Further, thickness measurements of every division in the identified deposits were compiled. The data were then statistically analyzed to show the median height of each division in a given flow event and illustrate the variability of architecture of the turbidites and HEBs that comprise the Carper Sandstone.

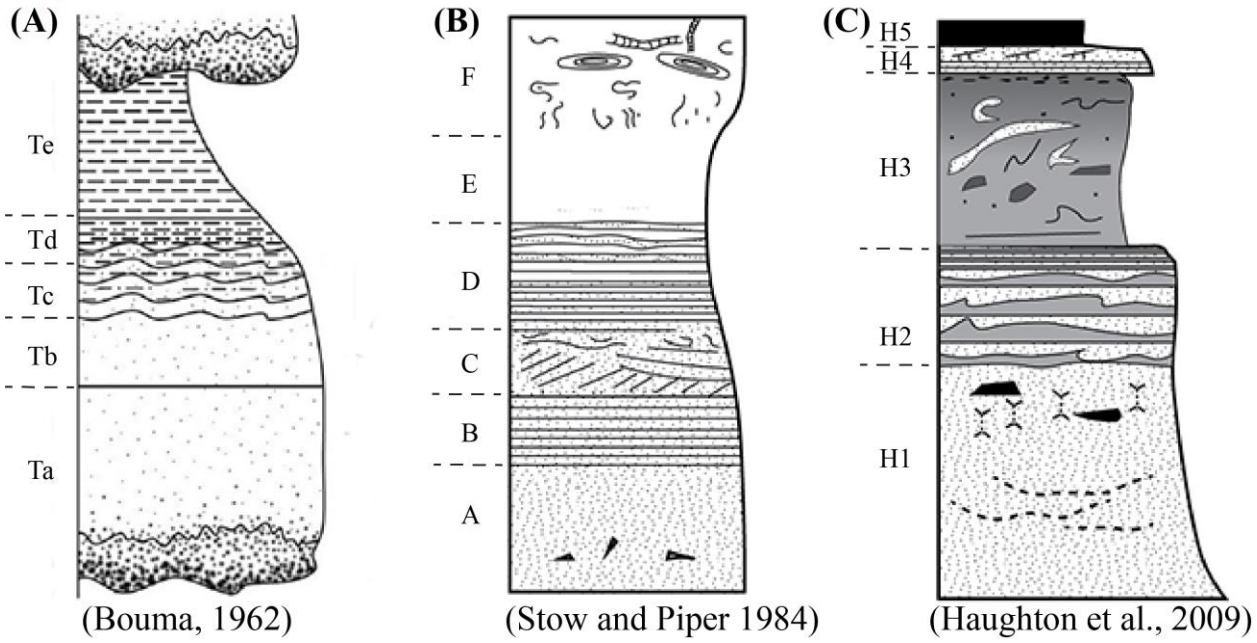


Figure 3-35. The evolution of deep-sea sediment gravity flow facies models. A) Idealized turbidite Bouma sequence, B) Turbidite deposit composed of silt-sized grains, and C) Typical deposits of a co-genetic turbidite and debrite, known as a Hybrid Event Bed. The descriptions of the internal divisions are found in the citations for each diagram. Note that the diagram on the left is a modified image taken from (Bozetti, 2017).

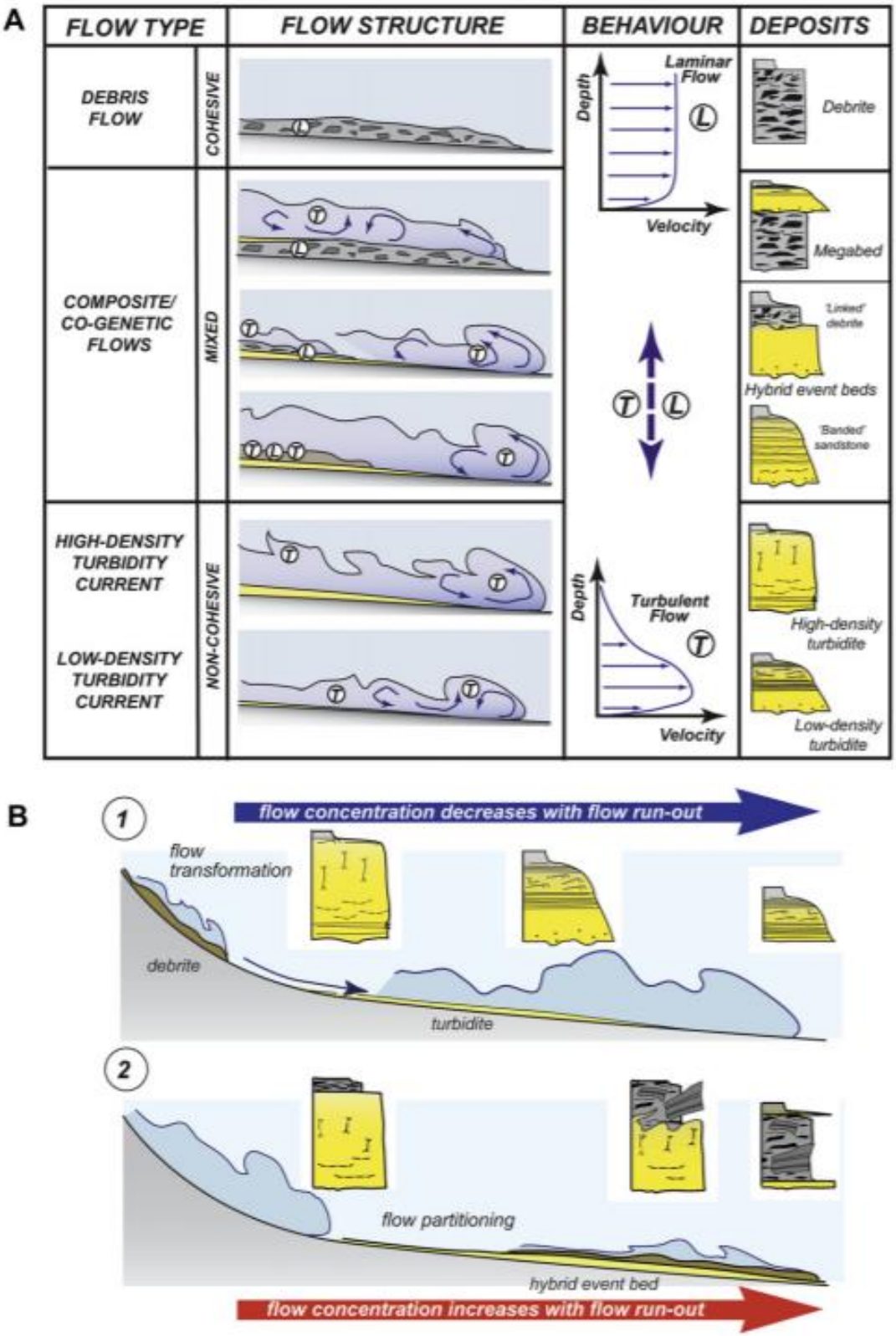


Figure 3-36. A) Classification scheme for event beds emplaced by subaqueous sediment gravity flows. B) Spatial variability of flow concentration and resulting stratigraphy (Haughton et al., 2009).

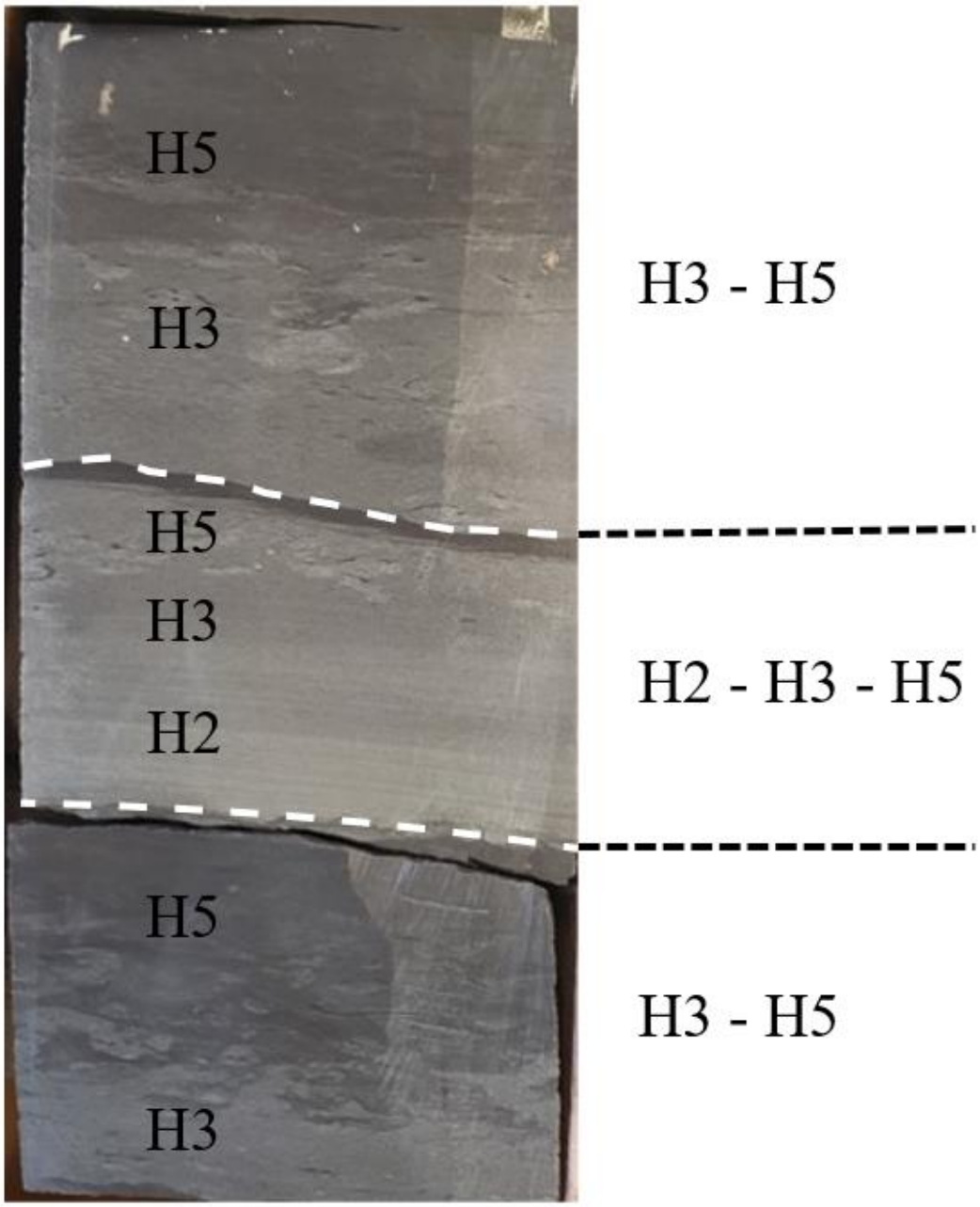


Figure 3-37. An example of a HEB assemblage (e.g., [Haughton et al., 2009], Figure 3-35) in a Carper core. The HEB assemblage is identified, internal down, and measured. Core is approximately 9 cm (3.5 in) wide.

Turbidites

Twenty turbidite deposits were identified. The most common architectural configurations were *Ta-Te* (7) followed by *Ta-Tb* (3), *Ta-Tb-Te* (3), and *Ta-Tb-Td* (2). No complete (*Ta-Tb-Tc-Td-Te*) Bouma sequence was observed. Turbidites found in the core often lacked identifiable divisions, and thus appeared as a subtle transition from clean sandstone (*Ta*) to clean mudstone (*Te*). The average turbidite thickness was approximately 60.5 cm (23.8 in), with a 36.0 cm (14.2 in) thick Ta division, an 8.6 cm (3.4 in) Tb division, an 8.7 cm (3.4 in) Tc division, a 2.3 cm (0.9 in) Td division, and a 5.1 cm (2.0 in) Te division. Average thicknesses are further broken down by specific divisions in Figure 3-38.

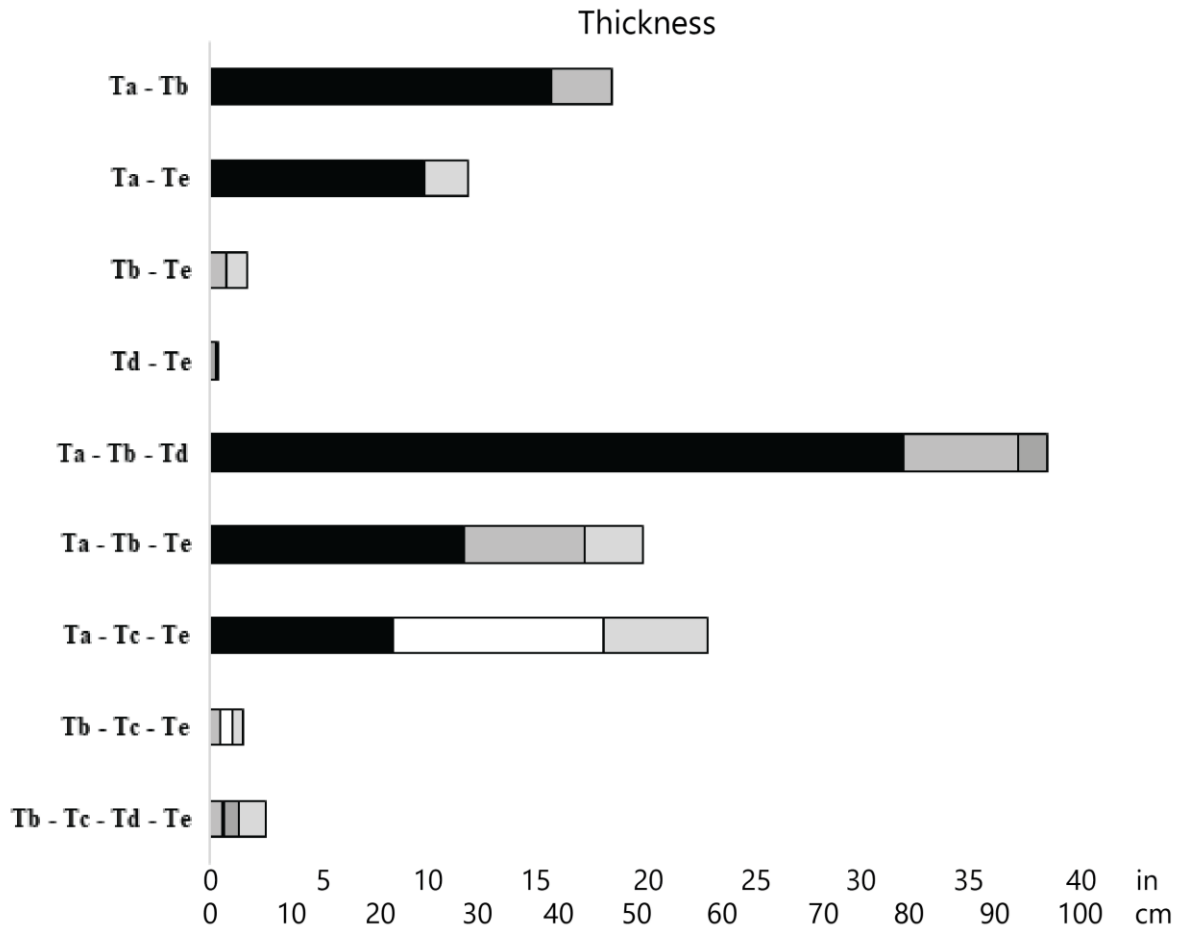


Figure 3-38. The average thickness of each division for the range of observed turbidite deposits.

Hybrid Event Beds

A total of 53 HEBs were identified consisting of 18 different architectures. The most common architectures were incomplete: *H3-H5* (12) followed by *H1-H3-H5* (8), *H1-H3* (7), and *H1-H3-H4-H5* (6). No other architecture occurred more than three times throughout the core. One complete HEB sequence (H1 through H5) was found in the Quaranta 5 core (3,352 ft). Much like the turbidites, massive sand (lithofacies Sm / H1) and mudstone (lithofacies M / H5) are more common than well-defined planar to low-angle cross-bedding (lithofacies Sp / H4) and interlaminated sandstone and mudstone (lithofacies Sl / H2).

The average HEB in the core was approximately 47.0 cm (18.4 in) thick, with a 21.8 cm (8.6-in) H1 division, a 15.1 cm (5.9 in) H2 division, a 3.58 cm (1.4 in) H3 division, a 2.3 cm (1.0 in) H4 division, and a 5.0 cm (1.5 in) H5 division (Figure 3-40). The thickness of the H3 division in the Carper Sandstone is significantly different than the original muddy sandstone facies originally described by Haughton et al. (2003) in which the facies was measured to be on average 20 cm (7.9 in). Haughton et al. (2003) originally described an H3 section that transitioned from a hetergenous matrix with sand patches and floating clasts, to a floating mudstone breccia. The dissimilarity of thickness might explain why some of the internal architecture is absent in the Carper Sandstone. Average thicknesses are further broken down by specific divisions in Figure 3-39.

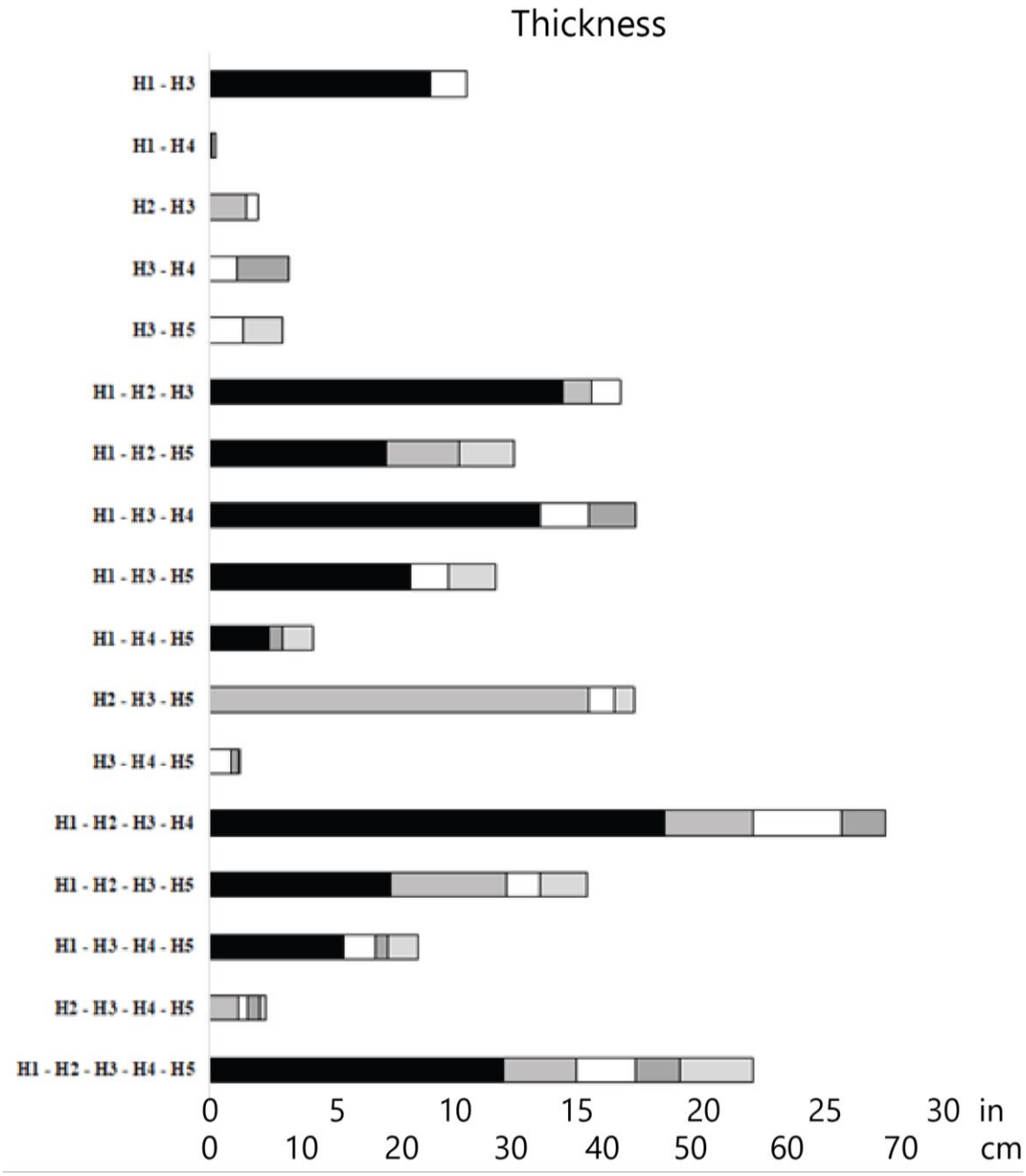


Figure 3-39. The average thickness of each division for the range of observed HEB deposits.

Internal Architecture

For all identified turbidite and HEB assemblages identified, the thickness of each division (Ta through Te, and H1 through H5) was measured. The average height of each division is visualized in Figure 3-40. The results show a general thinning upwards trend, except for the Turbidite Tc division being larger than the Tb division, and the H5 division being thicker than the H4 and H3 division (HEB). Beds of massive sandstone, representing the most ideal facies for reservoir development, are generally thicker than the other beds. In HEBs, where turbulence is often dampened, there is more parity in the bed size distribution. A result of that parity is a mudstone baffle that is relatively large compared to its turbidite counterparts.

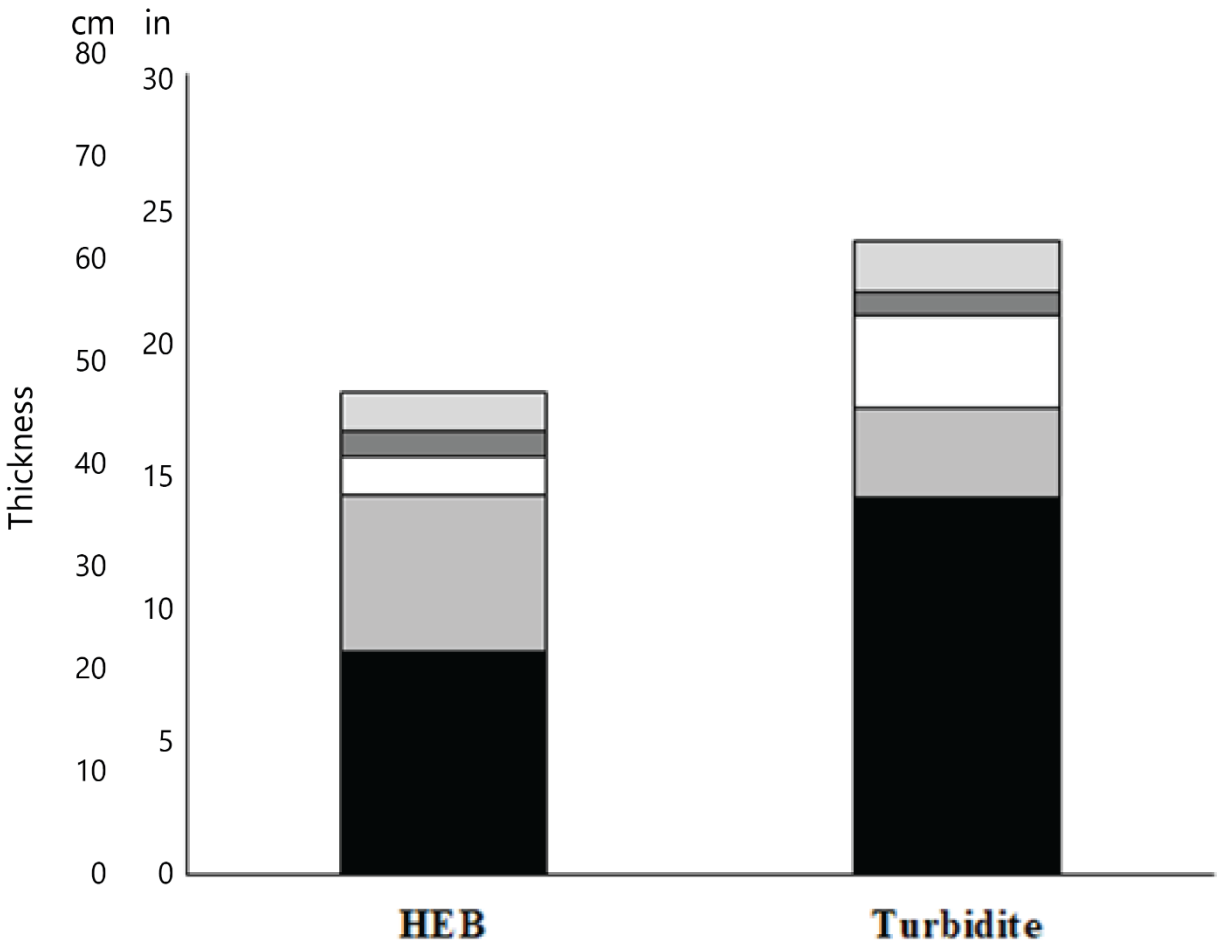


Figure 3-40. Average thickness of all divisions compiled into an idealized HEB and turbidite deposits for the Carper Sandstone.

Composition and Texture

Lineback (1968) previously described the composition of the Carper Sandstone in Illinois as consisting of approximately 60-70% quartz, 25% sericitic matrix, 4-12% carbonate, 2-5% brown organic fragments, and small amounts of chlorite, feldspar, clay, pyrite, and glauconite. Mineralogical analysis of 34 sandstone samples (Table 3-5) provides a refinement on Lineback's findings, with 47-69% quartz, 8-18% feldspar, 8-23% clays, 4-21% carbonates, and 0.5-2% other minerals and organic material. Based on the composition, the Carper Sandstone can generally be classified as argillaceous subarkose sandstone or subarkose wacke. The same classification was applied to the Carper Sandstone based on samples studied in the subsurface in Indiana (Al-Aswad, 1986). A subset of the samples (15) from the two most complete Carper cores available, the Quaranta 5 and Holsapple 2B, were also analyzed for clay mineral composition. Results from XRD analysis of the <16µm fraction glycolated oriented clay slides show, on average, 56% Illite, 22% chlorite, 17% illite-smectite, and 5% kaolinite.

Lineback (1968) furthermore described the Carper Sandstone as being composed of very-fine grained quartz sand with 70 to 90 µm angular to elongate grains. Petrographic analysis of 15 thin sections from the Quaranta 5 and Holsapple 2B cores indicate grain sizes range from approximately 50 to 120 µm, fitting into the grain size classification of coarse silt to very-fine sand. The samples were moderately-well to well-sorted.

In general, the carper Sandstone exhibits small pores that are highly occluded by authigenic carbonate and clay minerals (Figure 3-41). Most feldspar grains were observed to be at least partially dissolved and replaced by various authigenic clays (Figure 3-42). Partially dissolved feldspar grains are sometimes overwhelmed by clays and thus might lead to a bias in the point counting process. Porosity derived from routine core analysis and point counting were generally in agreement. Based on the textural analysis, 20-30% of porosity loss is due to compaction (Trask/Scherer method). The relatively tight packing may indicate cementation and dissolution happened before deep burial.

Am important implication of the compositional and textural data presented here is that the Carper Sandstone is not a petrophysically simple rock (i.e., rock with very little clay, a regular pore structure, and high-salinity water). This is supported by special core analysis of the Holsapple 2B (API 120352329600) core, which showed a typical grain density of 2.7+ g/cc owing to the higher density clay and carbonate cements common in the Carper. Clean quartz sandstone has a grain density of 2.65 g/cc. It is critical to account for this petrophysical complexity when performing any type of formation evaluation. Previous research has shown how even the relatively low clay content of the Cypress Sandstone and Aux Vases Sandstone can impact calculations of oil saturation from well logs (Leetaru, 1990; Giannetta et al., 2021). Given the high clay content, authigenic carbonates, and elevated grain density of the Carper, extra care must be taken in calculating water saturation from well logs.

Table 3-5. Bulk mineralogy of Carper Sandstone samples based on x-ray diffraction analysis of samples. The well API, sample depth, Carper lobe and gross lithology of the samples are also listed. Shaded rows correspond to samples that were also analyzed petrographically (Table 3-7).

				Bulk Mineralogy (%)								
API	**Depth**	**Lobe**	**Lithology**	**Clay**	**Quartz**	**K-feldspar**	**P-feldspar**	**Calcite**	**Dolomite**	**Siderite**	**Pyrite / Marcasite**	**Other**
1212126965	3331.2	D	Ss	7.1	57.4	2.7	8.1	5.7	13.5	2.7	2.8	0.0
1212126965	3344.0	D	Ss	7.9	71.4	2.3	10.0	0.5	4.1	2.4	1.4	0.0
1212126965	3350.2	D	Ss	7.7	61.4	2.5	10.4	0.5	12.5	3.2	1.9	0.0
1212126965	3355.2	D	Ss	8.7	62.9	2.6	9.1	3.0	8.6	2.1	3.0	0.0
1203523296	3686.2	C	Ss	8.3	67.0	3.7	14.0	0.5	1.7	3.8	1.1	0.0
1203523296	3697.5	C	Ss	7.4	69.2	3.6	14.4	0.4	1.6	2.8	0.7	0.0
1203523296	3723.0	A	Ss	24.6	38.7	5.7	17.9	1.0	2.4	6.9	2.8	0.0
1203523296	3726.3	A	Ss	9.9	68.3	3.4	13.2	0.4	1.0	2.6	1.2	0.0
1203523296	3736.0	A	Ss	8.7	65.2	3.6	14.3	0.8	1.5	4.2	1.7	0.0
1203523296	3742.2	A	Ss	10.7	65.7	3.2	13.0	1.0	0.8	4.6	1.0	0.0
1203523296	3752.2	A	Ss	16.3	58.5	2.7	13.3	1.3	0.6	5.2	2.2	0.0
1203523296	3758.7	A	Ss	21.2	42.2	5.7	11.6	1.4	1.6	10.8	5.6	0.0
1203523296	3761.8	A	Ss	7.1	73.9	2.3	11.1	0.4	0.9	3.1	1.2	0.0
1203523296	3766.1	A	Ss	7.1	71.8	3.1	12.6	0.5	0.8	2.5	1.6	0.0
1203523296	3776.6	A	Ss	8.8	67.1	3.6	14.7	0.8	1.2	3.0	0.7	0.0
1202300766	2286.0	A	Ss	21.9	51.2	1.9	16.9	0.3	6.6	0.5	0.0	0.5
1202300766	2301.0	A	Ss	22.8	53.2	1.3	17.5	0.1	4.1	0.3	0.0	0.6
1202300766	2311.0	A	Ss	26.6	48.8	1.2	16.2	0.1	6.3	0.1	0.0	0.4
1205523059	4846.5	S	Ss	10.4	63.7	0.6	7.1	0.0	17.3	0.0	0.0	0.5
1205523059	4848.0	S	Ss	11.1	63.6	0.3	4.9	0.0	19.0	0.0	0.0	0.5
1205523059	4849.2	S	Ss	10.2	56.4	0.3	6.3	0.0	25.6	0.0	0.0	0.5
1205523059	4850.8	S	Ss	8.8	67.4	0.3	6.2	0.0	16.3	0.0	0.0	0.6
1205523059	4852.0	S	Ss	12.1	68.4	0.4	7.2	0.0	11.0	0.0	0.0	0.5
1205523059	4853.3	S	Sh	17.6	24.0	0.1	6.6	0.0	50.8	0.0	0.0	0.8
1205523059	4854.0	S	Sh	8.4	49.4	0.3	6.5	0.0	34.7	0.0	0.0	0.5
1205523059	4855.0	S	Si	8.4	47.7	0.3	5.8	0.0	36.7	0.0	0.0	0.8
1205523059	4857.0	S	Sh	61.3	28.3	0.9	7.0	0.0	1.4	0.0	0.0	0.3
1205523059	4859.3	S	Ss	11.9	74.5	0.7	8.5	0.4	1.2	0.0	0.0	0.6
1205101748	3314.3	D	Ss	12.4	46.6	0.1	7.7	3.8	28.6	0.0	0.0	0.7
1205101748	3315.4	D	Ss	13.2	49.4	0.2	7.4	3.1	25.6	0.0	0.0	0.9
1205101748	3316.5	D	Sh	47.3	28.5	0.7	6.4	0.0	16.5	0.0	0.0	0.5
1205101748	3317.5	D	Sh	61.6	28.8	0.8	6.2	0.0	1.4	0.0	0.0	0.4
1205101748	3320.0	D	Ss	18.7	49.0	0.2	11.1	14.3	5.1	0.0	0.0	1.0
1205101748	3320.8	D	Ss	24.4	45.7	0.4	11.2	10.2	6.5	0.0	0.0	1.0
1205101748	3321.8	D	Ss	20.7	48.6	0.4	11.6	9.6	7.2	0.0	0.0	1.1
1205101748	3323.3	D	Ss	19.6	48.3	0.3	11.9	14.9	3.0	0.0	0.0	1.2

1205101748	3324.0	D	Ss	23.3	43.0	0.3	9.9	18.0	3.0	0.0	0.0	0.5
1205101748	3326.3	D	Sh	60.0	29.6	0.3	6.6	0.1	2.6	0.0	0.0	0.2
1207900686	4088.0	A	Sh	62.3	27.9	0.6	6.6	0.0	0.8	0.0	0.0	0.3
1207900686	4100.0	A	Ss	20.3	60.0	0.7	16.8	0.0	1.5	0.0	0.0	0.6
1207900686	4112.0	A	Ss	20.0	59.9	0.4	15.8	0.2	3.0	0.0	0.0	0.5
1202923336	3040.0	A	Ss	24.4	50.0	0.6	11.9	0.2	12.0	0.0	0.0	0.5
1202923336	3041.5	A	Sh	66.2	23.3	1.0	6.6	0.2	1.8	0.0	0.0	0.6
1202923336	3044.5	A	Sh	65.3	23.8	1.3	5.5	0.0	1.6	0.0	0.0	0.5
1202923336	3047.7	A	Sh	75.3	16.2	1.4	5.9	0.0	0.2	0.0	0.0	0.5
1202923336	3050.0	A	Sh	69.3	21.8	1.8	5.9	0.0	0.4	0.0	0.0	0.4
1202923336	3052.0	A	Sh	64.1	21.0	1.5	7.1	0.0	3.9	0.0	0.0	0.6
1202528436	4014.0	E	Ss	15.2	52.8	1.3	11.5	10.3	7.7	0.0	0.0	0.8
1202528436	4016.0	E	Ss	14.9	53.3	1.1	12.0	10.4	7.0	0.0	0.0	0.7
1202528436	4017.3	E	Ss	14.3	51.8	0.5	11.6	8.8	12.1	0.0	0.0	0.7
1202528436	4018.0	E	Ss	12.3	59.1	0.8	11.6	7.1	8.3	0.0	0.0	0.5
1202528436	4018.4	E	Ss	15.2	49.6	1.1	13.0	9.4	10.8	0.0	0.0	0.8
1202528436	4020.0	E	Ss	13.1	57.5	1.2	11.2	7.5	8.7	0.0	0.0	0.8
1202528436	4021.8	E	Ss	14.0	58.6	1.3	11.4	10.3	3.6	0.0	0.0	0.6

Table 3-6. Clay mineralogy of Carper Sandstone samples based on x-ray diffraction analysis of <16µm fraction glycolated oriented clay slides. The well API, sample depth, Carper lobe and gross lithology of the samples are also listed. Shaded rows correspond to samples that were also analyzed petrographically (Table 3-7).

API	Depth	Lobe	Lithology	Illite-Smectite (%)	Illite (%)	Kaolinite (%)	Chlorite (%)
1212126965	3331.2	D	Ss	25.39	60.67	4.15	9.79
1212126965	3344.0	D	Ss	17.29	58.14	5.54	19.03
1212126965	3350.2	D	Ss	21.50	62.21	3.62	12.67
1212126965	3355.2	D	Ss	29.21	50.56	5.72	14.50
1203523296	3686.2	C	Ss	19.07	53.52	5.88	21.52
1203523296	3697.5	C	Ss	15.36	56.02	4.10	24.52
1203523296	3723.0	A	Ss	15.63	45.10	3.79	35.47
1203523296	3726.3	A	Ss	15.46	49.21	3.58	31.75
1203523296	3736.0	A	Ss	13.15	54.92	5.13	26.80
1203523296	3742.2	A	Ss	12.74	55.24	3.42	28.60
1203523296	3752.2	A	Ss	16.06	52.26	6.58	25.11
1203523296	3758.7	A	Ss	11.36	67.86	4.59	16.19
1203523296	3761.8	A	Ss	16.16	60.07	5.08	18.70
1203523296	3766.1	A	Ss	17.66	57.00	4.27	21.08
1203523296	3776.6	A	Ss	13.01	55.61	4.30	27.08

Table 3-7. Grain size and sorting characteristics of Carper Sandstone based on petrographic analysis. Routine porosity and permeability measurements from core plugs are also listed.

API	Depth	Lobe	Porosity (%)	Permeability (mD)	Mean grain size (µm)	Median grain size (µm)	Mean (phi)	Grain size classification	Sorting classification
1212126965	3331.2	D	9.0	0.024	52	46	4.388	Coarse Silt	moderately well sorted
1212126965	3344.0	D	19.4	4.281	52	48	4.356	Coarse Silt	well sorted
1212126965	3350.2	D	12.0	0.069	53	52	4.308	Coarse Silt	well sorted
1212126965	3355.2	D	12.2	0.224	57	56	4.189	Coarse Silt	well sorted
1203523296	3686.2	C	14.6	0.824	65	63	4.005	Very fine sand	well sorted
1203523296	3697.5	C	14.8	0.543	64	58	4.085	Coarse Silt	moderately well sorted
1203523296	3726.3	A	12.6	0.191	69	64	3.975	Very fine sand	moderately well sorted
1203523296	3736.0	A	10.8	0.052	72	69	3.877	Very fine sand	moderately well sorted
1203523296	3742.2	A	11.8	0.055	70	66	3.927	Very fine sand	moderately well sorted
1203523296	3761.8	A	7.3	0.016	119	105	3.207	Very fine sand	moderately well sorted
1203523296	3766.1	A	15.7	3.816	79	75	3.723	Very fine sand	well sorted
1203523296	3776.6	A	12.3	0.291	79	74	3.753	Very fine sand	moderately well sorted

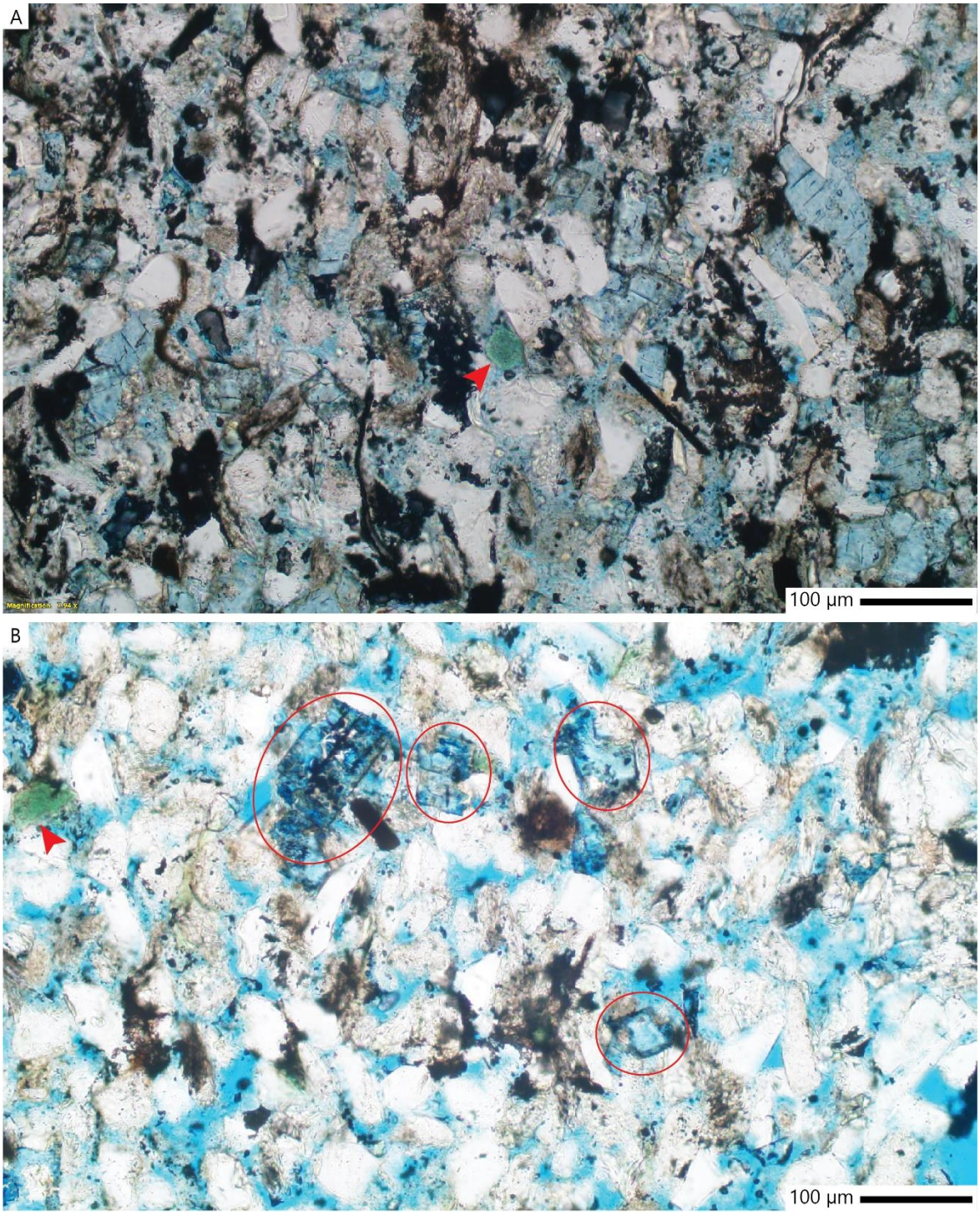


Figure 3-41. Thin sections from Quaranta 5 core. A) 1,015.4 m (3331.2 ft). 9.0% Φ, 0.02 mD k. A typical field of view showing high relief authigenic or detrital dolomite comprising a large proportion of the framework. There are small aggregates of dolomite and quartz in the span of 10-50 grains. Pore spaces between these aggregates are filled with various clays, but dominantly illite. The opaque grains are counted as hematite for simplicity, but they are more likely to be marcasite/pyrite based on XRD results (Table 3-5). The translucent green grains (red arrows) are glauconite, but there are too few to be exclusively categorized in point counting. B) 1,019.3 m (3,344 ft). 19.4% Φ, 4.28 mD k. Very-fine grained sandstone, quartz and feldspar framework grains. Small, poorly connected pores occluded by carbonate rhombs (red circles) and clusters and clay minerals.

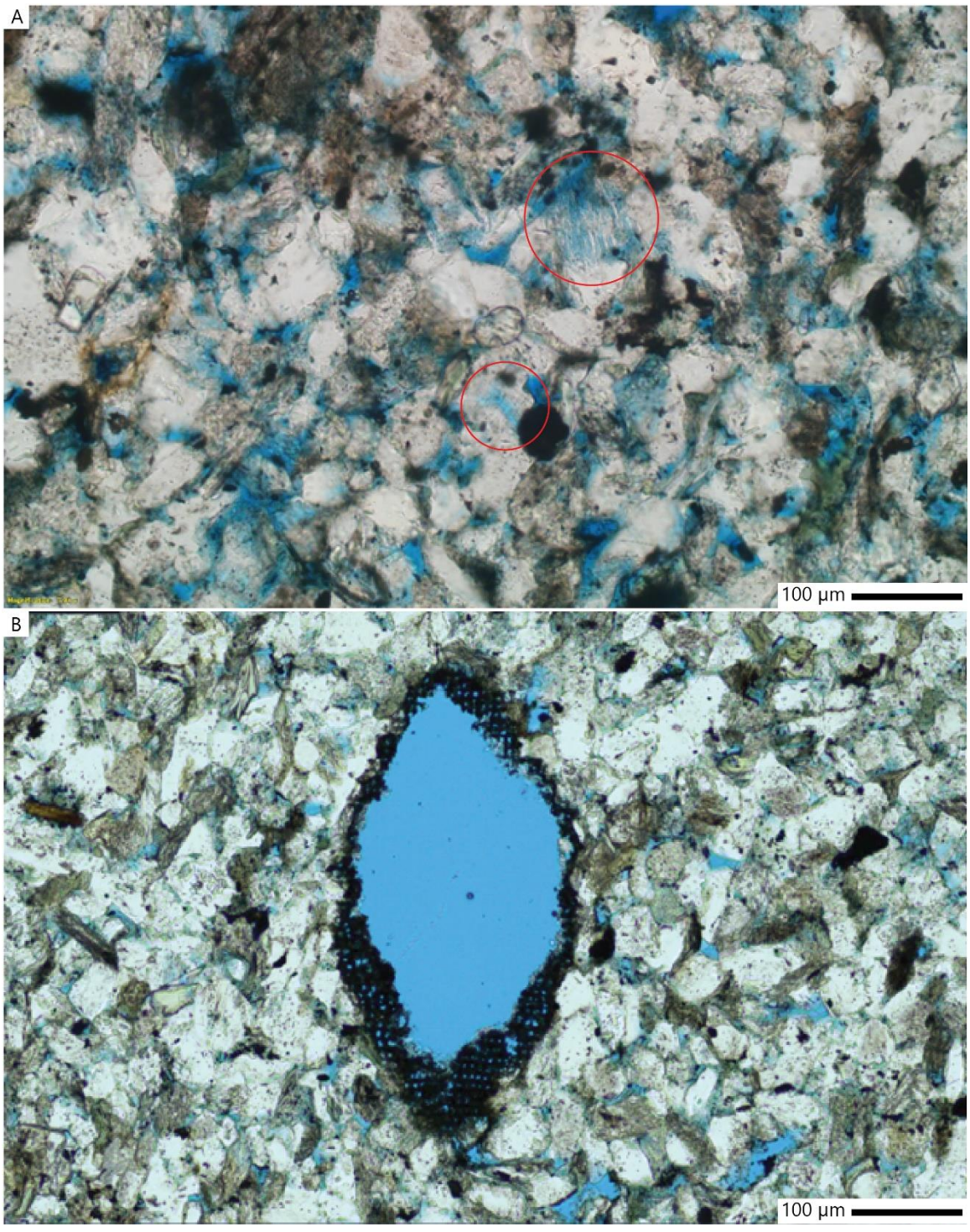


Figure 3-42. Thin sections from Holsapple 2B. A) 1,127 m (3697.5 ft). 14.8% Φ, 0.54 mD k. In the center of image are a few non-stained feldspar grains (red circles) that are partially dissolved and have been replaced by clay minerals in their secondary pore spaces. In the Holsapple 2B samples, quartz grains commonly have quartz overgrowths with irregular shapes that may indicate early-stage cementation that later dissolved and lined by authigenic clay minerals. B) 1,123.6 m (3,686.2 ft). 14.6% Φ, 0.82 mD k. Typical matrix field view with an oversized moldic pore in the center of the image. From the remnant structure of the mold, it can be inferred as a biogenetic fragment with its perimeter replaced by iron rich authigenic minerals.

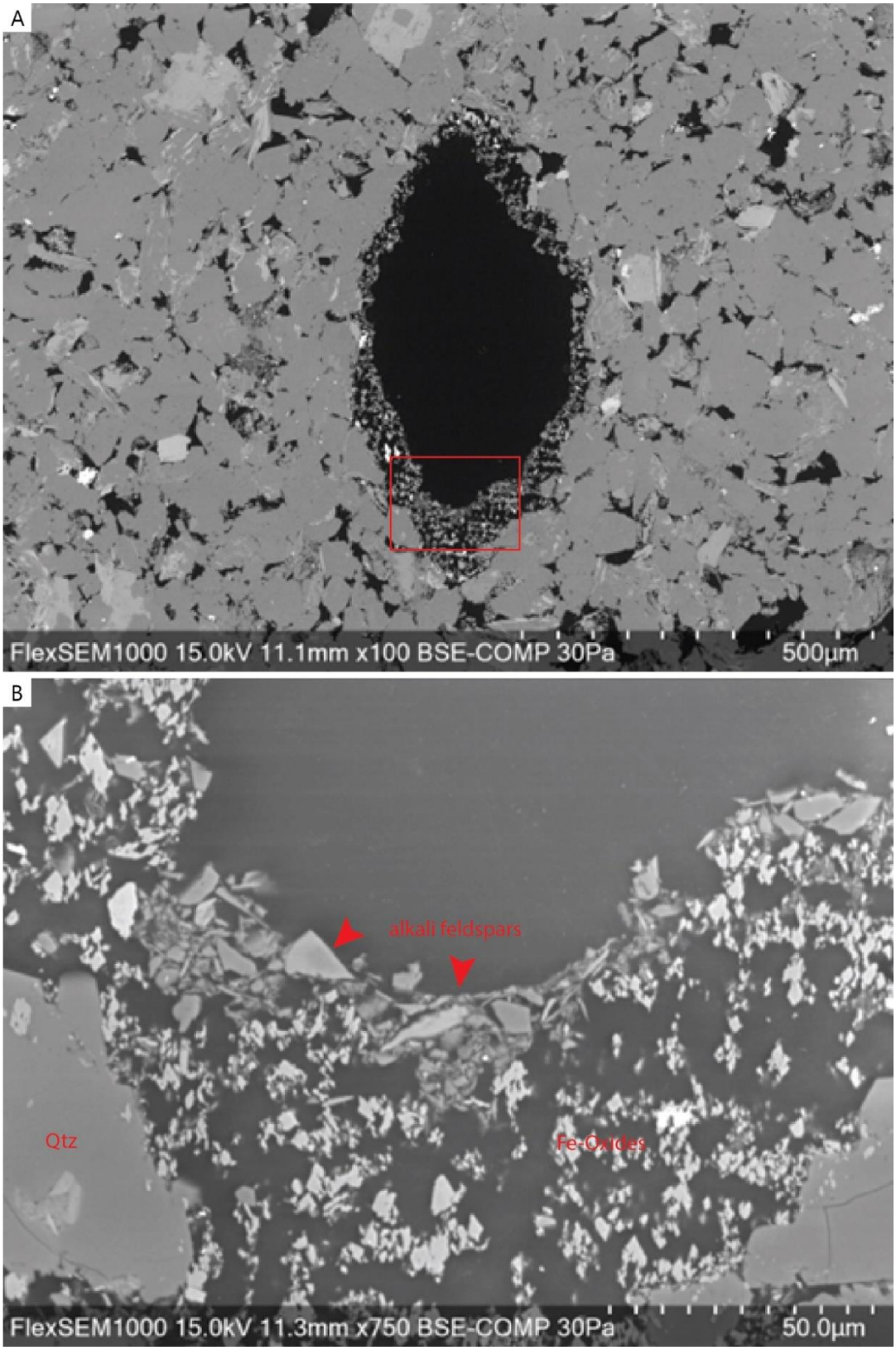


Figure 3-43. SEM images of the sample shown in Figure 3-42B showing dissolution of the bioclast and replacement with Fe-oxide minerals and lining of the interior of the moldic pore with authigenic alkali feldspars.

Depositional and Diagenetic Model

Reading and Richards (1994) proposed a 12-division classification scheme for deep water basin margin systems based on characteristics of the feeder system and grain size of the deposits. The Borden delta had a low slope gradient and the Carper Sandstone lobes originated at specific points along the northern slope of the Basin that progressively shift southwestward through time. As such, the overall Carper Sandstone system is interpreted to be mud-rich to mud/sand-rich single point-source submarine fans. In such systems, potential reservoir facies may occur as spatially restricted, heterogeneous channel sands that may not have a good top seal, thin but widespread levee margin sands, and laterally extensive lower fan and basinal thin-bedded turbidites (Reading and Richards, 1994). The Carper core that was available for study was generally biased towards the basinal facies (turbidites and HEBs), but it is possible that there are examples channel facies represented in some of the fields nearer to the point source of a given lobe. For example, St. James Field is located near the point source for the Carper D lobe and logs show 20 to 30 m or fairly clean, higher net:gross sandstone that may include channel facies (e.g. Figure 3-44).

The mineral suite reflects marine eogenetic environment (e.g., Worden and Morad, 2003). Compared to sandstones like the Cypress and Aux Vases in which kaolinite and chlorite are the dominant clay minerals, illite is by far the dominant clay mineral in the Carper. This likely reflects contributions from both diagenetic illite as well as depositional illite, since illite the is the most common flocculate at intermediate distances from the shoreline (Edzwald et al., 1974). The relatively high proportion of illite can also facilitate quartz pressure solution and cementation, leading to porosity loss and permeability reduction (Fisher et al., 2000). Authigenic glauconite, pyrite, and iron-rich dolomite reflect eodiagenesis in a marine environment which commonly hosts bacterially catalyzed interactions of organic matter and oxidizing inorganic solutes and minerals (Stonecipher, 2000).

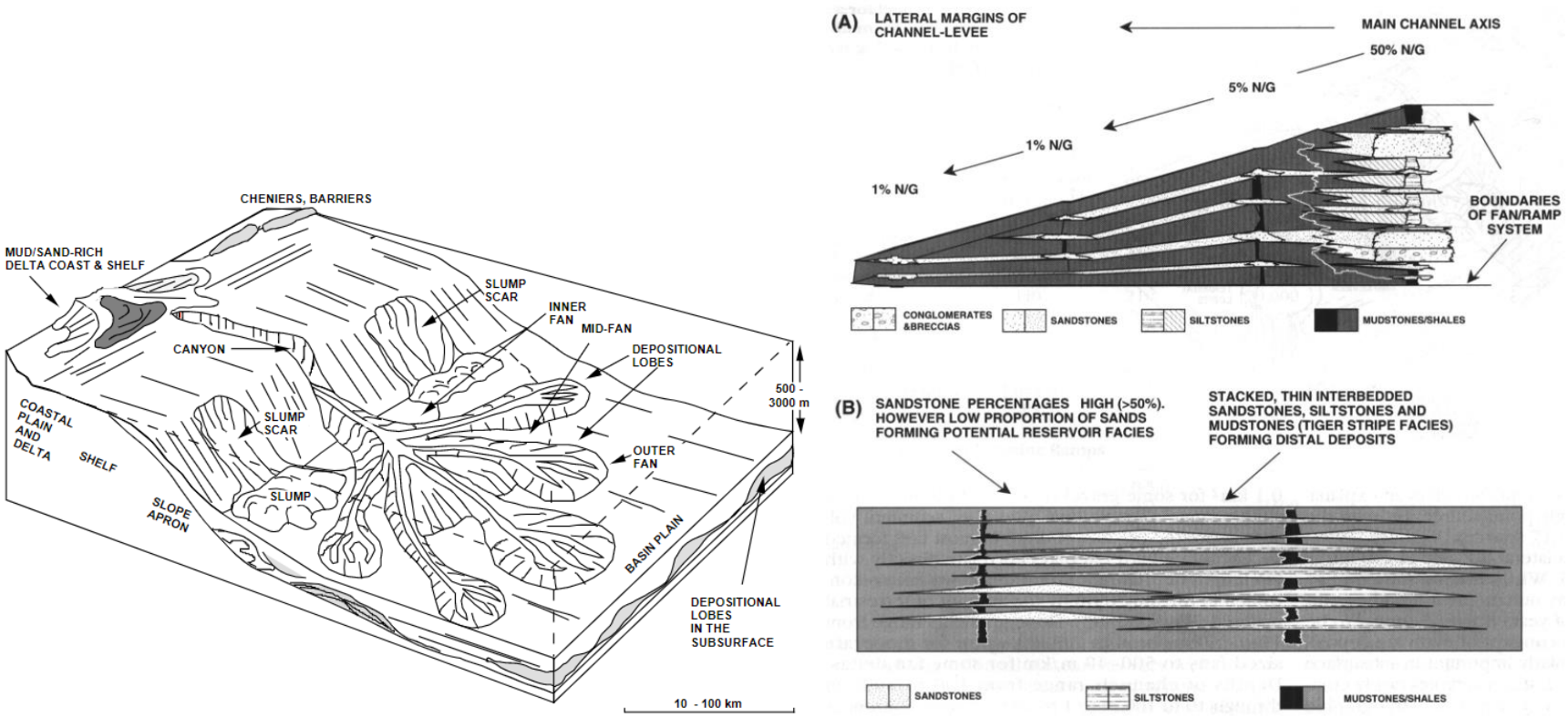


Figure 3-44. Left: Depositional block model of mud-rich to mud/sand-rich single point-source submarine fans. Right: Diagrammatic strike cross sections through the proximal channel A) and distal outer fan B) portions of the sediment gravity flow system. The model demonstrates how relatively thin sandstone bodies can persist laterally over great distances. From Reading and Richards (1994).

Reservoir Implications

As deep-water systems continue to be an excellent source of hydrocarbon extraction (Weimer and Link, 1991), the massive sandstones (lithofacies Sm) remain the highest quality reservoir of any internal division in a sediment gravity flow. However, fluctuations in the quality of the sandstone reservoir can depend on several factors. Internal architecture and resulting bed permeability is dependent on the location of the deposit in the basin, and the flow mechanisms that shaped it (Stow and Johansson, 2000). HEBs, for instance, have more heterogenous bed sets and are overall thinner than the observed turbidites (Figure 3-40).

In the case of the Carper, although these massive sandstones are the cleanest facies and have the best porosity and permeability locally, the very-fine grain size, compaction, and authigenic mineral cements result in values that are relatively low when compared to the more common Mississippian sandstone reservoirs in the Illinois Basin. Like the massive sandstone, the laminated sandstone (lithofacies Sp) maintains a coarser grain size with a similar porosity, but thin laminations of clay and mud material can serve to degrade permeability (e.g., Johnson et al., 1987). The commonly observed soft-sediment deformation of laminae, including instances of fluid-escape pipes can further complicate the permeability of the rock, introducing anisotropy that may not correspond to vertical.

The interbedded sandstone and mudstone (lithofacies Sl) and sandy mudstone (lithofacies Ms) have a high mud to sand ratio and low porosity and permeability, making them poor reservoir quality. When similar facies in H2-H3 divisions of HEBs have been analyzed elsewhere as hydrocarbon reservoirs they have been disregarded as stand-alone reservoirs for extraction or injection (Southern et al., 2017).

The mudstone beds (lithofacies M) in the Carper Sandstone represents an impermeable caprock. Sand-filled subaqueous sedimentary cracks in some of the thinner mudstone beds do potentially create tortuous pathways to hydraulically connect the cleaner sandstones across stacked HEBs or turbidities (Lonergan et al. 2000) and may have played an important role in allowing oil migration and emplacement over geologic time. Similarly, fracturing and sand injection into these cracks pose a potential risk to caprock fidelity (Hurst and Cartwright, 2007) in the event of future injection into the Carper Sandstone.

Results of the facies analysis showed a higher frequency of HEB deposits than turbidites, suggesting a deep-sea environment located on the fringe of the deltaic complex. This interpretation is obviously biased by the limited number of cores and the locations of the cores generally more in the distal parts of the Carper lobes rather than in the thicker channels. Results of the technique also showed two frequently occurring outcomes: i) basecut (absent coarse, sandy base) H3-H5 HEBs, and ii) turbidite and HEB sequences containing sandy bases, and a muddy cap, with little distinct architecture between. The diminutive size of the basecut orientations suggest that these sequences, whether HEB or turbidite, are limited in their ability to disrupt storage potential. Inversely, the flow events with a sandy base, a generally fining upward sequence, and a muddy cap were thicker overall and form the best reservoir rock observed in the cores.

Oil Reservoirs

The Carper Sandstone is the oldest productive siliciclastic reservoir of the Mississippian System in the Illinois Basin. In wells that produce oil from its reservoirs, the Carper is usually the objective formation, or it is comingled with deeper Devonian reservoirs.

The Carper was discovered in its namesake well (Carper 1, API 120230198400, Sec 30, T10N, R13W, Clark County, IL) in 1922 in Martinsville Field (Figure 3-45). The well was intended as a test of the (Ordovician)

Trenton limestone, but the oil shows in the Carper were sufficient for testing and eventual completion as a producing well (Moulton, 1926). Over 100 additional wells were completed in the Carper in the fields along the LaSalle Anticlinorium (Westfield, Johnson North, Martinsville; Figure 3-45) through about 1960. By the early 1960s, oil was discovered in the Carper Sandstone in fields south of the Loudon Anticline (Stevenson, 1964) and the southern end of the Mattoon Anticline (Figure 3-45). Carper development wells are typically drilled on a 20-acre spacing (~660 ft). Since the 1990s, there have been several successful wells drilled outside of established fields in Clay, Cumberland, Effingham, and Jasper Counties.

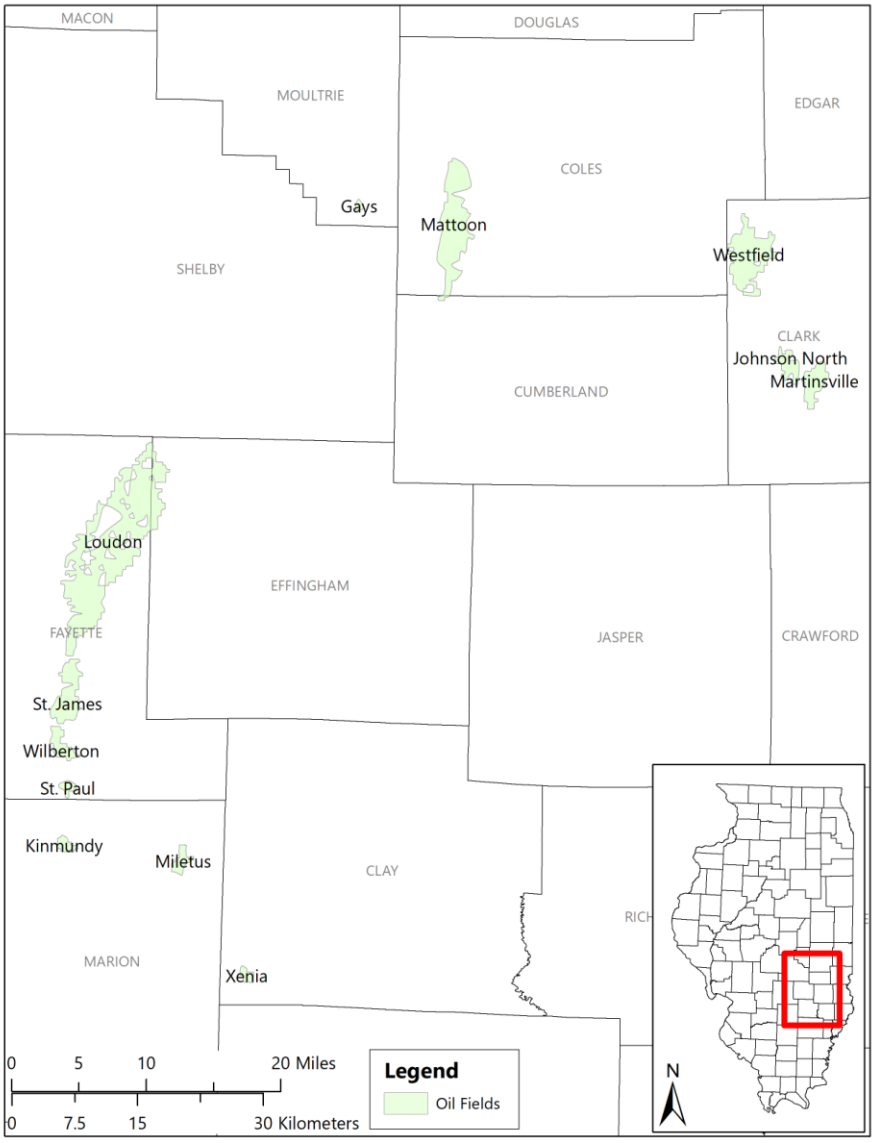


Figure 3-45. Map showing distributions of oilfields in which the Carper Sandstone contributes to oil production.

Porosity, Permeability, and Fluid Saturation

Compared to other Illinois Basin siliciclastic reservoirs, the Carper Sandstone is among the tightest due to its finer grain size and authigenic mineral cements. The ISGS database includes routine core analysis data for 1,501 core plugs collected from 73 cores. Typical values for depth, porosity, and permeability are summarized below (Table 3-8).

Table 3-8. Summary of properties for 1,501 Carper Sandstone core plug analysis from the ISGS database.

	Average	Median	P10	P90
Sample Depth (ft)	2,163.6	1,411.5	964.5	3,693.9
Porosity (%)	14.0	14.5	9.4	17.9
Permeability (mD)	3.3	1.3	0.2	6.6

Irreducible (or connate) water saturation (S_{WIRR}) is a function of porosity, rock type, pore size, grain size, diameter of interconnecting channels, wettability, and capillary pressure. Porosity-permeability relationships can be used to estimate S_{WIRR}, and in turn the potential initial oil saturation (S_{OI}) in oil reservoirs (Coates and Denoo, 1981). Although such methods are only well suited to petrophysically simple rocks, they can provide useful information on the expected oil saturation in a virgin Carper Sandstone reservoir. Rocks with small pores can have relatively high S_{WIRR} because of larger grain surface area, less room for the flow of fluids, low initial oil relative permeability (kR_O) and final water relative permeability (kR_W) values, and small saturation changes during two-phase flow (Morgan and Gordon, 1970).

A few examples from the Carper Sandstone may support a relatively high S_{WIRR}. Well records that include petrophysical calculations done by Shell during the opening of the St. Paul Field indicate 45% initial water saturation (S_{Wi}). Similarly, well log analysis of modern wells drilled in non-depleted areas shows 50% S_{Wi}. As shown in Table 3-9, the sandstone properties in many fields indicate an S_{OI} from about 40 to 64%. Using Mattoon Field as an example, it is likely that mobile oil is only produced from sandstone of the Carper A and B lobes, where the S_{OI} values are calculated at 41 and 51%, respectively. Pore throat size is also considered to be a determining factor in whether an interval is productive pay, with a minimum pore throat radius (R_{35}) for pay generally being 0.5 µm (Kolodzie, 1980). Despite the tight nature of the sandstone, Carper core data from nearly all Carper producing fields fall above the R_{35} cutoff of 0.5 µm (Figure 3-46).

Given the properties of the Carper Sandstone, it is best classified on the lower end of the spectrum of conventional reservoirs and/or on the upper end of the spectrum of tight-oil reservoirs (Figure 3-47). Tight oil reservoirs are usually defined as those reservoirs in which petroleum occurs in a free or adsorbed state in rocks adjacent to source rocks, has not experienced large-scale long-distance migration, and matrix permeability of <1 mD (Jia et al., 2016). Despite potentially lower in situ saturation, lower permeability rocks in tight oil reservoirs can have higher displacement efficiencies and a potentially higher proportion of the in-place saturation is movable in the presence of water (Liu et al., 2021). Such reservoirs can benefit from unconventional production techniques, including multi-stage hydraulically fractured (MSHF) horizontal wells, which tend to increase the production rates and ultimate recoveries (Aguilera, 2014; Figure 3-47).

*Table 3-9. Core analysis data organized by oil field and by interpreted Carper lobe (Lineback, 1968). The count column indicates the number of samples on which the statistics are based. Average porosity and average and median permeability values are recorded. *Fractional S_{WIRR} and S_O (1-S_{WIRR}) values are calculated based on the method of (Coates and Denoo, 1981).*

Field	Count	Lobe	Porosity (%)	Permeability (mD, avg)	Permeability (mD, med)	S_{WIRR}* (fractional)	S_O* (fractional)
Cumberland	69	A	10.8	0.4	0.2	0.71	0.29
Mattoon	29	A	13.7	13.7	1.4	0.59	0.41
Oak Point	30	A	14.7	2.1	1.3	0.65	0.35
Johnson North	149	A	14.9	5.4	2.2	0.60	0.40
Westfield	205	A	15.3	2.7	1.2	0.70	0.30
Martinsville	381	A	15.9	4.0	1.9	0.66	0.34
Mattoon	19	B	15.7	15.2	6.7	0.49	0.51
Cooks Mill	5	B	16.3	4.6	4.1	0.57	0.43
Stewardson	10	C	10.7	1.3	1.1	0.52	0.48
Cumberland	16	C	11.5	0.2	0.2	0.78	0.22
Mattoon	57	C	16.0	1.6	0.8	0.73	0.27
Gays	3	C	16.6	1.4	1.4	0.71	0.29
St. James	79	D	13.0	1.1	0.9	0.66	0.34
Wilberton	14	D	13.0	2.1	1.5	0.62	0.38
Kinmundy	24	D	13.9	0.6	0.4	0.75	0.25
St. Paul	41	D	15.1	1.8	0.9	0.67	0.33
Stewardson	6	D	17.4	15.2	14.3	0.45	0.55
Xenia	17	E	6.4	6.6	1.5	0.36	0.64
Oskaloosa	6	E	11.4	0.8	0.3	0.69	0.31

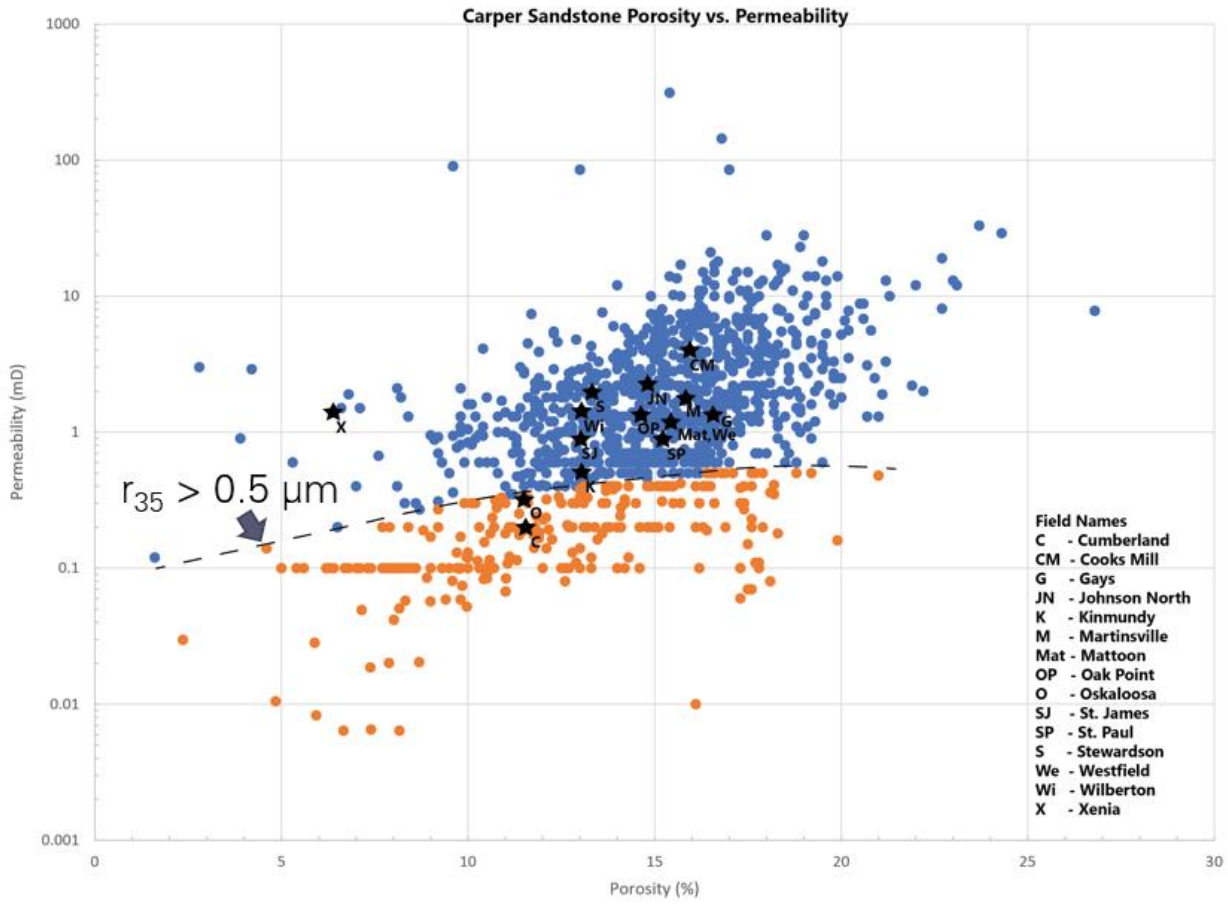


Figure 3-46. Scatter plot of porosity vs permeability with typical properties for a given oilfield plotted as stars. The data is separated into two populations; the blue points represent data above the 0.5 µm pore radius cutoff and the orange points are below the cutoff. Stars represent average properties for Carper productive fields and generally fall above cutoff.

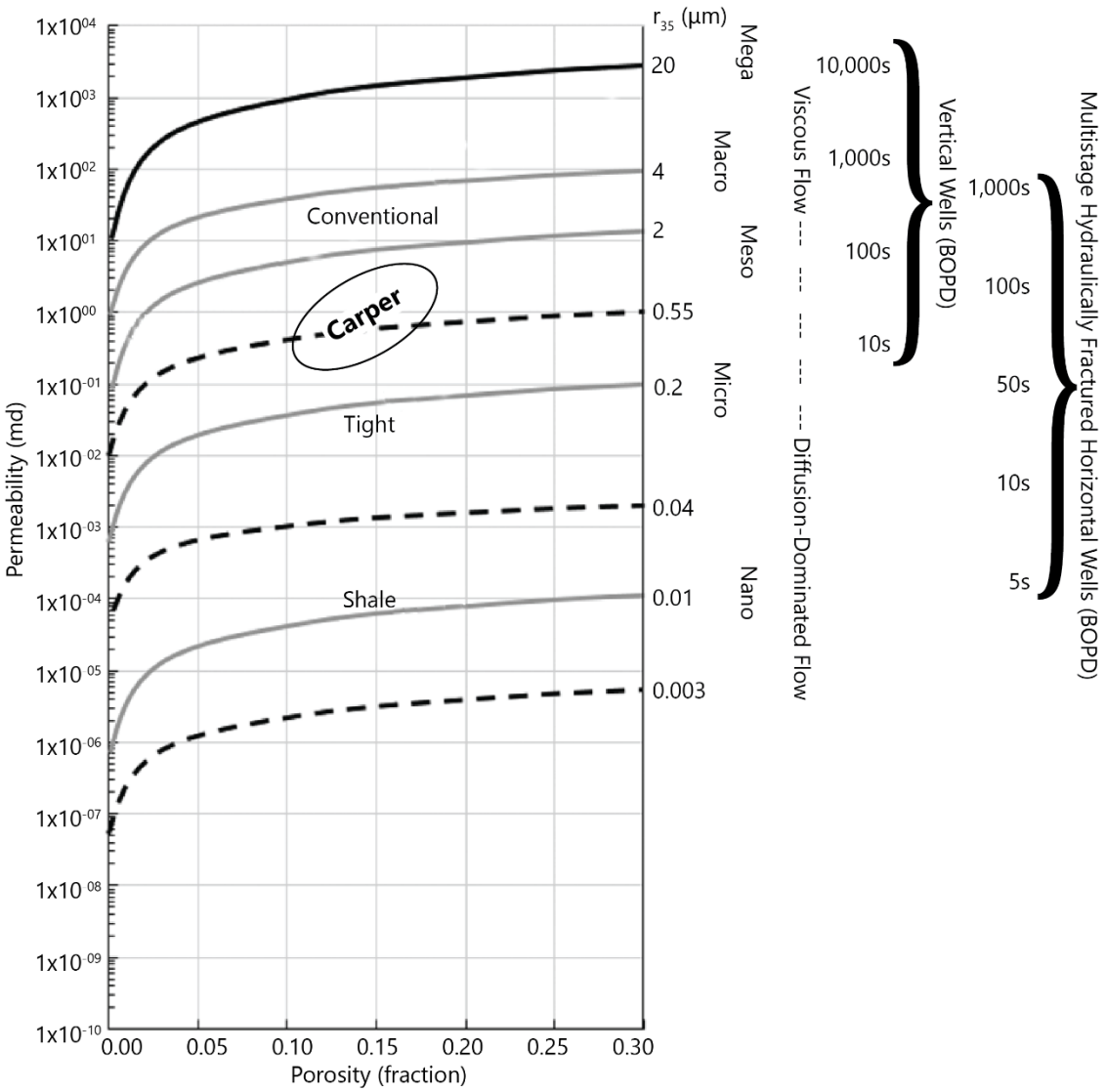


Figure 3-47. Flow units are determined as a function of porosity (fractional), permeability (md), pore-throat radii (r_{35} in micrometers). Designations of Conventional, Tight, and Shale reservoirs are shown on the graph as is an oval that represents the spread of Carper Sandstone core analysis data from Figure 3-46. On the right, theoretical ranges of oil rates (in barrels of oil per day, BOPD) for vertical wells and horizontal wells are shown. All rates are approximations and are affected by individual rock characteristics. Modified from Aguilera (2014).

Natural Fracturing

Natural fractures in the Carper Sandstone are commonly noted in drilling records, observed in core, and recorded on rare specialized geophysical logs (Figure 3-48). Drilling records and operators commonly report that drilling through the Borden Siltstone (particularly the "Osage" zone near the top and the Carper Sandstone near the base) requires precautions (including increased mud viscosity, admixed lost circulation material, and avoiding surges while tripping in or out of the well) to prevent drilling fluid loss. It is difficult to characterize the fracture properties (orientation, spacing, aperture, connectivity, etc.) because outcrops of Carper Sandstone are sparse and the sandstone bodies that comprise the lobes that occur in the subsurface of Illinois do not outcrop.

Despite the difficulty in characterization and uncertain properties, natural fractures play a significant role in controlling reservoir behavior. Natural fractures are a likely source of produced water for Carper wells, but the production rate decreases over time and wells can be readily drawn down with sustained pumping. This behavior indicates that natural fractures have limited connectivity and are not “infinite acting” as would be the case with a strong water drive like the thick Cypress Sandstone or Ullin Limestone. When completing wells in the Carper, hydraulic fracture stimulations increase the surface area of communication from reservoir to wellbore, which makes oil production from the low-permeability matrix possible but also links up natural fractures and brings on water. These hydraulic fractures likely allow pressure-depleted wells that are shut-in to slowly recharge over time as the fractures refill with fluids from the tight matrix.

The occurrence of natural fractures in the Carper also requires well tests (including DSTs) to be longer duration to reflect a true reservoir (matrix) response. This fact likely accounts for the limited application of DSTs in the Carper (only 28 recorded in the ISGS database, though more have likely been run). The tests that were run are generally unable to provide a good indication of the productive capacity of a given well (Stevenson, 1964).

Natural fractures also play an important role in controlling the distribution of oil saturation within the Carper Sandstone. Natural fractures provide a pathway for vertical migration of oil across intraformational mudstone beds which would otherwise create a high degree of vertical anisotropy in the Carper. As a result, fractures and facies changes lead to oil accumulation in sweet spots because oil can move up buoyantly along fractures and then laterally within the porous facies. Oil accumulations in multiple Carper Sandstone beds are therefore not limited to anticlines, but only some are productive.

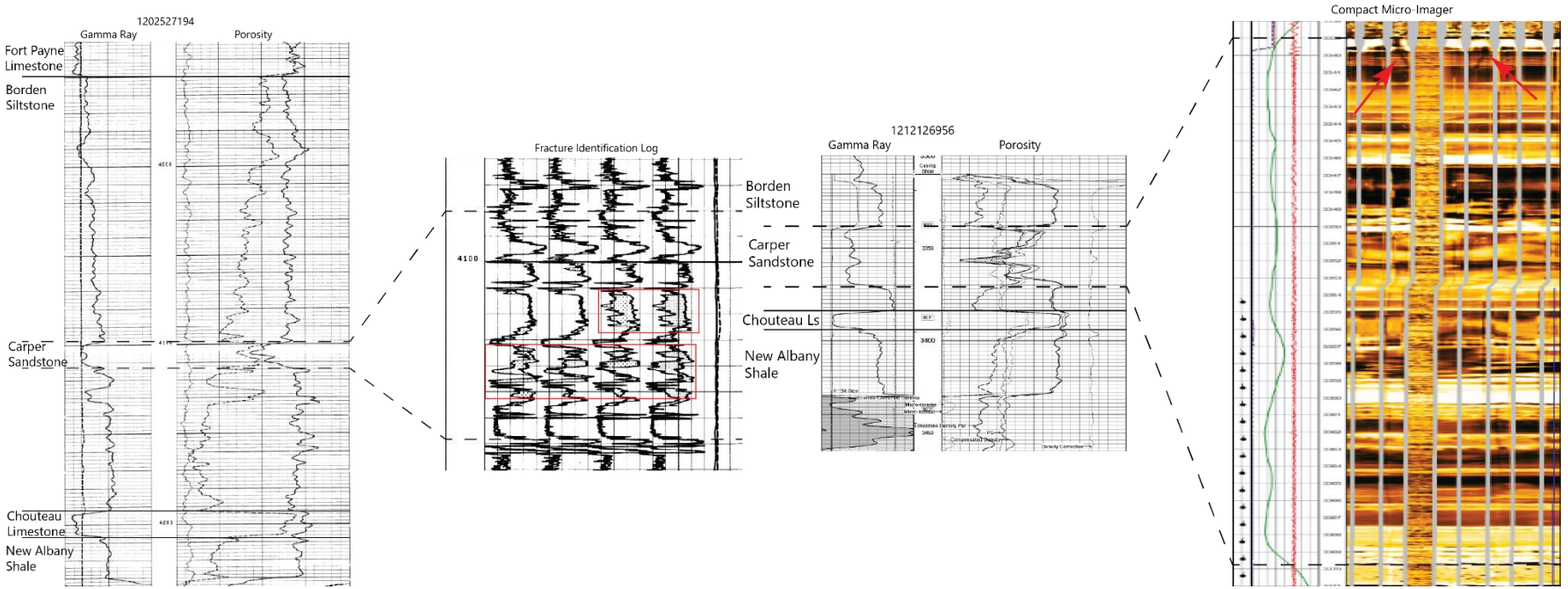


Figure 3-48. Example specialized geophysical logs from two wells indicating natural fractures in the Carper Sandstone. Left: Fracture identification log from the Overbeck-Pribble 1 well (API 120252719400). This log is derived from a wireline tool with four directional pads that measure resistivity resulting in four resistivity tracks. All four pads are expected to produce similar signatures in unfractured formations, but in formations with open-mode fractures, two of the resistivity tracks will show a separation in the resistivity curves indication invasion of drilling mud into the fractures (see red box). Right: Compact Micro-Imager log from the Quaranta 5 well (API 121212695601). This log works in a similar manner to the fracture identification log in that it uses a tool with resistivity sondes on multiple pads, but the higher resolution allows the data to be displayed as a wellbore image, with fractures generally indicated as dark vertical/subvertical lines (see red arrows). Both wells show indications of natural fractures in the Carper Sandstone.

Fluid Properties

Oil

There are several published reports that include data on oil properties (Rees et al., 1943; Armon et al., 1964, 1966; Mast, 1970; Hatch et al., 1991) for Illinois formations. Oils produced from Devonian, Mississippian, and Pennsylvanian reservoirs in Illinois, which includes the Carper Sandstone, fall into the "Illinois normal" category of Hemple fractional distillation according to Rees et al. (1943). In general, oil samples from the Carper have a gravity of 36° to 39° API units and a viscosity of 5 to 8 cP (Mast, 1970).

Company well records from the Holt-Ford Community 1 well (API 120510183100, Section 5, T5N, R3E) record values from additional oil analyses from the opening of the St. Paul Field in southern Fayette County. A separator test was conducted on the C.C. Ford 1 well (API 120510174800) and determined the gas-oil ratio to be 523.42 ft^3/bbl and a formation volume factor (B_{oi}) was measured at 1.17.

Carper oil samples were collected from three wells for this study, the G. Swits 2 (API 121392125900), Holsapple 2B (API 120352329600), and Quaranta 5 (API 121212696501). The density and viscosity of the oil was measured near ambient temperature and pressure. The density was measured with a Mettler Toledo Densito digital density meter and the viscosity with a Viscometer Viscolite d15. Oil properties are reported in Table 3-10. In all cases, the oil density and viscosity were higher than reported values for typical Carper oil.

*Table 3-10. Carper oil properties. Density and viscosity are reported at 60°F *Note – The volume of oil in the sample from the Swits well was too small to get a reliable viscosity measurement.*

API	Well Name	Sample Date	Depth (m (ft))	Reservoir Temperature (°C (°F))	Density (°API)	Viscosity (cP)*
121392125900	G. Swits 2	9/3/2020	928.5 (3,046)	33.1 (91.5)	29.3	n/a
120352329600	Holsapple 2B	8/24/2020	1,124.1 (3,688)	45.8 (114.5)	29.1	11.0
121212696501	Quaranta 5	9/30/2021	1,015.0 (3,330)	37.7 (99.8)	32.5	14.5

Brine

Brine composition and resistivity data is not readily available in published reports for the Carper Sandstone. For this study, brine samples were collected from three wells, G. Swits 2, Holsapple 2B, and Quaranta 5. Brine analysis was also discovered in the well records for the C.C. Ford 1 well (API 120510174800). Brine properties are summarized in Table 3-11. Resistivity for each of the samples was calculated using the method reported by Demir (1995) (equation x) and corrected for formation temperature assuming the typical Illinois Basin temperature gradient (equation y):

$$R_{w(T)} = \frac{957}{TDS^{0.778} * 1.017^{T}}$$

Where:

$R_{w(T)}$ = resistivity of formation water at reservoir temperature (ohm-m)

TDS = total dissolved solids (ppm)

T = Formation Temperature (°F)

$$T = \left(\frac{depth - 100}{100}\right) + 62$$

Although depth is generally a poor indicator of water salinity and thus resistivity, in the case of the Carper samples reported here, depth and resistivity yielded a strong correlation (Figure 3-49). Given the lack of available brine data for the Carper, the regression line equation reported in Figure 3-49 is assumed to provide a good approximation for the water resistivity in the Carper Sandstone at a given depth, at least in areas southwest of the LaSalle Anticline.

*Table 3-11. Carper brine properties. Depth is the depth to the top of the sandstone in the perforations. *Resistivity value is corrected to formation temperature. †The reported values for the C.C. Ford well are from brine analysis conducted by the company and reported in the well records.*

API	Well Name	Depth (m (ft))	Reservoir Temperature (°C (°F))	Salinity (TDS)	Density (g/mL)	Resistivity (ohm-m)*
121392125900	G. Swits 2	928.5 (3,046)	33.1 (91.5)	125,860	1.09	0.059
120352329600	Holsapple 2B	1,124.1 (3,688)	45.8 (114.5)	147,020	1.10	0.042
121212696501	Quaranta 5	1,015.0 (3,330)	37.7 (99.8)	142,790	1.10	0.049
120510174800†	C.C. Ford 1	1,002.2 (3,288)	35.0 (95.0)	141,350	1.10	0.052

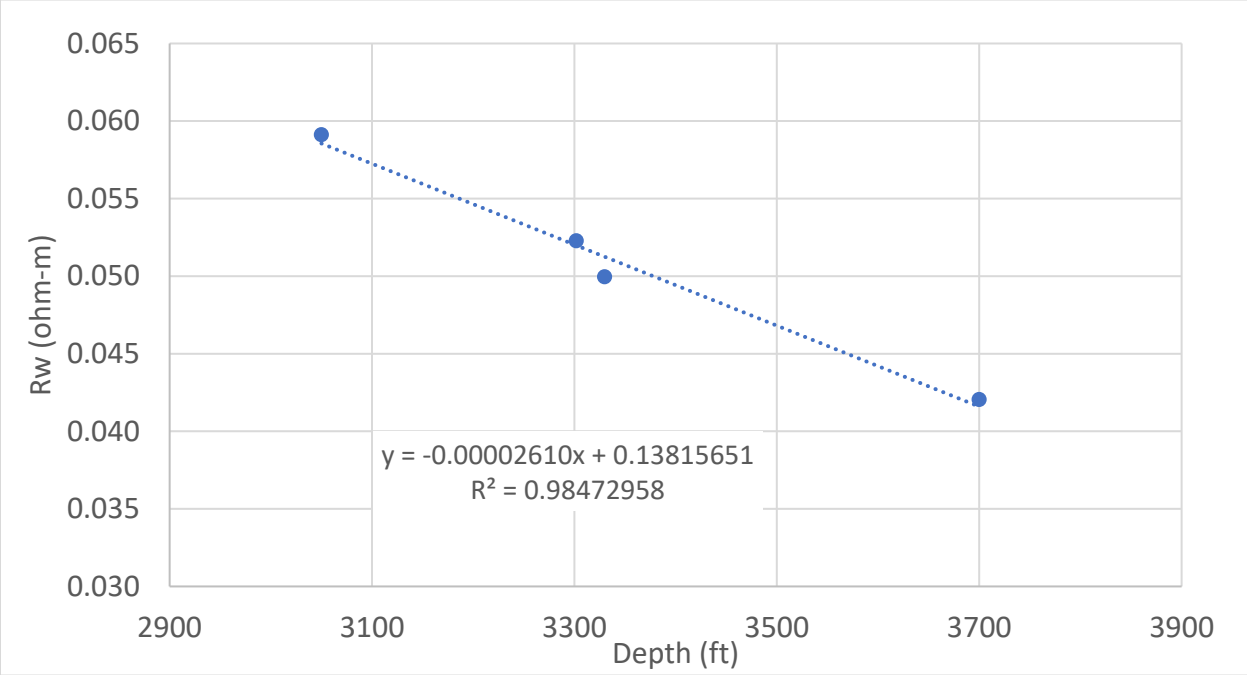


Figure 3-49. Graph of Depth vs Water Resistivity (R_W) based on data from four wells (Table 3-11). A regression line is plotted through the data points and the equation of the line is shown.

Well Completion Practices and Longevity

Approximately 750 oil wells have been completed in the Carper Sandstone in Illinois. We reviewed well records from over 200 wells representing all producing fields and spanning a range of completion dates to better understand the completion practices, initial production response, and the longevity of Carper oil wells.

There is relatively little information on the completion practices of wells drilled before the 1950s. In general, wells drilled in the 1960s were completed open hole (or with a gap in the casing when comingled with deeper zones) and subjected to a varying number of nitroglycerine shots. Wells drilled since 1960 show a mix of cased/perforated and open hole completions that were treated with mud cleanout acid and approximately 90% have been hydraulically fractured. On average, about 10,000 to 12,000 gallons of water are used with 1.3 to 1.5 pounds of sand per gallon (+/- some salt or walnut hulls). A few wells have been subjected to larger fracture operations of more than 50,000 gallons.

Initial production records show that 110 bbls of total daily fluid production is typical with few wells producing less than 20 bbls or more than 210 bbls per day. Initial production response does not correlate with size of the hydraulic fracture stimulation. Average oil cut is 50%, with higher values common in wells located on the crests of anticlines and lower values from wells drilled at the periphery of fields.

Of the wells reviewed for this study, the median lifespan of the well before plugging and abandonment (or plug back to a shallower formation) was 11 years. Approximately 25% of wells were completed and plugged within five years. It is unclear how long these wells were pumped, but it is assumed that the production decline was steep. A small subset of wells is apparently still open and presumably on pump after 60+ years of production.

The Carper Sandstone has very little secondary production. There are only six Carper waterflood units on record: two short lived (<5 years) units in Martinsville Field and four long term (24 to 41 year) floods in Wilberton and St. James Fields. There are several saltwater disposal wells in the Carper that inject 50 to 500 bbls of water per day at surface pressures from 0 to 300 psi.

Future Development Prospects

Carper Sandstone oil fields are developed on anticlinal traps, which have the highest oil saturations and mobility, but there is widespread evidence of stratigraphic or hydrodynamic traps in greenfield areas (down dip, far from production). Well records, core data, and well log analysis document oil indicators in large areas outside the existing boundaries of producing fields as well as a broad, generally non-productive area in the Effingham-Cumberland-Jasper County vicinity (Figure 3-50). Drill stem tests conducted in these areas indicate attempts to identify mobile oil, but in general most of the oil shows were non-productive. There are a few potential explanations for such widespread observations of oil indicators in the Carper Sandstone.

First, the geometry of the Carper Sandstone (widespread, laterally continuous beds) as well as its stratigraphic relationship with respect to the New Albany Shale source rock make it an obvious migration pathway or carrier bed that links the source rock with the producing reservoirs on anticlines. Oil migrating out of the New Albany Shale would have encountered the Carper Sandstone as the first porous unit above it across much of the northern part of the Illinois Basin. As previously discussed, the properties of the Carper make it a reservoir that could have accumulated oil but maintained a high S_{WIRR}.

Second, it is possible that the Carper Sandstone may also be interpreted as a residual oil zone (ROZ). An ROZ is defined as a volume of rock of significant scale into which oil accumulated and was later naturally displaced, leaving behind a low, largely immobile remaining oil saturation (West, 2014). ROZs are commonly thought of as the zone below the oil-water contact (OWC) that is at residual oil saturation (S_{OR}) with respect to water. Any oil accumulation in the Carper may have been reduced naturally over geologic time as natural fractures can allow accumulated oil to leak via buoyancy with the imbibition of water to reduce oil saturation. The ROZ interpretation is supported by oil properties (e.g., density and viscosity; Table 3-10) and composition data (e.g., attenuation of the light hydrocarbon fraction) that indicates some water washing. Likewise, sulfur water produced during DSTs also indicates water washing of oil that may have resulted in natural saturation reduction.

These two cases are not mutually exclusive as oil that accumulated in a carrier bed could have been further reduced through processes that form ROZs, and in either case, despite seemingly low saturation, areas with mobile oil are possible. There are examples of wells in these greenfield areas that have been successfully completed (Figure 3-50) including in western Cumberland County (e.g., API 120352217000, 120352228000, and 120352142700) and eastern Fayette County (e.g., API 120512597400 and 120512603800) down dip from St. James Field.

In 2020, the ISGS in partnership with operator Bi-Petro, Inc., conducted a Huff and Puff (HnP) using CO_2 to test the hypothesis that the vast expanse of Carper Sandstone that contains low oil saturation could be a viable target for CO_2-EOR and associated carbon storage. The test well is the Holsapple 2B (API 120352329600) in Cumberland County, IL, in an off-structure greenfield ROZ at least 15 miles from the nearest Carper oil production (Figure 3-50). This well was drilled in 2016 as a wildcat test of conventional oil production from the Carper, but no oil was produced despite observed oil saturation in core. Well log derived oil saturation was at or below residual oil saturation with respect to water (S_O = ~25%) in this and other wells in the greenfield. The well was hydraulically fractured, and natural fractures were also suspected based on high water production during the initial oil production attempt that could not be explained by the core derived permeability (0.2 mD).

The HnP test injected 1,000 tons of CO_2 and produced 50 bbls of oil and 360 tons of CO_2, storing the remaining 640 tons of CO_2 in the reservoir. Both oil recovery and CO_2 storage exceeded reservoir simulation forecasts based on the pretest assumptions (natural fracture network and low viscosity oil only within the tight matrix), which showed that CO_2 would remain in fractures and have limited contact with matrix bound oil.

Based on the revised understanding of the Carper Sandstone geology, reservoir properties, development and production history, and response to CO_2 stimulation, we present these suggestions for ongoing and future development opportunities.

1. Renewed attempts at development in existing fields using techniques for unconventional reservoirs (e.g., horizontal wells), especially in areas where many Carper wells were only pumped for a few years.
2. Application of EOR techniques (e.g., chemical, CO_2 floods) in existing fields.
3. Application of EOR techniques in virgin greenfield areas.

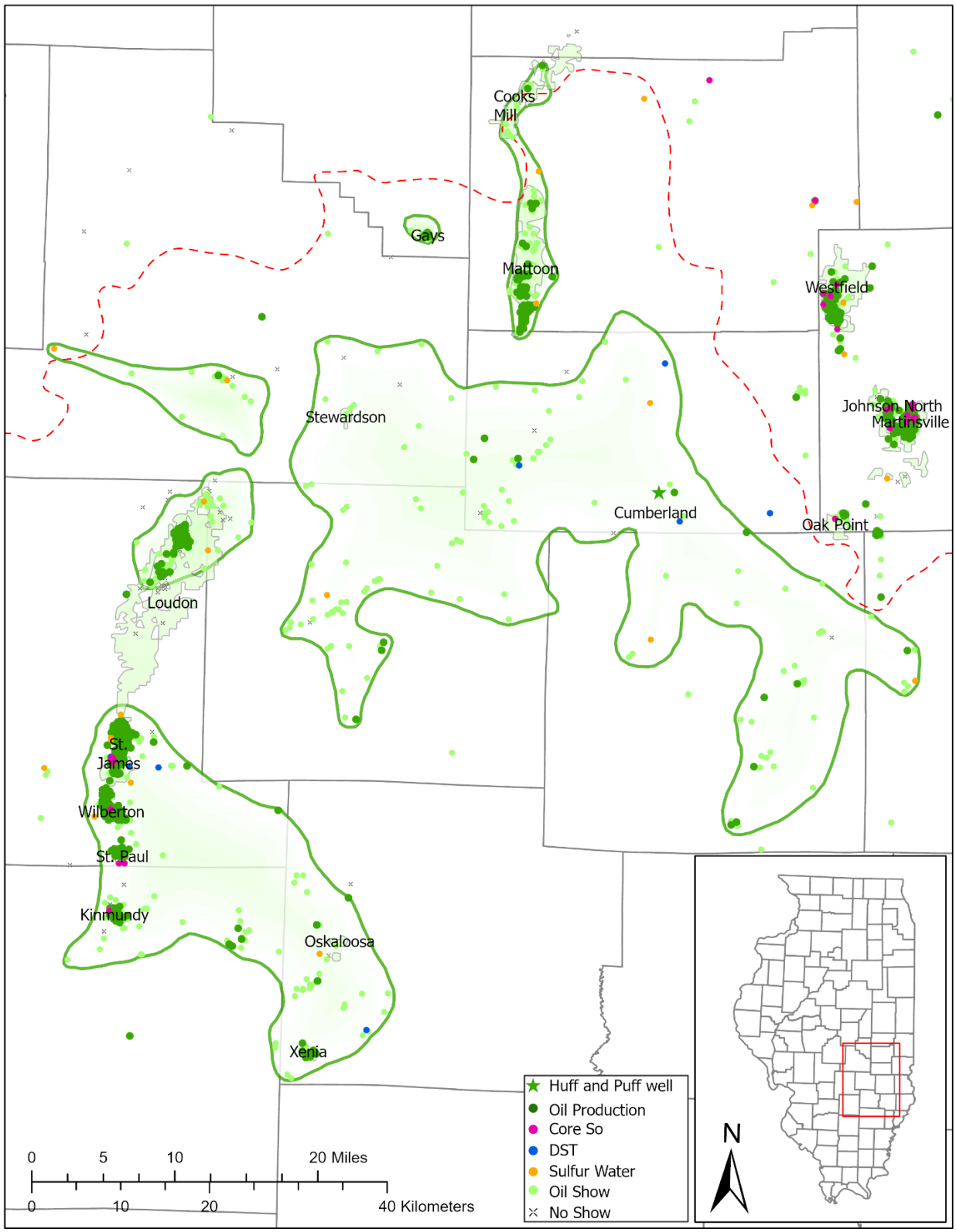


Figure 3-50. Map showing the distribution of oil indicators from well data in the Carper Sandstone. Green polygons outline fairways where most wells indicate oil saturation. The red dashed line represents a dept cutoff south of which the Carper Sandstone is likely at a depth suitable for miscible CO_2 injection for enhanced oil recovery.

CONCLUSIONS

The Mississippian Carper Sandstone is an atypical reservoir when compared to other Mississippian sandstones in the Illinois Basin. The Carper Sandstone was deposited as subaqueous sediment gravity flows with both turbidite and hybrid event bed deposits identified from core in Illinois. The Carper has a complex mineralogical composition (clays, carbonate cements), a finer grain size, (very-fine sandstone to coarse siltstone), moderate to low porosity and low permeability, natural fractures, and widespread indications of low in situ oil saturation. These factors together make the Carper an oil reservoir that, despite successful development on anticlines where oil saturations are the highest, is under exploited. Even areas where development drilling has taken place commonly have wells that were short lived indicating potential for future development using unconventional techniques possibly combined with EOR technology, such as CO_2.

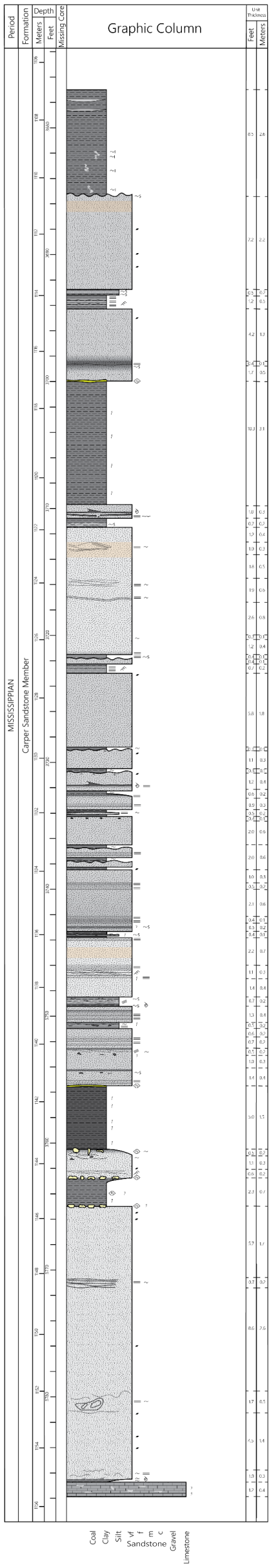
Hundreds of wells document unproduced oil shows in greenfield (downdip, far from established production) areas. Expulsion of oil from the New Albany Shale source rock into and through the Carper allowed it to act as a carrier bed for hydrocarbon migration, but the low in situ saturation indicate potential natural reduction of oil over geologic time and the development of a broad ROZ fairway within the Carper Sandstone. While a recent CO_2 HnP demonstrated that previously immobile oil could be recovered in a greenfield area, field-scale implementation of Carper CO_2 flooding must account for its atypical properties to economically produce oil.

Based on the findings of this study, there are three main areas that stand out as the most promising for future development of the Carper Sandstone:

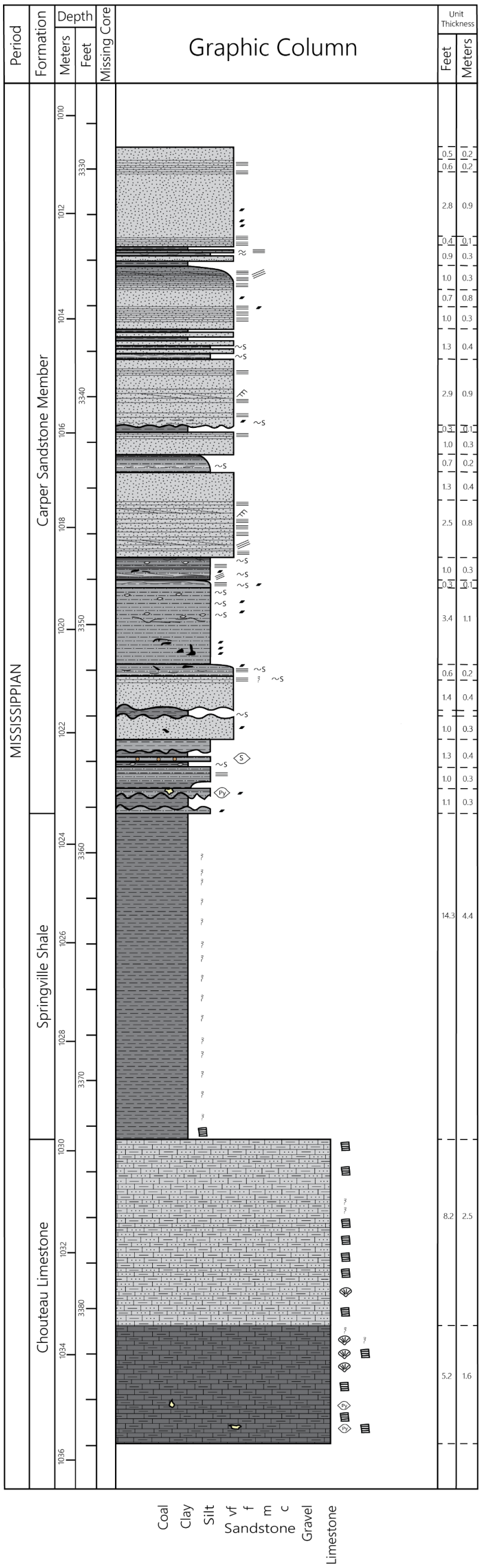
Existing Fields: Many existing fields contain Carper development wells that were complete and then plugged after only a few years of production. Poor productivity in these areas may have been the result of applying conventional well completion techniques and production practices. Significant quantities of remaining oil in place likely exist in these areas that could be targeted with horizontal wells and possibly CO_2-EOR.

Expanded Field Boundaries: Oil saturation in the Carper Sandstone is no doubt highest on anticlines, but widespread oil shows beyond the boundaries of fields indicate there may be no clear oil-water contact at the edge of existing fields. This fact presents an opportunity to extend the boundaries of existing fields by targeting the Carper with horizontal wells and CO_2-EOR and to exploit the reduced in situ oil saturation. CO_2 injection in these areas may also bank oil up dip and improve oil production within the field boundaries.

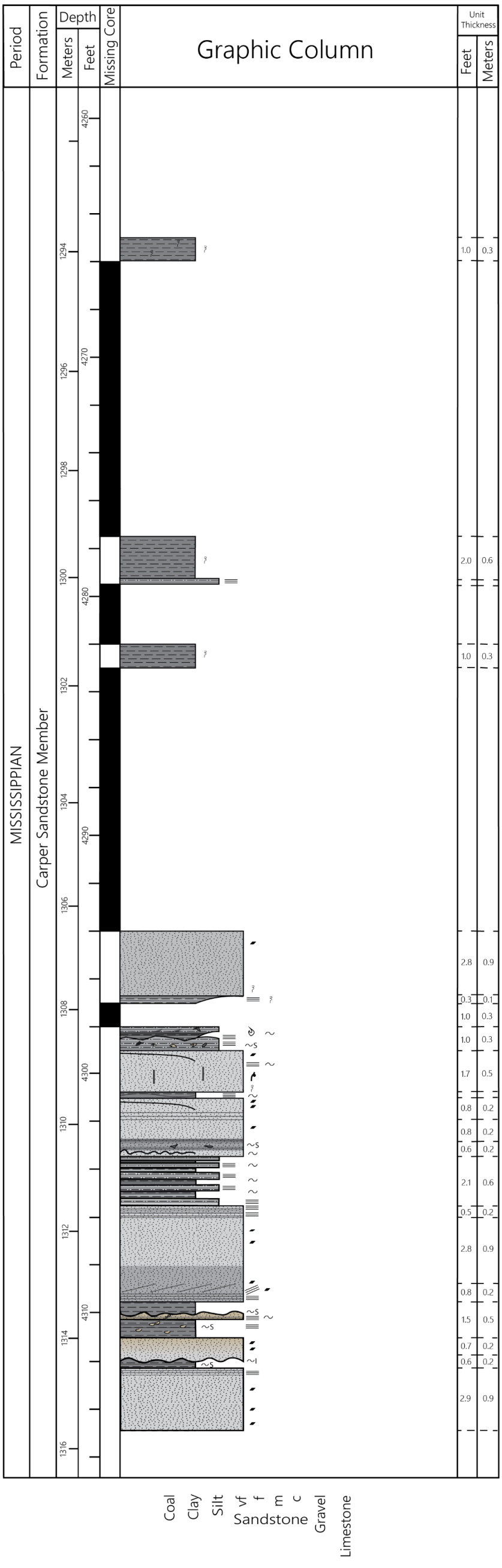
Greenfield Areas: Widespread distribution of low oil saturation in greenfield areas is an obvious target for CO_2-EOR and associated storage. While it is expected that most oil is at residual saturation with respect to water, a handful of wells in greenfield areas have shown some mobile oil. While oil saturation is low, the Carper covers a vast area, and the lack of legacy wellbores is favorable for contained CO_2 injection.



Holsapple 2B


Period
Formation
Depth
Meters
Feet
Missing Core
Graphic Column
Unit Thickness
Feet
Meters
MISSISSIPPIAN
Carper Sandstone Member
Springville Shale
Chouteau Limestone
1010
3330
1012
1014
3340
1016
1018
1020
3350
1022
1024
3360
1026
1028
3370
1030
1032
3380
1034
1036
0.5 0.2
0.6 0.2
2.8 0.9
0.4 0.1
0.9 0.3
1.0 0.3
0.7 0.8
1.0 0.3
1.3 0.4
2.9 0.9
0.3 0.1
1.0 0.3
0.7 0.2
1.3 0.4
2.5 0.8
1.0 0.3
0.3 0.1
3.4 1.1
0.6 0.2
1.4 0.4
1.0 0.3
1.3 0.4
1.0 0.3
1.1 0.3
14.3 4.4
8.2 2.5
5.2 1.6
S
Py
Coal
Clay
Silt
vf
f
m
c
Sandstone
Gravel
Limestone

Quaranta 5



Lindsay Community 1

3.1.4 Middle Devonian

Authors: Mansour Khosravi, Charles Monson, and Nathan Grigsby

The Geneva Dolomite Member, which is part of the Middle Devonian Grand Tower Limestone, has been a significant oil producer in the Illinois Basin for a century. It has yielded the bulk[1] of Devonian oil production in Illinois, with individual wells producing as much as half a million barrels (Huff and Seyler, 2010). A 2002 Geneva discovery near Miletus Field (Marion County, Illinois) saw the highest initial production (3,000 barrels/day) achieved by any Illinois well in several decades (Leighton, 2010). The Grand Tower also contains the Dutch Creek Sandstone Member, a generally thin and discontinuous sandstone unit that can nevertheless be a prolific producer (Huff and Seyler, 2010).

As with numerous other producing units in the Illinois Basin, the Geneva and Dutch Creek often exhibit oil shows or other oil indicators (e.g., sulfur) even in locations where primary production is not viable, raising the possibility that residual oil zones (ROZs) may be present and potentially exploitable. In this report, we discuss the production history, geological context, and stratigraphy of the Geneva/Dutch Creek. ROZ potential will be treated in a future report.

Background

The Geneva/Dutch Creek has been a significant oil producer in the Illinois Basin for a century. Major early Geneva fields in Indiana include the Siosi and Fairbanks in Sullivan County, western Indiana, which were discovered in 1926 and 1950, respectively, and had produced 8.4 million bbo between them through 1999 (Seyler et al., 2003). Major 20th-century Illinois discoveries included Sandoval Field (discovered 1908, but Geneva first exploited 1938); Patoka Field (discovered 1937, with approximately 10 million bbo attributable to Geneva production as of 2003); and Tonti Field (Geneva reservoir discovered 1940, after which total field production nearly tripled) all in Marion County (Seyler et al., 2003). The late 1990s and early 2000s saw something of a renaissance in Geneva discoveries, including at St. James Field (Fayette County), Lillyville Field (Effingham County), Miletus Field, and under Stephen A. Forbes State Park just south of Miletus (Seyler et al., 2003). Discovery and exploitation of Geneva resources in existing fields, resulting in major and rapid increases in production, has been a common theme in many of these fields.

Locations along the Salem and Loudon Anticlines and Du Quoin Monocline have exhibited particularly good Geneva production, while the Dutch Creek is the primary oil-producing member of the Grand Tower Limestone eastward, at and near Clay City Anticline in particular (Figure 3-51).

[1] More specific estimates of the percentage of Devonian oil production coming from the Geneva are difficult if not impossible to obtain, since production from the Geneva is often commingled with production from Mississippian formations. However, very high initial production rates for Geneva wells indicate the high productivity of the reservoir.

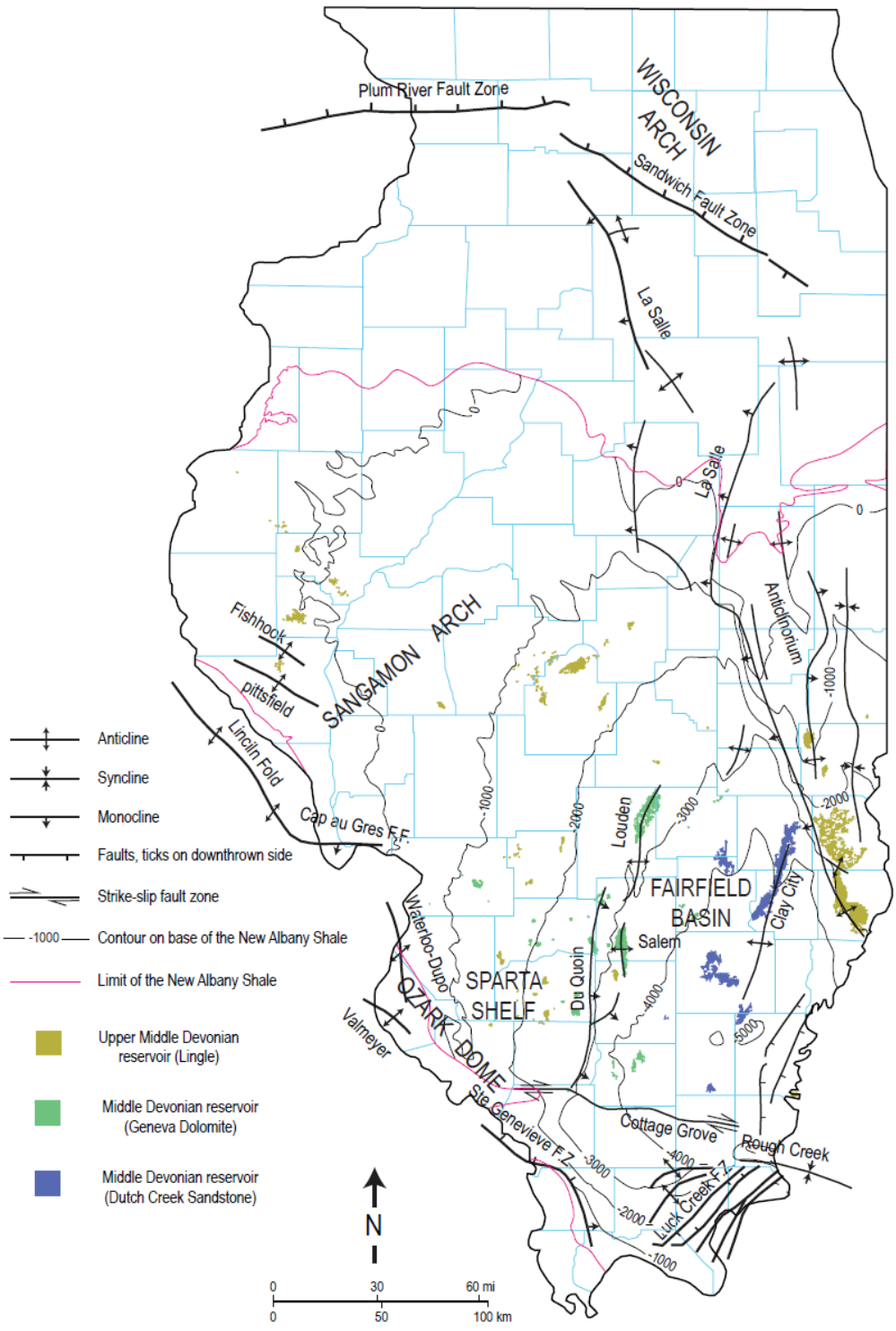


Figure 3-51. Regional structure map showing the location of major structural features in south-central Illinois (modified from Nelson, 1995). The Geneva Dolomite is one of the major oil-producing members of the Grand Tower Limestone in the western part of southern Illinois, whereas the Dutch Creek Sandstone, the lowest member of the Grand Tower, is the primary oil-producing member eastward.

Geologic characterization

Geological Setting

The Middle Devonian deposits in the Illinois Basin correspond to the lower part of the Kaskaskia sequence described by Sloss (1963). The deposition of the Kaskaskia sequence began with a significant marine transgression over the Lower Devonian strata in central and southern Illinois (Treworgy and Devera, 1990). The central and southern parts of the Basin continued to be beneath sea level during the Silurian and Devonian, when the Tippecanoe sequence was deposited without interruption, resulting in a conformable relationship with the overlying Kaskaskia sequence (Collinson et al., 1967; Spirakis, 1974; Collinson and Atherton, 1975; Droste and Shaver, 1987; Devera and Fraunfelter, 1988; Mikulic, 1990). Paleomagnetic data have indicated that Illinois was located between 10° and 20° south latitude with a prevailing warm equatorial climate during the Middle Devonian (Martin, 1975; Droste and Shaver, 1983), leading to the deposition of carbonate sediments with abundant and diverse fauna (Treworgy and Devera, 1990).

Stratigraphy

The Middle Devonian deposits in Illinois and southern Indiana consist predominantly of shallow-water carbonates in the lower part and argillaceous limestone in the upper part (North, 1969). Stratigraphic columns of the Devonian succession are shown in Figures 3-52 and 3-53. The Middle Devonian succession is divided into the Grand Tower Limestone and the Lingle Formation in the southern and southeastern parts of the Illinois Basin, south of the Sangamon Arch (Whiting and Stevenson, 1965; Collinson and Atherton, 1975; Devera and Hasenmueller, 1990; Nelson, 1995). These formations are equivalent to the Jeffersonville and North Vernon limestones, respectively, of Indiana (Figure 3-53). The Grand Tower is conformably overlain by the Lingle, which is mainly composed of highly calcareous shale and argillaceous and micritic limestones in southern and southeastern Illinois (North, 1969; Devera and Hasenmueller, 1990). The lower boundary of the Grand Tower/Dutch Creek is a major unconformity showing the base of the Kaskaskia sequence (and the top of the Tippecanoe Sequence) and rests on Lower Devonian or Silurian deposits (Collinson and Atherton, 1975).

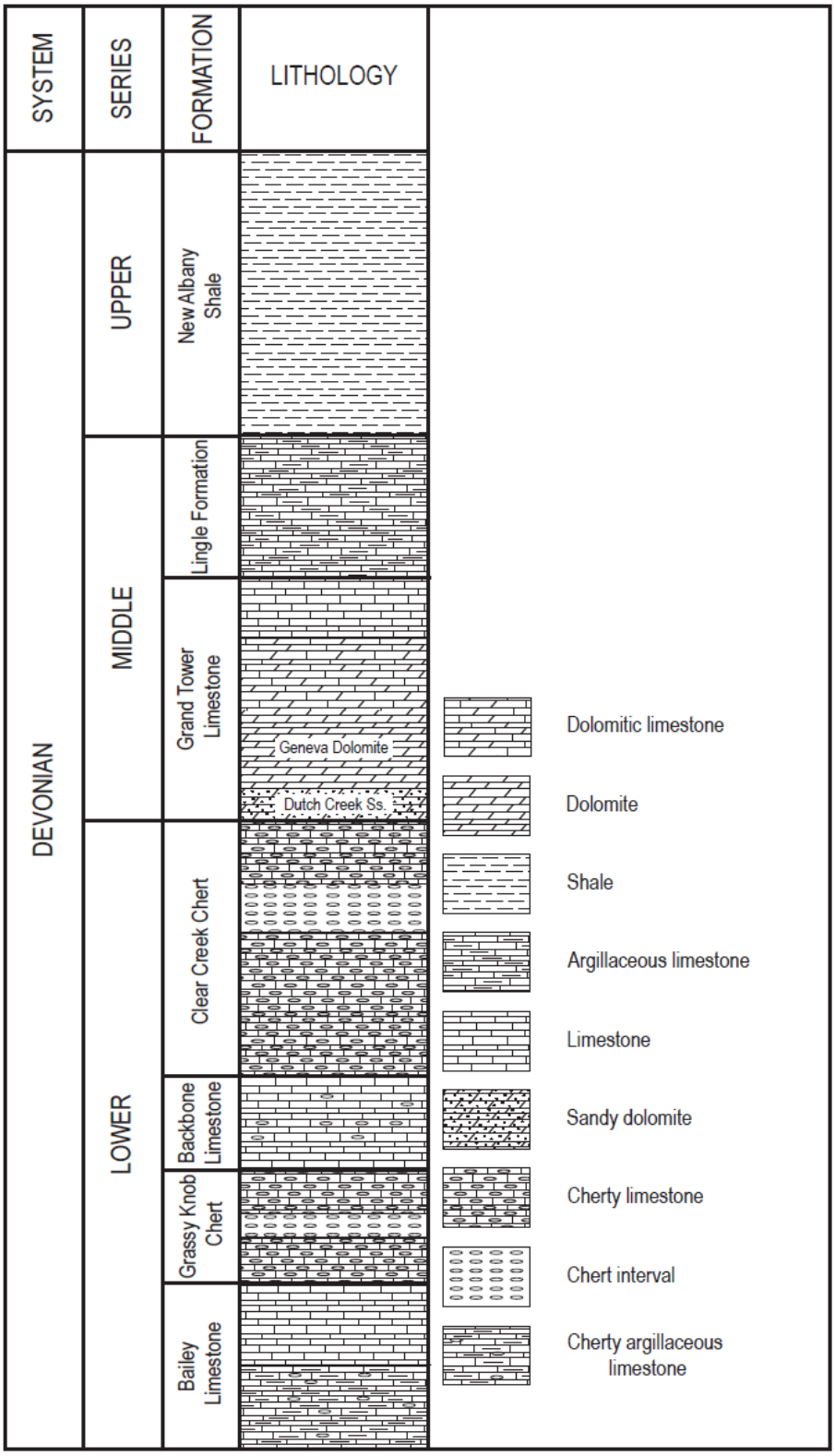


Figure 3-52. Devonian stratigraphic column in south-central Illinois.

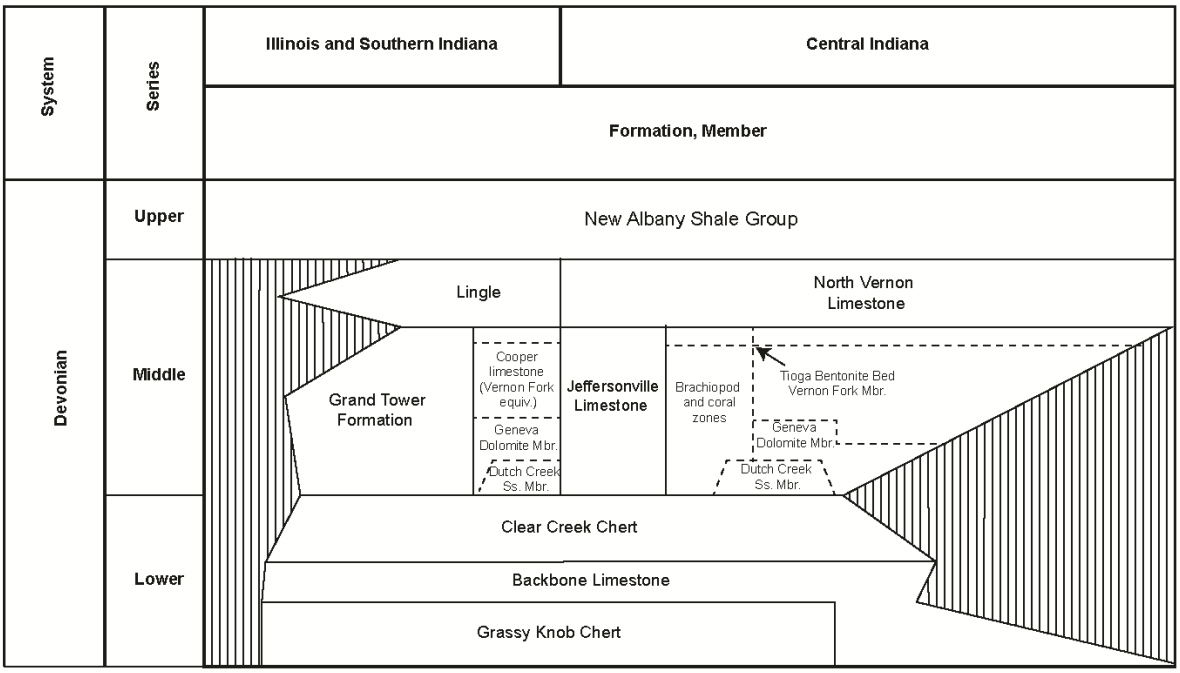


Figure 3-53. Stratigraphic column and correlation of the Lower Devonian through Upper Devonian deposits in Illinois and Indiana (modified from Droste and Shaver, 1975, 1987; adapted from Seyler et al., 2003).

The Grand Tower Limestone is divided into three members: the lower Dutch Creek Sandstone, the middle Geneva Dolomite, and an upper unit that is sometimes referred to as the Cooper Limestone (Meents and Swann, 1965; Collinson and Atherton, 1975) but has been described as "unnamed member (Vernon Fork equivalent)" by others (Seyler et al., 2003). The Grand Tower also contains a thin bentonite bed, the Tioga, 10-30 feet below the top of the formation (Collinson and Atherton, 1975).

The Dutch Creek Sandstone, basal member of the Grand Tower, is a highly porous and permeable sandstone to sandy carbonate unit that is productive in southeastern and eastern Illinois. It pinches out in most parts of western, northern and central Illinois (Figures 3-54 through 3-57) where the Geneva Dolomite directly overlies Lower Devonian deposits (Meents and Swann, 1965) (see further discussion in Lithology, Facies, and Depositional Environments section). The Geneva occurs across a broad swath of south-central to southwestern Indiana through east-central Illinois, while the Dutch Creek is present in southeastern Illinois, southwestern Indiana, and parts of western Kentucky (Figure 3-54).

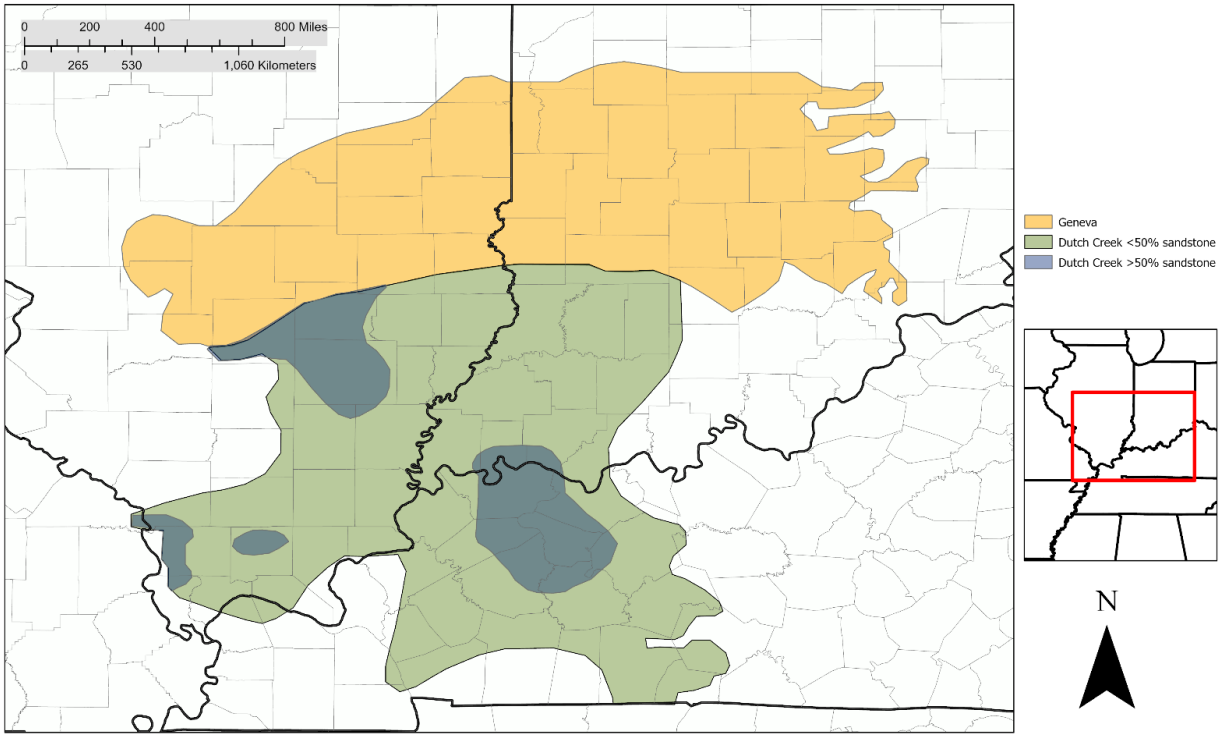


Figure 3-54. Distributions of Geneva Dolomite and Dutch Creek Sandstone members of the Grand Tower and Jeffersonville limestones, adapted from Devera and Fraunfelter (1988).

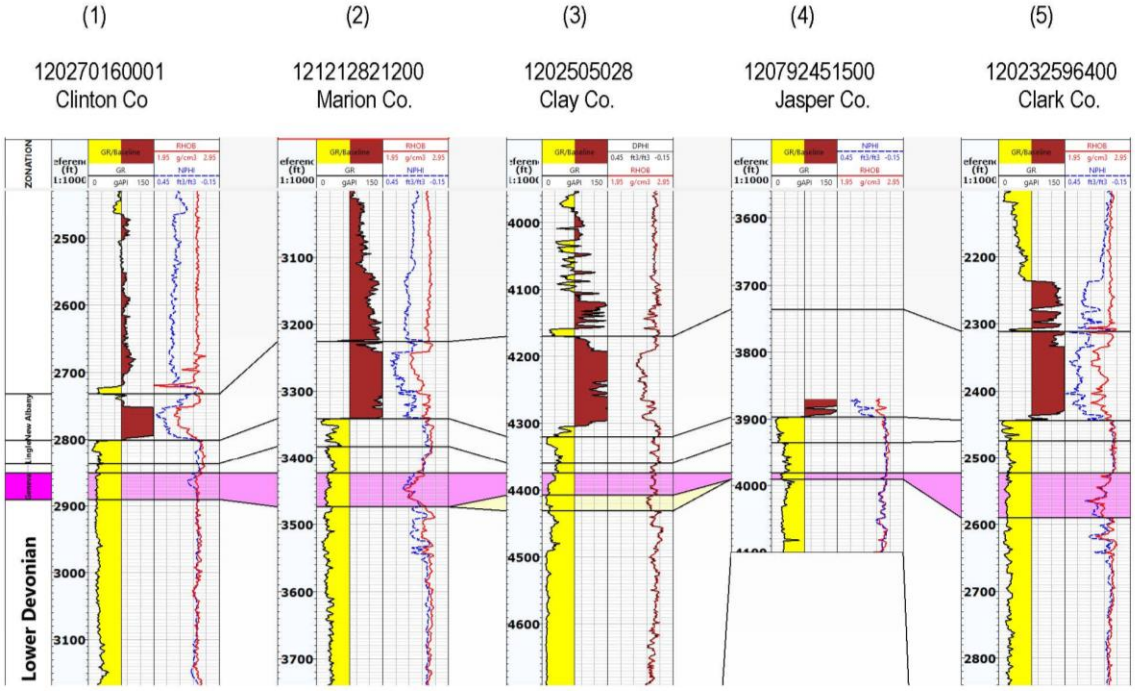


Figure 3-55. East-west stratigraphic cross section from Clinton County to Clark County showing the thickness and distribution of Geneva Dolomite (in purple) and Dutch Creek Sandstone (in yellow). See Figure 3-57 for trace of cross-section. Abbreviations: GR= Gamma ray; RHOB=Density; NPHI= Neutron porosity; DPHI=Density porosity.

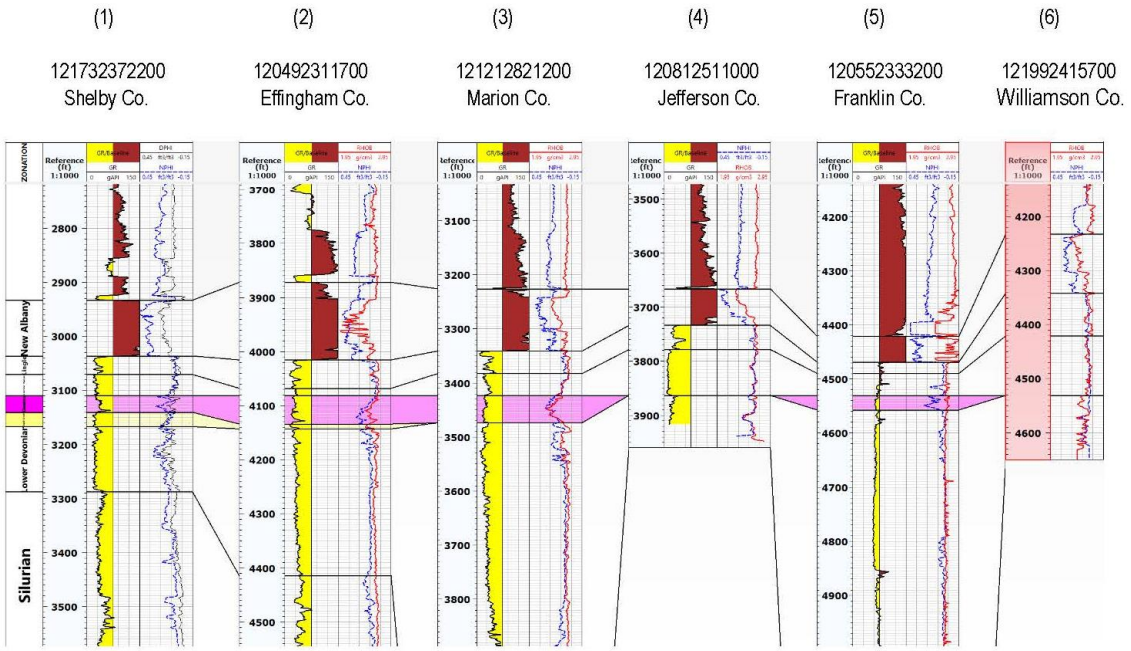


Figure 3-56. North-south stratigraphic cross-section from Shelby County to Williamson County showing the thickness and distribution of the Geneva Dolomite Member (in purple) and Dutch Creek Sandstone (in yellow). See Figure 3-57 for trace of cross-section. Abbreviations: GR= Gamma ray; RHOB=Density; NPHI= Neutron porosity; DPHI=Density porosity.

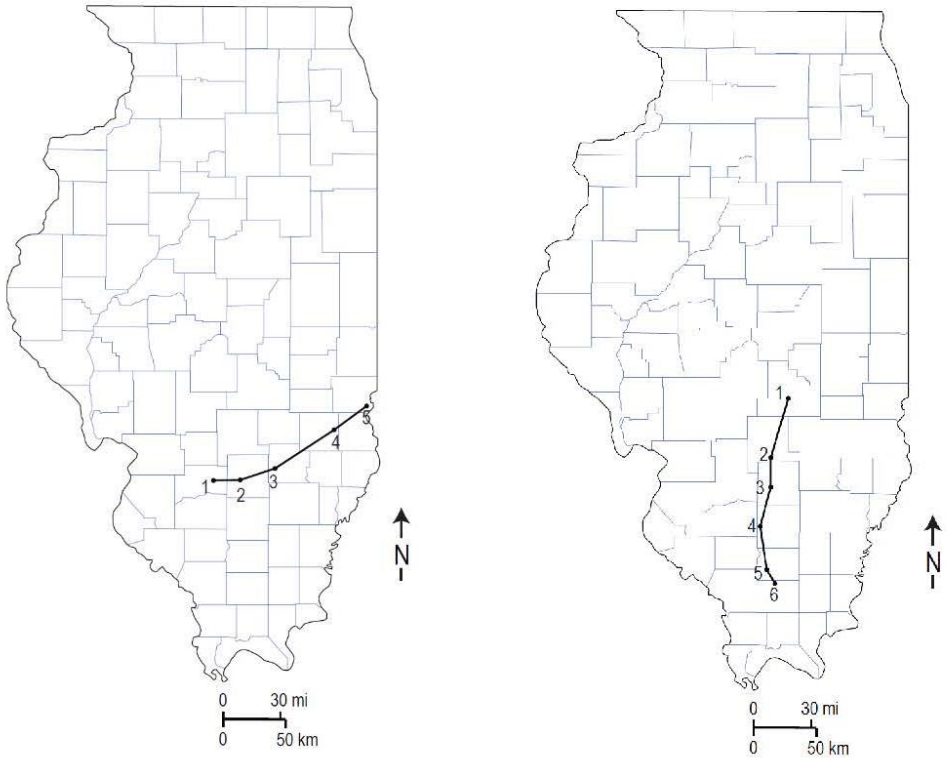


Figure 3-57. Traces of stratigraphic cross-sections in Figure 3-55 (at left) and Figure 3-56 (at right).

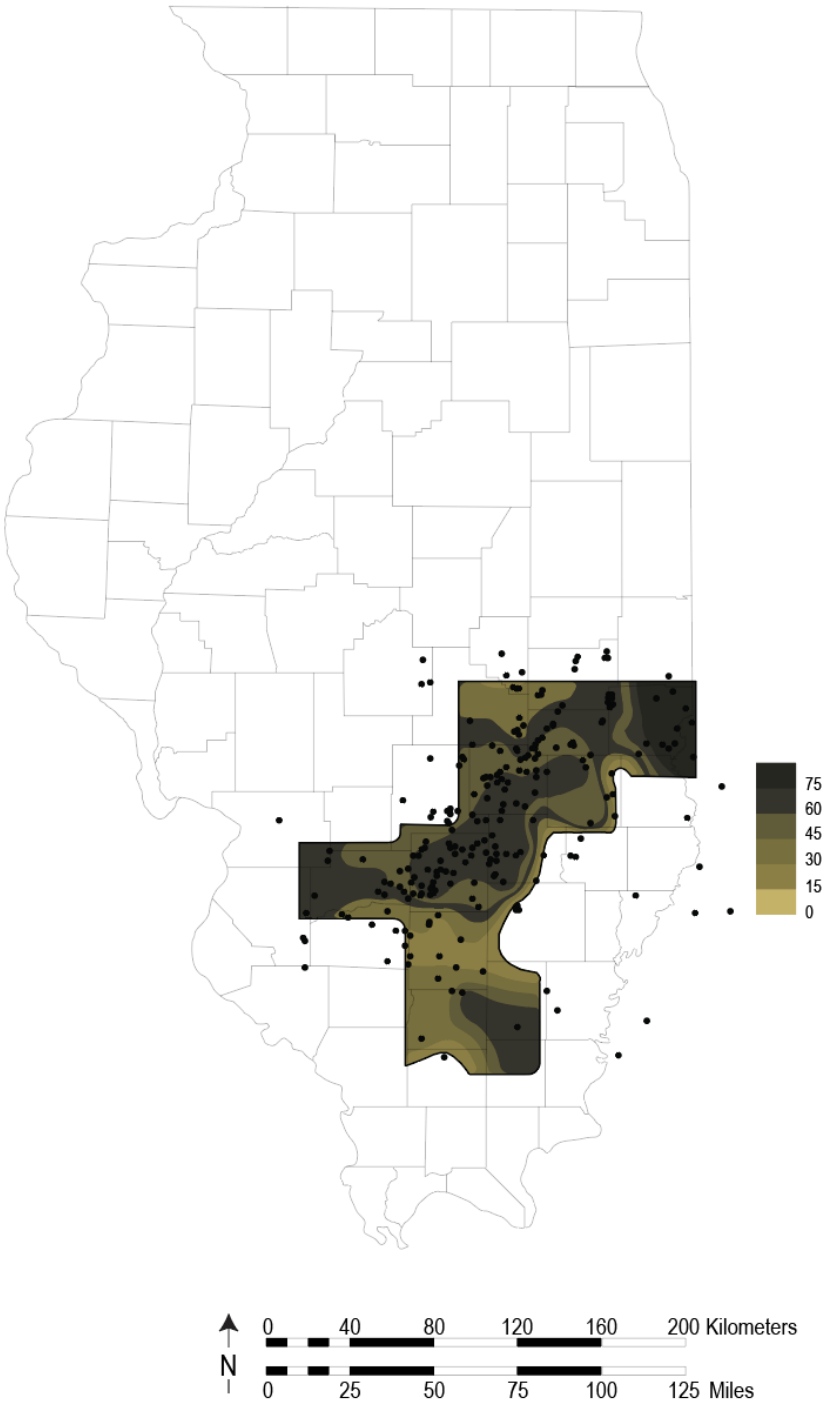


Figure 3-58. Thickness map of the Geneva Dolomite; contour interval 15 ft. Note greater thickness in the general area of the Loudon Anticline, where there has been considerable production from the Geneva (Figure 3-51). Black dots=well control.

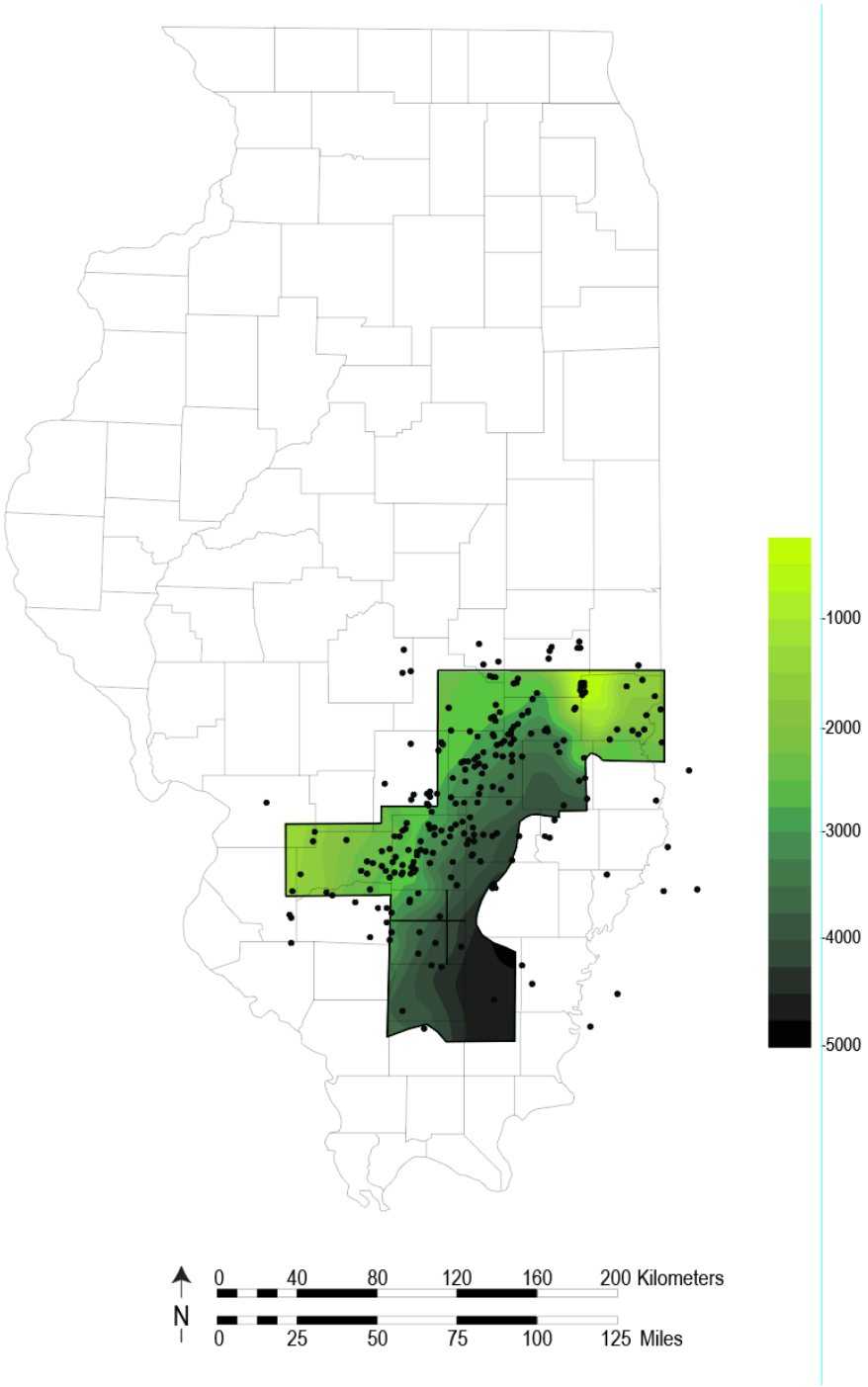


Figure 3-59. Structure map of the Geneva Dolomite, focusing on high-production areas such as the Loudon and Salem Anticlines (Figure 3-51). Depth values in feet subsea; contour interval 250 ft. Black dots=well control.

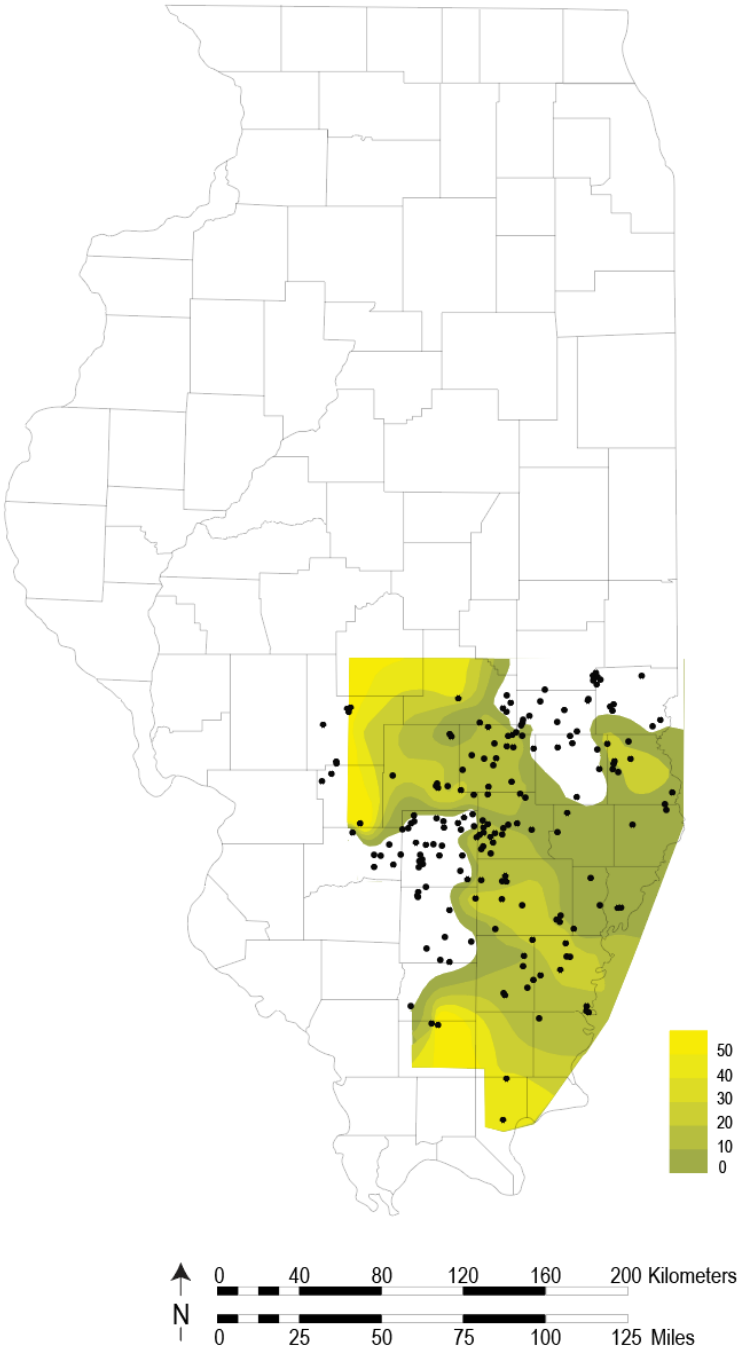


Figure 3-60. Thickness map of the Dutch Creek Sandstone. in southeast Illinois, where most Dutch Creek production has occurred. Contour interval 10 ft. Black dots=well control.

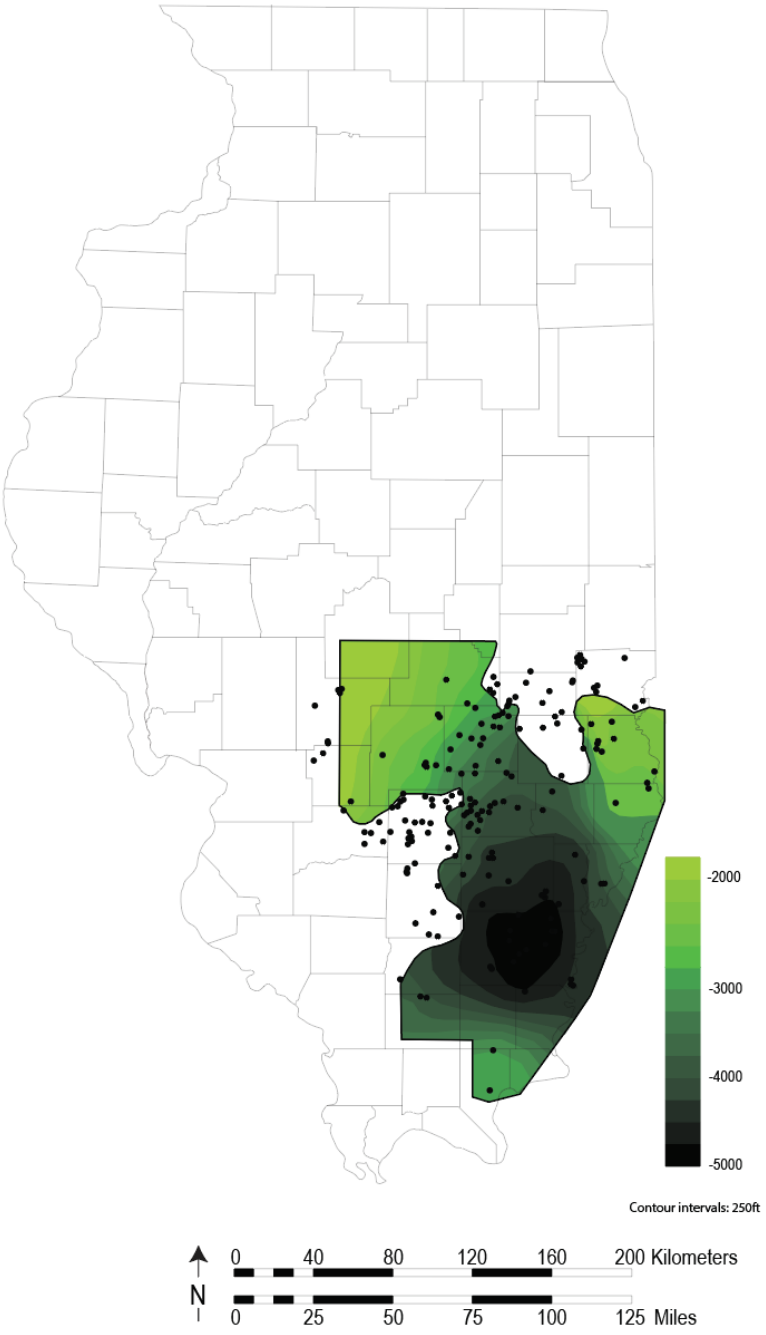


Figure 3-61. Structure map of the Dutch Creek Sandstone (in feet subsea) in southeast Illinois, where most Dutch Creek production has occurred. Contour interval 250 ft. "Bullseye" pattern of very deep Dutch Creek surface corresponds to the Fairfield Basin (Figure 3-51).

The Geneva Dolomite is typically 50 ft thick or less but may be over 75 ft locally (Figure 3-58). It occurs deeper in the subsurface to the southeast (Figure 3-59) and is found at roughly 3000 to 3500 feet below mean sea level in areas of high production such the Louden and Salem Anticlines (Figure 3-51). The Dutch Creek is typically less than 20 ft in thickness but may exceed 50 ft (Figure 3-60) and, like the Geneva, shallows to the northwest (Figure 3-61).

Lithology, Facies, and Depositional Environments

Cooper: The dense, sparsely fossiliferous, pure, and lithographic Cooper Limestone conformably overlays the Geneva Dolomite and acts as a seal or baffle for the prolific reservoir horizons. The Cooper often shows signs of periodic subaerial exposure such as mudcracks, which, together with stromatolites and other indicators, suggest a restricted shelf-lagoon to tidal-flat environment which may be responsible for Geneva dolomitization via Mg enrichment through seawater evaporation (Seyler et al., 2003).

Geneva: The Geneva consists of dark brown to brown sucrosic dolomite apparently formed through a postdepositional reflux dolomitization process (Seyler et al., 2003). Diagenetic events, such as dolomitization and dissolution, were the primary controls on the development of the reservoir characteristics of the Geneva Dolomite. Hydrocarbon production from the Geneva Dolomite is associated with intercrystalline, moldic, and vuggy porosities resulting from the dolomitization and dissolution of fossil content (Seyler et al., 2003) and structurally controlled trap development induced by tectonic activities (Nelson, 1995). Geneva Dolomite carbonates appear to have been deposited in a high-energy, shallow marine environment as a skeletal shoal or bank (Droste and Shaver, 1975).

Dutch Creek: Imprecise or conflicting treatments of the Dutch Creek in the literature have led to some confusion about its lithology and geographical distribution. The "Dutch Creek Formation"—demoted to member rank by later writers—was named from an exposure in Union County (southwestern Illinois) by Savage (1920), who described it as an iron-oxide-stained quartz sandstone. Numerous authors have followed suit by characterizing it primarily as a quartz arenite, supermature quartz arenite, or fossiliferous sandstone (Tissue, 1974; Collinson and Atherton, 1975; Densmore, 1997). Others, however, have described it as an extremely heterogeneous and discontinuous rock unit over its entire range, grading laterally and vertically into sandy dolomite and limestone (e.g., Meents and Swann, 1965) and entirely absent at many locations where the Geneva occurs (see also Figures 3-56 through 3-58). The discrepancy appears to stem in part from conflicting ideas as to the degree of carbonate content that can be present before the Dutch Creek appellation is no longer applicable.

Calcareous cement is a common attribute of Dutch Creek sandstones (Smunt, 1962; Collinson and Atherton, 1975), and the member can grade both laterally and vertically into sandy dolomite or limestone (Meents and Swann, 1965; Collinson and Atherton, 1975) and/or be interbedded with sandy carbonates (Collinson and Atherton, 1975). Meents and Swann (1965) restricted the term Dutch Creek to actual sandstone ("because sandy limestone occurs throughout the Grand Tower, the name Dutch Creek is only used where beds of sandstone are present"), but adjoining areas marked as "sandy limestone at base" on their map have been identified as containing Dutch Creek deposits in many well records (ILOIL). As shown in Figure 3-54, Devera and Frauenfelter (1988) mapped the Dutch Creek as being essentially continuous over a large area of western Indiana and eastern Illinois, with the bulk of its occurrences being less than 50% sandstone (i.e., sandy limestone or dolomite), with patches of greater than 50% sandstone that account for much of the Dutch Creek production.

Depositional setting of the Dutch Creek has generally been interpreted as tidal sand deposits on a shallow carbonate shelf (Smunt, 1964; Devera and Fraunfelter, 1988; Densmore, 1997; Wallenberg et al., 2016). Lines of evidence to support this interpretation include tentaculid and crinoid fossils (with the former being unidirectionally oriented, consistent with post-mortem alignment by waves); bimodal cross-strata dips; and reactivation surfaces (Devera and Fraunfelter, 1988).

Reservoir Properties

Generally high-porosity and high-permeability reservoir rock (Table 3-12) is one of the qualities that makes the Geneva both a productive unit and an attractive ROZ target. As suggested above, intervals that were particularly fossiliferous initially appear to have yielded the most high-porosity reservoir rocks due to fossil dissolution, e.g., the 13.7% porosity and 624 md permeability core sample obtained from Patoka Field (Seyler et al, 2003). Porous intervals are often traceable over significant distances using geophysical logs (Seyler et al., 2003). Summers (2006) observed a positive correlation between depth and pore size and permeability in the Geneva in Marion County, Illinois, with vuggy porosity becoming an increasingly greater component of the porosity distribution than intergranular with increasing depth beneath the top Geneva.

Table 3-12. Aggregate porosity-permeability data from Geneva and Dutch Creek wells in Illinois State Geological Survey files (where available).

	Minimum	Maximum	Mean	Median	Standard Deviation
Porosity (%)	4	30	17	18	6
Permeability (mD)	0	355	36	10	57

Seyler et al. (2003) noted that the "hydrocarbon charge for the Geneva reservoirs is…likely to have migrated from the black shales in the New Albany, located in deeper portions of the Illinois Basin, into the updip, though stratigraphically lower, Geneva Dolomite"; this would undoubtedly apply to Dutch Creek production as well. Geneva closure is often associated with tectonic structures such as the Louden and Salem anticlines, but underlying Silurian pinnacle reefs are also sometimes associated with prolific Geneva production. Dutch Creek production is also associated with structural highs (Huff and Seyler, 2010).

Conclusions

The Devonian Geneva and Dutch Creek Members—both members of the Grand Tower Formation—have excellent track records (especially the Geneva) as primary producers in the Illinois Basin, particularly in southeastern to south-central Illinois. Factors such as original density of fossil content (Geneva) and relative amount of carbonate cementation or matrix (Dutch Creek) are major controls on porosity and permeability, with maximum porosities of 30% and maximum permeability of 355 mD from Geneva/Dutch Creek samples on file at ISGS. Structural controls have proven important as well. Dutch Creek exploitation in particular has been relatively minor outside of proven areas such as the Clay City Anticline, and may offer further opportunities elsewhere, although patchy distribution of high-porosity sandstone is a complicating factor.

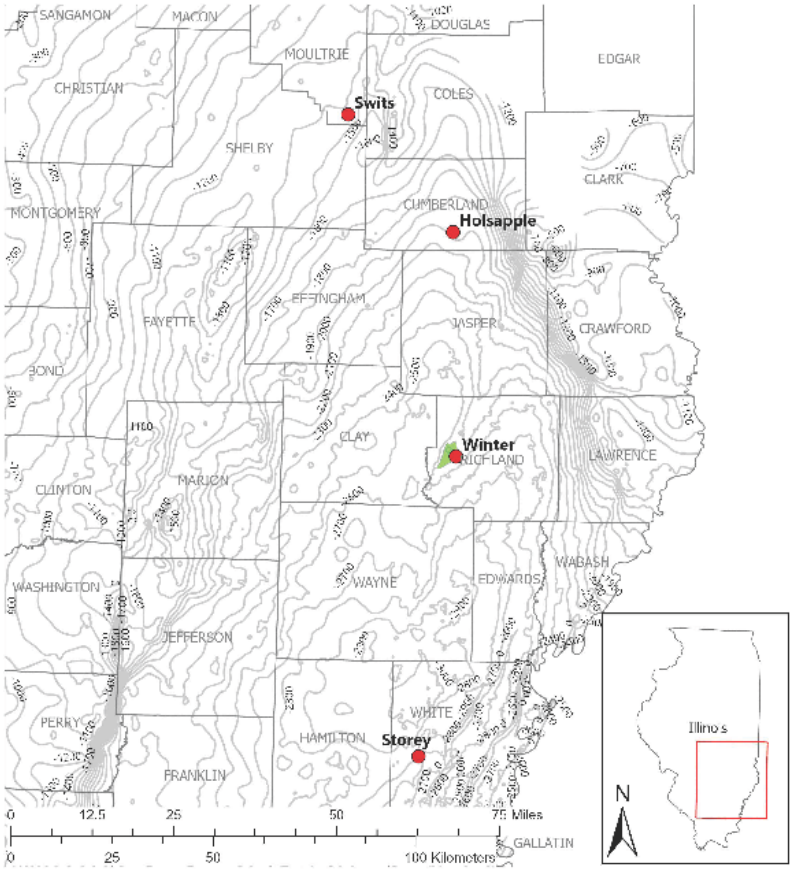
3.2 Model Oil Source and Migration into ROZ Fairways

Authors: Donna Willette

Summary and Results

Geochemistry

Initial research and sampling was conducted on selected oils and rock extracts collected from production wells centered around Noble Field (Figure 3-62) and across the east-central and southern Illinois Basin. The goal was to quantify previous research regarding the source of oils recovered from Carper and Cypress hydrocarbon reservoirs and provide a better understanding of ROZ accumulations and pathways. Detailed studies in the 1990's and 2000's indicated that the New Albany Shale was the likely source rock for over 4 billion barrels of generated, in-place oil within Ordovician, Devonian, Mississippian, and Pennsylvanian reservoirs (Hatch et al., 1991; Lewan et al., 2003).



Initial research involved comparison of selected oils and rock extracts from various shale horizons within the Devonian and Mississippian stratigraphic intervals. Analysis of high-resolution gas chromatography of both the extracts and oils suggested an oil-source correlation with the New Albany Shale. Initial Holsapple oil sample has significant water-washing. Saturate biomarker correlations also indicate an affinity for the New Albany Shale as well as the Springville Shale as possible source for the oils (Table 3-12).

Figure 3-62. Location of wells selected for geochemistry and modeling. Structure contour map of current structural configuration using a Mississippian reservoir interval.

Results are as follows:

Sterane/hopane ratio – In general, high concentrations of steranes relative to hopanes indicates greater influence of planktonic or benthic algae typical of marine organic matter rather than bacterial/terrestrial input. All extracts and oils meet the criteria of marine input. Fraileys Shale is anomalously low which may indicate degraded organic matter.

C_{26}/C_{25} Tricyclic Terpanes – This ratio is another biomarker indicator of terrestrial or marine input of orgranic matter. This ratio is also greatly affected by organic matter quality, i.e., organic richness and oxidation. Nothing definitive can be determined from the extract/oil comparison.

C_{29}/C_{30} hopanes – Ratios of selected hopanes and terpanes can discriminate between organic matter that is dominantly preserved/generated in carbonate environments versus clastic environments. Based upon a ratio > 0.7, the extracts and oils were generated in carbonate environments.

C_{21}/C_{22} Tricyclic Terpanes – This is another ratio utilized to distinguish carbonate-influenced organic matter (OM) from OM generated from clastic environments. Both extracts and oils are strongly (> 0.60) skewed for OM generated under carbonate depositional conditions.

Table 3-12. Summary of Biomarker comparison between oils and selected shale rock extracts.

Biomarker Ratio	Borden Siltstone Extract	Fraileys Shale Extract	New Albany Extract	Springville Shale Extract	Holsapple #2B^ OIL	G. Swits #2 OIL
Sterane/hopane ratio	0.56	0.14	0.62	0.65	1.18	1.35
C_{26}/C_{25} Tricyclic Terpanes	1.0	0.83	1.22	0.92	1.63	1.27
C_{29}/C_{30} hopanes	0.83	1.12	1.00	0.95	0.76	0.75
C_{21}/C_{22} Tricyclic Terpanes	2.20	2.17	2.40	2.60	1.15	1.63
C_{35} hopane/C_{34} hopane (s)	0.86	0.76	0.66	0.66	0.49	0.69
Ts / (Ts+Tm)	0.49	0.14	0.47	0.48	0.75	0.67

C_{35} hopane/C_{34} hopane (s) – If organic matter is deposited under strong, anoxic conditions, the biomarker ratio should be greater than one. Both extracts and oil suggest water stratification conditions that are predominantly dysoxic. This result is also in keeping with new research that suggests that the New Albany Shale OM was primarily deposited under dysoxic conditions with short bursts of anoxia.

Ts / (Ts+Tm) – This ratio is an indicator of relative maturity (the thermal history the OM has experienced). As the ratio increases it indicates higher thermal maturity for the oil or source rock (extract). Extracts from the Borden Siltstone, New Albany Shale, and Springville Shale generated equivalent low-maturity ratios. The Fraileys Shale indicated very low-maturity potential source rock or contains OM that is severely oxidized or degraded. The oils (having undergone thermal expulsion) indicate relative higher maturities – with the Holsapple oil having undergone higher thermal stress than the G. Swits oil.

Summary: A general comparison indicates that the sterane, hopane, and tricyclic terpanes biomarkers indicate that all shales and oils were generated from predominantly marine OM in carbonate environments with indications of fluctuating dysoxic water column conditions. The relative ratio similarities between the Springville and New Albany Shales suggests similar types of OM preserved under somewhat similar conditions. Both the Fraileys Shale and Borden Siltstone extracts generated ratios dissimilar enough to the other shales to suggest either different types of OM input, different preservation conditions, and/or oxidation of the OM. Nothing in the general comparison precluded the initial

interpretation that the New Albany Shale (perhaps a little from the Springville Shale) generated the oils in the Holsapple and G. Swits wells. In addition, a comparison of oils recovered from wells located in Christian and Richland counties (> 40 miles apart) indicate that both oils were generated from the New Albany Shale (Figure 3-63). This research confirms that oils in ROZ zones studied for this project were initially generated from the New Albany Shale.

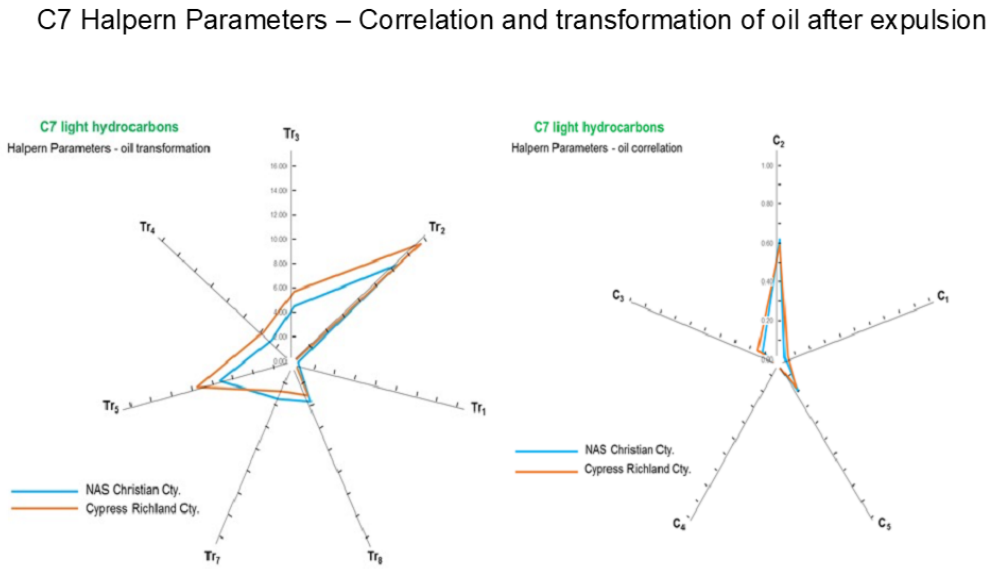


Figure 3-63. Usage of C7 light hydrocarbon ratios to discern oil correlation and transformation.

Basin Modeling

Assessment of oil expelled into migration pathways is hampered by the unroofing and erosion of portions of the Pennsylvanian, Permian, Triassic, Jurassic, and Cretaceous stratigraphic intervals within the Illinois Basin. With little/no evidence of depositional thickness and subsequent extent of erosional events – the estimates of depositional unroofing were based on vitrinite reflectance values of kerogen in Pennsylvanian coal seams, in which the Ro values were significantly higher than current temperature and burial thresholds. Initial research regarding thicknesses of the missing section range from 2000' to over 6000' (Cluff and Byrnes, 1991). For the purposes of the comparative modeling of point-specific wells, the inputs into the missing intervals were similar for all four wells. Approximately 3500' was deposited, then eroded in the Late Pennsylvanian-Permian-Early Mesozoic timeframe with 500' deposited, then eroded during the Cretaceous timeframe, and finally a nominal amount of deposition and erosion during the Quaternary. An elevated heat flow event was included during Permian time which coincides with a known elevated hydrothermal occurrence associated with intrusive activity in southern Illinois. Figure 3-64 is a diagram indicating the calculated heat flow throughout basin development and it roughly corresponds to recent calculations of heat flow evolution within the. basin. Controls for burial history and thermal history remained the same between the four wells. In addition, the models used for hydrocarbon generation related to initial hydrogen index and total organic content remained the same between wells, just differing in the starting organic richness content between the Maquoketa and New Albany shales – the New Albany Shale containing higher/richer hydrogen indices.

Comparison of oil expelled highlights the relative position of the wells in the basin evolution and architecture. As the Paleozoic platform was likely shallower in what is now Cumberland and Moultrie counties, the temperature and depth of burial were less than the Paleozoic basin in southern Illinois. Calculated oil expelled for the New Albany Shale, at its deepest burial, was 10mg/g rock (Figure 3-65). The amount expelled is considered non-trivial but would require longer timeframes to saturate both microporosity in the shale and carrier beds/fractures through more porous intervals. It is also important to note that the shallowest burial indicated by the G. Swits well, suggests that the Maquoketa oil contribution to available pore space was significantly reduced in this part of the basin. Further south and deeper in the basin, both the Carrie Winter and Storey wells indicate that this area generated large volumes of oil from the New Albany Shale, 25 and 30 mg/g rock respectively. This result reinforces the conclusion that the New Albany Shale was a major, if not the major, contributor of generated oil in the basin. Oil expelled from the Maquoketa Shale is less than half of the volume expelled from the New Albany Shale. How this impacts the ultimate distribution of oil within the basin will be discussed in the next section.

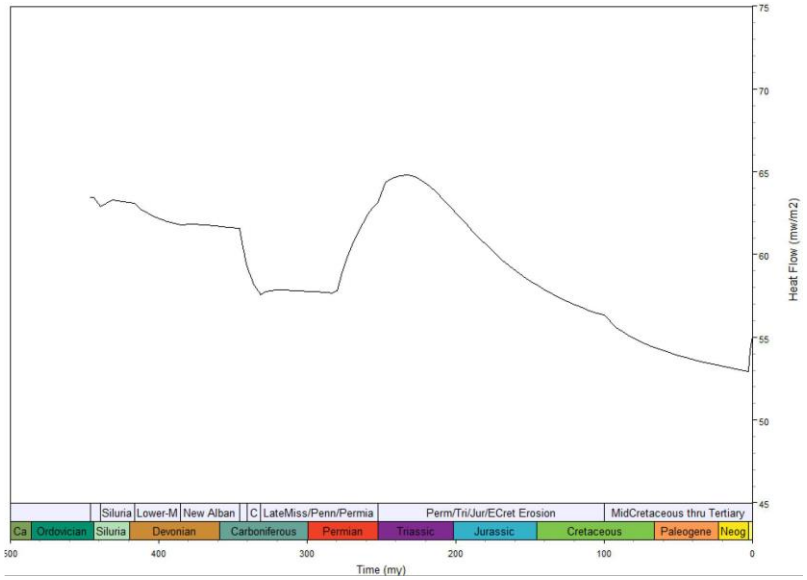
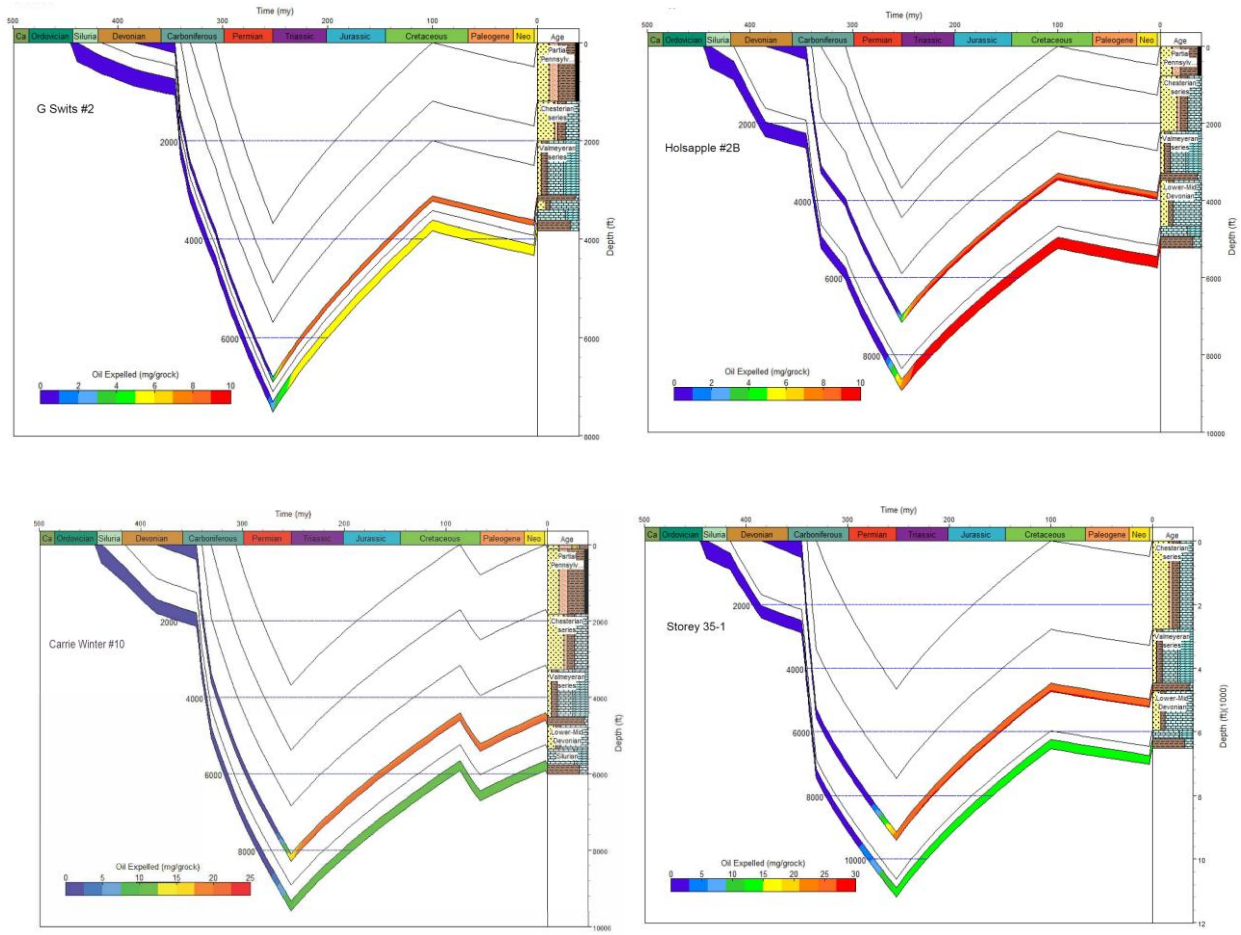


Figure 3-64. Calculated heat flow from Illinois Basin stratigraphy.

The timing and rates of oil expulsion are depicted in Figure 3-66. High rates of expulsion for Maquoketa Shale are of longer duration than New Albany Shale but return to no-expulsion at least 10 million years before New Albany shale according to the modeling for the Storey and Carrie Winter wells. Expulsion rates for New Albany Shale are considered very high for a clay-rich shale. This suggests that any Maquoketa generated oil in the basin plumbing likely was mobilized and replaced by New Albany generated oil – in areas of connected fractures and carrier beds. Moving north in the basin as depicted by modeling of the Holsapple well, expulsion rates for the New Albany Shale are significantly less relative to Storey and Carrie Winter wells but the rate for Maquoketa Shale is about the same relative to the aforementioned wells. This reflects the burial position in this portion of the Illinois Basin where proximity to incipient development of inverted uplift structural configurations associated with the LaSalle anticlinorium impacted the source kitchen burial time/temperature. Therefore, the New Albany Shale, while still being able to expel significant amounts of oil, was buried to shallower depths which impacted the rate of expulsion. This is the result of the New Albany Shale containing very rich and reactive organic matter. The Maquoketa Shale contained less rich and reactive organic matter – differences in burial depths appear not to impact the rate of expulsion as significantly. Maquoketa Shale rates of expulsion occurred earlier

and diminished approximately 10 million years before the relatively high rates of generation ceased in the New Albany Shale. This suggests that any Maquoketa generated oil in the basin plumbing likely was mobilized and replaced by New Albany generated oil – in areas of connected fractures and carrier beds. The shallow basin platform area in what is now Moultrie County (G. Swits well), produced burial and temperature conditions which suggest that onset of oil generation between the Maquoketa and New



Albany Shales were similar but the expulsion reduction in the Maquoketa Shale occurred at least 2-5 million years before the New Albany Shale.

Figure 3-65. Comparison of calculated oil expelled from the Maquoketa and New Albany Shale in different areas of the Illinois basin.

Summary

The New Albany Shale generated significantly large volumes of oil in the Illinois Basin and at rates that overwhelmed more modest generation of hydrocarbons from the Maquoketa Shale. The Maquoketa Shale generated oil was likely eroded (along with large volumes of New Albany Shale oil) from reservoirs developed in the late Pennsylvanian/Permian during unroofing of the Illinois Basin. Early Paleozoic reactivation structures captured the large volumes of New Albany Shale generated oil which may have re-mobilized any Maquoketa Shale oil down-structure and into carrier beds in an up-dip configuration. These beds may have provided access to basin edges where erosion and weathering resulted in the

disappearance of these oils except in deep basin, early formed structures along the Cottage Grove Fault System.

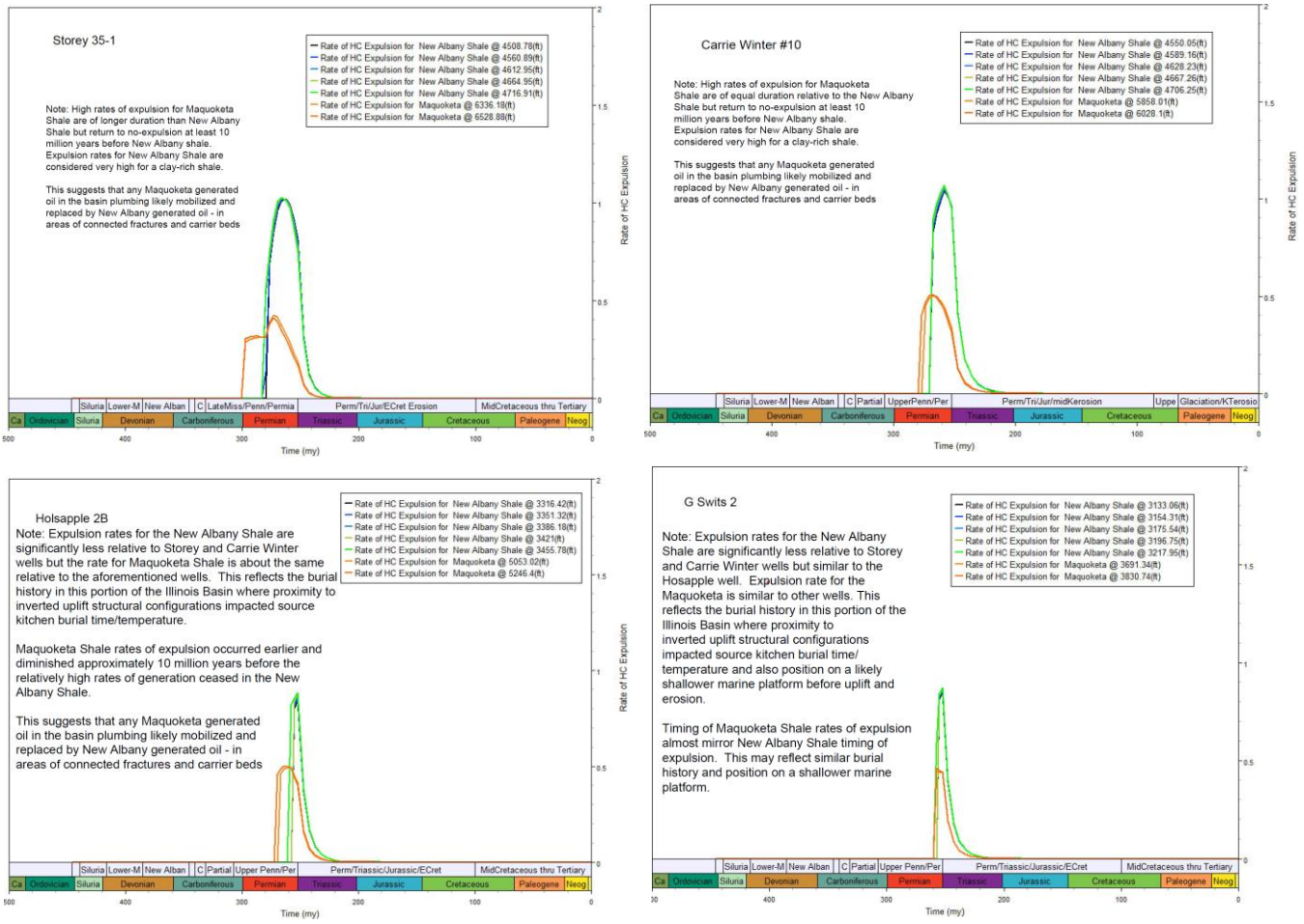


Figure 3-66. Comparison of timing and rate of oil expulsion within different parts of the basin.

4. Greenfield Field Laboratory: Stacked ROZ Storage Complex

The Greenfield field laboratory site is in Cumberland County, Illinois, with evidence of stacked greenfield ROZs. This greenfield field laboratory has two active wells that were drilled prior to the beginning of the project. The wells are outside of recognized, named oilfields, and while production was attempted at high flow rates, no oil was produced from the Carper Sandstone. The wells have modern logs, core, and production data. In addition to the Carper, preliminary well log analysis indicated potential greenfield ROZs in the Cypress and Pennsylvanian in both wells.

This chapter will detail a short-term CO_2 injection (Huff and Puff) test designed to acquire oil rate changes due to CO_2 injection that was performed from Fall 2020 to Fall 2021 in the Holsapple 2B well. Pressure transient tests were performed before and after the CO_2 injection test. The results were used to calibrate reservoir simulations to test how a greenfield ROZ responds to various injection strategies.

4.1. Holsapple 2B Huff and Puff Test

Authors: Nathan Grigsby, Fang Yang, Dmytro Luhktai, and Nathan Webb

Naturally occurring residual oil zones (ROZs) have been commercially developed in the Permian Basin by operators who apply carbon dioxide enhanced oil recovery (CO_2-EOR) to mobilize the residual oil. These ROZs occur beneath main pay zones (MPZs) (i.e. brownfield ROZs) and in areas where the entire mobile oil column was swept, with no overlying MPZ remaining (i.e. greenfield ROZs). Evidence is emerging that ROZs exist in other basins, but more work needs to be done to identify and characterize them, and to determine if CO_2-EOR can be used to economically produce them.

In the Illinois Basin, the Carper Sandstone (lower Mississippian) is a prospective ROZ. Conventional oil production from MPZs in the Carper commonly occurs on anticlines in the northern half of the basin. However, drilling records indicate oil shows in many areas of the basin where the Carper occurs but is not productive. In 2015, a well was drilled into the Carper in Cumberland County, IL, a greenfield ROZ area that does not occur on a structural high and is approximately 10 miles from the nearest oil field with Carper oil production. Despite core from the well with observed (low) oil saturation and well log analysis indicating oil saturation in this and adjacent wells, conventional oil production from the well was not achieved. The Carper Sandstone in this well is thus interpreted to contain a greenfield ROZ.

To this end, a single well CO_2 injection test was conducted in this well to increase the understanding of greenfield ROZs and provide data to calibrate reservoir simulations to test how a greenfield ROZ would respond to development-scale CO_2-EOR. This topical report details the Greenfield ROZ field laboratory test, including pre-test reservoir characterization, test selection, design and execution of the test, and results and interpretation.

The objectives for the Greenfield ROZ field laboratory test can be broken down into two broad categories:

1. Characterize the geology and reservoir fluids of the ROZ.
    a. The geologic properties of the target reservoir (i.e. porosity, permeability, heterogeneity, anisotropy) must be well understood to optimize design specifications for any CO_2 injection test (e.g. CO_2 injection rate, duration of injection, cumulative volume of CO_2 injected and oil produced), so much of the characterization was completed before the injection test by interpretation of log, core, and production data. A robust understanding of the geologic properties of the reservoir is also necessary to understand the applicability of the findings. A CO_2 injection test can produce additional data that can be used to further

refine the geologic interpretation to better estimate how the formation would respond to potential larger scale CO_2-EOR projects.

b. Fluid characterization refers to current oil saturation, residual oil saturation to water and to CO_2, and composition of the oil and brine. A CO_2 injection test will provide field data to constrain the residual oil saturation to CO_2.

2. Demonstrate the efficacy of CO_2-EOR and storage in a siliciclastic greenfield ROZ.

   a. There is significant uncertainty about the EOR potential of greenfield ROZs in siliciclastic reservoirs. A CO_2 injection test will provide field data to begin to understand whether CO_2 be used to produce the oil in a siliciclastic greenfield ROZ, and if so, the quantity that could be produced and under what conditions. Test data will also help quantify the amount of CO_2 that can be injected and stored. In addition to providing evidence that CO_2 can be used to produce oil from siliciclastic ROZs, the injection test will also provide information (such as injectivity of CO_2 and the resulting oil rate production) that can be used to calibrate reservoir simulations to test various injection/production scenarios.

4.1.1 Pre-Test Reservoir Characterization

A robust understanding of the reservoir and petrophysical properties of the target interval is necessary to establish initial conditions for reservoir simulations and minimize uncertainty about injected CO_2 behavior. The injection test will be performed in the Holsapple 2B well (API 120352329600) in south-central Cumberland County, IL, in the Carper Sandstone (Figure 4-1). A full suite of well logs (Gamma ray [GR], spontaneous potential [SP], array resistivity, cross plotted porosity, photoelectric factor [Pe]) and whole core from the Carper were collected when the well was completed and were available for analyses and interpretation. The operator's log analysis indicated oil in one 15 ft thick Carper sandstone bed. This conclusion was supported by oil in the core samples. The entire 15 ft zone was perforated, and the sandstone bed was slickwater fracked. The well was pumped at ~200 bbls/day for ~6 months and produced only trace amounts of oil.

The Carper Sandstone greenfield ROZ in the Holsapple 2B well is an excellent candidate for a CO_2 injection test for several reasons: 1.) It contains core validated oil saturation that is confirmed to be non-mobile by months of pumping. 2.) It is >10 mi away from Carper production, ensuring that residual oil in the Carper is the result of natural processes and not depletion from oilfield practices. 3.) The Carper is overlain by approximately 500 ft of Borden mudstone that will be an effective seal for CO_2. 4). The Holsapple 2B well less than a decade old and has excellent data with core, modern geophysical and cement bond logs, and production data. 5.) The operator of the well is amenable to and interested in the test.

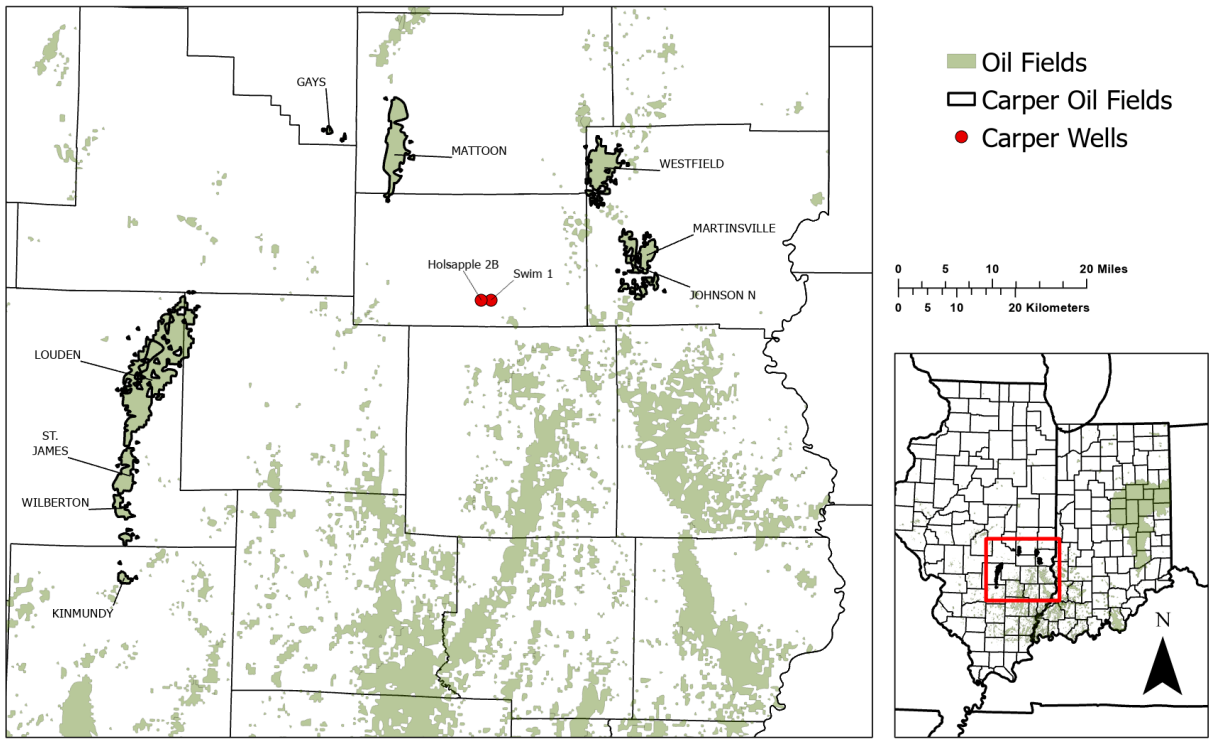


Figure 4-1. Map of the Greenfield ROZ Field laboratory. The Holsapple 2B and Swim 1 wells are shown with red circles. Oil fields are shaded green, and those that have Carper production have black borders.

Geologic Characterization

The design of the CO_2 injection test is contingent upon geologic factors that would control the injected CO_2, including lateral variability in petrophysical properties, (e.g., heterogeneity, anisotropy, thickness). The Holsapple 2B well is in a greenfield setting where data is sparse, so regional data were examined to understand Carper reservoir characteristics to support the geologic interpretation and to draw inferences about the lateral extent and potential variability of the injection interval. A more careful interpretation of all available data near the well was then conducted to minimize uncertainty of the geologic properties of the target interval.

Regional Setting

All available log, core, drilling, and production data for the Carper Sandstone were compiled and analyzed. The Carper occurs in the lower portion of the Borden Siltstone (Figure 4-2) as lobes that tongue into the northern Illinois Basin (Lineback, 1968; Figure 4-3). The injection well is in central Cumberland County and penetrates Carper sandstone bodies that are part of the A, C, and D lobes (Figure 4-3). The target injection interval is within the Carper C (Figure 4-4).

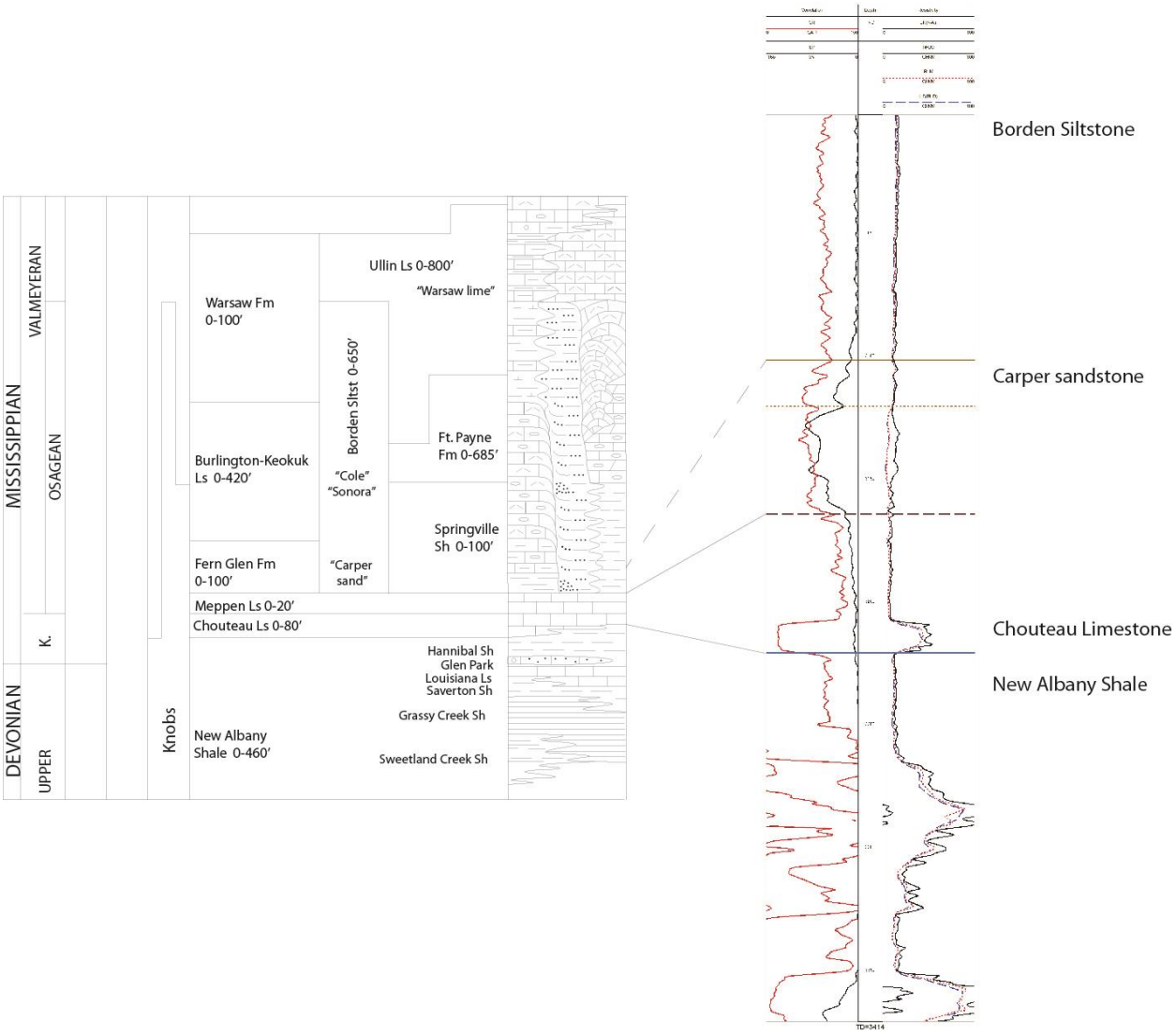


Figure 4-2. Example geophysical log showing the typical stratigraphy of the Carper Sandstone.

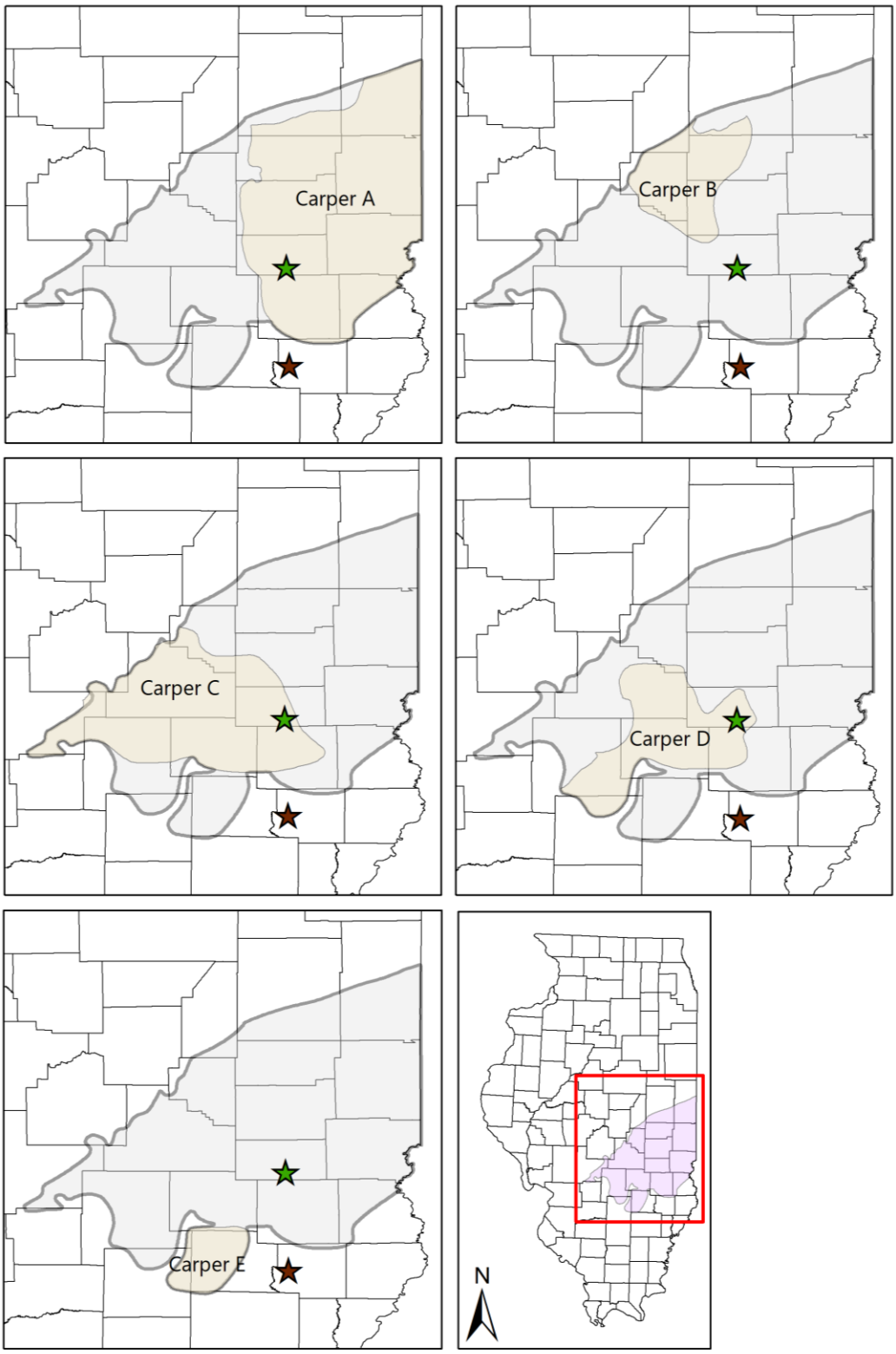


Figure 4-3. Series of maps showing the overall extent of the Carper Sandstone in Illinois (shaded in grey) and the distribution of individual lobes within that extent (shaded in tan). The Holsapple well is indicated by the green star. Modified from Lineback (1968).

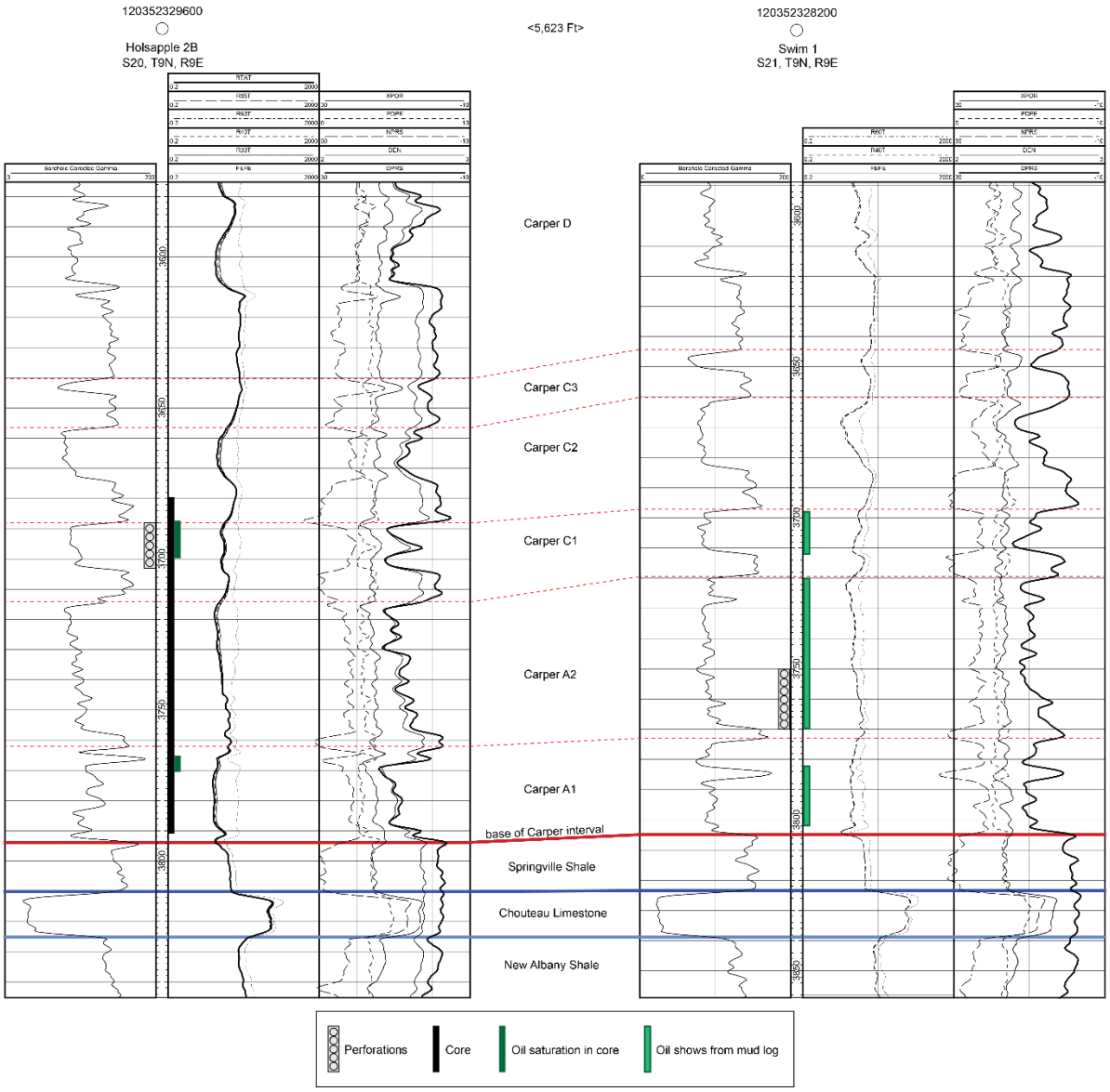


Figure 4-4. Two-well cross section showing the Holsapple 2B well and the adjacent Swim 1. In both wells, Carper sandstone bodies occur over a thickness of more than 200 ft. The Carper C1 sandstone is 15 ft thick and is the zone that is perforated in the Holsapple 2B well. Perforations are indicated by grey circle-filled boxes. Core is indicated by the black bar. Oil reported by operator is indicated by the green bars. The distribution of oil saturation is better constrained in the Holsapple well (which had core) vs. the Swim well (which reported oil based on observations during drilling).

Data from all available Carper core analysis reports in Illinois were compiled and analyzed (Figure 4-5). The Holsapple well has lower average porosity (11%) and permeability (0.6 mD) than other wells, which tend to have average porosity between 13 and 16% and permeability between 2 and 4 mD. This may indicate that the core data is erroneous, but it is more likely that the other wells, which were preferentially drilled in oil fields, have different petrophysical properties. Three of the oil fields with core; St. James, Kinmundy, and Wilberton Fields produce oil from the Carper D, but their porosity and permeability are not significantly different than the wells that produce oil from the Carper A; Westfield, Martinsville, and Mattoon Fields.

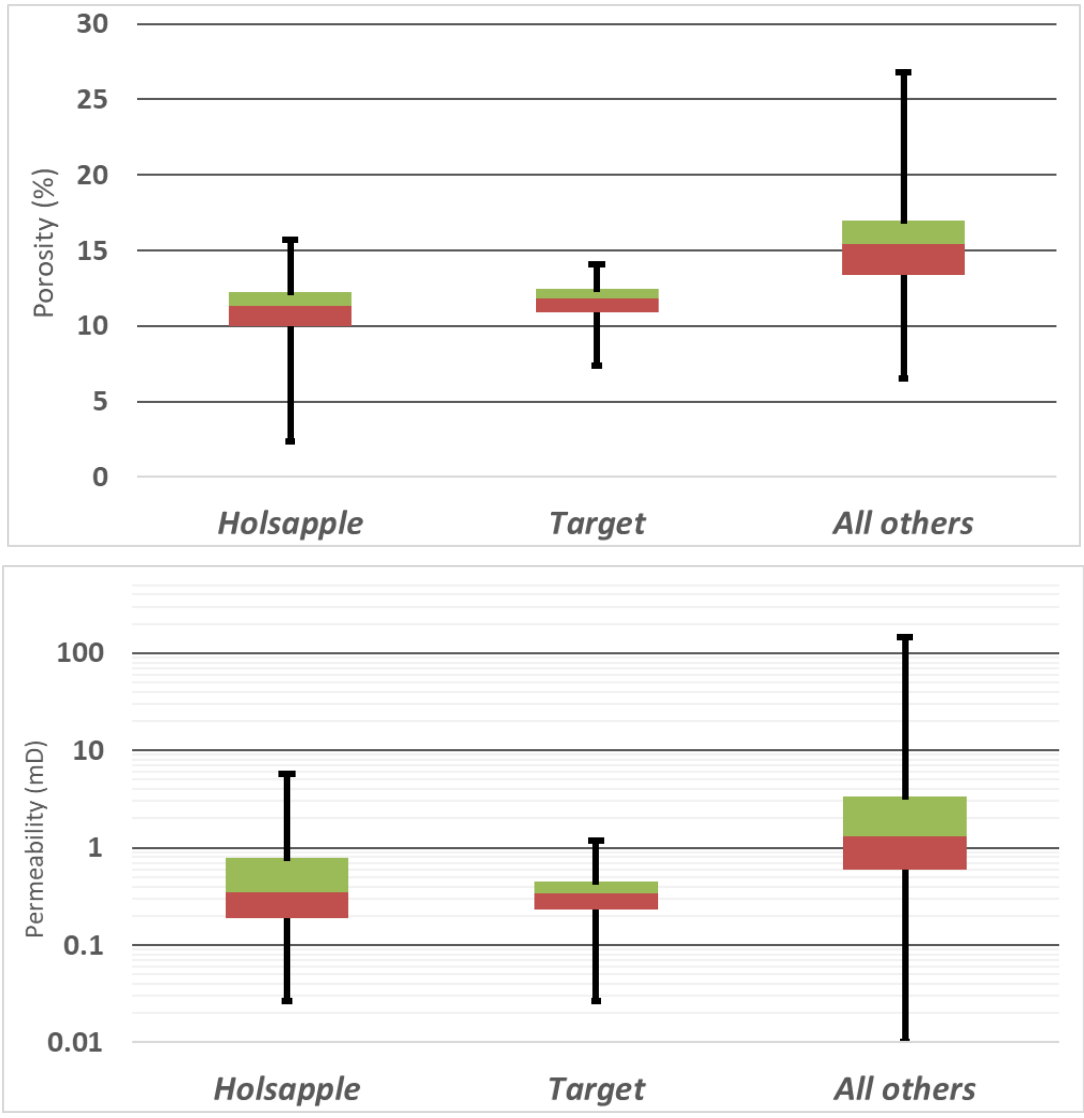


Figure 4-5. Box and Whisker plots of porosity (top) and permeability (bottom) from core analysis reports for the Carper Sandstone. The porosity and permeability from the target well (Holsapple) and the 15-foot target interval within the well are lower than the other fields.

Site Geology

The geologic interpretation of the Carper sandstone at the greenfield test site is based on core (Figure 4-5) collected from the Holsapple #2B well and the full suite of well logs from the Holsapple #2B and the Swim #1 well (Figure 4-4). Nearby wells and oilfields in adjacent counties that produce from the Carper also provide important geological information. The target interval in the Holsapple #2B well is a thin (~4.6 m [15ft] thick) shaly sandstone between the depths of 1,125-1,129 m (3,690-3,705 ft), referred to as the Carper "C1" (Figure 4-4).

Core from the Holsapple #2B well shows the Carper sandstone to be composed of very-fine grained sandstone to coarse siltstone. The rock is well indurated and carbonate cemented. Within the target C1 interval, the reservoir facies is dominated by structureless sandstone with a ~0.3 m (1 ft) bed of interlaminated shale and sandstone occurring in the middle of the interval. Samples were taken for

petrography and X-ray diffraction (XRD) analysis to constrain the grain size, mineralogy, controls on porosity and permeability, but this data was not available for the pre-test characterization. Analysis of the Holsapple #2B core indicates porosity ranging from 7 to 14% and permeability of approximately 1 mD or less over the entire Carper Sandstone (Figure 4-5). The target interval has porosity between 10-14%.

Gamma Ray, SP, resistivity, and neutron-density porosity logs all indicate that the target C1 interval is isolated vertically from other Carper Sandstone bodies by 3+ m (10+ ft) thick beds of shale above and below. Separation of neutron porosity (NPOR) and density porosity (DPOR) logs suggest that the interval has some shale. Neutron and density porosity diverge in the middle of the interval, suggesting a shale rich interval. This is accompanied by a slight deflection on SP, GR, and resistivity curves, which suggests that the feature is 0.3-1 meter (1-3 ft) thick (above the resolution of the porosity logs but below the resolution of the SP, GR, and resistivity logs). Neutron-density porosity logs suggest that "clean" sections of the target interval are between 12-14% porosity. These characteristics extend to the nearby Swim #1 well (Figure 4-1 and 4-5).

On the geophysical log, density porosity is well supported by core measured values, but the neutron and cross plotted porosity are significantly higher (Figure 4-6). The anomalously high neutron and cross plotted porosity values are likely due to a high proportion of clay mineral cement within the Carper.

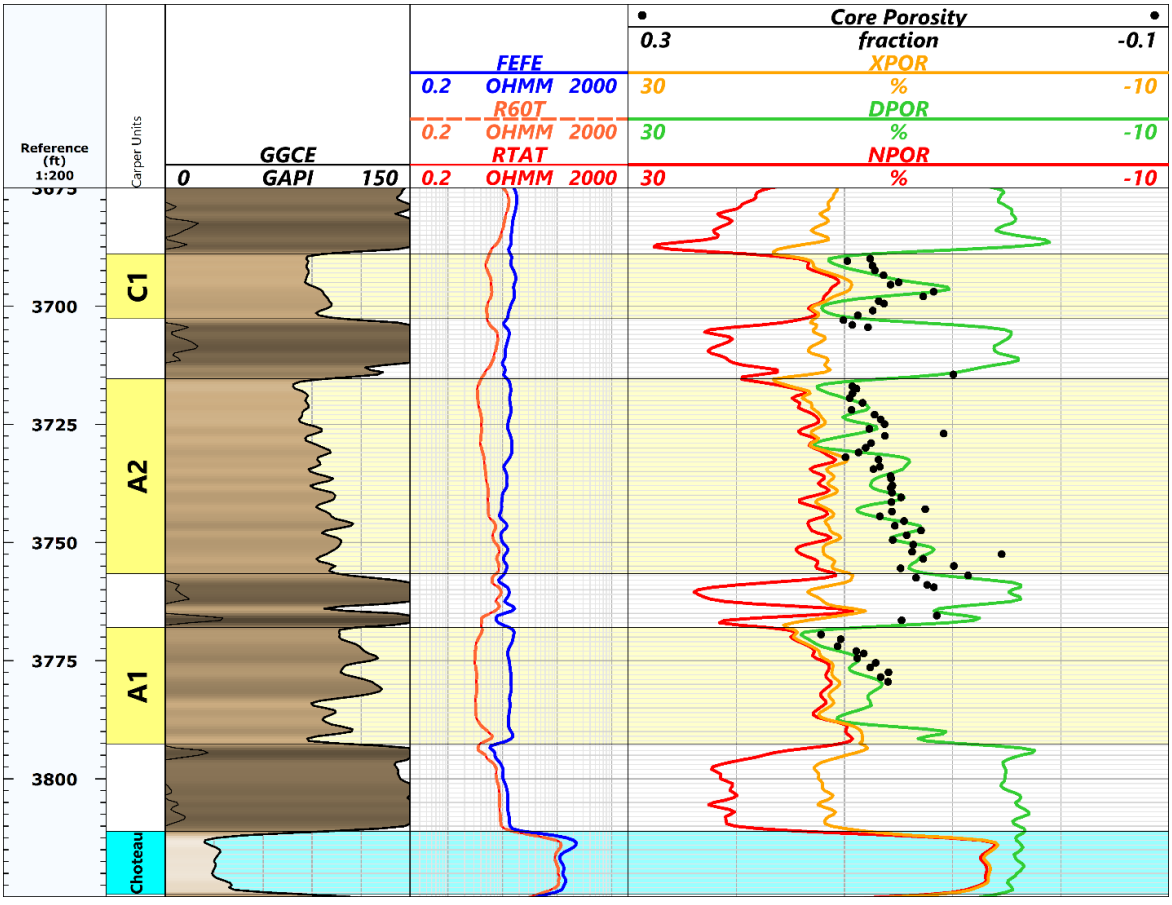


Figure 4-6. Triple combo log and core-derived porosity for the Holsapple 2B well. Core-derived porosity matches density porosity but is significantly less than neutron and cross plotted porosity. The mismatch between core and neutron/cross plotted porosity is much more pronounced in the intervals with high Gamma Ray and is indicative of clay causing the neutron porosity log to overestimate porosity.

Fluid Characterization

Regional Setting

Historical records of the Carper were evaluated to determine its regional ROZ potential. Scout tickets, production records, core analysis reports, completion reports, and drill stem tests were all checked for oil indicators and assigned indicator values to denote if the well had oil, and if that oil was productive.

A map of these indicator values shows that the Carper is productive on structural highs in Westfield, Martinsville, Johnson North, Mattoon, Gays, Louden, St James, Wilberton, and Kinmundy Fields, and a high proportion of wells that encounter the Carper off-structure have oil shows without production (Figure 4-7). This distribution of oil shows and oil production suggests that the Holsapple 2B well is within a Carper ROZ fairway.

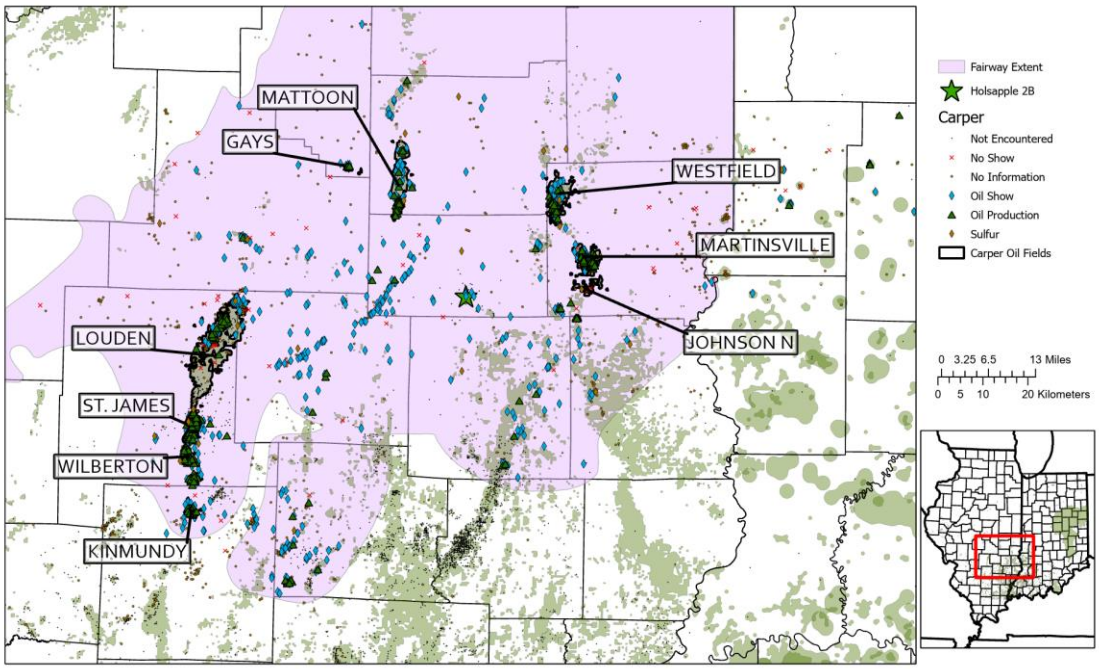


Figure 4-7. Locations of wells with Carper oil shows are shown in blue dots, Carper production shown in red dots, core analysis reports with Carper porosity and permeability shown with green asterisks, and injection well shown in black star. The estimated extent of Carper Sandstone shown in thick black line, and oil fields shaded green. Westfield and Martinsville have clusters of oil production and core analysis reports in Clark County that are believed to have the best chance of being analogous to Holsapple 2B well.

Site Fluid Characterization

Pre-injection fluid characterization involved a determination of oil and water saturation (S_O and S_W respectively) and oil and water composition.

Chemical analysis of brine samples from the injection interval reported a total dissolved solids (TDS) of 88,844.65 parts per million (ppm), which will create an R_w of 0.074 ohm-m at the reservoir temperature of 36 °C (97 °F) as determined from the typical temperature gradient of the Illinois Basin.

Months of production yielded no oil samples from the Holsapple 2B well, so the properties of the oil were estimated from the values published in Mast (1970). All these samples had similar density and viscosity (Figure 4-8), so it was assumed that the oil in the Holsapple 2B well had a density and viscosity of 37 API and 6 cP, respectively.

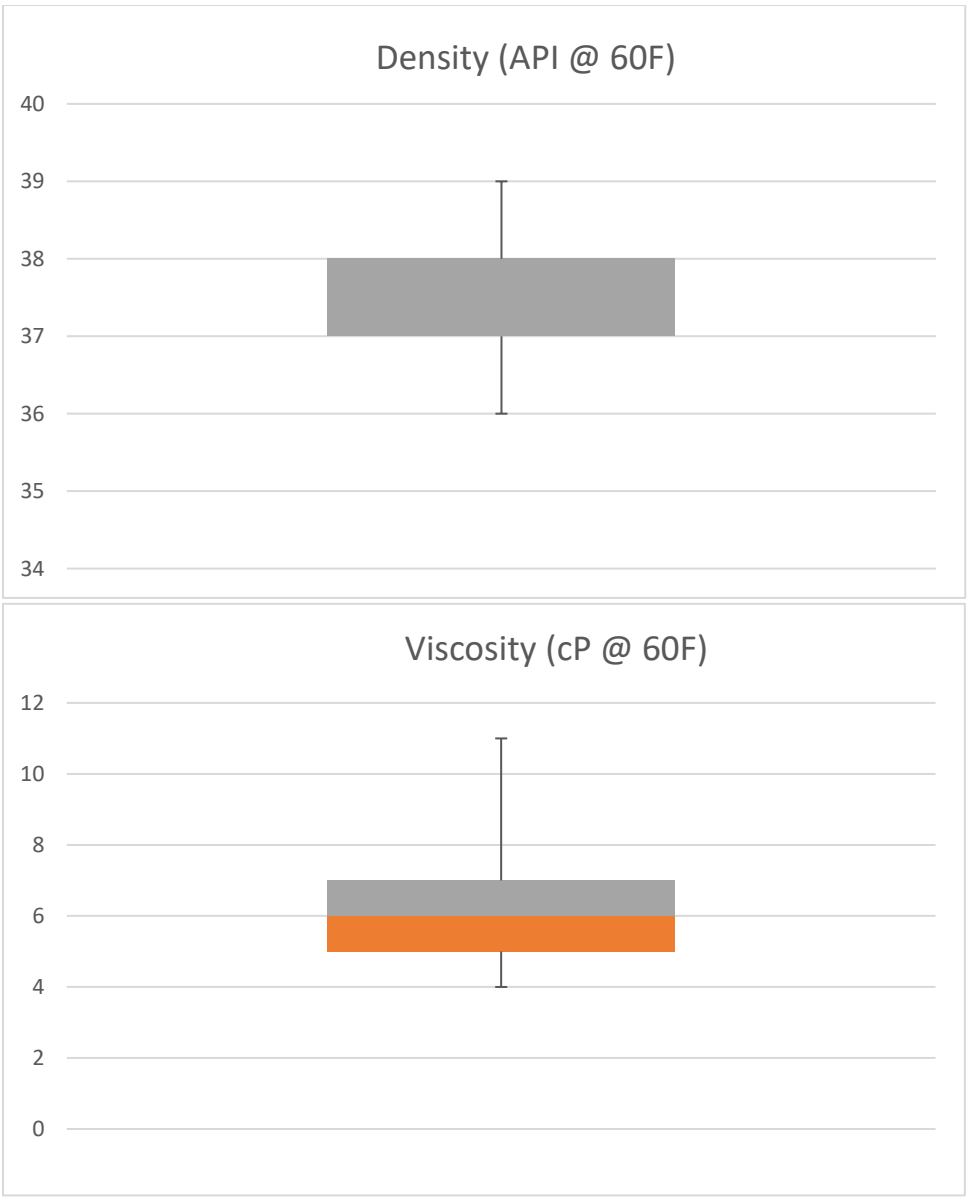


Figure 4-8. Box and Whisker plots of density (top) and viscosity (bottom) of Carper oils reported in Mast (1970).

Well Log Analysis

Logs were analyzed to characterize the fluid saturation distribution within the Carper, but the presence of clay dispersed within the sandstone makes log derived S_w problematic. Archie's equation assumes that the formation is shale free (which is not the case) and dual water calculations rely on the assumption that the clay dispersed within the target formation contains the same properties as a nearby shale.

Archie water saturation (S_W) was calculated using the raw neutron, density, and cross plotted porosity logs (NPOR, DPOR, XPOR respectively) using an R_w of 0.074 ohm-m and a cementation exponent (*m*) of 2 (Figure 4-9). Oil saturation (S_O) is assumed to occupy the remaining pore space (1-S_W). The disagreement between the porosity logs creates a large difference in calculated S_w. This difference is most pronounced in shale rich intervals, where high NPOR and XPOR results in the lowest observed S_w (~50%), while low DPOR results in S_w ~100%.

The absolute value of core measured S_O is unreliable (due to displacement of in situ fluids during the coring process), but the relative value of core measured S_O is useful to detect the presence or absence of oil and general trends in oil saturation distribution. In this case, the cored interval (3685-3786 ft) only had oil saturation within the target interval (C1 from 3686.5-3700 ft) and directly beneath a shale break in the lowest Carper interval (A1 from 3765.5-3770.5 ft). The entire Carper A2 was cored with no oil observed and the middle of the target interval also has a ~5 ft span with no oil (3692.2-3698.3 ft) (Figure 4-4).

The comparison of the preliminary log analysis and core measured oil saturation suggests that the target interval has the highest potential to have oil, that there are no thick intervals of overlooked oil, but there is potentially some oil in the uppermost portion of the lowermost Carper interval. These observations also support DPOR derived S_w and show that NPOR and XPOR derived S_w grossly overestimate the quantity and distribution of oil saturation (Figure 4-9).

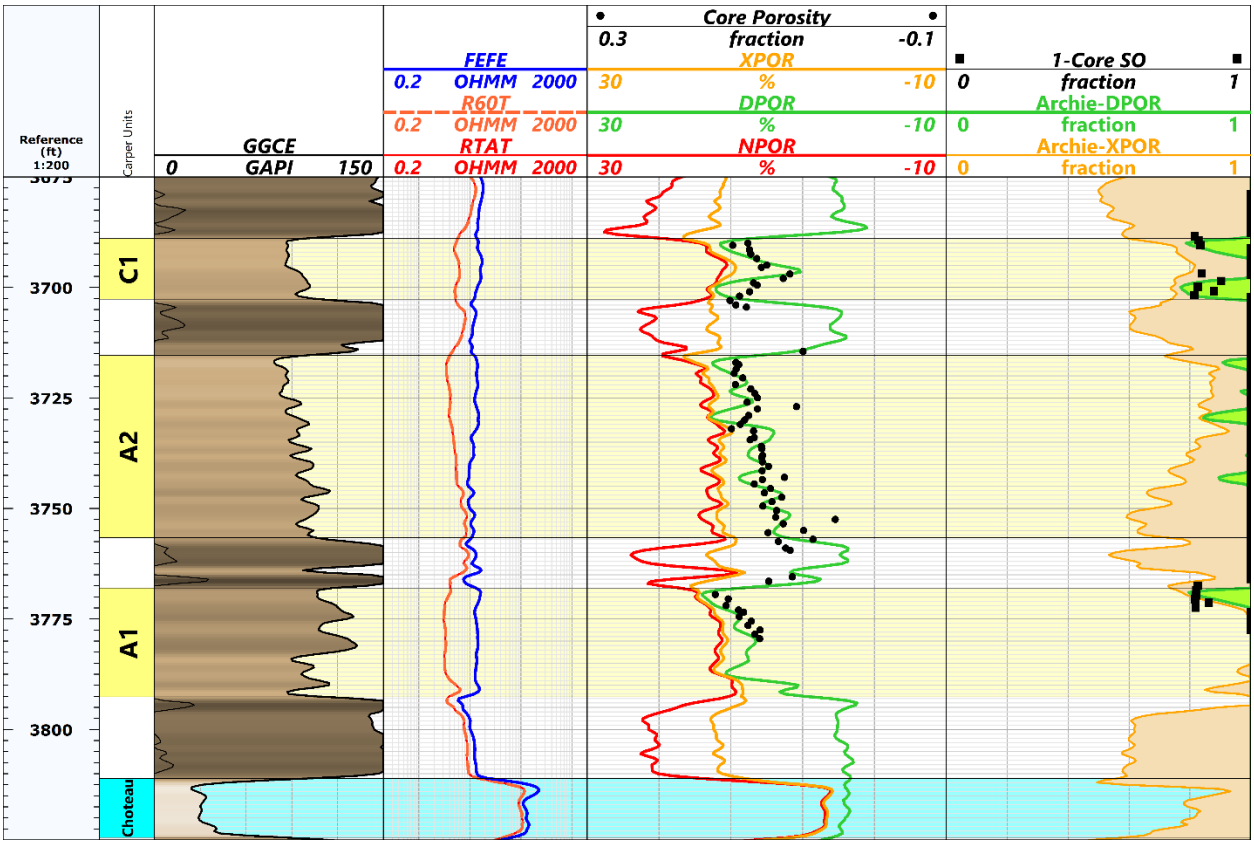


Figure 4-9. Log and core derived water saturations and volume of shale plotted against depth. The Carper C1 is the target interval. Archies Sw is calculated using the raw DPOR and XPOR logs assuming an Rw = 0.074 and an m of 2. Archies Sw derived from DPOR more closely approximates the oil observed in core (oil only present in C1 and top of A1 units) while XPOR derived Archies Sw is erroneously low, especially in shale rich intervals. This mirrors the over-estimation of NPOR in clay-rich intervals.

There was significant uncertainty in S_O, so dual water saturations were also calculated to constrain the S_O in the target interval as much as possible. The volume of shale (Vshale) was calculated via both GR and neutron-density porosity. The shales above and below the target interval each had the highest GR response (~160 API) and NPOR/DPOR separation (23% NPOR and 2% DPOR) in the entire Carper. These values were used as the shale baselines.

The interval above the target interval had the lowest GR of the entire Carper, so its GR was selected for the sand baseline. However, both Pe and GR were higher than the values typically observed in clean sandstone (the GR was ~75 API [typically <50 API in clean sandstones] and the Pe was ~2.5 in the Carper [1.8 in quartz]). This suggests that sandstone units within the Carper contain clays that could disrupt the dual water equations. NPOR and DPOR converged at ~16% at the top and base of the target interval but diverged in the middle (Figure 4-6). The divergence between NPOR and DPOR is believed to be caused by thin shale laminations observed in the core, so the sandstone baseline was set at 16%.

The two calculated Vshale curves generally agreed, but the neutron-density Vshale did a better job of detecting the thin shale break in the middle of the target interval, so it was used.

The target interval has a calculated S_O of approximately 25%. This likely represents the residual oil saturation to water (S_{ORW}) of the Carper. However, this number carries a moderate amount of uncertainty with it. The elevated Pe and GR response in the target interval suggests that not all the porosity is effective, and it is likely that porosity is being overestimated. Core flood experiments are planned to validate S_{ORW}, but the data was not available before CO_2 injection.

Historical Production

Production of oil and water from the target well can be used to estimate permeability, pressure, and to history match models used for reservoir simulations. The target interval was hydraulically fractured and put on pump in mid-November 2016. Only the last two months of daily production rates were available, but this data shows that it consistently produced 150-200 bbls of fluid per day until the well was shut-in in May 2017 (Figure 4-10). Only trace amounts of oil were produced during the six months of production. The daily fluid production from the well is commensurate with nearby Carper production, which produces on the order of 100-200 bbls of fluid per day.

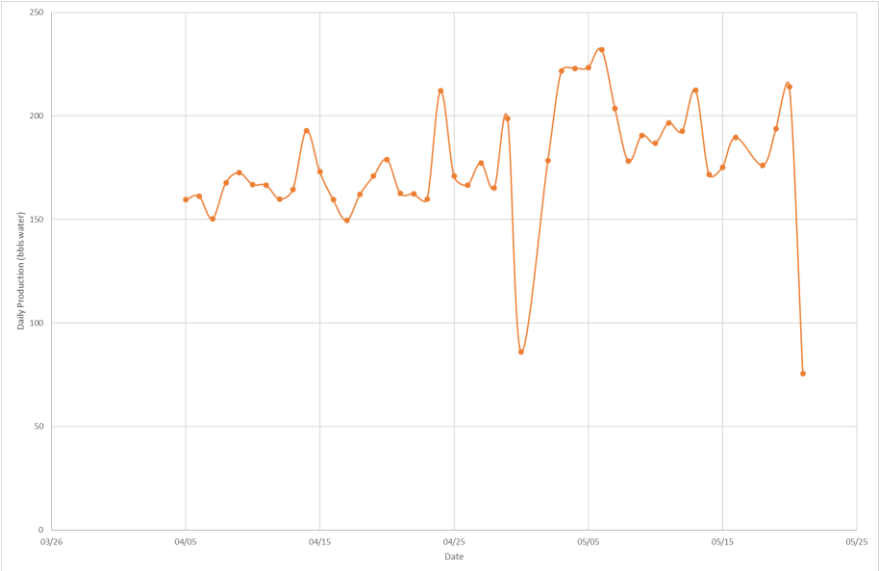


Figure 4-10. Water production from the Holsapple 2B well provided by the operator.

Test Selection

There are two types of CO_2 injection tests being considered for this project; a single well Huff and Puff (HnP) or two single well chemical tracer tests (SWCTTs) separated by a CO_2 injection. Before deploying either test in the field, it was necessary to first evaluate which of the two tests would be more likely to

meet the Greenfield ROZ field laboratory test objectives while remaining within the budget and time constraints of the project.

Huff and Puff

A Huff and Puff (HnP) involves three steps; 1. Injection of CO_2, 2. A shut-in or soak period, 3. Re-opening and producing the well. The shut-in period allows CO_2 time to contact oil, reducing its viscosity, mobilizing it, and allowing it to be produced. Multi-well HnPs have been widely used for several decades to produce oil left in reservoirs that have undergone primary and secondary recovery, but single well HnP are also commonly used as pilot tests to determine the CO_2-EOR potential of a depleted reservoir.

The HnP proposed here will inject as much CO_2 possible into the target well given the budget and time constraints of the project. Reservoir simulations based on the preliminary ROZ characterization would be used to constrain CO_2 injectivity, soak time, and resulting expected oil production.

Single Well Chemical Tracer Test

The Single Well Chemical Tracer Test (SWCTT) was invented by Deans et al. (1971) to assess residual oil saturation after secondary and tertiary recovery. A partitioning tracer (an ester) is added to produced water and injected into formation. This is followed by a "push" injection; a volume of tracer-free water that pushes the tracer 3-9 meters (10-30 feet) into the formation. The well is shut in and allowed to soak, during which time a chemical reaction occurs, and a secondary tracer (alcohol) is created. Water is produced and the rate of which the parent (ester) and daughter (alcohol) chemical tracers is compared. Oil saturation is then calculated by comparing the arrival time of the partitioning and secondary tracers:

$$S_{OR} = \frac{{}^{Q_A}/_{Q_B} - 1}{{}^{Q_A}/_{Q_B} - 1 + K_D} \qquad \text{Equation 4-1}$$

Where:

S_{OR} = Residual oil saturation

Q_A = Produced volume necessary for peak secondary tracer concertation

Q_B = Produced volume necessary for peak partitioning tracer concentration

K_D = A partition coefficient defined by:

$$K_D = \frac{C_O}{C_e} \qquad \text{Equation 4-2}$$

Where:

K_D = Partitioning coefficient

C_o = Concentration of tracer in oil

C_e = Concentration of tracer in water

The proposed SWCTT test would involve two SWCTT tests; one before CO_2 injection to establish residual oil saturation to water, and one after CO_2 injection to establish residual oil saturation to CO_2. Pre injection reservoir simulations will be used to estimate the volume of CO_2 necessary to reduce a 3-9 m (10-30 ft) radius around the injection well to residual saturation (to CO_2) to ensure that the post injection SWCTT measures the proper saturation. The tracers partitioning coefficient and interpretation of produced fluid and resulting oil saturations will be provided by vendor.

Comparison of Tests

The expected outcomes of both tests were compared to determine if and how they would meet objectives. Each test has strengths and weaknesses. Single well HnPs are often used as pilot tests to determine the effectiveness of a larger scale CO_2-EOR project. This accomplishes objective 2; To demonstrate the efficacy of CO_2-EOR and storage in a siliciclastic ROZ. However, the test provides no information on (pre- or post-injection) oil saturation and would not directly inform ROZ characterization. SWCTTs are designed to measure in situ oil saturation, so a SWCTT before and after a CO_2 flood will measure residual oil saturation to water and to CO_2 respectively (assuming the reservoir is at residual oil saturation to water and that the CO_2 flood sweeps the necessary radius to residual oil saturation to CO_2). This information could be used to inform both the ROZ characterization and the efficacy of CO_2. However, the added cost of two SWCTT tests results in diminished budget for CO_2, reducing the amount that could be injected. This is expected to result in less oil production and a less compelling demonstration of the efficacy of CO_2-EOR and storage.

Pre-Test Reservoir Simulations

Reservoir simulations were used to constrain injection parameters (e.g. cumulative volume, rate, and duration for either type of test) and to estimate resulting oil production and CO_2 storage. Preliminary simulations used a simple homogenous model with petrophysical properties based on values from the core analysis report (Table 4-1). A homogenous model was used because the geologic conceptual model of the Carper sandstone (as a gravity flow deposit) assumed broad lateral continuity and minimal lateral heterogeneity and anisotropy. This was supported by observations of the target interval being approximately 15 feet thick, and the matrix corrected density porosity log was similar (~10-12%) in the Swim and Barkley wells (the only other wells with porosity logs), suggesting that the core derived properties were representative of the Carper within the model domain. Reservoir pressure was estimated to be 1,597 psi at the top of the formation by assuming the freshwater gradient of 0.433 psi/ft. This is very near the minimum miscibility pressure of CO_2, which is estimated to be around 1,300 psi.

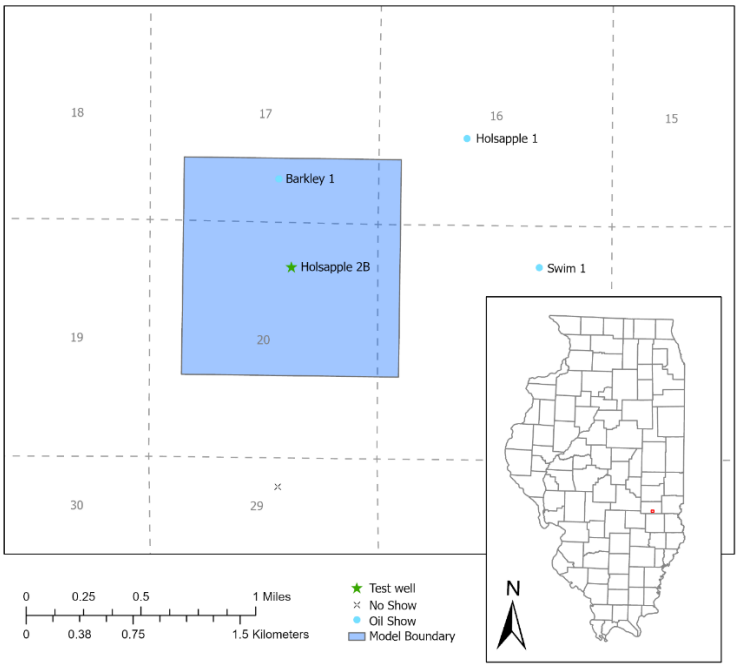


Figure 4-11. Map of Greenfield model bounds.

Table 4-1. Parameters of simple homogeneous model.

Parameter	Value
Top depth measured (meters/feet)	1,124 / 3,688
Top depth subsea (meters/feet)	962 / 3,155
Thickness (meters/feet)	4.6 / 15
Porosity (%)*	12
Permeability (mD)*	0.2
Temperature (°F)	113
Pressure (psi)**	1,597
Cell count #x*#y*#z	100*100*30
Cell size Δx*Δy*Δz (ft*ft*ft)	50*50*3

*Porosity and permeability values are averages based on core measurements. **Reservoir pressure calculated at measured depth at the formation top based on freshwater gradient of 0.433 psi/ft.

Simulations based on the preliminary simple model consistently produced fluids on the order of 10 bbls per day; an order of magnitude below the historical production of ~200 bbls (>100 bbls) per day (Figure 4-10). Additional model runs were conducted to determine the effective permeability required to yield the historically observed water production by varying the permeability and thickness (Table 4-2). These simulations concluded that the 15 ft target interval would need an effective permeability two orders of magnitude over the core derived permeability (10-20 mD instead of 0.2 mD). Even if all Carper units (142 ft in cumulative thickness) were in communication, the effective permeability would still need to be two orders of magnitude higher than values observed in the core (approximately 1 mD). A natural fracture network, overlooked by log and core analyses, was therefore interpreted to be present in the Carper in this area. It is unclear if the shale units above and below the target interval are effective seals or if natural fractures allow pressure communication between sandstone units.

Table 4-2. Effective permeability requirements for observed fluid production.

Permeability, md	Thickness, ft	Rate at 2 months, stb/day	Permeability-Thickness, md-ft
20	15	248	300
15	15	192	225
10	15	134	150
1	150	182	150
0.2	750	234	150

Fracture Modeling

A natural fracture network will exert a large control on any injection of CO_2 by providing the highest permeability conduit for flow. Therefore, a dual porosity, dual permeability model was used to model the natural fracture network to better understand how a natural fracture network will influence the test. The

matrix properties were assumed to be those observed in core analysis and used for the preliminary simple model (Table 4-1)(ϕ=11.5%, *k*=0.2 mD). No information about the parameters of the fracture network (e.g. intensity, spacing, orientation, permeability) was available, so different fracture network properties were tested until a range was found that would meet historical fluid production from the well. Table 4-3

Anisotropic vertical fractures were required to meet historical water production rate. The x direction was set to the regional principal stress orientation (Carlson et al., 2018). The fracture permeability in X direction (Kxf) was set equal to the fracture permeability in Z direction (Kzf). The fracture permeability in Y direction (Kyf) needed to be at least 0.02 times Kxf to create the historically observed fluid production. These permeabilities were created by setting the fracture spacing in X direction to one fracture per meter (LY=3ft), and the fracture spacing in Y direction (LX) to 150 ft. The fracture porosity was set to 0.1% based on the assumption that the fracture width was 1 mm, and the effective fracture permeability in X direction would be 83.3 mD based on Crain's equation (Proceedings of the International Field Exploration and Development Conference 2020, 2021).

A 2% oil saturation was added to the fractures to get the simulation to run.

There was significant uncertainty in the fracture network parameters, so an additional model with a denser fracture network was created that could also be responsible for the historically observed water production (Table 4-3).

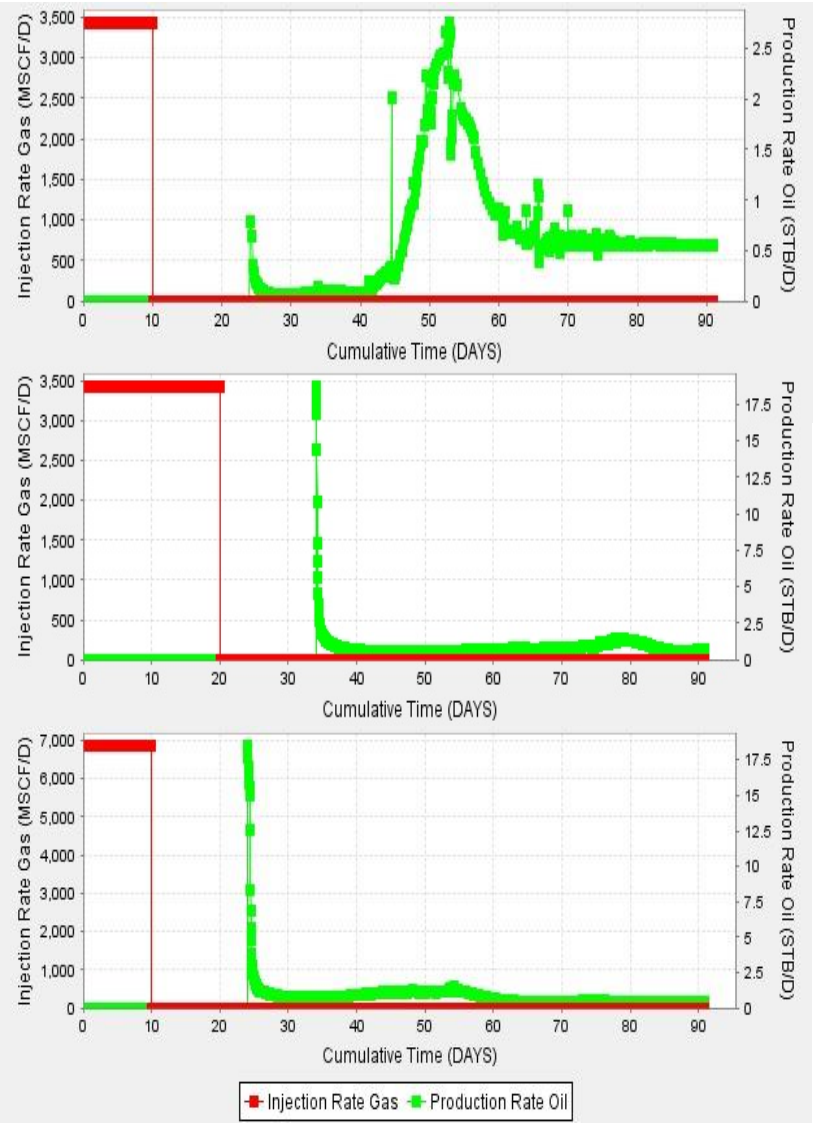
Table 4-3. Input parameters for preliminary fracture models.

Parameter	**Coarse fracture model**	**Dense fracture model**
Matrix porosity (øm)	11.5%	11.5%
Matrix permeability (kX,kY,kZ) (mD)	(0.2,0.2,0.1)	(0.2, 0.2, 0.1)
Fracture porosity (øf)	0.102%	1.02%
Fracture effective permeability* (kXeff, kYeff, kZeff) (mD)	(83.3, 1.7, 83.3)	(8330, 166.6, 8330)
Fracture spacing (LX,LY,LZ) (ft)	(150, 3, 15)	(15, 0.3, 15)
Fluid relative permeability in fractures	Vertical equilibrium curve with Sor= 2% and Swr=5%	Vertical equilibrium curve with Sor= 2% and Swr=5%

CO_2 Injection Scenarios

Simulations using the two fracture models (Table 4-3) were run to understand how the reservoir would respond to CO_2 injection and aid in test selection, constrain design specifications (CO_2 injection volume, rate), and estimate how much oil and CO_2 would be produced.

Oil production was evaluated based on its sensitivity on CO_2 injection rate, injection time, soak period, injection scheme (continuous injection vs. half-day injection), and prior water injection vs. no water injection. Simulation results showed continuous CO_2 injection with no water injection was preferable. Oil production increased with higher cumulative CO_2 injection or higher CO_2 injection rate (Figure 4-12).



200 ton/day for 10 days:

Peak oil = 3 stb/day

Cum oil at 1-month = 18 stb

200 ton/day for 20 days:

Peak oil = 19 stb/day

Cum oil at 1-month = 25 stb

400 ton/day for 10 days:

Peak oil = 19 stb/day

Cum oil at 1-month = 46 stb

Figure 4-12. Injection and production rates vs time showing higher cumulative CO_2 injection and higher injection rate yielded more oil production.

However, the pump available to inject CO_2 has a design capacity of 60 tons/day. To account for potential efficiency losses, a rate of 30 tons/day was deemed to be the injection limit. It is logistically easier to inject during daylight hours, so models injected CO_2 at a rate of 30 tons per day for 12 hours followed by a 12-hour shut period. With this rate limit, shorter soak time and higher cumulative injection yielded slightly better cumulative oil production (Table 4-4 and Table 4-5).

Simulations consistently showed that CO_2 would remain in the fractures and had only limited contact with oil held in matrix. Extending the soak time primarily moved CO_2 laterally in the fractures and had little effect on its interaction with matrix (Figure 4-13 and Figure 4-14).

Table 4-4. Simulation results for the coarse fracture model.

Case name	Case description	Total CO_2 injection, ton	Peak oil rate, stb/d	Cum. oil at 1 month, stb	Total time, day
HnP_LY3_30t_7i7s	30t/d half day injection for 7 days, soak 10 days	105	0.6	9	44
HnP_LY3_30t_7i14s	inject 7 days, soak 14 days	105	0.6	9	51
HnP_LY3_30t_7i21s	Inject 7 days, soak 21 days	105	0.6	9	58
HnP_LY3_30t_10i7s	inject 10 days, soak 7 days	150	0.5	11	47
HnP_LY3_30t_10i14s	inject 10 days, soak 14 days	150	0.5	10	54
HnP_LY3_30t_10i21s	inject 10 days, soak 21 days	150	0.5	10	61
HnP_LY3_30t_14i7s	inject 14 days, soak 7 days	210	0.5	10	51
HnP_LY3_30t_14i14s	inject 14 days, soak 14 days	210	0.5	10	58
HnP_LY3_30t_14i21s	inject 14 days, soak 21 days	210	0.4	10	65

Table 4-5. Simulation results for the dense fracture model.

Case name	Case description	Total CO_2 injection, tonne	Peak oil rate, stb/d	Cumulative oil at 1-month, stb	Total time, day
HnP_LY03_30t_7i7s	30t/d half day injection for 7 days, soak 10 days	105	1.3	13	44
HnP_LY03_30t_7i14s	inject 7 days, soak 14 days	105	1.1	12	51
HnP_LY03_30t_7i21s	Inject 7 days, soak 21 days	105	1.1	12	58
HnP_LY03_30t_10i7s	inject 10 days, soak 7 days	150	1.5	14	47
HnP_LY03_30t_10i14s	inject 10 days, soak 14 days	150	1.7	14	54
HnP_LY03_30t_10i21s	inject 10 days, soak 21 days	150	1.5	14	61
HnP_LY03_30t_14i7s	inject 14 days, soak 7 days	210	1.6	15	51
HnP_LY03_30t_14i14s	inject 14 days, soak 14 days	210	1.8	14	58
HnP_LY03_30t_14i21s	inject 14 days, soak 21 days	210	1.6	14	65

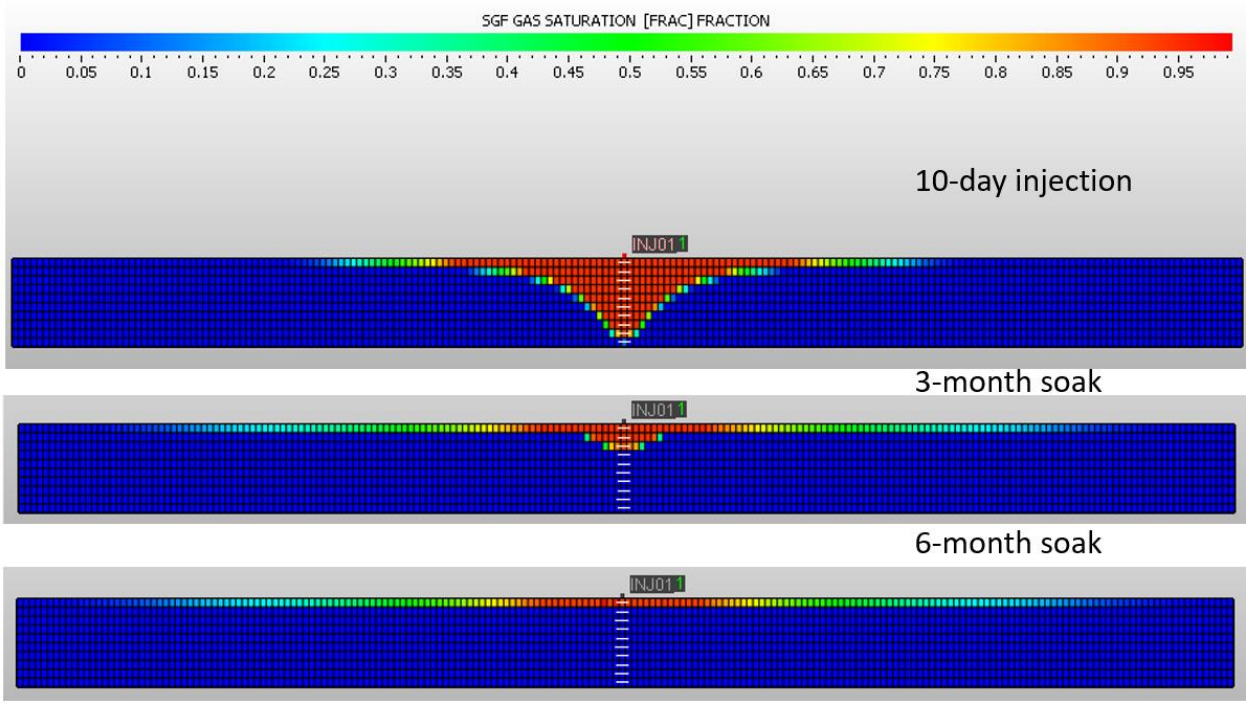


Figure 4-13. Gas saturation in fractures after 10 days of CO_2 injection and at various soak periods.

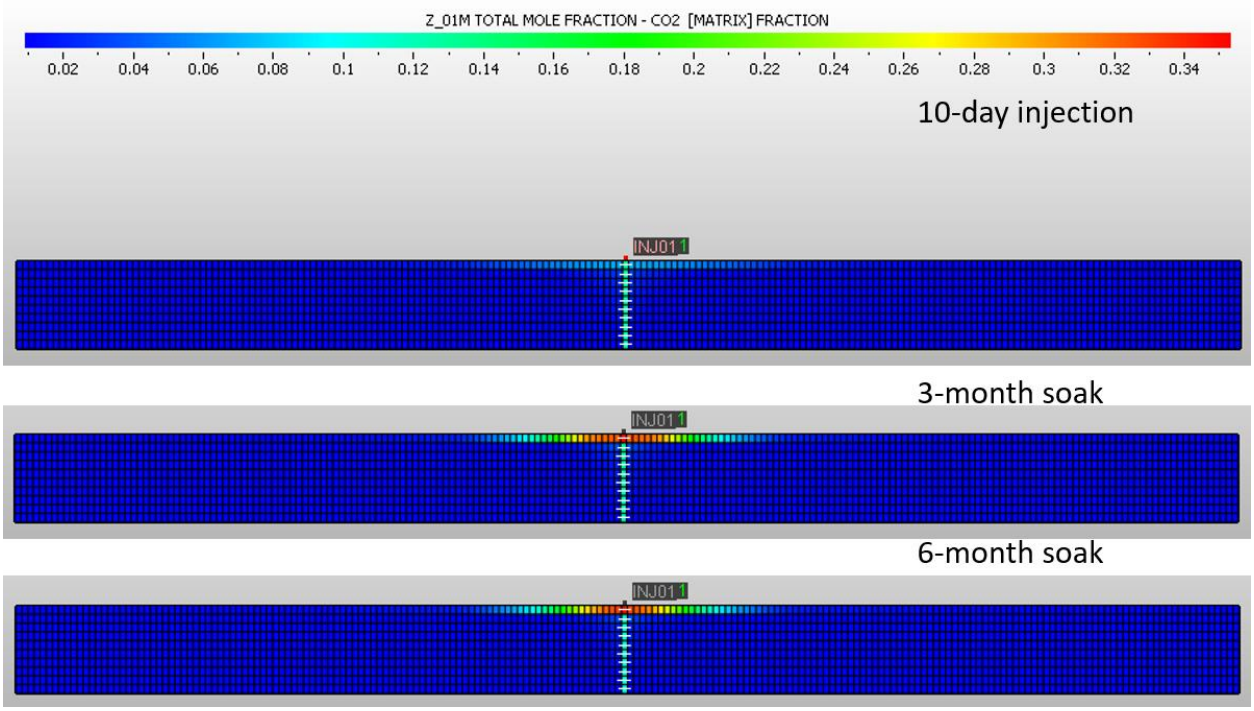


Figure 4-14. CO_2 mole fraction in matrix after 10 days of CO_2 injection and at various soak periods (CO_2 saturation was too low to show in matrix).

Simulation Conclusions

Simulations validated previous assumptions that the natural fracture network in the Carper Sandstone will exert a large control on any injection of CO_2 by providing the highest permeability conduit for flow. To meet the historical water production rate, the natural fractures were found to be two-directional vertical with a fracture spacing no greater than 3 ft in the dominant fracture direction. A sensitivity study on various injection schemes, rates, times, and soak periods suggested continuous CO_2 injection at higher rate would yield higher oil production. With the injection rate limited by pump capacity, oil production favored higher cumulative CO_2 injection. Soak period had little effect on oil production with shorter soak time being preferable. Regardless of the test design, both the peak oil rate and cumulative oil production were expected to be low (less than 2 stb/day and 20 bbls at 1-month production). The CO_2 storage in the simulated cases was minimal as most CO_2 was produced to optimize oil production.

The low permeability matrix and natural fracture network of Carper posed a significant challenge for CO_2-EOR and associated storage. Injected CO_2 consistently remained in the fractures and had limited contact with oil held within the matrix. This resulted in very low storage efficiency and oil production.

The parameters of the natural fracture exert a large influence on simulations but are highly uncertain due to lack of data. Therefore, well tests before CO_2 injection must be designed to reduce uncertainty in the natural fracture network.

Test Selection

The success of the SWCTT relies on reducing the oil saturation near the wellbore to residual saturation (to CO_2). Reservoir simulations consistently found that injected CO_2 would remain in fractures and bypass oil in the matrix. Furthermore, the added cost of the tracer tests would reduce the budget for CO_2, thus decreasing the odds of mobilizing oil per the simulations. It was also determined that residual oil saturation to water and CO_2 could be determined via core flood experiments on existing core. The uncertainty in the interaction between fracture and matrix, coupled with the added expense, means that SWCTT is less likely to succeed.

Simulations predict a HnP would not produce economic amounts of oil, but even if the reservoir is not reduced to residual saturation (to CO_2), any production would demonstrate that the oil could be produced from a siliciclastic ROZ (and a geologically problematic reservoir, at that). Results of the HnP could also be used to refine reservoir models to better understand how a larger scale test could be designed to economically produce oil. SWCTT may yield similar information, but the reduced volume of CO_2 that could be injected would reduce the chances of both oil production and CO_2 storage.

Based on these predictions, the HnP was selected as the preferred well test with the understanding that natural fractures, low permeability matrix, questionable miscibility, and low oil saturation would reduce the magnitude of oil production.

4.1.2 Field Operations

The overall objectives of the HnP were to produce oil to demonstrate the efficacy of CO_2-EOR in the Carper Greenfield ROZ and to produce data that could be used to better understand the ROZ. Core and log analyses confirmed oil saturation in the target interval, but months of pumping demonstrated the saturation to be low enough for the oil to be immobile with respect to water. Lack of nearby production meant that this oil was reduced to residual saturation naturally (i.e., a greenfield ROZ). Fluids would be produced before CO_2 injection to confirm that the reservoir did not contain mobile oil, so any oil produced after CO_2 injection could be attributed to CO_2-EOR. Reservoir simulations suggest that oil production will be minimal, so failing significant oil production, the secondary objective of the test was to produce data that could be used to refine reservoir simulations of field development.

The field test consists of six phases: Pre-Test, Pressure Transient Tests, Baseline Production, CO_2 Injection, Soak/Vent, Post CO_2 Production. Each phase contains design, equipment, operations, and findings subsections.

- Design covers the objectives and expected operations and outcomes of each phase based on the information available at the time (before the phase was conducted).
- Equipment subsections provide details of the equipment used during the phase.
- Operations covers the equipment used, field work, and data acquired. Ideally this would follow the design exactly, but unexpected complications commonly required alterations during the operation phase.
- The description of each phase concludes with an analysis of the data and a description of how the findings altered the design of the next phase.

Summary

Pre-test activities determined that the reservoir had pressure and temperature sufficient to ensure a miscible CO_2 test and uncovered evidence that the Carper may be naturally fractured. The bottom of the wellbore was also found to be filled with sand, which required the pump to be placed above the perforations rather than below as originally designed. The pressure transient tests confirmed that the Carper contained an extensive fracture network. Baseline production yielded 5,000 bbls of water with no oil, validating no mobile oil in the presence of water in the reservoir. Approximately 1,000 tons of CO_2 were successfully injected over a 25-day period. A four-week soak period, followed by four weeks of venting vapor CO_2, and six weeks flowing fluids were required before the pump could be turned on for post-CO_2 production. Post-CO_2 production continued for approximately five months. A total of approximately 60 bbls of oil and 350 tons of CO_2 were produced.

Both test objectives were met. Both oil production and CO_2 storage significantly outperformed simulated scenarios and field operations produced data (oil, water, and CO_2 production rates, and oil and gas samples) that were used to improve our understanding of the rock and fluid properties of the Carper ROZ.

Table 4-6. Summary of field activities.

Phase	Subphase	Date	Summary
Pre-Test Characterization		2/28/2020—9/2/2020	Found evidence that Carper contains a natural fracture network and is above MMP for CO_2 test
Pressure Transient Tests		9/3/2020-10/6/2020	Confirmed existence of extensive fracture network
Baseline Production		10/16/2020-11/09/2020	Produced 5,000 bbls water, 0 bbls oil. Confirmed immobile oil
CO_2 injection		11/13/2020-12/13/2020	Injected 1,000 tons CO_2
Soak/Vent	Soak	12/13/2020-12/22/2020	One week soak
	Vent	1/15/2021-2/12/2021	Vented 150 tons of CO_2 to pull fluids into well
Post CO_2 Production	Flow	3/2/2021-4/15/2021	Vented 100 tons CO_2 and naturally flowed 1,600-2,500 bbls of fluid to surface to establish stable fluid level above pump
	Pump 1	4/21/2021-5/18/2021	Produced 60 tons CO_2, 5,100-7,500 bbls water, and 24 bbls oil
	Pump 2	6/10/2021-9/27/2021	Produced 60 tons CO_2, 14,000-25,000 bbls water, and 23 bbls oil

Pre-Test

Design

Pre-test activities involved taking inventory of what was on site, moving equipment on site, and compiling and analyzing all available data.

Operations

Preliminary reconnaissance of the Greenfield site was conducted on February 28, 2020. The site consists of the Holsapple 2B (test) well, the Holsapple 1B (disposal) well, and a pad and berm for the tank battery (Figure 4-15). At the time of the initial inspection, there were no tanks set up, and both wells were capped, but underground electrical lines and flow lines were in place.



Figure 4-15. Map of the field site showing the location of the tank battery, disposal well and test well.

In July 2020, 3 210 bbl fiberglass tanks (two for brine storage and one for oil storage) and a 5-foot by 20-foot gunbarrel oil/water separator were setup and the firewall surrounding them was repaired. In August 2020, work began to prepare the wells for testing. The wellhead was equipped with an Echometer Well Analyzer and a wireline was run in the well with a PPS 58 pressure/temperature gauge. The Echometer determined that the depth of the pre-test static fluid level was at 330 ft (GL). The wireline tagged the fluid at 367 ft (GL) (3,321 ft above perforations).

Wireline tagged TD at 3,720 ft (KB), (243 ft above the reported PBTD). The cable head was covered with sand when it was pulled up, so it was believed that the lower 243 ft of the wellbore filled with sand after the well was shut in. The PPS 58 wireline gauge was positioned at top perforation depth 3,688 ft (KB) and a T-bar was installed. Pressure at the perforation depth was 1,591 psia and temperature was 45.8 °C (114.5 °F). Both pressure and temperature were higher than expected and suggest that injected CO_2 will maintain miscibility.

Capillary Suction Time Test

Capillary suction time (CST) tests were conducted to investigate the sensitivity of the clay-containing formations. CST testing defines the time to move a water front between two electrodes, which is related to the ability of the fluid to flocculate or disperse clays in a sample. A Carper Sandstone core sample was used in the test to see if fresh water could be injected as part of the Pressure Transient Test without lowering the permeability of the formation due to shocking the clay cements The results demonstrated that, while the fresh (DI) water did have an impact (lengthening the time, thus indicating some clay dispersion), there was not an appreciable difference when compared to formation brine (Table 4-7).

Table 4-7. Results of the capillary suction tests.

Fluid	Time (base fluid; seconds)	Time (Carper slurry; seconds)	CST Ratio*
Di Water	15.4	28.9	0.87
Formation Brine	12.4	26.5	1.14
2% KCL	11.2	23.2	1.08

Updated Production Data

Only the final two months of production data were initially available from the operator that showed that the reservoir was able to produce ~200 bbls of fluid per day. This rate was much more than the core-derived permeability could produce and indicated that a natural fracture network may be present. The rest of the production data (first 5 months) was made available from the operator before field work began. The complete data shows that the well produced up to 400-600 bbls of fluid per day in the weeks following the initial completion (Figure 4-16).

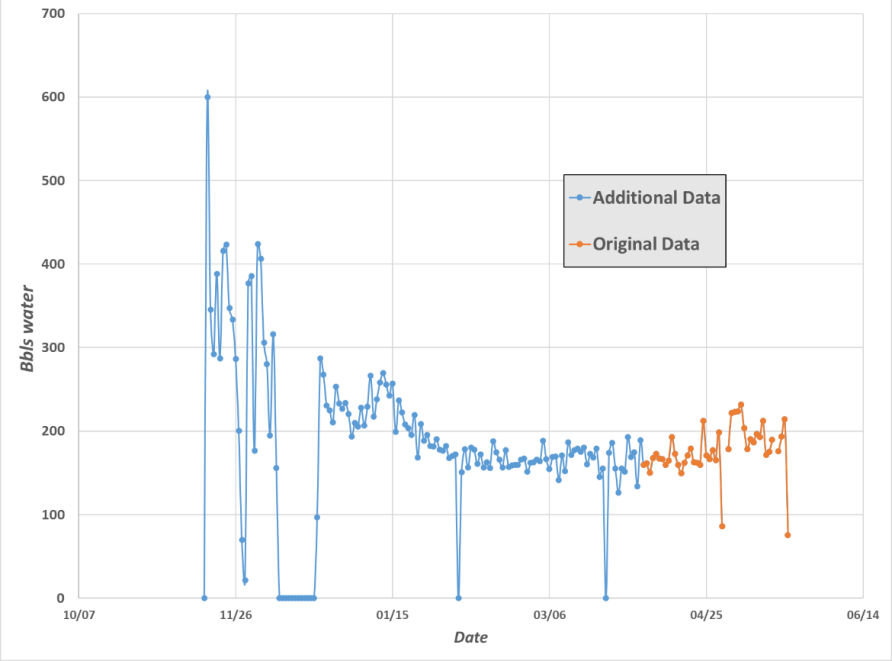


Figure 4-16. Complete historical production immediately after the well was completed in November 2016 until it was shut in in May 2017.

Findings

The pre-test activities yielded information that significantly altered the understanding of the Carper. The bottom hole pressure, temperature, and associated fluid level were much higher than previously reported. The higher pressure suggests that the test will be under miscible conditions, which will dramatically increase the odds of oil recovery. Furthermore, the higher reservoir temperature shifts the calculated R_W from 0.074 ohm-m to 0.062 ohm-m. This lower R_W results in higher log derived S_O. However, the shallow TD of the well resulting from the fill in the wellbore was a source of concern because the optimal placement of the pump would be below the perforations.

The more complete production history has two important ramifications. The high production rate observed soon after the well was completed suggests that the natural fracture network of the reservoir is more extensive than expected. Reservoir simulations concluded that the 15-foot perforated interval would need an effective permeability two orders of magnitude greater than the permeability observed in the core to produce 200 bbls/day (~20 mD as opposed to 0.2 mD). The properties of the matrix were well constrained by core, so this higher apparent permeability would come from a more extensive fracture network.

The high production rate also provides evidence of well behavior during draw-down. A rate over ~350 bbls/day could draw the well down to an untenable level, but the well was able to maintain a pumping rate of ~200 bbls/day while maintaining fluid level (based on pressure readings from the submersible pump that was used indicating a few hundred feet of fluid above the pump intake). Therefore, the baseline production phase was designed to produce fluids at 350 bbls/day until the well showed signs of being drawn down, at which time the rate would be reduced to 200 bbls/day to keep fluid above the pump.

In summary, the pre-test activities' observations are as follows:

- The Carper current reservoir pressure is above MMP; the HnP is likely to be miscible.
- The lower portion of the well is filled with sand.
- Fresh water could be used for injection testing without reacting with the Carper Sandstone.
- More complete production history bolstered the idea of a natural fracture network but suggested that it was more extensive than previously thought.
- 200 bbls/day is a good pumping rate to limit the drawdown of the well.

Pressure Transient Test

Design

The objective of the pressure transient test is to reduce uncertainty in the properties of the target interval to optimize the design of the HnP. Generally, a pressure transient test is generally designed to estimate the productive effective permeability and net thickness, but the apparent disagreement between fluid production projections from flow simulations using core derived permeability and historical fluid production rates indicated the presence of a natural fracture network within the target interval. A natural fracture network is expected to strongly influence the fate and transport of injected CO_2, so the pressure transient test was designed to confirm the existence of the natural fracture network, determine the extent of its influence within the reservoir, and determine if the fracture network was allowing communication between sandstone bodies.

Data available to design the pressure transient tests were core permeability and porosity, well log porosity and thickness, two months of production records (from 2017), completion information (perforation and casing), a fluid level measurement acquired during pre-test characterization, and a conceptual framework of the regional geology. Reservoir simulation using the core data and production records estimated that permeability 10 times greater than core analyses permeability was required to match the observed historical fluid production. Discussions with Illinois Basin operators with Carper production confirmed inferences that the formation was naturally fractured, which could be the reason the production-based estimate of permeability via simulation was much higher than core permeability (Table 4-2).

To reduce costs, the pressure transient tests were designed to use the 5.5" well casing (not smaller diameter tubing and packer) and with available ISGS low-rate triplex pumps. Use of casing instead of tubing and packer increases period in which wellbore storage could dominate the pressure response of the reservoir and cause

the test to fail in terms of undetectable very early reservoir response. The maximum rate on the ISGS pumps was projected to meet most injection test requirements unless fracture pressure or permeability was higher than expected. If the tests failed, a loss of 2-4 days was projected, but the cost was minimal, so tubing could be installed, and larger pumps could be acquired and used if necessary.

The design of the pressure transient test has two components: injection parameters (water injection rate, total volume injected, and injection duration) and data acquisition (data required for interpretation). Injection parameters were selected to create a measurable pressure response given the properties of the reservoir. Because the objective of the test was to detect a natural fracture network, there was a focus on minimizing the wellbore storage effect. Minimal water injection was assumed based on the low core permeability, but high historical water production indicated that a much higher rate would be necessary to create a measurable pressure response. It was determined that an injection rate of approximately 6 gallons per minute (GPM) would be adequate to create the necessary pressure response. To reduce costs, the preliminary pressure transient test was designed to be conducted using city water from a nearby house, the two-210 bbl tanks at the Holsapple tank battery for water storage, and a buried flowline to move water from the tanks to the well. If this was determined to be ineffective, larger tanks would be brought to the site and another test, with a higher injection rate, would be conducted.

Pre-test activities included a fluid level shot using an Echometer. The shot indicated fluid level was about 400 ft from surface which gave a calculated pressure (1591 psia) close to that of the freshwater gradient (1,600 psia). Ideal injection tests start with the test liquid to surface; however, this can only be done with lower density fluid, which in this case was freshwater. Therefore, water was continuously added to the test well in small increments to allow the freshwater to slowly displace the brine from the wellbore and fill up to surface.

Injection test planned: The injection test plan, in chronological order as step rate test, mini-frac test, multi-rate test, and pressure falloff test. The **step-rate test was designed** to determine fracture pressure. It was designed to reach fracture pressure by injecting up to 3-4 GPM. At a depth of 3,688 ft, the fracture pressure was projected to be 2,950 to 3,320 psi based on fracture gradient of 0.8 to 0.9 psi/ft. Surface pressure up to 2,000 psia would be needed to have step rate test data above the fracture pressure.

The **mini-frac test** was planned to validate the fracture pressure from the step-rate test and estimate fracture closure pressure. The mini frac test is a constant rate test chosen to exceed the fracture pressure during the test. The constant rate would be selected based on the step rate test results.

Depending on the results of the step rate test prior to reaching fracture pressure, a **multi-rate, steady-state test**, a series of constant rate injection periods with the intent of establishing steady state, would be added to enable the calculation of permeability from each constant rate injection period.

A long duration **pressure falloff test** was planned to have a 7-10 day constant rate injection period, followed by a 10-14 day shut-in period. The pressure falloff test provides data to calculate permeability and identify large-scale geologic features that may influence the relationship between bottomhole injection pressure and rate.

Operations

Water injection was facilitated by a pair of triplex (three plunger rods) positive displacement, reciprocating, plunger pumps; a CAT 230 (capable of 2.3 GPM and 1,500 PSI) and a CAT 760 (capable of 3.6 GPM and 5,000 PSI). Both pumps were required to deliver the approximately 6 GPM flow rate in the test design specifications.

Immediately prior to conducting the step rate test, surface pressure was approximately zero psi and freshwater (test fluid) was near surface (<40 ft). The first rate of the step rate test was planned for 0.4 GPM for 5 to 10 mins and expected to increase pressure 75-150 psi. However, the first rate did not increase pressure appreciably (<5 psi). Similarly, subsequent rate changes realized very little pressure increase, and it became obvious that there was either much higher permeability, extensive natural fracture system and/or lengthy hydraulic fracture. Because it was obvious inadequate pressure could be attained with up to 4 GPM estimating fracture pressure was no longer possible and focus shifted to constant rate injection falloff and multi-rate, steady-state tests. Below is a summary of the tests that were performed:

- Multi-rate, steady state tests over four rates of 20 mins and 24-hour duration. Several short term (<8 hrs) were injected for overnight falloff tests before starting a 7 day injection period and 14 day shut-in.
- A long-term falloff test was conducted for about 20 days.

Pressure Transient Analyses

The injection test consisted of four injection periods separated by and ending with shut-in periods (Figure 4-17). The first three shut-in periods were analyzed using derivative analyses; the 4th and final shut-in was not analyzable due to pressure disturbance attributable to a leak from the wellhead. Qualitatively, the derivative plot (Figure 4-18) showed the very characteristic trend of hydraulic fracture, a positive ½ slope, that dominated nearly the entirety of the shut-in periods. Consequently, the derivative plot showed no indications of natural fractures. Similarly, there was no evidence of radial composite effect found from injecting fresh water into an oil reservoir that has differing fluid viscosity and/or compressibility (oil and brine).

Analyses of the derivative plots of the three analyzable shut-in periods gave hydraulic fracture half lengths of 500 to 650 ft, and horizontal permeability estimates from 8.2 to 9.7 mD. The initial pressure estimate is 1588 psia, which is 23 psia less than the pressure used for pre-test reservoir simulations based on the freshwater gradient (Table 4-1).

Compared to the permeability from core, the higher permeability from derivative analyses inferred another source of permeability, e.g., natural fractures.

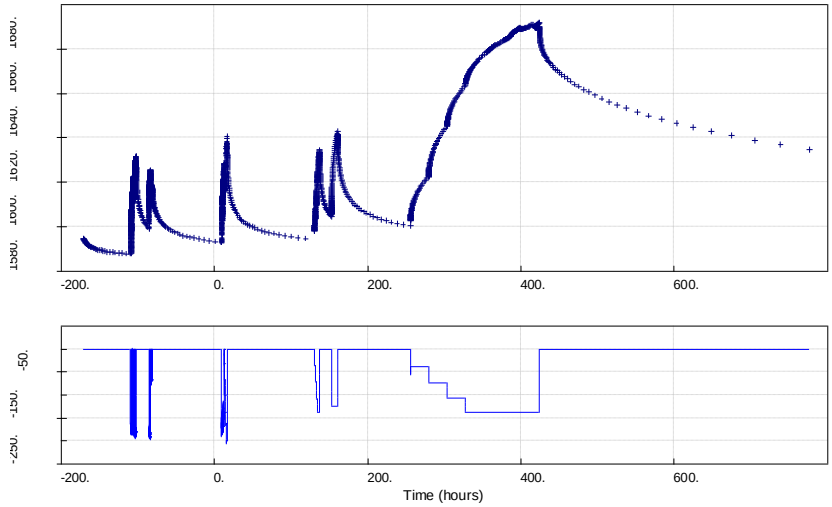


Figure 4-17. Injection pressure and rates for pressure transient testing with freshwater. Four injection periods separated by shut-in periods. Final shut-in was not analyzable due to an unknown pressure disturbance in the wellbore, most likely due to a wellhead leak.

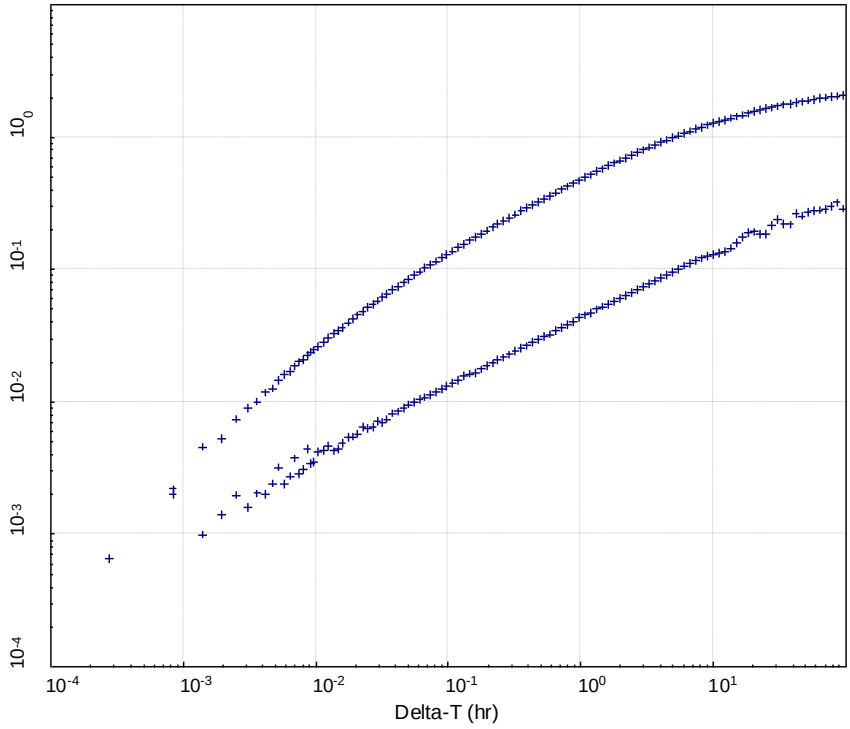


Figure 4-18. Derivative of 3rd shut-in period. Positive ½ slope indicative of linear flow from the hydraulic fracture. Horizonal derivative indicative of radial flow developing near end of shut-in period (>80 hrs) was used to estimate horizontal permeability.

Disposal Well Test

An additional pressure transient test was conducted on the disposal well to validate that the produced water from the upcoming Baseline Production and Huff and Puff tests could be injected into the disposal well at the anticipated rate (up to 400 bbls/day). Analyses of the pressure falloff tests of the disposal well determined that the disposal well had adequate injectivity.

Baseline Production Phase

Design

The goals of the Baseline Production Phase were twofold; 1) To understand how pumping draws down the well, and 2) to provide oil-free production data against which to compare Post-CO_2 Production. Based on the historical behavior of the well, the test was designed to begin production at a rate of approximately 350 bbls/day and reduce to ~200 bbls/day if Echometer derived fluid level approached 2,500 ft below surface. The Baseline Production Phase was planned to last for one month, during which time pumping rate, fluid level, bottom hole pressure (BHP), total fluid production, water production, and oil production would be measured and recorded for analysis. Once production concluded, the well would be shut in to allow the reservoir to repressurize to MMP (approximately 1,250 psi) before starting CO_2 injection.

Equipment

Fluid was produced by a variable speed pumping unit and downhole rod pump capable of 200 to 350 bbls/day fluid throughput. Downhole equipment was deployed according to the wellbore schematic (Figure 4-19). 114 joints (plus 8’ and 4’ pup joints) of 2-7/8” J-55 6.5 lb/ft EUE tubing were used, and a

Spirit Hybrid-X Downhole Gas/sand/solids separator was installed to prevent sand grains from entering and destroying the pump. The standing valve and 4’ Standard Steel Downhole Pump Assembly (25-225-THC12-4-2-3) was deployed with a 2’ X 7/8” rod sub, 11 x 1.5” sinker bars, 128 x 7/8” rods, and 8’, 6’, and 2’ 7/8” rod subs. A 22’ 1-1/4” polished rod (33-300C622) with 10’ liner (20-405K212) was made up and connected to the bridle. A Lufkin Morgan 228-246-86 pump base (set to long 86” stroke) was set up and driven by 3-phase 25 HP electric motor, with a 7 C drive sheave.

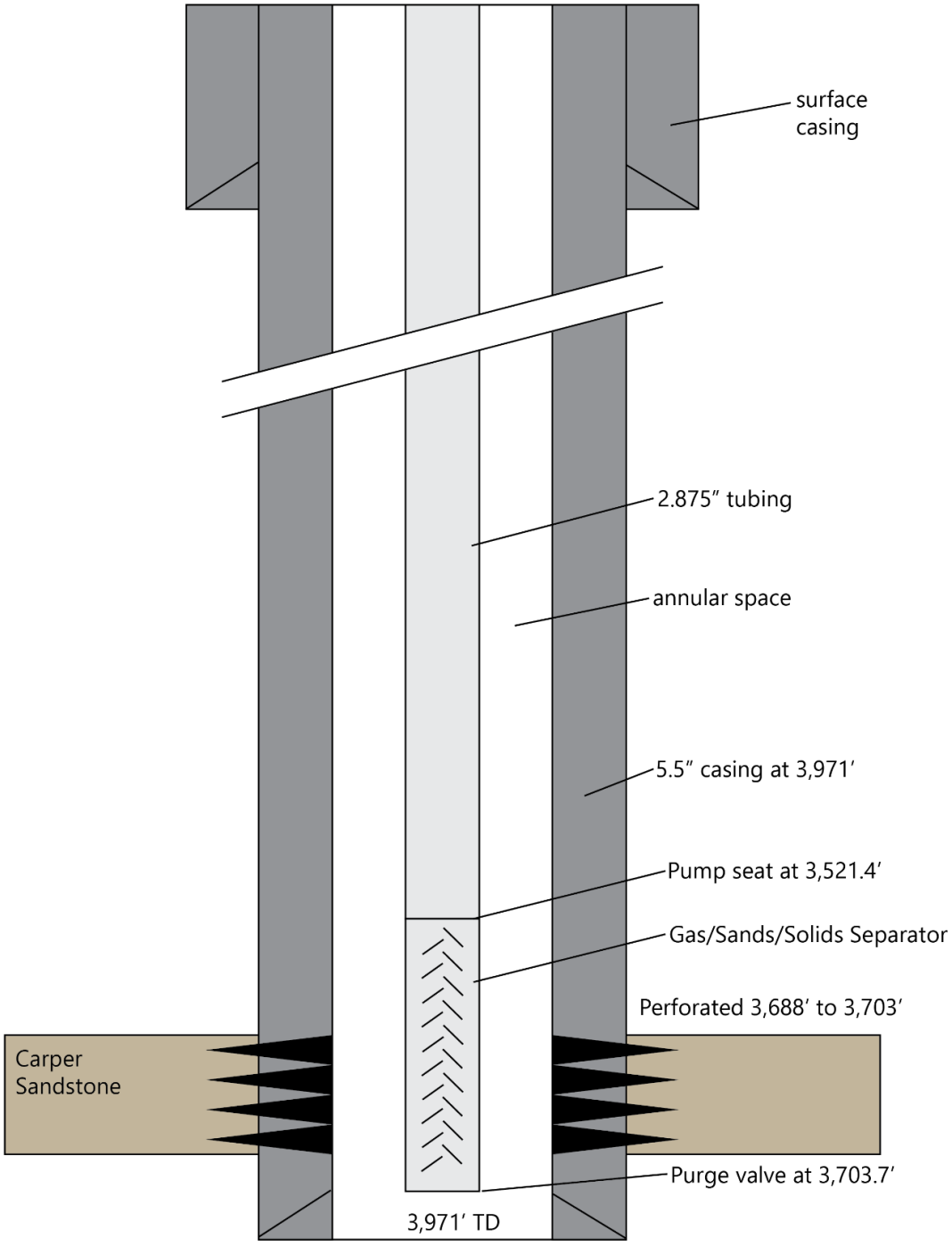


Figure 4-19. Wellbore schematic of the Holsapple 2B well.

Produced fluid would flow through a buried fiberglass flowline to the tank battery and into the gunbarrel separator which would partition the water and oil for storage in the 210 bbl tanks. One of the brine tanks was fitted with three float switches; 10 feet from the base to activate a pump to drain the tank to the disposal well, 4 feet from the base to shut down the disposal pump to prevent air from entering the pump, and 12 feet from the base to shut down the pumping unit to prevent overflow in case the disposal well did not activate or if its pumping rate was not enough to keep up with production. The water that would remain in the base of both tanks and the void space above the shutoff switch reduced the working brine storage capacity from 420 bbls (two 210 bbl tanks) to approximately 225 bbls.

Produced fluids were metered at three locations; a turbine meter upstream of the gunbarrel separator measured total fluids produced, an ultrasonic meter with two transducers between the gunbarrel tank and the oil and water tanks measured oil and water individually, and a turbine flowmeter between the brine tanks and the disposal well measured disposed fluids.

The Echometer installed during the pressure transient tests was used to track fluid level (from which BHP can be calculated), pressure, temperature, and acoustic velocity for the duration of baseline production.

Throughout the different stages of project operations, an enclosed trailer was on site to house data logging equipment and other tools and small equipment needed to support operations. Due to the remote location of the Holsapple-2B well, internet connectivity was established first to allow remote monitoring and data backup. Connectivity was addressed by setting up a cell signal booster tower which was used in conjunction with an Android cellphone (later replaced by a more robust Verizon Nighthawk M5 5G WiFi 6 Mobile Router) serving as an internet hot spot. A Wi-Fi router was used to bring all computers and data logging equipment online.

A Campbell Scientific CR1000 data logger was set up as a central hub. This CR1000 was equipped with a receiving antenna and a suite of signal conditioning electronics to allow other data loggers to connect to the hub. The hub received data from sensors equipped on the Holsapple 2B well, the Holsapple 1B disposal well, as the CO_2 injection pump skid, and the tank battery. Each location had a CR1000 data logger that logged the local data and transmitted it to the main hub. The main hub data logger was connected to a desktop PC and accessed via Loggernet software to view and graph live data and create backups. CloudBerry Remote Assistant software was used to connect to the PC remotely.

Each data logger had an onboard memory card to store data, all the data sent to the hub was backed up on the PC and synced to cloud storage. This redundancy minimized data loss which became an issue as memory cards would fail due to ambient heat and humidity.

The trailer also housed a second PC that was dedicated to controlling the Echometer device attached to well. The PC logged all the Echometer data using Echometer's Total Well Management software and could be remotely accessed via CloudBerry software. At the tank battery, Campbell Scientific enclosures were used to house the Flexim FLUXUS F608 ultrasonic flow meter and a laptop PC that was connected back to the router in the trailer via 300 ft of ethernet cable. This PC was used in conjunction with the Flexim unit to data log oil and brine flow rates at the tank battery (laptop data was logged, backed up the data using a custom script and allowed for remote access to view data real time using same software mentioned above).

The trailer was connected to 120V shore power at the wellhead. All systems in the trailer had backup power sources as well; The main PC was connected to an APC Back-UPS Pro 700, CR1000 data logger hub

and the Echometer system had a marine 12V battery backup. A Milwaukee fan was used to keep all above electronics cool during hot weather.

Table 4-8. Baseline data acquisition equipment.

Location	Data stream	Unit
Wellhead	BHP and fluid level	Echometer
	WH pressure, flow rate, Annulus pressure	NuFlo MC-11 Plus flow meters, Siemens Sitrans P pressure transmitters and BDC thermocouple temperature sensors
Pump skid	Pressure, temperature	Siemens Sitrans P pressure transmitters and BDC thermocouple temperature sensors
Upstream of tank battery	Total fluid production rate	Omega 2" FTB-1441
Tank battery	Oil and water production rate	Flexim G601 with two transducers between gunbarrel and oil/water tanks
Between water tank and disposal well	Water disposal rate	Omega 1" FTB-1425

Operations

The Baseline Production Phase began on October 8th when an attempt was made to remove the sand from the wellbore. A sand pump ran four runs with good recovery followed by six with very little sand recovery. The final sand tag was 3,733' below Kelly Bushing, which was still approximately 200' above the PBTD recorded when the well was drilled (3,970'). Due to budgetary constraints, it was decided to use the sand separator and spot the pump above perforations.

Baseline production was conducted from Friday, October 16th until Monday, November 9th. Production began production at 7 strokes/minute which yielded a production rate of approximately 350 bbls/day. Production was stopped twice; First to limit fluid drawdown on Monday, October 26th and again on Tuesday, October 29th because of a power outage.

Findings

The Baseline Production phase met both of its goals. Twenty-five days of production resulted in over 5,000 bbls of water produced with no observed oil, confirming that the oil in the Carper is not mobile. It was also established that pumping at approximately 350 bbls/day would draw down fluid level. These findings matched expectations, so the design of the CO_2 Injection phase did not change.

There was good agreement between both turbine meters and the ultrasonic meter. Total fluids produced, produced water, and disposed water all showed a total of over 5,000 bbls of water were produced with no oil (Figure 4-20). The agreement between ultrasonic and produced turbine data suggests that both meters were working properly. The slightly lower volume of disposed water was greater than the on-site brine storage capacity and may suggest that the brine disposal meter was underestimating volume.

The Echometer derived fluid level and BHP also behaved as expected (Figure 4-21). The Echometer did run out of nitrogen on three occasions, but data gaps caused by these outages occurred in non-critical times and the missing data could be inferred. BHP was tracked after baseline concluded and reached MMP on November 16th.

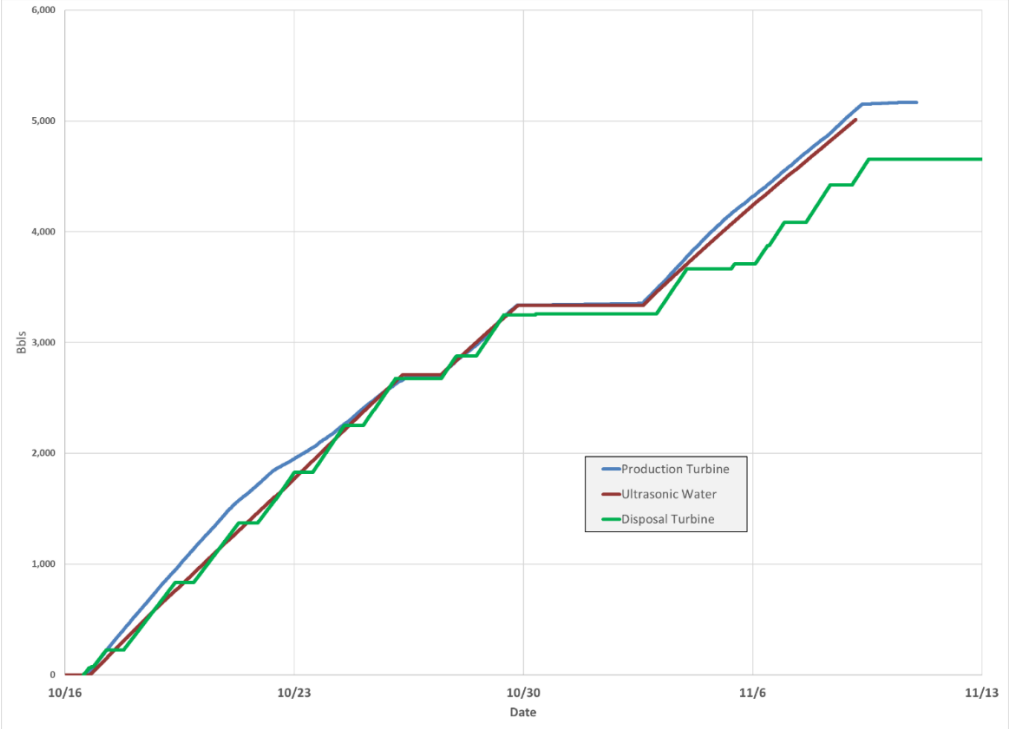


Figure 4-20. Cumulative water produced as measured by the production turbine meter (blue line), ultrasonic water meter (red line), and disposal turbine meter (green line). Production turbine and ultrasonic data both show that ~5,000 bbls of water was produced. The lower volume of the disposal meter (~4,700 bbls) is believed to represent the storage capacity of the brine tanks.

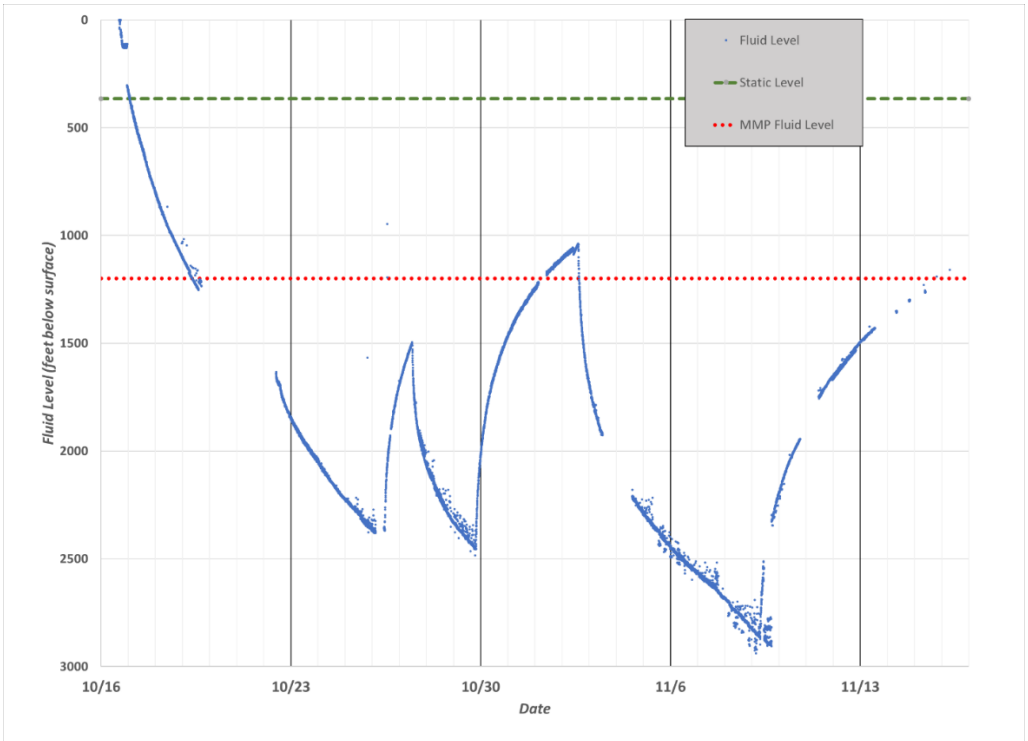


Figure 4-21. Echometer derived fluid level and bottom hole pressure over the course of Baseline Production.

Pre-CO_2 Injection Reservoir Simulations

The reservoir model was calibrated to both pressure transient tests (water injection test and step rate test) by adjusting fracture properties. The step rate test showed hydraulic fracture dominated flow, so a hydraulic fracture was added to the reservoir model using 1 ft wide cells along the well with increased permeability that mimics a hydraulic fracture. However, the property set that matched bottomhole pressure to that of water injection test (Figure 4-22) could not match that of the step rate test (Figure 4-23). Possible reasons for low pressure increase in the step rate test could be leaking to other zones or extended hydraulic fracture half lengths. The dense natural fracture model developed during pre-test simulations created a significant reduction in pressure buildup once the hydraulic fracture was imposed, so the updated coarse natural fracture model was believed to be more representative and used for simulations going forward.

The reservoir model was then adjusted to match pressure data from Baseline Production (Figure 4-21) by varying hydraulic fracture half length, hydraulic fracture permeability, natural fracture spacing, and natural fracture effective permeability (Figure 4-24). The resulting model has a hydraulic fracture with a half-length of 511 ft and a permeability of 8,000 mD, and the natural fracture spacing is 150 ft in X direction and 3 ft in Y direction with an effective permeability of 12 mD. The maximum relative permeability to water is 0.35.

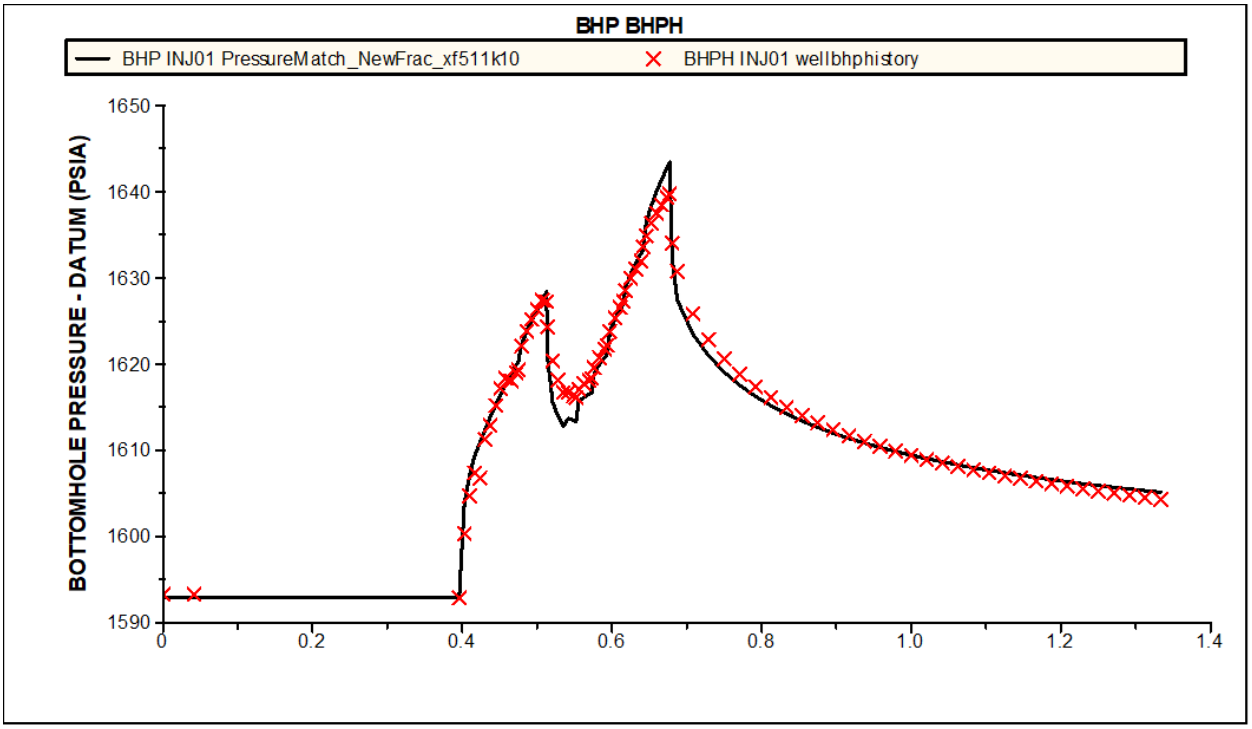


Figure 4-22. Simulated bottomhole pressure (black line) to match that of water injection test (red cross) by adding a hydraulic fracture with a half-length of 511 ft and a permeability of 8,000 mD.

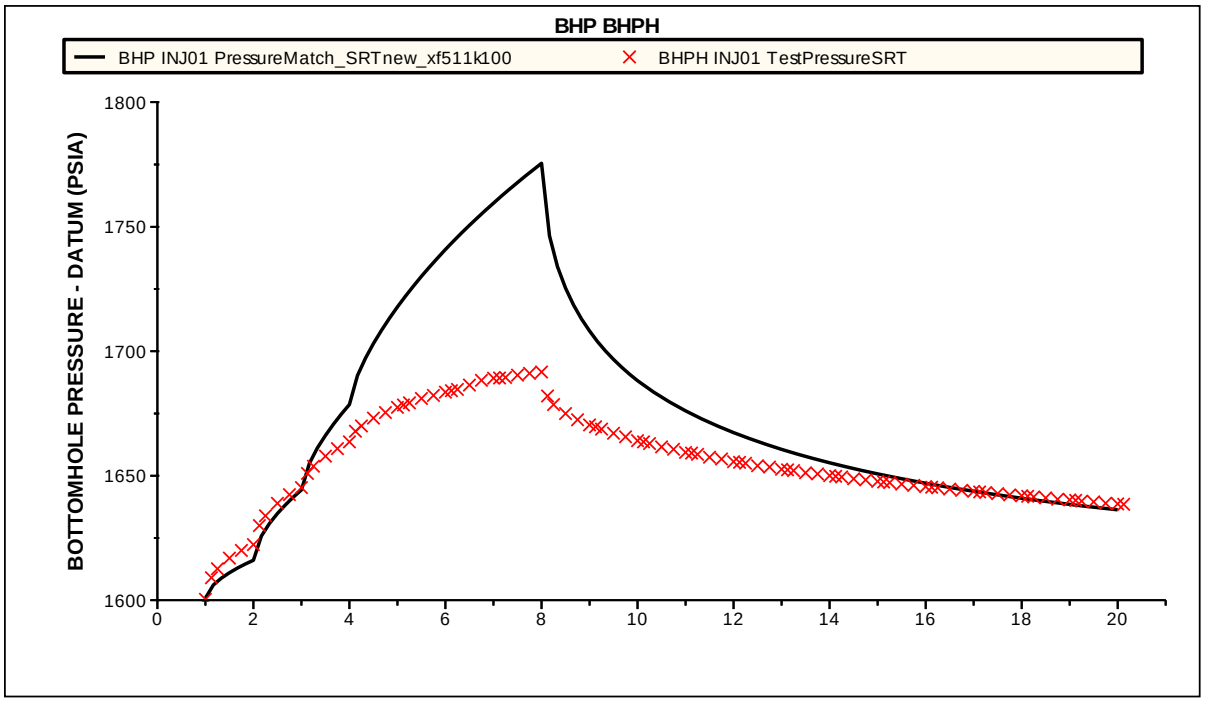


Figure 4-23. Simulated bottomhole pressure (black line) attempting to match that of step rate test (red crosses) by adding a hydraulic fracture with a half-length of 511 ft and a permeability of 8,000 mD.

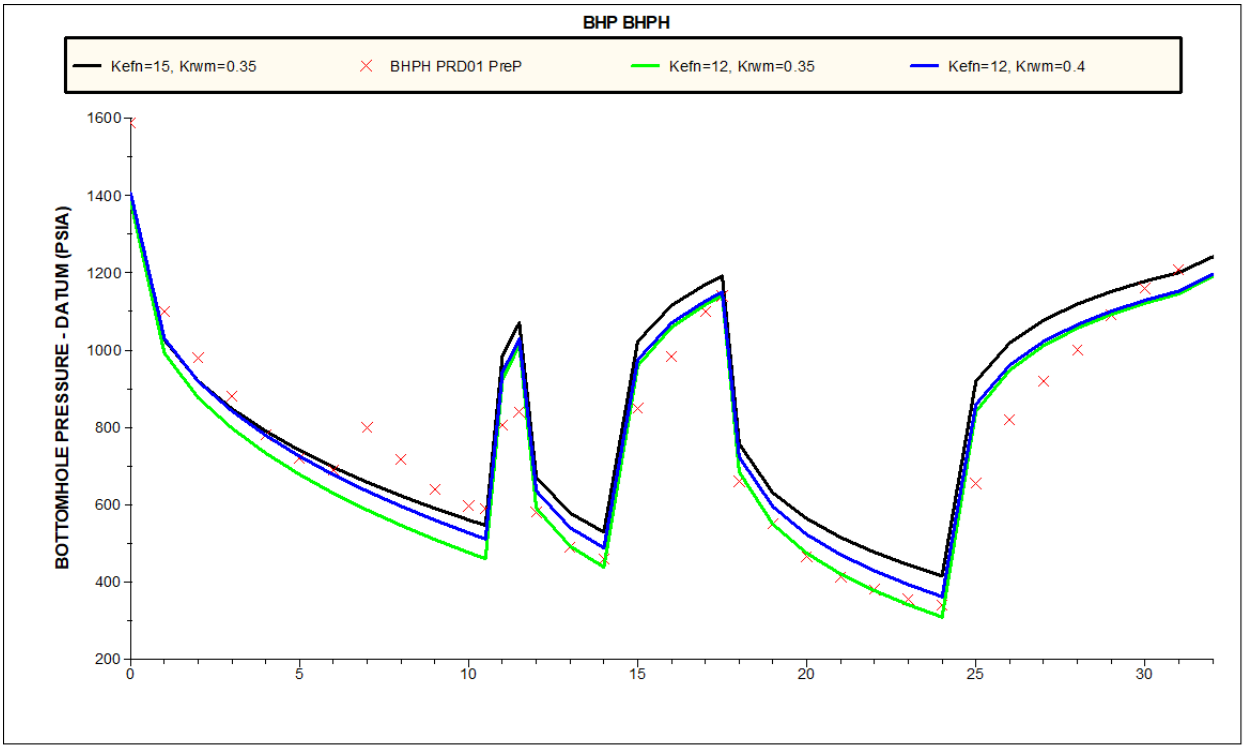


Figure 4-24. Simulated bottomhole pressure (solid lines) matched that of baseline production test (red cross). Blue, black, and green lines are reservoir simulations with various permeabilities (Black: khf = 8,000mD, kefn = 15mD, krwmax=0.35; Green = khf = 8,000 mD, kefn = 12mD, krwmax=0.35; Blue: khf = 8000 mD, kefn= 12 mD, krwmax=0.4).

Once the model was tuned to produce a reasonable history match, CO_2 injection scenarios were conducted. These simulations were run concurrently with CO_2 injection and used to better understand how the soak and production parameters would impact oil production.

Two cases were simulated with an initial reservoir pressure of 1,270 psi. Fluid level was measured by the Echometer at 1,000 feet below surface (2,688 ft fluid column above perforations) on February 11th, 2020. This fluid column height gives a calculated reservoir pressure of 1,270 psi. The CO_2 was injected at 40 tons/day for 25 days, then soaked for 7 or 14 days, and then produced for 1 month constrained by a total fluid production rate of 280 stb/d. Table 4-9 lists the predicted oil performance with different soak periods. The shorter 7-day soak period yields slightly better oil performance in terms of both cumulative oil production and peak oil rate (Table 4-9 and Figure 4-25).

About 64% of the injected CO_2 was produced after 1 month of production for the 7-day soak case (Figure 4-26). The CO_2 storage for the 14-day soak case was comparable. Visual examination of the modeled distribution of CO_2 and oil in the matrix and fractures shows that CO_2 stayed in fractures and had limited contact with oil in the matrix (Figure 4-27), suggesting fracture dominated flow. This is in line with published observations in which fractures would dominate flow when the matrix permeability is less than 1 mD and the fracture-matrix permeability ratio is above 10,000 (Matthai and Belayneh, 2004).

Table 4-9. Simulated oil production performance as a function of soak time.

Soak Period (days)	**Cumulative oil at 1 month (stb)**	**Peak oil rate (stb/d)**	**Peak oil time (day of production)**
7	13	1.6	5
14	12	1.5	4

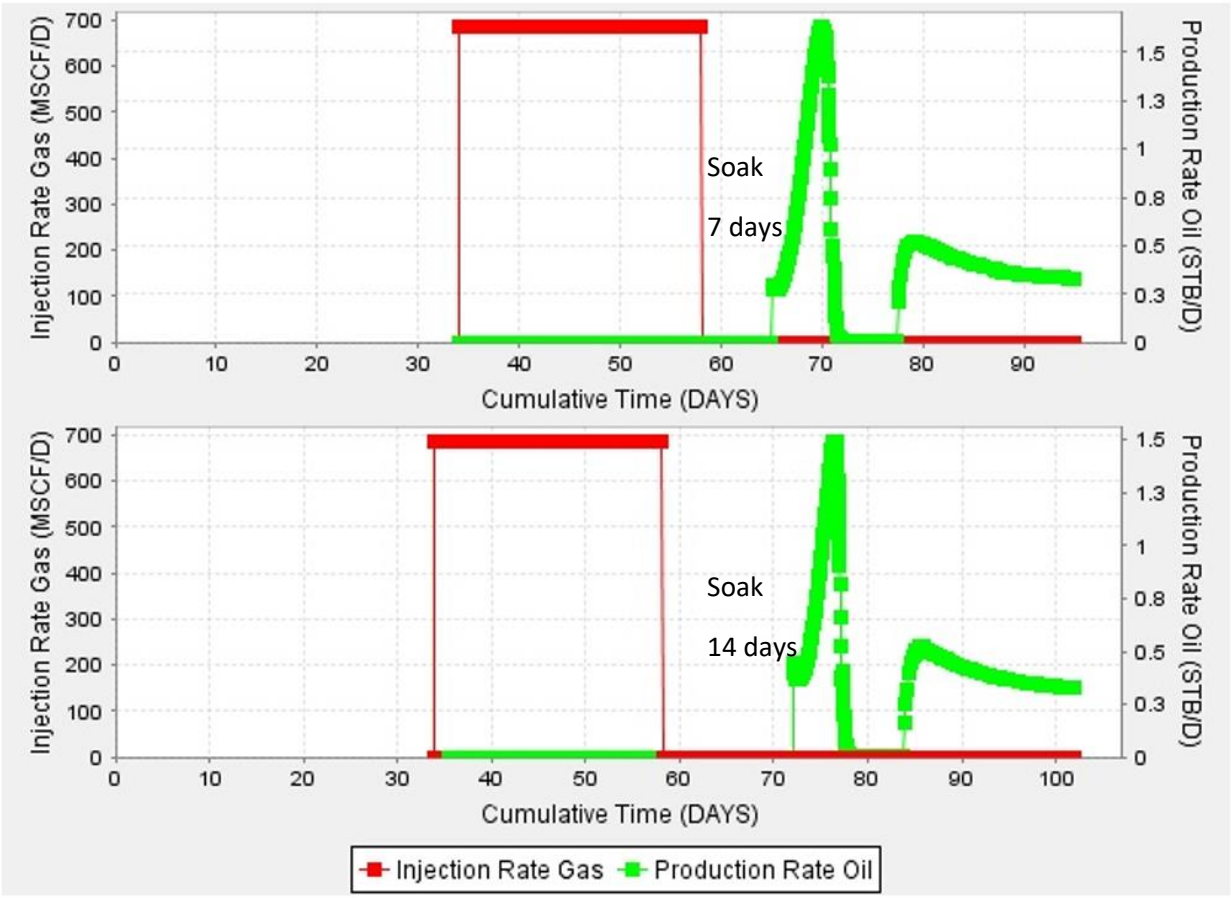


Figure 4-25. Oil rate vs time at various soak periods.

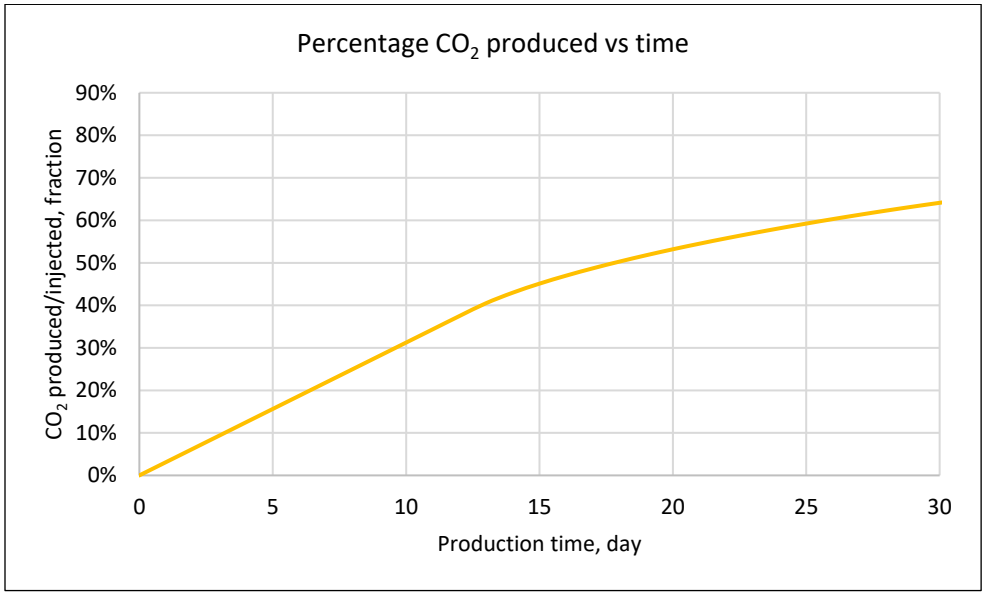


Figure 4-26. Produced CO_2 as a percentage of injected CO_2 vs time for the 7-day soak case.

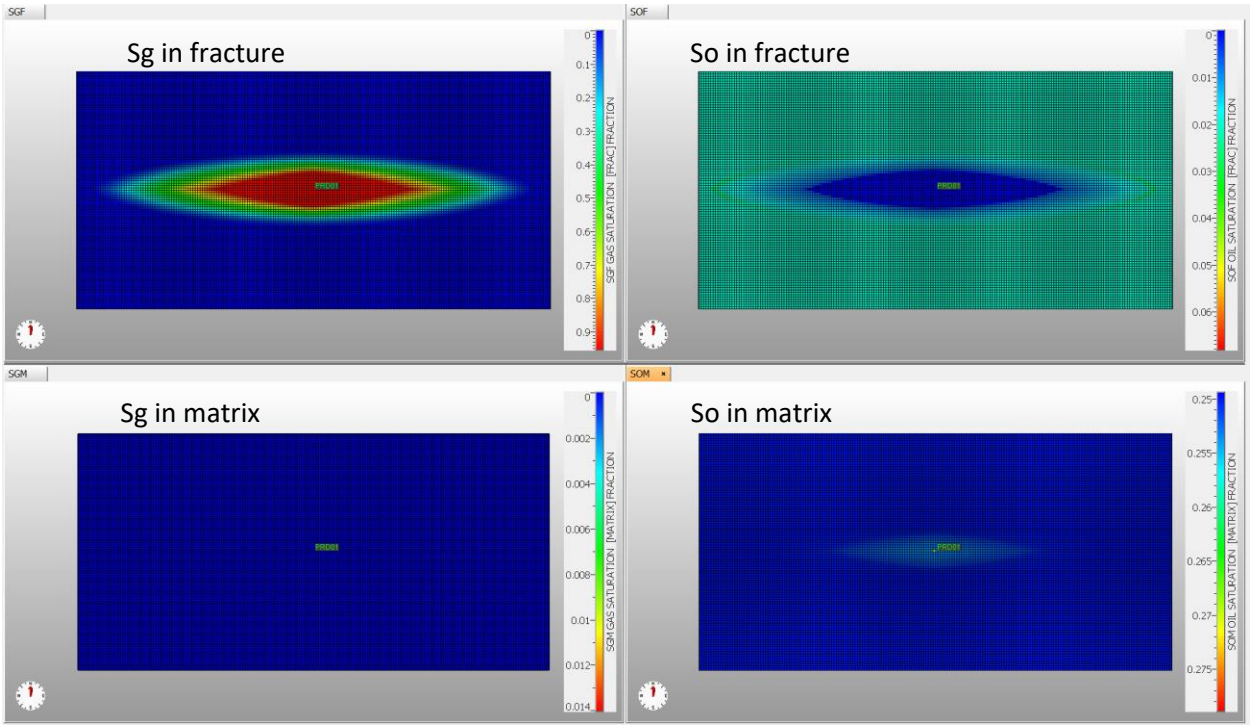


Figure 4-27. Top view of gas and oil saturation in both fracture and matrix at the end of CO_2 injection.

CO_2 Injection

Design

The goal of the CO_2 Injection Phase was to safely inject as much CO_2 as the budget allowed at the highest rate possible into the Carper sandstone target interval in the Holsapple well. The CO_2 Injection Phase was designed to leverage the equipment and experience gained from previous ISGS CO_2-EOR projects (Finley, 2009; Frailey et al., 2012a; Frailey et al., 2012b). The pressure transient tests and the Baseline Production phase had shown that the target interval had sufficiently high injectivity that CO_2 could be injected at pump capacity, which has a maximum injection rate of 12 GPM (~70 tons of CO_2/day). Accounting for efficiency losses, it was expected that a rate of approximately 50 tons/day could be maintained. The budget allowed for the purchase of 1,000 tons of CO_2. Based on the injection rate of the pump and an assumption of continuous injection, the CO_2 injection phase was expected to take approximately 20 days.

Equipment

The equipment for CO_2 injection can be broadly broken down into three components: the CO_2 storage tank, the CO_2 pump skid, and an in-line heater. The CO_2 storage tank used for this project was a 50-ton insulated trailer that the CO_2 vendor MACARB parked on site (Figure 4-28). This trailer was equipped with sensors that recorded its mass. The trailer was equipped with telematics and the trailer mass and pressure data was uploaded to a website hourly and used to track how much CO_2 was left in the vessel. Smaller trucks were deployed when the weight reached 10 tons that delivered 20 tons of CO_2 to refill the 50-ton vessel to ensure continuous injection.



Figure 4-28. 50-ton storage trailer parked on site. CO_2 exits the trailer via the hose on the left (covered in frost) and returns via the hose on the right. Pump skid is visible in the background.

The CO_2 pump skid was constructed for a previous ISGS CO_2-EOR project (Figure 4-29). Previous ISGS CO_2 injection projects discovered that, because CO_2 in the storage tanks is very close to vapor pressure, moving CO_2 from the tanks directly to the main pump creates a substantial vapor locking risk. These projects determined that a booster pump between the storage tank(s) and the main pump was necessary to minimize this risk. The booster pump was a Blackmer CRL1.25 vane pump driven by a 2HP electric motor controlled by a Toshiba VF-S11 VFD. The booster pump was set to increase the pressure of the CO_2 approximately 20 psi before entering the main pump. The main pump is a General Pump Emperor Series HTF2421S triplex pump powered by a 15 HP Siemens electric motor with a capacity of ~12 GPM (~70 tons per day). CO_2 moved from the main pump to a Natco 250,000 btu inline heater that was used to increase the temperature of the CO_2 before it was injected (Figure 4-30). A schematic of the system is shown in Figure 4-31.



Figure 4-29. Image of the CO_2 pump skid. CO_2 enters the skid from the right and goes to the inline heater to the left. The booster pump is visible below the red cylinder and the main pump is visible behind box.



Figure 4-30. Image of the inline heater. CO_2 comes in from the pump skid on the right (not pictured) and goes to the well to the left.

Pressure and temperature sensors were installed at several points on the pump skid, inline heater, well head, and downhole (Figure 4-31). Data from temperature and pressure sensors at the booster pump inlet and outlet, main pump outlet, heater outlet, and wellhead were all recorded by a central data logger. The pump skid was equipped with NuFlow liquid turbine flow meter to measure the injection flow rate and a transmitter to send a signal to a data recorder.

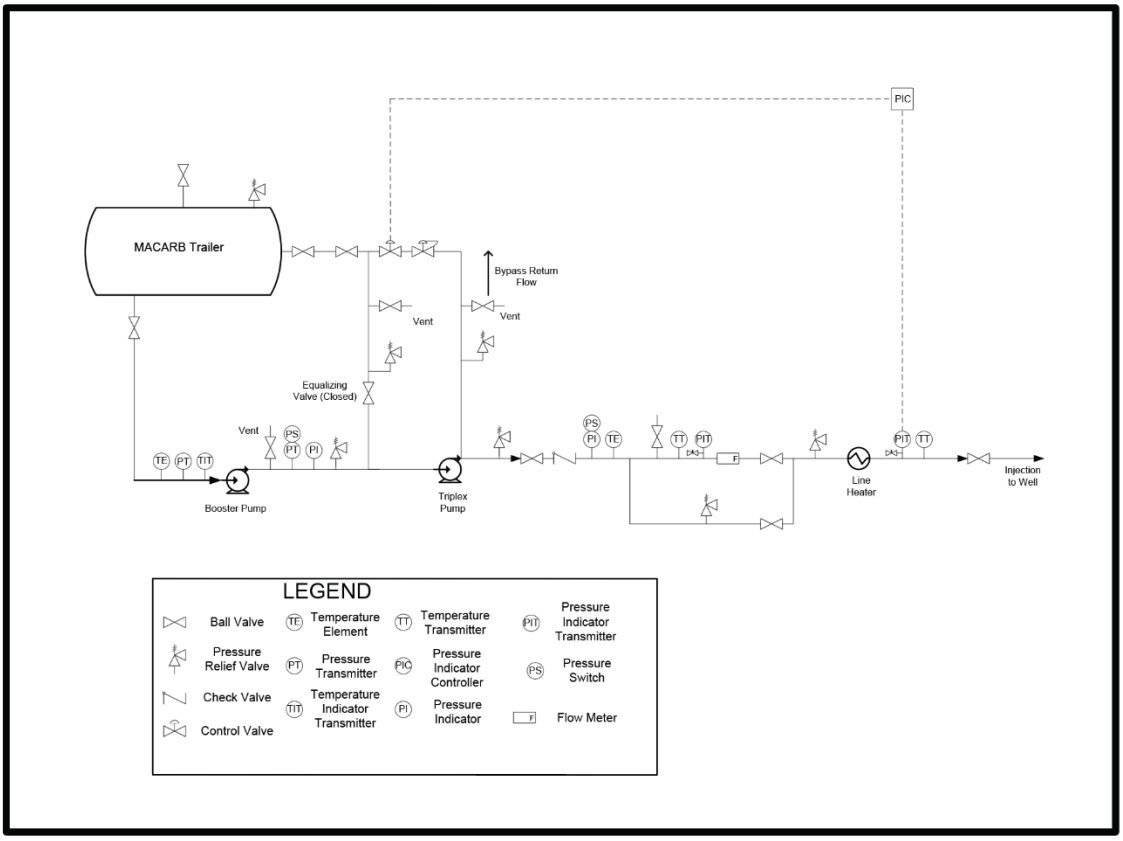


Figure 4-31. Schematic for the CO_2 injection surface equipment including storage tank, pump skid, and inline heater. Modified from Frailey et al. (2012).

Operations

The CO_2 injection phase began on Friday, November 13th when approximately 40 tons of CO_2 were delivered to the storage trailer. About 13 tons of CO_2 were injected over the next week to test the system. Full scale CO_2 injection began on Friday, November 20th.

Several issues were encountered that delayed the start of injection.

- The booster pump was assembled incorrectly, which was not discovered until attempting to start injection. Diagnosing and fixing the problem delayed the start of injection about one week (from November 13th until November 20th).
- The pump lost prime and shut down when the CO_2 storage tank got under 15%. This resulted in two brief outages on Saturday, November 21st and Sunday, November 22nd. To resolve the issue and keep the storage tank above 15%, CO_2 deliveries were made more frequently, and the injection rate was reduced to approximately 35 tons/day on Wednesday, November 25th.

A total of 1,014 tons of CO_2 (52 truckloads) were delivered over the next few weeks. CO_2 injection concluded around midnight on Sunday, December 13th. Once CO_2 injection concluded, the well was shut in and the CO_2 storage tank, pump skid, and flow lines were bled down and removed from the site.

Findings

Two data sources were used to measure the total volume of CO_2 injected; 1. The turbine flowmeter downstream of the main pump on the pump skid and 2. The mass of CO_2 reported delivered by MACCARB (Figure 4-32).

Pressure and temperature of the CO_2 measured upstream of the main pump were used to calculate the density of CO_2. This density was then used to convert the GPM reported by the turbine flowmeter to tons of CO_2/day by using Equation 4-3:

$$CO_2\left(\frac{tons}{day}\right) = CO_2 density * 0.133681 * \frac{GPM}{2000} \qquad \text{Equation 4-3}$$

MACCARB provided an invoice with each shipment that reported when the delivery trailer was on site and what mass of CO_2 was delivered. The cumulative mass of CO_2 delivered was calculated every hour by spreading the tons delivered in each shipment over the time that the trailer was on site. The mass of the 50-ton storage tank was then subtracted from the cumulative mass delivered to estimate the cumulative tons injected (Figure 4-32).

There was significant disagreement between the two methods. They were reasonably close in the beginning and started to diverge as injection continued. It is believed that the data provided by the vendor was a more accurate representation of the mass of CO_2 injected. This conclusion was based on several uncertainties in the flowmeter data:

- The flowmeter requires a correction factor to translate the rotations of the turbine to flow rate (GPM). This correction is dependent on flow rate, and it is possible that it became incorrect as the flow rate changed.
- The calculation to convert GPM reported by the flowmeter to tons of CO_2/day relies on temperature and pressure data. Temperature and pressure data from gauges upstream of the main pump were used, but it is not clear if these were representative of the CO_2 stream downstream of the pump.
- Several problems were discovered in the flowmeter when it was taken apart and inspected after injection. A fibrous substance was found wrapped around the flowmeter axel (Figure 4-34) and a bearing was missing. It is believed that additional friction caused by these issues would have resulted in the flowmeter underestimating flow.

The discrepancy between the two methods complicated the estimation of total mass of CO_2 injected and injection rate. The raw turbine meter data suggests that 840 tons of CO_2 were injected while the MACCARB data suggests 1,010 tons were injected. Both data sources suggest that CO_2 was injected at a rate of approximately 50 tons/day at the beginning of the test and 35 to 40 tons/day after the rate was reduced (Figure 4-33).

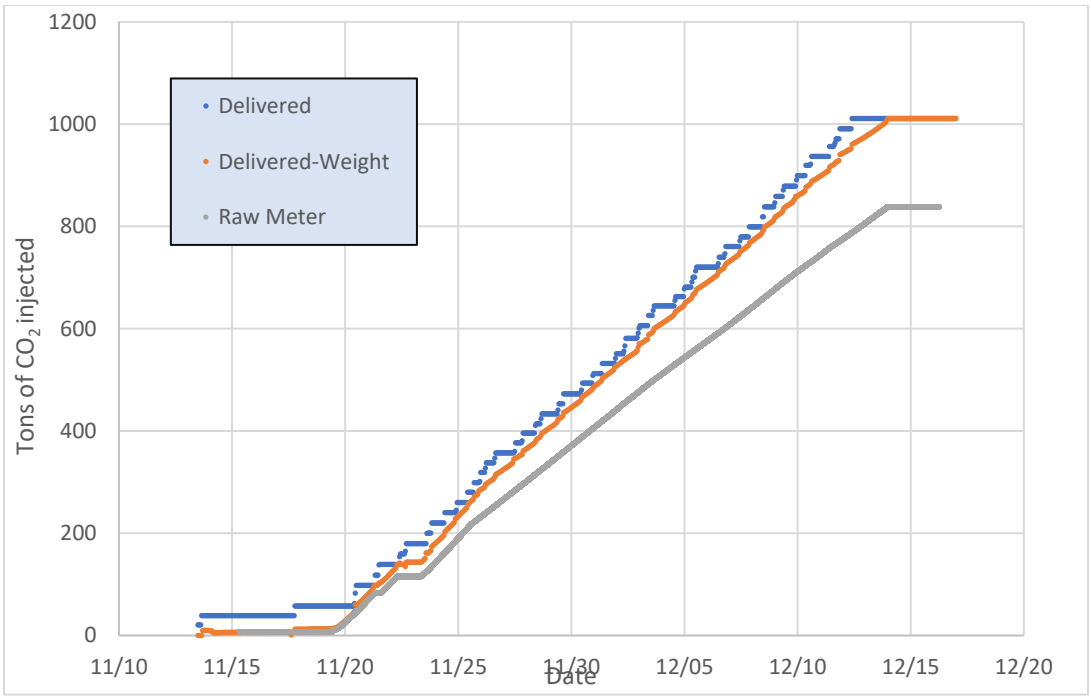


Figure 4-32. Cumulative CO_2 injected over the duration of the CO_2 injection phase. The total mass derived from the flowmeter (grey dots) was significantly lower than the mass derived from the mass delivered minus the tank mass (orange dots).



Figure 4-33. Rate of CO_2 injection derived from turbine meter data (yellow dots) and tank mass data (blue dots). The turbine meter data was calculated by transforming the observed gallons per minute recorded every 15 seconds to tons/day based on Equation 4-3. Hourly tank data (blue dots) had significant scatter, so daily average (orange line) was calculated to remove noise. The turbine meter data appears to agree with the raw tank mass data but is slightly lower than the daily averaged tank mass data.



Figure 4-34. Fibrous material found wrapped around the flowmeter axel after CO_2 injection.

Soak/Vent

Design

The soak phase of a Huff and Puff is generally designed to allow CO_2 time to contact oil while keeping oil near enough to the wellbore to be produced when production resumes. As previously described, the pump had to be set above perforations due to fill in the bottom of the well. Because the pump is unable to pump CO_2, it was deemed necessary to vent CO_2 through the annulus to pull reservoir fluids (oil and/or brine) into the well and above pump before starting the pump for the Post-CO_2 Production phase. Thus, the Soak/Vent phase is defined here as the time interval following the conclusion of CO_2 injection and before reservoir fluids entered the well.

Reservoir simulations conducted during CO_2 injection indicated that the optimum soak time for oil production would be one week and that approximately 150 tons of CO_2 would need to be vented before reservoir fluids would re-enter the wellbore. Based on these simulations, the plan was to shut-in the well for one week and then begin venting at the highest rate possible through the gas prover until there was an indication of reservoir fluids in the wellbore, at which time the pump could be turned on and the Post CO_2 Production Phase could begin. However, several unexpected operational challenges were encountered that caused the actual operations to deviate significantly from this design, resulting in a prolonged soak period.

There was uncertainty in how to recognize when reservoir fluids had entered the well and were approaching the surface since the only data sources were wellhead pressure and fluid level. Failure to recognize reservoir fluids approaching the surface could have resulted in reservoir fluids passing through the prover and onto the ground, resulting in lost data and an environmental hazard. Other single well CO_2 injection tests found that slugging reservoir fluids creates an increase in annulus pressure as CO_2 rises and vaporizes followed by a sharp decline when reservoir fluids enter the well (Wehner al., 1998). Data was tracked and evaluated daily to determine if CO_2 was venting properly and if there were signs of reservoir fluids entering the well.

The capability of the equipment played an important role in the design of the Soak/Vent phase. The gas prover used to meter vented CO_2 has a maximum operating pressure of 100 psi, so a choke was installed

upstream of the prover to reduce pressure to ~25 psi to allow a factor of safety for unexpected pressure spikes. Also, the gas prover cannot meter liquid, so a gas/liquid separator had to be installed midway through venting to filter out any produced fluids from the gas stream.

The Echometer was used to track the CO_2 fluid level (the contact between liquid and vapor CO_2) through the duration of the venting phase. The Echometer signal cannot propagate through liquid CO_2, so although it could be used to track the CO_2 fluid level, it could not detect reservoir fluids beneath a column of liquid CO_2. Thus, it did not provide useful information when liquid CO_2 was to surface and required periodic shut ins to identify the fluid level to determine if venting was substantially changing reservoir pressure from which we could infer reservoir liquid at the bottom of the well (without downhole sensors, our only means of detecting reservoir fluids in the wellbore was through indirect observations).

Equipment

The Echometer was used to track fluid level (the contact between liquid and vapor CO_2) in the annulus over the duration of the venting phase. The Echometer signal was not expected to propagate through liquid CO_2, so it was used to track the liquid/vapor CO_2 interface but did not provide useful information when liquid CO_2 was to surface.

CO_2 flowed from the well annulus through the Natco inline heater that was previously used during CO_2 injection to raise the temperature of liquid CO_2 produced from the well. An adjustable well choke with 1/64" graduations allowing precise pressure and flow rate was installed at the outlet of the inline heater. The choke was necessary to reduce the wellhead pressure (several hundred PSI) down to approximately 25 PSI for the safe operation of the downstream equipment.

A gas/liquid separator was installed downstream of the line heater to collect any reservoir fluids that may have traveled up the well annulus with the flowing CO_2 (Figure 4-35). The gas/liquid separator was a 24" x 6', 133-gallon capacity tank with 2" mechanical dump valve rated to 250 psi. The liquid outlet of the gas/liquid separator was connected to a buried flowline that allowed ejection of accumulated fluids to the tank battery, so even if oil and/or brine started flowing from the well, the produced fluids would be collected and metered.

Vented CO_2 was metered by a gas prover connected to the gas outlet of the gas/liquid separator with interchangeable orifice plates. Electronic gauges recorded pressure and temperature within the prover and atmospheric pressure was at a 5-second frequency. The pressure and temperature data along with the specific gravity of CO_2 (1.52) and the diameter of the orifice plate were used to calculate the volumetric flow rate of CO_2 being vented based on the following equation:

$$Q = V * Ct * Cp * Cg \qquad \text{Equation 4-4}$$

Where:

Q = Venting rate (Mcf/hr)

V = Venting rate of orifice plate at given pressure for standard conditions (atmospheric pressure = 14.65 lbs/in, flowing temperature = 60 °F, Specific Gravity = 0.600) [Mcf/hr] (from Table 4-10)

Ct = multiplier for flowing temperature

Cp = multiplier for atmospheric pressure

Cg = multiplier for specific gravity

Prover temperature and atmospheric pressure were expected to vary throughout venting and were incorporated into the flow rate calculations during operations, but the flow rate could be approximated for each orifice plate by assuming standard conditions and 25 psi (Table 4-10).

Table 4-10. Venting rate for each orifice size assuming specific gravity = 1.52, temperature = 50 F, atmospheric pressure = 14.77 psi, venting pressure = 25 psi.

Orifice Diameter (inch)	**Venting Rate (tons/day)**
0.125	0.6
0.250	2.0
0.375	4.3
0.500	7.7
0.750	17.1
1.000	31.1

A handheld infrared gas analyzer (IRGA) was used in the field to acquire real-time gas composition measurements to ensure vented gas did not have a hydrocarbon concentration high enough to require installation of a flare pit. The IRGA device reads all hydrocarbons as "methane," but it was believed that an increase in observed "methane" would be a qualitative indicator that hydrocarbons were entering the wellbore and volatilizing. Gas samples were collected in bags and sent out for analysis to determine what hydrocarbons were present in the "methane."



Figure 4-35. Photo of the gas/liquid separator. Vented gas enters separator from the blue hose on the right, Gas prover shown on left. Wellhead visible on the right.

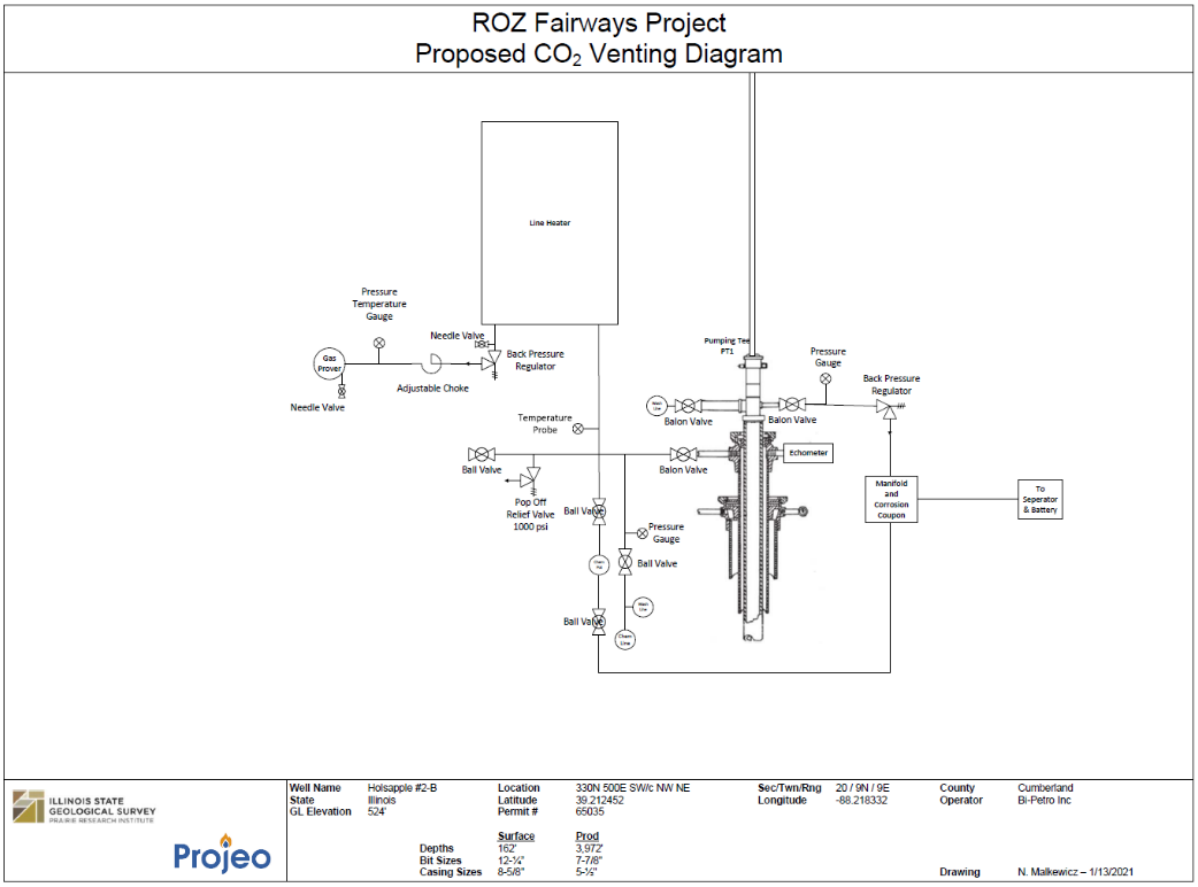


Figure 4-36. Schematic for CO_2 venting after the line heater was installed.

Operations

There are no operations to report for the soak portion of the Soak/Vent phase. Operations for the vent phase include short term tests that were necessary to establish how to vent CO_2 and a venting phase in which the well was left to vent continuously unattended with pressures and temperatures being remotely monitored.

Short-Term Tests

Short-term vent tests were conducted on December 22nd, 2020, and throughout the week of January 5th-7th, 2021 to ensure that the gas prover was working properly, that the Echometer could be used to estimate the CO_2 fluid level (the vapor/liquid contact), and to determine if and how CO_2 could be safely vented unattended. For these initial tests, the adjustable well choke and gas prover were connected directly to the wellhead; the inline heater was not yet on site and the gas/liquid separator was not yet plumbed in.

The first short term vent test, a modified isochronal test, took place on December 22nd, 2020, eight days after the well was shut in at the end of CO_2 injection. CO2 was vented through four different orifice plates (1/8", ¼", 3/8" ½") for 30 minutes each with 30-minute shut-in periods between each flow. The adjustable well choke was manually adjusted to maintain 25 PSI at the prover through each flow period. This was followed by venting through the ¼" orifice plate for 90-minutes. The well was shut in at the conclusion of the test with a total of ~7 tons of CO_2 vented.

Echometer shots taken before venting determined that the BHP was 1606 psi. The Echometer was used to track how the BHP and associated CO_2 fluid level changed during venting (Figure 4-37). The Echometer data behaved as expected; BHP and fluid level generally rose during venting as exiting vapor CO_2 allowed liquid CO_2 to enter the wellbore, and slowly decreased when the well was shut as liquid CO_2 decompressed, filled the upper wellbore with vapor and pushed the remaining liquid back into the formation. The rate at which the BHP changed was correlated to the rate at which CO_2 was vented. The Echometer also correctly tracked the rise in CO_2 fluid level and predicted liquid CO_2 to surface after 30 minutes of venting through the ½" orifice, which was validated by a visible change to vented gas (the vented stream changed from a gaseous appearance to that of a "jet lighter" stream pushing out solid CO_2 hydrate) and necessitated shutting in the well.

The first test demonstrated that the Echometer could be used to track the liquid CO_2 level, that venting at over 7.7 tons/day would bring liquid CO_2 to surface after 30 minutes, and that the well could be vented at a constant rate. Liquid CO_2 did not reach the surface at lower rates, but the final venting interval (90-minutes of venting through the ¼" orifice plate) did create an increase in BHP and associated fluid level that did not equilibrate, so additional, longer-scale tests were needed to demonstrate that venting through the ¼" orifice plate would not bring liquid CO_2 to surface (since it cannot be accurately measured when produced through the gas prover) before the well could be left venting unattended.

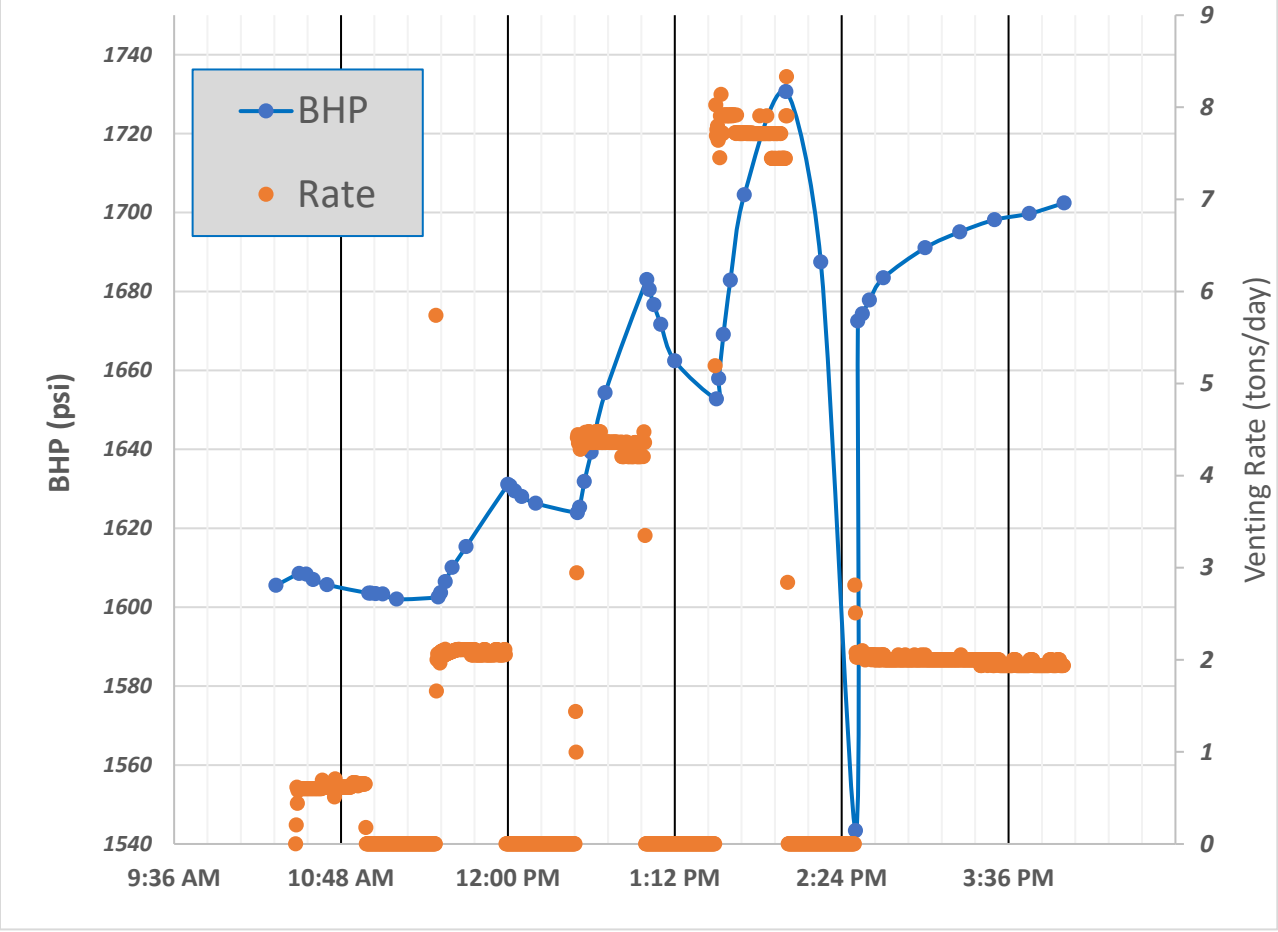


Figure 4-37. Venting rate derived from gas prover data (orange dots and secondary y axis) and Echometer derived bottom hole pressure (blue line and primary y axis) for the initial short term venting test on December 22nd. The test involved four 30-minute venting periods with different orifice sizes followed by a 90-minute vent.

The next round of short-term tests took place from Tuesday, January 5th to Thursday, January 7th with an objective to identify a rate that could be used to vent CO_2 unattended (Figure 4-38).

Tests on 1/5/2021 involved approximately 5 hours of continuous venting through the ¼" orifice plate at roughly 2 tons/day. This resulted in liquid CO_2 reaching the surface. CO_2 hydrates were also observed, with visible flakes blowing out of the gas prover.

Tests on 1/6/2021 involved several short vent periods through the 1/8" orifice at a rate of roughly 0.6 tons/day. Fluids did not reach the surface, but CO_2 hydrate formation continued to be an issue.

Due to the ambient temperature being below freezing and the issues with hydrate formation, the well choke and prover were wrapped with fiberglass insulation before testing on 1/7/2021.Venting resumed with the 1/8" orifice at roughly 0.6 tons/day for 90 minutes before flow stopped completely and pressure at the gas prover spiked from 25 to >100 PSI. Upon inspection of the gas prover, a large accumulation of CO_2 hydrate had developed within the body of the prover that blocked the orifice and stopped flow (Figure 4-39).

The second round of tests confirmed that the Echometer could be used to track the liquid CO_2 level but also demonstrated that the formation of hydrates was an issue that had to be dealt with.

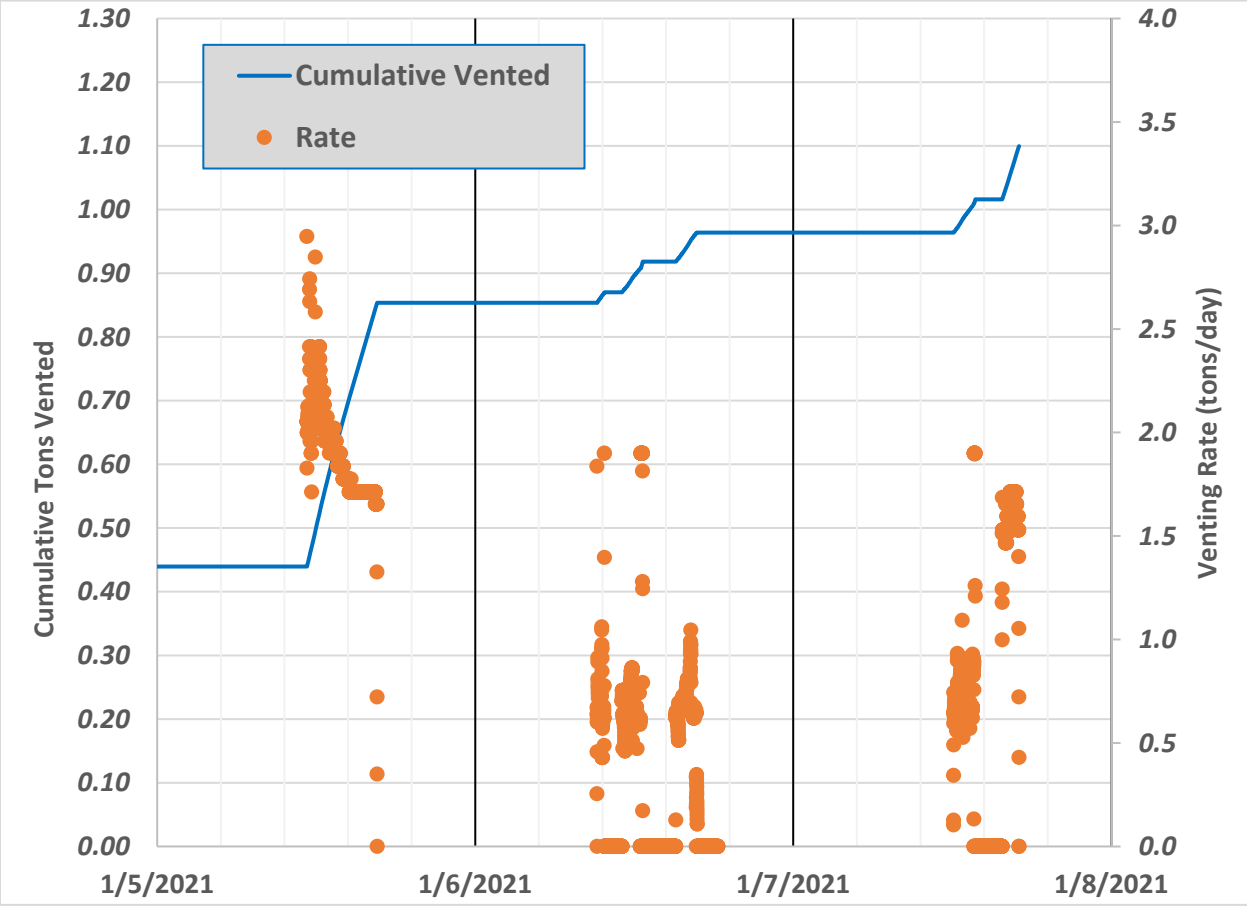


Figure 4-38. CO_2 venting rate (orange dots and secondary y axis) and cumulative CO_2 vented (blue line and primary y axis) for the second short term venting test.



Figure 4-39. Image of CO_2 hydrate obstructing the gas prover. Picture taken at the end of the vent test on January 7th.

Venting

CO_2 hydrate was forming after the choke within the gas prover due to the pressure drop across the choke from 600+ psi to approximately 25 psi causing a temperature drop of the CO_2 from approximately 50 °F upstream of the choke to -2°F (-16.7°C) at the prover. Neither of these pressure/temperature points are within the hydrate range of CO_2, but CO_2 was migrating through the hydrate range between these two points (CO_2 moved leftward along the yellow line on Figure 4-40). To mitigate this issue, the inline heater used for CO_2 injection was installed upstream of the choke on 1/14/2021. The heater was set to 150°F (65.6°C), which warmed the CO_2 to approximately 130°F (54.4°C) upstream of the choke which dropped to approximately 50°F (10°C) at the orifice plate, before dropping to ambient temperature and pressure (green line on Figure 4-40). This increase in temperature was adequate to prevent hydrate formation during venting.

The addition of the inline heater had the added benefit of ensuring that liquid CO_2 would not reach the gas prover. Liquid CO_2 could now flow to the surface and get warmed to a vapor in the heater before passing through the choke.

Following installation of the inline heater, staff remained onsite for several hours while venting through the ½" orifice plate to confirm that the issues with liquid CO_2 flowing to surface and the formation of CO_2 hydrates had been eliminated.

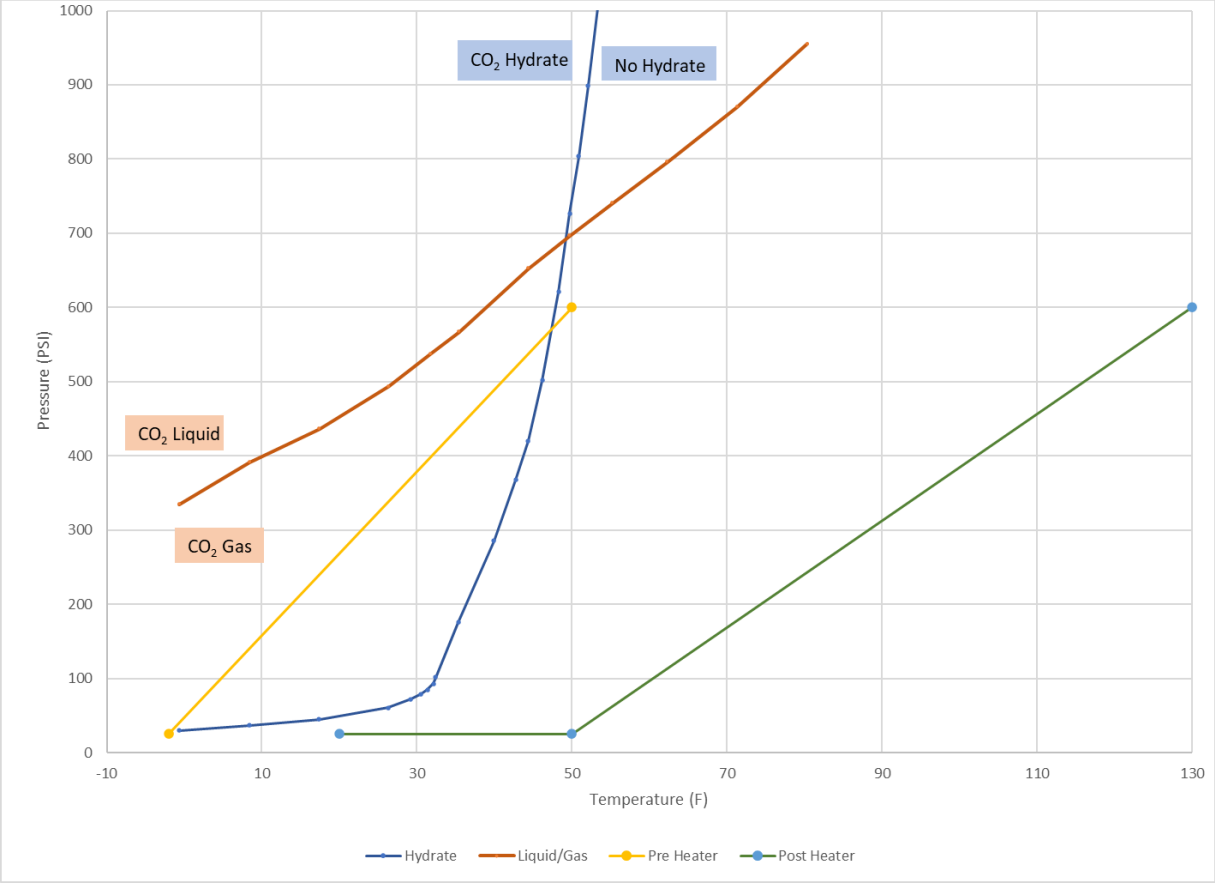


Figure 4-40. Phase diagram for CO_2. Hydrate was forming during preliminary venting tests when the pressure dropped from ~600 psi to ~25 psi and temperature dropped from ~50 °F to -2 °F, when the yellow line crossed the blue line. The inline heater was used to increase the temperature to avoid the formation of hydrate (the green line is shifted to the right and never crosses the blue line).

The ¼" orifice plate was then used to vent continuously at approximately 2 tons/day (Figure 4-41). The well was shut-in for 24 hours on January 19th. Echometer derived fluid level dropped once venting stopped and equilibrated at 500 ft below surface (Figure 4-42).

The ½" orifice plate was installed when venting resumed on January 20th. The venting rate equilibrated at approximately 7.75 tons/day until was shut in on January 25th to again check the CO_2 fluid level. Fluid level was determined to be 600 ft from surface (Figure 4-42).

No reservoir fluids (oil or water) had been observed during venting, but it was believed that as venting progressed there was a risk of reservoir fluids entering the wellbore and flowing to surface. The gas prover could not meter fluids and reservoir fluids would pose a potential environmental risk so the gas/liquid separator was plumbed in between the heater and gas prover on January 27th to catch any fluids that might be produced. CO_2 now had to pass through the hose and reside in the gas/liquid separator tank after being heated and before being vented, so adding the gas liquid separator increased the effect of ambient temperature on vented CO_2, but the risk of hydrate formation was negligible because this cooling took place after CO_2 passed through the choke and was reduced to 25 psi (horizontal section of the green line on Figure 4-40).

Gas composition was measured with the IRGA device following shut in as venting resumed on 1/27/2021 and indicated 2.5% methane concentration. Pressure on the orifice plate slowly increased once venting began. This resulted in the rate increasing from ~7.75 tons/day on January 27th to ~8 tons/day on February 4th when the well was shut in again to measure fluid level. The vented gas contained 4.1% methane immediately before the well was shut in.

Venting resumed on 2/8/2021 with the ½" orifice plate. Gas composition taken an hour after venting resumed contained 14% methane. Venting continued at 8 tons/day until the evening of 2/11/2021, when pressure rapidly increased by approximately 100 psi before breaking over and sharply decreasing by approximately 400 psi overnight and stabilizing in the morning of February 12th (Figure 4-43). Over the preceding month of nearly continuous venting, annulus pressure had risen steadily (between 3 and 10 psi per day). This pressure behavior was interpreted to be fluid slugging indicative of reservoir fluids entering well and marked the conclusion of the Venting Phase. The gas sniffer was used to measure gas composition and the well was shut in (and remained so for a few weeks following due to frigid ambient temperatures). The Echometer continued to track fluid level until the post CO_2 Production Phase began.

Findings

The goal of the soak/vent phase was to vent CO_2 to pull reservoir fluids into the wellbore. Data streams acquired during this phase can be broken down into two components; operational data (Echometer derived fluid level and BHP and wellhead pressure) and gas prover data used to calculate the volume of CO_2 vented.

Gas prover data (temperature, pressure, and orifice size) were tracked over the duration of the phase and used to calculate the rate and total volume of CO_2 vented. According to this data, a total of 146.5 tons of CO_2 were vented during the "venting" subphase (Figure 4-41).

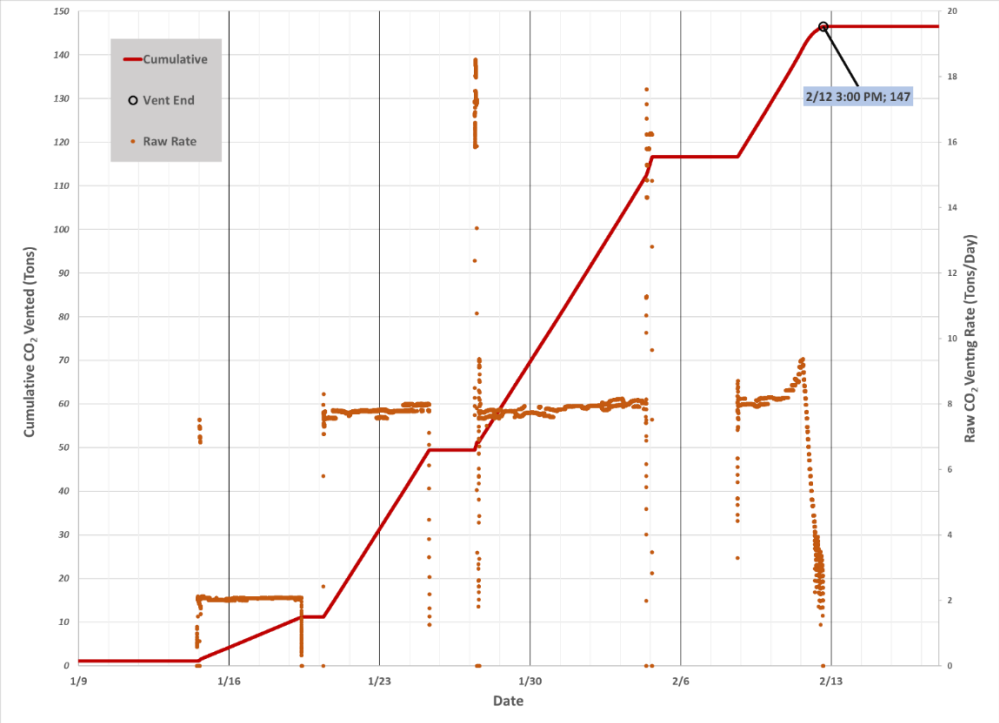


Figure 4-41. Rate and cumulative CO_2 vented during the "venting" subphase based on pressure, temperature, and orifice size. The end of the Venting phase is marked with a hollow circle on the cumulative curve.

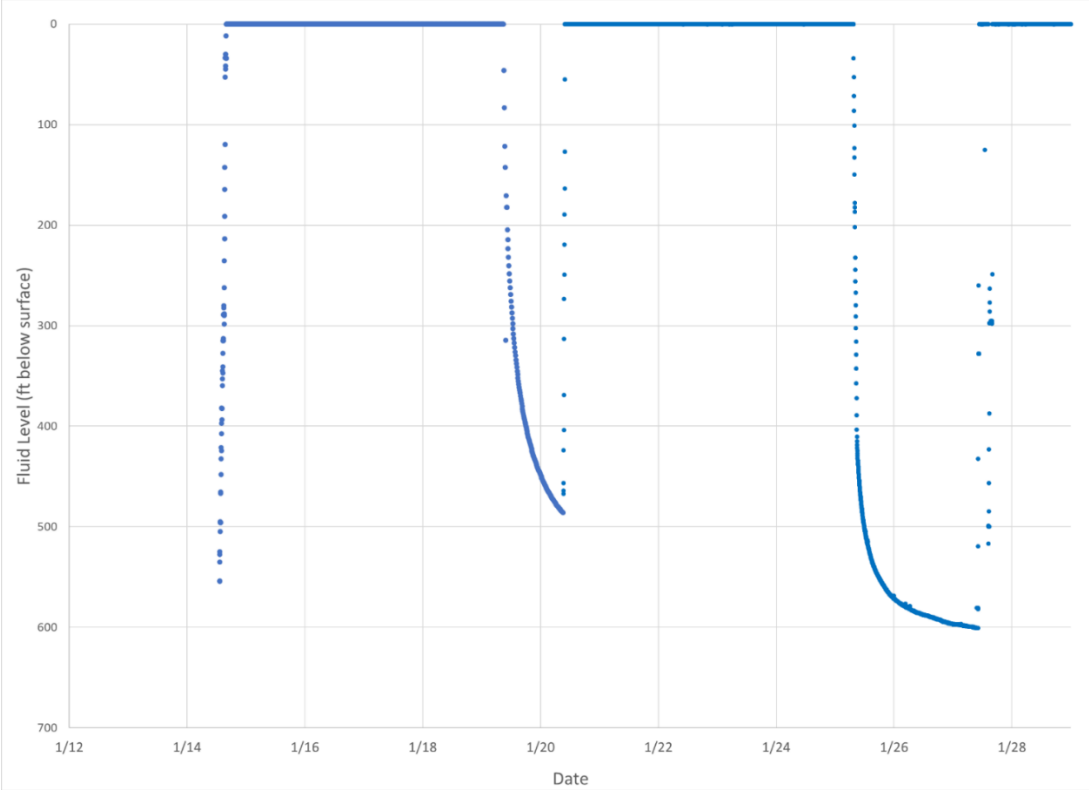


Figure 4-42. Echometer Fluid Levels during the venting phase.

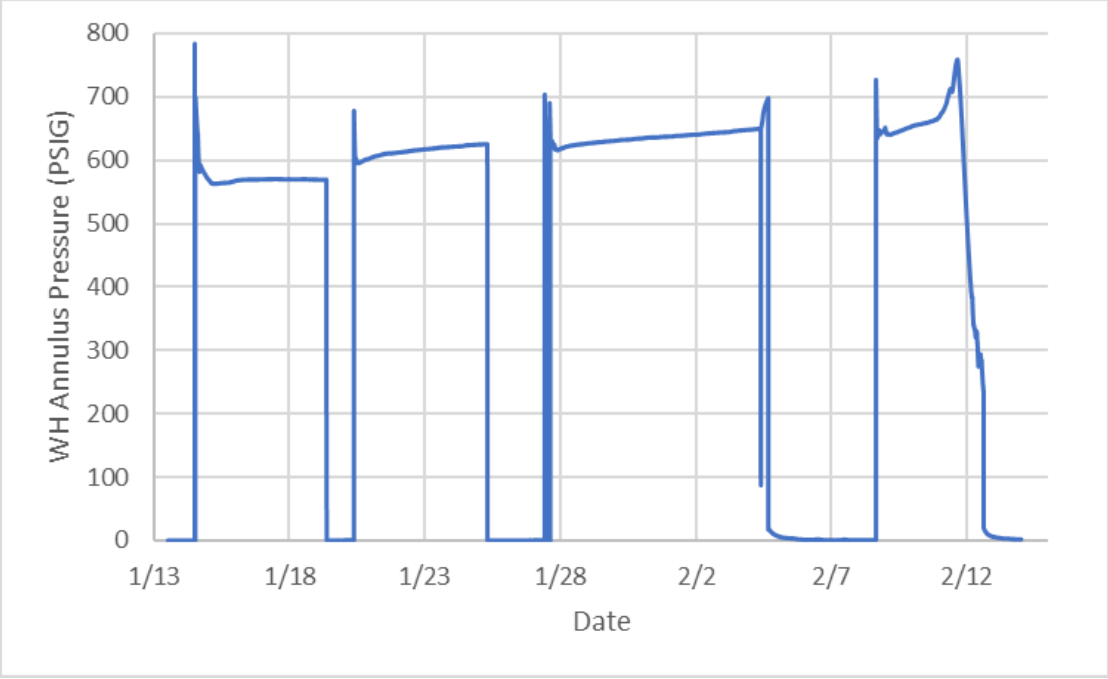


Figure 4-43. Well Head Annulus pressure for the Venting phase. Pressure steadily increased at about 3-10 psi per day while venting, except for the evening of February 11th when it increased over 100 psi before rapidly decreasing over 400 psi. This pressure behavior was interpreted to be fluid slugging indicative of reservoir fluids entering well and marked the conclusion of the Venting Phase.

Gas Composition Alteration

Gas composition data from the IRGA meter was meant to be a qualitative check to determine if hydrocarbons were entering the well, but an attempt was made to use it to refine both the amount of CO_2 vented and the Echometer derived BHP and fluid level.

The percent methane data displayed a general trend of increasing with time that matched expectations, but the data came with two important caveats. The IRGA device could only be used when somebody was on site, so each data point represents a point in time. Careful consideration was therefore required to understand what each data point represented. For example, the 14% methane data point on February 9th was taken soon after venting resumed following a lengthy shut-in period. This data point was significantly higher than the value taken immediately before shutting in (4%) and after venting resumed for four days (7%). This point is therefore believed to represent shut in conditions as hydrocarbon gas accumulated in the headspace of the well and not the proportion of hydrocarbons when actively venting. So, this data point was appropriate to be used for Echometer derived fluid levels when the well was shut in (it is representative of the gas column that the Echometer shot traveled through) but not for the proportion of hydrocarbon in the vented gas since methane concentration dropped once venting resumed.

A polynomial line was regressed through the data points believed to be representative of the vented gas (all the data points except the 14% reading). The equation defining the line was used to estimate the proportion of methane in the vented gas (Figure 4-44 This interpolation method ignores when the well was venting or shut in but had a good fit and was considered a reasonable approximation of the increase in methane concentration over time.

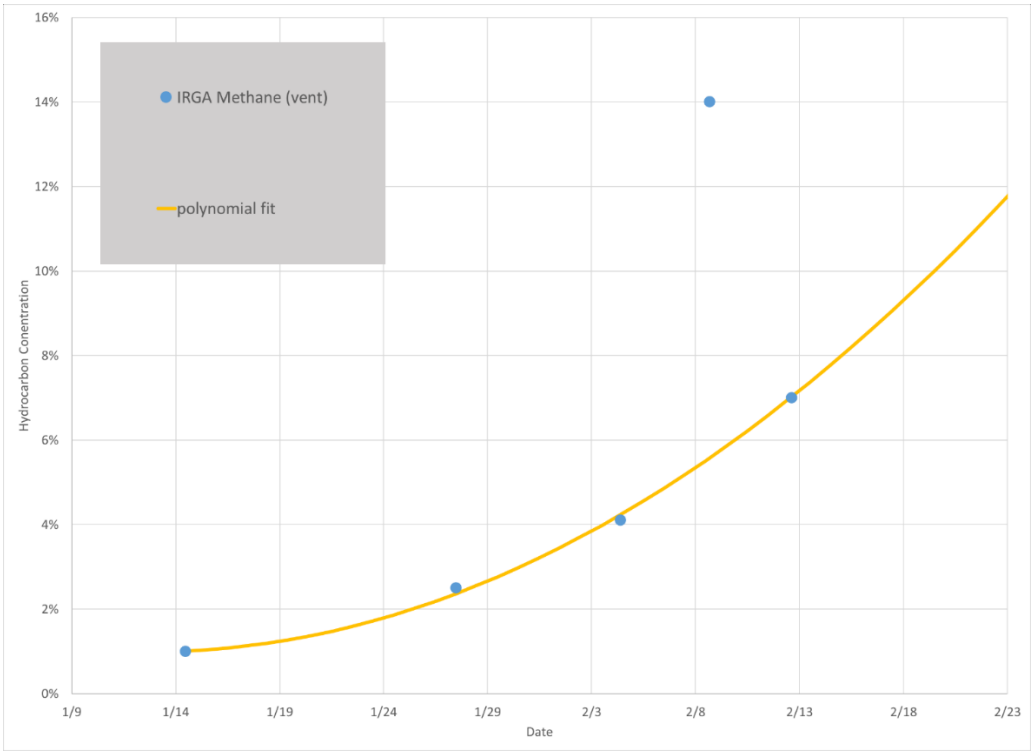


Figure 4-44. Estimated change in methane percentage during venting. Blue dots are observed methane and yellow line is polynomial curve fit to observed data.

The second important consideration is that device does not distinguish between types of hydrocarbons. The specific gravity of the gas is an important parameter in both the Echometer and vented data calculations. Different hydrocarbons have different specific gravities (Table 4-11), so this introduces a source of uncertainty.

Table 4-11. Specific gravities of the hydrocarbons that may be present in the vented gas.

Gas	**Specific Gravity**
CO_2	1.52
Heptane	3.46
Hexane	2.98
Pentane	2.49
Butane	2.01
Propane	1.52
Ethane	1.04
Methane	0.55

The specific gravity of the vented gas can be modified by the proportion and specific gravity of the hydrocarbons in the stream according to the following equation:

$$SGadjust = 1.52\ (1\text{-}HC\%) + HC\ specific\ gravity\ (HC\%) \qquad \text{Equation 4-5}$$

Where:
SGadjust = Specific gravity of vented gas adjusted for hydrocarbon
HC% = Hydrocarbon percentage of vented gas
HC specific gravity = Specific gravity of hydrocarbon constituent

Hydrocarbons with specific gravity below that of CO_2 (methane, ethane) will buffer their impact on apparent venting rate; increasing hydrocarbon concentration decreases the overall specific gravity of the vented gas which increases the total venting rate, which increases the amount of CO_2 vented. The true volume of CO_2 vented will be greater than simply subtracting the percentage of "methane" from the raw orifice data but less than assuming that methane is the only hydrocarbon constituent present. Hydrocarbons with specific gravity higher than CO_2 will have the opposite effect, increasing hydrocarbon concentration will increase the specific gravity of the vented gas and decrease the total venting rate, further reducing the apparent amount of CO_2 vented. The CO_2 venting rate for each data point was modified by the following equation:

$$Q_{HC} = Q^*(Cg/0.63)^*(1\text{-}HC\%) \qquad \text{Equation 4-6}$$

Where:
Q_{HC}= Rate of vented CO_2 adjusted for hydrocarbon
Q = Raw venting rate for given conditions from Equation 4-4
Cg= Specific gravity multiplier based on SG adjust

Equations 4-5 and 4-6 were used with the proportion of hydrocarbon as defined by the polynomial curve from Figure 4-44 to calculate a new venting rate of CO_2 at every data point to calculate new cumulative volume of CO_2 vented (Figure 4-45). Even the most extreme case (assuming the hydrocarbon is entirely heptane with a specific gravity of 3.46) only reduces the cumulative CO_2 vented from 146.54 to 139.17. This is an unlikely scenario but was considered here to constrain the theoretical maximum effect of hydrocarbon on the apparent vented CO_2.

The change in overall CO_2 vented is small, but the data do start to diverge towards the end of the phase, so it was believed that hydrocarbons had the potential to become an important consideration as production progresses.

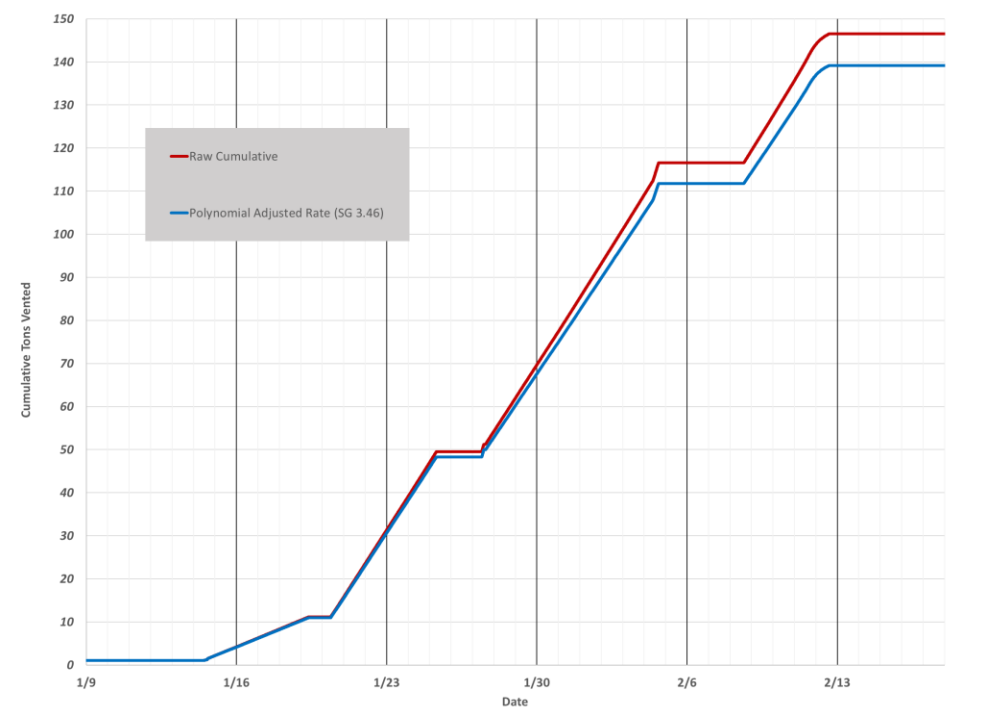


Figure 4-45. Cumulative CO_2 vented using the raw data (red line) and heaviest hydrocarbon (specific gravity = 3.46) assuming a concentration of hydrocarbon from the polynomial curve from Figure 4-44. Values are similar at the beginning of venting and begin to diverge towards the end of the phase as the concentration of hydrocarbon increases, but even assuming the heaviest hydrocarbon only reduces the amount of CO_2 vented from 146 to 140 tons.

Hydrocarbon data derived from the GC analysis was also used to correct the acoustic velocity for Echometer pressure transient fluid level shots during well testing and in post data evaluation. Concentrations of each of the components derived from the GC analyses (CO2, N2, H2S, C1, C2, C3, IC4, NC4, IC5, NC5 and C6+) were used to calculate the specific gravity of the vented gas when each sample was taken (Table 4-12). This specific gravity was assumed to be representative of the gas within the borehole (that the Echometer shots were traveling through) and used to correct acoustic velocity via the Acoustic Velocity Determination tool embedded in the TWM software from the time that the sample was taken until the next sample was taken. Surface temperature, bottomhole temperature and pressure against the Echometer device was also used in conjunction with the gas analyses to correct individual fluid level shots. New values would then be used for calculation of fluid level and all post processing of the pressure transient data.

Table 4-12. Echometer venting fluid level data.

Date	Fluid Level (ft)	Pressure (psi)	Gas Composition	Gas Gravity	Calculated BHP	Notes
12/21/20	402	676	100% CO2	1.517	1721	End of post-injection week-long shutin period before modified isochronal test.
1/14/21	510	697	99% CO2	1.508	1708	End of week-long shutin after experiencing hydrate issues. Just before venting with heater.
1/27/21	500	705	97.5% CO2	1.493	1719	End of 2-day shutin period after venting 50 tons.

Post-CO_2 Production Phase

Design

The goal of the Post-CO_2 Production phase was to produce fluids from the well and measure the amount of CO_2, oil, and water produced. Because baseline production concluded with no oil observed, any oil produced during Post-CO_2 Production could be attributed to CO_2-EOR. It was also important to measure how much CO_2 was produced to understand how much remained stored in the reservoir.

The Venting Phase concluded when there were indications of reservoir fluids entering the well, but the resulting wellhead pressure remained too high (>300 psi) to begin pumping. Attempts to bleed off annulus pressure resulted in the well flowing reservoir fluids to the surface. Thus, it was apparent that the well needed to flow for a period to further reduce the reservoir pressure to the point that artificial lift was required. This makes the line between the end of the Venting Phase and the beginning of the Post-CO_2 Production Phase transitional, but the beginning of the Post CO_2 Production Phase is defined here as when the well started to produce reservoir fluids to the surface on 3/2/2022.

The Post-CO_2 Production phase is divided into two subphases. The goal of the first subphase, defined here as **Flowing**, was to condition the well so that the pump could be turned on and left unattended. The second subphase, defined here as **Pumping**, is a more traditional production period, with continuous pumping and fluid production. The amount of CO_2, oil, and water produced, and water disposed were measured during both subphases.

The Flowing subphase was necessary because attempts to start pumping would stimulate flowing, in which the CO_2 within the formation would carry fluids up both the tubing and annulus at which point the pumping unit would be shut down. The magnitude of the well flow rate was difficult to estimate but had the potential to overwhelm the gas/liquid separator or to put excessive pressure on the well stuffing box. The flowing fluid also contained gas bubbles, which would put extra pressure on the tubing. These uncertainties required personnel to be onsite to stimulate flow, monitor the system, and choke back the flow if pressures got too high. Each cycle of flow and shut in would release pressure from the reservoir. Cycling continued until the well stopped flowing on its own and the pump could be left running unattended.

The design of the Pumping subphase was less complicated; the pump would be turned on and the strokes per minute would be adjusted to match the fluid production rate established during Baseline Production

(350 bbls/day). Fluid level and well head pressure would be continuously logged and remotely monitored every day to ensure everything remained within safe operating parameters.

The expected production performance (oil cut, CO_2 production) of the Pumping subphase were based on reservoir simulations and fluid drawdown observed during the Baseline Production phase.

Reservoir simulations consistently indicated that higher production rate resulted in higher oil production, so the pumping phase was designed to produce at the maximum pump capacity (350 bbls/day) and decrease to 200 bbls/day as the reservoir showed signs of depletion. Operational challenges encountered during venting effectively prolonged the soak period. The conclusion of CO_2 injection (December 13th) to the beginning of Post CO_2 fluid production (March 2nd) was two and a half months.

Equipment

All the equipment used for Post-CO_2 Production was installed during previous phases and described in their respective sections. Post-CO_2 Production used the same pumping unit, tank battery, and associated meters installed during baseline production and the gas liquid separator and gas prover installed during CO_2 venting.

Data acquisition equipment was a combination of meters installed during Baseline Production Phase; Total fluids metered by turbine meter upstream of tank battery, ultrasonic meter with two transducers metered oil and water individually, and turbine meter between tank battery and disposal well metered disposed water, and the Soak/Vent Phase; the gas/liquid separator and gas prover.

There are several important operational constraints of the equipment:

The gas/liquid separator and gas prover have pressure and rate constraints. The prover is only rated to handle 100 psi. The gas liquid separator has a maximum flowing rate of 50 GPM (2,300 bbls/day). Also, the operator suggested keeping less than 450 psi on the tubing. These constraints meant that the well had to be constantly monitored and choked off or shut in when rates or pressures threatened to exceed design specifications of the equipment.

Larger orifice plates were used for the flowing subphase to de-restrict the flow of CO_2 as much as possible for two reasons; 1. It was believed that trapped CO_2 bubbles were causing the excessive and unpredictable flowing, and 2. The potential for very high flow rates created a risk of increased pressure on the gas/liquid separator. Small orifice plates would hold more pressure in the gas/liquid separator, increasing the risk of equipment damage.

The fluid level had to remain above the pump and the pressure on the tubing had to be < 450 psi for the pump to be active. The polished rod would get hot when not in contact with fluid, which would occur when establishing flow after starting the pumping unit or when the tubing was filled with vapor CO_2 instead of fluids. The heat posed a risk of warming the polished rod or damage to the stuffing box, so careful monitoring and the installation of a polished rod lubricator were required. These constraints also meant that the pump could only be used briefly unless the tubing was consistently full of fluid.

Flowing Subphase

Flowing Operations

Daily operations during the flowing subphase involved stimulating flow by a brief period of pumping and/or opening well chokes to promote rapid venting, monitoring pressure, adjusting well chokes once fluid flow was established to constrain flow rate to safe levels, then leaving the well chokes set to prevent uncontrolled pressure or flowrate while leaving the well unattended.

The flowing subphase took place between March 2nd until April 15th. Details of the field work each day can be found in the daily activity logs in Appendix A. The goal for each day evolved over the course of the subphase from maximizing flow while personnel were on site to adjusting pumping rate, choke settings, and orifice plates to prolong flow for as long as possible until the pump could be run for hours without stimulating significant flow. Between April 13th and April 15th, the well was pumped without any associated flowing, created confidence that continuous pumping could start in earnest and marked the conclusion of the flowing subphase.

IRGA data was taken throughout the phase to estimate how much hydrocarbon was being vented. Four samples were collected over the course of the subphase for more detailed gas chromatograph (GC) analysis.

Flowing Data

A turbine meter in the flowline upstream of the gunbarrel separator was used to measure total fluids produced, a turbine meter downstream of the brine tank was used to measure total fluids disposed, an ultrasonic meter with transducers on oil and water legs was used to measure oil and water entering the oil and brine tanks, and the gas prover was used to measure CO_2 vented. Data from these instruments was continuously logged and was analyzed to determine how much oil, water, CO_2 were being produced.

Vented CO_2 was measured in the same way as during the venting phase. Venting rates were generally higher but less sustained than the venting phase (Figure 4-46). Not much CO_2 was vented until the end of the subphase when the well was able to flow consistently for multiple days. Raw data suggests that ~85 tons of CO_2 were vented during the flowing subphase and that a total of ~240 tons were vented throughout the venting and flowing phases.

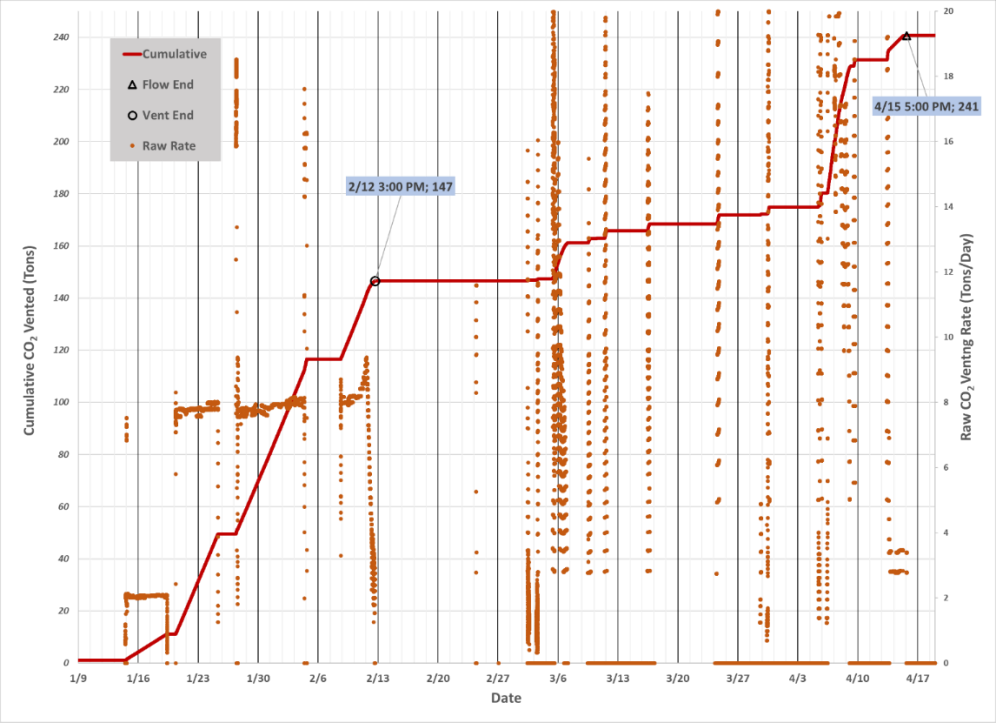


Figure 4-46. Rate and cumulative CO_2 vented through the flowing subphase based on pressure, temperature, and orifice size. The end of the venting subphase is marked with a hollow circle and the end of the flowing subphase is marked with a hollow triangle on the cumulative curve.

Both production and disposal turbine meters largely behaved as expected, with production measured when the well was known to be flowing and disposal following the general trend in a stairstep pattern as the disposal pump turned on and off (Figure 4-47). However, the production turbine metered 2,432 bbls of fluid produced and the disposal turbine metered 1,731 bbls of water disposed. The difference between the two (701 bbls) was significantly greater than the on-site storage capacity (225 bbls) and suggests that the production meter was overestimating the volume of fluid produced or the disposal meter was underestimating the volume of water disposed.

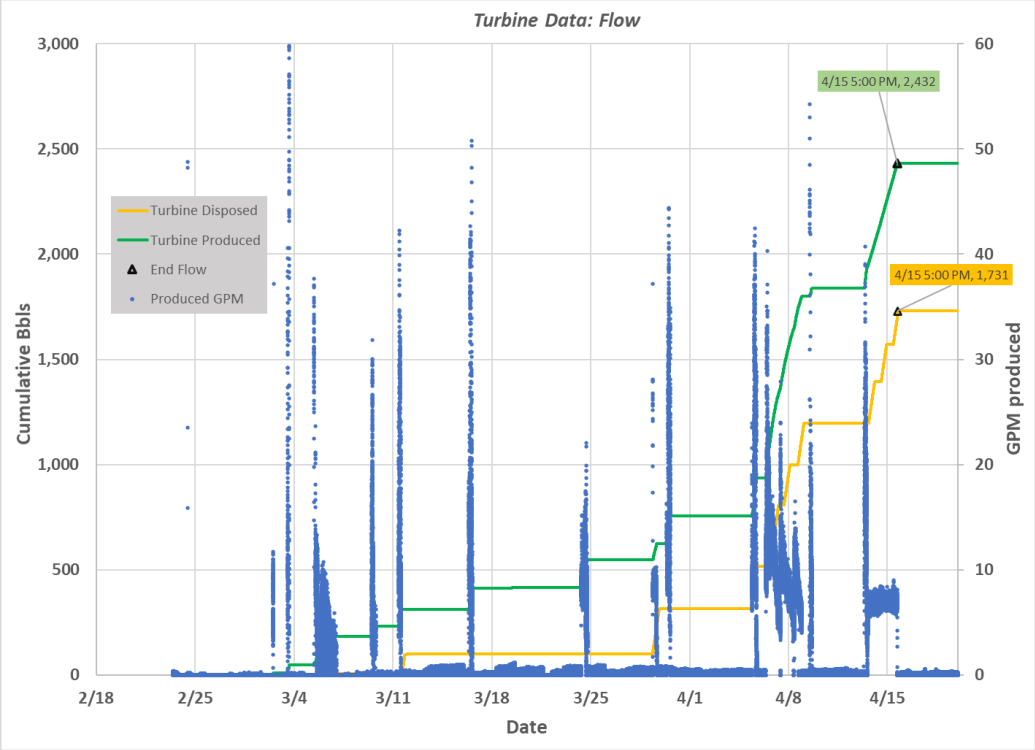


Figure 4-47. Cumulative water produced (green line) and disposed (yellow line) as measured by the turbine meters. Production rate shown with blue dots.

The ultrasonic meter was the primary measure of oil and water produced (Figure 4-48). The ultrasonic meter works by measuring the velocity of fluid (of known density) flow through a pipe of known diameter. The measurements are only reliable when the fluid completely fills the pipe. No oil was observed until midway through the flowing subphase after which time it slowly increased throughout the rest of the subphase. Oil cut for the Flowing subphase was very low (0.3%) with 1,600 bbls of water and only 4.8 bbls of oil observed. Interestingly, oil was usually reported by the ultrasonic meter when the well was not producing (in the middle of the night or over the weekend when the well wasn't flowing) and showed up as isolated data points surrounded by no detect values. This is most apparent at the end of the flowing subphase when the cumulative ultrasonic oil production increases from 2.20 bbls when the well was shut in on April 15th to 4.81 before the Pumping subphase began on April 21st. This "extra data" also appears in the water data, which increased from 1,598 bbls to 1,612 bbls after shutting in but was masked by the large cumulative volume. The source of this extra data is believed to be caused by a small error in the meter that only became apparent because of the very small volume of oil produced. Since oil production was so small, there was generally only a trickle of oil running through the 2" diameter pipe that connected the gunbarrel oil/water separator to the oil tank, making ultrasonic measurements unreliable.

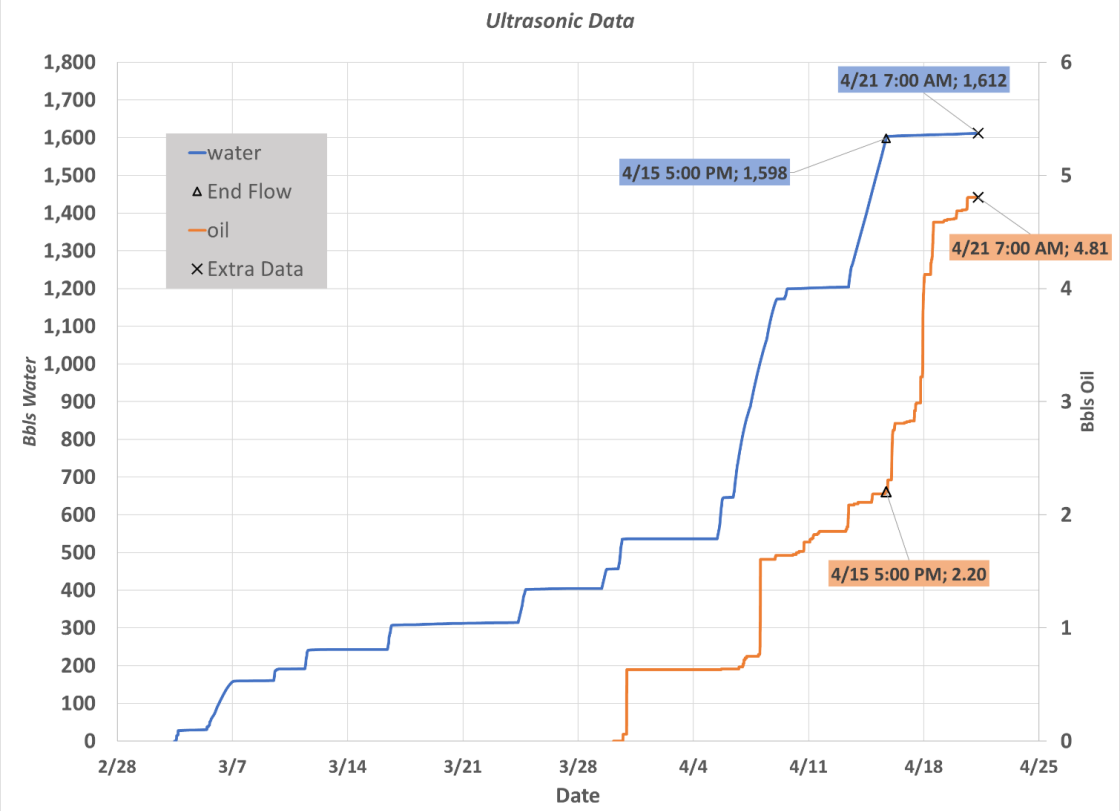


Figure 4-48. Cumulative oil and water production observed by the ultrasonic meter at the end of the flowing subphase. 1,598 bbls of water and 2.2 bbls of oil were produced at the end of the flowing subphase. The cumulative volumes of water and oil continued to increase after the well was shut in.

Interpretation

Multiple flow meters were used to provide redundant data (Figure 4-47 and Figure 4-48). The turbine fluid produced was expected to be the sum of the ultrasonic water and ultrasonic oil and the Ultrasonic Water was expected to be equal to the turbine fluid disposed. Deviation from these expectations was used as a sign of equipment failure. There was significant disagreement between the volume of water produced as indicated by the produced turbine and combined ultrasonic data. The difference between the data streams was calculated at each data point to determine the cause and which meter was most representative of the fluid being produced (Figure 4-49). Examination of the data and observations from the field suggested that the disagreement was caused by CO_2 dissolved in the produced brine. It was believed that bubbles of CO_2 caused turbulent flow through the turbine meter, which caused it to overestimate the volume of fluid produced. Conversely, CO_2 dissolved in brine reduced the density of the fluid passing through the ultrasonic meter, which caused it to underestimate flow.

The cumulative volumes of water produced indicated by the turbine production and ultrasonic water meters diverged whenever there was production. The daily production rate of the turbine meter was consistently 41% greater than the rate observed by the ultrasonic meter (Figure 4-50), but rate did seem to play a role with slightly more divergence at higher rates. Higher production rates gave the CO_2 less time to break free in the gas/liquid separator and allowed more CO_2 to pass through the meters, which resulted in a more pronounced effect.

The volume of water measured by the production turbine meter was immediately greater than the volume measured by the disposal turbine meter. Produced water needed to fill both brine tanks before the disposal pump kicked on and water was disposed. However, the difference between the two quickly surpassed the capacity of the two brine tanks and continued to increase. CO_2 dissolved in the fluid could also explain this difference if CO_2 outgassed after the production turbine and before the disposal turbine (i.e. in the gunbarrel or brine storage tanks).

The relationship between Ultrasonic water minus turbine disposed behaved as expected for the early flow periods; cumulative water indicated by the ultrasonic water meter increased when the well was producing and the disposal turbine meter caught up when water was disposed, but during the last two flow periods the disposal turbine data caught up and passed the ultrasonic water data (more water was disposed than produced).

CO_2 dissolved in the fluid could also explain this behavior. Early flow periods were on the order of hours. The volume of water produced to the brine tanks during these brief flow periods was not great enough to trigger disposal, so brine sat in the storage tanks for several days and gave CO_2 time to outgas. The last two flow periods involved more prolonged production, during which the brine tanks filled and emptied several times. These cycles decreased the amount of time the CO_2 charged brine spent in the storage tanks and increased the amount of CO_2 that made it to the disposal turbine meter, thereby causing the disposal turbine meter to overestimate brine production.

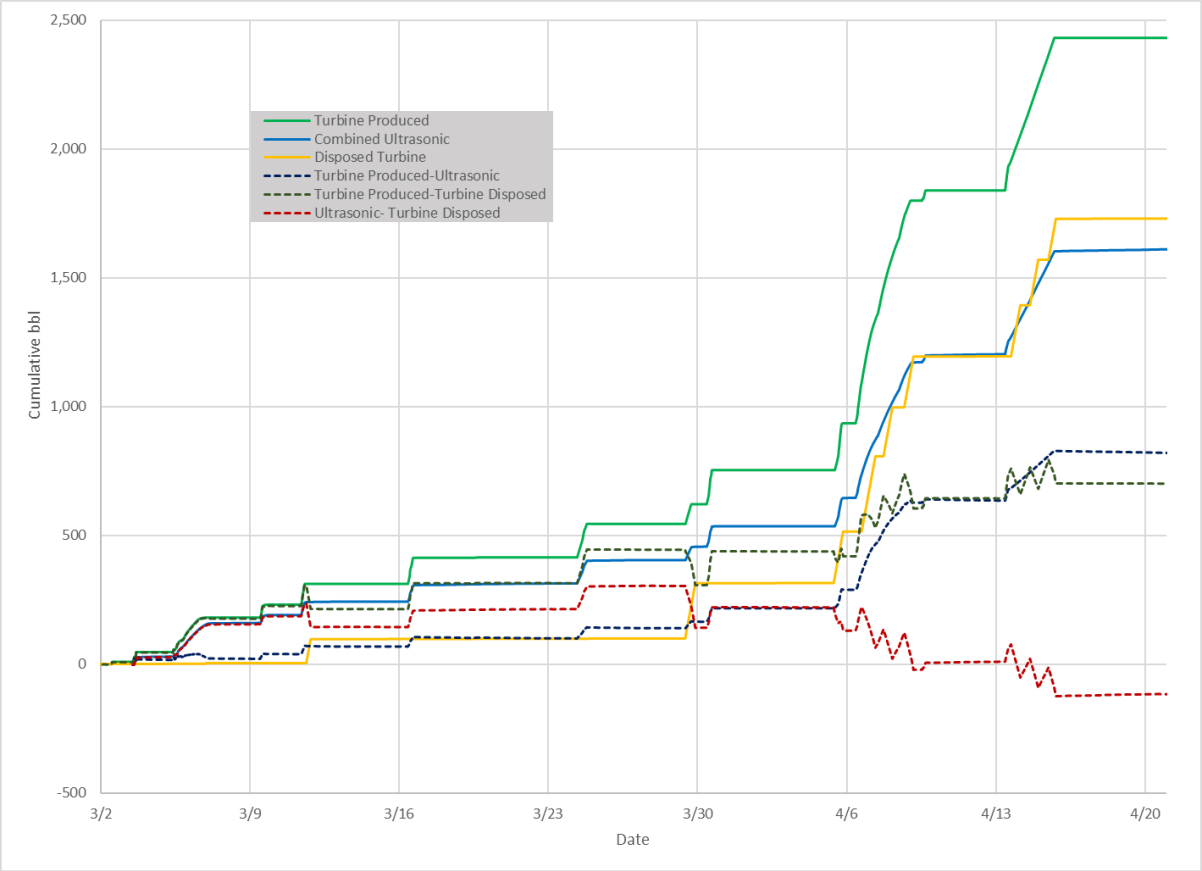


Figure 4-49. Cumulative production recorded by produced turbine meter (green line), disposed turbine meter (yellow line), and ultrasonic water meter (blue line) for the flowing subphase.

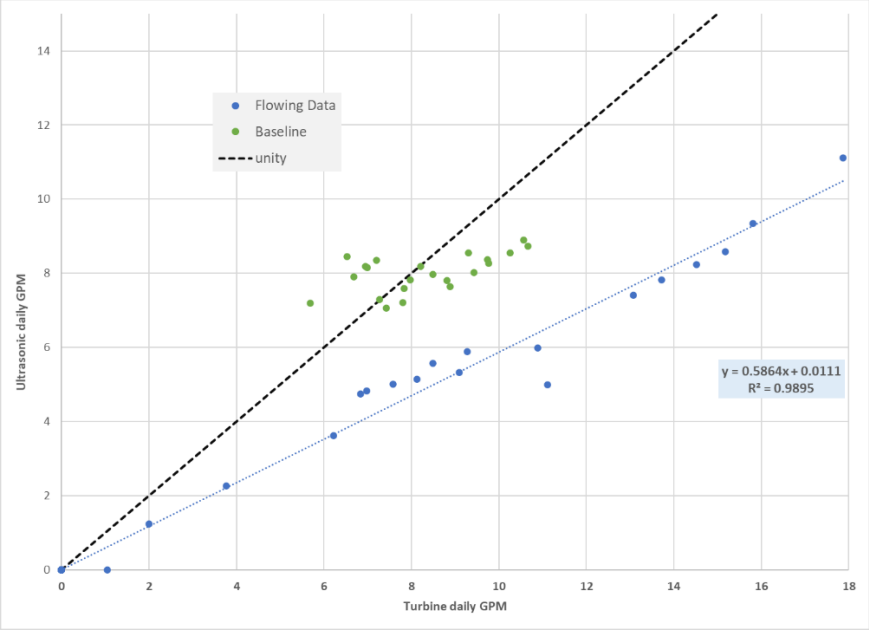


Figure 4-50. Average GPM observed by the turbine meter plotted against the average GPM observed by the ultrasonic water meter during Baseline Production and the Flowing subphase. Turbine daily average was consistently ~41% greater than the ultrasonic daily average. This behavior is significantly different than the daily average GPMs observed during baseline production, which were clustered around the unity line.

Only the first point from the IRGA data of the flowing subphase fell along the trend observed during the venting phase and all the GC samples all had significantly less hydrocarbon than the IRGA data (Figure 4-51). It was therefore believed that the IRGA meter was incorrectly calibrated. The polynomial line derived during the venting phase would overestimate hydrocarbons and was abandoned. Samples were taken weekly for GC analysis throughout the rest of production to track the composition and hydrocarbon proportion of the vented gas.

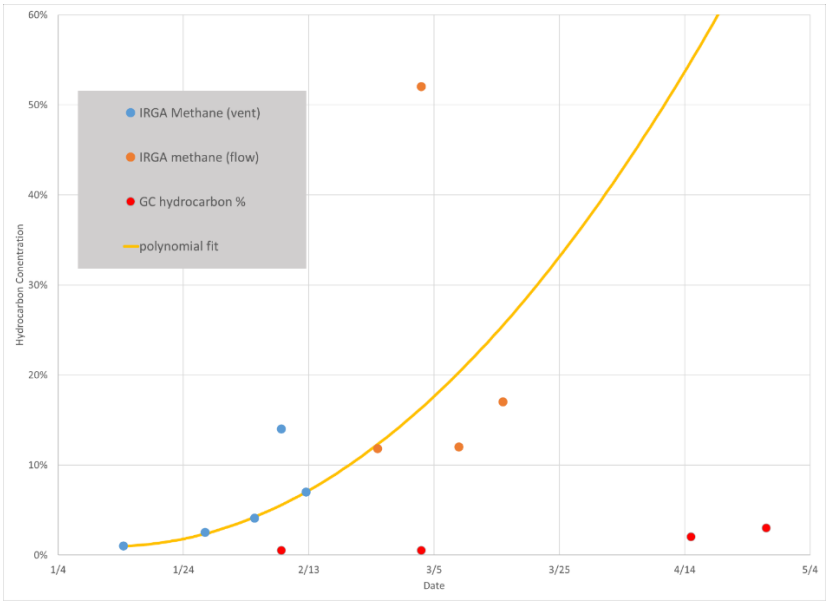


Figure 4-51. Percent methane observed throughout venting (blue dots) and flowing phases (orange dots). GC data (red dots) fall significantly beneath the IRGA data, so it was believed that the IRGA data was erroneous.

Oil Indicators

The Ultrasonic data from the flowing subphase measured little oil production. This was supported by visual inspections of the accumulated oil in the oil tank throughout the phase. However, there were several indications that oil was being produced but not measured.

- Strong odor of hydrocarbon
- Oil in the sight glass on gas/liquid separator
- Oil in samples collected from the bleeder valve on the wellhead
- A skim of oil observed floating on brine in the brine storage tank

Hydrocarbon odor was noticed near the well from the beginning of the flowing subphase. This could not be quantified but was an early indication that at least some oil was being produced.

Oil started appearing in the sight glass on the gas/liquid separator soon after the start of the flowing subphase. The proportion of oil/water appeared to be variable but was almost always observed and recurrent after emptying the sight glass. It was believed that oil could be coating the outside of the glass giving the impression that it had more oil than it appeared, but this was the first hard evidence that liquid hydrocarbon was being produced and not metered.

A bleeder valve on the wellhead was cracked open to allow fluid flowing from the annulus to be collected directly into a cup on Wednesday, April 7th (Figure 4-52). This sample contained brownish water with an estimated 5% oil cut. Subsequent samples taken from the bleeder valve contained about the same oil cut.

A layer of oil was visible in the top of the brine tank. It was difficult to determine how much oil this represented, and it was possible that it was residual oil left in the brine tank or gunbarrel separator, but the very limited amount of oil in oil tank meant that even a small amount of oil in the brine tank would indicate that a high proportion of oil production had been missed. Oil in the brine tank provided an explanation of how oil could be produced without being metered; the oil was not separating from the brine in the gunbarrel oil/water separator and was entering the brine tank. Strapping the brine tank produced inconsistent results. An oil thief sampling device was used to gather samples from the brine tank and identified oil in the top, middle, and even lowermost portion of the brine tank (Figure 4-53). These thieved samples were still foaming which was indicative of CO_2 in the brine tanks.



Figure 4-52. Fluid sample taken from the bleeder valve on April 7th. The sample contains approximately 5% oil cut and was evidence that oil was being produced but not measured.



Figure 4-53. Jars filled with samples thieved from the brine tank on April 15th from the bottom (left), middle (middle), and top (right). These samples validated that oil was present in the brine tank that a de emulsifier was required to break the oil free of water.

Updated Design for Pumping Subphase

Oil observed in the brine tank was an indication of an issue with the oil/brine separation process that had to be mitigated before continuing. Investigation revealed two potential causes of oil in brine tank, one mechanical and one chemical. The oil leg running from the outlet of the gunbarrel separator to the oil storage tank had a section of pipe that reduced from 2" to ½". This could act as a p-trap and prevent flow from the gunbarrel into the oil tank. The oil leg was re-plumbed to be continuous 2" pipe. Also, the oil deep in the brine tank suggested that the oil was having a hard time breaking out of emulsion with the brine. A chemical demulsifier treatment (Jacam OEB 9103P Emulsion Breaker Paraffin Solvent) was added to the flowline upstream of the gunbarrel separator to break the emulsion.

<u>Pumping Subphase</u>

Operations

The Pumping subphase began on Tuesday, April 21st when the oil leg of the gunbarrel separator was replumbed, the demulsifier treatment was added, and the pumping unit was turned on. The pumping unit was started at 7 strokes/minute and left running continuously. This pump speed was expected to create the same rate observed during baseline production (8 GPM or 350 bbls/day). Well head and gas prover data, ultrasonic oil and water, turbine produced and disposed, and Echometer data were compiled and analyzed daily. Fluid levels in the oil and water tanks were also measured daily and the brine tank was thieved weekly to validate the volume of oil produced and to ensure that no more oil was entering brine tank.

The Pumping subphase started with high production rates (10 GPM) caused by significant flowing. The rate declined over the next week before stabilizing around 4-6 GPM (125-175 bbls/day) (depending on whether measured by the turbine or ultrasonic meter). This decrease in production rate was coupled with a decrease in CO_2 venting rate.

Reservoir simulations consistently found that higher production rates would produce more oil, so steps were taken try to increase the production rate. Production was stopped briefly on Tuesday, April 27th for a dynamometer test to determine if the decline in fluid production rate was indicative of a problem with the pump.

Data was collected using Echometer's Polished Rod Transducer which contains an accelerometer and a strain gauge. The transducer operates by measuring the change in diameter of the polished rod and converts the diameter change to change in load on the polished rod. Total Well Management software (supplied with equipment) generates a surface and downhole card(s) for evaluation using data from the transducer.

The first issue that the dynamometer card displayed was that the downhole pump was experiencing gas interference due to CO_2 gas breaking out of the oil/brine emulsion (consistent with the venting issues prior to dynamometer test). The general shape of the downhole card revealed minor flowing well interference, fluid was rising faster than the plunger which, in turn, was holding the traveling valve open and lowering the load on the surface pump. This was also expected as the well was observed to flow after the pump was shut down, sometimes for a couple of days. The up-stroke portion of the pump cycle on the downhole card showed load loss, and there was a steep reduction in load at the beginning of the up-stroke, which is indicative of leaking tubing.

The dynamometer test was fully evaluated after realignment of the polished rod and after the rod string was pulled. Inspection of the rods revealed a couple of rods with quarter sized holes that validated the leaking tubing and contributed to the operating inefficiencies.

It was believed that CO_2 was causing the low efficiency, so the back pressure regulator was adjusted to keep 75 - 100 Psi on the tubing at the suggestion of the operator.

Operator cut demulsifier off on Wednesday, April 28th and turned it back on Wednesday, May 5th

Fluid level generally dropped but started rising on May 8th. The pump speed was increased to 8 strokes/minute on Tuesday, May 11th, and the annulus choke was closed to create back pressure on the annulus to help drive down fluid level, both of which resulted in a noticeable increase in oil production.

Fluid production stopped unexpectedly early in the morning of Tuesday, May 18th. On-site inspection determined that the pumping unit was still operating, but the polished rod had shifted relative to the horse head of the pumping unit and needed to be realigned. It was determined at this point that the duration of pumping (approximately one month) and volume of fluids produced (5,000-6,000 bbls) had matched those from the Baseline Production phase so the conditions of the Post-CO_2 Production phase had been met. This break in pumping marks the end of the first pumping subphase.

Pumping Findings

The first Pumping phase concluded with 5,000-7,500 bbls water, 24-30 bbls oil, and 301 tons of CO_2 produced (Table 4-13). The generally stable production rate resulted in smooth cumulative production curves (Figure 4-54 and Figure 4-55). The production rate was around 8 GPM at the beginning of the subphase and decreased over the next few days before leveling off at around 5 GPM for the duration of the subphase.

Table 4-13. Injection and production data at the end of the first pumping period.

Phase	Data	Source	Phase Value	Total Value
Baseline	Water (bbl)	Turbine produced	5,153	
		Turbine disposed	4,653	
		Ultrasonic	5,010	
	Oil (bbl)	Ultrasonic	0	
CO_2 Injection	CO_2 (ton)	Turbine	840	
		Truck weight	1,010	
Vent	CO_2 (ton)	Gas Prover	147	
Flow	Water (bbl)	Turbine produced	2,432	
		Turbine disposed	1,731	
		Ultrasonic	1,612	
	Oil (bbl)		5	
	CO_2 (ton)	Gas Prover	94	241
1^{st} Pumping phase	Water (bbl)	Turbine produced	5,020	7,452
		Turbine disposed	4,174	5,905
		Ultrasonic	3,519	5,131
	Oil (bbl)		25	30
		Tank strap	24	
	CO_2 (ton)	Gas prover	60	301

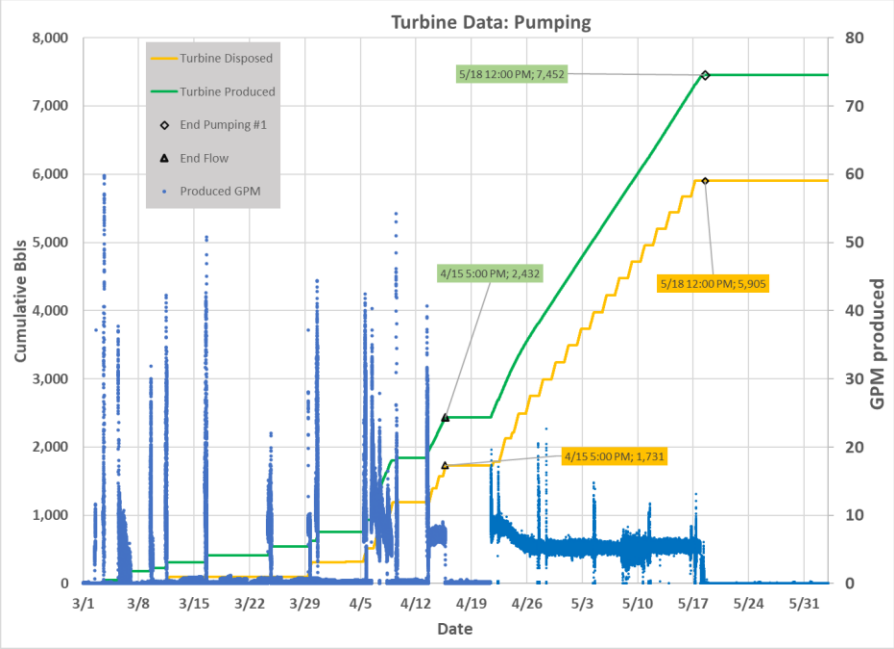


Figure 4-54. Cumulative produced total fluid (green line), water disposed (yellow line), and produced GPM observed by the turbine meters (blue dots) for the duration of the Post CO_2 production phase. A total of 7,452 bbls of fluid were produced and 5,905 bbls water were disposed.

The overall character of the ultrasonic production curve was similar to the turbine data. The cumulative volume increased consistently while the pump was active (Figure 4-55). A total of 5,131 bbls of water and 29.5 bbls of oil were produced before the well was shut in, but both continued to register after pumping had concluded until the meter was turned off on May 25th. This additional data was believed to be caused by a rounding error.

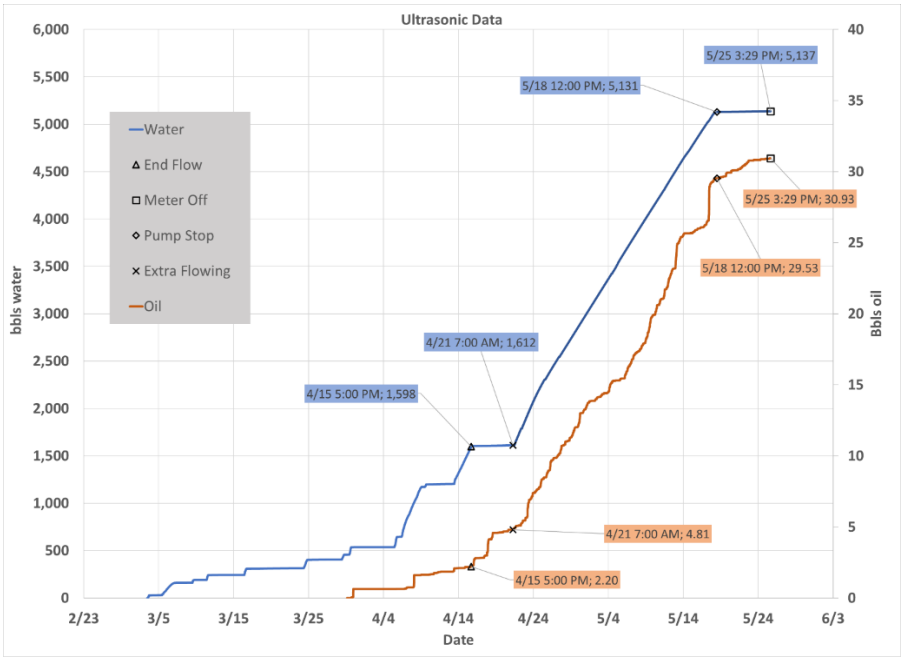


Figure 4-55. Cumulative oil and water production observed by the ultrasonic meter during the flowing and pumping subphases. A total of 5,131 bbls of water and 29.5 bbls of oil were produced during the first pumping subphase.

The CO_2 venting rate was more stable in the pumping subphase than the flowing subphase (Figure 4-56). The rate increased immediately after pumping began, broke over and decreased after a few days before stabilizing at approximately 1 ton/day. Some variability occurred when attempts were made to increase production. A total of 301 tons of CO_2 were vented at the end of the first pumping period.

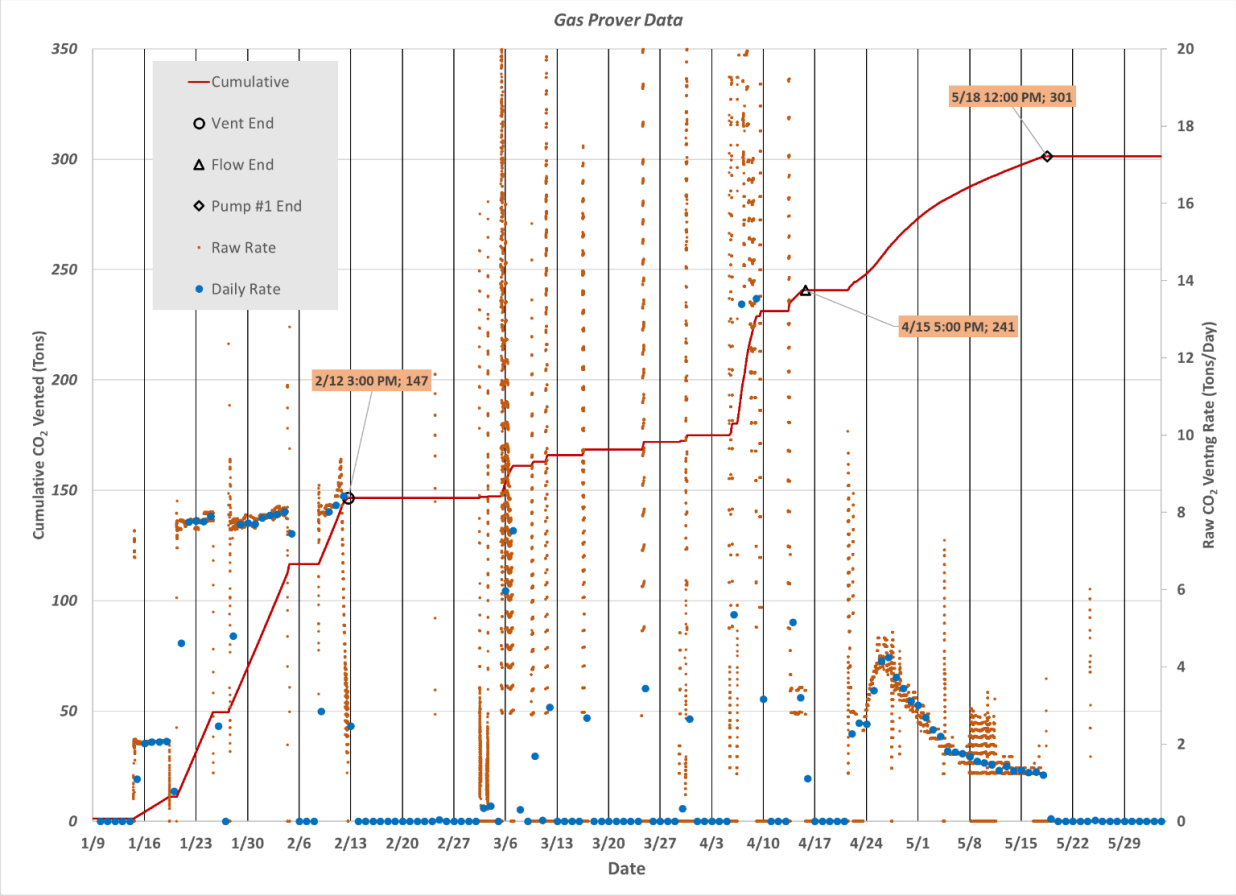


Figure 4-56. Rate and cumulative CO_2 vented through the flowing subphase based on pressure, temperature, and orifice size. The end of the venting subphase is marked with a hollow circle, the end of the flowing subphase is marked with a hollow triangle, and the end of the first pumping subphase is marked with a hollow diamond on the cumulative curve.

Echometer derived fluid level was calculated and checked daily. Fluid level slowly decreased once pumping started until May 9th, when it unexpectedly increased for two days (Figure 4-57). The increase in pumping rate and increase in backpressure on the annulus on May 11th resulted in an immediate decline in fluid level that continued until the pumping unit was shut off on May 18th. Observations of pumping unit behavior from the field combined with the lack of production suggested that the well was pumped off, but Echometer derived fluid level indicated about 1,000 feet of fluid above the pump. The fluid level increased after pumping ended before starting to level off around static fluid level (1,100 ft below surface).

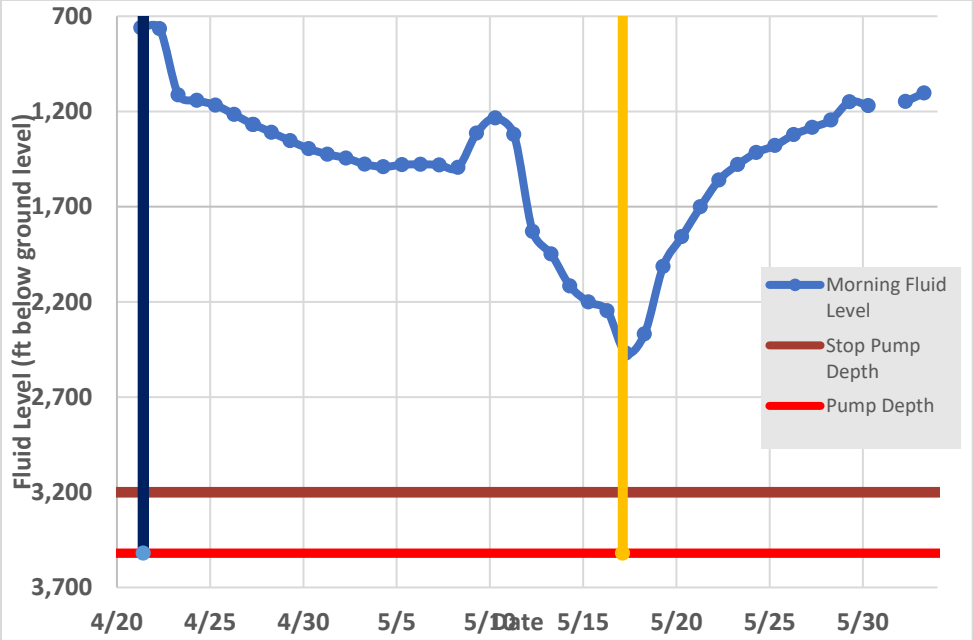


Figure 4-57. Echometer derived fluid level taken every morning over the duration of the first pumping subphase. Fluid level steadily drops once the pump is turned on April 21st until May 8th, when it unexpectedly begins to rise. Fluid level drops at a higher rate once the pump was turned up to 8 strokes/minute and rises again once pumping concluded on May 18th (shown with a vertical yellow line). Fluid level was believed to be pumped down to the pump (lower horizontal red line).

Uncertainty with the ultrasonic oil data was a concern so the oil tank was strapped daily as a secondary check. Unfortunately, the low rate of oil production created uncertainty in both data sources.

The oil leg of the gunbarrel separator was replumbed before the pumping subphase to be a continuous run of 2" pipe, which the ultrasonic meter requires to be full of fluid to function properly. The oil recorded by the ultrasonic meter appeared as single data points surrounded by no detect values, but a constant trickle of oil was visually observed entering the oil tank on several occasions beginning on April 27th. It was therefore believed that the rate of oil production was too low to fill the 2" pipe and the ultrasonic data was unreliable.

Tank strap measurements rely on measuring the level of the oil in the tank. One inch of fluid in the 210-bbl tank represents 1.16 bbls of oil (often more than was produced each day), so even a small discrepancy in the measurement, which was taken manually, could mask daily oil production. While the tank strap data contained some obviously erroneous measurements (there were some days where the measured cumulative oil production dropped) it was believed to be a more accurate measure of the cumulative oil produced than the ultrasonic data.

Tank strap values and cumulative ultrasonic data were compared each day throughout the subphase (Figure 4-58). Ultrasonic production showed up as soon as the subphase began. During this time, oil was observed in the base of the oil tank, but part of the base was still exposed so the tank strap method was still recording zero oil. Tank strap oil started showing up on Monday, April 27th when it went from zero to ~5 bbls. There was good agreement between the two data streams for the rest of the subphase and an estimated 4-5 bbls of oil were produced before the well was shut in on May 18th. The oil production appeared to be accelerating in the four to five days before the well was shut in (Figure 4-58).

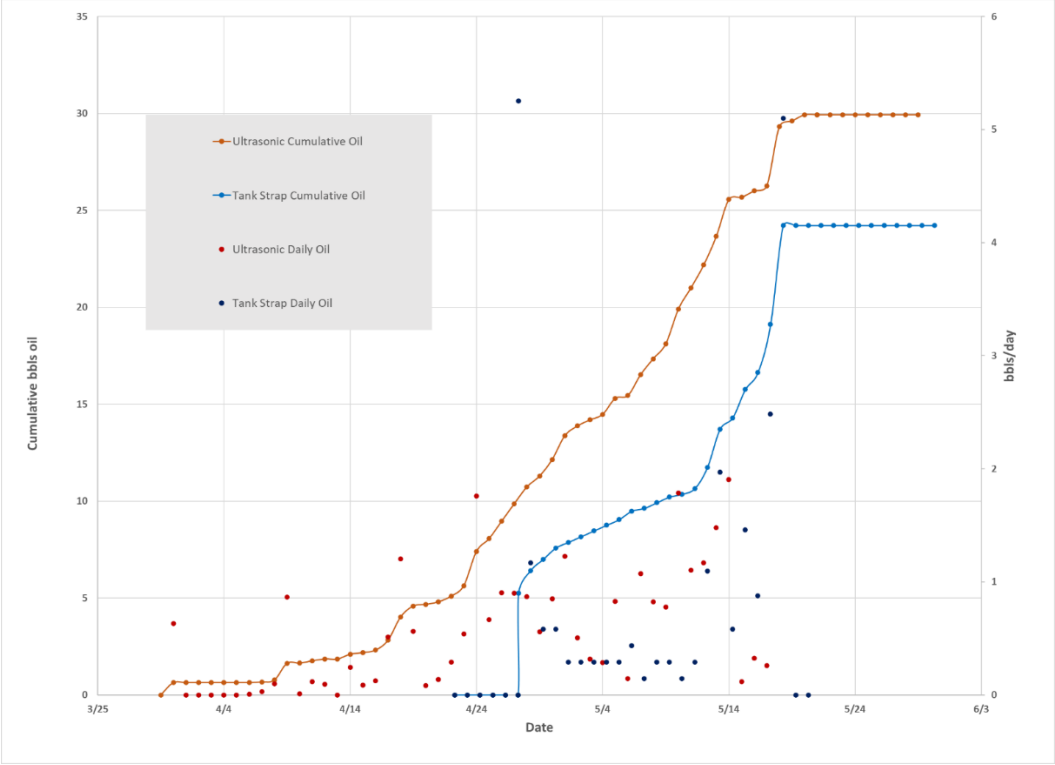


Figure 4-58. Cumulative and daily oil data observed by the Ultrasonic (orange line and red dots) and tank strap (light blue line and dark blue dots). The Ultrasonic meter measured a total of 30 bbls of oil while the tank strap measured 24 bbls.

There were indications that underestimation of CO_2 and oil observed in the flowing subphase continued during the pumping phase. Fluid samples thieved from the brine tank consistently had bubbles and significant oil cuts (Figure 4-59) The disagreement between the turbine and ultrasonic meters also continued throughout pumping. It is therefore believed that the volume of oil and CO_2 reported here underestimate the amount removed from the reservoir, but no data is available that allows for this error to be quantified.



Figure 4-59. Fluid samples thieved from the brine tank on April 23rd, 2021 (upper image) and April 27th, 2021 (lower image) showing that oil was found in the brine tank during the Pumping Phase.

The linear relationship between turbine produced and ultrasonic water meters observed in the Flowing subphase (Figure 4-50) continued into the pumping subphase (Figure 4-60). The turbine production was consistently 30% greater than the ultrasonic production (the difference was 41% in the flowing subphase). If the disagreement between the two meters was caused by CO_2 in the produced fluids, the better agreement may suggest that either the proportion of CO_2 had decreased over the course of production, or the lower production rate was allowing CO_2 more time to break free of the fluid.

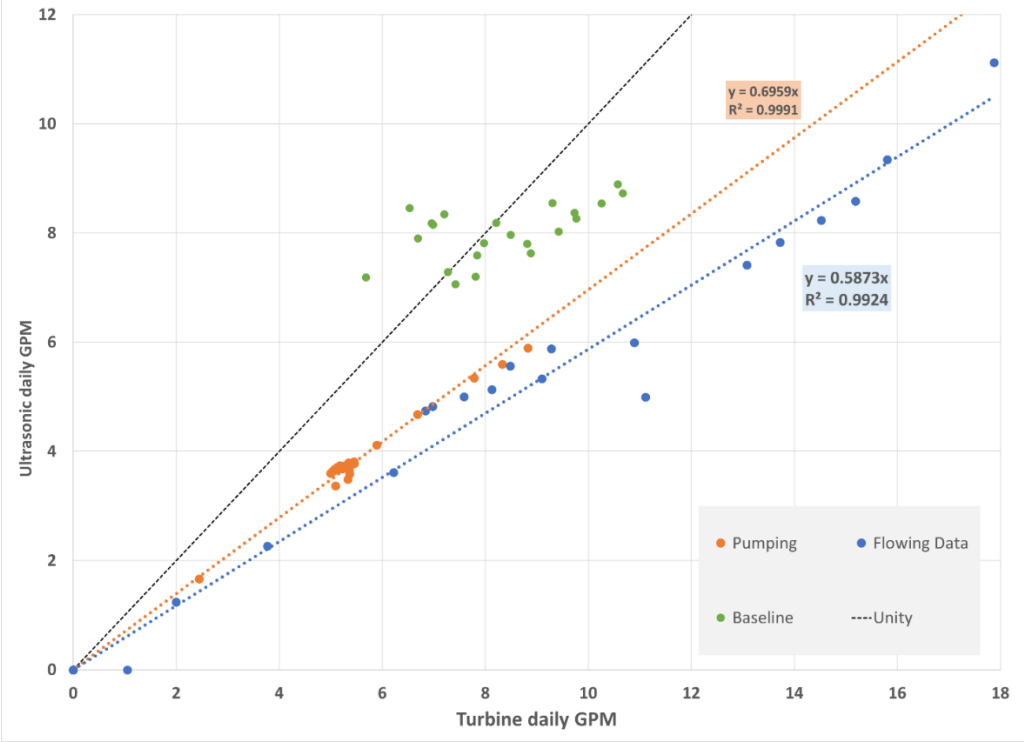


Figure 4-60. Average GPM observed by the turbine meter plotted against the average GPM observed by the ultrasonic water meter for the post CO_2 production phase. Turbine daily average was consistently 30% greater than the ultrasonic daily average.

The trends in the differences between production turbine, disposal turbine, and ultrasonic water data streams observed in the flowing subphase also continued throughout the pumping subphase but the more prolonged, consistent production of the Pumping subphase allowed for more time for the data to diverge (Figure 4-61).

The turbine production meter reported significantly higher production than others. The difference between production turbine and combined ultrasonic (oil + water) data widened as the production progressed, consistent with the 30% greater rate (Figure 4-60). The production turbine meter observed 1,500 bbls more fluids than the disposal turbine meter. The disposal turbine meter measured about 800 bbls more than the Ultrasonic water meter.

The disagreement between turbine produced and turbine disposed suggests that either the production meter was overestimating the volume of fluids produced or the disposal meter was underestimating it. The ultrasonic water production is 50% of the pump capacity (7 strokes/minute was expected to create a

rate of about 8 GPM, but the ultrasonic only measured around 4 GPM). It was believed that these differences could be caused by CO_2 in the fluids as described in the flowing subphase.

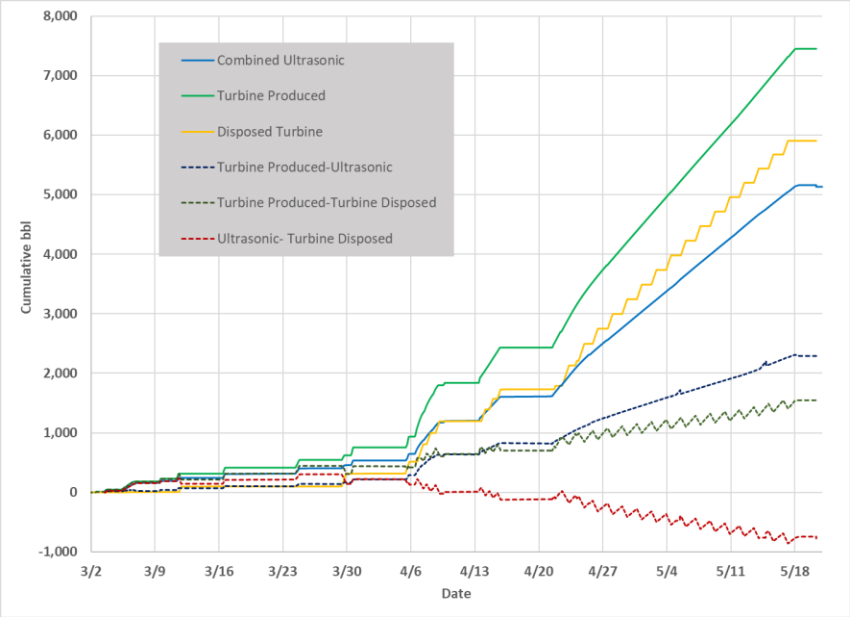


Figure 4-61. Cumulative water recorded by production turbine meter (solid green line), disposal turbine meter (solid yellow line), and ultrasonic water meter (solid blue line) for the flowing and first pumping subphases. Turbine produced was significantly greater than any of the others. Turbine disposed was slightly less than the combined ultrasonic but overtook it during pumping subphase and continued to diverge.

Pumping #2

The conditions necessary to conclude the Post CO_2 Production Phase had been satisfied, but the operator was optimistic that the higher oil cut observed at the end of the first pumping period would be indicative of the expected oil cut during continued pumping with the well pumped off. Additional pumping offered an opportunity to pursue economic oil production and to continue gathering data to better understand the EOR and associated storage performance of the ROZ. Thus, pumping and data acquisition resumed on June 10th and continued until September 27th.

Operations

While checking the damage caused when production stopped, the rods and tubing were pulled from the well and 5-6 holes up to 0.25-in diameter were discovered in two joints of tubing at approximately 1,500 feet below surface. It was believed that these holes were responsible for the interruption in production; Once fluid level in the annulus dropped below them, the pumping unit circulated fluid from the tubing back into the annulus rather than bringing it to surface. The damaged tubing joints were replaced, the rods and tubing were run in, and pumping resumed on Thursday, June 10th. The pumping unit was set to 4.6-5.0 strokes/minute which resulted in a fluid production rate of 4.5 GPM. The pumping unit speed was increased to 5.3-5.5 strokes/minute (increasing fluid production rate to 7.5 GPM) on Tuesday, June 15th. This rate was maintained with less drawdown than was observed in the first pumping subphase.

The disposal turbine meter stopped reporting data on July 16th (Figure 4-61). Upon disassembly, flakes of rust were observed to prevent the turbine from spinning freely. Rust flakes continued to lodge in the disposal turbine meter because of the lack of an upstream filter and it was frequently disassembled and cleaned. Thus, the turbine meter functioned only intermittently for the remainder of the production period.

While disassembling the turbine meter to remove rust flakes, some oil was consistently found in the brine effluent, indicating failure of the brine/oil emulsion to fully break up despite application of demulsifier chemical treatment. However, on a few occasions during the pumping period, the demulsifier treatment was not active, due to delays in having the chemical tank refilled when it was empty, or inadvertently failing to turn the chemical pump back on following routine maintenance of the surface equipment. Daily oil production was noticeably impacted (including days of zero oil production) when the demulsifier treatment was inactive (Figure 4-64).

A Murphy switch on the tank battery tripped and shut the pumping unit down on July 29th. It was determined that the disposal well was building pressure faster and holding it longer than before, likely due to the accumulation of rust flakes at the flow meter in the disposal line. Pumping resumed on August 5th and continued until the test concluded on September 28th.

Data

The production turbine meter functioned consistently throughout the phase, but the disposal turbine meter was intermittently disabled by rust flakes and did not provide a reliable figure for cumulative volume of disposed fluid (Figure 4-62). The ultrasonic water meter displayed a similar trend, but the ultrasonic oil meter recorded erroneous production even when the pumping unit was not operating, and the well was shut in (Figure 4-63). Tank strap measurements of cumulative oil production totaled less than half of the production reported by the ultrasonic meter (Figure 4-64).

The CO_2 production rate oscillated between 0.3-1 tons/day at the beginning of the Pumping #2 subphase but stabilized at 0.3 tons/day on August 25th and remained consistent for the remainder of the production period (Figure 4-65). Daily fluid levels behaved as expected; fluid levels dropped when the pump was active and sharply increased when the well was shut in (Figure 4-66).

Pumping concluded on September 27, 2021, with a total of 14,095-25,043 bbls of water, 47-115 bbls oil, and 357 tons of CO_2 produced (Table 4-14). The data provided here are the raw values reported by the relevant meter. The disagreement between meters will be discussed and resolved in the next section.

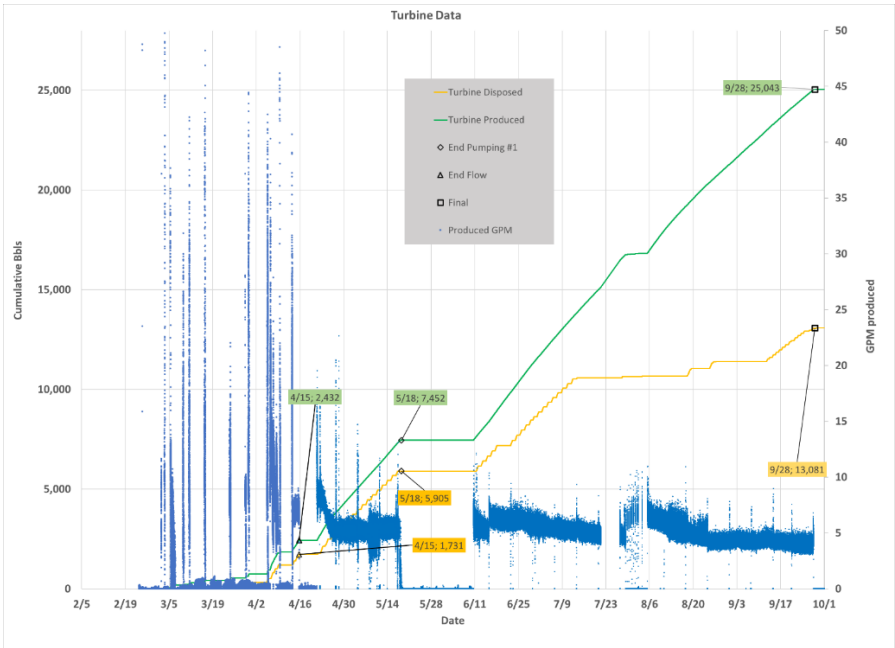


Figure 4-62. Cumulative produced total fluid (bbls; green line), water disposed (bbls; yellow line), and fluid production rate (GPM; blue dots) observed by the turbine meters for the duration of the Post CO_2 production phase. A total of 25,043 bbls of fluid were produced and 13,081 bbls water were disposed.

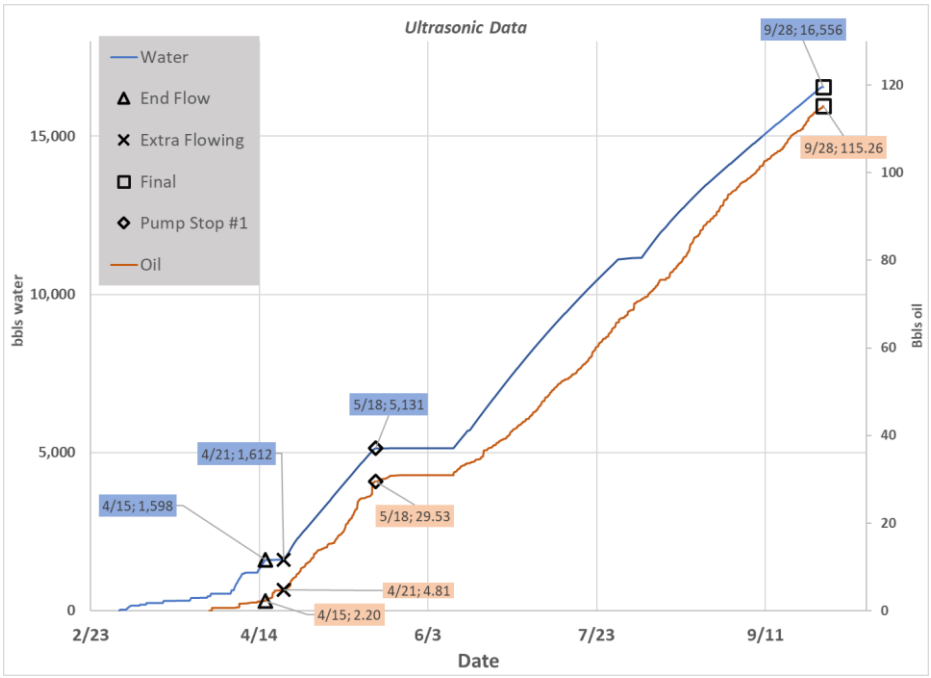


Figure 4-63. Cumulative oil and water production observed by the ultrasonic meter during the flowing and first and second pumping subphases. A total of 16,556 bbls of water and 115 bbls of oil were produced.

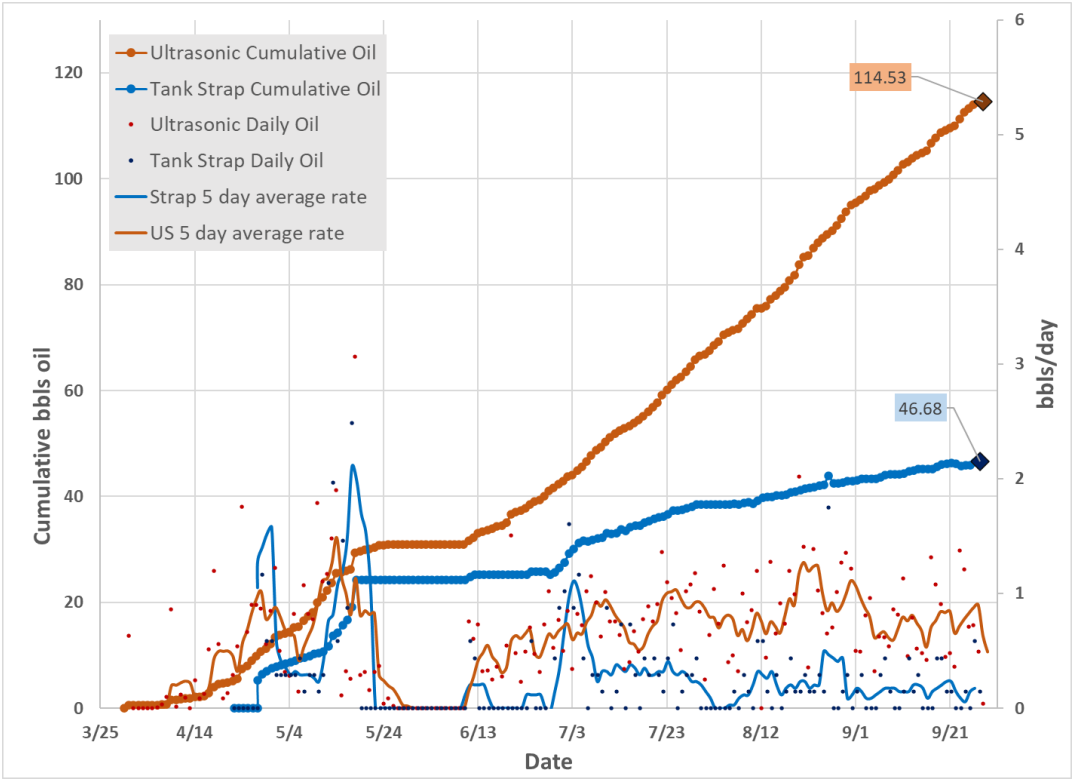


Figure 4-64. Cumulative and daily oil data observed by the Ultrasonic (orange line and red dots) and tank strap (light blue line and dark blue dots) at the end of the Post-CO_2 Production Phase. The Ultrasonic meter measured a total of 114 bbls of oil while the tank strap measured 47 bbls.

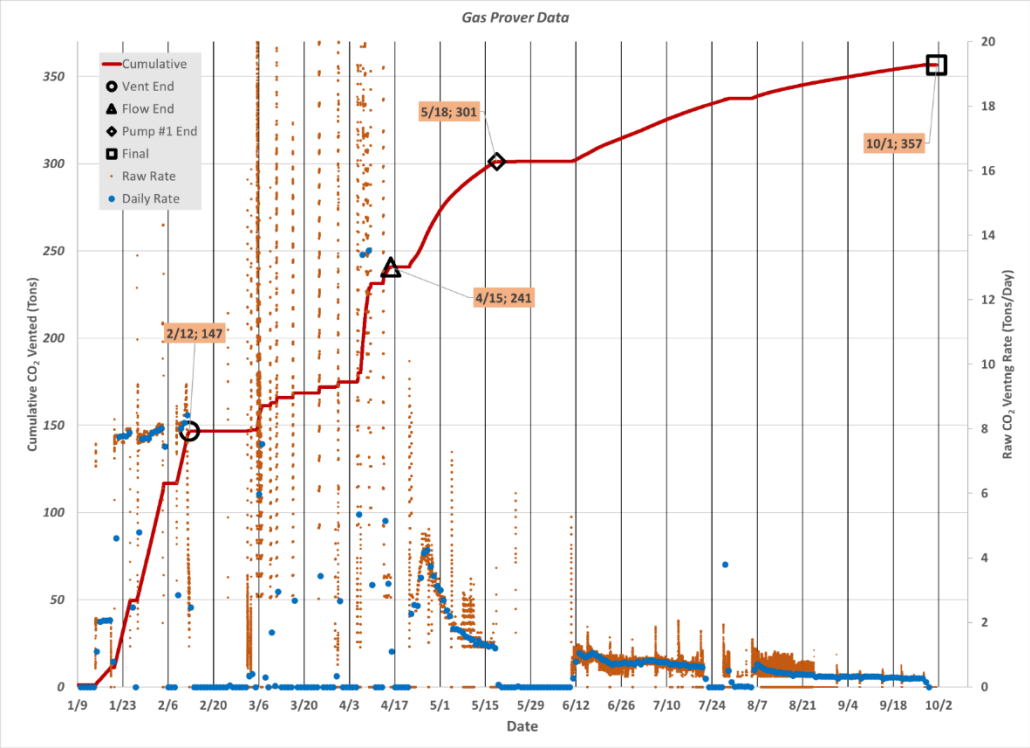


Figure 4-65. Final gas prover data. The gas prover measured a total of 357 tons of CO_2 vented over all phases.

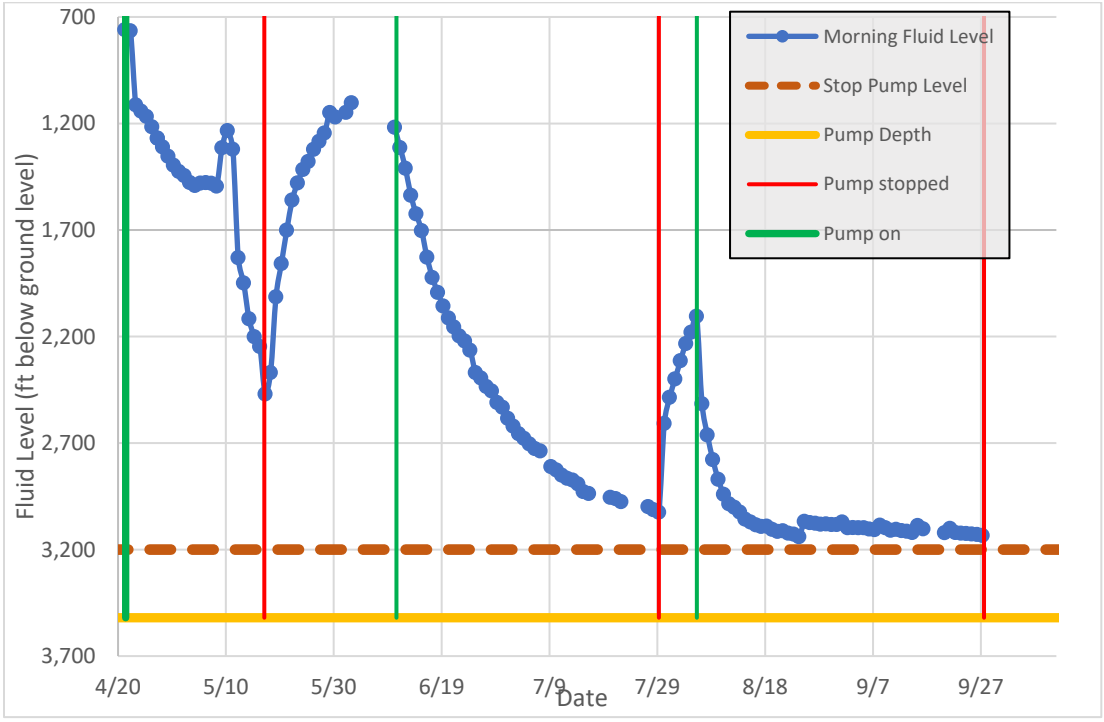


Figure 4-66. Echometer derived fluid level for The Post CO_2 Production Phase. Fluid level steadily declined during production (right of vertical green lines) and increased when the pump was not active (right of vertical red lines).

Table 4-14. Final raw data showing the mass and volume of the fluids injected and produced from the Holsapple well. There were redundant instruments used to measure fluids being injected and produced through most project phases.

Project Phase	Data	Source	Value	Total
Baseline	Water (bbl)	Turbine produced	5,153	
		Turbine disposed	4,653	
		Ultrasonic	5,010	
	Oil (bbl)	Ultrasonic	0	
CO_2 Injection	CO_2 (ton)	Turbine	840	
		Truck weight	1,010	
Vent	CO_2 (ton)	Gas Prover	147	
Flow	Water (bbl)	Turbine produced	2,432	
		Turbine disposed	1,731	
		Ultrasonic	1,612	
	Oil (bbl)		5	
	CO_2 (ton)	Gas Prover	94	241
1st Pumping	Water (bbl)	Turbine produced	5,020	7,452
		Turbine disposed	4,174	5,905
		Ultrasonic	3,519	5,131
	Oil (bbl)		25	30
		Tank strap	24	
	CO_2 (ton)	Gas prover	60	301
2nd Pumping	Water (bbl)	Turbine produced	17,591	25,043
		Turbine disposed	7,176	13,081
		Ultrasonic	8,964	14,095
	Oil (bbl)		65	95
		Tank strap	23	47
	CO_2 (ton)	Gas prover	56	357

Data Corrections

CO_2

Gas prover data was assumed to be representative of the amount of CO_2 produced, but the venting rate was calculated based on the assumption that the vented gas was pure CO_2. There was evidence that the proportion of hydrocarbon in the vented gas increased over time, so the raw gas prover data was believed

to overestimate the amount of CO_2 vented. Attempts were made to account for this over the course of testing by correcting the CO_2 venting rate by the proportion of methane measured by the IRGA device (see the "gas composition alteration" subsection at the end of the Venting section [Figure 4-45]), but preliminary analysis of GC data suggested that the IRGA device was overestimating the amount of hydrocarbon in the vented gas (see interpretation subsection at the end of the Flowing section [Figure 4-51]). GC analyses of all the vented gas samples, available after testing had concluded, provided data that could be used to more reliably correct the amount of CO_2 vented.

The proportion of CO_2 and the overall specific gravity of the vented gas derived from the GC analyses decreased over time (Figure 4-67). Lines were regressed through both datasets. The equation defining the line fit to the specific gravity data (blue box and dashed line in Figure 4-67) was used to correct the specific gravity term in Equation 4-4 to calculate the total venting rate for each data point. This new venting rate was then multiplied by the proportion of the vented gas that was CO_2 as defined by the line fit to the CO_2 proportion data points (yellow box and dashed line in Figure 4-67) to derive a new cumulative volume of CO_2 curve (Figure 4-68). The concentration of CO_2 remained above 90% and the change in specific gravity was low, so the total amount of CO_2 vented only decreased from 357 to 349 tons. This decrease in vented CO_2 is caused by vaporized hydrocarbons and represents additional EOR.

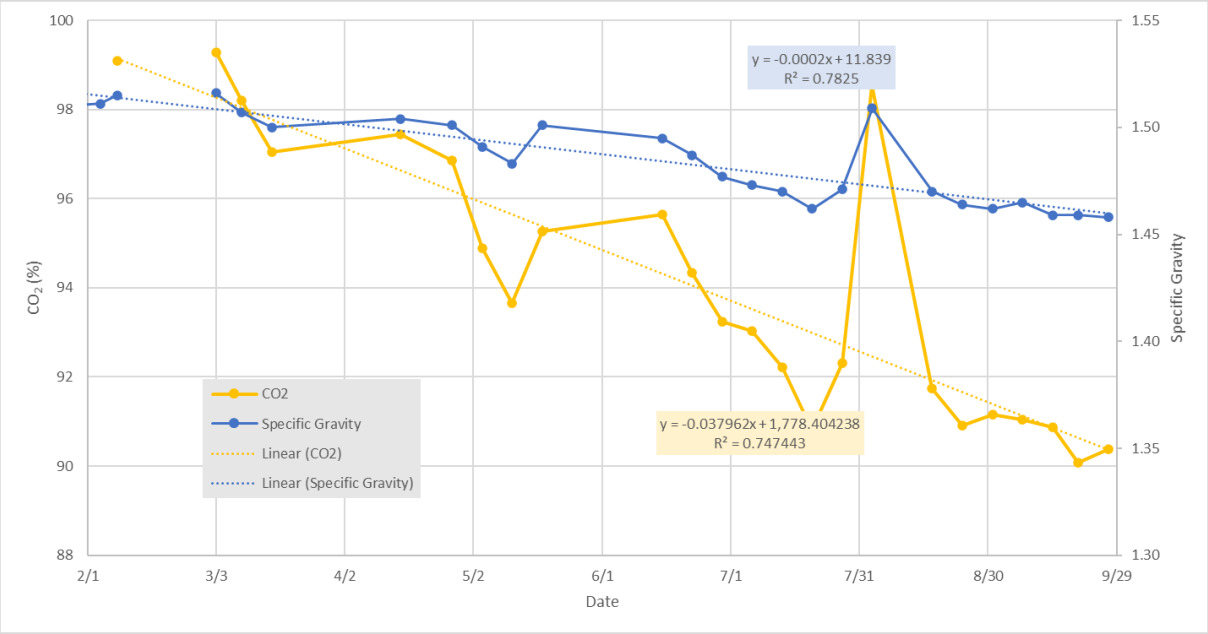


Figure 4-67. Concentration of CO_2 and specific gravity of vented gas as derived from GC samples. The concentration of CO_2 decreases over time, but never gets below 90% except for a single data point believed to be erroneous. This is coupled with a decrease in the specific gravity of the vented gas. Equations defining the lines regressed through each of the data (dashed lines) were used to adjust the amount of CO_2 vented.

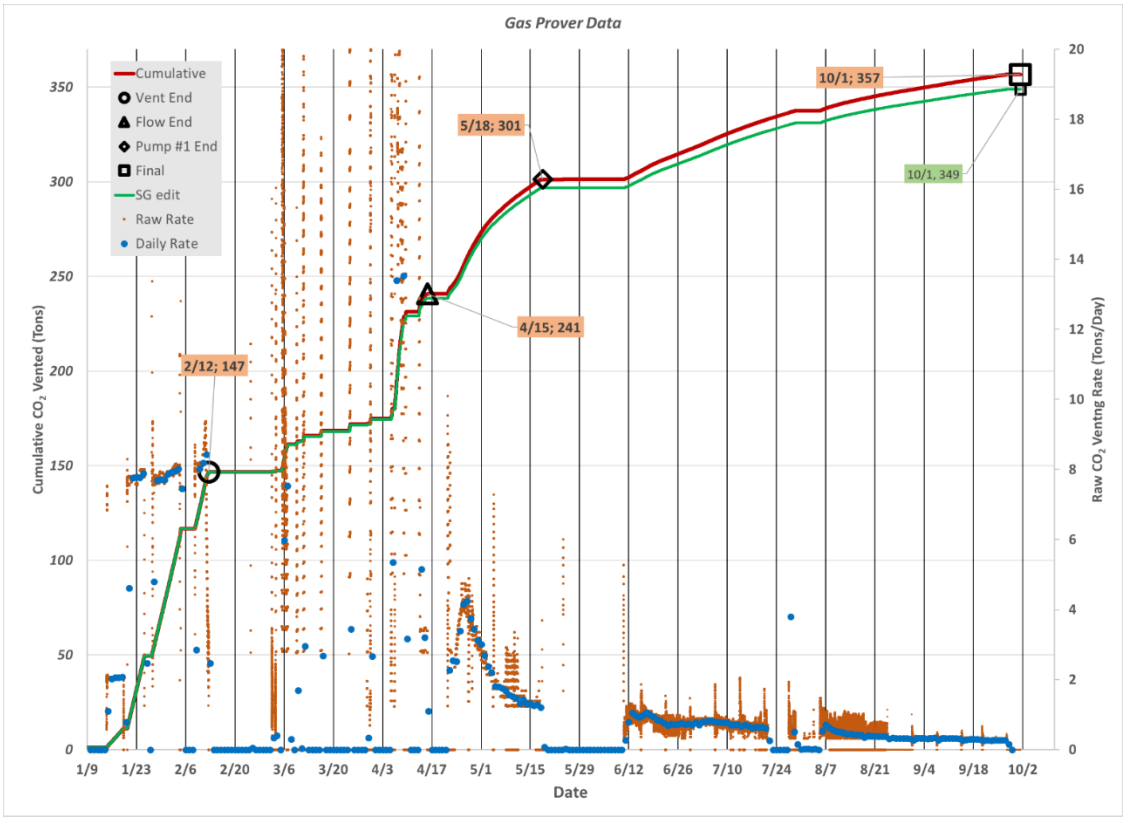


Figure 4-68. Volume of CO_2 produced after accounting for hydrocarbons derived from GC data. Cumulative volume of CO_2 produced derived from raw gas prover data is shown in red line and cumulative volume of CO_2 produced adjusted for hydrocarbon shown in green. Accounting for hydrocarbons reduces the total amount of CO_2 vented from 357 tons to 349 tons.

Oil

Oil observed in the brine tank and disposal turbine meter represents oil that did not properly demulsify from the brine and thus was not measured. Based on this evidence, the measured oil production underestimated the true oil production. No data was available to quantify this error, so a conservative estimate was developed.

Throughout the flowing subphase, oil production was indicated at the wellhead through observations of the scent of hydrocarbon gas in the vented gas stream, oil in the gas/liquid separator sight glass, and through periodic fluid samples collected from the bleeder valve on the wellhead. Despite this, oil was not accumulating in the oil tank downstream of the gunbarrel separator. Plumbing issues between the gunbarrel separator and the oil tank were discovered at the end of the flowing subphase and are interpreted to have caused all preceding oil production to be diverted into the brine tank. Oil was observed in the brine tank at the end of the flowing subphase (Figure 4-53). Since brine exits the bottom of the gunbarrel before being plumbed into the top of the brine tanks, an oil/brine emulsion had to have filled the gunbarrel separator during the flowing subphase. Oil production for the Flowing Subphase was estimated by assuming 0.5 bbl of oil production on days with water production between 50-100 bbls and 1 bbl of oil produced on days with water production over 100 bbls. This is consistent with the oil cut observed during the Pumping Phases and results in an estimated 15 bbls of oil production that we attribute to the Flowing Subphase that was not metered (Figure 4-69).

15 bbl of oil is considered a conservative estimate for several reasons. This estimate assumes that the oil cut during the flowing phase was comparable to the oil cut during the pumping phase, but the indirect indicators of oil production (i.e., hydrocarbon odor, oil in sight glass) were more pronounced during flowing. The production rate was much higher during the Flowing Subphase, which reservoir simulation results concluded would have resulted in a higher oil cut. Conventional wisdom also suggests that the best oil response would occur when the well starts producing and the oil cut would decline over time. These factors suggest that the flowing subphase should have a better oil response.

The updated estimate adds oil production to the Flowing Subphase but does not change the oil produced during pumping. We assumed that replumbing the oil tank before pumping began prevented additional oil from entering the brine tank, but oil was observed in samples thieved from the brine tank throughout the duration of the pumping period and in the disposal meter near the end of testing. It is not clear whether this oil entered the brine tank during flowing and remained there for the rest of production or oil continuously entered the brine tank over the entire course of production. However, the demulsifier was found to be turned off or set too low several times during pumping, and the unexpectedly viscous nature of the oil produced may have prevented the demulsifier from working properly.

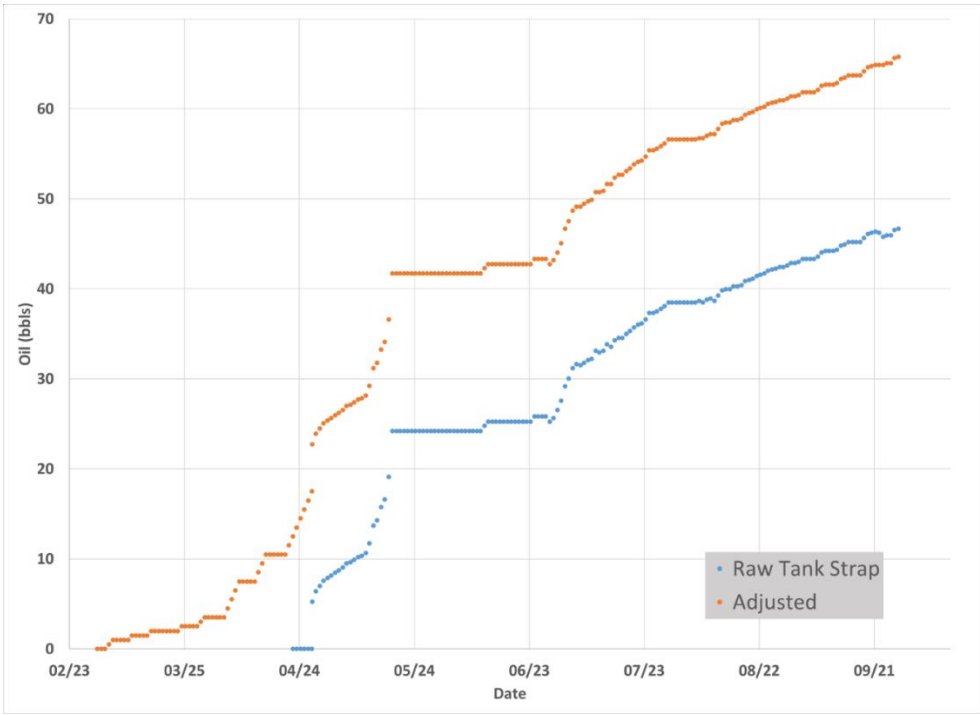


Figure 4-69. Cumulative oil production as measured by raw tank strap measurements (blue) and adjusted for missing flowing data (orange).

Water

Three meters were used to measure water production; the Production Turbine Meter upstream of the gunbarrel separator measured the volume of total fluid produced, the Ultrasonic Water Meter between gunbarrel separator and brine storage tank measured the fluid entering the brine tank, and the Disposal Turbine Meter downstream of the brine tank measured the volume of fluid disposed. The redundant meters were used to identify if a meter was not functioning properly, but there was significant disagreement among all three meters that began during the Flowing Phase (Figure 4-49) and continued throughout both Pumping Phases (Figure 4-61 and Figure 4-70).

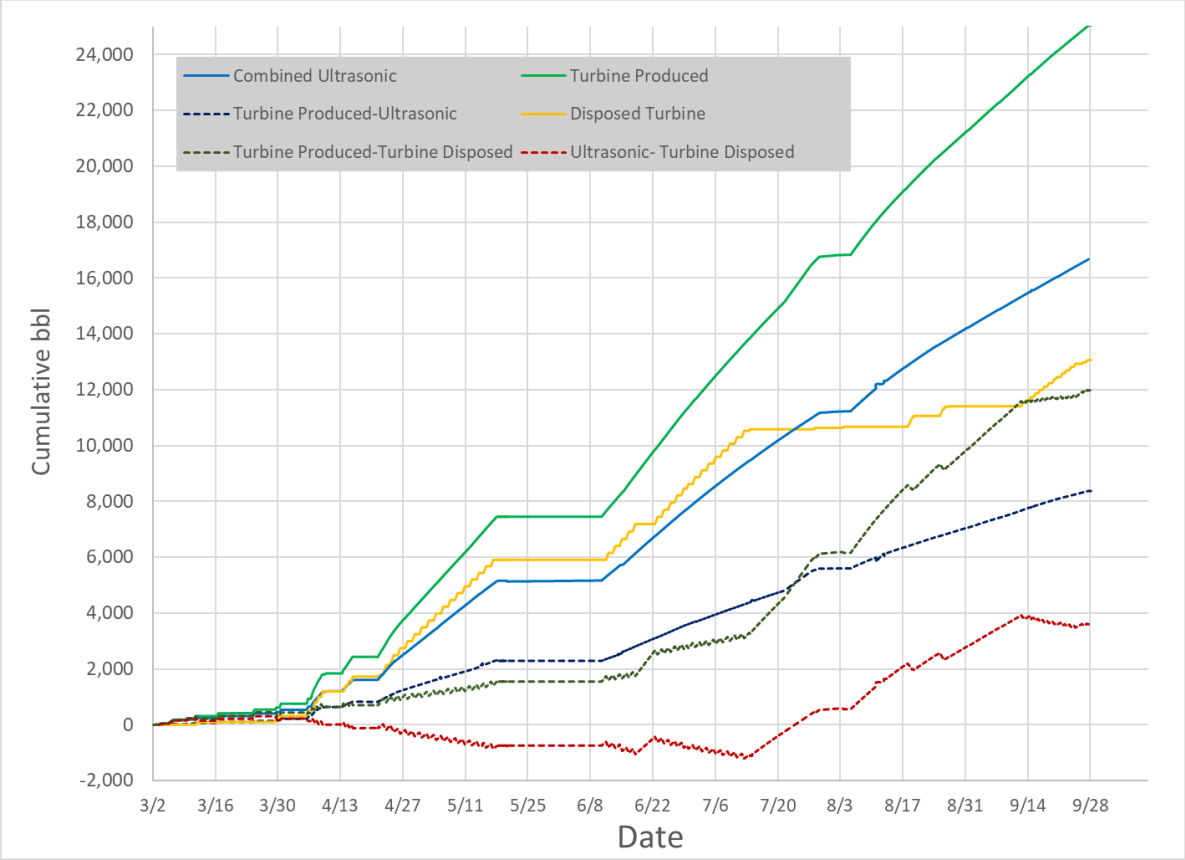


Figure 4-70. Cumulative water recorded by production turbine meter (solid green line), disposal turbine meter (solid yellow line), and ultrasonic water meter (solid blue line) for the post CO_2 production phase (flowing and first and second pumping subphases). Turbine produced was significantly greater than any of the others. Turbine disposed was slightly less than the combined ultrasonic but overtook it during pumping subphase and continued to diverge.

The Production Turbine meter was located immediately downstream of the gas liquid separator. Turbulent flow created by the churning of the fluid leaving the separator could have caused the meter to overestimate flow, particularly during the flowing phase when production rates were the highest.

Oil and/or CO_2 in the produced fluid could have also created the disagreement by causing the Ultrasonic Water Meter to underestimate flow. The production rate measured by the Ultrasonic Water Meter was approximately equal to the production rate measured by the Production Turbine Meter during the Baseline Production Phase (in which brine alone was produced without entrained oil or CO_2), but it was consistently 40% lower than the Production Turbine Meter during the Flowing Subphase (Figure 4-50), and consistently 30% lower than the Production Turbine Meter during the Pumping Phases (Figure 4-60 and Figure 4-71). The Flowing Subphase was likely to have a higher proportion of CO_2 in the produced fluid, and the higher production rate observed during Flowing Phase (>8 GPM as opposed to <6-7 GPM measured during pumping phases) would allow for less time for the CO_2 to break free in the in the gas/liquid separator and vent through the prover. This higher proportion of CO_2 in the produced fluid amplified the disagreement in the flowing subphase. Also, improper plumbing during the Flowing Subphase resulted in oil being directed to the brine tank (through the Ultrasonic Meter on the brine tank). The plumbing was resolved after the Flowing Subphase, so oil would have less (or no) impact on the Ultrasonic Meter during the Pumping Phases. Unfortunately, the impact of turbidity on the Produced Turbine meter, and the amount of oil and CO_2 dissolved in fluid is unknown and likely changed over time.

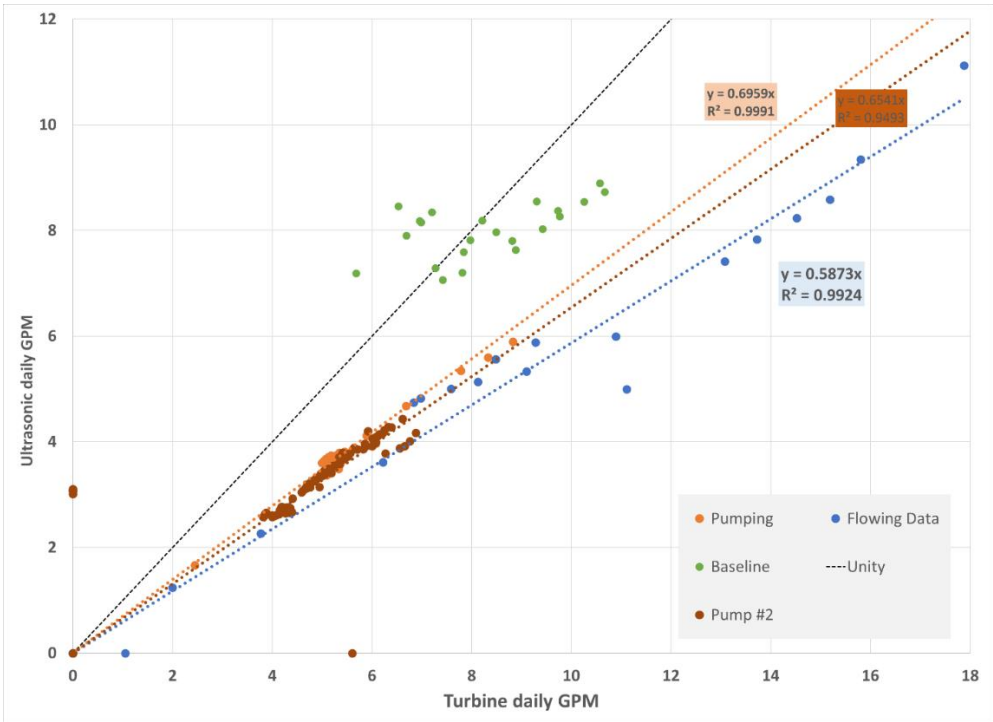


Figure 4-71. Average GPM observed by the turbine meter plotted against the average GPM observed by the ultrasonic water meter after the 2nd Pumping Phase. Turbine daily average was consistently 40% greater than the ultrasonic daily average during the Flowing Phase (blue dots and line), 30% greater during the 1st pumping phase (orange dots and line) and 35% greater during the 2nd pumping phase (red dots and line).

The Disposal Turbine Meter was the meter least likely to be influenced by oil or CO_2 in the produced fluid; Oil would be diverted to the oil tank, and any remaining CO_2 entrained in the oil/brine emulsion would have time to outgas in the gunbarrel separator and brine tanks before reaching the meter. Also, the controlled flow from the brine tank to the disposal well would likely be laminar, so the Disposal Turbine Meter was believed to be the most accurate representation of the water produced. However, rust flakes caused the Disposal Turbine Meter to stop functioning several times during the Pumping Phases, so it could not be used directly to estimate the volume of water produced. Therefore, an attempt was made to use its data to correct the data from the ultrasonic meter.

Evaluation of the data revealed two periods during the Flowing Phase, and three periods during the Pumping Phases, in which both the Ultrasonic Water and Turbine Disposed Meters were consistently active. These intervals displayed negative slopes, where the Disposal Turbine Meter was increasing at a greater rate than the Ultrasonic data. Lines regressed through these intervals showed that data were correlated (high R^2 values). The slope was -50 during the Flowing Phase and -30 during the Pumping Phases (three pumping intervals are visible in Figure 4-72). This suggests a linear disagreement between the two meters, which was consistent with oil and/or CO_2 causing the Ultrasonic meter to underestimate flow.

These slopes were used to correct the data from the Ultrasonic meter for the flowing phase by multiplying the rate by 1.31 and pumping phases by multiplying the rate by 1.23. Doing so results in negligible slope during these intervals, which suggests that the Ultrasonic Water Meter was approximating the Disposal Turbine Meter data (Figure 4-73). Correcting the Ultrasonic data increases the total amount of water produced from 16,556 to 20,492 bbls.

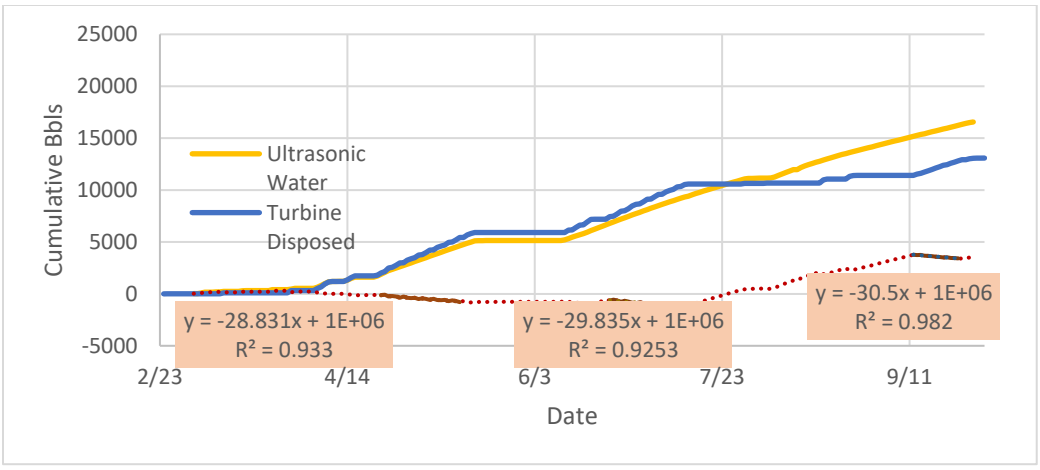


Figure 4-72. Cumulative fluid produced as measured by the Ultrasonic water and Turbine disposed meters. The red dashed line represents the difference between the two (Ultrasonic minus Turbine disposed). Lines were regressed through the intervals when both meters were active. The negative slope observed was used to correct the data from the Ultrasonic meter.

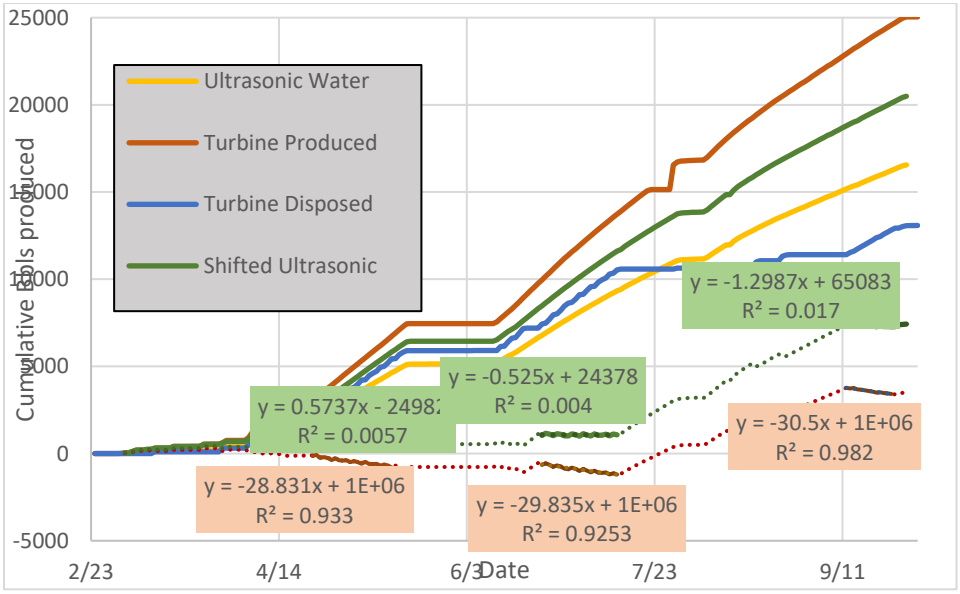


Figure 4-73. Cumulative volume of water produced over the Post-CO_2 Production Phases. Cumulative water produced as measured by the raw Ultrasonic Water (solid yellow line), Production Turbine (solid red line), and Disposal Turbine Meters (solid blue line), and the calculated shifted ultrasonic values (solid green line) all increase over time. The cumulative volume of water produced measured by the Disposal Turbine meter is consistently greater than the Raw ultrasonic water meter, as shown by the negative slope and high R^2 value of the dotted red line when both meters were active. This slope approaches zero when the ultrasonic data is corrected.

Post HnP Injection Test

Following the conclusion of Pumping on September 27th, a low-volume water injection test was planned to compare reservoir response to water injection before and after CO_2 injection. The pumping unit was switched on to fill the brine tanks on October 16th in preparation for an injection test. The rods and tubing were then pulled from well and the wellhead was replumbed for injection. Before the test, the Echometer derived fluid level was 2,240 ft from surface and the surface pressure was 0 psi, indicating that reservoir pressure was recovering more slowly than expected. Injection began at 2:50 PM on October 19th and

concluded at 11:30 AM on October 21st. Based on tank measurements, 197.2 bbls of water were injected, 17.5 bbls of which were stored in the wellbore. The injection rate was 106 bbls/day (3.1 gal/min). Echometer derived fluid level at the end of the test was at 1,643 ft from surface and the surface pressure was 2.5 psi, with injected water never filling the well casing to surface, resulting in a failed test. Once injection concluded, the well was shut in and the Echometer was used to track the fluid level. The remaining equipment was demobilized on November 3rd.

Field Activity Conclusions

Field activities for the Greenfield ROZ HnP took place from early 2020 to the end of 2021. 1,010 tons of CO_2 were injected, and 349 tons were produced, along with 20,492 bbls of water and 63 bbls of oil (Table 4-15). Disagreement between meters creates some uncertainty in these values, but inferences were made to estimate true values.

The measured oil production was not enough to be economic but is a technical success in that it provides validation of the efficacy of CO_2-EOR to mobilize oil from a siliciclastic greenfield ROZ in the ILB. The low oil recovery is attributed to the reservoir properties of the Carper Sandstone; Natural fractures within a low permeability, very-fine grained sandstone to coarse siltstone resulted in limited contact between CO_2 and matrix bound oil. Both EOR and CO_2 storage exceeded expectations defined by pre-test reservoir simulations.

Project critical data can be broken down into rate and volume of CO_2 injected, rates and volumes of fluid (oil, water, total fluid) and gas produced and pressure responses. These data will be evaluated to better characterize the rock and fluid properties of the Carper Greenfield ROZ.

Table 4-15. Final corrected values for oil, water, and CO_2 produced over all phases of the HnP.

Phase	**Dates**		**Phase Total**	**Project Total**
Baseline Production	10/16/2020-11/09/2020	Water (bbls)	5,000	
		Oil (bbls)	0	
CO_2 Injection	11/13/2020-12/13/2020	CO_2 (tons injected)	1,010	
CO_2 Venting	1/15/2021-2/12/2021	CO_2 (tons)	147	
Flowing	3/2/2021-4/15/2021	Oil (bbls)	11	
		Water (bbls)	2,110	
		CO_2 (tons)	92	239
Pumping 1	4/21/2021-5/18/2021	Oil (bbls)	24	35
		Water (bbls)	4,330	6,440
		CO_2 (tons)	57	296
Pumping 2	6/10/2021-9/27/2021	Oil (bbls)	28	63
		Water (bbls)	14,052	20,492
		CO_2 (tons)	53	349

4.1.3 Post-Test Interpretation

The field test had two objectives; to demonstrate the efficacy of CO_2-EOR in a siliciclastic greenfield ROZ, and to characterize the rock and fluid properties of the ROZ. The HnP accomplished the first objective by producing oil and storing CO_2 and accomplished the second objective by producing fluids (oil, gas, brine) whose properties and composition were analyzed. Fluid properties and results from core flood tests using proxies for the produced fluids were used to improve the characterization of the ROZ following the conclusion of field activities.

Hydrocarbon Properties

A total of eleven Carper oil samples were acquired for this project: Nine from the Holsapple 2B well collected at various stages of field activities (Table 4-16), one from the G. Swits 2 well in Gays oil field about 25 miles to the northwest, and another from the Quaranta 5 well in Kinmundy oil field about 50 miles to the southwest. The density and viscosity were measured for all samples. Four of the samples were also submitted for gas chromatographic (GC) analysis; The first sample taken from the Holsapple 2B well (before CO_2 injection), the last sample taken from the Holsapple 2B well (Post CO_2 production), and the samples from the G. Swits 2 and Quaranta 5 wells. Twenty-seven gas samples acquired throughout field activities were also submitted for GC analysis. This data was evaluated to determine the composition of the produced oil, and if (and how) the oil was potentially altered by injected CO_2.

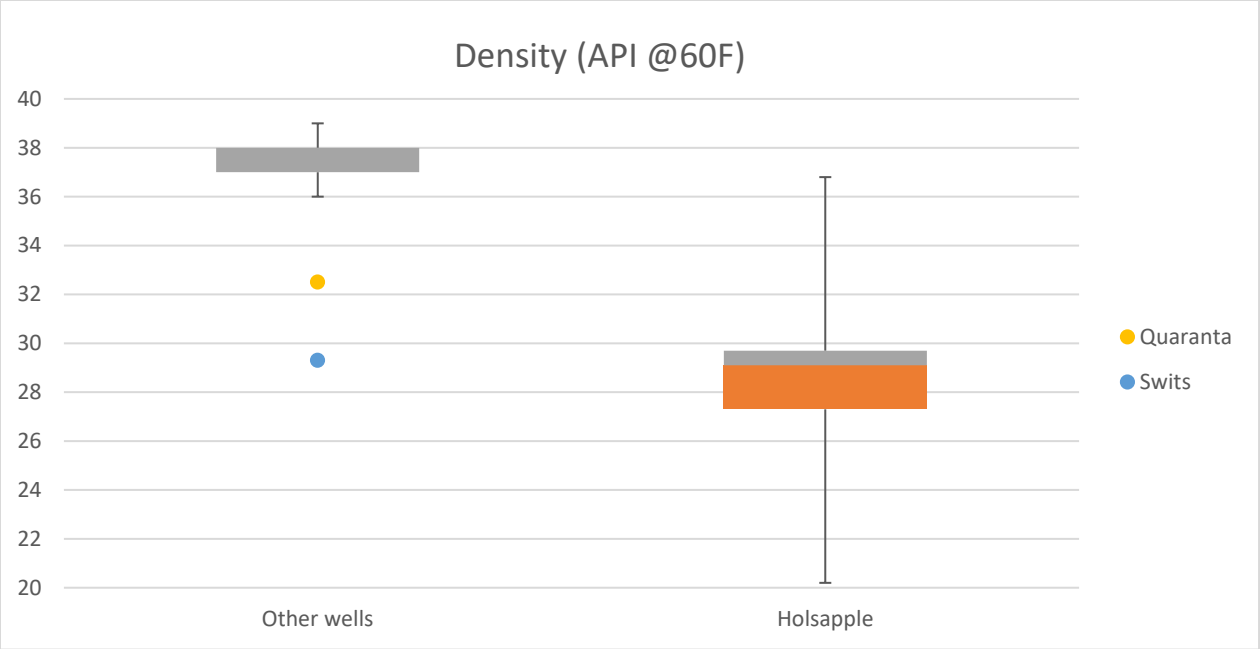
Density and Viscosity

All oil samples were measured for density and viscosity, except for the sample from the G. Swits 2 well, the volume of which was too small to be measured for viscosity. Samples were consistently denser and more viscous than published values of Carper oil (Mast, 1970; Figure 4-74).

It was unclear if the elevated density and viscosity of the samples is representative of in-situ conditions or to what degree they were influenced by interaction with injected CO_2. Two of the samples from the Holsapple 2B well were acquired before CO_2 injection, and the two from other wells were acquired via primary recovery, so there is evidence to suggest that the newly acquired samples are representative of in-situ conditions. While the first sample from the Holsapple 2B well was acquired at the beginning of field activities and had been sitting atop a water column in the wellbore for three years, the consistency of the density over time suggests that the samples are representative of the in-situ oil (Figure 4-75).

Table 4-16. Density and viscosity measurements of oil samples acquired throughout HnP field operations.

Date	**State in Project Timeline**	**Sample Location**	**Density @60 °F**	**Viscosity @60 °F**	**Comment**
8/24/20	Before well testing	Wellbore	29.1	11	Submitted for whole oil GC
10/4/20	After water inj test; pre-CO_2	Wellbore	29.7	63	
2/23/21	Post-CO_2; well flowing	Gas/liq sep	36.8	7.1	
3/3/21	Post-CO_2; well flowing	Gas/liq sep	26.8	7.1	
4/6/21	Post-CO_2; well flowing	Gas/liq sep	27.3	69	
4/27/21	Post-CO_2; sustained pumping	Brine tank	20.2	74	Possibly impacted by tank residue?
5/4/21	Post-CO_2; sustained pumping	Oil tank	29.1	28	
7/13/21	Post-CO_2; sustained pumping	Gas/liq sep and oil tank	29.7	39	Two samples; measured the same
9/7/21	Post-CO_2; sustained pumping	Siphon tube	27.7	32	Submitted for whole oil GC



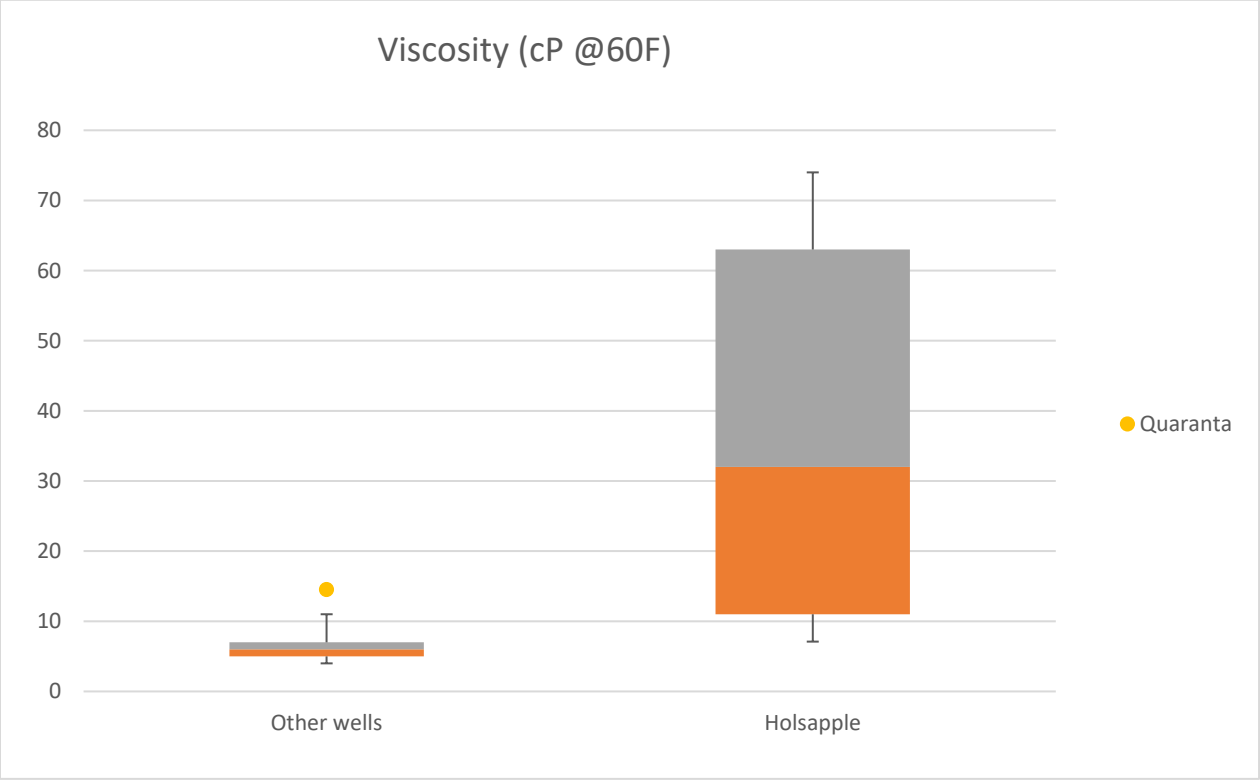


Figure 4-74. Box and Whisker plots of the density (top) and viscosity (bottom) of oil samples from the Carper. Published values for Carper sandstone crude oil from around the basin are on the left and samples collected from the Holsapple 2B well (Table 4-16) are on the right. Samples from the G. Swits 2 well are shown with a blue dot and from Quaranta 5 well are shown with yellow dot. Samples acquired for this project were consistently denser and more viscous with higher variability in properties.

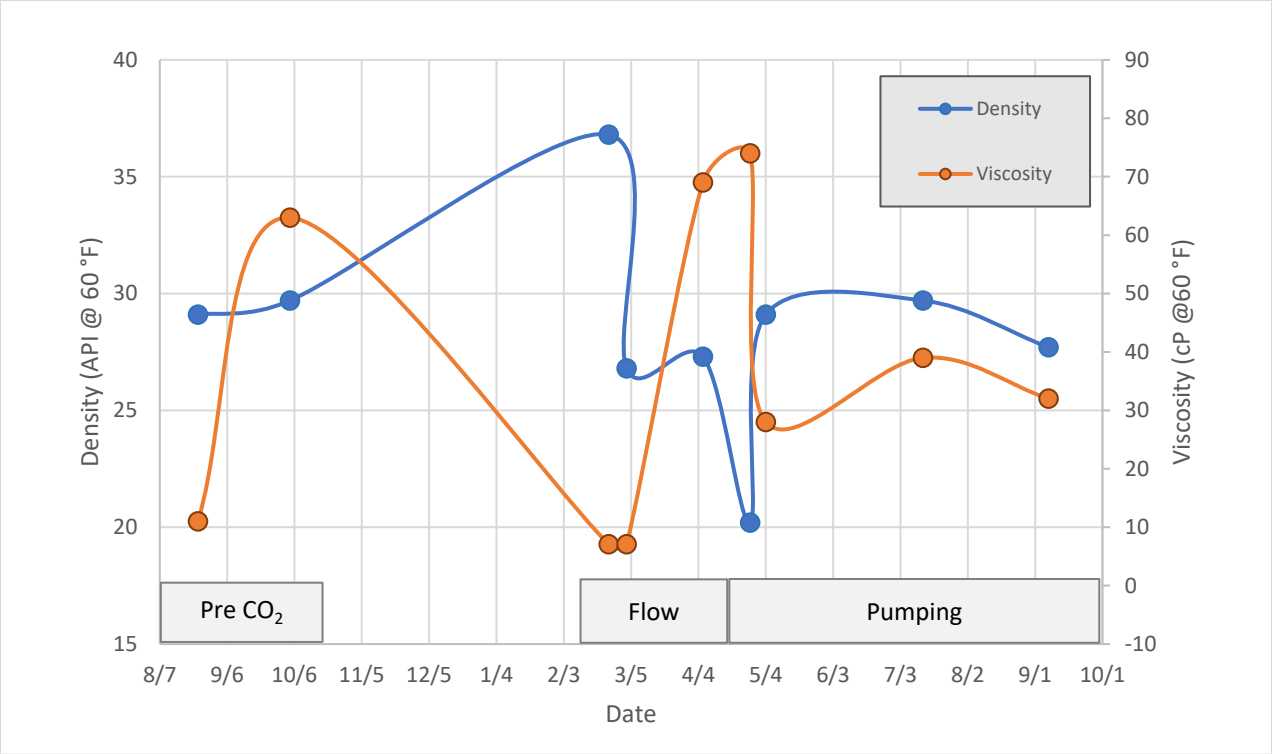


Figure 4-75. Density and viscosity of oil samples taken from the Holsapple 2B well over time.

Gas Chromatographic Data

Two oil samples from the Holsapple 2B well (one taken before CO_2 injection and one taken during the post CO_2 production period; Table 4-16), Carper oil samples from the G. Swits 2 and Quaranta 5 wells, and twenty-seven gas samples from the Holsapple 2B well across the duration of the production period (1/27/2021 to 9/27/2021) were submitted to Stratum Reservoir for GC analysis. Stratum Reservoir's full report is included in Appendix x. The summary of the conclusions are as follows:

Holsapple 2B Oil Alteration Characteristics

All but the Quaranta 5 oil sample exhibit variable light hydrocarbon evaporation. The pre-CO_2 injection Holsapple 2B oil is the most severely altered oil (nC_6-nC_{10} and BTX depletion). The post-CO_2 injection Holsapple 2B and G. Swits 2 oils are mildly altered (nC_6-nC_{10} depletion). The degree and pattern of evaporation suggests that the relatively high density (29.1° API) of the pre-CO_2 injection Holsapple oil reflects a combination of light hydrocarbon evaporation and water washing (BTX depletion) with the increased level of alteration due to exposure of oil to air in the well bore during the prior three years while the well was shut in. Slightly less depletion of the nC_6-nC_{10} fraction, the presence of high BTX aromatics and fewer C_{11}+ *n*-paraffins observed in the post-CO_2 injection Holsapple 2B oil probably represents the true Carper oil characteristics and suggests that the high density (27.7° API) and depletion of the nC_6-nC_{10} fraction is likely due to mild in-reservoir evaporative fractionation. Holsapple 2B oils are lower maturity oils derived from Type II marine kerogens. G. Swits 2 and Quaranta 5 oils are suggested to be slightly lower maturity and derived from a similar Type II marine kerogen.

Post-CO_2 Injection Gas Characteristics

The 27 produced gas samples from the Holsapple 2B well had a composition of 90%+ CO_2 and approximately 5% hydrocarbon (C_1-C_5) gases, the latter of which increased slightly through the production period at the expense of CO_2 (Figure 4-76). The hydrocarbon gases are wet (C_2+ averages 36%).

Nine of 27 gases, selected for carbon isotopes (C_1, C_2, C_3, nC_4 and CO_2) and deuterium isotope (C_1) analyses, are isotopically variable with February and March-2021 gas characteristics reflecting startup production (i.e., near well bore) of a mix of predominantly injected CO_2 and ~1% HC gas (predominantly thermogenic with minor biogenic component), whereas April through September, 2021 gas characteristics reflect a mix of injected CO_2 and ~5.4% thermogenic hydrocarbon gas and thermogenic CO_2 gas. The gases are suggested to have been generated at early oil-window maturity and slight increases in April through September 2021 (i.e., similar maturity as Holsapple 2B oils). Ethane and propane isotopes suggest a slight increase in maturity over time.

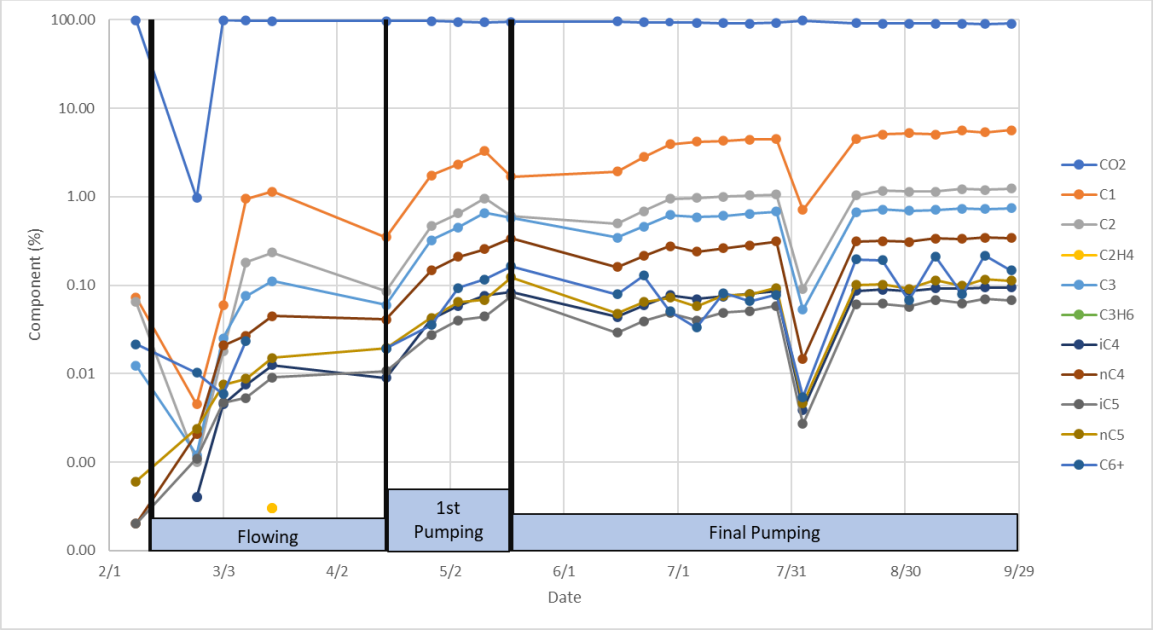


Figure 4-76. GC analysis of gas samples acquired over the course of field activities.

Conclusions

Analysis of oil and gas samples acquired throughout field activities determined that the oil within the Carper ROZ is denser and more viscous than previously anticipated. Our interpretation of the GC analysis of Carper oil samples is that the measured properties are generally representative of the in-situ oil. This conclusion has important ramifications for the conceptual understanding of the ROZ, the mechanisms responsible for CO_2-EOR and associated storage observed in the HnP, and the parameters used for reservoir simulations.

Core Analyses

Routine core analyses (porosity/permeability) were conducted soon after the well was completed and used for the pre-test characterization of the Carper, but more detailed analyses of the samples were conducted in parallel with field activities to better understand the rock properties.

X-Ray Diffraction

X-Ray diffraction (XRD) analysis of the core from the Holsapple 2B well determined the Carper Sandstone composition to be 40-75% quartz with as much as 29% clay. The clay fraction was typically ~50% illite, ~30% chlorite, ~15% illite-smectite, and ~5% kaolinite (Table 4-17).

The matrix density measured as part of routine core analyses had an average of 2.70 g/cc. XRD analysis revealed that this elevated density is primarily the result of siderite and chlorite. This finding supports pre-test observation that the density porosity log (DPOR) closely approximated core derived porosity, but only when calculated on a limestone matrix (Figure 4-6).

Table 4-17. XRD analysis of core from the Holsapple 2B well.

			Bulk mineral data								Results: <16 µm Glycolated Smear			
Depth	Poro	Perm (mD)	%clay	%Quartz	%K-feldspar	%P-feldspar	%Calcite	%Dolomite	%Siderite	%Pyrite/Marcasite	%Illite-Smectite	%Illite	%Kaolinite	%Chlorite
3679.0			29%	39%	5%	10%	1%	2%	10%	3%	15%	66%	4%	16%
3686.2	14.60%	0.824	8%	67%	4%	14%	1%	2%	4%	1%	19%	54%	6%	22%
3697.5	14.80%	0.543	7%	69%	4%	14%	0%	2%	3%	1%	15%	56%	4%	25%
3705.2			24%	43%	6%	9%	2%	3%	11%	2%	15%	67%	4%	14%
3723.0			25%	39%	6%	18%	1%	2%	7%	3%	16%	45%	4%	35%
3726.3	12.60%	0.191	10%	68%	3%	13%	0%	1%	3%	1%	15%	49%	4%	32%
3736.0	10.80%	0.052	9%	65%	4%	14%	1%	2%	4%	2%	13%	55%	5%	27%
3742.2	11.80%	0.055	11%	66%	3%	13%	1%	1%	5%	1%	13%	55%	3%	29%
3752.2			16%	58%	3%	13%	1%	1%	5%	2%	16%	52%	7%	25%
3758.7			21%	42%	6%	12%	1%	2%	11%	6%	11%	68%	5%	16%
3761.8	7.30%	0.016	7%	74%	2%	11%	0%	1%	3%	1%	16%	60%	5%	19%
3766.1	15.70%	3.816	7%	72%	3%	13%	1%	1%	2%	2%	18%	57%	4%	21%
3776.6	12.30%	0.291	9%	67%	4%	15%	1%	1%	3%	1%	13%	56%	4%	27%

Core Flood

Core flood tests were conducted by Stratum Reservoir to bolster the understanding of the reservoir and well behavior by providing endpoint saturations and to help constrain reservoir simulations by providing relative permeability curves. The tests involved saturating the core with brine, flooding with oil to determine S_{WIRR}, flushing with water to determine S_{ORW}, and then flushing with CO_2 to establish S_{ORCO2}.

Core floods were conducted on two different samples (Table 4-18). The first used Carper crude oil and a synthetic brine representative of samples from the Holsapple 2B well on a core taken from a depth of 3700.3 ft (Sample #24). Details of the testing procedure are provided in Appendix C and the results are provided in Table 4-18 and Figure 4-77. S_{ORW} was significantly higher than expected (74% as opposed to approximately 25% predicted by well log analyses during pre-test characterization), so a second core flood was conducted to support or refute the values derived from the first core flood. A sample was selected less than a foot away (Sample #23 from a depth of 3699.8) and used the same synthetic brine with a synthetic oil blend. Results of the second core flood are presented in Table 4-18, Figure 4-78, and Figure 4-79.

Table 4-18. Results of the core floods.

Sample #			23		24	
Depth (ft)			3699.8		3700.3	
Permeability (mD)		to Air	0.527		0.161	
		Klinkenberg	0.385		0.100	
Porosity (fraction)			0.131		0.118	
Cycle			SS Water-Oil	SS CO2-Water/Oil	USS Water-Oil	SS CO2-Water/Oil
Initial Conditions	Fluid Saturation, fractional pore space	water	0.357	-	0.336	-
		oil	0.643	-	0.664	-
Effective Permeability to oil, mD			0.078	-	0.032	-
Terminal Conditions	Fluid Saturation, fractional pore space	gas	-	0.517	-	0.575
		water	0.741	0.404	0.397	0.269
		oil	0.259	0.079	0.603	0.156
	Effective Permeability to Fluid, mD		0.005	0.045	0.003	0.028
	Relative Permeability to Fluid, fraction		0.013	0.117	0.034	0.279
Oil Recovery	Fraction, pore space		0.384	0.180	0.061	0.447
	Fraction, oil in place		0.597	0.280	0.092	0.673

CO2-WATER/OIL CORE FLOOD

Steady-State Method Wettability Restored-State Samples

Net Confining Stress: 1900 psi Temperature: 95°F

Illinois State Geological Survey
ROZ Associated Storage
Cumberland County, Illinois
File: HH-107518
Date: 11-10-21

Sample Number:	24
Sample Depth, feet:	3700.30
Permeability to Air, md:	0.161
Klinkenberg Permeability, md:	0.100
Porosity, fraction:	0.118
Effective Permeability to Oil, md:	0.0316
Initial Water Saturation, fraction:	0.397

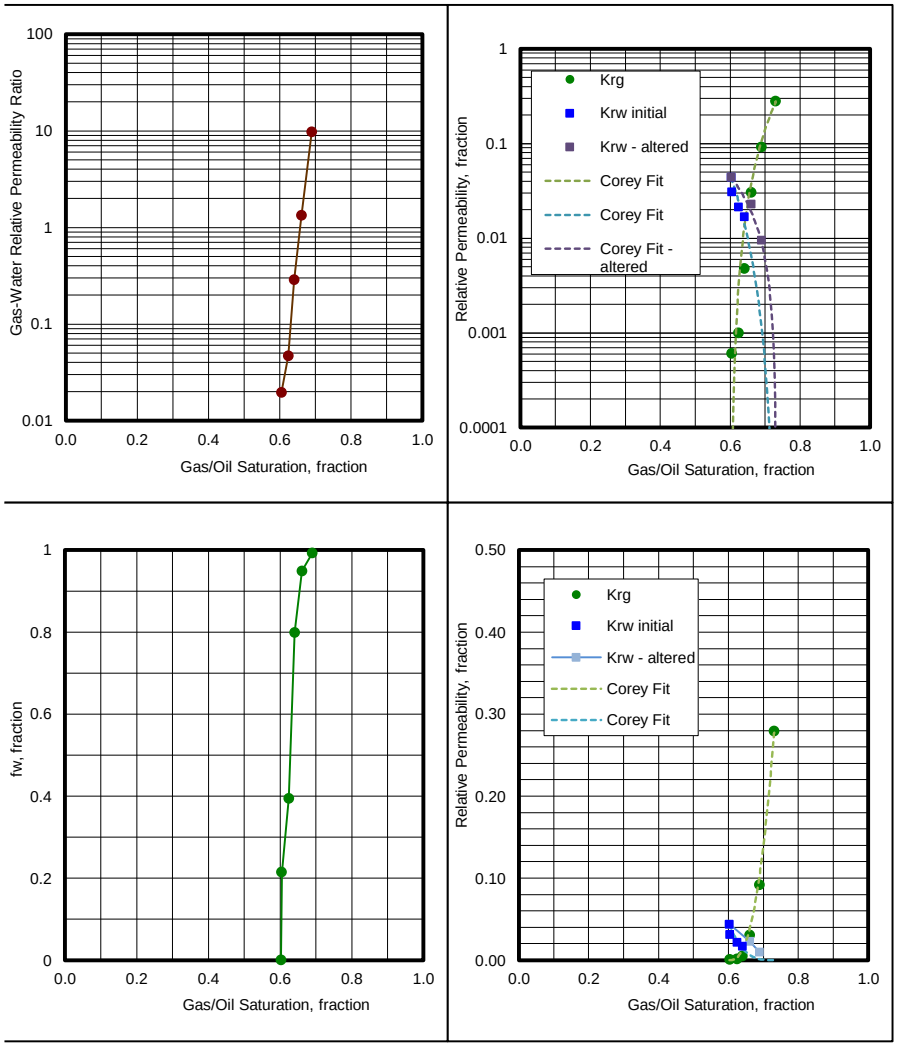


Figure 4-77. Gas-oil relative permeability curves for sample #24.

WATER-OIL RELATIVE PERMEABILITY

Steady-State Method Wettability Restored-State Samples
Net Confining Stress: 1900 psi Temperature: 95°F
Oil:Water Viscosity Ratio: 12.57

Illinois State Geological Survey	Sample Number: 23
ROZ Associated Storage	Sample Depth, feet: 3699.80
Cumberland County, Illinois	Permeability to Air, md: 0.527
File: HH-107518	Permeability to Brine, md: 0.305
Date: 09-30-22	Porosity, fraction: 0.131
	Initial Water Saturation, fraction: 0.357
	Effective Perm to Oil at Swi, md: 0.0778

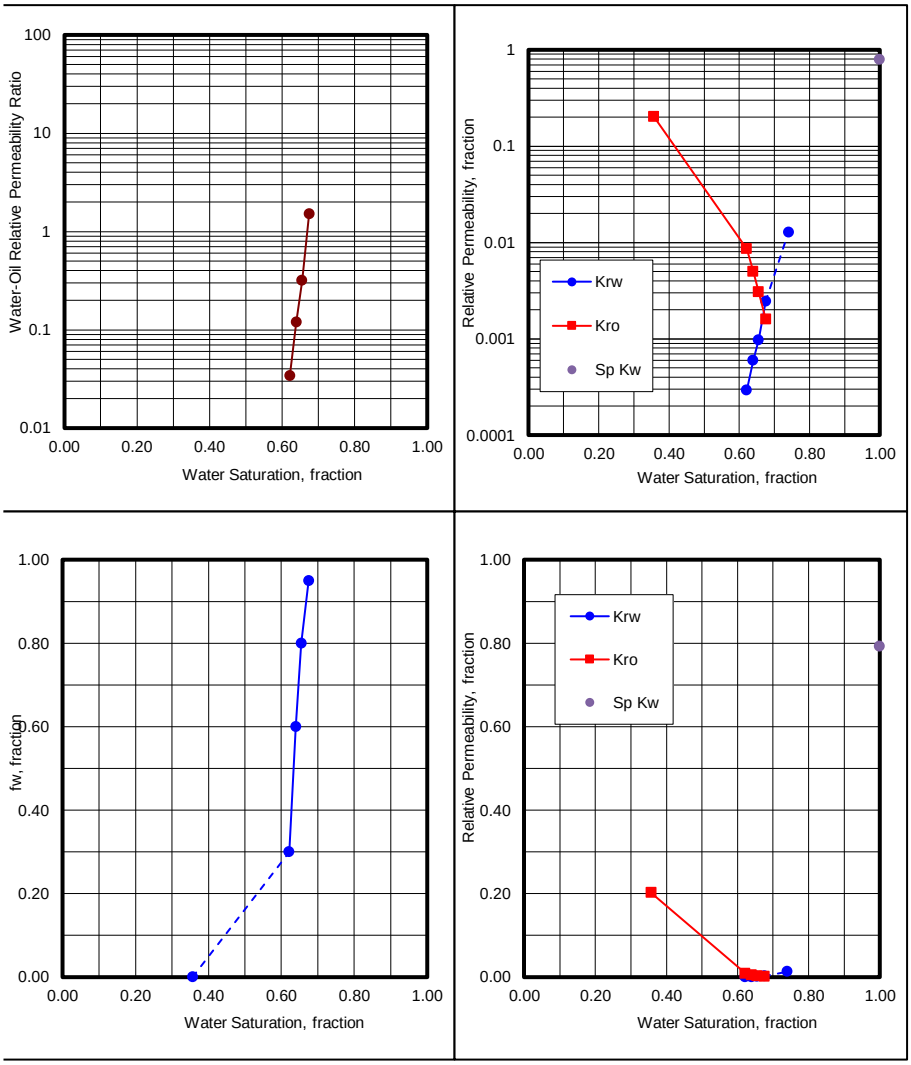


Figure 4-78. Water-oil relative permeability curves for sample #23.

CO2-WATER/OIL CORE FLOOD

Steady-State Method Wettability Restored-State Samples

Net Confining Stress: 1900 psi Temperature: 95°F

Illinois State Geological Survey
ROZ Associated Storage
Cumberland County, Illinois
File: HH-107518
Date: 09-30-22

Sample Number:	23
Sample Depth, feet:	3699.80
Permeability to Air, md:	0.527
Klinkenberg Permeability, md:	0.385
Porosity, fraction:	0.131
Effective Permeability to Oil, md:	0.0778
Initial Water Saturation, fraction:	0.741

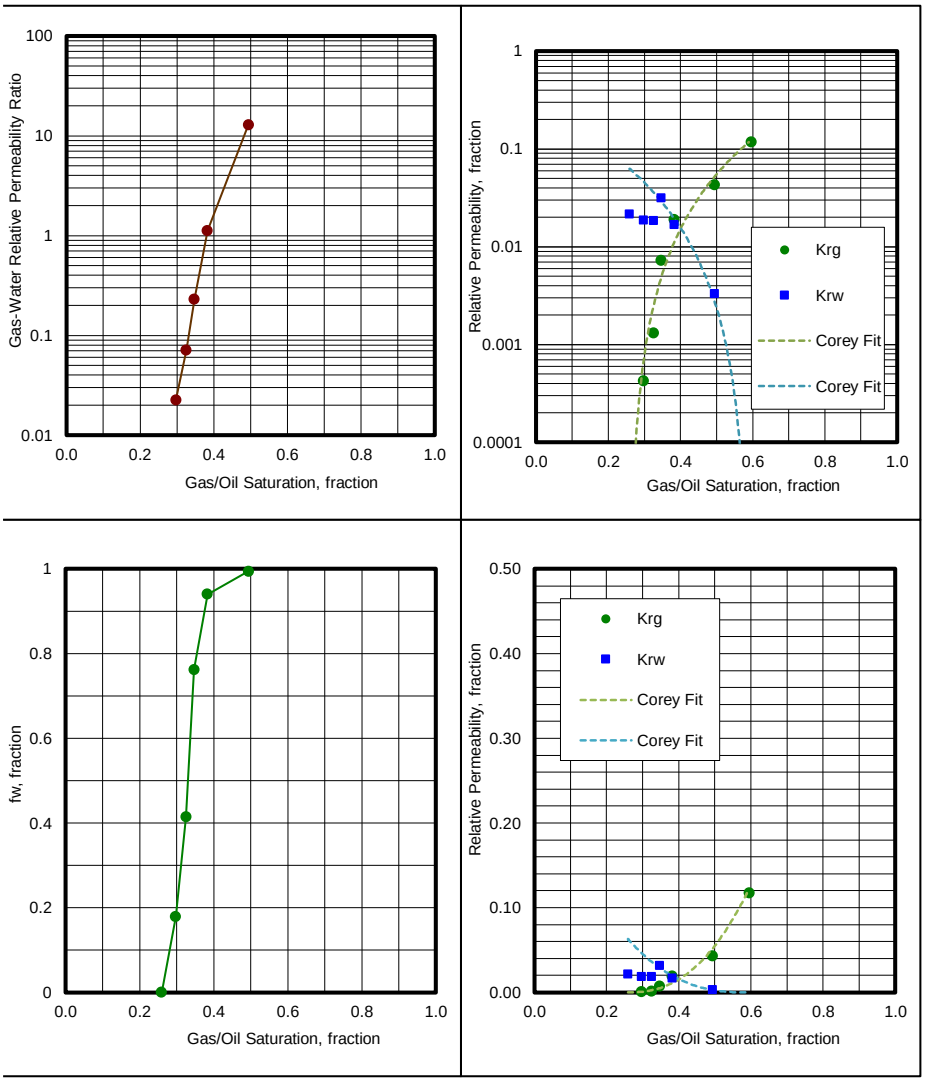


Figure 4-79. Gas-oil relative permeability curves for sample #23.

Both tests produced consistent results for S_{WIRR} (between 33.6-35.7%) and S_{ORCO2} (between 7.9-15.6%), but the first test measured an S_{ORW} of 60.3% while the second test measured S_{ORW} of 25.9% (Table 4-18). Both tests found that CO_2 could mobilize residual oil from the matrix. Reservoir simulations based on pre-test characterization consistently found that CO_2 would remain in fractures without encountering the matrix-bound oil. As a result, these simulations underestimated the amount of oil produced (and CO_2 stored), and most of the oil produced in the simulation is attributed to oil saturation added to the fractures

just to get the models to run. CO_2 entering the matrix and mobilizing the oil within is a plausible explanation for field-observed oil production and CO_2 storage exceeding expectations.

The Carper ROZ is interpreted to have formed via natural waterflooding over geologic time, which would result in an in-situ oil saturation equal to S_{ORW}. Analyses of well logs conducted during pre-test characterization found that S_O was approximately 25%. This was assumed to be S_{ORW} and used as the initial condition for reservoir simulations. This is in line with the S_{ORW} determined by the second core flood, but if the in situ S_O was closer to S_{ORW} measured in the first core flood test (~60%), the Carper would contain much more oil. Difficulties with interactions between the natural Carper crude oil and core Sample 24 resulted in permeability reductions to the core. It is therefore believed that the natural crude oil damaged the core used for the first core flood and caused an erroneously high S_{ORW}, but this discrepancy in S_{ORW} has important ramifications for the mechanism for oil production, OOIP, and EOR potential, so log analyses were re-evaluated to determine if a combination of parameters could create an S_O of approximately 60% in the target interval.

Updated Log Analyses

Data and observations made as a result of field activities caused us to reevaluate pre-test well log analyses. The consideration of natural fractures in the analysis had the largest influence on calculated S_O, but fluid samples and temperature data acquired during testing indicated a lower R_W, XRD of core data yielded data that improved understanding of rock properties, and core flood data suggests that S_{OR} is potentially much higher than anticipated (60% from Table 4-18 as opposed to 25% from Figure 4-9).

Higher S_O could explain the results of the reservoir simulations, which consistently underestimated the amount of oil produced. Log analyses were re-evaluated to determine the source of this error. Pre-test analyses were based on a water sample acquired before testing that had a TDS of 88,884 ppm. This TDS results in an Rw of 0.073 ohm-m at 97 °F (the formation temperature based on the typical temperature gradient of the Illinois Basin). But a water sample acquired on 10/26/2020 had a much higher TDS (145,092 ppm) and a wireline gauge indicated a higher reservoir temperature (115 °F). These new data result in a revised R_W of 0.042 ohm-m at reservoir conditions. This lower R_W increases calculated S_O using the same input parameters, but not to the levels observed in the first core flood test.

Typical values for Archies cementation exponent (*m*=2) and tortuosity factor (a=1) were used in pre-test analyses because the natural fracture network was unknown, and because they produced expected results (i.e., low S_O in intervals with core derived oil that was non-productive [3686.5-3700 ft and 3765.5-3770.5 ft in Figure 4-9] and approximately 100% S_W in intervals that were cored with no oil reported [all other depths in Figure 4-9]).

Sixteen core plugs from the Holsapple 2B well were measured for resistivity to constrain Archie parameters.

The Formation Factor (F) of each sample was derived via Equations 4-7 and 4-8. The logarithm of core derived porosity was cross-plotted against the logarithm of Formation Factor. The line regressed through the data was used to determine the core derived *m* (2.13 [the slope of the line]) and *a* (0.715 [F at the y intercept of the line; $10^{-0.1458}$]) (Figure 4-77).

$$R_O = \frac{R * A}{l} \qquad \text{Equation 4-7}$$

Where:
R= measured resistance (ohms)
A= cross sectional area of sample (m^2)
l= length of sample (m)

$$F = \frac{R_O}{R_w} \qquad \text{Equation 4-8}$$

Where:
F= Formation Factor
R_W = resistivity of water used (0.071 ohm-m)

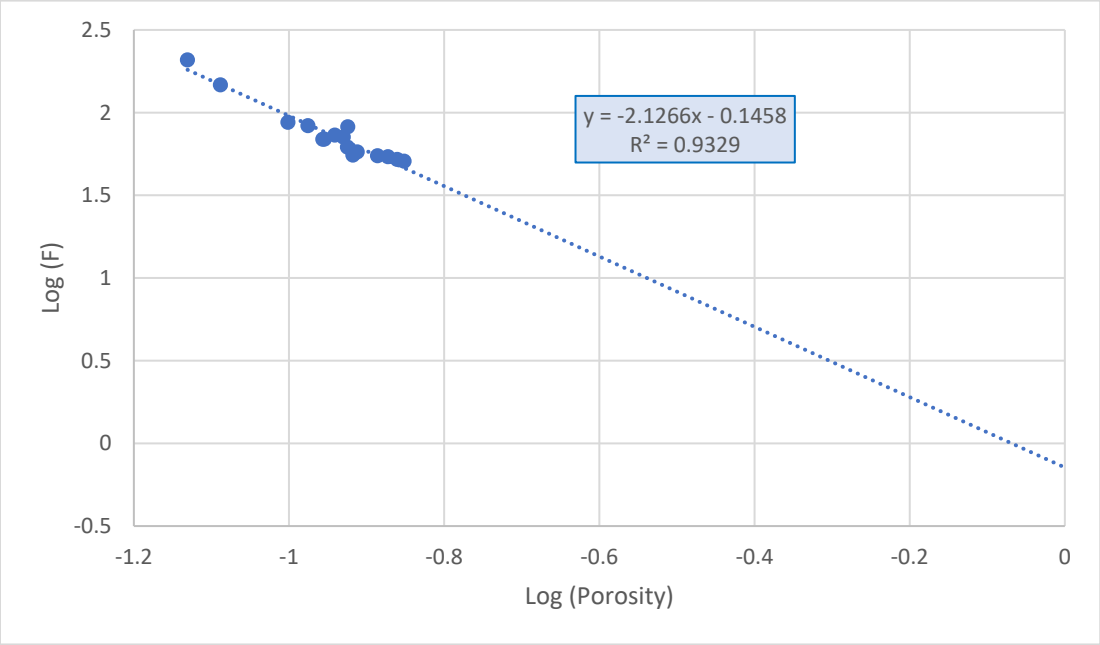


Figure 4-80. Cross plot used to estimate Archie parameters m and a. The data suggests that m is 2.1266 (the slope of the line) and a is 0.7149 (F at the y intercept of the line; $10^{-0.1458}$).

Cementation exponents were calculated for each sample using Equation 4-9 and assuming an *a* of 0.72 (Table 4-19). Laboratory measured resistivity and calculated *m*'s for sixteen core plugs from the Carper in the Holsapple 2B well. The average *m* of these samples (2.12) was slightly higher than the *m* used for the pre-test analyses (2). However, it is important to recognize that this core-derived resistivity is indicative of the of the matrix only, and that the Carper contains a natural fracture network that could significantly decrease the *m* of the Carper as a whole (Aguilera, 1980; Asquith, 1985; Ransom 1984). While there are models to predict *m* for naturally fractured reservoirs (Aguilera and Aguilera, 2002; Rasmus, 1983), the information available is not adequate to properly constrain the parameters of the natural fracture network in the Carper, so *m* was adjusted to create 40% S_O predicted by the first core flood test.

$$m = \frac{a^\theta}{F} \qquad \text{Equation 4-9}$$

Table 4-19. The laboratory measured resistivity and calculated Archie's cementation exponents (m) for sixteen core plugs from the Carper in the Holsapple 2B well.

Plug Depth (ft)	Porosity (%)	Ro	Formation Factor	m when a=0.72
3685.7	12.09	3.92	55.22	2.05
3686.5	13.79	3.69	51.96	2.16
3687.4	11.91	5.82	81.91	2.22
3688.5	11.75	5.04	71.05	2.14
3689.2	11.11	4.90	68.97	2.08
3690.6	9.97	6.19	87.22	2.08
3691.4	10.58	5.90	83.15	2.11
3692.8	7.40	14.76	207.94	2.18
3693.9	8.16	10.42	146.80	2.12
3694.9	11.46	5.17	72.88	2.13
3695.3	11.06	4.88	68.78	2.07
3696.6	11.90	4.38	61.72	2.09
3697.9	13.01	3.89	54.73	2.12
3698.9	14.08	3.60	50.70	2.17
3699.8	13.42	3.83	53.98	2.15
3700.3	12.25	4.10	57.68	2.09

It is necessary to reduce *m* to 1.55 to create calculated S_W values in the target Carper C1 interval that are in line with the S_{ORW} derived from the first core flood test (Figure 4-77). This *m* is on the low end reported for sandstones (Table 4-20) and puts significant S_O in the Carper A2, which was cored without observed oil. It is possible that geologic differences between the Carper C1 and A2 create a much lower *m* in the Carper C1 (such as a fracture network that is not present in the A2 or a different amount or type of clay), but it is much more likely that that *m* is over 2 in the Carper, S_O is approximately 25%, the first core flood that found S_{ORW} of 62% was erroneous, and the second core flood that found S_{ORW} of 25% is representative of the Carper.

Table 4-20. Typical ranges of cementation exponent (m) and tortuosity factor (a) parameters for sandstone from literature (modified from Worthington, 1993).

m	a	Reference
1.64—2.23	0.47—1.8	Hill and Milburn (1956)
1.3—2.15	0.62—1.65	Carothers (1968)
0.57—1.85	1.0—4.0	Porter and Carothers (1970)
1.2—2.21	0.48—4.31	Timur et al. (1972)
0.02—5.67	0.004—17.7	Gomez-Rivero (1976)

Dual water calculations were also evaluated to determine if clay could create approximately 60% S_O in the Carper C1 and approximately 0% S_O in the Carper A2. However, both the Gamma Ray and neutron-density separation were similar in the A2 and C2, so the two units have similar volumes of clay. This means that there is no combination of parameters that puts approximately 60% S_O in the oil-bearing intervals without putting significant S_O in the Carper A2 (where it was known to not occur).

Re-evaluation of well logs was not able to detect a significant difference in S_O between the Carper C1 and A2 units. These results suggest that the first core flood test produced erroneous results, and that S_{OR} (and in situ S_O) is approximately 25% (consistent with the second core flood test).

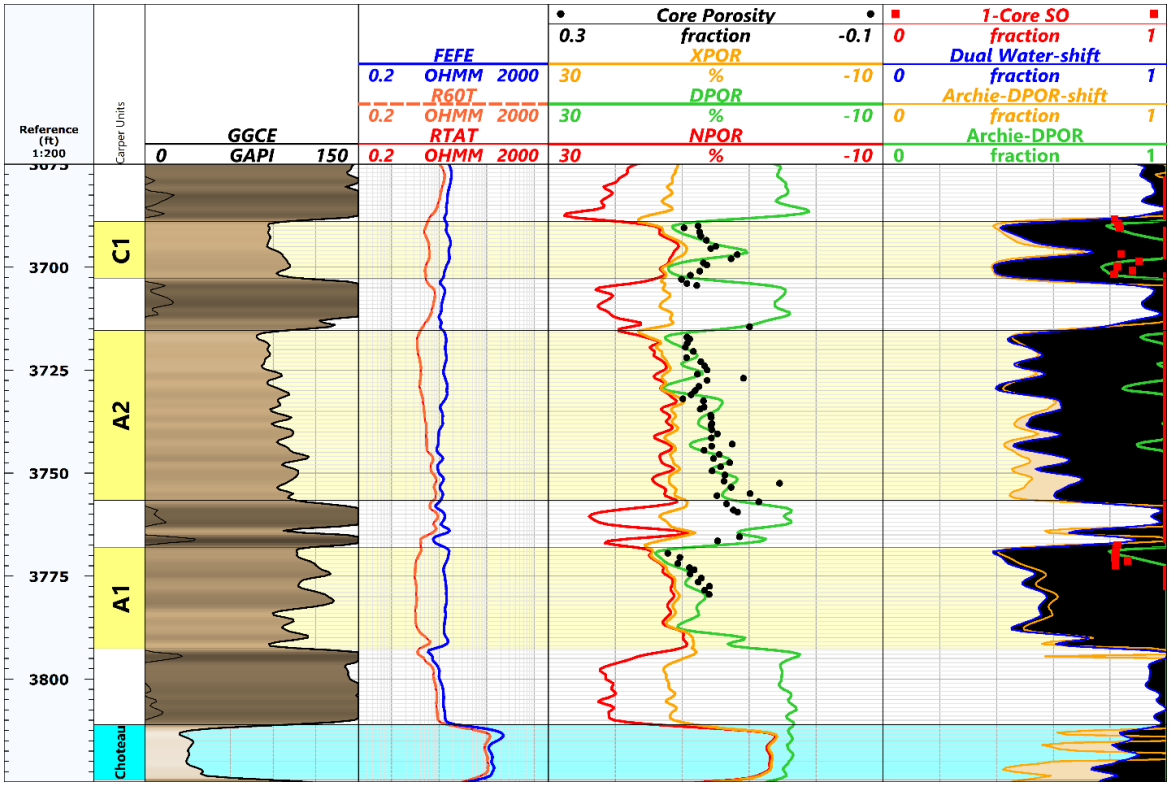


Figure 4-81. Log and core derived water saturations and volume of shale plotted against depth. The target interval is isolated with black dashed lines. Archies Sw is calculated using the raw DPOR log values assuming an Rw = 0.042 and an m of 1.5.

4.1.4 Post-Test Reservoir Simulations

Simulations were run to calibrate the reservoir model to observed oil, water, and CO_2 production from the Holsapple 2B well. These simulations were used to aid in design decisions while the test was active, and to provide context to better understand field observations.

First, the base model that was calibrated to the pressure transient test and Baseline Production (described in the Pre-CO_2 Injection reservoir simulation section and Figure 4-24) was used to simulate field activities (Figure 4-70) by imposing the CO_2 injection rates measured during the CO_2 Injection Phase (Figure 4-33), the CO_2 production rate measured during the CO_2 Venting Phase (Figure 4-41), and the actual water production rate measured during the Post-CO_2 Production Phases. The model was used to predict performance of the Production Phase by imposing a maximum total fluid rate of 280 stb/day with a minimum BHP of 100 psi (Figure 4-78). Simulated gas production rates matched well. Simulated oil production rates showed rates less than 0.5 stb/d (Figure 4-79).

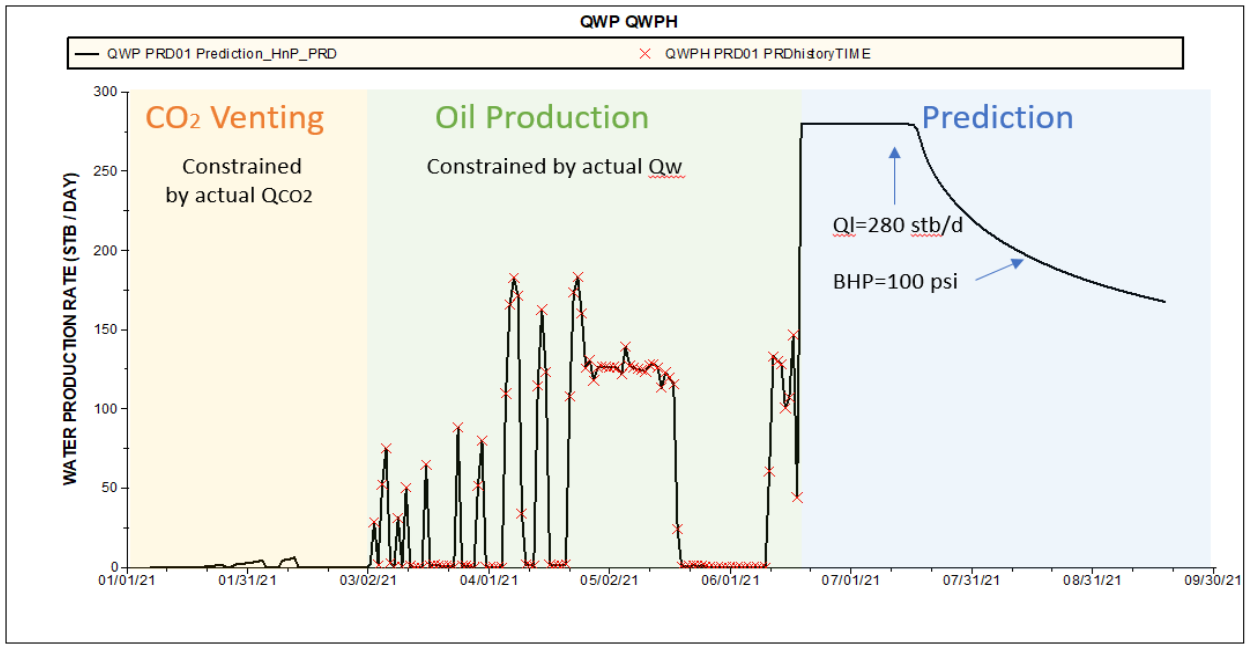


Figure 4-82. Simulated water production rate for the base model (red cross showing the actual water production rate during the production period).

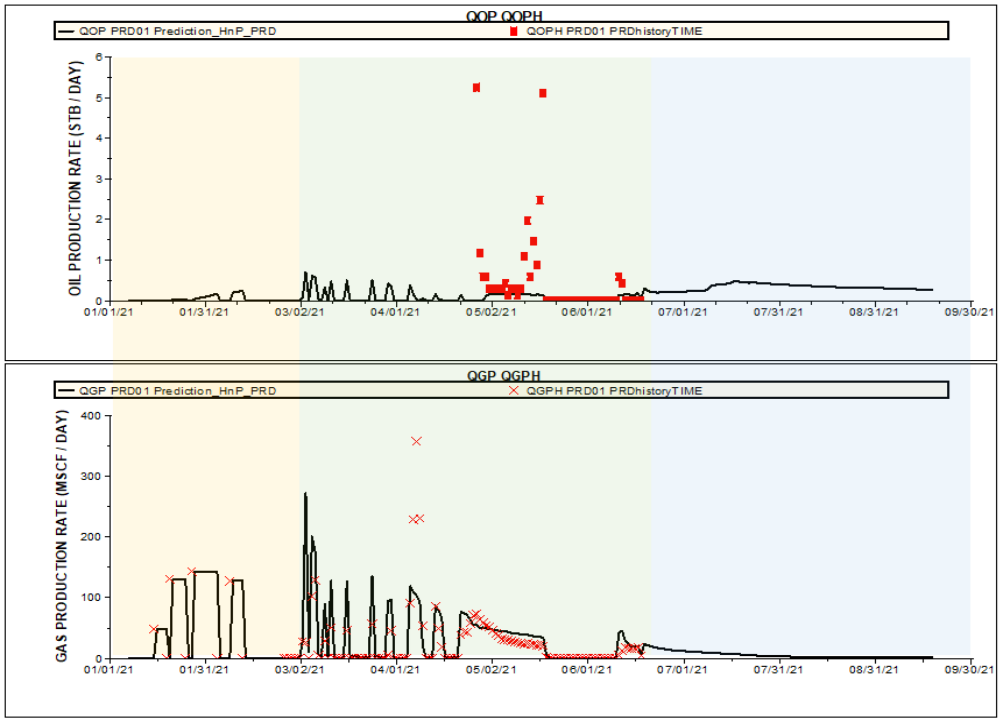


Figure 4-83. Simulated oil and gas production rates for the base model (red data showing the actual rates).

Next, history match was carried out to calibrate the model to better understand the mechanism responsible for EOR and associated CO_2 storage. As shown in Figure 4-80, simulated oil production rates varied from actual rates. The real field oil production is more prone to variability in field operations, which does not display a natural reservoir production decline trend. Therefore, the goal of history matching was to match the cumulative oil production.

The following parameters were adjusted to match cumulative oil production:

- Relative permeability
- Oil composition/EOS data
- Oil saturation in matrix

Relative permeability curves were adjusted based on their uncertainty; however, they had little effect on cumulative oil production.

The base model had S_{OR} and S_{OI} of 25% in the matrix based on log analysis and 2% in the fractures.

The base model had EOS properties derived from the literature (36.8 API and 7cP at 60 °F). However, the EOS data was tuned based on an on oil and gas analysis of samples acquired from the Holsapple well to be 32.4 API and 11 cP at 60 °F (Table 4-16 and Figure 4-74). Simulations were run using both sets to determine how impactful the difference was.

As shown in Figure 4-80, simulation results showed that oil production data was not matched with heavy oil EOS data, even when the S_{OI} and S_{OR} in matrix were increased to 35%. More oil could be produced with lighter oil (7cP oil) (green line), which created a better history match.

For the best matched case, the simulated peak oil production rate was 1.2 stb/d (measured 2.5 stb/d, which was affected by operation rather than following natural decline trend), and the simulated total oil production at 7 months was 66 stb (measured 63 stb). The produced CO_2 was 14% of injected CO_2 after venting and 27% at 7-month production (Figure 4-82).

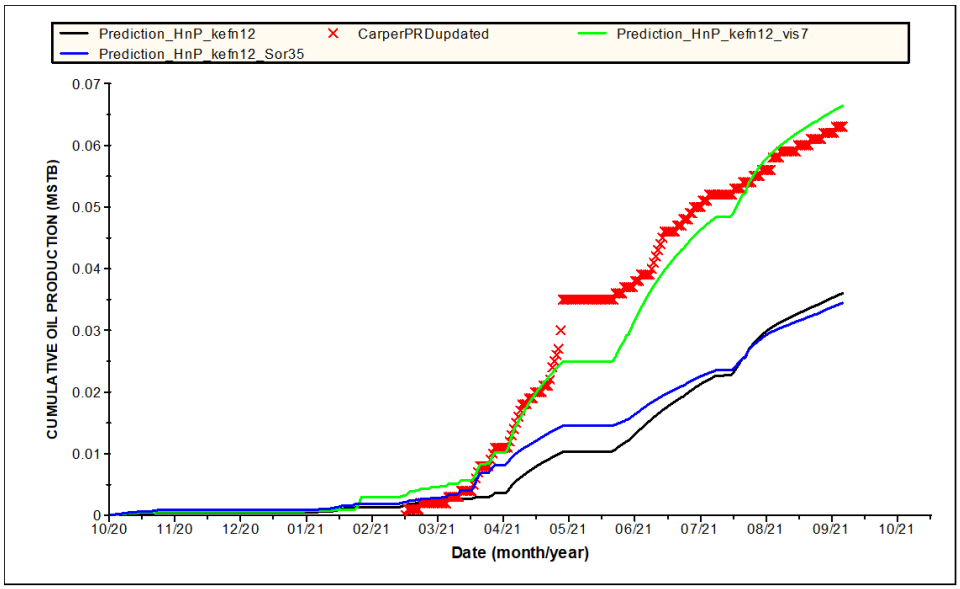


Figure 4-84. Cumulative oil production vs time with various oil saturations and EOS data. The black line shows the simulated results with low oil saturation in the matrix (25%) and heavier oil (11cP), the blue line shows the simulated case with high oil saturation in the matrix (35%) and heavier oil, the green line shows simulated case with low oil saturation in the matrix and lighter oil (7cP), and red crosses show field production data from HnP test).

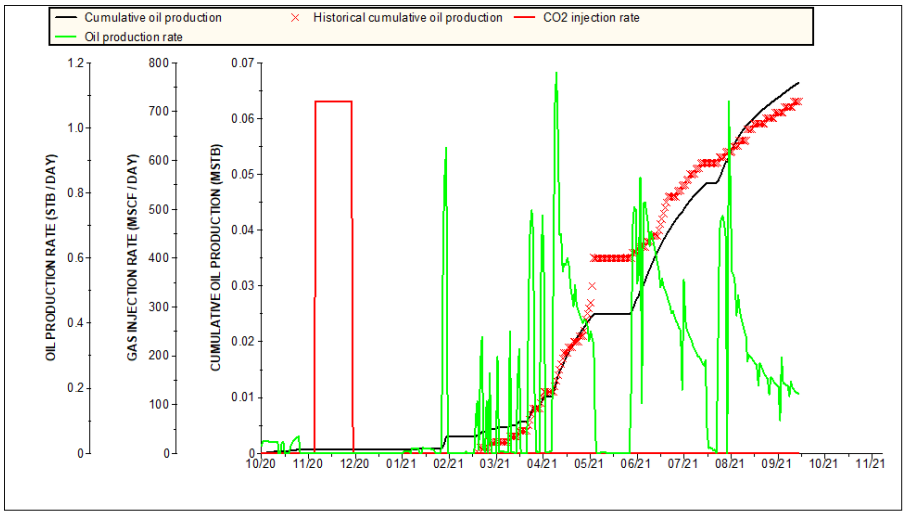


Figure 4-85. Rate and cumulative oil production for the best matched case.

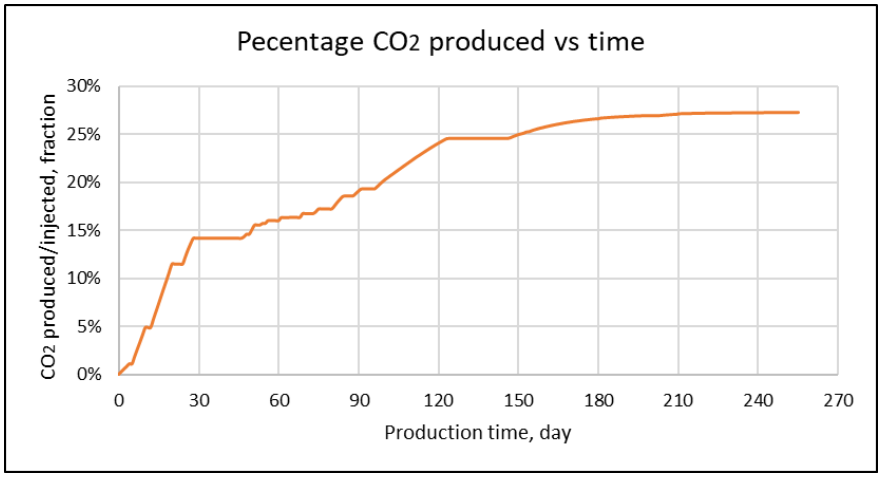


Figure 4-86. Produced CO_2 as percentage of injected CO_2 vs production time.

The base model calibrated to pre-HnP tests was able to approximate observed water and CO_2 production but not oil production. Further calibration to HnP tests with adjustment in oil composition was able to better match oil production. The oil in the matched case was lighter than the oil sampled from Holsapple 2B well; however, it was within observed range of oil properties in the Illinois Basin (Mast, 1970).

The simulations suggest that the hydraulic fracture and natural fracture network dominate fluid flow. Injected CO_2 remains in the fractures and has limited interaction with the matrix. Most oil is produced from the fractures and the adjacent matrix; injected CO_2 moved far enough away from the well via fractures to not be produced when production resumed.

The fracture dominated flow can be attributed to low matrix permeability (0.2 mD) and high fracture-matrix permeability ratio (200,000:1). Study on fluid flow partitioning between fractures and matrix concluded that factures would dominate flow when matrix permeability is less than 1 mD and fracture-matrix permeability ratio is above 10,000:1 (Matthai and Belayneh, 2004).

Summary and Conclusions

A Huff and Puff test was conducted in the Carper Sandstone in the Holsapple 2B well. Field activities occurred from September 2020 to September 2021, during which time 1,010 tons of CO_2 were injected and 63 bbls oil, 349 tons of CO_2, and 20,492 bbls of water were produced. The remaining 661 tons of CO_2 were stored in the subsurface. This test achieved both of its objectives of demonstrating the efficacy of CO_2-EOR and associated storage in a Greenfield ROZ and increasing the understanding of the Carper ROZ.

The oil produced demonstrates that CO_2 can mobilize the oil within the Carper greenfield ROZ. The amount of oil was not economic, but several operational constraints likely reduced the amount of oil produced. It is therefore believed that the Carper ROZ could be a viable CO_2-EOR target where it is thicker, has higher permeability, has higher oil saturation, or occurs as part of a stacked reservoir complex. In addition to the produced oil, a significant amount of the injected CO_2 was stored in the subsurface. This test was not designed to optimize CO_2 storage and CO_2 was only injected into 15 feet of the over 200 feet of porous Carper Sandstone observed in the Holsapple 2B well (Figure 4-4). This suggests that the Carper could also be leveraged as a target CO_2 storage.

The HnP also produced data that was used to better understand the Carper ROZ. The test allowed for acquisition of oil and gas samples and more detailed analyses of existing core. Furthermore, the measured CO_2 injection and fluid and gas production and resulting pressure response were used to better understand reservoir response and calibrate reservoir simulations to test field scale scenarios.

Analysis of oil samples determined that the Carper oil is denser and more viscous than published values (i.e., Mast 1970). It is believed that the natural waterflood that created the Carper ROZ preferentially stripped the light hydrocarbons, leaving behind a more dense, viscous oil that had limited potential to mix with CO_2.

Core flood tests found that the residual oil saturation to water of the Carper is likely about 25%, and that CO_2 could mobilize residual Carper oil from the matrix. However, the limited mixing potential of the oil suggests that Darcy flow was the primary driver of oil production. This should have resulted in reduced oil production, but real world production exceeded expectations set by reservoir simulations.

The mechanism responsible for oil production is not well explained. Reservoir simulations consistently found that injected CO_2 would remain in the fractures and have only limited contact with the matrix bound oil. Simulations were able to match observed oil production, but only when the oil saturation of the fractures was increased. Simulated oil production was primarily from oil saturation added to the fractures in the model that allowed the simulation to run. In reality, there is no oil saturation in the fractures as it would have been produced and observed during initial attempts at production prior to CO_2 injection.

However, core floods determined that CO_2 could displace this oil from the matrix, so a more likely explanation is that the interaction between the fracture and matrix (likely a diffusion process given the permeability contrast) was not properly represented in reservoir simulations. Attempts to introduce diffusion into the reservoir simulations failed, likely reflecting a software limitation.

While a natural fracture network was inferred, its extent and connectivity remains poorly understood because the reservoir response to all well tests indicated dominance of the hydraulic fractures. Reservoir response from the pre-test pressure transient test and baseline production were used to calibrate reservoir models, but the pressure response observed in the post test pressure transient test was indicative of a reservoir that was pressure depleted following the flowing and pumping subphases. This suggests that the fracture network in direct communication with the wellbore likely has limited extent.

4.2 Strategies to Maximize Storage, EOR, and Net Present Value

Authors: Nathan Webb, Fang Yang, and Nathan Grigsby

Development strategies for a greenfield ROZ were determined using a reservoir simulation approach calibrated to a field laboratory CO_2 Huff and Puff (HnP) experiment. A development strategy, as defined here, is the combination of well spacing, pattern type and size, perforated intervals, and well orientation that is used in the CO_2 flood of a given formation as part of an EOR and storage program. In the case of the Greenfield site, there is currently a single formation, the Carper Sandstone, that possesses a validated residual oil zone (ROZ) that would be the target of CO_2-EOR and storage.

Oil recovery and CO_2 storage due to CO_2 flood were used as metrics for selecting development strategies of the Carper Sandstone Greenfield ROZ. A static reservoir model of the Carper sandstone was used as input to determine the injection potential (injectivity), CO_2-EOR, and storage potentials of the formation via dynamic reservoir simulations.

Methods

The Carper Sandstone is naturally fractured, and a natural fracture network would exert a large control on any injection of CO_2 as fractures would provide the highest permeability conduit for flow. Therefore, a dual porosity and dual permeability model was used to model the natural fracture network to better understand how it would influence the test. The matrix properties were assumed to be those observed in core analysis (ϕ=11.5%, k=0.2 mD). No information about the parameters of the fracture network (e.g. intensity, spacing, orientation, permeability) was available, so different fracture network properties were tested until a range of fracture properties was identified that would meet historical fluid production from the well.

Two base fracture models that encompass the range of fracture properties (a coarse fracture model and a dense fracture model) were used to assist in CO_2 HnP pilot test design and predict oil production. Oil production was evaluated based on its sensitivity to CO_2 injection rate, injection time, soak period, injection scheme (continuous injection vs. discontinuous injection), and prior water injection vs. no water injection. Simulation results showed continuous CO_2 injection with no water injection was preferable. More oil production was expected with higher CO_2 injection rate or higher cumulative CO_2 injection. With an injection rate limit of 60 ton/day (constrained by pump capacity), shorter soak time and higher cumulative injection yielded slightly better cumulative oil production.

Prior to the HnP pilot test, a water injection and step-rate test was conducted, followed by a baseline production test. The reservoir model was calibrated to both tests. The step-rate test showed hydraulic fracture dominated flow, so a hydraulic fracture was added to the reservoir model using 1 ft wide cells along the well with adjusted permeability and porosity. The reservoir model was also adjusted to match pressure data from the baseline production test by varying hydraulic fracture half length, hydraulic fracture permeability, natural fracture spacing, and natural fracture effective permeability.

The calibrated model was used to evaluate CO_2-EOR performance in field-scale development. The hydraulic fracture, however, was not included in the field-scale model as wells are likely not to be hydraulic fractured. A line drive well pattern was considered for field development. Sensitivity studies were conducted on pattern type (direct line drive, staggered line drive), pattern size (40-acre, 80-acre), pattern width-length ratios (1:4, 1:8), CO_2 injection rate, gas production rate, and injection scheme (WAG vs. continuous CO_2 injection). Simulation results showed that a larger pattern with greater distance between injection and producer pairs would slow CO_2 breakthrough, thus a direct line drive in 80-acre

pattern with a pattern width-length ratio of 1:8 was preferred. Lower rate CO_2 injection delayed CO_2 breakthrough and lateral movement, resulting in higher sweep efficiency and cumulative oil production.

However, CO_2 quickly spread laterally beyond pattern boundaries with significant gravity override, and CO_2 remained in fractures rather than go to matrix. Therefore, additional engineering measures were considered to enhance the EOR performance, including using side water injectors to overcome the CO_2 plume movement outside of the pattern, adding a shaly layer in the middle to offset gravity override, and considering soak-alternating-gas (SAG) injection to slow CO_2 breakthrough and enhance CO_2 interaction with matrix. Promising oil performance was observed combining all these measures. A series of SAG cases with various soak-to-injection ratio were run to determine an optimum soak-to-injection ratio. A baseline SAG case using this ratio was then simulated to evaluate the CO_2-EOR performance.

Field Development Simulation Results

The baseline SAG case simulated direct line drive CO_2-EOR in an 80-acre pattern with a pattern width to length ratio of 1:8 (660 ft :5280 ft). An inner well placement is shown below (Figure 4-87): a row of injectors followed by a row of producers, except the side injectors are converted to water injectors, and more water injectors are added above and below to keep CO_2 in the pattern. The important input parameters are listed in Table 4-21.

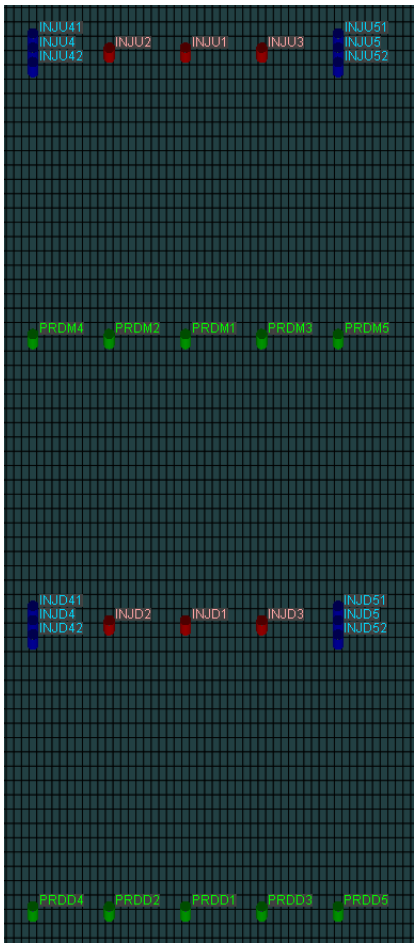


Figure 4-87. Inner well placement of direct line drive. CO_2 injectors shown in red, water injectors shown in blue, and producing wells shown in green.

Table 4-21. Model input parameters.

Parameter	Value
Number of cells (NX, NY, NZ)	(300, 150, 5)
Cell dimension (DX, DY, DZ) (ft)	(66, 132, 3)
Reservoir temperature (°F)	113
Reservoir pressure (psi)	1593 psi at 3688 ft
Initial oil saturation in matrix	25%
Initial oil saturation in fracture	2%
Matrix porosity (øm)	11.5%
Matrix permeability (kX,kY,kZ) (mD)	(0.2,0.2,0.1)
Fracture porosity (øf)	0.051%
Fracture effective permeability* (kXeff, kYeff, kZeff) (mD)	(83.3, 1.7, 83.3)
Fracture spacing (LX, LY, LZ) (ft)	(300, 6, 100)
Fluid relative permeability in fractures	Vertical equilibrium curves with Sor= 2% and Swr=5%

**Fracture effective permeability is the product of fracture permeability and fracture porosity*

The CO_2 was injected at 40 ton/d/well for 25 days with simultaneous side well water injection at 200 stb/d/well. It was then soaked for 25 days (all wells shut in), followed by 15-days of production at a maximum liquid rate of 865 stb/d/well (based on volumetric balance of injection) and a maximum gas production rate of 20 ton/d/well. The cycle was repeated for a total simulation time of five years.

The metrics used to evaluate the CO_2-EOR and storage performance include CO_2-EOR, CO_2 storage, oil recovery factor, net utilization factor, CO_2 storage factor, and storage efficiency. They were calculated using the equations below:

$$CO_2EOR = N_{p,CO_2} - N_{p,WF} \quad \text{Equation 4-10}$$

$$G_{store} = G_{inj,CO_2} - G_{p,CO_2} \quad \text{Equation 4-11}$$

$$RF = \frac{CO_2EOR}{OOIP} \quad \text{Equation 4-12}$$

$$NUF = \frac{G_{store}}{CO_2EOR} \quad \text{Equation 4-13}$$

$$SF = NUF \times RF \quad \text{Equation 4-14}$$

$$E_{CO_2} = \frac{G_{store}}{HCPV} \quad \text{Equation 4-15}$$

Where:

- CO_2-EOR = incremental oil produced
- $N_{p,CO2}$ = cumulative oil production of CO_2 flood (Mstb)
- $N_{p,WF}$ = cumulative oil production of waterflood (Mstb)
- G_{store} = CO_2 storage (MMscf or Mrb)
- $G_{inj,CO2}$ = CO_2 injected (MMscf)
- $G_{p,CO2}$= CO_2 produced (MMscf)

- RF = oil recovery factor (fraction)
- OOIP = original oil in place (Mstb)
- NUF = net utilization factor
- SF = CO_2 storage factor (MMscf/Mstb)
- E_{CO2} = CO_2 storage efficiency (Mrb/Mrb)
- HCPV = hydrocarbon pore volume (Mrb).

The OOIP in the equations is the OOIP of the pattern area rather than the whole field OOIP. Injected CO_2 that moves out of pattern area was not accounted for in storage efficiency calculations. At five years, the cumulative oil production is 1.87 Mstb, and oil recovery is 0.65% (Figure 4-88). About 14% of injected CO_2 was produced (Figure 4-89). Net utilization factor and storage factor are up to 452 mscf/stb and 2.9 mscf/stb respectively (Figure 4-90). The CO_2 storage is up to 106% of hydrocarbon pore volume (HCPV) and 26% of total pore volume (TPV) (Figure 4-91).

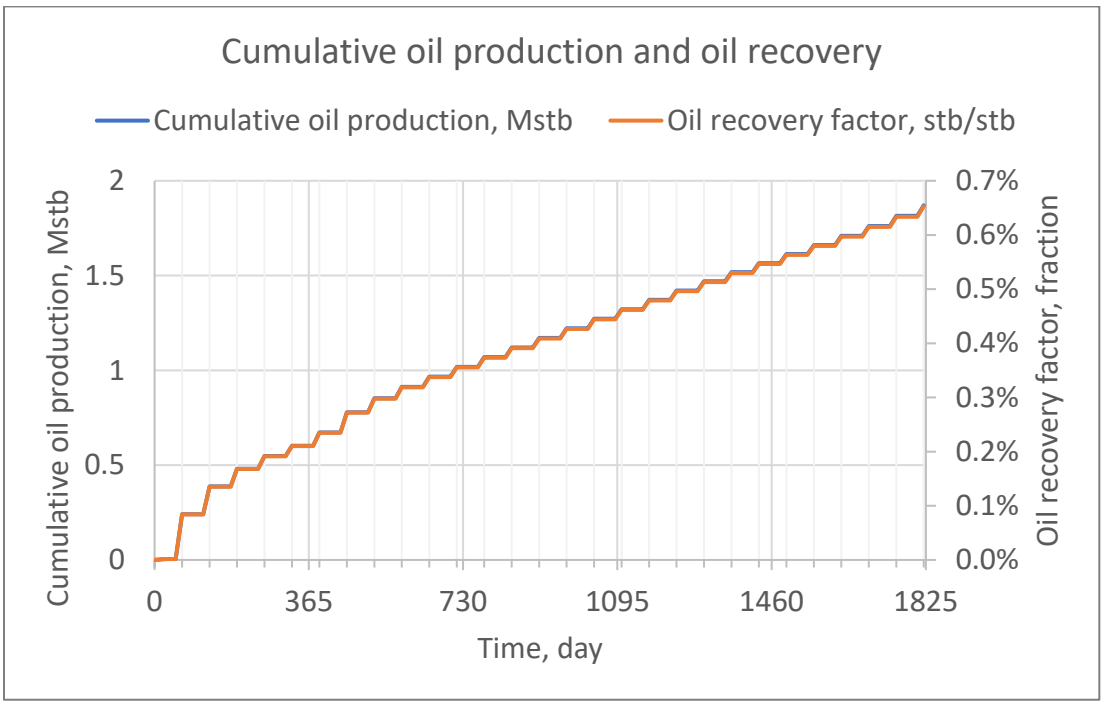


Figure 4-88. Cumulative oil production and oil recovery with time.

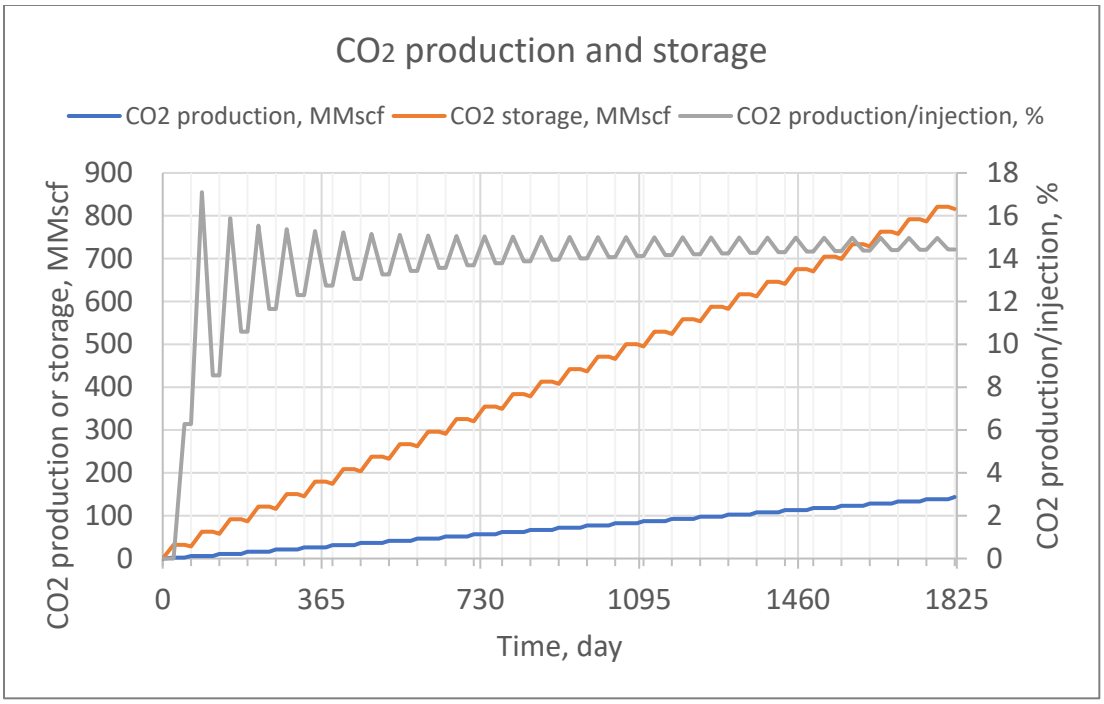


Figure 4-89. CO_2 production and storage with time.

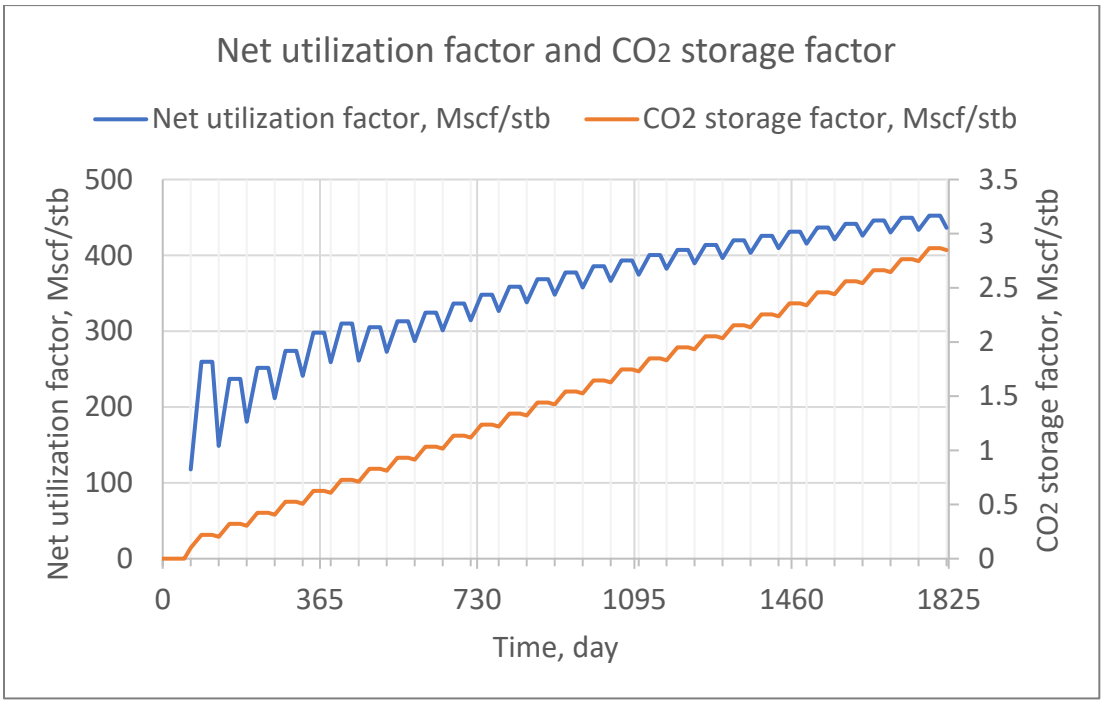


Figure 4-90. Net utilization factor and CO_2 storage factor with time.

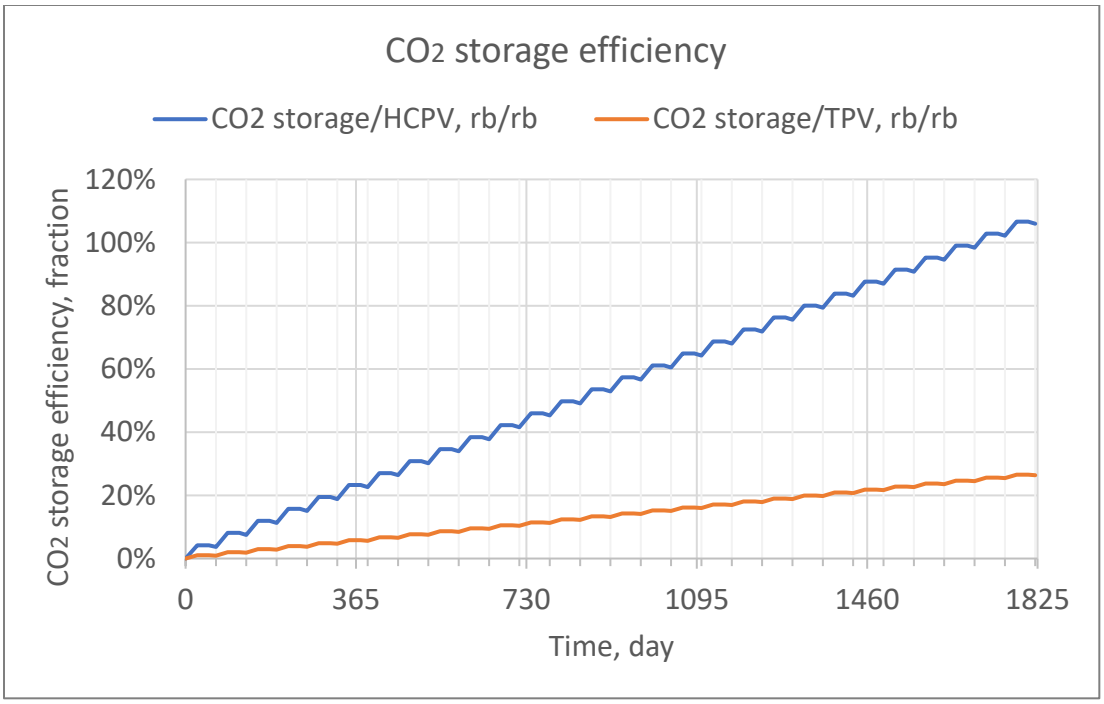


Figure 4-91. CO_2 storage efficiency with time.

Preliminary SAG simulation showed promising oil production from the Carper Sandstone. As more data becomes available (e.g. fluid production and pressure data from the HnP pilot test, relative permeability measurements, and oil composition measurements), the reservoir model will be further calibrated by adjusting initial and residual fluid saturation and equation of state (EOS) data based on oil composition. The line drive cases and results will be updated accordingly.

Conclusion

To maximize CO_2-EOR and storage Carper Sandstone Greenfield ROZ, a tight sandstone with natural fractures, the following development strategies are suggested:

- Direct line drive with large pattern with great distance between injection and producer pairs to slow CO_2 breakthrough (80-acre pattern with a pattern width to length ratio of 1:8 in this study),
- Soak-alternating-gas to slow CO_2 movement towards producers and enhance CO_2 interaction with matrix,
- Side water injectors to keep CO_2 in the pattern, and
- A relatively low CO_2 injection rate given a set cumulative injection to slow CO_2 movement in high-permeability direction, thus achieving higher sweep efficiency.

5. Brownfield Field Laboratory: Stacked ROZs and Conventional Reservoir Storage Complex

A detailed study was conducted on the Brownfield field laboratory site with evidence of stacked complex with a brownfield ROZ and several depleted conventional reservoirs. The brownfield field laboratory is within the extended boundary of Noble Field, Richland County, IL, which has recorded and measured oil production from conventional oil reservoir(s) for which an ROZ is part of a stacked oil reservoir complex that includes the Cypress Sandstone. A new well was drilled in the fall of 2019 to collect new geophysical logs, core, fluid samples, and conduct a drill stem test. This chapter will detail the geology of the Brownfield stacked reservoir complex and the findings resulting from the test well that was drilled in 2019.

5.1 Geology of the Stacked Reservoirs in the Noble Oil Field, Richland County, IL

Authors: Nathan Webb and Nathan Grigsby

This manuscript is currently in review for publication as part of the ISGS Circular Series.

Noble Oil Field (Figure 5-1), part of the Clay City Consolidated oil field in southwestern Richland County, Illinois, was discovered in 1937. More than 46 MMBO (7.3 million m^3) have been produced from seven stacked reservoirs (Figure 5-2) in the field (Webb and Grigsby, 2020). Roughly 53% of Noble Field's cumulative oil production is derived from an oil reservoir in the Mississippian Cypress Sandstone, with another 37% coming from the Ste. Genevieve Limestone. The remainder of the oil production comes from five other Mississippian-age formations, both siliciclastic and carbonate (Figure 5-2). The field represents a stacked reservoir complex of naturally occurring residual oil zones (ROZs) and depleted and bypassed conventional oil reservoirs that is typical of the Illinois Basin.

Oil production from Noble Field has been ongoing since the late 1930s. In its early years, the field was developed to rapidly maximize the return on drilling investment. The earliest wells were drilled and completed in the relatively thin, spatially restricted carbonate reservoirs of the Ste. Genevieve Limestone where they quickly depleted reservoir pressure, often within five years. Once production from those reservoirs declined, wells were commonly plugged back and recompleted in the larger, more continuous reservoir in the top of the Cypress Sandstone to produce a steadily declining amount of oil with an ever-increasing water cut for decades to follow. Additional reservoirs were targeted in the Aux Vases Formation and the Yankeetown/Renault sandstones and later in deeper formations including the St. Louis, Salem, and Ullin Limestones, with production commonly comingled from several stacked reservoirs. The result of this strategy is significant oil production, but a likewise significant amount of mobile and residual oil that remains in 1) pressure-depleted reservoirs, 2) bypassed reservoir compartments, and 3) a brownfield ROZ in the Cypress Sandstone that underlies the main pay zone (MPZ).

Carbon dioxide enhanced oil recovery (CO_2-EOR), which promises to recover a portion of the remaining oil while storing CO_2 in the depleted reservoirs (Verma, 2015), can be an effective method to further develop such mature fields containing stacked storage complexes. Implementing CO_2-EOR and associated storage in a stacked reservoir complex requires a systematic approach of reservoir characterization and design of development strategies that co-optimize EOR with associated storage (depending on business objective) among the varied and contrasting geology of the stacked reservoirs. In this study, Noble Field is treated as an archetypal stacked ROZ and conventional reservoir complex, and we complete reservoir characterization of the seven oil producing formations in the field. This characterization is then used to develop robust geocellular models of the formations within the stacked reservoir complex that can be

used in reservoir simulations to predict the oil production and associated CO_2 storage of various development strategies to better understand how to co-optimize CO_2-EOR and storage.

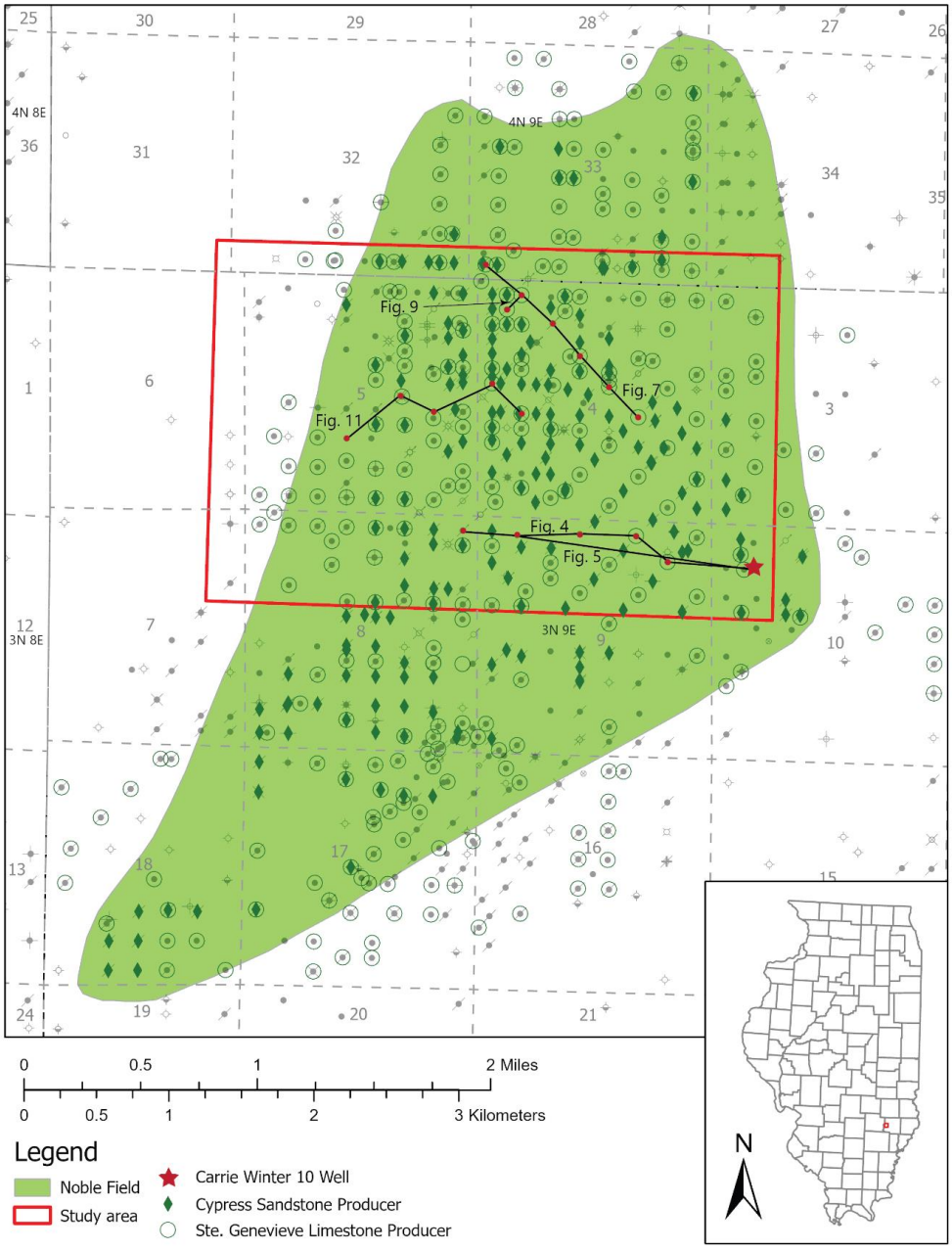


Figure 5-1. Map showing the approximate extent of Noble Field, shaded in green, in western Richland County, as estimated from early reports published following the field's discovery. Sections are labeled and outlined with grey dashed lines. The study area for this report is outlined in red. The Carrie Winter 10 well location is shown with a red star. All well locations are symbolized, those that produced from the Cypress are overlain with a green diamond and those that produced from the Ste. Genevieve Limestone are circumscribed by a green circle.

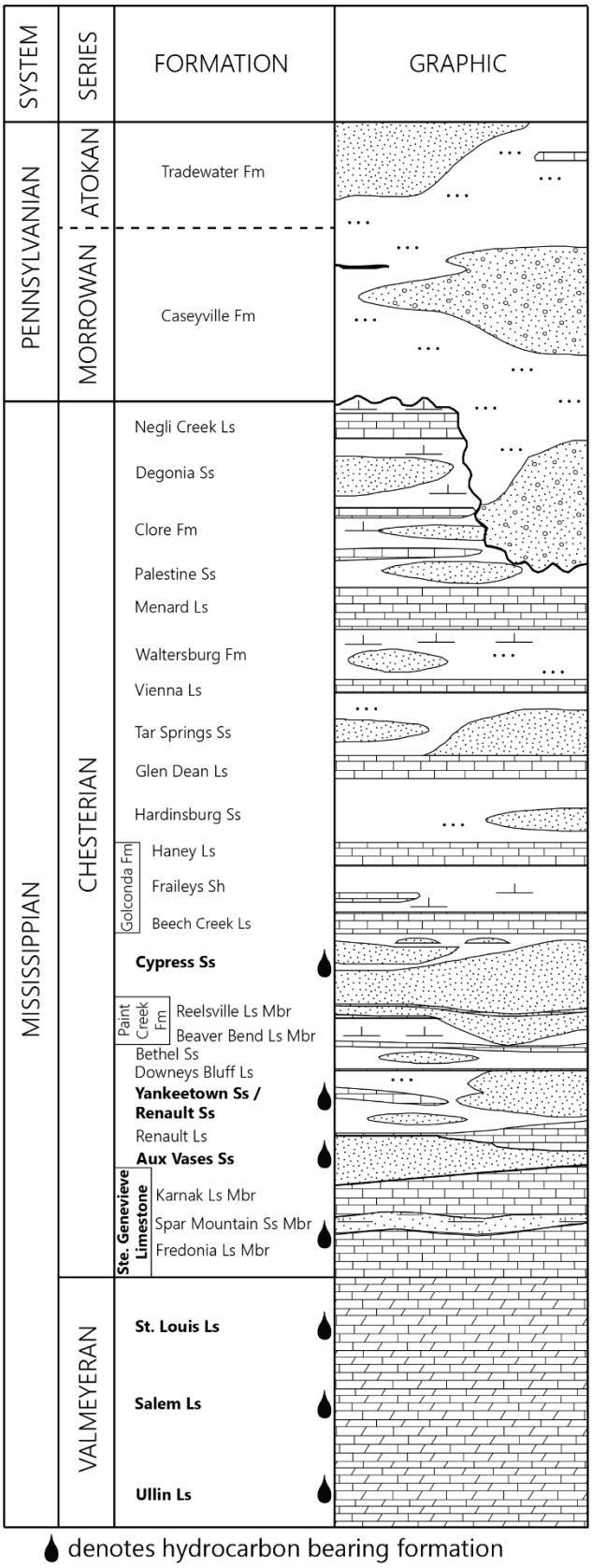


Figure 5-2. Generalized stratigraphic column of Noble Field. Modified from Webb and Grigsby (2020).

Study Area and Methods

The study area was defined as a rectangular area of 3.75 mi^2 (9.8 km^2) in the northern half of Noble Field where the well density is the highest (Figure 5-1). A stratigraphic column details the middle Mississippian to lower Pennsylvanian strata in Noble Field and indicates the hydrocarbon-bearing formations that compose the stacked reservoir complex (Figure 5-2). Webb and Grigsby (2020) previously summarized the stratigraphy of Noble Field, which includes approximately 2,000 to 2,200 ft (610 to 671 m) of Pennsylvanian-aged strata that overlie and truncate Chesterian formations along the sub-Absaroka unconformity (Figure 5-2). Approximately 2,200 to 2,400 ft (671 to 732 m) of Mississippian strata occur in the field, including approximately 800 ft (244 m) of cyclic Chesterian siliciclastics and carbonates, 1,200 to 1,400 ft (366 to 427 m) of Valmeyeran carbonates, and 50 to 300 ft (15 to 91 m) of Valmeyeran to Kinderhookian mudstone and limestone. Devonian strata, including the New Albany Shale and underlying carbonates, occur at a depth of roughly 4,415 ft (1,346 m) and are approximately 550 to 870 ft (168 to 265 m) thick. Silurian carbonates occur at a depth of approximately 4,960 to 5,280 ft (1,512 to 1,609 m) and range in thickness from 360 to 680 ft (110 to 207 m). The Ordovician system is encountered at approximately 5,650 ft (1,722 m). The deepest well in the field, the C.T. Montgomery 18-B well (API 121590068100, Section 4, T3N, R9E), reaches a depth of 6,800 ft (2,073 m) in the Ordovician St. Peter Sandstone.

In November 2019, the Carrie Winter 10 well (API 121592652800) was drilled as part of this study in SE ¼, NW ¼, NW ¼, Section 10, T3N, R9E (Figure 5-1) to a total depth (TD) of 3,831 ft (1,168 m) in the Ullin Limestone (Figure 5-2). The resulting samples and geophysical logs from this well provide a one-dimensional reference point for all stacked reservoirs in the field from which to build the characterization. Oil shows were observed in six formations within the Carrie Winter 10 well (Table 5-1). These formations are discussed below. All the logs associated with this well can be downloaded from the ILOIL website (https://isgs-oas.isgs.illinois.edu/reports/rwservlet?oilsummary&121592652800).

Geophysical logs from approximately 840 wells were used to correlate the tops and bases of the stacked reservoirs as well as other significant stratigraphic markers in the field well beyond the model boundaries. The correlation picks were used to develop surfaces that will be used in the creation of the geocellular model. Most of the wells penetrated the Cypress Sandstone, Aux Vases Formation, and the top of the Ste. Genevieve Limestone. Fewer wells penetrated the progressively deeper formations: St. Louis Limestone (350 wells), Salem Limestone (290 wells), and Ullin Limestone (77 wells). Geophysical logs available for correlation and mapping included 1940s-to 1970s-era electric logs with spontaneous potential (SP) and resistivity curves (generally long normal, short normal, and lateral resistivity) and more recent logs, including neutron density porosity, gamma-ray, SP, and induction resistivity traces. Most of the deeper wells had porosity logs. Porous reservoirs within the carbonate formations were identified from the logs to gain a better understanding of their thickness, spatial distribution, and heterogeneity. Geologic descriptions found in the text are based on a combination of literature review, well log interpretation, and observations from the Carrie Winter 10 well.

*Table 5-1. Top, base, and thickness data for the six oil-bearing formations encountered in the Carrie Winter 10 well. The number of producing wells from each formation is estimated based on ISGS records of perforation intervals. [+]Net:Gross (N:G) is a ratio of the ϕ-H to the total formation thickness. *Carrie Winter 10 well does not have a complete section through the Ullin, so data from nearby Coen #99 well (API 121592608600) was used instead. Top and base depth adjusted to the estimated depths in the Carrie Winter 10 well.*

Formation	Top (ft [m])	Base (ft [m])	Thickness (ft [m])	Porosity Cutoff (%)	ϕ-H (ft [m])	N:G[+]	Production Wells (est.)
Cypress Ss	2,571 [783.6]	2,726 [830.9]	155 [47.2]	12	25.3 [7.7]	16.3%	195
Aux Vases Fm	2,864 [872.9]	2,882 [878.4]	18 [5.5]	11	0.3 [0.1]	1.7%	77
Ste. Genevieve Ls	2,908 [886.4]	3,082 [939.4]	174 [53.0]	16	4.2 [1.3]	2.4%	284
St. Louis Ls	3,082 [939.4]	3,268 [996.1]	186 [57.0]	8	1.3 [0.4]	0.7%	149
Salem Ls	3,268 [996.1]	3,700 [1,127.8]	432 [131.7]	8	8.0 [2.4]	1.9%	173
Ullin Ls*	3,700 [1,127.8]	4,110 [1,252.7]	410 [125.0]	6	19.8 [6.0]	4.8%	14

Geology

Ullin Limestone

The Ullin Limestone occurs at a depth of approximately 3,700 ft (1,128 m) and contains the deepest producing oil reservoir in Noble Field. The formation is approximately 300 to 400 ft (91 to 122 m) thick. Regionally, the Ullin Limestone is divided into two members (Figure 5-3). The lower and thicker Ramp Creek Member is overlain by the thinner Harrodsburg Member along a gradational contact (e.g., Lineback, 1966). The Ramp Creek Member is composed of a biohermal facies that overlies and grades laterally into a transported facies (Lasemi et al., 1998). The transported facies is generally a very-fine grained, winnowed, bryozoan-crinoidal grainstone, and the biohermal facies is a highly porous, fenestrate-fragment coquina (Lasemi et al., 1998). The Ramp Creek Member is highly porous and generally contains a brine aquifer. In the Harrodsburg Member, porous intervals occur in sandwave and mound apron facies, interpreted to have been deposited by storm currents in a broad ramp setting (Lasemi et al., 1998), that consist of poorly cemented, light-colored grainstones composed of fragments of bryozoan and crinoids, the latter of which becomes less abundant upwards and corresponds with increased porosity (Jobe and Saller, 1995; Lasemi and Grube, 1995). Non-porous inter-sandwave facies consist of a cherty lime mudstone to wackestone. The porous zones are commonly less than 10 ft (3 m) thick and can stack to form porous intervals up to 40 ft (12 m) thick (Lasemi and Grube, 1995).

In Noble Field, there are approximately 60 wells TD in the Ullin Limestone, usually penetrating 30 to 50 ft (9 to 15 m) into the Harrodsburg Member (Figure 5-4). Observed porosity zones range in thickness from 5 to 20 ft (1.5 to 6 m). The uppermost one or two porous zones can be oil-bearing, and a handful of wells in the field are perforated in this interval, though the production is almost universally comingled with other formations. The underlying porous zones typically produce sulfur water. Three wells in the field penetrate the entire thickness of the Ullin Limestone, with the Coen #99 well (API 121592608600) being the most recent and centrally located (Figure 5-5). There are 121 ft (37 m) of formation above 6% porosity

(a total of 20.3 pore-ft [6.2 pore-m]) in the Coen #99 well (Figure 5-5). CO_2-EOR may be possible in the relatively thin and compartmentalized reservoirs of the Harrodsburg Member, but the thick brine aquifer of the Ramp Creek Member (Figure 5-5) is an excellent candidate for CO_2 storage.

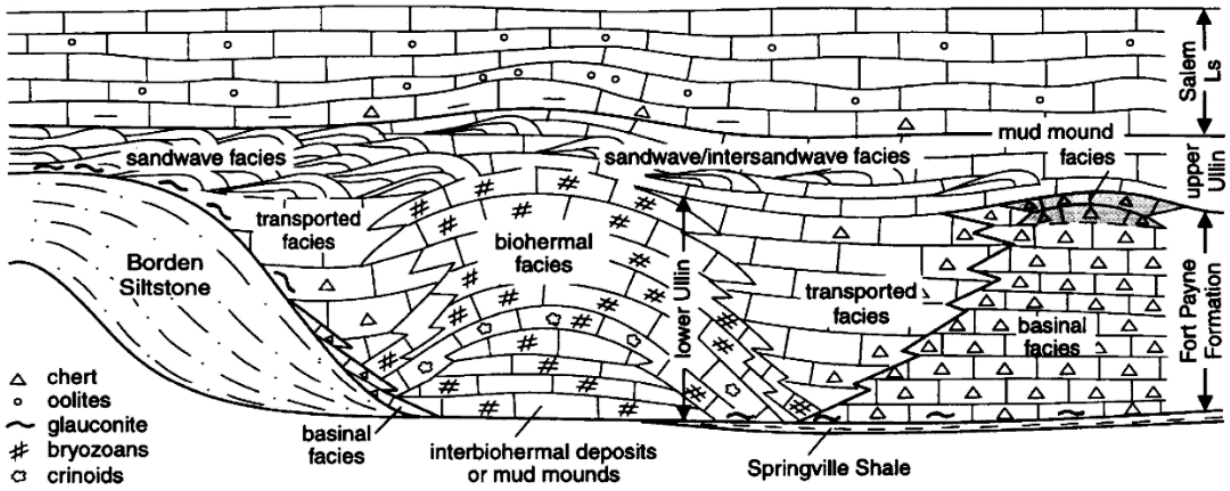


Figure 5-3. Diagrammatic cross section showing the Ullin Limestone in context with overlying and underlying formations that illustrates the distribution of facies within the formation. Oil reservoirs in Noble Field occur within the sandwave facies of the Harrodsburg Member (upper Ullin on this diagram). From Lasemi et al. (1998).

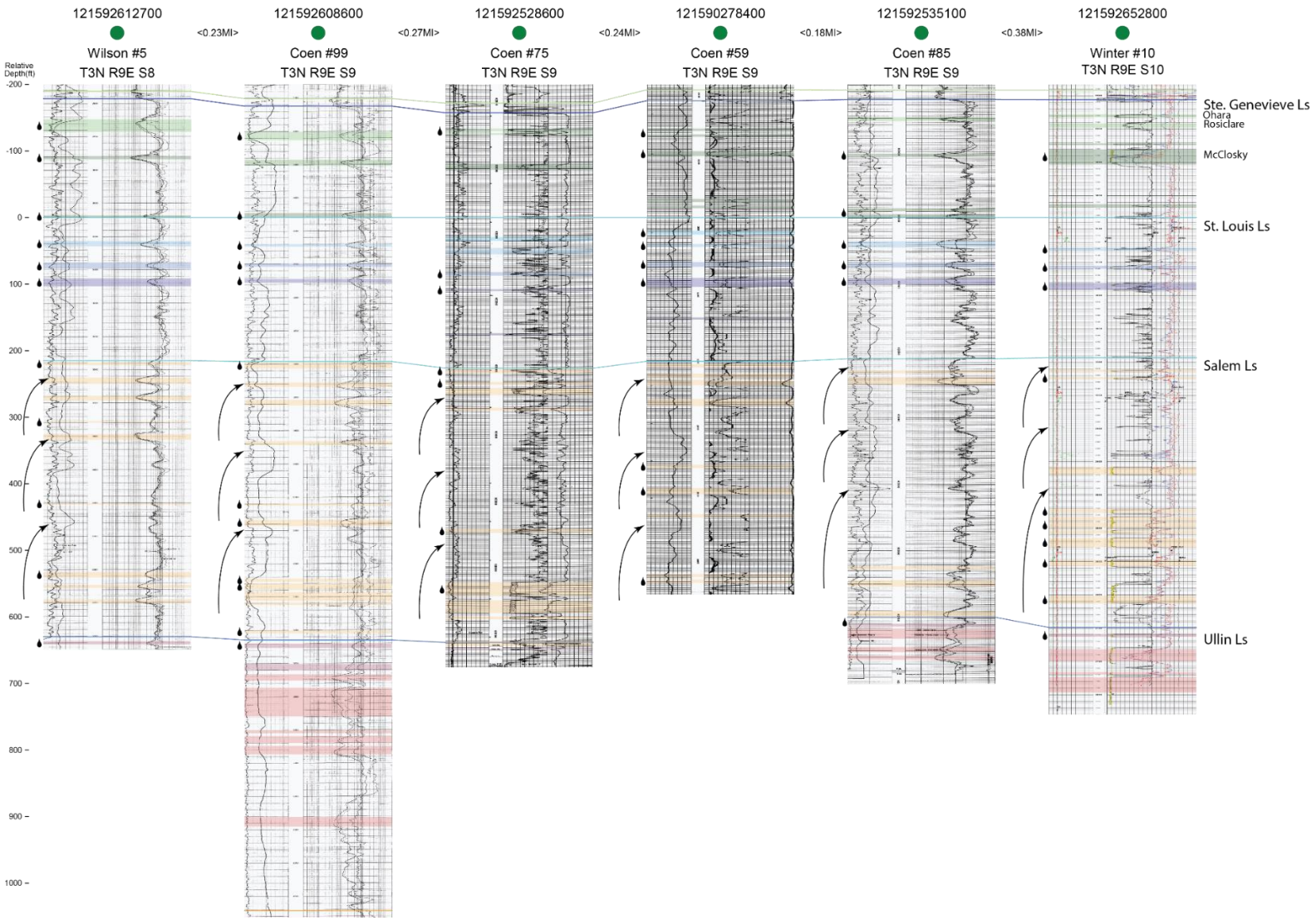


Figure 5-4. West-East cross section in Noble Field showing the stratigraphy of the Middle-Mississippian carbonate succession. Intervals of porosity are shaded; Pink = Ullin Ls., Yellow = Salem Ls., Purple/Blue = St. Louis Ls., Green = Ste. Genevieve Ls. Arrows highlight the gamma ray/SP log motif indicating the three fining upward cycles of sedimentation within the Salem Ls. (e.g., Cluff and Lineback, 1981).

Being relatively pure limestone, the Ullin Limestone has a characteristically low gamma ray and strongly negative SP signature throughout. Neutron and density porosity curves generally track well together with minimal separation (on limestone matrix) and clearly indicate porous zones (Figure 5-5). Microlog response aids in the identification of the porous and permeable intervals by showing low resistivity and a positive separation (Figure 5-5).

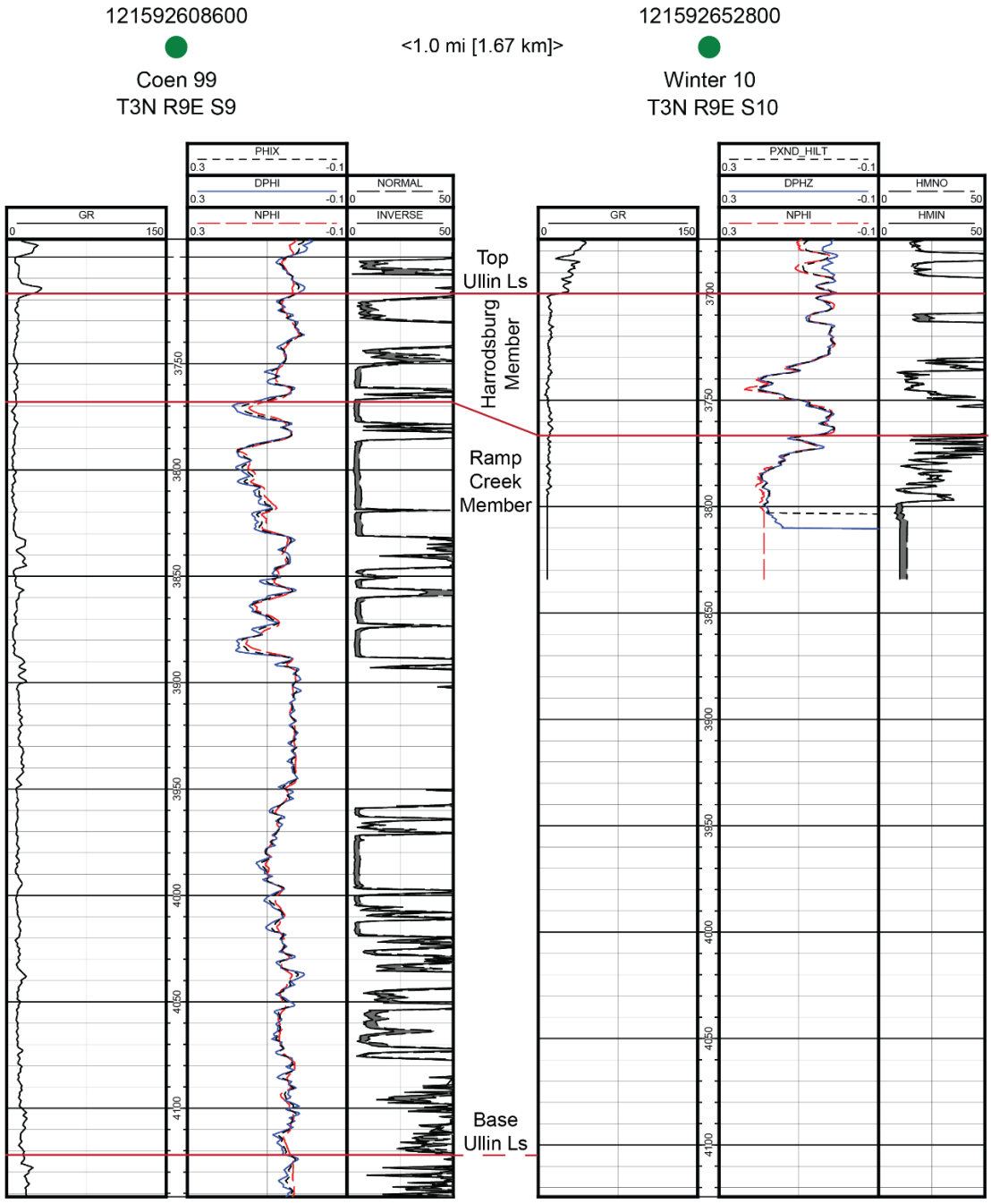


Figure 5-5. Gamma ray, porosity, and microlog curves through the Ullin limestone in two wells in Noble Field. The JO Coen 99 well penetrates the entire formation, whereas the Carrie Winter 10 well reaches TD within the upper part of the Ramp Creek Member. Note the significant thickness of rock in the Ramp Creek Member with porosity at or above 10% and showing positive microlog separation.

Salem Limestone

The Salem Limestone occurs at a typical depth of 3,300 ft (1,006 m) and is approximately 400 ft (122 m) thick. The dominant lithology of the Salem Limestone is wackestone to packstone with rounded, broken fossil fragments and whole small fossils, commonly with oolite-like overgrowth within a micrite to sparite matrix (Lineback, 1972). Facies analysis has indicated that the Salem Limestone was deposited as part of a subtidal high-energy shoal complex on a carbonate platform (Brown, 1990). A recent literature review and more detailed description of the facies based on quarry exposures is presented by Keith and Thompson (2018). In a regional subsurface study, Cluff (1984) described the cyclical nature of Salem Limestone deposition and identified three shallowing upward cycles (Figure 5-6). Each cycle has a typical succession from bottom to top:

1. coarse-grained skeletal wackestones and lime mudstones interbedded with highly porous and permeable oolitic and skeletal grainstones
2. bioturbated oolitic and skeletal packstones with thin grainstone beds, usually with irregular porosity and permeability
3. impermeable argillaceous lime mudstones, pelletal packstones, and dolomitic mudstones that commonly form effective seals over the underlying porous grainstones.

Oil production from the Salem is common in many fields in Illinois and Indiana, and oil reservoirs are commonly found in the oolitic and skeletal grainstones that occur in the basal part of the cycles (Stevenson, 1978; Keller and Becker, 1980). Whether the grainstones are porous and oil-bearing is highly dependent on whether the grains have been calcite-cemented (Stevenson, 1978). Porosity and permeability are controlled by compaction and cementation, with early syntaxial rim cement around echinoderm grains both inhibiting compaction and filling pore spaces and closing off pore throats (Dodd et al., 1993). An analysis of porosity in the Salem fields in Indiana indicated the lower limit of producible porosity in the Salem (and St. Louis) Limestone was 6% with productive intervals generally at least 5 ft (1.5 m) thick (Keller and Becker, 1980). However, more recent operations that target the Salem in the Wabash Valley region have had success completing thicker intervals of lower porosity rock with more aggressive fracture stimulations and acid treatments (Hoy, 2014).

In Noble Field, the three cycles can be readily observed on well logs (Figure 5-4). Porous zones are commonly up to 20 ft (6 m) thick and are best developed in the first (lower) and third (upper) cycles within the Salem. The geophysical log characteristics of these porous oolitic and skeletal grainstones include low resistivity, strongly negative (left) SP deflection, moderate to high density and neutron porosity with minimal separation (when run on limestone matrix), and low gamma ray response (Cluff, 1984).

Oil production from the Salem in Noble Field is sporadically distributed. Salem production is almost always comingled with other formations, making it difficult to understand reservoir performance. However, some of the first Salem completions were single zone completions. The CT Montgomery 16B well (API 121590140500), located near the top of the structure, was completed in 1954 in two intervals (totaling 19 ft [6 m]) in the lower Salem with an initial production (IP) of 108 bbl (17.2 m^3) oil and 23 bbl (3.7 m^3) water per day. The well was reworked after 22 years to include perforations in additional zones. Similarly, the Palmer-Taylor 18 well (API 121590058100) was completed in two zones (totaling 20 ft [6 m]) in the lower Salem in 1957 with an IP of 10 bbl (1.6 m^3) oil and 5 bbl (0.8 m^3) water per day and was converted to water injection after 19 years. Despite the inherent heterogeneity and compartmentalization of Salem reservoirs, there is a good amount of porous rock

in the formation, in particular the lower Salem, which would likely be a fair candidate for CO_2-EOR and associated storage.

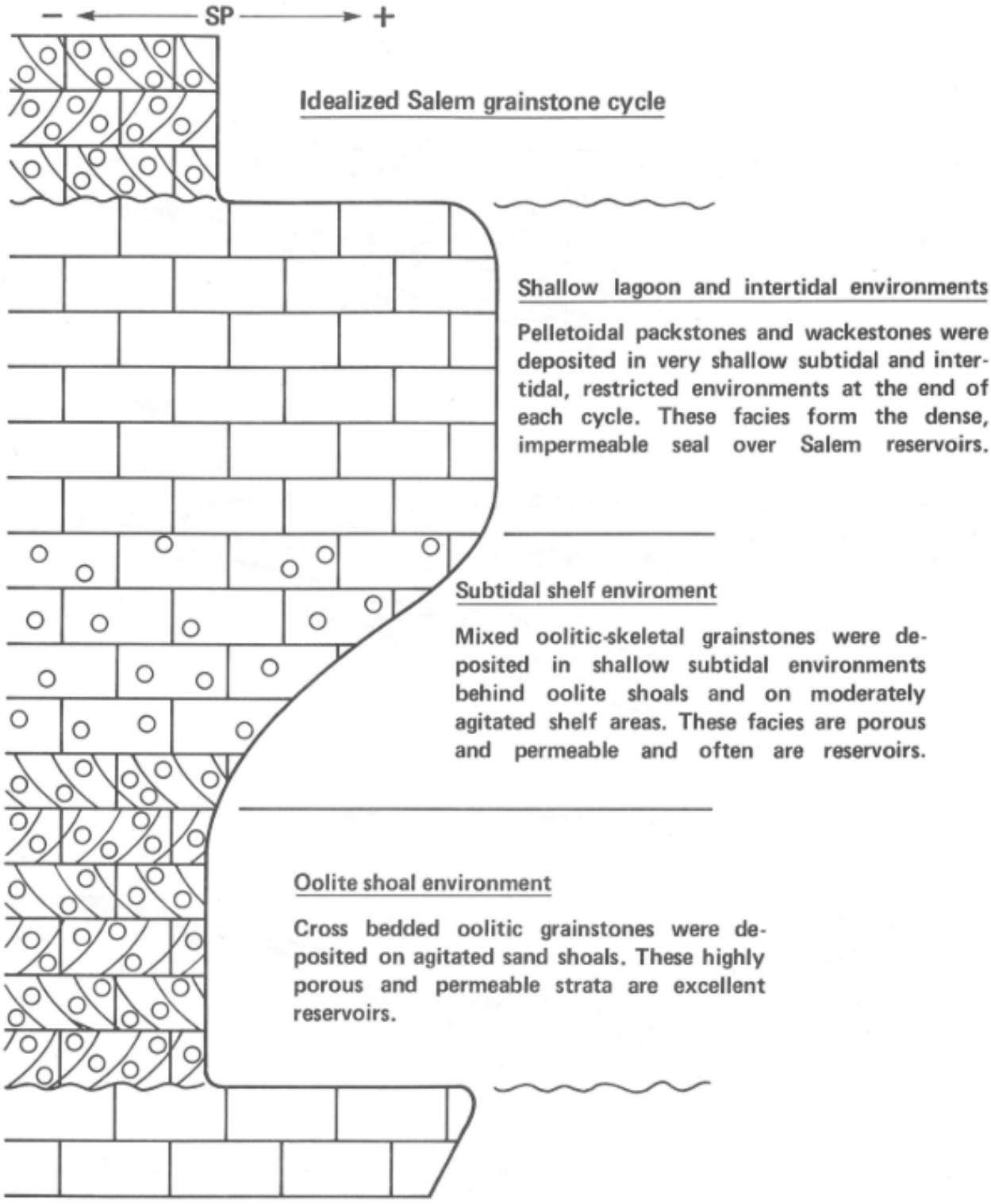


Figure 5-6 Idealized facies distribution within a shallowing upward cycle typical of the Salem Limestone. SP log response can be used to identify the cycles in oil wells. From Cluff and Lineback (1981).

St. Louis Limestone

The St. Louis Limestone occurs at approximately 3,100 ft (945 m) and is 200 ft (61 m) thick. The St. Louis Limestone is characterized by cherty lime mudstone interbedded with various facies, including skeletal wackestone, skeletal packstone, microsucrosic dolomite, and minor anhydrite (Lineback, 1972; Treworgy, 1991) generally reflecting deposition in a supratidal to sabkha environment (Keith and Thompson, 2018). Oil reservoirs in the St. Louis Limestone occur within microsucrosic dolomite beds that originated as lime mudstones and have high porosity and moderate permeability (Bristol and Howard, 1966; Cluff, 1984). Oil production characteristics from early St. Louis wells along the Clay City Anticline in Jasper County to the northeast indicated an active water drive with possible contributions from solution gas (Bristol and Howard, 1966). On geophysical logs, the dolomite beds can be distinguished by significant separation between the two porosity curves (neutron porosity 4% to 8% higher than density porosity) and Pe < 4 and often have low resistivity and high density (>10%) and neutron porosity (>20%).

In Noble Field, a number of these dolomite beds occur in the St. Louis Limestone, generally in the upper half of the formation, with each bed being typically 2 to 8 ft (0.6 to 2 m) thick. Many of the observed dolomite beds are difficult to trace from well to well; however, there are three beds (referred to here as the St. Louis A, B, and C) that are more consistent and can be correlated throughout the field (Figure 5-7). The St. Louis A, B, and C beds are separated from one another by approximately 15 to 25 ft (5 to 8 m) of non-porous limestone (Figure 5-7). Despite the continuity of the dolomite beds on cross sections, the porosity (as indicated on logs) can vary markedly from >20% to only a few percent, meaning reservoir continuity between wells is likely tenuous. A few additional thin dolomite beds occur within the formation both above and below the three primary beds, but they are less continuous.

St. Louis oil production in Noble Field is somewhat sporadically distributed. As with the Salem, St. Louis production is almost always comingled with other formations, making it difficult to understand reservoir performance, but the first St. Louis completions were single zone completions. The CT Montgomery 15B well (API 121590140400), located near the top of the structure, was completed in 1954 in the upper St. Louis with an IP of 85 bbl (14 m^3) oil and no water per day. The well was plugged back after 36 years and perforated in the Cypress. Although the microsucrosic dolomite beds that comprise the St. Louis reservoirs have good porosity and are widespread, their limited thickness likely makes their EOR and associated storage prospects marginal.

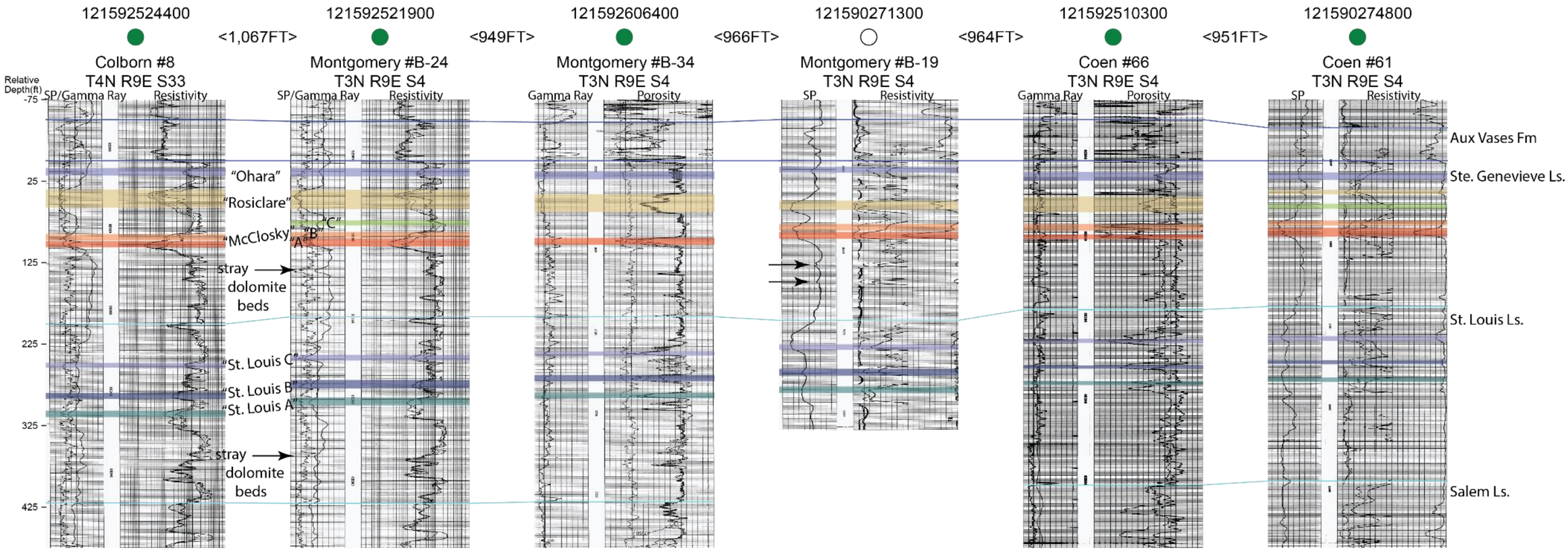


Figure 5-7. Cross section showing typical log response and continuity of porosity zones within the St. Louis and Ste. Genevieve Limestones. Formation names are listed along the right margin of the cross section. Informal names and subdivisions used in this report are annotated on the cross section.

Ste. Genevieve Limestone

The Ste. Genevieve Limestone is divided into three members in Illinois, from bottom to top: Fredonia Limestone Member, Spar Mountain Sandstone Member, and Karnak Limestone Member (Figure 5-8). In Noble Field, the Ste. Genevieve Limestone is approximately 200 ft (60 m) thick with the Fredonia being 130 ft (40 m), the Spar Mountain being 50 ft (15 m), and the Karnak composing the remaining 20 ft (6 m). Lithologic similarities of the Ste. Genevieve Limestone to the Salem Limestone reflect a return to an overall high-energy subtidal shoal depositional setting on a carbonate platform with the sandy, oolitic grainstone reservoirs described below being deposited mainly in tidal shoals and channels (Choquette and Steinen, 1980).

The Fredonia Limestone Member is generally composed of gray to brown fine-grained packstone, wackestone, and lime mudstone interspersed with beds of coarser grained ooid grainstones that can contain very-fine grained quartz sand. The limestone contains brachiopod fossil fragments and can be calcite-cemented. The lower two-thirds of the member contains thin stringers of microsucrosic dolomite. The upper third contains lenses of light brown to white, medium to coarse ooid grainstone that is very porous when not cemented by calcite (Bell and Cohee, 1938). The oolitic facies of the Fredonia occur in lenses and form prolific oil reservoirs (Workman and Bell, 1937), which are commonly referred to as McClosky sand or McClosky oolite (Nelson, 2022; Figure 5-9). Detailed studies of this interval indicate that the oolites occur as uncemented porous lenses that are typically flat-bottomed and convex-upward, generally <10 ft (3 m) thick, and elongate from 0.5 mi (0.8 km) to a few miles (kilometers) in length, and 0.13 to 0.75 mi (0.2 to 1.2 km) in width (e.g., Carr, 1973; Choquette and Steinen, 1980). Correlating and mapping these thin, discontinuous bodies can be difficult, though slice mapping has been suggested as an effective technique (Zuppann, 1993). In Noble Field, the distribution of McClosky lenses is sporadic, leading early developers of the field to encounter roughly 10% dry holes that commonly offset wells with high IPs (Wasson, 1938; Lee, 1939).

The Spar Mountain Sandstone Member of the Ste. Genevieve Limestone is lithologically variable, consisting of mixed carbonates and siliciclastics. Nelson et al. (2002) describes the Spar Mountain in the northern Fairfield Basin as being composed of oolitic and skeletal limestone that contains 20% or more detrital quartz silt and sand grains. In Noble Field the porous sandy oolitic zone, referred to as the Rosiclare sand or Rosiclare lime (Nelson, 2022), can be as much as 30 ft (9 m) thick (Figure 5-10) and is characterized by poorly sorted quartz sand grains and dark, large ooids, but can be composed purely of ooids in some places (Lee, 1939).

The Karnak Limestone Member is generally composed of brown, crystalline, fossiliferous limestone that is argillaceous and dolomitic in places (Lee, 1939) and is lithologically similar to the Fredonia Limestone Member. In some areas, the Karnak contains a zone of oolitic to peloidal grainstone that is porous and oil-bearing in places and is referred to as the Ohara lime.

Geophysical log response through the Ste. Genevieve Limestone is generally like that of the St. Louis Limestone and the Salem Limestone. Oil production from the Ste. Genevieve Limestone is well distributed across the field. Well records document incredible IPs, in some cases exceeding 2,000 bbl (318 m^3) of oil. The Arbuthnot 1 discovery well of Noble Field (API 121590012100), which is approximately 50 ft (15 m) structurally lower that the top of the structure, was completed open hole in the Rosiclare and McClosky reservoirs for a reported IP of 2,500 bbl (398 m^3) of oil in 1937. The M Eberhardt 1 well (API 121590141000), drilled higher on the structure in early 1938, was completed in the Rosiclare for 2,623 bbl (417 m^3) of oil. Four months later, the same well was deepened

approximately 50 ft (15 m) to target a McClosky reservoir. Early Ste. Genevieve wells commonly flowed oil to surface for a short period, and production declined rapidly with the wells often requiring artificial lift within a few months (Wasson, 1938). Compartmentalization of Ste. Genevieve reservoirs may be a challenge, but production has been prolific, and the reservoir quality is outstanding. Given these facts and the success of waterflooding in the formation, the CO_2-EOR and associated storage potential of the Ste. Genevieve is expected to be good.

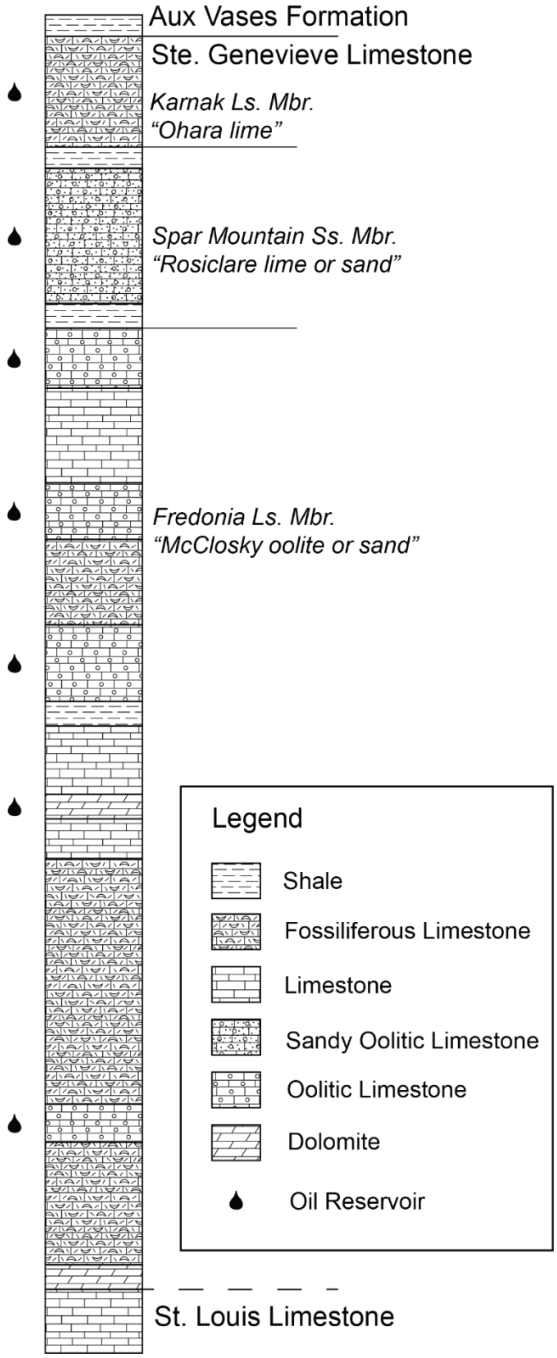


Figure 5-8. Diagrammatic stratigraphic column through the Ste. Genevieve Limestone showing the three members, lithologic variability, and the various horizons at which oil reservoirs are commonly found. Modified after Stevenson (1969).

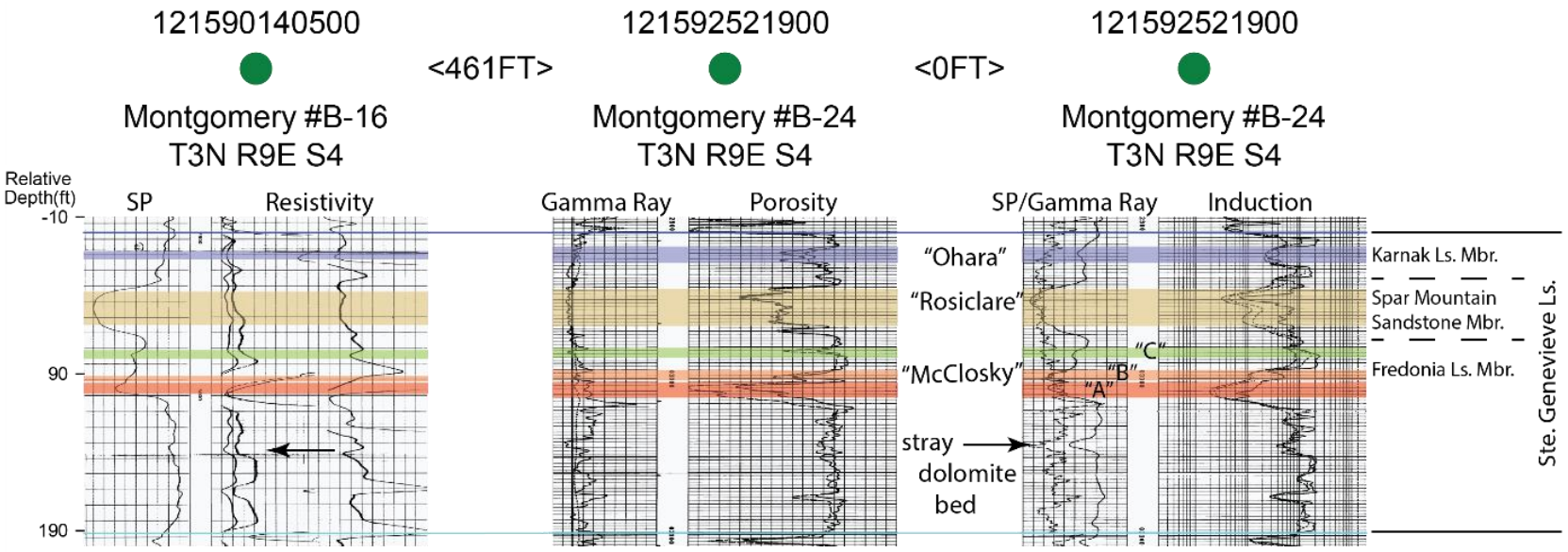


Figure 5-9. Type logs from two wells, showing the character of the Ste. Genevieve Limestone in an old e-log from the Montgomery #B-16 well (left) and in porosity (middle) and induction (right) logs from the offset Montgomery #B-24 well. Formation names are listed along the right margin of the cross section. Informal names and subdivisions used in this report are annotated on the cross section.

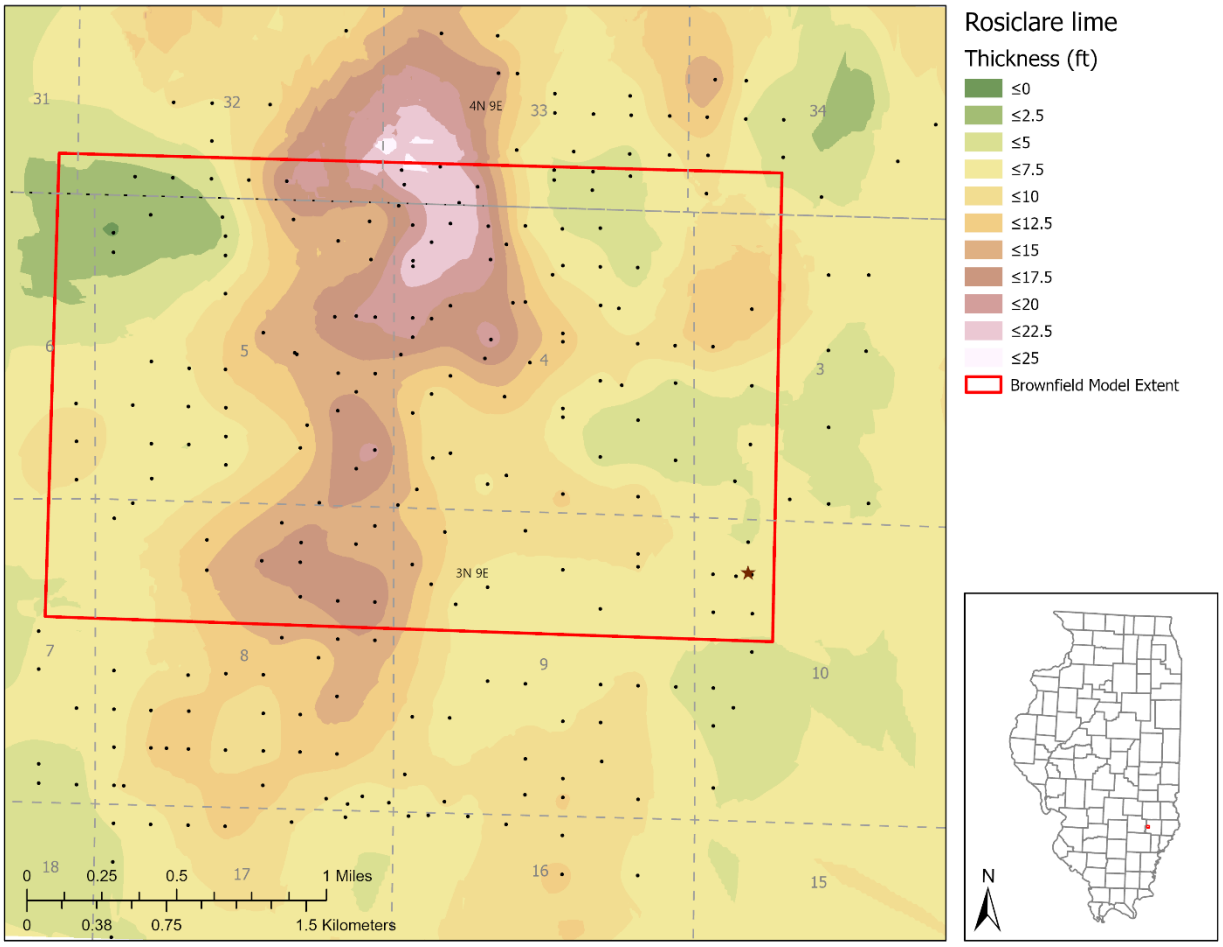


Figure 5-10. Isopach map showing the thickness of the porous "Rosiclare lime" interval within the Ste. Genevieve Limestone. The black dots are the data points used to make the map. The brown star is the Carrie Winter 10 well. The red outline is the study area from Figure 5-1.

Aux Vases Formation

The Aux Vases Formation occurs at a depth of approximately 2,850 ft (869 m) and is roughly 50 ft (15 m) thick. The formation is lithologically variable, consisting of a lower calcareous, fine-grained sandstone to fossiliferous limestone or dolomite that can be sandy or oolitic, a middle sandy oolitic limestone, and an upper fine-grained shaly sandstone (Lee, 1939). The predominance of an upper siliciclastic interval and a lower interval with carbonates is a common occurrence within the Aux Vases in this part of the Illinois Basin (Leetaru, 2000). The Aux Vases Formation has been studied in detail throughout the Illinois Basin at King Field (Leetaru, 1991), Boyd Field (Leetaru, 1993), Zeigler Field (Seyler, 1998), Energy Field (Huff, 1993), Dale Consolidated Field (Udegbunam et al., 1993), Storms Consolidated Field (Leetaru, 1996), Stewardson Field (Rice et al., 1993), as well as a regional study by Leetaru (2000).

In the central part of the Illinois Basin, the Aux Vases is comprised of a belt of lenticular sandstone bodies 16 to 33 ft (5 to 10 m) thick that are commonly elliptical in map view with their long axes oriented northeast-southwest. The lenticular sandstone bodies intergrade laterally with lenses of sandy limestone and are encased by reddish to greenish gray mudstone. The lenses have flat bases, are convex-upward, and are generally interpreted as tidal sand bars (Seyler, 1986; Cole, 1990) and

likely formed in a tidally influenced siliciclastic wedge that prograded over underlying carbonate-rich sediments (Leetaru, 2000).

On geophysical logs, the SP response in the sandstone is less strongly negative, and gamma ray is higher than the thick, clean Cypress Sandstone, indicating that Aux Vases sandstone is more shaley in general. Modern logs with neutron and density porosity, micro-logs, and PE curves are particularly useful in tracking the lithologic changes in the formation and identifying thin stringers of porosity in dolomites developed in the lower half of the formation (Figure 5-11). Core analysis data from the formation are limited, but typical porosities are in the 13 to 14% range (P10 = 10.1%; P90 = 21.4%) with corresponding single-digit permeabilities.

Oil reservoirs within the Aux Vases are highly facies-dependent, and production perforations generally target the upper, sandier portion of the formation (Figure 5-11). Wells completed in the Aux Vases are sporadically scattered around the field, and production from the Aux Vases is almost universally comingled with other zones. A few well records indicate single zone completions in the Aux Vases and shed light on its productivity. The Schilling 1 well (API 121590269000) was completed in 12 ft (4 m) of upper Aux Vases sandstone for 126 bbl (20 m^3) of oil and 5 bbl (0.8 m^3) of water in 1965 and remains open as of 2022. On the same lease, the Schilling 2 well (API 121590269100) was completed in the same 12 ft (4 m) of upper Aux Vases sandstone for 144 bbl (23 m^3) of oil and no water in 1965 and was plugged in 1997. The Rosenberg 2 well (API 121590282001), originally a St. Louis producer for three years, was reentered and completed with 20 ft (6 m) of perforations in the Aux Vases for a reported IP of 6 bbl (1 m^3) of oil and no water in 1969 and was plugged in 1989. Given the lithologic variability and compartmentalization expected in the Aux Vases, CO_2-EOR and associated storage potential in the formation is likely limited.

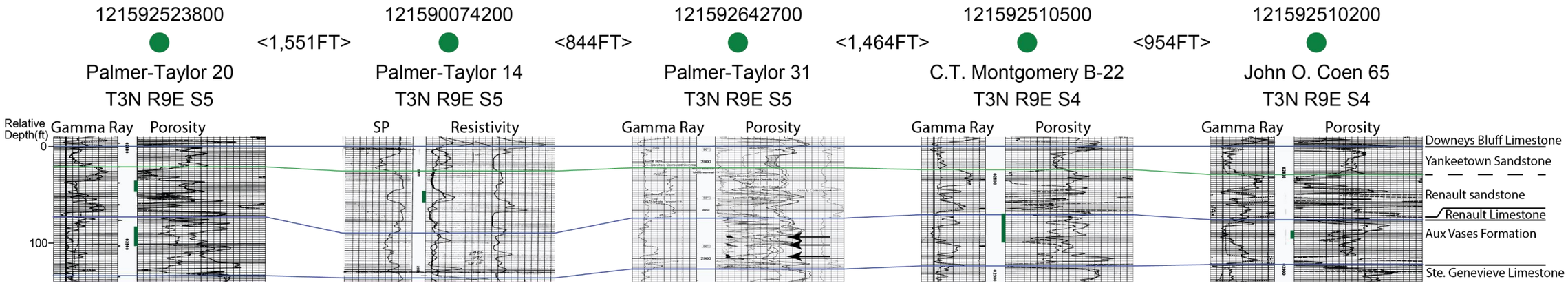


Figure 5-11. Cross section showing the interval from the top of the Ste. Genevieve Limestone up through the base of the Downeys Bluff Limestone (which is the datum). Production perforations in the Aux Vases Formation and the Renault Sandstone are shown with green bars. The Aux Vases Formation is lithologically complex. Oil is generally produced from the sandstone in the upper part of the formation, but porous sandy dolomites also occur in the lower part of the formation (see black arrows), as indicated by neutron-density porosity separation on limestone matrix. Formation names are listed along the right margin of the cross section.

Yankeetown Sandstone and Renault Sand

Two relatively thin lenticular sandstone units, the Renault Sand and Yankeetown (Benoist) Sandstone, occupy a 50- to 80-ft-(15- to 24-m) thick interval that overlies the Renault Limestone and occurs at an average depth of 2,780 ft (847 m) (Figure 5-11). A sandstone body approximately 10 ft (3 m) thick occurs 10 to 20 ft (3 to 6 m) above the Renault Limestone and is commonly referred to as the Renault Sand (Nelson, 2022). Twenty to 30 ft (6 to 9 m) of shaly to clean Yankeetown Sandstone is indicated on geophysical logs at the top of this interval directly underlying the Downeys Bluff Limestone. A regional study of the Benoist Sandstone indicates that its thickness in Noble Field should average around 10 ft (3 m) of net clean sandstone (Leetaru et al., 2005). Both sandstone bodies can be calcareous.

Relatively few wells in Noble Field produce oil from the sandstones in this interval, mainly in the central part of Section 5 (Figure 5-1), and there are few definitive records on their production performance. The EOR and storage potential of these reservoirs in the study area are therefore considered to be trivial, and the formations were not characterized in detail.

Cypress Sandstone

The Cypress Sandstone occurs at an average depth of approximately 2,600 ft (792 m) and is a thick, continuous sandstone that generally has a blocky appearance on SP and gamma ray logs. The thickness of the sandstone can vary from 90 to 175 ft (27 to 53 m). There is generally a 20- to 30-ft (6- to 90-m) thick shaly interval between the top of the sandstone and the base of the Beech Creek Limestone (Figure 5-12). The thick Cypress Sandstone has been interpreted to represent amalgamated fluvial deposits within an incised valley system (Nelson et al., 2002; Webb and Grigsby, 2020). Refer to Webb and Grigsby (2020) for the complete geologic characterization of the Cypress Sandstone in Noble Field.

The top of the Cypress Sandstone contained a relatively thick oil column (MPZ was originally up to approximately 50 ft [15 m] underlain by a 20- to 30-ft [6- to 9-m] thick ROZ; Figure 5-12) where the high porosity, permeability, and relative homogeneity of the reservoir rock has resulted in excellent production. The mobile oil column of the MPZ has since moved up because of the prolific oil production from the Cypress. Initial production values from wells completed in the Cypress Sandstone typically range from 100 to 300 bbl of oil (15.9 to 47.7 m^3) with 0 to 300 bbl of water (0 to 47.7 m^3) (Webb and Grigsby, 2020). The highest initial production recorded was 1,896 bbl of oil (302 m^3) from the C.T. Montgomery B-2 well (API 121590139100) in northwestern sec. 4, T3N, R9E. The ROZ is underlain by a thick brine aquifer, which can result in water coning issues due to high vertical permeability. Producing wells are generally long-lived but can develop a high water cut over time. Previous calibrated reservoir simulations indicated that an additional 3 to 3.5 million bbl (477,000 to 556,500 m^3) of oil could be produced from the Cypress Sandstone with CO_2-EOR and that, depending on the development strategy, 30+ million tonnes of associated CO_2 storage are possible in the MPZ and ROZ. There is significant additional storage available in the thick brine aquifer that makes up the bulk of the Cypress Sandstone in Noble Field.

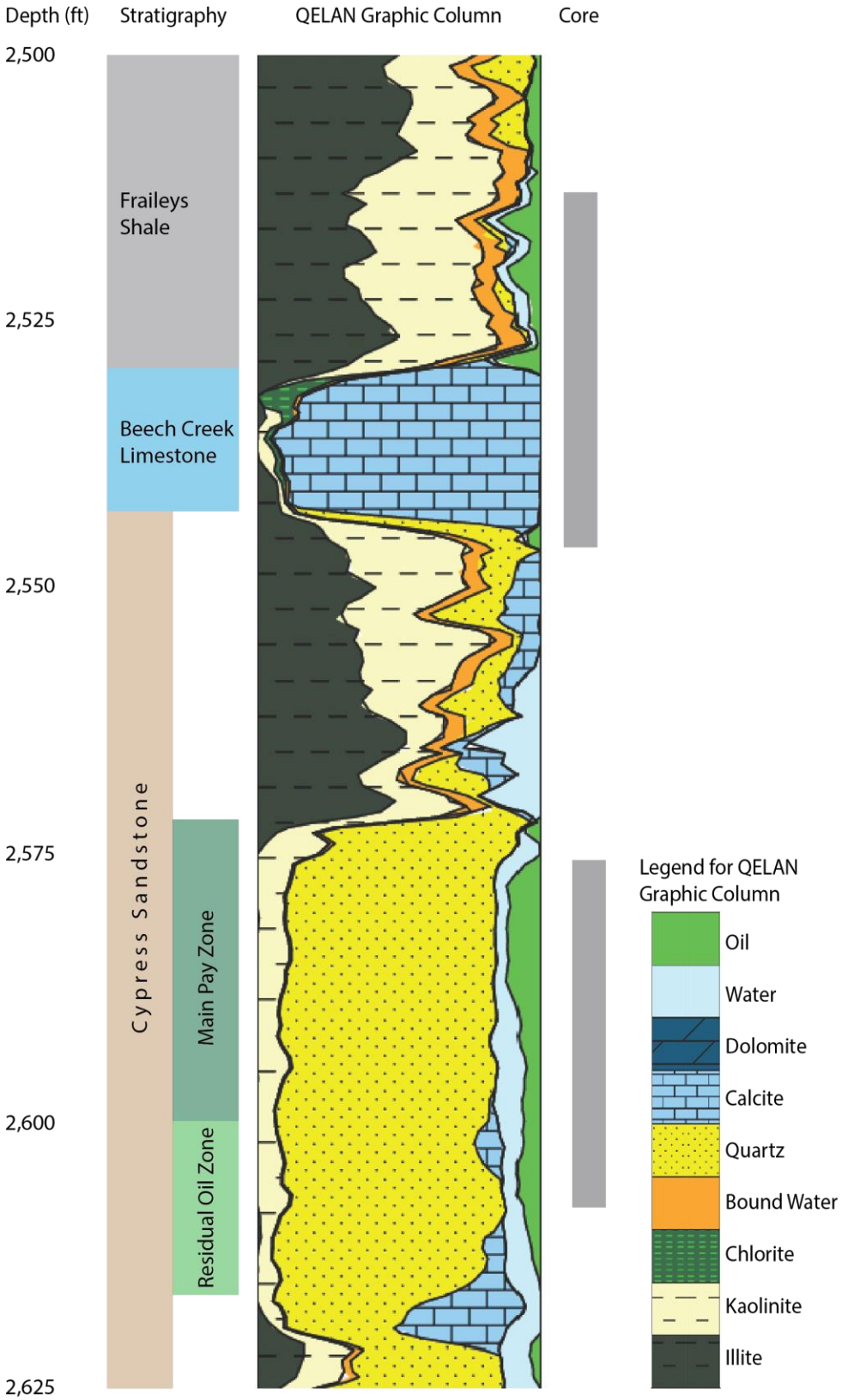


Figure 5-12. Diagram showing stratigraphy, lithology (based on Schlumberger QELAN analysis), and core in the Cypress Sandstone and overlying units in the Carrie Winter 10 well.

Stacked Reservoir Characterization

Continuity

Noble Field is a typical example of an Illinois Basin oil field with production from multiple stacked reservoirs. The field is located on an anticlinal structure, and oil production is derived from several conventional reservoirs of both siliciclastic and carbonate lithology, as discussed above. An ROZ is also present in the Cypress Sandstone (Webb and Grigsby, 2020).

When assessing the stacked reservoir complex at Noble Field for CO_2-EOR and associated storage, it is important to consider the applicability of different well pattern sizes to the potential efficacy of a CO_2 flood, as each formation has a unique reservoir geometry. As such, a reservoir continuity approach was employed to better understand the potential connectivity of well pairs in each formation to aid in the design of the optimum well patterns and perforation intervals at various distances for each formation. Reservoir continuity is the percentage of pay in a well that is connected between any two given wells (George and Stiles, 1978). Infill drilling with smaller injection patterns generally results in maximized per-well oil recovery (Barber et al., 1983), but the size of the selected flooding pattern must be balanced between reservoir continuity and the economics of drilling and completing new wells or converting legacy wells.

Reservoir continuity was determined using an analytical method developed by Stiles (1976). Forty well pairs in the field were correlated at various distances from 258 to 4,173 ft (79 to 1,272 m), and the thickness of porous formation above a 6% porosity cutoff was determined. The well pairs were selected to represent a range of different orientations to account for anisotropy of the porous reservoirs. Wells with the same thickness of porous rock are 100% continuous, whereas 0% continuity occurs in wells where one well has some thickness of porous rock and the other well has none. Reservoir continuity is presented graphically as a % continuity at a given distance (Figure 5-13). Of the six formations characterized above, the Aux Vases Formation was excluded from the reservoir continuity determination due to significant lithologic changes across Noble Field.

The results of the stacked reservoir continuity analysis (Figure 5-13) show the Cypress Sandstone has the highest reservoir continuity at any well spacing with greater than 90% continuity at 2,500 ft (762 m). The thin lenticular porosity zones in the Ullin Limestone are the least continuous, showing no continuity at approximately 1,750 ft (533 m). The other three carbonate formations have moderate continuity with the Salem Limestone slightly outperforming the Ste. Genevieve and St. Louis reservoirs across the range of well spacings.

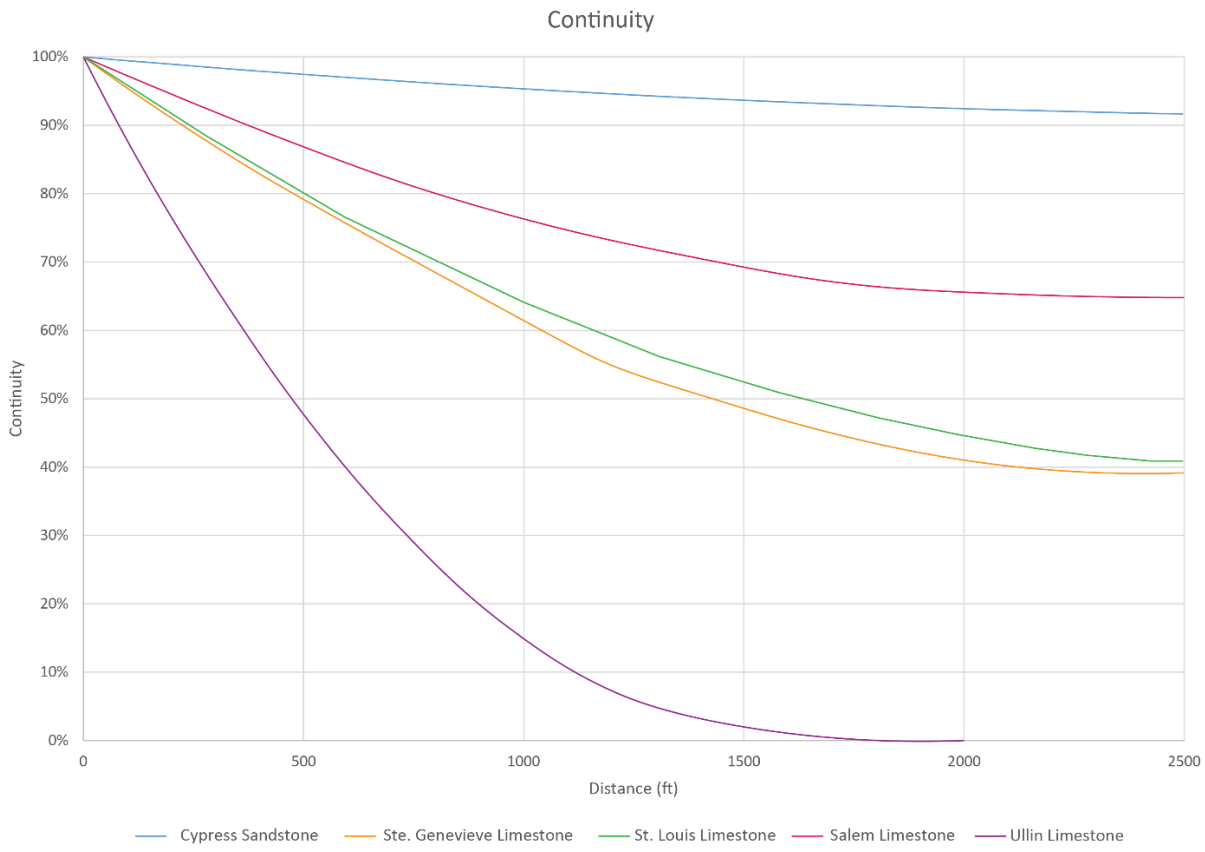


Figure 5-13. Graph showing reservoir continuity of five formations (Cypress Sandstone, Ste. Genevieve Limestone, St. Louis Limestone, Salem Limestone, and Ullin Limestone).

Porosity and Permeability

Porosity and permeability data were analyzed for the stacked reservoirs in Noble Field, and summary values are tabulated below (Table 5-2). Due to limited data within the model area, core analysis data from Richland and adjacent counties were included in the analysis. The Cypress Sandstone and Aux Vases Formation have reservoirs developed in sandstones, and the core data reflects this with generally higher porosity values. The Cypress Sandstone has somewhat higher porosity than the Aux Vases, but permeability is higher by an order of magnitude because the Cypress is a clean sandstone lacking the higher proportion of clay and carbonate cement common in the Aux Vases. Of the carbonate reservoirs, the Ste. Genevieve Limestone has somewhat higher porosity but much higher permeability, again by an order of magnitude, than the other formations. Average porosity in the St. Louis, Salem, and Ullin Limestones is less than 10%.

Table 5-2. Reservoir properties. Temperature and pressure are estimated based on typical depts and established rules of thumb including geothermal gradient and freshwater gradient. Core analyses data for the Aux Vases, St. Louis, Salem, and Ullin were extremely limited within Noble Field, so data was pulled from adjacent counties (Richland, Jasper, Clay, Wayne) to develop statistics. Samples is the total number of plugs that were analyzed.

	Reservoir				**Core Analysis**	**Porosity (%)**				**Permeability (mD)**				
Formation	Lithology	Dominant Porosity Type	Temp (F)	Pressure (psia)	Samples	Mean	Median	P10	P90	Mean	Median	P10	P90	Depth
Cypress Sandstone	Sandstone	Intergranular	87.5	1,160	355	16.9	17.2	13.2	20.3	452	365	9.8	1,081.0	2,650
Aux Vases Formation	Shaley Sandstone; Dolomite	Intergranular; Intercrystalline	89.5	1,250	5,807	15.2	15	8.9	21.9	32.6	3.3	0	86.0	2,850
Ste. Genevieve Limestone	Oolitic and Skeletal Grainstone	Intergranular	90.5	1,290	244	12.1	13.1	3.9	18.6	432	115	0	1,272.5	2,950
St. Louis Limestone	Microsucrosic Dolomite	Intercrystalline; dissolution	92.0	1,360	142	9.3	8.3	3.1	15.8	0.9	0	0	2.1	3,100
Salem Limestone	Oolitic and Skeletal Grainstone	Intergranular	94.0	1,440	847	7.9	7.7	2.7	13.4	12.4	1	0	22.8	3,300
Ullin Limestone	Skeletal Grainstone	Inter and intragranular	98.0	1,620	80	6.9	7.1	2.2	12.2	35.7	0.8	0	112.5	3,700

Porosity Cutoffs

The porosity and permeability dataset summarized in Table 5-2 was used to develop porosity to permeability transforms and to determine porosity cutoffs for each of the carbonate reservoirs. Porosity and permeability data for each formation were plotted on semilog plots (e.g., Figure 5-14). The Winland R_{35} method (Kolodzie, 1980), which approximates pore throats >0.5 µm based on 35% mercury saturation (R_{35}), was used to differentiate reservoir rock from non-reservoir rock using the following equation:

$$R_{35} = 0.732 + 0.588 * 10^{kH} - 0.864 * 10^{\emptyset} \quad \text{Equation 5-1}$$

Where:

R_{35} = the pore aperture radius corresponding to the 35th percentile of mercury saturation.

kH = horizontal permeability from core analysis reports (in mD).

Ø = porosity from core analysis reports (in %).

Data points with an R_{35} value above 0.5 µm were defined as reservoir, and those less than 0.5 µm were defined as non-reservoir. Two lines, derived from the porosity to permeability transforms developed by Lucia (1995) (Equation 5-2), were projected through the reservoir and non-reservoir data. The rock fabric number for each line was iteratively updated until a good match was achieved. Lucia (1995) only provided equations for integer rock fabric numbers (1,2,3), so the constants a and b were calculated for intermediate rock fabric numbers using Equations 5-3 and 5-4.

$$k = e^{a} * b^{\theta} \quad \text{Equation 5-2}$$

$$a = 22.56 - 12.08 * \ln(fabric\ number) \quad \text{Equation 5-3}$$

$$b = 8.671 - 3.603 * \ln(fabric\ number) \quad \text{Equation 5-4}$$

In the Ste. Genevieve Limestone, for example, the non-reservoir data points, which represent calcite-cemented rock, fell along the rock fabric number 3 line and the reservoir data points, which represent ooid grainstone rock, aligned with a 1.2 rock fabric number (Figure 5-14). The equation describing the line fit to the reservoir data points was used to calculate each simulated porosity value to permeability (Equation 5-5). The porosity at which the data along the 1.2 transform transitioned from non-reservoir to reservoir was used as the porosity cutoff (11.5%). These porosity cutoffs were updated when necessary to create more reasonable reservoir characteristics or to history match reservoir simulations. In most cases, a higher porosity cutoff was used to limit reservoir continuity to achieve the trends observed in Figure 5-13 and for reservoir simulations to properly predict oil production.

$$k = e^{20.35756} * 8.014095^{\theta} \quad \text{Equation 5-5}$$

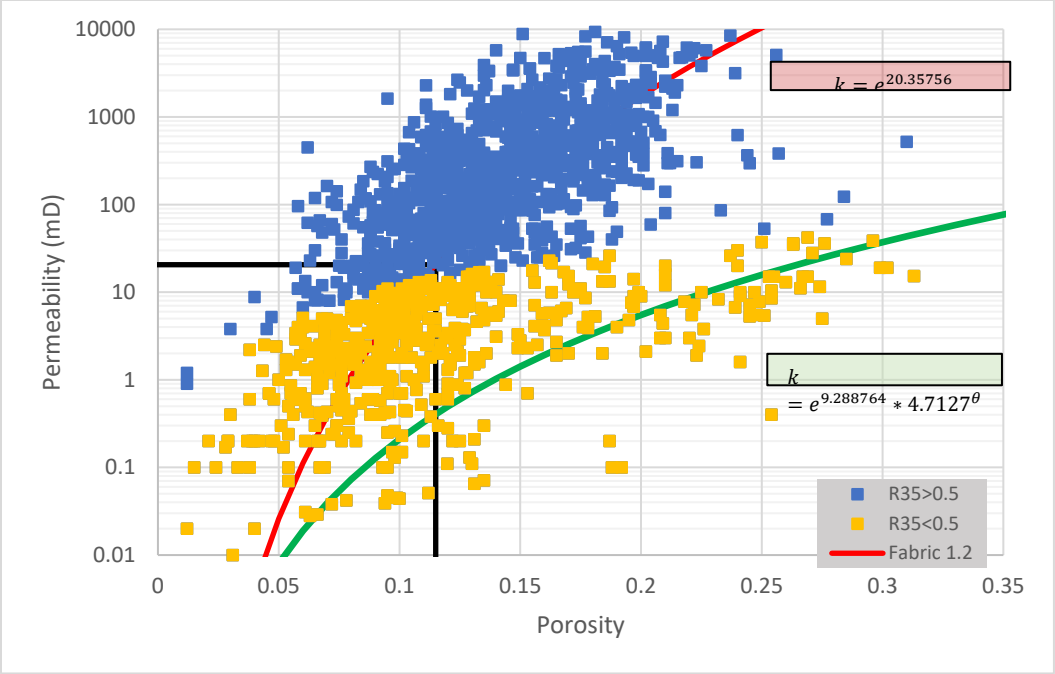


Figure 5-14. Core derived porosity and permeability for the Ste. Genevieve Limestone. Data defined as non-reservoir ($R_{35} < 0.5$) are shown with yellow squares and data defined as reservoir ($R_{35} > 0.5$) are shown with blue squares. The red line fits the reservoir data and corresponds to porosity to a permeability transform based on a rock fabric number of 1.2. The equation defining this line (shown in the red box) was used to calculate permeability for each cell from its simulated porosity value.

Field Development and Production History

To better constrain estimates of the potential EOR resource of the stacked reservoirs, it is important to understand the development and production history of the field. Noble Field was developed rapidly following discovery in 1937 (Figure 5-15). Wells drilled from 1937 through the late 1950s typically reached total depth within the Ste. Genevieve Limestone (approximately 2,900 ft [884 m]). Wells completed in the Ste. Genevieve Limestone were prolific oil producers but were quickly depleted and commonly plugged back and perforated in the Cypress Sandstone, resulting in Cypress production coming on strong by 1939-1940 (Figure 5-16). By the 1950s, the Cypress Sandstone was the most productive reservoir in the field (Bell and Kline, 1956).

In the mid-1940s, Pure Oil Company, the largest operator in the field at that time, was facilitating some pressure maintenance of the Ste. Genevieve Limestone reservoirs using dump floods in which the brine aquifer in the overlying Cypress Sandstone was opened in selected wells, allowing water to flow by gravity into the highly permeable Ste. Genevieve reservoirs with very little control (Squires, 1946; Witherspoon, 1952). In August 1954, Pure began waterflooding the Ste. Genevieve Limestone reservoirs over a 1,200 acre (4.9 km^2) portion of the field, using dedicated injection wells to inject produced water from the Cypress Sandstone (Witherspoon and Jackson, 1955). The waterflooding was not organized into specific well patterns, but the effect of a more systematic reintroduction of pressure to the depleted reservoirs can be observed in the cumulative production graph (Figure 5-16). Around the same time in 1954, a few wells were drilled to test the Salem and St. Louis reservoirs, following successful tests further north along the Clay City Anticline in Jasper County (Bell and Kline, 1956). Wells drilled since the late 1960s generally penetrate the deeper Valmeyeran carbonate reservoirs (approximately 3,000 to 3,700 ft [914 to 1,128 m];

Figure 5-15). Though a few deep wells reached the Ullin Limestone in the 1950s through 1970s, most wells that target that formation have been drilled since the late 1980s.

Estimating annual oil production history of the field is fraught with uncertainty. Early reporting by the Illinois State Geological Survey (ISGS) (e.g. Bell, 1939) provided annual data on field-wide production. However, by 1948, development expanded and interfingered with other fields, and Noble Field was merged into the Clay City Consolidated field at which point tracking published values for fieldwide production became impossible.

Historically, monthly Pipeline Production reports produced by Petroleum Information/Dwights LLC (now IHS Markit, a subsidiary of S&P Global) have provided oil production data reported at the lease level. Illinois did not impose a severance tax on oil production prior to 2013, so well-level data is not available. The lease-level data is available digitally for years since 1980, but for the years in which the field underwent the most intense development (Figure 5-15), the records only exist in bound books. The format of the reports has changed over time with leases being categorized alternatively by operator or by location. Operators and/or lease names change, making them difficult to track without *a priori* knowledge of the changes. In some cases, simple transcription errors in the reports can cause leases to be miscategorized or misplaced in the reports for several months or years at a time. On top of these issues, production is generally comingled from two or more stacked reservoirs, making proportional attribution of production per formation difficult. Only through diligent tracking of well completion and workover records, of which the ISGS data is no doubt incomplete, can a picture of formation-level production be assembled. It is possible to reconstruct production history from these records with the explicit understanding of the many assumptions required to do so and that the resulting history may, at best, be a reasonable approximation of reality. Presumably the most accurate production history for the mature fields in Illinois reside in company files that have been handed down through generations.

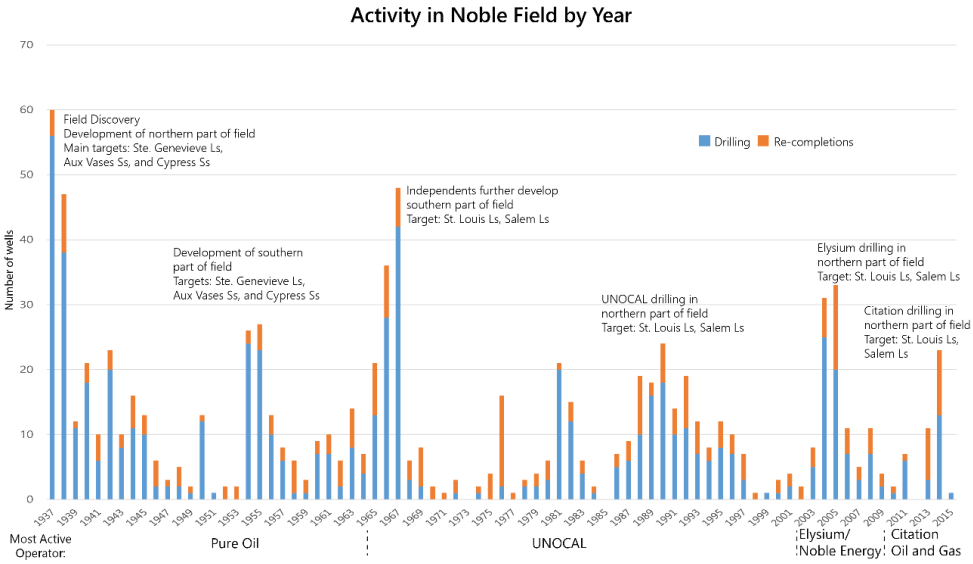


Figure 5-15. Annotated graph of annual drilling activity and well recompletions in Noble Field. Historical drilling activity provides a context for determining the relative historical productivity of all formations in the field. Data were available up to the first quarter of 2015. From Webb and Grigsby (2020).

For Noble Field, the December issue of the Pipeline Production report from each year was used to develop the production history. This was previously done to develop the production history for the Cypress Sandstone in the field (Webb and Grigsby, 2020) but was refined here to parse out Ste. Genevieve

production. From this exercise, cumulative oil production from the study area within Noble Field is approximately 39 MMBO. Of that total, the 20.5 MMBO is attributed here to the Cypress Sandstone, 14.6 MMBO to the Ste. Genevieve Limestone (9.1 MMBO primary production, 5.5 MMBO waterflood), and 3.4 MMBO to all other formations.

The Cypress Sandstone is by far the most prolific producing oil reservoir in the field (Figure 5-16), making up 51% of the total field production. The Ste. Genevieve is the second largest contributor at 36% of the total field production. The Aux Vases Formation, and Salem, St. Louis, and Ullin Limestone reservoirs are commonly commingled together, making it difficult to differentiate their contributions. Thus, the remaining reservoirs in the field were grouped together and account for 13% of the field production.

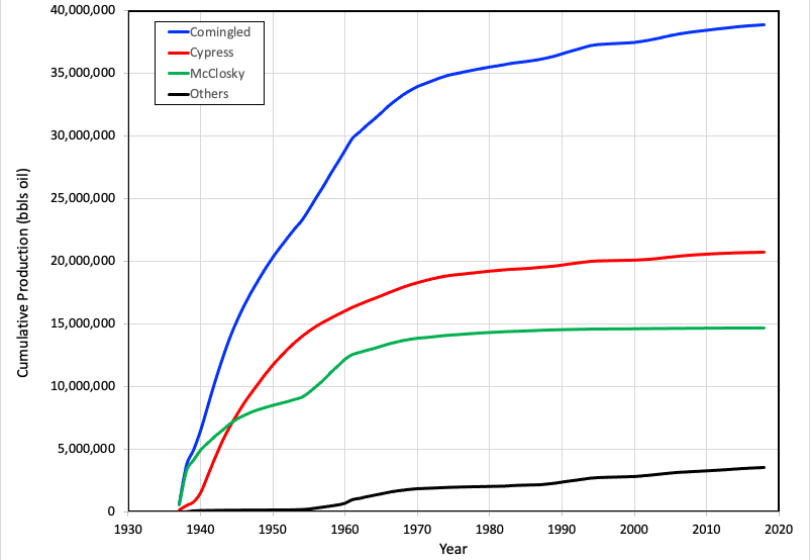


Figure 5-16. Graph of cumulative production showing the total comingled field production, relative contribution of the two most prolific reservoirs (Cypress and Ste. Genevieve), and a grouping of all remaining reservoirs.

Summary of Reservoir Characterization

In summary, the Noble Field is a prototypical Illinois Basin oil field with comingled oil production from several stacked reservoirs. Two reservoirs within the Cypress Sandstone and Ste. Genevieve Limestone have by far been the most performant in terms of oil production since the discovery of the field. The Cypress Sandstone contains a thick MPZ that benefits from nearly ubiquitous high-quality reservoir rock across the field. The Ste. Genevieve Limestone contains reservoirs that are far more compartmentalized but can be relatively thick and have exceptionally high porosity and permeability. The other formations, while together contributing a not insignificant amount of production to the overall field, have inherent heterogeneity and compartmentalization that has made them secondary reservoirs.

When viewing Noble Field through the lens of CO_2-EOR and associated storage opportunities, there are separate cases to be made depending on whether the business case favors oil production or favors CO_2 storage. As with primary and secondary production, the Cypress Sandstone and Ste. Genevieve Limestone appear to be the obvious targets for CO_2-EOR because of the sheer scale of the reservoirs and unsweep (depleted/bypassed MPZ and ROZ) oil saturation in the former and the success of waterflooding in the latter. Previous calibrated reservoir simulations of the Cypress Sandstone alone indicated recovery of more than 11% of OOIP after 20 years of CO_2 injection (Webb et al., 2019). For CO_2 storage, the thick brine aquifers within the Cypress Sandstone and Ullin Limestone are the most attractive targets. While all the

other stacked formations in the storage complex will contribute to EOR and storage, based on their past performance, their contribution will likely be subordinate.

Geocellular Modeling

In characterizing the geology of the oil productive formations in Noble Field, a framework was developed for understanding the reservoir types as described above. The reservoirs observed exhibit complex variations of lithology, continuity, thickness, heterogeneity, and pore-space attributes (e.g., porosity, permeability, anisotropy). For this framework to be useful in determining potential future recovery from CO_2-EOR, the observed reservoir attributes must be translated into a representative digital (geocellular) model.

Grigsby and Webb (2020) discussed in detail the process whereby the geological conceptual framework for the thick Cypress Sandstone was translated into a geocellular model of porosity, permeability, and fluid saturation, using data derived from core and geophysical logs. That model was leveraged in this study, and below we describe the development of models for the other stacked reservoirs in the field.

Geocellular models were constructed for each of the six oil-bearing formations within Noble Field (Table 5-1): The Cypress and Aux Vases Sandstones and the Ste. Genevieve, St. Louis, Salem, and Ullin Limestones. The models of each of the individual formations were merged into a single model of the entire stacked complex. The model boundaries were designed to include the Brownfield ROZ characterization well (Carrie Winter 10) and extend to the west over the structural high of the field (Figure 5-1). The thickness of the stacked model was set to span the top of the shallowest formation (-2,000 ft subsea elevation; top of Cypress Sandstone) to the base of the deepest formation modeled (-4,000 ft subsea elevation; base of Ullin Limestone). The top and base surfaces developed during reservoir characterization were used to delineate the stratigraphic boundaries between each of the formation models. Few wells penetrate the whole thickness Ullin, so it was assigned a constant thickness of 300 ft projected from its upper boundary to approximate its lower boundary. The grid was constructed using a cell spacing of 100 ft/100 ft/3 ft (x/y/z) and the final grid for the stacked model has 127/86/667 (x/y/z) cells (7.3 M total cells).

Porosity was modeled independently for each formation by isolating the log data that fell within the formation and shifting the data to stratigraphic space. Logs were then corrected for lithology and analyzed to identify anisotropy and quantify lateral variability. Variograms were developed to honor the transitional behavior and are provided in the appendix (Table 5-4). Sequential Gaussian Simulations were used to create multiple realizations of the porosity distribution. Formation specific porosity to permeability transforms were developed and used to calculate permeability for each cell from simulated porosity. All the formation models were merged and shifted back to structural space. The resulting stacked reservoir model was vetted by geologists to confirm it properly represented the conceptual geologic frameworks of each formation in the study area.

The Carrie Winter 10 well was used to characterize the oil saturation for each formation because the modern logging suite (including a dielectric log that permits S_W calculations that are insensitive to formation R_W) and core/drill cuttings available for the well were designed to allow for a more detailed evaluation of geologic properties and oil/water saturation. Archies water saturation (S_W; [Archie, 1942]) was calculated for each of the formations in the Carrie Winter 10 well. Oil saturation (S_O) was assumed to occupy the remaining pore space (S_O=1-S_W). Dual water calculations (Waxman and Smits, 1968; Clavier et al., 1984) were also used to mitigate the influence of shale and further constrain S_W for the Cypress and Aux Vases. Oil shows from visual evaluation of drill cuttings were used to validate the presence of oil

where S_O was calculated from logs. There are, however, two important considerations to the use of the Carrie Winter 10 well data. First, reservoir simulations require initial conditions, but the log data likely represent somewhat depleted reservoirs due to production in offset wells. Also, the well is near the eastern edge of the model and off the crest of the structure, so it is possible that the initial S_O values observed in the well are not representative of the rest of the field. Other wells within the Carrie Winter lease and throughout the field were also assessed to determine if the S_O values observed in the Carrie Winter 10 well were consistent over the model boundaries.

Porosity cutoffs for each formation were determined based on analysis of core porosity data using the Winland R_{35} method (Kolodzie, 1980). Once applied to the model, OOIP was calculated for each formation assuming 65% S_{Oi}. Oil-water contacts were introduced into the Cypress Sandstone and Ullin Limestone, which are both known to contain thick brine aquifers below the original oil column. The remaining formations were populated with oil saturation in any cells above the porosity cutoff as well perforation data in the field indicates no internal oil-water contacts.

Ullin Limestone

The Ullin Limestone is a thick (>400 ft [122 m]) pure limestone but is the deepest oil-producing formation at the field, and only the upper tens of feet (Harrodsburg Member) contain oil reservoirs in discontinuous lenticular bodies, so wells that do penetrate the Ullin often avoid the lower brine aquifer (Ramp Creek Member). Only one well has a porosity log through the entire Ullin Limestone within the model boundaries, so it was necessary to construct two models—one for the upper 30 ft (9 m) that was conditioned to data from the 39 wells that have porosity logs in the Harrodsburg member of the Ullin, and another for the Ramp Creek Member that was made by extrapolating values from the single well with porosity logs that cover the whole formation. The average of the NPHI and DPHI curves was used to develop variograms and condition simulations. Variograms for the Harrodsburg Member were developed to match the transitional behavior observed in the logs. No data was available to develop variograms for the Ramp Creek Member, so an omnidirectional variogram with a single range was used to create more laterally extensive features.

For the Ullin Limestone, a line with rock fabric number 3 was projected through the non-reservoir core analysis data points and a line with rock fabric number 1.3 was projected through the reservoir core analysis data (Figure 5-17). The equation describing the reservoir data points was used to calculate each simulated porosity value to permeability (Equation 5-6). Initially, the porosity at which the data along the 1.3 transform transitioned from non-reservoir to reservoir was used as the porosity cutoff (7%), but it was decided to increase the porosity cutoff to 8% to limit the connectivity of the upper oil-bearing interval to better represent perceived compartmentalization (e.g., Figure 5-13). The resulting model has discontinuous porous oil reservoirs in the Harrodsburg Member and thicker, more laterally extensive porous rock in the Ramp Creek Member (Figure 5-18).

$$k = e^{20.35756} * 8.014095^{\theta} \qquad \text{Equation 5-6}$$

Drill cuttings from the Carrie Winter 10 indicate oil saturation in a five-foot-thick, porous interval within 10 ft of the top of the formation (Figure 5-19). Observations throughout the field suggest that the oil is restricted to this upper interval, but the dielectric log predicts oil anomalously throughout the entire Ullin (Figure 5-19). Higher Archie exponents were required (*m* of 2.2 and *a* of 1.1) to increase S_W over the whole Ullin and create a water saturation profile that was more in line with expectations (e.g., brine aquifer within the Ramp Creek Member).

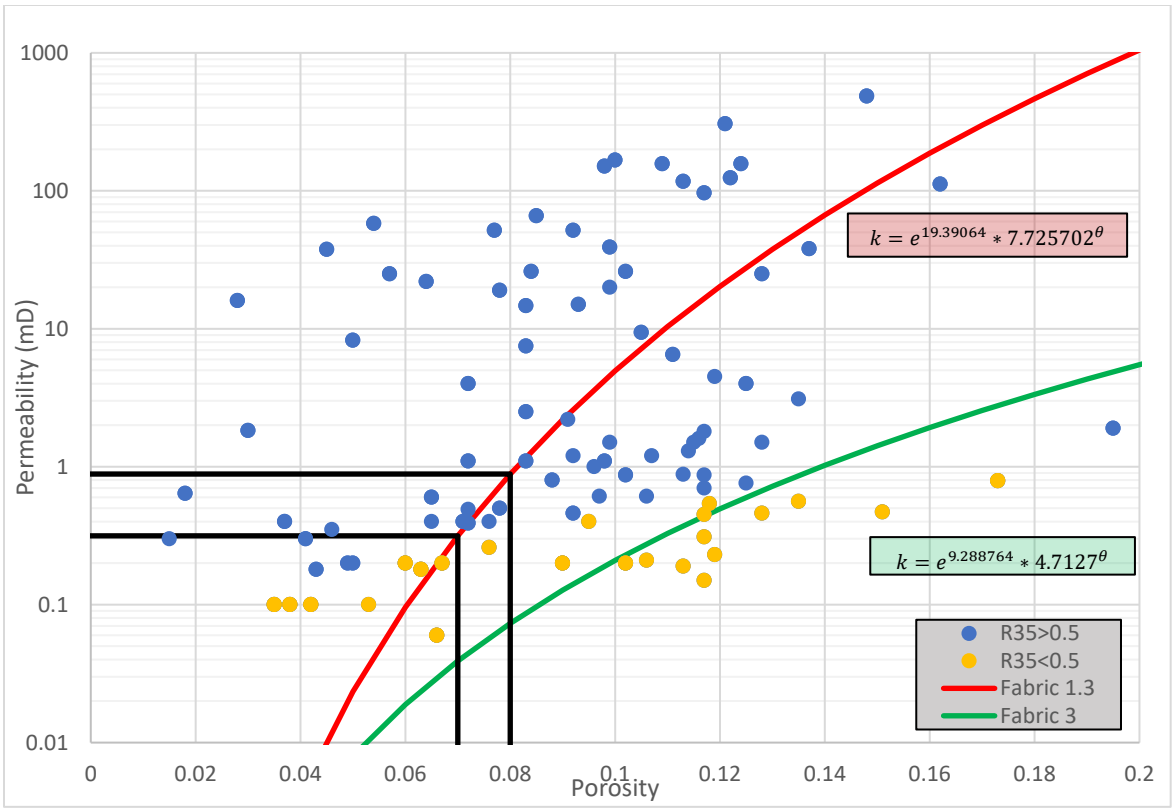


Figure 5-17. Core derived porosity and permeability for the Ullin. Data defined as non-reservoir (R_{35} < 0.5) are shown with yellow squares, and data defined as reservoir (R_{35}>0.5) are shown with blue squares. The red line fits the reservoir data and corresponds to porosity to a permeability transform based on a rock fabric number of 1.3. The equation defining this line (shown in the red box) was used to calculate permeability for each cell from its simulated porosity value.

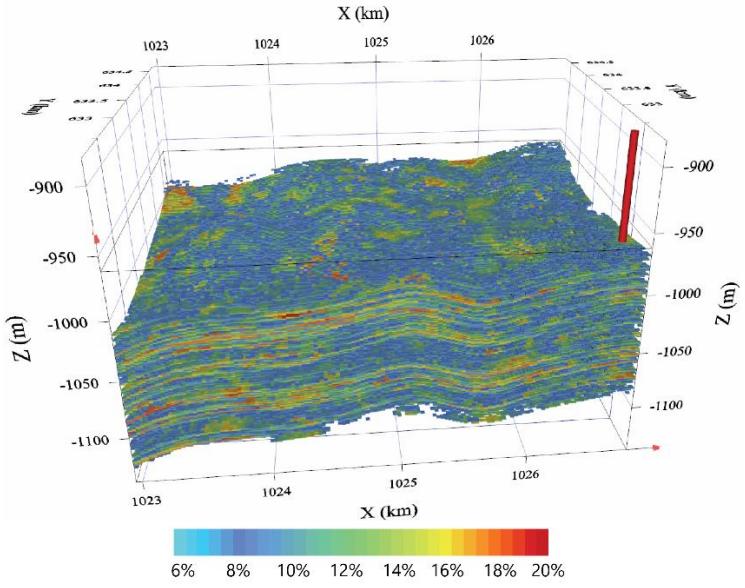


Figure 5-18. Porosity model of the Ullin Limestone after an 8% porosity cutoff is applied. 10x vertical exaggeration. Location of the Carrie Winter 10 well shown with a red cylinder in the southeastern corner. Extent of model area shown in Figure 5-1.

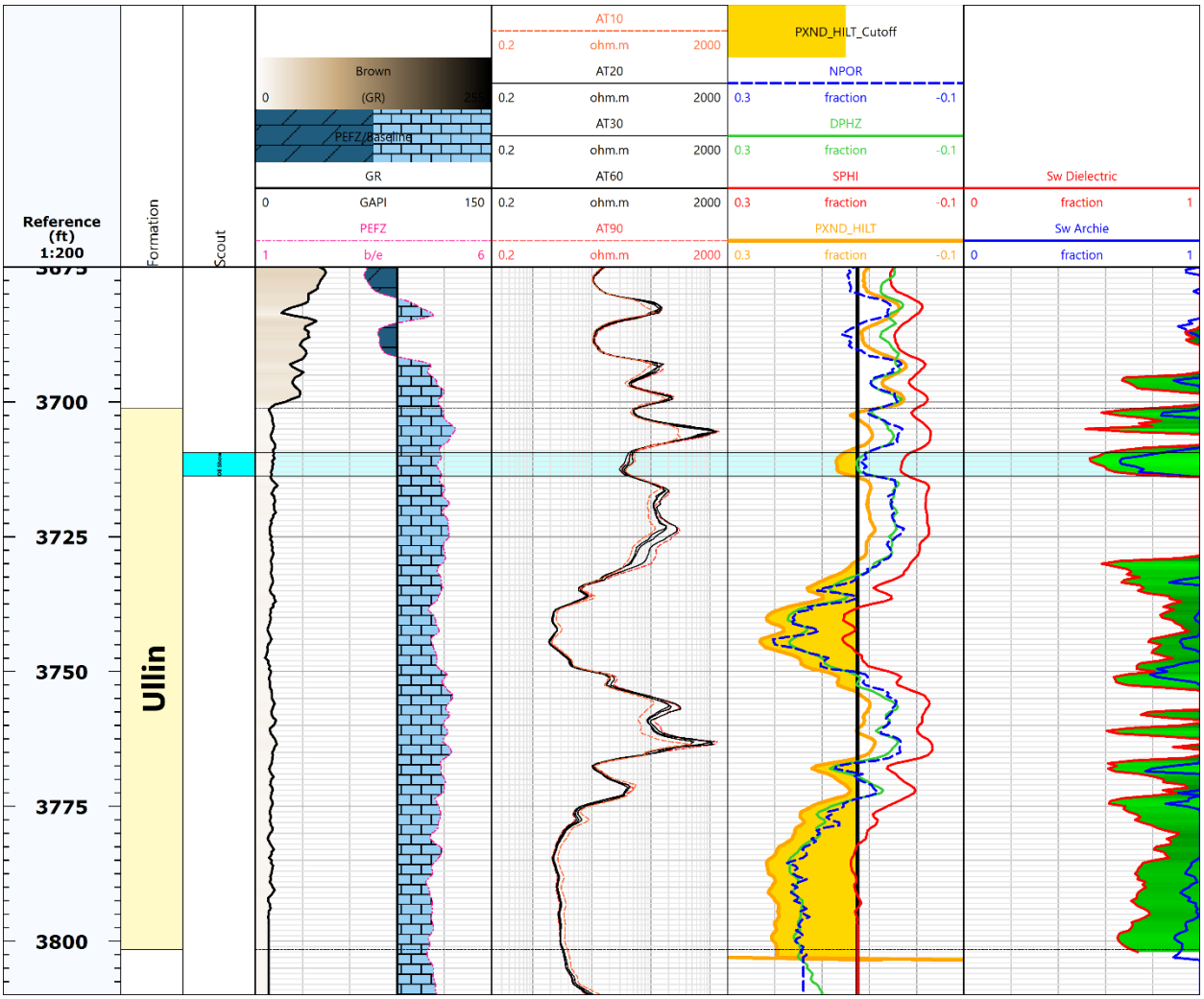


Figure 5-19. Well logs and calculated water saturation through the Ullin Limestone in the Carrie Winter 10 well. Archies S_W shown in blue curve, S_W derived from the dielectric log shown with red curve and green fill, and oil show observed in drill cuttings is shaded blue. Intervals above the 8% porosity cutoff are shaded yellow on the porosity curve, and a Pe cutoff of 4 barns/electron is used to differentiate between dolomite and limestone. Neutron and Density porosity overlie for the whole Ullin and Pe is ~5 barns/electron, demonstrating that it is a pure limestone. Oil in the Ullin is believed to only occur in discontinuous porous units in the uppermost 30 ft, but the calculated S_Ws predict S_O over the whole thickness. The cause of this error is unknown.

Salem Limestone

The Salem Limestone is thick (approximately 400 ft [122 m]), but the reservoirs within it occur as thin intervals of porosity scattered throughout the otherwise low-porosity (<5%) limestone. Reservoir continuity assessment determined that the Salem was the most laterally continuous target carbonate (Figure 5-13), so variograms were constructed with long x/y ranges and no nugget to create thin, laterally extensive reservoir units (Figure 5-20).

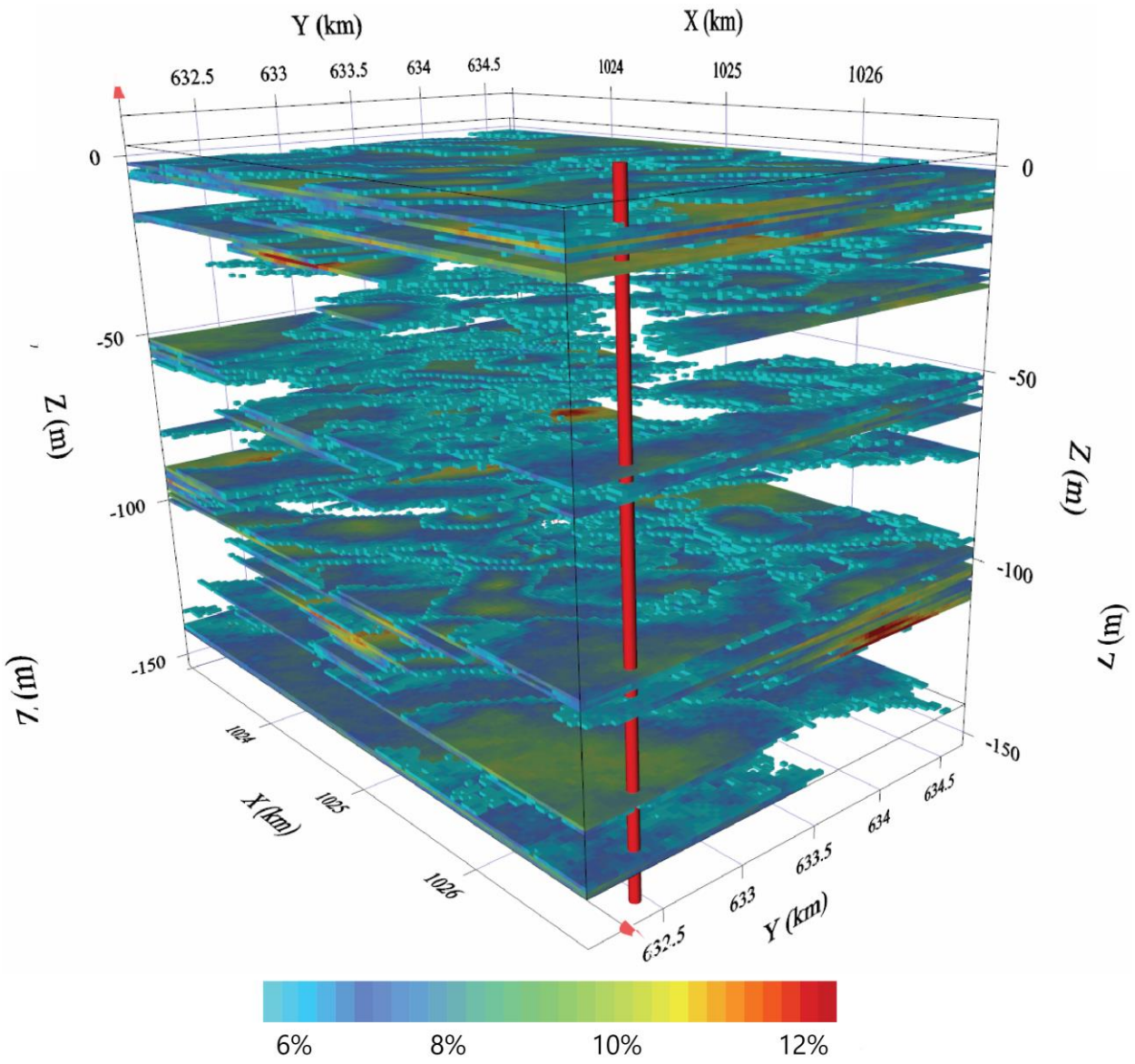


Figure 5-20. Distribution of porosity in the Salem model in stratigraphic space after a 12% porosity cutoff has been applied. 20x vertical exaggeration. The 5% porosity cutoff removes most of the cells and those that remain occur in thin, laterally continuous layers. Extent of model area shown in Figure 5-1. Carrie Winter 10 well is represented by the red cylinder in the southeast corner of the model.

For the core analysis data from the Salem Limestone, a trend of non-reservoir data representing skeletal wackestones and lime mudstones fell along the rock fabric number 3 line, and the data from reservoir facies of oolitic and skeletal grainstones aligned with a 1.2 rock fabric number (Figure 5-21). The equation describing the reservoir data points was used to calculate each simulated porosity value to permeability (Equation 5-5). The preliminary porosity cutoff was selected where the data along the 1.2 transform transitioned from non-reservoir to reservoir (8.3%). It was determined that this cutoff allowed for too much reservoir continuity, so a slightly higher value (9%) was used to reduce the connectivity. The resulting porosity model is shown in Figure 5-22.

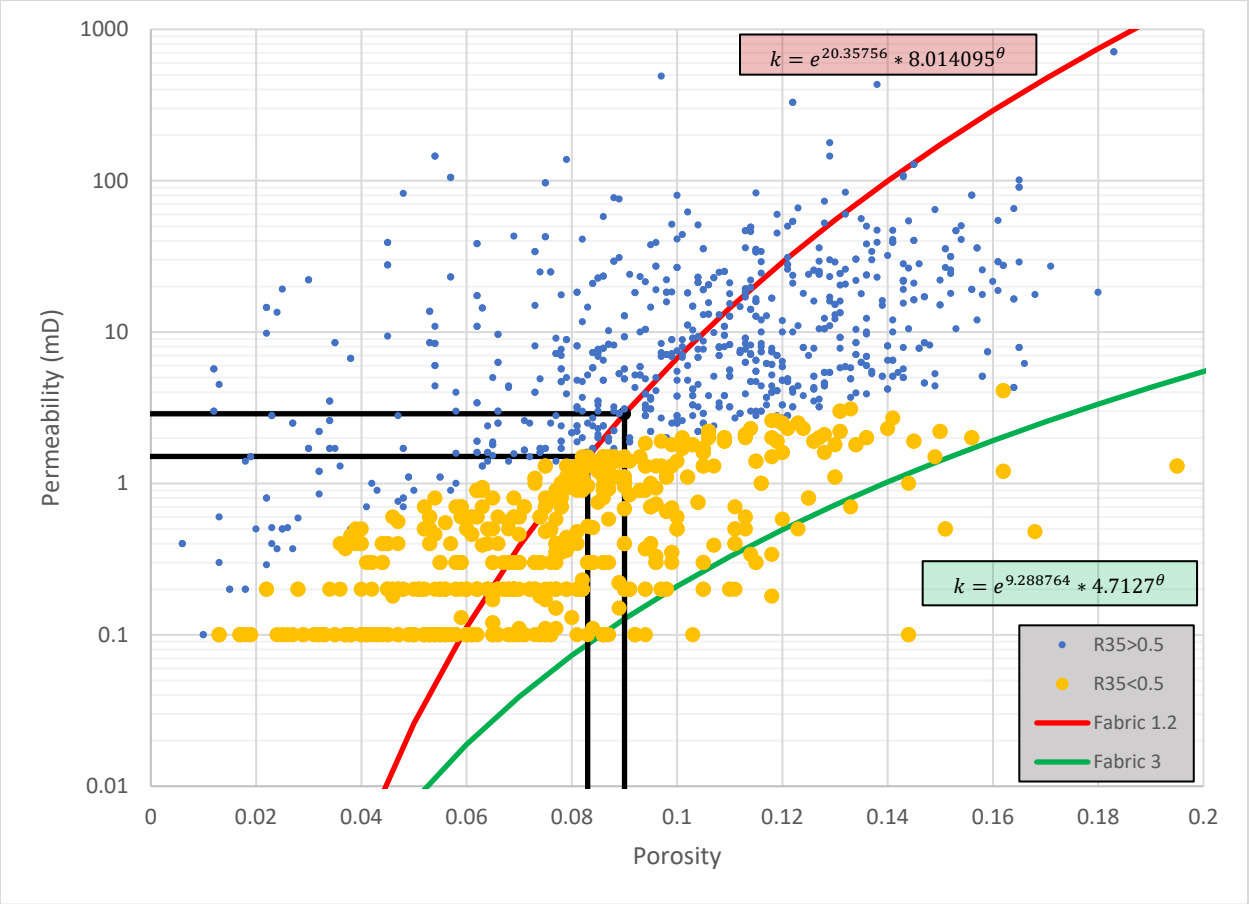


Figure 5-21. Core derived porosity and permeability for the Salem. Data defined as non-reservoir (R35 < 0.5) are shown with yellow squares and data defined as reservoir (R35 > 0.5) are shown with blue squares. The red line fits the reservoir data and corresponds to porosity to a permeability transform based on a rock fabric number of 1.2. The equation defining this line (shown in the red box) was used to calculate permeability for each cell from its simulated porosity value.

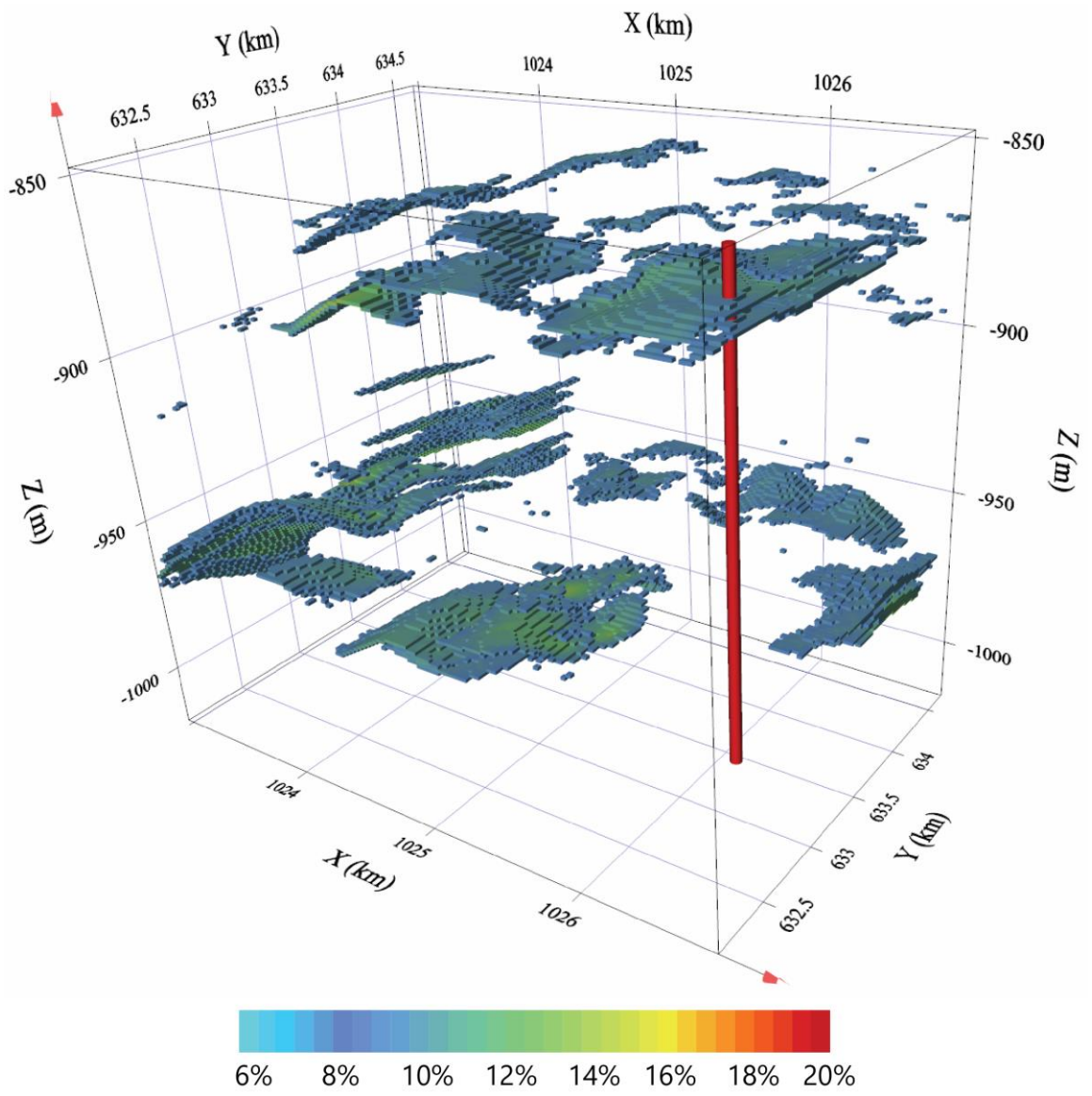


Figure 5-22. Active cells in the Salem Limestone porosity model after the 9% porosity cutoff has been applied. 20x vertical exaggeration. The location of the Carrie Winter 10 well is shown with a red cylinder. The model is in approximately the same orientation as Figure 5-20 but has been shifted to structural space and has a more aggressive porosity cutoff (9% porosity cutoff used here as opposed to the 5% cutoff used in Figure 5-20). Extent of model area shown in Figure 5-1. Carrie Winter 10 well is represented by the red cylinder in the southeast corner of the model.

The Salem Limestone is approximately 400 ft (122 m) thick in the Carrie Winter 10 well. The Salem is a pure limestone with two shale breaks, so DPHI on a limestone matrix was used to calculate S_W. S_O was calculated wherever there is porosity, but the lowest third (from 3,520-3,660 ft) has the highest concentration of oil saturation. This distribution of oil saturation (oil throughout, but most porosity and oil in the lower third of the formation) is consistent with oil shows across the field. Initial oil saturation is difficult to quantify, but the interval between the two shale breaks (3,464-3,470 ft) had the highest S_O (calculated values of approximately 70%). This interval may represent native S_O and the lower S_Os observed in the historically productive lower Salem may represent a depleted reservoir.

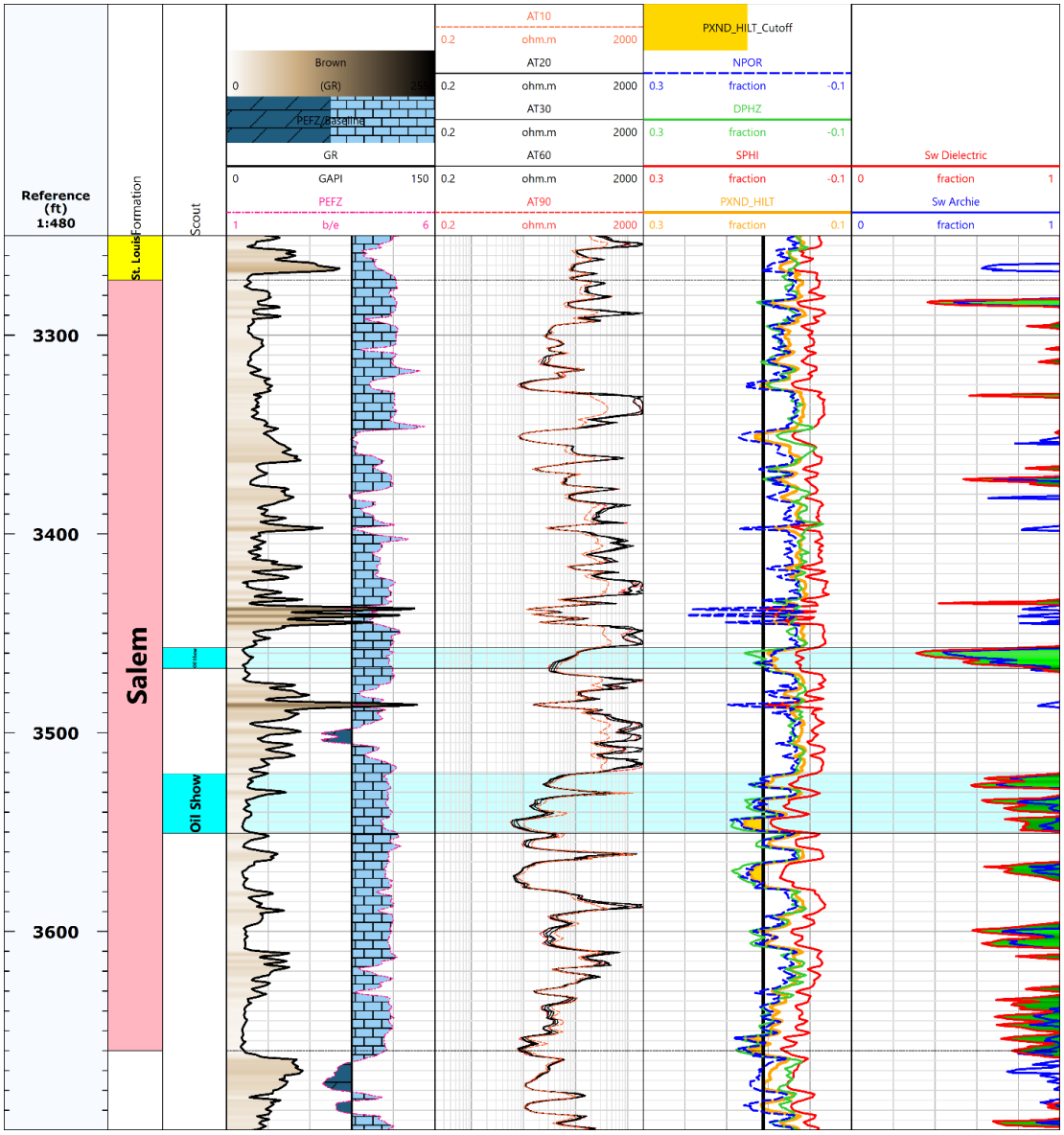


Figure 5-23. Well logs and calculated water saturation through the Salem Limestone in the Carrie Winter 10 well. Archies S_W shown in blue curve, S_W derived from the dielectric log shown with red curve and green fill, and oil shows observed in drill cuttings are shaded blue. Intervals above the 9% porosity cutoff are shaded yellow on the porosity curve, and a Pe cutoff of 4 barns/electron is used to differentiate between dolomite and limestone. Neutron and density porosity overlie and Pe~ 5 barns/electron for the whole Salem, demonstrating that it is a pure limestone. Calculated S_Ws predict oil within porous units scattered throughout the Salem, with the highest proportion in the lower third. This distribution of oil matches what is observed throughout the rest of Noble Field. Most of the S_Os are around 40%, but an interval between two shale breaks (3,458-3,467 ft) does get to 70%. This interval is supported by an oil show in the cuttings.

The scout ticket for the Carrie Winter 3 well (API 121592617100), 619 ft (189 m) west of the Carrie Winter 10 and drilled in 2006, records five oil shows in the Salem Limestone. These oil shows correspond to occurrences of oil calculated by Archie's S_W (Figure 5-24). The uppermost oil show in the lower Salem was perforated (from depths of 3,515 to 3,525 ft) and yielded an IP of 15 bbls oil and 5 bbls water per day. Both the perforated interval and the interval between the shale breaks (that has the highest S_O in the Carrie Winter 10 well) have approximately 60% S_O in the Carrie Winter 3 well.

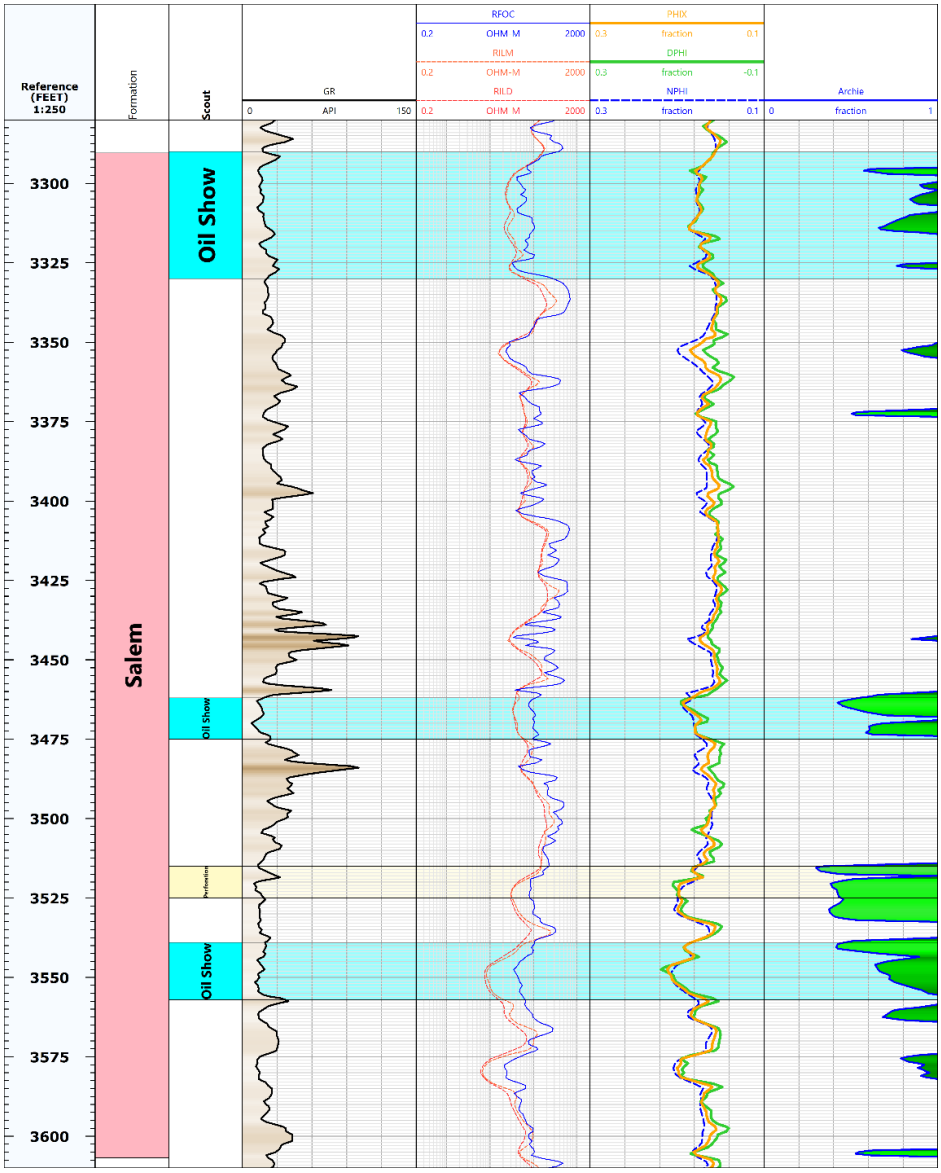


Figure 5-24. Well logs and calculated water saturation through the Salem Limestone in the Carrie Winter 3 well. Archies S_W shown in blue curve and green fill, oil shows observed in drill cuttings are shown with blue fill, and perforated interval is shown with a yellow fill. Neutron and Density porosity overlie for the whole Salem, demonstrating that it is a pure limestone. Calculated S_Ws predict oil within porous units scattered throughout the Salem, with the highest proportion in the lower third. This distribution of oil matches what is observed in the drill cuttings and throughout the rest of Noble Field. The perforated interval (3515-3525) produced an IP of 15 bbls oil/5bbls water, confirming that it contains mobile oil.

St. Louis Limestone

The reservoirs within the St. Louis Limestone occur as two to three layers of porous dolomite embedded within the upper third of the otherwise non-porous limestone. The change in lithology masks the reservoir on the DPHI log (the higher density of the dolomite matrix offsets the reduction in bulk density created by the increase in pore space), so NPHI was used to condition simulations. The variogram required three sills to properly represent the near and far transitional behavior of the St. Louis reservoirs. The resulting model contains three discontinuous bands of porosity embedded within a low porosity background (Figure 5-25).

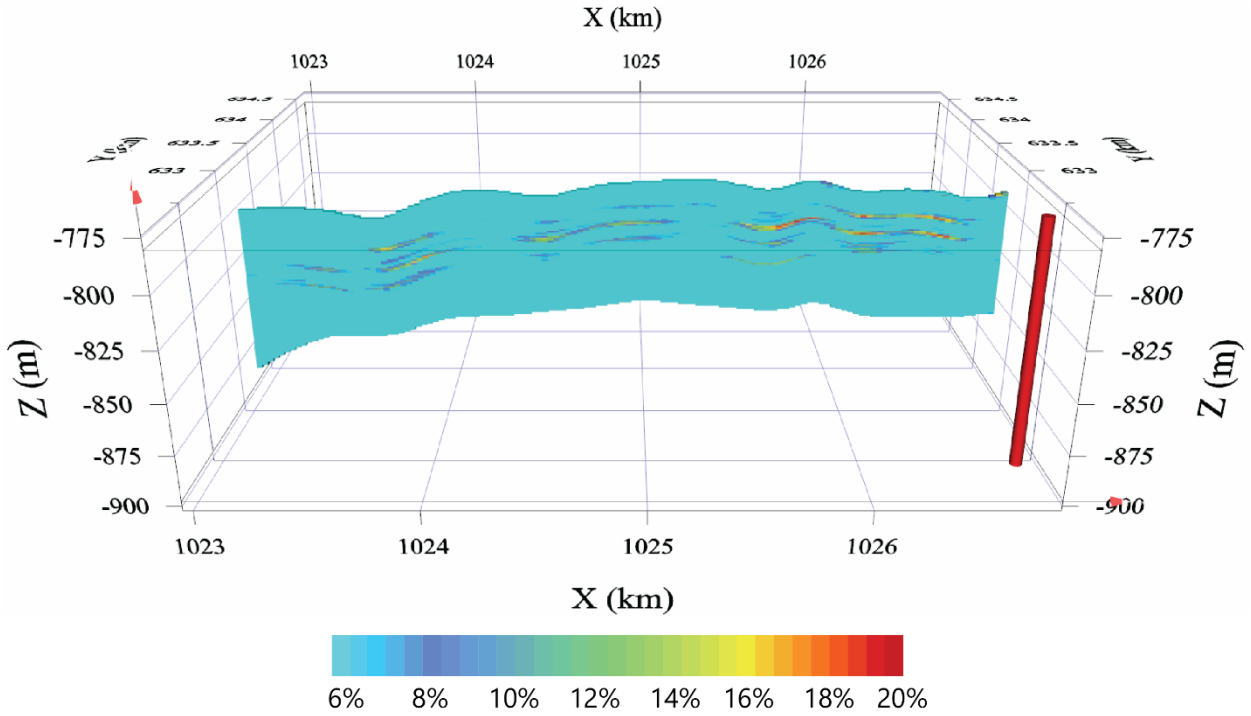


Figure 5-25 West-East slice through the St. Louis porosity model. The model is in structural space with 10x vertical exaggeration, and the slice is taken from the approximate middle of the model (row 40 or 4,000 feet from the southern boundary). The model has low porosity (<6%), except for three bands of porosity that occur in the upper half. Carrie Winter 10 well is represented by the red cylinder in the southeast corner of the model.

The reservoir core analysis data points representing the porous microsucrosic dolomite in the St. Louis Limestone aligned with a rock fabric number of 1.4 (Figure 5-26), so the permeability for the St. Louis was calculated using Equation 5-7. The core data transitioned from reservoir to non-reservoir at 11%, so this was selected as the porosity cutoff. The resulting porosity model is shown in Figure 5-27.

$$k = e^{18.4954} * 7.45869^{\theta} \qquad \text{Equation 5-7}$$

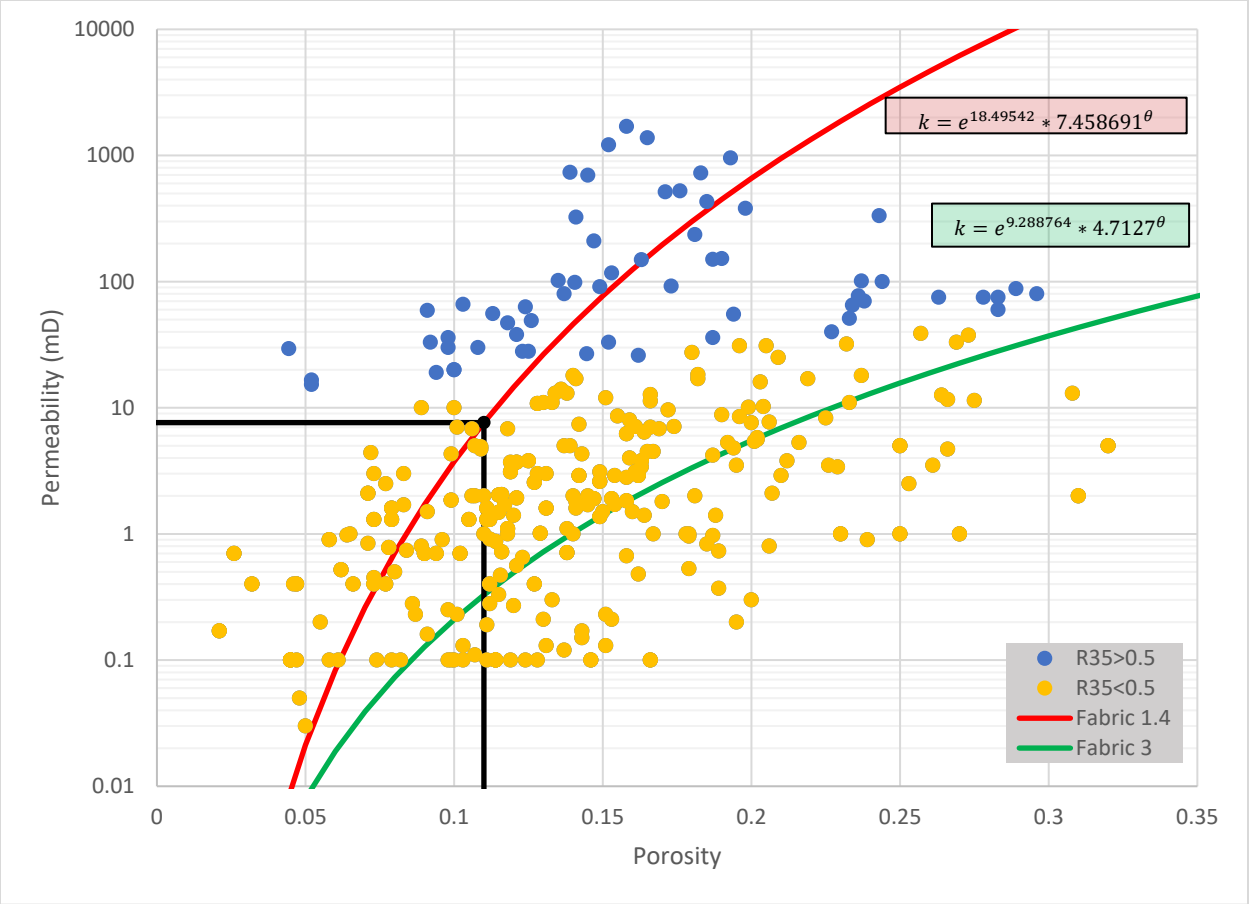


Figure 5-26. Core derived porosity and permeability for the St. Louis. Data defined as non-reservoir (R35 < 0.5) are shown with yellow squares and data defined as reservoir (R35>0.5) are shown with blue squares. The red line fits the reservoir data and corresponds to porosity to a permeability transform based on a rock fabric number of 1.4. The equation defining this line (shown in the red box) was used to calculate permeability for each cell from its simulated porosity value.

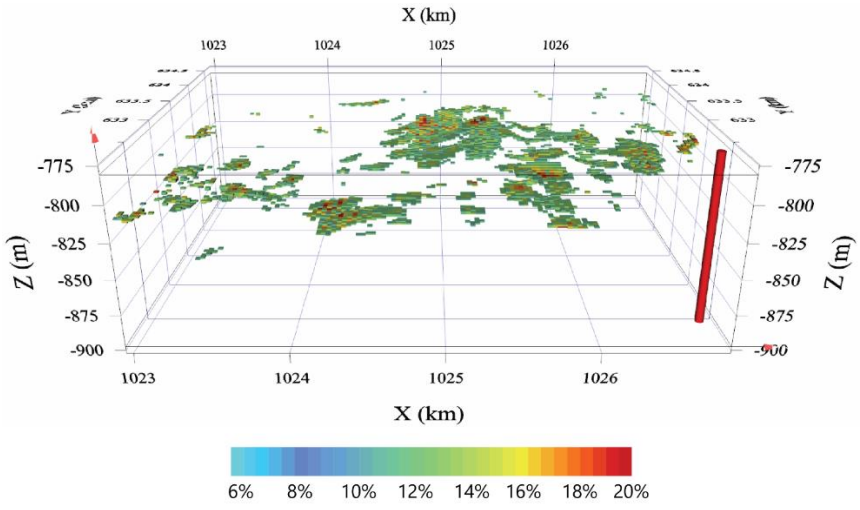


Figure 5-27. Active cells in the St. Louis porosity model after the 9% porosity cutoff has been applied. The location of the Carrie Winter 10 well is shown with a red cylinder. The model is in approximately the same orientation as Figure 5-20 but has been shifted to structural space and has a more aggressive porosity cutoff. Extent of model area shown in Figure 5-1. Carrie Winter 10 well is represented by the red cylinder in the southeast corner of the model.

Water saturation was calculated for the St. Louis by converting porosity to a dolomite matrix. Converting the entire St. Louis to a dolomite matrix creates erroneously high porosity in the nonporous limestone that separates the dolomite reservoirs, but the 8% porosity cutoff filters out these intervals. There was no data to estimate R_W, so a value of 0.05 ohm-m was used.

The resulting Archie S_W only calculates S_O in the dolomite intervals (Figure 5-28). This distribution of oil and water is validated by oil shows in the Carrie Winter 10 well and in other wells across the field. Agreement between dielectric and Archie S_Ws suggests that the R_W used for Archie's calculation (0.05 ohm-m) is reasonable. Dielectric S_W does detect two additional occurrences of oil, one in an upper dolomite (from 3,147-3,150 ft) and another below the upper dolomite (from 3,166.5-3,168 ft). Archie S_W also identifies S_O in these intervals if a 6% porosity cutoff is used.

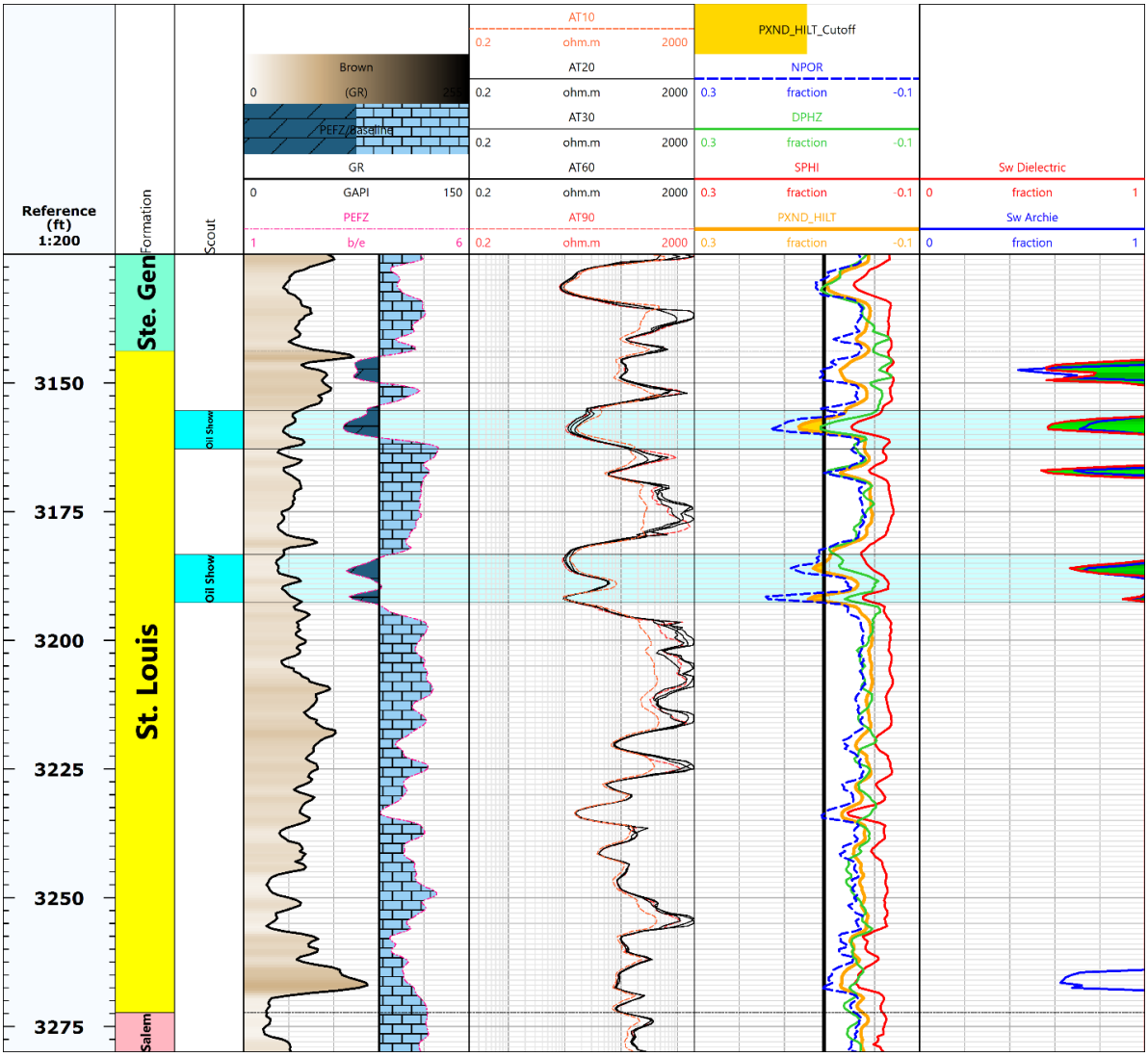


Figure 5-28 Well logs and calculated water saturation through the St. Louis Limestone in the Carrie Winter 10 well. Archies S_W shown in blue curve, S_W derived from the dielectric log shown with red curve and green fill, and oil shows observed in drill cuttings are shown with blue fill. Intervals above the 6% porosity cutoff are shaded yellow on the porosity curve, and a Pe cutoff of 4 barns/electron is used to differentiate between dolomite and limestone. Calculated S_W predicts oil within two porous dolomitic units (where Pe/10 4 and NPOR>DPHZ). Both intervals had oil shows observed in drill cuttings.

The upper dolomitic reservoir in the St. Louis Limestone was perforated in the Carrie Winter 7 well (API 121592631000), 936 ft (285 m) southwest of the Carrie Winter 10 and drilled in 2011, from 3,163-3,169 ft and yielded an IP of 12 bbls oil and 50 bbls water per day. Archie's S_W, based on the same input parameters used for Carrie Winter 10, calculates approximately 50% S_O in both dolomitic intervals, though the upper interval has a thicker, more consistent interval of oil saturation (Figure 5-29). The high water cut suggests that this S_O represents mobile oil in a partially depleted reservoir, and production from this Carrie Winter 7 could explain the reduced S_O in Carrie Winter 10.

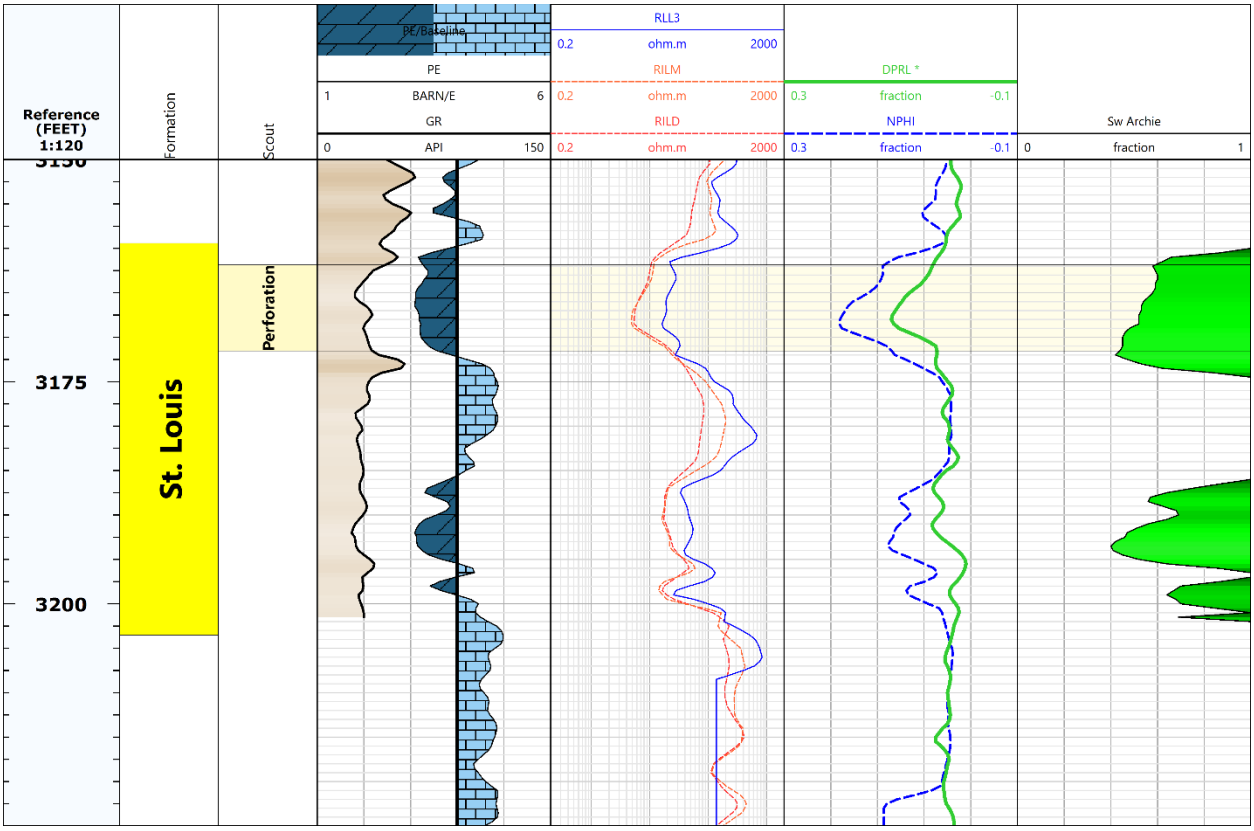


Figure 5-29. Well logs and calculated water saturation through the St. Louis Limestone in the Carrie Winter 7 well. Archies S_W shown in blue curve and green fill and perforated interval shown with yellow fill. Calculated S_W predicts oil within two porous dolomitic units (where Pe <0.4 and NPHI>DPRL). The upper S_O interval is supported by perforations, which had an IP of 12 bbls oil and 50 bbls water.

Ste. Genevieve Limestone

The complex lithology and shale within the Ste. Genevieve Limestone make NPHI erroneously high, so DPHI was used to develop variograms and condition simulations. The Ste. Genevieve is the second most productive formation in Noble Field, but it is also interpreted to be more laterally discontinuous than the Cypress, Salem, and St. Louis (Figure 5-13). This conceptual model suggests that the Ste. Genevieve reservoirs are highly porous and permeable but also highly compartmentalized. The variograms were thus designed to create a model with porous, compartmentalized reservoirs (Figure 5-30).

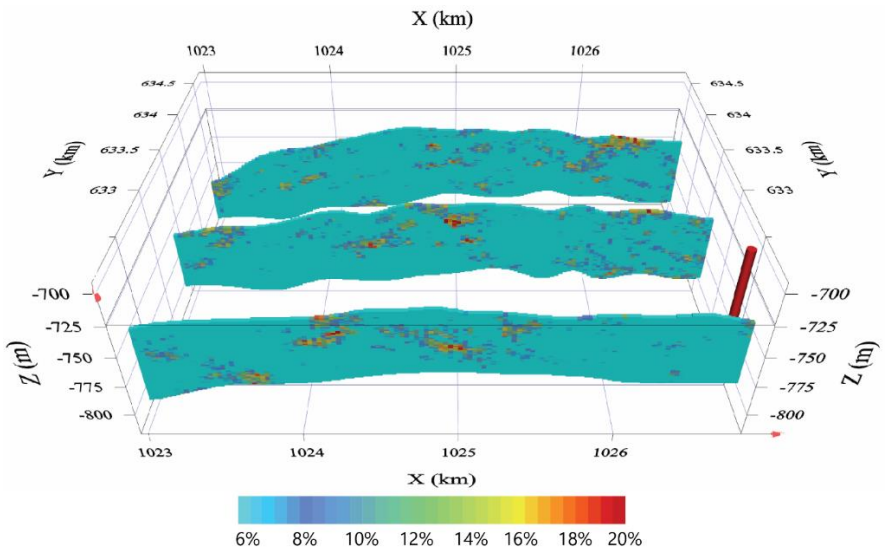


Figure 5-30. Slices through the Ste. Genevieve model before the porosity cutoff is applied. The reservoir units are represented as clusters of cells with high porosity (warm colors) embedded within a nonporous (light blue) background. 10x vertical exaggeration. Extent of model area shown in Figure 5-1. Carrie Winter 10 well is represented by the red cylinder in the southeast corner of the model.

For the available core analysis data from the Ste. Genevieve Limestone, a trend of non-reservoir data fell along the rock fabric number 3 line, and the data from reservoir facies aligned with a 1.2 rock fabric number (Figure 5-14). The equation describing the reservoir data points was used to calculate each simulated porosity value to permeability (Equation 5-5). The porosity at which the data along the 1.2 transform transitioned from non-reservoir to reservoir was used as the porosity cutoff (11.5%). The resulting porosity model is shown in Figure 5-31.

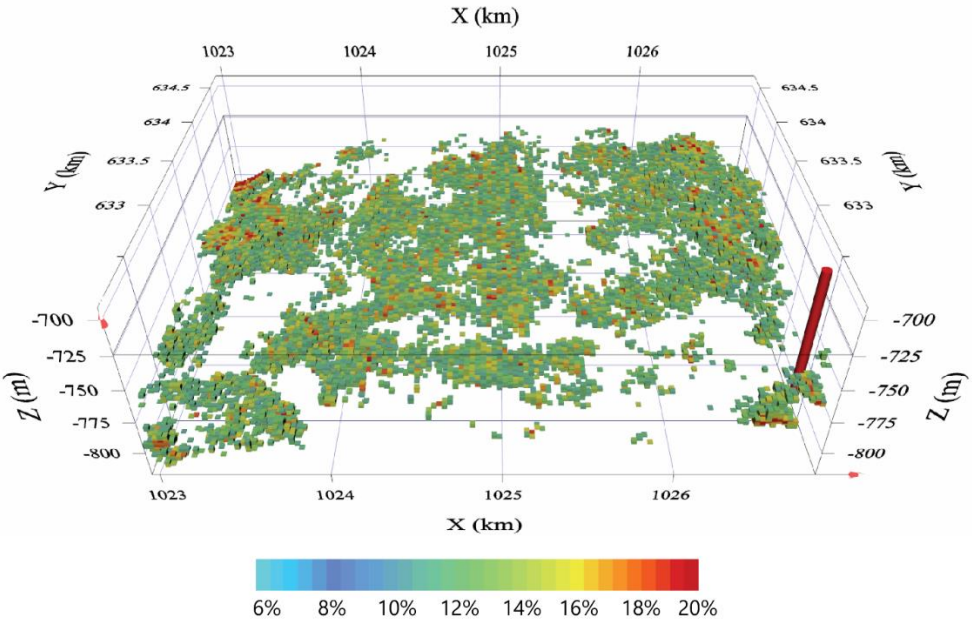


Figure 5-31. Active cells in the Ste. Genevieve porosity model after the 11.5% porosity cutoff has been applied. Extent of model area shown in Figure 5-1. Carrie Winter 10 well is represented by the red cylinder in the southeast corner of the model.

There are two oil shows in the Fredonia Limestone Member (McClosky) of the Ste. Genevieve in the Carrie Winter 10 well, one in a thin (~5 ft [1.5 m]), low-porosity (~5%) upper interval, and the other in a thicker (~20 ft [6.1 m]), more porous interval. The basal 5 ft (1.5 m) of the interval has shale, which causes Archie's equation to calculate oil. Both the upper oil show and lower shale-rich interval are masked when the 11.5% porosity cutoff is imposed (Figure 5-32). The resulting oil-bearing portion of the McClosky has 3 ft (0.9 m) of moderate oil saturation (50% S_O) above 10 ft (3.1 m) of depleted reservoir (20% S_O). This zone was tested but did not produce oil.

The scout ticket for the Carrie Winter 4 well (API 121592624600), 224 ft (68 m) west of the Carrie Winter 10 and drilled in 2008, does not record any oil shows, but the McClosky was perforated and had an IP of 11 bbls oil and 0 bbls water. Archie's S_W has a similar character in Carrie Winter 4 as in Carrie Winter 10, with 10 ft (3.1 m) of high oil saturation perched above a shale break at the base of the formation. The reservoir in the Carrie Winter 4 is structurally 5 ft (1.5 m) higher than in the Carrie Winter 10, which would explain why the interval of moderate oil saturation is thinner in the latter well. The S_O is also much higher in the Carrie Winter 4 well (approaching 70%), which could suggest that the McClosky production from the Carrie Winter 4 partially depleted (reduced the saturation of) the mobile oil column in Carrie Winter 10.

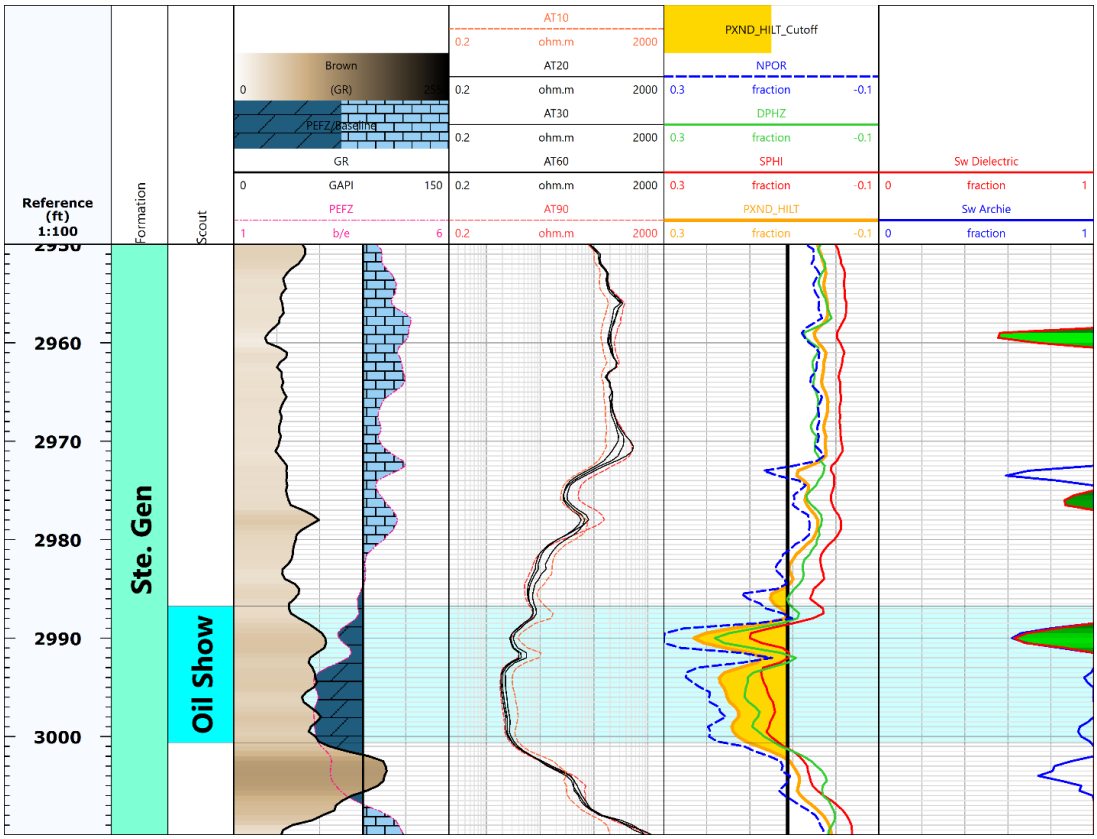


Figure 5-32. Well logs and calculated water saturation through the Ste. Genevieve Limestone in the Carrie Winter 10 well. Archies S_W shown in blue curve, S_W derived from the dielectric log shown with red curve and green fill, and oil shows observed in drill cuttings are shown with blue fill. Intervals above the 6% porosity cutoff are shaded yellow on the porosity curve, and a Pe cutoff of 4 barns/electron is used to differentiate between dolomite and limestone. Calculated S_Ws predict oil within porous units at the base of the Ste. Genevieve, which is supported by an oil show in the cuttings. Both dielectric S_W and drill cuttings suggest there is oil in an upper unit, but it is thin and has low (4%) porosity.

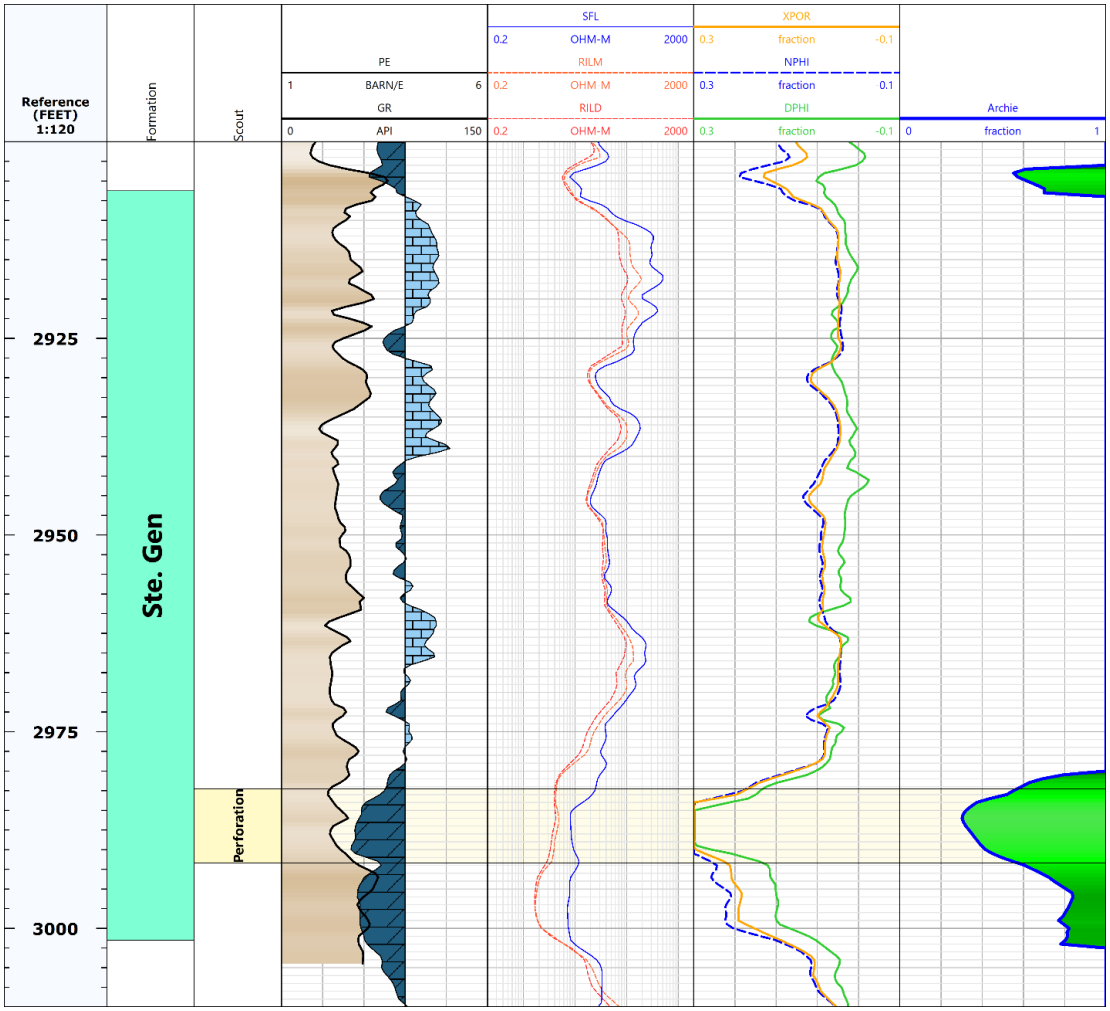


Figure 5-33. Well logs and calculated water saturation through the Ste. Genevieve Limestone in the Carrie Winter 4 well. Archies S_W shown in blue curve and green fill, and perforated interval is shown with yellow fill. A Pe cutoff of 4 barns/electron is used to differentiate between dolomite and limestone. Neutron is higher than Density porosity for the whole Ste. Genevieve, which suggests that it is not a pure limestone. Calculated S_{WS} predict oil within porous units at the base of the Ste. Genevieve. This interval was perforated and had an IP of 11 bbls oil and 0 bbls water, which demonstrates that it contains mobile oil.

Aux Vases Formation

Shale above and below the main sandstone reservoir in the upper Aux Vases Formation creates an erroneously high NPHI response (>30%), so a GR cutoff of 50 API was used to separate "sandstone" from "shale" facies. Data within the sandstone facies were assigned the cross-plotted porosity value, and data within the shale facies were assigned 5% porosity. The synthetic log was used to construct omnidirectional variograms and condition sequential gaussian simulations to create realizations of the porosity distribution.

Porosity and permeability from core analysis reports for the Aux Vases Formation from Richland and adjacent counties were plotted against each other (Figure 5-34). The equation defining the power line regressed through them was used to calculate permeability for each cell based on the simulated porosity value. An 11% porosity cutoff was then applied to remove cells with permeability below 1 mD. The resulting model is shown in Figure 5-35.

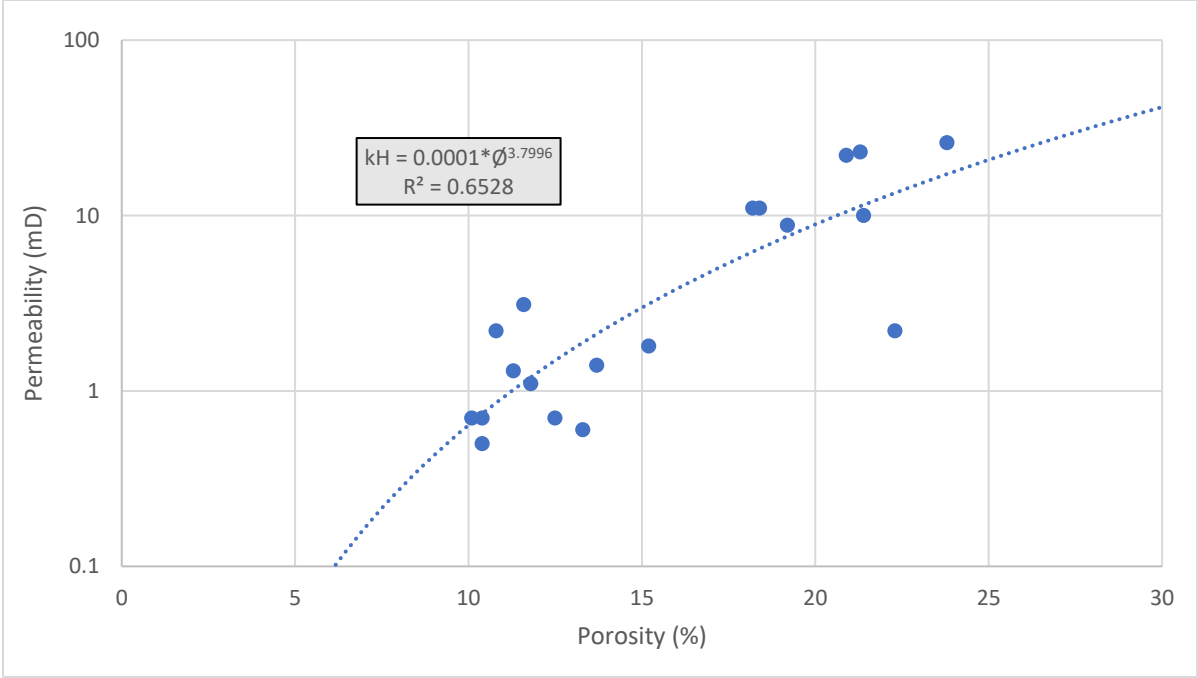


Figure 5-34. Cross plot of porosity and permeability for the Aux Vases from core analysis reports. The equation defining the power line regressed through the data was used to calculate permeability assigned to each cell from simulated porosity.

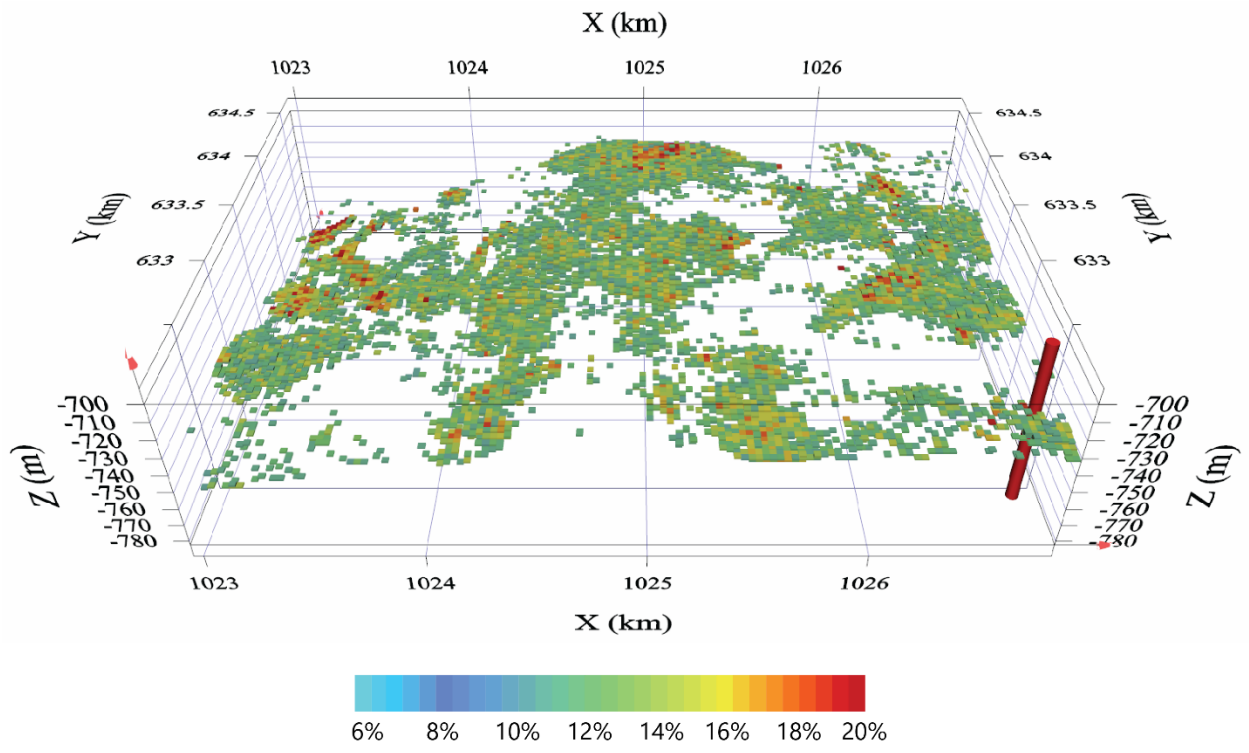


Figure 5-35. Porosity distribution of the Aux Vases after 11% porosity cutoff is applied. 20x vertical exaggeration. Extent of model area shown in Figure 5-1. Carrie Winter 10 well is represented by the red cylinder in the southeast corner of the model.

The Aux Vases Sandstone reservoir is sandwiched between a non-porous limestone and a shale unit. Elevated Pe (approximately 2.5) and pronounced NPHI/DPHI log separation, coupled with low raw gamma ray (around 20 API) and potassium measured by the spectral gamma ray log (<0.5%) suggest the presence of a chlorite-rich clay mineral suite within the sandstone. This mineralogy is consistent with what has been observed in the Aux Vases Formation elsewhere in the basin (Smoot, 1960; Seyler, 1988; Udegbunam et al., 1993) and is important to consider when calculating S_W (Asquith, 1990; Leetaru, 1990).

Archie S_W based on the PHIX log predicts 50% S_O in the Aux Vases, but dual water calculations reduce this S_O to 30% and correctly predict 0% S_O in the underlying shale (Figure 5-36). This may represent a depleted reservoir in the Carrie Winter 10 well.

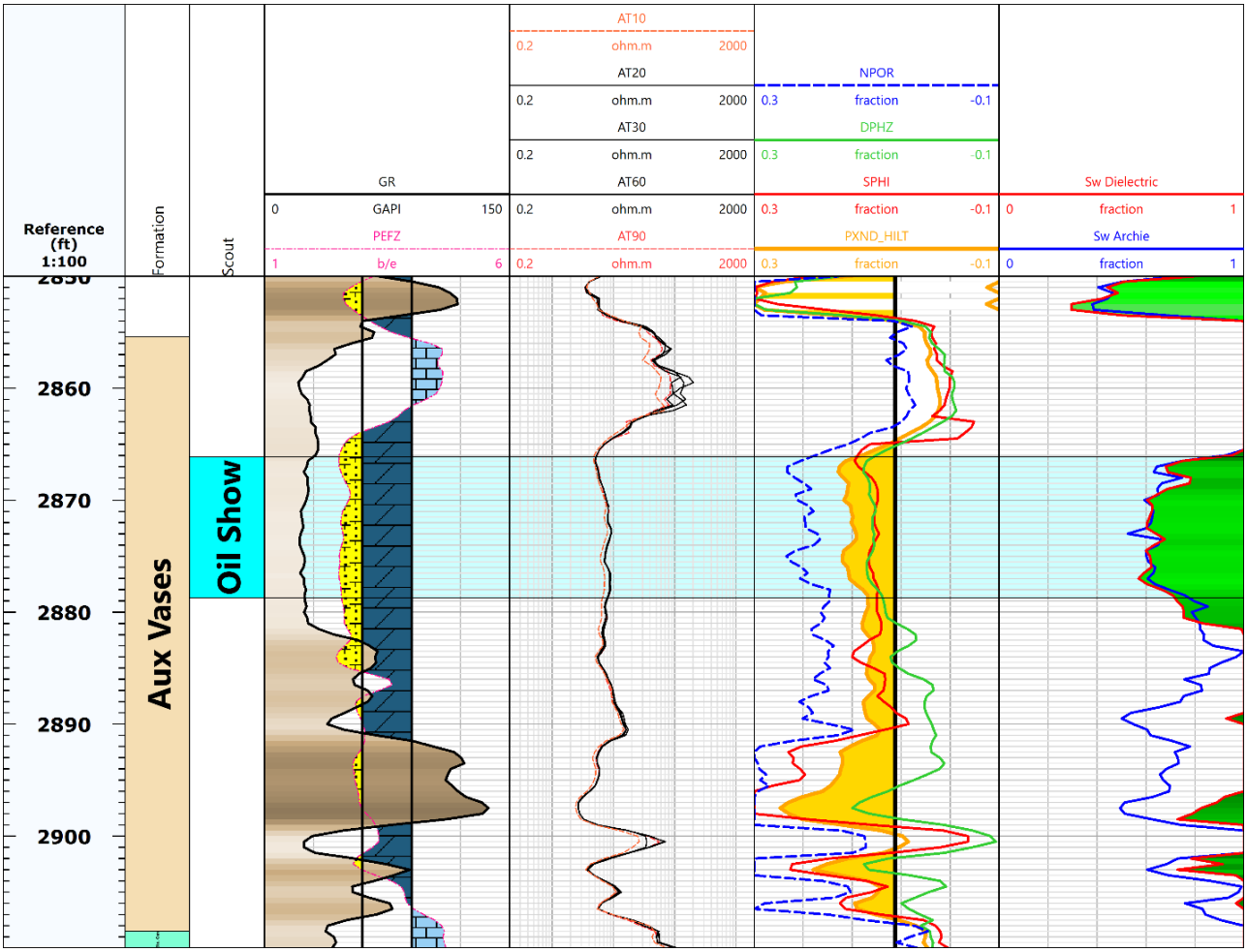


Figure 5-36. Well logs and calculated water saturation through the Aux Vases in the Carrie Winter 10 well. Archies S_W shown in blue curve, S_W derived from the dielectric log shown with red curve and green fill, and oil shows observed in drill cuttings are shown with blue fill. A Pe cutoff of 3 barns/electron is used to differentiate quarts from carbonate, and a Pe cutoff of 4 barns/electron is used to differentiate between dolomite and limestone. Archies S_W predicts oil throughout the entire Aux Vases, but dielectric S_Ws correctly compensate for the influence of clay and only predicts S_O where it was observed in the cuttings (between 2867-2878).

A drill stem test (DST) was completed in the Aux Vases Formation (2,860-2,885 ft) in the Carrie Winter 7, but poor results indicated that the Aux Vases did not warrant a completion in this well. Archie's and dual water S_W were similar in the Carrie Winter 7 (Figure 5-37) as those in the Carrie Winter 10 well.

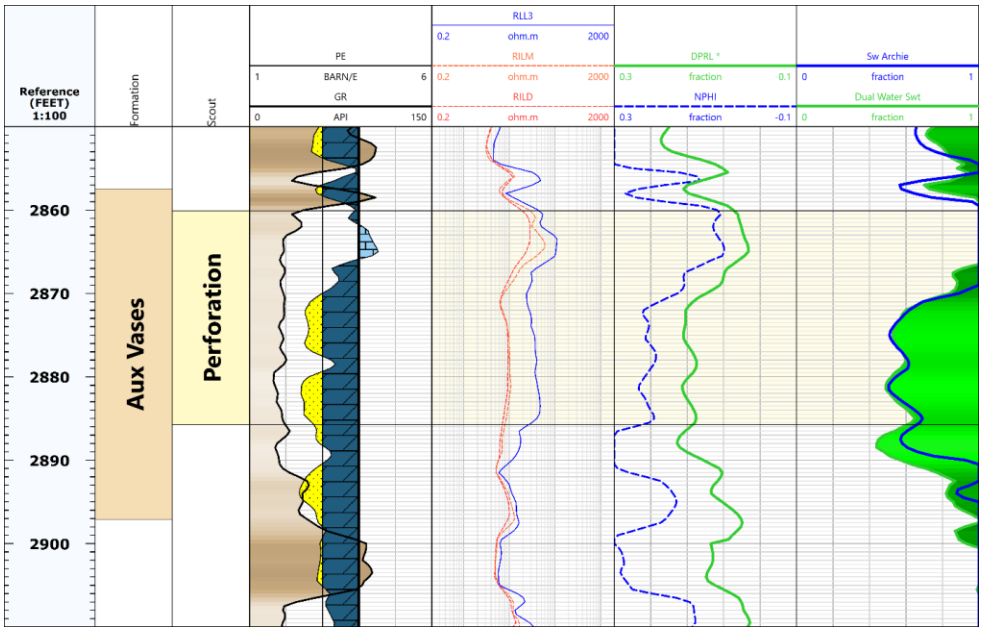


Figure 5-37. Well logs and calculated water saturation through the Aux Vases in the Carrie Winter 7 well. Archies S_W shown in blue curve, dual water Sw shown in green curve with green fill, and perforated interval is shown with a yellow fill. Neutron is significantly greater than Density porosity for the whole Aux Vases because it is a sandstone, and the logs were run on a limestone matrix. Archies S_W predicts oil throughout the entire Aux Vases, but dual water Sw correctly compensates for the influence of clay and only predicts S_O between 2868-2890. A DST between 3515-3525 found that the formation contained an uneconomic amount of oil.

Cypress Sandstone

The model for the thick Cypress Sandstone was developed by leveraging the geocellular model created for a previous project (Grigsby and Webb, 2020). This previous model was the combination of two models. First, normalized spontaneous potential logs (NSP) were used to create a "depositional model" in which the distribution of sand and shale facies were represented. An NSP to porosity transform was developed to calculate porosity for each of the cells. Then, a "diagenetic model" was constructed with neutron-density porosity logs to represent layers of calcite cement that correspond to oil-water contacts within the thick sandstone and can act as baffles to vertical fluid movement (Webb and Grigsby, 2020). The final model had 11% porosity assigned to cells that had cement in the diagenetic model and NSP-derived porosity from the depositional model.

Variograms developed for previous projects were used for simulations to populate the new model with NSP values. These variograms were elongated along a NW/SE orientation to create the anisotropy observed at the field.

The NSP to porosity transform (Equation 5-8) and the porosity to permeability transform (Equation 5-9) developed in the previous project were used to calculate porosity and permeability for each cell. The calcite cement layers were then imprinted on the model by assigning a small vertical permeability (kZ [0.1 mD]) to layers x and y. A 12 % porosity cutoff was imposed, but the porosity and connectivity of the thick Cypress are generally very high, so the cutoff had only limited impact (Figure 5-38 and Figure 5-39).

$$\theta_{NSP} = 0.04e^{0.0164*NSP} \qquad \text{Equation 5-8}$$

$$k = 0.0338 * \theta_{NSP}^{3.279} \qquad \text{Equation 5-9}$$

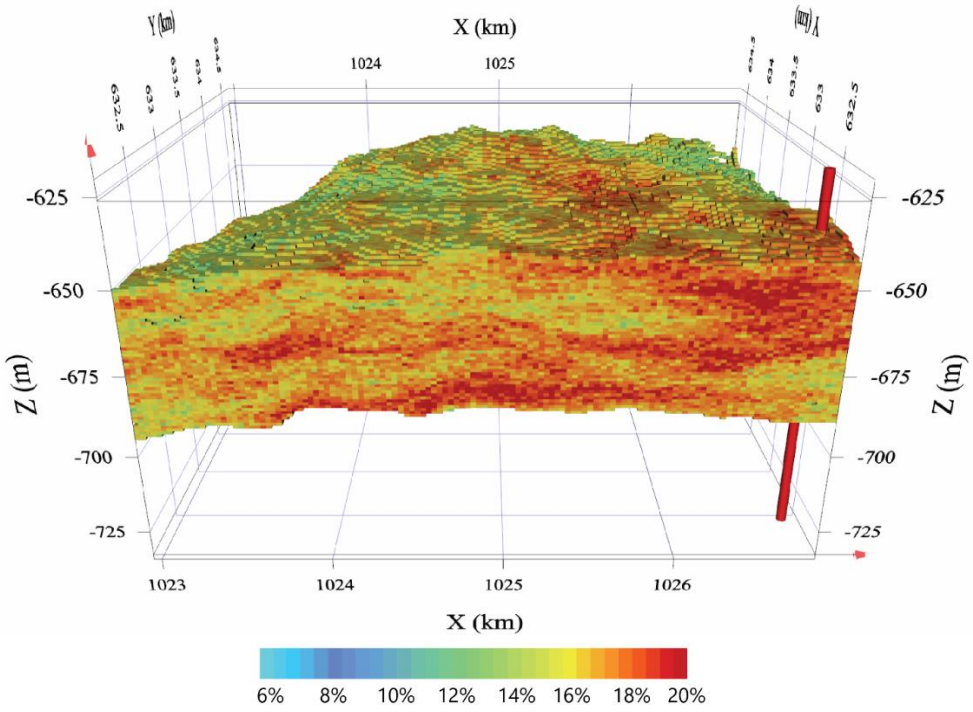


Figure 5-38. Three-dimensional view of the Cypress porosity model. Extent of model area shown in Figure 5-1. Carrie Winter 10 well is represented by the red cylinder in the southeast corner of the model.

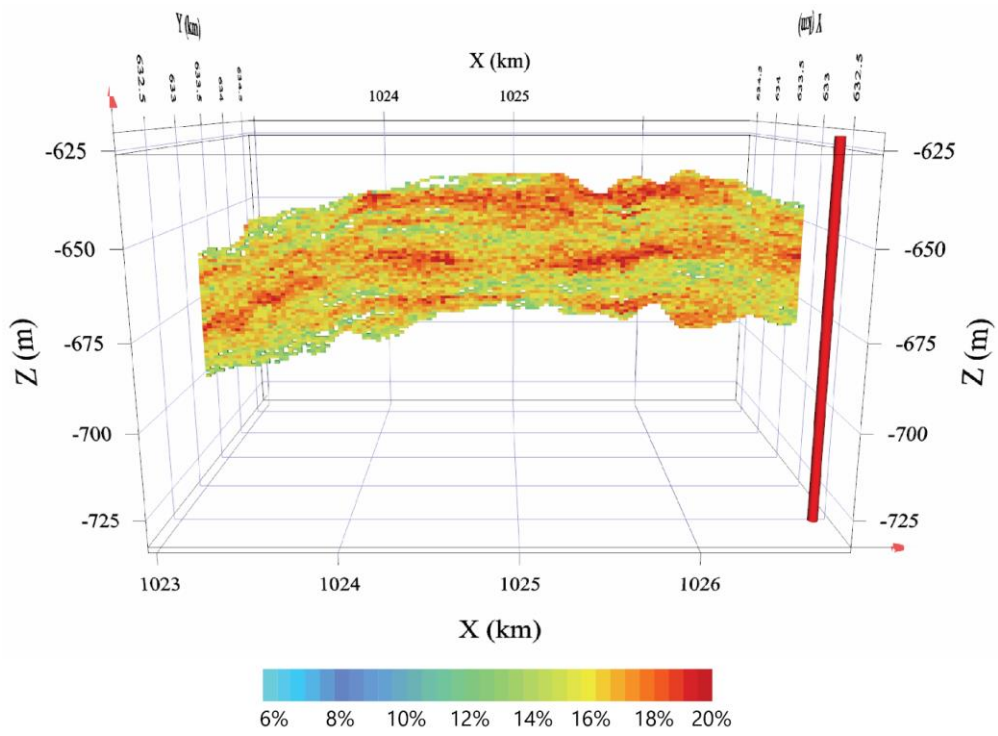


Figure 5-39. W-E cross section through the Cypress Sandstone porosity model after the 12% porosity cutoff is applied. Carrie Winter 10 well is represented by the red cylinder in the southeast corner of the model.

Water saturation was calculated for the thick Cypress for hundreds of wells in Noble Field in the previous project. Interpretation of these logs determined that the Cypress Sandstone contains a brownfield ROZ that underlies the original MPZ.

Unfortunately, the Carrie Winter 10 well has several characteristics that make interpretation of the log-derived S_O difficult (Figure 5-40). The deep resistivity log in the Carrie Winter 10 well appears to be erroneously high from 2,600-2,613 ft (in the middle of the anticipated ROZ). This high resistivity results in an oscillation in S_W curve in the oil-bearing portion of the formation. Vertical fractures containing calcite mineralization were observed on both the FMI log and core in this interval and may contribute to the high resistivity through this interval.

The interval between 2,615-2,625 ft contains a calcite layer, which was expected at the OWC, above an interval of extremely high GR (>300 API) from 2,620-2,625 ft, which was originally interpreted as a shale break. However, the SGR in this high GR interval shows that it is composed entirely of uranium. Furthermore, both NPHI and DPHI are approximately 18% (no separation), Pe is under 2, and the resistivity log has good separation. It is believed that this GR spike is caused by uranium-enriched water trapped beneath the calcite layer.

Fortunately, several other wells within the Carrie Winter lease were evaluated for the previous project. Two of these wells, the Carrie Winter 4 and Carrie Winter 7 (Figure 5-41), were logged with a pulsed neutron tool in 2017 (Webb et al., 2019). These wells all had an OWC that was consistent with the OWC pick in the Carrie Winter 10 well and had 35% S_O in the ROZ.

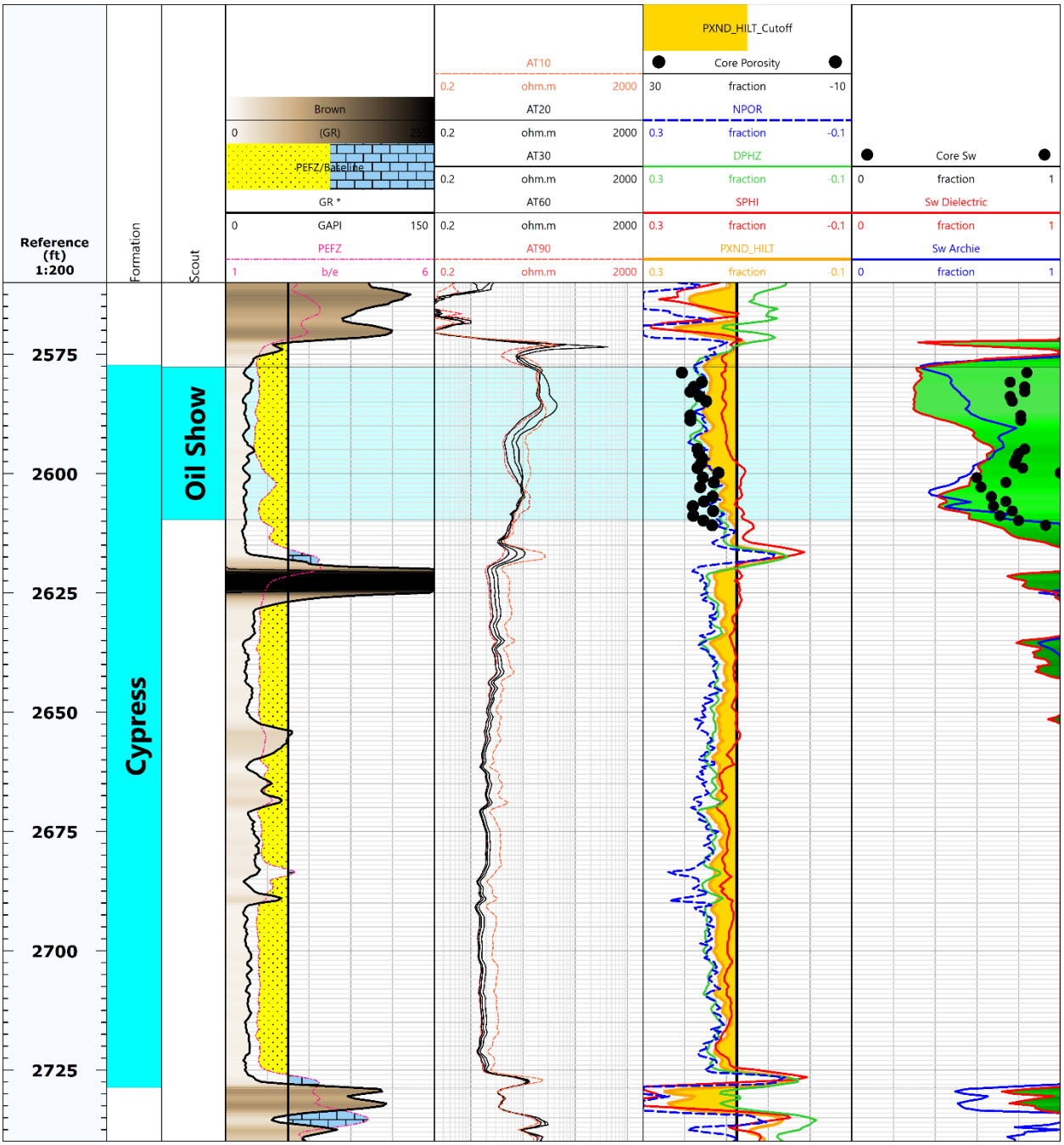


Figure 5-40. Well logs, core, and calculated water saturation through the Cypress Sandstone in the Carrie Winter 10 well. Archies S_W shown in blue curve, S_W derived from the dielectric log shown with red curve and green fill, SW calculated from core shown with black dots, and oil show observed in drill cuttings shown with blue fill. The porosity curves were run on a sandstone matrix, so Neutron and Density porosity overlap except in the upper shale rich portion of the Cypress. Archie and Dielectric S_Ws predict oil within the uppermost 35 feet of the sandstone, which is supported by core, an oil show in the cuttings, and the DST. Unfortunately, an oscillation in S_W between 2,590-2,610 ft prevents a more detailed characterization of the ROZ.

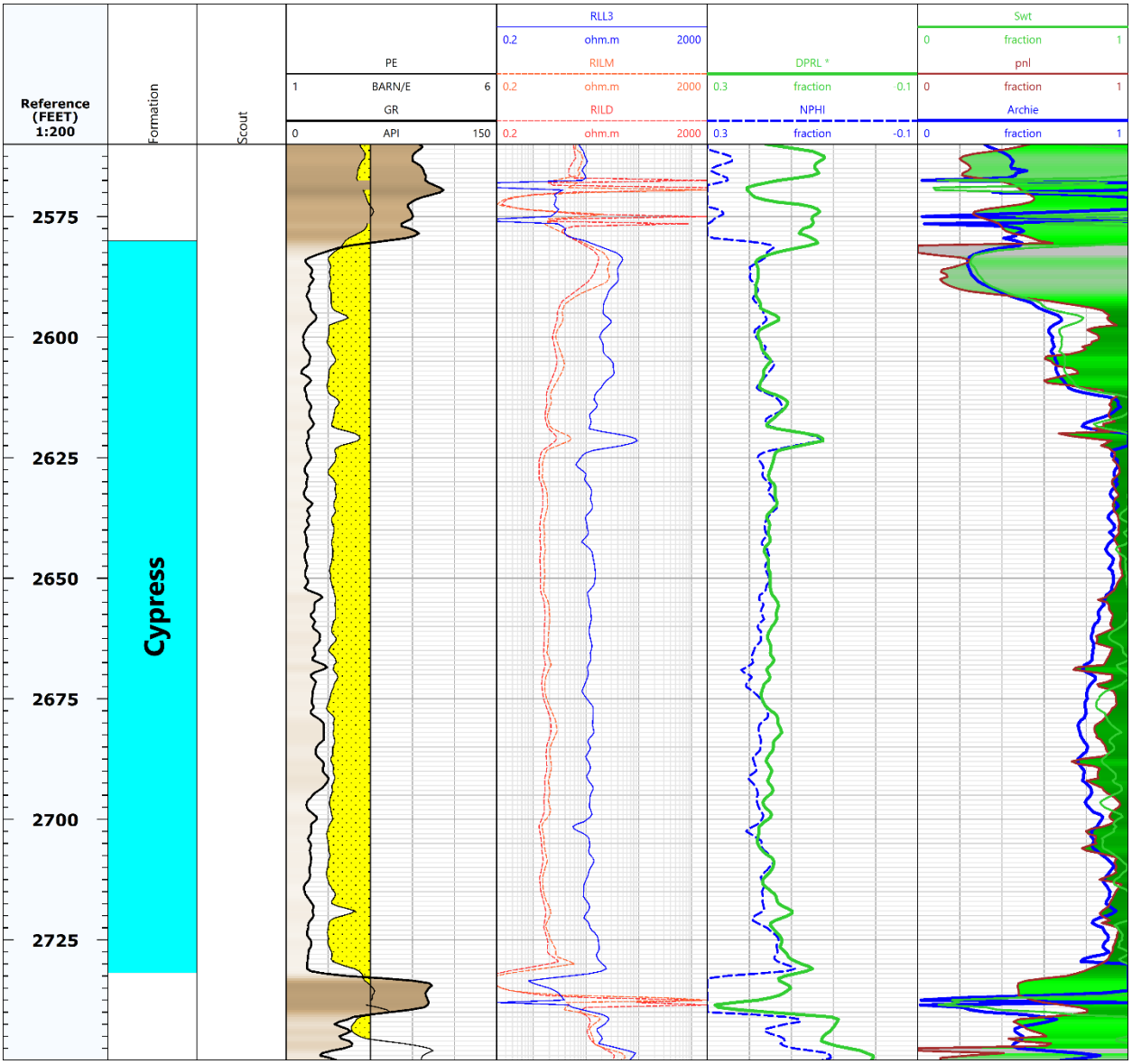


Figure 5-41. Well logs and calculated water saturation through the Cypress in the Carrie Winter 7 well. Archies S_W shown in blue curve, dual water Sw shown in green curve, pulsed neutron S_W shown in brown curve with green fill. All three S_Ws predict oil above 2612, but Archies and dual water S_W stabilize at 65% in the ROZ and PNL S_W does not.

Final Stacked Model

Models for each formation were returned to structural space and combined into a single model. Inactive cells (those that fell below the porosity cutoff and layers between formations) were masked. Realizations were vetted by geologists, and the one deemed most representative of the geology was selected to be used for reservoir simulations. The resulting porosity model is shown in Figure 5-42.

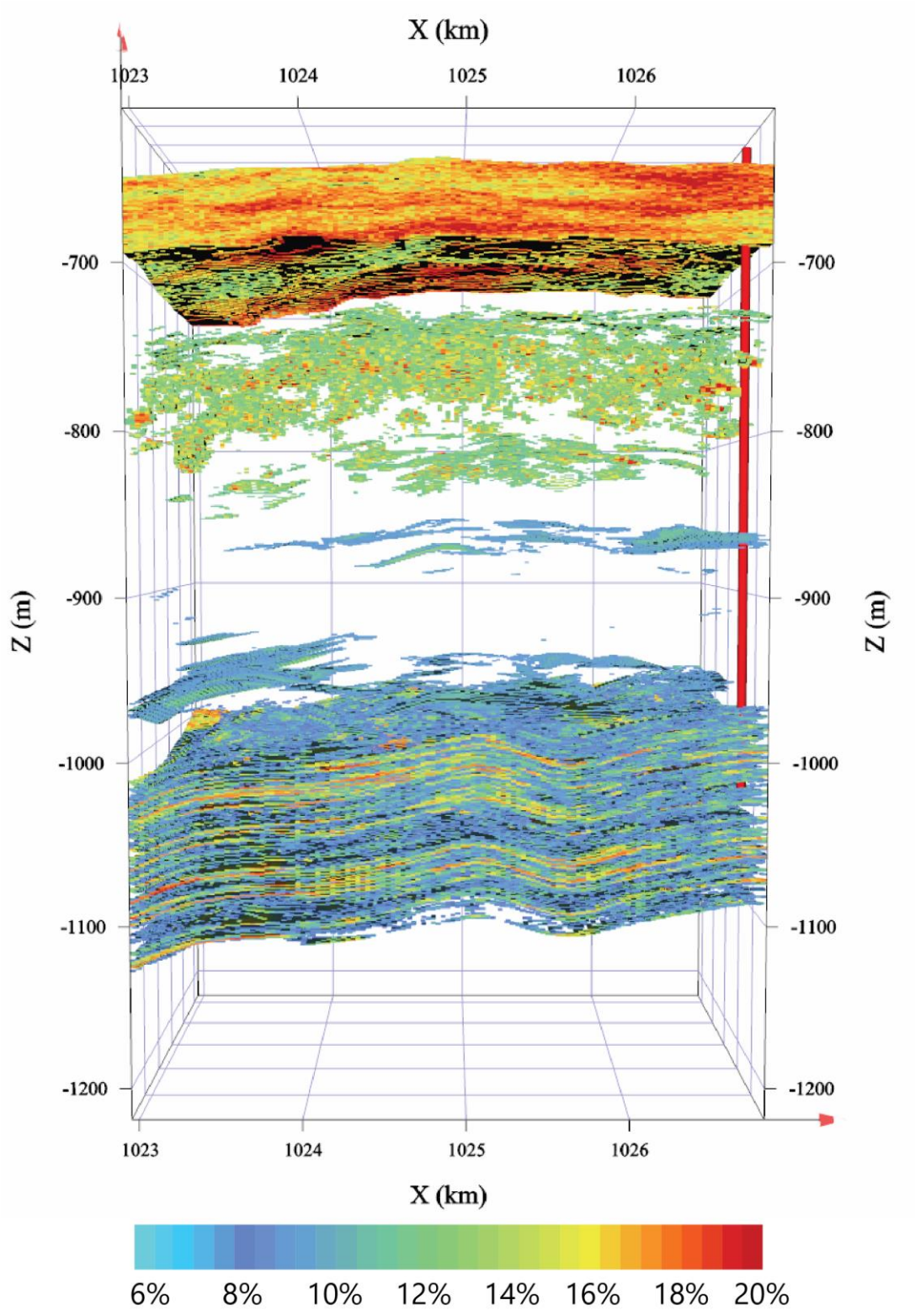


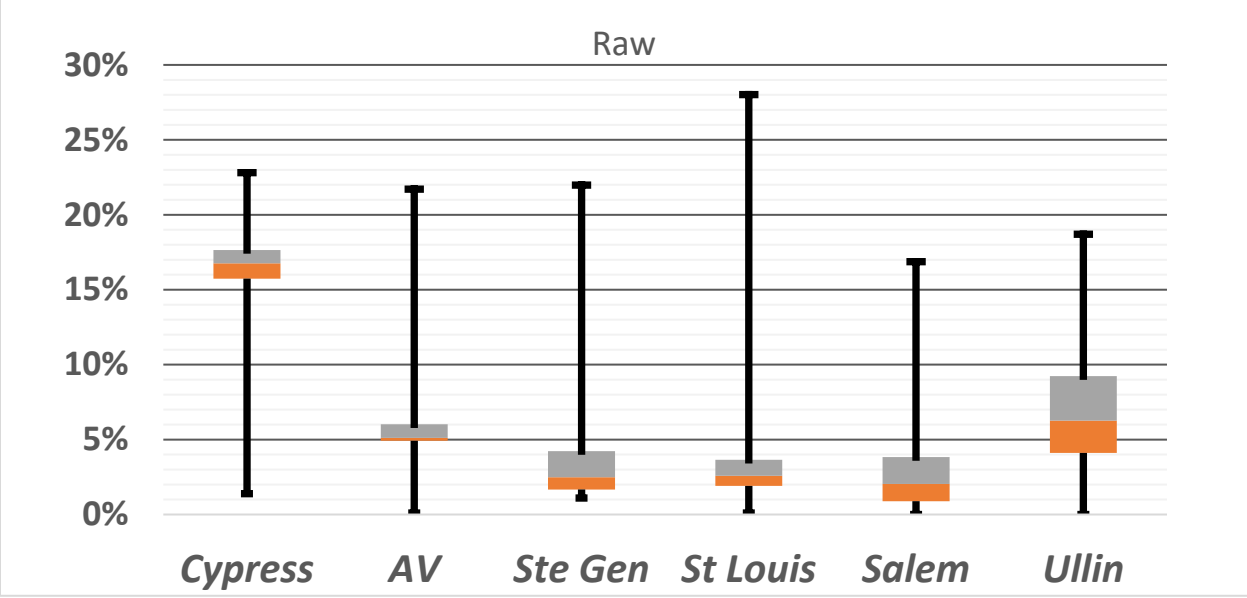
Figure 5-42. Final Stacked porosity model after porosity cutoffs have been applied. Carrie Winter 10 well is represented by the red cylinder in the southeast corner of the model.

In addition to visual inspection of each formation, statistics for each geocellular model before and after porosity cutoffs were applied were evaluated to ensure that they met expectations. The statistics for the final models before and after the porosity cutoffs were applied are provided in Table 5-3, Figure 5-43, and Figure 5-44.

Geologic characterization determined that the Cypress reservoir was a thick, homogenous sandstone. This is reflected in the effect of the porosity cutoff on the geocellular model, which, despite being the highest of the formations modeled, makes only a negligible impact on cell count and petrophysical properties. Conversely, the reservoirs within the Aux Vases Formation and the St. Louis, Ste. Genevieve, and Salem Limestones exist as compartments scattered throughout nonreservoir rock. The porosity cutoff correctly removes a large proportion of non-reservoir cells and pulls permeability of the remaining cells up over 1 mD. The Ullin reservoir was determined to have the lowest continuity of the formations evaluated (Figure 5-13), but the porosity cutoff does not create a dramatic reduction in active cells nor an increase in petrophysical properties. This is because the continuity assessment focused on the upper oil-bearing interval of the formation. The bulk of the model represents the deeper aquifer portion of the Ullin that is believed to be much more continuous.

Table 5-3. Summary table of values (raw and post-porosity cutoff) within the final stacked reservoir model of Noble Field.

Formation		Active Cell Count	% Reduction	Median porosity (%)	Average Permeability (mD)	S_O	OOIP (bbl)**
Cypress Sandstone	Raw	523,357		16.8	320	65% MPZ, 35% ROZ, 0% aquifer	
	12% cutoff	497,610	5	16.8	335		56,321,528
Aux Vases Formation	Raw	199,797		5.1	1.7	65%	
	11% cutoff	9,874	95	13.0	32		4,332,240
Ste. Genevieve Limestone	Raw	687,919		2.5	7.8	65%	
	11.5% cutoff	32,511	95	14.1	160		15,894,263
St. Louis Limestone	Raw	415,848		2.6	1.4	65%	
	11% cutoff	6,714	98	13	84		3,132,329
Salem Limestone	Raw	1,266,351		2.0	0.2	65%	
	9% cutoff	22,205	98	9.9	12		7,848,235
Ullin Limestone	Raw	1,476,115		6.3	20	65% in top 30 ft, 0% aquifer	
	8% cutoff	496,404	66	11.0	59		8,975,103



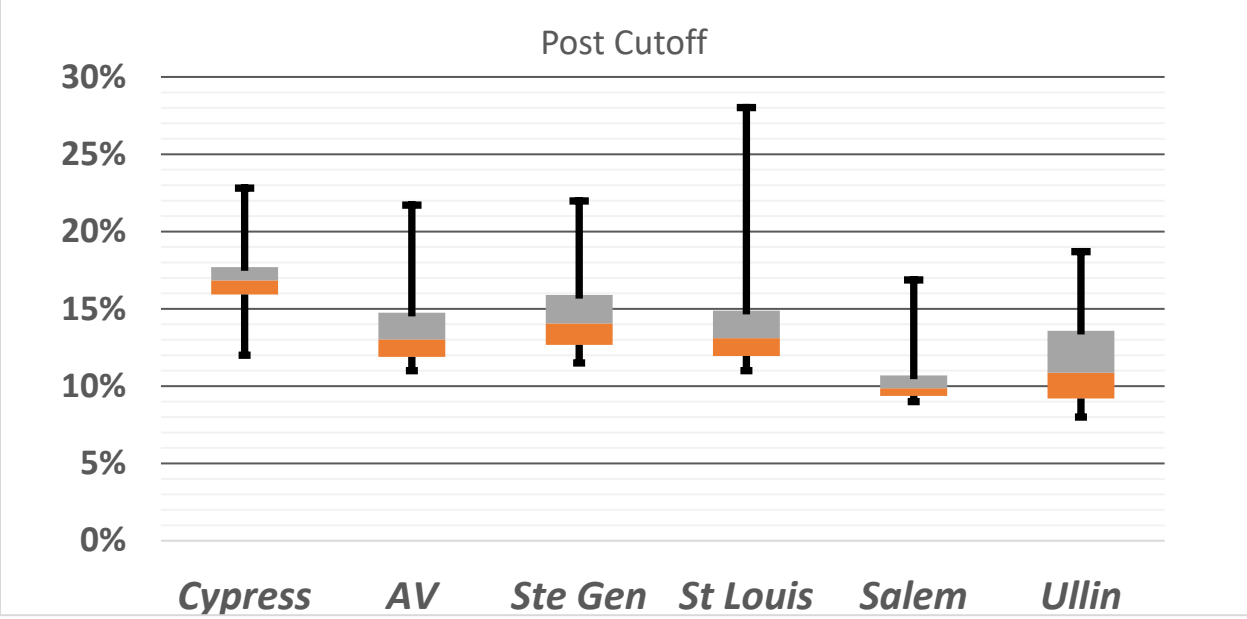
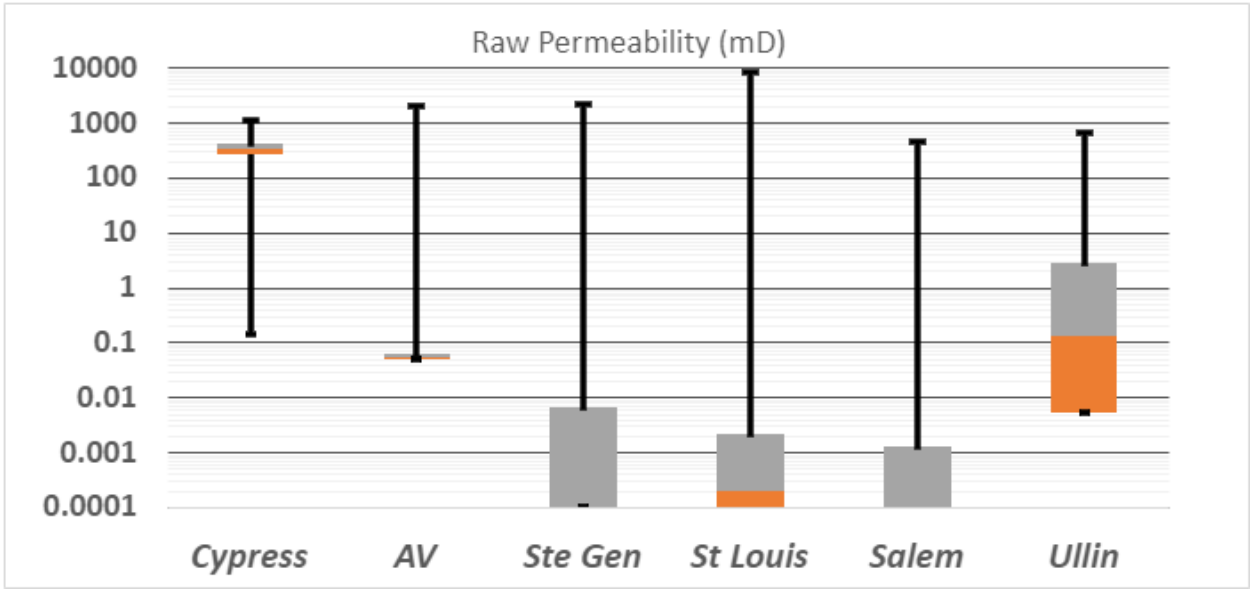


Figure 5-43. Box and whisker plots of the porosity of each of the formations modeled before (top) and after (bottom) porosity cutoffs were applied.



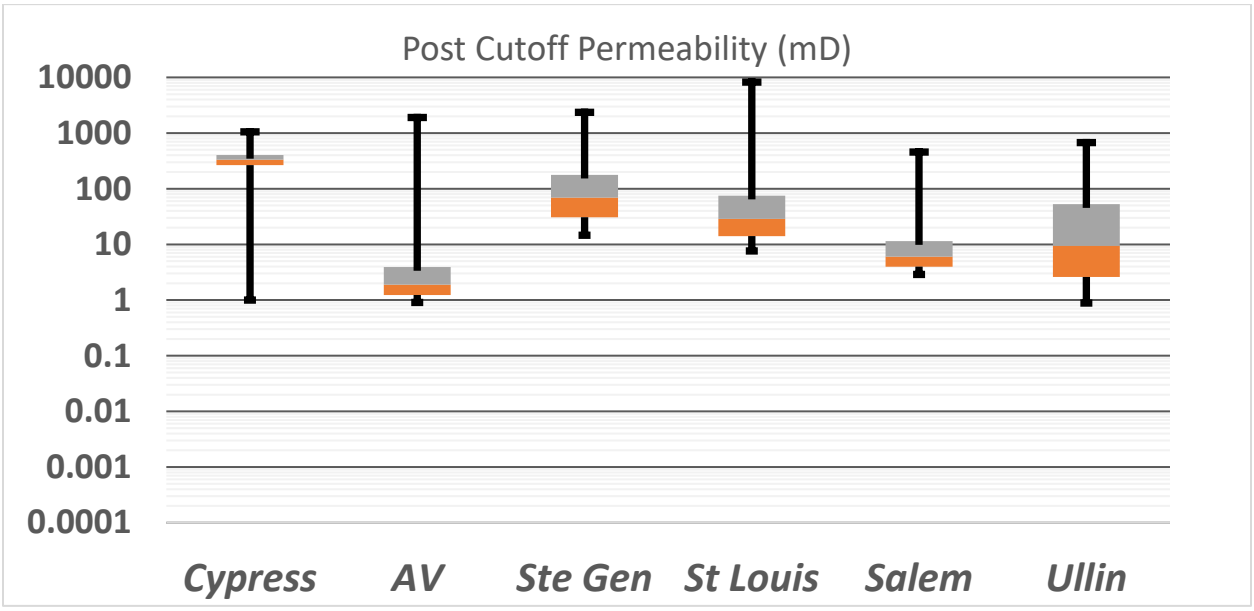


Figure 5-44. Box and whisker plots of the permeability of each of the formations modeled before (top) and after (bottom) porosity cutoffs were applied.

Conclusions

Noble Field contains a stacked reservoir complex with depleted conventional oil reservoirs in both carbonate and siliciclastic rocks and a siliciclastic ROZ and is characteristic of the type of mature brownfield setting common across the Illinois Basin. Given the geologic makeup of the reservoirs and the amount of residual oil that remains in depleted and bypassed MPZs and the ROZ, the field is an obvious target for CO_2-EOR and associated storage in which CO_2 promises to recover a portion of the remaining oil, but the storage potential is adequate to make the oil production carbon negative.

Geologic characterization was undertaken to better understand the reservoir properties and historical productivity of the stacked reservoirs within the field. The Cypress Sandstone and Ste. Genevieve Limestone reservoirs have been responsible for approximately 90% of the oil production over the past eight decades with the remainder being attributed to pay zones in several other formations. The Cypress Sandstone is the shallowest oil reservoir in the field and is unique among the stacked reservoirs in that it is thick and relatively homogeneous with exceptional continuity, and it contains an ROZ below the partially depleted MPZ. Reservoirs within the Aux Vases Formation generally occur within a thin, shaley sandstone in the upper part of the formation, though porous dolomites also occur in the lower half. The Ste. Genevieve and Salem Limestones are lithologically similar with each containing oolitic to skeletal grainstone reservoirs that are relatively thin and compartmentalized within otherwise non-porous limestone. The St. Louis Limestone has reservoirs mainly developed in thin but widespread microsucrosic dolomite beds. Reservoirs within the Ullin Limestone are restricted to thin stringers of porosity that occur in the uppermost part of the formation. Both the Cypress Sandstone and the Ullin Limestone contain thick brine aquifers below their oil reservoirs that would be well suited to saline carbon storage.

Geocellular models were constructed to represent the reservoir properties, including porosity and permeability relationships, thickness and spatial distribution, and lateral continuity, defined as part of the geologic characterization. Well log analyses, based largely on a newly drilled well with an advanced suite of logs, were used to develop water saturation estimates that helped better constrain the current saturation in the partially depleted reservoirs. Ultimately, the stacked reservoir model developed herein will provide input for dynamic reservoir simulations that, once calibrated to the production history of the field, will be used to test various CO_2 development scenarios to predict the co-optimized performance of CO_2-EOR and associated storage in the stacked reservoir complex.

Appendix 5-1

Table 5-4. Statistics for the horizontal and vertical variograms used to develop the geocellular models for the stacked reservoir complex.

Formation	Direction	Nugget	Close Sill	Close Range, m (ft)	Far Sill	Far Range, m (ft)	very far sill	very far range, m (ft)
Upper Ullin Limestone	x/y	0.1	0.45	(3,000)	0.45	(10,000)		
	z			(20)		(200)		
Lower Ullin Limestone	x/y *z*	0.1	0.9	(8,000) (10)				
Salem Limestone	N125°	0.0	0.2	15,240 (50,000)	0.5	60,960 (200,000)		
	N215°			30,480 (100,000)		91,440 (300,000)		
	z			6 (20)		23 (75)		
St. Louis Limestone	N130°	0.01	0.49	244 (800)	0.4	1829 (6,000)	0.1	2195 (7,200)
	N220°			183 (600)		1097 (3,600)		1829 (6,000)
	z			3 (10)		6 (20)		30 (100)
Ste. Genevieve Limestone	N45°	0.1	0.45	457 (1,500)	0.45	2,743 (9,000)		
	N135°			549 (1,800)		1,829 (6,000)		
	Z			3 (10)		6 (20)		
Aux Vase Formation	x/y	0.1	0.5	366 (1,200)	0.4	2,438 (8,000)		
	Z			3 (10)		61 (200)		
Cypress Sandstone	N110°	0.1	0.5	1,676 (5,500)	0.4	18,288 (60,000)		

5.2 Carrie Winter 10 Report

Authors: Nathan Webb and Nathan Grigsby

A new research well, the Carrie Winter #10, was drilled in Noble Oil Field (Figure 5-45) to validate the existence and properties of a brownfield residual oil zone (ROZ) in the thick Cypress Sandstone. Fresh core was extracted, and modern open-hole logs were obtained to quantify oil saturation and determine fluid contacts. Because the porosity and permeability of the Cypress Sandstone is relatively high, a low-invasion coring bit that directs drilling fluid away from the core was used to maximize the preservation of *in situ* fluid saturations in the core. A drill stem test (DST) was conducted to determine whether mobile oil was present, to test pressure communication across a calcite cemented zone at the top of the ROZ, to acquire reservoir fluid samples, and short-term pressure transient test data for reservoir-scale permeability estimates. The design of the coring, fluid sampling, pressure transient testing and logging program of the research well corresponds to Task 5 of the project SOPO.

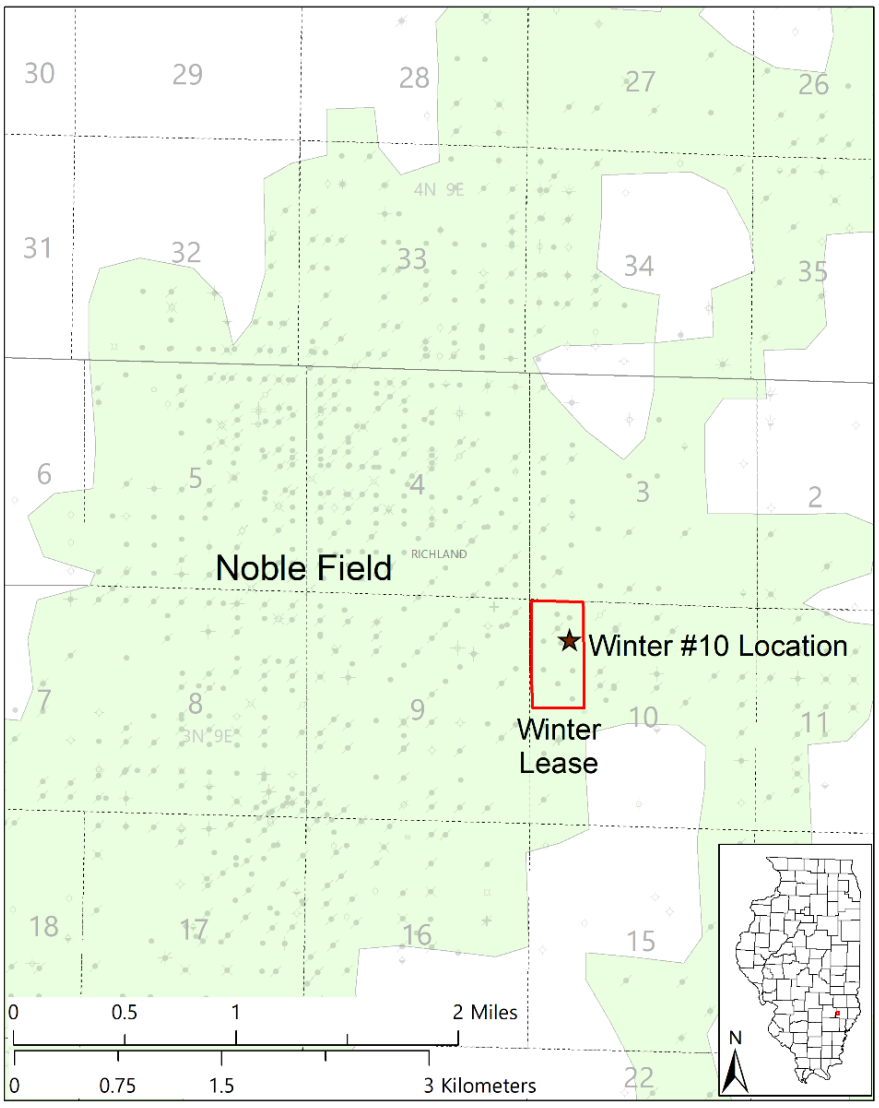


Figure 5-45. Map showing location of the Winter Lease and Winter #10 well in the context of Noble Field.

Well Summary

Podolsky Oil Company (Podoco) was the oil industry partner for the brownfield laboratory site on the project and made available an undrilled location on the 80-acre Carrie Winter lease, W ½, NW ¼, Section 9, T3N, R9E, Richland County, IL (Figure 5-45). Podoco obtained a drilling permit issued by Illinois Department of Natural Resources on April 25, 2019.

Design

In the autumn of 2019, a drilling program was designed in coordination with Podoco to drill a research well to an objective depth (approx. 3,800 ft.) in the Mississippian Ullin Limestone (Figure 5-46). The Ullin Limestone was selected because it is the deepest oil producing formation in the field and the resultant well and geophysical logs would provide data for all stacked reservoirs in the field.

Collection of up to 180 ft of full diameter core was planned for the well, starting in the Fraileys Shale, continuing through the Beech Creek Limestone, and through the entirety of the Cypress Sandstone. The objective of the core was to provide material to analyze the oil reservoir (main pay zone and ROZ), seal system, and the overall geology of the succession.

A full suite of Schlumberger geophysical logs was planned for the well. Schlumberger was mobilized from outside of the Basin because of their Dielectric Scanner, which is a logging tool that provides an alternative to the resistivity-based water saturation calculation against which to calibrate water saturation calculations from conventional logs in this and adjacent wells, and from Schlumberger Reservoir Saturation Tool (pulsed neutron) logs that were run in four nearby wells in the field in 2017.

A drill stem test (DST) was also planned for the Cypress ROZ. The Cypress ROZ is separated from the overlying MPZ and underlying brine aquifer by dense calcite cements. The DST was designed to test whether the calcite cements form a barrier to vertical fluid movement.

Drilling

Drilling commenced on November 7, 2019. Drilling time was recorded on a 5 ft. interval from surface to 2,400 ft. and on a 1 ft. interval from 2,400 ft. to TD. Samples were collected on a 10 ft. interval below 2,150 ft. and increased to a 5 ft. sampling interval at 2,400 ft. Each sample was evaluated on site for odor and oil shows. The drilling progress is summarized in Table 5-5.

Drilling through the Pennsylvanian was most consistent in terms of rate of penetration except for some thick shales that occur in the basal Pennsylvanian interval at approximately 1,750, 1,850, and 1,950 ft (Figure 5-47). The Chesterian section had variable rate of penetration due to the relatively thin units and variable lithology. The top of the Ste. Genevieve Limestone marks a significant lithological change to dominantly limestone and resulted in a consistently slower rate of penetration.

Difficulties encountered during drilling included low rate of penetration while drilling (especially some lower Pennsylvanian shales) and exceedingly low while coring due to worn out bits and lost circulation due to encountering a natural fracture in the upper part of the Cypress Sandstone that resulted in less core being collected to remain within budget for the project.

Table 5-5. Summary of the drilling progress in November 2019.

Date	Event
11/17/2019	Well spudded.
11/17/2019-11/21/2019	Drilling through surficial deposits, Pennsylvanian and upper Chesterian strata.
11/21/2019	Core point selected at 2,516 ft.
11/22/2019	Core bit stops penetrating around noon; Core #1 laid down in afternoon (2,516 ft. to 2,549 ft.). Core bit is ruined, decided to drill through 30 ft. of upper Cypress shaley interval to top of sandstone to save backup bit for coring Cypress MPZ/ROZ.
11/23/2019	Core barrel jambs at 2,604'; Core #2 laid down late afternoon (2,579' to 2,604'; three feet of loss).
11/24/2019	Core #3 laid down in pre-dawn hours (2,604' to 2,611'). Drill stem test run through mid-afternoon.
11/24/2019-11/27/2019	Drilling through remainder of Chesterian and Valmeyeran strata.
11/27/2019	Well TD reached at 3,831'; Schlumberger onsite and logging begins in the evening.
11/28/2019	Logging complete by mid-day.

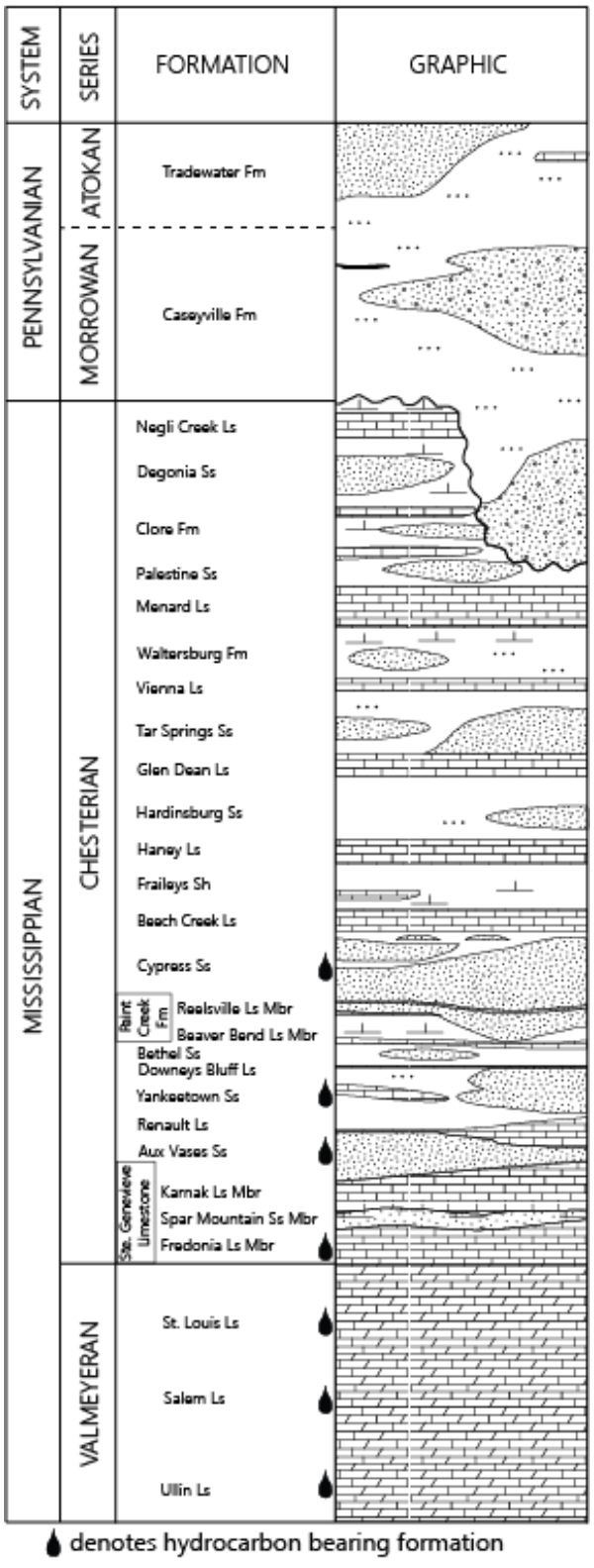


Figure 5-46. Generalized stratigraphic column of Noble Field showing the seven oil reservoirs in the field that make up the Brownfield stacked storage complex.



Figure 5-47. Rate of penetration vs depth as recorded by iBall Bloodhound.

Methods

Bloodhound

An iBall Instruments Bloodhound gas detector and chromatograph system was used to record gas signatures and rate of penetration (Figure 5-47) while drilling from 255 ft. to TD. The Bloodhound provided quantitative data on total gas (C1 to iC4 / nC4), O_2, CO_2, and H_2S.

Core

Sixty-six feet of 4.25-in diameter core were collected from the Fraileys Shale and Beech Creek Limestone (the seal system) and the Cypress Sandstone MPZ and ROZ (Figure 5-47). A low invasion thermally stable polycrystalline diamond (TSP) coring bit was used. The low invasion bit has fluid jets on the face of the bit that directs drilling fluid away from the core to avoid flushing the core with drilling fluid (Figure 5-49). When the core was being laid down, it was quickly wiped down, measured, marked for footage, and then double wrapped in polyvinyl ethylene stretch wrap (a composition known to have low reactivity with crude oil). The core was then wrapped in heavy aluminum foil and all seams were taped.

The core was geologically described. The Fraileys Shale section of the core was sampled for mercury injection/capillary pressure analysis to determine its seal capacity. It was also sampled for X-ray fluorescence and X-Ray diffraction to determine elemental composition and mineralogy.

The core through the Cypress Sandstone was sampled for whole core analysis, core plug analysis, thin sections, and X-ray fluorescence and X-Ray diffraction. A 10-inch whole core sample was collected out of every foot of core. From the remaining two inches of core between the whole core samples, a horizontal and vertical plug was collected. End trims from the plugs were collected for thin section preparation.

Core plugs were subjected to routine core analysis including Dean-Stark extraction and porosity and permeability determination using a Vinci PoroPerm machine. Electrical resistivity was measured using a Vinci PC/RI system.

Whole core samples were typically broken due to the natural fracture in the formation, so a modified technique was required for whole core desaturation. The samples were cleaned of excess drilling fluid and submerged in a brine solution to measure the fluid displacement of the samples as a means of validating the bulk volume of the broken samples.

The whole core and core plug samples underwent Dean-Stark extraction to determine the in-situ saturations. This process also cleans the core before it is returned to storage. The initial mass of each sample was measured. The samples were then placed in the Dean-Stark apparatus. A 75% Toluene/25% Methanol mixture of known density was added into the sample container until the sample was wholly submerged. The heating mantle was set to maintain the temperature inside the Dean-Stark apparatus between 180 to 220°C to start the evaporation process. Solvent and water boiled and evaporated into the condensing coil where the solvent was returned to the sample chamber and the water was collected in a water trap from which it was routinely removed and measured, and its density determined. Once water was fully removed from the sample (as indicated by the cessation of water accumulating in the trap), the solvent mixture was replaced, and the Dean-Stark cycle is restarted. Each cycle takes 48 to 72 hours depending on oil saturation and was repeated until the solvent mixture remains clear at the end of the cycle indicating that all the oil has been removed from the sample. Following the final cycle, the sample is removed from the container and placed in a fume hood to let the residual solvent evaporate after which the sample is placed into an oven at 138°C to completely dry. Final mass of the dry sample was measured for the saturation calculation where the volume of oil is calculated from the loss in weight of the sample and adjusted by subtracting the mass of the water removed from the sample.

Clean, dry samples were fully saturated with 10% KCl brine mixture (10% potassium chloride by weight mixed with deionized water) of known density to verify the bulk and pore volume of the sample. To achieve 100% saturation, the process is done in a container under vacuum for 24 to 48 hours to help remove residual gasses in the brine and the sample. Once saturation is complete, the sample is weighed and its fluid displacement is again measured. The mass and the volume of displaced brine is recorded.



Figure 5-48. Photograph of low-invasion TSP coring bit used to collect core through the MPZ and ROZ within the Cypress Sandstone. The TSP cutting nibs show considerable wear and resulted in excessivly low rate of penetration while coring.

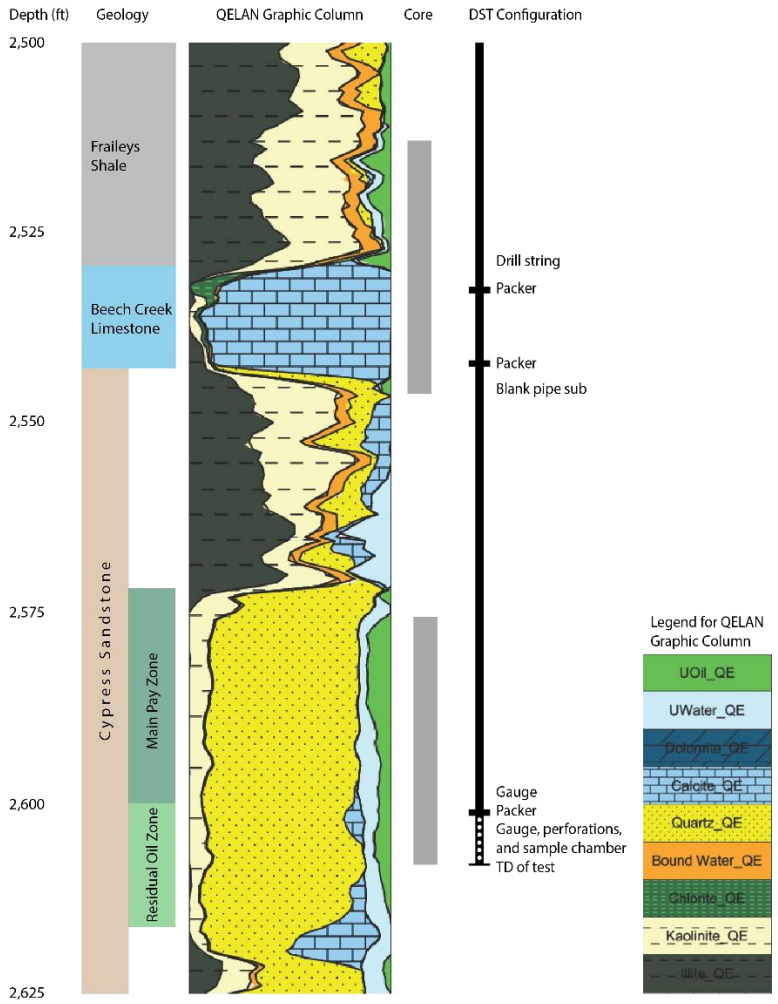


Figure 5-49. QELAN graphic column with geological interpretation, cored intervals, and DST configuration annotated and plotted against depth.

Log Analysis

Schlumberger collected Platform Express, Array Induction, Borehole Compensated Sonic, Spectral Gamma Ray, Fullbore Formation MicroImager, and Dielectric Scanner open hole logs through the depth interval containing the stacked reservoirs (~2,400 to 3,800 ft). Schlumberger used these logs to conduct industry standard petrophysical QELAN log analyses.

The overarching goal of these analyses were to validate the presence of a brownfield ROZ in the thick Cypress Sandstone and to better understand its petrophysical (both rock and fluid) properties. The sophisticated log suite was also leveraged to evaluate five additional formations to constrain input parameters for reservoir simulations: The Aux Vases, Ste. Gen, St. Louis, Salem, and Ullin.

Well logs typically found throughout the Illinois Basin (resistivity, neutron-density porosity, and gamma ray) were independently analyzed and compared to the ELAN analysis to determine if they could be used to properly characterize the petrophysical properties of the target formations. Four additional wells in the Carrie Winter lease were also evaluated to support the analysis of the Carrie Winter #10 well (Table 5-6). All of these wells had resistivity, gamma ray, and neutron-density porosity logs and two also have pulsed neutron logs (PNLs) in the Cypress in 2018.

Table 5-6. Statistics for each of the target formations in the other wells in the Carrie Winter lease.

		CW3	CW4	CW6	CW7
	API	121592617100	121592624600	121592624800	121592631000
	TD (ft)	3627	3043	3563	3240
Formation Top (ft)	Cypress	2569	2577	2570	2580
	Aux Vases	2862	2860	2871	2860
	McCloksy	2937	2979	2971	2990
	St Louis	3131	-	3123	3080
	Salem	3293	-	3511	-
	Ullin	3615	-	-	-
Extra logs			PNL		PNL
Perforations		DST in Cypress, Salem producer	McClosky producer	DST in Cypress, McClosky, & St. Louis producer	DST in AV, St. Louis producer

Rock Properties

The composite log developed by Schlumberger includes a geologic characterization that lists the proportion of quartz, kaolinite, chlorite, illite, limestone, and dolomite and assigns total and effective porosity. Logs present in other wells throughout Noble (resistivity, neutron-density porosity, and gamma ray) were independently analyzed to determine if they could properly identify and characterize reservoirs in each of the target formations. A good match between the sophisticated ELAN and interpretation of traditional well logs would improve confidence that other wells could be used to create representative field-scale geocellular models of each of the target formations.

Rock properties must also be understood to properly calibrate water saturation calculations. Even a low proportion of dolomite or the right kind of clay can shift calculated water/oil saturation a few percentage points. The low oil saturations in an ROZ make this error significant.

Fluid Properties

The primary objective of these log analyses is to validate that an ROZ exists in the thick Cypress. Oil saturation was also calculated for the Aux Vases, McClosky, St. Louis, Salem, and Ullin to aid in reservoir simulations.

Well logs are commonly used to estimate oil saturation (S_O) by calculating water saturation (S_W) and assuming that the remaining pore space is occupied by oil (S_O=1-S_W). Water saturation profiles (S_W versus depth) can be created by using established methods of calculating S_W from resistivity and neutron-density porosity logs (e.g., Archie; Archie, 1942) or Dual Water (Waxman and Smits, 1968; Clavier et al., 1984). An ROZ below an MPZ will have S_W that varies with depth according to a predictable behavior shown in Figure 5-50 (Koperna and Kuuskraa, 2006; Harouaka et al., 2013; Yang and Qing, 2016). Within the MPZ, water saturation is low and at irreducible saturation. Below the base of the MPZ at the top of the ROZ, water saturation increases to a constant water saturation (i.e., the residual oil saturation), referred to here as the ROZ transition zone. Below the constant water saturation within the main ROZ, the water saturation increases to 100% in the underlying aquifer, referred to here as the capillary transition zone. The lower boundary of irreducible water saturation is defined here as the producing oil-water contact (POWC) and the depth where water saturation increases to 100% is the oil-water contact (OWC). The ROZ is defined here as the interval between the POWC and the OWC. These definitions make a distinction between MPZ, main residual oil zone (MROZ), and two capillary transition zones.

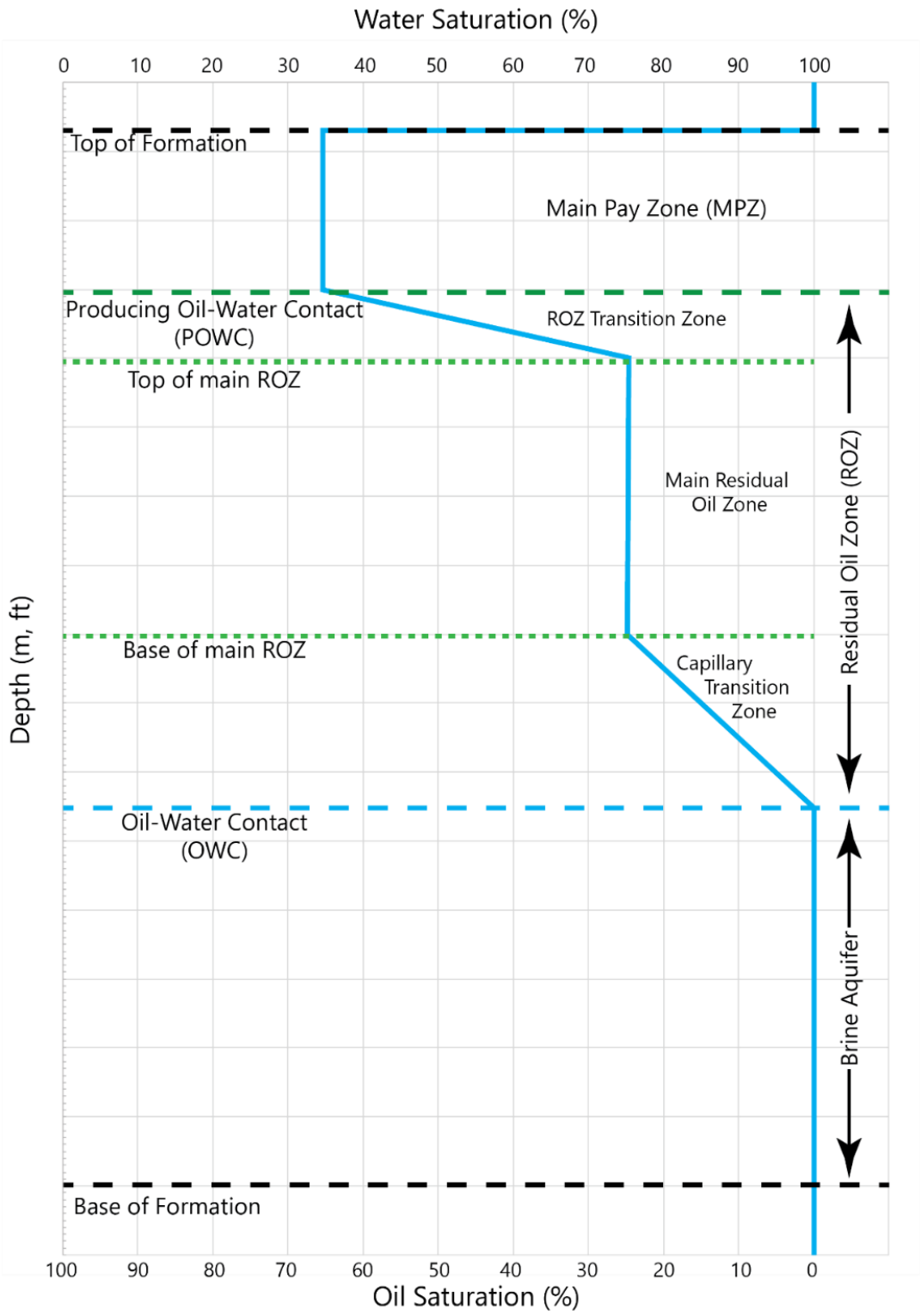


Figure 5-50. Ideal Saturation Profile. Top and base of the porous formation indicated with black dashed lines, water saturation profile shown with solid blue line. The ROZ exists between the producing oil-water contact (POWC – green dashed line) and the oil-water contact (OWC), below which water saturation becomes 100%. Irreducible water saturation is 35%, and residual oil saturation in this figure is 25% (75% S_W). The ROZ is comprised of the ROZ transition zone, main ROZ, and capillary transition zone.

The composite log contains a calculated S_W. These are helpful to understand the distribution of S_O within the Carrie Winter #10 well, but additional analyses were conducted to determine if traditional logs could be used to properly estimate oil saturation and determine where it is mobile. This method was developed for a previous project to better understand the ROZ potential in the thick Cypress, in which it was compared to four PNLs at Noble and used throughout Illinois to constrain the boundaries and characteristics of the Cypress ROZ fairway.

Archies and dual water equations are used to calculate S_W. Bulk Volume Water (BVW), Moveable Hydrocarbon Index (MHI), and Apparent Water Resistivity (Rwa) are then calculated to identify where the oil is at irreducible saturation (Swirr), mobile, and where it is immobile (i.e. at S_{OR}).

The moveable hydrocarbon index (MHI) was developed as a quick look method to identify reservoirs that contain movable hydrocarbons by comparing the water saturations of the uninvaded formation and the flushed zone (Asquith, 1985; Asquith and Krygowski, 2004). Mud filtrate invades permeable hydrocarbon-bearing zones and displaces the hydrocarbons from the flushed zone immediately adjacent to the drilled wellbore, resulting in the flushed zone having a higher water saturation than the uninvaded formation. For hydrocarbon-bearing zone in which the hydrocarbon has been flushed or moved by the mud filtrate, MHI is calculated as follows:

$$MHI = \frac{S_w}{S_{xo}} = \sqrt{\frac{R_{xo}/R_t}{R_{mf}/R_w}}, \qquad \text{Equation 5-10}$$

where:

- S_{xo} = water saturation of the flushed zone
- R_t= resistivity of the uninvaded zone (ohm-m)
- R_{xo} = resistivity of the flushed zone (ohm-m)
- R_{mf} = resistivity of the mud filtrate (ohm-m at formation temperature).

It is generally accepted that, for sandstones, an MHI <0.7 (<0.6 for carbonates) indicates that hydrocarbons are present and that the formation has adequate hydrocarbon mobility (Asquith 1985; Asquith and Krygowski 2004). If this holds true, the MHI will be <0.7 in the productive portion of a sandstone reservoir (i.e., the MPZ and ROZ transition zone) and >0.7 in the unproductive portion (i.e., the ROZ and 100% S_W intervals).

Apparent Water Resistivity

Apparent Water Resistivity (R_{WA} in ohm-m) is mathematically defined by assuming 100% S_W and using Archie's equation as follows:

$$R_{wa} = \frac{\phi^m * R_t}{a}, \qquad \text{Equation 5-11}$$

where:

- ϕ = porosity
- m = cementation exponent
- a = tortuosity factor.

Each interval (MPZ, ROZ, 100% S_W) will have a characteristic R_{WA} signature. Resistive hydrocarbon-filled pore space will result in a very high R_{WA} in the MPZ. Conversely, conductive brine filling the pore space

within a 100% S_W interval will result in the lowest R_{WA} (equal to the R_W) of the formation. An ROZ is a mixture of oil and water and will have an R_{WA} value between that of the MPZ and 100% S_W interval.

The minimum R_{WA} can be compared to the known value for R_w for the formation; this can be used to validate a 100% S_W interval below the ROZ. The depth at which R_{WA} meets the true R_W (the known resistivity of the formation water) can be used to pick the OWC.

Bulk Volume Water

Bulk volume water (BVW) is the product of water saturation and porosity and is commonly used to identify MPZs that will produce water-free oil (i.e., S_W is at irreducible saturation [S_{WIRR}]). BVW is calculated as follows:

$$BVW = S_w * \emptyset \qquad \text{Equation 5-12}$$

The assumption is that BVW is constant at S_{WIRR} for similar grain sizes and increases with decreasing grain sizes (Table 5-7**;** Asquith, 1985; Asquith and Krygowski, 2004). Therefore, an interval of the upper reservoir that has a constant BVW indicates an MPZ at S_{WIRR} within a homogenous formation. If the MPZ is at S_{WIRR}, BVW will maintain a stable value related to the grain size in the MPZ and begin to increase immediately below the POWC. A thick MPZ that exhibits two different but constant BVW values indicates that the zone is at S_{WIRR} but has two unique grain sizes. In the aquifer, BVW is expected to be equal to porosity.

Table 5-7. Relationship between grain size and bulk volume water at S_{WIRR} in sandstone reservoirs; from Asquith (1982).

Grain Size		**Bulk Volume Water at S_{WIRR}**
Coarse	0.5-1.0 mm	0.020-0.025
Medium	0.25-0.5 mm	0.025-0.035
Fine	0.125-0.25 mm	0.035-0.050
Very Fine	0.062-0.125 mm	0.050-0.070
Silt	<0.0625 mm	0.070-0.090

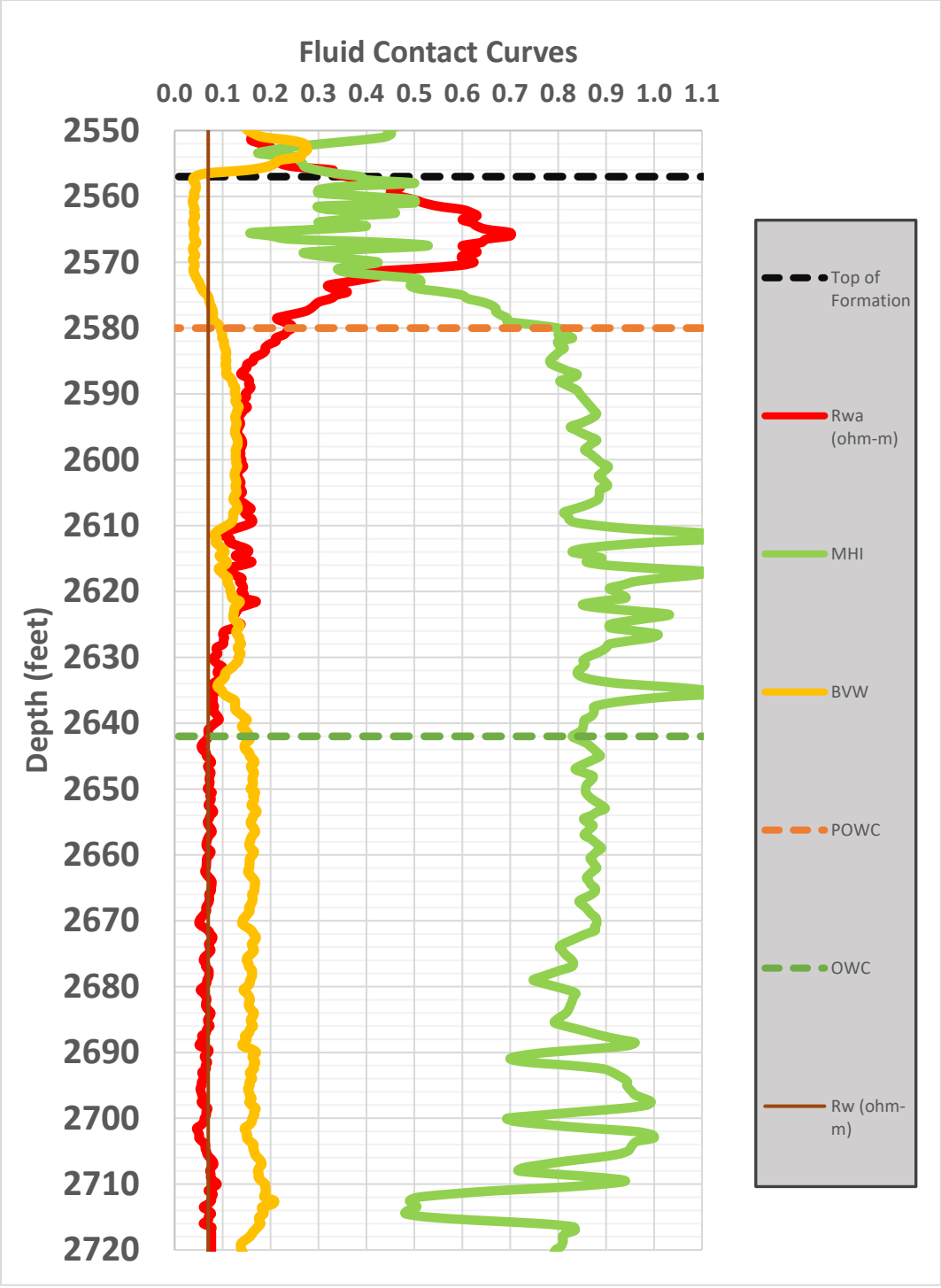


Figure 5-51. Idealized Fluid Contact Curves. Moveable hydrocarbon index (solid green line), R_{WA} (solid red line), and BVW (solid orange line) curves plotted against depth. The POWC (dashed orange line), top and base of the ROZ (dashed red and blue lines), and OWC (dashed green line) are the same depths from Figure 4.1. BVW is low and constant within the MPZ and increases to the value of porosity as water saturation increases. MHI is less than 0.7 in the MPZ and increases to greater than 0.7 where there is no moveable hydrocarbon (in the ROZ and 100% S_W zone). R_{WA} is very high in the MPZ, decreases and stabilizes in the ROZ, and decreases again before stabilizing at the true R_W in the 100% S_W zone. This behavior can be used to aid in selection of POWC and OWC.

Drill Stem Test

A drill stem test (DST) was conducted on the Cypress ROZ. A DST is a pressure transient test used to estimate reservoir properties prior to well completion. The Cypress ROZ is separated hydraulically from the overlying MPZ and underlying brine aquifer by dense calcite cements. Drilling stopped approximately 5 ft above the lower calcite cement and a packer was set against the upper calcite cement so that the DST tool would open in the ROZ only (Figure 5-48). By isolating the ROZ, the test was designed to determine whether there was mobile oil in the ROZ. Fluid samples were collected from the DST sample chamber and in different portions of the drill string.

Fluids

Fluids collected from the DST were analyzed for resistivity and composition. Resistivity was measured using a Western Atlas International Core Laboratories resistivity cell and a GenRad 1689M. The Illinois State Water Survey conducted analyses to determine the cations, anions, pH, alkalinity, and TDS of the samples.

In mid-2021, the well was completed as an oil producer in the MPZ of the Cypress Sandstone and an oil sample was collected. A Mettler Toledo Density Meter Densito (sn C121827019) was used to determine the density of the oil and a Viscolite 700, model VL7-100B-d15-TS [M2.0] was used to measure the viscosity.

Results

Bloodhound

The Bloodhound gas detector generally indicated gas levels elevated above background readings within each of the hydrocarbon bearing formations, including the Cypress Sandstone, Aux Vases Formation, Ste. Genevieve Limestone, St. Louis Limestone, Salem Limestone, and the upper part of the Ullin Limestone (Figure 5-50). Above the Ste. Genevieve Limestone, elevated hydrocarbon gas readings occurred generally within the Cypress Sandstone and Aux Vases Formation. However, from the Ste. Genevieve Limestone to the total depth of the well, elevated gas readings were noted throughout. This may be evidence of either a pervasive natural fracture system allowing gases to escape throughout the carbonate succession, or the localized generation of hydrocarbon gasses due to the inclusion of carbonaceous material within the rocks.

Within the Cypress sandstone itself, the highest hydrocarbon gas readings occur within and just below the ROZ (Figure 5-51). It is possible that gases were held in these zones and prevented from migrating upwards due to the impermeable carbonate cements associated with the ROZ.

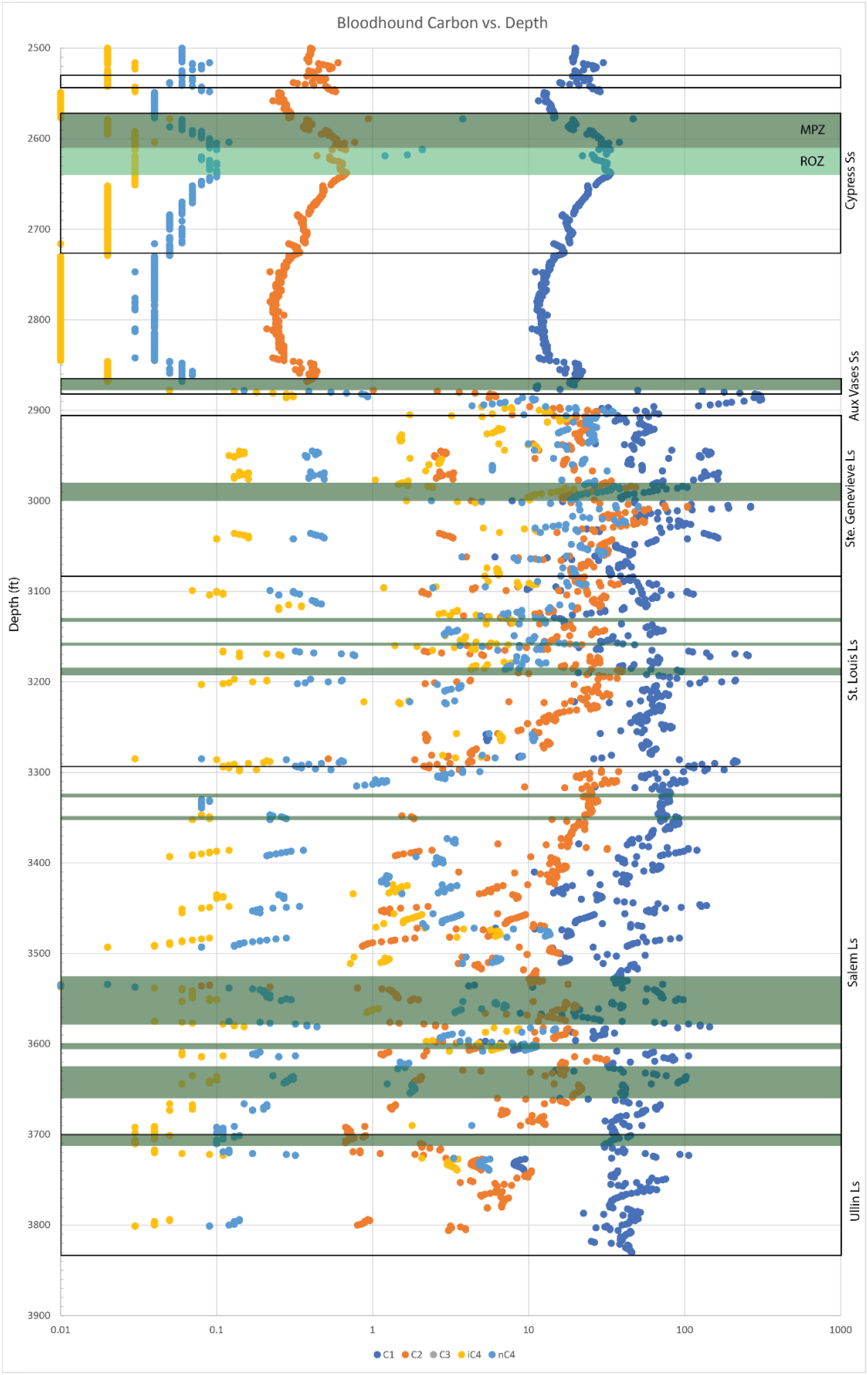


Figure 5-52. Depth graph of total gas data (C1 to iC4 / nC4) from the Bloodhound gas detector. Green shaded areas indicate zones with oil shows as indicated from drill cuttings and log analyses. Formation names are labeled on the right.

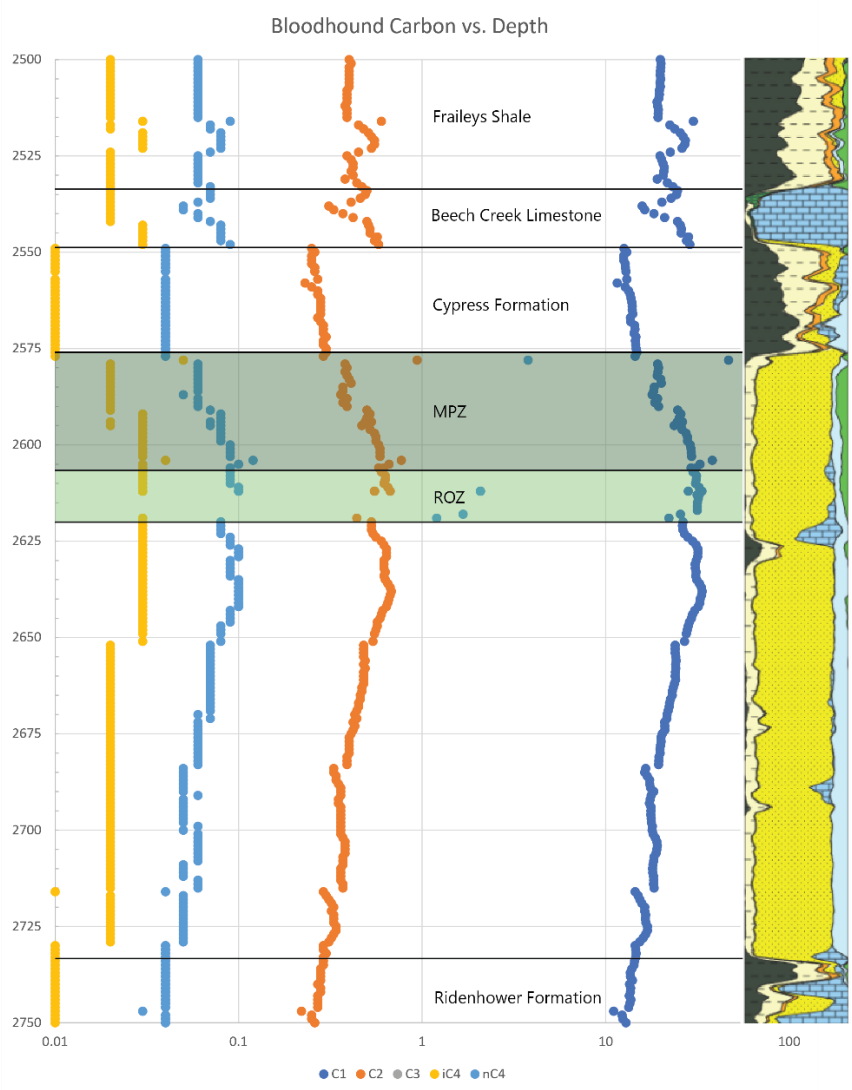


Figure 5-53. Depth graph of total gas data (C1 to iC4 / nC4) from the Bloodhound gas detector through the Cypress Formation. Green shaded areas indicate the MPZ and ROZ within the thick sandstone. zones with oil shows as indicated from drill cuttings and log analyses. Formation names are labeled and graphic QELAN column is shown on the right.

Core Analysis

Within the Cypress Sandstone, identifying and quantifying oil saturation in the ROZ was the key objective of the coring. As such, it was important to take measures to preserve the in-situ saturation of the core.

The Winter #10 research well provided a rare opportunity to collect core through the Fraileys Shale and Barlow Limestone, the seal system for the Cypress Sandstone. These units occur in outcrop, but there are no known cores for the two units in the basin interior. The new core provides material with which to characterize mineralogy, organic content, and the ability of the formations to hold a CO_2 column of given height.

Table 5-6 shows the 1” core plug data from the Winter #10 core. The plug samples were partially dried, so water saturation values are not reported. Oil saturation is reported with respect to pore volume based on the measured amount of oil removed during dean stark extraction.

Task 3.2 in the project SOPO is concerned with characterizing overlying seals within the ROZ fairways.

Table 5-8.

	Horizontal Plugs				Vertical Plugs						
Sample Depth (ft)	Porosity (%)	Klinkenberg Permeability (mD)	Residual Oil (%)	Residual Oil (g)	Porosity (%)	Klinkenberg Permeability (mD)	Residual Oil (%)	Residual Oil (g)	V vs H Porosity (% difference)	V:H Perm	
2578.9	22.5	529.4	16.2%	0.539	21.3	501.9	15.6%	0.559	6%	95%	MPZ
2580.9	18.7	259.2	24.4%	1.314	18.3	96.2	22.5%	0.804	2%	37%	
2581.9	20.2	477.6	17.0%	0.614	19.4	31.5	17.9%	0.576	4%	7%	
2582.9	20.9	548.4	16.7%	0.707	20.5	257.5	18.5%	0.786	2%	47%	
2583.9	19.1	292.4	23.9%	0.905	18.3	84.3	23.4%	0.845	4%	29%	
2584.9	17.9	525.0	23.4%	0.826	18.5	150.2	24.5%	0.684	3%	29%	
2585.9					19.4	286.8	19.4%	0.478			
2587.9	20.9	706.0	18.8%	0.770	22.3	901.2	16.8%	0.319	6%	128%	
2588.9	20.9	646.8	19.5%	0.658	20.3	411.5	18.7%	0.733	3%	64%	
2594.9	19.5	655.1	17.2%	0.635	19.8	501.2	18.0%	0.742	1%	77%	
2595.9	19.2	397.1	20.0%	0.750	18.9	87.0	19.5%	0.697	2%	22%	
2596.9	18.6	410.9	21.2%	0.751	19.3	134.2	18.5%	0.644	4%	33%	
2597.9	18.8	435.9	22.3%	0.763	17.7	64.6	19.5%	0.671	6%	15%	
2598.9	19.5	519.7	18.0%	0.610	18.2	372.8	17.1%	0.355	7%	72%	
2599.9	15.5	250.8	0.2%	0.004	20.5	210.8	92.4%	1.220	28%	84%	ROZ
2600.9	18.5	347.2	40.3%	1.262	16.5	58.1	19.3%	0.641	12%	17%	
2601.9	16.4	292.7	25.9%	0.721	16.0	139.8	25.6%	0.815	2%	48%	
2602.9	19.0	363.0	37.8%	1.198	18.1	260.2	24.3%	0.870	5%	72%	
2604.9	16.6	88.2	33.1%	1.145	16.5	267.8	28.1%	0.985	1%	304%	
2605.9	18.3	286.0	26.1%	0.787	17.6	26.7	26.3%	0.267	4%	9%	
2606.9	20.4	293.5	31.6%	1.286	19.9	242.0	21.4%	0.789	3%	82%	
2607.9	16.5	148.4	23.5%	0.726	15.6	22.9	0.8%	0.023	5%	15%	
2608.9	20.3	252.0	28.6%	1.056	18.7	101.3	14.8%	0.577	8%	40%	
2609.9	18.4	130.0	20.5%	0.692	19.0	58.4	0.8%	0.029	3%	45%	
2610.9	16.7	180.8	7.3%	0.200	15.9	15.1	0.9%	0.020	5%	8%	

Log Analysis

Thick Cypress

The massive Cypress is a very clean sandstone and consists of ~90% quartz with <10% clay, except for two thin limestone layers at ~2625 and ~2685 (Figure 5-54). These limestone layers are believed to be calcite cement that forms at the oil water contact.

Spectral Gamma Ray reveals that the upper Cypress is ~90% shale composed of ~50% illite and ~50% kaolinite, but the clay within the thick Cypress is mostly kaolinite with almost no illite. The upper Cypress is a convenient, and often used, pick for a shale baseline, so the difference in clay composition between the upper and thick Cypress could have important ramifications for shaly sand calculations, which assume that the clay distributed throughout the target formation has the same properties as the clay in the shale baseline. Spectral gamma ray also shows high proportion of Uranium directly beneath the calcite layer. The ELAN analysis interprets this as shale, but resistivity and microlog separation suggest good permeability and neutron-density porosity suggests clean sand, so this is believed to be caused by uranium in the water trapped beneath the impermeable calcite layer.

Illite is more radioactive than kaolinite and creates a higher gamma ray response, so using the gamma ray (GR) deflection in the upper Cypress as the shale baseline will result in a GR derived volume of shale (Vshale) that underestimates the true volume of clay in the thick Cypress. However, kaolinite also has a very low cation exchange capacity (CEC) and associated propensity for brine double layer, which reduces the properties (microporosity and excess conductivity) that shaly sand techniques are used to compensate for. Despite the problems with the shale baseline, the low proportion of kaolinite rich clay suggests that Archie's equation will do a good job of approximating S_W.

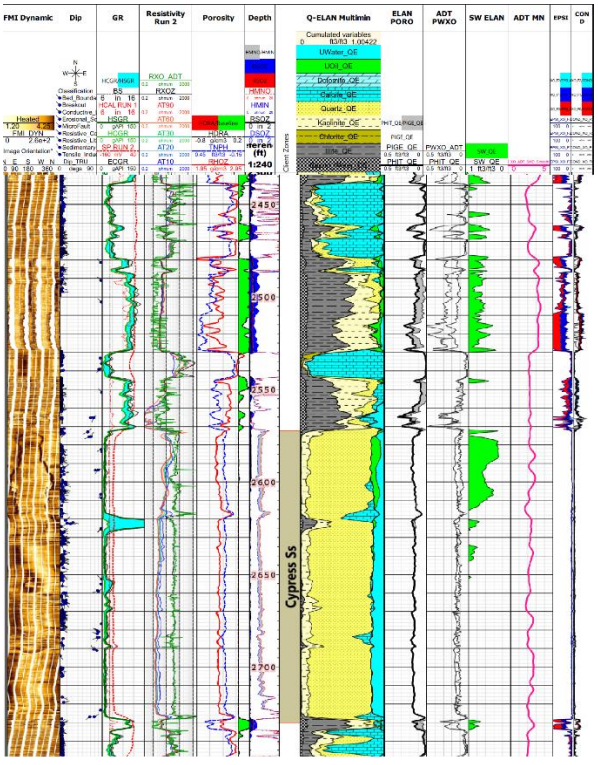


Figure 5-54. Composite log for the thick Cypress Sandstone in the Carrie Winter #10 well.

Density porosity based on a sandstone matrix (density of 2.65 g/cc), neutron porosity corrected for a sandstone matrix, and cross plotted porosity all overlay (Figure 5-55). This suggests that the influence of clay is negligible. Porosity is 15-20% throughout the thick Cypress. Core derived porosity compares well with neutron-density porosity despite having more scatter.

Sonic porosity is significantly greater than the neutron-density porosity in the upper oil-bearing portion of the Cypress, increases to ~37% for 20 feet at the calcite layer before dropping to negative three for 15 feet before rebounding and behaving as expected.

The deep and medium resistivity curves increase above the shallow resistivity curve between 2600-2610 ft (Figure 5-56). The cause of this behavior is unknown. The spike at 2612 ft coincides with the impermeable calcite cement layer. A vertical fracture extending from the calcite layer at 2620 ft to the top of the Cypress, observed in the FMI log and core, could be a potential explanation.

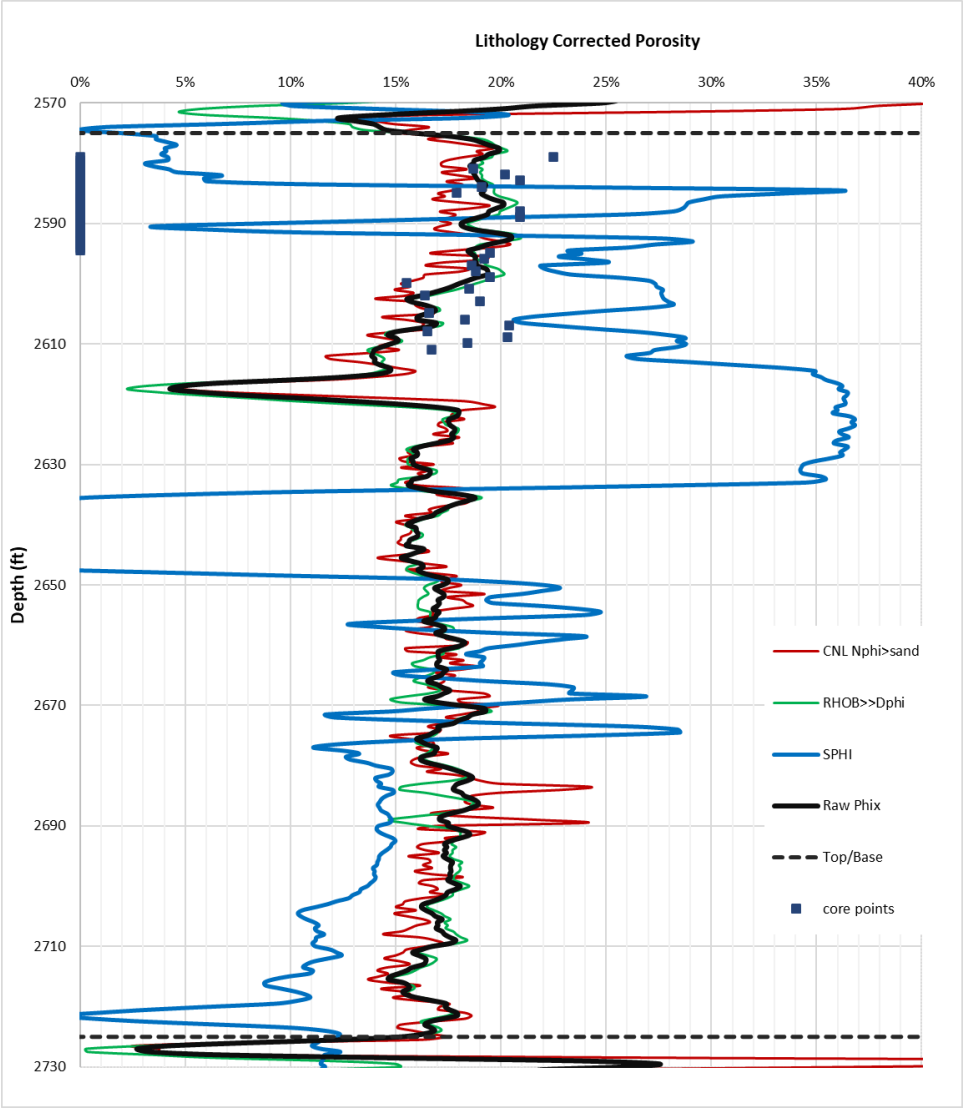


Figure 5-55. Porosity logs for the Cypress in the Carrie Winter #10 well. Neutron porosity corrected for a sandstone matrix shown with red line, density porosity derived from bulk density assuming a matrix density of 2.65 g/cc shown with green line, sonic porosity shown with blue line, and cross plotted porosity shown with black line. Core derived porosity shown with blue squares.

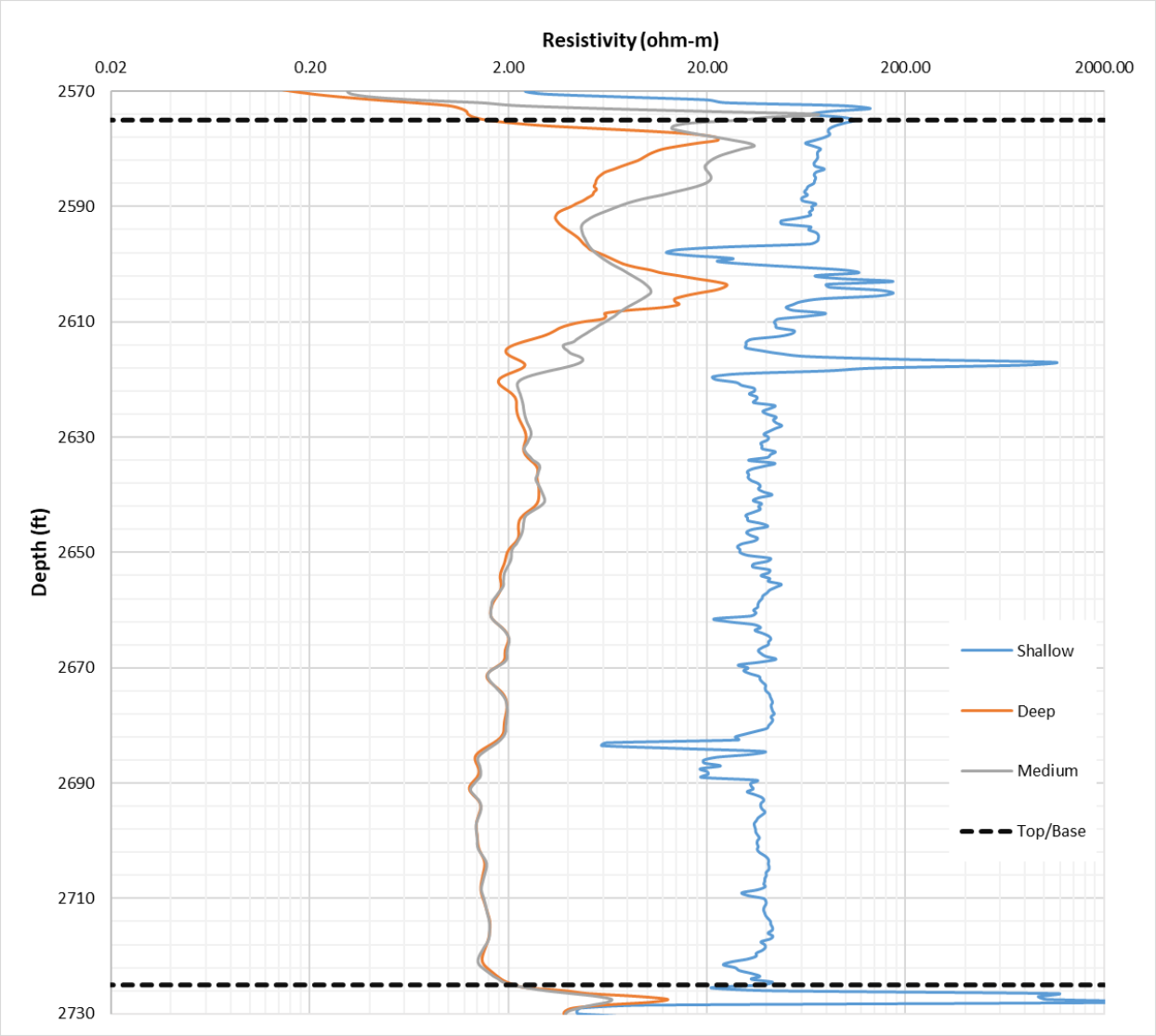


Figure 5-56. Resistivity in the Cypress sandstone in the Carrie Winter #10 well. Deep resistivity shown with orange line, medium resistivity shown with grey line, and shallow resistivity shown with blue line.

The ELAN analysis shows an S_W profile in the Cypress (Figure 5-54) that is indicative of a brownfield ROZ (Figure 5-50). The top ~15 feet of the formation has ~ 65% oil saturation, which is underlain by 25 feet of ~20% oil saturation. Most of this oil occurs above the limestone layer at 2620 ft, but isolated intervals of low oil saturation (~10-20%) were detected down to the depth of 2654 ft. This interpretation suggests that the POWC is at ~2590 ft and the OWC coincides with the limestone layer at 2616 ft.

The spike in resistivity at 2600-2610 ft causes S_W profiles based on Archie and Dual Water calculations to deviate from the expected behavior (Figure 5-57). This complicates the selection of the POWC and ROZ S_O, but the OWC is still apparent. Strict interpretation of the fluid contact curves puts immobile oil the uppermost Cypress that is underlain by and interval of mobile oil from 2595-2614 ft. This interpretation is supported by S_O observed in the core analysis (core derived S_O is higher between 2600-2610 ft than 2580-2600 ft) but doesn't match the conceptual understanding of ROZs.

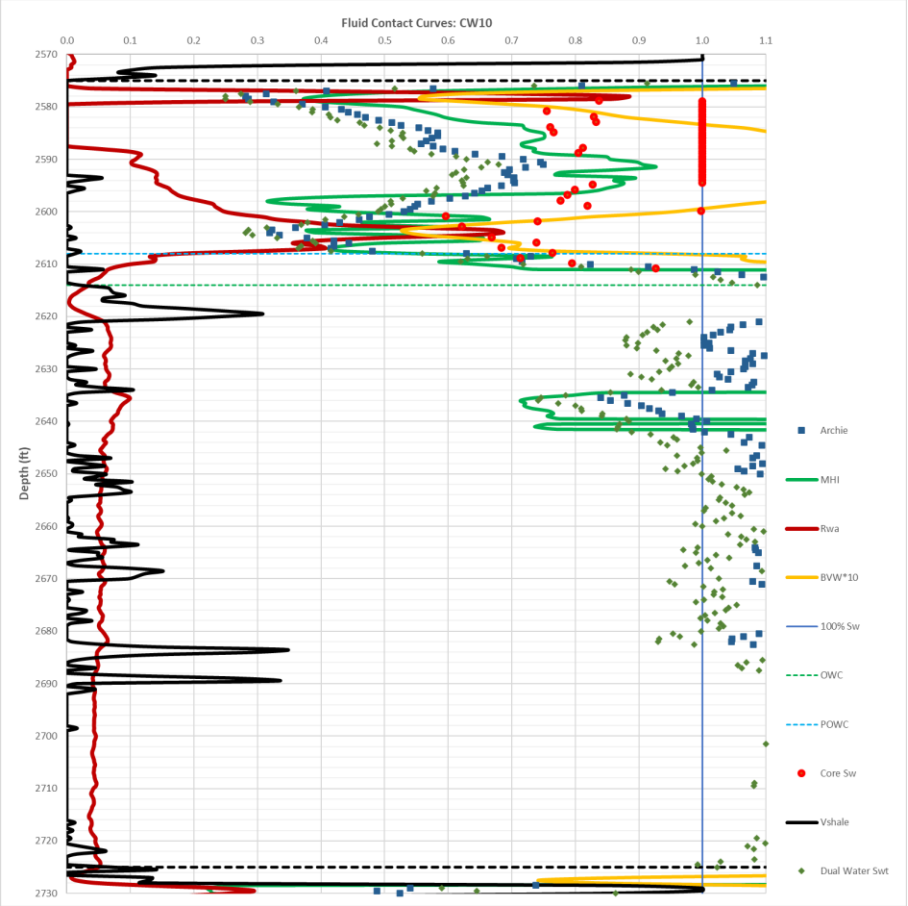


*Figure 5-57. Fluid Contact Curves for the Cypress in the Carrie Winter #10 well. Archie derived S_W shown with blue dots, Dual Water S_W shown with green dots, MHI shown with green line, BVW *10 shown with yellow line, R_{WA} shown with red line, and GR derived Vshale shown with black line.*

The Cypress rock properties were largely the same in all of the wells in the Carrie Winter lease. Porosity is ~20%, deep resistivity in aquifer is ~1.2 ohm-m, and GR ~15 API. All the other Carrie Winter wells have a calcite cement layer at the OWC, but none of the other wells have the anomalous spike in resistivity above the calcite observed in the Carrie Winter #10 well, nor did they have the spike in GR beneath the calcite cement layer. The cleaner resistivity curve creates Sw profiles indicative of brownfield ROZs in all the other Carrie Winter wells. The OWC is within three feet and S_O stabilizes at ~25% between the POWC and OWC in all wells (Table 5-9).

Table 5-9. Fluid contacts and residual oil saturation of four wells in the Carrie Winter lease.

	POWC (ft)	**OWC (ft)**	**ROZ S_O**
CW3	-2105	-2137	25
CW4	-2110	-2134	30
CW6	-2106	-2134	25
CW7	-2114	-2135	25

Aux Vases

The Aux Vases is a complicated mixture of sandstone, limestone, and shale. ELAN analysis predicts that the whole sand interval has 40% S_O (Figure 5-58).

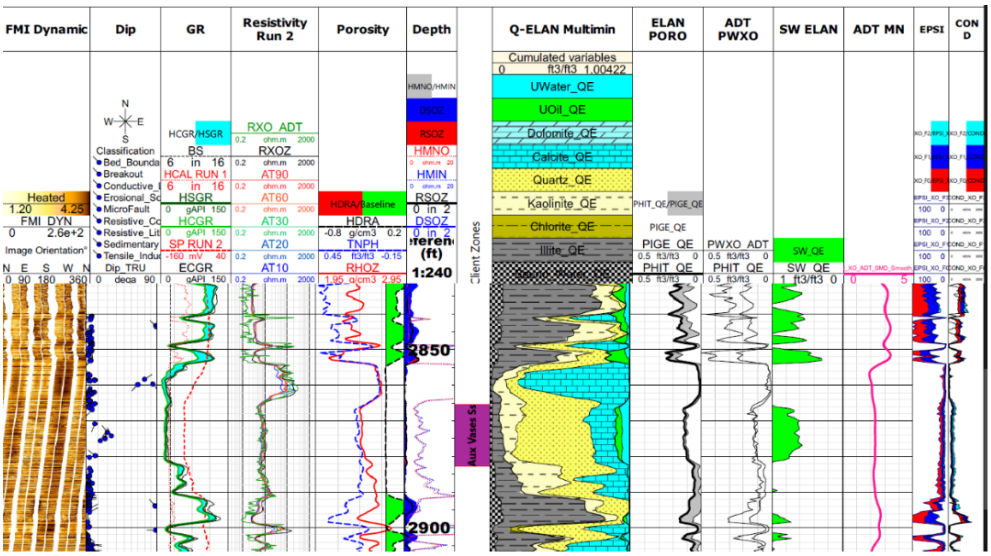


Figure 5-58. Composite log for the Aux Vases in the Carrie Winter #10 well

The Aux Vases is difficult to characterize with traditional well logs. The complex lithology creates uncertainty in porosity and R_W unknown without underlying aquifer to estimate via R_{Wa}. Uncertainty in these input parameters makes oil saturation difficult to quantify, but MHI in each of the other Carrie Winter wells is >0.7, which suggests that none of the oil is mobile. This is supported by the drill stem test in the nearby Carrie Winter # 7 well that determined that the interval of greatest S_O was uneconomic (Figure 5-59).

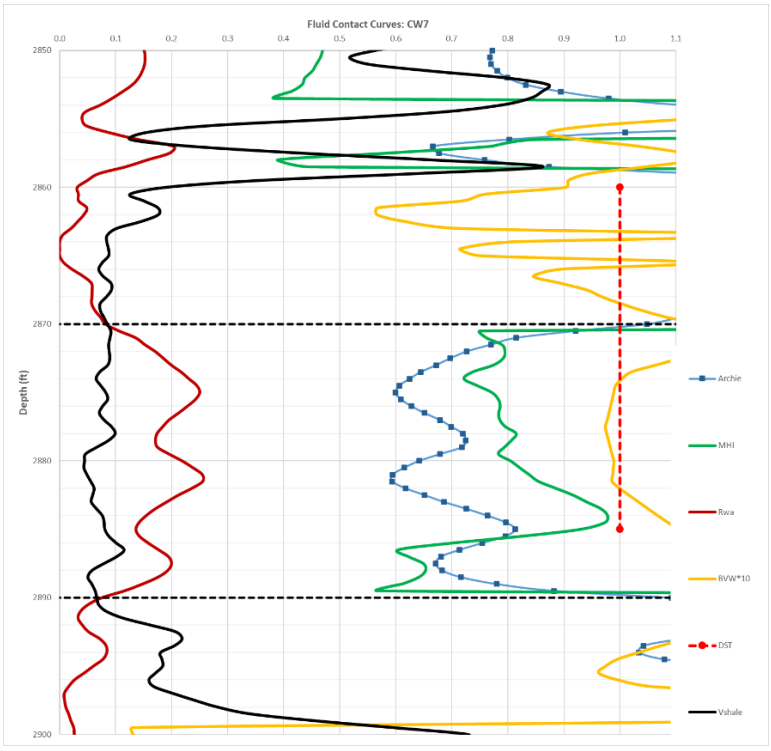


*Figure 5-59. Fluid Contact Curves in the Carrie Winter #7 Aux Vases. Archie derived SW shown with blue line, MHI shown with green line, BVW *10 shown with yellow line, RWA shown with red line, and GR derived Vshale shown with black line. Oil saturation is ~40% in the porous portion of the Aux Vases (isolated by black dashed lines). A drill stem test from 2860-2885 ft deemed the oil uneconomic and MHI is >0.7, which suggests that the oil is not mobile.*

Ste. Gen/McClosky

The McCloksy member of the Ste. Gen is productive throughout the field, but ELAN analysis only puts <40% S_O in a two-to-three-foot porous interval near the top (Figure 5-60). Fluid contact curves based on the traditional logs agrees with this interpretation (Figure 5-61). It predicts ~30% S_O from 2989 to 2991.5 ft. MHI never gets below 0.8 so it is deemed non-productive.

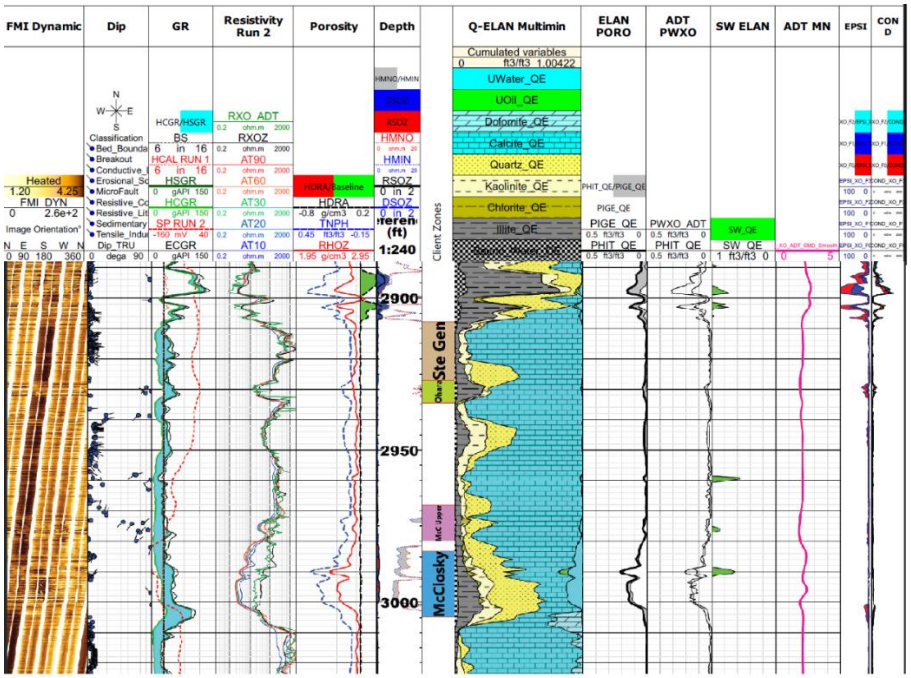


Figure 5-60. Composite log for the McClosky in the Carrie Winter #10 well

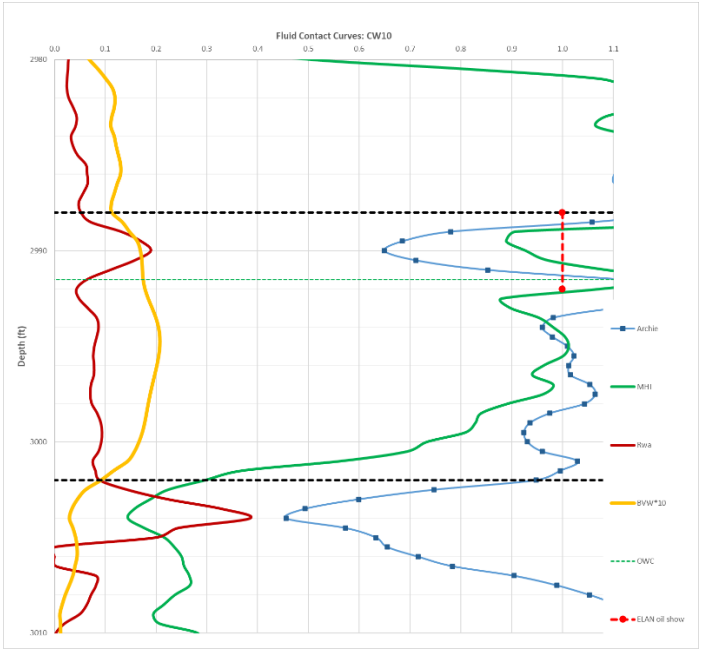


*Figure 5-61. Fluid contact curves for the McClosky in the Carrie Winter #10 well. Archie derived S_W shown with blue line, MHI shown with green line, BVW *10 shown with yellow line, RWA shown with red line, and GR derived Vshale shown with black line. There is only three feet of S_O in the McClosky and MHI>0.7 suggests that it is not mobile.*

The Carrie Winter #4 and #6 wells both produced oil from the McClosky. The Carrie Winter #4 was perforated from 2984 to 2991 and had an initial production (IP) of 11 bbls of oil and 0 water. Analysis of Carrie Winter #4 shows 13 feet of S_O within the perforated interval, five feet of which is believed to be mobile (~ 60% S_O and MHI <0.7) (Figure 5-62).

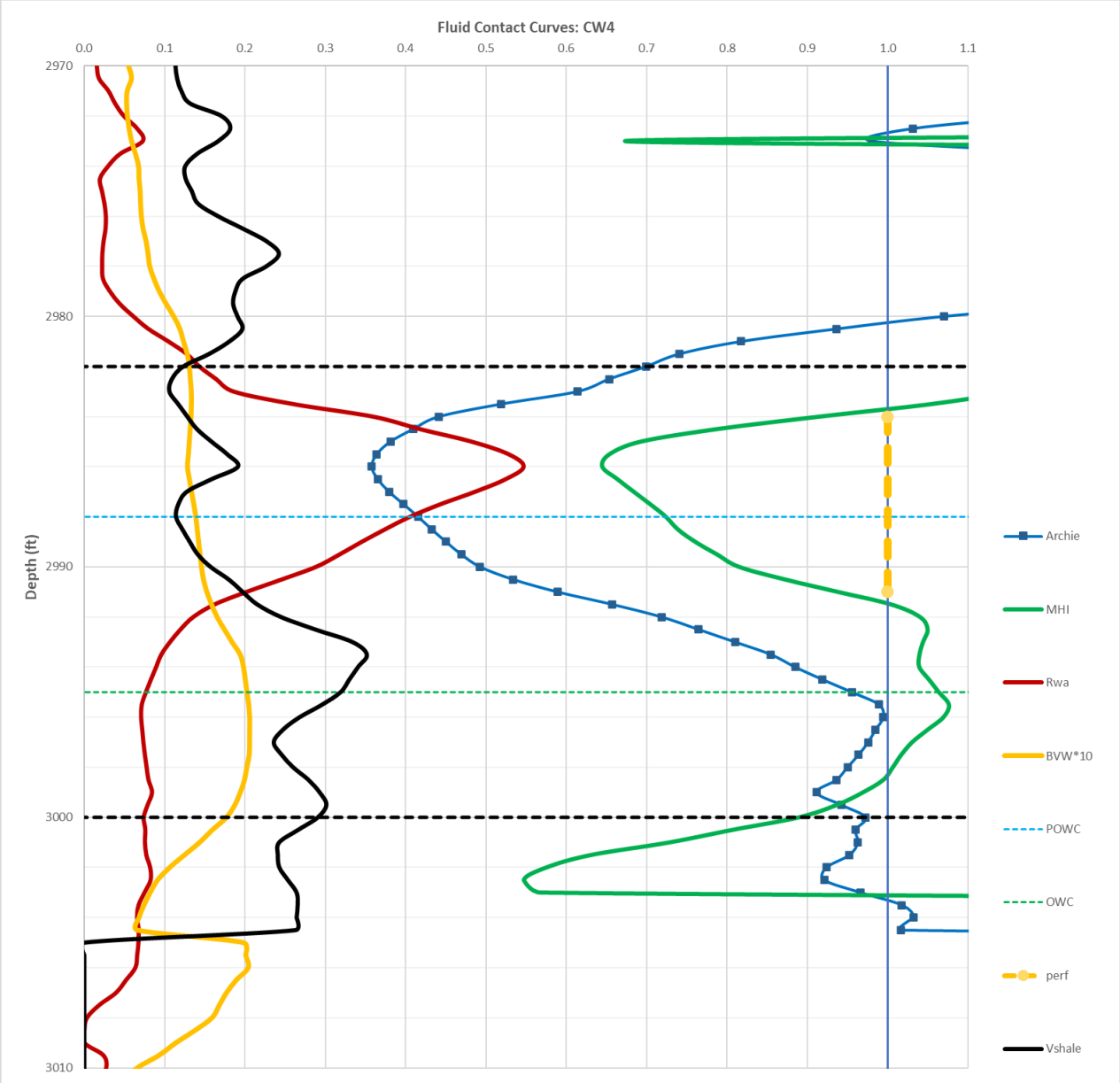


*Figure 5-62. Fluid Contact Curves for the McClosky in the Carrie Winter #4 well. Archie derived S_W shown with blue line, MHI shown with green line, BVW *10 shown with yellow line, RWA shown with red line, and GR derived Vshale shown with black line. Interval from 2984 to 2991 ft was perforated and had an initial production (IP) of 11 bbls of oil and 0 bbls of water. This interval corresponds to a S_O of 50-60% and MHI<0.7.*

St. Louis

St. Louis is mostly nonporous limestone, but the reservoirs occur within three dolomitized units that are typically 5-10% porosity. ELAN analysis identifies ~40% oil saturation in the lower two of these three dolomitic intervals (Figure 5-63).

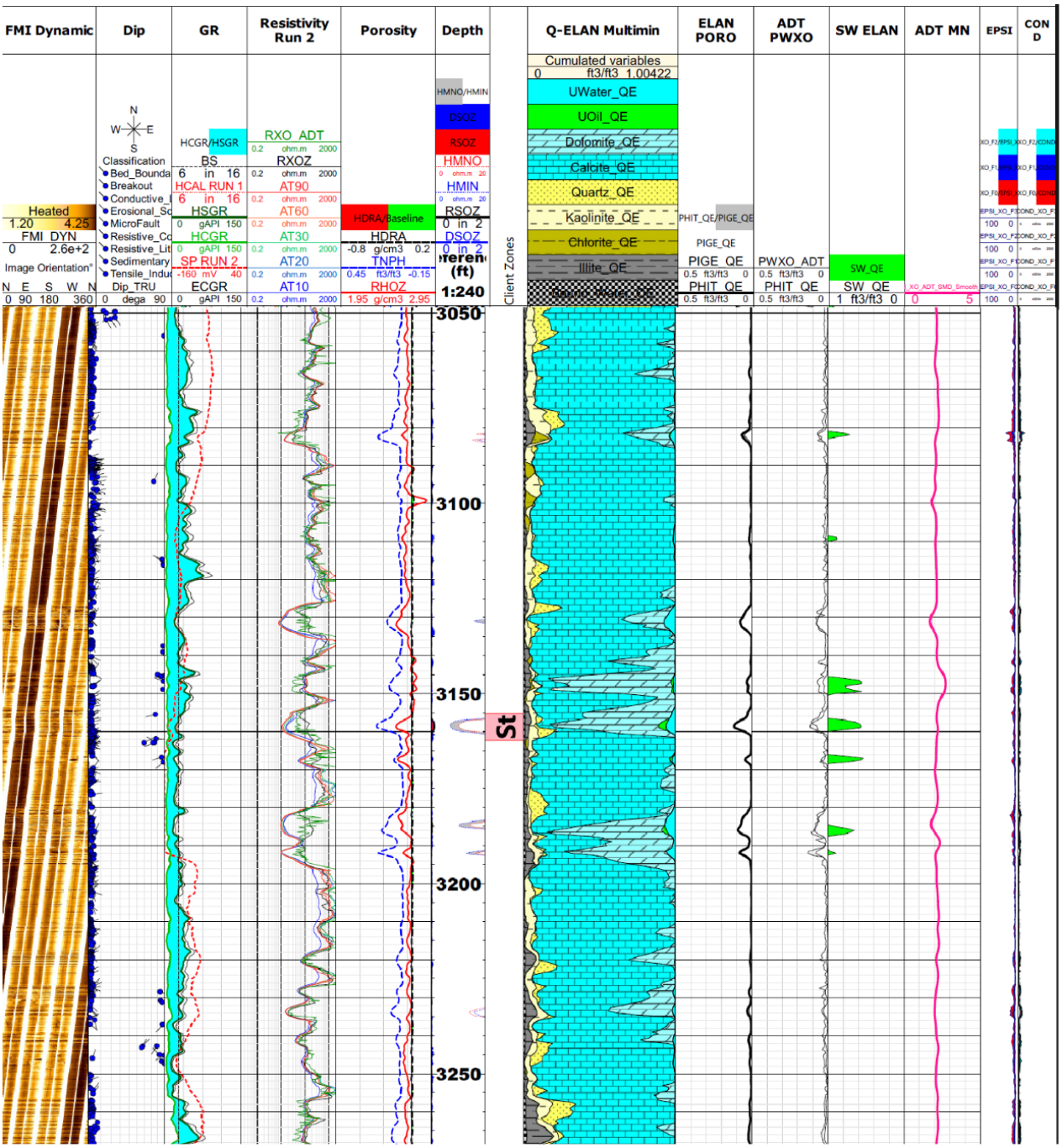


Figure 5-63. Composite log for the St. Louis in the Carrie Winter #10 well.

Analysis of the traditional logs was conducted by using neutron porosity and then applying a 5% porosity cutoff over the whole St. Louis interval (Figure 5-64). This produces the same S_O as the ELAN analysis except in two places; immobile oil occurs in the porous interval at 3130-3135 ft but 3145-3150 ft is below the porosity cutoff and masked. The interval at 3130-3135 ft is mostly limestone and slightly dolomitic, so calculated S_O is believed to be caused by the neutron log underestimating porosity. The MHI within the oil-bearing intervals is near the 0.7 cutoff. It is likely that these intervals contain mobile interval but are too thin for the resistivity logs to reach their true values.

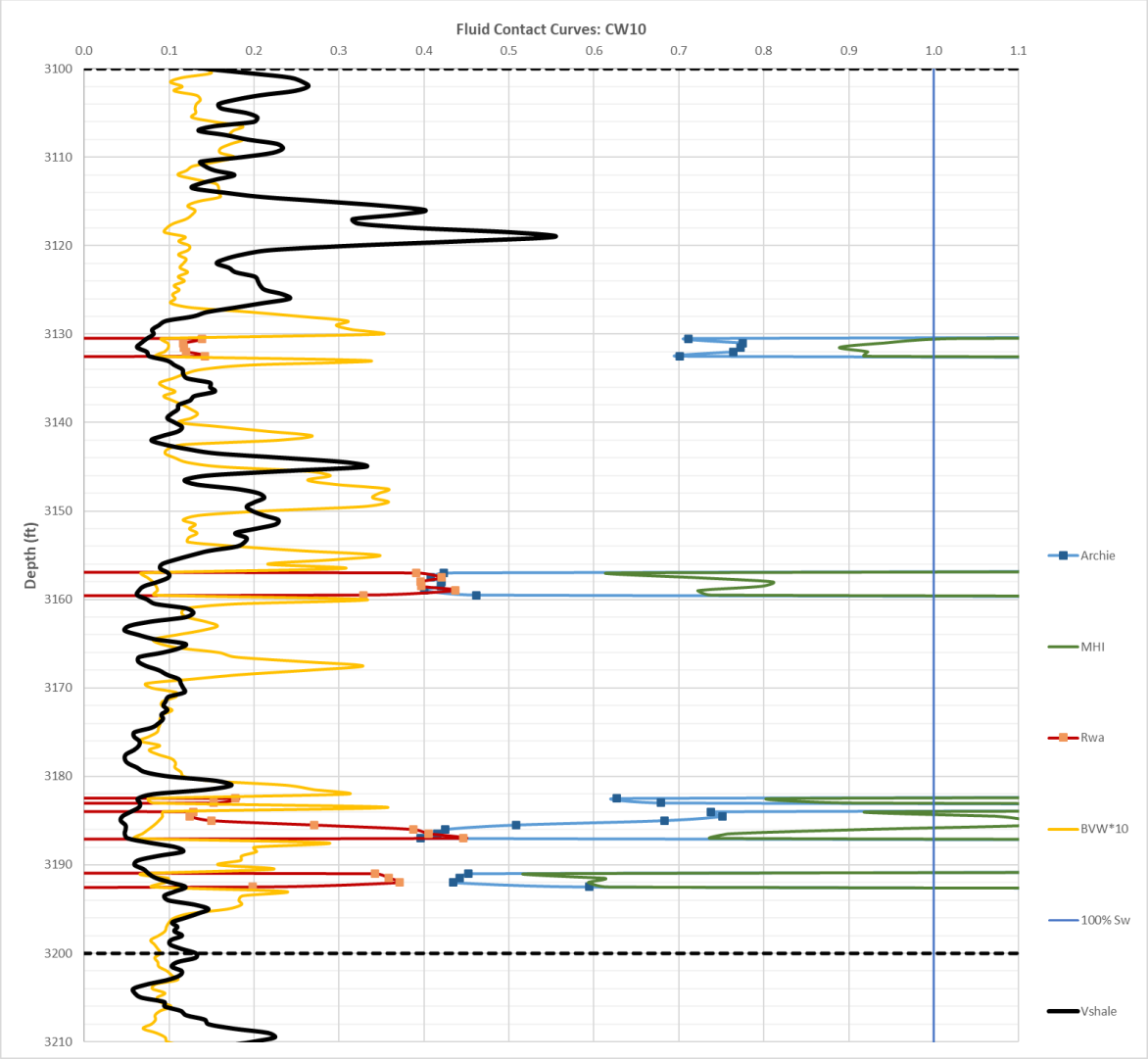


*Figure 5-64. Fluid Contact Curves for the St. Louis in the Carrie Winter #10 well. Archie derived S_W shown with blue line, MHI shown with green line, BVW *10 shown with yellow line, R_{WA} shown with red line, and GR derived Vshale shown with black line.*

Carrie Winter #7 is a St. Louis producer. It was perforated from 3161-3169 ft and had an IP of 12 bbls oil and 50 bbls water. Fluid contact curve analysis based on the same input parameters detects mobile oil in Carrie Winter #7 and not in Carrie Winter #10. The perforated interval in Carrie Winter #7 has 20-40% S_O and MHI< 0.7 (Figure 5-65). MHI also suggests that the lower interval also has productive oil, but it is under 10% porosity, so it may not be economic.

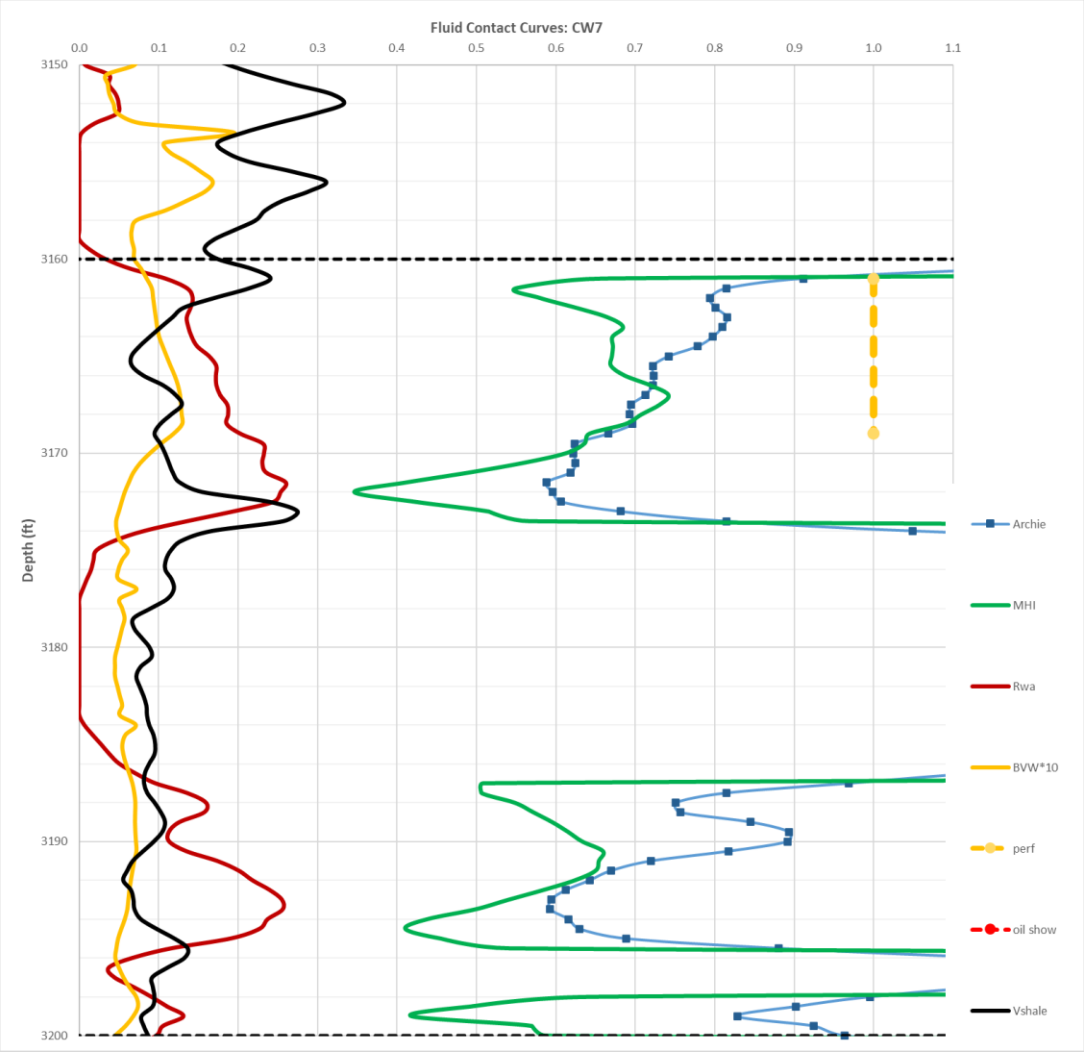


*Figure 5-65. Fluid Contact Curves for the St. Louis in the Carrie Winter #7 well. Archie derived S_W shown with blue line, MHI shown with green line, BVW *10 shown with yellow line, RWA shown with red line, and GR derived Vshale shown with black line. Interval from 2984 to 2991 ft was perforated and had an initial production (IP) of 11 bbls of oil and 0 bbls of water. This interval corresponds to a S_O of 30-40% and MHI<0.7.*

Salem

Salem is a very thick (~400 ft) limestone unit with multiple oil-bearing intervals. ELAN puts oil in most of the porous intervals (Figure 5-66). The highest concentration of S_O occurs in the basal 15 feet, but an interval between 3460-3470 ft has the highest S_O. This interpretation generally matches expectations based on historical records from the field, as oil shows occur throughout the Salem, but the lower Salem is the interval most often targeted for oil production.

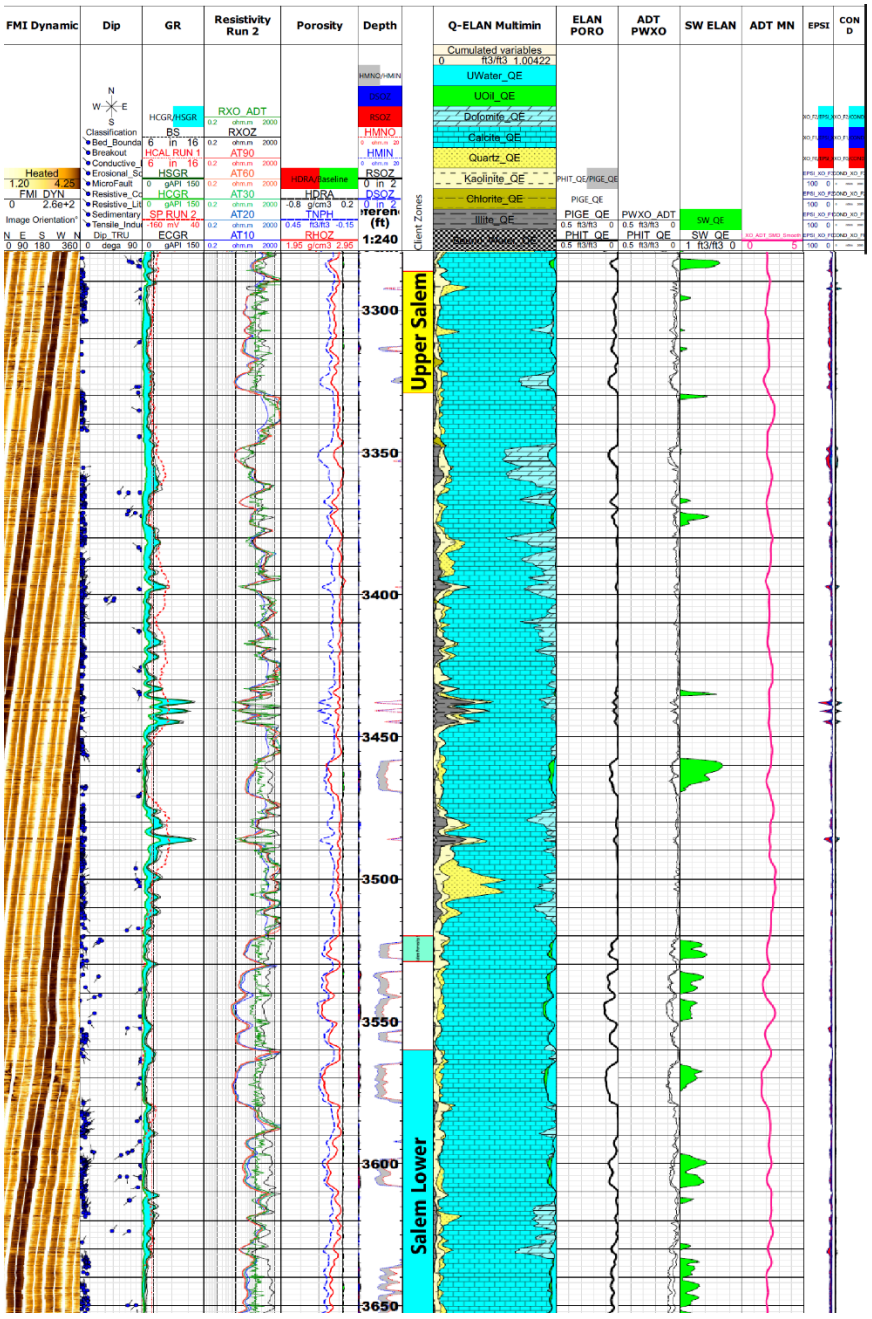


Figure 5-66. Composite log for the Salem in the Carrie Winter #10 well

Fluid contact curve calculations were conducted by assuming that the entire interval was limestone and applying a 5% porosity cutoff (Figure 5-67). Oil was detected in the same intervals as the ELAN analysis, but MHI shows that only the interval from 3460-3465 ft is mobile. A thin interval at ~3370 ft does get below the 0.7 MHI cutoff, but it occurs as a single data point within a dolomitic interval, so it may be erroneous. The lower Salem is typically productive, but analysis puts low S_O (~20-30%) and MHI well above the cutoff for mobile oil. It is likely this interval is depleted in Carrie Winter #10.



*Figure 5-67. Fluid Contact Curves for the Salem in the Carrie Winter #10 well. Archie derived S_W shown with blue line, MHI shown with green line, BVW *10 shown with yellow line, R_{WA} shown with red line.*

The uppermost porous interval of the lower Salem (3515-3525 ft) was perforated in the Carrie Winter #3 well and had an IP of 15 bbls oil/5bbls water. The scout ticket for the well also lists oil shows in four other intervals. Fluid contact curve analysis does a good job identifying these intervals (Figure 5-68). The perforated interval has the thickest interval below the MHI cutoff (~20 ft) and the highest S_O (~50%). Calculated S_O occurs in the intervals that had oil shows reported on the scout ticket. The intervals listed with very slight show of oil (vsso) on scout tickets have low S_O above the MHI cutoff, but the interval listed with a slight show of oil (sso) has ~40 S_O and appears to be mobile.

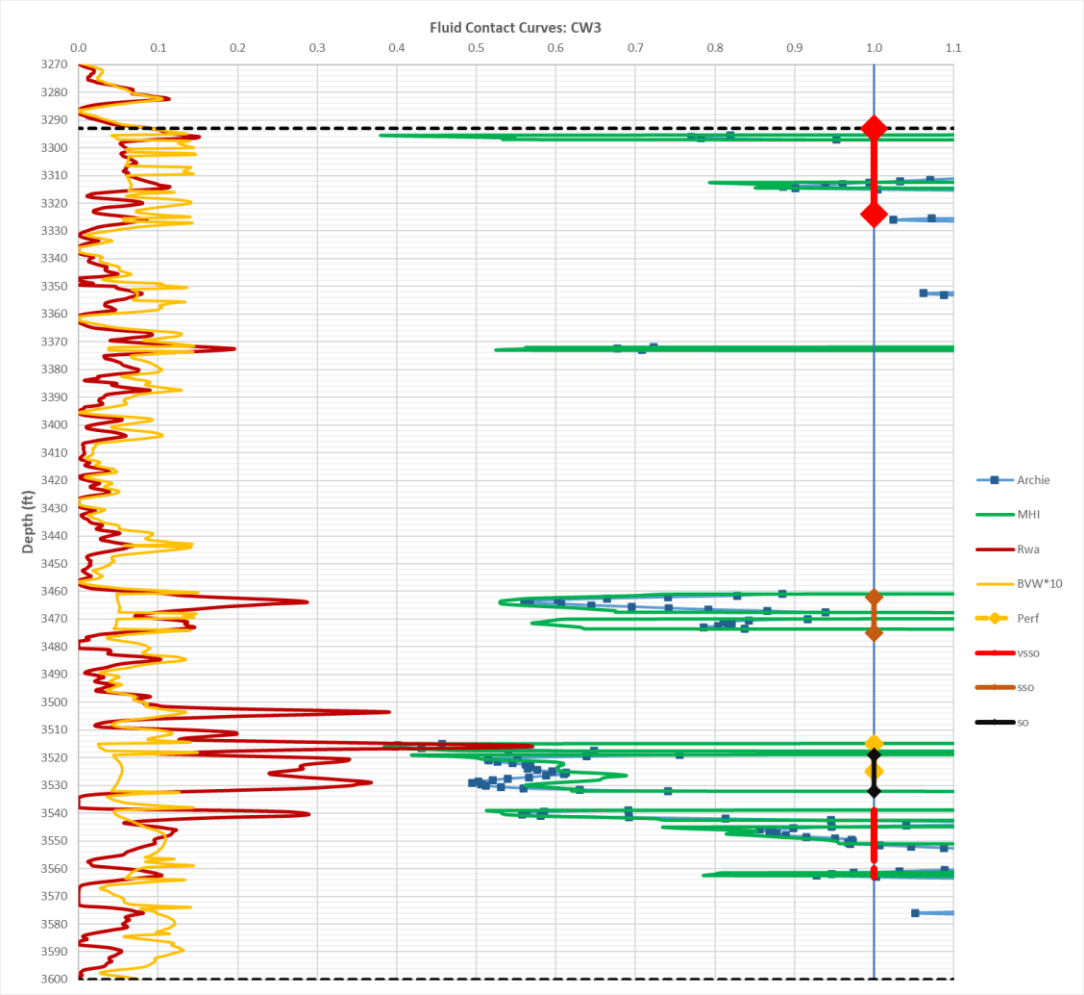


*Figure 5-68. Fluid Contact Curves for the Salem in the Carrie Winter #4 well. Archie derived S_W shown with blue line, MHI shown with green line, BVW *10 shown with yellow line, R_{WA} shown with red line. The well was perforated from 3515 to 3525 ft (yellow line) and had an IP of 15 bbls oil/5bbls water. Depths for Oil show (vertical black line), slight show of oil (vertical dark orange line), and very slight oil show (vertical red line) recorded on scout ticket also shown where x=1.*

Ullin

The Ullin is a pure limestone that can be split into thin upper and lower massive units. Oil in the Ullin is believed to only occur in the upper tens of feet, but ELAN analysis puts 20-40% S_O wherever the Ullin has porosity (Figure 5-69). This could be an indication of a historically overlooked ROZ in the lower Ullin. Independent analysis was conducted to support or refute this possibility.

The Ullin is the deepest of the oil-bearing intervals at Noble Field and thus has the worst data coverage. The only other well that reaches the Ullin in the Carrie Winter lease, Carrie Winter #3, only reaches the top ~10 feet, so interpretations of the lower Ullin are based entirely on the Carrie Winter #10 well.

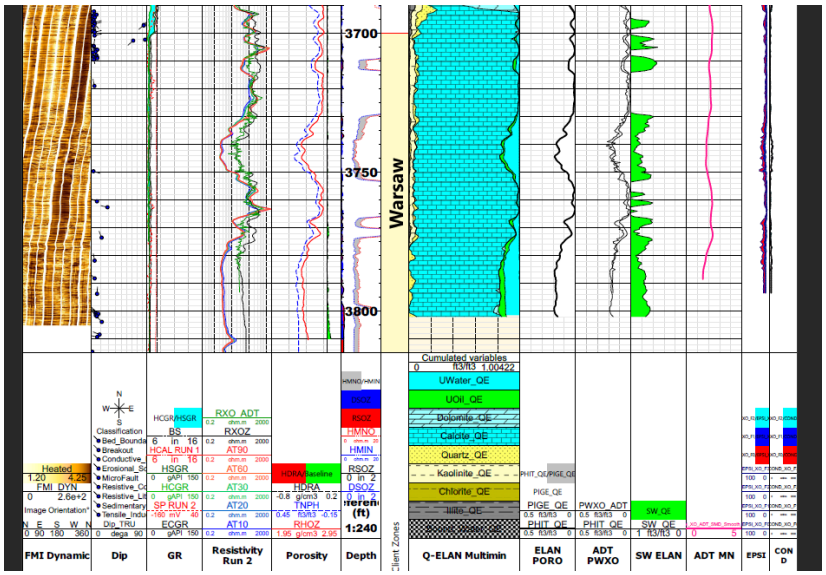


Figure 5-69. Composite log for the Ullin (Warsaw) in the Carrie Winter #10 well.

Interpretation of GR, porosity, and Pe logs suggests that the Ullin is a remarkably pure limestone. GR is ~ 10 API over the whole interval. Neutron, density, and cross plotted porosity all overlay over the whole Ullin. The crossplot of Pe and Bulk Density aligns perfectly with a limestone lithology (Figure 5-70). Binning the data by NPHI also matches porosity predicted by the bulk density.

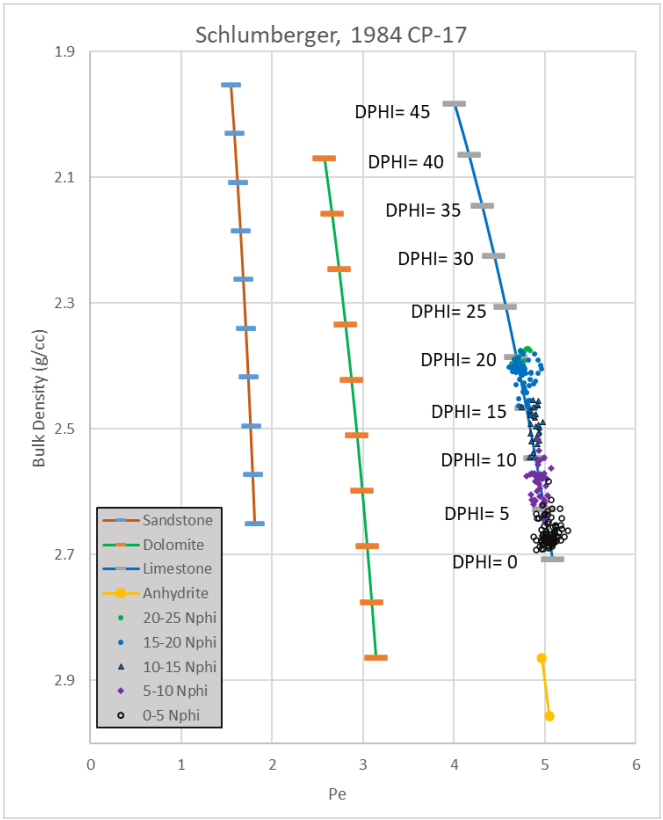


Figure 5-70. Cross plot of Pe and bulk density. Points are binned and colored by neutron porosity and align with the limestone lithology line.

All indications suggest that Ullin is pure limestone, so lithology isn't the cause of excess oil. Using an R_W of 0.09 and a porosity cutoff of 6% creates an alternative interpretation where 3710-3712 ft is the only oil-bearing interval (Figure 5-71). This matches historical observations, but water sample would be required to reduce uncertainty in R_W and discount the possibility of an ROZ.

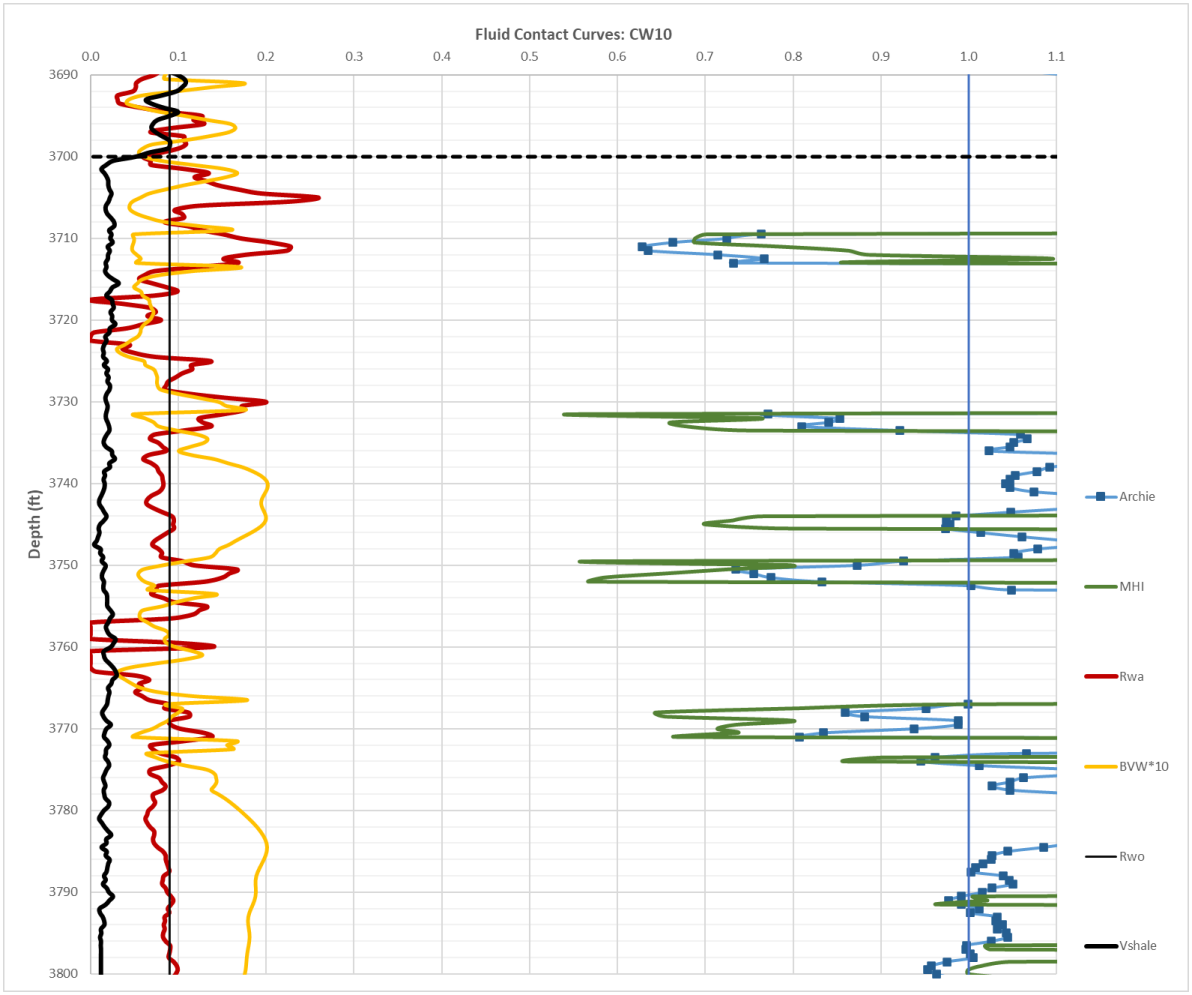


*Figure 5-71. Fluid Contact Curves for the Ullin in the Carrie Winter #10 well. Archie derived S_W shown with blue line, MHI shown with green line, BVW *10 shown with yellow line, R_{WA} shown with red line, and GR derived Vshale shown with thick black line.*

Drill Stem Test

The orange and gray data are the DST (lower gauges) and the blue is the VIT (upper gauge). The final flow period is between 4.7 and 4.9 hrs. The DST gauges saw pressure decrease of several 100 psi (off the bottom of the graph and data NOT shown). The VIT gauge shows a 5 psi decrease and then a buildup. Communication across the calcite layer could be the formation or in the wellbore (only if packer did not seal well.) Will work on estimate of Kv/kh between the gauges (i.e. across the calcite interval).

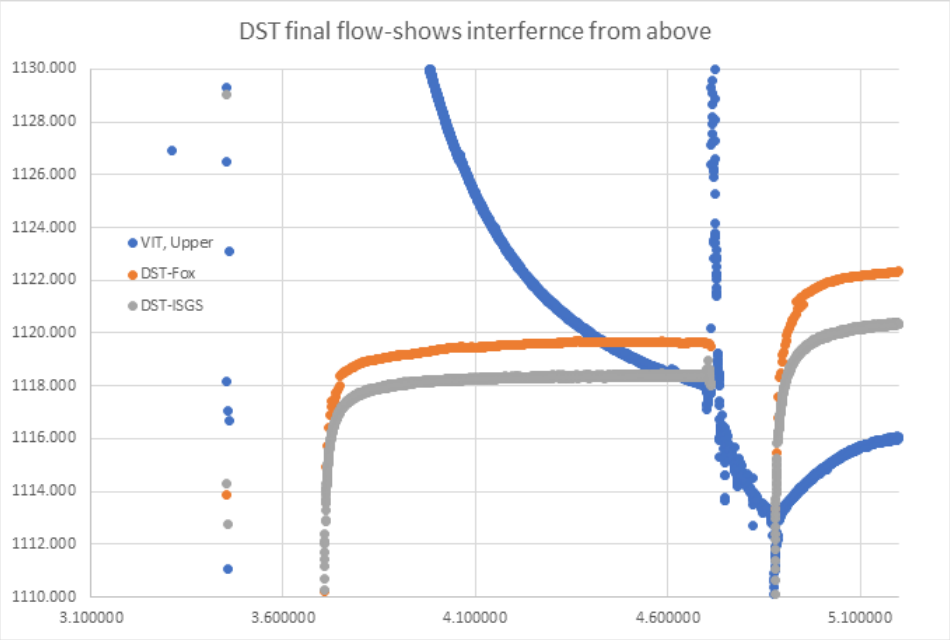


Figure 5-72.

Fluid

Four fluid samples were collected at the conclusion of the DST. Samples 1, 2, and 3, were collected when the drill string (top, middle, and bottom of the 1,260 ft fluid column, respectively). Sample 1 had a lot of mud and not enough water for all analyses (thus no TDS). Sample 4 was the sample from the DST sample chamber and thus, I would think, is most representative of the formation brine.

Water resistivity (Rw) of the brine, critical for accurate well log analysis, was measured at 0.074 ohm-m @ 90°F, consistent with past measurements.

Oil sample collected in August 2021 measured 33.8 API @60°F, 8.8 cP @60°F.

Table 5-10. Anion analysis conducted at the ISGS for Cypress brine samples from the John O. Coen #92 well (API 121592607500, Section 4, T3N, R9E) show a Cl^- concentration of 58,744.6 mg/L, a Br^- concentration of 460.2 mg/L and a SO_4^- concentration of 1,115.31 mg/L. Cation analysis for the same sample are listed in the following table.[1]

ICP analyses by the Illinois State Water Survey
Samples received: 1/15/2020
Samples analyzed: 1/24/2020
Report date: 1/27/2020
All concentrations are in mg/L

Sample name/#	Al	As	B	Ba	Be	Ca	Cd	Co	Cr	Cu
MDL:	**0.037**	**0.11**	**0.023**	**0.00085**	**0.00055**	**0.029**	**0.012**	**0.013**	**0.0058**	**0.0016**
Top	0.58	<1.1	3.31	1.54	<0.0055	1362	<0.12	<0.13	0.228	<0.016
Middle	0.47	<1.1	5.48	1.23	<0.0055	2022	<0.12	<0.13	0.346	<0.016
Bottom	<0.37	<1.1	6.40	0.625	<0.0055	2367	<0.12	<0.13	0.203	<0.016
DST	<0.37	<1.1	6.36	0.455	<0.0055	2378	<0.12	<0.13	<0.058	<0.016

Sample name/#	Fe	K	Li	Mg	Mn	Mo	Na	Ni	P	Pb
MDL:	**0.024**	**0.016**	**0.11**	**0.027**	**0.0015**	**0.022**	**0.036**	**0.043**	**0.073**	**0.041**
Top	0.31	145	6.4	746	0.832	<0.22	18391	<0.43	<0.73	<0.41
Middle	0.79	200	9.4	1065	1.87	<0.22	26731	<0.43	<0.73	0.42
Bottom	<0.24	227	10.8	1258	1.12	<0.22	30492	<0.43	<0.73	<0.41
DST	0.28	230	10.9	1263	2.35	<0.22	30861	<0.43	<0.73	<0.41

Sample name/#	S	Sb	Se	Si	Sn	Sr	Ti	Tl	V	Zn
MDL:	**0.22**	**0.059**	**0.13**	**0.066**	**0.086**	**0.00037**	**0.00056**	**0.047**	**0.047**	**0.0097**
Top	268	<0.59	<1.3	10.2	<0.86	50.1	0.0120	<0.47	<0.47	0.586
Middle	321	<0.59	<1.3	13.5	<0.86	72.2	0.0077	0.49	<0.47	0.802
Bottom	391	<0.59	<1.3	9.76	<0.86	81.6	<0.0056	0.65	<0.47	0.108
DST	359	<0.59	<1.3	6.47	<0.86	82.7	<0.0056	<0.47	<0.47	0.268

[1]Dagger (‡) indicates MDL is elevated and was estimated because of a difficult matrix.

ICP analyses by the Illinois State Water Survey
Samples received: 1/15/2020
Samples analyzed: 1/15-17/2020
Report date: 1/27/2020
All concentrations are in mg/L

Sample name/#	pH	alkalinity	TDS, 180 C	F	Cl	Br	NO3-N	SO4
MDL:		**4**	**7**	**0.07**	**0.16**	**0.08**	**0.04**	**0.21**
Top								
Middle	7.45	369	75,520	<7	5283	<8	<4	86
Bottom	7.21	327	87,220	<7	4666	<8	<4	79
DST	7.19	204	86,000	<7	5314	<8	<4	89

Resistivity by the Illinois State Geological Survey
Samples received: 1/15/2020
Samples analyzed: 3/25/2020
Report date: 3/25/2020

Sample name/#	Resistivity (Rw; ohm-m)	Measured Temp (F)	**Resistivity (Rw; ohm-m; temp corrected to 90F)**
Top	0.141	69.1	0.111
Middle	0.117	63.3	0.084
Bottom	0.108	60.4	0.075
DST	0.104	62.9	0.075

5.3 Drill Stem Test Analysis

Author: Scott Frailey

Published as Technical Report DOE-UIUC-31700-5, OSTI ID: 1905587

Test Objective

The objectives of the enhanced drill stem test (DST) are 1) to confirm there is no mobile oil from the suspected residual oil zone (ROZ), 2) estimate vertical and horizontal permeability in the ROZ, and 3) test vertical communication between the Cypress main pay zone (MPZ) and the ROZ, across the upper calcite layer.

Test Type

A traditional DST was completed by Fox Testing, the DST service provider. A traditional DST is open at the surface. A qualitative inference of fluid entering the drill string can be made by observing air bubbling in a bucket at the surface. The Fox Testing tool assembly allowed for a maximum of two flow periods. In the Fox report, two pressure gauges were in the test interval: one referenced as "inside" and the other as "outside" gauges.

To assess vertical communication across the upper calcite layer, the traditional DST tool was enhanced by placing a gauge above the uppermost packer. The pressure recorded on this gauge was designed to behave like a vertical interference test (VIT).

In this report, the gauge used for a traditional DST is called the DST gauge, and the gauge used for the VIT is called the VIT gauge.

Test Design

At the time of the DST, the well was drilled to 2611 ft, 5 ft above the lower calcite at the base of the ROZ (determined after the DST and additional drilling commenced). To isolate the DST test interval to the ROZ (between the upper and lower calcite), the DST packer was set at the upper calcite layer at 2601 ft. If the two calcite layers were completely impermeable, the test interval thickness would be 15 ft (2601-2616 ft) with 10 ft (2601-2611 ft) open to the DST tool via the drilled wellbore. Based on the well logs and characterization analyses that followed the DST, relevant Cypress subintervals and thickness are in Table 5-11.

Table 5-11. Cypress subintervals and thicknesses at C. Winters #10 determined from well logs run after DST and well drilled from 2611 to TD of the well. At the time of the DST, the MPZ and the upper 10 ft of the ROZ were drilled.

Cypress Subinterval	Subinterval depth, ft	Thickness, ft
MPZ	2574-2599	25
Upper Calcite	2599-2601	2
ROZ	2601-2616	15
Lower Calcite	2616-2619	3
Aquifer	2619-2729	110
Total* Cypress	-	150

*Total porous and permeable Cypress

Based on anticipated relative high brine flow rates of the test intervals, flow periods of 10 mins each were planned to avoid the DST's recovered fluids rising and killing the well during the final flow period. The first and second shut-in periods were 60 and 180 mins, respectively (Table 5-12). Sampling rate of the pressure gauges was chosen to ensure adequate data for pressure transient analyses during the shut-in periods. The flow periods' durations were chosen to maximize the radius of investigation, clean up the test interval

of mud and mud filtrate (primarily 1st flow period), and minimize the possibility of too much fluid entering the drill string and killing the well.

For the VIT, when the DST was open (for fluid recovery) and closed, if communication occurred within the formation (not the wellbore) across the upper calcite, the VIT gauge should show a delayed pressure decrease when the gauge is opened followed by a delayed pressure increase when the DST tool was closed. The VIT pressure change should be much less (<80-90%) than the DST gauge below the upper calcite if communication is measured through the formation. If communication is in the wellbore (e.g., due to a leaky packer), the VIT pressure should change without delay and be similar value as the DST gauge below the upper calcite. However, the VIT and DST gauges are 8 ft apart; therefore, depending on vertical permeability, communication vertically across the upper calcite layer may be too rapid (a few seconds) to distinguish from communication in the wellbore.

Table 5-12. Actual DST parameters of the 1st and 2nd flow and shut-in periods of the C. Winters #10 DST. (Serial numbers of gauges are in parenthesis.)

Test Attribute	Cypress ROZ
Interval open to DST, ft	2601-2611
Test interval depth, ft	2601-2615
Test interval height, ft	10
1st Flow /SI Periods, mins	10/60
2nd Flow /SI Periods, mins	10/190
DST (in zone) Gauge depth, ft (MD)	2603.5 (8900, 0568)
VIT (above zone) Gauge depth, ft (MD)	2595.5 (0602)

DST (Measured) Results

Pressure and temperature are direct measurements during each flow and shut-in period. Cumulatively, the volume of fluid recovered during both flow periods is estimated when the DST assembly is pulled from the wellbore and disassembled (Table 5-13). Initial and final pressures (Table 5-13) allow qualitative interpretations of the DST functionality and the tested formation. (Qualitative interpretation includes indications of tool failure and if formation behaves infinite or limited in volume.) Estimates of the volume of fluid produced during each flow period are possible using the pressure at the beginning and end of each flow period or using the rate of change of pressure as a function of time (dp/dt) during each flow period.

The recovered fluid was reported as 17.67 bbl (Table 5-13) of muddy salt water, which was from the cumulative total of 20 mins from the 1st and 2nd flow periods (10 mins each). This is the equivalent of 2,544 bbl per day (bpd) during these 20 mins. No trace of oil was recovered.

Table 5-13. C. Winters #10 DST's direct estimate of fluid recovery and measurements of pressure and temperature of the 1st and 2nd flow and shut-in periods. Only brine was recovered from the test; no oil was recovered. (Directly from Fox Testing DST report.)

DST Measurements	Values
1st Initial and Final Flowing pressure, psig	425.23/403.70
1st Final SI pressure, psig	1101.77
2nd Initial and Final Flowing pressure, psig	740.56/928.31
2nd Final SI pressure, psig	1104.57
Fluid volume recovered, bbl	17.67

The initial flow pressure should be close to 0 psig because the DST pipe is initially empty (i.e. no hydrostatic pressure due to recovered fluid), but this DST's 1st flow period started at 425.23 psig which is over 850 ft of fluid. This is indicative of fluid entering the DST assembly prior to the 1st flowing period. Prior to the 1st flow period, a pressure decrease was recorded that can only be attributed to the gauge being exposed to atmospheric pressure by opening the DST tool. This makes estimating the flow rate from the individual flow periods challenging because the analyses of the shut-in data require an estimate of the rate immediately before the shut-in. If fluid entered the DST tool prior to the start of a flow period, this rate will not be indicative of the recovered fluid but will be related to the measured pressures at the beginning and end of each flow period.

If there is no leak during the 1st shut-in period, the final pressure of the 1st flow period should be close to the initial pressure of the 2nd flow period because the fluid levels in the DST pipe are the same. This DST had differing pressures (403.70 and 740.56 psig); so, the start of the 2nd flow period is 336.86 psig higher than the pressure at the end of the 1st flow period. This implies that over 680 ft of fluid entered the drill string during the first shut-in period, indicating that the shut-in tool failed. Qualitatively, both shut-in periods looked like pressure build-up and the tool did shut-in. So, if there was a shut-in tool failure, it did not interfere with a traditional-looking pressure buildup. (Additionally, the DST report showed 1260 ft of fluid recovered. Using the absolute pressure, a greater height of fluid would have been recovered. So, there is inconsistency between the recovered fluid and pressure data.)

Comparison of the final SI for each flow period indicates whether the reservoir is of a limited extent and the two flow periods depleted pressure. For this DST, the 2nd final shut-in pressure exceeded the 1st final shut-in pressure, which is indicative of some type of flow impediment and that the initial shut-in period of 60 mins was inadequate to return pressure to near initial pressure compared to the 2nd final shut-in pressure. Additionally, it indicates that the interval tested is not laterally limited.

Fluid and Rock Properties

To conduct pressure transient analyses of C. Winter's #10 DST acquired pressure data, fluid properties were estimated based on correlations. Brine properties are a function of formation temperature, initial formation reservoir pressure, and brine salinity. Oil properties are a function of formation temperature, initial formation reservoir pressure, API gravity, and gas-oil ratio.

Because the DST recovered no oil, only brine properties were estimated. The brine was sampled and analyzed. The TDS was estimated at 86,000 ppm. McCain's (1991, SPE 18571) correlation was used to estimate brine volume factor, viscosity, and compressibility. Newman (1973) correlation was used to estimate pore compressibility. The properties used in the pressure transient analyses are in Table 5-14.

Table 5-14. Brine properties and pore compressibility from correlations and measured properties required to use these correlations.

Test Attribute	Cypress ROZ	Comment
Brine Salinity, TDS**	86,000	
Temperature, F	90.35	From 2nd SI of DST
Initial pressure (p*), psia	1122	
Brine formation volume factor, rb/stb	1.0056	
Brine viscosity, cp	0.87208	
Brine compressibility	2.7573×10^{-6}	
Porosity, fraction*	0.15216/0.16498	2601-2616 / 2601-2724

Brine density, lbm/ft^3	66.258	0.46012 psi/ft
Pore compressibility, psi^{-1}	3.5562x10^{-6}	For 0.16359 porosity
Wellbore radius, ft	0.32708	Diameter 7.85 in DST Report

*average porosity for two intervals shown: DST test interval and upper calcite layer to base of Cypress. Porosity values were very close so thickness-weighted average was used in PTA (0.16359).

Rate Estimates for 1st and 2nd Flow Periods

In addition to fluid properties, the flow rates preceding the shut-in periods are necessary inputs to pressure transient analyses. Because the flow rate is related directly to the fluid recovered and accumulated downhole in the drill string during the DST, the flow rate *cannot* be measured directly with a meter. Because the drill string fills with recovered fluid during the DST flow periods and fluid level builds up with time, the instantaneous flow rate decreases with time due to the increase in back pressure (i.e., hydrostatic pressure due to fluid level) on the test formation as the drill string fills with recovered fluid. There are two methods used to estimate flow rate during each of the two flow periods: 1) hydrostatic pressure end point and 2) dp/dt methods. Regardless of which method is used, each should be constrained by the total fluid recovered and the duration of the total flowing time (sum of the fluid recovered during two flow periods). Each method was used to estimate the volume recovered during each flow rate, which was normalized to the total volume (17.67 bbl) recovered from the DST (Table 5-13).

The difference between the end and start flowing pressure (during each flow period), combined with the brine density, gives the column of brine present in the drill string, which is converted to barrels of brine by using the unit volume of the drill string (0.01403 bbl/ft).

Hydrostatic Pressure Method

Because of the pressure fluctuations during the 1st flow period and the relatively high initial flowing pressure (compared to the expected 0 psig when the tool initially opens to atmospheric pressure), two estimates of rate were made using two different estimates of the initial flowing pressures.

dp/dt Method

The dp/dt method uses the slope of the pressure increase during the flow periods. This is generally a straight line, but for this test was very noisy early in both flow periods, but particularly noisy at the beginning of the first flow period (Figures 5-73a and 5-73b). The rate equation for using dp/dt (psi/hr) is given below:

$$q = 2.0736 \times 10^5 \, (dp/dt) \, (V_u/r)$$

and uses the unit volume (V_u, bbl/ft) of the DST pipe and density (lb/ft^3) of the fluid recovered. For this DST, density was 66.14 lb/ft^3 and unit volume was 0.01403 bbl/ft.

The rates from the dp/dt method (Table 5-15) for each flow period gave a value relatively close to the fluid recovered volume and showed the 1st rate higher than the 2nd rate as expected in a DST.

Table 5-15. Volume of fluid estimated and normalized from each flow period and each applicable method.

	1st Flow Period (10 mins)				2nd Flow Period (10 mins)				Total
Method	**Vol-calc bbl**	**Rate (Vol-calc) bpd**	**Vol-norm bbl**	**Rate (Vol-norm) bpd**	**Vol-calc bbl**	**Rate (Vol-calc) bpd**	**Vol-norm bbl**	**Rate (Vol-norm) bpd**	**Recovered Volume calculated**
dp/dt (recorded pressure)	5.42	818.1	9.5	1435	4.67	685.5	8.10	1189	10.1
dp/dt (expected pressure)	11.87	1790	-	-	14.88	2185	-	-	26.8
Hydrostatic pressure (recorded pressure)	5.72	863.0	8.27	1248	6.57	965	9.33	1408	12.29
Hydrostatic pressure (expected pressure)	11.9	1790	-	-	-	-	-	-	-

Vol-calc: volume calculated directly from one of the two methods; Vol-norm: Vol-calc normalized to 17.67 bbls fluid recovered by DST (report); Rate: Vol-norm divided per flow period duration converted to days (from minutes). Recorded pressure is directly flow linear trend established through recorded pressure during each flow period. `Expected pressure' is the expected pressure if starting with fluid -free drill string and no fluid entering well during shut-in periods.

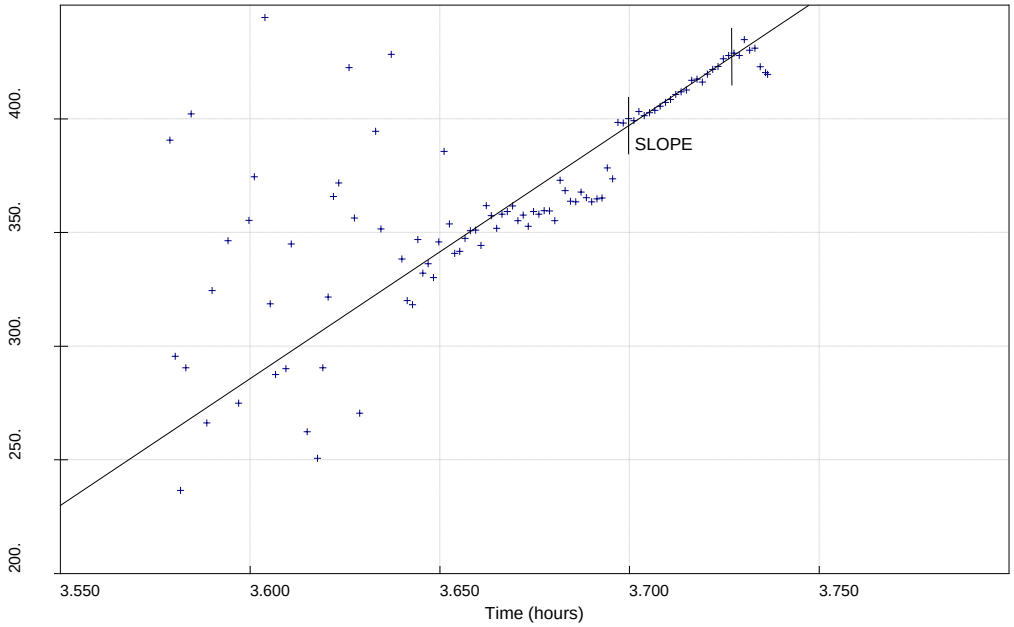


Figure 5-73a. Cartesian graph of pressure vs. time during 1st flow period. Noisy data immediately following start of flow period from 3.58 to 3.65 hrs. Linear trend from 3.70 to3.73 hrs used to calculated dp/dt of 1116 psi/hr for rate calculation.

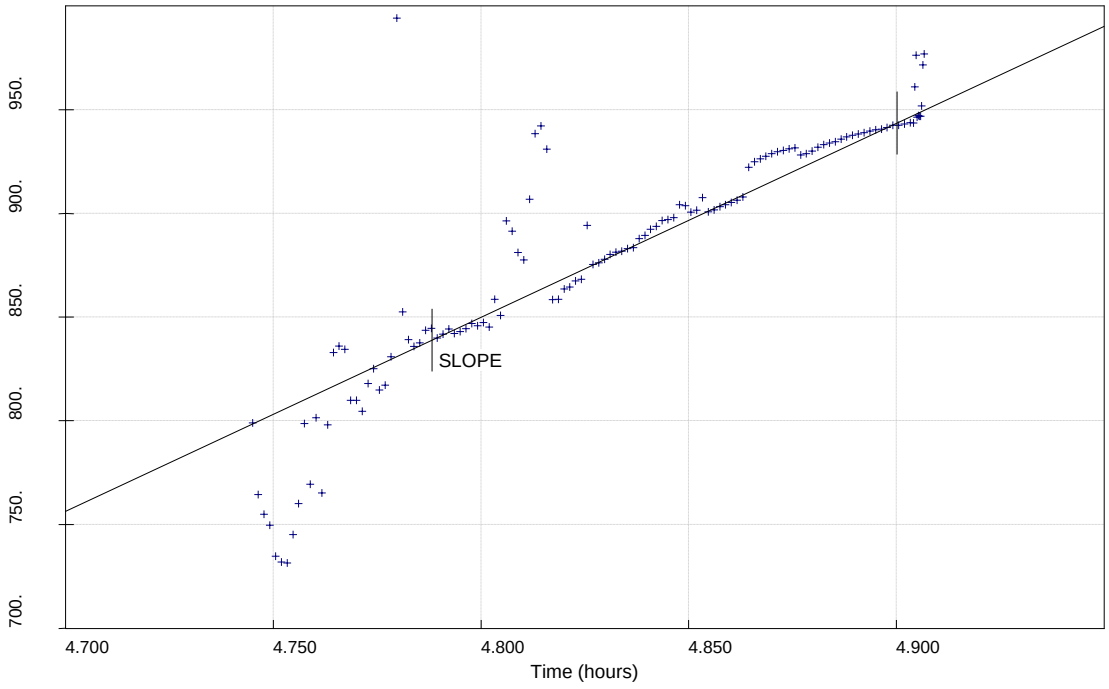
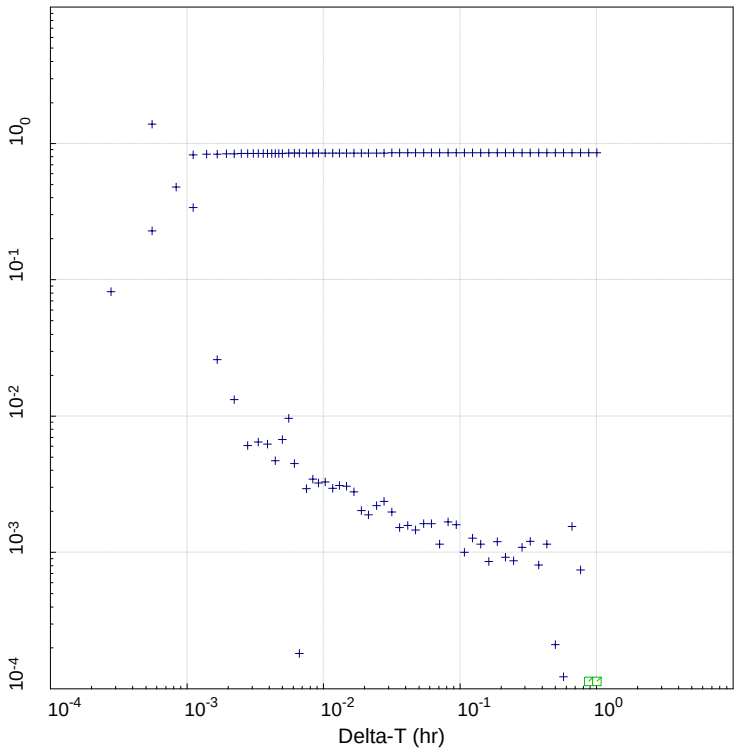


Figure 5-73b. Cartesian graph of pressure vs. time during 2nd flow period. Noisy data from 4.74 to 4.78 and 4.80 to 4.82 hrs. Linear trend from 4.78-4.80 and 4.82 to 4.91 hrs used to calculated dp/dt of 935.0 psi/hr for rate calculation.

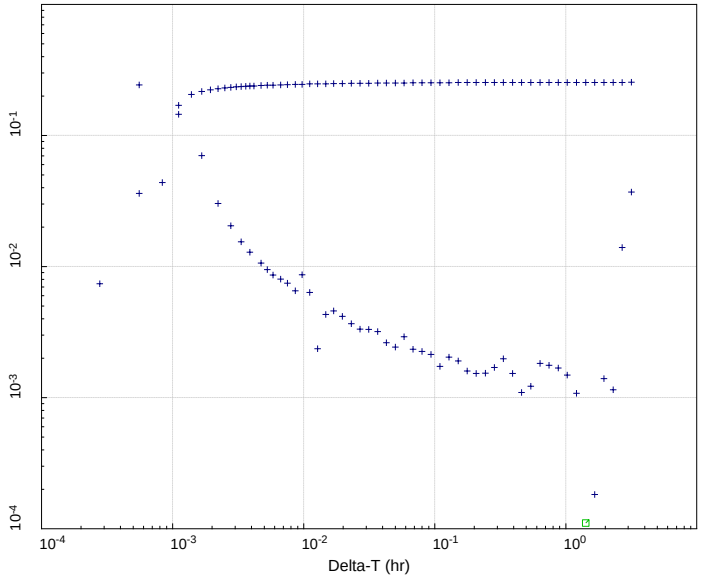
Rates used for analyses. The dp/dt and hydrostatic pressure method using recorded pressure data gave similar volumes produced and were 30% and 43% of the recovered fluid volume from the DST. The methods using the expected values over predicted by >50%. The dp/dt estimate of the 1st flow rate was greater than that of the 2nd flow rate but was not for the hydrostatic pressure method. For these reasons, the flow rates estimated from the dp/dt method using the recorded pressure (818.1 and 685.5 bpd; row 1, Table 5-15) was used for the derivative analyses to estimate permeability. These rates are *not* normalized to the total fluid recovered because the estimates are not relatively close to the recovered volume and that fluid is suspected of entering the DST tool prior to the flow period based on the initial pressure measured for each flow period.

Pressure Transient Interpretation and Results

Derivative analyses. The derivative plot consists of pressure and pressure derivative (Figures 5-74a and 5-74b) of each shut-in period of the DST, which each follows one of the two flow periods. The initial pressure data typically is dominated by fluids in the drill pipe and the later pressure data is mostly influenced by the geologic formation (i.e. the tested interval). Because only 10 ft of Cypress was open below the DST packer, the remainder of the Cypress that was above and below the 10 ft interval could contribute to flow. Flow from above and/or below an open interval causes a partial penetration effect which is indicated by a negative half-slope (-1/2) on the derivative curve. Both flow periods' derivative has a -1/2 slope which is well developed and is sustained across two log-cycles of time; this duration is relatively convincing that it is the partial penetration effect.



Figures 5-74a. Derivative plot of 1st shut in. Nearly horizontal derivative present between 0.1 and 1.0 hrs is indicative of radial flow from which horizontal permeability can be estimated. A negative half slope, present between 0.003 and 0.2 hrs, is indicative of spherical flow due to partial penetration effect from which vertical permeability can be estimated. (Pressure is upper trend and pressure derivative is lower trend.)



Figures 5-74b. Derivative plot of 2nd shut in. Nearly horizontal derivative present between 0.1 and 2.0 hrs is indicative of radial flow from which horizontal permeability can be estimated. A negative half slope, present between 0.0005 and 0.2 hrs, is indicative of spherical flow due to partial penetration effect from which vertical permeability can be estimated. (Pressure is upper trend and pressure derivative is lower trend.)

Following the negative half-slope on both shut-ins is a nearly horizontal derivative indicative of radial flow from which horizontal permeability can be estimated. No other slope is present on the derivative, and therefore, no other geologic feature is indicated. The permeability-thickness produced, calculated from the 1st and 2nd shut-in, were 56,000 and 43,000 md-ft, respectively. Generally, the 2nd shut-in is used for permeability-thickness estimates because of the longer flow and shut-in period; however, the flow period preceding the 2nd shut-in was the same duration as the first. Because the 2nd flow period appears more stable (and therefore flow rate from this period more accurate) than the 1st flow period (Figures 5-73a and 5-73b) and the derivative is less erratic (Figures 5-74a and 5-75b), the 2nd shut-in's permeability-thickness estimate is considered more likely.

The k_v/k_h ratio was estimated to be 0.0685 from the 2nd shut-in derivative where the negative half-slope was present, which assumes that the 125 ft ROZ and aquifer subinterval were tested. If the entire Cypress (150 ft) was tested, the k_v/k_h would be 0.118. For the 40 ft MPZ and ROZ, k_v/k_h is 0.00225.

The Formation MicroImager (FMI) log indicates a vertical fracture (about 50 ft vertically) throughout most of the MPZ of the Cypress. However, there is no evidence of linear flow from a single, vertical fracture response on the pressure derivative. An early positive ½ slope is indicative of an infinite-acting vertical fracture; for a finite-acting vertical fracture, the ½ slope is preceded by a positive ¼ slope. Neither a ¼ nor ½ slope are present early on the derivative.

Semilog analyses. In addition to horizontal permeability, semilog analyses give an estimate of the initial pressure of the formation tested. The superposition method that accounts for preceding flow periods was used for the semilog analyses. When the same interval of shut-in time on the derivative is used to estimate permeability on the semilog analyses, the permeability estimates are identical; therefore, for this analyses, semilog analyses was not used to estimate horizontal permeability. To estimate the initial pressure from the superposition plot, the straight-line trend is extrapolated to infinite shut-in time (x=0 on superposition plot).

If the extrapolated pressures of the two shut-in periods are similar, the interval tested may be large. If the extrapolated pressure of the 2nd shut-in period is noticeably lower than that of the 1st shut-in, the DST fluid recovered was adequate to decrease the formation pressure, and the formation tested may have limited extent.

The superposition plot of the 1st and 2nd shut-in periods extrapolated to 1119 and 1122 psia, respectively, which are relatively close. Consequently, there is no indication of a limited extent to the test interval. Generally, the 1st shut-in is used for initial pressure because of the single and lesser cumulative volume of fluid withdrawn; for this reason, the 1st shut-in's initial pressure estimate was considered the best estimate. The semilog pressure data is directly from the DST gauge (8900) at 2603.5 ft (Table 5-12). Using 14.7 psia as atmospheric pressure, the fluid gradient is 0.425 psi/ft.

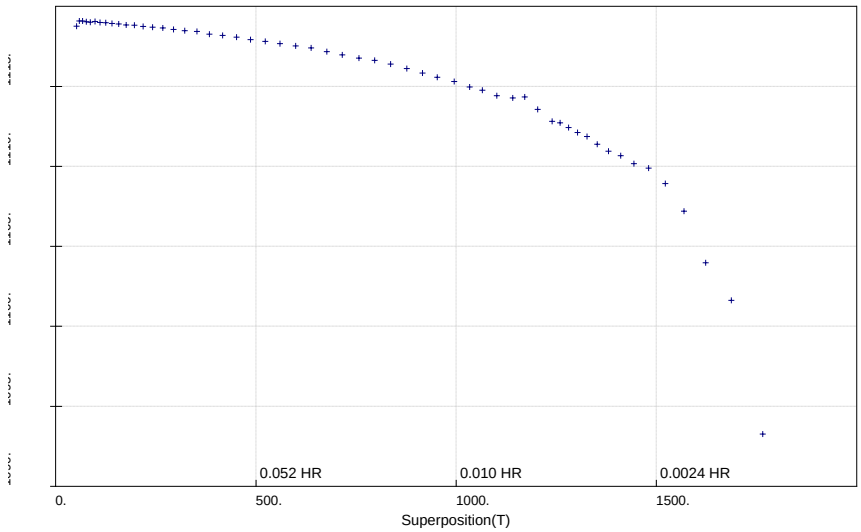


Figure 5-75a. Superposition (semilog) plot of 1st shut in. (Pressure, P, on y-axis.) Linear trend from 100 to 250 was used for extrapolation to the estimate initial pressure. (The superposition function's units are dimensionless.)

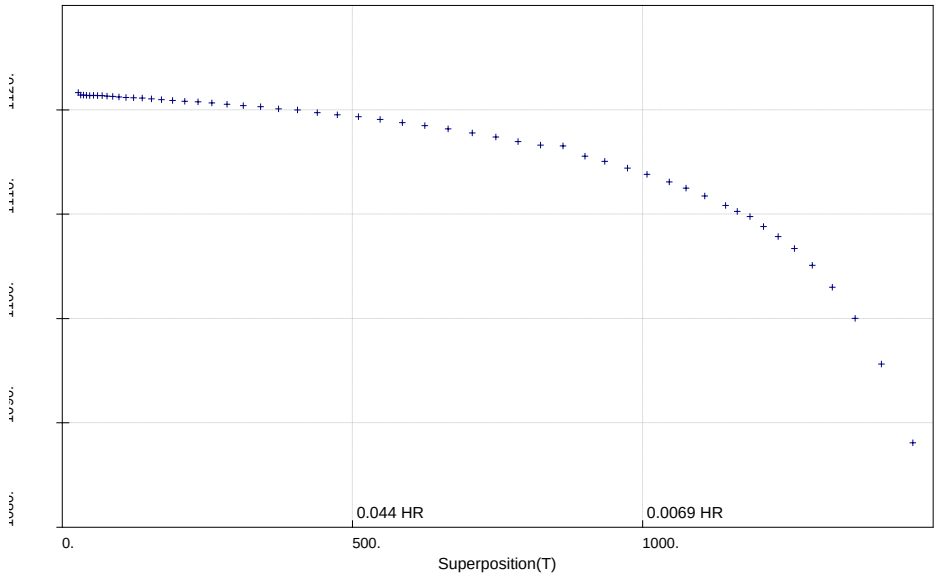


Figure 5-75b. Superposition (semilog) plot of 2nd shut in. (Pressure, P, on y-axis.) Linear trend from about 100 and 200 was used for extrapolation to estimate initial pressure. (The superposition function's units are dimensionless.)

Interpretation. To estimate permeability, the thickness of the tested interval must be assumed. Because the DST had 10 ft open to the DST tool (distance between packer set at upper calcite layer and TD of well at the time of test) and partial penetration effect is indicated on derivative, there are four options of the tested interval: 1) the entire Cypress, 2) the 15 ft between the two calcite layers (ROZ), 3) the MPZ and ROZ, and 4) the ROZ and the underlying aquifer. Based on Table 5-11, these four options have thicknesses of 150, 15, 40, and 125 ft, respectively. Using permeability-thickness of 13,500 md-ft and these thicknesses, horizontal permeability is 290, 2900, 1075, and 340 md, respectively. Because of the presence of a partial penetration effect on the derivative, option 2 seems unlikely because 10 ft of open formation

to the DST influenced by a total of 15 ft is unlikely to create a partial penetration effect across two log cycles of time.

The arithmetic average horizontal permeability of the core from the MPZ and ROZ are 500 and 250 md, respectively; the average of MPZ and ROZ together is 375 md. Comparing permeability from the derivative analyses and the core (from MPZ and ROZ), the test of ROZ only (option 2) and MPZ and ROZ (option 3) are unlikely (Table 5-16). No core was taken from the aquifer; so, core permeability is unavailable for comparison; at the time of this report, a permeability transform calibrated to the core was not available. Option 3 not being likely is supported by the lack of oil recovered from the DST, which if tested, the MPZ should have mobile oil. The interpretation of well logs and geologic characterization indicates that the lower calcite has much lower permeability in comparison to the upper calcite, which contradicts the derivative analyses.

Table 5-16. Comparison of permeability from derivative and core analyses.

Tested Subinterval	Option	Derivative Analyses		Core Analyses*	
		Horz Perm (md)	k_v/k_h	Horz Perm (md)	k_v/k_h
MPZ, ROZ and aquifer	1	290	0.118	-	
ROZ	2	2900	-	250	0.213
MPZ and ROZ	3	1075	0.00225	375	0.203
ROZ and aquifer	4	340	0.0685	-	

*no core was taken from the aquifer; no permeability data available for aquifer.

Based on comparison of permeability (Table 5-16), option 1 or 4 are likely if the permeability of the MPZ and ROZ are representative of the aquifer. The k_v/k_h ratio from core, calculated using harmonic average of vertical permeability and arithmetic average of horizontal perm, did not compare well with k_v/k_h from the derivative analyses for the MPZ and ROZ subinterval test (option 3). A k_v/k_h of 0.118 over a 150 ft test interval consisting of two low permeability calcite intervals seems high. A k_v/k_h of 0.0685 over a 125 ft test interval consisting of one low permeability calcite layer seems high, but more reasonable compared to a k_v/k_h of 0.118 across two calcite layers. (General observations of k_v/k_h of 0.1 is over 10 ft.)

A summary of the pressure transient results from the DST are in Table 5-17.

Table 5-17. Final estimates of the DST

Test Attribute	Value	Comment
Permeability-thickness, md-ft	43,000	2nd shut-in
Initial pressure, psia*	1119	1st shut-in
Thickness tested, ft	40	MPZ and ROZ
k_v/k_h	0.0685	2nd shut-in
Reservoir response	Radial, infinite-acting, and partial penetration	

* at 2603.5 ft

Results: Vertical Communication Across Lower (of Two) Calcite Layer (at Base of Cypress ROZ)

To compare the pressure trends between the VIT gauge (above upper calcite) and the DST gauge (below upper calcite), the clocks of the respective gauges must be synchronized using a pressure perturbation that affects both gauges simultaneously. This can be accomplished only before and after the packer is set for the DST. An example of a pressure perturbation on both gauges (Figure 5-76) is at about 3.20216 hrs

(DST gauge) and 3.21583 hrs (VIT gauge). To synchronize these gauges, 0.01367 hrs (49.212 secs) were added to the VIT gauge.

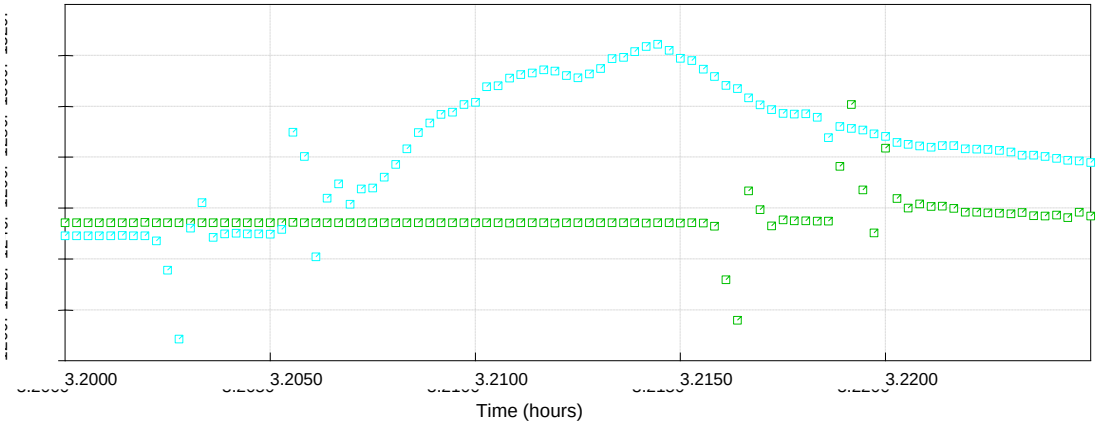


Figure 5-76. example of difference in time between VIT and DST pressure gauges. Blue is the VIT gauge; green is the DST gauge.

Opening and closing the DST to allow fluid to be recovered from the test interval decreases and increases the pressure of the test interval, respectively. If there is vertical communication across the upper calcite, the VIT gauge will have a delayed response to the pressure change noticed on the DST gauge. The magnitude of the VIT pressure change should be much less than that of the DST gauge due to the reduced vertical flow above the upper calcite compared to horizontal flow through the ROZ.

Cartesian analyses. To understand the pressure gauge responses qualitatively prior to analyses, Cartesian graphs of the pressure data comparing the synchronized gauges were completed. Prior to the first flow period, the VIT gauge was not constant and continued to decrease through the 1st flow and shut-in period. Consequently, the open and close actions of the DST did not create a detectable pulse on the VIT pressure gauge. The action of opening the DST to flow caused a sharp pressure increase that masked part of the pressure data early in the 2nd flow period; however, a 2nd trend developed that was interpreted as pre-pulse so that an estimate of the delay in VIT pressure response could be determined (Figure 5-77). The delay estimate is 61.2 seconds.

The DST action of closing the 2nd flow period (start of 2nd shut-in), caused the VIT gauge pressure to decrease about 4 psi, which masked early VIT pressure data. An extrapolation of the pre-shut in VIT pressure allowed for a 46.4-second estimate of the arrival of the 2nd shut-in pulse following the DST tool closure (Figure 5-79). The pulse estimate is 3.354 psi (at 5.4 hrs) above the minimum pressure at about 4.9 hrs (Figure 5-80). Table 5-18 summarizes the pulse and delay times from Cartesian analyses of VIT.

Some of the changes in pressure may be due to changing mud level in the annulus throughout the test. To minimize this effect, the level should be maintained to surface throughout the DST.

Table 5-18. Delay in pressure response and magnitude of pressure change at VIT gauge at specific DST events.

DST Event	Delay, seconds	Pressure change, psi	Comment
Prior to the 1st flow	-	-	Used to synchronize clocks
Start of the 1st flow	13.302	40.0	
Start of the 1st shut-in	None observed	None observed	
Start of the 2nd flow	61.2		Pressure change not observed
Start of the 2nd shut-in	46.4	3.35	Decreasing VIT trend; max pulse
Following the 2nd shut-in	-	-	Validated clock synchronization

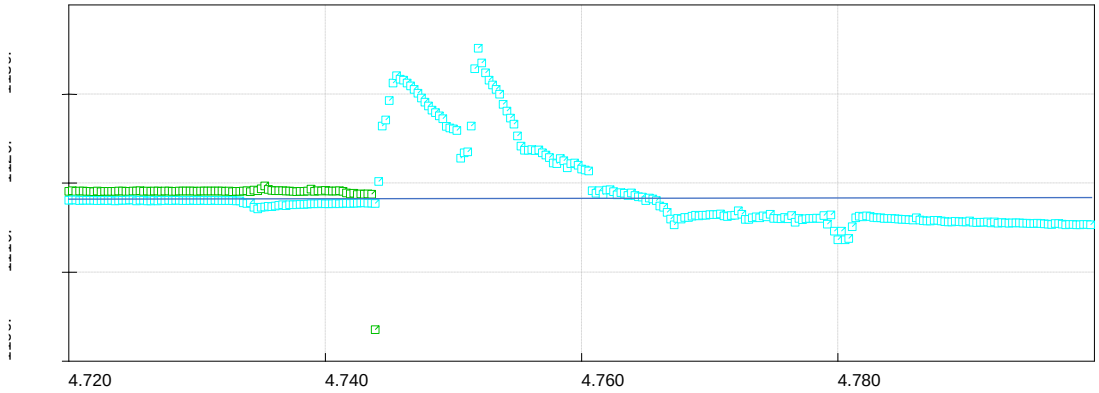


Figure 5-77. Start of 2nd flow period. Action of opening DST tool increased pressure on the VIT gauge (light blue) by about 12 psi. The DST gauge (green) decreased rapidly (off bottom of graph). Horizontal blue line used to establish 2nd trend (4.761 to 4.766 hrs]) similar to end of 1st shut-in (4.72 to about 7.744 hrs). The delay in VIT pulse is 61.2 seconds (4.761 - 4.744 hrs).

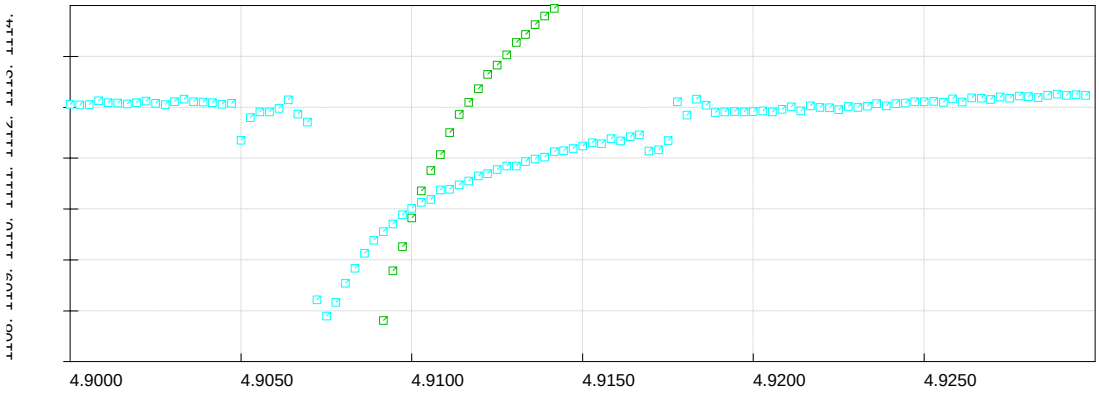


Figure 5-78. Start of 2nd shut-in (end of 2nd flow period). DST closing action caused the VIT gauge (light blue) to lose pressure (4.907 hrs) and mask pulse arrival. Early DST gauge pressure (green) shows the increase in pressure due to the start of 2nd shut-in.

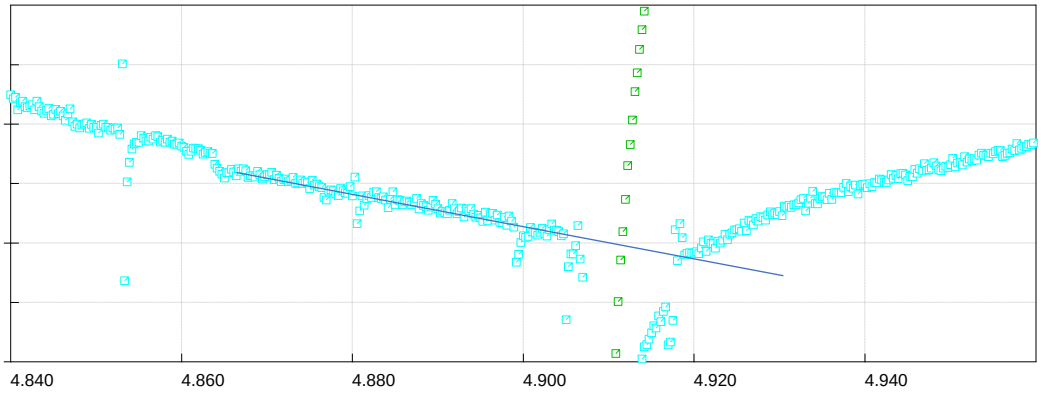


Figure 5-79. Start of 2nd shut-in (end of 2nd flow period). Trend line used to extrapolate to shut-in VIT pressure (light blue) of 1112.85 psi at about 4.92 hrs to estimate the 2nd shut-in pulse arrival at the VIT gauge. Early DST gauge pressure (green) shows the increase in pressure due to the start of 2nd shut-in.

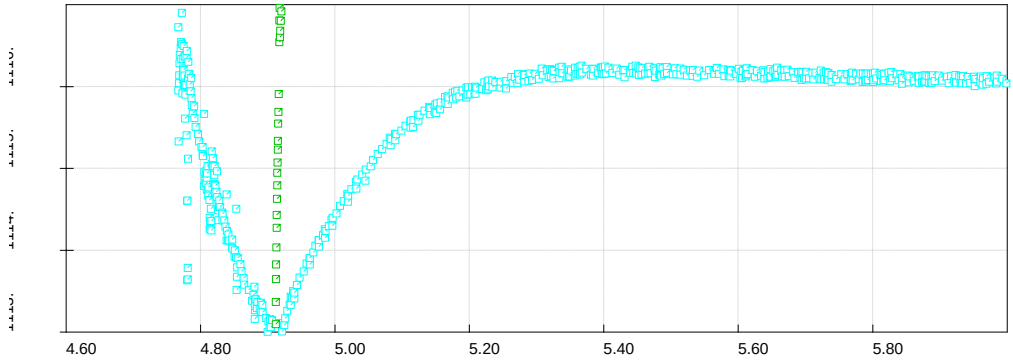


Figure 5-80. Start of 2nd shut-in (end of 2nd flow period). VIT pulse (light blue) starts at about 4.9 hrs and reaches a maximum at about 5.4 hrs. Pulse should have continued to increase, but trend is to continue to decrease. (Early DST gauge pressure, green, shows the increase in pressure due to the start of 2nd shut-in.) Pressure pulse at maximum pressure is 3.35 psi.

Pulse test analyses. Simulation (analytical) was used to match the pressure data of the 2nd pulse of the VIT caused by the DST's 2nd flow and shut-in periods. The pressure fluctuations caused by opening and closing the DST were ignored. Similarly, the small but continuous VIT pressure decrease was ignored. So, only the data attributed to the pulse was part of this analysis. In Figure 5-81, this is the pressure data from about 4.75 to 5.3 hrs.

Unlike the analyses of the DST data, which is immediately influenced by the ROZ test interval followed by any part of the Cypress above the upper calcite and/or below the lower calcite, the VIT gauge is influenced by the average vertical permeability between the VIT and DST gauges. The distance between gauges is 8 ft, which includes the 2 ft thickness of the upper calcite.

The simulation process is manually iterative with initial properties derived from the DST analyses (Table 5-17). After several iterations, a horizontal permeability of 400 md and a k_v/k_h of 0.04 gave the simulated curve (blue line) in Figure 5-81. This horizontal permeability compares very well with the core data arithmetic average permeability of 375 md (Table 5-16). The VIT estimated k_v/k_h is very low compared to the k_v/k_h derived from the harmonic average of vertical permeability from the core (0.213); this is likely because of the relatively low k_v/k_h of the upper calcite layer present between the VIT and DST gauges.

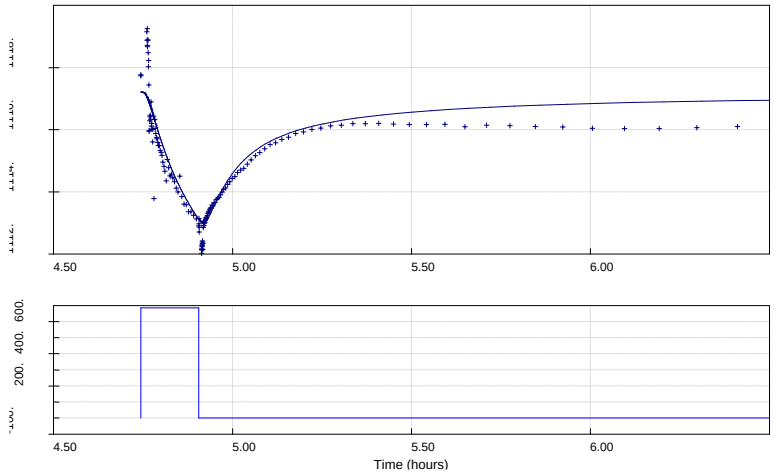


Figure 5-81. Simulation of the VIT pulse (solid blue line on the upper graph) caused by the DST's 2nd flow period and shut-in. The VIT pressure data (blue +) attributed to opening and closing the DST tool was ignored. Similarly, the general trend of VIT pressure decrease was not attributed to the pulse and was not part of the analyses. (on this plot pressure at time >5.3 hrs).

Compared to the DST analyses of the MPZ and ROZ, the k_h and k_v/k_h are very different, supporting the conclusion from the DST that a DST MPZ and ROZ test only is unlikely. Because the VIT indicates vertical communication across the upper calcite, the DST interpretation of the MPZ, ROZ, and aquifer test (Option 1, Table 5-16) seems more likely.

Comparing the DST results for an MPZ, ROZ, and aquifer test, the VIT k_v/k_h is about 1/3 of the DST k_v/k_h (0.118), and the VIT k_h is about 30% greater than the DST k_h. Because the VIT was not affected by the aquifer, this is not a direct comparison of the same part of the formation. This is another indication that the upper calcite has lower k_v/k_h compared to the average k_v/k_h from the DST tested intervals.

Conclusion

Based on a comparison of DST results, core data, and VIT indication of upper calcite permeability, the DST test interval was most likely the MPZ, ROZ, and aquifer. The DST indicated a partial penetration effect and no vertical fracture flow. The permeability-thickness product of the test interval is 43,000 md-ft and a k_v/k_h of 0.118 over the vertical height of this interval (150 ft). Furthermore, the ROZ had no recovered (i.e. mobile) oil.

Recommendation

The suspected cause of the VIT pressure decrease throughout the test was a decrease in mud level during the DST; therefore, the annulus mud level should be maintained for the duration of the DST test. Because closing and opening action of the DST tool caused pressure changes that masked the early part of the VIT pulse, a closer look at the DST mechanism for shut-in should be inspected and the procedure reviewed to minimize or eliminate pressure fluctuations in the wellbore that affect the VIT gauge. The pre-DST pressure data that showed a pressure decrease of 100s psi below the hydrostatic mud pressure, which had to be because the DST temporarily opened to the atmosphere, the DST equipment and procedure prior to and while setting the DST packer should be reviewed. Similarly, because the final pressure of the 1st flow period did not compare well to the initial pressure of the 2nd flow period, fluid entering the DST during the 1st shut-in period is indicated. This part of the DST tool should be inspected. The difference

between the recovered fluid volume and the estimated fluid volume is supportive of fluid entering the DST tool other than during the two flow periods.

5.4 Strategies to Maximize Storage, EOR, and Net Present Value

Authors: Nathan Webb, Roland Okwen, and Nathan Grigsby

Development strategies for the stacked brownfield ROZ site were identified using an approach that integrates the application of dimensionless performance curves (DPCs) and reservoir continuity (RC). A development strategy, as defined here, is the combination of well spacing, pattern type and size, perforated intervals, and well orientation that is used in the CO_2 flood of a given formation as part of an EOR and storage program. In the case of an EOR and Storage program that targets a stacked reservoir complex in which the target formations possess dissimilar geology, it follows that development strategies that maximize the EOR or Storage in one formation may not do so for another. In such cases, a process must take place to identify the development strategies that holistically co-optimize EOR and storage for the entire field.

Prior to this co-optimization, it is important to identify the development strategies that will separately maximize EOR and Storage in each formation. Oil recovery and CO_2 storage were used as metrics for selecting development strategies of six vertically stacked reservoirs that include depleted reservoirs and ROZs. Pattern size, degree of reservoir heterogeneity, RC, and DPCs were used to make initial CO_2-EOR and storage estimates for each formation. The formations studied included (in increasing depth) the Cypress Sandstone, Aux Vases Formation, and the Ste. Genevieve, St. Louis, Salem, and Ullin Limestones. The injection potential (injectivities), and CO_2-EOR, and storage potentials of the formations were determined via dynamic reservoir simulations. Simulation results were used to validate initial CO_2-EOR and CO_2 storage estimates.

Methods

Dimensionless Performance Curves

The Midwest Geological Sequestration Consortium (MGSC) dimensionless performance curve (DPCs) tool (Okwen and Frailey, 2015) was used to estimate CO_2-EOR and storage for six stacked reservoirs. Input parameters to the DPCs tool include degree of reservoir heterogeneity, miscibility type, injection type, and pattern size. The degree of reservoir heterogeneity ranges from low, moderate, to high. The CO_2 flood can be either miscible or immiscible and could be continuous injection or water-alternating-gas injection. Lastly, the CO_2 flood pattern sizes considered include 20-, 40-, and 80-acres. Miscible, continuous injection floods for 20-, 40-, and 80-acres pattern sizes were estimated for each formation. Furthermore, the degree of reservoir heterogeneity for each formation was determined subjectively, based on the interpreted depositional environment for each formation. Formations with thin or spatially compartmentalized reservoirs were assigned a high heterogeneity whereas thick and continuous formations were assigned a low heterogeneity.

Outputs from the DPCs tool include EOR and CO_2 storage for 20-, 40-, and 80-acre pattern size and for each formation (Table 5-19 and Table 5-20).

Table 5-19. Reservoir continuity and dimensionless CO_2-EOR by formation.

Formation	Heterogeneity classification	Continuity (%)			Np/HCPV**		
		933 ft [20-ac]	1320 ft [40-ac]	1867 ft [80-ac]	20-ac	40-ac	80-ac
Cypress Ss	Low	95.2	94	92.6	0.102	0.122	0.134
Aux Vases Fm*	Moderate	–	–	–	0.096	0.111	0.120
Ste. Genevieve Ls	Moderate	63.8	52.5	42.7	0.061	0.058	0.051
St. Louis Ls	High	66	56	46.2	0.056	0.052	0.044
Salem Ls	Moderate	77.1	71.5	66	0.074	0.079	0.079
Ullin Ls**	Moderate - low	18.3	5	0	0.019	0.006	0.000

Note: *The Aux Vases Formation was excluded from the reservoir continuity determination due to significant facies change within the Noble Field. So, continuity factors were not applied to the resulting EOR estimate.

*****Reservoir continuity is based on the porous lenses that occur in the uppermost part of the Ullin Limestone. Only two wells in the field penetrate the entire thickness of the Ullin including the lower saline aquifer.***

Table 5-20. Reservoir continuity and dimensionless CO_2 storage by formation.

Formation	Heterogeneity classification	Continuity (%)			CO_2 storage/HCPV**		
		933 ft [20-ac]	1320 ft [40-ac]	1867 ft [80-ac]	20-ac	40-ac	80-ac
Cypress Ss	Low	95.2	94	92.6	0.339	0.456	0.449
Aux Vases Fm*	Moderate	–	–	–	0.041	0.426	0.413
Ste. Genevieve Ls	Moderate	63.8	52.5	42.7	0.026	0.224	0.176
St. Louis Ls	High	66	56	46.2	0.312	0.206	0.158
Salem Ls	Moderate	77.1	71.5	66	0.032	0.305	0.273
Ullin Ls**	Moderate - low	18.3	5	0	0.036	0.023	0.000

Note: *The Aux Vases Formation was excluded from the reservoir continuity determination due to significant facies change within the Noble Field. So, continuity factors were not applied to the resulting storage estimate.

*****Reservoir continuity is based on the porous lenses that occur in the uppermost part of the Ullin Limestone. Only two wells in the field penetrate the entire thickness of the Ullin including the lower saline aquifer.***

Reservoir Continuity

The CO_2-EOR and storage estimates from DPCs are corrected further to account for reservoir continuity. Reservoir continuity, or the percentage of pay in a well that is connected between any two given wells (George and Stiles, 1978), needs to be well understood to design the optimum well patterns and perforation intervals. Infill drilling with smaller injection patterns results in maximized per-well oil recovery (Barber et al., 1983), but the size of the selected flooding pattern must be balanced between reservoir continuity and the economics of drilling and completing new wells or converting legacy wells.

Reservoir continuity was determined using an analytical method developed by Stiles (1976). Well pairs in the field were correlated at various distances (from 79 to 1,272 m) and the thickness of porous formation above a certain cutoff (in this case 6%) was determined. Wells with the same thickness of porous rock are 100% continuous whereas 0% continuity occurs in wells where one well has some thickness of porous rock and the other well has none. Reservoir continuity is presented graphically as a % continuity at a given well spacing (Figure 5-82). Of the six formations assessed for development strategies, the Aux Vases Formation was excluded from the reservoir continuity determination due to significant facies change within the Noble Field.

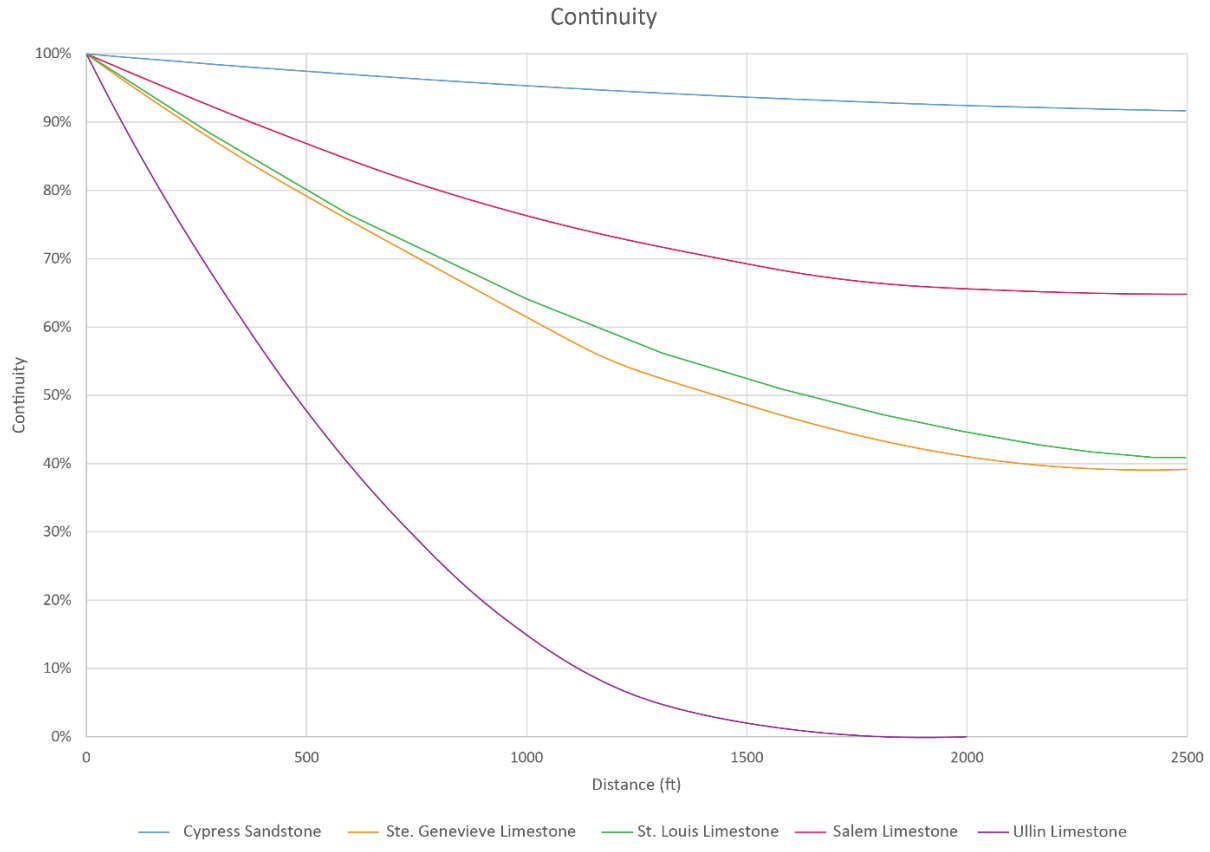


Figure 5-82. Graph showing reservoir continuity of five formations (Cypress Sandstone, Ste. Genevieve Limestone, St. Louis Limestone, Salem Limestone, and Ullin Limestone).

Production History

To better constrain estimates of the potential EOR resource of the stacked reservoirs, the field production history was evaluated. Production history data is derived from monthly accountings of oil production reported at the lease level. Production data is also comingled amongst the many producing formations in the field. Thus, assembling the production history of the field requires detailed tracking of well completions and recompletions through time and making subjective decisions regarding the attribution of production based on the behavior of lease-scale production. The result is an imperfect but reasonable approximation of the relative productivity of the stacked reservoirs in the brownfield site.

The Cypress Sandstone is by far the most prolific oil production in the field (Figure 5-83), making up 51% of the total field production. The Ste. Genevieve is second largest contributor at 36% of the total field production. The Aux Vases, and Salem, St. Louis, and Ullin Limestone reservoirs are commonly commingled together, making it difficult to differentiate their contributions. Thus, the remaining reservoirs in the field were grouped together and account for 13% of the field production.

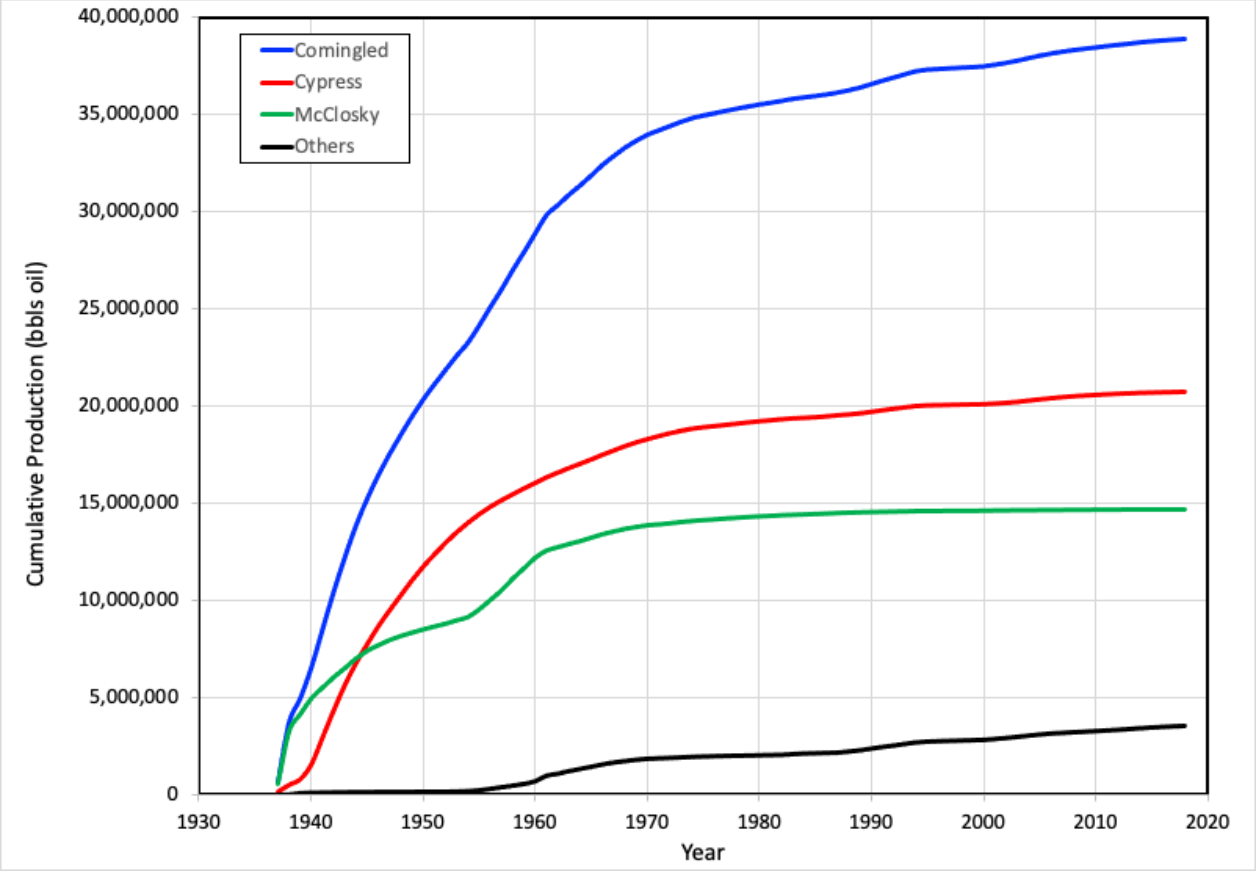


Figure 5-83. Graph of cumulative production showing the relative contribution of the two most prolific reservoirs (Cypress and Ste. Genevieve) and a grouping of all remaining reservoirs.

Formation Injectivity

The relative injection potentials of the stacked reservoirs or formations (Cypress, Aux Vases, Ste. Genevieve, St. Louis, Salem, and Ullin) were assessed by simulating CO_2 injection via a single well that penetrates all the formations (Figure 5-84). Six injection scenarios were simulated using the single well. In the first scenario, all formations are perforated, and the proportion of CO_2 injected into each formation

was calculated. The perforations of formation with the highest proportion of CO_2 injected were plugged in subsequent simulations. Results from the simulation scenarios were then used to rank the formations by injection potential (Table 5-21). Results in Table 5-21 indicate that the Cypress Sandstone has the highest and the Ste. Genevieve Limestone has the lowest injection potential.

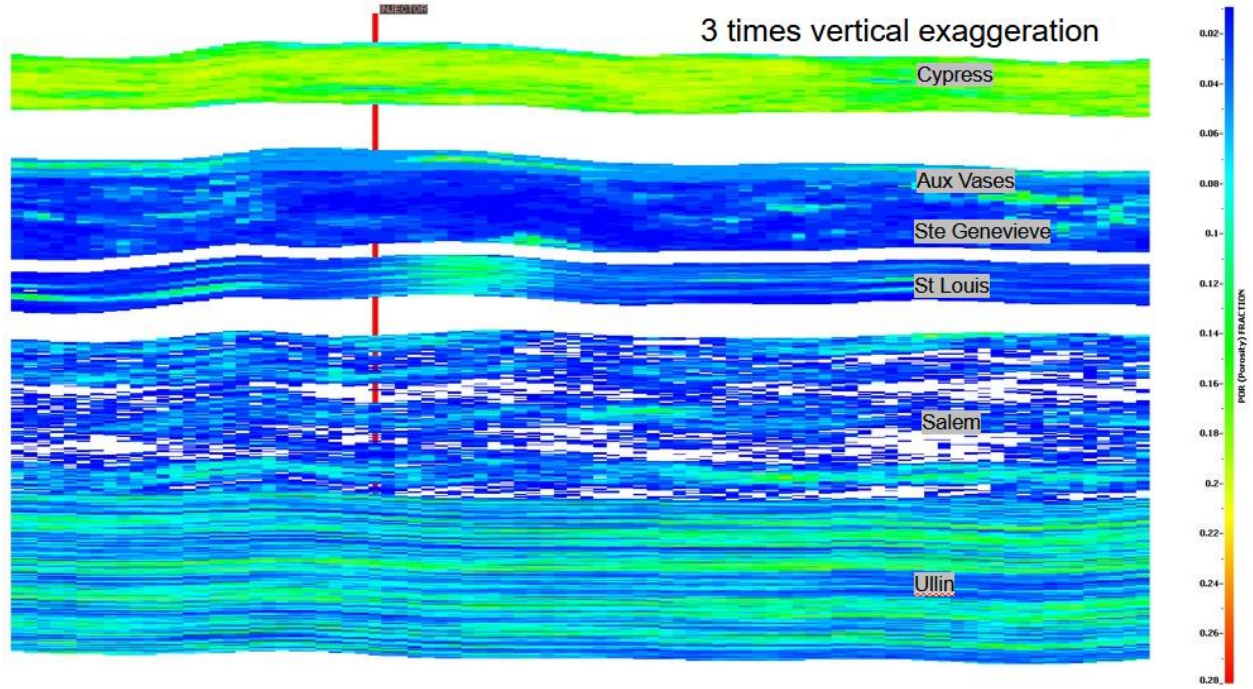


Figure 5-84. Example cross section through the stacked reservoir model showing how the location of the simulated injection well (red) can impact injectivity. The St. Louis Limestone is generally a lower porosity (darker blue) formation in comparison to the Ste. Genevieve Limestone, but the placement of the well in the model is near a porosity "sweet spot" in the St. Louis, thus increasing its relative injectivity.

Table 5-21. CO_2 injection potential by formation.

SCENARIO NUMBER	FORMATIONS	CUMULATIVE INJECTION (TONNES)	CO_2 INJECTION PROPORTION BY FORMATION (%)					
			CY	AV	SG	SL	Sa	U
1	CY, AV, SG, SL, SA, U	237,523	96.0	0.01	0.0	0.1	0.2	3.7
2	AV, SG, SL, SA, U	9,550	-	0.3	0.0	1.9	4.5	93.3
3	AV, SG, SL, SA	655	-	5.0	0.4	28.6	66.0	-
4	AV, SG, SL	223	-	14.7	1.2	84.1	0.0	-
5	AV, SG	35	-	92.3	7.7	-	-	-
6	SG	2	-	-	100	-	-	-

NOTE: CY: CYPRESS SANDSTONE, AV: AUX VASES FORMATION, SG: STE. GENEVIEVE LIMESTONE, SL: ST. LOUIS LIMESTONE, SA: SALEM LIMESTONE, AND U: ULLIN LIMESTONE.

Development Strategies

The development strategies for the stacked reservoirs at the brownfield site are ultimately controlled by the size of the (EOR and/or storage) resource in each formation and the injectivity of the formations, both of which are controlled by the geology of the formations in question. The production history of the field demonstrates that the Cypress Sandstone has been the most prolific oil producer at the Brownfield site.

Table 5-21 shows that the Cypress Sandstone is (by two orders of magnitude) the formation that will most readily accept CO_2 injection. Therefore, the prescribed development strategy for the Brownfield should prioritize the Cypress Sandstone and treat other formations as secondary resources.

CO_2-EOR Potential

In terms of EOR strategies, the 80-acre pattern yields the highest potential recovery from the Cypress (Table 5-19). All other formations in the field perform better with smaller 40- or 20-acre patterns. Since the Ste. Genevieve Limestone ranks second in oil production, the smaller pattern size should prioritize that formation and should therefore be 40-acre (Table 5-19). Thus, a sequential strategy in which the Cypress is targeted first with an 80-acre pattern size followed by a change to a smaller 40-acre pattern size to target the remaining formations would lead to the maximum EOR performance.

CO_2 Storage Potential

Storage potential does not correlate directly with the EOR resource because the Cypress Sandstone and the Ullin Limestone have large porous intervals lacking oil saturation, thus making them targets as saline storage resources in addition to storage associated with EOR. Again, the Cypress Sandstone has by far the largest injection potential (Table 5-21). For CO_2 storage, the Cypress Sandstone is most performant when developed with a 40-acre pattern size. The Ullin Limestone has more favorable CO_2 storage performance with a 20-acre pattern. Therefore, depending on the preferred target formation, either a 40-acre or 20-acre well pattern would result in maximum storage performance.

Conclusions

The development strategies suggested here are meant to maximize EOR and storage separately and are biased towards most prolific formations (regarding oil production and potential injectivity, respectively) at the Brownfield site. For EOR, the strategy is to first prioritize the Cypress Sandstone with an 80-acre pattern followed by targeting the remaining formations with a smaller pattern. For storage, the strategy is to target the Cypress with a 40-acre pattern or target the Ullin Limestone with a 20-acre pattern. However, these strategies ignore the realities of actual field development in which efforts would be made to co-optimize pattern sizes for the best possible combination of EOR and storage performance, all while considering the economics of the project.

6. Co-optimization, LCA, and Classification of Stacked Reservoir EOR and Storage Resources

Based on subtasks 4.6 and 5.6 in which injection strategies were identified for maximum storage, EOR, and NPV (separately), this task involves reservoir simulation to test development strategies to co-optimize CO_2-EOR and associated storage in stacked ROZ complexes. The detailed reservoir process information will be merged into a broader techno-economic assessment of potential integrated CCUS technology deployments that include nearby CO_2 sources and the optimal, least-cost solutions for transporting CO_2 in candidate pipeline networks. Results from the techno-economic assessment will enable LCA of the fully integrated CCUS process. A key component of the techno-economic assessment includes the evaluation of the impact of the 2018 change to the 45Q federal tax code, which provides significant new credits for incentivizing deployment of CCUS technologies.

6.1 CO_2 Sources and Pipelines to Supply Field Lab Sites

Authors: Ashley S.B. Douds (Indiana Geological and Water Survey) and Kevin Ellett (Carbon Solutions, LLC)

Introduction

Passage of the Inflation Reduction Act (IRA) in August 2022 has spurred interest in exploring options for carbon capture and storage (CCS) in the United States as a greenhouse gas emission mitigation strategy. The enhancements to the I.R.C. § 45Q tax credits within the IRA increased the incentives for storage in saline geologic formations and utilization of emissions from qualifying sources of CO_2 including direct air capture (DAC), industrial and power generation facilities[1]. Depending on the project type, a separate tax credit amount is available: permanent storage or other industrial uses of CO_2, including enhanced oil recovery (EOR).

Two residual oil zone (ROZ) fields within the Illinois Basin were identified as potential targets for EOR using CO_2 from qualifying sources, a greenfield and a brownfield. Throughout the Illinois Basin, median oil saturation of ROZ calculated from log analysis is 23% with 16% and 30% representing one standard deviation[3], which have deterred traditional development in the greenfield case, and led to field abandonment in the brownfield case. New analysis, conducted as a part of this study, indicate the oil saturation (So) of the subject brownfield and greenfield to average around 25%. This report analyzes the unit cost differences between developing either field as EOR targets using an optimal pipeline network from available I.R.C. § 45Q qualifying CO_2 emission sources with proximity to either the brownfield or greenfield.

METHODS

Case and Scenario Development

Residual oil zones are characterized by low oil saturations which inhibit oil recovery from the reservoir using conventional methods. However, several ROZ have successfully produced oil with the use of enhanced oil recovery techniques including injecting the reservoir with CO_2, reenergizing the oil, and enabling oil to move towards a producing well[4]. Therefore, oil that had previously been stranded in the reservoir is produced, and at the same time some amount of CO_2 is sequestered in the formation during this process. As part of the Department of Energy-sponsored Illinois Residual Oil Zone-GeoLab project, the Illinois State Geological Survey (ISGS) conducted a series of reservoir simulations to determine the volume of CO_2 that can be sequestered in the reservoir while co-producing oil. This type of project does qualify

for the enhanced I.R.C. § 45Q tax credits outlined in the Inflation Reduction Act of 2022 of up to $60 per tonne of CO_2 used for EOR[1].

This study evaluates the main drivers of EOR and carbon storage project costs associated with Mississippian-aged reservoirs in east-central Illinois. The sites investigated for this study include the 4,400-acre Noble Field in Richland County, Illinois, identified in this study as the brownfield; and the 440,000-acre Carper Cumberland ROZ prospect centered on Cumberland County, Illinois, identified as the greenfield (Figure 6-1). The brownfield reservoirs used for EOR and carbon storage include the Cypress Sandstone and the Ste. Genevieve Limestone. Oil saturations in the two reservoirs are heterogenous and average 25 to 35%, having been simulated to reflect partial depletion from decades of oil production. Greenfield reservoirs of interest for this study include the Carper and Geneva residual oil zones (ROZ) and the saline aquifer of the Geneva. The Carper and Geneva ROZ intervals have calculated oil saturations of 25% and are modeled as EOR and CO_2 storage zones; the Geneva saline aquifer is modeled as a CO_2 storage interval only.

Proximal ethanol plants and coal-fired power plants were considered as potential CO_2 sources to evaluate differences between the lower volume emission, lower estimated capture cost ethanol plants and the higher volume emission, higher estimated capture cost coal-fired power plants. The scenarios were run for two different project lengths: a 20-year injection period, representing the lifecycle of the project; and a 12-year injection period representing the length of time I.R.C. § 45Q tax credits are applicable for a CO_2 sequestration project.

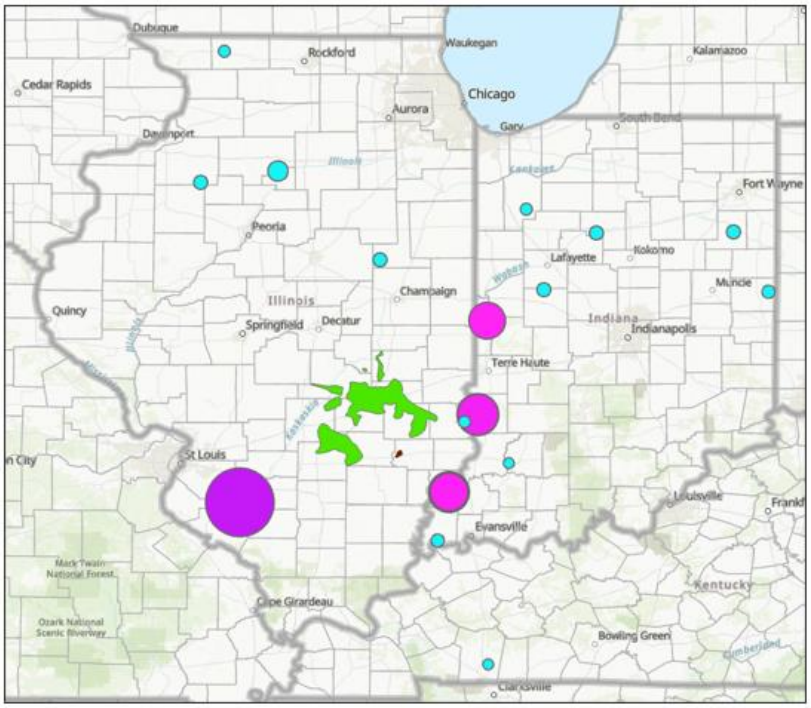


Figure 6-1. Pink circles are coal fired power plants and blue circles are ethanol plants, each is sized proportional to its estimated amount of capturable CO_2. Greenfield and brownfield outlines are shown on the map in green and brown shading, respectively.

Pipeline simulation for the brownfield and greenfield cases were modeled independently. The case for each field consisted of a 20-year project period based on the life cycle analysis (LCA) results conducted within this project and a 12-year project period that runs the length of the 45Q tax credits, with a 0.1

capital recovery rate. For the greenfield and brownfield cases, all 21 source facilities were available to the *SimCCS Gateway* model, and one greenfield case focused solely on the ethanol facilities to evaluate the total unit cost differences.

In addition to varying the project length, brownfield cases include three scenarios (pessimistic, representative, and optimistic) to evaluate a range of expected estimates for capital and operating expenditures (CAPEX and OPEX) needed to establish and operate the project, as well as uncertainty in the total CO_2 storage capacity of the field. The representative case uses average CAPEX and OPEX costs and storage capacity; the pessimistic case includes high-end CAPEX and OPEX costs with a reduced storage capacity by 10%; and the optimistic case uses low-end CAPEX and OPEX costs and storage capacity 10% higher than the representative case. As part of this project, the ISGS conducted a series of dynamic reservoir simulations to evaluate the potential for injecting CO_2 into the Mississippian aged Carper and Geneva reservoirs within the Greenfield and the Cypress and Ste. Genevieve of the Brownfield for both enhanced oil recovery (EOR) and CO_2 storage. This study uses an aggregation of the inputs from the models to develop storage and cost estimates with the Brownfield scenario inputs given in Table 6-1.

Table 6-1. Brownfield scenarios built with output from ISGS model runs.

	12 year			20 year		
	pessimistic case	**representative case**	**optimistic case**	**pessimistic case**	**representative case**	**optimistic case**
Cumulative CAPEX and OPEX ($/tCO2)	19.2	15.3	11.4	21.6	17.7	13.8
storage capacity (megatonnes)	9.99	11.1	12.21	9.99	11.1	12.21

The greenfield cases are more complex with a varying number of injector-producer patterns leading to a broader range of CO_2 storage capacity and cost estimates (Table 6-2). A broad range of capturable CO_2 available from the sources shown in Figure 6-1 is also considered in the greenfield cases. Owing to the larger reservoir volume available in the greenfield, one set of scenarios utilized all the sources available in the study to maximize CO_2 storage, and the other set of scenarios considered using CO_2 emissions solely from ethanol plants to evaluate the effect that lower capture costs could have on overall project costs and development strategies. Details of the greenfield scenarios are outlined in Tables 6-2 and 6-3.

Table 6-2. Parameters used for the six greenfield scenarios using CO_2 from designated coal-fired power plants and ethanol plants. The total annual CO_2 emissions from all these sources is 31.22 Mt CO_2/yr.

Coal-fired power plants and ethanol plants						
Scenario name	Time (years)	Pattern size (acres)	CO_2 available from sources	pattern scaling factor	CO_2 storage, Mt using scaling factor	CAPEX and OPEX ($/tCO2)
12 yr, 40-acre	12	40	375	41	116	16.11
12 yr, 80-acre	12	80	375	41	347	2.60
20 yr, 40-acre	20	40	624	41	172	11.79
20 yr, 80-acre	20	80	624	41	564	1.74
P90, high perm	12	80	375	41	366	3.56
P90, high perm	20	80	624	41	585	2.31

Table 6-3. Parameters used for the six greenfield scenarios using CO_2 from designated ethanol plants. The total annual CO_2 emissions from all these sources is 3.92 Mt CO_2/yr.

Ethanol plants only						
Scenario name	Time (years)	Pattern size (acres)	CO_2 available from sources	pattern scaling factor	CO_2 storage, Mt using scaling factor	CAPEX and OPEX ($/tCO2)
12 yr, 40-acre	12	40	47	5	14	16.11
12 yr, 80-acre	12	80	47	5	42	2.60
20 yr, 40-acre	20	40	78	5	21	11.79
20 yr, 80-acre	20	80	78	5	69	1.74
P90, high perm	12	80	47	5	45	3.56
P90, high perm	20	80	78	5	71	2.31

Assessment of Potential CO_2 Capture Facilities

The CO_2NCORD (CO_2 National Capture Opportunities and Readiness Data) software and database tool was used to evaluate emission sources throughout the region with the potential to supply CO_2 for brownfield and greenfield project development. CO_2NCORD combines a comprehensive database of point source CO_2 emission information from facilities and individual emission stream processes with the most recent peer-reviewed, literature-based capture cost estimates to provide detailed estimates of where CO_2 could be captured, how much could be captured, and at what cost. A total of twenty-one I.R.C. § 45Q eligible capture facilities were selected for this study based on their proximity to both the greenfield and brownfield storage sites and the industrial sector they represent. Only ethanol and coal-fired power plants were considered because these two emission sectors have been the focus of most carbon capture research and demonstration projects to date.

Although ethanol plants have a relatively small CO_2 output, their current estimated capture cost is one of the lowest of all industrial CO_2 sources in the CO_2NCORD database. Prior assessments of capture on the fermentation emission stream from ethanol plants have suggested unitized capture costs of under \$20/tCO_2. However, current results from CO_2NCORD estimate that the average cost of capture for ethanol facilities across the U.S. is most likely about \$25/tCO_2 with recent rates of inflation driving up the overall cost estimate. Note that our estimates for annual capturable emissions and costs used in this study are for the fermentation emission stream only (Table 6-4). Additional co-located emission streams at ethanol plants (e.g., natural gas combustion) are not considered due to their significantly higher estimated cost of capture.

In CO_2NCORD, the estimated cost of retrofitting coal-fired power plants for carbon capture is dependent on the design and age of individual boiler units within the plant. Economies of scale are also predicted to be a significant cost driver on these facilities whereby the unitized cost of capture (\$/tCO_2) decreases as the overall size and volume of the capture unit increases. The most significant uncertainty for including coal-fired power plants in this study is predicting which facilities might remain operational during the timespan of the proposed EOR projects. Although publicly available information indicates that coal-fired power plants other than Prairie State Generating Station may close in this region, the project team decided to include the potential for certain units within three additional power plants to move forward with carbon capture as a means for remaining operational (Table 6-4).

Table 6-4. List of CO_2 emission facilities from the ethanol and coal-fired power generating sectors that were included in this study.

Capture Facility	Sector	Capturable Emissions (MMTA)	Average capture cost ($/tCO2)
Marquis Energy LLC	Ethanol	0.90	24.98
Valero Linden Plant	Ethanol	0.39	24.98
One Earth Energy LLC	Ethanol	0.36	24.98
Valero Bluffton Plant	Ethanol	0.36	24.98
Big River Resources Galva LLC	Ethanol	0.33	24.98
The Andersons Marathon Holdings LLC	Ethanol	0.33	24.98
Valero Mt. Vernon Plant	Ethanol	0.30	24.98
Cardinal Ethanol, LLC	Ethanol	0.30	24.98
Lincolnland Agri-Eenrgy LLC	Ethanol	0.18	24.98
Adkins energy LLC	Ethanol	0.16	24.98
Iroquois Bio Energy Company	Ethanol	0.15	24.98
Commonwealth Agri-Energy LLC	Ethanol	0.10	24.98
Grain Processing Corp	Ethanol	0.06	24.98
Cayuga Generating Station - Unit 1	Power Generation - Coal	2.49	78.63
Cayuga Generating Station - Unit 2	Power Generation - Coal	2.48	78.75
Gibson Generating Station - Unit 1	Power Generation - Coal	2.9	75.37
Gibson Generating Station - Unit 2	Power Generation - Coal	2.59	77.77
Merom Generating Station - Unit 1	Power Generation - Coal	2.97	74.85
Merom Generating Station - Unit 2	Power Generation - Coal	2.86	75.66
Prairie State Generating Station - Unit 1	Power Generation - Coal	5.5	67.31
Prairie State Generating Station - Unit 2	Power Generation - Coal	5.51	67.38

CO_2 Transport Network Generation

Following the parameterization of CO_2 capture and storage facilities as described above, *SimCCS Gateway* was used to generate candidate pipeline networks for the various greenfield and brownfield scenarios (Figures 6-2 through 6-4). Candidate networks provide an optimal, least-cost route of transporting CO_2 from all potential sources to all potential storage sinks based on an underlying spatial cost surface model. In *SimCCS Gateway*, the open-source CostMAP software tool[5] was used to provide a nationwide cost surface model at 1 km resolution. The candidate pipeline networks shown in Figures 6-2 through 6-4 thus represent all potential least-cost pipeline routes that the SimCCS Gateway software may select from when finding an optimal solution to any scenario given the specific constraints of each scenario.



Figure 6-2. Map of candidate network for greenfield 1 (ethanol only). Blue circle is the midpoint of the greenfield, red dots are locations of potential carbon emission sources.

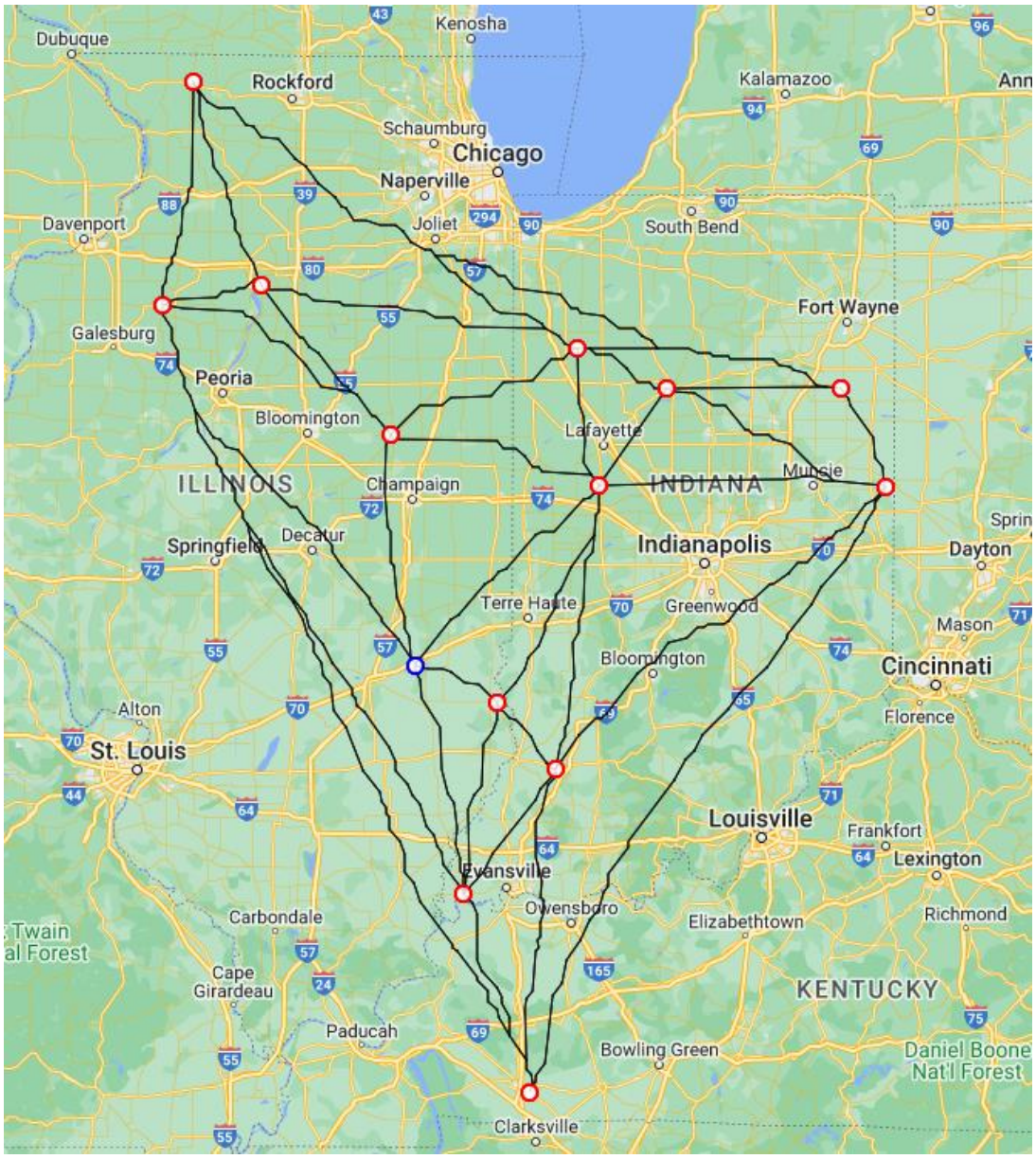


Figure 6-3. Map of candidate network for greenfield 2: ethanol and coal-fired power plant sources. Blue circle is the midpoint of the greenfield, red dots are locations of potential carbon emission sources.

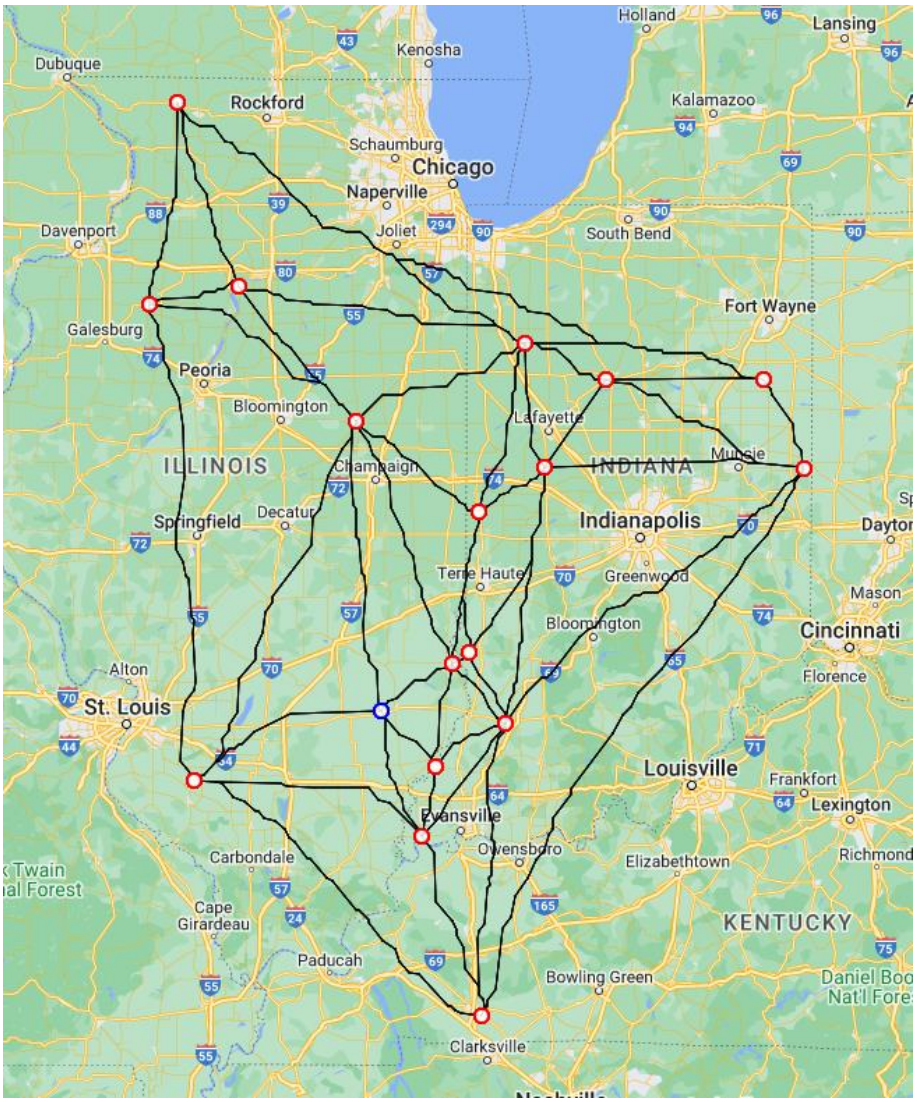


Figure 6-4. Map of candidate network for brownfield case. Blue circle is the midpoint of the brownfield, red dots are locations of potential carbon emission sources.

RESULTS

Brownfield Case

In the Brownfield case, *SimCCS Gateway* selected all sources of CO_2 emissions from ethanol plants due to the lower capture cost as outlined in Table 6-4, except for the 20-year pessimistic scenario. For that scenario, *SimCCS Gateway* opted to pull CO_2 from the Merom Unit 1 most likely because the pipeline would already be near the facility and building a pipeline to another ethanol facility would have driven up the pipeline costs more than including CO_2 from a power plant increased the capture cost (Table 6-5). All scenarios use the same cumulative CO_2 storage range (Table 6-1; high, low, average), but when the timeframe is shortened from 20 years to 12 years, the increased annual amount of CO_2 needed for the brownfield requires the project to build pipelines to additional ethanol plants in the 12-year scenario (Figures 6-5 and 6-6). However, the shortened project timeframe decreases the operating expense (OPEX); therefore, the total unit cost for the 12-year versus the 20-year case is lower in all cases (Figure 6-7). While the transportation and capture unit costs do not vary much between the pessimistic,

representative, and optimistic scenarios, the storage unit cost declines in accord with the total unit cost (Figure 6-7), indicating this variable has the highest impact on the total unit cost for the project. Therefore, upfront storage costs (CAPEX) and ongoing operating costs (OPEX) are a large driver of costs for the brownfield case.

Table 6-5. SimCCS Gateway results from all brownfield model runs.

Project length (years)	Case Name	Number of CO_2 Emission Sources	*Unit Cost ($/tCO$_2$)*			
			Capture	Transport	Storage	Total Cost
12	pessimistic	3	24.98	6.13	19.2	50.31
	representative	4	24.98	6.42	15.3	46.7
	optimistic	4	24.98	6.20	11.4	42.58
20	pessimistic	3	25.93	5.34	21.6	52.87
	representative	2	24.98	6.57	17.7	49.25
	optimistic	3	24.98	7.17	13.8	45.95

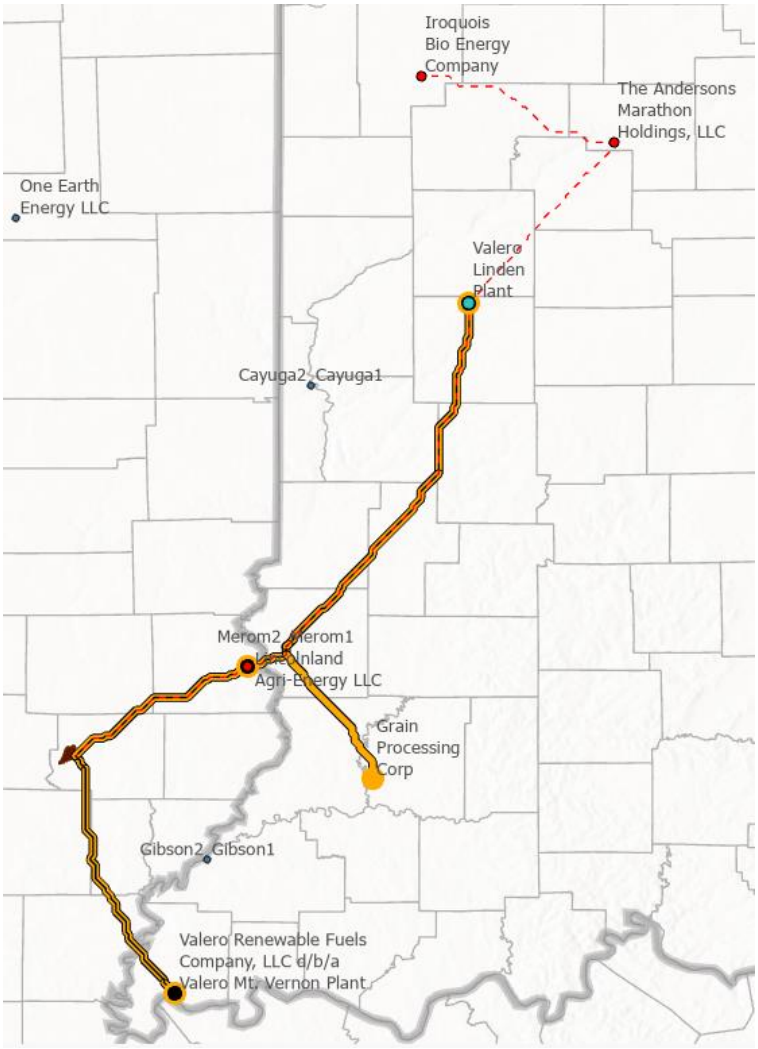


Figure 6-5. Brownfield 12-year cases. Orange pipelines and sources = Representative Case; Black pipelines and sources = Pessimistic Case; Red pipelines and sources = Optimistic Case.

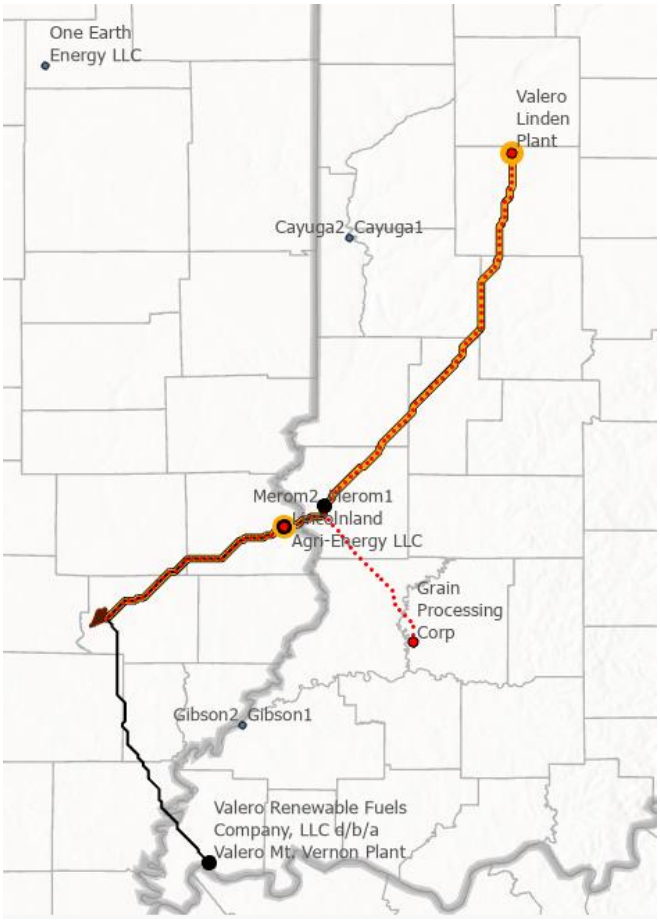


Figure 6-6. Brownfield 20-year cases. Orange pipelines and sources = Representative Case; Black pipelines and sources = Pessimistic Case; Red pipelines and sources = Optimistic Case.

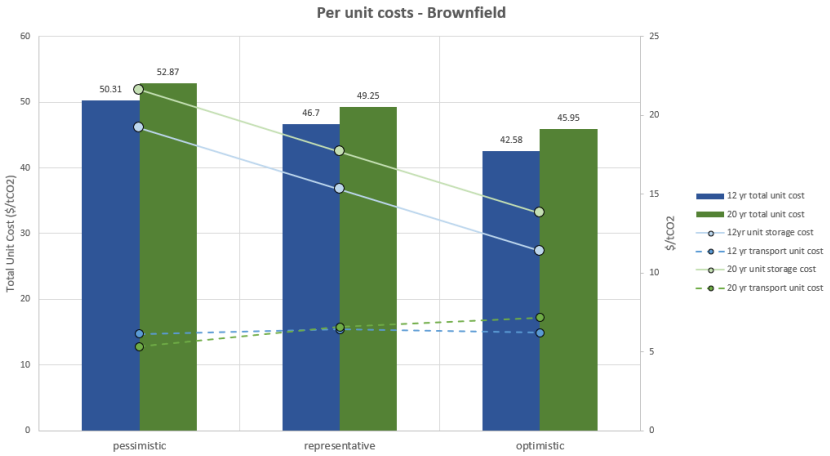


Figure 6-7. Graphical results of Brownfield scenarios.

Greenfield Cases

The greenfield cases run in *SimCCS Gateway* allow for evaluating the impacts on the total unit cost due to changes in project length, injection/producer well spacing, and CO_2 emission sources. Similar to the brownfield case, a set of scenarios were run for the entire 20-year project length and a set for 12 years that reflects the amount of time I.R.C. § 45Q tax credits are available for any qualifying CO_2 sequestration project. The well spacing variables include 40-acre and 80-acre cases. In addition, cases were run to evaluate the impact of CO_2 emission sources on the costs for the project. One case relies only on the lower emission volume, lower cost ethanol plants (greenfield 1) and the other case sources CO_2 from ethanol plants and from higher emission volume, higher cost coal-fired power plants (greenfield 2).

A two-step process was used to determine the amount of CO_2 that could be stored in the greenfield cases. First, the annual CO_2 source capacity was determined and multiplied by the length of the project. A scaling factor for the injector/producer well patterns was determined and applied to each case (ethanol only versus ethanol and coal-fired power plants) ensuring the same number of patterns are used in each scenario without exceeding the CO_2 storage capacity of the field once full-scale development has occurred (Tables 6-2 and 6-3). In each case, the 12 year, 80-acre, P90 scenario was the limiting scenario. The pattern scaling factor describes a repeating pattern of CO_2 injection and producing wells either drilled at 40 or 80-acre spacing over a 1 mi^2 area. Each pattern will have the same number (either 5 or 41) of Carper ROZ, Geneva ROZ, and Geneva aquifer wells.

Project length (years)	Case Name	Number of CO_2 Emission Sources	*Unit Cost ($/tCO$_2$)*			
			Capture	Transport	Storage	Total Cost
12	40 acre	4	24.98	4.71	16.11	45.8
	80 acre	10	24.98	5.3	2.6	32.88
	80 acre P-90	11	24.98	5.75	3.56	34.29
20	40 acre	4	24.98	5.03	11.79	41.8
	80 acre	9	24.98	5.27	1.74	31.99
	80 acre P-90	10	24.98	5.39	2.31	32.68

Table 6-6. Greenfield cases with only ethanol plants as the CO_2 source.

Ethanol-only CO_2 Source – Greenfield 1

In the greenfield case using only ethanol plants as the CO_2 source, the capture unit cost is constant because all ethanol plants were assigned the industry-wide average cost estimate. Modeled transportation unit costs represent a relatively narrow range from $4.71 and $5.75/t$CO_2$. Therefore, the storage unit cost has the highest impact on the variability of project total unit cost in each scenario, which represents the amount of CAPEX and OPEX required to develop the greenfield (Figure 6-8). At the highest level, the difference between the 40-acre and 80-acre cases is that the first case requires double the number of wells drilled to develop the field, which directly relates to storage unit costs. This relationship is graphically depicted in Figure 6-9 illustrating the direct linear relationship between storage and total unit costs, whereas the transport and capture costs show no relationship. It is also noteworthy that as the amount of CO_2 is stored increases, the total unit cost of the project declines exponentially.

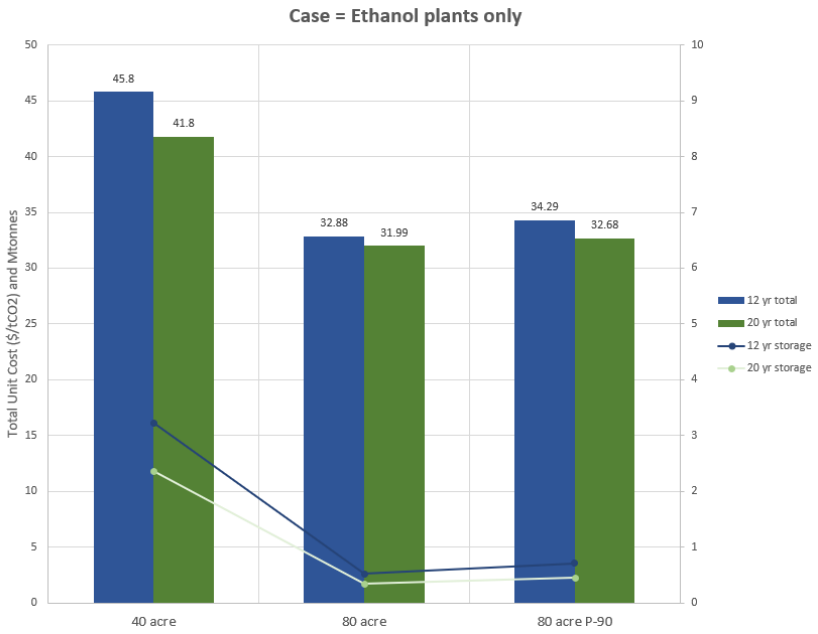


Figure 6-8. Relative difference in total unit cost between 12 yr and 20 yr ethanol only cases. Storage unit costs are the bggest driver in total unit cost changes between scenarios.

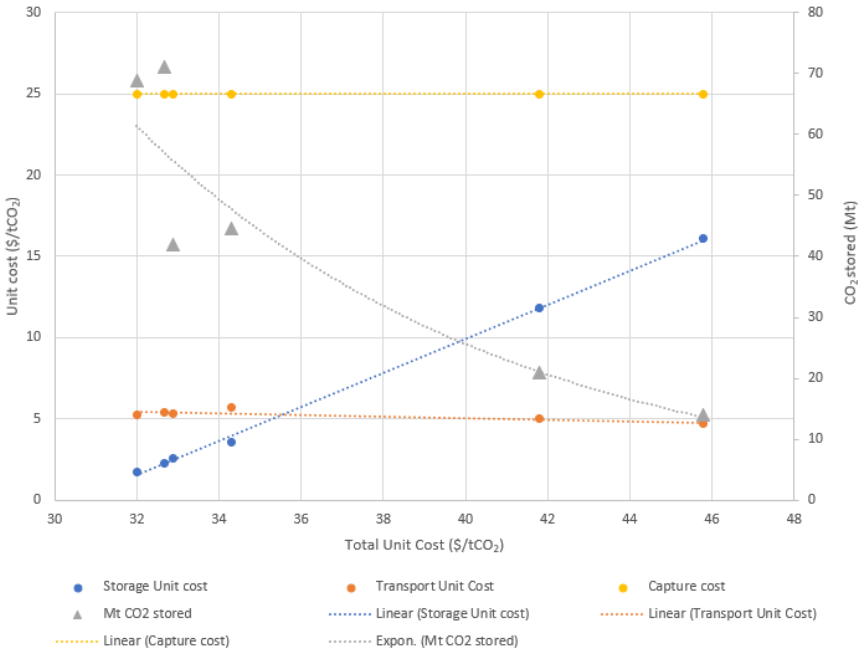


Figure 6-9. Relationship between total unit costs for the ethanol only greenfield project (greenfield 1), individual unit costs, and the amount of CO_2 stored.

In addition to the capital required (CAPEX) to drill the injector and producing wells in these patterns, the length of the project has an impact on the number of years that field operating and maintence costs need to be accounted for. Figure 6-10 graphically illustrates how OPEX costs are dwarfed by the initial CAPEX required to develop the field. These costs are decided at the early stages of the project, which front-loads the CAPEX required to develop the project.

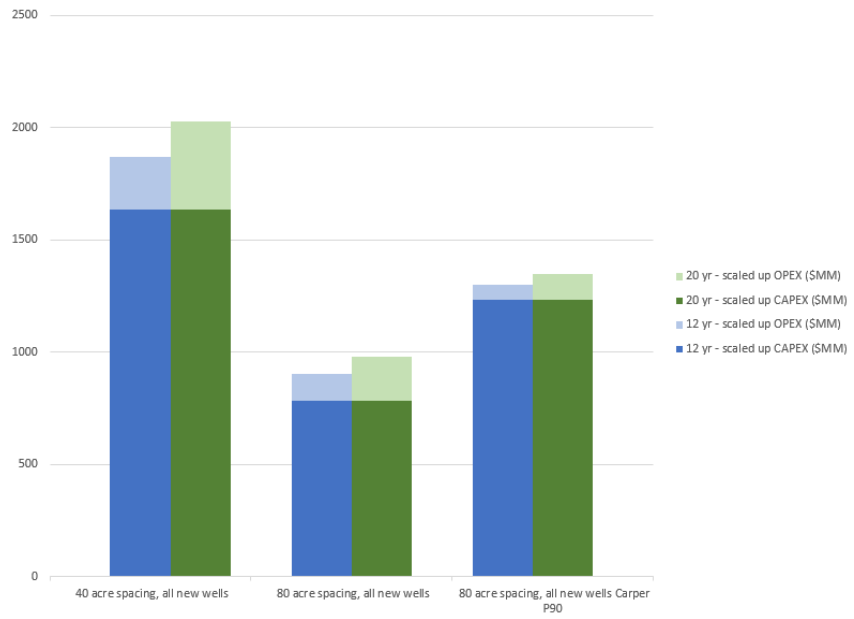


Figure 6-10. Relative costs of OPEX and CAPEX for the ethanol only greenfield case.

Ethanol and Coal-Fired Power Plant CO_2 Sources – Greenfield 2

In these scenarios, *SimCCS Gateway* can select any of the available sources for the project to fill the greenfield. As a result, the capture unit costs vary between each scenario depending on the amount of CO_2 pulled from each facility to reach field capacity (Table 6-7). As in the first greenfield case, the storage capacity of the greenfield is limited by the CO_2 emissions from available sources. Since more sources are available to the model, with higher CO_2 output, the stored CO_2 is an order of magnitude larger than the first greenfield case (Figure 6-11). Modeled transportation unit costs vary from $1.24 and $3.65/tCO2, much less than the first greenfield case (Table 6-7) owing to the significantly larger volumes of CO_2 being transported. In these scenarios, capture unit cost is the biggest driver of total unit cost variability (Figure 6-12).

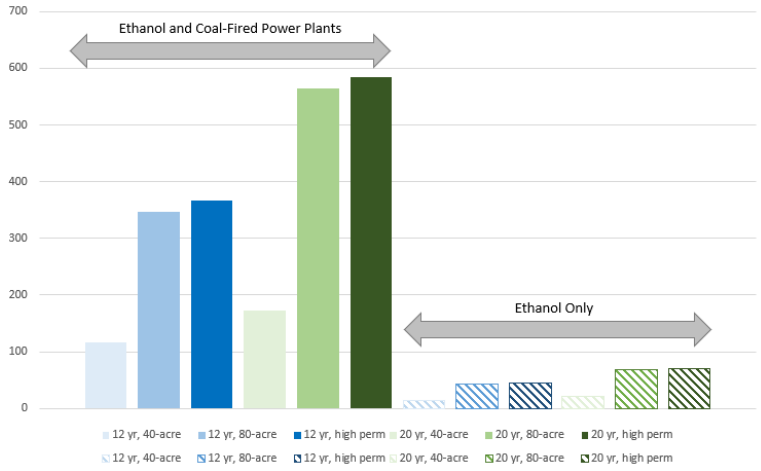


Figure 6-11. CO_2 storage capacity used for both greenfield cases.

Table 6-7. Greenfield cases using ethanol plants and coal-fired power plants as the CO_2 source.

Scenario name	Project length (years)	Pattern size (acres)	Number of CO_2 Emission Sources	*Unit Cost ($/tCO$_2$)*			
				Capture	Transport	Storage	Total Cost
12 yr, 40-acre	12	40	15	50.13	3.32	16.11	69.56
12 yr, 80-acre	12	80	21	65.97	1.38	2.6	69.96
12 yr, P90, high perm	12	80	21	66.64	1.32	3.56	71.52
20 yr, 40-acre	20	40	14	48.01	3.69	11.79	63.49
20 yr, 80-acre	20	80	20	65.65	1.42	1.74	68.81
20 yr, P90, high perm	20	80	21	66.11	1.37	2.31	69.79

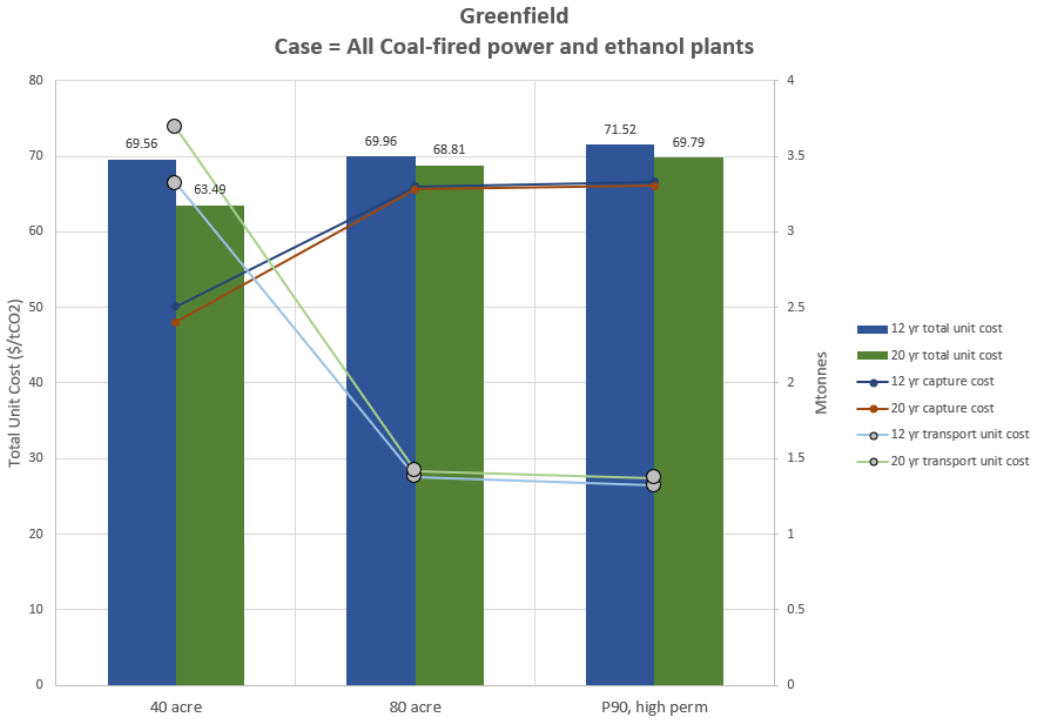


Figure 6-12. Transport and capture unit costs relative to total unit cost of greenfield scenario two.

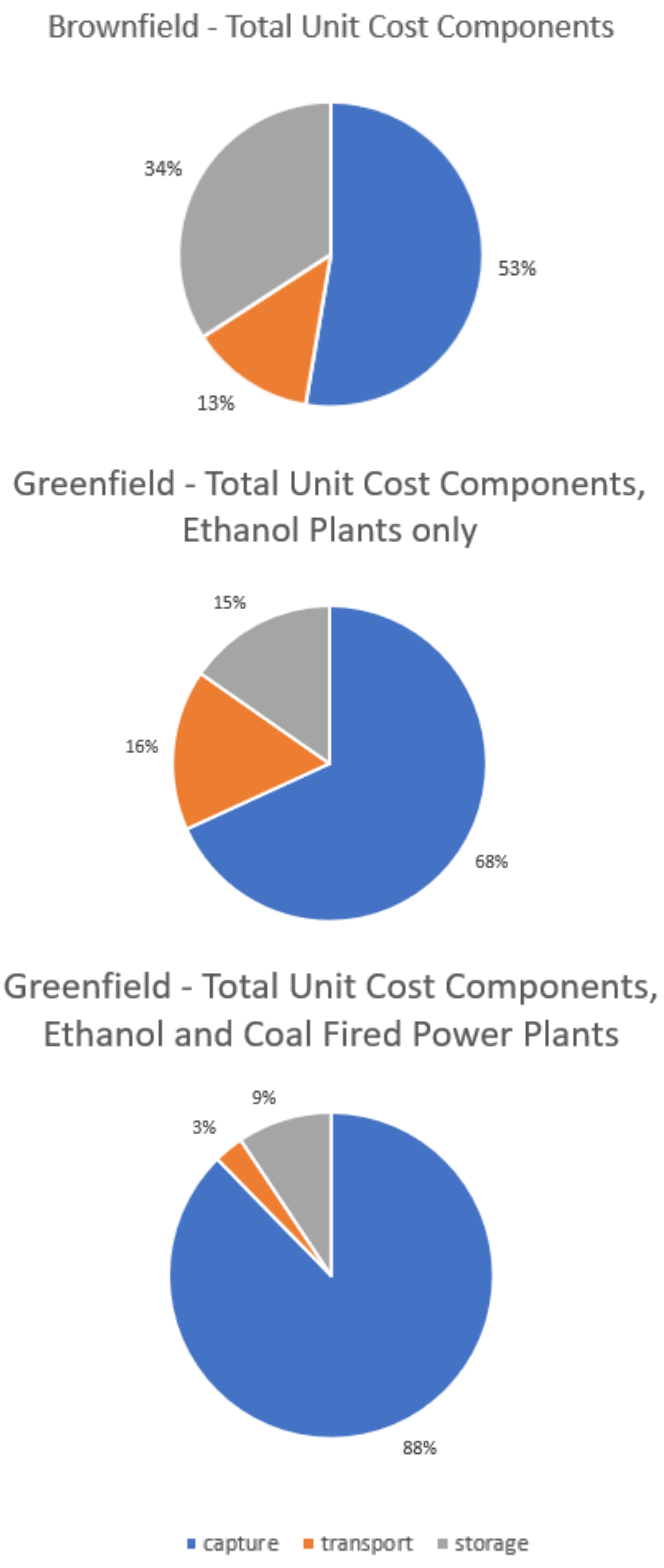


Figure 6-13. Percent of total unit cost for each of the components of the project: capture, transport, and storage. In all cases, capture costs are the largest portion of the total unit cost indicating that technological advancement lowering these costs would be beneficial to similar projects.

CONCLUSIONS

Renewed interest in EOR projects was brought about following the passage of the Inflation Reduction Act of 2022 which extended and enhanced I.R.C. § 45Q tax credits for qualifying CCUS projects. Two residual oil zone fields within the Illinois Basin, an underdeveloped greenfield and a depleted brownfield, were modeled in *SimCCS Gateway* to connect qualifying CO_2 industrial sources to the ROZ fields. The results of each case were evaluated for variations in capture, transport, and storage unit costs relative to the total unit cost for the project. Qualifying coal fired power plant and ethanol facilities within the states of Indiana, Illinois, and Kentucky were selected as the CO_2 sources for the three cases.

Each case was run at a 20-year maximum timeframe and a 12-year case to carve out the amount of time I.R.C. § 45Q tax credits would apply to the project. Due to smaller field capacity, the brownfield case only required CO_2 from 2-4 ethanol plants, greenfield case 1 (ethanol plants only) required CO_2 from 4-11 facilities. In contrast, the greenfield case 2 (ethanol + coal fired power plants) required 14-21 CO_2 industrial sources to meet field capacity.

Between the three cases, storage unit cost had the greatest sensitivity on total unit cost for the brownfield and greenfield 1 (ethanol only) cases. This implies that field development costs play a large role in project economics for these projects. Variations in the total unit cost for the greenfield 2 case (ethanol and coal fired power plants) were impacted most by the capture unit costs. Capture costs are the dominant factor in the high total unit cost for coal fired power plants, so reducing these costs could improve economics for decarbonization.

When evaluating the components of the total unit costs for each project (capture, transportation, and storage) on a percentage basis, capture costs were consistently the largest portion of the total unit costs (53%-88%, Figure 6-13). This implies that working to reduce the costs associated with carbon capture at industrial facilities should be the focus of technology development to improve project economics.

The results from this study can help inform decision making regarding the potential feasibility of enhanced oil recovery projects in ROZ fields. The enhanced 45Q tax credit plus revenue from future oil production should offset some of the total project costs. Improvements in field development costs and capture costs are two areas that would benefit this type of project. Although reducing field development costs may be difficult to achieve, technology enhancements that lower capture costs could benefit the economics.

6.2 Co-Optimized Economic CO_2-EOR and Storage

6.2.1 Brownfield

Authors: Roland Okwen and Nathan Webb

Introduction

The objective of this study is to develop strategies to make the best or most effective combined use of (i.e., co-optimize) carbon dioxide-enhanced oil recovery (CO_2-EOR) and associated CO_2 storage systematically in a stacked storage complex that includes depleted main pay zones (MPZs) and a Residual Oil Zone (ROZ) within a Brownfield Field Laboratory (inside the boundaries of Noble Field, Richland County, Illinois). Reservoir simulations will be used to test development strategies (well pattern size, perforation interval, injection type, and sequencing of the formations [commingled vs. sequential]) to determine the co-optimized EOR and associated storage performance in the integrated stacked reservoir complex.

Development Strategies

Prior to co-optimizing CO_2-EOR and CO_2 storage in stacked reservoirs, development strategies that separately maximize EOR and storage in each formation were identified for the stacked brownfield ROZ site. CO_2-EOR and CO_2 storage were used as metrics for selecting development strategies for six vertically stacked reservoirs that include depleted reservoirs and ROZs. Pattern size, degree of reservoir heterogeneity, reservoir continuity (RC), and dimensionless performance curves (DPCs) were used to make initial CO_2-EOR and CO_2 storage estimates for each formation. The formations studied included (in increasing depth) the Cypress Sandstone, Aux Vases Formation, and the Ste. Genevieve, St. Louis, Salem, and Ullin Limestones. The injection potential (injectivities), CO_2-EOR, and CO_2 storage potentials of the formations were determined via dynamic reservoir simulations. Simulation results were used to validate initial CO_2-EOR and CO_2 storage estimates.

The development strategies are biased towards the two most prolific formations (regarding oil production and potential injectivity, respectively) at the Brownfield site, the Cypress Sandstone and Ste. Genevieve Limestone, which together accounts for approximately 90% of the oil produced from the field. For CO_2-EOR, the strategy is to first prioritize the Cypress Sandstone (which contains both a depleted MPZ and a ROZ) with an 80-acre pattern, followed by targeting the remaining formations with a smaller pattern. For storage, the strategy is to target the Cypress with a 40-acre pattern or target the Ullin Limestone with a 20-acre pattern. However, these strategies ignore the realities of actual field development in which efforts would be made to co-optimize pattern sizes for the best possible combination of CO_2-EOR and CO_2 storage performance while considering the project's economics.

In the proceeding sections, we present (1) descriptions of the geology and static reservoir models of the brownfield laboratory site, (2) dynamic reservoir model description including calibration of the static reservoir model and simulated scenarios, (3) simulation results of simulated cases, and (4) discussions on the interpretation of modeling results of the simulated cases and determination of strategies to co-optimize CO_2-EOR and CO_2 storage.

Geology and Static Reservoir Model

The brownfield laboratory site (Noble Field) contains a stacked complex with a brownfield ROZ and several depleted conventional reservoirs. The field hosts seven oil-bearing formations, six of which are well-developed and producing. The formations include the Cypress Sandstone, Aux. Vases Sandstone, Ste. Genevieve Limestone, St. Louis Limestone, Salem Limestone, and Ullin Limestone. All these formations are Mississippian in age.

Each formation underwent geologic characterization (Webb and Grigsby, 2023). Lithofacies classification schemes relate the spatial occurrence of facies with reservoir properties and depositional environments were interpreted to define conceptual models for each stacked reservoir present at the brownfield laboratory site (Table 6-8). Geocellular models were constructed for the stacked reservoirs using digitized geophysical logs and core data (Figure 6-14). The models were iteratively refined with the conceptual model.

Dynamic reservoir models were initialized based on the geocellular models. The reservoir models include inputs of field laboratory-derived data (e.g., fluid and rock properties), well location, and configuration.

Model Description

The three-dimensional geocellular model of the stacked reservoirs described in section 2, reservoir fluids equation of state (EOS), rock properties, and relative permeabilities were used as input to dynamic simulations.

The geocellular model of the stacked reservoir consists of 127 × 86 × 667 gridblocks in the x-, y-, and z-directions, respectively (Figure 6-14), including infinite-acting aquifers attached to the edges of the model. Each gridblock is 100 ft × 100 ft × 3 ft (30.5 m × 30.5 m × 0.91 m). The porosity cutoff applied to the model ranges from 8% to 12% and varies from one formation to another (Table 6-9). The application of porosity cutoff reduced the number of active gridblocks in the model from 7.3 million to 1.1 million. The infinite-acting aquifers were modeled using the Carter-Tracy analytical aquifer function (Carter and Tracy, 1960), using average reservoir properties (i.e., porosity and permeability) and model dimensions (thickness, length, and width) as input parameters. An infinite-acting aquifer function is not attached to the top and bottom of the model. Vertical production and injection wells were used to simulate primary recovery and waterflooding.

Fluid and Rock Properties

A CO_2-oil-water compositional Nexus® model was used to describe fluid properties and phase behavior as a function of temperature and pressure. The compositional model consists of a Peng-Robinson equation-of-state (PR-EOS) of crude oil with CO_2 as one of its components. A gas-oil ratio of 72 scf/stb, typical of Illinois Basin crude oil (Finley, 2005; Sims, 1993), was assumed. In addition, crude oils from the stacked formations are considered to have similar compositions because density and viscosity measurements from oil samples derived from Mississippian-aged reservoirs across the Illinois Basin are remarkably consistent (Armon et al., 1964, Armon et al., 1966), implying a similar composition.

Table 6-8. Attributes of six oil-producing formations in the vicinity of the Brownfield well.

Formation	Top Depth (ft)	Reservoir Thickness (ft)	Porosity (average %)	Porosity (median %)	Permeability (average mD)	Permeability (median mD)	Reservoir lithofacies	Reservoir continuity	Depositional environment
Cypress Sandstone	2,575	>150	16.9	17.2	452	365	Very fine to fine-grained sandstone	Thick and continuous sheet over entire field	Multistory fluvial channel deposit
Aux Vases Sandstone	2,865	30	14.9	13.3	6	2	Very-fine grained shaley sandstone	Thin and continuous, but porosity controlled by facies changes and shale content	Coastal - tidal flat deposits
Ste. Genevieve Limestone	2,975	<10	13.5	13.8	410	212	Oolitic and skeletal grainstones	Uncemented, flat-bottomed, convex-upward lenses <10 ft thick, elongate, from 0.5 mi to several miles in length, 0.125 to 0.75 mi in width	Shallow-water high energy shoals and bars
St. Louis Limestone	3,150	Multiple; Variable	9.3	9.6	2	<1	Microsucrosic dolomite	Thin, continuous sheets	Altered lime mudstones deposited in restricted lagoonal settings
Salem Limestone	3,275	Multiple; Variable	5.5	4.7	7	<1	Oolitic and skeletal grainstones	Discreet lenses that occur within the lower part of three shoaling upward cycles	Shallow-water high energy shoals and bars
Ullin Limestone	3,700	Multiple; Variable	insufficient data				Bioclastic bryozoan (+/- crinoid) grainstones	Thin aprons adjacent to discontinuous bryozoan boundstone mounds	Buildups and storm-generated sand waves

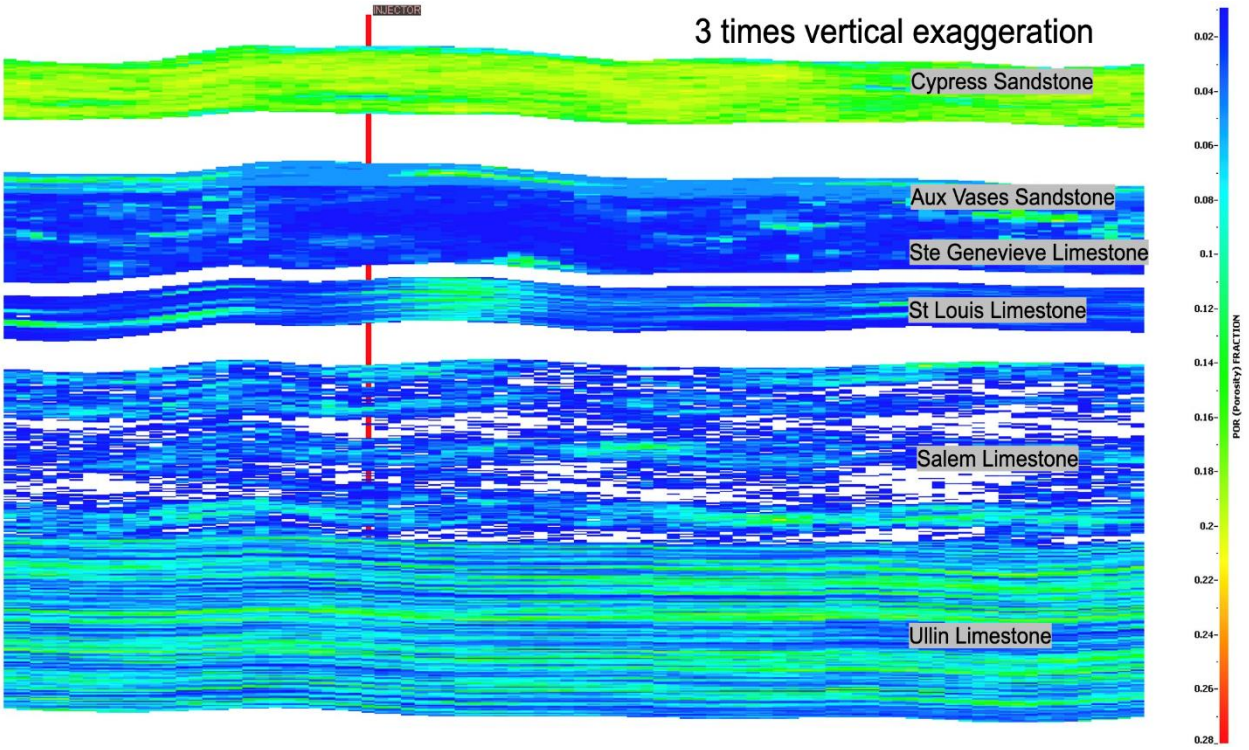


Figure 6-14. Cross section through the geocellular model. The Cypress (red), Aux Vases (green), and Ullin (purple) are shown as solid colors, whereas the Ste. Genevieve (blue), St. Louis (yellow), and Salem (orange) show the interpolated heterogeneity and discreet reservoir bodies common to the carbonate reservoirs (see Figure 6-18).

Table 6-9. Reservoir parameter of the stacked formations.

Formation	**Cypress Ss**	**Aux Vases Fm**	**Ste. Genevieve Ls**	**St. Louis Ls**	**Salem Ls**	**Ullin Ls***
Depth (ft)	2,570	2,865	2,910	3,080	3,270	3,700
Temperature (^{O}F)	88	90	90	92	94	98
Porosity cutoff (%)	12	11	8	11	9	8
Average porosity (%)	16.79	13.54	14.48	13.67	10.18	11.6
Average permeability (md)	334.62	32.45	160	83.49	11.7	59.22

A calibrated PR-EOS, depicting crude oil phase behavior and fluid properties using laboratory measurements of viscosity, density, and composition (Table 6-10) of a Cypress crude oil sample (Okwen et al., 2023) was used as input to the dynamic model. The relative permeabilities of reservoir fluids were generated using Corey's function (Corey, 1954) to mimic water-wet conditions. The end-point saturations and relative permeabilities, chosen based on previous simulation work in the ILB (Knepp et al., 2009), are presented in Table 6-11 and Figure 6-15.

Table 6-10. Composition of Cypress oil sample measured by simulated distillation by volume percent. (Okwen et al., 2023).

Carbon number	Volume %	Carbon number	Volume %
< 5	0.5	18	3.4
5	0.5	19	3.3
6	0.5	20	3.0
7	2.9	22	5.0
8	5.7	24	4.3
9	5.8	26	3.3
10	4.0	28	3.8
11	3.9	30	3.1
12	3.3	32	2.8
13	4.6	34	2.2
14	3.8	36	1.8
15	4.0	38	1.9
16	3.8	40	1.5
17	4.2	40^{+}	13.1

Table 6-11. Saturation and relative permeability endpoints.

Parameter	Value
Irreducible water saturation, S_{wr}	0.35
Residual oil saturation to water, S_{orw}	0.25
Residual oil saturation to gas, S_{org}	0.03
Critical gas saturation, S_{gc}	0.10
Water relative permeability at residual oil saturation, $k_{rw,max}$	0.20
Gas relative permeability at irreducible water saturation, $k_{rg,max}$	0.90
Oil relative permeability at irreducible water saturation, $k_{row,max}$	0.80
Oil relative permeability at residual gas saturation, $k_{rog,max}$	0.80

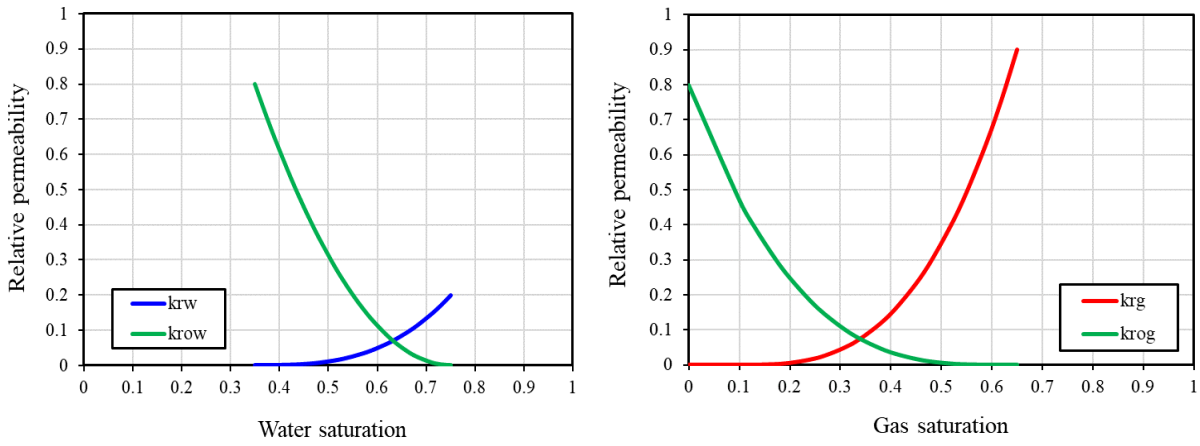


Figure 6-15. Water-oil relative permeability (left) and gas-oil relative permeability (right). The Stone II method (Stone, 1973) was used to approximate 3-phase (water-oil-gas) relative permeability, i.e., simultaneous flow of three phases (Okwen et al., 2023).

Initial Conditions

All producers and injectors were assigned a wellbore radius of 0.327 ft (3.924 inches I.D.) with zero skin because there is no historical record of well stimulations (except in Ste Genevieve). Except for the residual

oil zone in the Cypress, the specified initial oil saturation of the stacked reservoirs is 65%. The initial oil saturation of the residual oil zone is 35%, which is 10% greater than the residual oil saturation to water (S_{orw}, Table 6-11). In addition, only the Cypress Sandstone and Ullin Limestone have aquifers underlying the MPZ. The aquifer in the Ullin Limestone is thicker but less permeable and has lower reservoir connectivity than the aquifer in the Cypress Sandstone. As a result, the Cypress Sandstone and Ullin Limestone are each expected to have high associated CO_2 storage potential.

McCain correlation (McCain, 1991) was used to estimate brine properties (density, viscosity, and compressibility) from the average reservoir temperatures and salinities of the formations (Table 6-12). In addition, the rock compressibility of the formations were estimated from the average porosities of the formation using the Newman correlation (Newman, 1973).

Table 6-12: Input parameters used to simulate primary production and waterflood.

Parameter	**Formation**					
	Cypress	Aux Vases	Ste Genevieve	St. Louis	Salem	Ullin
*Datum (ft, MD)	2605	2865	2910	3080	3270	3700
Average temperature (^{O}F)	89	90	90	92	94	98
Brine density (lb/ft^3)	67.4	67.4	67.4	67.4	67.4	67.4
Initial pressure (psia)	1232.8	1354.4	1375.4	1454.9	1543.8	1744.8
Rock compressibility (psi^{-1})	3.44 x 10^{-6}	4.53 x 10^{-6}	5.83 x 10^{-6}	6.16 x 10^{-6}	8.10 x 10^{-6}	7.17 x 10^{-6}
Brine viscosity (cp)	0.93	0.92	0.92	0.91	0.89	0.87
Brine compressibility (psi^{-1})	2.75 x 10^{-6}	2.74 x 10^{-6}	2.74 x 10^{-6}	2.75 x 10^{-6}	2.75 x 10^{-6}	2.76 x 10^{-6}
$^{+}$Well radius (in)	3.92	3.92	3.92	3.92	3.92	3.92
Producing BHP (psia)	1000	50	50	50	50	50
**Maximum BHP (psia)	2619.7	2879.7	2924.7	3094.7	3284.7	3714.7
*Note: *550 ft ground elevation, $^{+}$zero skin factor, ** maximum injection pressure*						

Methods

Dynamic Reservoir Model

Reservoir simulations were performed using the geocellular model of the stacked reservoirs, initial reservoir parameters, and fluid properties as inputs. The purpose of the reservoir simulations is to determine strategies to co-optimize CO_2-EOR and associated storage in vertically stacked reservoirs and ROZs based on field laboratory data that have been incorporated into reservoir models.

Reservoir simulations of individual formations were also performed to assess their CO_2 EOR and storage potentials. Prior to co-optimizing storage and CO_2-EOR (subtask 6.1), development scenarios (via reservoir simulation) that will maximize storage, EOR, and net present value were identified. For individual formations, sensitivity to different well spacing, and completion interval of injection and production wells were simulated. Finely gridded pattern models were used to identify the most promising development scenarios for use in larger full-field models. For the entire stacked ROZ complex, simultaneous and sequential injection into each formation were simulated.

Historical production of the Cypress Sandstone and Ste. Genevieve limestone was replicated because both formations are prolific oil-producing formations. Before simulating CO_2 injection, oil within the formations is depleted to residual saturations via primary recovery and waterflooding. Optimum CO_2 EOR and storage field development strategies were identified by simulating multiple CO_2 injection scenarios. Field development strategies were selected using the following metrics:

- CO_2-EOR (Mstb),
- CO_2 storage (G_{store} [million tonnes]),
- oil recovery factor (RF, [stb/stb]),
- net utilization factor (NF, [Mscf/stb]),
- CO_2 storage factor (SF, [Mscf/stb]), and
- carbon balance of oil produced (CB, [tonnes/stb]).

This section begins with descriptions of the inputs used to initialize dynamic reservoir models, simulated scenarios, and development strategies, including a presentation of simulation results by formations and the entire stacked reservoirs and discussions.

Model Calibration

Except for the Ste Genevieve Limestone, extensive waterflooding was not performed in the stacked formations at Noble Field. As a result, 40 years of waterflooding was simulated for the Ste Genevieve Limestone.

Primary Production and Waterflood

Based on field production history, the Ste. Genevieve Limestone contains the only reservoirs that were systematically waterflooded as part of the field development. There has been significant saltwater disposal into the brine aquifer within the Cypress Sandstone and some scattered water injection wells target other formations, but only the St. Genevieve had sustained water injection in quasi-organized well patterns over a large area. The simulated primary production and waterflood periods are 25 - 65 years and 40 years, respectively. Specifically, 65 years of primary production from the Cypress, Aux Vases, and St Louis, 45 years of primary production from Salem and Ullin, and 25 years of primary production plus 40 years of waterflooding from the Ste Genevieve.

The well spacing used to simulate primary production is based on formation type. Historically, the regulated well spacings for sandstone and carbonate formations in Illinois prior to 2020 were 10 acres and 20 acres, respectively (Hedin, 2020). As a result, 10-acre well spacing was used to simulate primary recovery from the Cypress and Aux Vases, and 20-acre well spacing was used for the Ste Genevieve, St Louis, Salem, and Ullin. Also, waterflooding of the Ste Genevieve was simulated using an injection pattern size of 40 acres. The input parameters used to simulate primary production and waterflood for each formation are presented in Table 6-12.

Simulation results show that the Cypress Sandstone and Ste Genevieve Limestone are the most prolific, while Salem Limestone is the least prolific oil-producing formation (Table 6-13). Oil production from the Cypress is significantly higher than that of Ste Genevieve because it is more permeable and relatively homogeneous than the Ste Genevieve, which has limited reservoir connectivity. Similarly, the Ste Genevieve is a more prolific oil-producing formation than the Ullin, St. Louis, Aux Vases, and Salem because it is more permeable (Table 6-8). Oil production from the top of the Ullin is high compared to Salem due to pressure maintenance from an underlying aquifer. Water injection into the Ste Genevieve caused pressure buildup increases in reservoir pressure in the overlying Aux Vases and underlying St Louis

formations, thus boosting oil production from both formations (Figure 6-16). As a result, the oil rate curves of Ste Genevieve, Aux Vases, and St. Louis have two maxima, the first at the start of primary production and the other during the early stage of water injection into the Ste Genevieve (Figure 6-16). The fluid saturations used to initialize CO_2 EOR simulations are assumed equivalent to saturations at the end of primary production; for Cypress, Aux Vases, St Louis, Salem, and Ullin Formations; and waterflood; for the Ste Genevieve Limestone. Baseline simulations that involve the continuation of either primary production or waterflood (depending on the formation) were performed to determine incremental oil production due to CO_2 EOR. For example, the baseline simulation for the Cypress Sandstone and Ste Genevieve Limestone involve the continuation of primary production and waterflood, respectively.

The average oil saturations in each formation before CO_2 injection starts range between 61% and 31% (Table 6-14). Except for the Aux Vases, results in Table 6-14 show a correlation between residual oil saturation and reservoir continuity i.e., residual oil saturation decreases with increasing reservoir continuity. The residual oil saturation for Ste Genevieve is lower than those of St Louis and Salem because Ste Genevieve was waterflooded. Similarly, the residual oil saturation of St. Louis is lower than that of Salem due to pressure buildup from water injection in Ste Genevieve.

Table 6-13. Estimated primary production and waterflooding oil recovery of each formation.

Formation	**OOIP (Mstb)**	**Primary production (Mstb)**	**Waterflood (Mstb)**	**Prim Oil rec**	**WF Oil rec**
Cypress	55,469.0	20,672.3	-	37.3%	0.0%
Aux Vases	3,671.5	586.1	-	16.0%	0.0%
Ste Genevieve	35,602.0	8,997.2	3,588.4	25.3%	10.1%
St. Louis	3,456.8	631.8	-	18.3%	0.0%
Salem	7,560.9	293.3	-	3.9%	0.0%
Ullin	8,649.7	1,148.0	-	13.3%	0.0%
Total	114,410	32,328.7	3,588.4	28.3%	10.1%

Table 6-14. Estimated average residual oil saturation at the end of either primary recovery or waterflooding of each formation.

Formation	*Continuity (%) 933 ft [20-ac]	Average residual oil saturation	Endpoint
Cypress	95.2	31 %	Primary recovery
Aux Vases	-	49 %	Primary recovery
Ste Genevieve	63.8	40 %	Waterflood
St. Louis	66	47 %	Primary recovery
Salem	77.1	61 %	Primary recovery
Ullin	18.3	52 %	Primary recovery
*Note: * .(cite Brownfield development strategies deliverable report)*			

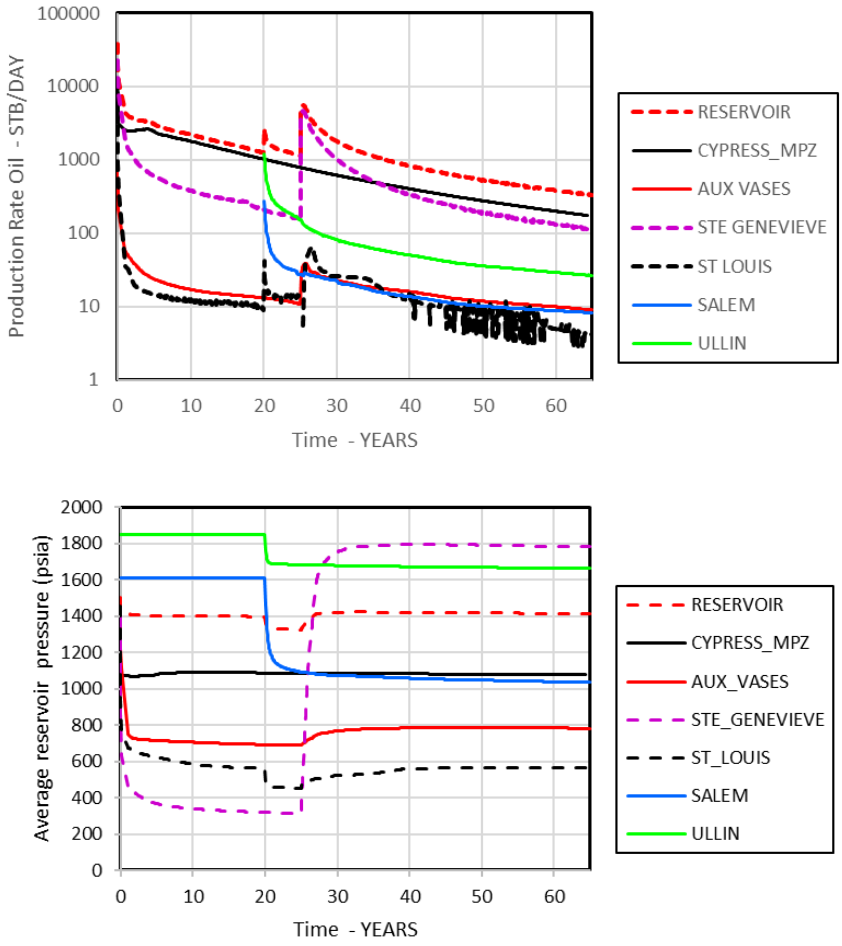


Figure 6-16. Oil production rate (top) and average reservoir pressure (bottom) by formation during primary production (Year 0 – year 65 for Cypress, Aux Vases, and St Louis, year 0 – year 25 for Ste Genevieve, and year 20 – year 65 for Salem, and Ullin) and waterflooding (year 25 – year 65 for Ste Genevieve).

Simulated Scenarios

Multiple brownfield development scenarios, including sensitivities of reservoir performance (i.e., CO_2-EOR and CO_2 storage) to changes in injection schemes and 5-spot pattern size, were simulated to determine strategies to develop stacked brownfield ROZs. Injection schemes simulated were continuous and water-alternating-gas (WAG) (Jarrell et al., 2002), including simultaneous and sequential injection of CO_2 into multiple reservoirs. CO_2 flood simulations used 40-acre and 80-acre five-spot patterns in the Ste Genevieve Limestone and Cypress Sandstone, respectively. An extensive list of the cases simulated is presented in the appendix. The simulated cases (Table 6-15) selected to determine strategies for developing stacked brownfield ROZs were grouped into the following scenarios; (1) baseline cases, (2) Conventional EOR with Associated Storage (CEOR-AS), (3) Advance EOR with Associated Storage (AEOR-AS), and (4) Advanced EOR with Maximum Storage (AEOR-MS).

Baseline Dases

Two baseline cases (IOR and EOR), in which primary and/or water flooding is simulated for the duration of a CO_2 flood project, were simulated. In the IOR baseline, producers (existing wells) are pumped off (i.e., 50 psia producing bottomhole pressure (BHP). In the EOR baseline, the producing BHP is 1200 psia which is equivalent to the producing BHP of the miscible CO_2 flood cases simulated in this study. In addition, the producers in the EOR baseline are pattern wells.

Conventional EOR with Associated storage (CEOR-AS)

Four water-alternating-gas (WAG) simulations were simulated to assess the impact of flooding the Cypress and Ste Genevieve separately or sequentially on reservoir performance. Results from a preliminary sensitivity study (not shown but cases included in Appendix 6-1) on the effect of water cycle duration on oil production indicate that a 7-day water cycle yielded the highest oil production and decreases as the water cycle duration increases. As a result, a 7-day water cycle was adopted for WAG simulations.

In the short sequential WAG cases, CO_2 is injected into Ste Genevieve for three years and into the Cypress for the remaining 17 years. This strategy was adopted because oil production from the Ste Genevieve steeply declined (e.g., from 7,650 stb/day to 837 stb/day) while oil production from the Cypress declined at a slower pace (e.g., from 3,190 stb/day to 2,560 stb/day) after three years of primary recovery (Figure 6-16).

Advanced EOR with Associated Storage (AEOR-AS)

Five continuous CO_2 flood cases were simulated to assess the effect of flooding the Cypress and Ste Genevieve separately or commingling injection into both reservoirs on reservoir performance. For the same reason stated in section 3.4.2, a short sequential continuous injection case in which CO_2 is injected into Ste Genevieve for three years and into the Cypress for the remaining 17 years was simulated. These simulations were performed to explore the feasibility of increasing oil production and CO_2 storage.

Advanced EOR with Maximum Storage (AEOR-MS)

Two continuous CO_2 flood cases that include CO_2 injection into Cypress aquifer were simulated to assess the feasibility of increasing CO_2 storage. The simulations were also performed to assess the sensitivity of CO_2 storage to changes in well completion strategy i.e., injecting CO_2 via a single vertical well perforated through the entire thickness or at the bottom (33 ft) of the Cypress aquifer. This scenario is analogous to the “stacked storage” concepts depicted in Hovorka, 2013 which involves re-injecting produced CO_2 into a saline aquifer.

Table 6-15. Summary of reservoir simulation scenarios for the brownfield. All EOR scenarios use vertical wells in regular 5-spot patterns. The pattern size in the Ste. Genevieve Limestone is 40-acre and the pattern size in the Cypress Sandstone is 80-acre.

Scenario	Case #	Development	Injection type	Water cycle duration	Constraints / Description
Baseline Cases					
IOR (Economic) Baseline	1	Commingled	N/A	N/A	Cypress primary production; Ste. Genevieve waterflood. Using existing (historical) wells
EOR Baseline	2	Commingled	N/A	N/A	Cypress primary production; Ste. Genevieve waterflood. Using EOR well patterns
Conventional EOR with Associated Storage (CEOR-AS)					
Cypress Sandstone only	3	N/A	WAG	7-day	5-spot pattern CO_2 floods (WAG) of the Cypress. Plus 7 days Max water cycle duration
Ste. Genevieve Limestone only	4	N/A	WAG	7-day	5-spot pattern CO_2 floods of the Ste Genevieve. 7 days maximum water injection duration
Cypress Sandstone and Ste. Genevieve Limestone	5	Short sequential	WAG	7 days (Ste. Gen only)	Three years conventional production from Cypress and EOR from Ste. Gen. Cypress EOR begins at year three.
Cypress Sandstone and Ste. Genevieve Limestone	6	Short sequential	WAG	7-day	Three years conventional production from Cypress and EOR from Ste. Gen. Cypress EOR begins at year three.
Advanced EOR with Associated Storage (AEOR-AS)					
Cypress Sandstone only	7	N/A	Continuous	N/A	5-spot pattern CO_2 floods of the Cypress (80-acre patterns).
Ste. Genevieve Limestone only	8	N/A	Continuous	N/A	5-spot pattern CO_2 floods of the Ste Genevieve (40-acre patterns).
Cypress Sandstone and Ste. Genevieve Limestone	9	Commingled	Continuous	N/A	5-spot pattern CO_2 floods of the Cypress (80-acre patterns) and Ste Genevieve (40-acre patterns).
Cypress Sandstone and Ste. Genevieve Limestone	10	Separate	Continuous	N/A	
Cypress Sandstone and Ste. Genevieve Limestone	11	Short sequential	Continuous	N/A	Three years conventional production from Cypress and EOR from Ste. Gen. Cypress EOR begins at year three.
Advanced EOR with Maximum Storage (AEOR-MS)					
Cypress Sandstone (plus aquifer) and Ste. Genevieve Limestone	12	Commingled	Continuous	N/A	Rate = 1,000 Mscf/day
Cypress Sandstone (plus aquifer) and Ste. Genevieve Limestone	13	Commingled	Continuous	N/A	Rate = 1,000 Mscf/day, perforated bottom 33 ft of aquifer

Results

Simulation Results

Simulation results indicate that cases in the "Conventional EOR with Associated Storage" (CEOR-AS) scenario will produce more oil and water than corresponding cases in the "Advanced EOR with Associated Storage" (AEOR-AS) scenario (Table 6-16) because injection schemes used in the former and latter are WAG and continuous, respectively. The mobility of CO_2 is lower in WAG than in continuous injection floods; as a result, sweep efficiencies, thus oil production, in the simulated CEOR-AS cases are higher than those of the AEOR-AS. Higher water production in the CEOR-AS cases is a result of water injected to stabilize the CO_2 front. On the other hand, significantly larger volumes of CO_2 are injected and produced in the AEOR-AS than CEOR-AS cases (Table 6-16) because CO_2 injection is interrupted in CEOR-AS cases during the water injection phase of a WAG cycle. The switch from water to CO_2 injection in WAG simulations varies from well to well due to reservoir heterogeneity. Thus, the CEOR-AS cases are designed to maximize oil production (recovery) and minimize CO_2 utilization.

Furthermore, oil production and CO_2 storage of the cases (cases 12 and 13, Table 6-16) in the Advanced EOR with Maximum Storage (AEOR-MS) scenario are greater that of a corresponding case (case 9, Table 6-16) in the AEOR-AS scenario because additional volumes of CO_2 is injected via a dedicated well into to the Cypress aquifer underlying the Cypress ROZ. Increased oil production is achieved in the AEOR-MS case due to pressure propagation and movement of CO_2 from the Cypress aquifer to Cypress ROZ. Additionally, the proportion of CO_2 injected into the MPZ, via wells completed in the MPZ and ROZ, increased due to pressure buildup in the ROZ thereby increasing the pressure and oil production from the MPZ. Therefore, CO_2 injection into the Cypress aquifer positively impacts oil recovery from MPZ and ROZ by increasing the average pressure within the Cypress Sandstone.

The metrics (equations 1– 6) used to evaluate the performances of the simulated cases include; CO_2-EOR (Mstb), CO_2 storage (G_{store} [thousand tonnes]), oil recovery factor (RF, [stb/stb]), net utilization factor (NUF, [Mscf/stb]), CO_2 storage factor (SF, [Mscf/stb]), CO_2 storage efficiency (E), and carbon balance of oil produced (CB, [tonnes/stb]) or net utilization factor (NF, [Mscf/stb]).

$$CO_2EOR = N_{p,CO_2} - N_{p,baseline} \ [stb] \quad \textbf{(1)}$$

$$G_{store} = G_{inj,CO_2} - G_{p,CO_2}[Mscf \times \frac{1}{18.854} \frac{tonne}{Mscf}] \quad \textbf{(2)}$$

$$RF = \frac{CO_2EOR}{OOIP} \left[\frac{stb}{stb}\right] \quad (3)$$

$$SF = NF \times RF \left[\frac{Mscf}{stb}\right] \quad (4)$$

$$E_{CO_2} = \frac{G_{store}B_{gCO2}}{PV} \left[\frac{rb}{rb}\right] \quad (5)$$

$$NUF = CB = \frac{G_{store}}{CO_2EOR} \left[\frac{Mscf}{stb}\right] \left[\frac{Mscf}{stb} \times \frac{1}{18.854} \frac{tonne}{Mscf}\right] \quad \textbf{,(6)}$$

where $N_{p,}CO_2$, $N_{p,baseline}$, $G_{inj,}CO_2$, $G_{p,}CO_2$, OOIP, and PV are the cumulative oil production of CO_2 flood (Mstb), baseline cumulative oil production (Mstb), CO_2 injected (MMscf), CO_2 produced (MMscf), original oil in place (pre-primary production, Mstb), and pore volume (Mrb), respectively.

Table 6-16. Summary of results of reservoir simulation scenarios for the brownfield.

Sim #	Scenario	Case	Cumulative oil production (Mstb)	CO_2 storage (Mtonnes)	Cumulative Gas Injection (MMscf)	Cumulative Water Production (Mstb)	Cumulative CO_2 production (MMscf)
Baseline Cases							
	IOR (Economic) Baseline	1	121	n/a	n/a	6,901	n/a
	EOR Baseline	2	313	n/a	n/a	14,894	n/a
Conventional EOR with Associated Storage (CEOR-AS)							
53	Cypress Sandstone only	3	884	338	6,762	76,596	73
51	Ste. Genevieve Limestone only	4	391	162	11,458	3,999	8,343
49	Cypress Sandstone and Ste. Genevieve Limestone	5	903	297	5,932	65,147	212
52	Cypress Sandstone and Ste. Genevieve Limestone	6	922	307	6,174	65,117	213
Advanced EOR with Associated Storage (AEOR-AS)							
59a	Cypress Sandstone only	7	483	870	46,913	3,855	30,077
58a	Ste. Genevieve Limestone only	8	339	221	36,380	1,221	32,014
34	Cypress Sandstone and Ste. Genevieve Limestone	9	731	1,006	73,540	5,441	54,545
35	Cypress Sandstone and Ste. Genevieve Limestone	10	748	892	69,384	5,572	52,120
50	Cypress Sandstone and Ste. Genevieve Limestone	11	501	780	32,386	4,649	17,410
Advanced EOR with Maximum Storage (AEOR-MS)							
54	Cypress Sandstone (plus aquifer) and Ste. Genevieve Limestone	12	900	1,357	73,544	5,485	55,182
56	Cypress Sandstone (plus aquifer) and Ste. Genevieve Limestone	13	823	1,358	73,544	5,489	55,173

These metrics were used to compare and subsequently identify field development strategies for co-optimizing CO_2-EOR and CO_2 storage in stacked brownfield reservoirs. Cases with the highest metrics values are highlighted in gray (Table 6-17). The CEOR-AS (short sequential WAG case 5 and case 6) and AEOR-MS (continuous CO_2 flood and injection into Cypress aquifer [case 54]) cases have the highest CO_2-EOR ($\geq$ 900 Mstb). The continuous injection cases in the AEOR-AS (case 9) and AEOR-MS (cases 12 and 13) scenarios have the highest G_{store}. The cases with the highest RF (Table 6-17) were WAG (case 3 and case 4) and continuous injection into the Ste Genevieve (case 8). WAG injection scheme was used in CEOR-AS simulations to reduce CO_2 mobility (i.e., flood conformance), increase CO_2 breakthrough time (Harouaka et al., 2013), and improve volumetric displacement efficiency (Jarrell et al., 2002); therefore, CEOR-AS cases were expected to have the highest CO_2-EOR. Higher EOR was achieved in case 12 (continuous injection into the Cypress MPZ, Cypress ROZ, Cypress aquifer, and Ste Genevieve) due to increased average reservoir pressure and CO_2 injection into the Cypress ROZ and Cypress MPZ. Average reservoir pressure in the Cypress ROZ is increased from pressure propagation and movement of CO_2 from the Cypress aquifer to Cypress ROZ. Pressure buildup in the ROZ increases the proportion of CO_2 injected into the MPZ (via wells completed in the MPZ and ROZ) thereby increasing CO_2 injection and average reservoir pressure of Cypress MPZ. As expected, cases with the highest G_{store} (cases 9, 12, and 13) are those with the highest volumes of CO_2 injected (Table 6-16). The highest CO_2-EOR and lower G_{store} cases yielded the lowest CB and ECO_2. For example, the CB and ECO_2 of the top two cases with the highest CO_2-EOR (case 5 and case 6) are both less than 0.4 tonne/stb and equal to 7%, respectively. The continuous injection cases in both the AEOR-AS and AEOR-MS scenarios (cases 7 –13) have net carbon-negative oil (NCNO) production (i.e., CB > 0.4) due to higher storage efficiencies (ECO_2 > 12%). Out of the eleven CO_2 flood cases in Table 6-17, eight cases produce NCNO and three are net carbon positive (i.e., three out of four CEOR-AS cases).

Table 6-17. CO_2-EOR, associated storage, and carbon balance metrics within a 360-acre model area after 20 years of CO_2 injection. A CB of 0.4 tonne/stb is net carbon neutral.

Scenario	Case #	CO_2-EOR, Mstb	G_{store}, Mtonnes	RF, %	NUF, Mscf/stb	SF, Mscf/stb	ECO_2, %	HCPV injected	CB, tonne/stb
Baseline Cases (no CO_2)									
IOR (Economic) Baseline	1	121	n/a	0.6	n/a	n/a	n/a	n/a	n/a
EOR Baseline	2	313	n/a	1.6	n/a	n/a	n/a	n/a	n/a
Conventional EOR with Associated Storage (CEOR-AS)									
Cypress Sandstone only	3	884	338	6.9	7.6	0.85	12	12.9	0.38
Ste. Genevieve Limestone only	4	391	162	6.2	8.0	0.83	10	1.3	0.41
Cypress Sandstone and Ste. Genevieve Limestone	5	903	297	4.7	6.3	0.62	7	10.7	0.33
Cypress Sandstone and Ste. Genevieve Limestone	6	922	307	4.8	6.5	0.47	7	7.4	0.33
Advanced EOR with Associated Storage (AEOR-AS)									
Cypress Sandstone only	7	483	870	3.8	34.9	1.20	30	1.8	1.80
Ste. Genevieve Limestone only	8	339	221	5.4	12.9	0.64	18	2.4	0.65
Cypress Sandstone and Ste. Genevieve Limestone	9	731	1,006	3.8	26.0	0.72	24	1.8	1.38
Cypress Sandstone and Ste. Genevieve Limestone	10	748	892	3.9	23.1	0.92	25	1.1	1.19
Cypress Sandstone and Ste. Genevieve Limestone	11	501	780	2.6	29.9	0.81	19	0.8	1.56
Advanced EOR with Maximum Storage (AEOR-MS)									
Cypress Sandstone (plus aquifer) and Ste. Genevieve Limestone	12	900	1,357	4.7	20.4	1.57	15	1.8	1.17
Cypress Sandstone (plus aquifer) and Ste. Genevieve Limestone	13	823	1,358	4.3	22.3	1.09	15	1.8	1.28

Discussion

Oil field operators typically perform CEOR-AS CO_2 floods involving different WAG ratios to improve oil recovery, delay breakthrough time and reduce CO_2 utilization by improving flood conformance. As a result, CEOR-AS CO_2 floods inject and store smaller amounts of CO_2 compared to continuous CO_2 floods e.g., AEOR-AS and AEOR-MS simulations. Examples of CEOR-AS CO_2 floods include the Slaughter Estate Unit (Rowe et al., 1982), Willard (San Andres) Unit (Johnson, 1971), Little Creek, SACROC Unit (Kane, 1979), and Levelland (Graham et al., 1980).

CO_2 injection into the Cypress aquifer in AEOR-MS cases does not only increase the amount of CO_2 stored but increases the average reservoir pressure in the Cypress and amount of CO_2 in-place in the Cypress-ROZ. The CO_2 in-place in the Cypress-ROZ consist of a combination of CO_2 injected the pattern injectors and CO_2 migration from underlying Cypress aquifer. A larger proportion of CO_2 delivered via pattern injectors is injected into the Cypress-MPZ due to pressure propagation from the Cypress aquifer to the Cypress-ROZ. The increased average reservoir pressure, the CO_2 in-place in the Cypress-ROZ, and the volume of CO_2 injected into the Cypress-MPZ further enhanced CO_2-oil miscibility development, thereby increasing oil production (case 10 vs cases 12 and 13 in Table 6-17). The cumulative oil production in case 13 is lower compared to case 12 because CO_2 is injected into the bottom 20 ft of the Cypress aquifer, while the entire Cypress aquifer is perforated in case 12. As a result, the pressure propagation and amount of CO_2 migrating from the Cypress aquifer decreased.

The CO_2-EOR and CO_2 storage of the Ste Genevieve is adversely affected in simulated cases having commingled injection wells because CO_2 is preferentially injected into the Cypress, which is shallower, thicker, and more permeable than Ste Genevieve (Tables 6-8 and 6-9). The CO_2-EOR and CO_2 storage of case 8 in which the Ste Genevieve is flooded separately are higher than that of the commingled CO_2 injection case (Case 9) because more CO_2 is injected in the former (Table 6-18). Higher cumulative water and CO_2 production in case 8 are a result of a correspondingly high CO_2 injection (Table 6-18). As a result, the CO_2-EOR and CO_2 storage in the Ste Genevieve is lower due to lower due to lower than anticipated CO_2 injection (poor conformance) that resulted to lower recovery and storage efficiencies (Table 6-18). Therefore, due diligence is needed when commingling injection to ensure the permeability-thickness product (k-H) of the reservoirs or formations considered are not significantly different to avoid adversely affecting the desired proportion of fluid injected into the least permeable formation.

Table 6-18. CO_2-EOR and CO_2 storage performances for separate and commingled Ste Genevieve CO_2 floods. Higher values are highlighted in gray.

Case	Ste. Genevieve Limestone only (case 8)	Cypress Sandstone and Ste. Genevieve Limestone (case 9)
Development	Separate	Commingled
Injection type	Continuous	Continuous
Cumulative oil production (Mstb)	339	277
CO_2 storage (Mtonnes)	221	200
Cumulative Gas Injection (MMscf)	36,380	30,775
Cumulative Water Production (Mstb)	1,221	1,047
Cumulative CO_2 production (MMscf)	32,014	27,545
RF, %	5.4	4.4
ECO_2, %	18	14

Development Strategies

The performances of the simulated cases, based on the metrics described in Equations 6-1 through 6-4, presented in Table 6-17 were ranked for each metric (Table 6-19) to select a strategy to co-optimize CO_2-EOR and CO_2 storage. The six highest values for each metrics were highlighted in gray to identify a case with highest overall ranking (Table 6-19). Results in Table 6-19 show that CO_2-EOR and CO_2 storage are co-optimized in AEOR-AS and AEOR-MS cases. Specifically, CO_2-EOR and CO_2 storage can be co-optimized using the AEOR-MS case (case 12) with commingled injection into the Cypress MPZ , Cypress ROZ, and Ste Genevieve and continuous injection via a single vertical well perforated across the entire thickness of the Cypress aquifer (Tables 6-15 through 6-17) because it ranks highest overall compared to the other 10 CO_2 flood cases. Specifically, case 12 ranks sixth or higher for all the metrics (Table 6-19). Most importantly, case 12 has the 3rd highest CO_2-EOR and the second highest G_{store}. Therefore, excluding the economic metrics, the following analogies can be made:

1. CO_2-EOR is maximized in CEOR-AS cases, specifically case 6 and case 5, because both cases have the lower CO_2 net utilization factors and higher flood conformances that AEOR-AS and AEOR-MS cases.
2. Changing the injection scheme from WAG in CEOR-AS cases to continuous injection in AEOR-AS increases CO_2 at the detriment of the CO_2-EOR for AEOR-AS cases.
3. Increases to both CO_2-EOR and CO_2 storage, compared to AEOR-AS cases, is achieved in AEOR-MS cases because of additional CO_2 injection into the Cypress aquifer. The increased CO_2-EOR is attributed to increases in average reservoir pressure of the Cypress, CO_2 in-place in the Cypress-ROZ, and CO_2 injection into the Cypress-MPZ due to additional CO_2 injection into the Cypress aquifer.

Table 6-19. Overall rankings of simulated CO_2 flood cases. The first-six highest ranks are highlighted in gray.

Scenario	Case #	EOR	G_{store}	RF	NF	SF	ECO_2	HCPV injected	CB
Baseline Cases (no CO_2)									
IOR (Economic) Baseline	1	n/a	n/a	n/a	n/a	n/a	n/a	n/a	n/a
EOR Baseline	2	n/a	n/a	n/a	n/a	n/a	n/a	n/a	n/a
Conventional EOR with Associated Storage (CEOR-AS)									
Cypress Sandstone only	3	4th	7th	1st	9th	5th	8th	1st	9th
Ste. Genevieve Limestone only	4	10th	11th	2nd	8th	6th	9th	9th	8th
Cypress Sandstone and Ste. Genevieve Limestone	5	2nd	9th	5th	11th	10th	10th	2nd	10th
Cypress Sandstone and Ste. Genevieve Limestone	6	1st	8th	4th	10th	11th	10th	3rd	10th
Advanced EOR with Associated Storage (AEOR-AS)									
Cypress Sandstone only	7	9th	5th	9th	1st	2nd	1st	5th	1st
Ste. Genevieve Limestone only	8	11th	10th	3rd	7th	9th	5th	4th	7th
Cypress Sandstone and Ste. Genevieve Limestone	9	7th	3rd	9th	2nd	8th	2nd	5th	3rd
Cypress Sandstone and Ste. Genevieve Limestone	10	6th	4th	8th	4th	4th	3rd	10th	5th
Cypress Sandstone and Ste. Genevieve Limestone	11	8th	6th	11th	3rd	7th	4th	11th	2nd
Advanced EOR with Maximum Storage (AEOR-MS)									
Cypress Sandstone (plus aquifer) and Ste. Genevieve Limestone	12	3rd	2nd	5th	6th	1st	6th	5th	6th
Cypress Sandstone (plus aquifer) and Ste. Genevieve Limestone	13	5th	1st	7th	5th	3rd	6th	5th	4th

Additional CO_2 Storage Potential

The results documented in this report reflect associated CO_2 storage in the two most prolific oil reservoirs in the Brownfield. However, CO_2 storage can also be increased by injecting CO_2 into the brine aquifer that makes up the bulk of the Ullin Limestone. Three cases involving CO_2 storage into Ullin using one, two, and three injection wells were simulated to assess its storage potential.

While this study was focused on associated storage within Brownfield stacked reservoirs that contain MPZs and ROZs, when considered in the context of the greater Illinois Basin, there are additional underlying brine formations, including the St. Peter Sandstone and the Mt Simon Sandstone, that regional studies have shown to have significant CO_2 storage potential (e.g., NETL, 2012). Future development of the Brownfield should consider the opportunities for saline storage that underlie the field.

Summary and Conclusion

The objective of this study was to develop strategies for the best possible combination of carbon CO_2-EOR and associated CO_2 storage in a stacked storage complex that includes depleted MPZs and a ROZ within the Brownfield Field Laboratory. The development strategies are biased towards the two most prolific formations, the Cypress Sandstone and Ste. Genevieve Limestone, which together account for approximately 90% of the oil that has been produced from the field. Because of significant differences in the two reservoirs (e.g., thickness, continuity, compartmentalization), different pattern sizes were required to maximize the performance of CO_2 injection in each reservoir, but shared wells allow optimization of field development.

CO_2-EOR is maximized in CEOR-AS cases, which use a WAG injection strategy, because both cases have the lower CO_2 net utilization factors and higher flood conformance than AEOR-AS and AEOR-MS cases. The AEOR-AS cases increases associated CO_2 storage by switching to a continuous CO_2 injection strategy at the detriment of the CO_2-EOR for AEOR-AS cases. The AEOR-MS cases have increased CO_2-EOR and associated CO_2 storage because of additional CO_2 injection into the Cypress aquifer. The increased CO_2-EOR is attributed to increases in average reservoir pressure of the Cypress, CO_2 in-place in the Cypress-ROZ, and CO_2 injection into the Cypress-MPZ.

Appendix 6-1

Formation	Case #	Case	Description	Production BHP @ datum (psia)	Status	Comments/results
Cypress	1	Economic Baseline	Cypress primary production; Ste. Genevieve waterflood. Using existing (historical) wells	1200	Completed	Baseline
		EOR Baseline	Cypress primary production; Ste. Genevieve waterflood. Using EOR well patterns			
	2	CO_2EOR_Cypress	Cypress extended primary	1200	Completed	0.00E+00
	3	CO_2EOR_Cypress_Only	Cypress CO_2 EOR ==> Miscible	1200	Completed	1200 psi producing BHP
	4	CO_2EOR_Cypress_Only_800psi	Cypress CO_2EOR ==> Near Miscible	800	Completed	800 psi producing BHP
	5	CO_2EOR_SteGen_11pc_PorCutOff	Ste Genevieve primary rec and extended waterflood	1200	Completed	0.00E+00
	6	CO_2EOR_SteGen_11pc_PorCutOff1200psi	Ste Gen CO_2 EOR ==> Miscible	1200	Completed	1200 psi producing BHP
	7	CO_2EOR_SteGen_11pc_PorCutOff800psi	Ste Gen CO_2EOR ==> Near Miscible	800	Completed	800 psi producing BHP
	8	Cypress CO_2 flood sensitivity	0.00E+00	0	0.00E+00	0.00E+00
	9	CO_2EOR_Cypress_Only_50MMSCFPD	Miscible flood. Field production rate constrained to 50 MMscf/d	1200	Completed	Issue: Out of pattern CO_2 injection. (Will try inverted 5-spot CO_2 flood)

Formation	Case #	Case	Description	Production BHP @ datum (psia)	Status	Comments/results
	10	CO_2EOR_Cypress_Only_50MMSCFPD_Qlid1001stbpd	Miscible flood. Field production rate constrained to 50 MMscf/d. Qliqsmax increase from 200 to 10001 stb/d	1200	0.00E+00	0.00E+00
	11	CO_2EOR_Cypress_only_1200psi_uncontrainedProd	Miscible flood. Field production and injection rates unconstrained	1200	Completed	Very high and probably unrealistic injection rates. Simulation runs very slow
	12	CO_2EOR_Cypress_Only_50MMSCFPD_Qlid1001stbpd	Miscible flood. Field production and injection rates unconstrained, field production gas production constrained at 50 MMscf/d	1200	Completed	0.00E+00
	13	CO_2EOR_Cypress_only_centralized_patterns	Miscible flood. Field production rates unconstrained	1200	Incomplete	0.00E+00
	14	CO_2EOR_Cypress_only_centralized_patterns	Miscible flood. Field production rates constrained to 50 MMscf/d	1200	Completed	Significant out of pattern injection and movement of CO_2 into underlying aquifer
	15	CO_2EOR_Cypress_only_Patbal_Inv5spot	Miscible flood. Field production rates unconstrained to 50 MMscf/d	1200	On hold	0.00E+00
	16	CO_2EOR_Cypress_periferal_Watinj_50mmscfpd	six 80-ac patterns with peripheral water injection. Field injection and production rates constrained to 50 MMScf/d	1200	Completed	Limited out of pattern injection and movement of CO_2 into underlying aquifer

Formation	Case #	Case	Description	Production BHP @ datum (psia)	Status	Comments/results
	17	CO_2EOR_Cypress_periferal_Watinj_unconstrained	six 80-ac patterns with peripheral water injection. Field injection and production rates unconstrained	1200	Completed	Exess gas & water production
	18	CO_2EOR_AuxVases_periferal_Watinj	Primary recovery (10-ac well spacing)	1200	0.00E+00	Baseline
Aux Vases	19	CO_2EOR_AuxVases_periferal_Watinj_restart	... 80-ac patterns with peripheral water injection. Field injection and production rates constrained to 50 MMScf/d	1200	Incomplete	0.00E+00
	20	CO_2EOR_AuxVases_periferal_Watinj_restart_40ac	… 40-ac patterns with peripheral water injection. Field injection and production rates unconstrained	1200	Incomplete	0.00E+00
	21	CO_2EOR_SteGen_11pc_PorCutOff	primary recovery plus CO_2 EOR baseline (20-ac well spacing)	1200	Completed	Baseline (old)
Ste Genevieve	22	CO_2EOR_SteGen_11pc_PorCutOff800psia	... 40-ac patterns with peripheral water injection. Unconstrained Field injection and production rates	800	Incomplete	Simulation fails
	23	CO_2EOR_SteGen_11pc_PorCutOff1200psia	... 40-ac patterns with peripheral water injection. Unconstrained Field injection and production rates	1200	Completed	Peripheral water injection
	24	CO_2EOR_SteGen_restart_pBHP500	0.00E+00	500	Incomplete	0.00E+00

Formation	Case #	Case	Description	Production BHP @ datum (psia)	Status	Comments/results
	25	OnePat_40ac_VIP	CO_2 flood Ste Gen to Ullin. Producer perforated in the oil only bearing intervals, blanket perforation for injectors	1200	Completed	0.00E+00
Pattern modeling	26	OnePat_80ac_VIP	CO_2 flood Ste Cypress and Aux Vase. Producer perforated in the oil only bearing intervals. Injectors perforated in the Cypress-MPZ, bottom 6 ft of Cypress-ROZ and Aux Vases	1200	Incomplete	Excessive gas injection/production mostly into the Cypress
	27	OnePat_40ac_StL_Ul	CO_2 flood Ste St Louis to Ullin. Producer perforated in the oil only bearing intervals, blanket perforation for injectors	1200	Completed	Very low gas injection (112 .8 MMscf in 25 years)
	28	OnePat_80ac_AV	CO_2 flood in Aux Vase. Producer and Injectors perforated in the entire Aux Vases	1200	Completed	0.00E+00
	29	OnePat_40ac_StL_Ul_NoAquifer	CO_2 flood Ste St Louis to Ullin. Producer and injectors perforated in the oil only bearing intervals.	1200	Completed	Very low CO_2 injection (2.192 MMScf in 25 years)
	30	OnePat_10ac_StL_Ul_NoAquifer	CO_2 flood Ste St Louis to Ullin. Producer and injectors perforated in the oil only bearing intervals.	1200	Completed	Improved CO_2 injection (98,127 MMscf in 25 years)
	31	SinglePattern_SteGen_10ac	CO_2 flood Ste St Louis to Ullin. Producer and injectors perforated in the oil only bearing intervals.	1200	Completed	0.00E+00
	32	SinglePattern_stackedRes_40ac (Similar to SteGent_40ac_Nexus)	CO_2 flood Cypress to Ullin. Producer and injectors perforated in the oil only bearing intervals.	1200	Completed	0.00E+00

Formation	Case #	Case	Description	Production BHP @ datum (psia)	Status	Comments/results
	33	Four_SteGent_10ac_Nexus	CO_2 flood Cypress to Ullin. Producer and injectors perforated in the oil only bearing intervals. Four 10_ac patterns	1200	0.00E+00	Four 10-ac patterns
Mltiple 5-spot Patterns	34	Cypress Sandstone and Ste. Genevieve Limestone	5-spot pattern CO_2 floods of the Cypress and Ste Genevieve. Continuous injection	1200	Completed	Simultaneous flooding. Nine 40-ac patterns and Four 80-ac patterns
	35	Cypress Sandstone and Ste. Genevieve Limestone	5-spot pattern CO_2 floods of the Cypress and Ste Genevieve. Continuous injection	1200	Completed	Sequential flooding. Nine 40-ac patterns followed by Four 80-ac patterns
	36	DevStrat_Sequential_Patterns_1100psPBHP	5-spot pattern CO_2 floods of the Cypress and Ste Genevieve	1100	0.00E+00	Sequential. Producing BHP = 1100 psia at datum
	37	DevStrat_Sequential_Patterns_baseline	5-spot pattern CO_2 floods of the Cypress and Ste Genevieve	1200	0.00E+00	Baseline Sequential. Producing BHP = 1200 psia at datum
	38	DevStrat_Sequential_Patterns_WAG	5-spot pattern CO_2 floods of the Cypress and Ste Genevieve	1200	0.00E+00	Sequential. Producing BHP = 1200 psia at datum
	39	DevStrat_Simulateneous_Patterns_baseline	5-spot pattern CO_2 floods of the Cypress and Ste Genevieve	1200	0.00E+00	Baseline Simultaneous. Producing BHP = 1200 psia at datum

Formation	Case #	Case	Description	Production BHP @ datum (psia)	Status	Comments/results
	40	DevStrat_Simulateneous_WAG	5-spot pattern CO_2 floods of the Cypress and Ste Genevieve	1200	0.00E+00	Simultaneous. Producing BHP = 1200 psia at datum
	41	DevStrat_Simulateneous_WAG_40ac	40-ac 5-spot pattern CO_2 floods of the Cypress and Ste Genevieve	1200	Completed	High Oil recovery (1041.2 Mstb in 13 years)
	42	DevStrat_Simulateneous_WAG_80ac	80-ac 5-spot pattern CO_2 floods of the Cypress and Ste Genevieve	1200	Completed	850 Mstb
	43	DevStrat_Simulateneous_WAG_20ac	20-ac 5-spot pattern CO_2 floods of the Cypress and Ste Genevieve	1200	Completed	0.00E+00
	44	DevStrat_WAG_20acStGen_180acCypress	5-spot pattern CO_2 floods of the Cypress (180-ac) and Ste Genevieve (20-ac)	1200	Completed	0.00E+00
	45	DevStrat_WAG_40acStGen_360acCypress1+	5-spot pattern CO_2 floods of the Cypress (360-ac) and Ste Genevieve (40-ac)	1200	Completed	0.00E+00
	46	DevStrat_WAG_180acCypress1	Single 5-spot pattern CO_2 floods of the Cypress (180-ac). Total liquid production rate = 400 stb/d	1200	Completed	0.00E+00

Formation	Case #	Case	Description	Production BHP @ datum (psia)	Status	Comments/results
	47	DevStrat_WAG_180acCypress_Qliq999	Single 5-spot pattern CO_2 floods of the Cypress (180-ac). Total liquid production rate = 999 stb/d	1200	Completed	0.00E+00
	48	DevStrat_WAG_180acCypress_Qliq999_ProdBHP500	Single 5-spot pattern CO_2 floods of the Cypress (180-ac). Total liquid production rate per well = 9990 stb/d, Producing BHP 500 psi	500	Running	0.00E+00
	49	Cypress Sandstone and Ste. Genevieve Limestone	Three years conventional production from Cypress and EOR from Ste. Gen. Cypress EOR begins at year three.	1200	0.00E+00	Sequential flooding. Nine 40-ac patterns folowed by Four 80-ac patterns
	50	DevStrat_Short_Sequential_Patterns	5-spot pattern continuous CO_2 floods of the Cypress and Ste Genevieve	0	0.00E+00	Sequential flooding. Nine 40-ac patterns followed by Four 80-ac patterns
	51	Ste. Genevieve Limestone only	5-spot pattern CO_2 floods of the Ste Genevieve	1200	Completed	7 days maximum water injection duration
	52	Cypress Sandstone and Ste. Genevieve Limestone	Three years conventional production from Cypress and EOR from Ste. Gen. Cypress EOR begins at year three. Plus 7 days Max water cycle duration	1200	Completed	
	53	Cypress Sandstone only	5-spot pattern CO_2 floods (WAG) of the Cypress. Plus 7 days Max water cycle duration	1200	Completed	

Formation	Case #	Case	Description	Production BHP @ datum (psia)	Status	Comments/results
	54	Cyypress_aquiferInj_Continuous	5-spot pattern CO_2 floods of the Cypress and Ste Genevieve. Plus CO_2 injection into Cypress aquifer (1000 mscf/d)	1200	Completed	
	55	Cypress_aquiferInj_Continuous_Pconstrained	5-spot pattern CO_2 floods of the Cypress and Ste Genevieve. Plus CO_2 injection into Cypress aquifer (Pressure constrained)	1200	Completed	
	56	Cypress_aquiferInj_Continuous_BottomAquifer	5-spot pattern CO_2 floods of the Cypress and Ste Genevieve. Plus CO_2 injection into Cypress aquifer (rate constrained (1000 mscf/d, bottom aquifer)	1200		
	57	DevStrat_SteGen_40acPatterns_WAG_14days_Wslug_1	5-spot pattern CO_2 floods of the Ste Genevieve, plus CO_2 injection into the Ullin	1200	Completed	14 days maximum water injection duration
	59a	Cypress Sandstone only	5-spot pattern CO_2 floods of the Cypress. Continuous injection. 80-acre pattern size	1200		
	58a	Ste. Genevieve Limestone only	5-spot pattern CO_2 floods of the Ste Genevieve. Continuous injection. 40-acre pattern size	1200		
Ullin Injection Potential	58	DevStrat_SteGen_40acPatterns_WAG_1day_Wslug	5-spot pattern CO_2 floods of the Ste Genevieve, plus CO_2 injection into the Ullin	1200	Completed	1 days maximum water injection duration
	59	Ullin_CO_2Inj_potential	Four CO_2 injection wells perforated from Cypress to Ullin. Producer perforated in the oil only bearing intervals, blanket perforation for injectors	0	0.00E+00	Unconstrained injection. Simulation stops well CO_2 reaches edge grid cells

Formation	Case #	Case	Description	Production BHP @ datum (psia)	Status	Comments/results
	60	Ullin_CO_2Inj_potential_1WELL	One CO_2 injection wells perforated from Cypress to Ullin. Producer perforated in the oil only bearing intervals, blanket perforation for injectors	0	0.00E+00	Unconstrained injection. Simulation stops well CO_2 reaches edge grid cells
	61	Ullin_CO_2Inj_potential_2WELLS	Two CO_2 injection wells perforated from Cypress to Ullin. Producer perforated in the oil only bearing intervals, blanket perforation for injectors	0	0.00E+00	Unconstrained injection. Simulation stops well CO_2 reaches edge grid cells
	62	Ullin_CO_2Inj_potential_3WELLS	Three CO_2 injection wells perforated from Cypress to Ullin. Producer perforated in the oil only bearing intervals, blanket perforation for injectors	0	0.00E+00	Unconstrained injection. Simulation stops well CO_2 reaches edge grid cells
	0					

Continuous StGen

Aquifer water injection (control simulation)

Baseline

6.2.2 Greenfield

Authors: Fang Yang and Nathan Grigsby

Introduction

This study aims to develop strategies to co-optimize carbon dioxide-enhanced oil recovery (CO_2-EOR) and associated CO_2 storage in stacked greenfield Residual Oil Zones (ROZs) in the Illinois Basin. Reservoir simulations were performed on a Greenfield ROZ field laboratory site to assess development strategies that could be utilized to co-optimize CO_2-EOR and associated CO_2 storage and provide estimates of oil recovery and CO_2 storage potential to guide economic and regional resource assessments.

Representative geocellular models, based on the geologic characterization of greenfield ROZ stacked reservoirs present at the Greenfield ROZ field laboratory site, along with rock and fluid properties and initial model conditions, were then used to construct reservoir models.

Reservoir simulations were conducted on two types of models: a multi-reservoir model that included the Carper Sandstone, Geneva Dolomite ROZ, and Geneva aquifer, and individual reservoir models of each target. Various types of pattern floods and injection schemes were considered, including staggered line drive, 5-spot pattern, Water-Alternating-Gas (WAG), Soak-Alternating-Gas (SAG), Huff and Puff (HnP), and dewatering. The simulation results were assessed to determine their impacts on both oil recovery and CO_2 storage.

Geologic Characterization

Overview

At the Greenfield ROZ field laboratory site (e.g., the Holsapple 2B well; API 120352329600) in Cumberland County, Illinois (Figure 6-17), stacked reservoirs include ROZs in the Carper Sandstone and Geneva Dolomite and a brine aquifer below the ROZ in the Geneva Dolomite. This area was studied because observations from well data in the area indicate a greenfield ROZ is present in the Carper; wells that encounter the Carper commonly report oil shows but there is no oil production within ten miles. In the Holsapple 2B well, oil was observed while drilling, was measured from core, and was calculated from well logs, but six months of pumping resulted in only trace amounts of oil produced. Well data in the area also has evidence of a greenfield ROZ in the Geneva Dolomite; a high proportion of wells that encounter the Geneva record oil shows or sulfur water (an indirect indicator of an ROZ) and the nearest production is approximately ten miles away. The lack of proximate oil production suggests greenfield ROZs in both formations (oil saturation is low enough to be immobile and is naturally occurring instead of the result of depletion from nearby wells), but also results in relative lack of wells and associated data in the vicinity of the Holsapple 2B well (Figure 6-17). This poor data density results in poorly constrained geocellular models that relied heavily on regional geologic interpretation.

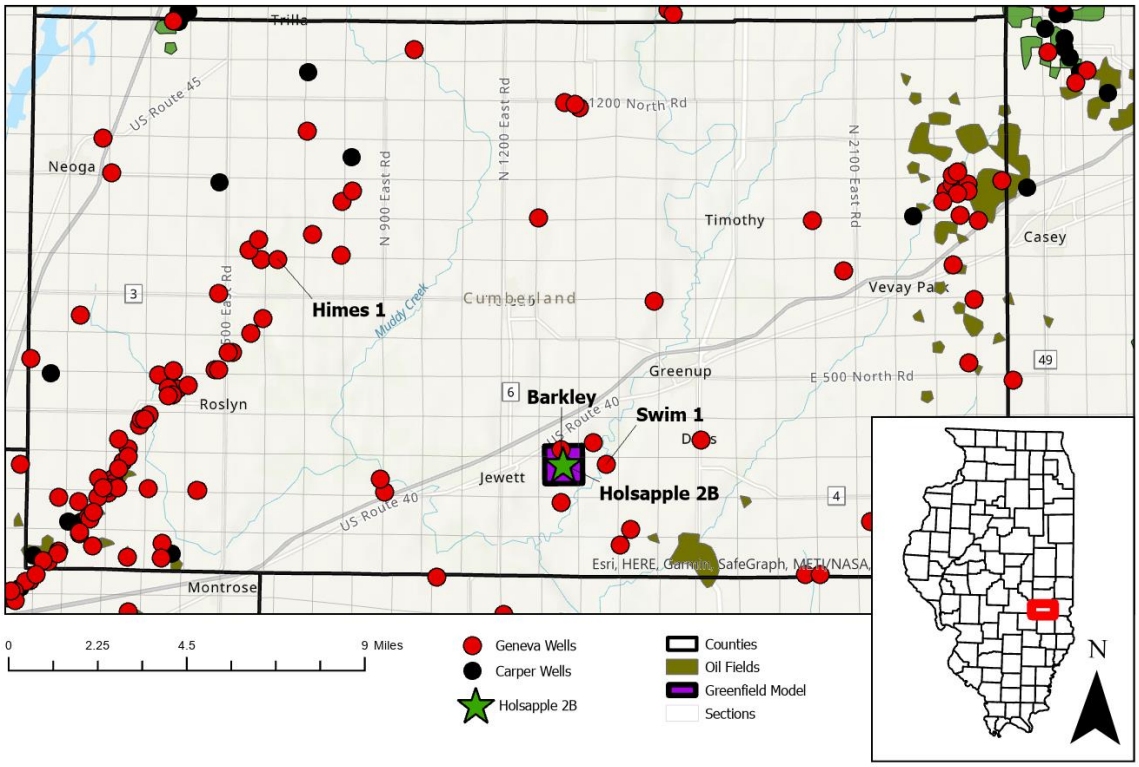


Figure 6-17. Map centered on Cumberland County showing the data available for geologic characterization and model development for the Carper Sandstone and Geneva Dolomite. Only 2 wells encounter the Carper (green star and red and black dots) and 1 encounters the Geneva (red dots) within the model boundaries (purple square).

Carper Sandstone

The (lower Mississippian) Carper Sandstone contains several stacked sandstone bodies embedded within impermeable mudstone in the lower part of the Borden Siltstone (Figure 6-18). The geologic interpretation of the Carper Sandstone at the greenfield site is based on core collected from the Holsapple 2B well and the full suite of well logs from the Holsapple 2B and the Swim 1 well (Figure 6-18). Nearby wells and oilfields in adjacent counties that produce from the Carper also provided important geological information (Figure 6-19). A brief description of the geology of the Carper is presented here to provide context, but a more complete characterization can be found in Chapters 4 and 5.

Analysis of the Holsapple 2B core indicates that the Carper is a very-fine grained sandstone to coarse siltstone with porosity ranging from 7 to 14% and permeability of approximately 1 mD or less. The absolute value of core measured S_O is unreliable due to displacement of in situ fluids during the coring process, but the relative value of core measured S_O is useful to detect the presence or absence of oil and general trends in oil saturation distribution. In this case, the cored interval (3,685-3,786 ft) only had oil saturation within the Carper C1 (from 3,686.5-3,700 ft) and directly beneath a shale break in the lowest Carper interval (A1 from 3,765.5-3,770.5 ft). The entire Carper A2 was cored with no oil observed and the middle of the target interval also has an approximately 5 ft span with no oil (3,692.2-3,698.3 ft). This distribution of oil and water matches scout tickets in the area, which commonly report oil shows in the Carper C1. Thus, the Carper C1 was defined as the target interval. The Carper C1 has the same thickness (15 ft) and porosity (10-14%) the Swim 1 well (approximately one mile to the east; Figure 6-18). Evaluation of all available well logs in the area determined that each of the Carper units are laterally continuous with

little variability over the scale of several miles (Figure 6-19). Natural fractures in the Carper Sandstone are commonly noted in drilling records, observed in core, and recorded on rare specialized geophysical logs. Drilling records and operators commonly report that drilling through the Borden Siltstone (particularly the "Osage" zone near the top and the Carper Sandstone near the base) requires precautions (including increased mud viscosity, admixed lost circulation material, and avoiding surges while tripping in or out of the well) to prevent drilling fluid loss.

Regional geologic characterization determined that the petrophysical properties in the Holsapple 2B well were representative of the area. However, based on comparison of all available Carper core data, the porosity and permeability in the Holsapple 2B well were significantly lower than other wells (Figure 6-20).

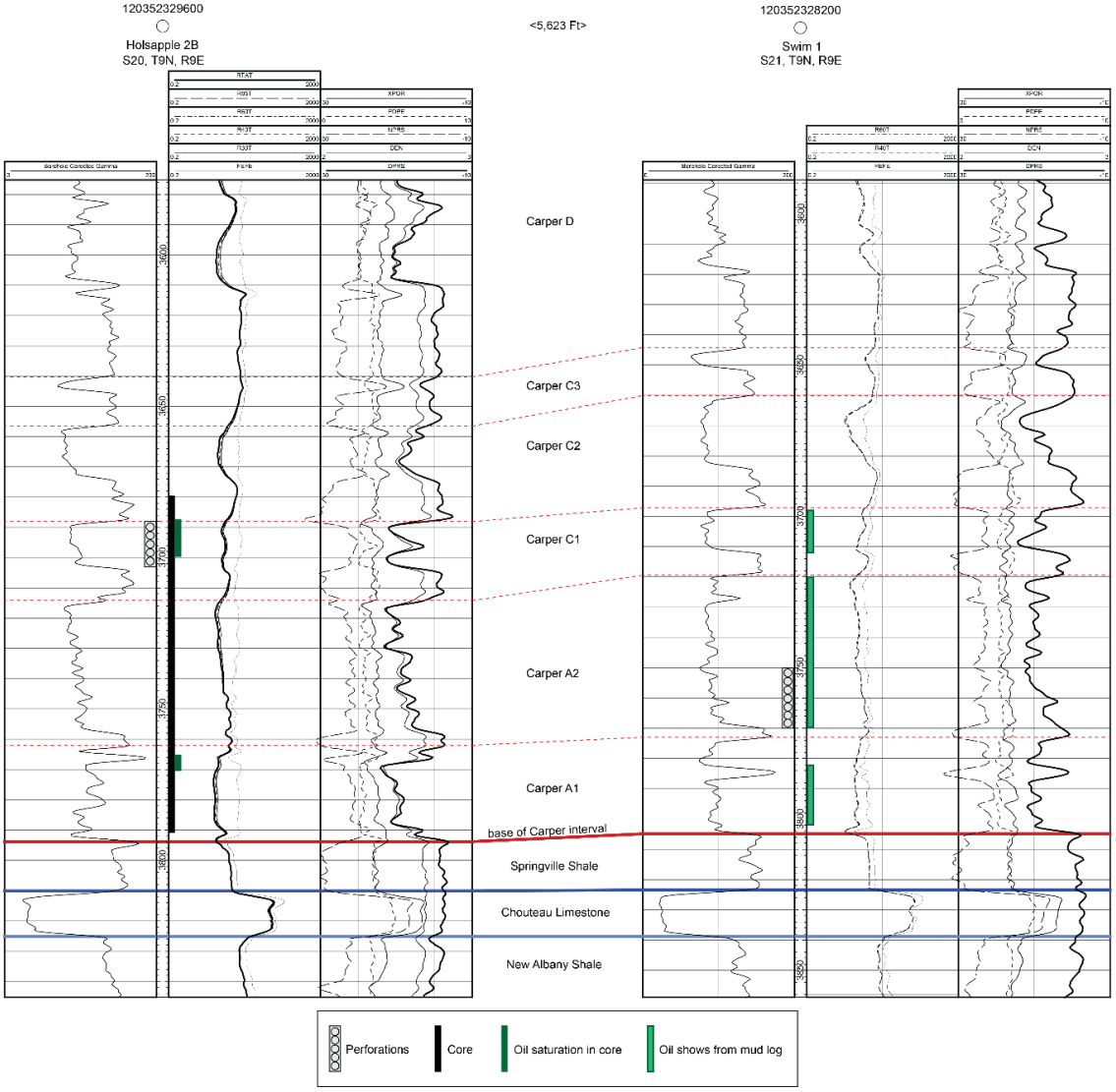


Figure 6-18. Two-well cross section showing the Holsapple 2B well and the adjacent Swim 1. In both wells, Carper sandstone bodies occur over a thickness of more than 200 ft. The Carper C1 sandstone is 15 ft thick and is the zone that is perforated in the Holsapple 2B well. Perforations are indicated by grey circle-filled boxes. Core is indicated by the black bar. Oil reported by operator is indicated by the green bars. The distribution of oil saturation is better constrained in the Holsapple well (which had core) vs. the Swim well (which reported oil based on observations during drilling).

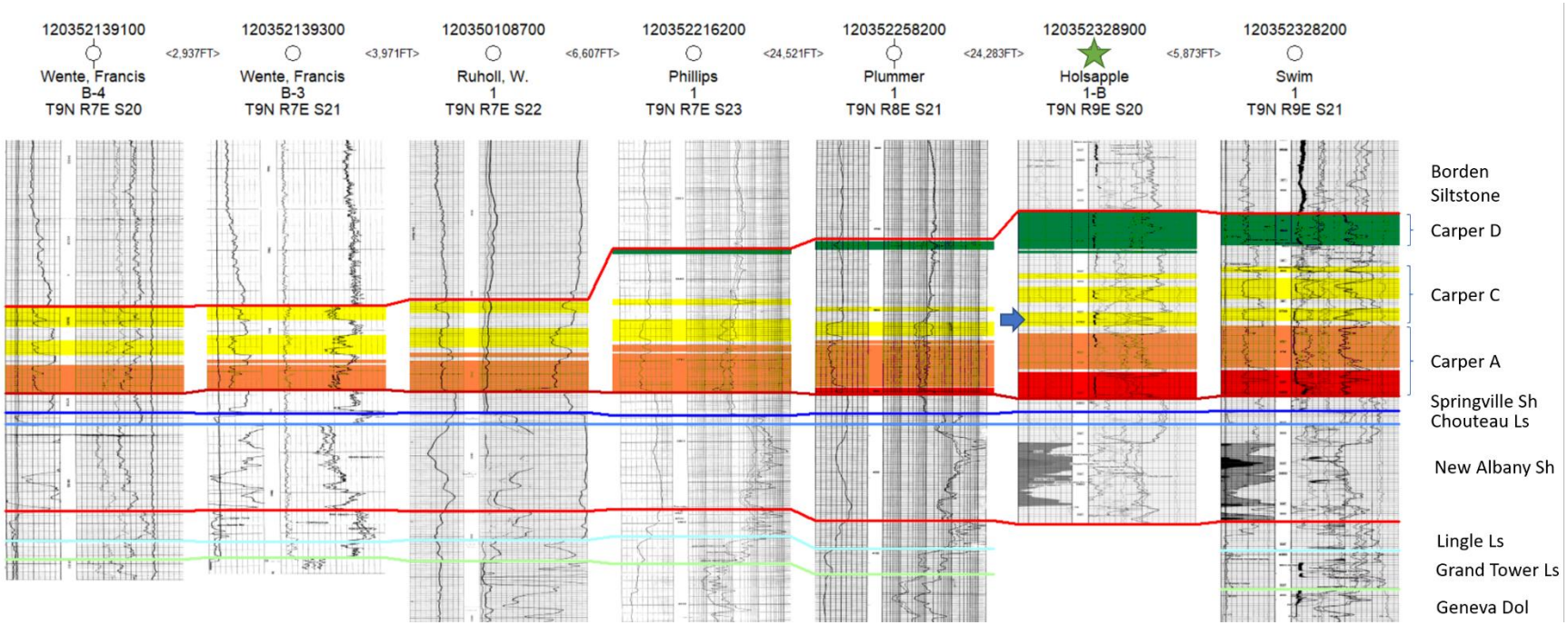


Figure 6-19. Approximately 13-mile-long west to east cross section showing the continuity of sandstone bodies within the overall Carper succession. The main 15 ft thick oil-bearing sandstone in the Holsapple 2B well (indicated by blue arrow) can be observed in all the wells in the cross section. Some of the underlying (red) and overlying (green) sandstone bodies that are present in the Holsapple 2B well thin and pinch out to the west.

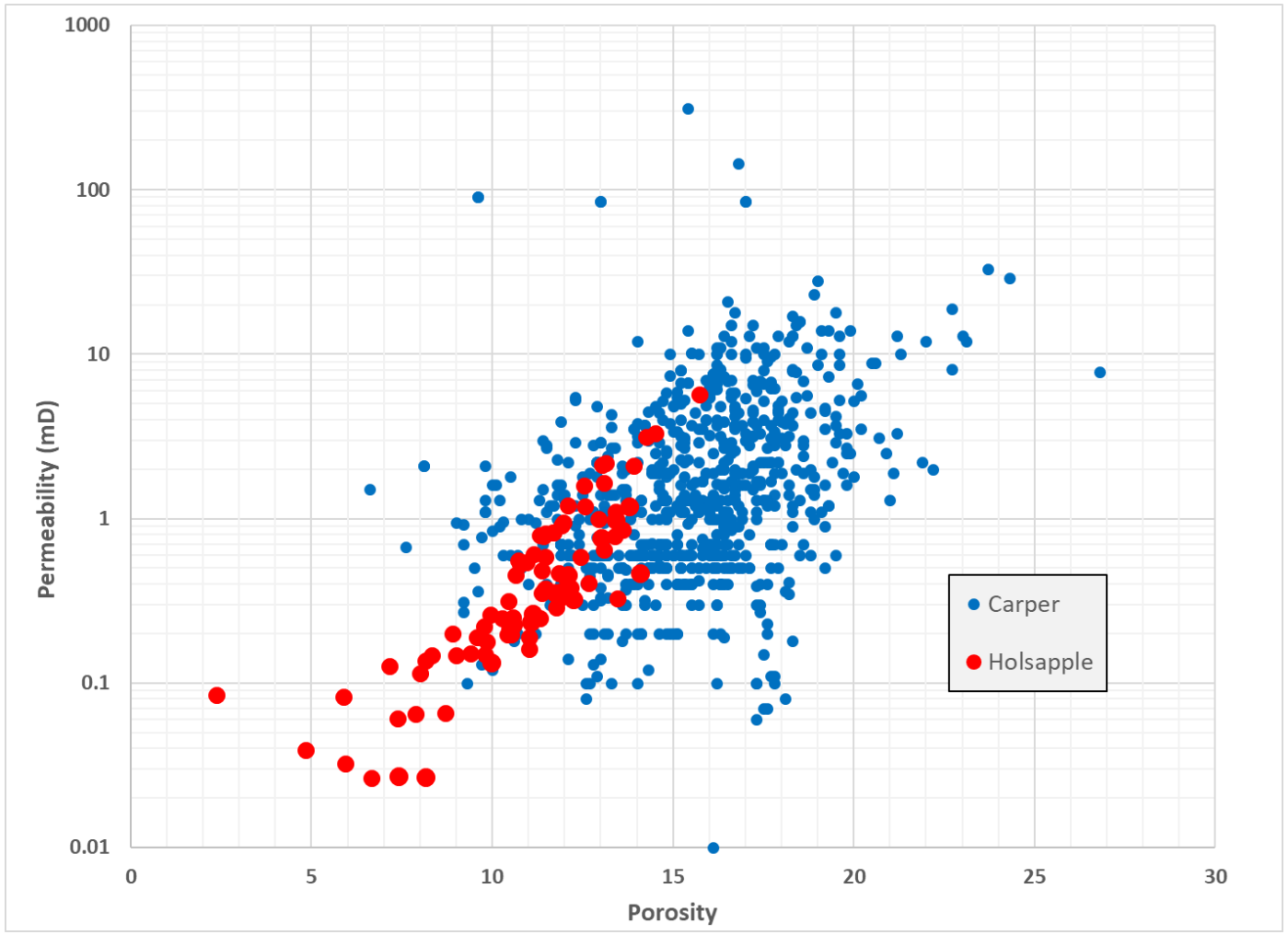


Figure 6-20. Porosity and permeability of the Carper Sandstone from core analysis reports. Porosity and permeability from the Holsapple well (red dots) are believed to be representative of the study area but are significantly lower than data from other wells (blue dots).

Geneva Dolomite

The Geneva Dolomite occurs as vugular, dolomitic intervals embedded within non-porous limestone in the middle Devonian Grand Tower Limestone (Figure 6-21). The Holsapple 2B well is not deep enough to encounter the Geneva, and only two wells within four miles encounter it, so wells from Lillyville oil field, which contains the nearest Geneva oil production about ten miles to the west, were used to understand the petrophysical properties of the Grand Tower. The nearest of these wells, the Himes 1 well (API 120352328300), is provided here as an example. Throughout the area, the dolomitic portion of the Grand Tower occurs beneath 40-50 ft of non-porous limestone in the Lingle and contains a thin upper oil-bearing unit that is sometimes called Jeffersonville and a thicker lower unit that appears to be fully saturated with water. Both porous intervals are consistently observed throughout the region and attributed to the Geneva here.

The two wells near the Holsapple 2B well were evaluated within this context to determine if the properties observed at Lillyville could be applied to the model. The Swim 1 well (API 120352328200) has modern porosity, resistivity, and Pe logs that could be used to differentiate dolomite from limestone but does not fully penetrate the Geneva. Conversely, the Barkley 1 well (API 120352214000) fully penetrates the Geneva but has older vintage porosity and resistivity logs and no Pe log.

Both wells have about 18 ft of 10% porosity below 30 ft of non-porous limestone. The scout ticket for the Swim 1 well lists a very slight show of oil in this interval and attributes it to the Grand Tower, but the drilling report states that it is “in part slightly vugular, and in part, slightly dolomitic,” and the Pe log is under four barnes/electron, so this is believed to be the upper ROZ bearing Geneva. About 17 ft of non-porous limestone separates this unit from an underlying dolomite, which the drilling report for the Swim 1 well describes as having “very good perm and impressive very good crystalline clear spherical medium to large or coarse grained vugular sandy dolomite.” It is not clear if the logs for the Swim 1 well fully penetrate this lower porous dolomite but based on resistivity and neutron/density porosity separation, it is about 40 ft thick in the Barkley 1 well. The distribution of porous dolomite embedded within non-porous limestone in the Devonian, and oil shows in the upper Geneva interval are consistent with observations from Lillyville Field (Figure 6-22), so the properties are believed to be laterally continuous throughout the area.

120352328200
○
Swim 1
S21, T9N, R9E

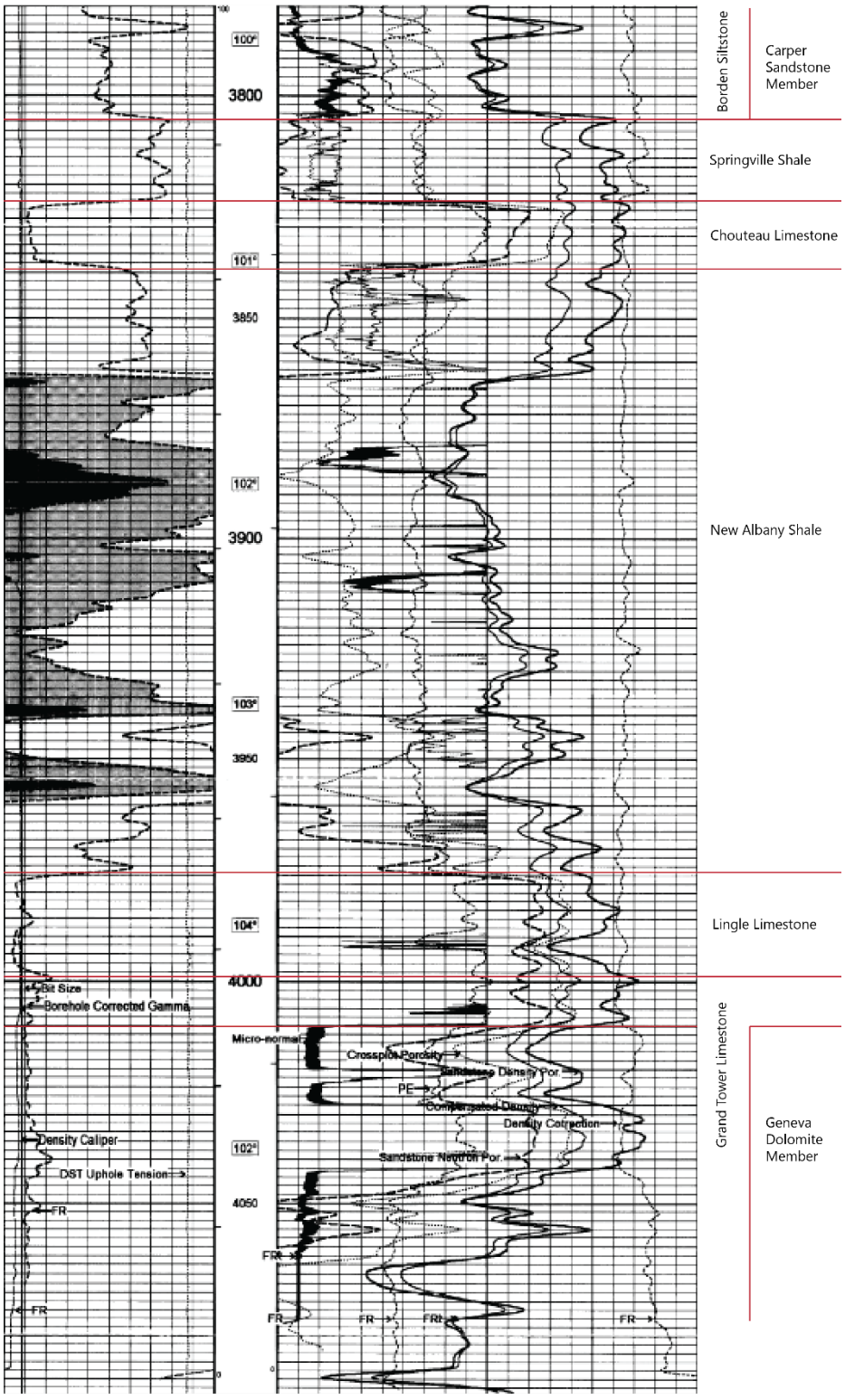


Figure 6-21. Type well for the Geneva Dolomite showing the relevent stratigraphy.

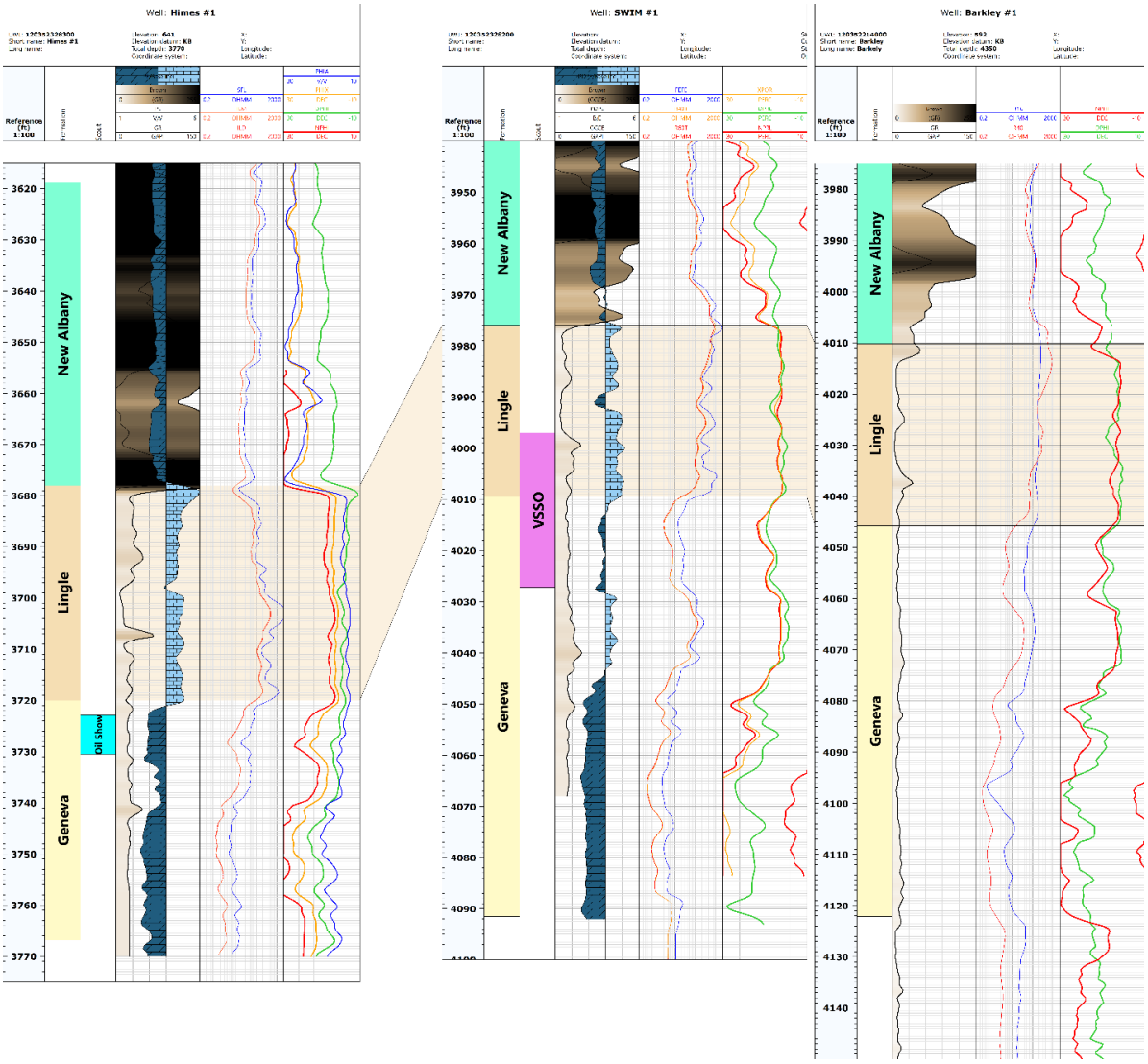


Figure 6-22. Three well cross section. The leftmost well (Himes #1) is indicative of wells in the vicinity of Lillyville oil field and right two wells represent the modeled area. A Barnes/electron cutoff of four is used to differentiate limestone from dolomite on the Pe log. Two porous intervals within the Geneva Dolomite are present in each well beneath non-porous Lingle Limestone. The upper Geneva interval has an oil show in Lillyville and a very slight show of oil (VSSO) in the Swim #1 well. The lower Geneva interval has very high porosity, but no oil is recorded in the area.

Reservoir Simulation

Geocellular Model

Regional geologic characterization determined that both Carper Sandstone and Geneva Dolomite are laterally continuous (with remarkably consistent thickness and reservoir properties) over an area of several square miles around the Holsapple 2B well, so a layer cake geocellular model was deemed adequate for pattern model simulations.

The layer cake geocellular model includes the ROZ bearing intervals of the Carper and Geneva, and the lower Geneva aquifer. The vertical extent was defined by the top of the Carper from the Holsapple 2B well and the base of the Geneva aquifer from the Barkley 1 well. Table 6-20 lists the petrophysical properties (depth, thickness, porosity, permeability, and initial oil saturation) of each unit of the modeled formations.

Table 6-20. Greenfield geocellular model petrophysical properties.

Formation	Depth, ft	Thickness, ft	Subsea top, ft	Porosity, %	Permeability, mD	Soi
Carper ROZ	3688-3703	15	-3160	11.5	0.2	25%
NA1	3703-4010	307	-3175	0	0	0
Geneva ROZ	4010-4028	18	-3482	10	20	20%
NA2	4028-4045	17	-3500	2	1	0
Geneva Aquifer (upper)	4045-4055	10	-3517	22	350	0
Geneva Aquifer (middle)	4055-4062	7	-3527	15	50	0
Geneva Aquifer (lower)	4062-4085	23	-3534	28	500	0

The porosity and permeability of the Carper Sandstone model were based on log and core data from the Holsapple 2B well. The porosity and permeability of the Geneva Dolomite intervals were estimated based on geologic records throughout the area. However, the complex lithology and lack of data make the petrophysical properties difficult to characterize, and the model contains a significant amount of uncertainty. A site-specific study would be required to constrain input parameters.

Archie's equation was used to calculate water saturation (with oil saturation assumed to occupy the remaining pore space; S_O=1-S_W) in every well in Cumberland County with digitized porosity and resistivity logs.

Simulation Inputs

Landmark's Nexus (version 5000.4.13), a commercial software package, was used to conduct numerical simulations. Nexus allows simulations of multiphase flow with multiple compositions for multiple reservoirs and models the reservoir, wells, and surface and subsurface facilities as a single system for a comprehensive representation of reservoir behavior. Two major CO_2 trapping mechanisms were modeled: structural/stratigraphic trapping and residual gas trapping. Solubility trapping was not considered due to a software malfunction. Mineral trapping was considered negligible because the storage units are primarily quartz and dolomite.

To model field-scale responses, a one-square-mile pattern model was used so the results could be easily upscaled to cover the regional area. The pattern model has closed boundaries to represent regionally repeating patterns based on the assumption of no flow between patterns. The closed boundary conditions were achieved by modifying the well factor, transmissibility, and pore volume of edge cells and corner cells to 50% and 25% of an inner cell, respectively.

All other major simulation inputs are described below by formation.

Carper Simulation Inputs

The parameters for the Carper Sandstone model were calibrated to field observations from a single well HnP test in the Holsapple 2B well (Chapter 4 and Appendix 7.1). The Carper Sandstone is naturally fractured and was hydraulic fractured in the Holsapple 2B well. It is assumed that both groups of fractures would be present if the Carper were developed, so a dual porosity and dual permeability approach was used to model fluid flow within and between matrix and both types of fractures (Table 6-21).

Table 6-21. Matrix and fracture properties of calibrated Carper model.

Parameters	Value
Initial oil saturation in matrix	25%
Initial oil saturation in fracture	2%
Matrix porosity (øm)	11.5%
Matrix permeability (kX,kY,kZ) (mD)	(0.2,0.2,0.1)
Fracture porosity (øf)	0.051%
Fracture effective permeability* (kXeff, kYeff, kZeff) (mD)	(12, 0.24, 12)
Fracture spacing (LX,LY,LZ) (ft)	(150, 3, 15)

Table 6-22 lists the major simulation inputs for the Carper Sandstone. The rock-fluid properties and initial conditions are based on information from the Holsapple 2B well. The rock compressibility was calculated from porosity using Newman Correlation (Newman, 1973). The water properties were calculated based on salinity and reservoir temperature and pressure using McCain correlations (McCain, 1991). The matrix relative permeability was generated using Corey's function embedded in Nexus. The endpoints and exponents were initially based on values typically observed in Illinois Basin sandstones and calibrated to field tests (Table 6-23, Figures 6-23 and 6-24). The fracture relative permeability followed vertical equilibrium curves with Sor= 2% and Swr=5% (Figures 6-25 and 6-26).

The initial reservoir pressure was assumed to follow a freshwater gradient of 0.433 psi/ft. The CO_2 was injected via the entire 15 ft Carper ROZ, and the maximum bottomhole pressure was constrained to be 2338 psi at 3688 ft, which followed an assumed fracture pressure gradient of 0.7 psi/ft with a 90% safety factor. Each producer was assumed to be hydraulicly fractured with a fracture half-length of 500 ft and a permeability of 8,000 mD, which is based on calibrated properties to Holsapple 2B well tests (Chapter 4 and Appendix 7.1).

Table 6-22. Simulation inputs of Carper Sandstone.

Category	Input parameter	Value/Description
Rock and fluid properties	Rock compressibility	5.55E-6 1/psi
	Relative permeability	Two sets: matrix and fracture
	Water salinity	88,000 ppm
	Water density	66.35 lb/ft3
	Water viscosity	0.72 cP
	Water compressibility	2.825 E-6 1/psi
Initial condition	Reference depth	3160 ft subsea (3688 ft in MD)
	Reservoir pressure	1612 psi (3688 ft x 0.433 psi/ft + 14.65 psi)
	Reservoir temperature	113 °F
Injection constraints	Perforation interval thickness	15 ft
	Maximum BHP	2328 psi (3688 ft x 0.7 psi/ft x 90% + 14.65 psi)

Table 6-23. Parameters used in Corey's relative permeability function for Carper Sandstone.

Formation	Matrix		Fracture	
Relative permeability table	Water-oil	Gas-oil	Water-oil	Gas-oil
Irreducible water saturation/ Critical gas saturation (fraction)	0.35	0.10	0.05	0
Residual oil saturation to water/gas (fraction)	0.25	0.18	0.02	0
Maximum water/gas relative permeability (mD)	0.35	0.90	0.98	1
Maximum oil relative permeability (mD)	0.80	0.80	0.95	1
Water/gas exponent	1.5	2	1	1
Oil exponent	1.5	2	1	1

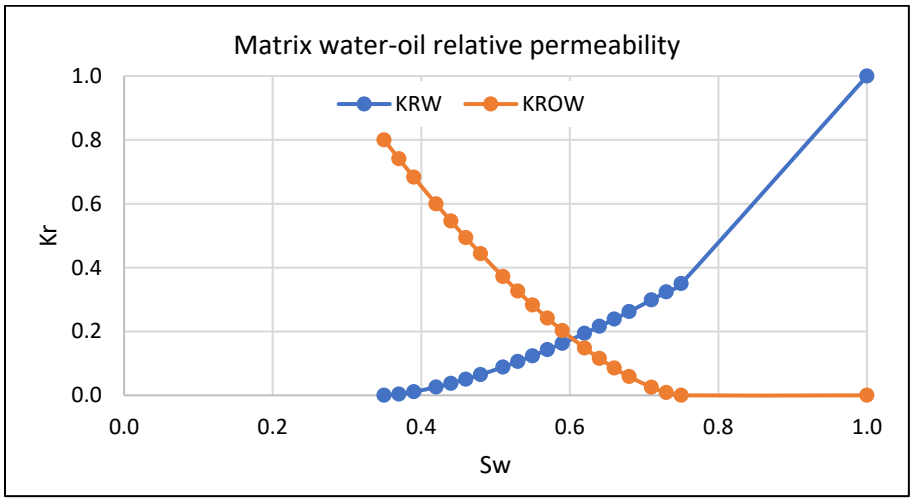


Figure 6-23. Carper matrix water-oil relative permeability curves.

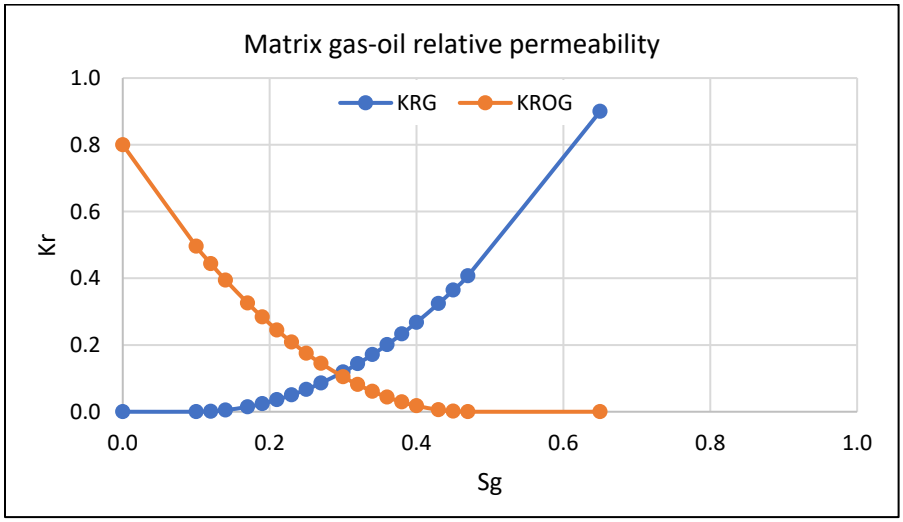


Figure 6-24. Carper matrix gas-oil relative permeability curves.

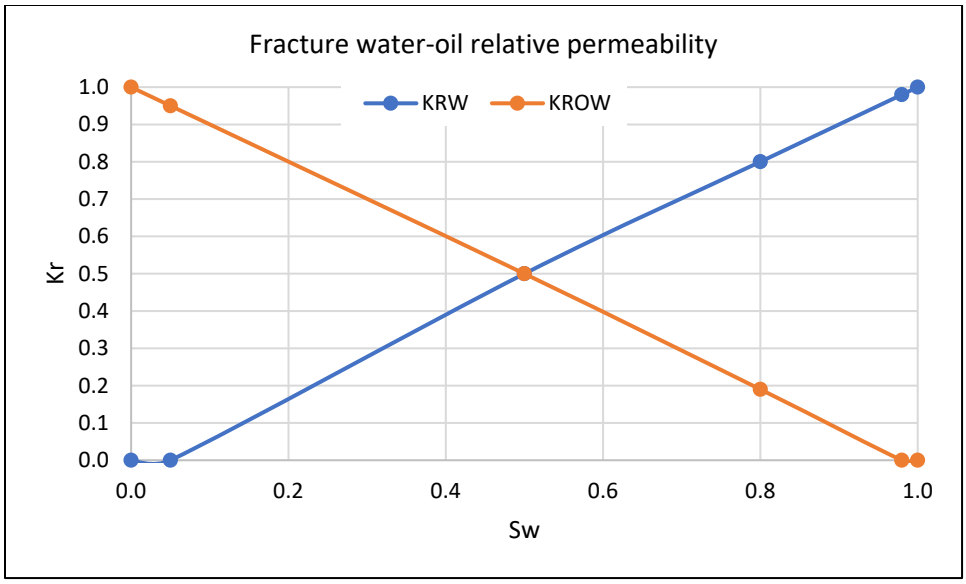


Figure 6-25. Carper fracture water-oil relative permeability curves.

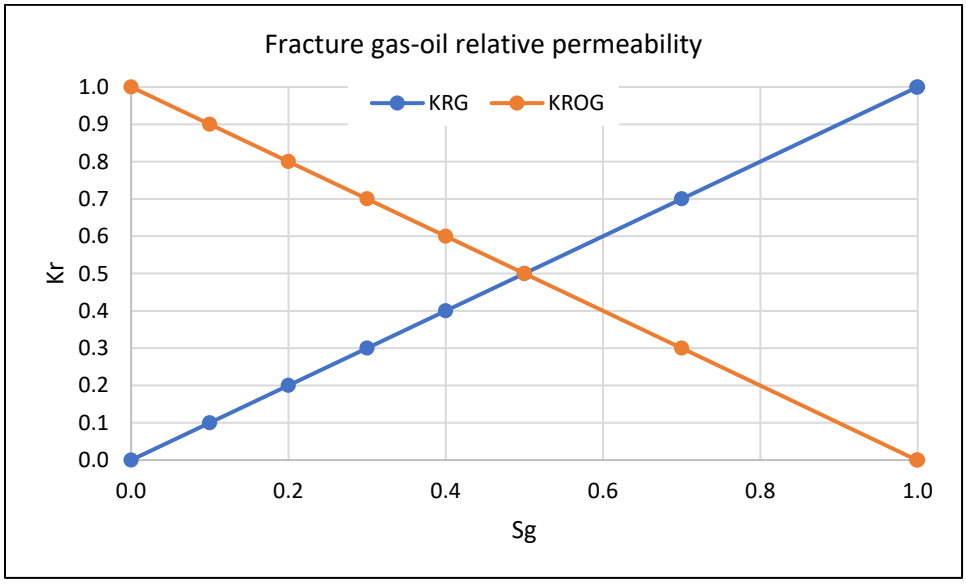


Figure 6-26. Carper fracture gas-oil relative permeability curves.

Geneva simulation Inputs

Table 6-24 lists the major simulation inputs for Geneva Dolomite. As with the Carper model, the rock and fluid properties were calculated using Newman Correlation (Newman, 1973) and McCain correlations (McCain, 1991). The relative permeability was generated using Corey's function embedded in Nexus, and the endpoints and exponent were based on literature (Bennion and Bachu, 2010; Table 6-25, Figures 6-27 and 6-28). For water-oil relative permeability, the endpoints were extracted from a relative permeability data set for CO_2EOR in Texas, a limestone reservoir with an average porosity of 9% and an average permeability of 30 mD (Aung, 2009). The Swr was adjusted to 0.05, and the oil exponent was adjusted from 3.6 to 2 because the Geneva Dolomite is a vuggy formation. For gas-oil relative permeability, the

endpoints and exponents were based on CO_2/brine drainage and imbibition relative permeability curves for carbonate formations (Bennion and Bachu, 2010) and adjusted to honor vuggy porosity and the clustering of Krg around 0.4 (Levine et al., 2014). The low Krg and high Swr are artifacts of measurement techniques (Benson et al, 2015).

The initial reservoir pressure was assumed to follow a pressure gradient of 0.465 psi/ft based on the Geneva salinity. The maximum bottomhole pressure followed an assumed fracture pressure gradient of 0.7 psi/ft with a 90% safety factor.

Table 6-24. Simulation inputs of Geneva Dolomite.

Category	Input parameter	Geneva ROZ	Geneva aquifer
Rock and fluid properties	Rock compressibility (1/psi)	8.23 E-6	3.62 E-6
	Relative permeability	Based on literature	Based on literature
	Water salinity (ppm)	125,000	125,000
	Water density (lb/ft3)	68.10	68.10
	Water viscosity (cP)	0.76	0.76
	Water compressibility (1/psi)	2.832 E-6	2.832 E-6
Initial condition	Reference depth (ft)	3482 subsea (4010 MD)	3517 subsea (4045 MD)
	Reservoir pressure (psi)	1879 psi	1896 psi
	Reservoir temperature (°F)	118	118.4
Injection constraints	Perforation interval (ft)	18	40
	Maximum BHP (psi)	2541 psi	2563

Table 6-25. Parameters used in Corey's relative permeability function for Geneva Dolomite.

Relative permeability table	Water-oil	Gas-oil
Irreducible water saturation/ Critical gas saturation (fraction)	0.05	0.10
Residual oil saturation to water/gas (fraction)	0.20	0.10
Maximum water/gas relative permeability (mD)	0.62	0.40
Maximum oil relative permeability (mD)	0.58	0.58
Water/gas exponent	2	1.6
Oil exponent	2	2

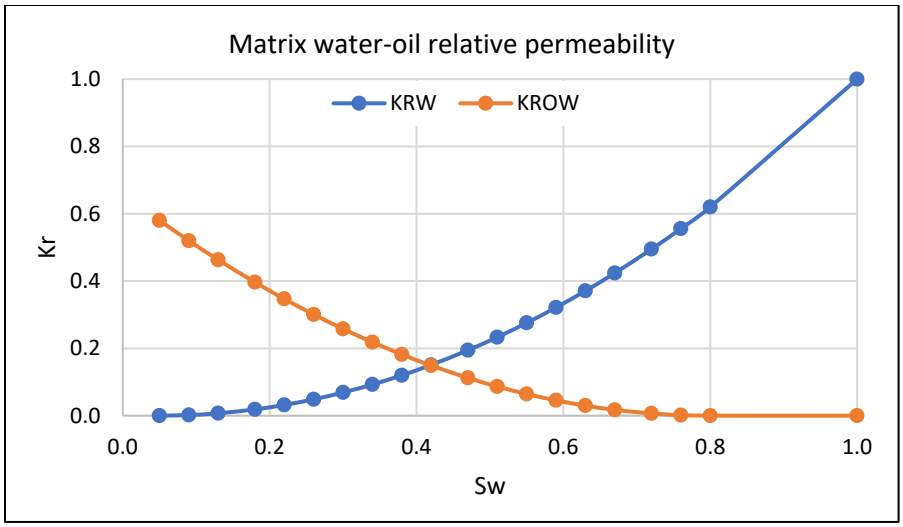


Figure 6-27. Geneva water-oil relative permeability curves.

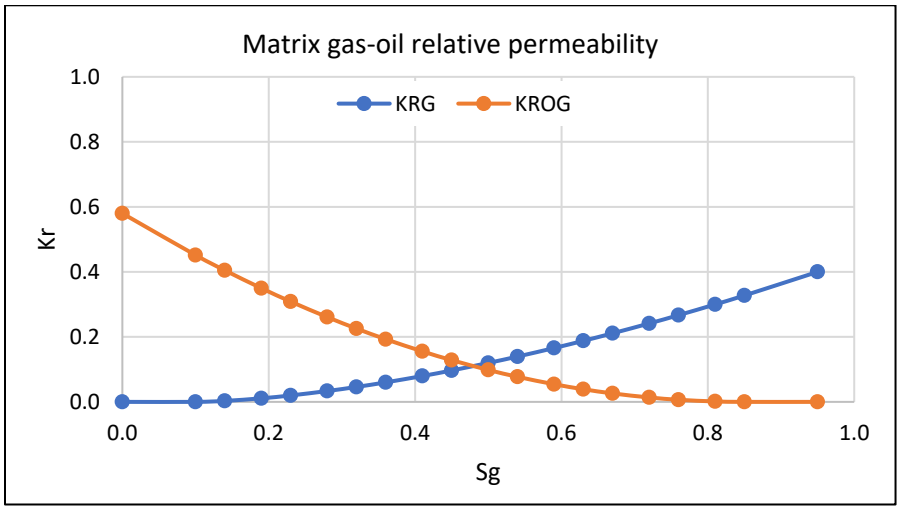


Figure 6-28. Geneva gas-oil relative permeability curves.

Simulation Scenarios

Two operational conditions were considered: developing both the Carper and Geneva ROZs simultaneously and developing Carper ROZ, Geneva ROZ, and Geneva aquifer separately. Accordingly, two types of models were considered: one multi-reservoir model that allowed simultaneous operation and three individual reservoir models to simulate each formation separately. These two model types had the same ariel extent and input parameters, but grid discretization and cell count were adjusted to accommodate various flood pattern sizes that could leverage co-using wells. The multi-reservoir model has 81×67×42 cells, with 65.19 ft x 78.81 ft wide cells, and variable cell thickness ranging from 1.5 ft to 2.3 ft. The geometry of the individual model grids varied by flood pattern size: for 40-acre patterns, the grids contained 80×80 cells areally, with cell spacing of 66 ft x 66 ft; for 80-acre pattern, the grid contained 80×40 cells areally, with cell spacing of 93.34 ft x 93.34 ft. The local grid refinement was used for the Carper model to include 1 ft wide cells around the producers that could be assigned high permeability to mimick hydraulic fractures.

Multi-reservoir Model

The Carper ROZ was preferred to be developed using a pattern that has a big length to width ratio with the long direction perpendicular to the high fracture permeability direction to avoid rapid CO_2 breakthrough and improve sweep efficiency. The Geneva ROZ and aquifer could be developed using regular 5-spot patterns. Wells were placed in a staggered line drive pattern to allow for wells to be used for all three formations in the multi-reservoir model where 160-acre patterns with a length to width ratio of 4:1 was used for Carper ROZ and 53-acre patterns with a length to width ratio of 4:3 was used for Geneva (Figure 6-29).

Two scenarios were considered: 1) no production from Geneva aquifer, where the CO_2 was injected into all formations, but production was limited to the ROZs, and 2) producing from all formations, where CO_2 was injected into all formations and all formations were produced. These simulations were run to determine if brine production from Geneva aquifer could be used to manage pressure and allow for more CO_2 injection.

For the scenario in which the Geneva aquifer was not produced, two cases were simulated: 1) NoLimit case, where there was no gas injection or production rate limit; injection was constrained by the maximum bottomhole pressures described in simulation inputs (Table 6-24) and production was constrained by a minimum bottomhole pressure of 25 psi, and 2) Qg1800 case, where the production was constrained by both pressure and a gas production rate of no greater than 1800 Mscf/day, which is 75% of the simulated maximum gas injection rate.

For the scenario in which all formations were produced, three cases (Qg1800PRD, Qg1200PRD, and Qg600PRD) were simulated with a gas production rate limit of 1800 Mscf/day, 1200 Mscf/day, and 600 Mscf/day, respectively.

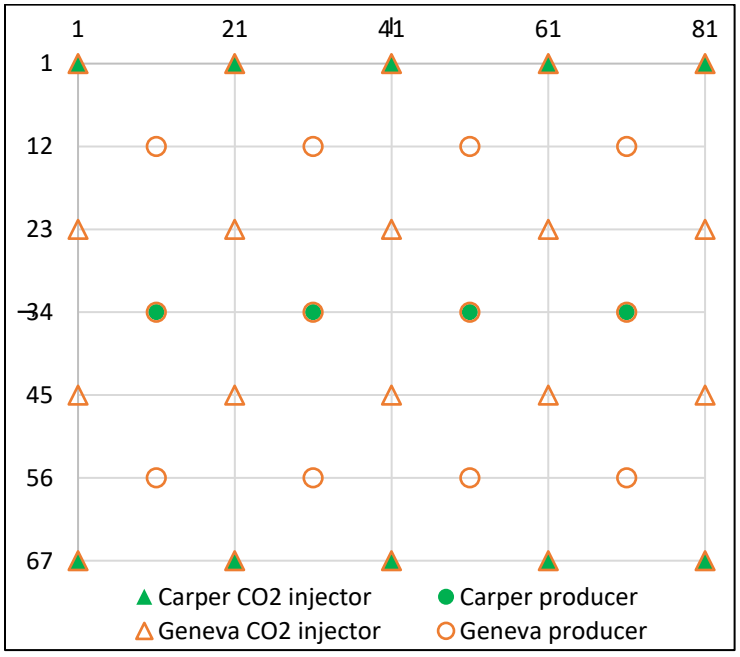


Figure 6-29. Staggered line drive pattern for the multi-reservoir model. The model has 81 x 67 x 42 cells. Each cell is 65.1852 ft in I direction and 78.806 ft in J direction. The injector spacing is 53 acres for Geneva and 160 acres for Carper, and the total model area is 640 acres (1 mi^2).

Individual Reservoir Models

Carper ROZ

The Carper Sandstone has a low permeability matrix (0.2mD) that is naturally fractured. The high contrast in permeability of the matrix and natural fractures can result in less effective conventional pattern floods with continuous CO_2 injection. Various CO_2 injection schemes were considered to determine how to optimize oil recovery and CO_2 storage. These injection schemes included continuous injection, water-alternating-gas (WAG), soak-alternating-gas (SAG, injection and production from different wells), and cyclic CO_2 injection (i.e., Huff and Puff (HnP, injection and production from the same well). The WAG cases considered two gas-water ratios: 2:1 and 1:1. The SAG schedule started with 25-day injection, 25-day soaking, and 15-day production, and was then optimized to 7-day injection, 14-day soaking, followed by 7-day production. The optimized SAG schedule was used for HnP. The well layout was the same as that of the multi-reservoir model, shown in Figure 6-29.

Preliminary results concluded that HnP resulted in the greatest oil recovery, so two additional HnP cases with two different pattern sizes were run (40 acre; CarperROZ_40ac, Figure 6-30 and 80 acre, CarperROZ_80ac, Figure 6-31) and initial dewatering were run to evaluate the CO_2-EOR and storage performance. Additionally, a medium permeability case (CarperP50_80ac, with a matrix porosity of 13%, a matrix permeability of 2 mD, and an effective fracture permeability of 20 mD) and a high permeability case (CarperP90_80ac, with a matrix porosity of 15%, a matrix permeability of 14 mD, and an effective fracture permeability of 83.3 mD) was run considering HnP and 5-spot pattern flood in 80-acre spacing schemes (Figure 6-32).

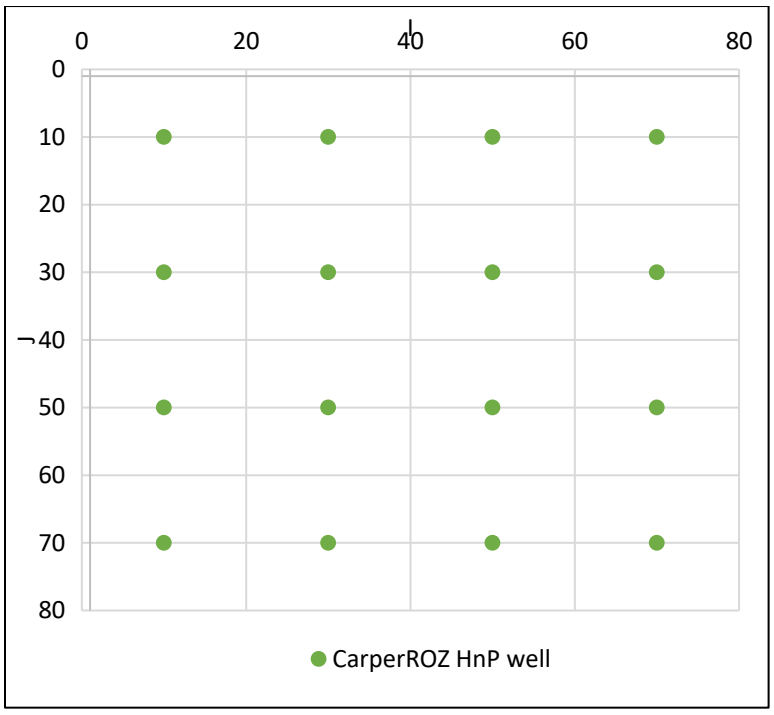


Figure 6-30. Well layout for 40-acre pattern in a 640-acre model area used to simulate HnP scenarios. The model has 80 x 80 cells in one layer. Each cell is 66 ft x 66 ft in I and J directions.

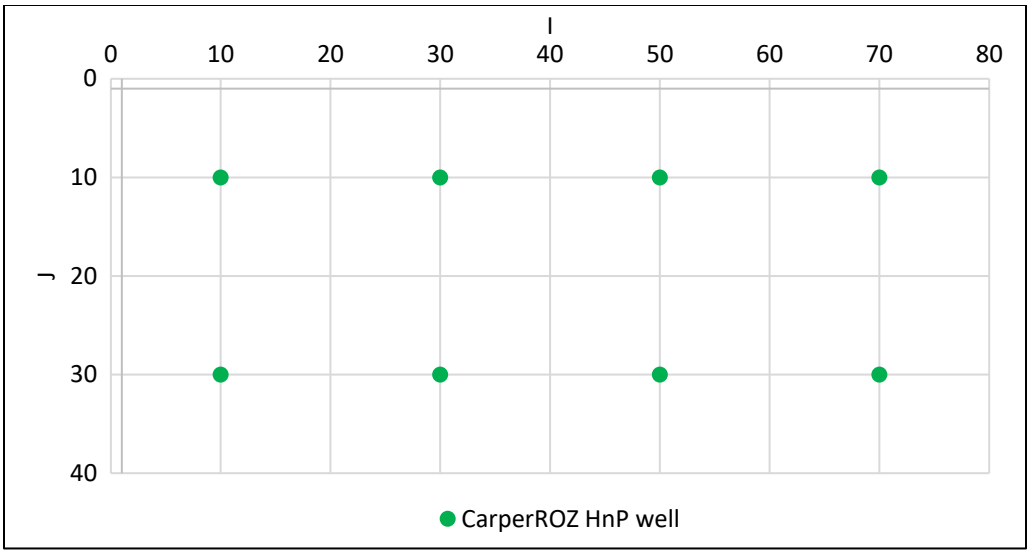


Figure 6-31. Well layout for the 80-acre pattern in a 640-acre model area used to simulate HnP scenarios for the Carper. The model has 80 x 40 cells in one layer. Each cell is 99.3375 ft x 99.3375 ft in I and J directions.

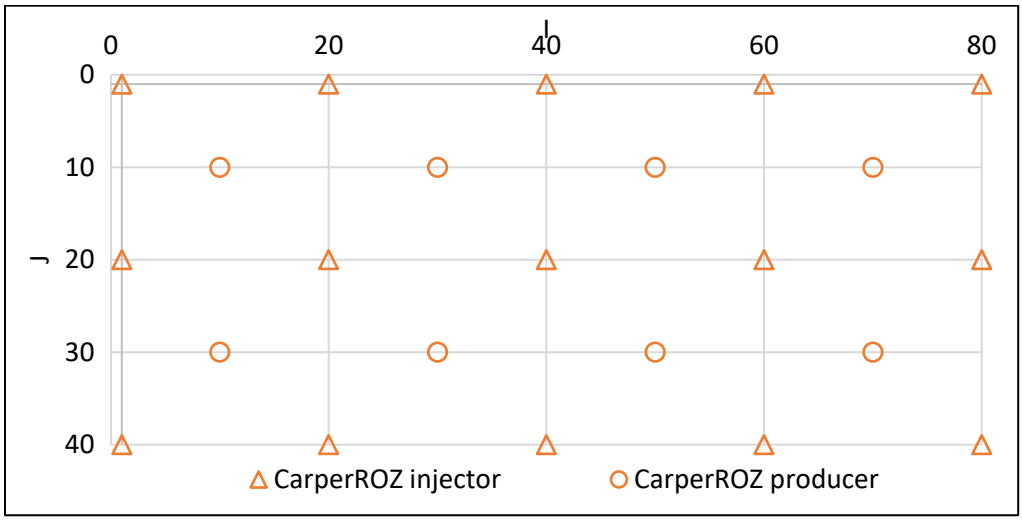


Figure 6-32. Carper high permeability estimate 80-acre pattern case well layout in a 640-acre model area. The model has 80 x 40 cells in one layer. Each cell is 99.3375 ft x 99.3375 ft in I and J directions.

Geneva ROZ

For the Geneva Dolomite, cases with various gas production constraints were run to determine a better development option using the well layout in the muti-reservoir model (Figure 6-29). The 5-spot pattern flood, in two pattern sizes: 40-acre (GenevaROZ_40ac case; Figure 6-33) and 80-acre (GenevaROZ_80ac case; Figure 6-34), was then used to develop Geneva ROZ.

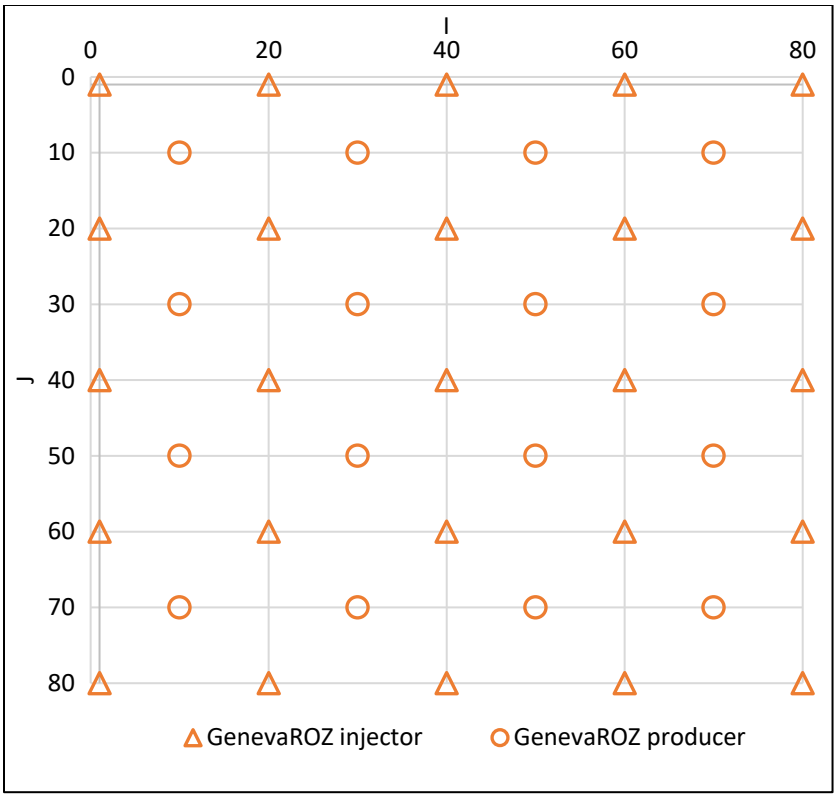


Figure 6-33. Well layout for the 40-acre 5-spot pattern in a 640-acre model area used to develop the Geneva ROZ. The model has 80 x 80 cells in one layer. Each cell is 66 ft x 66 ft in I and J directions.

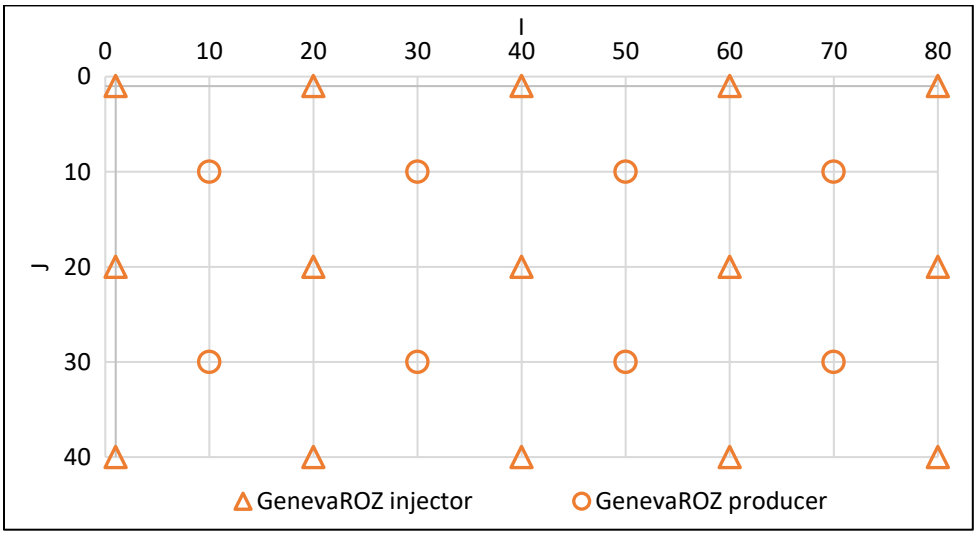


Figure 6-34. Well layout for the 80-acre 5-spot pattern in a 640-acre model area used to develop the Geneva ROZ. The model has 80 x 40 cells in one layer. Each cell is 99.3375 ft x 99.3375 ft in I and J directions.

Geneva Aquifer

The Geneva aquifer is intended for CO_2 storage. Although water production allows more CO_2 injection by releasing pressure, it increases the cost associated with producer drilling and water disposal. Therefore, in this individual reservoir model scenario, water production was not considered.

When the injectors were placed in a 53-acre spacing of the multi-reservoir model (Figure 6-29), very little CO_2 injection occurred due to pressure buildup. Therefore, scenarios for the separate Geneva aquifer model were designed to evaluate the well spacing necessary to optimize CO_2 storage. Five injectors were placed in a five-spot pattern in the middle of open boundary models. The CO_2 injection via the inner well represents a single well storage capacity at the corresponding well spacing because it has no boundary effect. The spacing between the wells was iteratively increased from 1 mi2 to 126 mi2. For cases with well spacing larger than 42 mi^2, a large model with an area equal to the well spacing was used. The model size was determined to be 42 mi^2 based on radius of investigation calculated using reservoir properties.

Simulation Results

The direct simulation outputs include oil production, CO_2 injection, CO_2 production, and water production.

The metrics used to evaluate the CO_2-EOR and storage performance include oil recovery factor, CO_2 storage, and net utilization factor. They were calculated using the equations below:

$$RF = \frac{CO_2 EOR}{OOIP} \quad \text{Equation 6-1}$$

$$CO_2\ EOR = N_{p,CO_2} - N_{p,WF} \quad \text{Equation 6-2}$$

$$G_{store} = G_{inj,CO_2} - G_{p,CO_2} \quad \text{Equation 6-3}$$

$$NUF = \frac{G_{store}}{CO_2 EOR} \quad \text{Equation 6-4}$$

Where:
CO_2 EOR = incremental oil produced
$N_{p,CO2}$ = cumulative oil production of CO_2 flood (Mstb)
$N_{p,WF}$ = cumulative oil production of waterflood (Mstb)
G_{store} = CO_2 storage (MMscf)
$G_{inj,CO2}$ = CO_2 injected (MMscf)
$G_{p,CO2}$= CO_2 produced (MMscf)
RF = oil recovery factor (fraction)
OOIP = original oil in place (Mstb)
NUF = net utilization factor (Mscf/stb)

For greenfield ROZs, no oil can be recovered from water flooding so the CO_2-EOR is the cumulative oil production from a CO_2 flood.

Multi-reservoir Model

The oil recovery factor, net utilization factor, CO_2 injection, CO_2 production as a percentage of injection, CO_2 storage, and water production for the multi-reservoir models are shown in Figures 6-35 through 6-40.

Producing the ROZs only (no production from Geneva aquifer; the NoLimit and Qg1800 cases) yielded more oil recovery, lower net utilization factor, and less water production, but also more CO_2 production and less CO_2 storage. Limiting gas production rate yielded less oil recovery and less CO_2 storage although it reduced CO_2 production and water production.

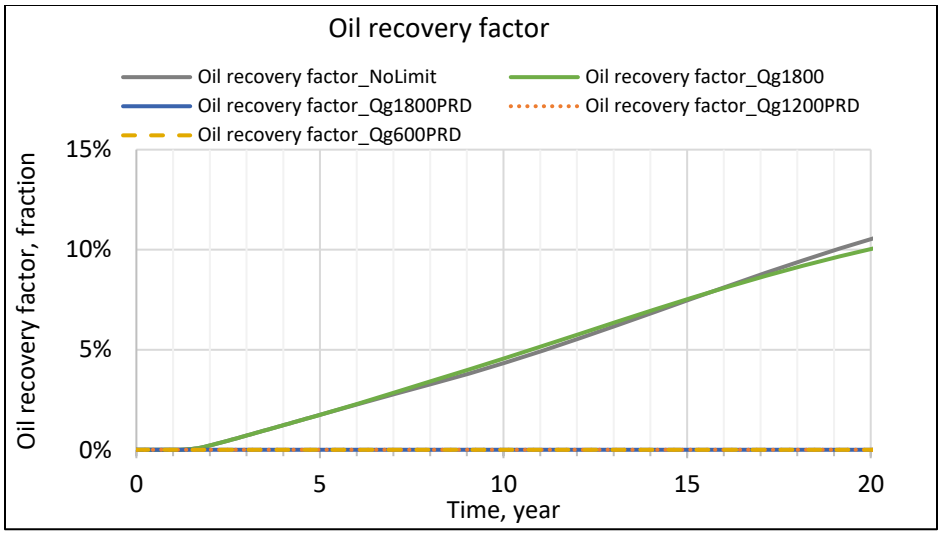


Figure 6-35. Oil recovery factor with time for cases with various operational constraints. Case NoLimit (grey line) and case Qg1800 (green line) have no production from Geneva aquifer, while other cases produce from all formations (yellow, blue, and orange lines, all overlapping along the x axis). Producing from the Geneva aquifer results in a significant reduction in oil recovery.

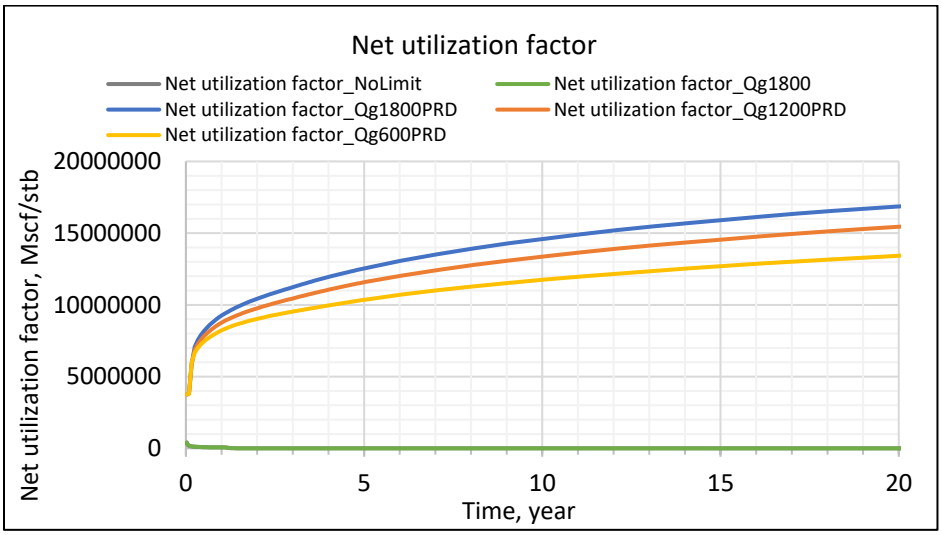


Figure 6-36. Net utilization factor with time for cases with various operational constraints. Case NoLimit and case Qg1800 have no production from Geneva aquifer, while other cases produce from all formations.

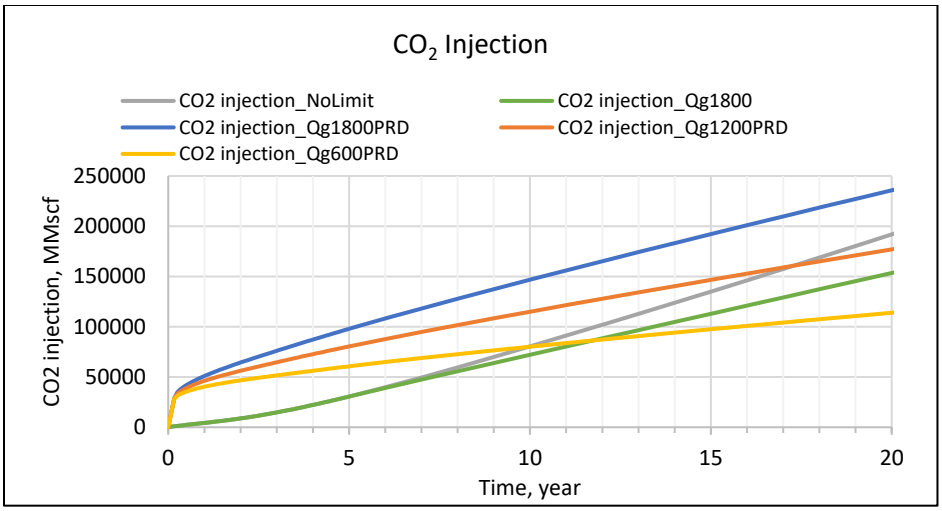


Figure 6-37. Cumulative CO_2 injection with time for cases with various operational constraints. Case NoLimit and case Qg1800 have no production from Geneva aquifer, while other cases produce from all formations.

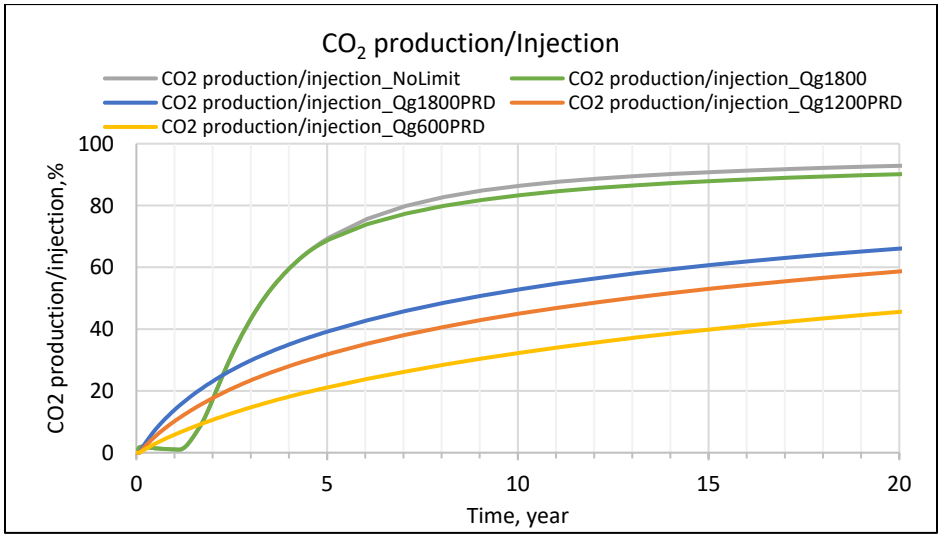


Figure 6-38. Cumulative CO_2 production as a percentage of injection with time for cases with various operational constraints. Case NoLimit and case Qg1800 have no production from Geneva aquifer, while other cases produce from all formations.

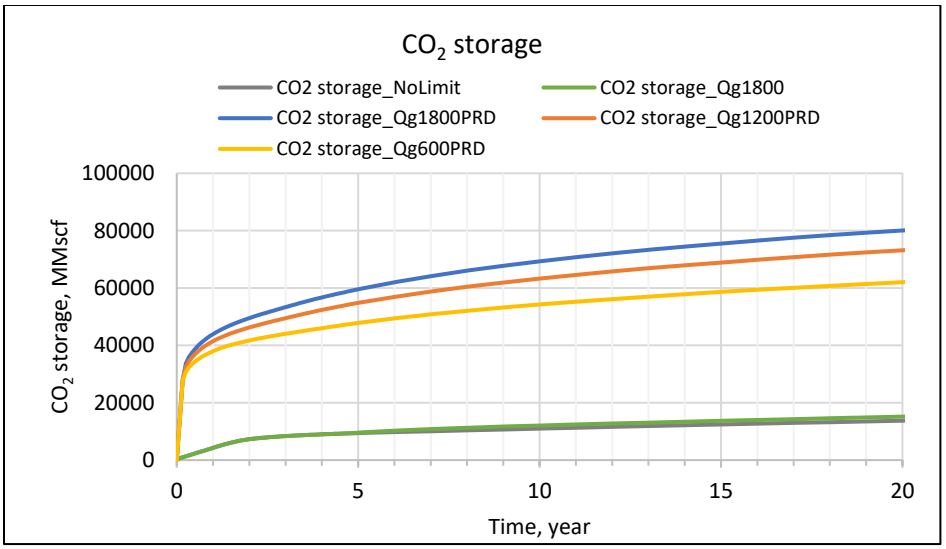


Figure 6-39. Cumulative CO_2 injection with time for cases with various operational constraints. Case NoLimit and case Qg1800 have no production from Geneva aquifer, while other cases produce from all formations.

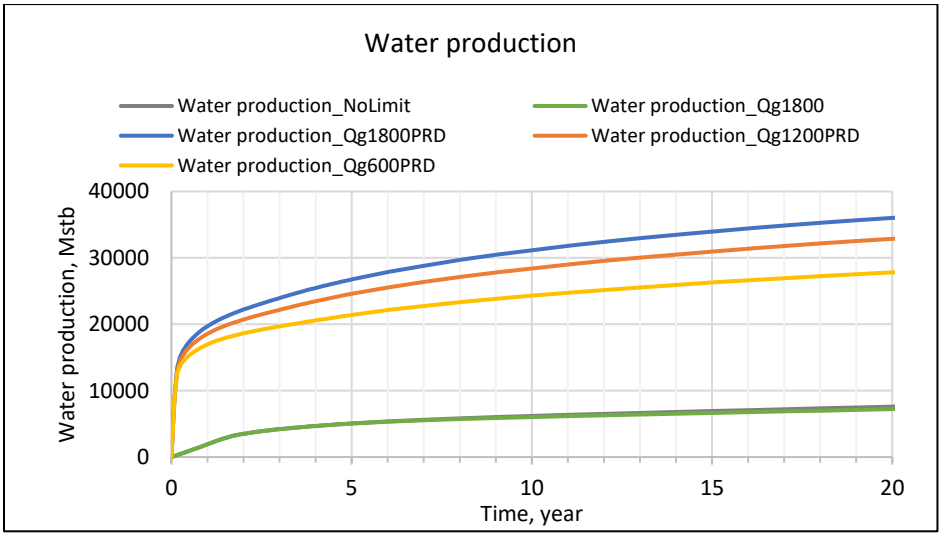


Figure 6-40. Cumulative CO_2 injection with time for cases with various operational constraints. Case NoLimit and case Qg1800 have no production from Geneva aquifer, while other cases produce from all formations.

With production from the ROZs only and no constraint on gas production rate (the NoLimit case), the CO_2 EOR and storage performance were compared among formations (Figures 6-41 through 6-46). The Geneva ROZ was the dominating contributor to the overall performance, and it has the most oil recovery (Figure 6-41), CO_2 injection (Figure 6-43), CO_2 storage (Figure 6-45), water production (Figure 6-46), and lowest net utilization factor (Figure 6-42) compared to other formations. This indicates that CO_2 preferably went into Geneva ROZ, which was attributed to the fact that the Carper has much lower permeability than Geneva ROZ, and the Geneva aquifer was limited by pressure buildup from CO_2 injection. Therefore, developing the formations separately was recommended to make the most of each formation.

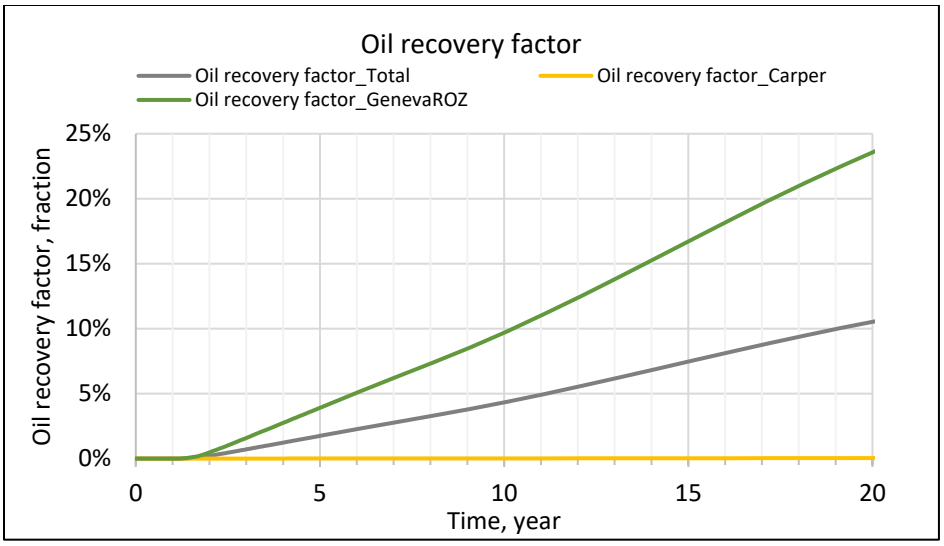


Figure 6-41. Oil recovery factor by formations with time for the NoLimit case.

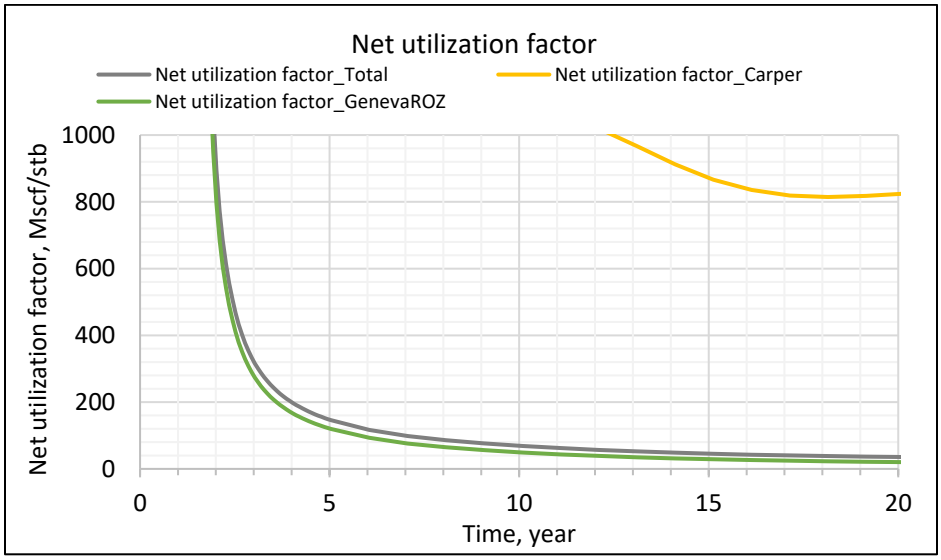


Figure 6-42. Net utilization factor by formations with time for the NoLimit case.

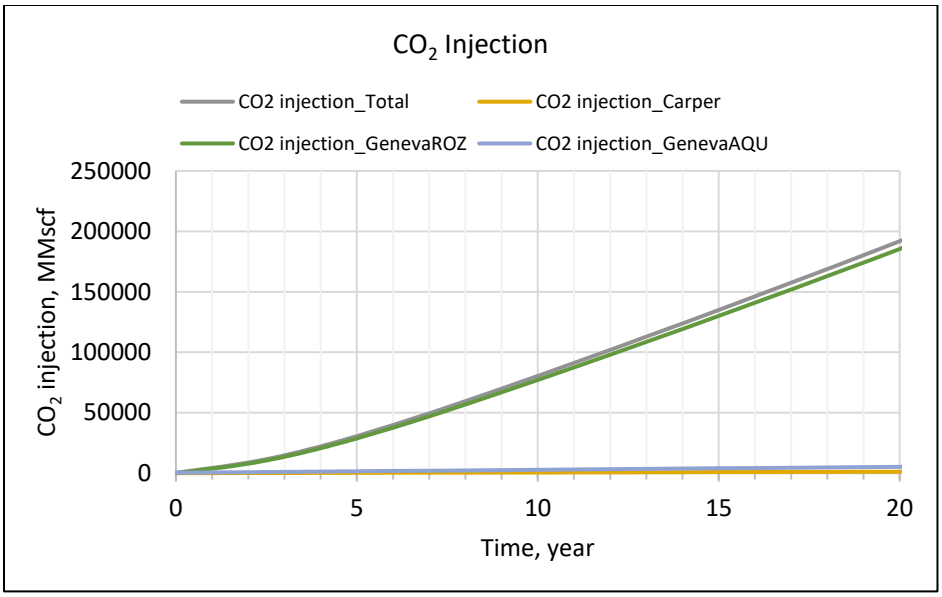


Figure 6-43. CO_2 injection by formations with time for the NoLimit case.

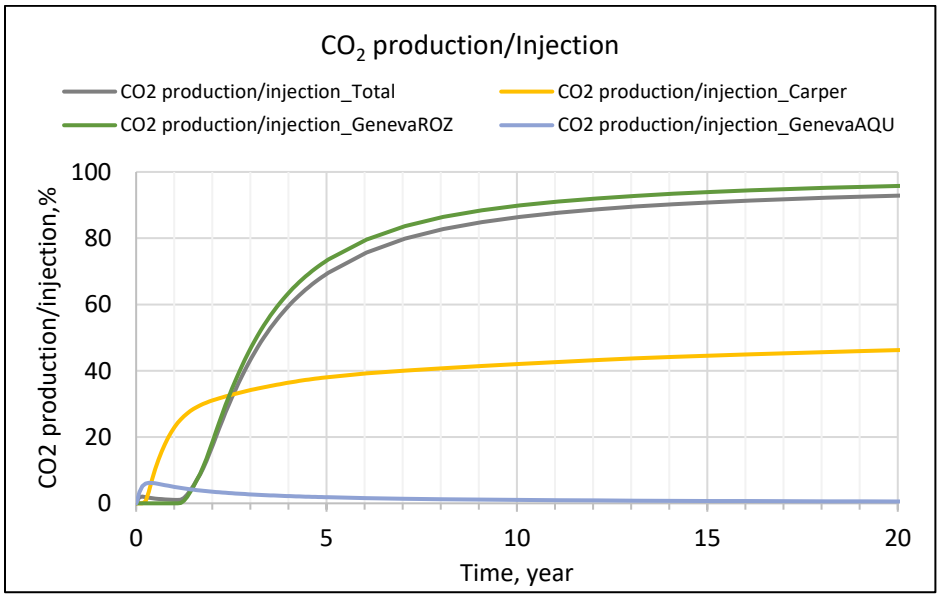


Figure 6-44. CO_2 production as a percentage of injection by formations with time for the NoLimit case.

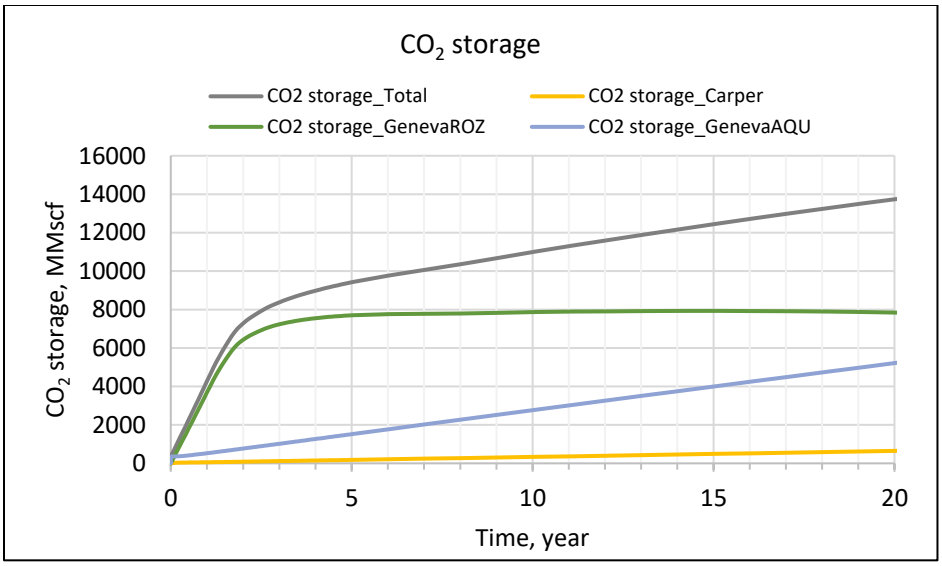


Figure 6-45. CO_2 storage by formations with time for the NoLimit case.

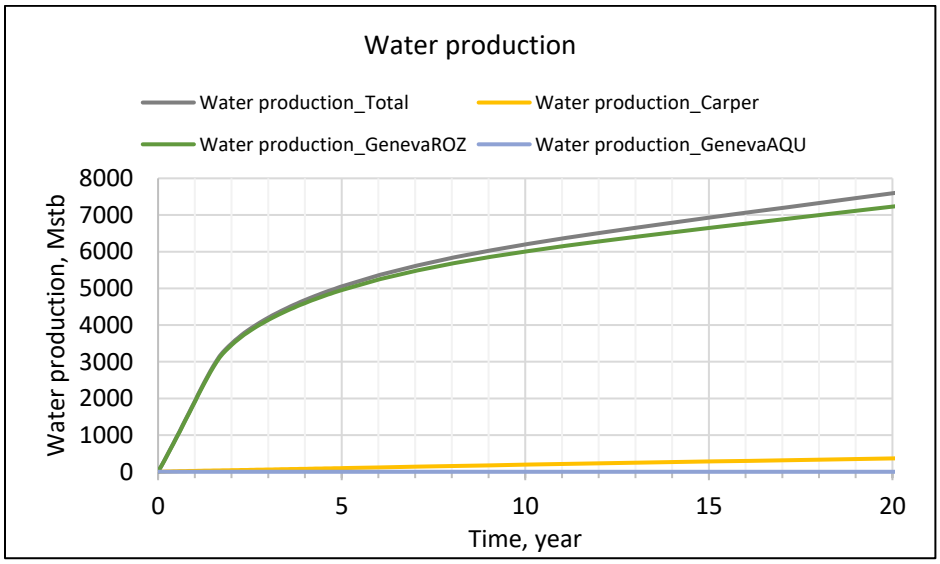


Figure 6-46. Water production by formations with time for the NoLimit case.

Individual Reservoir Models

Carper ROZ

Various injection schemes were compared in their impacts on oil recovery and CO_2 storage (Figures 6-47 through 6-50).

WAG injection schemes are effective in conventional reservoirs because they control gas mobility by reducing viscous fingering and density tonging, which increases CO_2 contact with un-swept zones and improves microscopic displacement (Alagorni et al., 2020). However, WAG was found to be ineffective in the simulations of tight Carper Sandstone. This is believed to be caused by the natural fracture network negating the fingering effect.

As shown in Figure 6-47, WAG yielded less oil production than continuous CO_2 injection, which could be the result of less total CO_2 injection in WAG due to water injection compared to continuous CO_2 injection. The CO_2 preferably went into fracture and had limited contract with matrix-bound oil and spread all over the Carper natural fracture system.

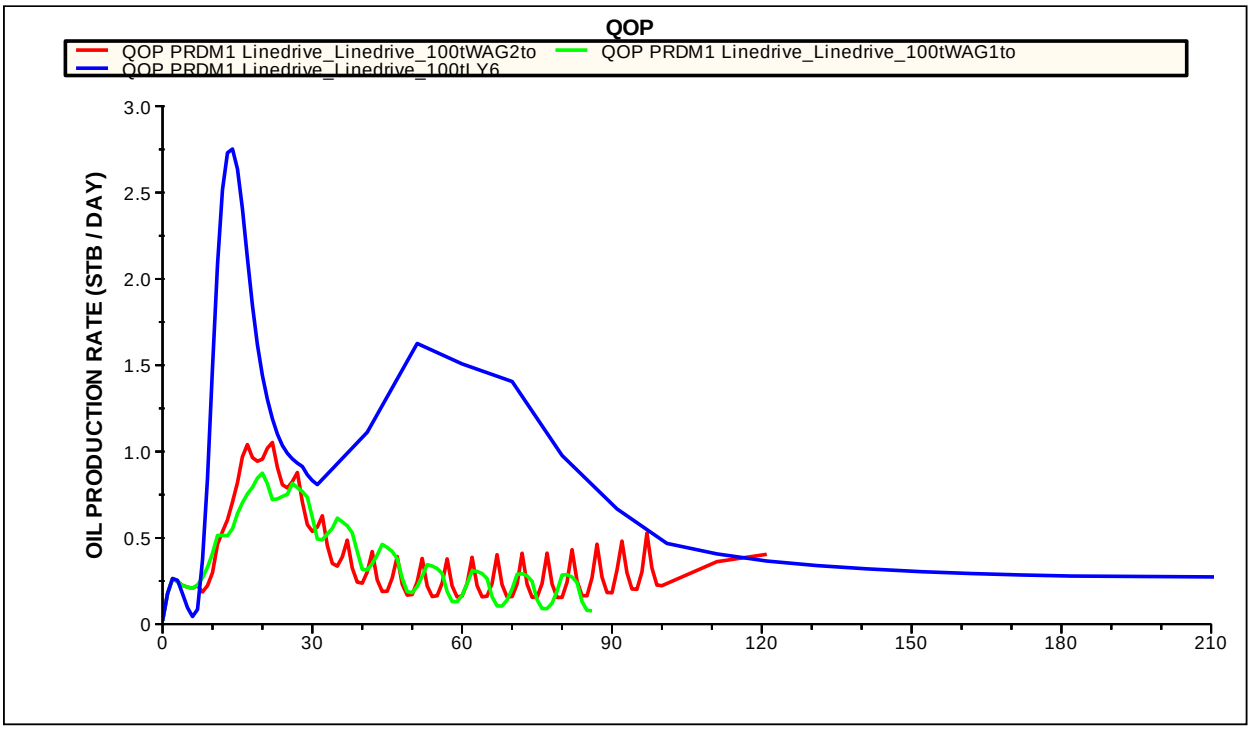


Figure 6-47. Continuous injection (blue line) vs. WAG (Red line-2:1 gas-water ratio, Green line-1:1 gas-water ratio) in oil production rate with time for a single well.

SAG greatly enhanced Carper oil recovery compared to continuous injection. As shown in Figure 6-48, only one oil peak occurred in the continuous injection case, with oil rate dropping dramatically after CO_2 breakthrough, while SAG allowed for oil peaks for each cycle, leading to much higher cumulative oil production. SAG mitigates the inadequate CO_2-crude oil interaction by adding a CO_2 soaking period just after CO_2 breakthrough. During the soaking period, CO_2 in the fracture dissolves and diffuses with the reservoir fluid, reducing oil viscosity, and the oil expands and is replaced by CO_2, leading to improvements in the recovery of residual oil (Wang et al., 2021; Xu et al., 2022).

The injection time, soaking time, and production time for the SAG scheme were optimized by checking the rate and pressure response. As shown in Figure 6-49, the CO_2 injection rate plateaued and the oil production rate dropped to close to zero within a week, and the reservoir pressure balanced with injection and production within a SAG cycle. As longer injection and production periods were not able to proportionally increase CO_2 injection and oil production, the injection and production periods were both reduced to 7 days and the soaking period was reduced to 14 days to allow pressure balance and shorter cycles of SAG. The optimized SAG case allowed for more frequent oil peaks and higher cumulative oil production (Figure 6-50).

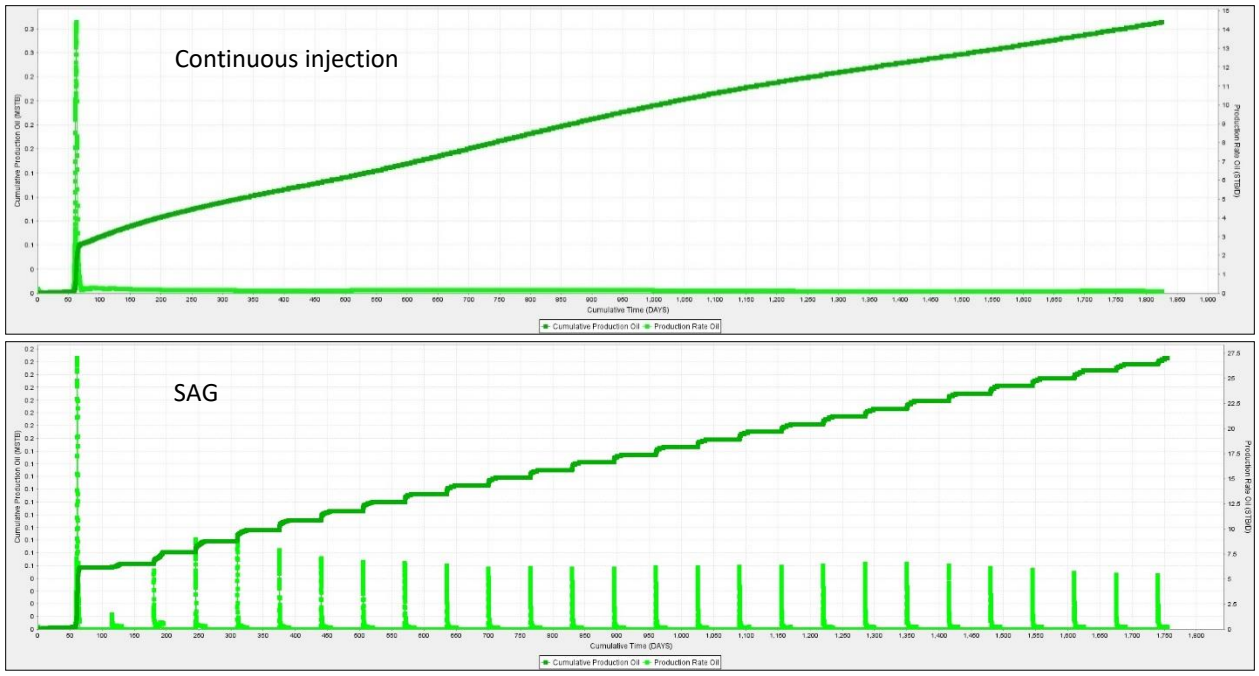


Figure 6-48. Continuous injection vs. SAG (Inject 25 days, soak 25 days, and produce 15 days) in field cumulative oil production with time. SAG has peak oil production in each cycle which create a total of 282 bbls oil production at year 5, while the continuous injection case has a single oil peak that quickly drops which results in a total of 213 bbls oil production at year 5.

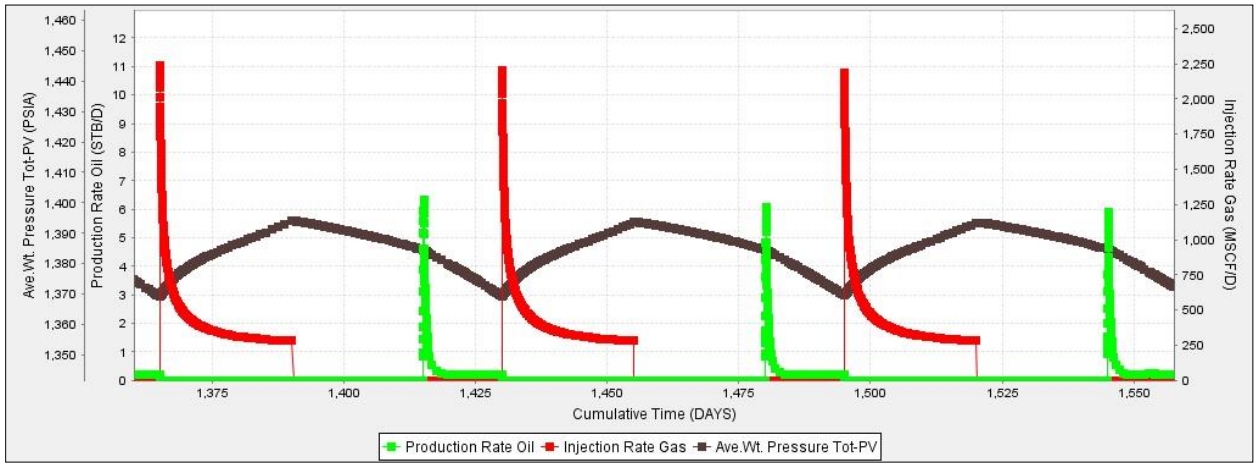


Figure 6-49. CO_2 Injection rate (red line), oil production rate (green line), and average reservoir pressure (brown line) with time for SAG optimization.

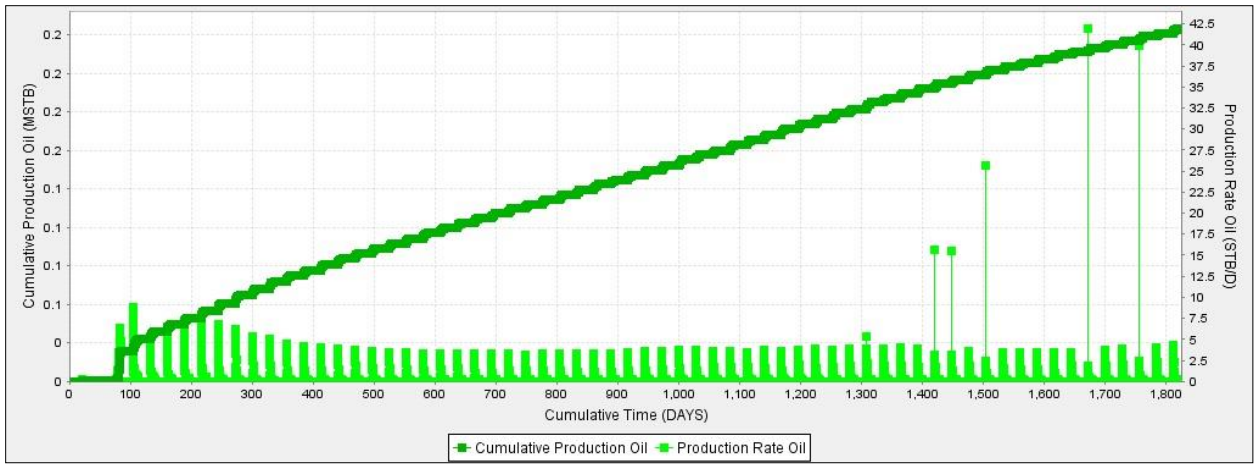


Figure 6-50. Optimized SAG (injection 7 days, soak 14 days, and produce 7 days) in field cumulative oil production with time.

SAG outperformed continuous injection, indicating CO_2 tended to replace oil near the well in the tight Carper sandstone. Therefore, HnP was considered as it focuses on the near well drainage area. Previous studies also show that HnP injection has the highest potential to enhance oil recovery in shale oil reservoirs (Sheng and Chen, 2014; Wan et al, 2013; Sheng and Chen, 2014; Sheng, 2015). As shown in Figure 6-51, HnP greatly increased oil recovery compared to SAG, especially when the production was constrained by gas production rate that maintained a stable high reservoir pressure (Figure 6-52). However, less CO_2 storage was observed with HnP compared to SAG (Figure 6-53).

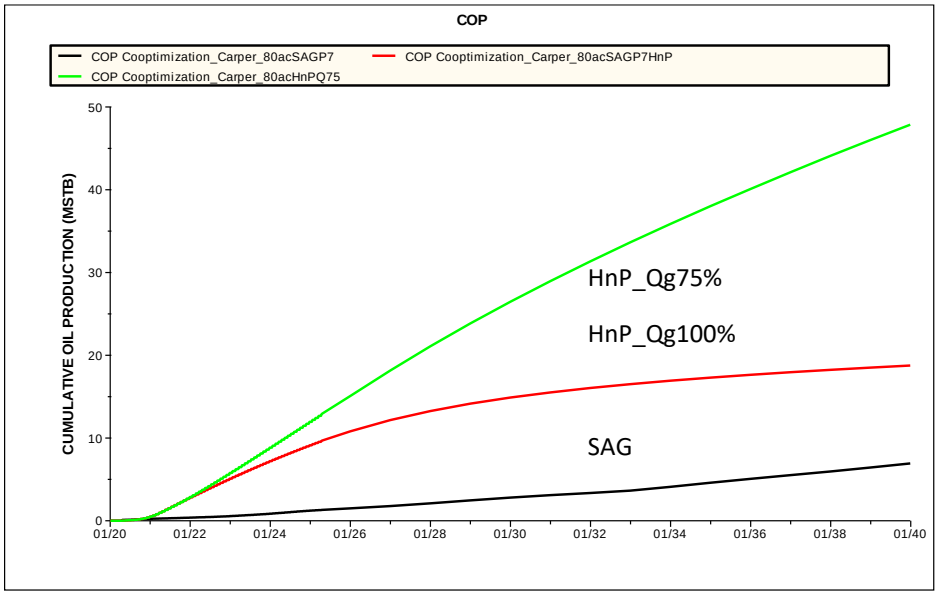


Figure 6-51. HnP (Green and red lines) vs. SAG (black line) in field cumulative oil production with time. HnP and SAG cycles shared the same schedule: injecting 7 days, soaking 14 days, and producing 7 days. The green line is a HnP case with maximum gas production rate set as 75% of maximum injection rate, and the red line is a HnP case with maximum gas production rate set as maximum injection rate.

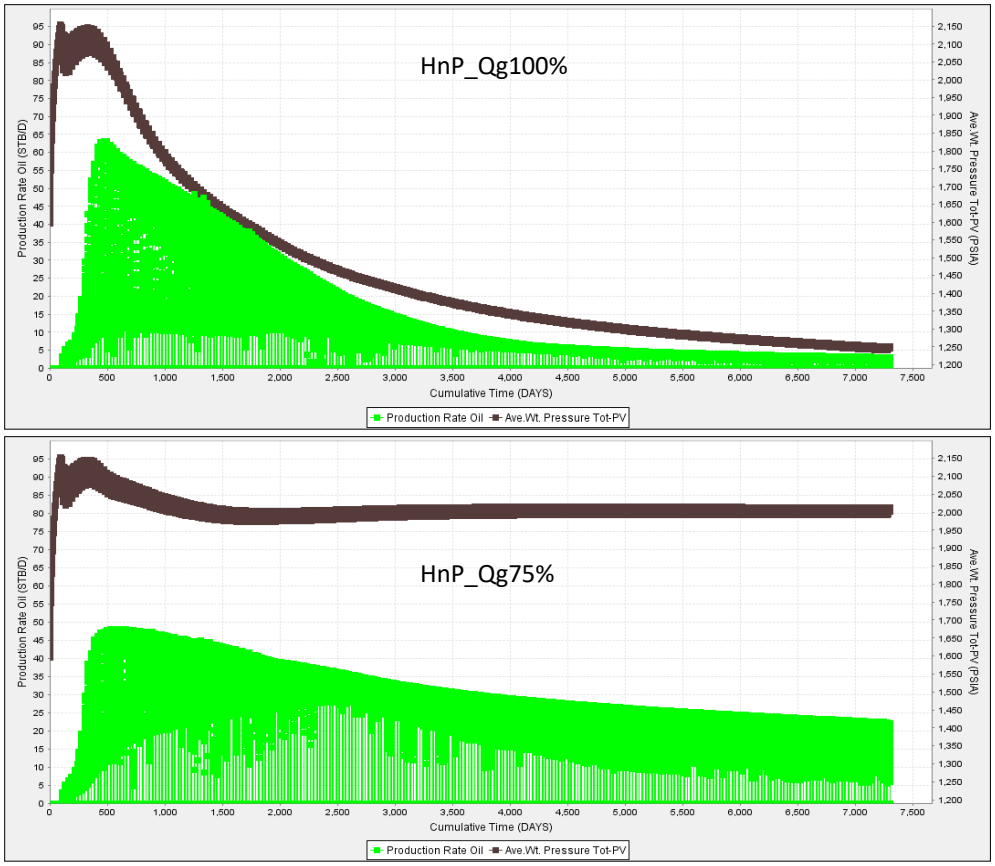


Figure 6-52. Oil production rate and average reservoir pressure with time for HnP cases with different gas production rate constraints (Top- 100% of maximum injection rate, bottom- 75% of maximum injection rate).

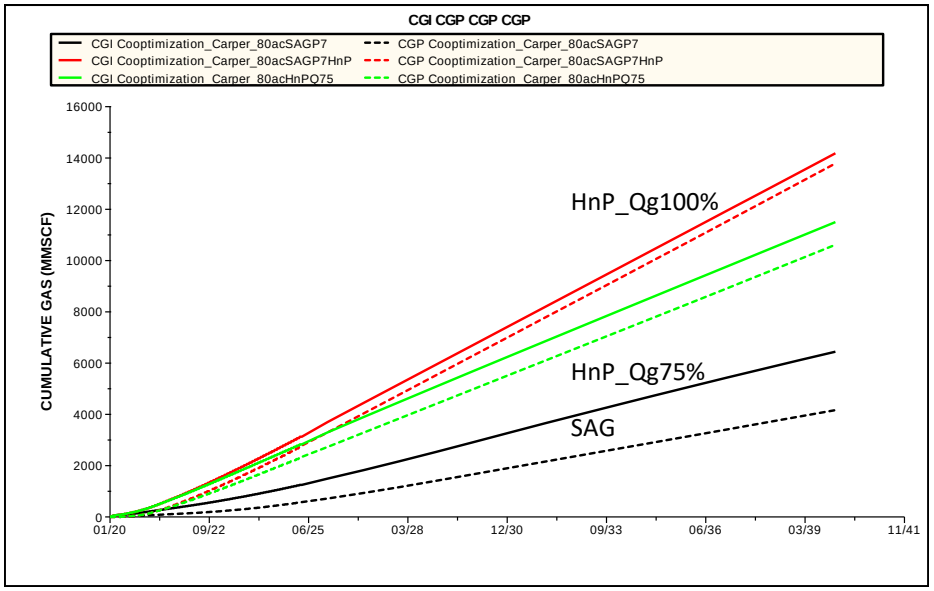


Figure 6-53. HnP (Green and red lines) vs. SAG (black line) in field cumulative gas injection and production with time. The CO_2 storage is the difference between injection and production. The green line is a HnP case with maximum gas production rate as 75% of maximum injection rate, and the red line is a HnP case with maximum gas production rate set as maximum injection rate.

To allow more CO_2 injection, dewatering was considered before starting the HnP cycles. Figure 6-54 and Figure 6-55 compare two Carper cases with and without dewatering before HnP. Dewatering lowered average pressure initially which allowed for more CO_2 injection, which led to slightly more oil production (1% more at 20 years) and more CO_2 storage (8% more at 20 years). Therefore, HnP with initial dewatering was considered a valid strategy to develop Carper ROZs.

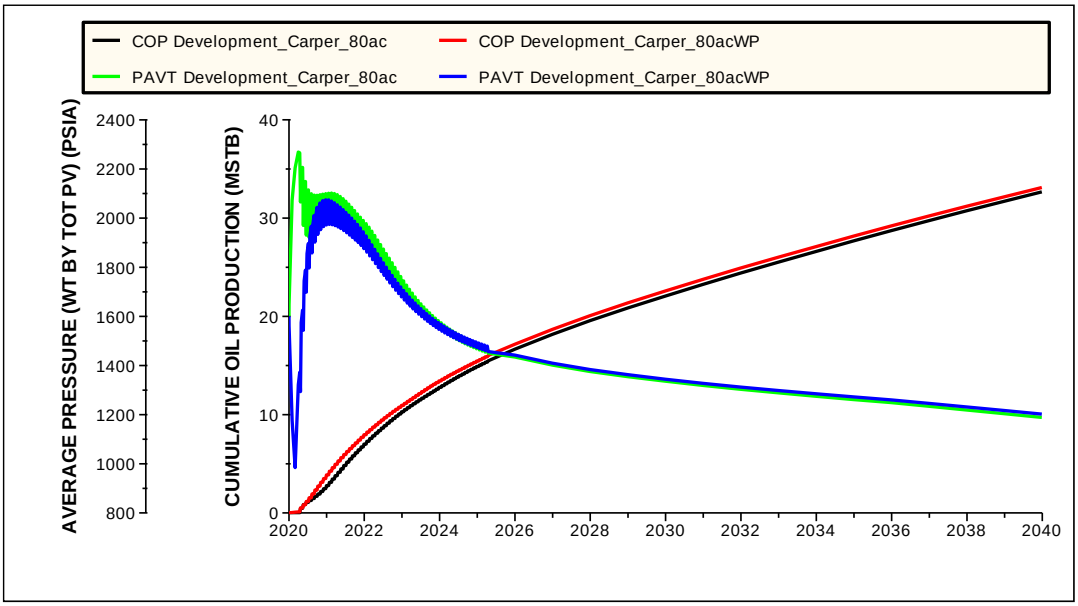


Figure 6-54. Cumulative oil production (red and black lines) and average reservoir pressure (blue and green lines) with (red and blue lines) and without (black and green lines) initial dewatering. The cases ending with 'WP' had a 3-month water production before the HnP cycles. The other case had no initial dewatering.

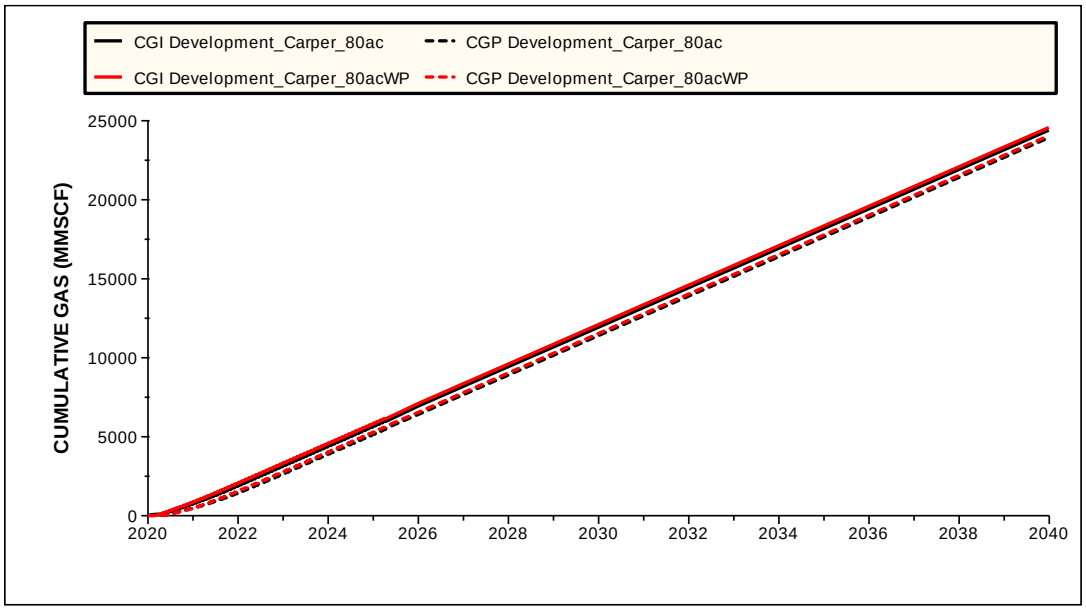


Figure 6-55. Cumulative CO_2 injection (solid lines) and production (dashed lines) with and without initial dewatering. The CO_2 storage is the difference between injection and production. The case ending with 'WP' (red lines) had a 3-month water production before the HnP cycles. The other case (black lines) had no initial dewatering.

The higher permeability cases, however, were more effective using 5-spot pattern flooding with continuous CO_2 injection as the permeability is in the conventional reservoir range. Figure 6-56 and Figure 6-57 showed that pattern flood yielded more oil production (90% more compared to HnP) and more CO_2 storage (50% more compared to HnP) at 5 months.

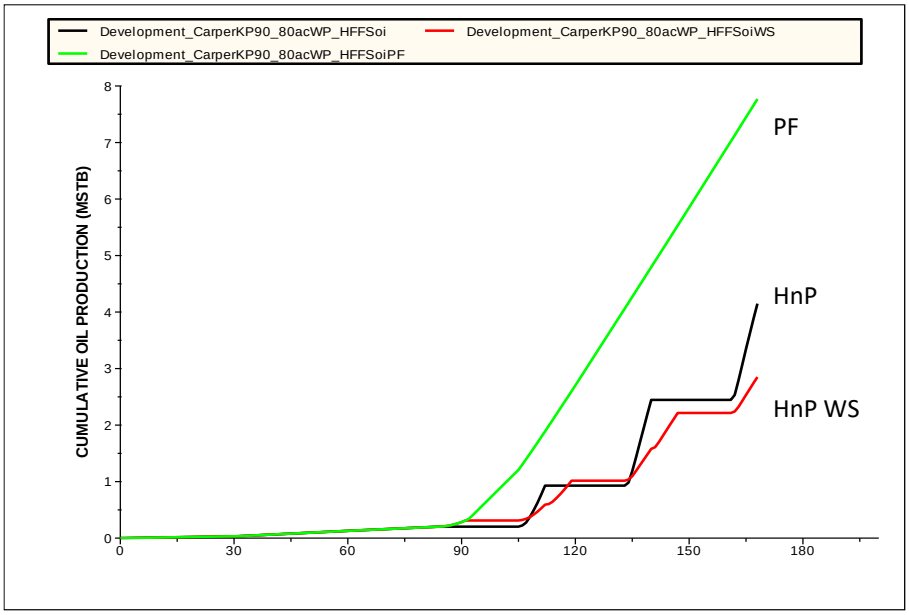


Figure 6-56. Cumulative oil production with time for Carper high permeability cases: HnP (black line), all wells had the same injection schedule; HnP WS (red line), when a well is injecting, a nearby well is producing; PF (green line), 5-spot pattern flood. The pattern flood produces significantly more oil over 180 days.

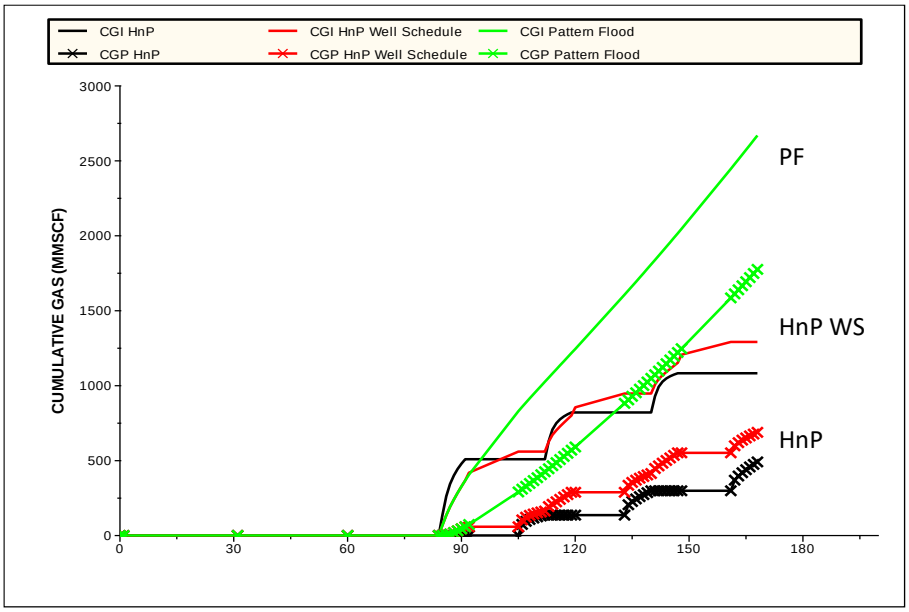


Figure 6-57. Cumulative CO_2 injection and production with time for Carper high estimate cases: HnP (red and black crosses), all wells had the same injection schedule; HnP WS (red and black lines), when a well is injecting, a nearby well is producing; PF (green line and crosses), 5-spot pattern flood.

Figures 6-58 through 6-63 show the performance of developing the Carper ROZ using HnP with dewatering in 40-acre and 80-acre spacings and developing a more permeable Carper ROZ using 5-spot pattern flood in 80-acre spacing. Table 6-26 lists Carper ROZ performance metrics at 20 years.

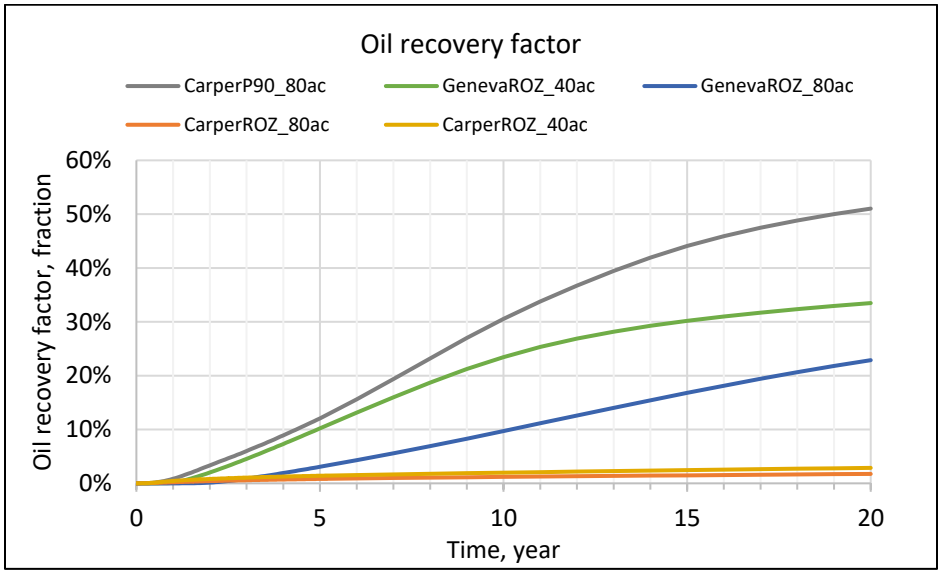


Figure 6-58. Oil recovery factor with time for the ROZs in different pattern sizes.

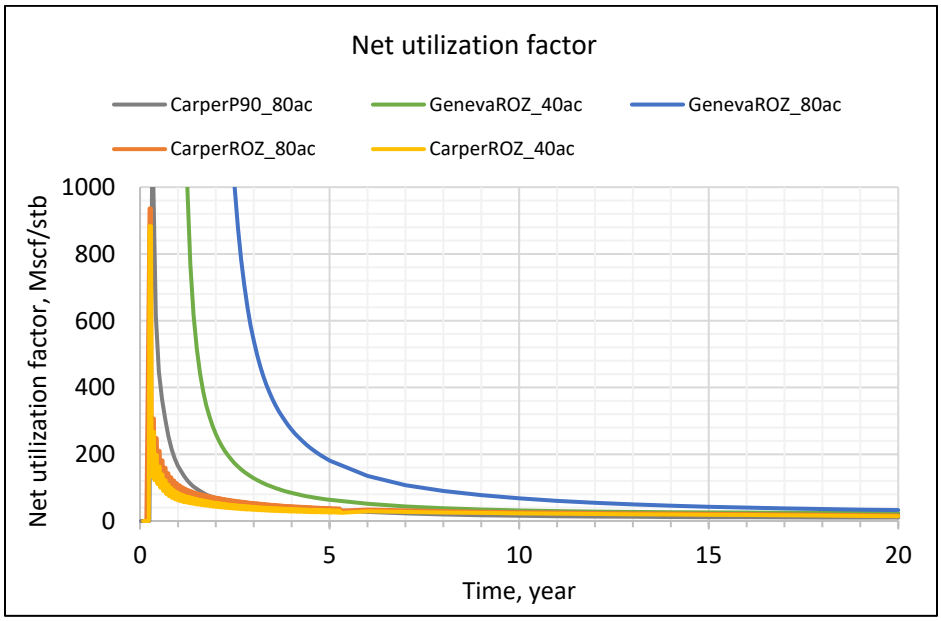


Figure 6-59. Net utilization factor with time for the ROZs in different pattern sizes.

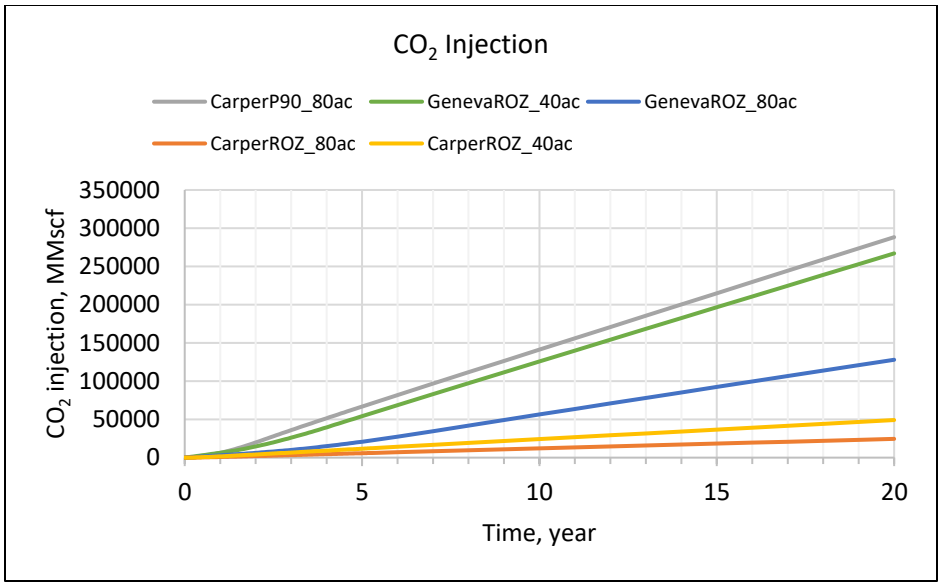


Figure 6-60. Cumulative CO_2 injection with time for the ROZs in different pattern sizes.

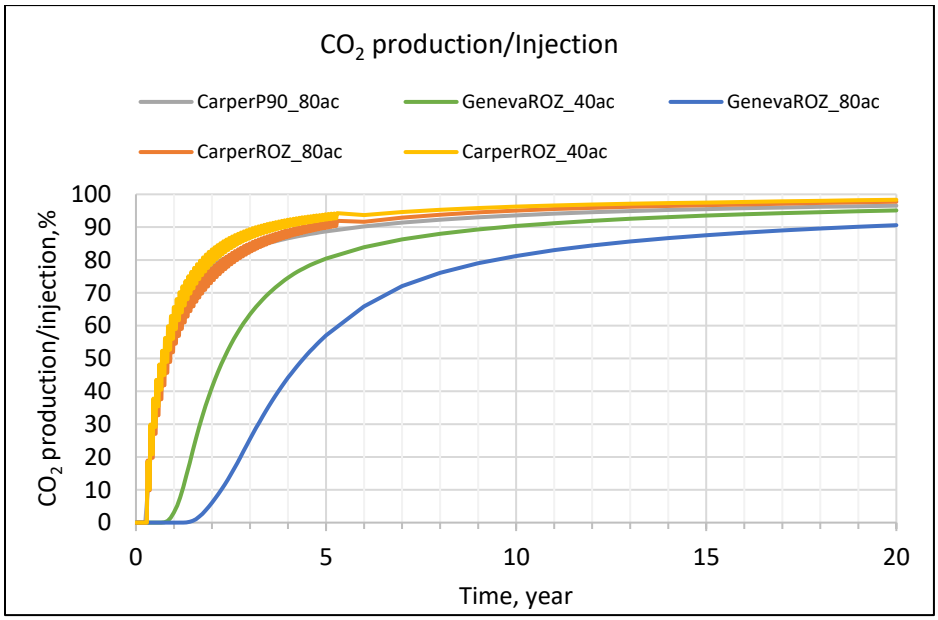


Figure 6-61. Cumulative CO_2 production as a percentage of injection with time for the ROZs in different pattern sizes.

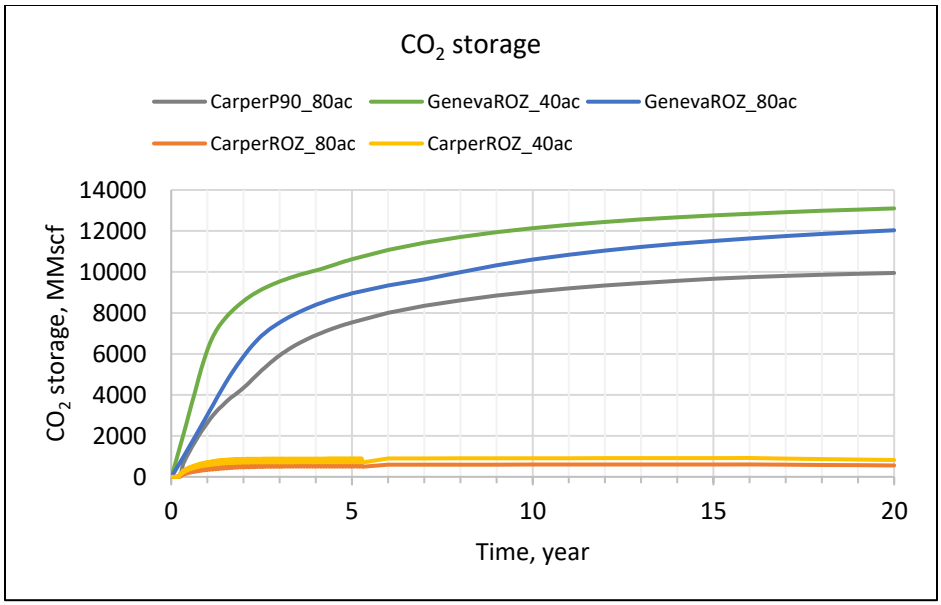


Figure 6-62. Cumulative CO_2 storage with time for the ROZs in different pattern sizes.

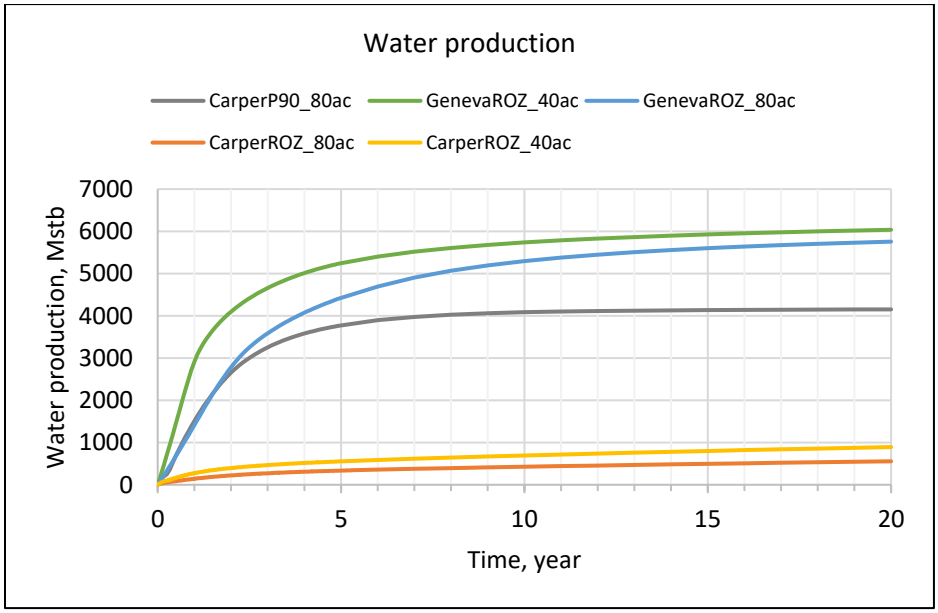


Figure 6-63. Cumulative water production with time for the ROZs in different pattern sizes.

Table 6-26. Carper ROZ performance in cumulative data

Scenario	Case name	CO_2-EOR, Mstb	Gstore, Mt	RF, %	NUF, Mscf/stb	SF, Mscf/stb	Eco2, %	HCPV injected	CB, tonne/stb
Low perm (0.2 mD) HnP in 40-ac spacing	Carper_40ac	57	43	2.9	14	0.4	7%	17	0.8
Low perm (0.2 mD) HnP in 80-ac spacing	Carper_80ac	33	29	1.7	17	0.3	5.2%	9.3	0.9
Med perm (2 mD) HnP in 80-ac spacing	CarperP50_80acHnP	71	140	3.7	37	1.4	15%	16	2.0
Med perm (2 mD) 5-spot pattern flood in 80-ac spacing	CarperP50_80acPF	181	221	9.5	23	2.2	28%	20	1.2
High perm (14 mD) 5-spot pattern flood in 80-ac spacing	CarperP90_80ac	966	525	51	10	5.3	62%	72	0.5

Mt: million metric tons, Mstb: thousand standard barrels

Overall, for tight Carper ROZ, the oil recovery factor, (1.7-2.9%) and net utilization factor (14-17 Mscf/stb) were low. The reason is that CO_2 stayed in fractures and had limited contact with oil in the matrix due to the high contrast of fracture and matrix permeability. This is consistent with previously published findings that suggest fractures dominate flow when the matrix permeability is less than 1 mD and the fracture-matrix permeability ratio is above 10,000 (Matthai and Belayneh, 2004).

For the more permeable Carper ROZ (the high permeability estimate case), however, the oil recovery factor was quite high (up to 51%). The net utilization factor was low (10Mscf/stb). The much higher permeability of the matrix (14 mD) allows for matrix dominated flow, which means that CO_2 can readily enter the matrix and displace oil. The more permeable Carper ROZ even outperformed the conventional Geneva ROZ, which was likely due to the natural fracture system spreading CO_2 all over the formation and allowed for more CO_2 interaction with oil.

Geneva ROZ

The performance of developing Geneva ROZ using 5-spot pattern flood in 40-acre and 80-acre spacings is shown in Figures 6-56 through 6-61. Table 6-27 lists Geneva ROZ performance metrics at 20 years.

The oil recovery factor was 23-33%. Small pattern size resulted in more oil recovery (Figure 6-56 and Table 6-27). The net utilization factor was 24-33 Mscf/stb. A high portion (84-95%) of injected CO_2 was produced, and a large amount of water production was needed for the operation.

Table 6-27. Geneva ROZ performance in cumulative data

Scenario	Case name	CO_2-EOR, Mstb	Gstore, Mt	RF, %	NUF, Mscf/stb	SF, Mscf/stb	Eco2, %	HCPV injected	CB, tonne/stb
5-spot pattern flood in 40-ac spacing	Geneva_40ac	548	691	33	24	8.0	72%	74	1.3
5-spot pattern flood in 80-ac spacing	Geneva_80ac	368	635	23	33	7.5	68%	36	1.7

Mt: million metric tons, Mstb: thousand standard barrels

Geneva Aquifer

Figures 6-64 and 6-65 show the achievable CO_2 injection rate for the Geneva aquifer with time under the BHP constraint. With small well spacings, the injection rate dropped quickly in the first two years and then slowly decreased to a low level (Figure 6-64). Larger well spacing delays and reduces the magnitude of this decrease in injection rate until no decrease is observed after 20 years with a well spacing of 100 mi^2 (Figure 6-65).

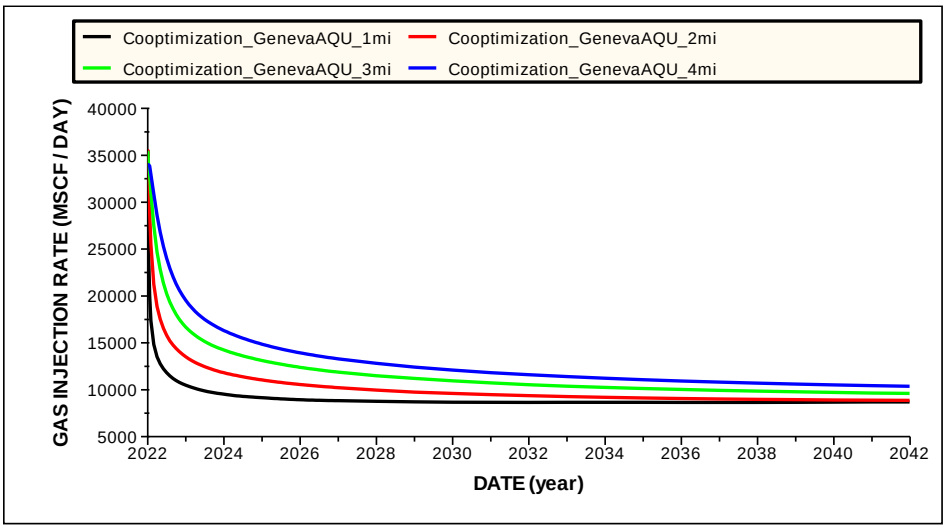


Figure 6-64. CO_2 injection rate with time for at various well spacings (1-4 mi^2). Increasing well spacing allows for greater gas injection rates.

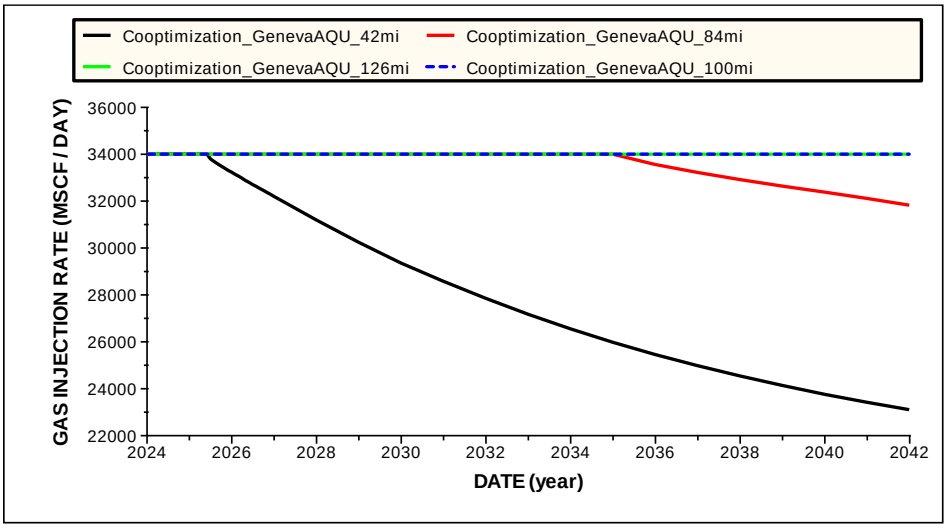


Figure 6-65. CO_2 injection rate with time at various well spacings (42-126 mi^2).

Table 6-28 lists the average CO_2 injection rate and cumulative CO_2 injection for a 100 mi^2 area at well spacings ranging from 1 mi^2 to 100 mi^2. The average injection rate is higher with larger well spacing, but smaller well spacing can achieve significantly more injection per 100 mi^2 at the cost of more wells.

Table 6-28. Average injection rate and cumulative CO_2 injection at various well spacings.

Time, year	1-mi spacing	2-mi spacing	3-mi spacing	4-mi spacing	100-mi spacing
Average CO_2 injection rate, Mt/yr (million metric tons per year)					
12	0.18	0.21	0.24	0.27	0.66
20	0.17	0.19	0.22	0.25	0.66
Cumulative injection for a 100 mi^2 area, Mt (million metric tons)					
12	213	124	97	82	8
20	346	194	148	123	13
Total wells	100	50	33	25	1

Table 6-29 summarizes the production and injection data for the stacked greenfield based on simulation results of the one square mile pattern model.

Table 6-29. Summary of cumulative injection and production from all formations.

Time, year	Pattern size, acre	CO_2 injection, Mt	CO_2 production, Mt	CO_2 storage, Mt	Oil production, Mstb	Water production, Mstb
12	40	12	9	3	484	6565
20	40	20	16	4	606	6929
12	80	12	4	8	227	5903
20	80	21	7	14	401	6311
12	80-P90	21	12	9	898	9560
20	80-P90	35	21	14	1334	9907

Mt: million metric tons, Mstb: thousand standard barrels

Discussion and Conclusions

Reservoir simulations were conducted on Carper and Geneva ROZs and the Geneva aquifer to optimize CO_2-EOR and associated CO_2 storage in a stacked greenfield ROZ storage complex.

The multi-reservoir model (in which all targets were developed simultaneously via shared wells) results showed that CO_2 was preferentially directed to the highly permeable Geneva formation. Therefore, it is necessary to develop each formation separately to optimize oil production and CO_2 storage. Additionally, the Carper and Geneva are very different geologically and require different development strategies.

Carper ROZ

The Carper based on the properties at the Holsapple 2B well had fracture dominated flow that limited CO_2 interaction with matrix oil, which led to very low oil recovery factor (1-3%) and low CO_2 storage (1-4 Mt/yr). The net utilization factor was 14-24 Msc/stb. The performance could be much better where the Carper has matrix dominated flow due to higher matrix permeability.

The following engineering measures are suggested to develop the tight Carper ROZ:

- HnP to better recover oil near wells as the cross-field interaction is limited by the tight matrix,
- Constrain gas production rate to maintain stable high reservoir pressure to allow more oil production and CO_2 storage, and
- Dewatering before HnP to lower reservoir pressure and allow more CO_2 injection.

The injection, soak, and production time of a HnP cycle need to be optimized based on rate and pressure response. At the Greenfield field laboratory (the Holsapple 2B well), 7-days was the optimum injection and production time, and the results were insensitive to soak time. A gas production rate limit of 75% of the maximum CO_2 injection led to balanced pressure and more oil production.

More HnP optimization can be done considering findings from literature: the optimum injection time is the time required for the near wellbore pressure to increase to the maximum injection pressure; and the optimum production time is the time required for the near wellbore pressure to decrease to the minimum production pressure (Sheng, 2017). Soaking pressure has more of an impact on oil recovery than soaking time (Gamadi et al., 2013). Soaking may not be necessary during the HnP gas injection in tight oil reservoirs because the benefits of soaking may not compensate for the loss of injection and production due to the time lost in the soaking period. The number of HnP cycles is determined by the economic rate cut-off (Chen et al., 2014; Sheng, 2017).

Sensitivity on the gas production rate limit is recommended to co-optimize oil production and CO_2 storage and a tighter constraint can reduce the amount of CO_2 production, thus recycling.

Dewatering can lead to increased oil production but also creates costs associated with additional water production.

Additionally, fluid diffusion between matrix and fracture was not included due to the limit of software capacity. Findings in literature suggested it could increase oil recovery by 3-9% in some cases (Alfarge et al., 2017; Ding et al., 2019) and not significantly in other cases (Sheng, 2017). The diffusion is more effective at high pressures and less effective at relatively low pressures (Alfarge et al., 2017; Ding et al., 2019). Further study can investigate the impact of diffusion on both oil recovery and CO_2 storage.

Geneva ROZ

The Geneva ROZ had better oil recovery factors (13-33%) and CO_2 storage (32-55 Mt/yr) than the Carper. The net utilization factor was 24-55 Msc/stb. To develop the conventional Geneva ROZ, a 5-spot pattern flood was recommended. Smaller pattern sizes lead to more oil recovery and CO_2 storage but also require more wells and results in more water production. Therefore, it is necessary to weigh the increased costs of wells against oil production and CO_2 storage to determine the optimum pattern size.

The WAG option was not considered for Geneva ROZ due to less CO_2 injection replaced by water injection and correspondingly, less CO_2 storage. Sensitivity study on WAG simulation results and economics could be performed to determine if WAG is beneficial for co-optimizing oil recovery and CO_2 storage.

Geneva Aquifer

The Geneva aquifer could store CO_2 at 0.18 Mt/yr with one well every square mile. However, the thin, highly permeable Geneva aquifer results in rapid pressure buildup, so wells need to be spread far apart to avoid interaction.

Appendix 6-2

Table 6-A1. Carper ROZ performance at 12 years

Scenario	Case name	CO_2-EOR, Mstb	Gstore, Mt	RF, %	NUF, Mscf/stb	SF, Mscf/stb	Eco_2, %	HCPV injected	CB, tonne/stb
Low perm (0.2 mD) HnP in 40-ac spacing	Carper_40ac	43	48	2.2	21	0.5	8%	10	1.1
Low perm (0.2 mD) HnP in 80-ac spacing	Carper_80ac	25	32	1.3	24	0.3	5%	5	1.3
Med perm (2 mD) HnP in 80-ac spacing	CarperP50_80ac HnP	49	115	2.6	44	1.1	13%	9	2.3
Med perm (2 mD) 5-spot pattern flood in 80-ac spacing	CarperP50_80ac PF	99	195	5.2	37	1.9	24%	9	2.0
High perm (14 mD) 5-spot pattern flood in 80-ac spacing	CarperP90_80ac	696	492	37	13	4.9	59%	43	0.7

Table 6-A2. Geneva ROZ performance at 12 years

Scenario	Case name	CO_2-EOR, Mstb	Gstore, Mt	RF, %	NUF, Mscf/stb	SF, Mscf/stb	Eco_2, %	HCPV injected	CB, tonne/stb
5-spot pattern flood in 40-ac spacing	Geneva_40ac	440	656	27	28	7.6	69%	43	1.5
5-spot pattern flood in 80-ac spacing	Geneva_80ac	202	582	13	55	6.9	62%	20	2.9

6.2.3 Economic Analysis of Brownfield and Greenfield ROZ Development Strategies

Authors: Nathan Webb and Scott Frailey

Introduction

The overall objective of this research is to identify economic strategies to co-optimize CO_2-EOR and associated storage in stacked, primarily siliciclastic, greenfield ROZs or a combination of stacked ROZs and conventional oil reservoirs. Given this, it was necessary to conduct an economic evaluation of the greenfield and brownfield reservoir simulation cases to determine whether any, despite having positive EOR and/or associated storage metrics, can be developed economically. This section will evaluate the economics of individual cases. A broader techno-economic assessment of the greenfield and brownfield sites considering regional CO_2 point sources and transport options is presented in a later section. The methods and assumptions herein are derived and updated from Webb et al. (2019).

Economic metrics were estimated for CO_2-EOR and associated storage cases to identify plausible commercial development strategies for the greenfield and brownfield sites. The comparative economic metrics were the internal rate of return (IRR) and net present value at 20% discount rate (NPV20), payout time for capital expense (CapEx), project life, profit/investment ratio, and cumulative cash flow for each case. Economic life was defined as the year in which net revenue was zero. All other metrics were calculated for each case's economic life.

While numerous CO_2-EOR cases were simulated, a general economic scenario was required to define expenses and revenue. The major elements of this scenario are as follows:

- A major CO_2 pipeline exists, and a trunk line is required to connect the CO_2-EOR project to the pipeline.
- The size (and cost) of the CO_2 recycling facility is based on the projection of the annual CO_2 production. (The sizes are 28,320, 59,472, 295,944, and 594,720 m^3/day (1, 2.1, 10.45, and 21 MMscf/d) at a cost of $1.5, $2.1, $5.8, and $7.9MM, respectively) (McKaskle et al. 2017).
- Existing wells not in CO_2 injection patterns are plugged. All wells in patterns require workover for CO_2 service and annual well work. Wells are pumped and have an associated artificial lift cost.
- The CO_2-EOR project is deployed as a single phase for the entire field.

Methods and Assumptions

For both Greenfield and Brownfield sites, economic metrics were calculated from annual injection/production data (CO_2 injection; water, oil, and CO_2 production) derived from reservoir simulations. Many assumptions of future prices and expenses are required for CO_2-EOR economic analysis, and all are summarized in Table 6-30. Unless otherwise specified, well and surface equipment estimates are based on responses from ILB oilfield operators. Plugged wells may require monitoring or re-plugging in the future, but these costs were not considered in the analysis. Goods and administrative (G&A) costs were assumed 20% of capital and operational expenses. Illinois has no severance tax on oil production. All capital expenses were expensed at time zero; depreciation was not used. All economic analyses were compiled before federal income taxes (FIT).

Table 6-30. Economic assumptions used for CO_2-EOR economic analysis.

Economic Input	Assumptions	Cost	Units	Notes
Capital Expenses				
Drill and complete new vertical well	2,500 to 4,000 ft TD	$350,000	Per well	Large fracture stimulation could add $50,000.
Surface facilities		$100,000	Per well	tank battery primarily for oil and water. Generally equal to the number of CO_2 gathering systems
Workover/convert existing well		$25,000	Per well	Highly time dependent. Typical range is $5,000 to $15,000 for carbon steel. Using $25,000 assuming CO_2 resistant.
Plugging		$5,000	Per well	
CO_2 recycling facility	0.365 BSCF/yr 0.767 BSCF/yr 3.835 BSCF/yr 7.67 BSCF/yr	$1.5 MM $2.1 MM $5.8 MM $7.9 MM	Per facility	Facility size based on peak annual CO_2 production rate
CO_2 gathering systems		$250,000	Per facility	System of pipes/manifolds that collect wells production and deliver to the surface equipment and the CO_2 Recycling facility. Need 10-20 producing wells per gathering system.
Operational Expenses				
Production well		$12,000	Per well per year	Rule of thumb is $1,000 per month.
Injection well	Injecting @500 psi	$6,000	Per well per year	Would be higher for higher injection pressure.
Royalty		12.5%		Confirmed
Ad valorem Tax		0.5%		Confirmed
Lift		$0.48	Per bbl-fluid	
Revenue				
Oil		$66	Per bbl	Average calculated over 5 years from data on EIA website
CO_2	EOR	$60	Per ton	26 U.S. Code § 45Q
CO_2	Storage	$85	Per ton	26 U.S. Code § 45Q

Specific well, surface facility, and CO_2 gathering system counts for each scenario determined the capital and operational expenses.

Greenfield

Reservoir simulations of the greenfield site focused on three different scenarios:

- 40-acre spacing case in which the Geneva Dolomite undergoes pattern flooding with dedicated injection/production wells and the Carper Sandstone undergoes huff and puff in dedicated wells.
- 80-acre spacing case in which the Geneva Dolomite undergoes pattern flooding with dedicated injection/production wells and the Carper Sandstone (low perm) undergoes huff and puff in dedicated wells.
- 80-acre spacing case in which the Geneva Dolomite and the Carper Sandstone (medium and high perm) undergoes pattern flooding with dedicated injection/production wells which are shared between the two formations.

All scenarios required all new wells with no plugging of old wells given this is greenfield development.

Wells: For both cases, well locations of Carper and Geneva producers are shared; however, the Carper wells are undergoing huff and puff, so they are counted separately. For the 80-acre case with P90 Carper properties, the Carper can be flooded, so the wells are shared. The single Geneva aquifer injector is shared with one of the Geneva ROZ injectors. All wells are assumed to be new. Therefore:

- 40-acre case: 48 total new wells (16 Geneva ROZ/Aquifer Injectors, 16 Geneva ROZ producers, 16 carper Huff and Puff wells) + $800k for fracture stimulation of 16 Carper producing wells
- 80-acre case (Carper Huff and Puff): 24 total new wells (8 Geneva ROZ/Aquifer Injectors, 8 Geneva ROZ producers, 8 carper Huff and Puff wells) + $400k for fracture stimulation of 8 Carper producing wells
- 80-acre case (Carper pattern flood): 16 total new wells (8 Geneva ROZ/Aquifer / Carper Injectors, 8 Geneva ROZ / Carper producers) + $400k for fracture stimulation of 8 Carper producing wells

Surface facilities and CO_2 gathering systems: One of each was assumed for the 80-acre case given the small number (<20) of producing wells and two of each were assumed for the 40-acre case.

CO_2 recycling facility:

- 40-acre case has peak CO_2 production of 16.6Bscf/yr, which requires a capacity of 19.19 Bscf/yr at a cost of $21.6 million.
- 80-acre case (Carper Huff and Puff) has peak CO_2 production of 8.3 Bscf/yr, which requires a capacity of 8.44 Bscf/yr at a cost of $10.0 million.
- 80-acre case (Carper pattern flood) case has peak CO_2 production of 21.7 Bscf/yr, which requires a capacity of 23.01 Bscf/yr at a cost of $23.7 million.

Brownfield

Reservoir simulations of the brownfield site focused on two main scenarios in which the Cypress Sandstone and Ste. Genevieve limestone were co-developed:

- An All New Wells scenario in which all existing wells are plugged and all new wells are drilled.
- An All Existing Wells scenario in which existing wells are reworked and those not used in the pattern floods are plugged.

Wells: In the 360-acre pattern model, there are four injection and four production wells in the Cypress Sandstone and nine injection and nine production wells in the Ste. Genevieve Limestone. Four wells are shared between the two formations, giving a total well count of 34 wells. Noble Field has an average of 0.2 existing wells per acre. So, in any 360-acre area in the field, one might expect to find 72 existing wells. In the "All new wells" scenario, these are all plugged and new wells drilled. In the "All existing wells" scenario, 38 existing wells are plugged, and 34 existing wells are worked over/converted.

Surface facilities and CO_2 gathering systems: Given the well count, two of each were assumed.

CO_2 recycling facility: One facility is needed with a capacity of 3.835 BSCF/yr at a cost of $5.8 million.

Results

In comparison to the simulation results, which has CO_2-EOR performance metrics after 20 years of injection, the economic metrics are calculated over the economic life of each project. The resulting economic metrics are shown in Tables 6-31 through 6-36. The economic metrics are reported with CO_2 cost of $0 per ton (Tables 6-31 and 6-34), $(30) per ton (Tables 6-32 and 6-35), and $(60) per ton (Tables 6-33 and 6-36). The $(30) and $(60) per ton are revenues to the project resulting from realization of half and full amount, respectively, of the 45Q tax credit for CO_2 utilization for EOR, which are plausible scenarios depending on the nature of the business partnership between the field operator and the CO_2 supplier. The economic metrics for the Greenfield site also include a row showing the operation of a single injection well injecting into the Geneva aquifer. The CO_2 revenues for this case are presented at $0 (Table 6-31), $(42.5) (Table 6-32), and $(85) per ton (Table 6-33), reflecting the higher values of the 45Q tax credit in scenarios where saline storage is the primary fate of the CO_2.

For the Greenfield cases, the payout period for those that proved economic (NPV @20% > $0) varied from one to three years, while the economic life varied from two to twenty years (twenty years was the maximum value based on the period of CO_2-EOR simulations). Net revenue from oil production only (no inclusion of CO_2-storage-related revenue) varied from approx. $3.5 to $75 million. All cases could only yield positive IRR if at least $30 per ton revenue was generated.

For the Brownfield cases, the payout period for those that proved economic varied from one to six years, while the economic life varied from two to twenty years. Net revenue from oil production only (no inclusion of CO_2-storage-related revenue) varied from approx. $7 to $52 million. Several cases had adequate oil production to yield positive IRR with CO_2 at $0 per ton.

Table 6-31. Greenfield cases with CO_2 at $0.

	Net Revenue ($million)	Capital Investment ($million)	CO_2 Costs ($million)	Operating Costs ($million)	Cumulative Cash Flow ($million)	IRR (%)	NPV @ 20% ($million)	Payback Period ($million)	Project Length ($million)
40-acre EOR cases									
Carper (low perm) + Geneva ROZs	$32.79	$(49.08)	$(159.96)	$(15.86)	$(143.00)	<0	$(76.25)	N/A	20
80-acre EOR cases									
80-acre Carper (med perm) HNP only	$3.50	$(12.42)	$(35.28)	$(2.99)	$(34.80)	<0	$(19.26)	N/A	20
80-acre Carper (med perm) Pattern Flood only	$9.64	$(18.30)	$(36.91)	$(5.47)	$(32.70)	<0	$(24.09)	N/A	20
80-acre Carper (high perm) Pattern Flood only	$54.21	$(27.78)	$(147.26)	$(6.40)	$(99.50)	<0	$(48.57)	N/A	20
80-acre Geneva ROZ Only	$20.64	$(15.30)	$(61.35)	$(6.98)	$(47.70)	<0	$(24.23)	N/A	20
80-acre Geneva ROZ + Aquifer	$20.64	$(15.30)	$(61.35)	$(6.98)	$(47.70)	<0	$(24.23)	N/A	20
80-acre Carper (low Perm) + Geneva ROZs	$22.12	$(24.60)	$(74.06)	$(9.63)	$(61.60)	<0	$(36.44)	N/A	20
80-acre Carper (high perm) + Geneva ROZs	$74.65	$(37.26)	$(208.62)	$(9.93)	$(143.90)	<0	$(66.18)	N/A	20
80-acre saline storage only									
Single well Geneva aquifer only	$(0.01)	$(1.74)	$-	$(0.14)	$(0.20)	<0	$(1.78)	N/A	20

Table 6-32. Greenfield cases with CO_2 at $(30) per ton for EOR and $(42.5) per ton for saline storage which represents realization of 50% of the 45Q tax credit.

	Net Revenue ($million)	Capital Investment ($million)	CO_2 Costs ($million)	Operating Costs ($million)	Cumulative Cash Flow ($million)	IRR (%)	NPV @ 20% ($million)	Payback Period ($million)	Project Length ($million)
40-acre EOR cases									
Carper (low perm) + Geneva ROZs	$32.79	$(49.08)	$256.37	$(15.86)	$273.30	39.4%	$33.98	3	20
80-acre EOR cases									
80-acre Carper (med perm) HNP only	$0.62	$(12.42)	$(0.26)	$(0.45)	$(0.10)	<0	$(12.42)	N/A	2
80-acre Carper (med perm) Pattern Flood only	$0.48	$(18.30)	$0.97	$(1.20)	$0.20	<0	$(18.05)	N/A	3
80-acre Carper (high perm) Pattern Flood only	$54.21	$(27.78)	$(147.26)	$(6.40)	$(99.50)	<0	$(48.57)	N/A	20
80-acre Geneva ROZ Only	$1.65	$(15.30)	$9.81	$(3.06)	$8.40	<0	$(9.04)	N/A	4
80-acre Geneva ROZ + Aquifer	$20.64	$(15.30)	$351.98	$(6.98)	$365.60	149.7%	$82.26	1	20
80-acre Carper (low Perm) + Geneva ROZs	$22.12	$(24.60)	$340.16	$(9.63)	$352.70	90.6%	$70.72	2	20
80-acre Carper (high perm) + Geneva ROZs	$74.65	$(37.26)	$220.52	$(9.93)	$285.20	56.0%	$49.02	2	20
80-acre saline storage only									
Single well Geneva aquifer only	$(0.01)	$(1.74)	$558.50	$(0.14)	$558.30	1604.5%	$132.21	1	20

Table 6-33. Greenfield cases with CO_2 at $(60) per ton for EOR and $(85) per ton for saline storage which represents realization of 100% of the 45Q tax credit.

	Net Revenue ($million)	Capital Investment ($million)	CO2 Costs ($million)	Operating Costs ($million)	Cumulative Cash Flow ($million)	IRR (%)	NPV @ 20% ($million)	Payback Period ($million)	Project Length ($million)
40-acre EOR cases									
Carper (low perm) + Geneva ROZs	$32.79	$(49.08)	$672.70	$(15.86)	$689.60	100%	$144.21	1	20
80-acre EOR cases									
80-acre Carper (med perm) HNP only	$0.62	$(12.42)	$1.04	$(0.45)	$1.20	<0	$(11.39)	N/A	2
80-acre Carper (med perm) Pattern Flood only	$1.26	$(18.30)	$3.92	$(1.88)	$3.30	<0	$(15.93)	N/A	5
80-acre Carper (high perm) Pattern Flood only	$54.21	$(27.78)	$(147.26)	$(6.40)	$(99.50)	<0	$(48.57)	N/A	20
80-acre Geneva ROZ Only	$2.70	$(15.30)	$22.14	$(3.44)	$21.40	21%	$0.15	2	5
80-acre Geneva ROZ + Aquifer	$20.64	$(15.30)	$765.32	$(6.98)	$779.00	311%	$188.75	1	20
80-acre Carper (low Perm) + Geneva ROZs	$22.12	$(24.60)	$754.38	$(9.63)	$766.90	194%	$177.89	1	20
80-acre Carper (high perm) + Geneva ROZs	$74.65	$(37.26)	$649.65	$(9.93)	$714.40	136%	$164.22	1	20
80-acre saline storage only									
Single well Geneva aquifer only	$(0.01)	$(1.74)	$1,117.01	$(0.14)	$1,116.90	3209%	$270.19	1	20

Table 6-34. Brownfield cases with CO_2 at $0.

	Case #	Net Revenue ($million)	Capital Investment ($million)	CO_2 Costs ($million)	Operating Costs ($million)	Cumulative Cash Flow ($million)	IRR (%)	NPV @ 20% ($million)	Payback Period ($million)	Project Length ($million)
Baseline Cases										
IOR (Economic) Baseline	1	$6.96	$-	$-	$(9.66)	$(2.70)		$(0.57)		20
EOR Baseline	2	$18.06	$(0.78)	$-	$14.38	$3.70	37.5%	$0.54	3	20
Conventional EOR with Associated Storage (CEOR-AS)										
Cypress Sandstone only	3	$34.94	$(3.66)	$(0.02)	$(17.00)	$17.90	98.9%	$7.28	2	8
Ste. Genevieve Limestone only	4	$20.31	$(3.96)	$(3.05)	$(4.89)	$12.40	41.6%	$2.45	3	15
Cypress Sandstone and Ste. Genevieve Limestone	5	$39.97	$(4.20)	$(0.11)	$(20.05)	$19.80	42.2%	$4.20	4	11
Cypress Sandstone and Ste. Genevieve Limestone	6	$40.32	$(4.20)	$(0.11)	$(20.05)	$20.20	42.4%	$4.27	4	11
Advanced EOR with Associated Storage (AEOR-AS)										
Cypress Sandstone only	7	$22.80	$(4.38)	$(11.23)	$(3.66)	$7.90	10.5%	$(1.54)	6	16
Ste. Genevieve Limestone only	8	$12.36	$(4.68)	$(3.42)	$(1.78)	$7.20	22.5%	$0.20	2	6
Cypress Sandstone and Ste. Genevieve Limestone	9	$23.68	$(4.92)	$(8.47)	$(5.00)	$10.20	26.6%	$0.82	3	9
Cypress Sandstone and Ste. Genevieve Limestone	10	$27.25	$(4.92)	$(9.78)	$(5.47)	$12.00	35.1%	$1.84	2	10
Cypress Sandstone and Ste. Genevieve Limestone	11	$8.98	$(4.92)	$(1.06)	$(1.83)	$6.10	11.8%	$(0.61)	2	4
Advanced EOR with Maximum Storage (AEOR-MS)										
Cypress Sandstone (plus aquifer) and Ste. Genevieve Limestone	12	$30.62	$(4.92)	$(12.08)	$(5.88)	$12.60	34.4%	$1.92	3	11
Cypress Sandstone (plus aquifer) and Ste. Genevieve Limestone	13	$26.09	$(4.92)	$(10.31)	$(5.46)	$10.30	27.2%	$0.89	3	10

Table 6-35. Brownfield cases with CO_2 at $(30) per ton for EOR which represents realization of 50% of the 45Q tax credit.

	Case #	Net Revenue ($million)	Capital Investment ($million)	CO_2 Costs ($million)	Operating Costs ($million)	Cumulative Cash Flow ($million)	IRR (%)	NPV @ 20% ($million)	Payback Period ($million)	Project Length ($million)
Conventional EOR with Associated Storage (CEOR-AS)										
Cypress Sandstone only	3	$36.93	$(3.66)	$8.47	$(19.33)	$26.10	203.3%	$13.27	1	9
Ste. Genevieve Limestone only	4	$20.31	$(3.96)	$1.59	$(4.89)	$17.00	67.0%	$4.97	2	15
Cypress Sandstone & Ste. Genevieve Limestone	5	$39.97	$(4.20)	$7.46	$(20.05)	$27.40	63.5%	$8.11	3	11
Cypress Sandstone and Ste. Genevieve Limestone	6	$40.32	$(4.20)	$7.65	$(20.05)	$27.90	63.6%	$8.23	3	11
Advanced EOR with Associated Storage (AEOR-AS)										
Cypress Sandstone only	7	$27.67	$(4.38)	$10.81	$(4.23)	$34.30	89.2%	$10.59	2	20
Ste. Genevieve Limestone only	8	$12.36	$(4.68)	$1.39	$(1.78)	$12.00	61.2%	$3.45	2	6
Cypress Sandstone and Ste. Genevieve Limestone	9	$30.85	$(4.92)	$12.81	$(6.57)	$37.10	129.8%	$15.06	1	13
Cypress Sandstone and Ste. Genevieve Limestone	10	$32.47	$(4.92)	$10.57	$(6.64)	$36.40	126.2%	$14.43	1	13
Cypress Sandstone and Ste. Genevieve Limestone	11	$28.73	$(4.92)	$14.56	$(8.58)	$34.70	67.2%	$8.37	2	20
Advanced EOR with Maximum Storage (AEOR-MS)										
Cypress Sandstone (plus aquifer) and Ste. Genevieve Limestone	12	$51.74	$(4.92)	$(0.05)	$(9.29)	$42.40	135.6%	$16.25	1	20
Cypress Sandstone (plus aquifer) and Ste. Genevieve Limestone	13	$47.32	$(4.92)	$(0.03)	$(9.25)	$38.00	130.0%	$15.08	1	20

Table 6-36. Brownfield cases with CO_2 at $(60) per ton for EOR which represents realization of 100% of the 45Q tax credit.

	Case #	Net Revenue ($million)	Capital Investment ($million)	CO_2 Costs ($million)	Operating Costs ($million)	Cumulative Cash Flow ($million)	IRR (%)	NPV @ 20% ($million)	Payback Period ($million)	Project Length ($million)
Conventional EOR with Associated Storage (CEOR-AS)										
Cypress Sandstone only	3	$38.73	$(3.66)	$17.37	$(21.68)	$34.40	327.6%	$19.30	1	10
Ste. Genevieve Limestone only	4	$20.31	$(3.96)	$6.24	$(4.89)	$21.70	95.9%	$7.49	1	15
Cypress Sandstone and Ste. Genevieve Limestone	5	$39.97	$(4.20)	$15.04	$(20.05)	$35.00	85.5%	$12.01	2	11
Cypress Sandstone and Ste. Genevieve Limestone	6	$42.25	$(4.20)	$15.79	$(22.57)	$35.50	85.4%	$12.16	2	12
Advanced EOR with Associated Storage (AEOR-AS)										
Cypress Sandstone only	7	$27.67	$(4.38)	$37.53	$(4.23)	$61.00	173.3%	$22.74	1	20
Ste. Genevieve Limestone only	8	$13.01	$(4.68)	$5.77	$(2.00)	$16.80	99.7%	$6.69	1	7
Cypress Sandstone and Ste. Genevieve Limestone	9	$35.93	$(4.92)	$37.66	$(7.70)	$65.90	233.1%	$29.50	1	16
Cypress Sandstone and Ste. Genevieve Limestone	10	$37.27	$(4.92)	$32.73	$(7.77)	$62.20	216.5%	$27.16	1	15
Cypress Sandstone and Ste. Genevieve Limestone	11	$28.73	$(4.92)	$38.33	$(8.58)	$58.50	103.9%	$16.52	1	20
Advanced EOR with Maximum Storage (AEOR-MS)										
Cypress Sandstone (plus aquifer) and Ste. Genevieve Limestone	12	$51.74	$(4.92)	$29.09	$(9.29)	$71.50	238.9%	$30.59	1	20
Cypress Sandstone (plus aquifer) and Ste. Genevieve Limestone	13	$47.32	$(4.92)	$29.13	$(9.25)	$67.20	233.3%	$29.42	1	20

Discussion

For the Greenfield site, because the setting requires all new wells, capital investment is generally an order of magnitude higher than the Brownfield site. As a result, none of the cases with CO_2 at $0 generate adequate revenue to make NPV @20% positive. The 80-acre Carper Sandstone huff and puff cases had the lowest capital and operating expenses due to fewer new wells being drilled and far less recycled CO_2. The case with the highest net revenue includes co-development of the (high perm) Carper Sandstone and the Geneva Dolomite due to the increased oil production from the former. However, the highest NPV @20% was the case in which the Geneva Dolomite ROZ + aquifer is developed on its own due to the increased CO_2 storage.

An alternative scenario at the Greenfield site is to use a single well to inject CO_2 into the saline aquifer in the Geneva Dolomite. The cost of the surface infrastructure (e.g., only one well to drill, no need for CO_2 recycling facility, etc.) is greatly reduced in this case. As a result, IRR exceeds 3,200% and NPV @20% is greater than $270 million, which is $80 to $100 million more than the most optimistic EOR cases.

For the Brownfield site, the ability to reuse (and plug) existing wells results in significantly reduced capital costs when compared to the Greenfield site. Net Revenue and NPV @20% metrics converge on Case 12, which includes co-development of the Cypress MPZ and ROZ with the Ste. Genevieve MPZ plus CO_2 storage within the Cypress Sandstone saline aquifer. The range of NPV @20% values among the different cases for the Brownfield site were generally narrower an order of magnitude lower than those of the Greenfield site with CO_2 at $(30) and $(60).

No single case tops all economic metrics. In this analysis, there are no solutions, only tradeoffs as selection of a development strategy based on economic criteria will be specific to the business strategy of an individual company. For example, payout or time to return capital investment may be more important to one company compared to the IRR for another. The Brownfield site generally offers lower economic risk because existing infrastructure results in lower capital investment. However, the presence of numerous legacy wellbores presents a different kind of risk in that improperly plugged wells may present leakage pathways for CO_2. Many of the Brownfield cases also are shorter lived as CO_2 recycling costs increase over time while the revenue generated from bringing in new CO_2 declines. Conversely, the Greenfield site requires greater capital investment, but the lack of legacy well penetrations and all new wells may be more attractive for operators adverse to dealing with legacy wellbore issues.

(Disclaimer: This economic analysis is intended to provide a comparison of economic metrics for different CO_2-EOR development strategies. Although representative of specific development scenarios, it is not intended to be used to make a specific commercial decision, since economic generalizations were made.)

6.3 Life Cycle Analysis of Brownfield and Greenfield Developments with Potential ILB CO_2 Sources

Authors: Easha Vivesh and Fang Yang

Introduction

Life Cycle Analysis (LCA) is a systematic approach for assessing the environmental effects of a technology, process, or product over the course of its full life cycle. When it comes to CO_2 Enhanced Oil Recovery (EOR) and associated storage, LCA is a useful method for evaluating the environmental impacts of various Carbon Capture Utilization and Storage (CCUS) strategies.

This study focuses on the CO_2 EOR and storage operations and evaluated the environmental impacts in terms of greenhouse gas (GHG) emissions for both brownfield and greenfield ROZ stacked reservoir complexes. First, the system boundary was defined based on project needs. Next, evaluation methods were selected based on suitability, and input data were collected from simulation results and assumptions based on literature. The LCA was then performed, and the results were analysed and compared. Last, conclusions were drawn to summarize the environmental impacts of developing brownfield and greenfield stacked reservoir complexes.

System Boundary

A CO_2 EOR and storage system has three components that generate GHG emissions, including upstream, gate-to-gate, and downstream. The upstream component covers the source of CO_2, which includes emissions associated with the capture, separation, purification, compression, and pipeline transport of CO_2 to a storage site. The gate-to-gate component is the CO_2 EOR and storage operations, including CO_2 injection, oil production, fluid separation, and CO_2 recycling. The downstream components may include crude oil pipeline transport, oil refining, transport to point of sale, and combustion of fuel products (Sminchak et al., 2020).

This study focuses on the gate-to-gate component as shown in Figure 6-66. It involves injecting CO_2 into oil reservoirs or saline aquifers and producing oil, water, and gas. The produced oil goes to an oil refinery, which is outside the gate-to-gate system boundary. The produced water can be stored to be used for water-alternating-gas injection or disposed. The produced CO_2 is recycled for EOR and storage. The produced natural gas is assumed to be negligible in this study.

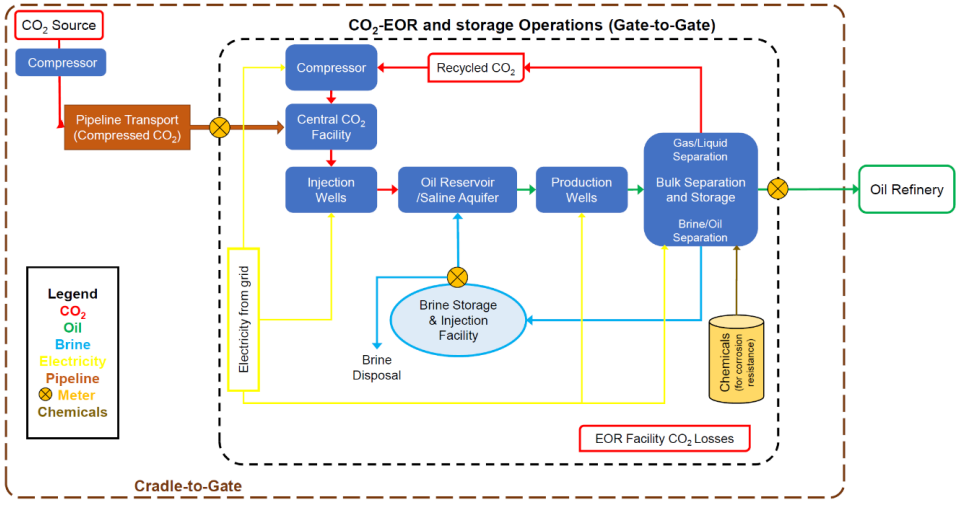


Figure 6-66. System boundary diagram illustrating cradle-to-gate and gate-to-gate components for a CO_2 EOR and storage system.

Methods and Inputs

Methods

The OpenLCA software is used for LCA in this study. It is an open-source software for Sustainability and Life Cycle Assessment created by GreenDelta. It offers a user-friendly interface and identifies main drivers throughout the life cycle by process, flow, and impact categories. It also connects to various well-established databases.

The general structure of OpenLCA includes project, product system, processes, and flows. A case is a project that consists of various product systems, which are process networks and connect processes with their respective flows. Flows are where inputs and outputs are defined for a given unit process. An input in flow can be selected from existing database by setting the category, and the source can be a provider in the database.

In this study, the CO_2 EOR and storage operations are represented by processes. Each process, such as CO_2 injection, oil production, and CO_2 storage, corresponds to a particular operation within the system being evaluated. The materials, energy, emissions connected to a particular process are represented as flows.

The TRACI 2.1 method is used for impact assessment as recommended by National Energy Technology Laboratory (NETL). The main environmental impact considered is the 100-year time horizon global warming potential (GWP), a measure of CO_2 mass emitted into the atmosphere during CO_2 EOR and storage.

The 'Current U.S. grid mix -US' was selected as electricity provider for assessing GWP from electricity usage. As there is no existing land use database in OpenLCA, a land use CO_2 emission factor of 8.12 Kg CO_2 eq/acre/year was used for assessing GWP from land use based on a reference CO_2 EOR LCA (Sminchak et al., 2020).

To gain a general understanding of how the gate-to-gate emissions compare to cradle-to-gate emissions, the volume of CO_2 used for each scenario was used to estimate the GWP of the upstream component. The 'Supercritical Pulverized Coal (SCPC) Power Plant, capture, cradle-to-gate – US' was assumed to be the CO_2 source for impact assessment.

Inputs

The main inputs in the gate-to-gate system considered are electricity and land use, which are controlled by field operations and well footprint, respectively. Input parameters for electricity and land use were derived from brownfield and greenfield simulation results and assumptions based on previously developed site-specific reservoir models (Sminchak et al., 2020).

Reservoir simulations tested various development strategies at greenfield and brownfield ROZ field sites to identify injection/production schemes that could be used to co-optimize CO_2 EOR and associated storage. Simulations were run for 12 and 20 years and reported the amount of CO_2 that would be injected, how much CO_2, oil, and water would be produced, and how many wells would be required.

Two development strategies were considered for the Brownfield ROZ site: Comingled (Case 9 in brownfield simulation report), in which all oil-bearing formations in the project area were targeted at the same time, and Separate (Case 10 in brownfield simulation report), in which each formation was targeted individually.

Three development strategies were considered for the Greenfield ROZ site: 40-acre (Case 40ac), 80-acre (Case 80ac), and an 80-acre high permeability (Case 80acP90), in which a higher permeability was used for one of the target formations (the Carper Sandstone).

Scaling factors were used to apply the results from the site-specific models to the estimated extent of the brownfield and greenfield stacked reservoirs. A scaling factor of 12 was applied to brownfield pattern model results to cover the approximate size of Noble Oil Field (6.75 mi^2). The Greenfield ROZ is believed

to cover a much larger regional extent, and a scaling factor of 41 based on CO_2 source availability from the SimCCS work was applied to greenfield pattern model results to cover 41 mi^2.

Table 6-37 lists LCA input data for both brownfield and greenfield.

Table 6-37. LCA input data for both brownfield and greenfield.

Field	Injection scheme	Time (year)	Reservoir Simulation Results				LCA inputs		
			CO_2 injection (Mt)	CO_2 production (Mt)	Oil production (Mstb)	Number of wells	CO_2 storage (Mt)	Electricity (kwh)	Land use (acre)
Brownfield	Comingled	12	28	16	6,996	312	11	1.15E+07	624
		20	47	35	10,224	312	12	2.42E+07	624
	Separate	12	26	16	7,344	312	10	1.10E+07	624
		20	44	33	10,428	312	11	2.31E+07	624
Greenfield	40-acre	12	484	368	19,833	656	116	2.57E+08	2624
		20	826	654	24,830	656	172	4.58E+08	2624
	80-acre	12	507	160	9,322	328	347	1.12E+08	1312
		20	867	303	16,427	328	564	2.12E+08	1312
	80-acre High Perm	12	845	479	36,821	328	366	3.35E+08	1312
		20	1,437	853	54,689	328	585	5.97E+08	1312

The first four columns are direct simulation results after applying scaling factors (12 for the brownfield site and 41 for the greenfield site). The remaining three columns are the LCA inputs calculated based on simulation results. The CO_2 storage was the difference between CO_2 injection and production. The electricity usage was estimated using 0.7 kwh/tonne of recycled CO_2 based on a reference CO_2 EOR operation (Sminchak et al., 2020). Recycled CO_2 was assumed to be equal to the produced CO_2 from reservoir simulation. The land use was estimated based on the number of wells used, assuming each well and associated facility occupies two acres of land.

LCA Results

This work focuses on GHG emissions associated with oil production and CO_2 storage. The GHG emissions are expressed in units of CO_2 mass equivalents (kg CO_2eq). The CO_2 emission factor is CO_2 emission per incremental oil produced in kg CO_2eq/stb.

Brownfield LCA Results

Gate-to-Gate GWP is dominated by electricity. The GWP generated by electricity was two orders of magnitude higher than the GWP from land use (Figure 6-67 and Table 6-38). Figure 6-68 shows the gate-to-gate GWP associated with the development strategies evaluated for the brownfield. For the two cases selected, the emission factors were 9-10 kgCO_2 eq/stb at 12 years and 13-14 kgCO_2 eq/stb at 20 years. The commingled injection yielded slightly higher emission factors than separate injection, but duration was much more of a factor than development strategy. However, the gate-to-gate GWP was dwarfed by the upstream emissions, which were two to three orders of magnitude higher than the gate-to-gate emissions (Table 6-38).

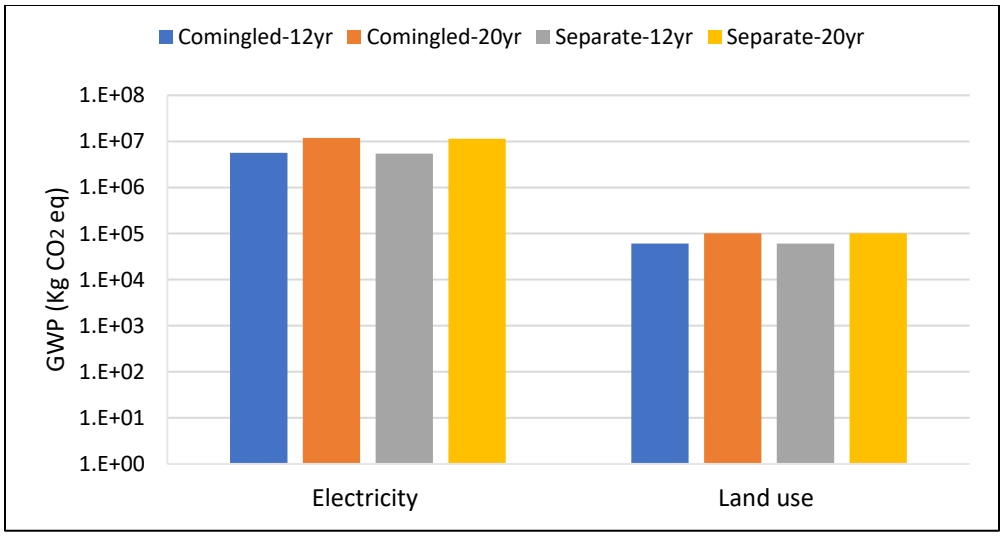


Figure 6-67. Global warming potential (GWP) of the Brownfield by electricity and land use. The GWP attributed to electricity is about two orders of magnitude greater than the GWP associated with land use.

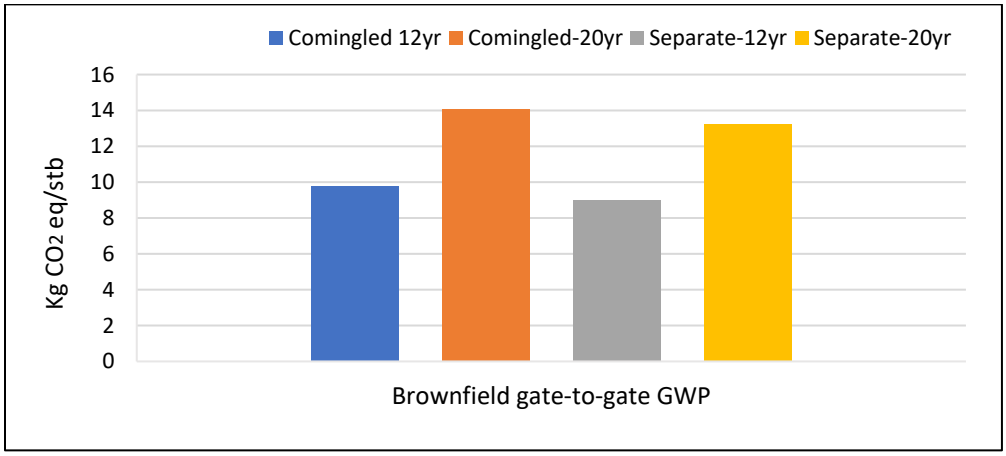


Figure 6-68. Global Warming Potential (GWP) of two development strategies after 12 and 20 years of operations.

Table 6-38. Brownfield LCA results.

Field	Injection scheme	Time (year)	Global warming potential (kg CO_2)			
			Electricity	Land use	Gate-to-Gate	Upstream CO_2 capture
Brownfield	Comingled	12	5.65E+06	60,803	5.72E+06	3.32E+09
		20	1.19E+07	101,338	1.20E+07	3.59E+09
	Separate	12	5.44E+06	60,803	5.50E+06	2.98E+09
		20	1.14E+07	101,338	1.15E+07	3.26E+09

Greenfield LCA Results

As with the Brownfield ROZ site, the Gate-to-Gate GWP at the Greenfield ROZ site was dominated by electricity (Figure 6-69 and Table 6-39). Figure 6-70 shows the gate-to-gate GWP associated with the development strategies evaluated for the Greenfield ROZ. The emission factors were 4.5-6.4 $kgCO_2$ eq/stb at 12 years and 5.4-9.1 $kgCO_2$ eq/stb at 20 years. The injection in 80-acre pattern yielded lower emission factors than the injection in 40-acre pattern. The high permeability case had lower emission factors than the low permeability case. However, the Cradle-to-Gate GWP was significantly greater than the Gate-to-Gate GWP.

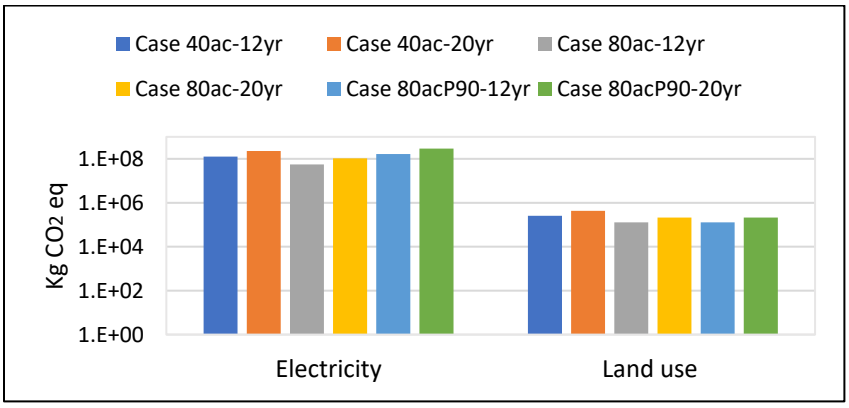


Figure 6-69. Global warming potential of greenfield by electricity and land use.

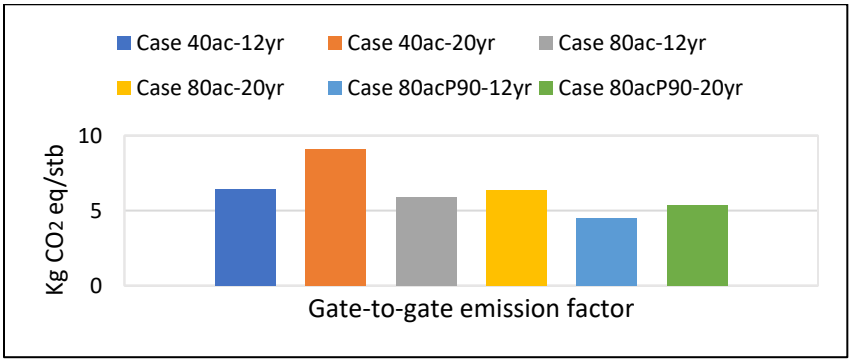


Figure 6-70. Gate-to-gate emission factor of greenfield CO_2 EOR and storage.

Table 6-39. Greenfield LCA results

Field	Injection scheme	Time (year)	Global warming potential (kg CO_2)			
			Electricity	Land use	Gate-to-Gate	Upstream CO_2 capture
Greenfield	40-acre	12	1.27E+08	2.56E+05	1.27E+08	3.47E+10
		20	2.25E+08	4.26E+05	2.26E+08	5.14E+10
	80-acre	12	5.51E+07	1.28E+05	5.52E+07	1.04E+11
		20	1.04E+08	2.13E+05	1.05E+08	1.69E+11
	80-acre High Perm	12	1.65E+08	1.28E+05	1.65E+08	1.09E+11
		20	2.94E+08	2.13E+05	2.94E+08	1.75E+11

Figure 6-71 shows gate-to-gate emission factors associated with CO_2 EOR and storage operations at the greenfield ROZ site. The emission factors were 4.5-6.4 $kgCO_2$ eq/stb at 12 years and 5.4-9.1 $kgCO_2$ eq/stb at 20 years. The injection in 80-acre pattern yielded lower emission factors than the injection in 40-acre pattern. The high permeability case had lower emission factors than the low permeability case.

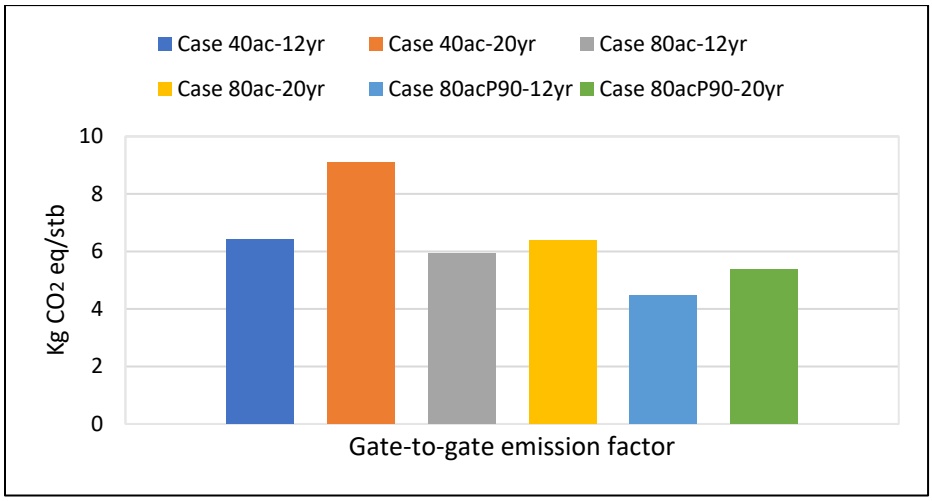


Figure 6-71. Gate-to-gate emission factor of greenfield CO_2 EOR and storage.

Similar to the brownfield ROZ site, electricity is the dominating factor contributing to the gate-to-gate emission. The GWP generated by electricity was two to three orders of magnitude higher than the GWP from land use (Figure 6-72).

Compared to upstream CO_2 capture, electricity plays a much less significant role in GHG emissions. The cradle-to-gate emissions were two to three orders of magnitude higher than the gate-to-gate emissions (Table 6-38).

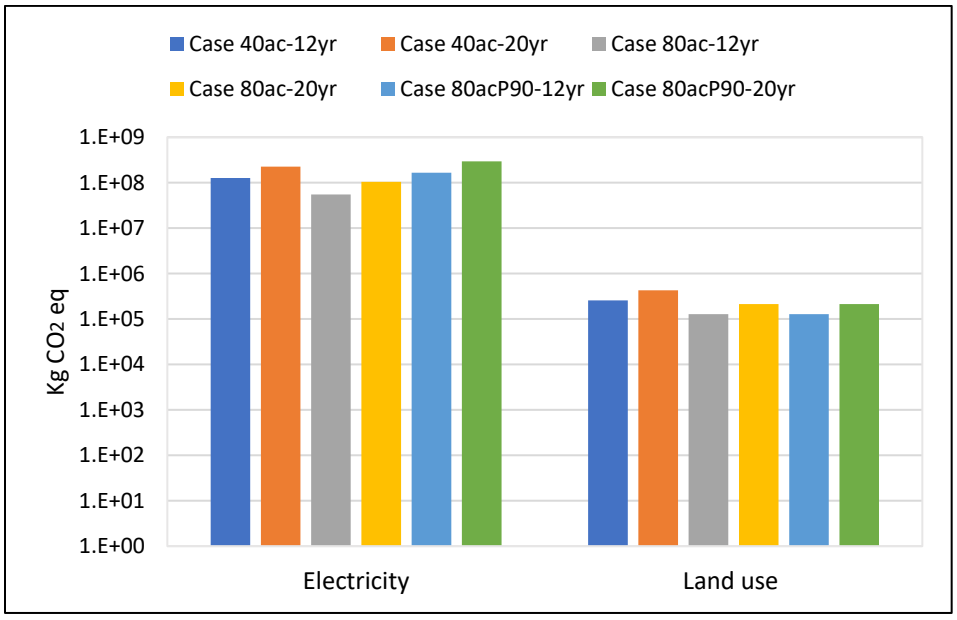


Figure 6-72. Global warming potential of greenfield CO_2 EOR and storage by electricity and land use.

Comparison

A previous study (Azzolina et al., 2017) suggested that the gate-to-gate emission factors are driven by net CO_2 utilization factors, and there is a linear relationship between the two factors based on cases with oil recovery factors between 5 and 20% and net CO_2 utilization factors between 5 to 20 Mscf/stb, which was representative of most CO_2 EOR sites, as shown in blue in Figure 6-73.

To evaluate the LCA results in this study, the gate-to-gate emission factors and net CO_2 utilization factors were calculated for both greenfield and brownfield. These data were plotted for each case and compared to the trend reported by Azzolina et al., (2017) (Figure 6-73).

Overall, the gate-to-gate emission factors in this study ranged from 4-14 $kgCO_2$ eq/stb, and the net CO_2 utilization factor ranged from 16-31 Mscf/stb (except one outlier). No linear relationship was observed between the two factors; however, they generally follow the trend. A correlation between the two factors may be developed with more data points plotted considering a large range of recovery factors and net CO_2 utilization factors.

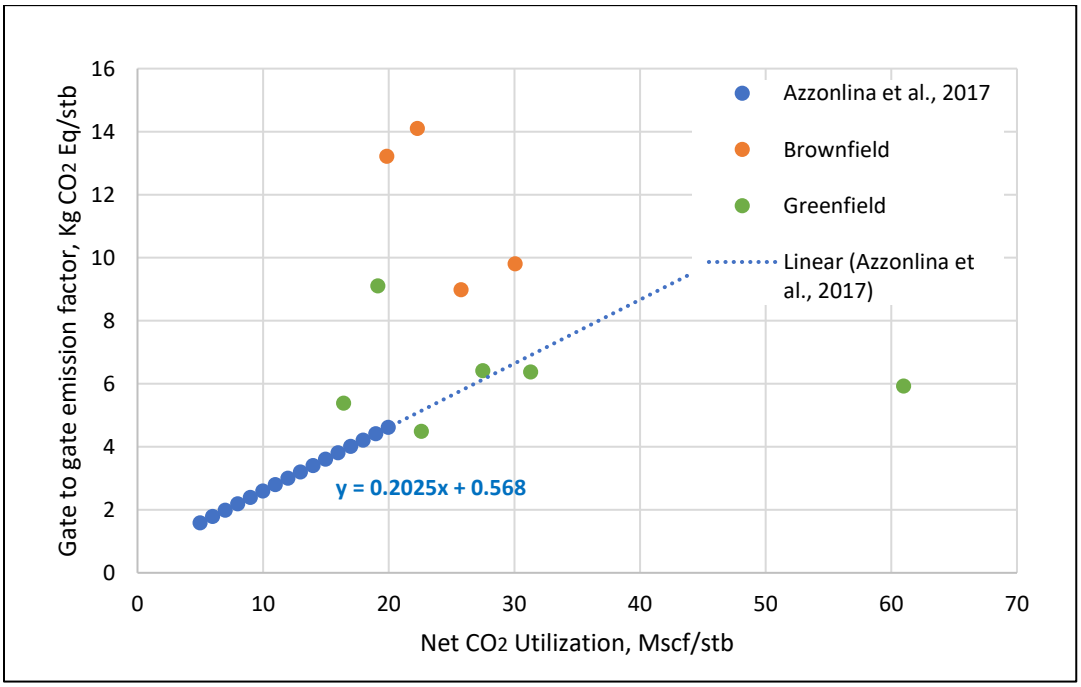


Figure 6-73. Gate-to-gate emission factor in relation to net CO_2 utilization factor.

Conclusions

The gate-to-gate emission factors were 9-14 $kgCO_2$ eq/stb for brownfield and 4-9 $kgCO_2$ eq/stb for greenfield. The two contributing factors were electricity and land use, and electricity is the dominating factor that generated 99% of the gate-to-gate emissions. However, the gate-to-gate emissions were found to be negligible compared to the cradle-to-gate emissions.

These findings suggest that the choice of development strategies evaluated here had only a negligible impact on GWP and upstream operations should be the focus of understanding a projects GWP.

6.4 CO_2 Storage and EOR Resource Assessment of Selected ILB ROZ Fairways

Authors: Nathan Webb, Nathan Grigsby, and Scott Frailey

A manuscript titled “Origin, distribution, and CO2 EOR and CO2 storage resource assessment of selected Residual Oil Zone Fairways in the Illinois Basin” was submitted to the journal Geoenergy Science and Engineering on October 26, 2023. What follows is a summary of that manuscript.

Introduction

In the Illinois Basin (ILB) exploratory analyses are required to recognize the existence of an ROZ. The methodology developed by Trentham and Melzer (2016) to explore for ROZs provides a useful framework for leveraging existing data (e.g., records from drilling, mud logging, drill stem testing, core analysis, well completions) to identify ROZs. While this approach is useful for mapping the extent of the ROZ fairway, characterization with specific consideration of the geologic setting is required to define the area, thickness, and oil saturation of ROZ prospects within the fairway. By defining ROZ prospects and characterizing their properties, CO_2-EOR and associated storage resource can be determined.

The aim of this study is to establish the existence of ROZs within the four formations identified by screening. ROZ fairway maps were developed for each formation based on regional geologic characterization results and assessment of well records. Nearly 50 ROZ prospects were defined within the fairways based on ROZ indicators and characterized using well log analysis. The resulting ROZ fairways and prospects were analyzed to create estimates of CO_2-EOR and associated CO_2 storage resources. Finally, the geologic history of the ILB was considered in the context of the mapped ROZ fairways and prospects to classify the ROZs and better understand the mechanisms that formed and controlled their distribution in the ILB.

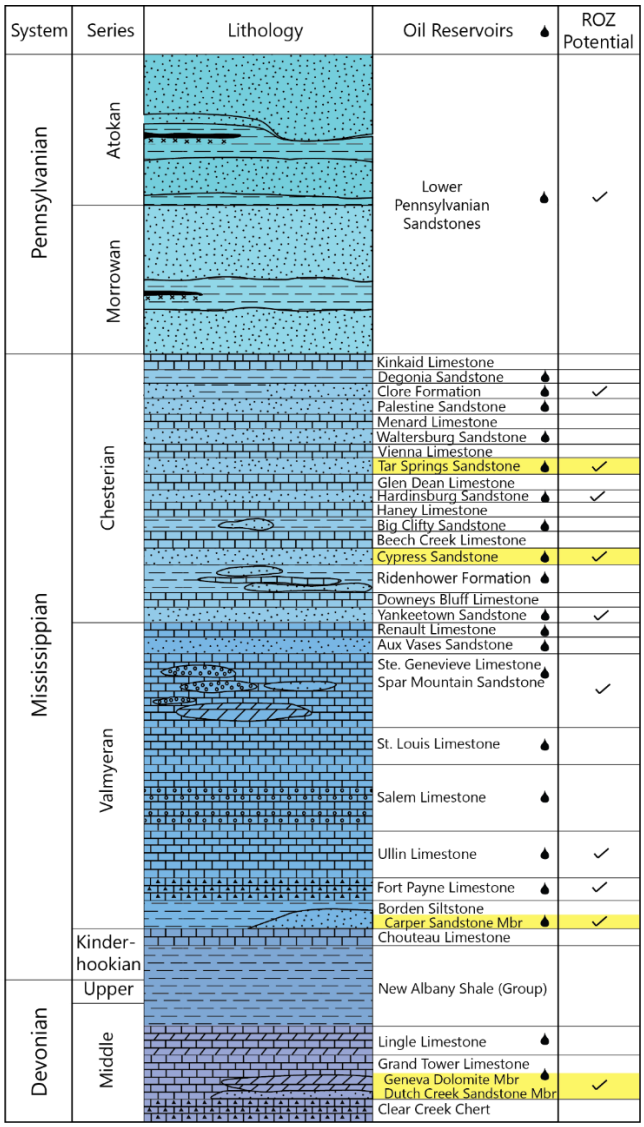


Figure 6-74. Generalized stratigraphic column of the upper Paleozoic succession in the Illinois Basin. Oil reservoirs are denoted by the black oil drop. Formations with potential for ROZ development have a checkmark. Those formations included in this study are highlighted in yellow.

Illinois Basin Petroleum System

The ILB is a Paleozoic sedimentary basin that hosts a petroleum system, which produced more than 4 billion barrels of oil since the early 20th century. The New Albany Shale is considered the primary source rock for the ILB petroleum system (Barrows and Cluff, 1984). Geochemical biomarkers have unequivocally linked oil produced from most ILB reservoirs to the New Albany Shale (Hatch et al., 1991). Oil generation in the New Albany Shale mostly occurred between 300 and 150 Ma (Pennsylvanian to Jurassic), coincident with the development of many geologic structures (e.g., LaSalle Anticlinorium) in the basin (Cluff and Byrnes, 1991).

Within a petroleum system, primary migration is any movement of petroleum within the fine-grained source rock, whereas secondary migration is the process by which oil migrates outside of the source rock to the trap generally as a separate, immiscible phase through water-saturated rock (England, 1994; Hunt

1995). Tertiary migration occurs when petroleum moves from one trap to another or to a seep (Hunt, 1995; Peters et al., 2012). Three parameters control secondary and tertiary migration (Tissot and Welte, 1984):

1. vertical buoyancy force due to the lower density of petroleum compared to the water,
2. capillary pressure that influences multiphase flow and counteracts buoyant forces,
3. lateral hydrodynamic flow related to tectonic uplift within the basin.

Oil migrates vertically and laterally through faults and open fractures and carrier beds until it accumulates within a trap formed by structure, stratigraphy, or faults. Carrier beds are migration pathways that link source rocks with reservoirs in conventional petroleum plays (Tissot and Welte, 1984).

In the ILB, buoyant forces are the primary driver of secondary migration as 66% of oil production occurs in reservoirs located above the oil generating part of New Albany Shale (Abrams, 1995; Lewan et al., 2002). However, a component of northward hydrodynamic flow has been suggested because the distribution of petroleum production extends considerably to the north beyond the area where source beds have generated oil (Bethke et al., 1991). This northward hydrodynamic flow is attributed to structural deformation and closing of the southern margin of the ILB via uplift of the Pascola Arch in the Bootheel region of Missouri (Figure 6-75) from late Paleozoic to Mesozoic time which created a hydrostatic head to drive groundwater flow to the north (Bethke et al., 1991).

Ultimately, oil that underwent secondary migration either:

1. accumulated in porous reservoirs within structural and/or stratigraphic traps that either exist today as accountable oil in place or were removed by erosion over geologic time, or
2. remained as residual oil in carrier beds, or
3. escaped to the atmosphere.

The modern distribution of oil reservoirs in the ILB can be interpreted to infer the migration pathways from the oil generating part of the New Albany Shale (Figure 6-75). The most intense oil generation from the New Albany Shale occurred in far southeastern Illinois centered over Saline, Gallatin, Hardin, and Pope Counties (Figure 6-75). The intense generation in this area and the pattern of lesser generation radiating outward has been interpreted to reflect the basin structure at the time of petroleum generation (Lewan et al., 2002). It corresponds closely with the thickest deposits of New Albany Shale slightly farther to the east along the border of Hardin County, Illinois, and Union/Crittenden Counties in Kentucky (Bergstrom et al., 1980). The area of most intense generation also corresponds with an area of active vulcanism during the Permian (within the window of oil generation) associated with Hicks Dome in Hardin County, Illinois.

Oil generated by the New Albany Shale in southern Illinois migrated most readily vertically along major fault systems, and faults and inferred fractures associated with major folds within the ILB (Figure 6-75). The fault systems include:

1. Cottage Grove Fault System. The Cottage Grove Fault System consists of a 113 km (70 mi) long, slightly north of west trending, master strike-slip fault with associated en echelon flanking faults and a belt of anticlines, with faulting occurring from Late Pennsylvanian to pre-Early Permian (Nelson, 1995).
2. Wabash Valley Fault system. The Wabash Valley Fault System consists of a series of north-northeast trending normal faults extending about 88 km (55 mi) long and up to 48 km (30 mi) wide with faulting occurring post-Late Pennsylvanian (Nelson, 1995).
3. Fluorspar Area Fault Complex. The Fluorspar Area Fault Complex is a complexly faulted area associated with the Illinois-Kentucky Fluorspar District that consists of structural elements

including the early Permian-age Hicks Dome (a cryptovolcanic feature with associated ultramafic dikes, stocks, and diatremes, and radial and concentric faults), northeast-trending fault blocks, and northwest trending strike-slip faults (Nelson 1995).

Major folds associated with deep-seated faults and inferred fractures include (Figure 6-75):

1. Clay City Anticline
2. Iola Anticline
3. LaSalle Anticlinorium
4. Loudon Anticline
5. Salem Anticline

The major folds are generally thought to be associated with Phanerozoic reactivation of fault and fold zones began as Proterozoic-Eocambrian normal faults (Marshak and Paulsen, 1996). Some folds have relatively steeply dipping beds and associated faulting and offset of Paleozoic strata (e.g., LaSalle Anticlinorium, flanked by the steeply westward-dipping Charleston Monocline), while others have more gentile dips without associated faulting in the Paleozoic section (e.g., Clay City Anticline). In the latter cases, fracturing associated with deformation of the anticlines is likely (and has been observed in core). These fault systems and folds with associated faults and fractures provided vertical conduits for oil to buoyantly migrate through several hundred meters of intervening tight mudstones and limestones, that would otherwise serve as an aquitard, into porous reservoirs within middle and upper Mississippian and lower Pennsylvanian strata. This results in ILB oilfields with multiple stacked oil saturated zones, many of which of commercial oil production.

Certain formations, such as the Cypress Sandstone and Tar Springs Sandstone have thick deposits of porous and permeable sandstone that have intraformational hydraulic connectivity at regional scales, allowing oil to migrate updip by buoyancy or be driven laterally by a hydrodynamic gradient resulting in residual losses due to both migration and the development of ROZs.

In the interior of the ILB where faults and major anticlines do not exist (e.g., the border between Hamilton, Jefferson, and Wayne County), oil accumulations develop in some of the deeper reservoirs and did not migrate into the stratigraphically younger formations.

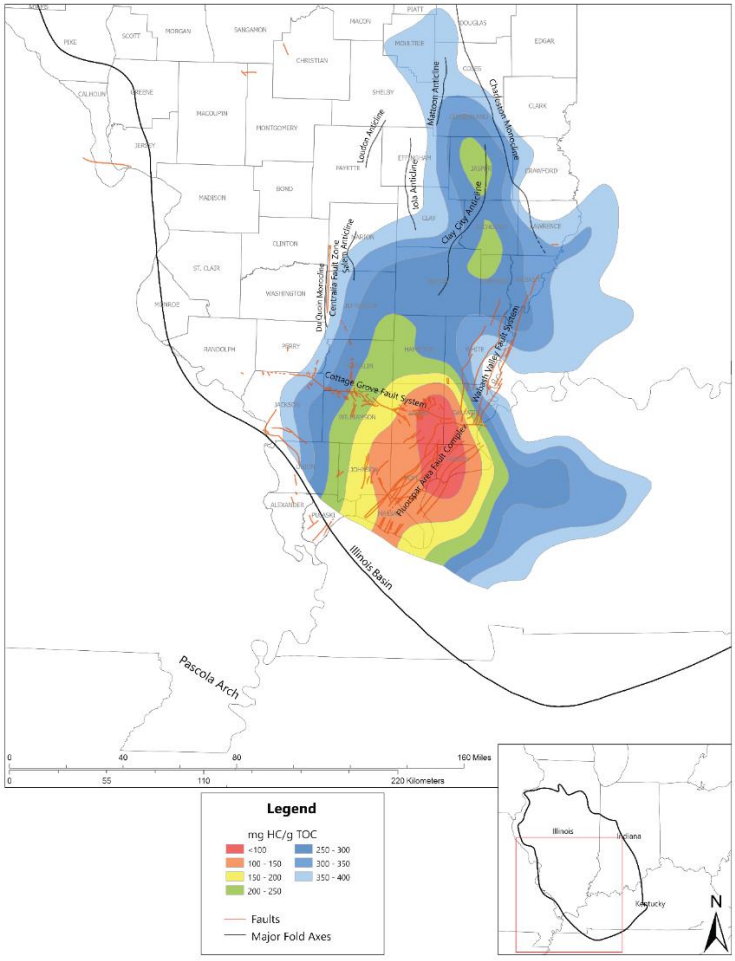


Figure 6-75. Contoured HI map of mature (> 400 mg HC/g TOC) New Albany Shale (NAS) source rock (TOC > 2.5 wt. %). Major structures (fault systems, anticlines) in southern Illinois are labeled, as is the Pascola Arch to the south. Orange lines are faults. Black lines are the axes of major folds. The outline of the Illinois Basin is shown with a thick black line. This map shows the areas of oil generation as well as vertical migration pathways (faults) and areas where major structural traps formed (folds). Contoured HI map derived from Lewan et al., 2002.

The ROZ-bearing formations being investigated here are stratigraphically both above and below the New Albany Shale (Figure 6-74). The Middle Devonian rocks are stratigraphically below the New Albany Shale but are generally structurally higher than the oil generating part of the New Albany Shale where they are productive. The Carper Sandstone is, in much of the Basin, the first porous formation that occurs above the New Albany Shale. The Cypress and Tar Springs Sandstones are overlying and separated from the New Albany Shale by more than one thousand feet of intervening strata, including hundreds of feet of mudstones of the Borden Siltstone and generally tight middle Mississippian limestones. Because of the significant thickness of impermeable rock that separates the Cypress Sandstone (the most prolific oil reservoir in the ILB) from the New Albany Shale, and the fact that oil is present in porous lenses within otherwise impermeable limestone (e.g., Ste Genevieve Limestone) or shale (e.g., Cypress Sandstone), fractures and faults have long been invoked as the most plausible pathway for oil to follow into these formations (Swann and Bell, 1958; Lewan, 1995). However, it is now understood that even relatively tight formations can act as carrier beds, as permeability of the rock and viscosity of the migrating petroleum do not limit migration at geologic time scales (Pepper, 2016).

ROZs originated within reservoirs in which oil has accumulated and was later displaced over geologic time, either by natural brine migration or by tectonic tilting or faulting. Studies have focused on the mechanisms of forming ROZs and localized ROZ indicators, but by understanding the regional consequences of ROZ formation, additional criteria emerged for ROZ identification. For example, if the Cypress Sandstone contains an ROZ, the thickness and areal extent of the sandstone across the basin implies huge fluid flux. Thus, a regional ROZ has broad implications for the Basin, raising questions as to where the displaced oil went and from where the invading water was sourced.

Melzer (2006) previously defined three types of ROZ (Figure 6-76) based on their formative mechanism. The three types include: Type 1. Regional tilt of a basin; Type 2. Breach of the reservoir seal with secondary healing, and; Type 3. Changed hydrodynamic conditions within the underlying aquifer.

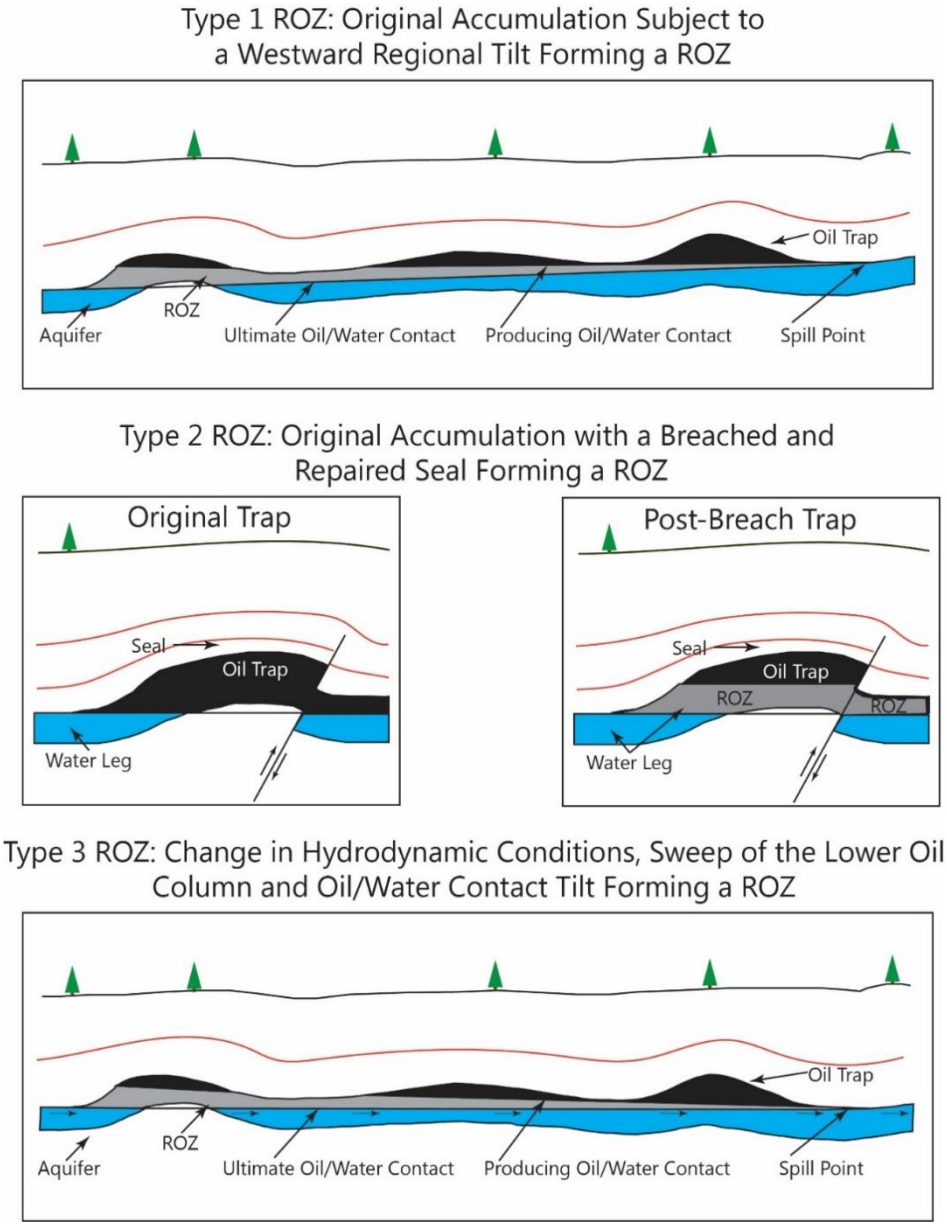


Figure 6-76. Three types of ROZs as defined by their formative mechanism. Modified from Melzer (2006).

Methods

ROZ Fairways and Prospects

Identifying and characterizing ROZ fairways and prospects follows a standardized workflow (Figure 6-77) adapted from Trentham and Melzer (2016).

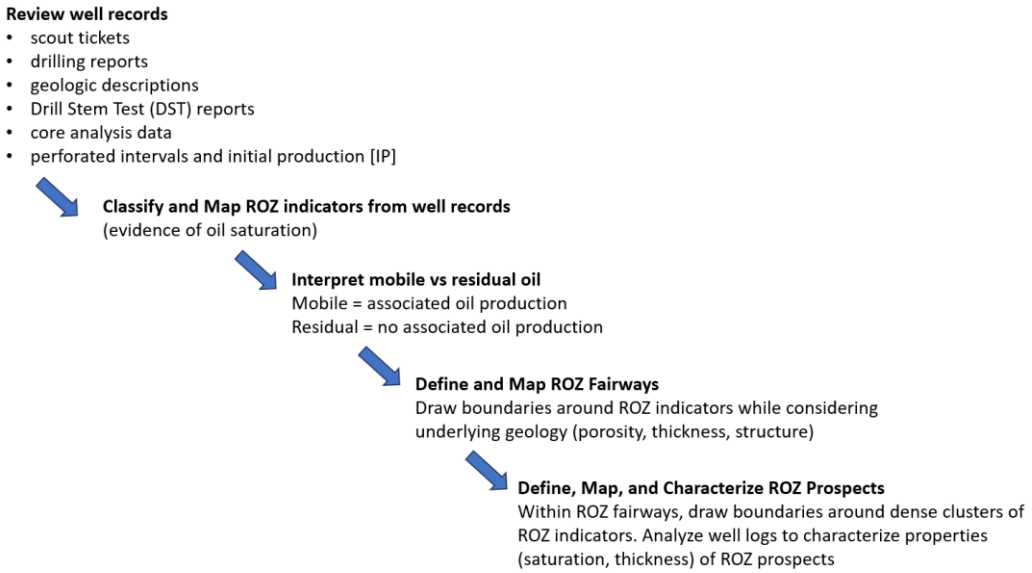


Figure 6-77. Workflow for identifying and characterizing ROZ fairways and prospects.

Well records (i.e., scout tickets, drilling reports, geologic descriptions, Drill Stem Test (DST) reports, core analysis data, perforated intervals and initial production [IP]) were evaluated to validate that the formation contained oil and, if so, to determine if the oil was mobile or immobile with respect to water. Each well was assigned an ROZ indicator according to the occurrence and mobility of oil (Table 6-40).

Table 6-40. Observed ROZ indicators from well records and their interpreted ROZ implications.

Observed ROZ Indicators	**ROZ Implication**
Formation encountered; no show of oil	Oil not present
Formation encountered; oil not reported	Oil may not be present
Indirect indicator (i.e., drill stem test does not collect oil, sulfur odor or water)	Oil may be present but likely immobile
Direct indicator (i.e., oil show in cuttings, oil saturation in core, drill stem test collected oil)	Oil present but potentially immobile
Oil production	Oil present and is mobile

ROZ indicators were mapped and overlaid on regional isopach and structure maps. Clusters of ROZ indicators of immobile oil without nearby oil production suggest naturally immobile in-place oil and thus ROZ presence (Table 6-40). The structure and isopach maps provide information on modern structural and stratigraphic traps that may be present, but ROZs could conform to paleotraps that may not exist in the modern traps. The results of this evaluation were used to define boundaries of **ROZ Fairways** for each formation (areas that were likely to contain ROZs).

Though there is evidence from ROZ indicators that ROZs are present within each ROZ fairway, ROZs are not necessarily expected to occur throughout each fairway. Local variations in reservoir properties and structure (faults, fractures, and folds) exert strong controls on the occurrence of petroleum traps generally, and ROZs specifically. Thus, **ROZ prospects** were defined as areas within a ROZ fairway that have a combination of well records indicative of the presence of an ROZ supported by quantitative well log analysis. Prospect is an oil and gas term used to refer to a potential oil and/or gas accumulation that is sufficiently well-defined to represent a viable drilling target. The ROZ prospects presented here are considered discrete brown- or greenfields within the larger ROZ fairways. Prospects, by definition, are potential oil accumulations that must be evaluated by drilling to determine whether they contain commercial quantities of petroleum (AAPG Wiki). Site-specific evaluations are required to determine that a prospect has adequate potential to be developed. Several ROZ prospects were mapped in each ROZ fairway as discussed below.

Evaluation of Well Records

Due to the large number of wells within the regional study area, it was not feasible to evaluate the well records of each well that encountered all four formations so wells were prioritized based on their potential to yield data that could be used to identify and characterize ROZs. First, records for the wells used in the preliminary screening were evaluated to validate that the proper ROZ indicator was assigned. Then, the well records for wells near those that had oil shows or production were evaluated to provide support. Wells with a total depth (TD) within or near a target formation were selected because they were more likely to have information (such as attempts at production or DSTs) that could be used to infer the mobility of oil than wells completed in different formations. Newer wells were also prioritized because they had the potential to have resistivity and neutron density porosity logs that could be digitized for well log analyses. It was also discovered that drilling reports for newer wells were more likely to report low oil saturations while intervals of low oil saturation were often overlooked on older wells.

ROZ fairway boundaries were defined between 1) wells with non-productive oil shows and adequate reservoir quality and 2) wells with “no shows” and/or unsuitable reservoir quality. ROZ fairway boundaries were iteratively updated by selecting wells near the boundaries for additional evaluation.

ROZ fairways have CO_2 EOR and storage potential, but site-specific research is required to evaluate whether there is adequate potential for development. ROZ prospects were therefore defined within each ROZ fairway by grouping wells with sufficient data to characterize, both in terms of qualitative analysis of ROZ indicator and quantitative well log analyses of ROZ properties (i.e., distribution, thickness, porosity, and saturation) that could be used to constrain CO_2-EOR and storage potential. Structure and thickness maps were used to delineate the boundaries of prospects where possible, but some prospects, particularly in greenfield areas, lack clearly defined structural closure. Also, because many of the ROZ prospects were defined based on data from established oil fields, fewer data were available at the periphery or outside of oil fields’ boundaries to define the outer boundaries of the ROZ prospects, so the geometry of downdip wells with ROZ indicators was compared with the modern hydrodynamic configuration of the reservoir to infer the presence of an ROZ.

Well Log Analysis

Rock and fluid properties of the four ROZs were characterized using fluid contact curves, a well log analysis method developed for a previous study of Cypress Sandstone ROZs (Webb et al., 2019b). Because ROZs have low S_O, small errors in input parameters can lead to ROZs being overlooked. The S_W profiles calculated from well logs rarely followed an ideal trend of stepwise decreases in S_O from MPZ through ROZ to brine aquifer (Figure 6-78).

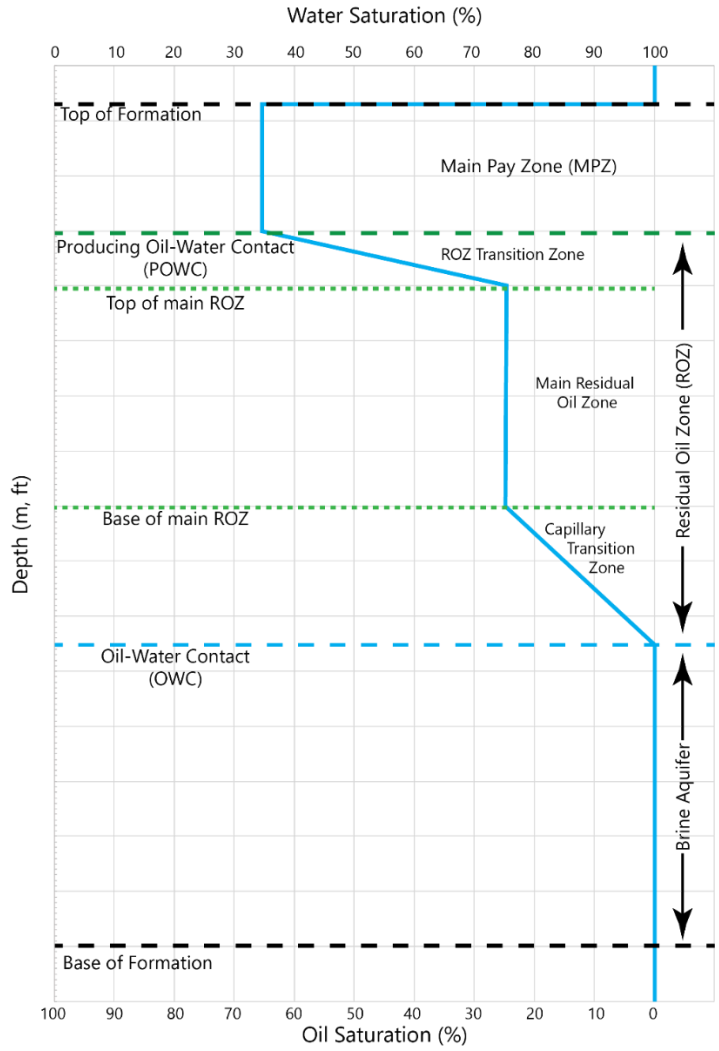


Figure 6-78. Ideal saturation curve of a brownfield residual oil zone (ROZ). Oil saturation (solid blue line) is greatest in the main pay zone (MPZ) where it is mobile. The producing oil water contact (POWC dashed green line) marks the boundary between the MPZ and ROZ, where oil saturation reduces and stabilizes at residual oil saturation to water in the residual oil zone (ROZ). The base of the ROZ is marked by the oil-water contact (OWC), where oil saturation drops to 0% in the underlying aquifer.

The average S_O (%) and average porosity (ϕ, %) were calculated for the ROZ in each well. The unit volume was also calculated using this equation:

$$\frac{bbls}{acre-ft} = 7{,}758\ \phi\ (1 - S_W)$$

EOR and Associated Storage Resource

To quantify the ROZ prospects' original oil in place (OOIP), porosity (ϕ), saturation (S_W), and thickness (h) values derived from well log analysis were applied to the area (A) of each ROZ prospect. OOIP (in barrels; bbl) was calculated using the standard volumetric equation:

$$Original\ oil\ in\ place\ (bbl) = \ 7{,}758\ \phi\ (1 - S_W)\ A\ h$$

Because analyzed wells were unevenly distributed, a method was required to estimate the area that each wells' calculated properties represented within multi-well prospects. A Voronoi map was generated in

ArcGIS (Analysis Tools > Proximity > Create Thiessen Polygons) that partitioned the area covered by the analyzed wells into Thiessen polygons based on the distance to each well (Figure 6-79). The Thiessen polygon for each analyzed well contains all locations closer to that well than to any other well. The Thiessen polygons were then clipped to the boundaries of the ROZ prospects. An oil volume for each well was found by using the unit volume for the ROZ multiplied by thickness (feet) and the area (acres) assigned to each well. The resulting OOIP values for each Thiessen polygons were summed to get the resulting best-estimate ROZ OOIP values for each prospect.

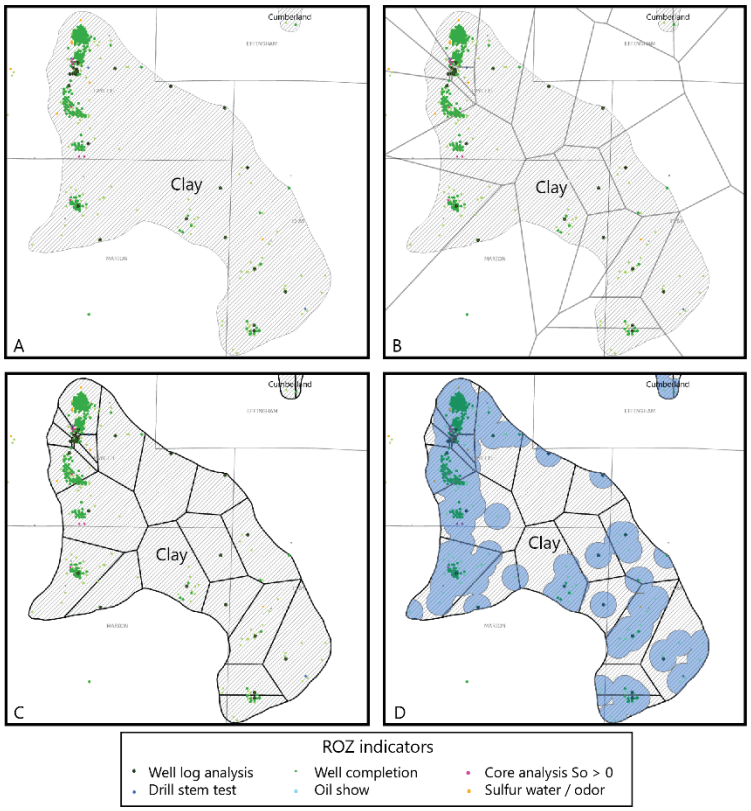


Figure 6-79. Example of the Carper ROZ Clay prospect showing how prospect boundaries were defined relative to ROZ indicators. Prospect boundaries extend beyond the ROZ indicators or were defined near them depending on local structure and thickness of the sandstone. A) Distribution of ROZ indicators within the prospect. B) Voronoi map showing how the area was partitioned into Thiessen polygons nearest to each well with adequate data for well log analysis. C) Thiessen polygons clipped to the prospect boundary. Oil saturation and thickness values calculated from well logs were multiplied by the area of their respective Thiessen polygon for volumetric analysis. D) 1-mi radius buffer drawn around wells with ROZ indicators (blue shading) to provide a low estimate of area used in the volumetric calculation for Carper Sandstone only. (Wells within oilfields, e.g., northwest corner of the map, have very close spacing and represent proportionally smaller areas compared to areas with a single well. Wells had mostly similar unit volumes so no outliers exist and incorrectly represent areas well beyond the oilfield.)

The entire area of the prospect represents a high estimate. Because Carper prospects were sparsely populated with well data, a low estimate used a 1-mile radius around each well with ROZ indicators (Figure 6-79D) in place of the entire prospect area.

The amount of oil recoverable via CO_2-EOR was estimated by applying EOR factors to the OOIP estimates (Table 6-41). CO_2 net utilization factors were used to estimate the associated CO_2 storage resource. Reservoir simulations of CO2 injection into the MPZ and Brownfield ROZ of the thick Cypress Sandstone at Noble Field were the source of the CO_2-EOR and net CO_2 utilization factors (Okwen et al., 2023) used

for the Cypress and Tar Springs ROZs. Similarly, reservoir simulations of CO2 injection into a greenfield ROZ in the Carper Sandstone (Yang et al., 2023) were the basis for the EOR and net utilization factors used to make estimates for the Carper ROZ. In all cases, the EOR and net utilization factors represent the most likely scenario. No estimates of EOR and associated storage resources were made for the Middle Devonian because no ROZ prospects were defined.

Table 6-41. EOR and storage factors based on reservoir simulation studies.

Development Strategy	**Formation**	**Strategy**	**CO_2-EOR Recovery Factor (% of OOIP)**	**Net Utilization (Mscf/stb)**
80-acre Water Alternating Gas	Cypress and Tar Springs Sandstones	Oil production	11.4	6
80-acre continuous CO_2 injection	Carper Sandstone (medium perm)	Oil production	9.5	23

Results

ROZ Fairways and Prospects

For this study, ROZ fairways are defined as the areas of the ILB that, based on regional mapping and data analysis, have the potential to contain ROZ prospects. Areas identified as ROZ fairways met both the presence of ROZ indicators (Table 6-40) and reservoir quality (thickness, porosity) criteria; areas that met only one or neither criterion was not considered a ROZ fairway. The distribution of the fairways is shown in Figure 6-80.

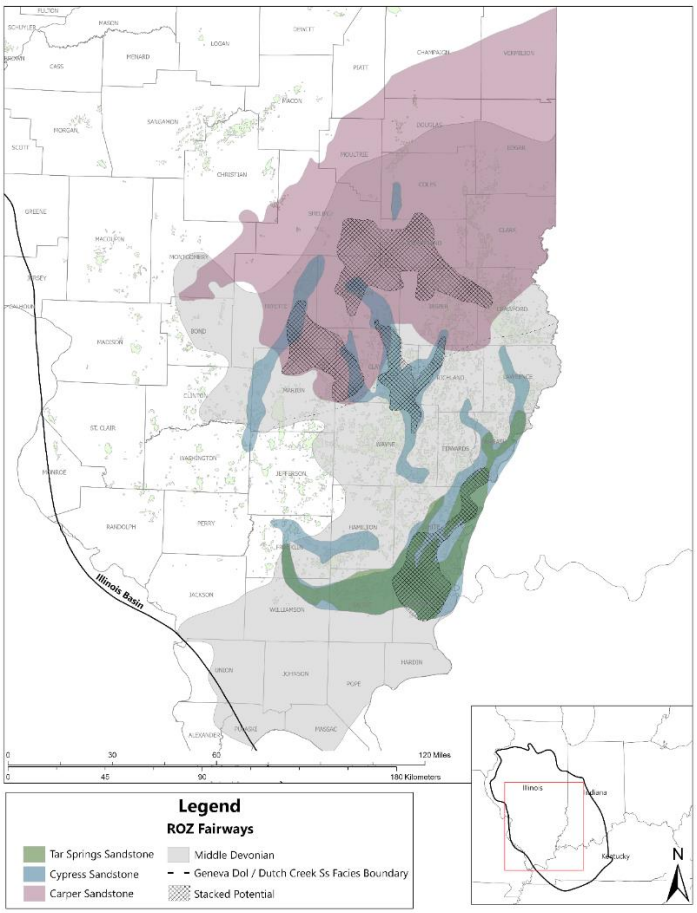


Figure 6-80. ROZ fairways (shaded). The Middle Devonian Fairway (grey) is split by a facies boundary with the Geneva Dolomite generally north of the black dashed line and the Dutch Creek Sandstone to the south. The Carper Sandstone fairway (rose) occurs entirely north of this dashed line, too. The Middle Devonian and Carper Fairways are relatively large and continuous fairways, Cypress Sandstone fairway (blue), and Tar Springs Fairway (green) are relatively smaller, discontinuous, and narrow.

Tar Springs ROZ

Fairway

The Tar Springs ROZ is stratigraphically the youngest ROZ evaluated. Tar Springs Sandstone oil production is concentrated in far southern and southeastern Illinois along the Cottage Grove and Wabash Valley Fault Systems, respectively (Cohee, 1942; See Figures 6-75 and 6-80). Tar Springs ROZs were observed in the tops of thick sandstones overlying thick brine aquifers near Tar Springs Sandstone oil fields. ROZ indicators constrain the interpreted Tar Springs ROZ fairway over an area covering approximately 2,200 km^2 (542,000 acres) throughout Williamson, Saline, Gallatin, Franklin, Wabash, and White Counties (Figure 6-81).

Prospects

Seven Tar Springs ROZ prospects were defined within the Tar Springs ROZ fairway (Figure 6-83; Table 6-42). Most evidence of Tar Springs ROZs was found in off-structure, data-sparse areas away from oil fields. Coupled with the lack of data, the variable geometry of the thick lower Tar Springs Sandstone and the occurrence of faults complicated the delineation of Tar Springs ROZ prospects. No Tar Springs ROZ prospects were defined in the southern and western areas of the fairway (within Franklin, Williamson,

and Saline Counties; Figure 6-81), because no wells in the area had digital neutron-density porosity logs that could be used to characterize and quantify oil saturation.

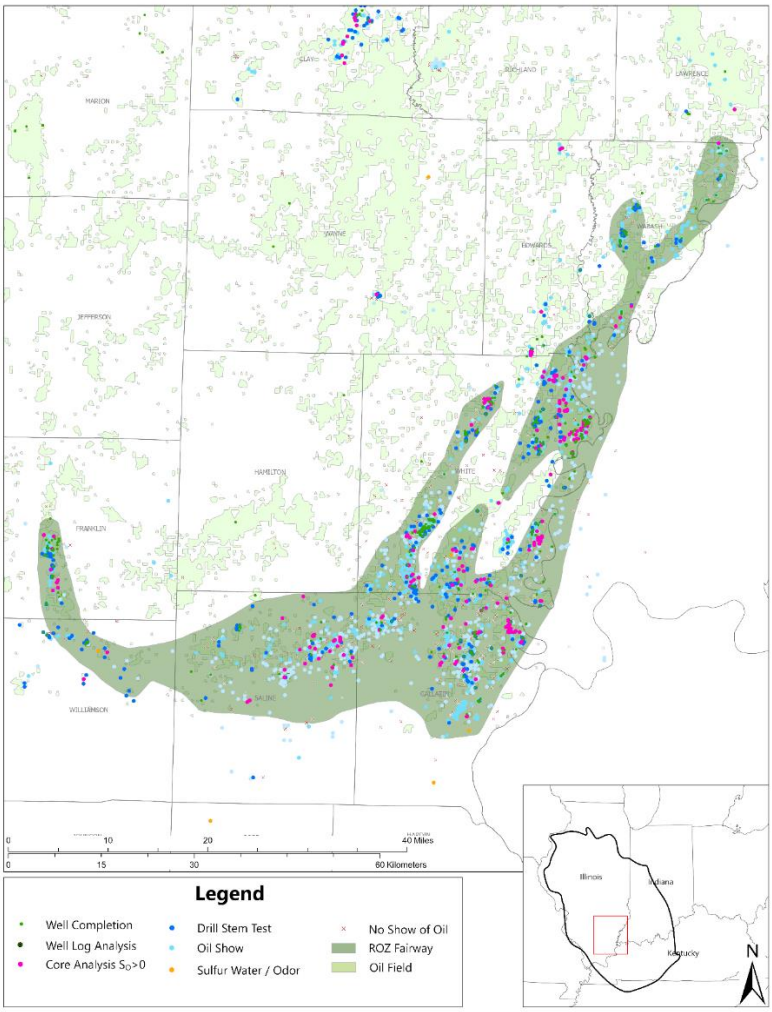


Figure 6-81. Map showing Tar Springs Sandstone ROZ Fairway (shaded in green) and distribution of ROZ indicators. Illinois oil fields are shaded in light green.

The Bruce 2 well (API: 120592566000), in the northern part of the Omaha prospect, is a representative example of a Tar Springs Greenfield ROZ (Figure 6-82). The upper Tar Springs Sandstone that is productive in Roland Field to the north is relatively non-porous in this well and has “no show of oil” listed on scout ticket. The scout ticket lists a “slight show of oil” in the top of the thick, lower sandstone body.

Table 6-42 summarizes the properties of the seven Tar Springs ROZ prospects based on calculations from well log analysis. All the prospects are centered on existing oil fields and six of the prospects host a MPZ in a thin upper sandstone with a Greenfield ROZ in a thick lower sandstone. Only the Herald prospect occurs in an area where the upper oil productive sandstone body is not present. In all cases, despite ongoing production in the fields, the MPZ had much higher calculated S_O values in the range of 37 to 53%, the latter approaching assumed S_{WIRR} based on analysis of the BVW curve and grain size. ROZ saturations were typically in the 20 to 30% range. In general, the ROZs were in rock of similar porosity to the MPZs, but the ROZs are universally thicker than the MPZs.

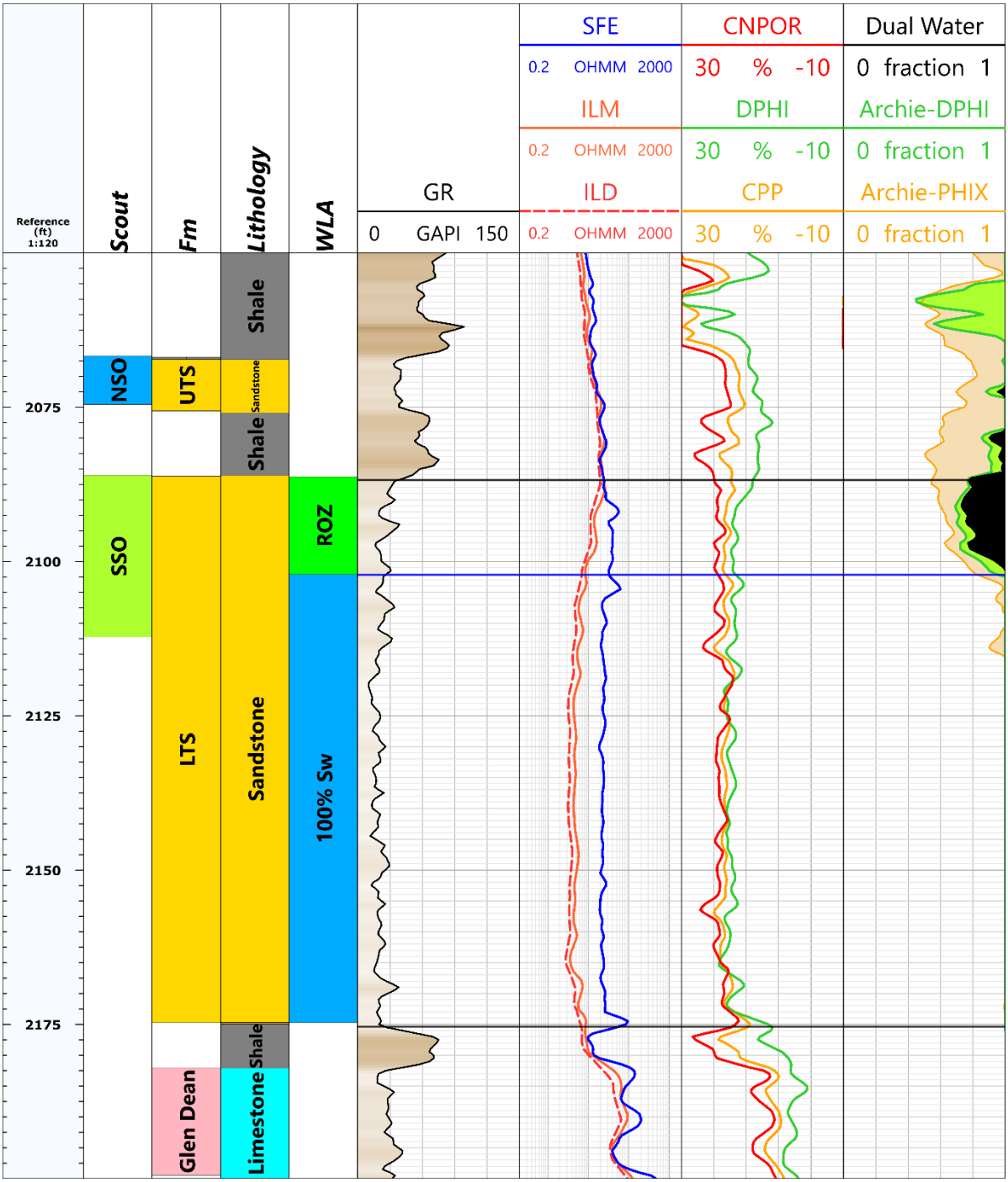


Figure 6-82. Example log analysis of a Tar Springs Greenfield ROZ taken from the Bruce 2 well (API: 120592566000). The "scout" track shows the depths of "no show of oil" (NSO) and "slight show of oil" (SSO) recorded on the scout ticket. Archie's Equation based on cross plotted porosity (Archie-PHIX; orange line and fill) erroneously calculates oil saturation in the shale break between the upper and lower Tar Springs Sandstone (labeled UTS and LTS in the Fm track, respectively). Archie's Equation based on density porosity (Archie-DPHI; green line and fill) removes most of the oil saturation from the shale break but still calculates it in an overlying shale unit with high density porosity. Dual Water calculations (black line and black fill) compensate for clay and properly calculate S_O. The target interval is bound by horizontal black lines and the interpreted oil water contact that defines the base of the ROZ is shown with a horizontal blue line.

Table 6-42. Average oil saturation, porosity, and thickness of Tar Springs ROZ prospects as derived from well log analysis.

Prospect Name	Wells analyzed	ROZ			Area (ac)	ROZ OOIP (MMBO)
		S_O (%)	ϕ (%)	Thickness (ft)		
Herald	7	24	12	36.0	12,951.4	107.5
Inman	3	22	14	23.7	19,739.5	156.5
New Harmony	2	29	16	20.0	19,911.1	177.2
New Haven	1	32	14	39.5	949.4	13.5
Omaha	3	16	18	11.8	5,692.7	10.9
Roland	15	24	16	36.2	14,160.8	154.4
Storms	3	24	13	10.0	1,010.6	2.5
					Total	622.5

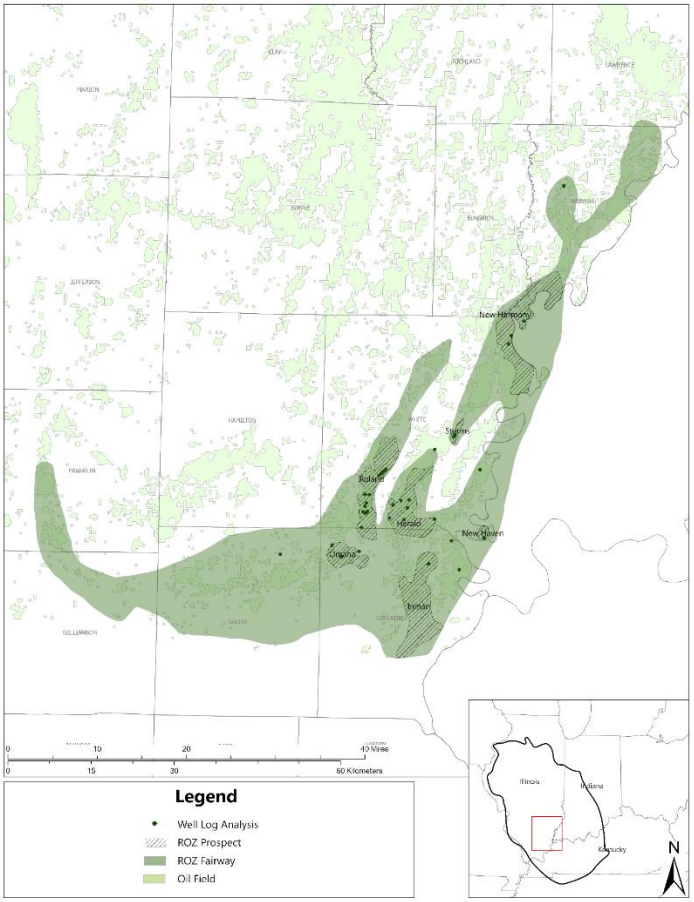


Figure 6-83. Tar Springs Sandstone ROZ prospects shown with annotated, crosshatched polygons. Green dots represent wells whose logs were used to characterize the ROZs.

Cypress ROZ

Fairways 6

The Cypress Sandstone was previously evaluated for ROZ potential in a regional study (Webb et al., 2019b) that identified a north-south trending ROZ fairway across southern Illinois and largely corresponded to a

tract of thick sandstone facies. In the present study, all of southern Illinois was explored for ROZs and the previous extent of the fairway has been revised. Multiple ROZ fairways are now recognized to occur within the Cypress Sandstone, and they can be broadly divided into three northern and one southern fairway (Figure 6-84). The combined area of the Cypress ROZ fairways is just over 5,500 km^2 (1.4 million acres).

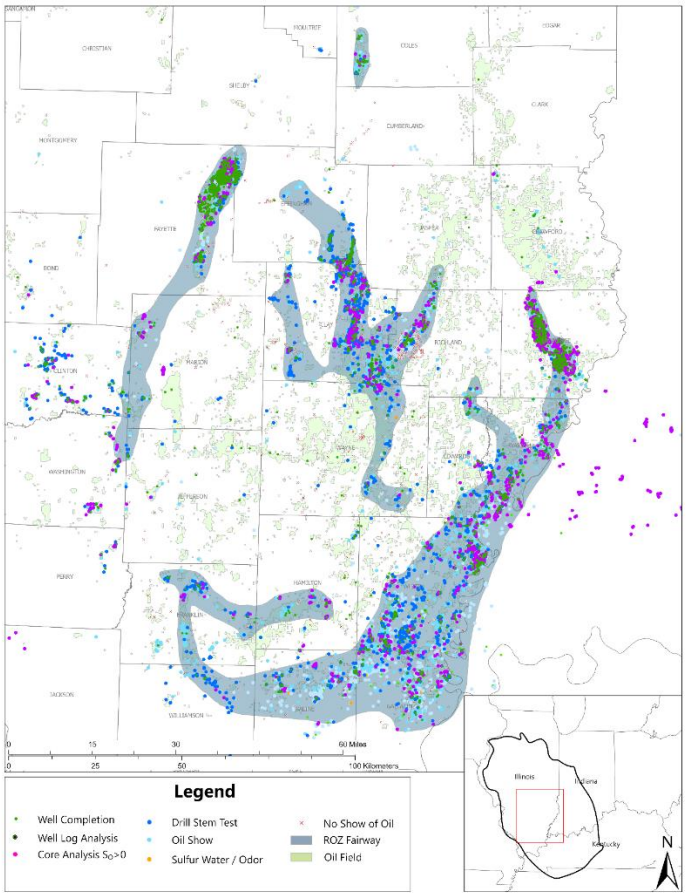


Figure 6-84. Map showing Cypress ROZ fairways (shaded in blue) and distribution of ROZ indicators. Illinois oil fields are shaded in light green.

Prospects

Webb et al. (2019b) identified 27 Cypress ROZ prospects. In the present study, many of these prospect boundaries were modified and eight of the prospects were no longer considered ROZ prospects based on the evaluation of additional ROZ indicators and well log analysis. A total of 33 Cypress ROZ prospects have been defined (Figure 6-86; Table 6-43). Most of the prospects are concomitant with or subdivide previously defined prospects. Six new prospects were defined within the southern fairway mostly along the southeastern border of the state.

The JR Coen 4 well (API: 121592533701) is a representative example of a Cypress Brownfield ROZ (Figure 6-85). The well is in the middle of Noble Field and surrounded by wells that produce oil from the top of the thick Cypress Sandstone. The well's scout ticket lists a good show of oil from 2,582 to 2,590 ft above a show of oil from 2,590 to 2,600 ft. The upper four feet were perforated (between the depths of 2486-2582), and the well had a comingled (with the Ste. Genevieve Limestone) initial production of 205 bbls oil and 90 bbls water in 24 hours.

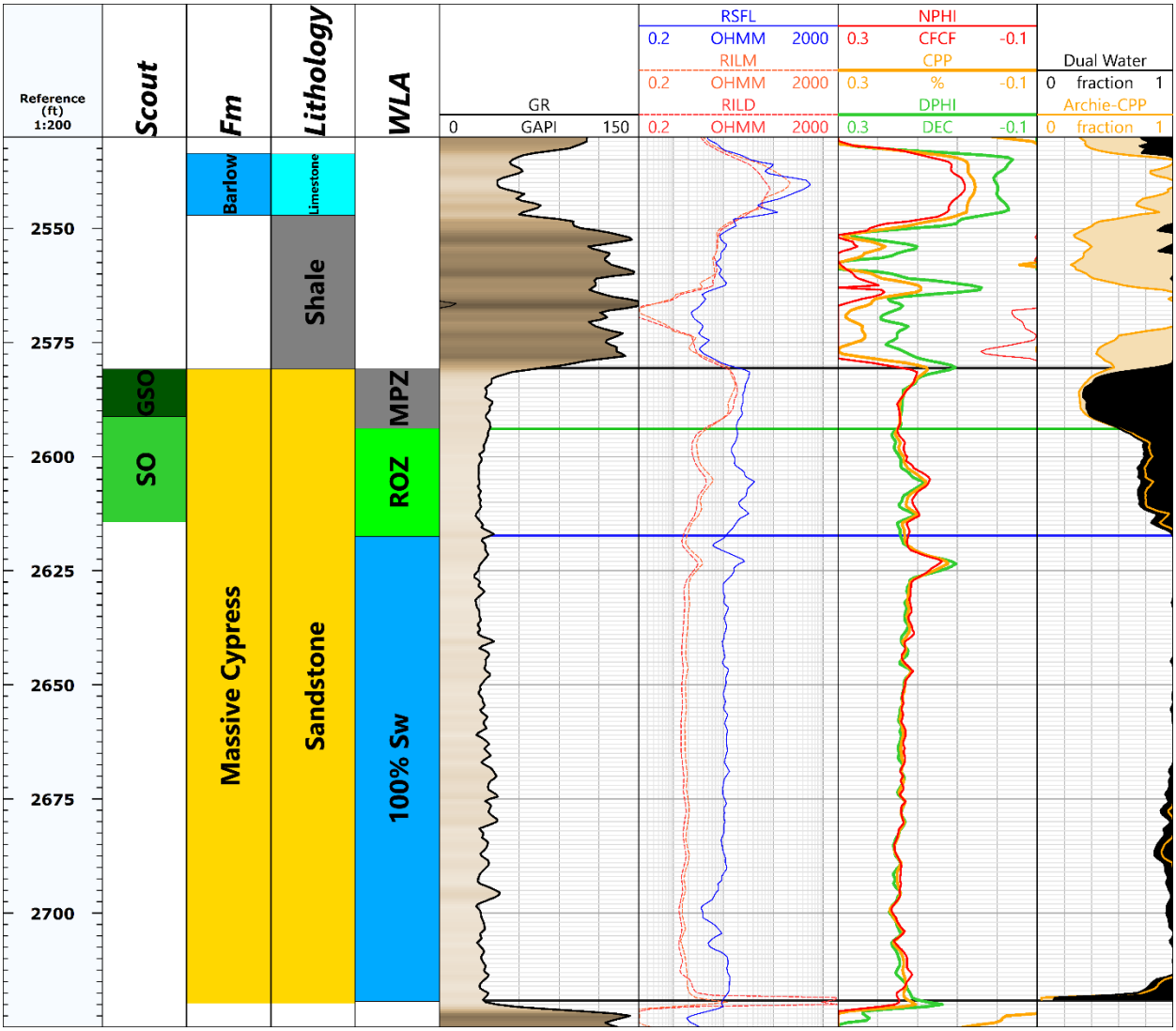


Figure 6-85. Example log analysis of a Cypress Brownfield ROZ taken from the JR Coen 4 well (API: 121592533701). The "scout" track shows the depths of "good show of oil" (GSO) and "show of oil" (SO) recorded on the scout ticket. Archies Equation based on cross plotted porosity (Archie-CPP shown with orange line and fill) and Dual Water Saturations (Dual Water curve shown with black line and fill) are lowest in the upper 5 feet (highest calculated oil saturation supported by a good show of oil listed on the scout ticket), increase to ~25% for 25 feet (supported by a "show of oil" listed on the scout ticket), before increasing to 100% for the lower aquifer bearing interval. This distribution of oil and water is indicative of a Brownfield ROZ in the Cypress. The target interval is bound by horizontal black lines and the interpreted producing oil water contact that defines the base of the MPZ is shown with a horizontal green line, and the oil water contact that defines the base of the ROZ is shown with a horizontal blue line.

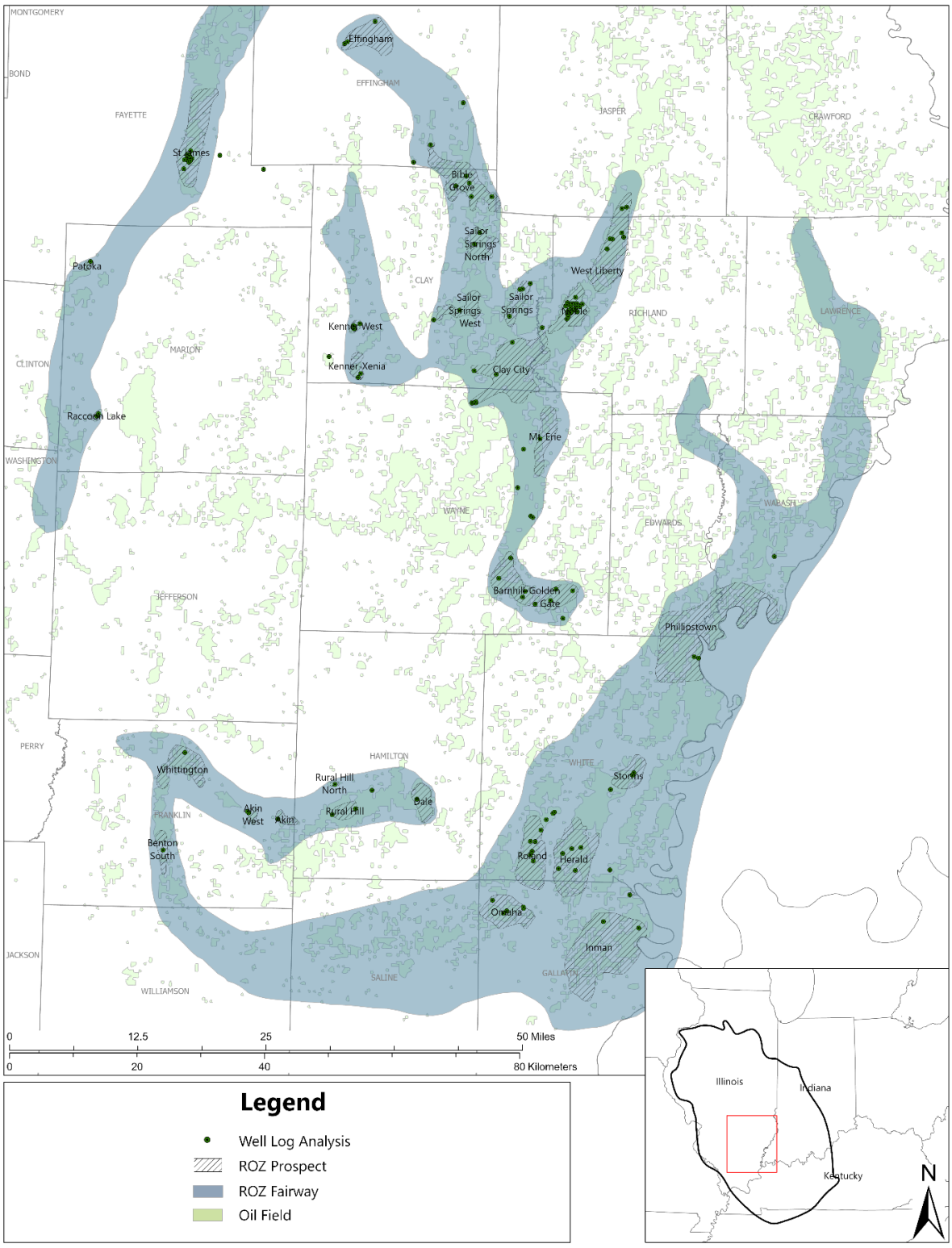


Figure 6-86. Cypress Sandstone ROZ prospects shown with annotated, crosshatched polygons. Green dots represent wells with logs that were used to characterize the ROZs.

Table 6-43. Properties of Cypress Sandstone ROZ prospects as derived from well log analysis. Sesser prospect is not in this table because there were no suitable digitized well logs within its boundaries.

Prospect Name	Wells analyzed	ROZ			Area (ac)	ROZ OOIP (MMBO)
		SO (%)	ϕ (%)	Thickness (ft)		
Akin	1	29	14	18.0	1,156.8	6.6
Akin West	2	32	10	36.8	738.9	5.3
Barnhill-Golden Gate	8	19	11	31.0	11,909.0	56.9
Benton South	1	15	18	12.5	2,151.0	5.4
Bible Grove	8	23	14	10.3	11,053.3	37.3
Clay City	7	26	16	25.0	18,890.9	122.0
Dale	1	20	15	14.0	3,337.5	11.2
Effingham	4	18	12	12.0	6,952.5	14.0
Herald	5	24	13	31.8	14,569.0	95.8
Inman	3	24	12	28.2	26,223.4	100.4
Kenner West	4	21	16	25.8	635.7	4.2
Kenner-Xenia	3	36	14	15.8	1,728.1	10.7
Mt. Erie	4	22	16	21.3	5,118.9	31.7
Noble	23	24	17	29.5	5,652.2	42.5
Omaha	5	29	10	40.1	7,549.5	67.5
Patoka	1	19	19	15.5	316.0	1.4
Phillipstown	3	23	12	12.0	32,908.3	69.6
Raccoon Lake	2	18	16	18.5	376.8	1.4
Roland	10	27	13	28.0	9,914.0	99.2
Rural Hill	2	16	14	23.5	2,056.2	11.3
Rural Hill North	1	19	7	16.0	208.0	0.4
Sailor Springs	4	28	15	23.5	3,214.3	47.6
Sailor Springs North	2	22	13	34.8	4,126.5	31.7
Sailor Springs West	2	19	14	18.3	3,739.0	11.5
St. James	14	23	16	38.8	15,641.6	77.6
Storms	3	21	14	20.8	4,129.2	20.0
West Liberty	7	27	17	11.7	11,997.7	40.5
Whittington	1	15	14	22.5	7,125.4	26.7
					Total	1,050.6

Carper ROZ

Fairway

The Carper Sandstone Member consists of a series of extensive lobate sandstone deposits of variable thickness (0 to 200 ft [0 to 61 m]) that occur within the Borden Siltstone (early Middle Mississippian) that tongues into the northern portion of the ILB (Swann et al., 1965; Lineback, 1968). The Carper is unlike any other Mississippian sandstone in the ILB in that it is finer grained, naturally fractured, well cemented by clay and carbonate minerals, and has lower porosity and permeability, all of which make it more akin to a tight oil reservoir (e.g., Yang et al., 2016) than the conventional oil reservoirs in the Tar Springs and Cypress Sandstones.

Given the widespread geographical distribution of oil shows almost everywhere the Carper Sandstone occurs, the Carper Sandstone ROZ fairway was defined coincidental with the spatial extent of the Carper Sandstone, covering an area of approximately 16,875 km^2 (4.2 million acres).

Prospects

Six Carper ROZ prospects were defined within the Carper ROZ fairway, generally within the northern half of the study area (Figure 6-89; Table 6-44). There are no ROZ prospects in the northeastern portion of the Carper ROZ fairway, because this area was not studied in detail due to the lack of neutron-density porosity logs. Some of the identified Carper ROZ prospects occur in association with anticlines where the Carper Sandstone is productive from MPZs, but the largest prospects occur over vast greenfield areas far removed from structural features.

The Swits 1 well (API: 121392124300) is provided here as a representative example of multiple Carper Sandstone bodies that contain both an MPZ and an ROZ (Figure 6-87). The well is in the middle of Gays field, which has four Carper Sandstone bodies separated by mudstones. Throughout the field, oil shows are listed for the upper three sandstone bodies, but only the lowermost sandstone is productive. The scout ticket for the Swits 1 well lists oil shows in the top two sandstone bodies, fluorescence in the third, and the lowermost sandstone was perforated and produced oil.

Table 6-44. Properties of Carper Sandstone ROZ prospects.

Prospect Name	Wells analyzed	ROZ			Area (ac; buffered)	ROZ OOIP (MMBO)
		SO (%)	ϕ (%)	Thickness (ft)		
Clay	23	24	9	25.7	95,949.9	505.8
Coles	0	No Logs	No Logs		20,891.8	268.7
Cumberland	46	23	11	60.1	163,741.8	1,811.2
Fayette	3	29	13	29.5	24,433.9	217.1
Moultrie	5	23	11	39.5	2,129.3	21.4
Shelby	1	18	13	30.0	12,159.6	74.1
					Total	2,898.2

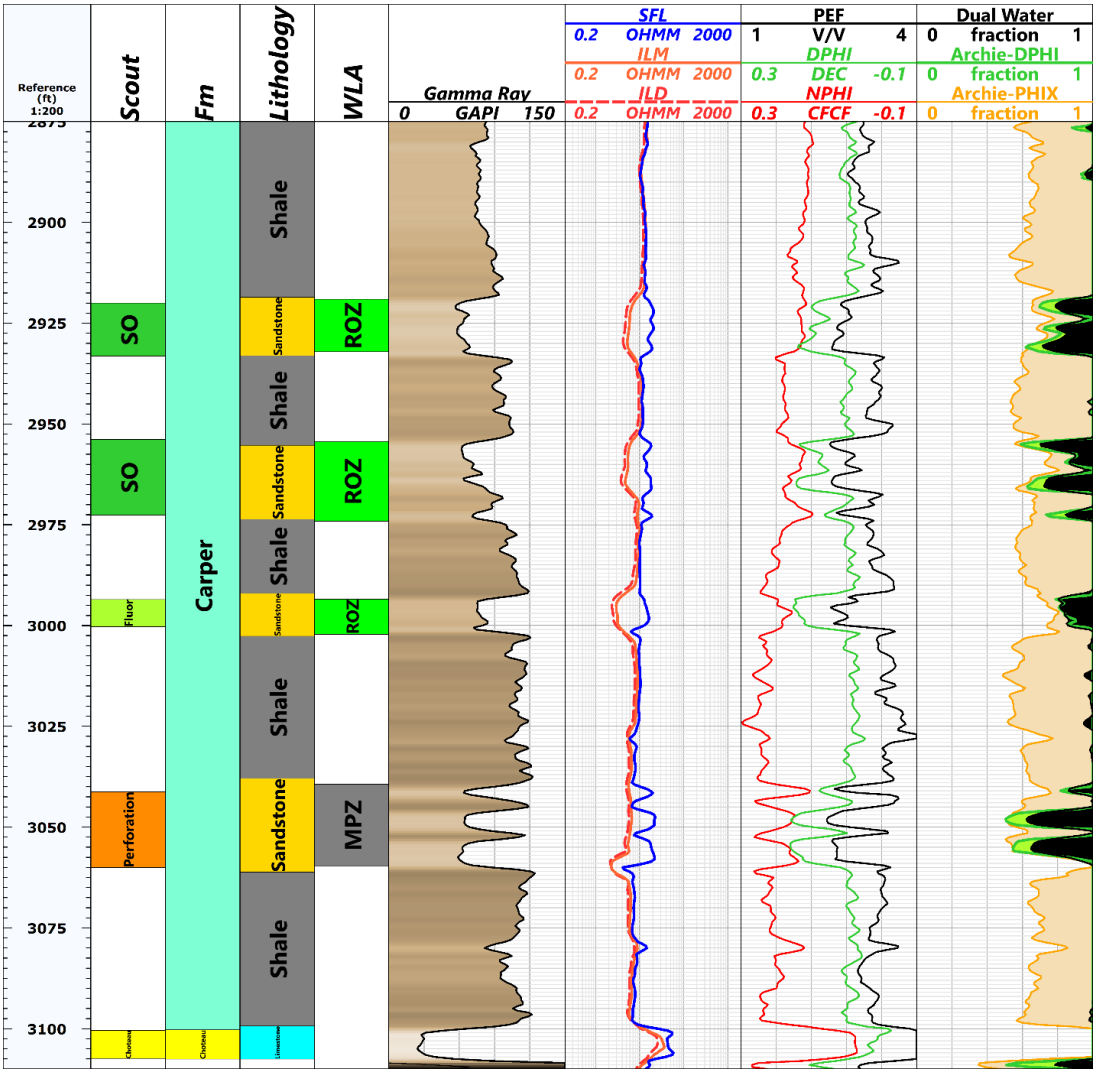


Figure 6-87. Example log analysis of a Carper MPZ and ROZ taken from the Swits well (API: 121392124300). Intervals listed with "show of oil" on the scout ticket shown with Sos, interval listed with "fluorescence" shown with Fluor, and perforated interval shown with Perforation on the leftmost track. Archie S_W calculated with raw cross plotted porosity (Archie-PHIX shown with the orange line and orange fill) is erroneously low in the shale intervals, where neutron porosity is erroneously high. Archie calculated with raw density porosity (Archie-DPHI shown with the green line and green fill) and Dual water Saturation (shown with blue line and black fill) do a better job of matching expectations; SW is 100% in the non-porous shale intervals, ~50% in the lowermost interval that was perforated and produced oil, and ~75% in the upper two porous intervals have oil shows and third porous interval has recorded fluorescence listed on the scout ticket. The log analysis qualitatively supports oil shows observed during drilling, but thin interbedded mudstones within the porous units complicate quantification of oil saturation.

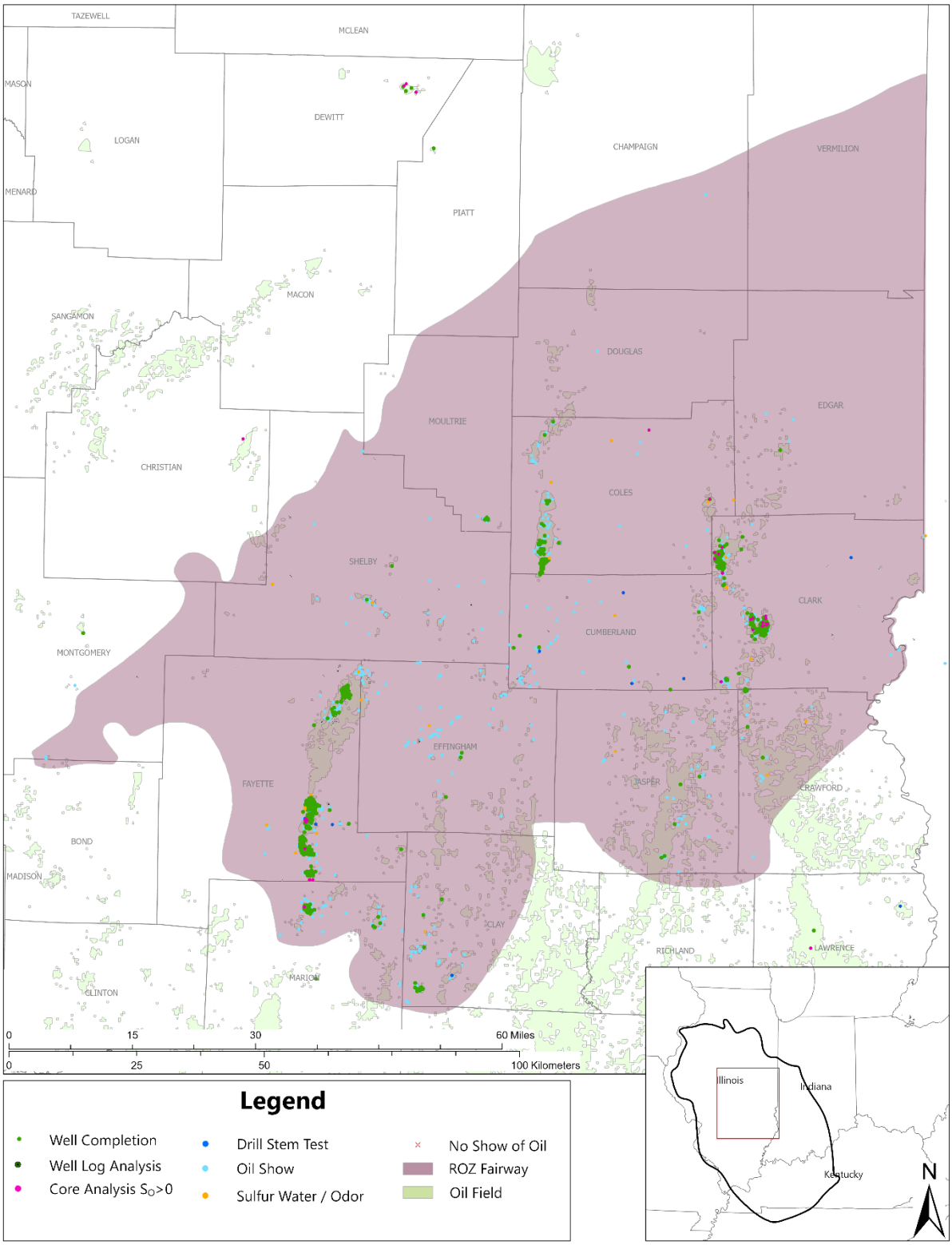


Figure 6-88. Map showing Carper Sandstone ROZ Fairway (shaded in purple) and distribution of ROZ indicators. Illinois oil fields are shaded in light green.

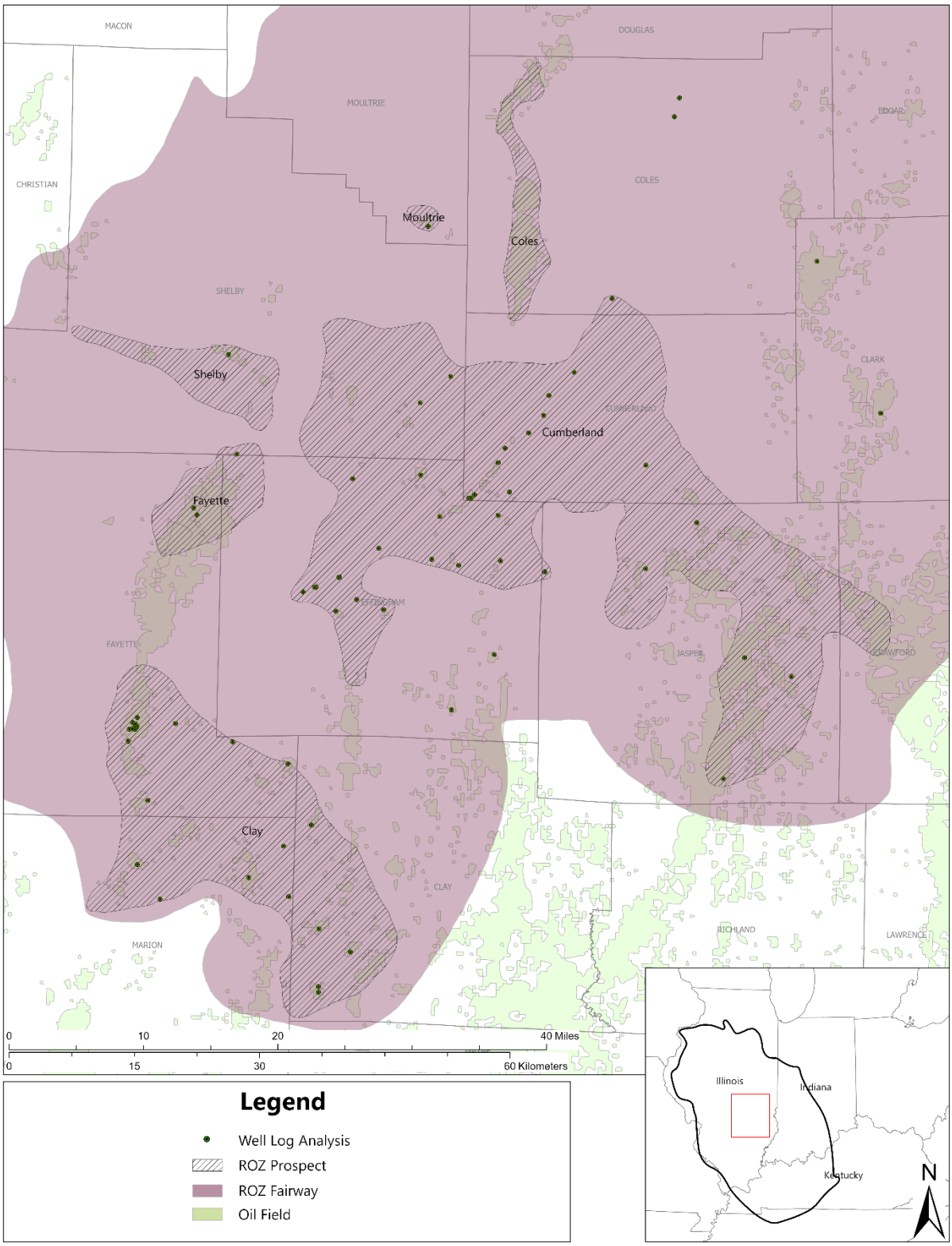


Figure 6-89. Carper Sandstone ROZ prospects shown with crosshatched polygons and annotated. Green dots represent wells whose logs were used to characterize the ROZs.

Middle Devonian ROZ

Fairway

The Middle Devonian ROZ is stratigraphically the lowest ROZ studied and among the deepest producing oil reservoirs in Illinois. North of a west-east trending facies boundary (Figure 6-80, dashed line) is the Geneva Dolomite, which consists of a laterally continuous vuggy, and in places sandy, dolomite embedded within a non-porous limestone. South of the facies boundary is the Dutch Creek Sandstone, which is a dolomitic sandstone embedded within a complex mixture of non-porous limestone and dolomite. The facies transition of the Geneva Dolomite into the Dutch Creek Sandstone along the boundary is diffuse.

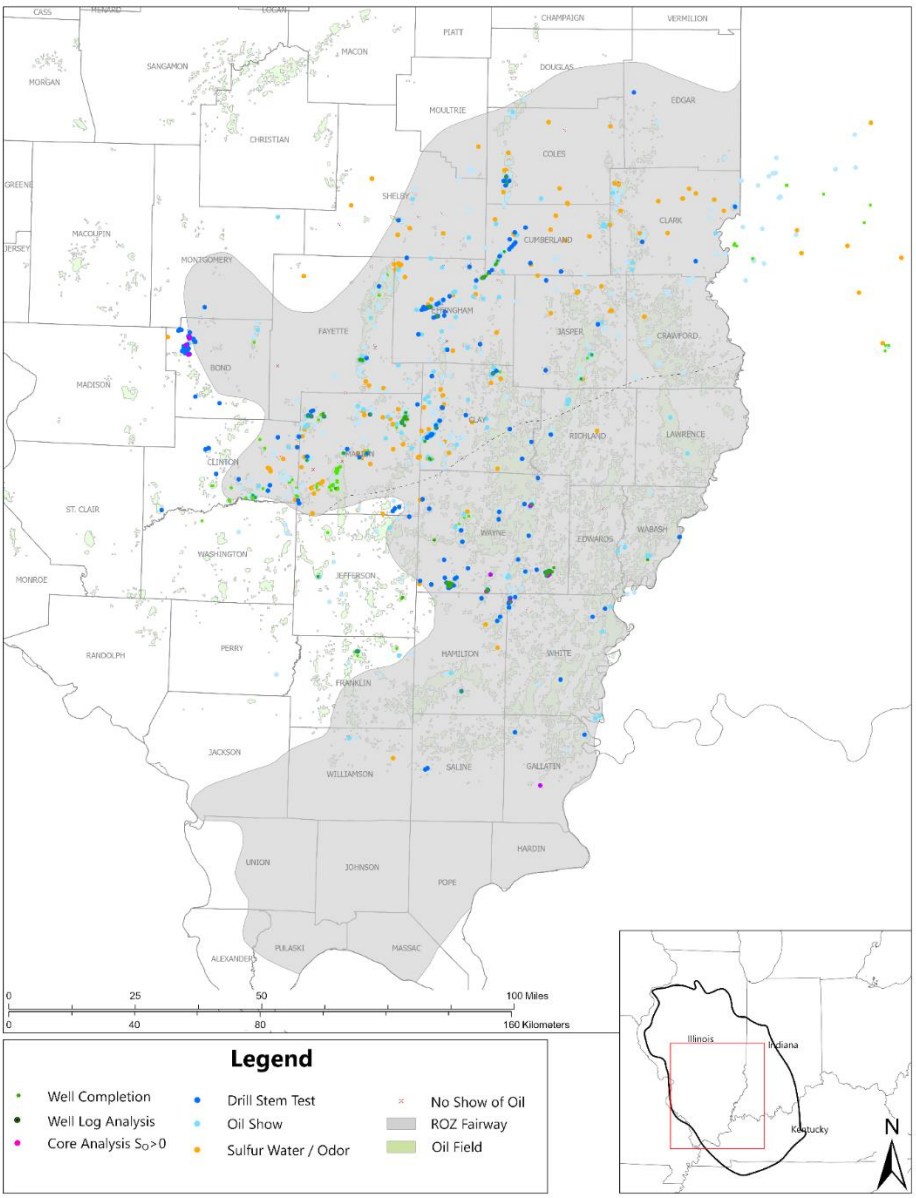


Figure 6-90. Map showing Middle Devonian ROZ Fairway (shaded in grey) and distribution of ROZ indicators. The dashed line represents the facies boundary between the Geneva Dolomite to the North and Dutch Creek Sandstone to the south. Illinois oil fields are shaded in light green.

Prospects

Several factors collectively complicated the well log analysis of the Middle Devonian ROZs The complex lithology, high degree of variability in the available formation water salinity (and thus resistivity) data, and thinness of Middle Devonian reservoirs introduce significant sources of uncertainty in the S_W calculations. Furthermore, few of the wells that encounter the Middle Devonian have neutron-density porosity logs necessary for S_W calculations. As a result, no Middle Devonian ROZ prospects were defined. A description of the well log analysis that supported the decision not to define prospects is provided in the appendix.

EOR and Associated Storage Resource

Estimates of OOIP for the Tar Springs, Cypress, and Carper ROZ prospects are shown in Tables 6-42 through 6-44. The calculation of ROZ OOIP for the Carper Sandstone includes only the low estimate (the buffered area within 1 mi (1.6 km) of wells with ROZ indicators); the high estimate of OOIP (based on the total unbuffered area of the ROZ prospects) is provided in Appendix 6-3. Approximately 4.6 billion bbls of oil are estimated in place in the ROZs.

The CO_2-EOR and associated storage estimates for the Tar Springs, Cypress, and Carper ROZ prospects (Table 6-45) result from the application of the simulation-derived recovery and net utilization factors (Table 6-41) to the best-estimate ROZ OOIP values (Tables 6-42 through 6-44). The storage estimate does not account for other accessible pore volume in the formation. In particular, the Cypress ROZ prospects generally have thick underlying brine aquifers that could provide significant additional associated CO_2 storage (e.g., NETL, 2012).

Table 6-45. Estimates of recoverable oil and associated CO_2 storage in the Tar Springs, Cypress, and Carper ROZ Prospects.

ROZ Prospects	EOR (MMBO)	Storage (million tonne)
Tar Springs	71.0	22.7
Cypress	119.8	38.3
Carper	275.3	333.1
Total	466.1	394.1

Discussion: ROZs in Illinois

Origin and Classification of ROZs

The Carper and Middle Devonian ROZ fairways are stratigraphically within a few 10s-100s of ft above and below, respectively, the New Albany Shale source rock. The Carper Sandstone, one of the first porous units to occur above the New Albany Shale, is an obvious secondary migration pathway for expelled oil to pass through to traps both up dip and up section. The Middle Devonian is an “upper source-lower reservoir” system in which oil migration was directed downward from the New Albany Shale. Further supporting downward migration, simulation studies have shown that fluid overpressures may develop above the source rock due to basin subsidence and deep burial resulting in downward impelling force that can overcome the buoyancy force of oil in water (Chi et al., 2010). Despite being stratigraphically below the New Albany Shale, commercial Middle Devonian reservoirs are developed in areas structurally up dip from the oil generating part of the source rock (Barrows and Cluff, 1984).

Over a large portion of the ILB, the Middle Devonian and Carper Sandstone were the most proximal porous and permeable geologic formations for oil expelled from the New Albany Shale to migrate with subsequent tertiary migration of the oil out of these formations to form ROZs (Figure 18). The regional

distribution of the ROZ fairways (Figures 6-88 and 6-90) reflects the widespread porosity development in both formations that coincides with the oil generating part of the New Albany Shale. The widespread and well-connected vuggy porosity development in the Middle Devonian was conducive to water washing of oil, which is supported by the common observation of sulfur water in the formation. Thus, the Middle Devonian is interpreted to be a Type 3 ROZ (originating from change in hydrodynamic conditions; *sensu* Melzer 2006).

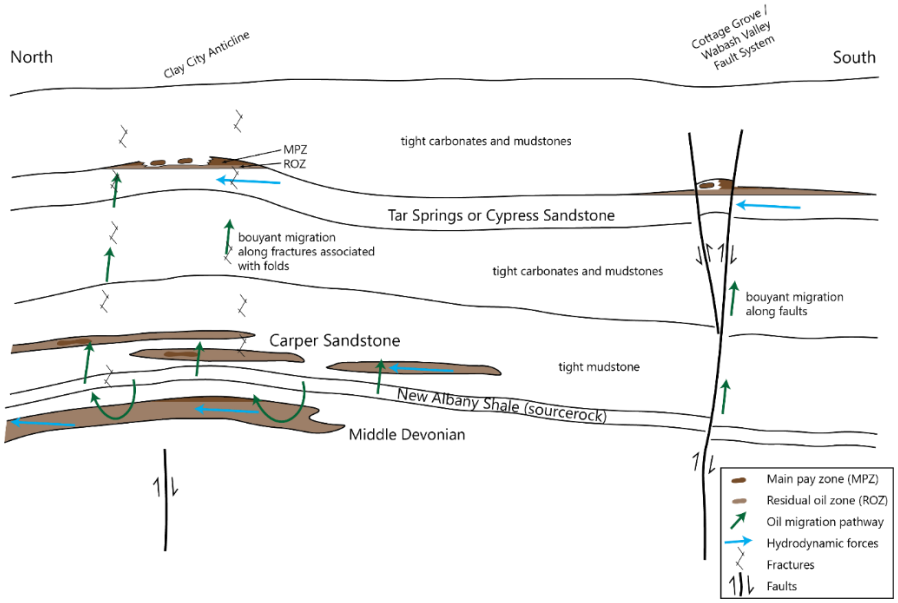


Figure 6-91. Generalized cross section showing the geometry and distribution of ROZs with respect to major structures (e.g., Clay City Anticline and Cottage Grove / Wabash Valley Fault systems), oil migration pathways, and basinal hydrodynamic forces.

Oil accumulation in the Carper was reduced over geologic time as natural fractures allowed tertiary migration of accumulated oil via buoyant leakage with water imbibition reducing oil saturation, resulting in development of a Type 2 ROZ (created by leakage along a breached seal; *sensu* Melzer, 2006). MPZs that occur on structural traps in the Carper have a relatively high S_{WIRR} (approx. 50%; Figure 6-88). Oil properties (e.g., density and viscosity) and composition data (e.g., attenuation of the light oil fraction) indicate water washing (Webb et al., 2023). Likewise, sulfur water produced from DSTs reflects the activity of sulphate reducing bacteria and is evidence of relatively fresh water washing of oil.

The Tar Springs and Cypress Sandstones are separated from the New Albany Shale source rock by over 1,000 ft of strata, most of which is composed of impermeable mudstones and tight carbonate rocks. Given the close association of Cypress and Tar Springs ROZ fairways with major faults and inferred fracturing along major folds (Figure 6-91), it is likely these are Type 2 ROZs (*sensu* Melzer, 2006). There are also indications of stratigraphic control on ROZ development in the Tar Springs and Cypress Sandstones. In both fairways, the sandstones are thick and have an oil column developed above, and in contact with, a brine aquifer. In areas where there are relatively thin sandstone lenses developed above the thick sandstone, those lenses tend to contain productive MPZs. Where lenses do not occur and oil saturation is developed in the top of the thick sandstone, with few exceptions (e.g., Noble Field), the oil accumulation is at reduced (with respect to S_{WIRR}) or residual oil saturation. The fact that the ROZs are developed within thick, clean sandstones and associated with underlying brine aquifers suggests that the ROZs may have also formed in response to a hydrodynamic gradient within the formations (i.e., Type 3 ROZs).

ROZ Fairway Boundaries

There are two factors that impact the mapped ROZ fairways: 1. The underlying geological controls on the secondary migration of oil in the ILB, and 2. The availability of data to constrain the fairway boundaries.

The Carper and Middle Devonian ROZ fairways are laterally extensive because of the conditions in which migration of oil occurred and ROZ indicators in a high proportion of the few wells present. Due to poor well control, the boundaries are uncertain. Nevertheless, the boundaries were chosen where geologic pinchouts were interpreted.

In comparison, the Cypress and Tar Springs ROZ fairways are considered better constrained because they are shallower, have more data control, and appear to be much more influenced by structure. In comparison to the Middle Devonian and Carper Sandstone ROZ fairways, the Tar Springs and Cypress Sandstone ROZ fairways, are narrow, somewhat linear features (Figure 6-80). The northernmost Cypress ROZ fairways occur in association with well-developed oil fields on significant structural folds (Clay City Anticline, Loudon Anticline, DuQuoin Monocline, Iola Anticline, and Mattoon Anticline; Figure 6-92). The southernmost Cypress and Tar Springs fairways coincide with oil fields developed along the Wabash Valley and Cottage Grove Fault Systems (Figure 6-92). Boundaries can be confidently established to the north where the formations deepen and ROZ indicators abruptly stop. The Tar Springs and Cypress Sandstone both contain rock asphalt and exhibit oil seeps in the subcrop and outcrop area of Kentucky in the southeastern portion of the ILB due to buoyancy driven oil migration (May 2013). Nevertheless, the southern boundary was established where well data diminishes.

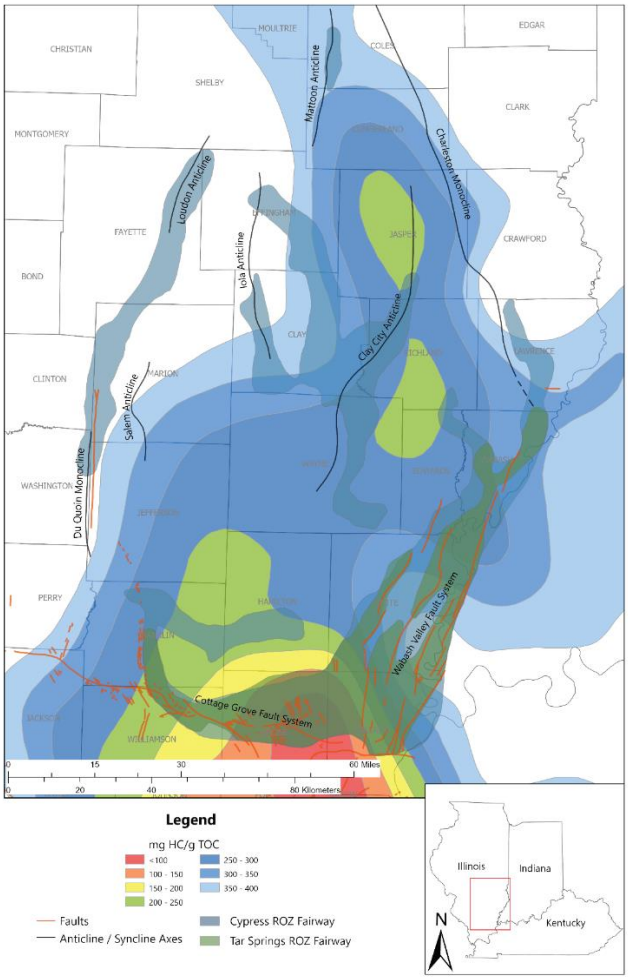


Figure 6-92. Map showing the Tar Springs and Cypress Sandstone ROZ Fairways in relation to mapped faults and significant structural anticline / syncline axes. The fairways are shaded over the oil generating part of the New Albany Shale with the most intense generation shown in red and the least intense shown in light blue.

ROZ Prospect Characteristics

The ROZs evaluated in this study have properties (e.g., saturation, thickness) that generally reflect their unique geology. The Tar Springs, Cypress, and Carper ROZs' OOIP are more certain than the Middle Devonian because of better data control and siliciclastic lithology (although the texture and complex mineralogy of the Carper introduce uncertainty in the calculation of ROZ S_O from well logs). Uncertainty in the OOIP of the Middle Devonian ROZ arises from poor data control and vuggy porosity.

In terms of oil saturation, average ROZ S_O values are between 23 and 32% (Figure 6-93), which is consistent with ROZ S_O values observed in Permian Basin fields (Harouaka et al., 2013) and in lab experiments (Honarpour et al., 2010). The broader range in oil saturations observed in the Tar Springs and Cypress when compared to the Carper are thought to reflect the higher reservoir quality of the former allowing lower S_{WIRR} of the paleo oil reservoirs and more efficient tertiary migration of oil. The much higher range of oil saturation observed in the Middle Devonian reflects the uncertainty in the log analysis to quantify the saturation, including intervals of mobile oil in the heterogeneous reservoir that were difficult to

differentiate, but also reflects geologic factors such as variation in pore size (i.e., the inclusion of both intercrystalline and vuggy porosity).

The Tar Springs and Cypress Sandstone ROZs have similar values for all ROZ properties (Figure 6-93). Conceptually this can be attributed to their similar geologic properties (e.g., grain size, mineralogy, porosity and permeability, depositional environment), but the high data density and straightforward well log analyses (thanks to adequate thickness coupled with simple lithology and well constrained TDS) of both also aided in characterization and led to repeatable results that were believed to converge on the true values.

The Carper Sandstone has similar S_O to the Tar Springs and Cypress, but significantly less porosity because it is finer grained with a higher clay content and some detrital to authigenic carbonate. Although the porosity is low, the Carper ROZs often occur in several stacked units, so the net thickness can be higher (Figure 6-93).

The complex lithology of the Geneva Dolomite creates a high degree of heterogeneity in porosity; consequently, net thickness results in uncertain calculations of S_O and unit volume (Figure 6-93). The Dutch Creek ROZ tends to occur within a thin, low porosity sandstone with varying amounts of dolomite that are embedded within a complex mixture of limestone and dolomite. This complex lithology, lack of modern well logs, and lack of brine data adversely affects characterization of Middle Devonian ROZs.

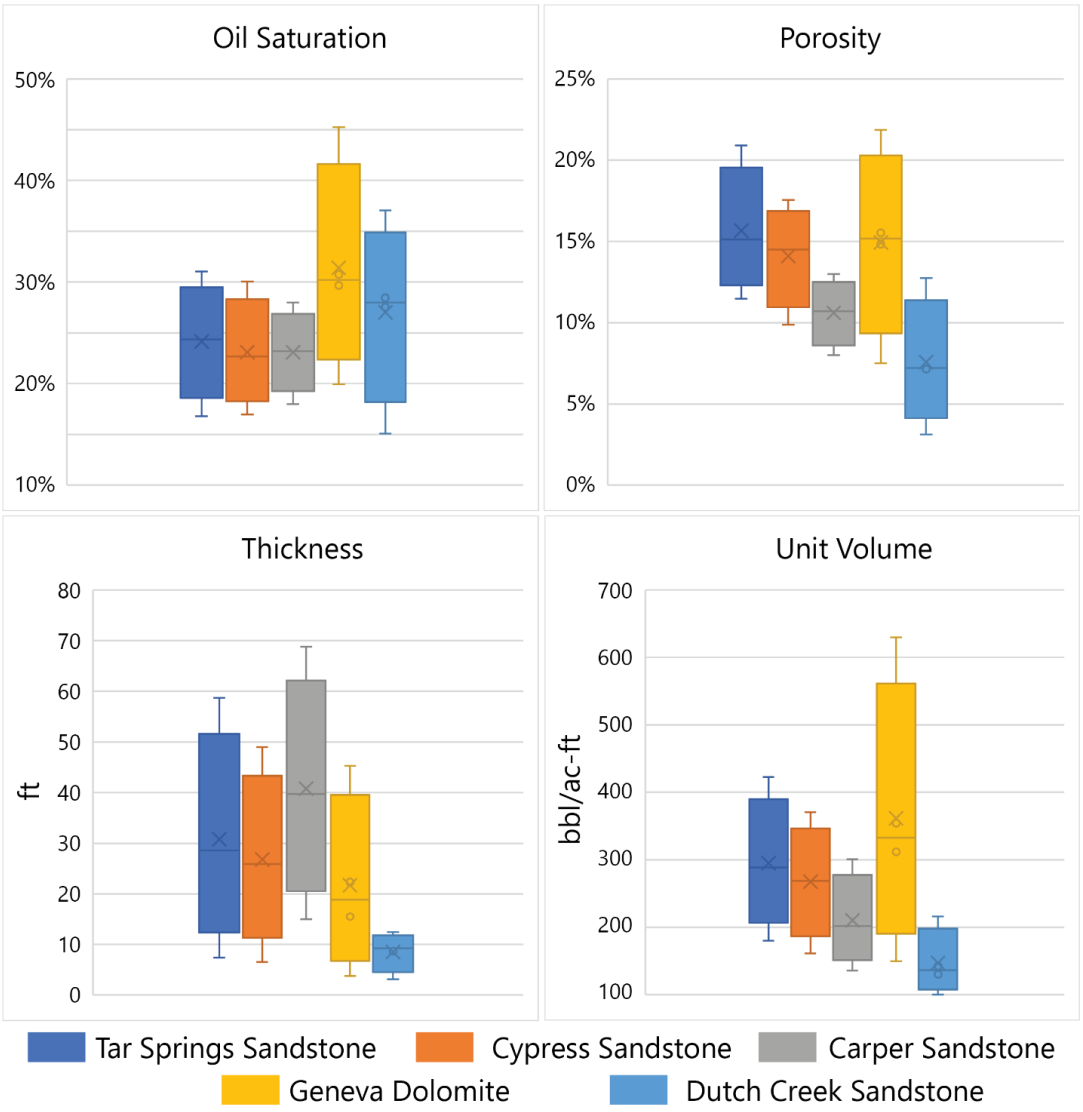


Figure 6-93. Box and whisker graphs showing ROZ properties, including oil saturation (upper left), porosity (upper right), thickness (lower left), and unit volume (lower right).

Stacked Storage

To maximize the utility of the CO_2 infrastructure investment, developers seeking to implement CO_2-EOR and associated storage may pursue areas with stacked storage in which two or more ROZs can be developed. Many Brownfield ROZs, especially those in the Cypress and Tar Springs, are within oil fields with mature oil reservoirs that occur in other formations that lack ROZs, but would be amenable to CO_2-EOR development. Other developers may prioritize CO_2 storage, with EOR being an added economic benefit. Several Greenfield ROZs were identified, especially in the Carper Sandstone (with additional potential in the Middle Devonian ROZ), that are overlying deeper brine aquifers that have significant storage potential.

There are several areas in Illinois with stacked ROZs fairways (Figure 6-80). Characterization of the ROZs allows for an estimate of the CO_2-EOR and storage in these areas, but the resource also exists apart from the defined prospects:

- The Tar Springs and Cypress ROZ Prospects in the White-Gallatin County area (i.e., Herald, Inman, Omaha, Roland, and Storms) include stacked Cypress and Tar Springs ROZs. These prospects are along the Wabash Valley Fault System, so fractures/faults are likely present and represent risk to seal integrity.
- Several Cypress ROZ Prospects in the Clay-Richland-Wayne County (LIST) are within brownfield ROZs that may extend beyond boundaries of existing oil fields. There is evidence to suggest that Carper and Middle Devonian ROZs exist within these prospects, but lack of data prohibits characterization (and prospect definition).
- The Carper Clay ROZ Prospect in the Fayette-Marion-Clay County area includes MPZs and ROZs in the Cypress and Carper Sandstones. The overlying Cypress ROZ appears to be limited to within, or very near, St. James oil field. Greenfield ROZs occur in the Carper Sandstone and Middle Devonian throughout the eastern half of Fayette County.
- The Carper Cumberland ROZ Prospect spans Effingham, Shelby, Cumberland, Crawford, and Jasper Counties and contains the Cypress Effingham ROZ prospect. Throughout the prospect, some isolated wells produce from the Middle Devonian (presumed to occur above pop-up reefs in the Silurian). Other isolated wells that encounter the Middle Devonian almost universally have oil indicators and thus define a greenfield ROZ.

Conclusions

ROZ fairways were identified within four formations in the Illinois Basin. In the Tar Springs and Cypress Sandstones, brownfield and greenfield ROZs occur in the upper portion of thick, clean sandstones and overlie brine aquifers. The Carper Sandstone contains a widespread greenfield ROZ fairway in which residual oil saturation occurs in multiple sandstone bodies that stack in some areas. Of the four ROZ fairways, the distribution Middle Devonian ROZ is the most uncertain, with widespread indications of oil within both the Geneva Dolomite and the Dutch Creek Sandstone.

The distributions of each formation's ROZ fairways are linked to geologic attributes of the Illinois Basin. There is evidence of ROZs forming by breached seals (Type 2 ROZ) and by intraformational hydrodynamic forces (Type 3 ROZ). The Middle Devonian and Carper Sandstone ROZs are stratigraphically near the source and thus likely received an oil charge over a relatively large area. The Tar Springs and Cypress Sandstone ROZ fairways are not as widespread because they are associated with fault systems and inferred fractures along major structural folds that provided local pathways for buoyant oil migration. There are several areas in Illinois with stacked ROZs that are co-located in greenfield and brownfields.

A methodology that combines several established well log analysis techniques (calculated water saturation, bulk volume water, moveable hydrocarbon index, and apparent water resistivity) was used with well records (such as oil shows and perforation depths) to quantify the oil saturation of the ROZs and characterize their distribution. Nearly 4.6 billion barrels of oil in place was estimated using volumetric method for 41 brownfield and greenfield ROZ prospects within the ROZ fairways. Residual oil saturation (S_{OR}) was 23 to 32% with saturations exceeding 40% found in the Geneva Dolomite. ROZs within defined prospects have thickness from less than 10 to nearly 70 ft. CO_2 EOR in the ROZ prospects is estimated 466 million barrels of oil, while the associated CO_2 storage is 394 million tonnes of CO_2.

Appendix 6-3

Middle Devonian ROZ

The Geneva Dolomite tends to be very productive where it occurs above Silurian reefs and non-productive where it does not (Seyler et al., 2003). A high proportion of wells with logs suitable for analysis are clustered in oil fields and indicate MPZs that equal the thickness of the porous formation. Only a handful of wells have suitable logs in off structure, presumably ROZ bearing areas of the fairway.

Table 6-A3. ROZ properties of the Middle Devonian ROZ.

Formation Name	Wells analyzed	ROZ		
		S_O (%)	ϕ (%)	Thickness (ft)
Geneva Dolomite	65	31	15	22.4
Dutch Creek Sandstone	13	26	7	9.3

The Root-Unkraut Comm #1 well (API: 120492514900) is provided here as a typical Geneva Dolomite ROZ example (Figure 6-A1). The well has a log suite that includes Pe and neutron density porosity. The scout ticket lists a very slight show of oil in the Geneva Dolomite from 3,788-3,822 ft and no show of oil in the lower Geneva Dolomite from 3,838-3,852 ft. A geologist's report corroborates with the scout ticket that the oil in the Geneva is in the top of the upper unit, but the depths are not listed.

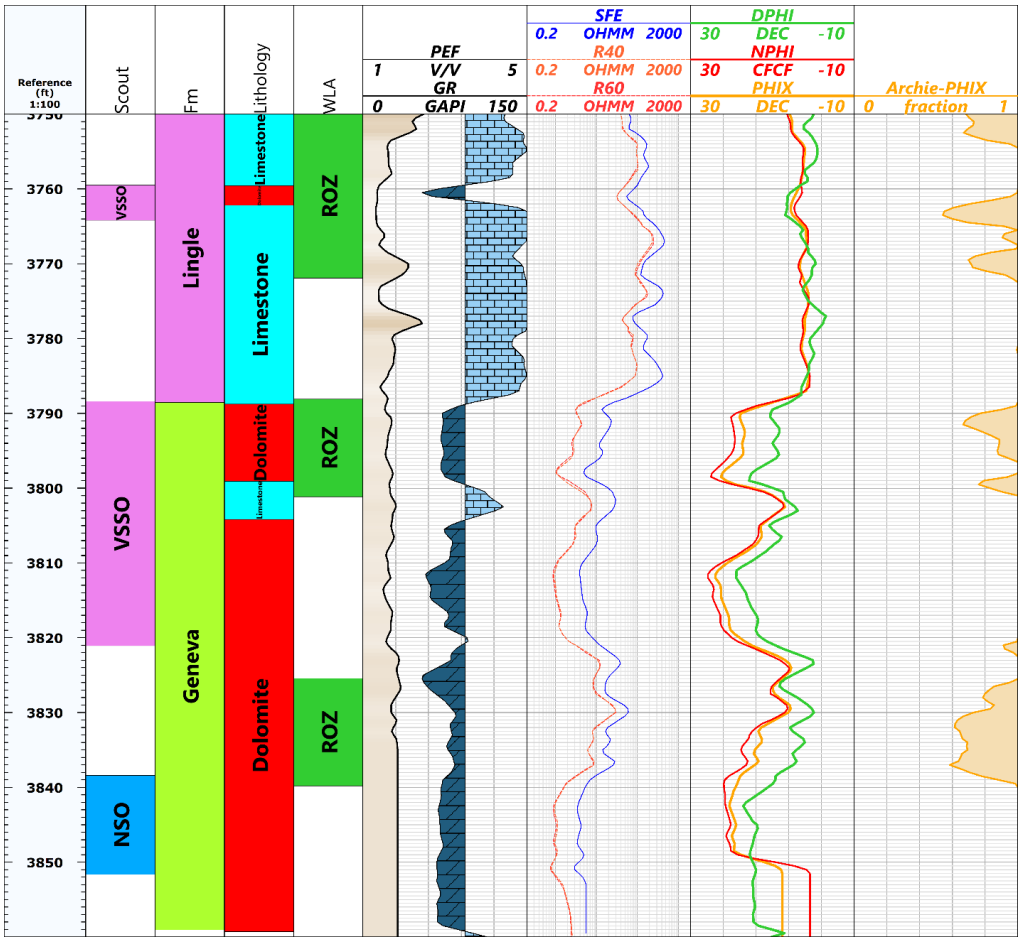


Figure 6-A1. Example log analysis of a Geneva ROZ taken from the Root-Unkraut Comm #1 well (API: 120492514900). Intervals listed with "very slight show of oil" on the scout ticket shown with VSSO, interval listed with "no show of oil" shown with NSO in the "scout" track. A Pe of 3 is used to differentiate limestone from dolomite. Archie S_w calculated with neutron-density porosity (Archie-PHIX, orange line and orange fill) generally agrees with the scout ticket, with calculated oil corresponding to very slight shows of oil listed in the Lingle and upper Geneva. However, Archies Equation also calculates oil in intervals not listed on the scout ticket. It is difficult to determine which of the calculated oil saturations are representative of reservoir condition.

Carper ROZ OOIP

The high estimate of OOIP (based on the total unbuffered area of the Carper ROZ prospects) is provided in Table 6-A4.

Table 6-A4. OOIP estimations over the full, unbuffered (with respect to well control) area of the Carper ROZ prospects.

Prospect	Area (ac; unbuffered)	ROZ OOIP (MMBO)
Clay	178,623.9	792.8
Coles	22,577.4	294.4
Cumberland	416,892.9	4,674.0
Fayette	27,740.6	249.6
Moultrie	2,240.3	22.5
Shelby	27,831.3	173.9

7. APPENDICES

7.1 Geochemical Characterization of Alteration of Holsapple 2B Oils and Correlation with Holsapple 2B Gases, Cumberland Co., Illinois

Author: Brooks A. Patterson (Stratum Reservoir)

Executive Summary

This study geochemically characterizes the process(es) responsible for alteration (abnormally low API gravity) of Holsapple 2B oils collected in Aug-2020 (Pre- CO_2 injection) and Aug-2021 (post CO_2 injection). In addition, Holsapple 2B gases sampled 1/27/21 – 9/27/21 (Post CO_2 injection) are characterized and correlated with the oils in order to determine if CO_2 has altered oil characteristics and production.

Holsapple 2B Oil Alteration Characteristics

High Resolution Gas Chromatography (HRGC) correlation and characterization of Pre- and Post-CO_2 injection Holsapple 2B oils, and recently collected G. Swits and Quaranta 5 oils indicates that all but Quaranta 5 oils exhibit variable light hydrocarbon evaporation. Aug-2020 pre-CO_2 injection Holsapple 2B oil is the most severely altered oil (nC$_6$-nC$_{10}$ depletion and BTX depletion). Aug-2021 post-CO_2 injection Holsapple 2B and G. Swits 2 oils are mildly altered (nC$_6$-nC$_{10}$ depletion).

The degree and pattern of evaporation suggests that low 29.1° API gravity measured in Holsapple Aug-2020 oil is due to the combination of light hydrocarbon evaporation and water washing (depletion of BTX aromatic HC's) with the increased level of alteration due to exposure of oil in the well bore during the prior four years while the well was shut in.

Slightly less depletion of nC$_6$-nC$_{10}$ HC's, the presence of high BTX aromatic HC's and less C$_{11}$+ n-paraffins observed in the post-CO_2 injection August-2021 Holsapple 2B oil probably represent the true Carper SS oil characteristics and suggest that the low 27.7° API gravity and nC$_6$-nC$_{10}$ HC depletion is likely due to mild in-reservoir evaporative fractionation.

Holsapple 2B oils are lower maturity oils derived from Type II marine kerogens. G. Swits and Quaranta 5 oils are suggested to be slightly lower maturity and derived from a similar Type II marine kerogen.

Post-CO_2 Injection Gas Characteristics

Twenty-seven Holsapple 2B post-CO_2 injection gases (1/27/2021 to 9/27/2021) are comprised of 90%+ CO_2 and ~5% C$_1$-C$_5$ HC gases. The HC gases are wet (C$_2$+ averages 36%). Both CO_2 and C$_1$-C$_5$ HC gases increase slightly with time.

Nine of 27 gases, selected for carbon isotopes (C$_1$, C$_2$, C$_3$, nC$_4$ and CO_2) and deuterium isotope (C$_1$) analyses, are isotopically variable with February and March-2021 gas characteristics reflecting startup production (i.e., near well bore) of a mix of predominantly injected CO_2 and ~1% HC gas (predominantly thermogenic with minor biogenic component), whereas April through September, 2021 gas characteristics reflect a mix of injected CO_2 and ~5.4% thermogenic HC gas and thermogenic CO_2 gas. The gases are suggested to have been generated at early oil-window maturity and slight increases in April through September 2021 ethane and propane isotopes suggest a slight increase in maturity over time.

Introduction and Objectives

ISGS client, Nathan Webb, requested that Stratum geochemically characterize Holsapple 2B oils collected in Aug 2020 and Aug-2021 to determine what process is responsible for the abnormally low gravity when

compared to Carper SS oils in the basin. To meet this objective, the Holsapple 2B oils were geochemically compared to G. Swits and Quaranta 5 oils. In addition, Holsapple 2B gases collected post-CO_2 injection (1/27/2021 and 9/27/2021) were available for characterization and correlation. Specifically, this study:

- Correlates 2020 and 2021 Pre- and post-CO_2 injection oils from Holsapple 2B with oils from G. Swits and Quaranta 5 wells and determines why Aug-2020 Pre- CO_2 injection oil is abnormally low gravity (i.e., what process has caused the oil to be a few degrees API low compared to oils in the region).
- Correlates 27 (Jan-2021 – Sept-2021) gas concentrations and 9 carbon isotopes (C_1-nC_4 and CO_2) and deuterium isotopes (C_1) and determines if post-CO_2 injection gas characteristics are stable or changing with time and possibly altering Holsapple 2B oil composition.

Conclusions (with supporting evidence)

Holsapple 2B Oil Characterization

High Resolution Gas Chromatography (HRGC) correlation and characterization of Pre- and post-CO_2 injection Holsapple 2B oils, and recently collected G. Swits and Quaranta 5 oils suggests that low 29.1° API gravity measured in Holsapple Aug-2020 oil is due to the combination of light hydrocarbon evaporation and water washing (depletion of BTX aromatic HC's) with the increased level of alteration due to exposure of oil in the well bore during the prior four years while the well was shut in.

Slightly less depletion of nC_6-nC_{10} HC's, the presence of high BTX aromatic HC's and less C_{11}+ *n*-paraffins observed in the post-CO_2 injection August-2021 Holsapple 2B oil probably represent the true Carper SS oil characteristics and suggest that the low 27.7° API gravity and nC_6-nC_{10} HC depletion is likely due to mild in-reservoir evaporative fractionation. These conclusions are evidenced as follows:

- G. Swits 2 and Holsapple 2B (2020 and 2021 samples) exhibit variable depletion of light HC's (depletion of nC_6-nC_{10} *n*-paraffins) greater than typically observed in dead oils. Quaranta 5 oil exhibits no nC_7+ hydrocarbon depletion.
- Holsapple 2B (Aug-2020, Pre-CO_2 injection) exhibits the most severe light HC depletion resulting in a well-developed concave nC_7-nC_{11} *n*-paraffin depletion distribution with an apex at nC_{11}. This deltoid shape is common in oils that have undergone severe exposure or in-reservoir evaporative fractionation (gas stripping).
- G. Swits 2 and Holsapple 2B (Aug-2021, post-CO_2 injection) oils light HC's are less depleted than the Holsapple 2B (Aug-2020, Pre-CO_2 injection) oil. Both exhibit convex depletion patterns suggesting that the light HC depletion is less severe than observed in the 2020 Holsapple 2B oil and may be due to a less severe evaporative process.
- Comparison of the study oil characteristics and compound class contents indicates that the most severely evaporated oil, Aug-2020 pre-CO_2 injection Holsapple 2B, contains lowest nC_6-nC_{10} paraffins and BTX aromatics and the greatest nC_{11}-nC_{30} paraffins. Aug-2021 post-CO_2 injection Holsapple 2B oil measured slightly greater nC_6-nC_{10} paraffins (17.5 ppt vs. 16.2 ppt), ~4x greater BTX aromatics (7.8 ppt vs. 2.1 ppt) and less nC_{11}-nC_{30} paraffins (45.5 vs. 68.5 ppt). API gravity correlates best with nC_6-nC_{10} levels (i.e., lower gravity oils are depleted in light *n*-paraffins).
- Holsapple 2B (Aug-2020 pre-CO_2 injection) oil measured greater nC_{11}-nC_{30} paraffins than the other study oils (possible concentration after depletion of light *n*- paraffins and BTX aromatics).

Table 7-1. Comparison of API, molecular fractions and BTX aromatics (red fill = low value, green fill = high value).

Characteristic	G. Swits 2	Holsapple 2B (2020)	Holsapple 2B (2021)	Quaranta 5
C_6+ Evaporation	Mild	Severe	Mild	Non
API Gravity (°)	29.3	29.1	27.7	32.5
nC_6-nC_{10} (ppt)	18.1	16.2	17.5	30.5
BTX Aromatics (ppt)	3.6	2.1	7.8	5.8
nC_{11}-nC_{30} (ppt)	47.9	68.5	45.5	60.6

- All four oils have low toluene/nC_7 ratios (0.1-0.3) and moderate nC_7/MCH ratios (0.75-0.83). High toluene/nC_7 (> 1.0) and low nC_7/MCH (< 0.5) ratios suggest evaporative fractionation; therefore, the study oils, particularly the 2020 pe-CO_2 injection Holsapple 2B oil, are not confirmed as stripped by evaporative fractionation. Lower nC_6-nC_{10} alkanes and BTX aromatics in the Aug-2020 Holsapple 2B oil appears due to the combination of light HC evaporation and water washing (partial removal of more soluble BTX) plausibly occurring while shut in for ~4 years.
- Iso-paraffin/*n*-paraffin ratios (Pr/nC_{17} and Ph/nC_{18}) separate Holsapple 2B oils (2020 and 2021) from G Swits 2 oil from Quaranta 5 oil and separation is supported by IP_{11}/nC_{10} – IP_{13}/nC_{12} ratios. These differences are consistent with maturity differences (Holsapple > G. Swits > Quaranta); however, may also be due to slight source differences.
- Oil maturity based on light and mid-HC ratios generally agree suggesting that the oils are early to peak oil-window maturity and Holsapple 2B oils are slightly greater maturity than G. Swits 2 oil which is slightly greater maturity than Quaranta 5 oil.

Holsapple 2B Gas Characterization

Twenty-seven Holsapple 2B post-CO_2 injection gases (1/27/2021 to 9/27/2021) are comprised of 90%+ CO_2 and ~5% C_1-C_5 HC gases. The HC gases are wet (C_2+ averages 36%). Both CO_2 and C_1-C_5 HC gases increase slightly with time.

Nine of 27 gases, selected for carbon isotopes (C_1, C_2, C_3, nC_4 and CO_2) and deuterium isotope (C_1) analyses, are isotopically variable with February and March 2021 gas characteristics reflecting startup production (i.e., near well bore) of a mix of predominantly injected CO_2 and ~1% HC gas (predominantly thermogenic with minor biogenic component), whereas April through September, 2021 gas characteristics reflect a mix of injected CO_2 and ~5.4% thermogenic HC gas and CO_2 gas. The gases are suggested to have been generated at early oil-window maturity and slight increases in April through September 2021 ethane and propane isotopes suggest a slight increase in maturity over time. Gas concentration and isotope data indicates the following:

- 26 of 27 post-CO_2 injection gases are predominantly CO_2 and excluding one sample, 2/24/2021 with suspect air contamination, range from 90.1% to 99.3% and CO_2 decreases slightly with time.
- Total C_1-C_5 HC gases are significant ranging from 127-82,380 ppm with an average of 43,901 ppm (~5% of the total gas). Methane is predominant HC gas, ranging from 35.4-80.7% and averaging 64.5%. The HC gases are wet with C_2+ ranging 19.3-64.6% and averaging 35.5%. Three gases (2/8/21-3/3/21) measured unusually low methane and are the wettest gases

(51.5-64.6% C_2+).

- C_6+ liquid HC's are present ranging 0.01-0.22%, often exceeding pentane contents and generally increase slightly with time.
- Gas carbon (C_1, C_2, C_3, nC_4 and CO_2) and deuterium (C_1) isotopes vary greater than instrumental error; generally increasing over time (i.e., becoming isotopically heavier).
- HC gases are predominantly thermogenic gases; however, minor contribution of light biogenic gas cannot be excluded particularly in gases collected 2/4 and 3/9, 2021. Thermogenic gas components appear to have been generated from two different sources or expulsions of predominantly marine source rock ($\delta^{13}C$ C_2 is ~ 2.5‰ light if generated from a single source).
- Gas maturities are suggested to have been generated at early oil-window and slightly increase with time (i.e., similar maturity as Holsapple 2B oils).

Carper SS Oil Alteration - Gas CO_2 Injection

Pre-CO_2 injection Holsapple 2B oil light HC's and BTX aromatics are severely depleted.

Post-CO_2 injection Holsapple 2B oil is less severely altered (> nC_6-nC_{10} HC's and BTX aromatics). One would not expect a decrease in the level of oil alteration in the period of one year (Aug-2020 – Aug-2021); therefore, it appears plausible that the pre-CO_2 injection Holsapple 2B oil was further altered during ~4 years residence in the shut-in wellbore while exposed to air and water, and the less severely altered Aug-2021 Holsapple 2B oil light HC depletion reflects the actual light HC depletion in the Carper SS.

Holsapple 2B (Post-CO_2 injection Aug-2021) oil exhibits similar degree of alteration as G. Swits oil (mild depletion of nC_6-nC_{10}); however, Holsapple 2B oil contains ~2x the BTX aromatics. Assuming both oils are representative of the Carper SS oil (i.e., minimal light HC evaporation during collection-transfer-shipping), both oils appear to have been subjected to mild evaporative fractionation. The difference in BTX aromatics is either due source expulsion/migration history or G. Swits 2 oil is water washed.

Materials and Methods

Sample Identification

Two Holsapple 2B oils collected on 8/24/2020 and 8/31/2021 and oils from G. Swits 2 and Quaranta 5 wells (Figure 7-1 well location map) were authorized by ISGS client for API gravity and High Resolution Gas Chromatography analyses (Table 7-2A, below). Additionally, 27 production gases from Holsapple 2B collected post-CO_2 injection (1/27/2021-9/27/2021) were analyzed for full C_1-C_6+ and fixed gas GC analyses. Nine of 27 gases were selected for offline carbon isotopes of C_1, C_2, C_3, $nC4$ and CO_2 and deuterium isotopes of C_1 (Table 7-2B, below).

Table 7-2A. Identification of oil samples and analyses

Sample Identification				Analyses	
Well	**Lab_No**	**Sample Date**	**Reservoir**	**API Gravity**	**GC ID's**
G. Swits 2	6132371276		Carper SS	1	G3200723.D
Holsapple 2B	6132371278	8/24/2020	Carper SS	1	G3200724.D
Holsapple 2B	6132772443	8/31/2021	Carper SS	1	G3210605.D
Quaranta 5	6132810649		Carper SS	1	G6210557.D

Table 7-2B. Identification of gas samples and analyses. Gas isotopes were analyzed using the offline method with exception of three gases that separated insufficient quantities of methane, propane and n-butane and required online isotope measurement.

Sample Identification				Analyses						
Well	Lab No	Sample Date	Sample Time	C_1-C_6+	$\delta^{13}C$ C_1	$\delta^{13}C$ C_2	$\delta^{13}C$ C_3	$\delta^{13}C$ *n* C_4	$\delta^{13}C$ CO_2	$\delta^{2}H$ C_1
Holsapple 2B	804927	1/27/2021	11:30	1						
Holsapple 2B	804928	2/4/2021	9:15	1	1	0	1	1	1	1
Holsapple 2B	783810	2/8/2021	16:15	1						
Holsapple 2B	804929	2/24/2021	11:10	1						
Holsapple 2B	785475	3/3/2021	11:22	1						
Holsapple 2B	804930	3/9/2021	15:15	1	1	1	1	1	1	1
Holsapple 2B	804931	3/16/2021	14:45	1						
Holsapple 2B	790000	4/15/2021	11:00	1						
Holsapple 2B	790666	4/27/2021	10:00	1	1	1	1	1	1	1
Holsapple 2B	791609	5/4/2021	10:00	1						
Holsapple 2B	791906	5/11/2021	10:00	1	1	1	1	1	1	1
Holsapple 2B	792447	5/18/2021	10:00	1						
Holsapple 2B	795356	6/15/2021	10:00	1	1	1	1	1	1	1
Holsapple 2B	795967	6/22/2021	11:00	1	1	1	1	1	1	1
Holsapple 2B	796760	6/29/2021	11:00	1						
Holsapple 2B	796929	7/6/2021	13:00	1						
Holsapple 2B	797669	7/13/2021	13:30	1	1	1	1	1	1	1
Holsapple 2B	798966	7/20/2021	13:30	1						
Holsapple 2B	799333	7/27/2021	11:00	1						
Holsapple 2B	800243	8/3/2021	13:00	1	1	1	1	1	1	1
Holsapple 2B	801600	8/17/2021	11:30	1						
Holsapple 2B	802131	8/24/2021	11:30	1						
Holsapple 2B	802581	8/31/2021	11:00	1						
Holsapple 2B	802928	9/7/2021	11:00	1						
Holsapple 2B	803655	9/14/2021	11:00	1						
Holsapple 2B	804362	9/20/2021	11:00	1						
Holsapple 2B	804932	9/27/2021	11:00	1	1	0	1	1	1	1
		Analysis Counts		*27*	*9*	*7*	*9*	*9*	*9*	*9*

black = offline, red = online

Oil data is shown on Table 7-3 at the end of the text portion of this report. Holsapple 2B gas concentration and isotope data are tabulated on Tables 7-4 and 7-5 at the end of the text portion of this report. Stratum Reservoir oil GC summary reports are located in Appendix 7-1. Isotech gas data reports for the Holsapple 2B gases are located in Appendix 7-2.

Background on the Geochemical Techniques

Analysis of Oils - Using Gas Chromatography to Determine Alteration and Reservoir Continuity

Geochemical determination of reservoir continuity is based on the well-established proposition that oils from separate reservoirs tend to differ from one another in composition (e.g., Slentz, 1981; Kaufman et al., 1990; Hwang and Baskin, 1994; Hwang et al., 1994). Depending on the field, these compositional differences exist for one or more of the following three reasons:

1. Processes that affect oil composition after oil enters a reservoir (e.g., processes such as biodegradation, water washing, and evaporative fractionation) do not operate to exactly the same extent in separate compartments.
2. Oil which a source rock generates at a given time differs slightly both from subsequently generated oil and previously generated oil due to continuous, subtle changes in the maturity of the source rock and changes in precisely which part of the source rock is in the oil window. Since no two compartments are of identical geometry, and since no two compartments have exactly the same filling history, it is difficult to achieve precisely the same homogenized composition in two separate compartments - even with oil from the same source.
3. More than one source rock may contribute oil to an accumulation, and the oils from different sources differ in composition. Since oils from different source rocks have different times of generation and/or different migration paths, the presence of more than one source may cause different compartments to fill with different mixes of oil from the respective sources. For example, Prudhoe Bay oil is known to be a mixture of petroleum from three source rocks (Masterson et al., 1997), and source variations are therefore a significant cause of the compositional differences in that field.

The technique assesses whether or not two oils are in fluid communication by comparing for each oil the relative abundances of the several hundred "inter-paraffin" peaks identifiable on a whole oil gas chromatogram or "GC". Inter-paraffin peaks are those compounds that elute from the GC between the normal-paraffins. The patterns for each sample are compared as follows:

- Corresponding inter-paraffin peaks are identified in all samples.
- For a given sample, several hundred ratios of closely spaced inter-paraffin peaks are compared with the corresponding ratios in the other samples.
- The ratios that differ the most between samples are identified.
- Values for these ratios for each sample are plotted on polar or "star" plots. On such diagrams, the composition of each oil is represented by a "star" in which each point on the star corresponds to the value for a given peak ratio.

Analysis of Gases

The gas samples were analyzed by Isotech Laboratories Inc. (Champaign, IL) for their chemical composition (methane, ethane, propane, butanes, pentane, C_6+, carbon dioxide, nitrogen, and oxygen) with a gas chromatograph calibrated with standards consisting of gas mixtures that span the range of compositions

observed in natural gas. The reproducibility of such analyses is generally 2% or better. Carbon isotopic compositions ($^{13}C/^{12}C$) of the hydrocarbon gases (methane, ethane, propane, n-butane and n-pentane) were determined using an off-line method where the chromatographically separated hydrocarbon gases are isolated and injected the inlet of an isotope ratio mass spectrometer. Reproducibility is generally ±0.1 per mil (‰) for production gases. Hydrogen isotopic composition ($^{2}H/^{1}H$) of methane was determined by reduction of water from combustion with zinc metal followed by dual-inlet isotope ratio mass spectrometry. Reproducibility of such analyses is generally ±3.5 per mil (‰). Carbon isotopic compositions were referenced to PDB (Peedee belemnite) and hydrogen isotopic compositions were referenced to SMOW (Standard Mean Ocean Water) calibrated by NBS (National Bureau of Standards) stable isotope standards.

Delta (δ) - Notation

The individual gas components: methane, ethane, propane, iso-butane and n-butane can be characterized by their stable carbon ($^{13}C/^{12}C$) and hydrogen ($^{2}H/^{1}H$) isotopic compositions. The heavy isotopes ^{13}C and ^{2}H (or deuterium, D) are the rare species and (on average) amount to ~1% of all carbon and ~150 ppm of all hydrogen, respectively. Small variations in $^{13}C/^{12}C$ and D/H ratios can be measured very accurately with modern mass spectrometers. For convenience, ratios are normally expressed in δ-notation as part per thousand (‰) variations relative to the PDB (carbon) and SMOW (hydrogen) isotope standards as follows:

$$\delta^{13}C\,(‰) = \left[\frac{(^{13}C/^{12}C)_{sample}}{(^{13}C/^{12}C)_{PDB}} - 1 \right] \times 1000$$

$$\delta D\,(‰) = \left[\frac{(D/H)_{sample}}{(D/H)_{SMOW}} - 1 \right] \times 1000$$

Because PDB and SMOW are enriched in ^{13}C and D relative to most natural gases, the latter almost always have negative $\delta^{13}C$ and δD values.

Carbon and hydrogen isotope ratios are conservative properties, which do not change significantly upon depressurization, solution or dissolution, or because of other physical processes, which take place during oil and gas production. Therefore, stable isotope concentrations in natural gases are independent of reservoir and sampling conditions rendering themselves as useful tracers for many gas field operations.

Results and Discussion

Holsapple 2B Oil Characteristics

This section discusses API and gas chromatography characteristics of the two "altered" Holsapple 2B oils (8/24/20 and 8/31/21) and G. Swits 2 and Quaranta 5 oils.

The four oils are slightly different gravities: 27.7° API (Post CO_2 injection Holsapple 2B, Aug-2021), 29.1° API (Pre-CO_2 injection Holsapple 2B, Aug-2020), 29.3° API (G. Swits) and 32.5° API (Quaranta 5). Gravities < 32° API appear to be abnormally low suggesting that all but Quaranta 5 oils are altered.

In-reservoir alteration processes such as biodegradation, evaporative fractionation and water washing are best identified using gas chromatography. Therefore, the next several figures explore each of the oil's molecular distributions.

Figure 7-2 is a whole oil gas chromatogram of oil from Holsapple 2B (3688') collected Aug-2020 after ~4 years being shut in (pre-CO_2 injection). The 29.1° API oil is paraffinic and non-biodegraded. However, C_7-C_{11} *n*-paraffins are severely depleted (concave pattern) either from long-term exposure or an in-reservoir process such as evaporative fractionation.

The next gas chromatogram, Figure 7-3, shows the Holsapple 2B (3688') collected Aug- 2021 (post-CO_2 injection). This 27.7° API oil is also paraffinic and non-biodegraded. As observed in the pe-CO_2 injected oil, C_7-C_{11} *n*-paraffins are depleted; however, the extent of depletion is less severe (convex pattern) and either from long-term exposure or an in- reservoir process such as evaporative fractionation.

Figure 7-4 compares the two Holsapple 2B light nC_4-nC_{11} HC gas chromatograms of oils collected Aug-2020 (top) and Aug-2021 (bottom). The nC_4-nC_{10} fingerprints appear different as the post-CO_2 injection nC_6-evaporation is more severe and the nC_7+ evaporation appears less severe than observed in the 2020 oil. The 2021 oil also contains ~4 times greater BTX (EB, TOL, MXYL, PXYL, OXYL, PB) and addition or enhancement of several mid-C_9+ non-identified compounds.

Figure 7-5 shows the nC_{12}-nC_{28} light HC gas chromatogram comparison of Holsapple 2B (3688') oils collected Aug-2020 (top) and Aug-2021 (bottom). The higher molecular weight fingerprints are very similar suggesting alteration has not differentially affected the mid to high molecular weight portion of the oil. However, the pre-CO_2 oil contains a greater quantity of *n*-paraffins than the post-CO_2 oil.

The next GC, Figure 7-6, is the gas chromatogram of oil from G. Swits 2. This 29.1° API oil is paraffinic and non-biodegraded. C_{11}- *n*-paraffins have been evaporated at similar degree as Holsapple 2B post-CO_2 oil and alteration appears due either to long-term exposure or an in-reservoir process such as evaporative fractionation.

Figure 7-7 shows the gas chromatogram of oil from Quaranta 5. The 32.5° API oil is paraffinic and non-biodegraded. This oil is not altered and exhibits minimal light hydrocarbon evaporation typical with collection of dead oils.

Figure 7-8 is a line diagram comparing API gravity, *n*-alkane and BTX compound classes (see Table 7-1 above). Decrease in API gravity correlates best with decreases in light *n*- paraffins. 2020 Pre-CO_2 injection Holsapple 2B oil measured slightly lower nC_6-nC_{10} paraffins (exposure or evaporative fractionation), lowest BTX aromatics (water washing) and greatest nC_{11}-nC_{30} paraffins (concentration). 2021 post-CO_2 injection Holsapple 2B oil measured similar nC_6-nC_{10} paraffins as G. Swits 2 oil (mild depletion), greatest

BTX aromatics (absence of water washing) and similar nC_{11}-nC_{30} paraffins as G. Swits 2 oil.

A ternary diagram of comparing the percentages of normal-paraffins, cyclo-paraffins and iso-paraffins in the study oils is shown on Figure 7-9. Oils that exhibit mild to moderate evaporation are more normal-paraffinic and less cyclo-paraffinic and iso-paraffinic than the non-altered Quaranta 5 oil.

The next diagram, Figure 7-10, is a cross-plot of light hydrocarbon parameters that are affected by evaporative fractionation (modified from Thompson, 1983 and 1987). Evaporative fractionation is a process in which dry gas enters an oil accumulation, and strips off light ends, preferentially removing the saturate vs. aromatic compounds straight-chain vs. cyclic and branched compounds; the gas then migrates to a shallower depth, and may drop out its condensate load as a "retrograde condensate" in a shallower reservoir. The residual oil would then be characterized by a high toluene/*n*-heptane ratio and a low *n*-heptane/methylcyclohexane ratio. Low toluene/nC_7 ratios (0.1-0.3) do not conclusively support that the Holsapple 2B oils are residual oils after evaporative fractionation and gas stripping. Increased toluene/nC_7 ratios do not fully correlate with the level of evaporation observed in the study oils.

A ternary diagram showing distribution of light hydrocarbons: 3-RP isoalkanes (Lacustrine), 5-RP cyclopentanes (Marine) and 6-RP cyclohexanes (Terrigenous) is on Figure 7-11. Mango (1994) referred to the importance of ring preferences in the formation of light hydrocarbons. In general, oils derived from marine kerogens tend to be enriched in the cyclopentanes (5-RP), those derived from predominantly lacustrine source rocks are enriched in iso-alkanes (3-RP), and oils from primarily terrigenous organic matter are usually enriched in cyclohexanes (6-RP). The study oils exhibit significant variations in cyclopentanes and cyclohexanes and insignificant variations in isoalkanes. These variations do not correlate fully with observed levels of evaporation suggesting that there is a possible source difference.

Figure 7-12 is a cross-plot comparing Pristane/Phytane (Pr/Ph) and nC_{17}/nC_{29}, both of which are subject to source differences. These mid-high molecular weight range parameters should not be influenced by the observed variable light hydrocarbon evaporation and water washing. Holsapple 2B oils measured lower Pr/Ph ratios than G. Swits 2 and Quaranta 5 oils suggesting a slight difference in source rock contribution (i.e., slightly greater terrigenous contribution to G. Swits and Quaranta 5 oils). Holsapple 2B oil measured intermediate nC_{17}/nC_{29} ratios, G Swits has the > nC_{17}/nC_{29} ratio and Quaranta 5 oil has the lowest nC_{17}/nC_{29} ratio.

Isoprenoid/*n*-alkane ratios are routinely used as indicators of biodegradation, maturity and organic facies (Figure 7-13). Holsapple 2B oils measured lower Pr/nC_{17} and Ph/nC_{18} ratios than G Swits 2 and Quaranta 5 oils (i.e., > nC_{17} and nC_{18} paraffins are consistent with greater paraffin content). The study oils plot in the "Mixed Oil/Gas Prone" region; however, they all plot very near the "Marine line" consistent with a predominant marine source. The differences among the study oils appears due to maturity (Holsapple 2B > G. Swits 2 > Quaranta 5) and not biodegradation.

Isoprenoid/*n*-alkane ratios, IP11/nC_{10} and IP13/nC_{12}, are also maturity indicators (Figure 7-14). Lower IP11/nC_{10} and IP13/nC_{12} ratios suggest that the two Holsapple 2B oils are more mature than the G Swits 2 oil and the Quaranta 5 oil.

Figure 7-15 compares Thompson light hydrocarbon ratios, nC_7/MCH and Heptane Values which are relative maturity indicators. Study oil nC_7/MCH vary insignificantly whereas the Heptane Values suggests that Holsapple 2B oils are slightly higher maturity than G Swits 2 and Quaranta 5 oils (similar maturity order as suggested on the previous figures).

The ratios of 2,4-DMP/2,3-DMP and 2-MH/3-MH are "temperature-of-generation" indicators (Koblova et al., 1980; Mango 1987) and reflect levels of thermal maturity of a homologous oil family. Of the two ratios, 2,4-DMP/2,3-DMP is thought to be the better temperature function (Mango, 1990). A parameter based on the 2,4-DMP/2,3-DMP ratio developed by BeMent et al. (1994), Ctemp {ºC=140+15[ln(2,4-DMP/2,3-DMP)]}, estimates the temperature of hydrocarbon expulsion. Figure 7-16 shows the estimated expulsion values (115-123° C) and suggests that the study oils were generated in the oil- window. However, this maturity trend conflicts with the previous maturity trends (e.g., 2021 Holsapple 2B oil < Quaranta 5 oil); possibly due to differential light HC evaporation or the oils do not constitute a homologous oil family.

Summary of Holsapple 2B Alteration Conclusions

High Resolution Gas Chromatography (HRGC) correlation and characterization of Pre- and Post-CO_2 injection Holsapple 2B oils, and recently collected G. Swits and Quaranta 5 oils indicates that all but Quaranta 5 oils exhibit variable light hydrocarbon evaporation. Aug-2020 pre-CO_2 injection Holsapple 2B oil is the most severely altered oil (nC_6-nC_{10} depletion and BTX depletion). Aug-2021 post-CO_2 injection Holsapple 2B and G. Swits 2 oils are mildly altered (nC_6-nC_{10} depletion).

The degree and pattern of evaporation suggests that low 29.1° API gravity measured in Holsapple Aug-2020 oil is due to the combination of light hydrocarbon evaporation and water washing (depletion of BTX aromatic HC's) with the increased level of alteration due to exposure of the oil in the well bore during the prior four years while the well was shut in.

Slightly less depletion of nC_6-nC_{10} HC's, the presence of high BTX aromatic HC's and less C_{11}+ *n*-paraffins observed in the post-CO_2 injection August-2021 Holsapple 2B oil probably represent the true Carper SS oil characteristics and suggest that the low 27.7° API gravity and nC_6-nC_{10} HC depletion is likely due to mild in-reservoir evaporative fractionation.

Holsapple 2B oils are lower maturity oils derived from Type II marine kerogens. G. Swits and Quaranta 5 oils are suggested to be slightly lower maturity and derived from a similar Type II marine kerogen.

Holsapple 2B Gas Characteristics, Source and Maturity

This section discusses the characterization of 27 Holsapple 2B gases collected 1/27/21- 9/27/21. Specifically, this study will determine:

- Hydrocarbon constituent concentrations of the gases.
- Methane, ethane, propane and CO_2 isotopic signatures of the gases.
- Gas collection time compositional/isotopic relationships.
- The type and maturity of the source rock(s) that generated the thermogenic gases.

The first diagram, Figure 7-17, compares %CO_2 and BTU line plot of 2021 post-CO_2 injection gases from Holsapple 2B. With the exception of gas collected 2/24/21 (suspect air contamination) the gases are predominantly CO_2 (90.1-99.3%) and CO_2 decreases slightly over time.

Figure 7-18 shows CO_2 content vs. $\delta^{13}C$ CO_2 for Holsapple 2B gases. The gases measured > 90% CO_2 and $\delta^{13}C$ CO_2 varies slightly (-41.3‰ to -39.4‰, Δ = 1.9‰); with a slight isotopic increase with time (If injected in 2020 why is CO_2 changing isotopically over time?). CO_2 is injected and its origin is not confirmed; however, these data suggest that the CO_2 is from hydrocarbon oxidation. The combination of decreasing CO_2 content and increasing $\delta^{13}C$ CO_2 suggests that the isotopically heavier CO_2 derived from kerogen

decarboxylation is increasing with time.

Figure 7-19 is a C_1-C_6+ line plot of 2021 post-CO_2 injection gases from Holsapple 2B. The HC gases are predominantly C_1 (0.001-5.7%). C_1 and C_2+ increase slightly over time. Gases collected 1/27/21-4/15/21 vary significantly more than gases collected 5/4/21- 9/27/21. C_6+ liquid HC's are present and often greater than pentanes.

The next diagrams, Figures 7-20 through 7-22 are a series of chemical composition time logs that compare the Holsapple 2B gases. Each sample collection time is identified on the left tracts and right margins. Figure 7-20 left track shows the total C_1-C_5 hydrocarbons and middle tract plots the well/reservoir unit concentrations in parts per million of the hydrocarbon gases methane through C_5 and the total gas (hydrocarbons). The right tract logs the down-hole concentrations in volume % of the hydrocarbon gases methane through C_5 of the normalized gas (100% = C_1+C_2+C_3+C_4+C_5). Total HC gas ranges from 127-82,380 ppm (left track) and increase with time. Abnormally low total HC gases occur in Feb-2021 (suspected air contamination) and Aug-3 (well shut in and CO_2 buildup). The gases measured significant quantities of C_2-*n*C_5 HC's. Normalized methane contents range from 35.4-80.7% (right track) and the C_2+ components ranging from 0 to 42.6% (average = 5.9%).

Figure 7-21 gas component time log shows that CO_2 is high ranging 9700-992,800 ppm (average = 91%). Methane is the predominant HC gas (35.4-80.7%, average = 64.5%) and stabilizes after April-2021. Ethane and propane are present and variable (10-12,300 ppm and 12-7420 ppm, respectively). Both ethane and propane increase significantly from 1/27/21 to 4/27/21 and then slightly from 4/27/21 to 9/27/21.

Figure 7-22 gas chemistry time log compares C_4+ gas component concentrations for post- CO_2 injection Holsapple 2B. C_4-C_5 concentrations are significant and variable in the study gases (butanes range 0-3440 ppm and pentanes range 2-1230 ppm). C_6+ contents are significant (54-2160 ppm) consistent with co-generation of liquid HC's.

The next several diagrams compare Holsapple 2B well gas isotope compositions. The first, Figure 7-23, shows the summary of the C_1, C_2, C_3, and *n*C_4 carbon isotopic compositions for Holsapple 2B storage gases collected 1/27/21-9/27/21 (9 of 27 were submitted for isotope analysis). The storage gases exhibit isotope trends typical of thermogenic gases (i.e., $C_1 < C_2 < C_3 <$ *n*C_4). Methane gases collected February and March are isotopically lighter than the later collected gases. Ethane could not be measured in two gases, 2/4/21 and 8/3/21.

Gas C_2+ wetness and carbon isotope summary log for Holsapple 2B gases collected between 1/27/2021 – 9/27/2021 (post-CO_2 injection) is shown on Figure 7-24. The gases are wet ranging from 19.3-64.6% C_2+ (center track) with wettest gases in February and early March (near air contaminated sample). Methane carbon isotopes range from -53.6 to -51.5‰ (Δ = 2.1‰ which exceeds online and offline instrumental error) with February-March gases significantly lighter than April-September gases. Ethane and propane carbon isotopes exhibit less variability with $\delta^{13}C$ C_2 ranging -42.9‰ to -42.2‰ (Δ = 0.7‰) and $\delta^{13}C$ C_3 ranging -36.3‰ to -35.2‰ (Δ = 1.1‰ and greater than instrumental error).

Figure 7-25 shows Holsapple 2B C_1-*n*C_4, CO_2 carbon and C_1 deuterium isotope tracts with relative gas isotope signatures. Pink rectangles show the off-line method instrumental error (±0.1‰ for carbon isotopes and ±2.0‰ for deuterium isotopes). Note that gases collected 2/4, 3/9 and 8/3 methane, propane and *n*C_4 required online analysis which has about two-times the instrumental error (±0.2‰ for

carbon isotopes and ±5‰ for deuterium isotopes). Black horizontal lines indicate compositional change; dashed horizontal lines are questionable compositional change due to greater online instrumental error. Excluding the 8/3/21 gas, the components generally get heavier with time.

Stable carbon isotopic compositions of the hydrocarbon gases plotted on the reciprocal carbon number Chung plot (Chung et al., 1988) for Holsapple 2B storage gases is on Figure 7-26. Chung postulated that gas components generated from a single source exhibit a semi-linear reciprocal isotope trend; therefore, this diagram suggests that the gases represent mixtures from more than one source with C_1-C_2 providing one possible relationship and C_1-C_3-nC_4 a different relationship. The C_1-nC_4 dashed red trend line approximates the trend of gas components from a single source with C_2 deviating -2.5‰ from the best-fit linear C_1-nC_4 tend line at greater than instrumental error. February and March gas methane is light possibly due to mixing with light biogenic gas. Extension of the two linear relationships to the left axis provides an estimate of the kerogen isotope that generated the gases ($\delta^{13}C$ kerogen ≈ -26‰ or -33‰). Lis et. al., 2006, reported average bulk isotopes for five low maturity New Albany Shale kerogens at -29.7‰ (mid- point between estimated kerogen isotopes from the two linear trends).

The stable carbon and hydrogen isotopic composition ($\delta^{13}C$ and δD) of methane in gas samples provides information about their genetic origin (Schoell, 1983; Whiticar et al., 1986 and Coleman et al., 1988). Both diagrams on Figure 7-27 indicate that the Holsapple 2B storage gases are wet lower maturity gases. C_2+ appears variable, possibly due to shut in (8/3/21 is the driest gas) and initial sampling (2/4/21 and 3/9/21 are intermediate) whereas April-September are wet (≥ 30%). The left diagram ($\delta D\ C_1 - \delta^{13}C\ C_1$) is probably more accurate suggesting that the gases are lower maturity gases or possibly mixed biogenic – thermogenic gases (particularly 2/4 and 3/9 gases).

Figure 7-28 is a "Bernard diagram" that provides a genetic characterization of natural gas based on the chemical ratio $C_1/(C_2+C_3)$ and the carbon isotopic value of methane ($\delta^{13}C_{Methane}$) for Holsapple 2B gases. These data suggest that the gases are of mixed biogenic – thermogenic origin and positioning suggests of predominantly Type II kerogen origin. Note that Milkov (2021) reported that the Bernard approach to differentiating Type II and Type III kerogen sourced gases is not reliable due to being based on small datasets (see next figure).

Milkov (2021) reported that separation of Type II shale gases and Type III coal gases using methane vs. ethane isotope diagrams and ethane-methane vs. methane isotope diagrams are more accurate than the previous Bernard diagram (Figure 7-29). These interpretative diagrams suggest that the Holsapple 2B gases were derived from Type II shale source rock. Data positions are consistent with lower maturity; however, a minor biogenic component cannot be ruled out. Gas type classifications are based on 6798 shale and coal gases from 23 countries on six continents.

Figure 7-30, "Clayton diagram", provides a genetic characterization, Gas Generation Index (GGI) and thermal maturity of natural gas based on the chemical ratio $C_1/\ \Sigma(C_1 \rightarrow C_5)$, and the carbon isotopic difference between methane and the generative kerogen ($\delta^{13}C_{Methane} - \delta^{13}C_{Kerogen}$) for Holsapple 2B gases. The GGI is defined as the fraction of generated gas to available gas. A bulk kerogen value of -29.7‰ was used and was selected as it is the average of 5 New Albany Shale low maturity kerogens (Lis et. al., 2006). This diagram suggests that 2/4/21 and 3/9/21 gases are mixed biogenic – thermogenic gases (high $C_1/\ \Sigma(C_1 \rightarrow C_5)$ and lower methane-kerogen isotopes). 4/27/21-9/27/21 gases are mature Type II gases (GGI's 0.6-0.65); 8/3/21 gas has a high methane content (well shut in) and similar methane-kerogen isotope as the 4/27/21-9/27/21 gases.

The next Clayton diagram provides a genetic characterization, Gas Generation Index (GGI) and thermal maturity of natural gas based on the chemical ratio $C_1/\ \Sigma(C_1 \rightarrow C_5)$, and the carbon isotopic difference between ethane and the generative kerogen ($d^{13}C_{Ethane}$ - $d^{13}C_{Kerogen}$) for Holsapple 2B gases (Figure 7-31). A bulk kerogen value of -29.7‰ was used and was selected as it is the average of 5 New Albany Shale low maturity kerogens (Lis et. al., 2006). This diagram suggests that the study gas ethane is lower maturity than methane (GGI < 0.4) and due to the deviation of ethane isotopes as observed on the Chung diagram (Figure 26). The estimated ethane isotope, if derived from the source rock that generated methane, propane and *n*-butane is -40‰ which suggests that the ethane is similar low maturity as methane (GGI ? 0.5).

The last Clayton diagrams, Figure 7-32, compares Holsapple 2B gas chemical ratio $C_1/S(C_1 \rightarrow C_5)$, and the carbon isotopic difference between propane and the generative kerogen ($\delta^{13}C_{propane}$ - $\delta^{13}C_{Kerogen}$). A bulk kerogen value of -29.7‰ was used and was selected as it is the average of 5 New Albany Shale low maturity kerogens (Lis et. al., 2006). This diagram suggests that the study gases are low maturity (GGI's ? 0.6) which is plausible and similar to methane. Gases collected 2/4, 3/9 and 8/3 have high $C_1/\ \Sigma(C_1 \rightarrow C_5)$ due to contribution of biogenic gas or having been shut in.

The next two diagrams are thermal maturity models based on C_1-C_3 carbon isotope signatures. The first, Figure 7-33, shows the inferred thermal maturity (equivalent vitrinite reflectance $\%R_O$) of the generative source based on the stable carbon isotopic relationships between ethane versus methane (A) and ethane versus propane (B) for gases from Holsapple 2B. This model is based on gas generation from a mix of Type II and Type III kerogens and thus is possibly inaccurate. The upper diagram shows that the gases are suggested to be immature. Gases with low $\delta^{13}C\ C_1$ < -50‰ plot well below the Ro ladder possibly due to being mixtures of light biogenic methane and heavier thermogenic gas. The lower diagram also suggests that the gases are immature.

Figure 7-34 is a similar model that infers thermal maturity (equivalent vitrinite reflectance $\%R_O$) of the generative source based on the stable carbon isotopic relationships between ethane versus methane (A) and ethane versus propane (B) for Type II organic matter. This model is based on gas generation from a Type II kerogen and is possibly accurate as the majority of gases appear to have been generated from Type II kerogen (Figures 7-28 and 7-29). A bulk kerogen value of -29.7‰ was used and was selected as it is the average of 5 New Albany Shale low maturity kerogens (Lis et. al., 2006). The upper diagram shows that the gases are suggested to be low maturity (Ro_{eq} < 0.5%). Gases with low $\delta^{13}C\ C_1$ < -50‰ plot below the Ro ladder possibly due to being mixtures of light biogenic methane and heavier thermogenic gas. The lower C_2-C_3 diagram also suggests that the gases are low maturity (Ro_{eq} < 0.5%); however, the maturity is caused by the low ethane isotopes which deviate from the linear on the Chung diagram (Figure 7-26). If ethane is derived from the same source as methane and propane it should have an approximate isotope of -40‰ and a Ro_{eq} ? 0.5%.

Figure 7-35 compares ?^{13}C methane versus normalized methane content for Holsapple 2B gases. The pink rectangle represents carbon isotope and compositional instrumental error (0.5‰ online - 0.2‰ offline and 2%, respectively). 2/4, 3/9 and 8/3 gases required online methane isotope analysis. 2/4 and 3/9 gases are isotopically lighter than the other 7 gases, possibly due to contamination of biogenic gas. The remaining 7 gas trend is consistent with maturity increase with time. April-May-June-5 gases are lower maturity than June- 22 gas which is lower maturity than 7/13, 9/27 and 8/3 gases (8/3 gas measured high methane when well was shut in).

$\delta^{13}C$ methane versus $\delta^{13}C$ CO_2 for Holsapple 2B gases is shown on Figure 7-36. The pink rectangle represents carbon isotope and compositional instrumental error (0.5‰ online - 0.2‰ offline and 2%, respectively). 2/4, 3/9 and 8/3 gases required online methane isotope analysis. 2/4 and 3/9 gases are isotopically lighter than the other 7 gases, possibly due to contamination of biogenic gas. Interestingly, methane and CO_2 become heavier, with time which suggests that the process affecting the increase in methane isotope with time (maturity or degradation) is also affecting the CO_2 isotopic signatures. A plausible explanation is that thermogenic CO_2 is mixing with lighter injected CO_2.

Figure 7-37 is a cross-plot of $\delta^{13}C$ ethane versus normalized ethane content for Holsapple 2B gases. The pink rectangle represents carbon isotope and compositional instrumental error (0.2‰ offline and 2%, respectively). 3/9 gas is isotopically lighter than the other 6 gases, possibly due to contamination of biogenic gas (biogenic gas may contain minor quantities of isotopically light ethane). The remaining 6 gas trend is consistent with a maturity increase with time. 4/27, 5/11 and 6/22 gases are lower maturity than 6/15, 7/1, 8/3 and 9/27 gases.

Comparison of $\delta^{13}C$ propane versus normalized propane content (Figure 7-38) in Holsapple 2B shows that 2/4, 3/9 and 8/3 gases, which required online methane isotope analysis, are isotopically slightly lighter than the other gases suggesting lower maturity. The remaining 6 gas trend is consistent with maturity increase with time (4/27 and 5/11 gases are lower maturity than 6/15, 6/22 and 7/13 gases which are lower maturity than 9/27 gas.

Summary of Holsapple 2B Gas Characterization Conclusions

Twenty-seven Holsapple 2B post-CO_2 injection gases (1/27/2021 to 9/27/2021) are comprised of 90%+ CO_2 and ~5% C_1-C_5 HC gases. The HC gases are wet (C_2+ averages 36%). Both CO_2 and C_1-C_5 HC gases increase slightly with time.

Nine of 27 gases, selected for carbon isotopes (C_1, C_2, C_3, nC_4 and CO_2) and deuterium isotope (C_1) analyses, are isotopically variable with February and March-2021 gas characteristics reflecting startup production (i.e., near well bore) of a mix of predominantly injected CO_2 and ~1% HC gas (predominantly thermogenic with minor biogenic component), whereas April through September, 2021 gas characteristics reflect a mix of injected CO_2 and ~5.4% thermogenic HC gas and thermogenic CO_2 gas.

Holsapple 2B gases were derived from Type II marine shale at early oil-window maturity. Slight increases in April through September 2021 ethane and propane isotopes suggest a slight increase in maturity over time.

Table 7-3. ROZ Oil Data

Well	Lab ID	Sample Date	API Gravity	n-paraffins	Cyclopara-ffins (%)	Branched (iso-) Paraffins (%)	BTX aromatics (%)	BTX aromatics (ppm)	C6-C10 n-paraffins (ppm)	nC11-nC30 paraffins (ppm)	3RP - isoalkanes	5RP - cyclopen tanes	6RP - cyclohexane
G Swits 2	6132371276		29.3	0.87	9.81	2.49	0.97	3.60	18.10	47.90	17.83	38.74	43.43
Holsapple 2B	6132371278	8/24/2020	29.1	0.91	5.73	2.51	0.59	2.10	16.20	68.50	20.47	28.05	51.47
Holsapple 2B	6132772443	8/31/2021	27.7	0.88	7.98	2.06	2.31	7.80	17.50	45.50	17.42	24.42	58.16
Quaranta 5	6132810649		32.5	0.70	20.77	8.65	1.28	5.80	30.50	60.60	20.67	43.37	35.96

Well	Lab ID	Sample Date	(B) TOL/nC7	(F) nC7/MCH	(H) Heptane Value	P2 - Whole Oil	P3 - Whole Oil	P2 + N2 - Whole Oil	2-MH/3-MH	2MH + 2,3DMP	3MH + 2,4DMP	2,4DMP/2,3 DMP	BeMent Temp (°C)
G Swits 2	6132371276		0.16	0.75	22.03	0.42	0.11	0.87	0.60	0.22	0.09	0.19	114.8
Holsapple 2B	6132371278	8/24/2020	0.18	0.83	24.97	0.33	0.08	0.57	0.75	0.19	0.12	0.32	122.8
Holsapple 2B	6132772443	8/31/2021	0.29	0.81	27.24	0.35	0.08	0.61	0.70	0.20	0.06	0.22	117.5
Quaranta 5	6132810649		0.09	0.83	20.55	1.24	0.31	2.58	0.68	0.69	0.50	0.26	119.6

Well	Lab ID	Sample Date	IP11/nC10	IP13/nC12	Pristane/ Phytane	Pristane/ nC17	Phytane/n C18	nC17/ nC29	CPI Hunt
G Swits 2	6132371276		0.32	0.42	2.00	0.85	0.52	6.31	1.03
Holsapple 2B	6132371278	8/24/2020	0.27	0.33	1.81	0.57	0.37	5.24	1.04
Holsapple 2B	6132772443	8/31/2021	0.22	0.34	1.80	0.53	0.36	5.20	1.02
Quaranta 5	6132810649		0.35	0.47	2.08	1.21	0.69	3.82	1.04

Table 7-4. Holsapple 2B Gas Data

					Gas Composition (ppm)																Isotopic Values (‰)					
Lab No.	Field	Well	Reservoir	Sample Date	H2	O2 + Ar	N2	CO2	CO	Methane	Ethane	Ethene	Propane	Propene	iso-Butane	n-Butane	iso-Pentane	n-Pentane	Hexanes+	Total HC Gas (C1→C5) ppm	$\delta^{13}CO_2$	$\delta^{13}C_1$	δDC_1	$\delta^{13}C_2$	$\delta^{13}C_3$	$\delta^{13}nC_4$
804927	ROZ	Holsapple 2B	Carper SS	1/27/2021		2084	7600	984600		4490	764		283		25	88	17	27	73	5694						
804928	ROZ	Holsapple 2B	Carper SS	2/4/2021		960	4400	986700		5930	1130		470		45	165	31	51	118	7822	-41.29	**-53.60**	-261.90		**-36.30**	**-32.80**
783810	ROZ	Holsapple 2B	Carper SS	2/8/2021		500	6800	991000		732	643		123		0	2	2	6	215	1508						
804929	ROZ	Holsapple 2B	Carper SS	2/24/2021	377	3227	986800	9700		45	10		12		4	21	11	24	102	127						
785475	ROZ	Holsapple 2B	Carper SS	3/3/2021		460	4900	992800		598	179		251		45	209	47	75	59	1404						
804930	ROZ	Holsapple 2B	Carper SS	3/9/2021		790	4400	982000		9520	1820		751		75	270	53	88	236	12577	-40.75	**-53.40**	-263.70	-42.91	**-36.00**	**-32.20**
804931	ROZ	Holsapple 2B	Carper SS	3/16/2021	2130	2591	11200	970400		11500	2330	3	1110		125	448	90	150		15753						
790000	ROZ	Holsapple 2B	Carper SS	4/15/2021		3847	13800	974400		3470	852		595		89	408	107	194	192	5715						
790666	ROZ	Holsapple 2B	Carper SS	4/27/2021		210	2800	968600		17500	4680		3220		409	1470	276	429	354	27984	-40.67	-52.11	-259.30	-42.54	-35.49	-32.47
791609	ROZ	Holsapple 2B	Carper SS	5/4/2021	168	1897	10200	948900		23300	6470		4520		584	2100	402	649	927	38025						
791906	ROZ	Holsapple 2B	Carper SS	5/11/2021	107	1046	7700	936600		32700	9580		6550		766	2560	442	686	1160	53284	-40.38	-51.82	-257.90	-42.36	-35.35	-32.24
792447	ROZ	Holsapple 2B	Carper SS	5/18/2021	126	1010	9600	952700		16900	6110		5750		829	3370	758	1230	1640	34947						
795356	ROZ	Holsapple 2B	Carper SS	6/15/2021	133	1655	10400	956500		19200	5000		3460		436	1610	291	477	790	30474	-40.54	-52.00	-259.20	-42.25	-35.19	-32.40
795967	ROZ	Holsapple 2B	Carper SS	6/22/2021	120	1967	9900	943300		28100	6890		4620		588	2150	392	647	1280	43387	-40.14	-51.79	-256.40	-42.33	-35.34	-32.38
796760	ROZ	Holsapple 2B	Carper SS	6/29/2021	116	470	6700	932500		39200	9520		6210		771	2750	483	725	503	59659						
796929	ROZ	Holsapple 2B	Carper SS	7/6/2021	109	670	7100	930300		41800	9650		5860		699	2380	399	578	332	61366						
797669	ROZ	Holsapple 2B	Carper SS	7/13/2021	106	1156	12000	922100		43000	9990		6110		745	2620	491	766	819	63722	-39.79	-51.49	-252.60	-42.18	-35.34	-32.31
798966	ROZ	Holsapple 2B	Carper SS	7/20/2021		2718	22200	908100		44300	10400		6460		795	2810	509	785	659	66059						
799333	ROZ	Holsapple 2B	Carper SS	7/27/2021	360	660	7400	923200		45000	10600		6770		855	3120	587	929	779	67861						
800243	ROZ	Holsapple 2B	Carper SS	8/3/2021		1000	4400	985400		7090	909		530		39	146	27	46	54	8787	-40.33	**-51.50**	-261.10		**-35.70**	**-32.60**
801600	ROZ	Holsapple 2B	Carper SS	8/17/2021		1473	11500	917400		44800	10400		6730		865	3130	611	1010	1950	67546						
802131	ROZ	Holsapple 2B	Carper SS	8/24/2021		762	13100	909100		50500	11700		7140		892	3160	616	1020	1920	75028						
802581	ROZ	Holsapple 2B	Carper SS	8/31/2021		1029	10700	911500		52100	11500		6970		860	3090	571	909	677	76000						
802928	ROZ	Holsapple 2B	Carper SS	9/7/2021		1173	10600	910500		50900	11400		7100		917	3370	683	1140	2110	75510						
803655	ROZ	Holsapple 2B	Carper SS	9/14/2021		600	8500	908700		55900	12200		7350		911	3320	622	983	792	81286						
804362	ROZ	Holsapple 2B	Carper SS	9/20/2021		1168	16800	900700		53600	11900		7290		940	3440	694	1160	2160	79024						
804932	ROZ	Holsapple 2B	Carper SS	9/27/2021		1057	11200	903800		56500	12300		7420		942	3410	678	1130	1470	82380	-39.40	-51.73	-253.40	-42.18	-35.21	-32.28

Isotopes in ed font were analyzed using online methodology

Table 7-5. Holsapple 2B Gas Ratio Data

				Normalized HC Gas Composition (Vol. %)								Calculated ratios											
Lab No.	Well	Reservoir	Sample Date	Methane	Ethane	Propane	Iso-Butane	n-Butane	Iso-Pentane	n-Pentane	CO2	C_{2+} (%)	$\frac{C_1}{C_2}$	$\frac{C_2}{C_3}$	$\frac{C_3}{\Sigma C_4}$	$\frac{C_3}{\Sigma C_5}$	$\frac{C_1}{(C_1+C_2)}$	$\frac{C_1}{(C_2+C_3)}$	$\frac{C_1}{(C_1 \rightarrow C_5)}$	$\frac{C_3}{(C_2+C_3)}$	$\frac{C_3}{(C_2+\Sigma C_4)}$	$\frac{C_3}{(C_2+\Sigma C_5)}$	$\frac{nC_4}{(nC_4+iC_4)}$	$\frac{nC_5}{(nC_5+iC_5)}$
804927	Holsapple 2B	Carper SS	1/27/2021	78.85	13.42	4.97	0.44	1.55	0.30	0.47	98.46	21.15	5.88	2.70	6.76	17.36	0.85	4.29	0.79	0.73	0.87	0.95	0.78	0.61
804928	Holsapple 2B	Carper SS	2/4/2021	75.81	14.45	6.01	0.58	2.11	0.40	0.65	98.67	24.19	5.25	2.40	5.38	13.78	0.84	3.71	0.76	0.71	0.84	0.93	0.79	0.62
783810	Holsapple 2B	Carper SS	2/8/2021	48.54	42.64	8.16	0.00	0.13	0.13	0.40	99.10	51.46	1.14	5.23	321.50	80.38	0.53	0.96	0.49	0.84	1.00	0.99	1.00	0.75
804929	Holsapple 2B	Carper SS	2/24/2021	35.43	7.87	9.45	3.15	16.54	8.66	18.90	0.97	64.57	4.50	0.83	0.40	0.29	0.82	2.05	0.35	0.45	0.29	0.22	0.84	0.69
785475	Holsapple 2B	Carper SS	3/3/2021	42.59	12.75	17.88	3.21	14.89	3.35	5.34	99.28	57.41	3.34	0.71	0.70	1.47	0.77	1.39	0.43	0.42	0.41	0.59	0.82	0.61
804930	Holsapple 2B	Carper SS	3/9/2021	75.69	14.47	5.97	0.60	2.15	0.42	0.70	98.20	24.31	5.23	2.42	5.28	12.91	0.84	3.70	0.76	0.71	0.84	0.93	0.78	0.62
804931	Holsapple 2B	Carper SS	3/16/2021	73.00	14.79	7.05	0.79	2.84	0.57	0.95	97.04	27.00	4.94	2.10	4.07	9.71	0.83	3.34	0.73	0.68	0.80	0.91	0.78	0.63
790000	Holsapple 2B	Carper SS	4/15/2021	60.72	14.91	10.41	1.56	7.14	1.87	3.39	97.44	39.28	4.07	1.43	1.71	2.83	0.80	2.40	0.61	0.59	0.63	0.74	0.82	0.64
790666	Holsapple 2B	Carper SS	4/27/2021	62.54	16.72	11.51	1.46	5.25	0.99	1.53	96.86	37.46	3.74	1.45	2.49	6.64	0.79	2.22	0.63	0.59	0.71	0.87	0.78	0.61
791609	Holsapple 2B	Carper SS	5/4/2021	61.28	17.02	11.89	1.54	5.52	1.06	1.71	94.89	38.72	3.60	1.43	2.41	6.16	0.78	2.12	0.61	0.59	0.71	0.86	0.78	0.62
791906	Holsapple 2B	Carper SS	5/11/2021	61.37	17.98	12.29	1.44	4.80	0.83	1.29	93.66	38.63	3.41	1.46	2.88	8.49	0.77	2.03	0.61	0.59	0.74	0.89	0.77	0.61
792447	Holsapple 2B	Carper SS	5/18/2021	48.36	17.48	16.45	2.37	9.64	2.17	3.52	95.27	51.64	2.77	1.06	1.46	3.07	0.73	1.42	0.48	0.52	0.59	0.75	0.80	0.62
795356	Holsapple 2B	Carper SS	6/15/2021	63.00	16.41	11.35	1.43	5.28	0.95	1.57	95.65	37.00	3.84	1.45	2.44	6.51	0.79	2.27	0.63	0.59	0.71	0.87	0.79	0.62
795967	Holsapple 2B	Carper SS	6/22/2021	64.77	15.88	10.65	1.36	4.96	0.90	1.49	94.33	35.23	4.08	1.49	2.52	6.63	0.80	2.44	0.65	0.60	0.72	0.87	0.79	0.62
796760	Holsapple 2B	Carper SS	6/29/2021	65.71	15.96	10.41	1.29	4.61	0.81	1.22	93.25	34.29	4.12	1.53	2.70	7.88	0.80	2.49	0.66	0.61	0.73	0.89	0.78	0.60
796929	Holsapple 2B	Carper SS	7/6/2021	68.12	15.73	9.55	1.14	3.88	0.65	0.94	93.03	31.88	4.33	1.65	3.13	9.88	0.81	2.70	0.68	0.62	0.76	0.91	0.77	0.59
797669	Holsapple 2B	Carper SS	7/13/2021	67.48	15.68	9.59	1.17	4.11	0.77	1.20	92.21	32.52	4.30	1.64	2.97	7.95	0.81	2.67	0.67	0.62	0.75	0.89	0.78	0.61
798966	Holsapple 2B	Carper SS	7/20/2021	67.06	15.74	9.78	1.20	4.25	0.77	1.19	90.81	32.94	4.26	1.61	2.88	8.04	0.81	2.63	0.67	0.62	0.74	0.89	0.78	0.61
799333	Holsapple 2B	Carper SS	7/27/2021	66.31	15.62	9.98	1.26	4.60	0.87	1.37	92.32	33.69	4.25	1.57	2.67	6.99	0.81	2.59	0.66	0.61	0.73	0.87	0.78	0.61
800243	Holsapple 2B	Carper SS	8/3/2021	80.69	10.34	6.03	0.44	1.66	0.31	0.52	98.54	19.31	7.80	1.72	4.91	12.45	0.89	4.93	0.81	0.63	0.83	0.93	0.79	0.63
801600	Holsapple 2B	Carper SS	8/17/2021	66.33	15.40	9.96	1.28	4.63	0.90	1.50	91.74	33.67	4.31	1.55	2.60	6.42	0.81	2.62	0.66	0.61	0.72	0.87	0.78	0.62
802131	Holsapple 2B	Carper SS	8/24/2021	67.31	15.59	9.52	1.19	4.21	0.82	1.36	90.91	32.69	4.32	1.64	2.89	7.15	0.81	2.68	0.67	0.62	0.74	0.88	0.78	0.62
802581	Holsapple 2B	Carper SS	8/31/2021	68.55	15.13	9.17	1.13	4.07	0.75	1.20	91.15	31.45	4.53	1.65	2.91	7.77	0.82	2.82	0.69	0.62	0.74	0.89	0.78	0.61
802928	Holsapple 2B	Carper SS	9/7/2021	67.41	15.10	9.40	1.21	4.46	0.90	1.51	91.05	32.59	4.46	1.61	2.66	6.25	0.82	2.75	0.67	0.62	0.73	0.86	0.79	0.63
803655	Holsapple 2B	Carper SS	9/14/2021	68.77	15.01	9.04	1.12	4.08	0.77	1.21	90.87	31.23	4.58	1.66	2.88	7.60	0.82	2.86	0.69	0.62	0.74	0.88	0.78	0.61
804362	Holsapple 2B	Carper SS	9/20/2021	67.83	15.06	9.23	1.19	4.35	0.88	1.47	90.07	32.17	4.50	1.63	2.72	6.42	0.82	2.79	0.68	0.62	0.73	0.87	0.79	0.63
804932	Holsapple 2B	Carper SS	9/27/2021	68.58	14.93	9.01	1.14	4.14	0.82	1.37	90.38	31.42	4.59	1.66	2.83	6.80	0.82	2.87	0.69	0.62	0.74	0.87	0.78	0.63

Table 7-5. Holsapple 2B Gas Ratio Data

Lab No.	Well	Reservoir	Sample Date	iC4 / nC4	Haworth Mud Log Ratios: GWR $\frac{\Sigma(C_2 \rightarrow C_5)}{\Sigma(C_1 \rightarrow C_5)} \times 100$	Haworth Mud Log Ratios: LHR $\frac{(C_1+C_2)}{(C_3+C_4+C_5)}$	Haworth Mud Log Ratios: OCR $\frac{(C_4+C_5)}{C_3}$	Gas - Gas ($\Delta^{13}C$ ‰): $C_2 - C_1$	Gas - Gas ($\Delta^{13}C$ ‰): $C_3 - C_2$	Gas - Kerogen ($\Delta^{13}C$ ‰): $\delta^{13}C_{ker}$	Gas - Kerogen ($\Delta^{13}C$ ‰): C_1 - Ker	Gas - Kerogen ($\Delta^{13}C$ ‰): C_2 - Ker	Gas - Kerogen ($\Delta^{13}C$ ‰): C_3 - Ker	Gas - Kerogen ($\Delta^{13}C$ ‰): $\delta^{13}C_{ker}$	Gas - Kerogen ($\Delta^{13}C$ ‰): C_1 - Ker	Gas - Kerogen ($\Delta^{13}C$ ‰): C_2 - Ker	Gas - Kerogen ($\Delta^{13}C$ ‰): C_3 - Ker	Gas - Kerogen ($\Delta^{13}C$ ‰): $\delta^{13}C_{ker}$	Gas - Kerogen ($\Delta^{13}C$ ‰): C_1 - Ker	Gas - Kerogen ($\Delta^{13}C$ ‰): C_2 - Ker	Gas - Kerogen ($\Delta^{13}C$ ‰): C_3 - Ker
804927	Holsapple 2B	Carper SS	1/27/2021	0.28	21.15	11.94	0.55			-26.0				-33.0				-29.7			
804928	Holsapple 2B	Carper SS	2/4/2021	0.27	24.19	9.27	0.62			-26.0	-27.60		-10.30	-33.0	-20.60		-3.30	-29.7	-23.9		-6.6
783810	Holsapple 2B	Carper SS	2/8/2021	0.00	51.46	10.34	0.08			-26.0				-33.0				-29.7			
804929	Holsapple 2B	Carper SS	2/24/2021	0.19	64.57	0.76	5.00			-26.0				-33.0				-29.7			
785475	Holsapple 2B	Carper SS	3/3/2021	0.22	57.41	1.24	1.50			-26.0				-33.0				-29.7			
804930	Holsapple 2B	Carper SS	3/9/2021	0.28	24.31	9.17	0.65	10.49	6.91	-26.0	-27.40	-16.91	-10.00	-33.0	-20.40	-9.91	-3.00	-29.7	-23.7	-13.21	-6.3
804931	Holsapple 2B	Carper SS	3/16/2021	0.28	27.00	7.19	0.73			-26.0				-33.0				-29.7			
790000	Holsapple 2B	Carper SS	4/15/2021	0.22	39.28	3.10	1.34			-26.0				-33.0				-29.7			
790666	Holsapple 2B	Carper SS	4/27/2021	0.28	37.46	3.82	0.80	9.57	7.05	-26.0	-26.11	-16.54	-9.49	-33.0	-19.11	-9.54	-2.49	-29.7	-22.41	-12.84	-5.79
791609	Holsapple 2B	Carper SS	5/4/2021	0.28	38.72	3.61	0.83			-26.0				-33.0				-29.7			
791906	Holsapple 2B	Carper SS	5/11/2021	0.30	38.63	3.84	0.68	9.46	7.01	-26.0	-25.82	-16.36	-9.35	-33.0	-18.82	-9.36	-2.35	-29.7	-22.12	-12.66	-5.65
792447	Holsapple 2B	Carper SS	5/18/2021	0.25	51.64	1.93	1.08			-26.0				-33.0				-29.7			
795356	Holsapple 2B	Carper SS	6/15/2021	0.27	37.00	3.86	0.81	9.75	7.06	-26.0	-26.00	-16.25	-9.19	-33.0	-19.00	-9.25	-2.19	-29.7	-22.3	-12.55	-5.49
795967	Holsapple 2B	Carper SS	6/22/2021	0.27	35.23	4.17	0.82	9.46	6.99	-26.0	-25.79	-16.33	-9.34	-33.0	-18.79	-9.33	-2.34	-29.7	-22.09	-12.63	-5.64
796760	Holsapple 2B	Carper SS	6/29/2021	0.28	34.29	4.45	0.76			-26.0				-33.0				-29.7			
796929	Holsapple 2B	Carper SS	7/6/2021	0.29	31.88	5.19	0.69			-26.0				-33.0				-29.7			
797669	Holsapple 2B	Carper SS	7/13/2021	0.28	32.52	4.94	0.76	9.31	6.84	-26.0	-25.49	-16.18	-9.34	-33.0	-18.49	-9.18	-2.34	-29.7	-21.79	-12.48	-5.64
798966	Holsapple 2B	Carper SS	7/20/2021	0.28	32.94	4.82	0.76			-26.0				-33.0				-29.7			
799333	Holsapple 2B	Carper SS	7/27/2021	0.27	33.69	4.53	0.81			-26.0				-33.0				-29.7			
800243	Holsapple 2B	Carper SS	8/3/2021	0.27	19.31	10.15	0.49			-26.0	-25.50		-9.70	-33.0	-18.50		-2.70	-29.7	-21.8		-6
801600	Holsapple 2B	Carper SS	8/17/2021	0.28	33.67	4.47	0.83			-26.0				-33.0				-29.7			
802131	Holsapple 2B	Carper SS	8/24/2021	0.28	32.69	4.85	0.80			-26.0				-33.0				-29.7			
802581	Holsapple 2B	Carper SS	8/31/2021	0.28	31.45	5.13	0.78			-26.0				-33.0				-29.7			
802928	Holsapple 2B	Carper SS	9/7/2021	0.27	32.59	4.72	0.86			-26.0				-33.0				-29.7			
803655	Holsapple 2B	Carper SS	9/14/2021	0.27	31.23	5.16	0.79			-26.0				-33.0				-29.7			
804362	Holsapple 2B	Carper SS	9/20/2021	0.27	32.17	4.84	0.86			-26.0				-33.0				-29.7			
804932	Holsapple 2B	Carper SS	9/27/2021	0.28	31.42	5.07	0.83	9.55	6.97	-26.0	-25.73	-16.18	-9.21	-33.0	-18.73	-9.18	-2.21	-29.7	-22.03	-12.48	-5.51
										Kerogen estimate Chung Fig. 26				Kerogen estimate Chung Fig. 26				Average 5 low maturity NAS kerogens (Lis et. al., 2006)			

Carper location Map
ISGS ROZ Oil Storage

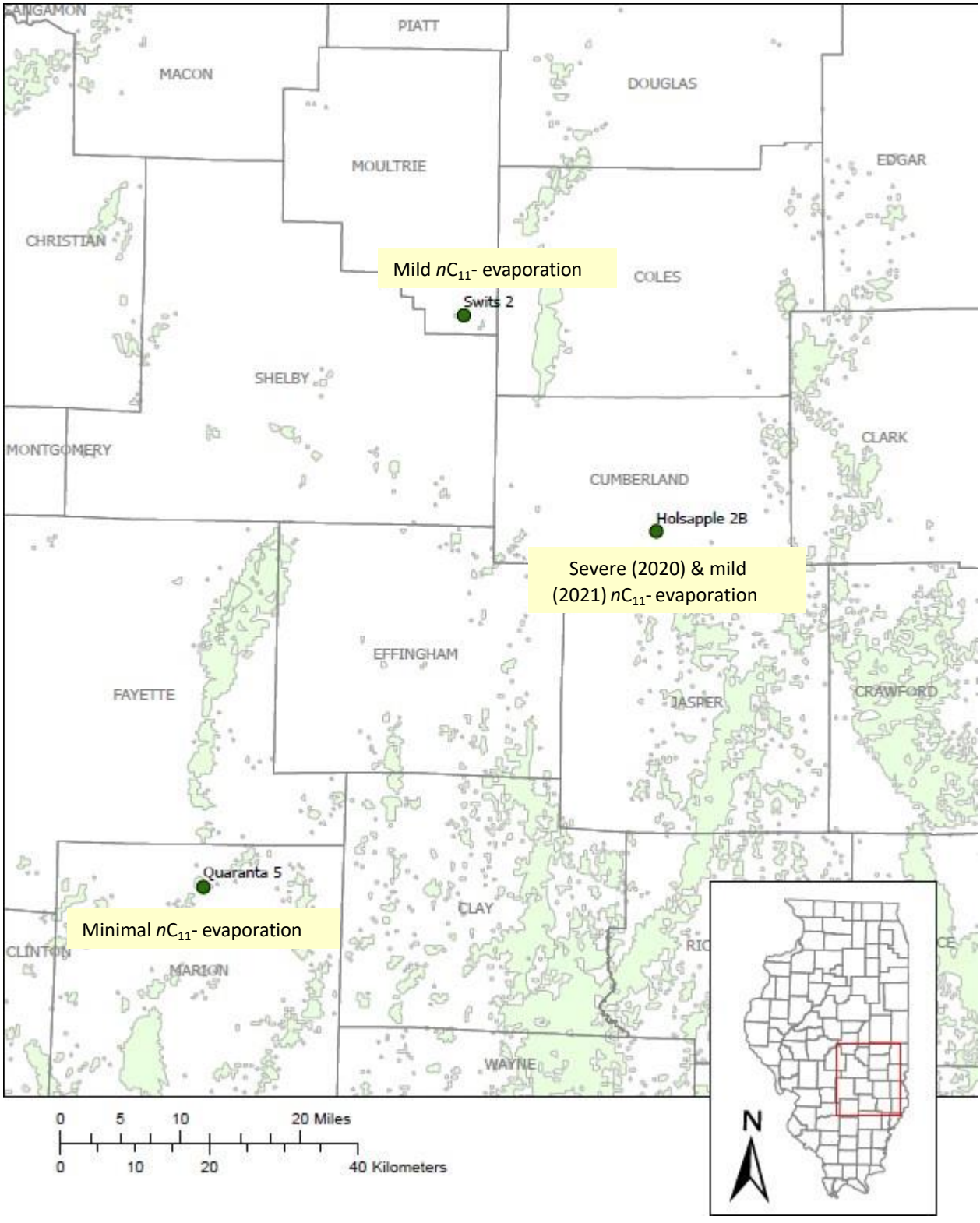


Figure 7-1. Southeast Illinois county map showing location of the three ROZ oil storage wells. Oils from the three study wells vary in gravity and amount of light hydrocarbon evaporation. Lower API does not correlate with the most severe evaporation observed in the 2020 Holsapple 2B oil. Twenty-seven post-CO_2 injection samples from Holsapple 2B (1/27/2021 – 9/27/2021) were included in the geochemical study.

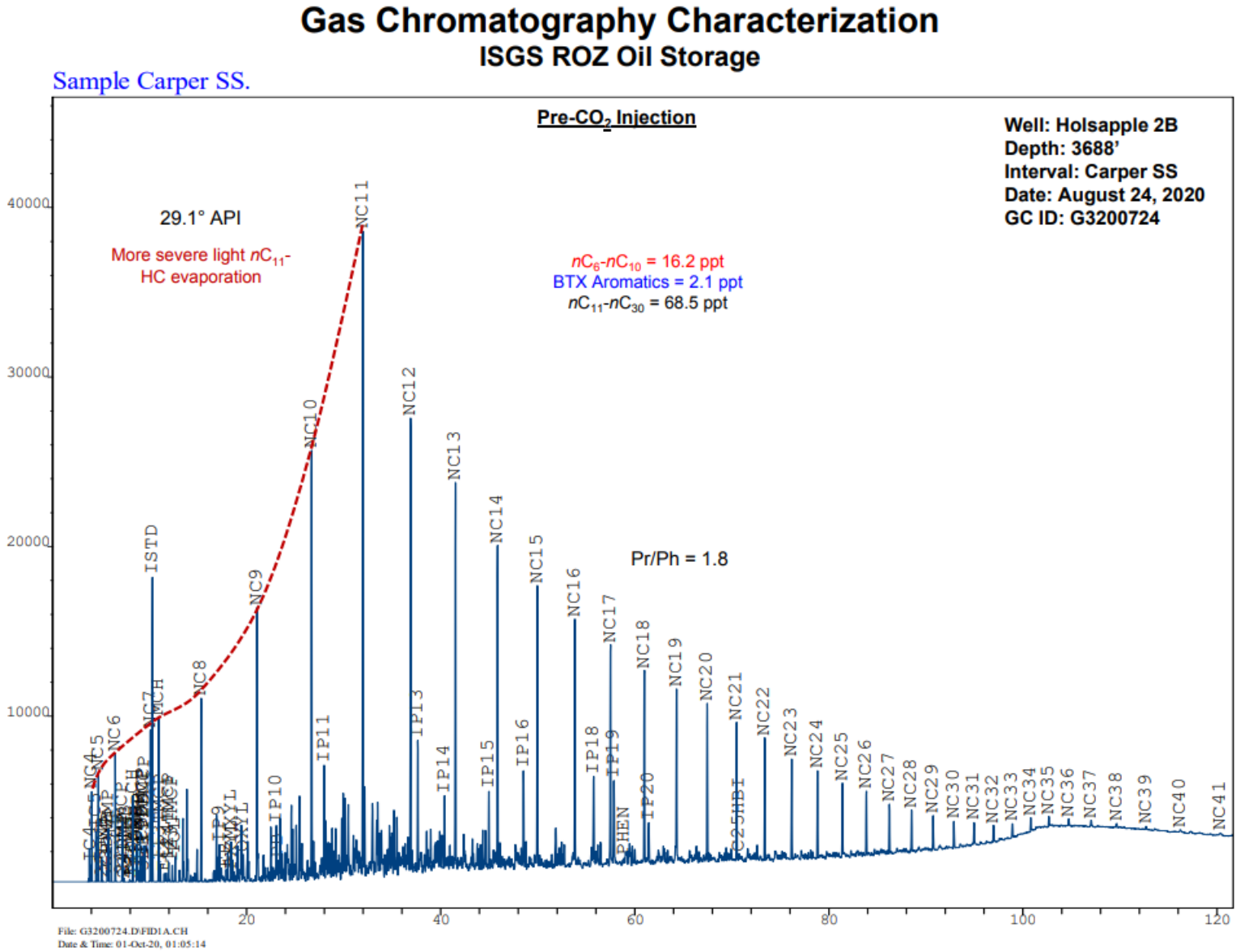


Figure 7-2. Whole oil gas chromatogram of oil from Holsapple 2B (3688') collected Aug-2020 after ~4 years shut in (pre-CO_2 injection). The 29.1° API oil is paraffinic and non-biodegraded. However, C_7-C_{11} n-paraffins are severely depleted (concave pattern) either from long-term exposure or an in- reservoir process such as evaporative fractionation.

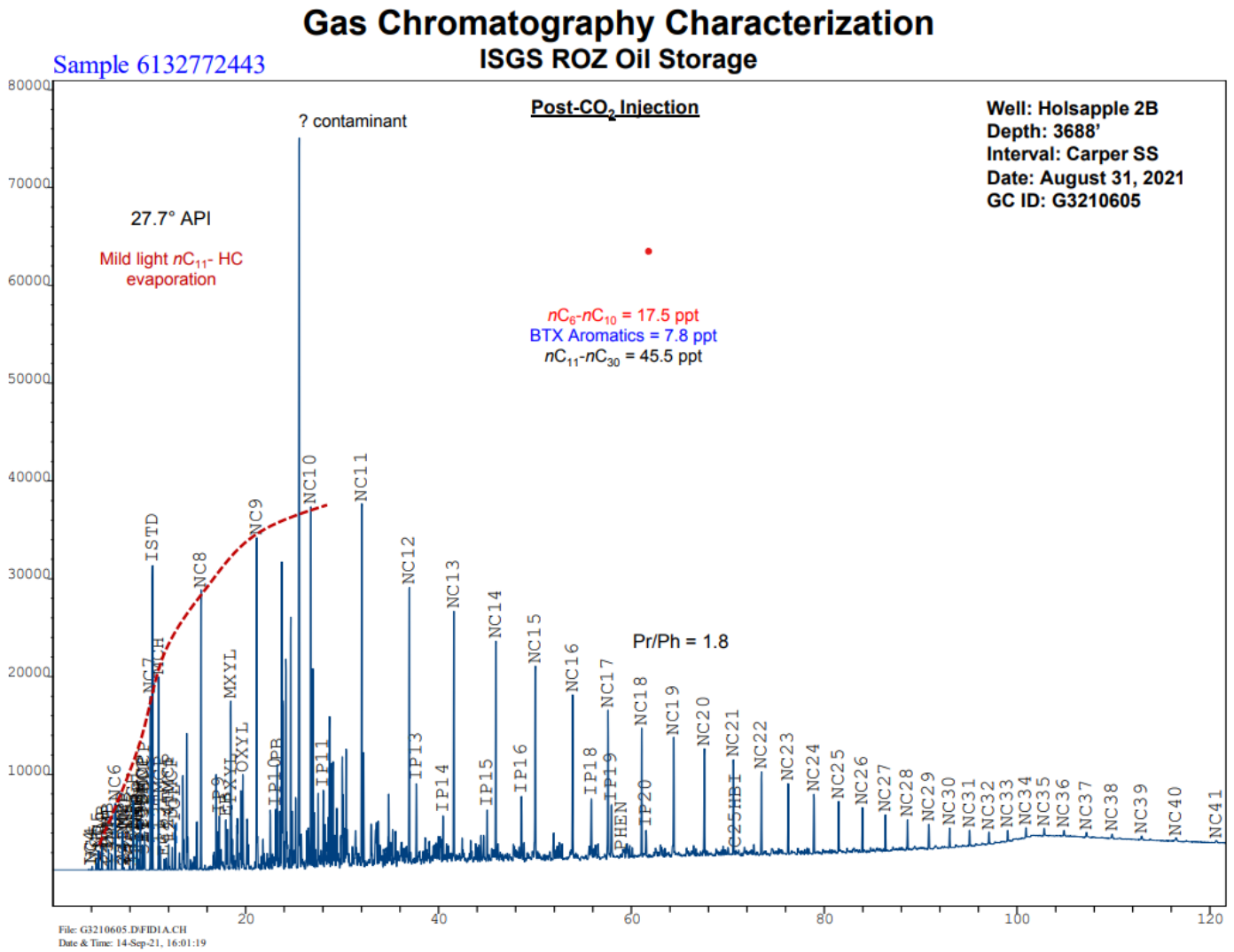


Figure 7-3. Whole oil gas chromatogram of oil from Holsapple 2B (3688') collected Aug-2021(post-CO_2 injection). This 27.7° API oil is also paraffinic and non-biodegraded. As observed in the pe-CO_2 injected oil, C_7-C_{11} n-paraffins are depleted; however, the extent of depletion is less severe (convex pattern) and either from long-term exposure or an in-reservoir process such as evaporative fractionation.

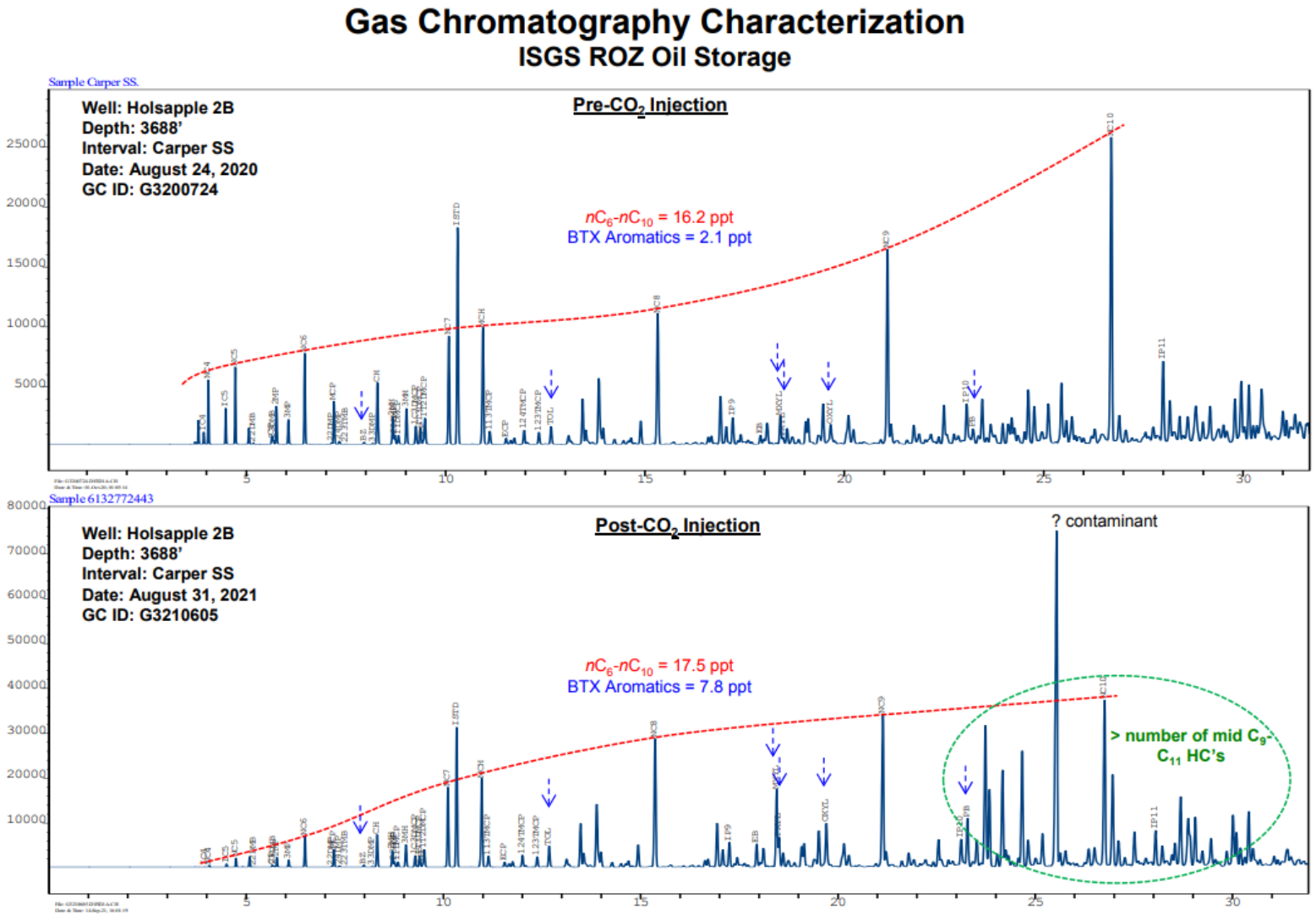


Figure 7-4. Light nC_4-nC_{11} light HC gas chromatogram comparison of Holsapple 2B (3688') oils collected Aug-2020 (top) and Aug-2021 (bottom). The nC_4- nC_{10} fingerprints appear slightly different; as the post-CO_2 injection nC_6- evaporation is more severe and the nC_7+ evaporation appears less severe than observed in the 2020 oil. The 2021 oil also contains ~4 times greater BTX (EB, TOL, MXYL, PXYL, OXYL, PB) and addition or enhancement of several mid-C_9+ non-identified compounds.

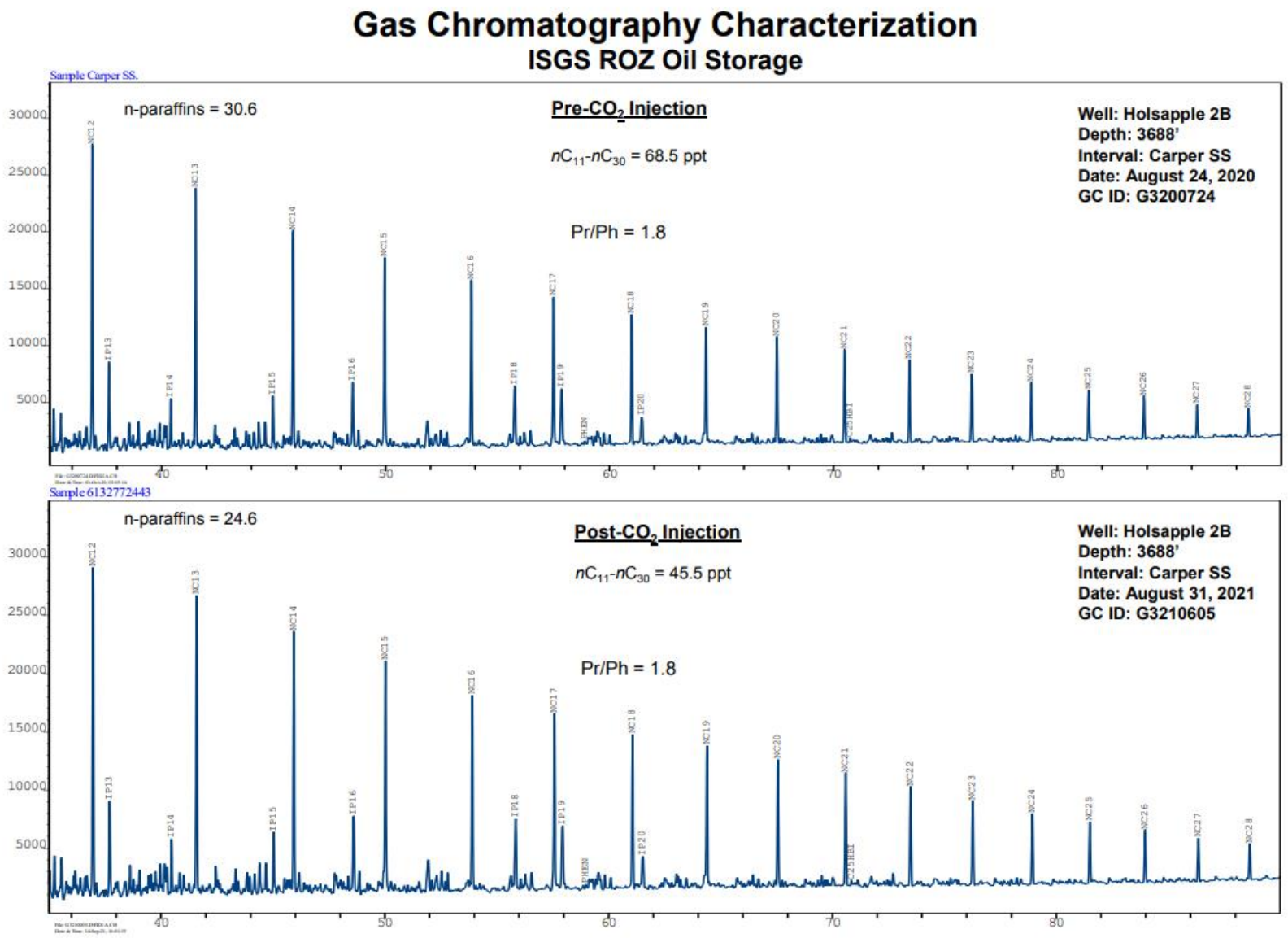


Figure 7-5. nC_{12}-nC_{28} light HC gas chromatogram comparison of Holsapple 2B (3688') oils collected Aug-2020 (top) and Aug-2021 (bottom). The higher molecular weight fingerprints are very similar suggesting alteration has not differentially affected the mid to high molecular weight portion of the oil. However, the pre-CO_2 oil contains a greater quantity of n-paraffins than the post-CO_2 oil.

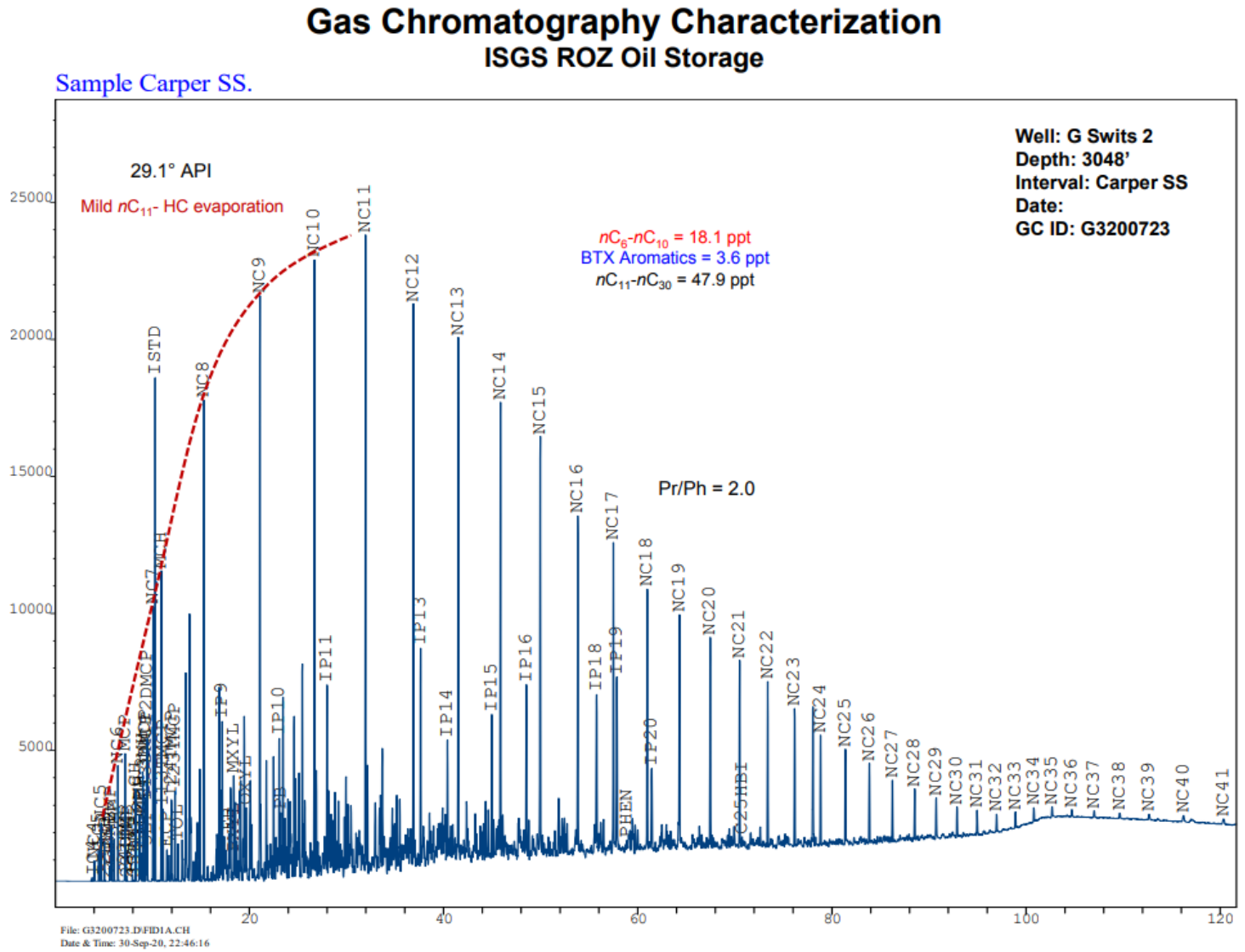


Figure 7-6. Whole oil gas chromatogram of oil from G Swits (3048'). This 29.1° API oil is paraffinic and non-biodegraded. C_{11}- n-paraffins have been evaporated at similar degree as Holsapple 2B post-CO_2 oil and alteration appears due either to long-term exposure or an in-reservoir process such as evaporative fractionation.

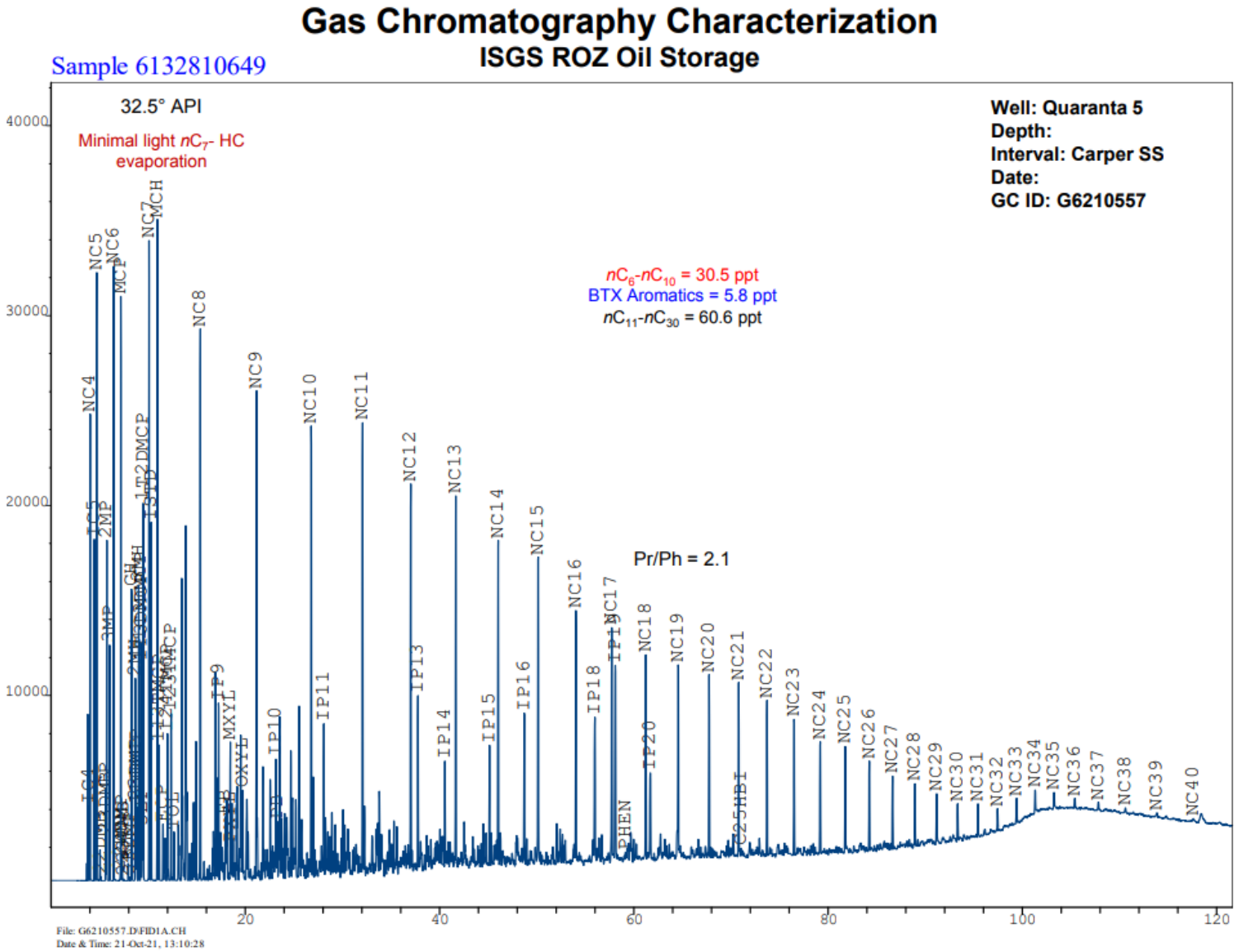


Figure 7-7. Whole oil gas chromatogram of oil from Quaranta 5. The 32.5° API oil is paraffinic and non-biodegraded. This oil is <u>not altered</u> and exhibits minimal light hydrocarbon evaporation typical with collection of dead oils.

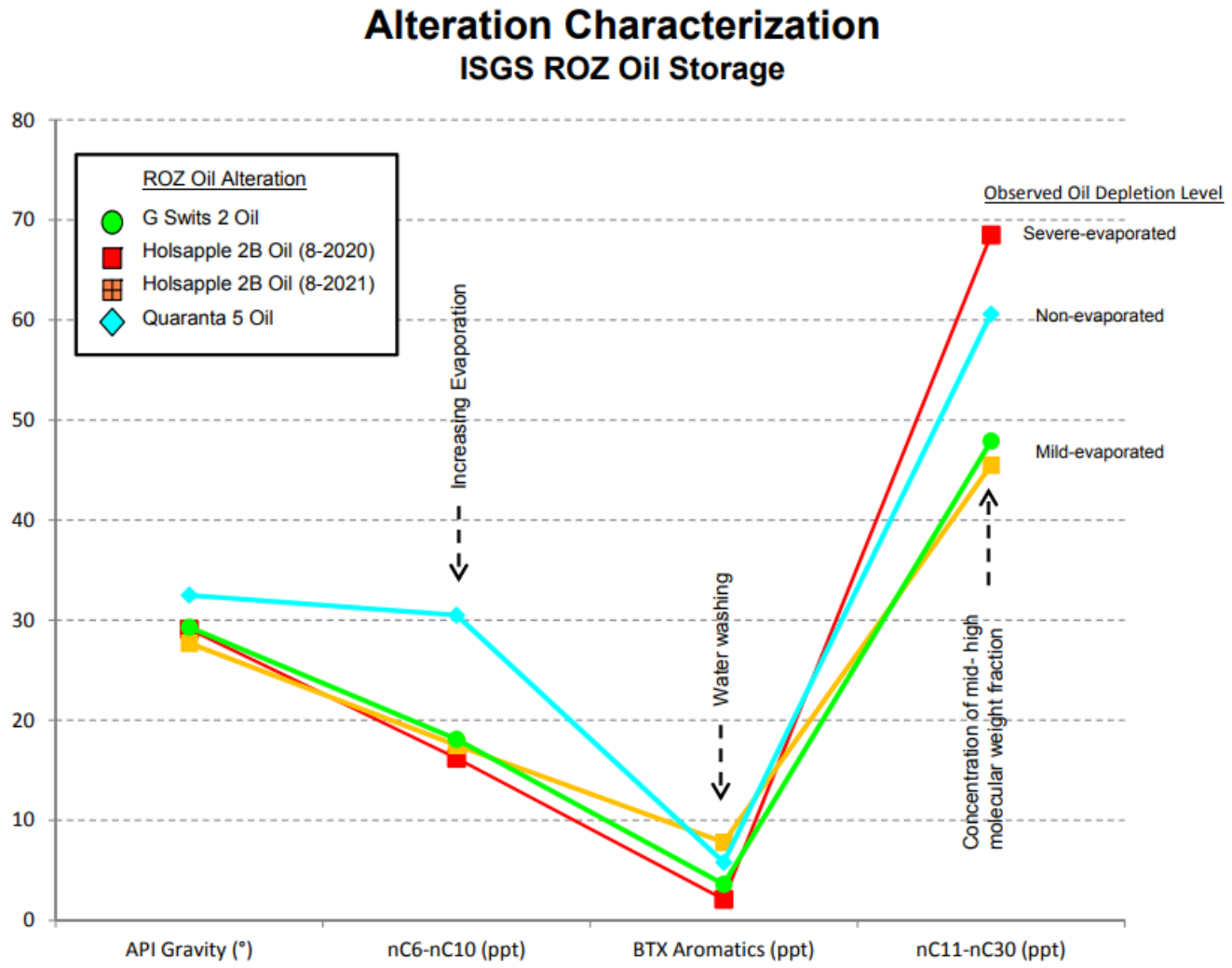


Figure 7-8. Line plot showing API gravity, n-alkane and BTX compound classes. Decrease in API gravity correlates best with decreases in light n- paraffins (see Table 7-1). 2020 Pre-CO_2 injection Holsapple 2B oil measured slightly lower nC_6-nC_{10} paraffins (evaporative fractionation), lowest BTX aromatics (water washing) and greatest nC_{11}-nC_{30} paraffins (concentration). 2021 post-CO_2 injection Holsapple 2B oil measured similar nC_6-nC_{10} paraffins as G. Swits 2 oil (mild depletion), greatest BTX aromatics (absence of water washing) and similar nC_{11}-nC_{30} paraffins as G. Swits 2 oil.

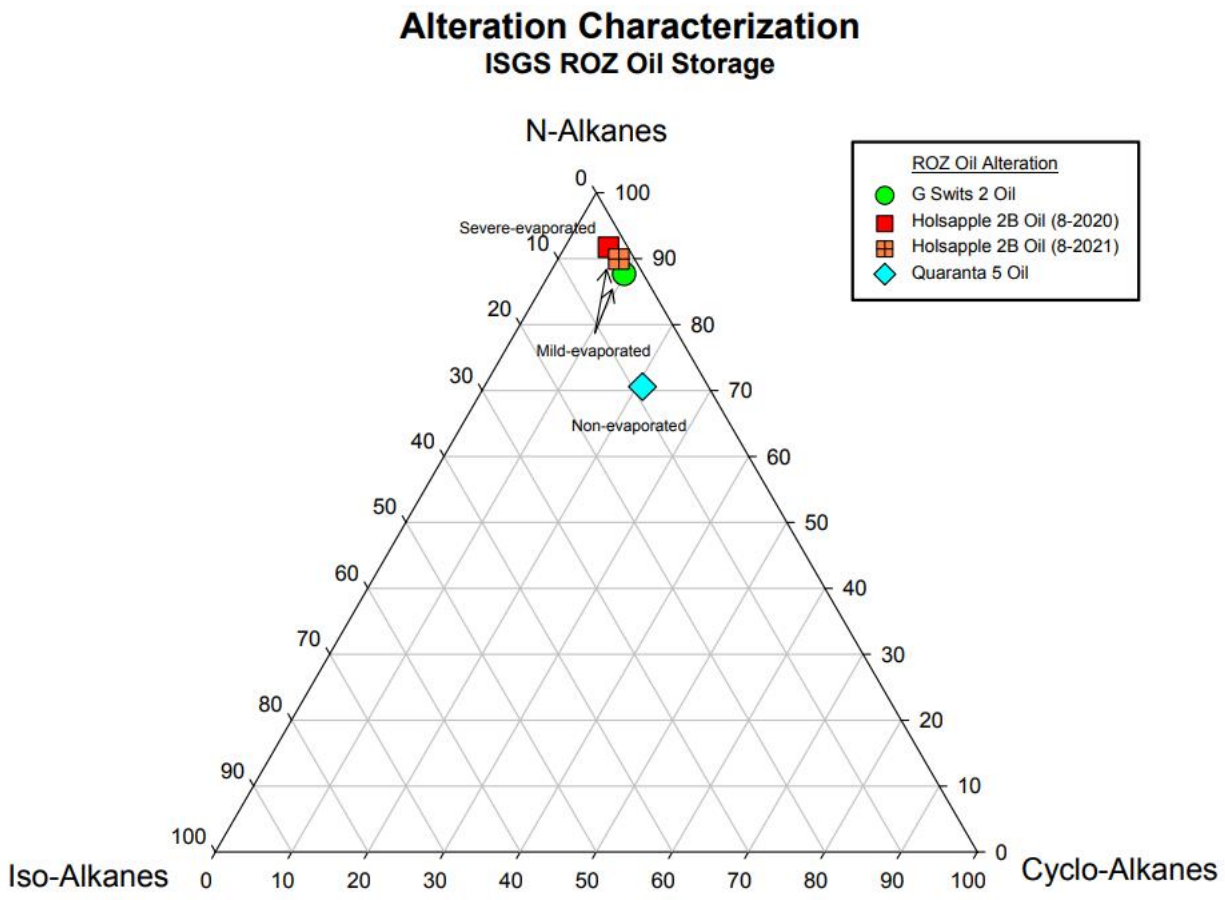


Figure 7-9. Ternary diagram of normal-, cyclo- and iso-alkanes. Oils that exhibit mild to severe evaporation contain more normal-alkanes relative to cyclo- and iso-alkanes than the non-evaporated Quaranta 5 oil.

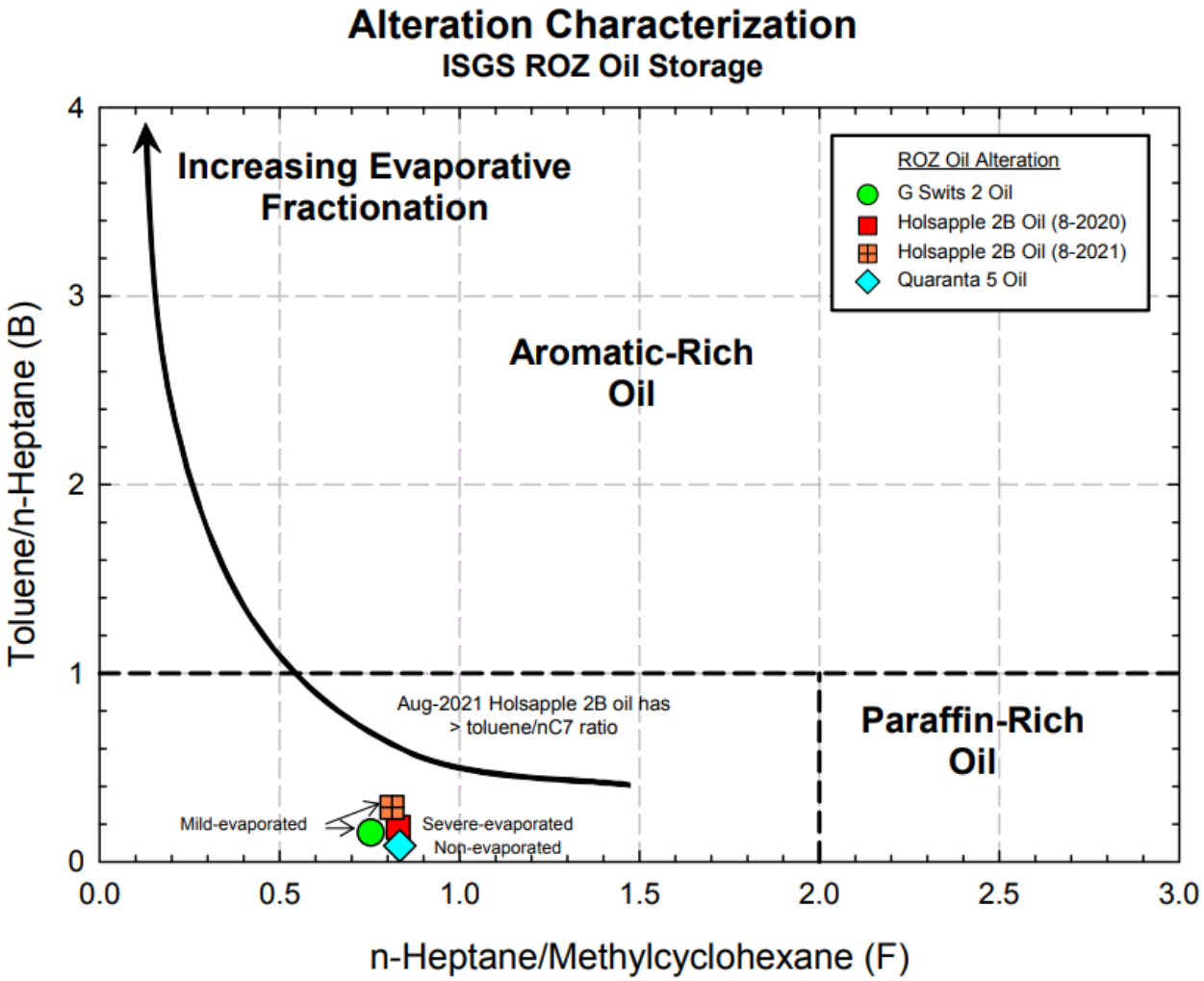


Figure 7-10. This is a cross-plot of light hydrocarbon parameters that are affected by evaporative fractionation (modified from Thompson, 1983 and 1987). Evaporative fractionation is a process in which dry gas enters an oil accumulation, and strips off light ends, preferentially removing the saturate vs. aromatic compounds straight-chain vs. cyclic and branched compounds; the gas then migrates to a shallower depth and may drop out its condensate load as a "retrograde condensate" in a shallower reservoir. The residual oil would then be characterized by a high toluene/n-heptane ratio and a low n-heptane/methylcyclohexane ratio. Low toluene/nC_7 ratios (0.1-0.3) do not conclusively support that the Holsapple 2B oils are residual oils after evaporative fractionation and gas stripping. Increased toluene/nC_7 ratios do not fully correlate with the level of evaporation observed in the study oils.

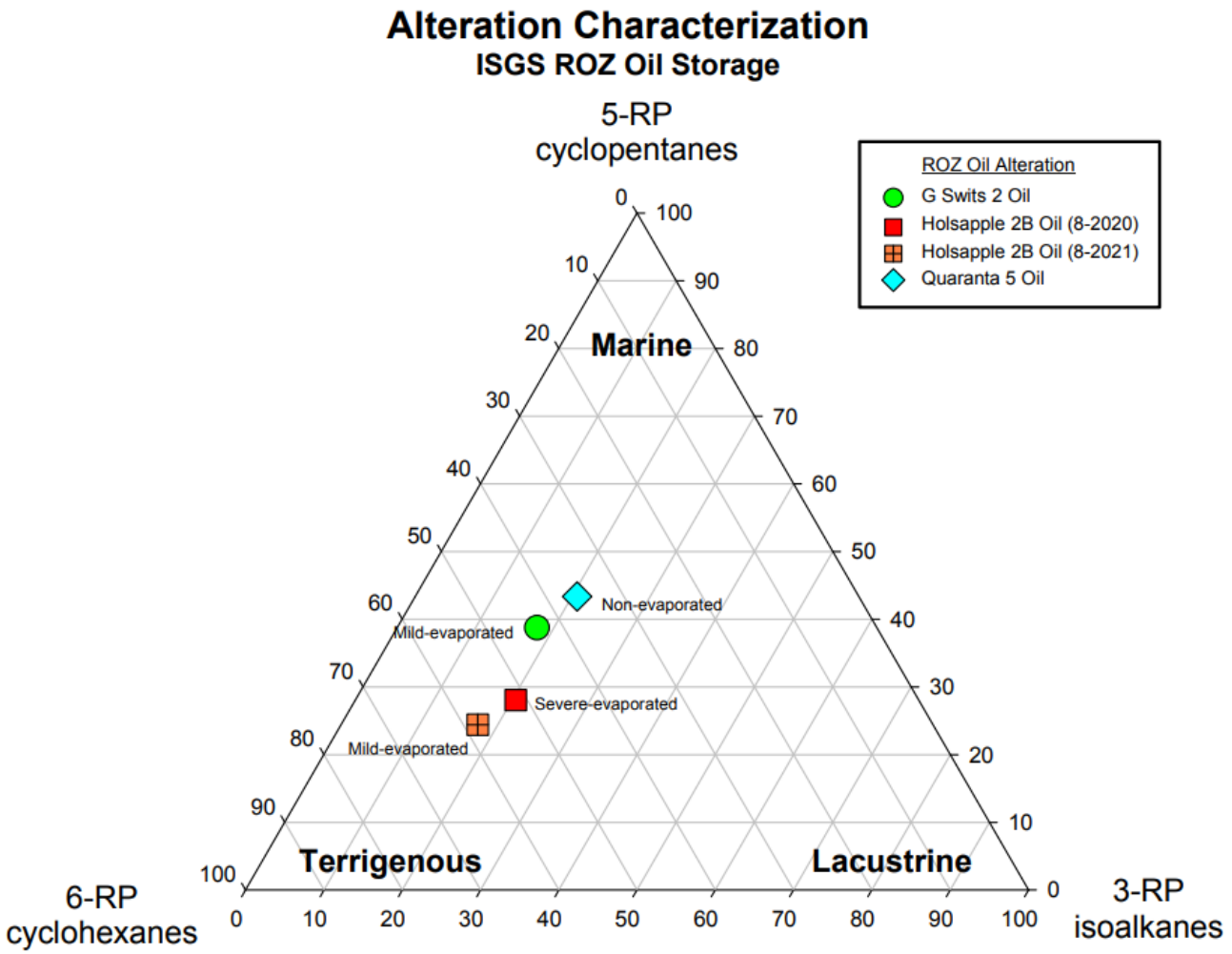


Figure 7-11. Ternary diagram showing distribution of 3-RP (Lacustrine), 5-RP (Marine) and 6-RP (Terrigenous) light hydrocarbons. Mango (1994) referred to the importance of ring preferences in the formation of light hydrocarbons. In general, oils derived from marine kerogens tend to be enriched in the cyclopentanes (5-RP), those derived from predominantly lacustrine source rocks are enriched in iso-alkanes (3-RP), and oils from primarily terrigenous organic matter are usually enriched in cyclohexanes (6-RP). The study oils exhibit significant variations in cyclopentanes and cyclohexanes and insignificant variations in isoalkanes. These variations do not correlate fully with observed levels of evaporation suggesting that there is a possible source difference.

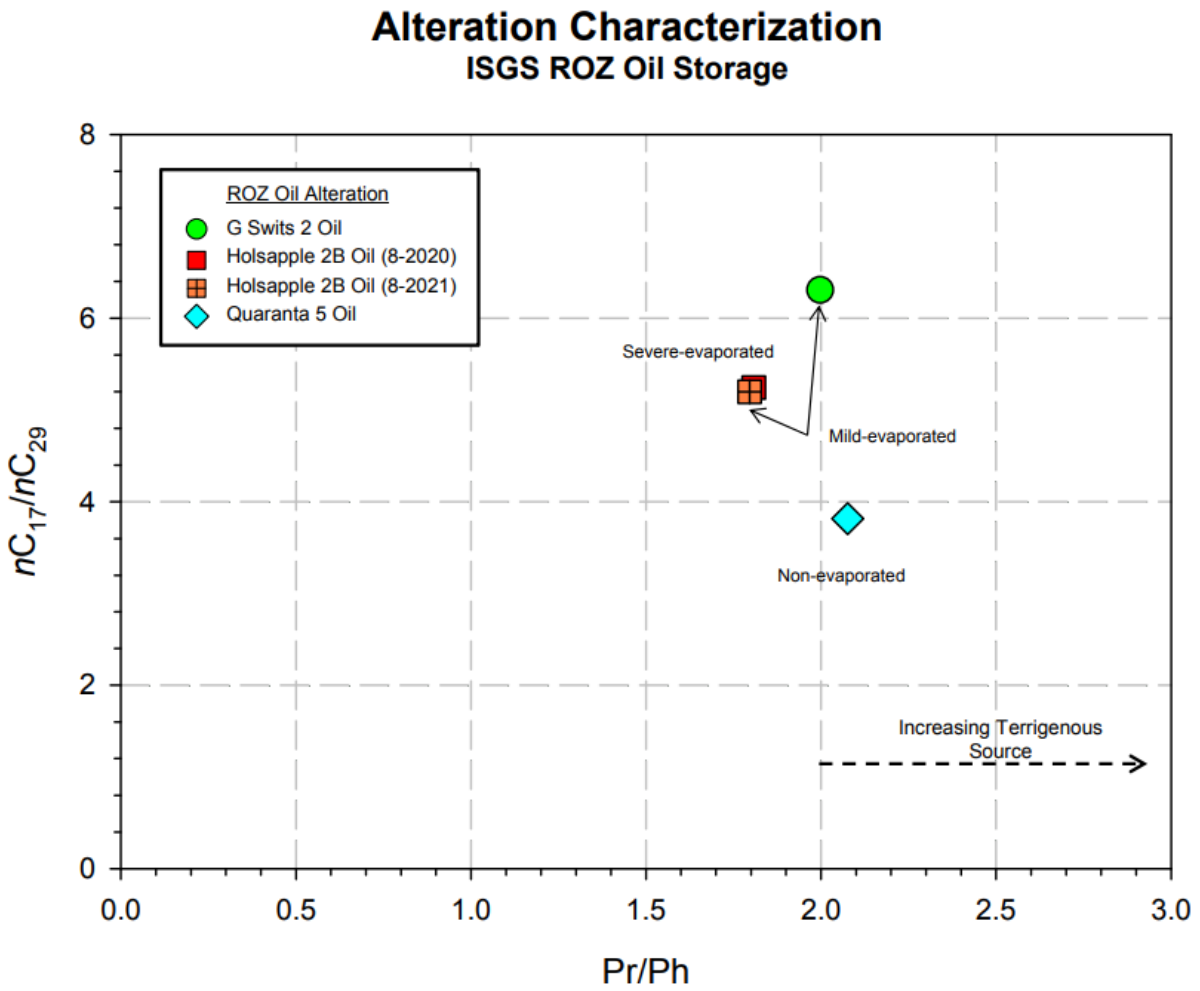


Figure 7-12. Cross-plot comparing Pristane/Phytane (Pr/Ph) and nC_{17}/nC_{29}, both of which are subject to source differences. These mid-high molecular weight range parameters should not be influenced by the observed variable light hydrocarbon evaporation and water washing. Holsapple 2B oils measured lower Pr/Ph ratios than G. Swits 2 and Quaranta 5 oils suggesting a slight difference in source rock contribution (i.e., slightly greater terrigenous contribution to G. Swits and Quaranta 5 oils). Holsapple 2B oil measured intermediate nC_{17}/nC_{29} ratios, G Swits has the > nC_{17}/nC_{29} ratio and Quaranta 5 oil has the lowest nC_{17}/nC_{29} ratio.

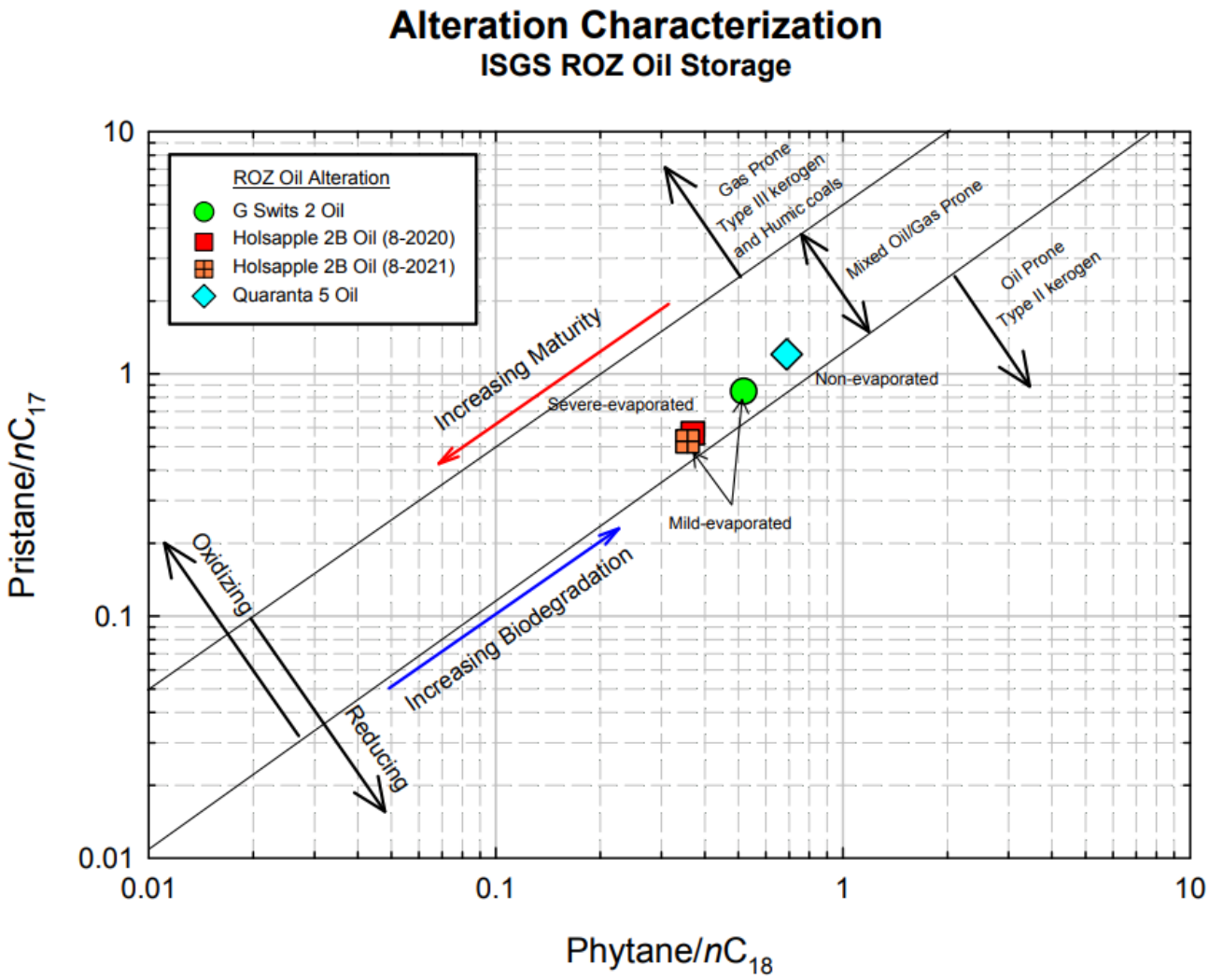


Figure 7-13. Isoprenoid/n-alkane ratios are routinely used as indicators of biodegradation, maturity and organic facies. Holsapple 2B oils measured lower Pr/nC_{17} and Ph/nC_{18} ratios than G Swits 2 and Quaranta 5 oils (i.e., > nC_{17} and nC_{18} paraffins are consistent with greater paraffin content). The study oils plot in the "Mixed Oil/Gas Prone" region; however, they all plot very near the "Marine line" consistent with a predominant marine source. The differences among the study oils appears due to maturity (Holsapple 2B > G. Swits 2 > Quaranta 5) and not biodegradation.

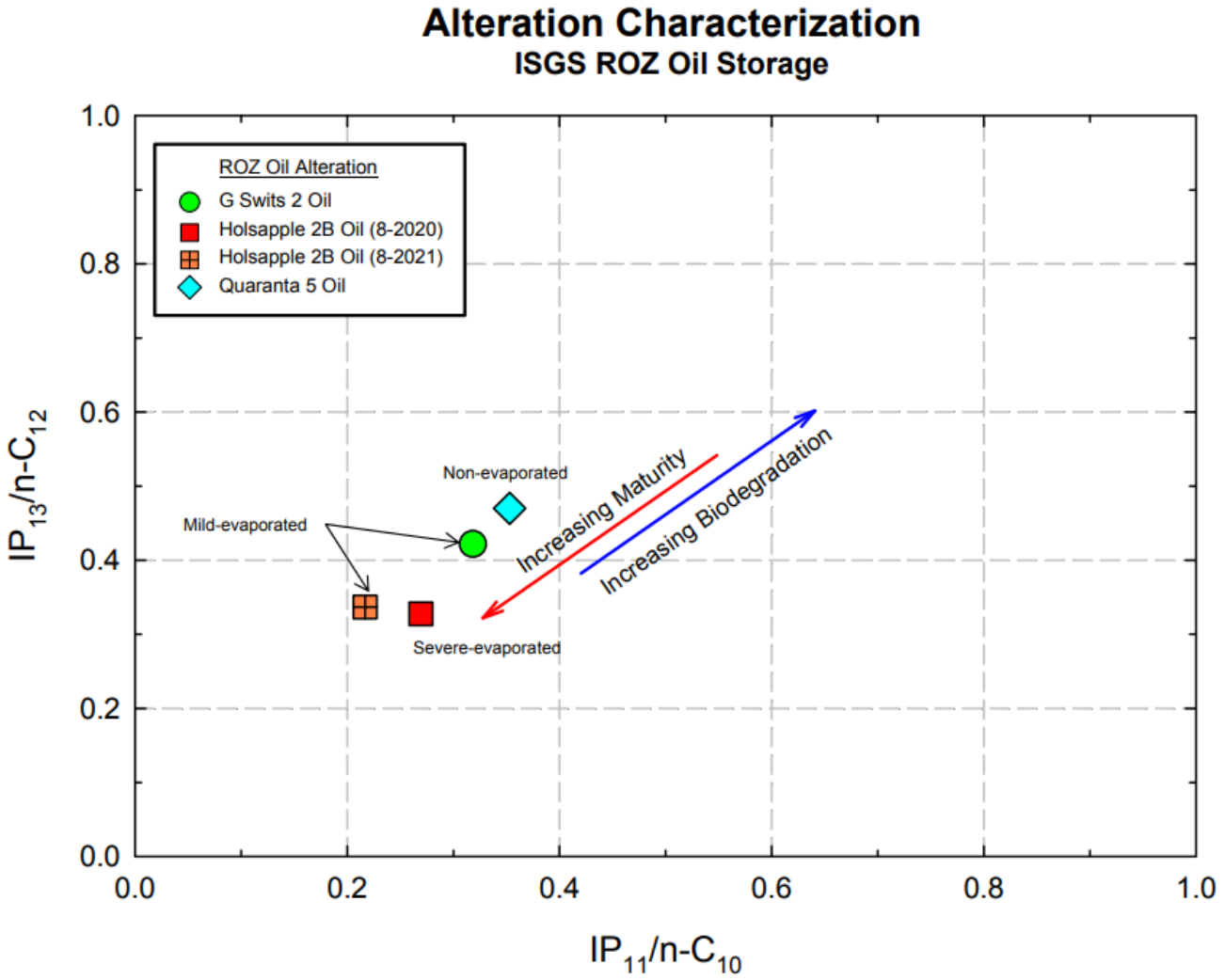


Figure 7-14. Isoprenoid/n-alkane ratios are also maturity indicators. Lower IP11/nC_{10} and IP13/nC_{12} ratios suggest that the two Holsapple 2B oils are more mature than the G Swits 2 oil and the Quaranta 5 oil.

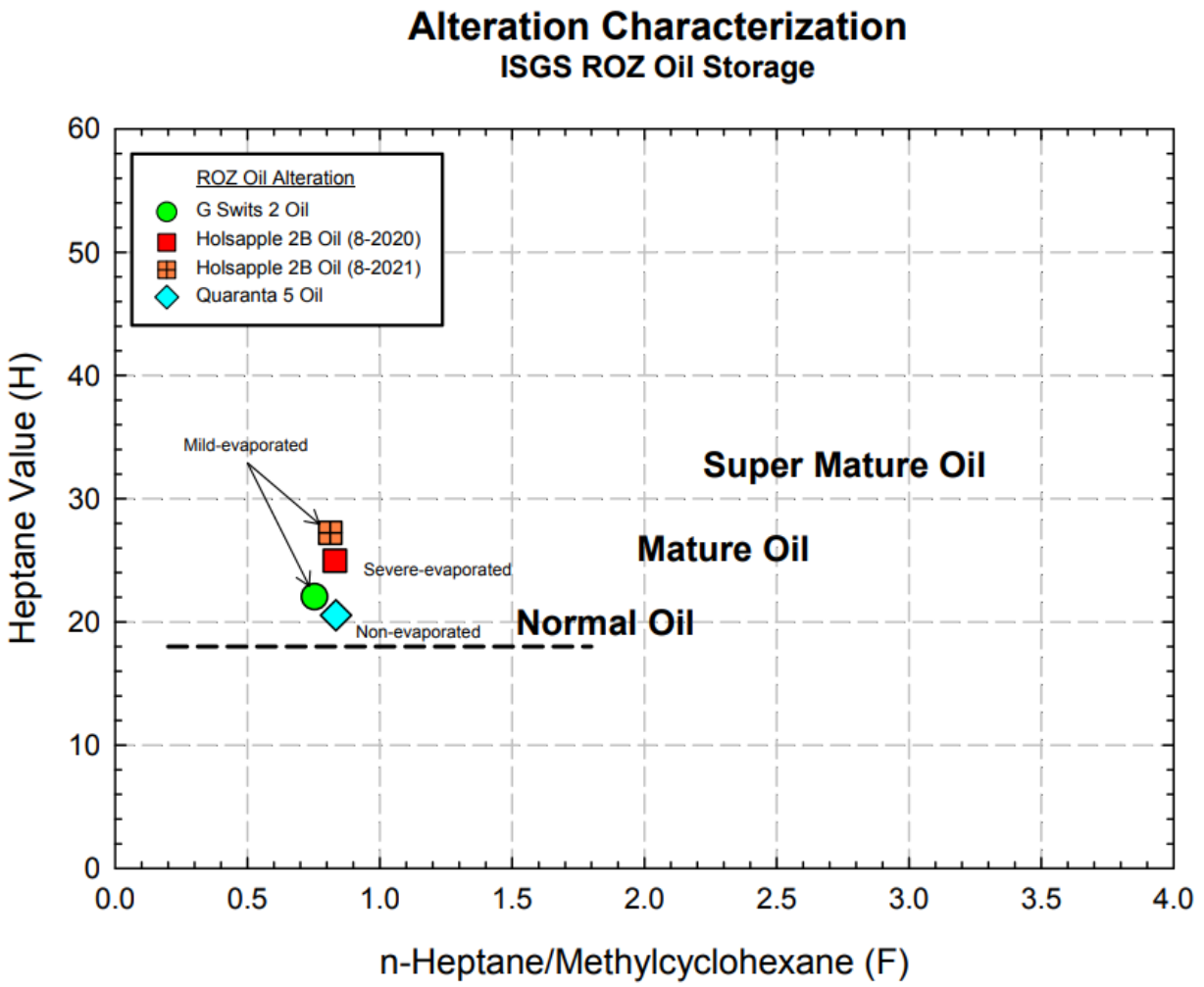


Figure 7-15. Thompson light hydrocarbon ratios, nC7/MCH and Heptane Value are relative maturity indicators. Study oil nC_7/MCH vary insignificantly whereas the Heptane Values suggests that Holsapple 2B oils are slightly higher maturity than G Swits 2 and Quaranta 5 oils (similar maturity order as suggested on the previous figures).

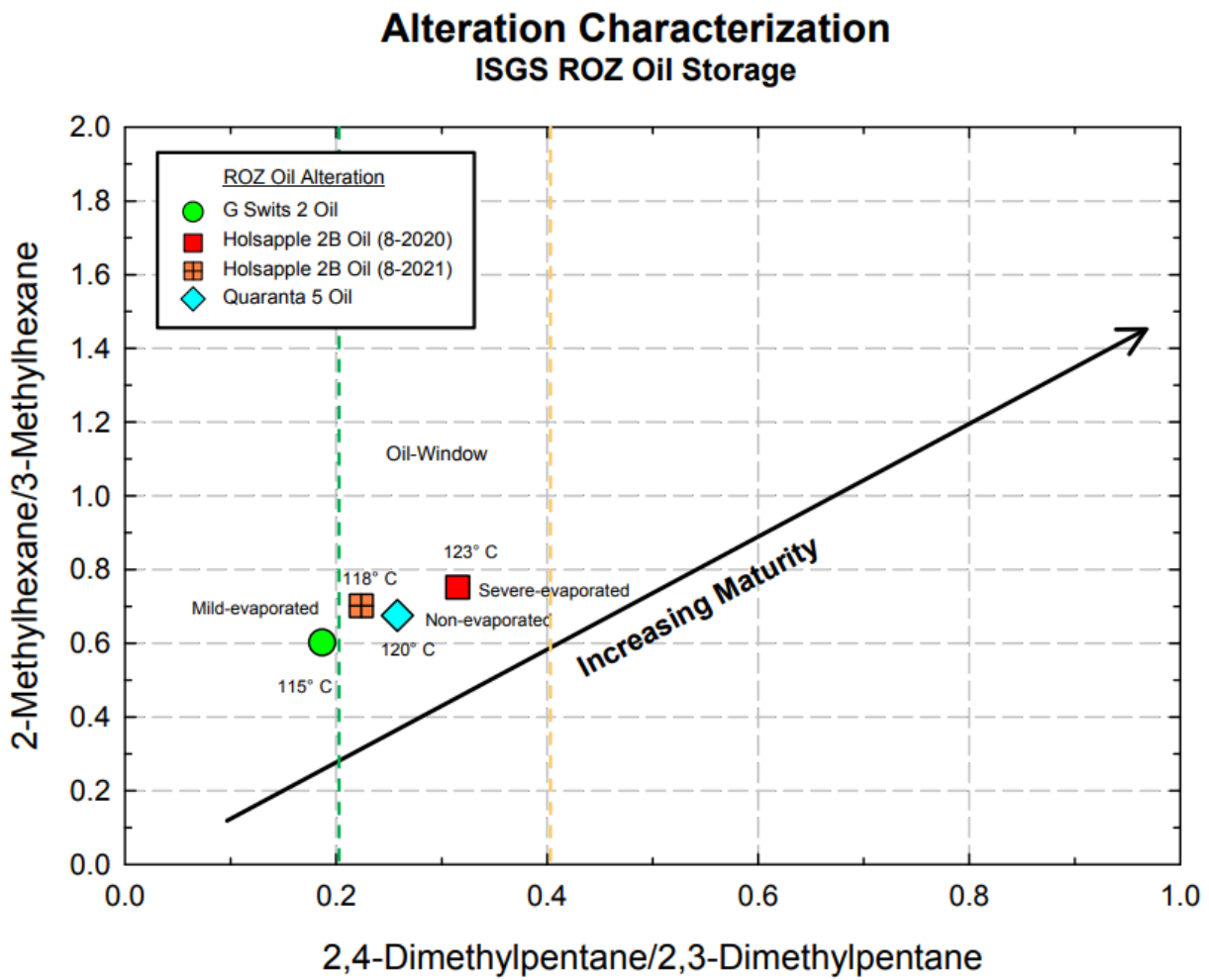


Figure 7-16. The ratios of 2,4-DMP/2,3-DMP and 2-MH/3-MH are "temperature-of-generation" indicators (Koblova et al., 1980; Mango 1987) and reflect levels of thermal maturity of a homologous oil family. Of the two ratios, 2,4-DMP/2,3-DMP is thought to be the better temperature function (Mango, 1990). A parameter based on the 2,4-DMP/2,3-DMP ratio developed by BeMent et al. (1994), Ctemp {ºC=140+15[ln(2,4-DMP/2,3-DMP)]}, estimates the temperature of hydrocarbon expulsion shows the estimated expulsion values (115-123° C) and suggests that the study oils were generated in the oil-window. However, this maturity trend conflicts with the previous maturity trends (e.g., 2021 Holsapple 2B oil < Quaranta 5 oil); possibly due to differential light HC evaporation or the oils do not constitute a homologous oil family.

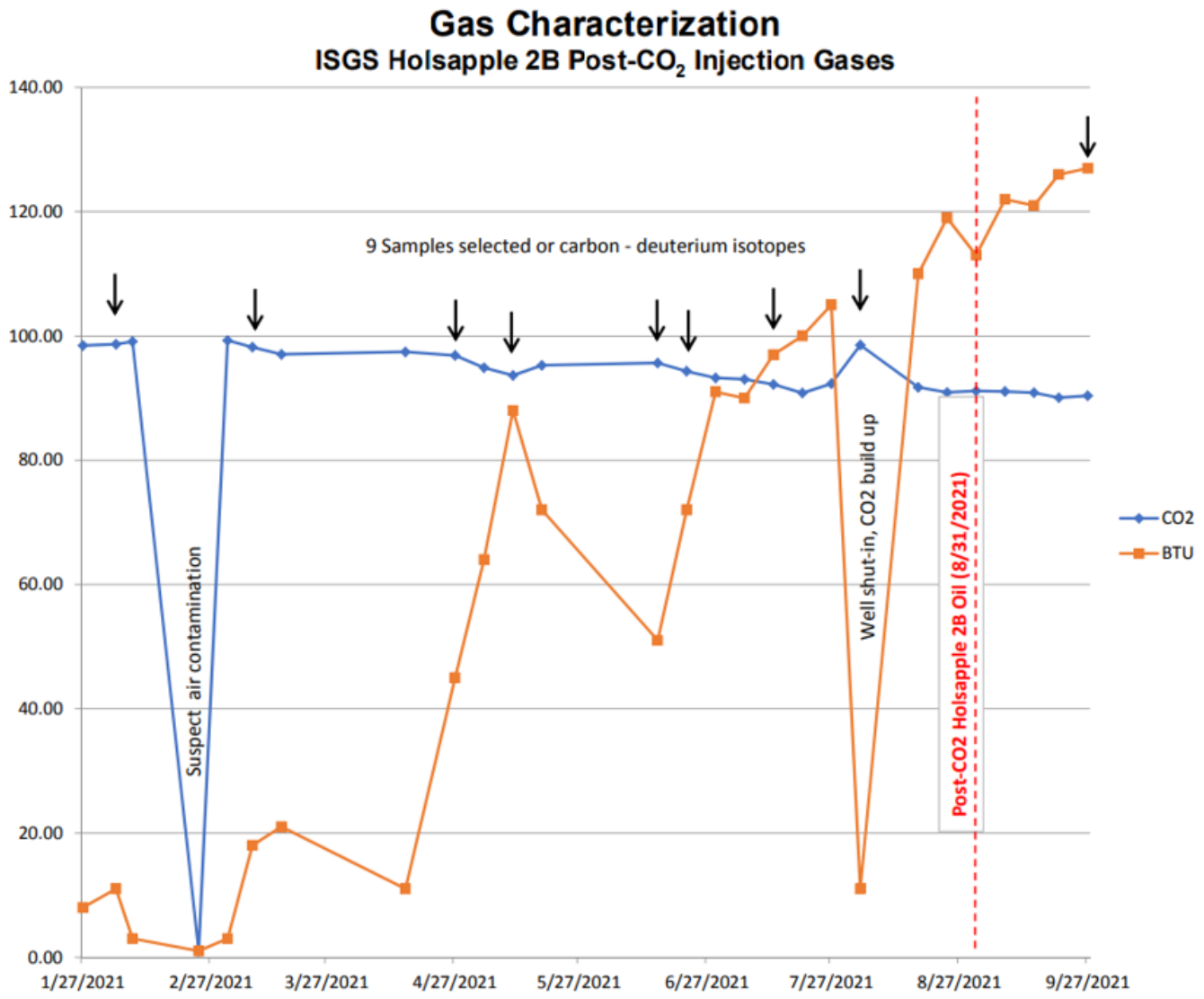


Figure 7-17. CO_2 and BTU line plot of 2021 Post-CO_2 injection gases from Holsapple 2B. With exception of gas collected 2/24/21 (suspect air contamination) the gases are predominantly CO_2 (90.1-99.3%) and CO_2 decreases slightly over time.

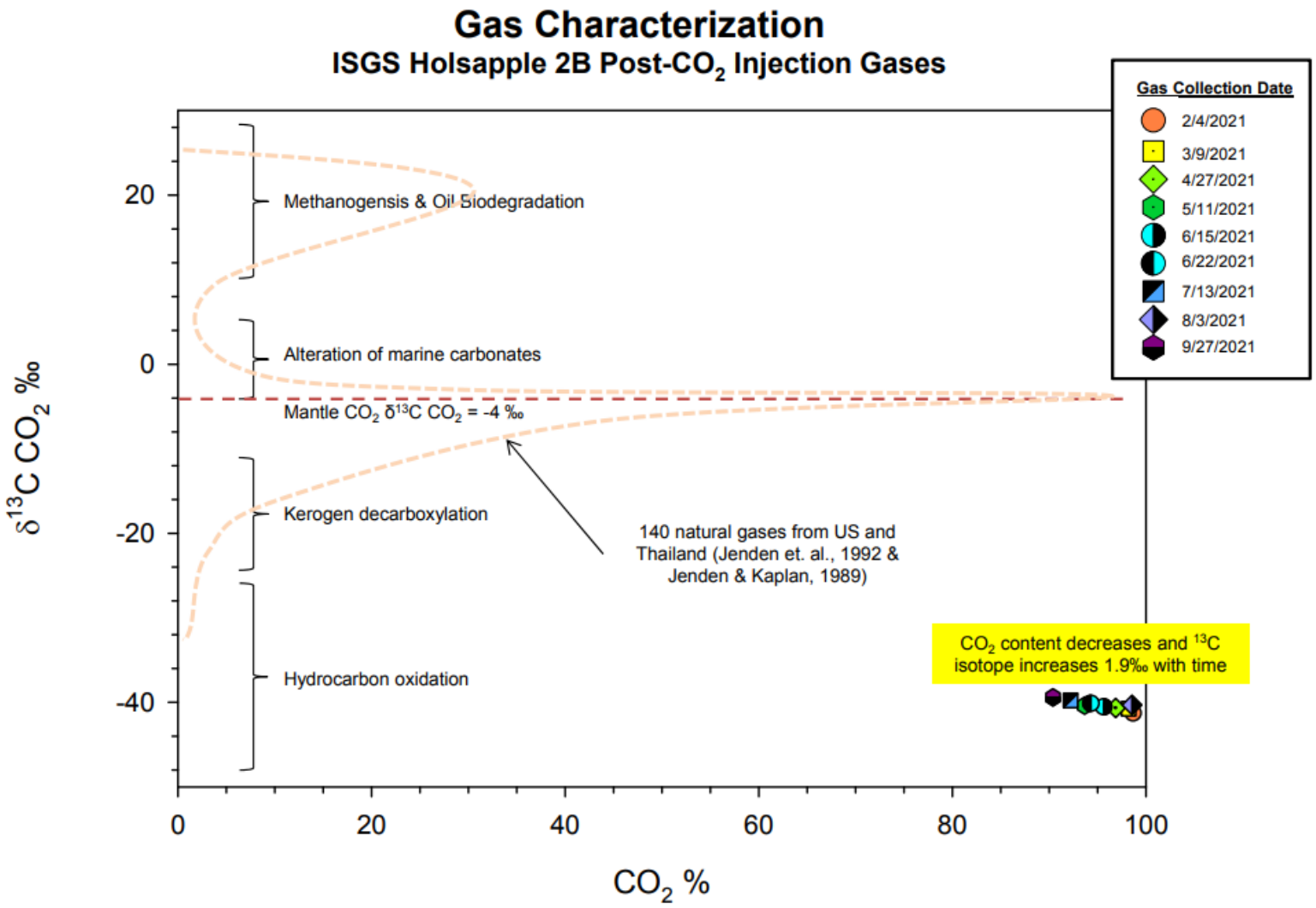


Figure 7-18. CO_2 content vs. $\delta^{13}C$ CO_2 for Holsapple 2B gases. The gases measured > 90% CO_2 and $\delta^{13}C$ CO_2 varies slightly (-41.3‰ to -39.4‰, Δ = 1.9‰); with a slight isotopic increase with time (If injected in 2020 why is CO_2 changing isotopically over time?). CO_2 is injected and its origin is not confirmed; however, these data suggest that the CO_2 is from hydrocarbon oxidation. The combination of decreasing CO_2 content and increasing $\delta^{13}C$ CO_2 suggests that the isotopically heavier CO_2 derived from kerogen decarboxylation is increasing with time.

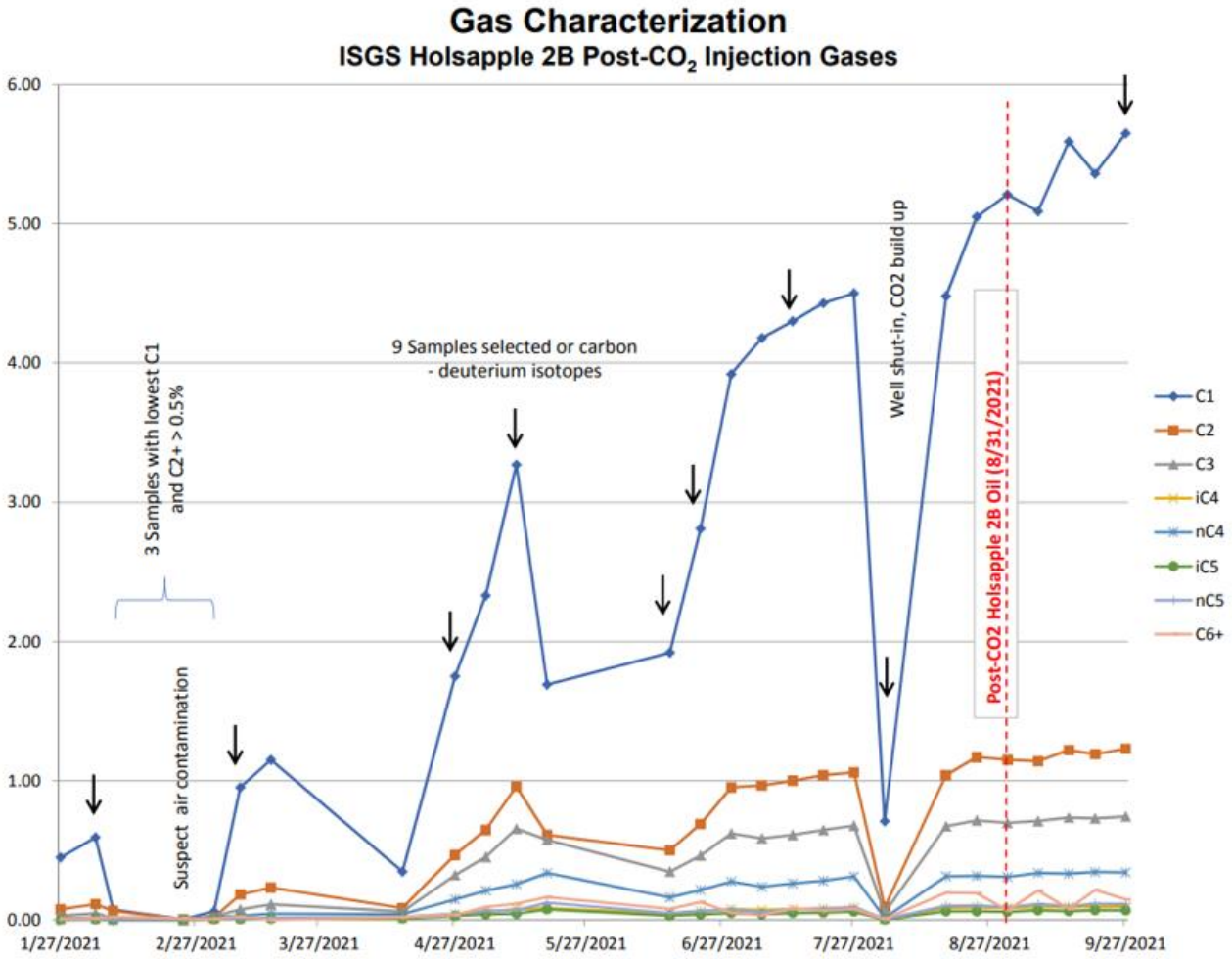


Figure 7-19. C_1-C_6+ line plot of 2021 Post-CO_2 injection gases from Holsapple 2B. The HC gases are predominantly C_1 (35.4-80.7%). C_1 and C_2+ increase slightly over time. Gases collected 1/27/21-4/15/21 vary significantly more than gases collected 5/4/21- 9/27/21. C_6+ liquid HC's are present and often greater than pentanes.

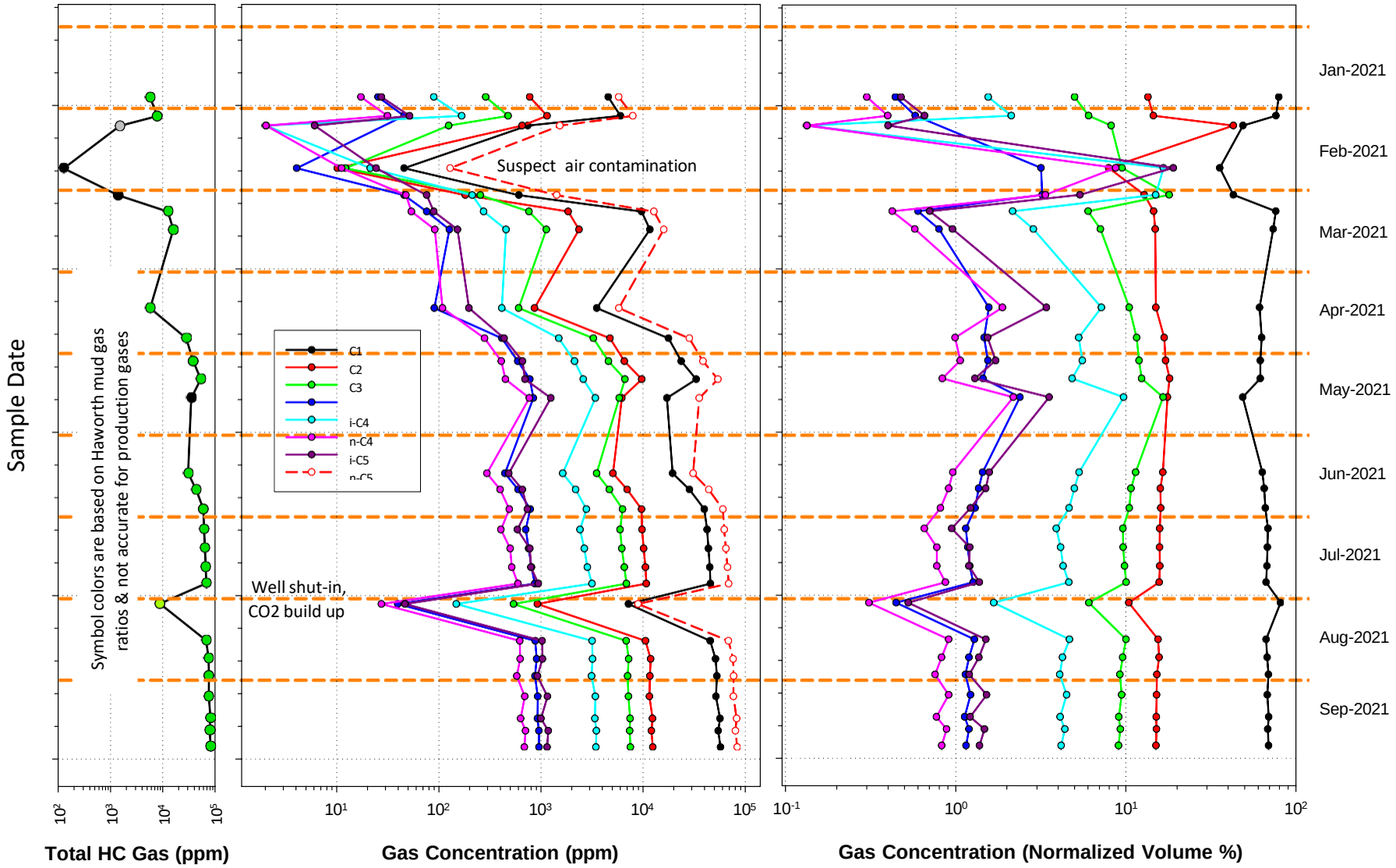


Figure 7-20. Gas concentration summary time logs for gases between 1/27/2021 and 9/27/2021 from Holsapple 2B (post CO_2 injection). Total HC gas ranges from 127-82,380 ppm (left track) and increases with time. Abnormally low total HC gases occur in Feb-2021 (suspected air contamination) and Aug-3 (well shut in and CO_2 buildup). The gases measured significant quantities of C_2-nC_5 HC's. Normalized methane contents range from 35.4-80.7% (right track) and the C_2+ components range from 0 to 42.6% (average = 5.9%) of the C_1-C_5 gases.

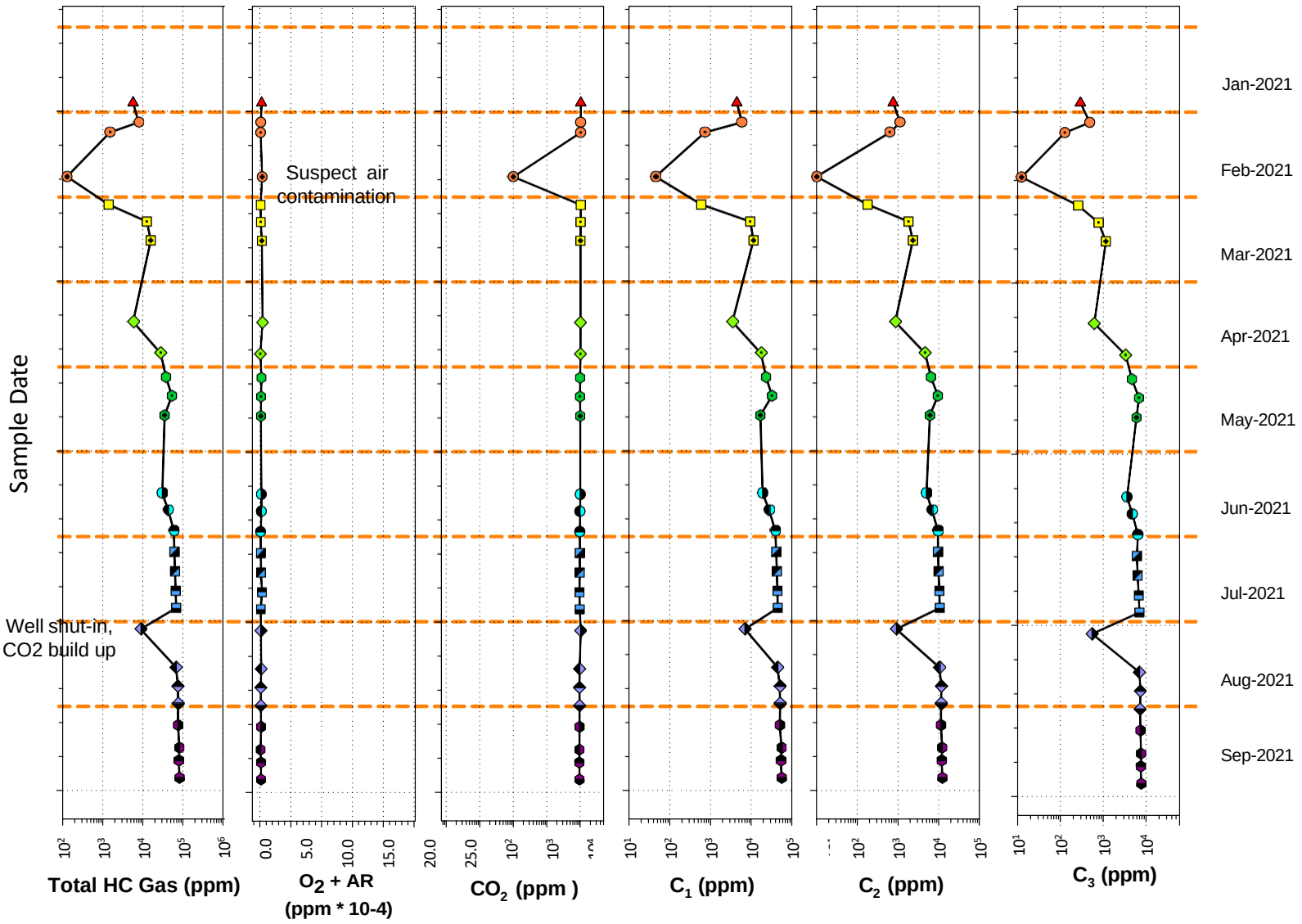


Figure 7-21. Gas raw chemistry time logs – 1 for gases collected between 1/27/2021 and 9/27/2021 from Holsapple 2B (post CO_2 injection). CO_2 is high ranging 9700-992,800 ppm (average = 91%). Methane is the predominant HC gas (35.4-80.7%, average = 64.5%) and stabilizes after April-2021. Ethane and propane are present and variable (10-12,300 ppm and 12-7420 ppm, respectively). Both ethane and propane increase significantly from 1/27/21 to 4/27/21 and then slightly from 4/27/21 to 9/27/21.

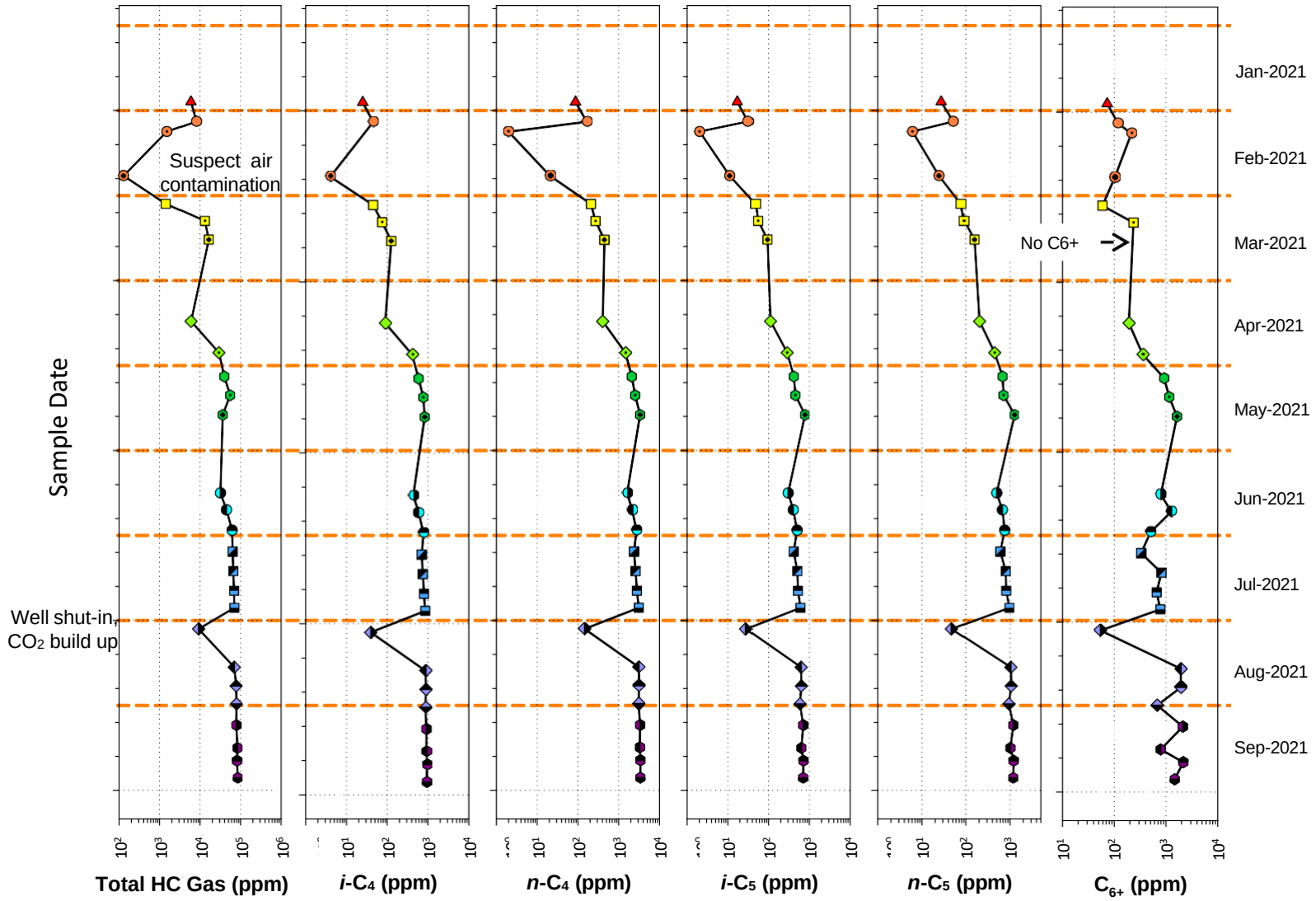


Figure 7-22. Gas raw chemistry time logs – 2 for gases collected between 1/27/2021 and 9/27/2021 from Holsapple 2B (post CO_2 injection). C_4-C_5 concentrations are significant and variable in the study gases (butanes range 0-3440 ppm and pentanes range 2-1230 ppm). C_6+ contents are significant (54-2160 ppm) consistent with co-generation of liquid HC's.

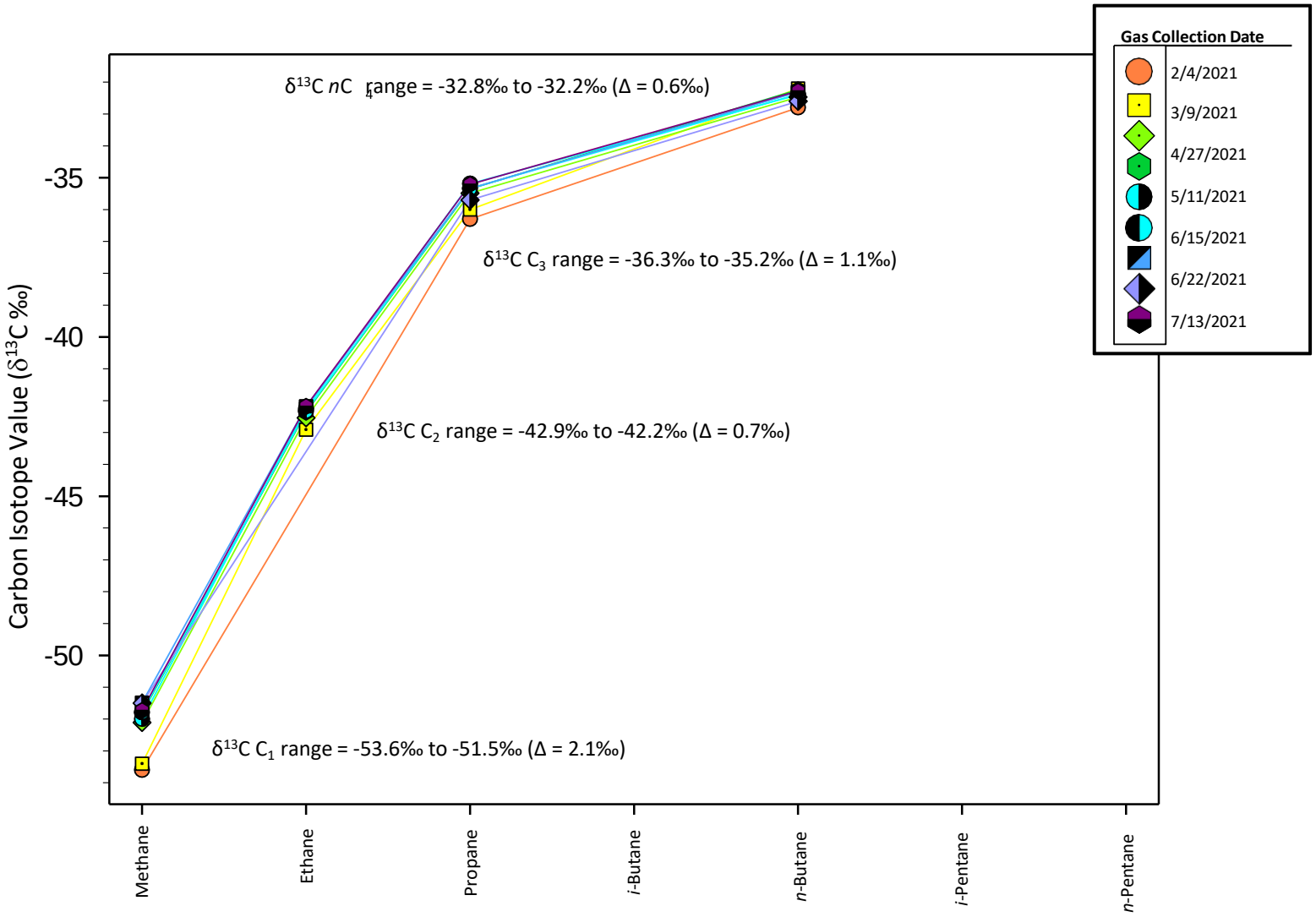


Figure 7-23. Summary of the C_1, C_2, C_3, and nC_4 carbon isotopic compositions for Holsapple 2B storage gases collected 1/27/21-9/27/21 (9 of 27 were submitted for isotope analysis). The storage gases exhibit isotope trends typical of thermogenic gases (i.e., $C_1 < C_2 < C_3 < nC_4$). Methane gases collected February and March are isotopically lighter than the later collected gases. Ethane could not be measured in two gases, 2/4/21 and 8/3/21.

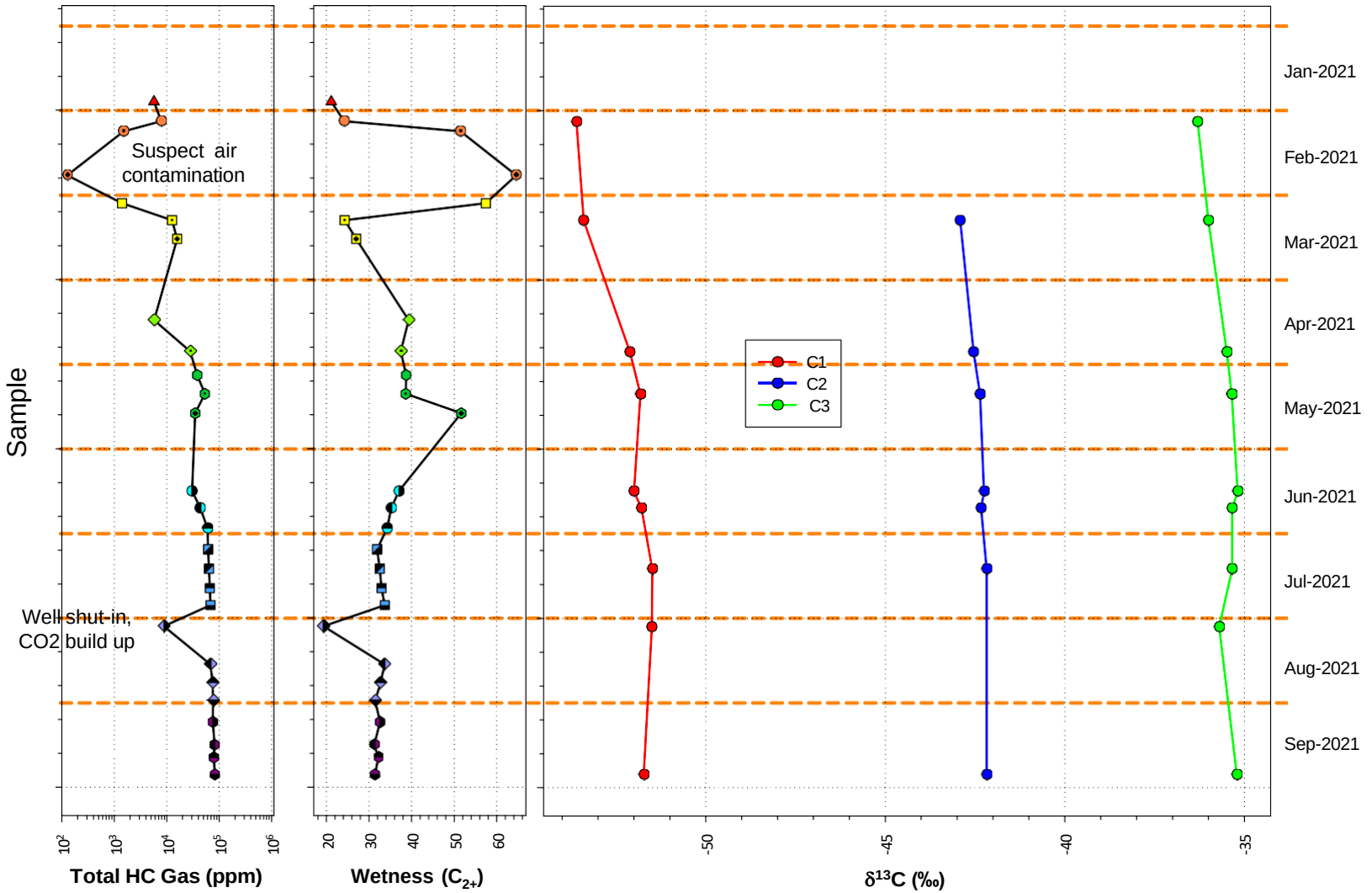


Figure 7-24. Gas C_2+ wetness and carbon isotope summary log for Holsapple 2B gases collected between 1/27/2021 – 9/27/2021 (post CO_2 injection). The gases are wet ranging from 19.3-64.6% C_2+ (center track) with wettest gases in February and early March (near air contaminated sample). Methane carbon isotopes range from -53.6 to -51.5‰ (Δ = 2.1‰ which exceeds online and offline instrumental error) with February-March gases significantly lighter than April- September gases. Ethane and propane carbon isotopes exhibit less variability with $\delta^{13}C$ C_2 ranging -42.9‰ to -42.2‰ (Δ = 0.7‰) and $\delta^{13}C$ C_3 ranging -36.3‰ to -35.2‰ (Δ = 1.1‰ and greater than instrumental error).

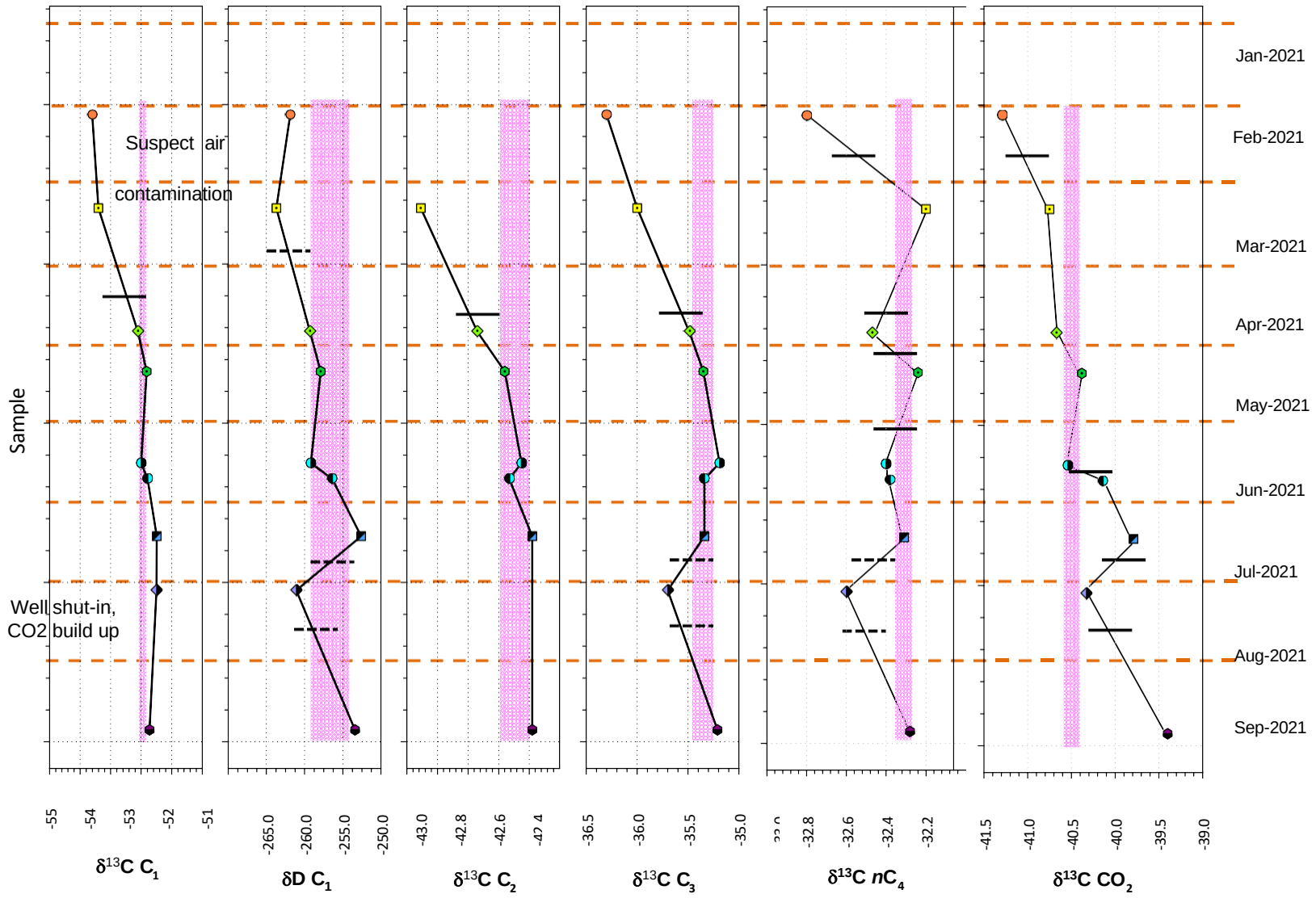


Figure 7-25. C_1-nC_4, CO_2 carbon and C_1 deuterium isotope tracts show the relative gas isotope signatures for Holsapple 2B storage gases collected 1/27/21 – 9/27/21. Pink rectangles show the off-line method instrumental error (±0.1‰ for carbon isotopes and ±2.0‰ for deuterium isotopes). Note that gases collected 2/4, 3/9 and 8/3 methane, propane and nC_4 required online analysis which has about two-times the instrumental error (±0.2‰ for carbon isotopes and ±5‰ for deuterium isotopes). Black horizontal lines indicate compositional change; dashed horizontal lines are questionable compositional change due to greater online instrumental error. Excluding the 8/3/21 gas, the components generally get heavier with time.

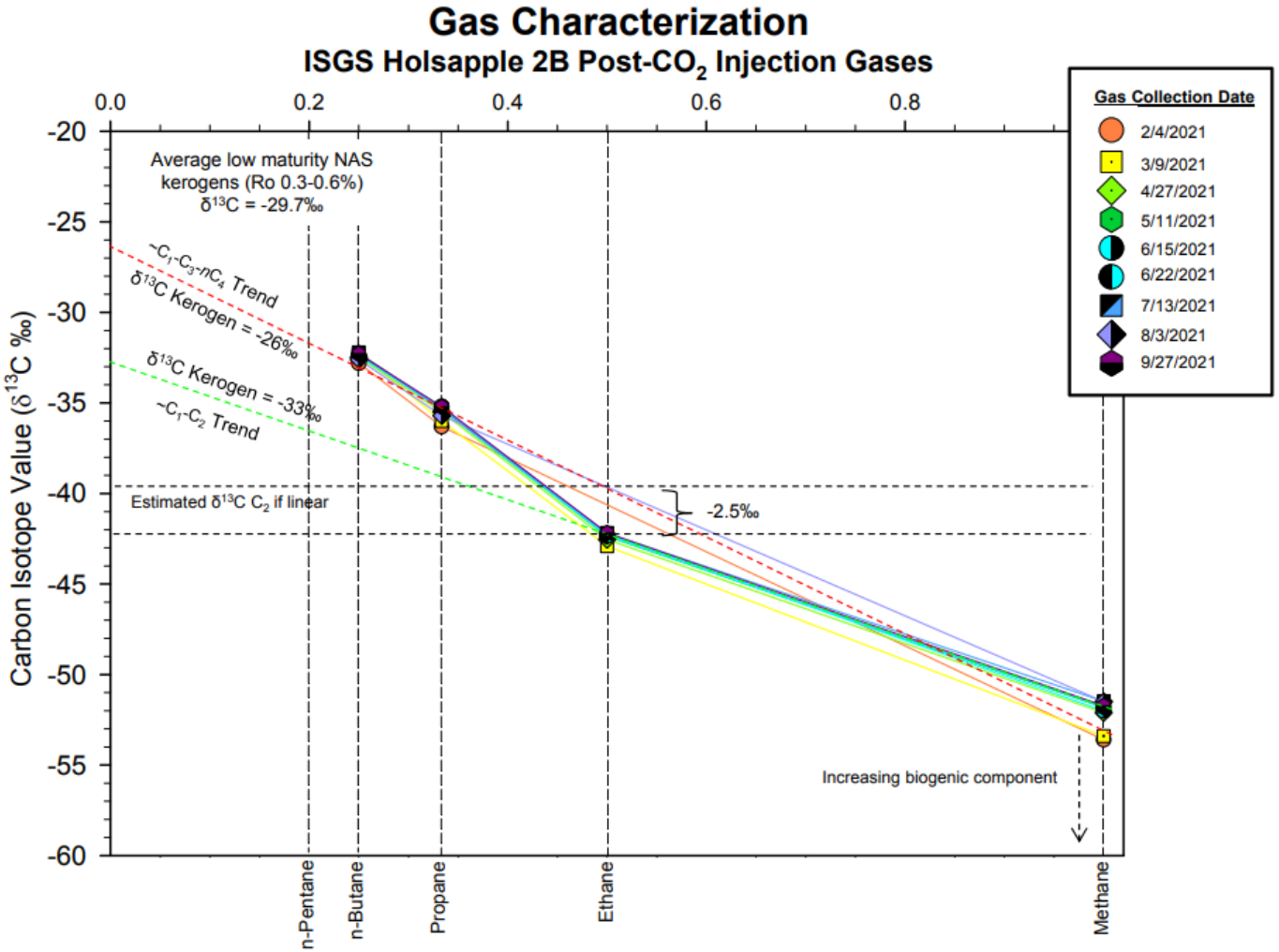


Figure 7-26. Stable carbon isotopic compositions of the hydrocarbon gases plotted on the reciprocal carbon number Chung plot (Chung et al., 1988) for Holsapple 2B storage gases. Chung postulated that gas components generated from a single source exhibit a semi-linear reciprocal isotope trend; therefore, this diagram suggests that the gases represent mixtures from more than one source with C_1-C_2 providing one possible relationship and C_1-C_3-nC_4 a different relationship. The C_1-nC_4 dashed red trend line approximates the trend of gas components from a single source with C_2 deviating -2.5‰ from the best-fit linear C_1-nC_4 tend line at greater than instrumental error. February and March gas methane is light possibly due to mixing with light biogenic gas. Extension of the two linear relationships to the left axis provides an estimate of the kerogen isotope that generated the gases ($\delta^{13}C$ kerogen ≅ -26‰ or -33‰). Lis et. al., 2006, reported average bulk isotopes for five low maturity New Albany Shale kerogens at -29.7‰ (mid-point between estimated kerogen isotopes from the two linear trends).

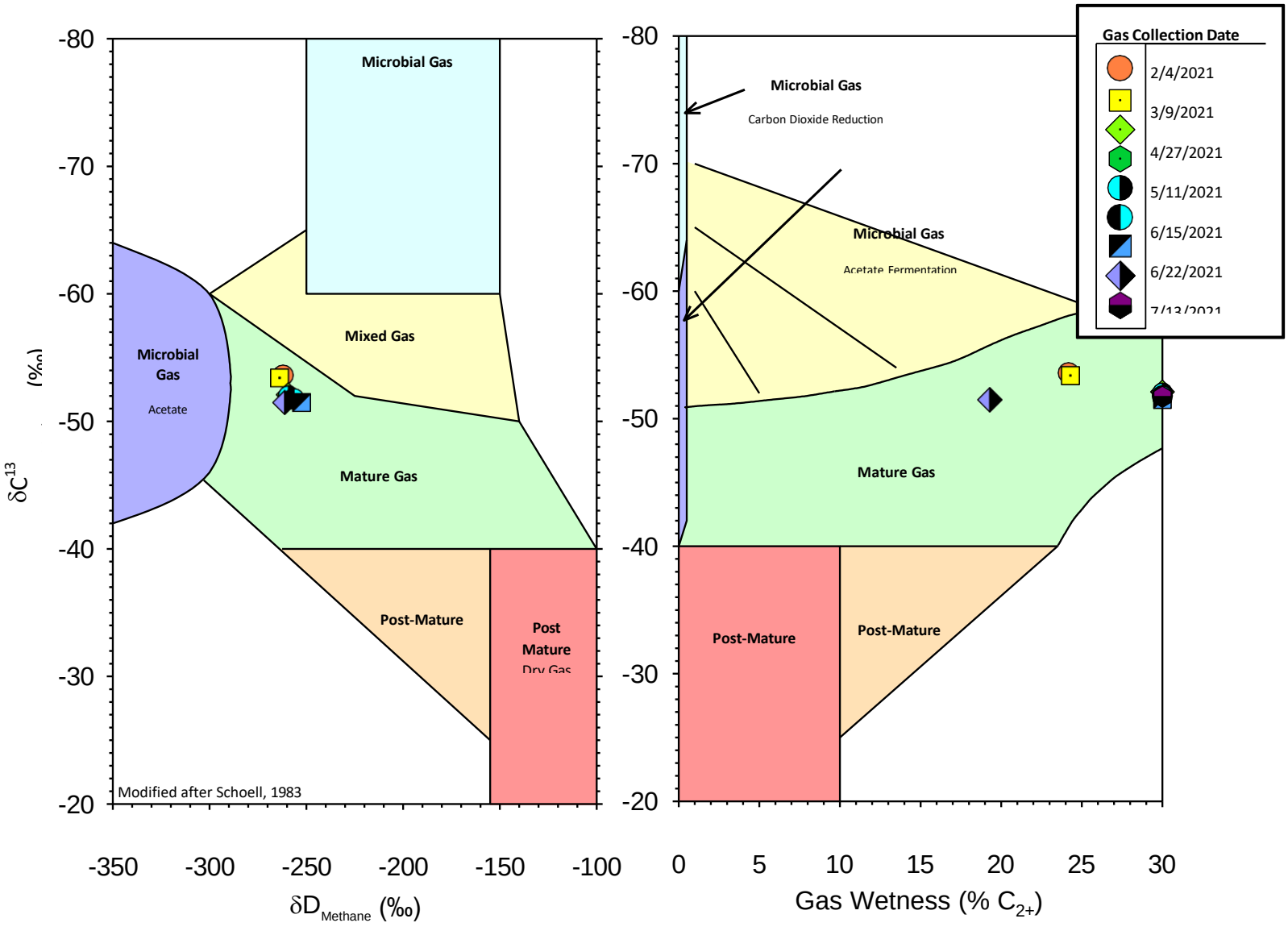


Figure 7-27. The stable carbon and hydrogen isotopic composition ($\delta^{13}C$ and δD) of methane in gas samples provides information about their genetic origin (Schoell, 1983; Whiticar et al., 1986 and Coleman et al., 1988). Both diagrams indicate that the Holsapple 2B storage gases are wet lower maturity gases. C_2+ appears variable, possibly due to shut in (8/3/21 is the driest gas) and initial sampling (2/4/21 and 3/9/21 are intermediate) whereas April-September are wet (≥ 30%). The left diagram ($\delta D\ C_1 - \delta^{13}C\ C_1$) is probably more accurate suggesting that the gases are lower maturity gases or possibly mixed biogenic – thermogenic gases (particularly 2/4 and 3/9 gases).

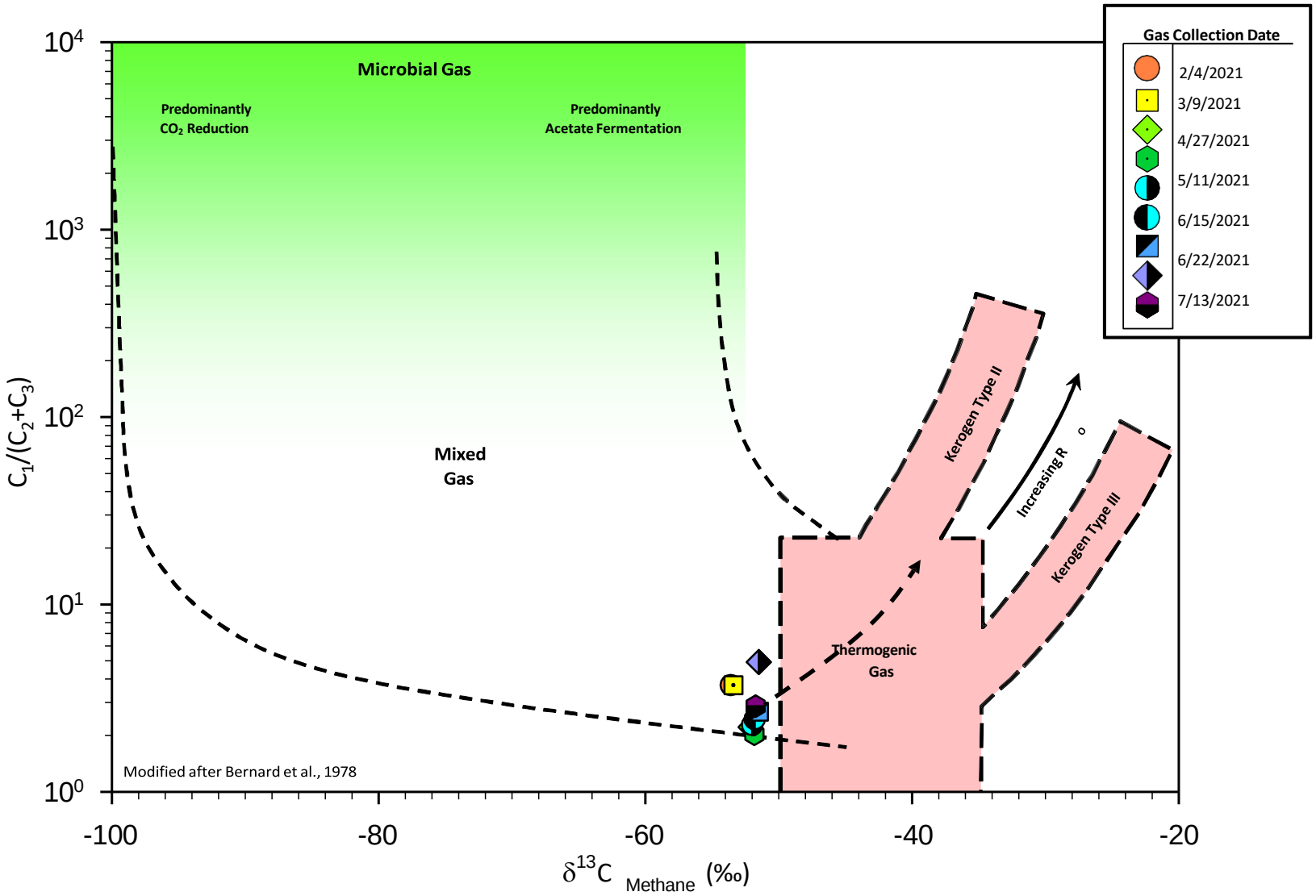


Figure 7-28. This Bernard diagram provides a genetic characterization of natural gas based on the chemical ratio $C_1/(C_2+C_3)$ and the carbon isotopic value of methane ($\delta^{13}C_{Methane}$) for Holsapple 2B gases. These data suggest that Holsapple 2B gases are of mixed biogenic – thermogenic origin and positioning suggests of predominantly Type II kerogen origin. Note that Milkov (2021) reported that the Bernard approach to differentiating Type II and Type III kerogen sourced gases is not reliable due to being based on small datasets.

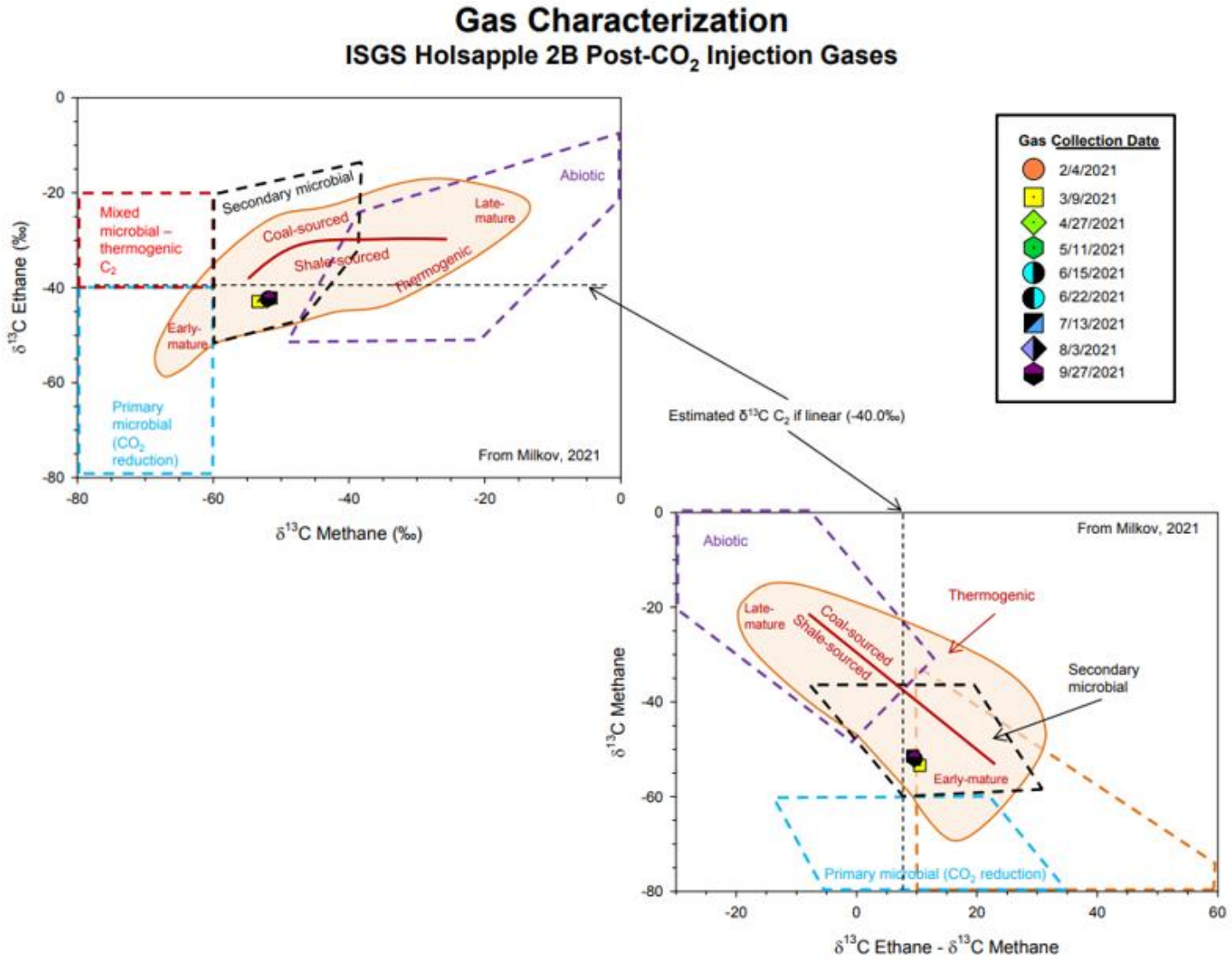


Figure 7-29. Milkov (2021) reported that separation of Type II shale gases and Type III coal gases using methane vs. ethane isotope diagrams and ethane-methane vs. methane isotope diagrams are more accurate than the previous Bernard diagram. These interpretative diagrams suggest that the Holsapple 2B gases were derived from Type II shale source rock. Data positions are consistent with lower maturity; however, a minor biogenic component cannot be ruled out. Gas type classifications are based on 6798 shale and coal gases from 23 countries on six continents.

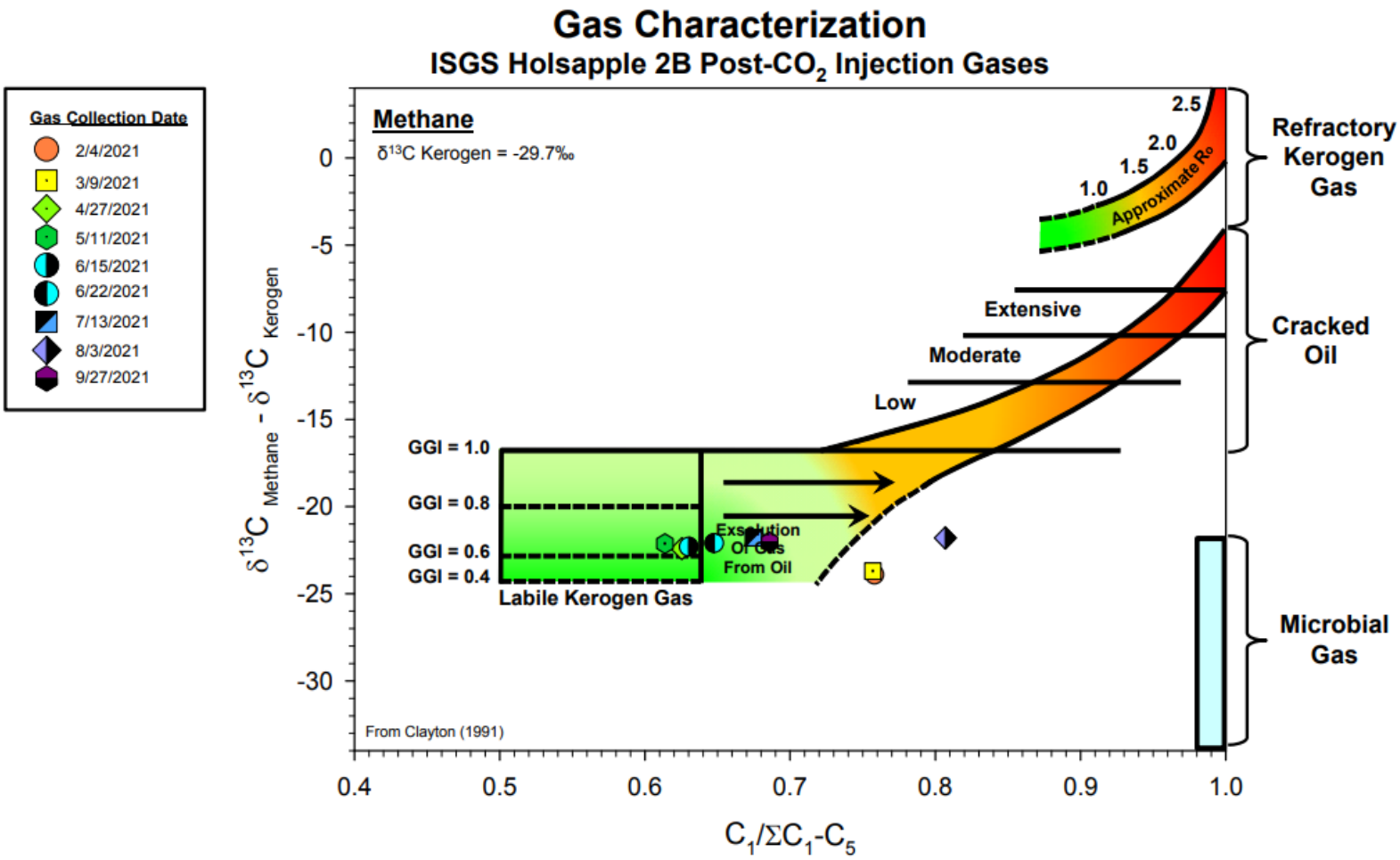


Figure 7-30. This Clayton diagram provides a genetic characterization, Gas Generation Index (GGI) and thermal maturity of natural gas based on the chemical ratio $C_1/\Sigma(C_1 \rightarrow C_5)$, and the carbon isotopic difference between methane and the generative kerogen ($\delta^{13}C_{Methane} - \delta^{13}C_{Kerogen}$) for Holsapple 2B gases. The GGI is defined as the fraction of generated gas to available gas. A bulk kerogen value of ***-29.7‰*** *was used and was selected as it is the average of 5 New Albany Shale low maturity kerogens (Lis et. al., 2006). This diagram suggests that 2/4/21 and 3/9/21 gases are mixed biogenic – thermogenic gases (high $C_1/\Sigma(C_1 \rightarrow C_5)$ and lower methane-kerogen isotopes). 4/27/21-9/27/21 gases are mature Type II gases (GGI's 0.6-0.65); 8/3/21 gas has a high methane content (well shut in) and similar methane-kerogen isotope as the 4/27/21-9/27/21 gases.*

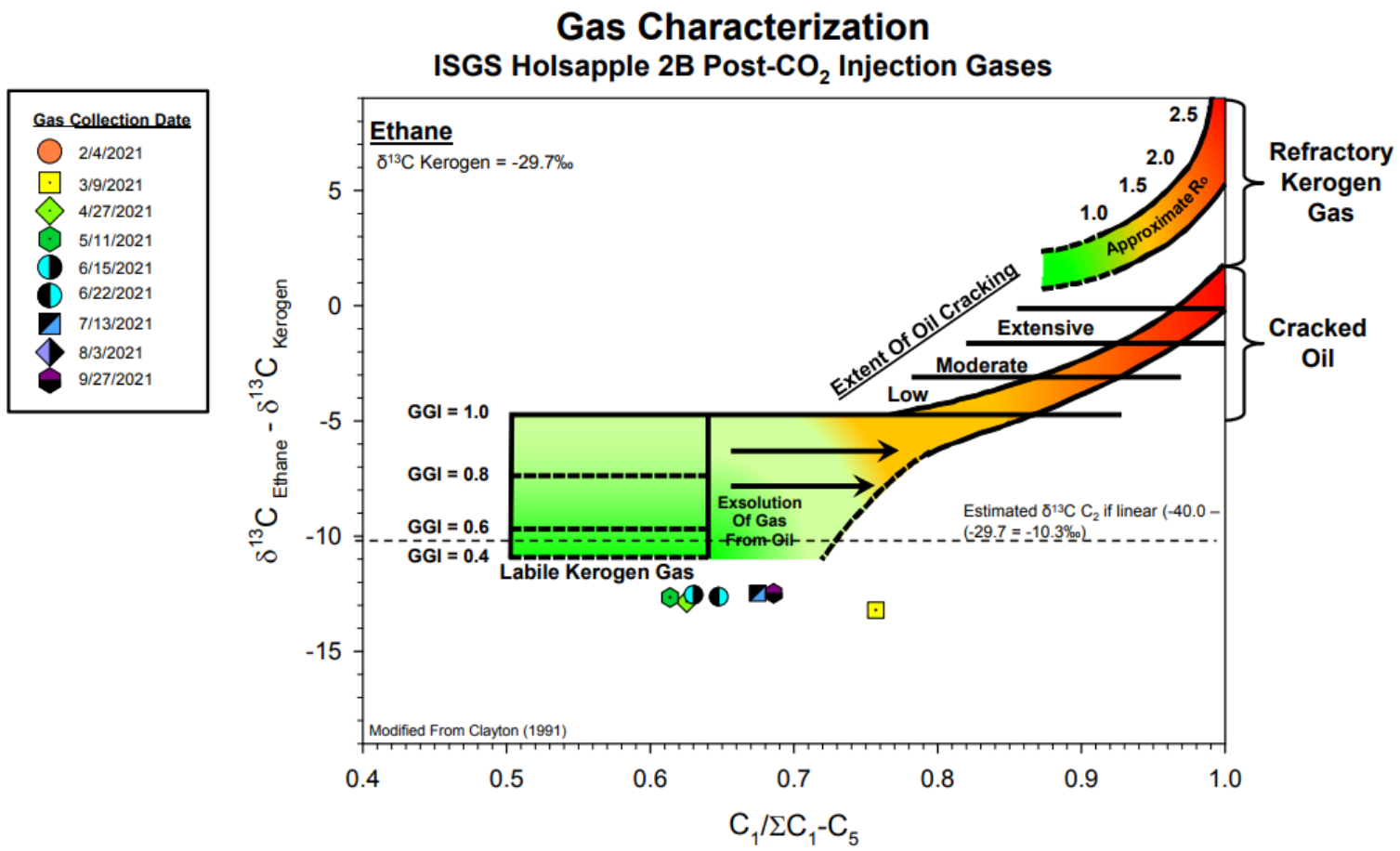


Figure 7-31. This Clayton diagram provides a genetic characterization, Gas Generation Index (GGI) and thermal maturity of natural gas based on the chemical ratio $C_1/\Sigma(C_1 \rightarrow C_5)$, and the carbon isotopic difference between ethane and the generative kerogen ($\delta^{13}C_{Ethane} - \delta^{13}C_{Kerogen}$) for Holsapple 2B gases. The GGI is defined as the fraction of generated gas to available gas. A bulk kerogen value of ***-29.7‰*** *was used and was selected as it is the average of 5 New Albany Shale low maturity kerogens (Lis et. al., 2006). This diagram suggests that the study gas ethane is lower maturity than methane (GGI < 0.4) and due to the deviation of ethane isotopes as observed on the Chung diagram (Figure 7-26). The estimated ethane isotope, if derived from the source rock that generated methane, propane and n-butane is -40‰ which suggests that the ethane is similar low maturity as methane (GGI ≅ 0.5).*

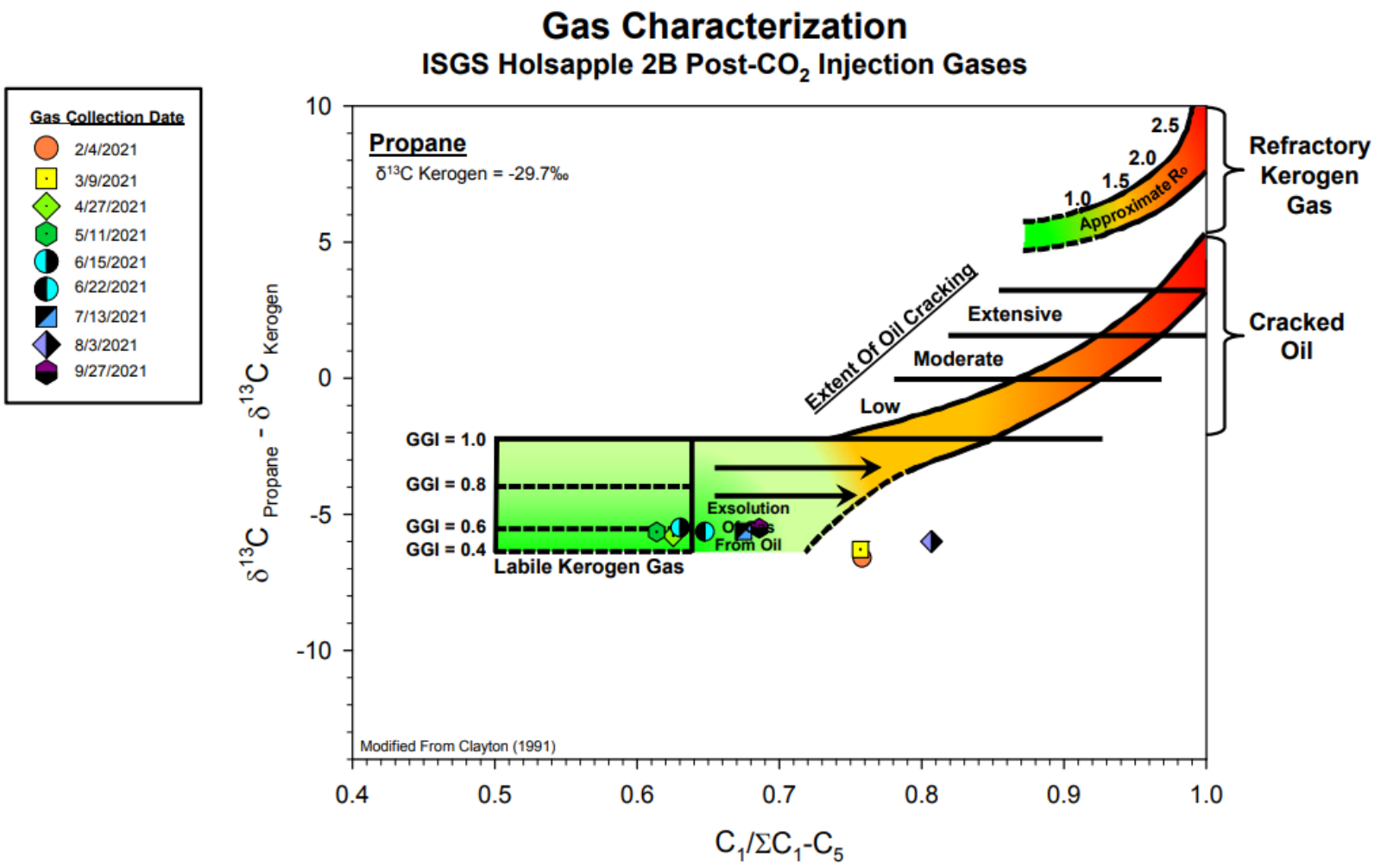


Figure 7-32. This Clayton diagram provides a genetic characterization, Gas Generation Index (GGI) and thermal maturity of natural gas based on the chemical ratio $C_1/\Sigma(C_1 \rightarrow C_5)$, and the carbon isotopic difference between propane and the generative kerogen ($\delta^{13}C_{propane} - \delta^{13}C_{Kerogen}$) for Holsapple 2B storage gases. The GGI is defined as the fraction of generated gas to available gas. A bulk kerogen value of -29.7‰ was used and was selected as it is the average of 5 New Albany Shale low maturity kerogens (Lis et. al., 2006). This diagram suggests that the study gases are low maturity (GGI's 0.6) which is plausible and similar to methane. Gases collected 2/4, 3/9 and 8/3 have high $C_1/\Sigma(C_1 \rightarrow C_5)$ due to contribution of biogenic gas or having been shut in.

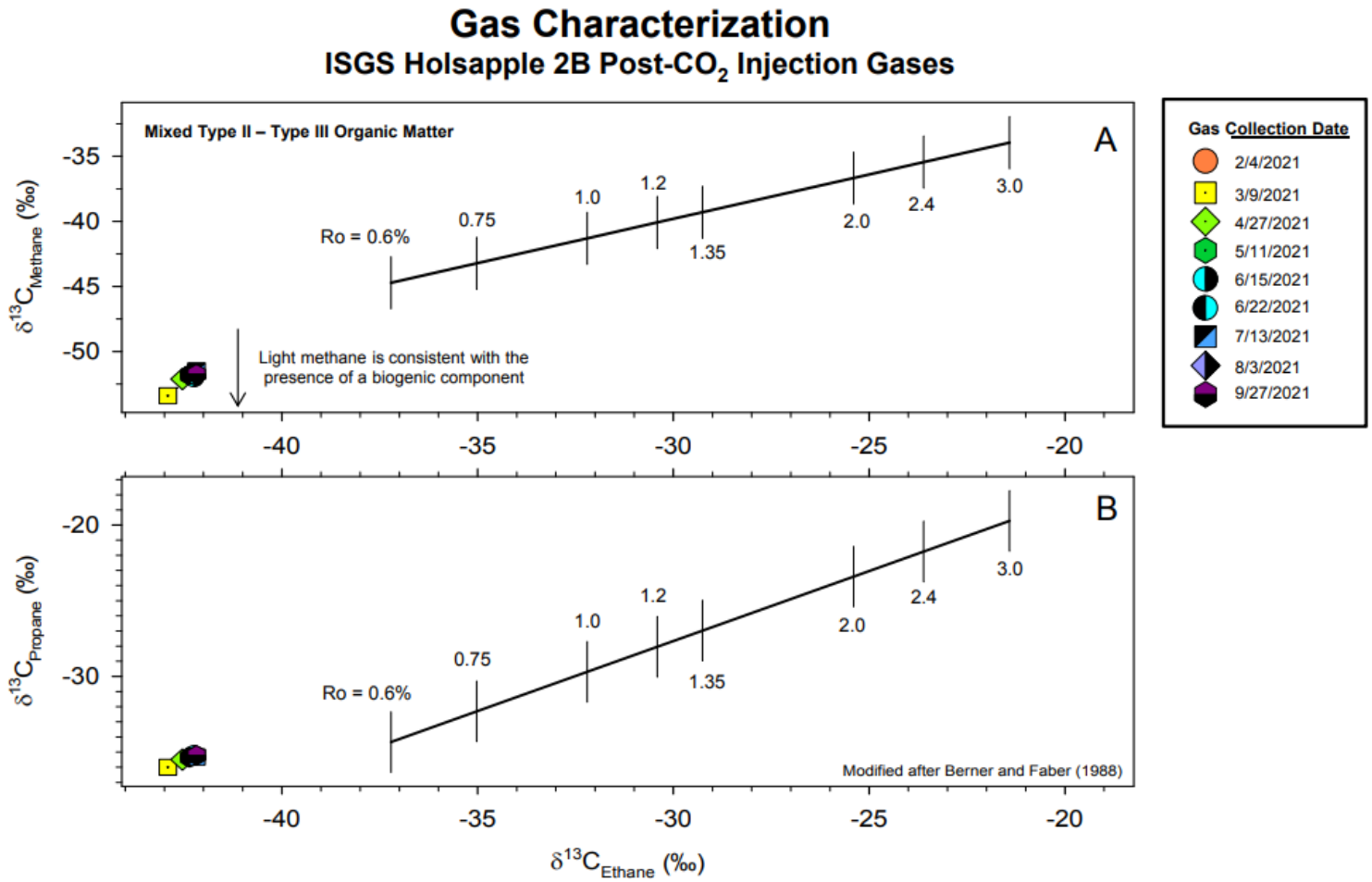


Figure 7-33. Inferred thermal maturity (equivalent vitrinite reflectance %R_O) of the generative source based on the stable carbon isotopic relationships between ethane versus methane (A) and ethane versus propane (B) for gases from Holsapple 2B. This model is based on gas generation from a mix of Type II and Type III kerogens and thus is possibly inaccurate. The upper diagram shows that the gases are suggested to be immature. Gases with low $\delta^{13}C$ C_1 < -50‰ plot well below the Ro ladder possibly due to being mixtures of light biogenic methane and heavier thermogenic gas. The lower diagram also suggests that the gases are immature.

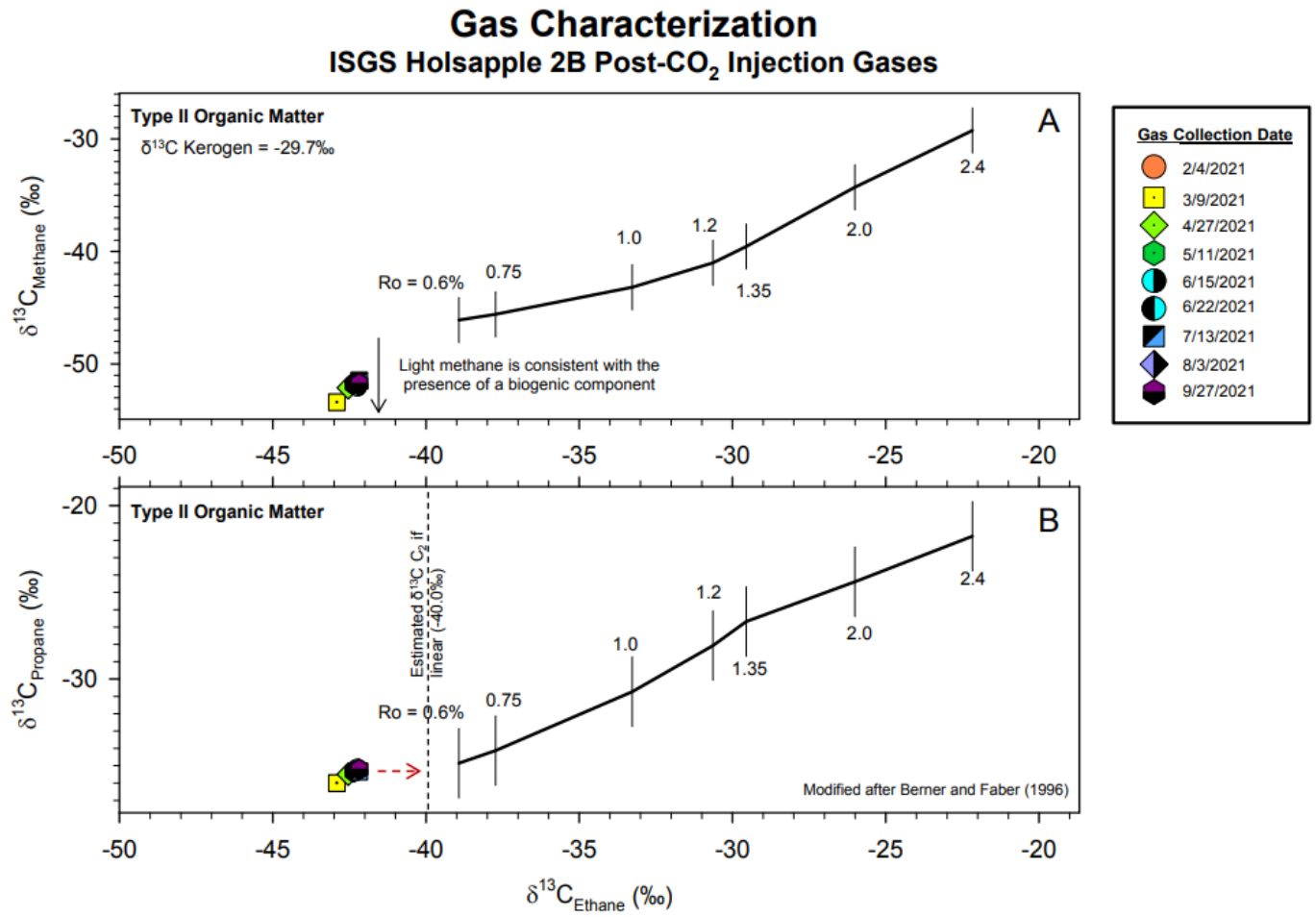


*Figure 7-34. Inferred thermal maturity (equivalent vitrinite reflectance %R_O) of the generative source based on the stable carbon isotopic relationships between ethane versus methane (A) and ethane versus propane (B), are shown for Type II organic matter for Holsapple 2B gases. A bulk kerogen value of -**29.7‰** was used and was selected as it is the average of 5 New Albany Shale low maturity kerogens (Lis et. al., 2006). The upper diagram shows that the gases are suggested to be low maturity (Ro_{eq} < 0.5%). Gases with low $\delta^{13}C$ C_1 < -50‰ plot below the Ro ladder possibly due to being mixtures of light biogenic methane and heavier thermogenic gas. The lower C_2-C_3 diagram also suggests that the gases are low maturity (Ro_{eq} < 0.5%); however, the maturity is caused by the low ethane isotopes which deviate from the linear on the Chung diagram (Figure 7-26). If ethane is derived from the same source as methane and propane it should have an approximate isotope of -40‰ and a Ro_{eq} ≅ 0.5%.*

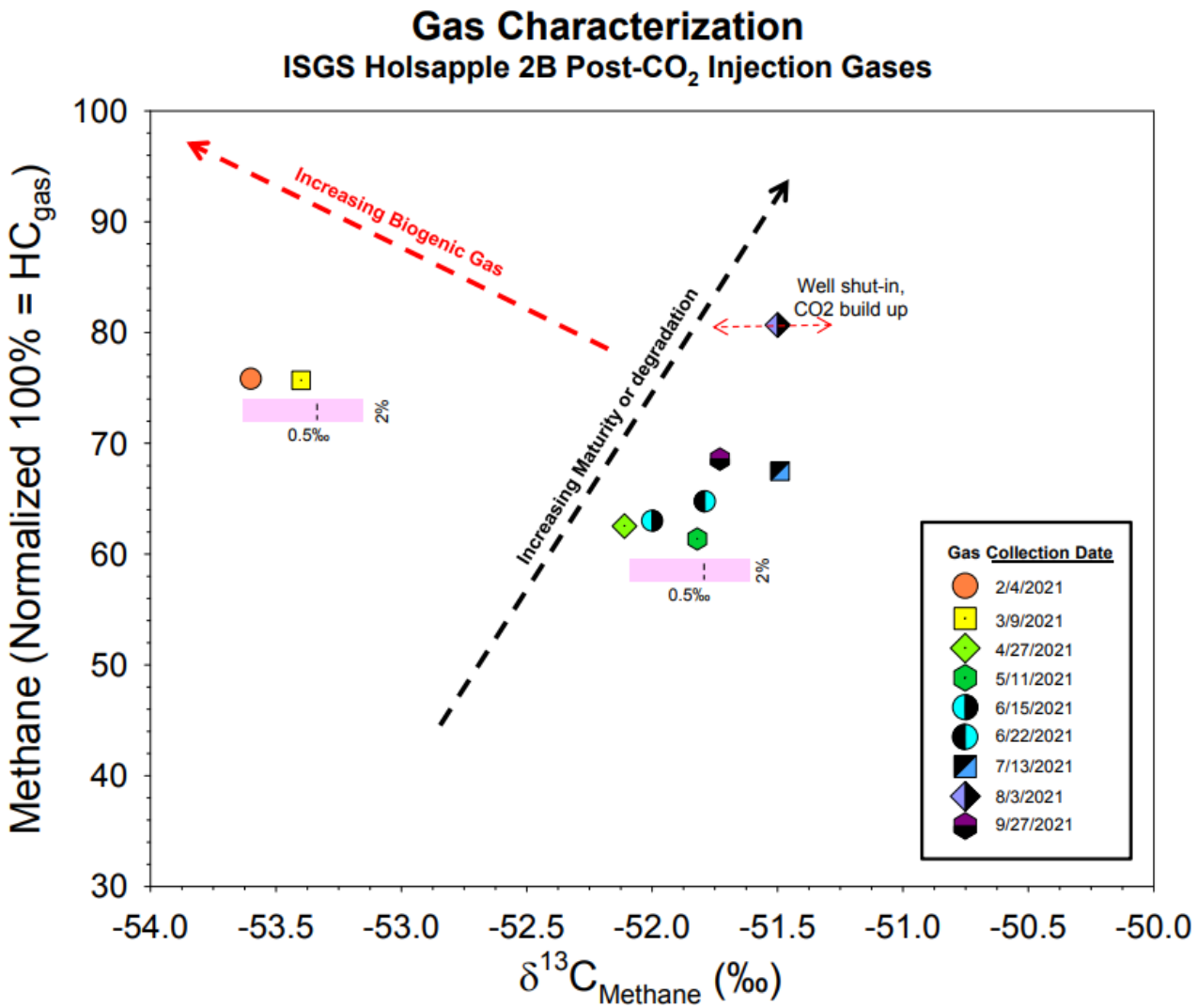


Figure 7-35. $\delta^{13}C$ methane versus normalized methane content for Holsapple 2B gases (9 of 27 were submitted for isotope analysis). The pink rectangle represents carbon isotope and compositional instrumental error (0.5‰ online - 0.2‰ offline and 2%, respectively). 2/4, 3/9 and 8/3 gases required online methane isotope analysis. 2/4 and 3/9 gases are isotopically lighter than the other 7 gases, possibly due to contamination of biogenic gas. The remaining 7 gas trend is consistent with maturity increase with time. April-May-June-5 gases are lower maturity than June-22 gas which is lower maturity than 7/13, 9/27 and 8/3 gases (8/3 gas measured high methane when well was shut in).

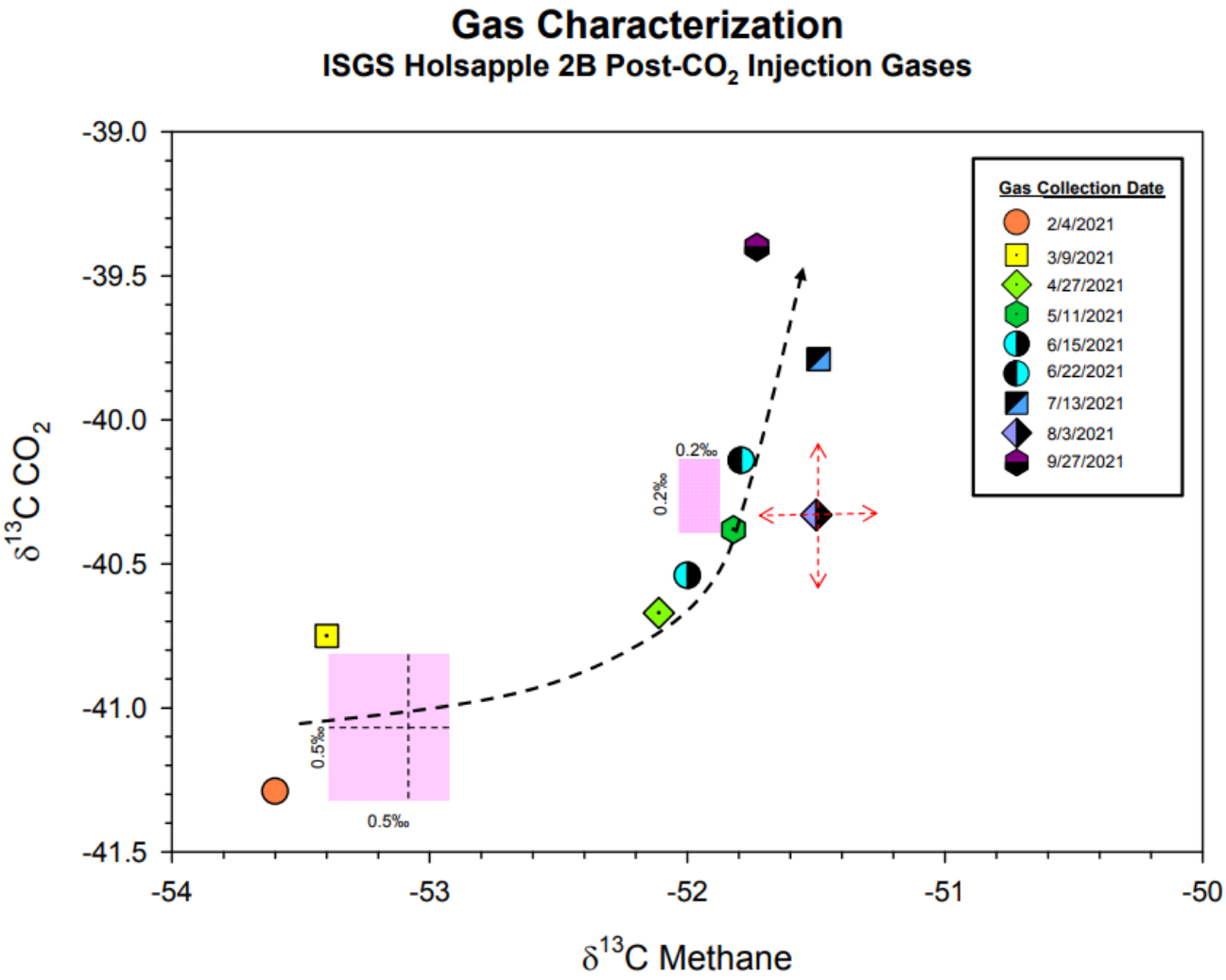


Figure 7-36. $\delta^{13}C$ methane versus $\delta^{13}C$ CO_2 for Holsapple 2B gases. The pink rectangle represents carbon isotope and compositional instrumental error (0.5‰ online - 0.2‰ offline and 2%, respectively). 2/4, 3/9 and 8/3 gases required online methane isotope analysis. 2/4 and 3/9 gases are isotopically lighter than the other 7 gases, possibly due to contamination of biogenic gas. Interestingly, methane and CO_2 become heavier, with time which suggests that the process affecting the increase in methane isotope with time (maturity or degradation) is also affecting the CO_2 isotopic signatures. A plausible explanation is that thermogenic CO_2 is mixing with lighter injected CO_2.

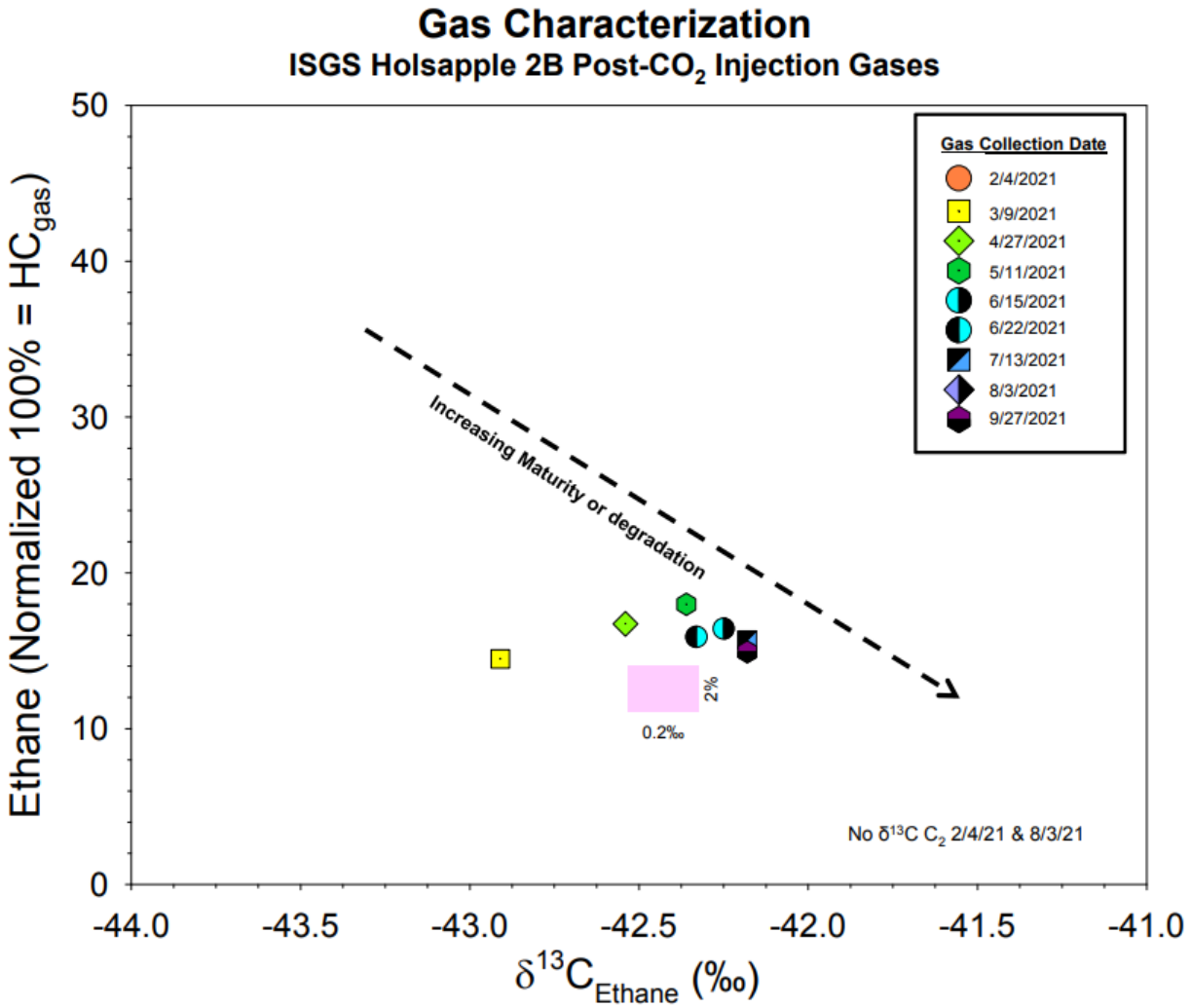


Figure 7-37. $\delta^{13}C$ ethane versus normalized ethane content for Holsapple 2B gases. The pink rectangle represents carbon isotope and compositional instrumental error (0.2‰ offline and 2%, respectively). 3/9 gas is isotopically lighter than the other 6 gases, possibly due to contamination of biogenic gas (biogenic gas may contain minor quantities of isotopically light ethane). The remaining 6 gas trend is consistent with a maturity increase with time. 4/27, 5/11 and 6/22 gases are lower maturity than 6/15, 7/1, 8/3 and 9/27 gases.

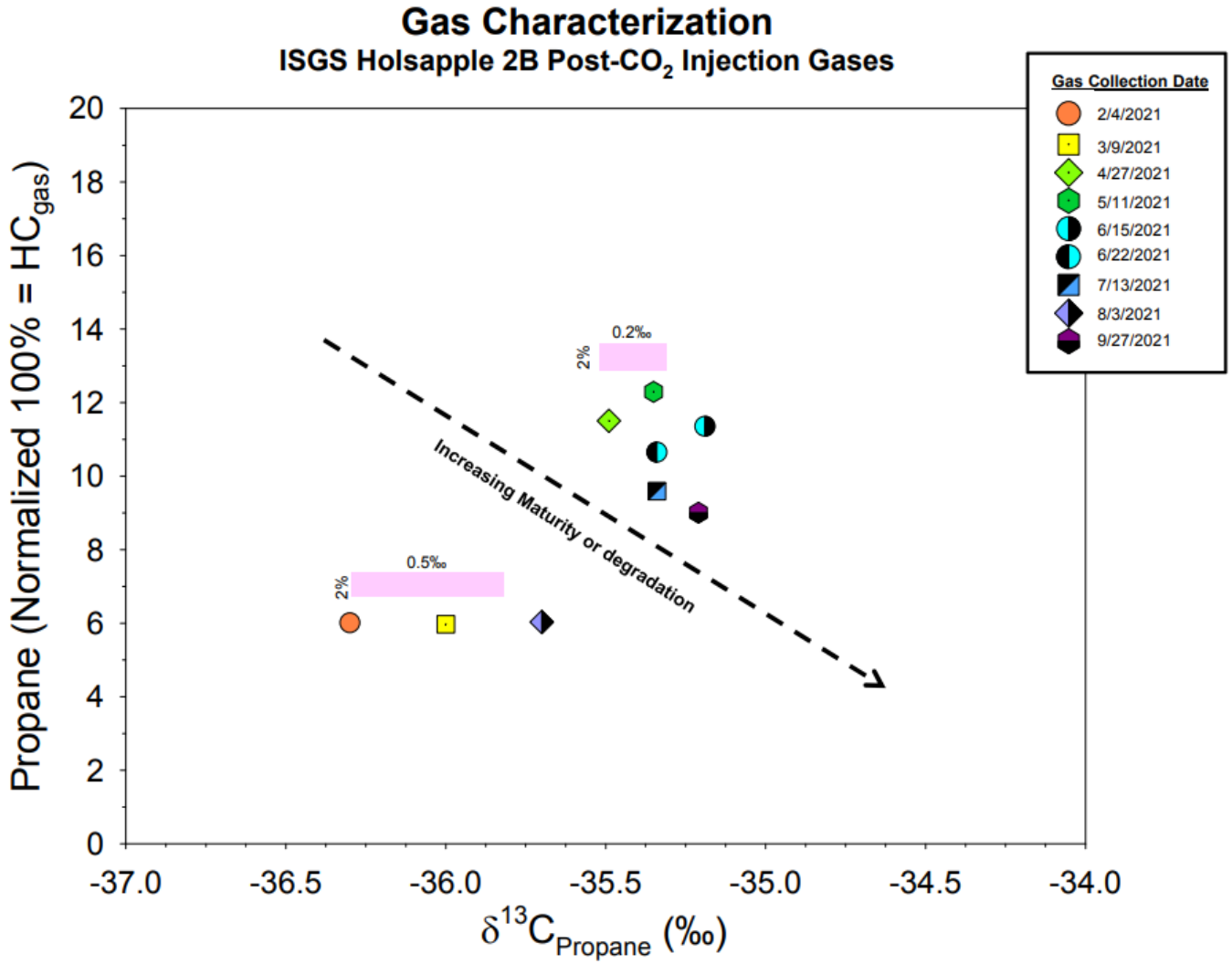


Figure 7-38. $\delta^{13}C$ propane versus normalized propane content for Holsapple 2B gases. The pink rectangle represents carbon isotope and compositional instrumental error (0.5‰ online - 0.2‰ offline and 2%, respectively). 2/4, 3/9 and 8/3 gases, which required online methane isotope analysis, are isotopically slightly lighter than the other gases suggesting lower maturity. The remaining 6 gas trend is consistent with maturity increase with time (4/27 and 5/11 gases are lower maturity than 6/15, 6/22 and 7/13 gases which are lower maturity than 9/27 gas.

Appendix 7-1

Stratum Oil Gas Chromatogram Reports

Sample Well, (Date), Interval

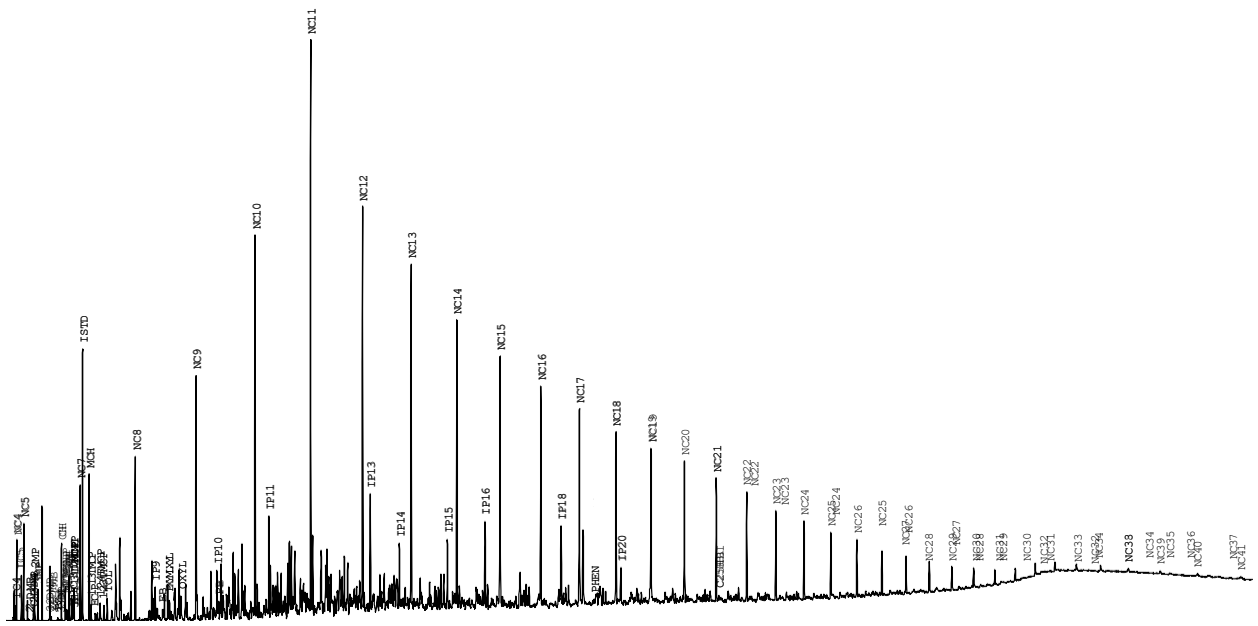
1) Holsapple 2B (8/24/2020) Carper SS
2) Holsapple 2B (8/31/2021) Carper SS
3) G. Swits 2 (2021) Carper SS
4) Quaranta 5 (2021) Carper SS

STRATUM RESERVOIR

WHOLE OIL GC

Company:	Illinois State Geological Survey	**Client ID:**	Carper SS.
Country:		**Project #: Lab**	HH-106658
Basin: Lease:		**ID: Reference**	6132371278
Block: Field:		**ID: Sample Type:**	
Well Name:			
Latitude:	Holsapple 2B	**Sampling Point:**	Oil
Longitude:	39.212452	**Collection Date:**	
		Formation:	
		Geologic Age: Top	August 24, 2020
GC Method:	G02G	**Depth: Bottom**	
		Depth:	

Whole Oil GC Trace G3200724.D



WGC parameters	
Pristane/Phytane	1.81
Pristane/nC17	0.57
Phytane/nC18	0.37
nC18/nC19	1.07
nC17/nC29	5.24
nC18/(nC18+nC19)	0.52
nC17/(nC17+nC29)	0.8
CPI Hunt[4]	1.0
CPI Marzi[5]	1.0
Normal Paraffins	30.6
Isoprenoids	5.7
Cycloparaffins	1.9
Branched (iso-) Paraffins	0.8
BTX aromatics	0.5
Resolved unknowns	60.1

Thompson[1]		
A.	BZ/*n* C_6	0.03
B.	TOL/*n* C_7	0.18
C.	(*n* C_6+*n* C_7)/(CH+MCH)	0.95
I.	Isoheptane Value	0.98
F.	*n* C_7/MCH	0.83
U.	CH/MCP	1.58
R.	*n* C_7/2MH	4.22
S.	*n* C_6/22DMB	103.30
H.	Heptane Value	24.97
	MCH/*n* C_7	1.21
	mpXYL/*n* C_8	0.27
	nC6/nC7	0.65

Mango[2]	
P_1	26.45
P_2	14.61
P_3	3.72
$5N_1$	8.08
N_2	10.41
$6N_1$	36.73
K_1	0.92
K_2	0.15
$5N_1/6N_1$	0.22
P_3/N_2	0.36
ln(24DMP/23DMP)	-1.15
Expulsion Temp ^{0}C	122.68

Halpern[3]	
Tr_1	2.35
Tr_2	12.79
Tr_3	4.03
Tr_4	3.03
Tr_5	7.06
Tr_7	1.93
Tr_8	4.00
C_1	0.07
C_2	0.55
C_3	0.17
C_4	0.05
C_5	0.15

[1]Thompson, K.F.M.,1983.GCA:V.47, p.303. [2]Mango, F.D.,1994.GCA: V.58, p.895. [3]Halpern,H.I.,1995,AAPG Bull.: V.79, p.801. [4]Hunt, 1979 [5]Marzi,1993,OrgG;20,130

Company: Well Name: Depth: Collection Date:	Illinois State Geological Survey Holsapple 2B	Client ID: HH-106658	Carper SS. Project #: Lab ID: 6132371278

Peak Label	Compound Name	Ret. Time	Area	Height	ppt (Area)	ppt (Hght)
IC4	Iso-alkane C4	3.927	1226	1013	0.11	0.19
NC4	Normal Alkane C4	4.044	6525	5403	0.57	1.04
IC5	Iso-alkane C5	4.478	3947	3010	0.35	0.58
NC5	Normal Alkane C5	4.717	8725	6472	0.77	1.24
22DMB	2,2-Dimethylbutane	5.169	124	81	0.01	0.02
CP	Cyclopentane	5.637	1097	686	0.10	0.13
23DMB	2,3-Dimethylbutane	5.669	524	356	0.05	0.07
2MP	2-Methylpentane	5.751	4987	3186	0.44	0.61
3MP	3-Methylpentane	6.049	3333	2044	0.29	0.39
NC6	Normal Alkane C6	6.460	12809	7612	1.13	1.46
22DMP	2,2-Dimethylpentane	7.135	186	107	0.02	0.02
MCP	Methylcyclopentane	7.193	6604	3574	0.58	0.69
24DMP	2,4-Dimethylpentane	7.329	474	249	0.04	0.05
223TMB	2,2,3-Trimethylbutane	7.486	51	21	0.01	0.00
BZ	Benzene	7.947	328	163	0.03	0.03
33DMP	3,3-Dimethylpentane	8.168	137	66	0.01	0.01
CH	Cyclohexane	8.284	10436	5151	0.92	0.99
2MH	2-Methylhexane	8.670	4658	2261	0.41	0.43
23DMP	2,3-Dimethylpentane	8.721	1504	754	0.13	0.15
11DMCP	1,1-Dimethylcyclopentane	8.811	1536	714	0.14	0.14
3MH	3-Methylhexane	9.013	6191	2976	0.54	0.57
1C3DMCP	1-cis-3-Dimethylcyclopentane	9.248	3239	1520	0.28	0.29
1T3DMCP	1-trans-3-Dimethylcyclopentane	9.362	2959	1380	0.26	0.27
3EP	3-Ethylpentane	9.424	410	314	0.04	0.06
1T2DMCP	1-trans-2-Dimethylcyclopentane	9.477	4830	2176	0.42	0.42
NC7	Normal Alkane C7	10.075	19639	9028	1.72	1.73
ISTD	Internal Standard	10.295	39524	18078	3.47	3.47
MCH	Methylcyclohexane	10.931	23670	9769	2.08	1.88
113TMCP	1,1,3,-Trimethylcyclopentane	11.101	2618	1089	0.23	0.21
ECP	Ethylcyclopentane	11.511	1171	499	0.10	0.10
124TMCP	1,2,4-Trimethylcyclopentane	11.963	2779	1160	0.24	0.22
123TMCP	1,2,3-Trimethylcyclopentane	12.334	2419	998	0.21	0.19
TOL	Toluene	12.639	3604	1469	0.32	0.28
NC8	Normal Alkane C8	15.315	29571	10899	2.60	2.09
IP9	Isoprenoid C9	17.196	6001	2214	0.53	0.43
EB	Ethyl-benzene	17.891	2032	743	0.18	0.14
MXYL	*m*-xylene	18.391	6469	2390	0.57	0.46
PXYL	*p*-xylene	18.454	1459	557	0.13	0.11
OXYL	*o*-xylene	19.652	5511	1643	0.48	0.32
NC9	Normal Alkane C9	21.078	45877	16319	4.03	3.13
IP10	Isoprenoid C10	23.064	10609	3335	0.93	0.64
PB	Propyl-benzene	23.225	4606	1259	0.40	0.24
NC10	Normal Alkane C10	26.693	76095	25518	6.68	4.90
IP11	Isoprenoid C11	27.991	20493	6848	1.80	1.32
NC11	Normal Alkane C11	31.975	120883	38469	10.61	7.38
NC12	Normal Alkane C12	36.901	84720	27124	7.44	5.21
IP13	Isoprenoid C13	37.638	27742	7908	2.44	1.52
IP14	Isoprenoid C14	40.404	14242	4550	1.25	0.87
NC13	Normal Alkane C13	41.520	76024	23063	6.68	4.43
IP15	Isoprenoid C15	44.968	16091	4733	1.41	0.91
NC14	Normal Alkane C14	45.862	63869	19292	5.61	3.70

Company:	**Illinois State Geological Survey**	**Client ID:**	**Carper SS.**
Well Name:	**Holsapple 2B**	**Project #:**	**HH-106658**
Depth:	**3688.00 -**	**Lab ID:**	**6132371278**
Collection Date:		**File Name:**	**G3200724.D**

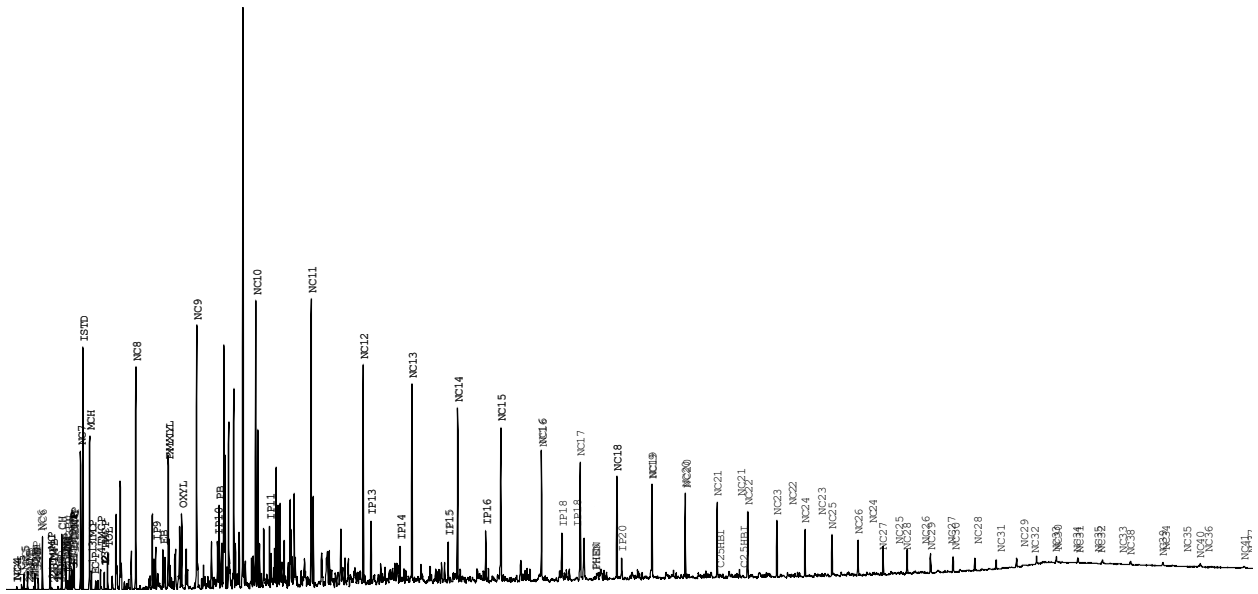
Peak Label	Compound Name	Ret. Time	Area	Height	ppt (Area)	ppt (Hght)
IP16	Isoprenoid C16	48.530	25252	5936	2.22	1.14
NC15	Normal Alkane C15	49.957	61737	16919	5.42	3.25
NC16	Normal Alkane C16	53.828	49495	14841	4.35	2.85
IP18	Isoprenoid C18	55.769	26555	5430	2.33	1.04
NC17	Normal Alkane C17	57.498	46588	13206	4.09	2.54
IP19	Isoprenoid C19 (Pristane)	57.856	26498	5118	2.33	0.98
PHEN	Phenanthrene	58.897	2692	489	0.24	0.09
NC18	Normal Alkane C18	60.987	39685	11585	3.48	2.22
IP20	Isoprenoid C20 (Phytane)	61.439	14653	2510	1.29	0.48
NC19	Normal Alkane C19	64.306	36965	10379	3.25	1.99
NC20	Normal Alkane C20	67.472	33973	9454	2.98	1.82
NC21	Normal Alkane C21	70.497	29365	8328	2.58	1.60
C25HBI	Highly Branch Isoprenoid C25	70.752	2111	504	0.19	0.10
NC22	Normal Alkane C22	73.396	26316	7367	2.31	1.41
NC23	Normal Alkane C23	76.172	22886	6041	2.01	1.16
NC24	Normal Alkane C24	78.837	19162	5278	1.68	1.01
NC25	Normal Alkane C25	81.400	16728	4465	1.47	0.86
NC26	Normal Alkane C26	83.865	14480	3890	1.27	0.75
NC27	Normal Alkane C27	86.242	11759	3011	1.03	0.58
NC28	Normal Alkane C28	88.533	9886	2558	0.87	0.49
NC29	Normal Alkane C29	90.749	8884	2107	0.78	0.40
NC30	Normal Alkane C30	92.892	6794	1640	0.60	0.32
NC31	Normal Alkane C31	94.963	6036	1387	0.53	0.27
NC32	Normal Alkane C32	96.973	4147	1039	0.36	0.20
NC33	Normal Alkane C33	98.919	4087	881	0.36	0.17
NC34	Normal Alkane C34	100.810	3706	861	0.33	0.17
NC35	Normal Alkane C35	102.687	3497	662	0.31	0.13
NC36	Normal Alkane C36	104.725	2812	473	0.25	0.09
NC37	Normal Alkane C37	107.028	2718	448	0.24	0.09
NC38	Normal Alkane C38	109.670	2466	319	0.22	0.06
NC39	Normal Alkane C39	112.716	1790	262	0.16	0.05
NC40	Normal Alkane C40	116.223	2096	238	0.18	0.05
NC41	Normal Alkane C41	120.352	1460	209	0.13	0.04

STRATUM RESERVOIR

WHOLE OIL GC

Company:	Illinois State Geological Survey	**Client ID:**	
Country:	UNITED STATES	**Project #:**	HH-107518
Basin:		**Lab ID:**	6132772443
Lease:		**Reference ID:**	Login 1707
Block:		**Sample Type:**	Oil
Field:		**Sampling Point:**	
Well Name:	Holsapple 2B	**Collection Date:**	Aug 31 2021 12:00AM
Latitude:	39.212452	**Formation:**	
Longitude:	-88.218332	**Geologic Age:**	
		Top Depth:	
GC Method:	G02G	**Bottom Depth:**	
Sample Prep:	NOPR	**Depth Units:**	

Whole Oil GC Trace G3210605.D



WGC parameters	
Pristane/Phytane	1.80
Pristane/nC17	0.53
Phytane/nC18	0.36
nC18/nC19	1.06
nC17/nC29	5.20
nC18/(nC18+nC19)	0.51
nC17/(nC17+nC29)	0.8
CPI Hunt[4]	1.0
CPI Marzi[5]	1.0
Normal Paraffins	24.6
Isoprenoids	4.5
Cycloparaffins	2.2
Branched (iso-) Paraffins	0.6
BTX aromatics	2.0
Resolved unknowns	65.2

Thompson[1]		
A.	BZ/*n* C_6	0.07
B.	TOL/*n* C_7	0.29
C.	(*n* C_6+*n* C_7)/(CH+MCH)	0.81
I.	Isoheptane Value	0.93
F.	*n* C_7/MCH	0.81
U.	CH/MCP	1.97
R.	*n* C_7/2MH	5.32
S.	*n* C_6/22DMB	173.60
H.	Heptane Value	27.24
	MCH/*n* C_7	1.23
	mpXYL/*n* C_8	0.80
	nC6/nC7	0.30

Mango[2]	
P_1	27.01
P_2	12.30
P_3	2.88
$5N_1$	7.76
N_2	8.97
$6N_1$	41.07
K_1	0.89
K_2	0.14
$5N_1/6N_1$	0.19
P_3/N_2	0.32
ln(24DMP/23DMP)	-1.50
Expulsion Temp ^{0}C	117.54

Halpern[3]	
Tr_1	4.55
Tr_2	15.71
Tr_3	4.21
Tr_4	2.95
Tr_5	7.16
Tr_7	2.04
Tr_8	4.33
C_1	0.05
C_2	0.59
C_3	0.13
C_4	0.05
C_5	0.18

[1]Thompson, K.F.M.,1983.GCA:V.47, p.303. [2]Mango, F.D.,1994.GCA: V.58, p.895. [3]Halpern,H.I.,1995,AAPG Bull.: V.79, p.801. [4]Hunt, 1979 [5]Marzi,1993,OrgG;20,130

Company: Well	**Illinois State Geological Survey**	**Client ID:**	
Name: Depth:	**Holsapple 2B**	**Project #:**	**HH-107518**
Collection Date:	**-**	**Lab ID:**	**6132772443**

Peak Label	Compound Name	Ret. Time	Area	Height	ppt (Area)	ppt (Hght)
IC4	Iso-alkane C4	3.944	68	48	0.00	0.01
NC4	Normal Alkane C4	4.061	479	385	0.03	0.04
IC5	Iso-alkane C5	4.497	907	682	0.05	0.08
NC5	Normal Alkane C5	4.737	2717	1975	0.14	0.22
22DMB	2,2-Dimethylbutane	5.190	67	39	0.00	0.00
CP	Cyclopentane	5.659	722	442	0.04	0.05
23DMB	2,3-Dimethylbutane	5.692	339	225	0.02	0.03
2MP	2-Methylpentane	5.774	3307	2100	0.17	0.24
3MP	3-Methylpentane	6.073	2534	1541	0.13	0.17
NC6	Normal Alkane C6	6.485	11631	6859	0.60	0.77
22DMP	2,2-Dimethylpentane	7.163	202	117	0.01	0.01
MCP	Methylcyclopentane	7.221	7380	3964	0.38	0.45
24DMP	2,4-Dimethylpentane	7.357	542	285	0.03	0.03
223TMB	2,2,3-Trimethylbutane	7.513	55	26	0.00	0.00
BZ	Benzene	7.976	867	430	0.05	0.05
33DMP	3,3-Dimethylpentane	8.198	204	95	0.01	0.01
CH	Cyclohexane	8.314	14530	7159	0.75	0.81
2MH	2-Methylhexane	8.701	7371	3559	0.38	0.40
23DMP	2,3-Dimethylpentane	8.752	2422	1210	0.12	0.14
11DMCP	1,1-Dimethylcyclopentane	8.842	2497	1161	0.13	0.13
3MH	3-Methylhexane	9.045	10501	5002	0.54	0.56
1C3DMCP	1-cis-3-Dimethylcyclopentane	9.280	5440	2548	0.28	0.29
1T3DMCP	1-trans-3-Dimethylcyclopentane	9.395	5098	2372	0.26	0.27
3EP	3-Ethylpentane	9.456	755	586	0.04	0.07
1T2DMCP	1-trans-2-Dimethylcyclopentane	9.510	8640	3892	0.44	0.44
NC7	Normal Alkane C7	10.110	39230	17747	2.02	2.00
ISTD	Internal Standard	10.331	68509	31222	3.52	3.52
MCH	Methylcyclohexane	10.968	48290	19829	2.48	2.24
113TMCP	1,1,3,-Trimethylcyclopentane	11.137	6083	2412	0.31	0.27
ECP	Ethylcyclopentane	11.547	2634	1124	0.14	0.13
124TMCP	1,2,4-Trimethylcyclopentane	12.000	6328	2622	0.33	0.30
123TMCP	1,2,3-Trimethylcyclopentane	12.372	5608	2299	0.29	0.26
TOL	Toluene	12.676	11366	4631	0.58	0.52
NC8	Normal Alkane C8	15.363	79751	28625	4.10	3.23
IP9	Isoprenoid C9	17.243	14886	5478	0.77	0.62
EB	Ethyl-benzene	17.936	13796	5126	0.71	0.58
MXYL	*m*-xylene	18.443	47544	17270	2.44	1.95
PXYL	*p*-xylene	18.503	16163	6586	0.83	0.74
OXYL	*o*-xylene	19.702	30203	9788	1.55	1.10
NC9	Normal Alkane C9	21.135	98125	34078	5.04	3.84
IP10	Isoprenoid C10	23.118	19925	6181	1.02	0.70
PB	Propyl-benzene	23.279	32460	10771	1.67	1.21
NC10	Normal Alkane C10	26.755	111701	37148	5.74	4.19
IP11	Isoprenoid C11	28.047	24210	8047	1.24	0.91
NC11	Normal Alkane C11	32.029	120016	37295	6.17	4.21
NC12	Normal Alkane C12	36.962	89228	28523	4.59	3.22
IP13	Isoprenoid C13	37.700	30032	8289	1.54	0.93
IP14	Isoprenoid C14	40.468	15797	4919	0.81	0.56
NC13	Normal Alkane C13	41.586	85907	25765	4.41	2.91
IP15	Isoprenoid C15	45.036	18330	5385	0.94	0.61
NC14	Normal Alkane C14	45.933	74308	22618	3.82	2.55

Company:	**Illinois State Geological Survey**	**Client ID:**	
Well Name:	**Holsapple 2B**	**Project #:**	**HH-107518**
Depth:	**-**	**Lab ID:**	**6132772443**
Collection Date:	**Aug 31 2021 12:00AM**	**File Name:**	**G3210605.D**

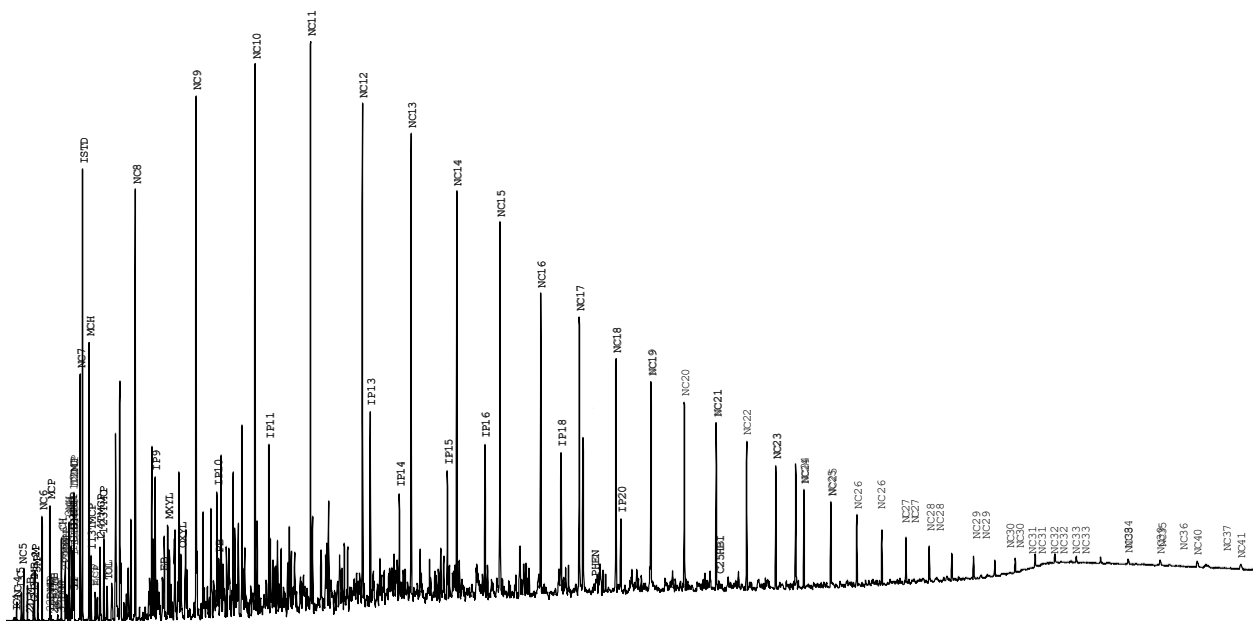
Peak Label	Compound Name	Ret. Time	Area	Height	ppt (Area)	ppt (Hght)
IP16	Isoprenoid C16	48.601	29035	6764	1.49	0.76
NC15	Normal Alkane C15	50.032	71208	20131	3.66	2.27
NC16	Normal Alkane C16	53.905	57772	17070	2.97	1.92
IP18	Isoprenoid C18	55.848	30441	6296	1.56	0.71
NC17	Normal Alkane C17	57.579	56118	15288	2.88	1.72
IP19	Isoprenoid C19 (Pristane)	57.940	29535	5590	1.52	0.63
PHEN	Phenanthrene	58.981	2828	526	0.15	0.06
NC18	Normal Alkane C18	61.070	46096	13323	2.37	1.50
IP20	Isoprenoid C20 (Phytane)	61.521	16443	2837	0.85	0.32
NC19	Normal Alkane C19	64.392	43425	12269	2.23	1.38
NC20	Normal Alkane C20	67.562	39915	11072	2.05	1.25
NC21	Normal Alkane C21	70.591	35665	9891	1.83	1.12
C25HBI	Highly Branch Isoprenoid C25	70.845	2617	628	0.13	0.07
NC22	Normal Alkane C22	73.491	31084	8638	1.60	0.97
NC23	Normal Alkane C23	76.268	27441	7371	1.41	0.83
NC24	Normal Alkane C24	78.933	23252	6186	1.20	0.70
NC25	Normal Alkane C25	81.500	20400	5394	1.05	0.61
NC26	Normal Alkane C26	83.968	17667	4651	0.91	0.52
NC27	Normal Alkane C27	86.347	14270	3790	0.73	0.43
NC28	Normal Alkane C28	88.640	12310	3191	0.63	0.36
NC29	Normal Alkane C29	90.859	10796	2620	0.56	0.30
NC30	Normal Alkane C30	93.007	8637	2092	0.44	0.24
NC31	Normal Alkane C31	95.080	7099	1711	0.37	0.19
NC32	Normal Alkane C32	97.092	5536	1292	0.28	0.15
NC33	Normal Alkane C33	99.034	5402	1212	0.28	0.14
NC34	Normal Alkane C34	100.932	4648	1080	0.24	0.12
NC35	Normal Alkane C35	102.808	4357	850	0.22	0.10
NC36	Normal Alkane C36	104.871	3676	644	0.19	0.07
NC37	Normal Alkane C37	107.214	3891	578	0.20	0.07
NC38	Normal Alkane C38	109.857	3443	508	0.18	0.06
NC39	Normal Alkane C39	112.940	3607	468	0.19	0.05
NC40	Normal Alkane C40	116.494	3812	440	0.20	0.05
NC41	Normal Alkane C41	120.665	2305	288	0.12	0.03

STRATUM RESERVOIR

WHOLE OIL GC

Company:	Illinois State Geological Survey	**Client ID:**	Carper SS.
Country:	UNITED STATES	**Project #:**	HH-106658
Basin:		**Lab ID:**	6132371276
Lease:		**Reference ID:**	
Block:		**Sample Type:**	Oil
Field:	Gays	**Sampling Point:**	
Well Name:	G Swits 2	**Collection Date:**	
Latitude:	39.470398	**Formation:**	
Longitude:	-88.523715	**Geologic Age:**	
		Top Depth:	3048.00
GC Method:	G02G	**Bottom Depth:**	
Sample Prep:	NOPR	**Depth Units:**	

Whole Oil GC Trace G3200723.D



WGC parameters	
Pristane/Phytane	2.00
Pristane/nC17	0.85
Phytane/nC18	0.52
nC18/nC19	1.08
nC17/nC29	6.31
nC18/(nC18+nC19)	0.52
nC17/(nC17+nC29)	0.9
CPI Hunt[4]	1.0
CPI Marzi[5]	1.0
Normal Paraffins	26.1
Isoprenoids	6.8
Cycloparaffins	2.9
Branched (iso-) Paraffins	0.7
BTX aromatics	0.8
Resolved unknowns	62.0

Thompson[1]		
A.	BZ/*n* C_6	0.06
B.	TOL/*n* C_7	0.16
C.	(*n* C_6+*n* C_7)/(CH+MCH)	0.81
I.	Isoheptane Value	0.55
F.	*n* C_7/MCH	0.75
U.	CH/MCP	0.79
R.	*n* C_7/2MH	4.37
S.	*n* C_6/22DMB	159.42
H.	Heptane Value	22.03
	MCH/*n* C_7	1.33
	mpXYL/*n* C_8	0.27
	nC6/nC7	0.32

Mango[2]	
P_1	21.89
P_2	13.33
P_3	3.41
$5N_1$	14.23
N_2	14.68
$6N_1$	32.45
K_1	0.82
K_2	0.12
$5N_1/6N_1$	0.44
P_3/N_2	0.23
ln(24DMP/23DMP)	-1.68
Expulsion Temp ^{0}C	114.83

Halpern[3]	
Tr_1	1.56
Tr_2	10.07
Tr_3	3.83
Tr_4	2.30
Tr_5	6.13
Tr_7	2.79
Tr_8	3.96
C_1	0.03
C_2	0.63
C_3	0.12
C_4	0.03
C_5	0.19

[1]Thompson, K.F.M.,1983.GCA:V.47, p.303. [2]Mango, F.D.,1994.GCA: V.58, p.895. [3]Halpern,H.I.,1995,AAPG Bull.: V.79, p.801. [4]Hunt, 1979 [5]Marzi,1993,OrgG;20,130

Company: Well Name: Depth: Collection Date:	Illinois State Geological Survey G Swits 2	Client ID: HH-106658	Carper SS. Project #: Lab ID: 6132371276

Peak Label	Compound Name	Ret. Time	Area	Height	ppt (Area)	ppt (Hght)
IC4	Iso-alkane C4	3.925	157	109	0.01	0.02
NC4	Normal Alkane C4	4.041	933	750	0.08	0.14
IC5	Iso-alkane C5	4.475	1443	1119	0.13	0.21
NC5	Normal Alkane C5	4.714	2821	2126	0.25	0.40
22DMB	2,2-Dimethylbutane	5.166	45	26	0.00	0.01
CP	Cyclopentane	5.634	923	574	0.08	0.11
23DMB	2,3-Dimethylbutane	5.667	259	193	0.02	0.04
2MP	2-Methylpentane	5.748	3171	2059	0.28	0.39
3MP	3-Methylpentane	6.046	2495	1555	0.22	0.29
NC6	Normal Alkane C6	6.457	7174	4289	0.62	0.81
22DMP	2,2-Dimethylpentane	7.133	113	68	0.01	0.01
MCP	Methylcyclopentane	7.190	8658	4731	0.75	0.89
24DMP	2,4-Dimethylpentane	7.326	397	212	0.03	0.04
223TMB	2,2,3-Trimethylbutane	7.483	41	16	0.00	0.00
BZ	Benzene	7.944	466	230	0.04	0.04
33DMP	3,3-Dimethylpentane	8.166	106	51	0.01	0.01
CH	Cyclohexane	8.281	6817	3392	0.59	0.64
2MH	2-Methylhexane	8.667	5053	2473	0.44	0.47
23DMP	2,3-Dimethylpentane	8.718	2126	1057	0.18	0.20
11DMCP	1,1-Dimethylcyclopentane	8.808	2194	1038	0.19	0.20
3MH	3-Methylhexane	9.011	8395	4054	0.73	0.77
1C3DMCP	1-cis-3-Dimethylcyclopentane	9.245	6497	3069	0.56	0.58
1T3DMCP	1-trans-3-Dimethylcyclopentane	9.360	6124	2872	0.53	0.54
3EP	3-Ethylpentane	9.419	658	596	0.06	0.11
1T2DMCP	1-trans-2-Dimethylcyclopentane	9.475	11656	5254	1.01	0.99
NC7	Normal Alkane C7	10.072	22093	10112	1.92	1.91
ISTD	Internal Standard	10.293	40377	18545	3.50	3.50
MCH	Methylcyclohexane	10.928	29317	11424	2.54	2.16
113TMCP	1,1,3,-Trimethylcyclopentane	11.098	6274	2660	0.54	0.50
ECP	Ethylcyclopentane	11.508	2704	1160	0.23	0.22
124TMCP	1,2,4-Trimethylcyclopentane	11.960	7180	3013	0.62	0.57
123TMCP	1,2,3-Trimethylcyclopentane	12.332	8058	3322	0.70	0.63
TOL	Toluene	12.636	3432	1386	0.30	0.26
NC8	Normal Alkane C8	15.314	49438	17712	4.29	3.34
IP9	Isoprenoid C9	17.196	15989	5880	1.39	1.11
EB	Ethyl-benzene	17.889	4823	1763	0.42	0.33
MXYL	*m*-xylene	18.389	10600	3887	0.92	0.73
PXYL	*p*-xylene	18.451	2553	957	0.22	0.18
OXYL	*o*-xylene	19.650	10212	2714	0.89	0.51
NC9	Normal Alkane C9	21.078	62258	21568	5.40	4.07
IP10	Isoprenoid C10	23.062	16540	5233	1.43	0.99
PB	Propyl-benzene	23.222	9012	2494	0.78	0.47
NC10	Normal Alkane C10	26.688	67662	22773	5.87	4.30
IP11	Isoprenoid C11	27.987	21531	7117	1.87	1.34
NC11	Normal Alkane C11	31.961	72963	23656	6.33	4.47
NC12	Normal Alkane C12	36.892	66117	20827	5.73	3.93
IP13	Isoprenoid C13	37.634	27870	8098	2.42	1.53
IP14	Isoprenoid C14	40.400	14882	4605	1.29	0.87
NC13	Normal Alkane C13	41.514	64218	19419	5.57	3.67
IP15	Isoprenoid C15	44.965	18684	5423	1.62	1.02
NC14	Normal Alkane C14	45.857	55649	16934	4.82	3.20

Company:	**Illinois State Geological Survey**	**Client ID:**	**Carper SS.**
Well Name:	**G Swits 2**	**Project #:**	**HH-106658**
Depth:	**3048.00 -**	**Lab ID:**	**6132371276**
Collection Date:		**File Name:**	**G3200723.D**

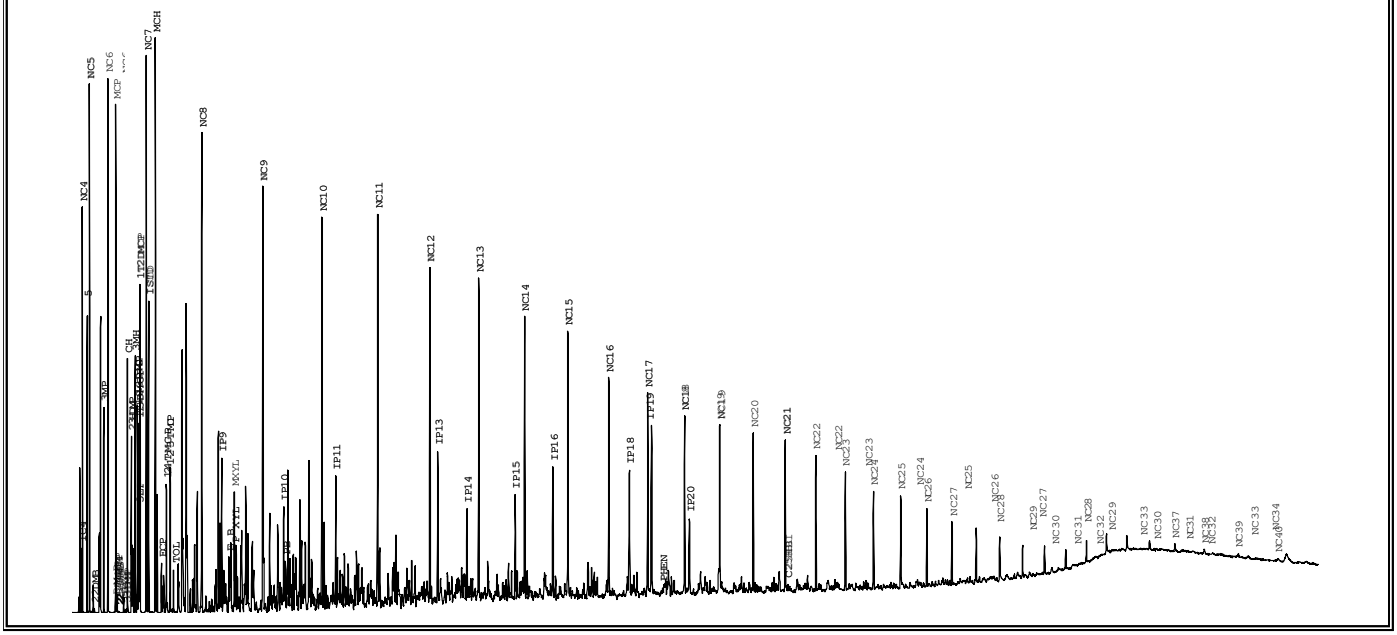
Peak Label	Compound Name	Ret. Time	Area	Height	ppt (Area)	ppt (Hght)
IP16	Isoprenoid C16	48.530	26638	6482	2.31	1.22
NC15	Normal Alkane C15	49.952	56419	15599	4.89	2.94
NC16	Normal Alkane C16	53.821	42970	12622	3.73	2.38
IP18	Isoprenoid C18	55.765	29532	5992	2.56	1.13
NC17	Normal Alkane C17	57.493	40793	11550	3.54	2.18
IP19	Isoprenoid C19 (Pristane)	57.856	34490	6572	2.99	1.24
PHEN	Phenanthrene	58.895	3194	533	0.28	0.10
NC18	Normal Alkane C18	60.981	33337	9708	2.89	1.83
IP20	Isoprenoid C20 (Phytane)	61.445	17264	3091	1.50	0.58
NC19	Normal Alkane C19	64.301	30908	8707	2.68	1.64
NC20	Normal Alkane C20	67.468	28328	7821	2.46	1.48
NC21	Normal Alkane C21	70.494	24406	6969	2.12	1.32
C25HBI	Highly Branch Isoprenoid C25	70.748	1843	461	0.16	0.09
NC22	Normal Alkane C22	73.390	21722	6178	1.88	1.17
NC23	Normal Alkane C23	76.167	18373	5157	1.59	0.97
NC24	Normal Alkane C24	78.833	15155	4130	1.31	0.78
NC25	Normal Alkane C25	81.394	13303	3575	1.15	0.68
NC26	Normal Alkane C26	83.859	11470	3006	0.99	0.57
NC27	Normal Alkane C27	86.234	9056	2323	0.79	0.44
NC28	Normal Alkane C28	88.528	7523	1949	0.65	0.37
NC29	Normal Alkane C29	90.743	6468	1551	0.56	0.29
NC30	Normal Alkane C30	92.887	4849	1161	0.42	0.22
NC31	Normal Alkane C31	94.956	3837	947	0.33	0.18
NC32	Normal Alkane C32	96.968	2800	697	0.24	0.13
NC33	Normal Alkane C33	98.921	2794	628	0.24	0.12
NC34	Normal Alkane C34	100.804	2359	555	0.20	0.11
NC35	Normal Alkane C35	102.679	2226	418	0.19	0.08
NC36	Normal Alkane C36	104.719	1554	289	0.14	0.05
NC37	Normal Alkane C37	107.022	1664	287	0.14	0.05
NC38	Normal Alkane C38	109.663	1621	245	0.14	0.05
NC39	Normal Alkane C39	112.681	1773	251	0.15	0.05
NC40	Normal Alkane C40	116.224	2774	278	0.24	0.05
NC41	Normal Alkane C41	120.335	1758	236	0.15	0.05

STRATUM RESERVOIR

WHOLE OIL GC

Company:	Illinois State Geological Survey	**Client ID:**	
Country:	UNITED STATES	**Project #:**	HH-107518
Basin:		**Lab ID:**	6132810649
Lease:		**Reference ID:**	ROZ Project
Block:		**Sample Type:**	Oil
Field:		**Sampling Point:**	
Well Name:	Quaranta 5	**Collection Date:**	
Latitude:	0	**Formation:**	
Longitude:	0	**Geologic Age:**	
		Top Depth:	
GC Method:	G02G	**Bottom Depth:**	
Sample Prep:	NOPR	**Depth Units:**	

Whole Oil GC Trace G6210557.D



WGC parameters	
Pristane/Phytane	2.08
Pristane/nC17	1.21
Phytane/nC18	0.69
nC18/nC19	1.03
nC17/nC29	3.82
nC18/(nC18+nC19)	0.51
nC17/(nC17+nC29)	0.8
CPI Hunt[4]	1.0
CPI Marzi[5]	1.0
Normal Paraffins	26.6
Isoprenoids	6.6
Cycloparaffins	7.8
Branched (iso-) Paraffins	3.3
BTX aromatics	1.1
Resolved unknowns	54.2

Thompson[1]		
A.	BZ/*n* C_6	0.03
B.	TOL/*n* C_7	0.09
C.	(*n* C_6+*n* C_7)/(CH+MCH)	1.07
I.	Isoheptane Value	0.57
F.	*n* C_7/MCH	0.83
U.	CH/MCP	0.55
R.	*n* C_7/2MH	3.35
S.	*n* C_6/22DMB	167.33
H.	Heptane Value	20.55
	MCH/*n* C_7	1.20
	mpXYL/*n* C_8	0.29
	nC6/nC7	0.73

Mango[2]	
P_1	21.26
P_2	15.71
P_3	3.96
$5N_1$	14.68
N_2	17.06
$6N_1$	27.33
K_1	0.87
K_2	0.12
$5N_1/6N_1$	0.54
P_3/N_2	0.23
ln(24DMP/23DMP)	-1.36
Expulsion Temp ^{0}C	119.67

Halpern[3]	
Tr_1	0.77
Tr_2	8.94
Tr_3	3.94
Tr_4	2.67
Tr_5	6.61
Tr_7	2.96
Tr_8	4.03
C_1	0.04
C_2	0.60
C_3	0.15
C_4	0.03
C_5	0.17

[1]Thompson, K.F.M.,1983.GCA:V.47, p.303. [2]Mango, F.D.,1994.GCA: V.58, p.895. [3]Halpern,H.I.,1995,AAPG Bull.: V.79, p.801. [4]Hunt, 1979 [5]Marzi,1993,OrgG;20,130

Company: Well Name: Depth: Collection Date:	**Illinois State Geological Survey Quaranta 5**	**Client ID:**	
		Project #:	**HH-107518**
		Lab ID:	**6132810649**

Peak Label	Compound Name	Ret. Time	Area	Height	ppt (Area)	ppt (Hght)
IC4	Iso-alkane C4	3.902	4596	3936	0.38	0.72
NC4	Normal Alkane C4	4.019	29598	24923	2.46	4.55
IC5	Iso-alkane C5	4.454	23200	18115	1.93	3.31
NC5	Normal Alkane C5	4.694	43022	32271	3.58	5.89
22DMB	2,2-Dimethylbutane	5.147	328	218	0.03	0.04
CP	Cyclopentane	5.617	7760	4831	0.65	0.88
23DMB	2,3-Dimethylbutane	5.650	2273	1640	0.19	0.30
2MP	2-Methylpentane	5.733	28120	18040	2.34	3.30
3MP	3-Methylpentane	6.033	20357	12495	1.69	2.28
NC6	Normal Alkane C6	6.448	54884	32621	4.56	5.96
22DMP	2,2-Dimethylpentane	7.126	607	368	0.05	0.07
MCP	Methylcyclopentane	7.184	57410	30990	4.77	5.66
24DMP	2,4-Dimethylpentane	7.321	2118	1110	0.18	0.20
223TMB	2,2,3-Trimethylbutane	7.476	202	92	0.02	0.02
BZ	Benzene	7.943	1900	922	0.16	0.17
33DMP	3,3-Dimethylpentane	8.164	423	203	0.04	0.04
CH	Cyclohexane	8.281	31470	15468	2.62	2.83
2MH	2-Methylhexane	8.672	22363	10763	1.86	1.97
23DMP	2,3-Dimethylpentane	8.722	8215	4111	0.68	0.75
11DMCP	1,1-Dimethylcyclopentane	8.811	8388	3915	0.70	0.72
3MH	3-Methylhexane	9.018	33090	15760	2.75	2.88
1C3DMCP	1-cis-3-Dimethylcyclopentane	9.252	26972	12617	2.24	2.30
1T3DMCP	1-trans-3-Dimethylcyclopentane	9.368	24849	11531	2.07	2.11
3EP	3-Ethylpentane	9.429	2410	2078	0.20	0.38
1T2DMCP	1-trans-2-Dimethylcyclopentane	9.485	44752	20134	3.72	3.68
NC7	Normal Alkane C7	10.091	75015	34030	6.24	6.22
ISTD	Internal Standard	10.309	41725	19001	3.47	3.47
MCH	Methylcyclohexane	10.949	89967	35106	7.48	6.41
113TMCP	1,1,3,-Trimethylcyclopentane	11.117	17071	7188	1.42	1.31
ECP	Ethylcyclopentane	11.529	7065	3009	0.59	0.55
124TMCP	1,2,4-Trimethylcyclopentane	11.985	18840	7822	1.57	1.43
123TMCP	1,2,3-Trimethylcyclopentane	12.359	21586	8865	1.80	1.62
TOL	Toluene	12.666	6488	2587	0.54	0.47
NC8	Normal Alkane C8	15.364	86633	29269	7.21	5.35
IP9	Isoprenoid C9	17.246	25684	9402	2.14	1.72
EB	Ethyl-benzene	17.944	9191	3381	0.76	0.62
MXYL	*m*-xylene	18.449	20009	7348	1.66	1.34
PXYL	*p*-xylene	18.511	4867	1884	0.41	0.34
OXYL	*o*-xylene	19.714	15965	4781	1.33	0.87
NC9	Normal Alkane C9	21.151	77874	26019	6.48	4.75
IP10	Isoprenoid C10	23.140	20297	6409	1.69	1.17
PB	Propyl-benzene	23.296	11112	3090	0.92	0.56
NC10	Normal Alkane C10	26.781	71964	24028	5.99	4.39
IP11	Isoprenoid C11	28.084	25392	8208	2.11	1.50
NC11	Normal Alkane C11	32.075	74815	24202	6.22	4.42
NC12	Normal Alkane C12	37.028	66954	20664	5.57	3.77
IP13	Isoprenoid C13	37.771	31482	9367	2.62	1.71
IP14	Isoprenoid C14	40.549	18306	5781	1.52	1.06
NC13	Normal Alkane C13	41.668	64480	19842	5.36	3.62
IP15	Isoprenoid C15	45.133	21852	6506	1.82	1.19
NC14	Normal Alkane C14	46.031	56820	17359	4.73	3.17

Company:	**Illinois State Geological Survey**	**Client ID:**	
Well Name:	**Quaranta 5**	**Project #:**	**HH-107518**
Depth:	**-**	**Lab ID:**	**6132810649**
Collection Date:		**File Name:**	**G6210557.D**

Peak Label	Compound Name	Ret. Time	Area	Height	ppt (Area)	ppt (Hght)
IP16	Isoprenoid C16	48.716	32605	8168	2.71	1.49
NC15	Normal Alkane C15	50.146	59691	16433	4.96	3.00
NC16	Normal Alkane C16	54.034	46323	13576	3.85	2.48
IP18	Isoprenoid C18	55.984	39655	7844	3.30	1.43
NC17	Normal Alkane C17	57.725	45742	12564	3.80	2.29
IP19	Isoprenoid C19 (Pristane)	58.090	55125	10519	4.58	1.92
PHEN	Phenanthrene	59.130	3323	572	0.28	0.10
NC18	Normal Alkane C18	61.229	38566	11004	3.21	2.01
IP20	Isoprenoid C20 (Phytane)	61.686	26547	4712	2.21	0.86
NC19	Normal Alkane C19	64.568	37447	10304	3.11	1.88
NC20	Normal Alkane C20	67.753	36137	9798	3.01	1.79
NC21	Normal Alkane C21	70.794	32755	9344	2.72	1.71
C25HBI	Highly Branch Isoprenoid C25	71.040	2251	552	0.19	0.10
NC22	Normal Alkane C22	73.707	30116	8358	2.51	1.53
NC23	Normal Alkane C23	76.500	26704	7282	2.22	1.33
NC24	Normal Alkane C24	79.182	22970	6052	1.91	1.11
NC25	Normal Alkane C25	81.761	21187	5706	1.76	1.04
NC26	Normal Alkane C26	84.245	18753	4846	1.56	0.89
NC27	Normal Alkane C27	86.637	15260	3935	1.27	0.72
NC28	Normal Alkane C28	88.943	13125	3420	1.09	0.63
NC29	Normal Alkane C29	91.174	11985	2756	1.00	0.50
NC30	Normal Alkane C30	93.336	8568	2039	0.71	0.37
NC31	Normal Alkane C31	95.421	7214	1810	0.60	0.33
NC32	Normal Alkane C32	97.445	5571	1269	0.46	0.23
NC33	Normal Alkane C33	99.409	6165	1423	0.51	0.26
NC34	Normal Alkane C34	101.318	5711	1294	0.48	0.24
NC35	Normal Alkane C35	103.250	5181	934	0.43	0.17
NC36	Normal Alkane C36	105.396	3254	584	0.27	0.11
NC37	Normal Alkane C37	107.820	3022	509	0.25	0.09
NC38	Normal Alkane C38	110.601	2850	378	0.24	0.07
NC39	Normal Alkane C39	113.859	2280	342	0.19	0.06
NC40	Normal Alkane C40	117.596	1591	245	0.13	0.05
NC41	Normal Alkane C41					

Parameter	Formula
WGC Parameters	
Pristane/Phytane	IP19/IP20
Pristane/nC17	IP19/NC17
Phytane/nC18	IP20/NC18
nC18/nC19	NC18/NC19
nC17/nC29	NC17/NC29
$nC_{18}/(nC_{18}+nC_{19})$	NC18/(NC18+NC19)
$nC_{17}/(nC_{17}+nC_{29})$	NC17/(NC17+NC29)
CPI Hunt[4]	((NC23+NC25+NC27+NC29+NC31)+(NC25+NC27+NC29+NC31+NC33))/(2*(NC24+NC26+NC28+ NC30+ NC32))
CPI Marzi[4]	((NC23+NC25+NC27)+(NC25+NC27+NC29))/(2*(NC24+NC26+NC28))
Normal Paraffins	C18+NC19+ NC20+NC21+NC22+NC23+NC24+NC25+NC26+NC27+NC28+NC29+NC30+NC31+NC32+NC33+ NC34+ NC35+NC36+NC37+NC38+NC39+NC40+NC41)/TOTAL_RESOLVED
Isoprenoids	100*(IP9+IP10+IP11+IP13+IP14+IP15+IP16+IP18+IP19+IP20+C25HBI)/TOTAL_RESOLVED
Cycloparaffins	100*(CP+MCP+CH+11DMCP+1T3DMCP+1T2DMCP+MCH+113TMCP+ECP+124TMCP+123TMC P+1C3DMCP+ 1C2DMCP)/TOTAL_RESOLVED
Branched (iso-) Paraffins	100*(IC4+IC5+22DMB+23DMB+2MP+3MP+22DMP+24DMP+223TMB+33DMP+2MH+23DMP+3M H+3EP)/ TOTAL_RESOLVED
BTX aromatics	100*(BZ+TOL+EB+MXYL+PXYL+OXYL)/TOTAL_RESOLVED (*OXYL added 05/21/2007)
Thompson[1]	
BZ/nC6	BZ/NC6
TOL/nC7	TOL/NC7
(nC6+nC7)/(CH+MCH)	(NC6+NC7)/(CH+MCH)
Isoheptane Value	(2MH+3MH)/(1C3DMCP+1T3DMCP+1T2DMCP)
nC7/MCH	NC7/MCH
CH/MCP	CH/MCP
nC7/2MH	NC7/2MH
nC6/22DMB	NC6/22DMB
Heptane Value	100*NC7/(CH+2MH+23DMP+11DMCP+3MH+1C3DMCP+1T3DMCP+1T2DMCP+MCH+NC7)
MCH/nC7	MCH/NC7
mpXYL/nC8	(MXYL+PXYL)/NC8
Mango[2]	
P1	100*NC7/(22DMP+24DMP+223TMB+33DMP+2MH+23DMP+11DMCP+3MH+1C3DMCP+1T3DMC P+3EP+ 1T2DMCP+NC7+MCH+ECP+TOL)
P2	100*(2MH+3MH)/(22DMP+24DMP+223TMB+33DMP+2MH+23DMP+11DMCP+3MH+1C3DMCP+1 T3DMCP+ 3EP+1T2DMCP+NC7+MCH+ECP+TOL)
P3	100*(3EP+33DMP+23DMP+24DMP+22DMP+223TMB)/(22DMP+24DMP+223TMB+33DMP+2MH+ 23DMP+ 11DMCP+3MH+1C3DMCP+1T3DMCP+3EP+1T2DMCP+NC7+MCH+ECP+TOL)
5N1	100*(ECP+1T2DMCP)/(22DMP+24DMP+223TMB+33DMP+2MH+23DMP+11DMCP+3MH+1C3DM CP+ 1T3DMCP+3EP+1T2DMCP+NC7+MCH+ECP+TOL)
N2	100*(11DMCP+1C3DMCP+1T3DMCP)/(22DMP+24DMP+223TMB+33DMP+2MH+23DMP+11DMC P+3MH+ 1C3DMCP+1T3DMCP+3EP+1T2DMCP+NC7+MCH+ECP+TOL)
6N1	100*(MCH+TOL)/(22DMP+24DMP+223TMB+33DMP+2MH+23DMP+11DMCP+3MH+1C3DMCP+1 T3DMCP+ 3EP+1T2DMCP+NC7+MCH+ECP+TOL)
K1	(2MH+23DMP)/(3MH+24DMP)
K2	(3EP+33DMP+23DMP+24DMP+22DMP+223TMB)/(2MH+3MH+11DMCP+1C3DMCP+1T3DMCP)
5N1/6N1	(ECP+1T2DMCP)/(MCH+TOL)
P3/N2	(3EP+33DMP+23DMP+24DMP+22DMP+223TMB)/(11DMCP+1C3DMCP+1T3DMCP)
ln(24DMP/23DMP)	ln(24DMP/23DMP)
Expulsion Temp ^{0}C	140+15{ln(24DMP/23DMP)}
Halpern[3]	
Tr1	TOL/11DMCP
Tr2	NC7/11DMCP
Tr3	3MH/11DMCP
Tr4	2MH/11DMCP

Parameter	Formula
Tr5	(2MH+3MH)/11DMCP
Tr7	1T3DMCP/11DMCP
Tr8	(2MH+3MH)/(22DMP+23DMP+24DMP+33DMP+3EP)
C1	22DMP/(22DMP+23DMP+24DMP+33DMP+3EP)
C2	23DMP/(22DMP+23DMP+24DMP+33DMP+3EP)
C3	24DMP/(22DMP+23DMP+24DMP+33DMP+3EP)
C4	33DMP/(22DMP+23DMP+24DMP+33DMP+3EP)
C5	3EP/(22DMP+23DMP+24DMP+33DMP+3EP)
C4	33DMP/(22DMP+23DMP+24DMP+33DMP+3EP)

Appendix 7-2

Holsapple 2B Carper SS Gases
(Post-CO_2 injection, 1/27/2021-9/27/2021)

Sample Date (remarks)

1) 1/27/2021
2) 2/4/2021 (selected for isotopes)
3) 2/8/2021
4) 2/24/2021
5) 3/3/2021
6) 3/9/2021 (selected for isotopes)
7) 3/16/2021
8) 4/15/2021
9) 4/27/2021 (selected for isotopes)
10) 5/4/2021
11) 5/11/2021 (selected for isotopes)
12) 5/18/2021
13) 6/15/2021 (selected for isotopes)
14) 6/22/2021 (selected for isotopes)
15) 6/29/2021
16) 7/6/2021
17) 7/13/2021 (selected for isotopes)
18) 7/20/2021
19) 7/27/2021
20) 8/3/2021 (selected for isotopes)
21) 8/17/2021
22) 8/24/2021
23) 8/31/2021
24) 9/7/2021
25) 9/14/2021
26) 9/20/2021
27) 9/27/2021 (selected for isotopes)

ISOTECH
a Stratum Reservoir brand
www.isotechlabs.com

Isotech Gas Data

Job 46945, 47111, 47509, 47576, 47643, 47689, 47727, 47940, 48021, 48114, 48128, 48210, 48266, 48308, 48397, 48542, 48600, 48676, 48732, 48808, 48860, 48920

CoreTrac IS-65021

Isotech Lab No.	Sample Name	Sample Date	Sample Time	Field Name	Location	GC Date	He %	H_2 %	Ar %	O_2 %	CO_2 %	N_2 %	CO %	C_1 %	C_2 %	C_2H_4 %	C_3 %	C_3H_6 %	iC_4 %	nC_4 %	iC_5 %	nC_5 %	C_6+ %	MS Date	$\delta^{13}CO_2$ ‰	$\delta^{13}C_1$ ‰	δDC_1 ‰	$\delta^{13}C_2$ ‰	$\delta^{13}C_3$ ‰	$\delta^{13}nC_4$ ‰	Specific Gravity	BTU	Comments
804927	210127_Holsapple_Produced_Gas	1/27/2021	11:30	Holsapple	Jewett, IL	11/10/2021	0.0070	nd	0.578	13.76	35.70	49.79	nd	0.107	0.0284	nd	0.0127	nd	0.0013	0.0046	0.0010	0.0016	0.0059								1.185	2	
804928	210204_Holsapple_Produced_Gas	2/4/2021	9:15	Holsapple	Jewett, IL	10/10/2021	nd	nd	nd	0.096	98.67	0.44	nd	0.593	0.113	nd	0.0470	nd	0.0045	0.0165	0.0031	0.0051	0.0118	12/14/2021	-41.29	-53.6	-261.9		-36.3	-32.8	1.511	11	d13C of methane, propane, and n-butane obtained online via GC-C-IRMS. Unable to separate ethane for isotope analysis.
783810	210208_Holsapple_Produced_Gas	2/8/2021	16:15	Holsapple	Jewett, IL	2/22/2021	nd	nd	nd	0.050	99.10	0.68	nd	0.0732	0.0643	nd	0.0123	nd	nd	0.0002	0.0002	0.0006	0.0215								1.515	3	
804929	210224_Holsapple_Produced_Gas	2/24/2021	11:10	Holsapple	Jewett, IL	10/10/2021	nd	nd	0.0127	0.31	0.97	98.68	nd	0.0045	0.0010	nd	0.0012	nd	0.0004	0.0021	0.0011	0.0024	0.0102								0.973	1	
785475	210303_Holsapple_Produced_Gas	3/3/2021	11:22	Holsapple	Jewett, IL	3/22/2021	nd	0.0377	nd	0.046	99.28	0.49	nd	0.0598	0.0179	nd	0.0251	nd	0.0045	0.0209	0.0047	0.0075	0.0059								1.516	3	
804930	210309_Holsapple_Produced_Gas	3/9/2021	15:15	Holsapple	Jewett, IL	10/10/2021	nd	nd	nd	0.079	98.20	0.44	nd	0.952	0.182	nd	0.0751	nd	0.0075	0.0270	0.0053	0.0088	0.0236	12/14/2021	-40.75	-53.4	-263.7	-42.91	-36.0	-32.2	1.507	18	d13C of methane, propane, and n-butane obtained online via GC-C-IRMS.
804931	210316_Holsapple_Produced_Gas	3/16/2021	14:45	Holsapple	Jewett, IL	10/10/2021	0.0063	nd	0.0091	0.25	97.04	1.12	nd	1.15	0.233	0.0003	0.111	nd	0.0125	0.0448	0.0090	0.0150	nd								1.500	21	
790000	210415_Holsapple_Produced_Gas	4/15/2021	11:00	Holsapple	Jewett, IL	5/5/2021	nd	0.213	0.0147	0.37	97.44	1.38	nd	0.347	0.0852	nd	0.0595	nd	0.0089	0.0408	0.0107	0.0194	0.0192								1.504	11	
790666	210427_Holsapple_Produced_Gas	4/27/2021	10:00	Holsapple	Jewett, IL	5/10/2021	0.0059	nd	nd	0.021	96.86	0.28	nd	1.75	0.468	nd	0.322	nd	0.0409	0.147	0.0276	0.0429	0.0354	12/9/2021	-40.67	-52.11	-259.3	-42.54	-35.49	-32.47	1.501	45	
791609	210504_Holsapple_Produced_Gas	5/4/2021	10:00	Holsapple	Jewett, IL	5/18/2021	0.0062	nd	0.0097	0.18	94.89	1.02	nd	2.33	0.647	nd	0.452	nd	0.0584	0.210	0.0402	0.0649	0.0927								1.491	64	
791906	210511_Holsapple_Produced_Gas	5/11/2021	10:00	Holsapple	Jewett, IL	5/18/2021	0.0081	0.0168	0.0056	0.099	93.66	0.77	nd	3.27	0.958	nd	0.655	nd	0.0766	0.256	0.0442	0.0686	0.116	12/9/2021	-40.38	-51.82	-257.9	-42.36	-35.35	-32.24	1.483	88	
792447	210518_Holsapple_Produced_Gas	5/18/2021	10:00	Holsapple	Jewett, IL	5/24/2021	nd	0.0107	0.0060	0.095	95.27	0.96	nd	1.69	0.611	nd	0.575	nd	0.0829	0.337	0.0758	0.123	0.164								1.501	72	
795356	210615_Holsapple_Produced_Gas	6/15/2021	10:00	Holsapple	Jewett, IL	6/25/2021	0.0053	0.0126	0.0055	0.16	95.65	1.04	nd	1.92	0.500	nd	0.346	nd	0.0436	0.161	0.0291	0.0477	0.0790	12/10/2021	-40.54	-52.00	-259.2	-42.25	-35.19	-32.40	1.495	51	
795967	210622_Holsapple_Produced_Gas	6/22/2021	11:00	Holsapple	Jewett, IL	6/28/2021	0.0074	0.0133	0.0067	0.19	94.33	0.99	nd	2.81	0.689	nd	0.462	nd	0.0588	0.215	0.0392	0.0647	0.128	12/9/2021	-40.14	-51.79	-256.4	-42.33	-35.34	-32.38	1.487	72	
796760	210629_Holsapple_Produced_Gas	6/29/2021	11:00	Holsapple	Jewett, IL	7/15/2021	0.0085	0.0120	nd	0.047	93.25	0.67	nd	3.92	0.952	nd	0.621	nd	0.0771	0.275	0.0483	0.0725	0.0503								1.477	91	
796929	210706_Holsapple_Produced_Gas	7/6/2021	13:00	Holsapple	Jewett, IL	7/15/2021	0.0098	0.0116	nd	0.067	93.03	0.71	nd	4.18	0.965	nd	0.586	nd	0.0699	0.238	0.0399	0.0578	0.0332								1.473	90	
797669	210713_Holsapple_Produced_Gas	7/13/2021	13:30	Holsapple	Jewett, IL	7/22/2021	0.0108	0.0109	0.0056	0.11	92.21	1.20	nd	4.30	0.999	nd	0.611	nd	0.0745	0.262	0.0491	0.0766	0.0819	12/9/2021	-39.79	-51.49	-252.6	-42.18	-35.34	-32.31	1.470	97	
798966	210720_Holsapple_Produced_Gas	7/20/2021	13:30	Holsapple	Jewett, IL	8/2/2021	0.0120	0.0106	0.0118	0.26	90.81	2.22	nd	4.43	1.04	nd	0.646	nd	0.0795	0.281	0.0509	0.0785	0.0659								1.462	100	
799333	210727_Holsapple_Produced_Gas	7/27/2021	11:00	Holsapple	Jewett, IL	8/4/2021	0.0118	nd	nd	0.066	92.32	0.74	nd	4.50	1.06	nd	0.677	nd	0.0855	0.312	0.0587	0.0929	0.0779								1.471	105	
800243	210803_Holsapple_Produced_Gas	8/3/2021	13:00	Holsapple	Jewett, IL	8/10/2021	nd	0.0360	nd	0.10	98.54	0.44	nd	0.709	0.0909	nd	0.0530	nd	0.0039	0.0146	0.0027	0.0046	0.0054	12/10/2021	-40.33	-51.5	-261.1		-35.7	-32.6	1.509	11	d13C of methane, propane, and n-butane obtained online via GC-C-IRMS. Unable to separate ethane for isotope analysis.
801600	210817_Holsapple_Produced_Gas	8/17/2021	11:30	Holsapple	Jewett, IL	8/26/2021	0.0114	nd	0.0073	0.14	91.74	1.15	nd	4.48	1.04	nd	0.673	nd	0.0865	0.313	0.0611	0.101	0.195								1.470	110	
802131	210824_Holsapple_Produced_Gas	8/24/2021	11:30	Holsapple	Jewett, IL	9/9/2021	0.0126	nd	0.0052	0.071	90.91	1.31	nd	5.05	1.17	nd	0.714	nd	0.0892	0.316	0.0616	0.102	0.192								1.464	119	
802581	210831_Holsapple_Produced_Gas	8/31/2021	11:00	Holsapple	Jewett, IL	9/14/2021	0.0120	nd	0.0059	0.097	91.15	1.07	nd	5.21	1.15	nd	0.697	nd	0.0860	0.309	0.0571	0.0909	0.0677								1.462	113	
802928	210907_Holsapple_Produced_Gas	9/7/2021	11:00	Holsapple	Jewett, IL	9/22/2021	0.0105	nd	0.0073	0.11	91.05	1.06	nd	5.09	1.14	nd	0.710	nd	0.0917	0.337	0.0683	0.114	0.211								1.465	122	
803655	210914_Holsapple_Produced_Gas	9/14/2021	11:00	Holsapple	Jewett, IL	9/29/2021	0.0125	nd	nd	0.060	90.87	0.85	nd	5.59	1.22	nd	0.735	nd	0.0911	0.332	0.0622	0.0983	0.0792								1.459	121	
804362	210920_Holsapple_Produced_Gas	9/20/2021	11:00	Holsapple	Jewett, IL	10/7/2021	0.0117	nd	0.0068	0.11	90.07	1.68	nd	5.36	1.19	nd	0.729	nd	0.0940	0.344	0.0694	0.116	0.216								1.459	126	
804932	210927_Holsapple_Produced_Gas	9/27/2021	11:00	Holsapple	Jewett, IL	10/10/2021	0.0130	nd	0.0057	0.10	90.38	1.12	nd	5.65	1.23	nd	0.742	nd	0.0942	0.341	0.0678	0.113	0.147	12/10/2021	-39.40	-51.73	-253.4	-42.18	-35.41	-32.28	1.458	127	

All gas component carbon isotope values are reported on a scale defined by a two point calibration of LSVEC and NBS 19

nd = not detected, na = not analyzed

7.2 Carper Water-Oil-CO_2 Relative Permeability

Illinois State Geological Survey
ROZ Associated Storage

Cumberland County, Illinois
File: HH-107518
Date: 09-30-22

SUMMARY OF RELATIVE PERMEABILITY PROCEDURES

Sample: 23

1. Each selected samples were CT scanned to evaluate the sample's integrity.
2. Each sample was installed in a hydrostatic coreholder at 500 psi net confining stress (NCS) and a 200 psi pore pressure was established. Each sample was miscibly cleaned by injecting alternating cycles of toluene, chloroform/methanol azeotrope and methanol through each sample. Solvent injection continued until the effluent was clear and methanol did not precipitate silver nitrate (AgNO3).
3. Each sample was unloaded and dried to a constant weight in a 140°F convection oven. Basic properties including permeability to air and porosity were measured at 1300 psi net confining stress
4. Each sample was pressure saturated under tagged synthetic formation brine. The brine was tagged with sodium iodide (NaI) as an x-ray blocker. The samples were then installed in a hydrostatic core holder, 1900 psi net confining stress (NCS) was applied, and 200 psi pore pressure was established. Synthetic formation brine was injected at a suitable constant rate until equilibrium differential pressure was observed. Specific permeability to brine was determined at three (3) injection rates.
5. The temperature was elevated to 95°F. Reservoir crude oil was injected at a suitable constant pressure to displace the brine while produced volumes and elapsed time were recorded. Injection continued until brine production stopped, and effective permeability to oil at residual brine saturation
   Note: Permeability reduction was noted. After discussions with the client, it was decided to replace the crude oil with a laboratory oil blend.
6. Tagged brine and oil blend were co-injected vertically upward at a series of increasing water-oil ratios to allow the water saturation in the sample to increase. Injection at each ratio was continued until an equilibrium differential pressure and saturation profile were observed. Brine alone was injected at a suitable constant rate until an equilibrium differential pressure was observed. Effective permeability to brine at residual oil saturation was determined at three (3) injection rates while scanning the sample.
   Note: Due to permeability and flow rate limitations the final water:oil ratio was not performed.
7. The system pore pressure was increased to 1600 psi and allowed to equilibrate overnight.
8. Tagged brine (equilibrated with CO_2 at test conditions) and carbon dioxide (CO_2) co-injected vertically downward at a series of increasing CO_2:water ratios to allow the CO_2 saturation in the sample to increase. Injection at each ratio was continued until an equilibrium differential pressure and saturation profile were observed. CO_2 alone was injected at a suitable constant rate until an equilibrium differential pressure was observed. Effective permeability to CO_2 at residual brine/oil saturation was determined at three (3) injection rates while scanning the sample.
   Note: Additional oil was produced during the CO2 flood.
9. The system was cooled to ambient temperature. The pore pressure was then reduced to ambient, and finally the net confining stress was reduced to ambient. Each sample was then unloaded, and
10. Each sample was unloaded and subjected to Dean-Stark analysis and soxhlet extraction to confirm final fluid saturations, and then dried to a constant weight.
11. Effective permeabilities to water, oil, and CO_2 were calculated using Darcy's law. Saturations at each point were determined using x-ray attenuation.

REFERENCES

Abrams, R. H., 1995, Long-range buoyancy-driven oil migration in the Illinois Basin: Stanford University, 79 p.

Aguilera, R., 2014, Flow Units: From Conventional to Tight-Gas to Shale-Gas to Tight-Oil to Shale-Oil Reservoirs: SPE Reservoir Evaluation & Engineering, v. 17, no. 02, p. 190–208, doi:10.2118/165360-PA.

Ahmad, N., 2003, Facies tract mapping technique, a sequence stratigraphic tool: Case study of lowstand Carper Sandstone play, Lower Carboniferous of Eastern Illinois Basin, North America, in ATC Conference and Oil Show: p. 21.

Alagorni, A H, Yaacob, Z B, Nour, A H, and Junin, R B. Effect of water alternating gas (WAG-N_2) after water or gas flooding on crude oil recovery in sandstone reservoirs. Energy Security and Chemical Engineering Congress. IOP Conf. Series: Materials Science and Engineering 736 (2020) 022015

Al-Aswad, A. A., 1986, Subsurface Lithostratigraphy and Depositional Environments of the Borden Group (Valmeyeran Series, Mississippian System) in Indiana (Winnowed Turbidites, Deltaic, Fine-Grained Sediments, New Providence Shale, Osagian Clastic Sediments): Bloomington, IN, Indiana University, 405 p.

Alfarge, D., Wei, M, and Bai, B., 2017, Factors affecting CO_2-EOR in shale-oil reservoirs: numerical simulation study and pilot tests. Energy and Fuels, 31, 8462-8480.

Anna, L. O., 2009, Geologic Assessment of Undiscovered Oil and Gas in the Powder River Basin Province, Wyoming and Montana: U.S. Geologicial Survey Digital Data Series DDS–69–U, p. 93pp.

Anna, L.O., 2011, Geologic assessment of undiscovered oil and gas in the Williston Basin Province, Montana, North Dakota, and South Dakota, chap. 3 *of* U.S. Geological Survey Williston Basin Province Assessment Team, Assessment of undiscovered oil and gas resources of the Williston Basin Province of North Dakota, Montana, and South Dakota, 2010: U.S. Geological Survey Digital Data Series 69–W, 76 p.

Archie, G. E., 1942, The Electrical Resistivity Log as an Aid in Determining Some Reservoir Characteristics: Transactions of the AIME, v. 146, no. 01, p. 54–62, doi:10.2118/942054-G.

Armon, W. J., Coburn, A. A., Mast, R. F., and Sherman, C. W., 1964, Physical Properties of Illinois Crude Oil. Part I, Illinois State Geological Survey (ISGS), Illinois Petroleum 78, 53 p.

Armon, W. J., Lawry, T. F., and Mast, R. F., 1966, Physical properties of Illinois Crude Oil. Part II, Illinois State Geological Survey (ISGS), Illinois Petroleum 81, 44 p.

Aryana, S., D. Cifrese, T. Smith, E. Hendrickson, and C. Craig, 2014, Flood Pattern Optimization of the Wertz Tensleep.

Asquith, G., 1985, COMBINING TECHNIQUES: 22-28 p.

Asquith, G., and D. Krygowski, 2004, Basic Relationships of Well Log Interpretation: Basic Well Log Analysis, AAPG Methods in Exploration, v. 16, p. 1–20.

Atherton, E., C. Collinson, and J. A. Lineback, 1975. Mississippian System. Handbook of Illinois Stratigraphy: Illinois State Geological Survey Bulletin 95, pp. 104-163.

Aung, M P W. Analysis on EOR/CO_2 Sequestration in Sacroc Unit, Texas using a compositional simulator. Master thesis. New Mexico Institute of Mining and Technology. 2009. http://www.prrc.nmt.edu/publications/media/pdf/thesis/Maung%20Ang%20Thesis_Final.pdf

Azzolina, N. A., Hamling, J. A., Peck, W. D., Gorecki, C. D., Nakles, D. V., & Melzer, L. S., 2017, A life cycle analysis of incremental oil produced via CO_2 EOR. *Energy Procedia*, *114*, 6588-6596.

Baas, J. H., J. L. Best, J. Peakall, and M. Wang, 2009, A Phase Diagram for Turbulent, Transitional, and Laminar Clay Suspension Flows: Journal of Sedimentary Research, v. 79, no. 4, p. 162–183, doi:10.2110/JSR.2009.025.

Barrows, M. H., and R. M. Cluff, 1984, New Albany Shale Group (Devonian-Mississippian) source rocks and hydrocarbon generation in the Illinois basin, in G. Demaison, and R. J. Murris, eds., Petroleum Geochemistry and Basin Evaluation: Tulsa, Oklahoma, American Association of Petroleum Geologists, p. 111–138.

Bell, A. H., 1939, Oil and gas development in Illinois in 1938: Urbana, IL, Illinois State Geological Survey, 28 p.

Bell, A. H., and V. Kline, 1956, Oil and gas development in Illinois in 1954: 143 p., doi:10.1038/312192a0.

Bennion, D.B., Bachu, S., 2010. Drainage and imbibition relative permeability curves at reservoir conditions for carbonate formations. In: SPE Paper 134028; SPE Annual Technical Conference and Exhibition, 19–22 September 2010, Florence, Italy.

Benson, S, Pini, R, and Krevor, S, 2015. Relative permeability analyses to describe multi-pahse flow in CO2 storage reservoirs. Global CCS institute. relative-permeability-analysis-describe-multi-phase-flow-co2-storage-reservoirs.pdf (globalccsinstitute.com)

Bergstrom, R. E., N. F. Shimp, and R. M. Cluff, 1980, Geologic and Geochemical Studies of the New Albany Shale Group (Devonian-Mississippian) in Illinois: Urbana, IL, 183 p.

Berner, U., 1989, Entwicklung und Anwendung empirischer Modelle fur die Kohlenstoffisotopenvariationen in Mischungen thermogener Erdgase: Ph.D. thesis, Technische Universitat Clausthal.

Berner, U., and E. Faber, 1996, Empirical carbon isotope/maturity relationships for gases from algal kerogens and terrigenous organic matter, based on dry, open-system pyrolysis: Organic Geochemistry, v. 24, p.947-955.

Berner, U., and E. Faber, 1988, Maturity related mixing model for methane, ethane and propane, based on carbon isotopes: Org. Geochem., v. 13, p. 67-72.

Bethke, C., J. Reed, and D. Oltz, 1991, Long-range petroleum migration in the Illinois Basin: AAPG Bulletin, v. 75, no. 5, p. 925–945.

Biodlz, K.T., 1991, The Los Angeles Basin: An overview. In Biddle. K.T., ed., Active Margin Basins: American Association of Petroleum Geologists Memoir 52, p. 5-24.

Borden, W. W., 1874, Report of a geological survey of Clarke and Floyd Counties, Indiana: Indiana Geological Survey, p. 133–189.

Bouma, A. H., 1962, Sedimentology of some flysch deposits, a graphic approach to facies interpretation: Amsterdam, Elsevier, 168 p.

Bredehoeft, J. D., K. Belitz, and S. Sharp-Hansen, 1992, The Hydrodynamics of the Big Horn Basin: A Study of the Role of Faults: American Association of Petroleum Geologists Memoirs, v. 76, no. 4, p. 530–546.

Bristol, H. M., and R. H. Howard, 1966, St. Louis (Mississippian) Oil Production in Jasper County, Illinois: Urbana, IL, 21 p.

Brokmeyer, R. J., D. C. Borling, W. T. Pierson, A. Exploration, and P. Sector, 1996, SPE 35191 Lost Soldier Tensleep $C0_2$ Tertiary Project, Performance Case History; Bairoil, Wyoming: p. 405–412.

Brown, M. A., 1990, Regional lithofacies and depositional environments of the Salem Limestone (Valmeyeran, Mississippian), south-central Indiana, in T. A. Thompson, ed., Architectural Elements and Paleoecology of Carbonate Shoal and Intershoal Deposits in the Salem Limestone (Mississippian) in South-Central Indiana: Bloomington, Indiana, Indiana Geological Survey, p. 1–12.

Bruno, M. S., J. Young, J. Diessl, K. Lao, N. White, B. Childers, & J. Xiang, 2014, Characterization of Pliocene and Miocene formations in the Wilmington Graben, Offshore Los Angeles, for large scale geologic storage of CO2. Energy Procedia, 63, p. 4897-4917.

Burton-Kelly, M. E., N. W. Dotzenrod, I. K. Foele, A. J. Gorz, S. C. Ayash, and W. D. Peck, 2015, Identification of Residual Oil Zones (ROZs) in the Williston and Powder River Basins: U.S. Department of Energy, National Energy Technology Laboratory, Carbon Storage R&D Project Review Meeting: Transforming Technology through Integration and Collaboration, August 18–20, 2015, no. March 2019, p. 1–23.

Burton-Kelly, M. E., N. W. Dotzenrod, I. K. Feole, W. D. Peck, M. D. Kurz, B. A. Kurz, S. A. Smith, and C. D. Gorecki, 2018, Identification of Residual Oil Zones in the Williston and Powder River Basins. United States: N. p., 2018. doi:10.2172/1430234.

Carlson, G., Johnson, K., Chuang, R., &Rupp, J. (2018). Spatially varying stress state in the central U.S. from Bayesian inversion of focal mechanism and in situ maximum horizontal stress orientation. Journal of Geophysical Research: Solid Earth,123, 3871–3890.

Carothers, J.E., 1968. A statistical study of the formation factor relation. Log Anal., 9(5): 13-20.

Carr, D. D., 1973, Geometry and origin of oolite bodies in the Ste. Genevieve Limestone (Mississippian) in the Illinois Basin: 81 p.

Carroll, W. K., 1979, Depositional Environments and Paragenetic Porosity Controls, Upper Red River Formation, North Dakota. Rep Invest ND Geological Survey, no. 66.

Carter, R.D., Tracy, G.W., 1960. An improved method for calculating water influx. Trans., AIME 219, 415–417.

Cartigny, M. J. B., D. Ventra, G. Postma, and J. H. van den Berg, 2014, Morphodynamics and sedimentary structures of bedforms under supercritical-flow conditions: New insights from flume experiments: Sedimentology, v. 61, no. 3, p. 712–748, doi:10.1111/SED.12076.

Chen, C., M.T. Balhoff, K.K. Mohanty, Effect of reservoir heterogeneity on primary recovery and CO2 huff 'n' puff recovery in shale-oil reservoirs, SPEREE 17 (3) (2014) 404-413.

Chi, G., D. Lavoie, R. Bertrand, and M. K. Lee, 2010, Downward hydrocarbon migration predicted from numerical modeling of fluid overpressure in the Paleozoic Anticosti Basin, eastern Canada: Geofluids, v. 10, no. 3, p. 334–350, doi:10.1111/J.1468-8123.2010.00280.X.

Chiquet, P., D. Broseta, and S. Thibeau, 2005, Capillary Alteration of Shaly Caprocks by Carbon Dioxide, in SPE Europec/EAGE Annual Conference: Society of Petroleum Engineers (SPE), p. 10, doi:10.2523/94183-ms.

Choquette, P. W., and R. P. Steinen, 1980, Mississippian non-supratidal dolomite, Ste. Genevieve Limestone, Illinois Basin: evidence for mixed-water dolomitization: Concepts and models of dolomitization, p. 163–196, doi:10.2110/pec.80.28.0163.

Chung, H. M., J. R. Gormly, and R. M. Squires, 1988, Origin of gaseous hydrocarbons in subsurface environments: theoretical considerations of carbon isotope distribution: Chemical Geology, v. 71, p.97-103.

Clavier, C., G. Coates, and J. Dumanoir, 1984, Theoretical and Experimental Bases for the Dual-Water Model for Interpretation of Shaly Sands: Society of Petroleum Engineers Journal, v. 24, no. 02, p. 153–168, doi:10.2118/6859-PA.

Clayton, C., 1991, Carbon isotope fractionation during natural gas generation from kerogen: Marine and Petroleum Geology, v. 8, p.232-240.

Cluff, R.M., 1984, Carbonate Sand Shoals in the Middle Mississippian (valmeyeran) Salem - St. Louis - Ste. Genevieve Limestones, Illinois Basin, in Carbonate Sands: SEPM (Society for Sedimentary Geology), p. 94–135, doi:10.2110/cor.84.05.0094.

Cluff, R.M. and Byrnes, A.P., 1991. Lopatin Analysis of Maturation and Petroleum Generation in the Illinois Basin. *in* M.W. Leighton, D.R. Kolata, D.F., Oltz, and J.J. Eidel, eds., Interior Cratonic Basins: Tulsa, Oklahoma, American Association of Petroleum Geologists Memoir 51, 425-452.

Cluff, R. M., and J. A. Lineback, 1981, Middle Mississippian carbonates of the Illinois Basin: Urbana, IL, Illinois State Geological Survey, 88 p.

Coates, G. R., and S. Denoo, 1981, The Producibility Answer Product: The Schlumberger Technical Review, v. 29, no. 2, p. 55–63.

Cohee, G. V., 1942, Lateral Variation in Chester Sandstones Producing Oil and Gas in Lower Wabash River Area With Special Reference to New Harmony Field: Urbana, IL, Illinois State Geological Survey, 1594–1607 p.

Cole, R. D., and W. J. Nelson, 1995, Stratigraphic Framework and Environments of Deposition of the Cypress Formation in the Outcrop Belt of Southern Illinois: Illinois State Geological Survey, 47 p.

Coleman, D. D., 1987, Gas identification by geochemical fingerprinting: American Gas Association, Operating Section Proceedings, p. 568-573.

Coleman, J. M., and D. B. Prior, 1981, Deltaic environments of deposition, in P. A. Scholle and D. Spearing, (eds.), Sandstone depositional environments: AAPG Memoir 31, p. 139-178.

Collinson, C. and E. Atherton, 1975, Devonian System, *in* Handbook of Illinois stratigraphy: Illinois State Geological Survey, Bulletin 95, p. 104–123.

Collinson, C., L.E. Becker, G.W. James, J.W. Koenig, and D.H. Swann, 1967, Illinois Basin, *in* International Symposium on the Devonian System: Alberta Society of Petroleum Geologists, v. 1, p. 940–962; Illinois State Geological Survey Reprint 1968-G.

Collinson, C., L.E. Becker, G.W. James, J. W. Koenig, D. H. Swann, M. P. Carlson, and F. H. Dorheim, 1967, Devonian of the North-Central Region, United States, in International Symposium of the Devonian System: CSPG Special Publications, p. 933–971.

Cook, B. R., 2012, Wyoming's miscible CO2 enhanced oil recovery potential from main pay zones: An economic scoping study: doi:10.1139/Zxx-xxx.

Cooper, J., 2016, Rangely Weber sand unit WAG management optimization. 14th Annual CO_2-EOR Carbon Management Workshop, Midland, Texas, USA, Midland CO_2 Conference.

Cooper, S. P., and J. C. Lorenz, n.d., Tensleep Formation Fracture Study Compendium.

Craddock, W. H. et al., 2012, Geologic Framework for the National Assessment of Carbon Dioxide Storage Resources – Powder River Basin, Wyoming, Montana, South Dakota, and Nebraska Geologic Framework for the National Assessment of Carbon Dioxide Storage Resources: Report of Project, v. 11, p. 1–285, doi:10.1016/j.ijggc.2012.09.018.

Craig, L., C. Connor, A. Armstrong, and K. Varnes, 1979, Paleotectonic investigations of the Mississippian System in the United States.

Crouch, J. and J. Suppe, 1993, Late Cenozoic Tectonic Evolution of the Los Angeles Basin and Inner California Borderland: A Model for Core Complex-Like Crustal Extension. Geological Society of America Bulletin 105: p. 1415-1435.

Cumings, Edgar Roscoe, 1922, Nomenclature and description of the geological formations of Indiana, in W. N. Logan, E.R. Cumings, C. A. Malott, S. S. Visher, W. M. Tucker, and J. R. Reeves, eds., Handbook of Indiana geology: Indianapolis, Indiana Department of Conservation, p. 403–570.

Daniel, R. F., and J. G. Kaldi, 2009, Evaluating Seal Capacity of Cap Rocks and Intraformational Barriers for CO2 Containment: p. 335–345, doi:10.1306/13171247ST59227.

Deans, H.A., 1971. Method of determining fluid saturations in reservoirs. U.S. Patent 3, 623–842.

Densmore, M. 1997, The Petrology and Petroleum Reservoir Potential of the Dutch Creek Sandstone in the South-Central Portion of the Illinois Basin. Unpublished M.S. thesis, Southern Illinois University at Carbondale, 64 p. plus 3 appendices.

Devera, J.A., and G.H. Fraunfelter, 1988, Middle Devonian paleogeography and tectonic relationships east of the Ozark Dome southeastern Missouri, southwestern Illinois and parts of southwestern Indiana and western Kentucky, *in* Second International Symposium on the Devonian System: Calgary, Alberta, Canadian Society of Petroleum Geologists, 18 p.

Devera, J.A., and N.R. Hasenmueller, 1990, Kaskaskia sequence: Middle Devonian and Upper Devonian Series through Mississippian Kinderhookian Series, *in* M.W. Leighton, D.R. Kolata, D.E. Oltz, and J.J. Eidel, eds., Interior cratonic basins: AAPG Memoir 51, p. 113–123.

Devera, J. A., W. J. Nelson, and R. D. Norby, 2011, Middle Devonian Series through Mississippian System, in D. R. Kolata, and C. Nimz, eds., Geology of Illinois: Illinois State Geological Survey, p. 167–186.

Ding, M, Gao, M, Wang, Y, Qu, Z, Chen, X., 2019, Experimental study on CO2-EOR in fractured reservoirs: Influence of fracture density, miscibility and production scheme. Journal of Petroleum Science and Engineering, 174, 476-485.

Dodd, J. R., T. A. Thompson, and D. O. Petzold, 1993, Anatomy of the grainstone shoal facies of the Salem Limestone (Mississippian) of southern Indiana Anatomy of the Grainstone Shoal Facies of the Salem Limestone (Mississippian) of Southern Indiana (A Preliminary Report): Bloomington, Indiana, 43 p.

Dolton, G. L., K. H. Carlson, and R. R. Charpentier, 1981, Estimates of Undiscovered Recoverable Resources of Conventionally Producible Oil and Gas in the United States: A Summary: 17 p.

Dolton, G., and J. Fox, 1996, Powder River Basin Province (033): Gautier, DL, Dolton, GL, Takahashi, KI, no. 033, p. 1–32.

Droste, J.B., and R.H. Shaver, 1975, Jeffersonville Limestone (Middle Devonian) of Indiana: Stratigraphy, sedimentation, and relation to Silurian reef-bearing rocks: American Association of Petroleum Geologists, Bulletin 59, p. 393–412.

Droste, J.B., and R.H. Shaver, 1983, Atlas of early and middle Paleozoic paleogeography of the southern Great Lakes area: Indiana Geological Survey, Special Report 32, 32 p.

Droste, J.B., and R.H. Shaver, 1987, Upper Silurian and Lower Devonian stratigraphy of the central Illinois Basin: Indiana Geological Survey, Special Report 39, 29 p.

Durham, D.L., and Yerkes, R.F., 1964. Geology and oil resources of the eastern Puente Hills area, southern California: United States Geological Survey Professional Paper 420-B, 62 p.

Edzwald, J. K., J. B. Upchurch, and C. R. O'Melia, 1974, Coagulation in Estuaries: Environmental Science and Technology, v. 8, no. 1, p. 58–63, doi:10.1021/ES60086A003.

England, W. A., 1994, Secondary migration and accumulation of hydrocarbons: The petroleum system – from source to trap, v. 77, p. 211–217.

Espinoza, D.N. and Santamarina, J.C., 2010. Water-CO2 mineral systems – Interfacial tension, contact angle, and diffusion. Implications to CO2 geological storage. Water Resources Research, 46, WO7537.

Ettensohn, F. R., S. F. Greb, D. R. Chesnut, D. C. Harris, C. E. Harris, C. F. Eble, P. D. Howell, A. E. Watson, and Johnson W.K., 2002, Mississippian Stratigraphy, Depositional Environments, and Tectonic Framework of the Central Appalachian Basin, Eastern Kentucky, U.S.A, in L. V. Hills, C. M. Henderson, and E. W. Bamber, eds., Carboniferous and Permian of the World: Canadian Society of Petroleum Geologists, p. 22–40.

Eves, K. E., and J. J. Nevarez, 2009, Update of Lost Soldier / Wertz Floods. Presented at the 15th Annual CO2 Flooding Conference, December 10-11, 2009, Midland, Texas.

Faber, E., 1987, Zur isotopengeochemie gasformiger Kohlen wasserstoffe: Erdol Erdgas Kohle, v. 103, p. 210-218.

Faber, E., and W. Stahl, 1984, Geochemical surface exploration for hydrocarbons in North Sea: AAPG Bulletin, v. 68, p.363-386.

Faber, E., W. J. Stahl, and M. J. Whiticar, 1992, Distinction of bacterial and thermogenic hydrocarbon gases: in R. Vially, ed., Bacterial Gas, Paris, Editions Technip, p. 63-74.

Fildani, A., W. R. Normark, S. Kostic, and G. Parker, 2006, Channel formation by flow stripping: large-scale scour features along the Monterey East Channel and their relation to sediment waves: Sedimentology, v. 53, no. 6, p. 1265–1287, doi:10.1111/J.1365-3091.2006.00812.X.

Findley, 2009. Enhanced Oil Recovery I: Loudon Single-Well Huff ‘n’ Puff. DOE contract: DE-FC26-03NT41994 Final report.

Fischer, D. W., J.A. LeFever, R.D. LeFever, L. D. Helms, J. A. Sorensen, S. A. Smith, E. N. Steadman, J. A. Harju, 2005, Mission canyon formation outline: p. 1—23.

Fischer, D. W., J. A. LeFever, R. D. LeFever, L. D. Helms, J. A. Sorensen, S. A. Smith, E. N. Steadman, and J. A. Harju, 2008, Red River Formation Outline: p. 1–16.

Fisher, Q. J., R. J. Knipe, and R. H. Worden, 2000, Microstructures of Deformed and Non-Deformed Sandstones from the North Sea: Implications for the Origins of Quartz Cement in Sandstones: Quartz Cementation in Sandstones, p. 129–146, doi:10.1002/9781444304237.CH10.

Fituri, H. S., 1987, Study of Selected Sandstone Reservoirs in the Indiana Portion of the Griffin Consolidated Field that lies above New Harmony: Indiana University, M.S. Thesis, 167 p.

Fonnesu, M., F. Felletti, P. D. W. Haughton, M. Patacci, and W. D. McCaffrey, 2018, Hybrid event bed character and distribution linked to turbidite system sub-environments: The North Apennine Gottero Sandstone (north-west Italy): Sedimentology, v. 65, no. 1, p. 151–190, doi:10.1111/SED.12376.

Foster, D.I., 1958, Summary of the stratigraphy of the Minnelusa formation, Powder River basin, Wyoming, IN Bibb, T.W., Jr., chairman, Powder River basin: Wyoming Geological Association Field Conference Guidebook, no. 13, p. 39-44.

Frailey, S.M., T.M. Parris, J.R. Damico, R.T. Okwen, and R.W. McKaskle. 2012a. CO_2 Storage and Enhanced Oil Recovery: Sugar Creek Oil Field Test Site, Hopkins County, Kentucky, C.C. Monson and J.H. Goodwin (eds): Illinois State Geological Survey, Open File Series 2012-4, 234 pp.

Frailey, S.M, I.G. Krapac, J.R. Damico, R.T. Okwen, and R.W. McKaskle. 2012b. CO_2 Storage and Enhanced Oil Revovery: Bald Unit Test Site, Mumford Hills Oil Field, Posey County, Indiana, J.H. Goodwin and C.C. Monson (eds): Illinois State Geological Survey, Open File Series 2012-5, 191pp.

Friedmann, S. J., and V. W. Stamp, 2006, Teapot Dome: Characterization of a CO2-enhanced oil recovery and storage site in Eastern Wyoming: Environmental Geosciences, v. 13, no. 3, p. 181–199, doi:10.1306/eg.01200605017.

Gamadi, T.D., J.J. Sheng, M.Y. Soliman, 2013, An experimental study of cyclic gas injection to improve shale oil recovery, in: Paper SPE 166334 Presented at the SPE Annual Technical Conference and Exhibition Held in New Orleans, Louisiana, USA.

Gautier, D. L., M. E. Tennyson, T. A. Cook, R. R. Charpentier, and T. R. Klett, 2012 (revised 2013), Remaining recoverable petroleum in ten giant oil fields of the Los Angeles Basin, southern California: U.S. Geological Survey Fact Sheet V. 1.1, 2 p.

Giannetta, L. G., N. D. Webb, S. K. Butler, and N. P. Grigsby, 2021, Using clay microporosity to improve formation evaluation in potential residual oil zones: Cypress Sandstone, Illinois Basin: AAPG Bulletin, v. 105, no. 8, p. 1595–1625, doi:10.1306/02262118214.

Gomez-Rivero, O., 1977. Some considerations about the possible use of the parameters a and m as a formation evaluation tool through well logs. Trans. SPWLA 18th Ann. Logging Symp., pp. J 1-24.0

Graham, B.D. et al.: Design and Implementation of a Levelland Unit CO_2 Tertiary Pilot, paper SPE 8831 presented at the 1980 SPE/DOE Enhanced Oil Recovery Symposium, Tulsa, April 20–23.

Greenhough, J. D., S. R. McCutcheon, and V. S. Papezik, 1985, Petrology and geochemistry of Cambrian volcanic rocks from the Avalon Zone in New Brunswick: Canadian Journal of Earth Sciences, v. 22, no. 6, p. 881–892, doi:10.1139/E85-092.

Grigsby, N. P., and N. D. Webb, 2020, Assessing the Cypress Sandstone for Carbon Dioxide-Enhanced Oil Recovery and Carbon Storage: Part II-Leveraging Geologic Characterization to Develop a Representative Geocellular Model for Noble Oil Field, Western Richland County, Illinois: ISGS Circular, v. 602.

Gupta, N., Parakh, S., Gang, T., Cestari, N., and Bandyopadhyay, P., 2022. Residual Oil Zone Recovery Evaluation and Forecast Methodology: A Wasson Field Case Study. *Proceedings – SPE Symposium on Improved Oil Recovery, 2022-April.* https://doi.org/10.2118/209474-MS

Harouaka, A., B. Trentham, and S. Melzer, 2013, Long overlooked residual oil zones (ROZ's) are brought to the limelight, in Society of Petroleum Engineers – SPE Canadian Unconventional Resources Conference 2013 – Unconventional Becoming Conventional: Lessons Learned and New Innovations: Society of Petroleum Engineers, p. 972–980.

Harris, C., 1992, Regional lithofacies and depositional environments of the Beech Creek Limestone (Chesterian), south-central Indiana, in A. S. Horowitz, and J. R. Dodd, eds., Chesterian sections (Late Mississipian) along Interstate 64 in southern Indiana: Indiana Geological Survey, p. 146–167.

Hatch, J.R, Risatti, J.B., and King, J.D., 1991. Geochemistry of Illinois Basin Oils and Hydrocarbon source rocks, *in* M.W. Leighton, D.R. Kolata, D.F., Oltz, and J.J. Eidel, eds., Interior Cratonic Basins: Tulsa, Oklahoma, American Association of Petroleum Geologists Memoir 51, 403-423.

Haughton, P. D. W., S. P. Barker, and W. D. McCaffrey, 2003, 'Linked' debrites in sand-rich turbidite systems – origin and significance: Sedimentology, v. 50, no. 3, p. 459–482, doi:10.1046/J.1365-3091.2003.00560.X.

Haughton, P. C. Davis, W. McCaffrey, and S. Barker, 2009, Hybrid sediment gravity flow deposits – Classification, origin and significance: Marine and Petroleum Geology, v. 26, no. 10, p. 1900–1918, doi:10.1016/J.MARPETGEO.2009.02.012.

Hedin, Craig R., 2020, IDNR Revisions to Spacing and Location of Wells, Illinois Oil and Gas Association, accessed May 19, 2023, https://ioga.com/2020/09/25/idnr-revisions-to-spacing-and-location-of-wells/#:~:text=The%20location%20of%20the%20well,a%20well%20to%20the%20same

Hefner, T. A. and K. T. Barrow, 1992, Rangely Field--U.S.A. Uinta/Piceance Basins, Colorado: v. 21, p. 29–56.

Henderson, T.C., Ridgway, K.D., Johnston, C.T., and Everett, T.A., Integrated reservoir characterization of enhanced oil recovery targets in mature basins: An example from the Tar Springs Formation, Rock Hill field, Illinois Basin, United States. AAPG Bulletin; 104 (10): 2077–2098.

Hild, G. P. and R. K. Wackowski, 1999, Reservoir Polymer Gel Treatments To Improve Miscible CO2 Flood: SPE Reservoir Evaluation & Engineering, v. 2, no. 02, p. 196–204, doi:10.2118/56008-PA.

Hill, H.J., and Milburn, J.D., 1956. Effect of clay and water salinity on electrochemical behaviour of reservoir rocks. Trans. AIME, 207: 65-72.

Honarpour, M. M., N. R. Nagarajan, A. Grijalba Cuenca, M. Valle, and K. Adesoye, 2010, Rock-Fluid Characterization for Miscible CO2 Injection: Residual Oil Zone, Seminole Field, Permian Basin, in SPE Annual Technical Conference and Exhibition: Society of Petroleum Engineers, doi:10.2118/133089-MS.

Hoover, B., S. Yaw, and R. Middleton, CostMAP: an open-source software package for developing cost surfaces using a multi-scale search kernel. International Journal of Geographical Information Science, 2020. 34(3): p. 520-538.

Hovorka, S. D., 2013, CCU&S via Stacked Storage— Case Studies from CO_2-EOR Basins of the United States: Energy Procedia, v. 37, p. 5166–5171, doi:10.1016/J.EGYPRO.2013.06.432.

Howard, R. H., 1990. Hydrocarbon Reservoir Distribution in the Illinois Basin: Chapter 21: Part I. Illinois Basin: Oil and Gas Systems. AAPG Memoir 51, pp. 299-327.

Howell, K. J., 2017, Sedimentology of multistorey fluvial sandstones of the Mississippian Cypress Formation, Illinois Basin, USA: University of Illinois, M.S. Thesis, 138 p.

Hoy, J. L., 2014, The Mississippian Play in the Illinois Basin, in PTTC Mississippian Lime Workshop: p. 39.

Hubbert, M. K., 1954, ENTRAPMENT OF PETROLEUM UNDER HYDRODYNAMIC CONDITIONS ENTRAPMENT v. 37, no. 8, p. 1954–2026.

Huff, B. G., 1993, Analysis of the Aux Vases (Mississippian) Petroleum Reservoirs of Energy Field, Williamson County, Illinois: Illinois State Geological Survey, Illinois Petroleum, 40 p.

Huff, B.G., and B, Seyler, 2010, Oil and gas geology, p. 283-298, in D.R. Kolata and C.K. Nimz (eds.), Geology of Illinois. University of Illinois at Urbana-Champaign.

Hunt, J.M., 1995. Petroleum geochemistry and geology (textbook). Petroleum Geochemistry and Geology (Textbook).(2 nd Ed.), WH Freeman Company.

Hwang, R. J., A. S. Ahmed, and J. M. Moldowan, 1994, Oil composition variation and reservoir continuity: Unity Field, Sudan: Org. Geochem., v. 21, p. 171-188.

Hwang R. J. and Baskin D. K., 1994, Reservoir connectivity and oil homogeneity in a large-scale reservoir. Middle East Petroleum Geoscience Geo94 2, 529-541.

Jafri, M. K., A. Lashin, E. Ibrahim, and M. Naeem, 2016, Petrophysical Evaluation of the Tensleep Sandstone Formation Using Well Logs and Limited Core Data at Teapot Dome, Powder River Basin, Wyoming, USA: Arabian Journal for Science and Engineering, v. 41, no. 1, p. 223–247, doi:10.1007/s13369-015-1741-7.

Jia, C., C. Zou, J. Li, D. Li, and M. Zheng, 2016, Evaluation criteria, major types, characteristics and resource prospects of tight oil in China: Petroleum Research, v. 1, no. 1, p. 1–9, doi:10.1016/S2096-2495(17)30026-1.

Jenden, P. D, D. R Hilton, I. R. Kaplan and H. Craig, 1992, Abiogenic hydrocarbon and mantle helium in oil and gas fields: US Geological Survey Professional Paper 1570, p. 31-56.

Jobe, H., and A. Saller, 1995, Oil reservoirs in grainstone aprons around bryozoan mounds, upper Harrodsburg limestone, Mississippian, Illinois Basin: American Association of Petroleum Geologists Bulletin, v. 79, no. 6, p. 783–800, doi:10.1306/8d2b1ba6-171e-11d7-8645000102c1865d.

Johnson, H. D., S. Levell, and A. H. Mohamad, 1987, Depositional Controls of Reservoir Thickness and Quality Distribution in Upper Miocene Shallow Marine Sandstones (Stage IVD) of the Erb West Field, Offshore Sabah, NW Borneo.

Johnson, R. C., 1985, Early Cenozoic History of the Uinta and Piceance Creek Basins, Utah and Colorado, with Special Reference to the Development of Eocene Lake Uinta: p. 247–276.

Johnston, J.W.: A Review of the Willard (San Andres) Unit CO_2 Injection Project, paper SPE 6388 presented at the 1971 SPE Permian Basin Oil and Gas Recovery Conference, Midland, TX, March 10 – 11.

Jones, N., 2016, Evaluation of ROZ in the Tensleep Formation, Northeastern Bighorn Basin, Wyoming. Enhanced Oil Recovery Institute, University of Wyoming.

Kaldi, J. G., 2011, Evaluating Reservoir Quality, Seal Potential and Net Pay, in CO2/CRC Professional Continuing Education Short Course.

Kane, A.V.: Performance Review of a Large Scale CO_2-WAG Project SACROC Unit — Kelly Snyder Field, J. Pet. Tech. (February 1979) 217–31.

Kaufman, R. L., A. S. Ahmed, and R. J. Elsinger, 1990, Gas Chromatography as a development and production tool for fingerprinting oils from individual reservoirs: applications in the Gulf of Mexico, in D. Schumaker, and B. F. Perkins, eds., Proceedings of the 9th Annual Research Conference of the Society of Economic Paleontologists and Mineralogists, October 1, 1990: New Orleans, p. 263-282.

Kaufman, R. L., H. Dashti, C. S. Kabir, J. M. Pederson, M. S. Moon, R. Quttainah, and H. Al-Wael, 1997, Characterizing the greater Burgan Field: Use of geochemistry and oil fingerprinting: SPE Paper No. 37803, p. 385-394.

Keith, B. D., and T. A. Thompson, 2018, Salem Limestone (Valmeyeran, Mississippian)—A high-energy carbonate shoal model: GSA Field Guides, v. 51, p. 339–358, doi:10.1130/2018.0051(13).

Keller, S. J., and L. E. Becker, 1980, Subsurface stratigraphy and oil fields in the Salem Limestone and associated rocks in Indiana: 63 p.

Kepferle, R. C., 1977, Stratigraphy, Petrology, and Depositional Environment of the Kenwood Siltstone Member, Borden Formation (Mississippian), Kentucky and Indiana: Washington D.C., 0–49 p.

Kleinstelber, S. W., 1990, Wertz Tensleep CO2 flood. Design and initial performance: JPT, Journal of Petroleum Technology, v. 42, no. 5.

Kolata, D. R., 2005. Bedrock geology of Illinois. Illinois State Geological Survey, Illinois Map 14, 2 sheets, scale 1: 500,000.

Kolata, D.R., and W.J. Nelson, 1990, Tectonic history of the Illinois Basin. In M.W. Leighton, D.R. Kolata, D.F. Olts, and J.J. Eidel, eds., Interior cratonic basins: American Association of Petroleum Geologists (AAPG), Memoir 51, p. 263-85.

Kolata, D. R. and Nelson, W. J., 2010. Tectonic history. In: Kolata and C. K. Nimz (eds.) Geology of Illinois. Illinois State Geological Survey, p. 77-89.

Kolodzie, S., 1980, Analysis of pore throat size and use of the waxman-smits equation to determine OOIP in spindle field, Colorado, in Proceedings - SPE Annual Technical Conference and Exhibition: Society of Petroleum Engineers, doi:10.2118/9382-ms.

Koperna, G. J., and V. A. Kuuskraa, 2006a, TECHNICAL OIL RECOVERY POTENTIAL FROM RESIDUAL OIL ZONES: BIG HORN BASIN: 121–124 p.

Koperna, G. J., and V. A. Kuuskraa, 2006b, TECHNICAL OIL RECOVERY POTENTIAL FROM RESIDUAL OIL ZONES: WILLISTON BASIN: v. 1, no. February, p. 121–124.

Kreisa, R. D., and R. K. Bambach, 1973, Environments of deposition of the Price Formation (Lower Mississippian) in its type area, southwestern Virginia: American Journal of Science, v. 273- A, p. 326–342.

Larter, S. and R. di Primio, 2005, Effects of biodegradation on oil and gas field PVT properties and the origin of oil rimmed gas accumulations: Organic Geochemistry, 36, p. 299-3310.

Lasemi, Z. and J. P. Grube, 1995, Mississippian “Warsaw” play makes waves in Illinois basin: Oil and Gas Journal, v. 93, no. 2, p. 47–51.

Lasemi, Z., R. D. Norby, and J. D. Treworgy, 1998, Depositional facies and sequence stratigraphy of a Lower Carboniferous bryozoan-crinoidal carbonate ramp in the Illinois Basin, mid-continent USA: Geological Society, London, Special Publications, v. 149, no. 1, p. 369–395, doi:10.1144/GSL.SP.1999.149.01.17.

Lasemi, Z., J. D. Treworgy, R. D. Norby, J. P. Grube, and B. G. Huff, 1994, Waulsortian Mounds and Reservoir Potential of the Ullin Limestone ("Warsaw") in Southern and Adjacent Areas in Kentucky: Illinois State Geological Survey, 65 p.

Lee, L. K., 1939, Geology of Basin Fields in Southeastern Illinois: AAPG Bulletin, v. 23, no. 10, p. 1493–1506.

Leetaru, H. E., 1990, Application of old electric logs in the analysis of Aux Vases Sandstone (Mississippian) reservoirs in Illinois: Urbana, IL, Illinois State Geological Survey, 21 p.

Leetaru, H. E., 1991, Reservoir heterogeneity and improved oil recovery of the Aux Vases (Mississippian) Formation at King Field, Jefferson County, Illinois: Urbana, IL, Illinois State Geological Survey, 49 p.

Leetaru, H. E., 1993, Improved oil recovery from the Aux Vases (Mississippian) Formation at Boyd Field, Jefferson County, Illinois: Urbana, IL, Illinois State Geological Survey, 30 p.

Leetaru, H. E., 1996, Reservoir Characteristics and Oil production in the Cypress and Aux Vases Formations at Storms Consolidated Field in White County, Illinois: Illinois State Geological Survey, 47 p.

Leetaru, H. E., 2000, Sequence Stratigraphy of the Aux Vases Sandstone: A Major Oil Producer in the Illinois Basin. AAPG Bulletin, v. 84, no. 3, p. 399–422.

Leetaru, H. E., K. Mize, and J. S. Cokinos, 2005, The Benoist (Yankeetown) Sandstone Play in the Illinois Basin: Illinois State Geological Survey, 46 p.

Leighton, M.W. 2010. History of Investigations on Illinois Geology, p. 3-58. In D.R. Kolata and C.K. Nimz (eds.), Geology of Illinois. University of Illinois at Urbana-Champaign.

Levine, J S, Goldberg, D S, Lackner, K S, Matter, J M, Supp, M G, Ramakrishnan, T S. Relative Permeability Experiments of Carbon Dioxide Displacing Brine and Their Implications for Carbon Sequestration. Environ. Sci. Technol. 2014, 48, 1, 811–818

Lewan, M. D., 1995, Feasibility study of material-balance assessment of petroleum from the New Albany Shale in the Illinois Basin: US Geological Survey Bulletin, v. 2137.

Lewan, M. D., M. E. Henry, D. K. Higley, and J. K. Pitman, 2002, Material-balance assessment of the New Albany-Chesterian petroleum system of the Illinois basin: AAPG Bulletin, v. 86, no. 5, p. 745–777, doi:10.1306/61EEDB8E-173E-11D7-8645000102C1865D.

Li, Z., M. Dong, S. Li, and S. Huang, 2006, CO2 sequestration in depleted oil and gas reservoirs—caprock characterization and storage capacity: Energy Conversion and Management, v. 47, no. 11–12, p. 1372–1382, doi:10.1016/J.ENCONMAN.2005.08.023.

Lillis, P. G., A. Warden, and J. D. King, 2003, Petroleum Systems of the Uinta and Piceance Basins — Geochemical Characteristics of Oil Types: Petroleum Systems and Geologic Assessment of Oil and Gas in the Uinta-Piceance Province, Utah and Colorado, no. April 2014.

Lineback, J. A., 1966, Deep-Water Sediments Adjacent to the Borden Siltstone (Mississippian) Delta in Southern Illinois: Illinois State Geological Survey, 48 p.

Lineback, J. A., 1968, Turbidites and Other Sandstone Bodies in the Borden Siltstone (Mississippian) in Illinois: Illinois State Geological Survey, 29 p.

Lineback, J. A., 1972, Lateral Gradation of the Salem and St. Louis Limestones (Middle Mississippian) in Illinois.

Lineback, J. A., and R. M. Cluff, 1985, Ullin-Fort Payne, a Mississippian shallow to deep water carbonate transition in a cratonic basin: p. 26.

Lis, G. P., A. Schimmelmann and M. Mastalerz, 2006, D/H ratios and hydrogen exchangeability of type II kerogens with increasing thermal maturity: Organic Geochemistry, No.37, p. 342-353.

Liu, H., Y. Luo, Y. Meng, G. Xiao, Y. Zhao, S. Zhou, and L. Shao, 2021, Effects of pore structure on the moveable oil saturation in water-driven tight oil sandstone reservoirs: Journal of Petroleum Science and Engineering, v. 207, p. 109142, doi:10.1016/J.PETROL.2021.109142.

Magoon, L. B., 1995, The play that complements the petroleum system – A new exploration equation: Oil and Gas Journal, v. 93, no. 40.

Marshak, S., and T. Paulsen, 1996, Midcontinent U.S. fault and fold zones: A legacy of Proterozoic intracratonic extensional tectonism? Geology, v. 24, no. 2, p. 151, doi:10.1130/0091-7613(1996)024<0151:MUSFAF>2.3.CO;2.

Martin, D.L., 1975, A paleomagnetic polarity transition in the Devonian Columbus Limestone of Ohio: A possible stratigraphic tool: Tectonophysics 28, p. 125–134.

Mast, R. F., 1970, Size, Development, and Properties of Illinois Oil Fields: Urbana, IL, 42 p.

Masterson, W. D., A. G. Holba, and L. I. P. Dzou, 1997, filling history of America's two largest oil fields: Prudhoe Bay and Kuparuk, North Slope, Alaska: Presented at Annual Meeting AAPG, Dallas, Texas, April 6-9, 1997.

Matthai S.K. and Belayneh, M., 2004, Fluid flow partitioning between fractures and a permeable rock matrix, Geophysical Research Letters, VOL. 31, L07602, doi:10.1029/2003GL019027

May, M. T., 2013, Oil-saturated Mississippian–Pennsylvanian Sandstones of South-central Kentucky, in F. J. Hein, D. Leckie, S. Larter, and J. R. Suter, eds., Heavy-oil and oil-sand petroleum systems in Alberta and beyond: p. 373–406, doi:10.1306/13371586St643557.

McCain, W. D., 1991, "Reservoir-Fluid Property Correlations—State of the Art." SPE Res Eng 6: 266–272. doi: https://doi.org/10.2118/18571-PA

McMahon, S., A. van Smeerdijk Hood, and D. McIlroy, 2017, The origin and occurrence of subaqueous sedimentary cracks: Geological Society Special Publication, v. 448, no. 1, p. 285–309,

doi:10.1144/SP448.15/ASSET/84882060-BDBE-4917-9774-9B4B5A7454D1/ASSETS/GRAPHIC/SP448-1839F09.JPEG.

Meents, W.F., and D.H. Swann, 1965, Grand Tower Limestone (Devonian) of southern Illinois: Illinois State Geological Survey, Circular 389, 36 p.

Melzer, S., 2006. Stranded oil in the residual oil zone. A report prepared for Advanced Resources International and U.S. Department of Energy Office of Fossil Energy - Office of Oil and Natural Gas. 91 p.

Middleton, R.S., et al., SimCCS: An open-source tool for optimizing CO2 capture, transport, and storage infrastructure. Environmental Modelling & Software, 2020. **124**: p. 104560.

Mikulic, D.G., 1990, Tippecanoe II Subsequence: Silurian System through Lower Devonian Series, *in* Interior cratonic basins: AAPG Memoir 51, p. 101–107.

Milkov, A. V., 2021, New approaches to distinguish shale-sourced and coal-sourced gases in petroleum systems: Organic Geochemistry, No. 158, p.1-14.

Milkov, A. V. and G Etiope, 2018, Revised genetic diagrams for natural gases based on a global dataset of > 20,000 samples: Organic Geochemistry, 25, p. 109-120.

Morgan, J. T., and D. T. Gordon, 1970, Influence of Pore Geometry on Water-Oil Relative Permeability: Journal of Petroleum Technology, v. 22, no. 10, p. 1199–1208, doi:10.2118/2588-PA.

Morse, D. G., 2001, Sedimentology, Diagenesis and Trapping Style, Mississippian Tar Springs Sandstone, Inman East Consolidated Field, Gallatin County, Illinois: Urbana, IL, Illinois State Geological Survey, Illinois Petroleum 157, 67 p.

Moulton, G. F., 1926, Areas for further prospecting near the Martinsville pool, Clark County: Illinois State Geological Survey, 12 p.

Muggeridge, A., Cockin, A., Webb, K., Frampton, H., Collins, I., Moulds, T., and Salino, P., 2014. Recovery rates, enhanced oil recovery and technological limits. Phil. Trans. R. Soc. A 372: 20120320.

Murphy, J. B., J. D. Keppie, J. Dostal, and A. J. Hynes, 1990, The geochemistry and petrology of the Late Precambrian Georgeville Group: A volcanic arc-rift succession in the Avalon terrane of Nova Scotia: Geological Society Special Publication, v. 51, p. 383–393, doi:10.1144/GSL.SP.1990.051.01.25.

Nelson, W. J., 1995, Structural features in Illinois: Illinois State Geological Survey Bulletin 100, 144 p.

Nelson, W. J., 2022, Informal Stratigraphic Names Used in the Petroleum Industry: Urbana, IL.

Nelson, W. J., L. B. Smith, J. D. Treworgy, L. C. Furer, and B. D. Keith, 2002, Sequence Stratigraphy of the Lower Chesterian (Mississippian) Strata of the Illinois Basin: Illinois State Geological Survey, Bulletin 107, 70 p.

NETL, 2012, The United States 2012 Carbon Utilization and Storage Atlas IV: 128 p.

Newman, G. H., Pore volume compressibility of consolidated, friable, and unconsolidated reservoir rocks under hydrostatic loading, SPE J. Petrol. Tech., 25 (1973), 129–134.

Newman, G.H., Chevron Oil Field Research Co., 1973. Pore-Volume Compressibility of Consolidates, Friable, and Unconsolidated Reservoir Rocks under Hydrostatic Loading. SPE 3835. Presented at SPE Rocky Mountain Regional Meeting, held in Denver, Colorado, 10-12 April 1972 Carbon Capture Provisions in the Inflation reduction Act of 2022, Clean Air Task Force. https://cdn.catf.us/wp-content/uploads/2022/08/19102026/carbon-capture-provisions-ira.pdf.

North, W.G., 1969, The Middle Devonian strata of southern Illinois: Illinois State Geological Survey, Circular 441, 49 p.

Núñez-López, V., and E. Moskal, 2019, Potential of CO2-EOR for Near-Term Decarbonization: Frontiers in Climate, v. 1, p. 5, doi:10.3389/FCLIM.2019.00005/BIBTEX.

Okwen, R.T., Frailey, S.M., Webb, N.D., and Grigsby, N.P., 2023. Assessing CO_2-Enhanced Oil Recovery and Storage: Part II – Development Strategies for Cypress Sandstone Residual Oil Zones. Illinois State Geological Survey (ISGS) Circular, In Press.

Okwen, R. T., S. M. Frailey, N.D. Webb, and N. P. Grigsby, 2023, Assessing CO2-Enhanced Oil Recovery and Storage: Part III – Development Strategies for Cypress Sandstone Residual Oil Zones, Illinois State Geological Survey Circular, 29 p.

Osmond, J. C., 1986, Petroleum Geology of the Uinta Mountains-White River Uplift, Colorado and Utah, *in* D.S. Stone, ed., New Interpretations of northwest Colorado geology: Rocky Mountain Association of Geologists, p. 213-222.

Peakall, J., J. Best, J. H. Baas, D. M. Hodgson, M. A. Clare, P. J. Talling, R. M. Dorrell, and D. R. Lee, 2020, An integrated process-based model of flutes and tool marks in deep-water environments: Implications for palaeohydraulics, the Bouma sequence and hybrid event beds: Sedimentology, v. 67, no. 4, p. 1601–1666, doi:10.1111/SED.12727.

Pelletier, B. R., 1958, Pocono paleocurrents in Pennsylvania and Maryland: Geological Society of America Bulletin, v. 69, no. 8, p. 1033–1064.

Pepper, A. S., 2016, Petroleum System Analysis: What Have We Learned Since Magoon and Dow's Memoir 60?, in AAPG Annual Convention and Exhibition, Calgary, Alberta, Canada: doi:10.3/JQUERY-UI.MIN.JS.

Peters, K. E., D. J. Curry, and M. Kacewicz, 2012, An overview of basin and petroleum system modeling: Definitions and concepts, in K. E. Peters, D. J. Curry, and M. Kacewicz, eds., Basin Modeling: New Horizons in Research and Applications: AAPG Hedberg Series, no. 4, p. 1–16.

Pierce, C. S., P. D. W. Haughton, P. M. Shannon, A. J. Pulham, S. P. Barker, and O. J. Martinsen, 2018, Variable character and diverse origin of hybrid event beds in a sandy submarine fan system, Pennsylvanian Ross Sandstone Formation, western Ireland: Sedimentology, v. 65, no. 3, p. 952–992, doi:10.1111/SED.12412.

Pitman, J. K., M. Henry, and B. Seyler, 1998, Reservoir Quality and Diagenetic Evolution of Upper Mississippian Rocks in the Illinois Basin: Influence of a Regional Hydrothermal Fluid-Flow Event During Late Diagenesis: US Geological Survey Professional Paper.

Porter, C.R. and Carothers, J.E., 1970. Formation factor-porosity relation derived from well log data. Trans. SPWLA 11th Ann. Logging Symp., pp. A 1-19.

Reading, H. G., and M. Richards, 1994, Turbidite systems in deep-water basin margins classified by grain size and feeder system: AAPG Bulletin, v. 78, no. 5, p. 792–822.

Rees, O. W., P. W. Henline, and A. H. Bell, 1943, Chemical characteristics of Illinois crude oils with a discussion of their geologic occurrence: Urbana: Illinois State Geological Survey.

Rice, R. J., R. D. Cole, and S. T. Whitaker, 1993, Reservoir characterization and potential for improved oil recovery within the Aux Vases Formation at Stewardson Field, Shelby County, Illinois: Urbana, IL, Illinois State Geological Survey, 36 p.

Rowe, H.G., York, S.D., and Ader, J.C.: Slaughter Estate Unit Tertiary Pilot Performance. J. Pet. Tech. (March 1982) 613–20.

Salvatore et al. 1995, Petrofacies and provenance of the Puente Formation (middle to upper Miocene), Los Angeles Basin, southern California: Implications for rapid uplift and accumulation rate. Journal of Sedientary Research A65, No. 4, p. 65-667.

Sanguinitoa, S. et al., 2020. Methodology for estimating the prospective CO2 storage resource of residual oil zones at the national and regional scale. International Journal of Greenhouse Gas Control 96, p. 1-8.

Sarmadivaleh, A., Al-Yaseri, Z, and Iglauer, S., 2015. Influence of Temperature and Pressure on quartz=water-CO2 contact angle and CO2=water interfacial tension. Journal of Colloid and Interface Science, 441, 59-64.

Savage, T.E., 1920, The Devonian Formations of Illinois: American Journal of Science 291, pp. 169-182.

Schoell, M., 1983, Genetic characterization of natural gases: AAPG Bulletin, v. 67, p. 2225-2238.

Schoell, M., 1988, Multiple origins of methane in the earth: Chemical Geology, v. 71, p. 1-10.

Schoell, M., and M. A. Beeunas, 1996, Episodic Migration of Natural Gas: A Worldwide Phenomenon of Dynamic Filling of Oil and Gas Fields: AAPG International Conference and Exhibition, Nice, France, Vol. 5, p. A126, Abstract.

Schowalter, T.T., 1979. Mechanics of secondary hydrocarbon migration and entrapment. AAPG Bulletin, 63, pp. 723-760.

Scotese, C. R., 2021, An Atlas of Phanerozoic Paleogeographic Maps: The Seas Come In and the Seas Go Out: Annual Review of Earth and Planetary Sciences, v. 49, no. 1, doi:10.1146/annurev-earth-081320-064052.

Scotese, C. R., and W. S. McKerrow, 1990, Revised World maps and introduction: Geological Society, London, Memoirs, v. 12, no. 1, p. 1–21, doi:10.1144/GSL.MEM.1990.012.01.01.

Seyler, B., 1998, Geologic and engineering controls on Aux Vases Sandstone reservoirs in Zeigler Field, Illinois: Urbana, IL, Illinois State Geological Survey, 79 p.

Seyler, B., and R. M. Cluff, 1991, Petroleum traps in the Illinois Basin. In: Leighton, M.W., Kolata, D.R., Oltz, D.F., Eidel, J.J. (eds.), Interior Cratonic Basins. AAPG Memoir 51, p. 36-401.

Seyler, B., J.P. Grube, and Z. Lasemi, 2003, The origin of prolific reservoirs in the Geneva Dolomite (Middle Devonian), west-central Illinois Basin: Illinois State Geological Survey, Illinois Petroleum 158, p. 36.

Seyler, B., J. P. Grube, and D. G. Morse, 2000, The Cypress Sandstone in Illinois, in Petroleum Technology Transfer Council Workshop.

Sheng, J., 2015, Enhanced oil recovery in shale reservoirs by gas injection, J. Nat.Gas Sci. Eng. 22, 252-259 (invited review).

Sheng, J, 2017, Optimization of huff-n-puff gas injection in shale oil reservoirs, Petroleum, Volume 3, Issue 4, Pages 431-437, ISSN 2405-6561, https://doi.org/10.1016/j.petlm.2017.03.004.

Sheng, J., K. Chen, 2014, Evaluation of the EOR potential of gas and water injection in shale oil reservoirs, J. Unconv. Oil Gas Resour. 5, 1-9.

Sloss, L.L., 1963, Sequences in the cratonic interior of North America: GSA Bulletin 74, p. 93–114.

Sminchak, J.R., S. Mawalkar, and N. Gupta, 2020, Large CO_2 Storage Volumes Result in Net Negative Emissions for Greenhouse Gas Life Cycle Analysis Based on Records from 22 Years of CO2-Enhanced Oil Recovery Operations, Energy & Fuels, v. 34, no. 3, p. 3566-3577: DOI:10.1021/acs.energyfuels.9b04540.

Smunt, F.M., 1964, The stratigraphy and petrography of the Dutch Creek Sandstone, Union and Alexander Counties, Illinois. Southern Illinois University, unpublished Master's thesis, 58 p.

Southern, S. J., I. A. Kane, M. J. Warchoł, K. W. Porten, and W. D. McCaffrey, 2017, Hybrid event beds dominated by transitional-flow facies: character, distribution and significance in the Maastrichtian Springar Formation, north-west Vøring Basin, Norwegian Sea: Sedimentology, v. 64, no. 3, p. 747–776, doi:10.1111/SED.12323.

SPE, 2017, CO_2 Storage Resources Management System.

Spencer, C. W., and R. J. Wilson, 1988, Petroleum geology and principal exploration plays in the Uinta-Piceance-Eagle Basins Province, Utah and Colorado: 35 p.

Spirakis, C.S., 1974, The sub-Kaskaskia unconformity of the Illinois Basin: Evanston, Illinois, Northwestern University, Ph.D. thesis, 100 p.

Squires, F., 1946, Flood Tide in Illinois: The Producers Monthly.

Stevenson, D. L., 1964, Carper Sand Oil Production in St. James, Wilberton, and St. Paul Pools, Fayette County, Illinois: Illinois State Geological Survey, 12 p.

Stevenson, D. L., 1969, Oil production from the Ste. Genevieve limestone in the Exchange area, Marion County, Illinois.

Stevenson, D. L., 1978, Salem Limestone oil and gas production in the Keenville Field, Wayne County, Illinois: 16 p.

Stonecipher, S. A., 2000, Applied Sandstone Diagenesis-Practical Petrographic Solutions for a Variety of Common Exploration, Development, and Production Problems: Applied Sandstone Diagenesis-Practical Petrographic Solutions for a Variety of Common Exploration, Development, and Production Problems, doi:10.2110/SCN.00.02.

Stow, D. A. V., and M. Johansson, 2000, Deep-water massive sands: nature, origin and hydrocarbon implications: Marine and Petroleum Geology, v. 17, no. 2, p. 145–174, doi:10.1016/S0264-8172(99)00051-3.

Stow, D. A. V., and D. J. W. Piper, 1984, Deep-water fine-grained sediments: Facies models: Geological Society Special Publication, v. 15, p. 611–646, doi:10.1144/GSL.SP.1984.015.01.38.

Stow, D. A. V., and G. Shanmugam, 1980, Sequence of structures in fine-grained turbidites: Comparison of recent deep-sea and ancient flysch sediments: Sedimentary Geology, v. 25, no. 1–2, p. 23–42, doi:10.1016/0037-0738(80)90052-4.

Summers, B.R., 2006, Petrophysical investigation of porosity distribution in the Geneva Dolomite Member of the Grand Tower Formation in Marion County, Illinois. Northern Illinois University, unpublished Ph.D. dissertation, 164 p.

Swann, D.H., 1963, Classification of Genevievian and Chesterian (Late Mississippian) rocks in Illinois: Illinois State Geologic Survey, Report of Investigations 216, 91 p.

Swann, D.H., 1964, Late Mississippian rhythmic sedimentation of the Mississippi Valley: American Association of Petroleum Geologists Bulletin, v. 79, p. 24 71-2483.

Swann, D. H., and A. H. Bell, 1958, Habitat of Oil in the Illinois Basin, in Habitat of Oil: American Association of Petroleum Geologists, p. 447–472.

Swann, D. H., J. A. Lineback, and E. Frund, 1965, The Borden Siltstone (Mississippian) Delta in Southwestern Illinois: Illinois State Geological Survey, 20 p.

Talling, P. J., 2013, Hybrid submarine flows comprising turbidity current and cohesive debris flow: Deposits, theoretical and experimental analyses, and generalized models: Geosphere, v. 9, no. 3, p. 460–488, doi:10.1130/GES00793.1.

Team, U. U.-P. A., 2003, The Uinta-Piceance Province—Introduction to a geologic assessment of undiscovered oil and gas resources: 25 p.

Thompson T. A., K. H. Sowder, and M. R. Johnson, 2016. Generalized stratigraphic column of Indiana bedrock. Indiana Geological Survey, Bloomington, Indiana.

Timur, A., Hemkins, W.B. and Worthington, A.E., 1972. Porosity and pressure dependence of formation resistivity factor for sandstones. Trans. CWLS 4th Formation Evaluation Symp., 30 pp.

Tissot, B. P., and D. H. Welte, 1984, Petroleum Formation and Occurrence: Petroleum Formation and Occurrence, doi:10.1007/978-3-642-87813-8.

Tissue, J.S., 1974, A Paleoenvironmental Analysis of the Middle Devonian Sandstones in the Upper Mississippi Valley. Unpublished M.S. thesis, University of Illinois at Urbana-Champaign, 83 p.

Trentham, R., and L. S. Melzer, 2016, A Cookbook Approach to Exploring for, and Evaluating, Residual Oil Zones in the San Andres Formation of the Permian Basin, in Southwest Section AAPG Annual Convention: doi:10.2118/167209-MS.Hill.

Treworgy, J. D., 1991, Kaskaskia Sequence - Mississippian Valmeyeran and Chesterian Series, in M. W. Leighton, D. R. Kolata, D. F. Oltz, and J. J. Eidel, eds., Interior Cratonic Basins: American Association of Petroleum Geologists, p. 125–142.

Treworgy, J. D., and J. A. Devera, 1991, Kaskaskia Sequence Overview - Middle Devonian Series through Chesterian Series, in M. W. Leighton, D. R. Kolata, D. F. Oltz, and J. J. Eidel, eds., Interior Cratonic Basins: American Association of Petroleum Geologists, p. 109–112.

Udegbunam, E. O., D. S. Beaty, and J. P. J. Fagan, 1993, Strategies for improved oil recovery from Aux Vases Reservoirs in McCreery and McCullum waterflood units, Dale Consolidated Field, Franklin County, Illinois: Urbana, IL, Illinois State Geological Survey, 39 p.

US-DOE, 2007, Carbon Sequestration Atlas of United States and Canada, 1st ed., 86 p.

U.S. Geological Survey Williston Basin Province Assessment Team, 2013, Executive summary—Assessment of undiscovered oil and gas resources of the Williston Basin Province of North Dakota, Montana, and South Dakota, 2010, chap. 1 *of* U.S. Geological Survey Williston Basin Province Assessment Team, Assessment of undiscovered oil and gas resources of the Williston Basin Province of North Dakota, Montana, and South Dakota, 2010 (ver. 1.1,November 2013): U.S. Geological Survey Digital Data Series 69–W, 4 p.

Verma, M. K., 2015, Fundamentals of Carbon Dioxide-Enhanced Oil Recovery (CO2-EOR)—A Supporting Document of the Assessment Methodology for Hydrocarbon Recovery Using CO2-EOR Associated with Carbon Sequestration: 19 p.

Wallenberg, A., D.H. Malone, J. Day, and J. Devera, 2016, Detrital zircon geochronology of the Devonian Dutch Creek Sandstone in the southern Illinois Basin. Geological Society of America *Abstracts with Programs* 48(7), doi: 10.1130/abs/2016AM-284406.

Wan, T., J.J. Sheng, M.Y. Soliman, 2013, Evaluation of the EOR potential in shale oil reservoirs by cyclic gas injection, in: Paper SPWLA-D-12-00119 Presented at the SPWLA 54th Annual Logging Symposium Held in New Orleans, Louisiana, 22-26.

Wang, Q, Shen, J, Lorinczi, P, Glover, P, Yang, S, and Chen, H. Oil production performance and reservoir damage distribution of miscible CO_2 soaking-alternating-gas (CO_2-SAG) flooding in low permeability heterogeneous sandstone reservoirs. Journal of Petroleum Science and Engineering, Volume 204, 2021, 108741, ISSN 0920-4105, https://doi.org/10.1016/j.petrol.2021.108741.

Wasson, T., 1938, Recent Oil Discoveries in Southeastern Illinois: AAPG Bulletin, v. 22, no. 1, p. 71–78.

Waxman, M. H., and L. J. M. Smits, 1968, Electrical Conductivities in Oil-Bearing Shaly Sands: Society of Petroleum Engineers Journal, v. 8, no. 02, p. 107–122, doi:10.2118/1863-A.

Webb, N.D., Z. Askari, N. Grigsby, D. Garner, H. Leetaru, and C. Carman, 2019a, Stacked Greenfield and Brownfield ROZ Fairways in the Illinois Basin Geo-Laboratory: Co-Optimization of EOR and Associated CO_2 Storage: Urbana, IL, 34 p.

Webb, N. D., S. M. Frailey, and H. E. Leetaru, 2019, A Nonconventional CO2-EOR Target in the Illinois Basin: Oil Reservoirs of the Thick Cypress Sandstone: Urbana, IL, 314 p.

Webb, N. D., and N. P. Grigsby, 2020, Assessing the Cypress Sandstone for Carbon Dioxide-Enhanced Oil Recovery and Carbon Storage: Part I—Reservoir Characterization of Noble Oil Field, Western Richland County, Illinois: Champaign, Ill.: Illinois State Geological Survey, Prairie Research Institute.

Webb, Nathan D., and Grigsby, N.P., 2023, Geologic Characterization of Stacked Reservoirs in the Noble Oil Field, Richland County, IL. Illinois State Geological Survey (ISGS) Circular, In Press.

Webb, N. D., N. P. Grigsby, J. D. Brown, and M. Yu, 2023, Reservoir Characterization of the Carper Sandstone Member of the Borden Siltstone: Urbana, IL.

Webb, N., N. Grigsby, S. Frailey, 2019, CO2 Storage and EOR Resource Assessment of the Cypress Sandstone Residual Oil Zone Play in the Illinois Basin, AAPG Search and Discovery Article #11263.

Wehner et al., 1998. CO2 Huff-n-Puff Process in a Light Oil Shallow Shelf Carbonate Reservoir. No. DE-FC22-94BC14986—18.

West, L. M., 2014, A Regional Assessment of Residual Oil Zones in the Permian Basin and Their Potential for Carbon Dioxide Capture Usage and Storage: Energy Procedia, v. 63, p. 7884–7890, doi:10.1016/J.EGYPRO.2014.11.824.

Whiticar, M. J., 1994, Correlation of natural gases with their sources: in L. B. Magoon, and W. G. Dow, eds., The Petroleum System, From Source to Trap, AAPG, p. 261- 283.

Whiticar, M. J., E. Faber, and M. Schoell. 1986. Biogenic methane formation in marine and freshwater environments: CO2 reduction vs. acetate formation-Isotope evidence. Geochim. Cosmochim. Acta. v. 50, pp. 693-709.

Whiting, L.L., and D.L. Stevenson, 1965, The Sangamon Arch: Illinois State Geological Survey, Circular 383, 25 p.

Widmyer, R.H., D.B. Williams and J.W. Ware, 1988, Performance evaluation of the Salem Unit Surfactant/ Polymer Pilot: Journal of Petroleum Technology, no. 11, p. 1217.

Willman, H. B., E. Atherton, T. C. Buschbach, C. Collinson, J. C. Frye, M. E. Hopkins, J. A. Lineback, and J. A. Simon, 1975, Handbook of Illinois Stratigraphy: Urbana, IL, Illinois State Geological Survey, Bulletin, 261 p.

Witherspoon, P. A., 1952, Some Important Aspects of Water Flooding in Illinois: Urbana, IL, Illinois State Geological Survey, 7 p.

Witherspoon, P. A., and E. G. Jackson, 1955, Summary of Water Flood Operations in Illinois Oil Pools During 1954: Urbana, IL, Illinois State Geological Survey, 63 p.

Worden, R. H., and Sadon Morad, 2003, Clay Mineral Cements in Sandstones, in R. H. Worden, and Sadoon Morad, eds., Clay Mineral Cements in sandstones: Oxford, UK, Blackwell Publishing Ltd., p. 3–41, doi:10.1002/9781444304336.

Worthington, P.F., 1993. The uses and abuses of the Archie equations, 1: The formation factor-porosity relationship. J. Appl. Geophys., 30: 215-228.

Xu, H, Jiang, H, Wang, J, Zhao, Q, Lei, Y, and Fan, L. Effect of CO_2 soaking time on replacement efficiency and reservoir properties of tight oil and gas reservoirs. Journal of Natural Gas Science and Engineering, Volume 97, 2022, 10435, ISSN 1875-5100, https://doi.org/10.1016/j.jngse.2021.104357.

Yang, C., and H. Qing, 2016, Possible occurrences of transition zones and residual oil zones below oil-water contacts in mature oil fields, southeast Saskatchewan: Interpretation, v. 4, no. 4, p. T591–T612, doi:10.1190/INT-2016-0008.1.

Yang, H., S. Li, and X. Liu, 2016, Characteristics and resource prospects of tight oil in Ordos Basin, China: Petroleum Research, v. 1, no. 1, p. 27–38, doi:10.1016/S2096-2495(17)30028-5.

Yerkes R.F., T. H. McCullon, J. E. Schoellhamer, and J.G. Vadder, 1965, Geology of the Los Angeles Basin California, an introduction: USGS Professional Paper 420-A.

Yin, P., N. Jones, M. Johnson, and S. Wo, 2014, ROZ Potential of Tensleep Sandstone in Bighorn Basin, Wyoming. Presented at 8th Annual Wyoming CO2 Conference, Casper, Wyoming.

Yin, P., S. Wo, M. Johnson, N. Jones, G. Murrell, and D. Mohrbacher, 2012, Residual oil zone potential of Tensleep Sandstone in the Bighorn Basin, Wyoming, in AAPG Annual Convention and Exhibition.

Yin, P., S. Wo, M. Johnson, N. Jones, G. Murrell, D. Mohrbacher, P. Yin, N. Jones, 2012, ROZ Potential of Tensleep Sandstone in Bighorn Basin, Wyoming: Dk, v. 40994, no. 9, p. 1689–1699, doi:10.1017/CBO9781107415324.004.

Zhang, Y., W. Yu, Z. Li, and K. Sepehrnoori, 2018, Simulation study of factors affecting CO2 Huff-n-Puff process in tight oil reservoirs: Journal of Petroleum Science and Engineering, v. 163, p. 264–269, doi:10.1016/J.PETROL.2017.12.075.

Zuppann, C. W., 1993, Complex oolite reservoirs in the Ste. Genevieve Limestone (Mississippian) at Folsomville Field, Warrick County, Indiana: Mississippian oolites and modern analogs, p. 73–89, doi:10.1306/st35571c6.